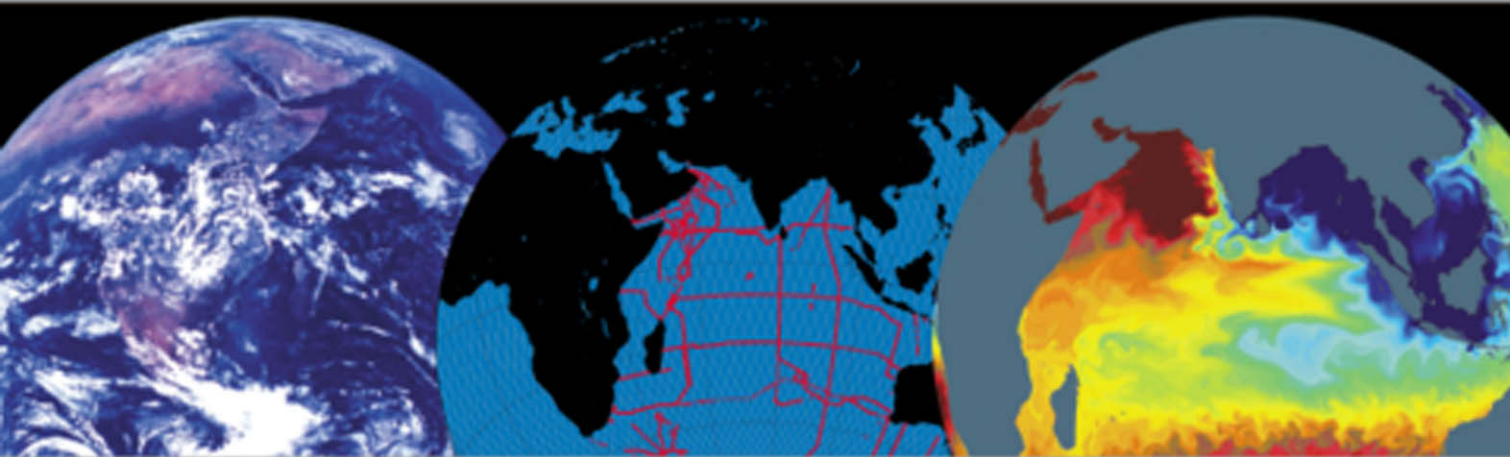




Ocean Circulation & Climate

Observing and Modelling the Global Ocean



Gerold Siedler John Church John Gould



INTERNATIONAL GEOPHYSICS SERIES. VOLUME 77



Ocean Circulation and Climate

Observing and Modelling the Global Ocean

This is Volume 77 in the
INTERNATIONAL GEOPHYSICS SERIES
A series of monographs and textbooks
Edited by RENATA DMOWSKA, JAMES R. HOLTON and H. THOMAS ROSSBY

A complete list of books in this series appears at the end of this volume.

Ocean Circulation and Climate

Observing and Modelling the Global Ocean

Edited by

Gerold Siedler

Institut für Meereskunde

Universität Kiel

Kiel, Germany

and

Instituto Canario de Ciencias Marinas

Telde, Spain

John Church

Antarctic CRC

and

CSIRO Marine Research

Hobart, Australia

John Gould

Southampton Oceanography Centre

Southampton, UK



ACADEMIC PRESS

A Harcourt Science and Technology Company

San Diego San Francisco New York Boston
London Sydney Tokyo

This book is printed on acid-free paper.

Copyright © 2001 by ACADEMIC PRESS

All Rights Reserved.

No part of this publication may be reproduced or transmitted in any form or by any means, electronic or mechanical, including photocopying, recording, or any information storage and retrieval system, without permission in writing from the publisher.

Explicit permission from Academic Press is not required to reproduce a maximum of two figures or tables from an Academic Press chapter in another scientific or research publication provided that the material has not been credited to another source and that full credit to the Academic Press chapter is given.

Academic Press

A Harcourt Science and Technology Company

Harcourt Place, 32 Jamestown Road, London NW1 7BY, UK

<http://www.academicpress.com>

Academic Press

A Harcourt Science and Technology Company

525 B Street, Suite 1900, San Diego, California 92101-4495, USA

<http://www.academicpress.com>

ISBN 0-12-641351-7

Library of Congress Catalog Number: 00-106870

A catalogue record for this book is available from the British Library

Typeset by Newgen Imaging Systems (P) Ltd, Chennai, India
Printed and bound in Spain by Grafos SA Arte Sobre Papel, Barcelona

01 02 03 04 05 06 GF 9 8 7 6 5 4 3 2 1

Contents

| | |
|----------------|-------|
| Contributors | xiii |
| Foreword | xvii |
| Preface | xviii |
| Acknowledgment | xx |

Section 1: The Ocean and Climate

Section 1 plates appear between pages 44 and 45

| | |
|---|-----------|
| 1.1 Climate and Oceans | 3 |
| <i>Hartmut Grassl</i> | |
| 1.1.1 WOCE and the World Climate Research Programme | 3 |
| 1.1.2 The scientific approach to the complex climate system | 4 |
| 1.1.3 Ocean–atmosphere interaction and climate | 5 |
| 1.1.4 Rapid changes related to the oceans | 6 |
| 1.1.5 Cryosphere and the oceans | 7 |
| 1.1.6 Anthropogenic climate change and the oceans | 7 |
| 1.1.7 Future climate research and ocean observing systems | 8 |
| 1.2 Ocean Processes and Climate Phenomena | 11 |
| <i>Allyn Clarke, John Church and John Gould</i> | |
| 1.2.1 A global perspective | 11 |
| 1.2.2 Air–sea fluxes | 12 |
| 1.2.3 Ocean storage of heat and fresh water | 17 |
| 1.2.4 Ocean circulation | 17 |
| 1.2.5 Ocean transport of heat, fresh water and carbon | 23 |
| 1.2.6 Climatic and oceanic variability | 24 |
| 1.2.7 Impacts of ocean climate | 27 |
| 1.2.8 Conclusion | 30 |
| 1.3 The Origins, Development and Conduct of WOCE | 31 |
| <i>B.J. Thompson, J. Crease and John Gould</i> | |
| 1.3.1 Introduction | 31 |
| 1.3.2 Large-scale oceanography in the 1960s and 1970s | 31 |
| 1.3.3 Ocean research and climate | 32 |
| 1.3.4 Implementation of WOCE (SSG initiatives) | 36 |
| 1.3.5 Implementation and oversight | 41 |
| 1.3.6 Was WOCE a success and what is its legacy? | 43 |

Section 2: Observations and Models

Section 2 plates appear between pages 76 and 77

| | |
|--|-----------|
| 2.1 Global Problems and Global Observations | 47 |
| <i>Carl Wunsch</i> | |
| 2.1.1 Different views of the ocean | 47 |
| 2.1.2 The origins of WOCE | 48 |
| 2.1.3 What do we know? | 51 |
| 2.1.4 The need for global-scale observations | 52 |
| 2.1.5 Where do we go from here? | 56 |

| | | |
|------------|--|-----------|
| 2.2 | High-Resolution Modelling of the Thermohaline and Wind-Driven Circulation | 59 |
| | <i>Claus W. Böning and Albert J. Semtner</i> | |
| 2.2.1 | The improving realism of ocean models | 59 |
| 2.2.2 | Historical perspective | 60 |
| 2.2.3 | Basic model design considerations: equilibrium versus non-equilibrium solutions | 62 |
| 2.2.4 | Examples of model behaviour in different dynamical regimes | 64 |
| 2.2.5 | Concluding remarks | 77 |
| 2.3 | Coupled Ocean–Atmosphere Models | 79 |
| | <i>Richard A. Wood and Frank O. Bryan</i> | |
| 2.3.1 | Why coupled models? | 79 |
| 2.3.2 | Formulation of coupled models | 79 |
| 2.3.3 | Model drift and flux adjustment | 84 |
| 2.3.4 | Initialization of coupled models | 86 |
| 2.3.5 | Coupled model simulation of present and past climates | 87 |
| 2.3.6 | Coupled model simulation of future climates | 93 |
| 2.3.7 | Climate models, WOCE and future observations | 94 |
| 2.3.8 | Summary and future developments | 95 |

Section 3: New Ways of Observing the Ocean

Section 3 plates appear between pages 172 and 173

| | | |
|------------|---|------------|
| 3.1 | Shipboard Observations during WOCE | 99 |
| | <i>B. A. King, E. Firing and T. M. Joyce</i> | |
| 3.1.1 | The role of hydrographic measurements | 99 |
| 3.1.2 | CTD and sample measurements | 102 |
| 3.1.3 | Current measurements in the shipboard hydrographic programme | 111 |
| 3.1.4 | Shipboard meteorology | 120 |
| 3.1.5 | Summary and conclusions | 121 |
| 3.2 | Subsurface Lagrangian Observations during the 1990s | 123 |
| | <i>Russ E. Davis and Walter Zenk</i> | |
| 3.2.1 | Determining currents in the ocean | 123 |
| 3.2.2 | Historical aspects: Stommel's vision to the WOCE Float Programme | 123 |
| 3.2.3 | The WOCE Float Programme | 127 |
| 3.2.4 | WOCE float observations | 129 |
| 3.2.5 | The future | 137 |
| 3.3 | Ocean Circulation and Variability from Satellite Altimetry | 141 |
| | <i>Lee-Lueng Fu</i> | |
| 3.3.1 | Altimeter observations | 141 |
| 3.3.2 | The ocean general circulation | 143 |
| 3.3.3 | Large-scale sea-level variability | 148 |
| 3.3.4 | Currents and eddies | 162 |
| 3.3.5 | Concluding discussions | 170 |

| | | |
|------------|--|------------|
| 3.4 | Air–Sea Fluxes from Satellite Data | 173 |
| | <i>W. Timothy Liu and Kristina B. Katsaros</i> | |
| 3.4.1 | Forcing the ocean | 173 |
| 3.4.2 | Bulk parameterization | 173 |
| 3.4.3 | Wind forcing | 174 |
| 3.4.4 | Thermal forcing | 177 |
| 3.4.5 | Hydrologic forcing | 179 |
| 3.4.6 | Future prospects | 179 |
| 3.5 | Developing the WOCE Global Data System | 181 |
| | <i>Eric J. Lindstrom and David M. Legler</i> | |
| 3.5.1 | Organization and planning for WOCE data systems | 181 |
| 3.5.2 | Elements of the WOCE Data System | 185 |
| 3.5.3 | The WOCE Global Data Set and future developments | 189 |

Section 4: The Global Flow Field

Section 4 plates appear between pages 300 and 301

| | | |
|------------|--|------------|
| 4.1 | The World Ocean Surface Circulation | 193 |
| | <i>Peter Niiler</i> | |
| 4.1.1 | Background | 193 |
| 4.1.2 | Methodology | 195 |
| 4.1.3 | The global mean velocity and velocity variance | 198 |
| 4.1.4 | The wind-driven Ekman currents | 201 |
| 4.1.5 | Future global circulation observations | 203 |
| 4.2 | The Interior Circulation of the Ocean | 205 |
| | <i>D. J. Webb and N. Sugino</i> | |
| 4.2.1 | Processes in the ocean interior | 205 |
| 4.2.2 | Observational evidence | 206 |
| 4.2.3 | Theory of gyre-scale circulation | 209 |
| 4.2.4 | The abyssal circulation | 211 |
| 4.2.5 | Conclusions | 213 |
| 4.3 | The Tropical Ocean Circulation | 215 |
| | <i>J. S. Godfrey, G. C. Johnson, M. J. McPhaden, G. Reverdin and Susan E. Wijffels</i> | |
| 4.3.1 | Flow and water mass transformation patterns | 215 |
| 4.3.2 | Equatorial phenomena in the Pacific Ocean | 216 |
| 4.3.3 | Equatorial Atlantic | 226 |
| 4.3.4 | Near-equatorial circulation in the Indian Ocean | 233 |
| 4.3.5 | Overall conclusions | 245 |
| 4.4 | Tropical–Extratropical Oceanic Exchange Pathways | 247 |
| | <i>Zhengyu Liu and S. G. H. Philander</i> | |
| 4.4.1 | The role of diffusion and advection | 247 |
| 4.4.2 | Tropical–subtropical exchanges of thermocline waters | 248 |
| 4.4.3 | Tropical–subpolar exchange of Intermediate Waters | 252 |
| 4.4.4 | Summary and further issues | 254 |

| | | |
|------------|--|------------|
| 4.5 | Quantification of the Deep Circulation | 259 |
| | <i>Nelson G. Hogg</i> | |
| 4.5.1 | Deep circulation in the framework of WOCE | 259 |
| 4.5.2 | Deep Western Boundary Currents | 260 |
| 4.5.3 | The interior: The Deep Basin Experiment | 266 |
| 4.5.4 | Summary | 269 |
| 4.6 | The Antarctic Circumpolar Current System | 271 |
| | <i>Stephen R. Rintoul, Chris W. Hughes and Dirk Olbers</i> | |
| 4.6.1 | Flow in the zonally unbounded ocean | 271 |
| 4.6.2 | Observations of the Antarctic Circumpolar Current | 274 |
| 4.6.3 | Dynamics of the ACC | 280 |
| 4.6.4 | Water mass formation and conversion | 291 |
| 4.6.5 | The Southern Ocean and the global overturning circulations | 296 |
| 4.6.6 | Conclusions | 300 |
| 4.7 | Interocean Exchange | 303 |
| | <i>Arnold L. Gordon</i> | |
| 4.7.1 | Interocean links | 303 |
| 4.7.2 | Bering Strait | 306 |
| 4.7.3 | Indonesian Seas | 307 |
| 4.7.4 | The Agulhas Retroflection | 310 |
| 4.7.5 | Discussion | 313 |

Section 5: Formation and Transport of Water Masses

Section 5 plates appear between pages 428 and 429

| | | |
|------------|--|------------|
| 5.1 | Ocean Surface Water Mass Transformation | 317 |
| | <i>William G. Large and A.J. George Nurser</i> | |
| 5.1.1 | The problem | 317 |
| 5.1.2 | Theory of surface water mass transformation | 318 |
| 5.1.3 | Ocean surface temperature, salinity and density | 321 |
| 5.1.4 | Surface fluxes of heat, fresh water and density | 326 |
| 5.1.5 | Surface water mass transformation and formation | 332 |
| 5.1.6 | Summary | 335 |
| 5.2 | Mixing and Stirring in the Ocean Interior | 337 |
| | <i>John M. Toole and Trevor J. McDougall</i> | |
| 5.2.1 | Scales of mixing and stirring | 337 |
| 5.2.2 | Background | 338 |
| 5.2.3 | The Temporal-Residual-Mean circulation | 340 |
| 5.2.4 | Lateral dispersion between the mesoscale and the microscale | 345 |
| 5.2.5 | Diapycnal mixing in and above the main thermocline | 346 |
| 5.2.6 | Mixing in the abyss | 352 |
| 5.2.7 | Discussion | 354 |
| 5.3 | Subduction | 357 |
| | <i>James F. Price</i> | |
| 5.3.1 | A little of the background on oceanic subduction | 357 |
| 5.3.2 | Surface-layer dynamics and thermodynamics of the subduction process | 360 |
| 5.3.3 | Development of steady, continuous models: Application to numerical model analysis and observations | 361 |
| 5.3.4 | Transient response of the thermocline to decadal variability | 365 |
| 5.3.5 | Summary and outlook | 370 |

| | |
|---|------------|
| 5.4 Mode Waters | 373 |
| <i>Kimio Hanawa and Lynne D. Talley</i> | |
| 5.4.1 Ventilation and mode water generation | 373 |
| 5.4.2 Definition, detection and general characteristics of mode waters | 374 |
| 5.4.3 Geographical distribution of mixed-layer depth and mode waters in the world's oceans | 376 |
| 5.4.4 Temporal variability of mode water properties and distribution | 384 |
| 5.4.5 Summary | 386 |
| 5.5 Deep Convection | 387 |
| <i>John Lazier, Robert Pickart and Peter Rhines</i> | |
| 5.5.1 Convection and spreading | 387 |
| 5.5.2 Plumes – the mixing agent | 391 |
| 5.5.3 Temperature and salinity variability | 393 |
| 5.5.4 Restratification | 396 |
| 5.5.5 Summary and discussion | 398 |
| 5.6 The Dense Northern Overflows | 401 |
| <i>Peter M. Saunders</i> | |
| 5.6.1 The sources | 401 |
| 5.6.2 Overflow paths | 402 |
| 5.6.3 Observed transport means and variability | 404 |
| 5.6.4 Processes in the overflows | 411 |
| 5.6.5 Analytical models of the overflow | 412 |
| 5.6.6 Numerical models of the overflow | 414 |
| 5.6.7 Overflow variability | 416 |
| 5.6.8 What have we learnt in WOCE? | 416 |
| 5.7 Mediterranean Water and Global Circulation | 419 |
| <i>Julio Candela</i> | |
| 5.7.1 Marginal seas | 419 |
| 5.7.2 Formation of Mediterranean Water | 421 |
| 5.7.3 Outflow of Mediterranean Water at the Strait of Gibraltar | 422 |
| 5.7.4 The effect of Mediterranean Water outflow on the circulation of the North Atlantic and the World Oceans | 427 |
| 5.8 Transformation and Age of Water Masses | 431 |
| <i>P. Schlosser, J. L. Bullister, R. Fine, W. J. Jenkins, R. Key, J. Lupton, W. Roether and W. M. Smethie, Jr</i> | |
| 5.8.1 Background | 431 |
| 5.8.2 Tracer methodology and techniques | 432 |
| 5.8.3 Exemplary results | 433 |
| 5.8.4 Outlook | 450 |

Section 6: Large-Scale Ocean Transports

Section 6 plates appear between pages 492 and 493

| | |
|--|------------|
| 6.1 Ocean Heat Transport | 455 |
| <i>Harry L. Bryden and Shiro Imawaki</i> | |
| 6.1.1 The global heat balance | 455 |
| 6.1.2 Bulk formula estimates of ocean heat transport | 456 |
| 6.1.3 Residual method estimates of ocean heat transport | 458 |
| 6.1.4 Direct estimates of ocean heat transport | 459 |
| 6.1.5 Discussion | 466 |
| 6.1.6 Challenges | 470 |
| 6.1.7 Summary | 473 |
| 6.1.8 Outlook for direct estimates of ocean heat transport | 474 |

| | | |
|------------|--|------------|
| 6.2 | Ocean Transport of Fresh Water | 475 |
| | <i>Susan E. Wijffels</i> | |
| 6.2.1 | The importance of freshwater transport | 475 |
| 6.2.2 | Indirect estimates of oceanic freshwater transport | 475 |
| 6.2.3 | Impacts of uncertainties on model development | 476 |
| 6.2.4 | Direct ocean estimates of freshwater transport | 478 |
| 6.2.5 | Comparison of direct and indirect flux estimates | 483 |
| 6.2.6 | Mechanisms of oceanic freshwater transport | 486 |
| 6.2.7 | Global budgets | 487 |
| 6.2.8 | Summary | 488 |
| 6.3 | Storage and Transport of Excess CO₂ in the Oceans: The JGOFS/WOCE Global CO₂ Survey | 489 |
| | <i>Douglas W. R. Wallace</i> | |
| 6.3.1 | Introduction | 489 |
| 6.3.2 | Background | 489 |
| 6.3.3 | The JGOFS/WOCE Global CO ₂ Survey | 495 |
| 6.3.4 | Synthesis of Global CO ₂ Survey data: Review | 503 |
| 6.3.5 | Conclusions and outlook | 520 |

Section 7: Insights for the Future

Section 7 plates appear between pages 588 and 589

| | | |
|------------|---|------------|
| 7.1 | Towards a WOCE Synthesis | 525 |
| | <i>Lynne D. Talley, Detlef Stammer and Ichiro Fukumori</i> | |
| 7.1.1 | Exploiting the WOCE data set | 525 |
| 7.1.2 | Data-based analyses | 526 |
| 7.1.3 | Model evaluation and development | 535 |
| 7.1.4 | Ocean state estimation | 535 |
| 7.1.5 | Summary and outlook | 542 |
| 7.2 | Numerical Ocean Circulation Modelling: Present Status and Future Directions | 547 |
| | <i>J. Willebrand and D. B. Haidvogel</i> | |
| 7.2.1 | Remarks on the history of ocean modelling | 547 |
| 7.2.2 | Space–time scales of ocean processes and models | 548 |
| 7.2.3 | Modelling issues | 549 |
| 7.2.4 | Atmospheric forcing and coupling | 553 |
| 7.2.5 | Organization of model development | 554 |
| 7.2.6 | Concluding remarks | 556 |
| 7.3 | The World during WOCE | 557 |
| | <i>Bob Dickson, Jim Hurrell, Nathan Bindoff, Annie Wong, Brian Arbic, Breck Owens, Shiro Imawaki and Igor Yashayaev</i> | |
| 7.3.1 | Assessing the representativeness of the WOCE data set | 557 |
| 7.3.2 | The state of the atmosphere during WOCE | 558 |
| 7.3.3 | The analysis of decadal change in intermediate water masses of the World Ocean | 563 |
| 7.3.4 | Climatic warming of Atlantic Intermediate Waters | 565 |
| 7.3.5 | Spin-up of the North Atlantic gyre circulation | 567 |
| 7.3.6 | Altered patterns of exchange in Nordic Seas | 569 |
| 7.3.7 | System-wide changes in the Arctic Ocean | 571 |
| 7.3.8 | Interdecadal variability of Kuroshio transport | 573 |
| 7.3.9 | Evidence of water mass changes in the Pacific and Indian Oceans | 576 |
| 7.3.10 | Summary and Conclusions | 580 |

| | |
|---|------------|
| 7.4 Ocean and Climate Prediction – the WOCE Legacy | 585 |
| <i>Neville Smith</i> | |
| 7.4.1 The long-term context | 585 |
| 7.4.2 Building from WOCE | 588 |
| 7.4.3 WOCE observations | 589 |
| 7.4.4 WOCE and climate prediction | 592 |
| 7.4.5 The mean state and long-term change | 595 |
| 7.4.6 Ocean variability and prediction: GODAE | 597 |
| 7.4.7 Institutionalizing the benefits of WOCE | 600 |
| 7.4.8 Conclusions | 601 |
| References | 603 |
| Acronyms, abbreviations and terms | 686 |
| Index | 693 |

This Page Intentionally Left Blank

Contributors

Arbic Brian

(arbic@mit.edu)

Massachusetts Institute of Technology, Cambridge, MA 02139, USA, and Woods Hole Oceanographic Institution, Woods Hole, MA 02543, USA

Bindoff Nathan

(n.bindoff@utas.edu.au)

Antarctic CRC, GPO Box 252-80, Hobart, Tasmania 7001, Australia

Böning C. W.

(cboening@ifm.uni-kiel.de)

Institut für Meereskunde, Universität Kiel, 24105 Kiel, Germany

Bryan Frank O.

(bryan@ncar.ucar.edu)

National Center for Atmospheric Research, PO Box 3000, Boulder, CO 80307, USA

Bryden Harry L.

(harry.bryden@soc.soton.ac.uk)

Southampton Oceanography Centre, Empress Dock, Southampton SO14 3ZH, UK

Bullister John

(bullister@pmel.noaa.gov)

NOAA/PMEL, R/E/PM Bin C15700, 7600 Sand Point Way NE Building 3, Seattle, WA 98115-0070, USA

Candela Julio

(jcandela@cicese.mx)

Departamento de Oceanografía Física, Centro Investigación Científica y de Educación Superior de Ensenada (CICESE), Km. 107 Carretera Tijuana-Ensenada, 22860 Ensenada B. Cfa., Mexico

Church John A.

(john.church@marine.csiro.au)

Antarctic CRC and CSIRO Marine Research, GPO Box 1538, Hobart, Tasmania 7001, Australia

Clarke Allyn

(ClarkeA@mar.dfo-mpo.gc.ca)

Fisheries and Oceans Canada, Bedford Institute of Oceanography, Dartmouth NS, B2Y 4A2, Canada

Crease J.

(jimc@diu.cms.udel.edu)

College of Marine Studies, University of Delaware, Lewes, DE 19958-1298, USA

Davis Russ E.

(rdavis@ucsd.edu)

Scripps Institution of Oceanography, La Jolla, CA 92093-0230, USA

Dickson Bob

(r.r.dickson@cefas.co.uk)

Centre for Environment, Fisheries and Aquaculture Science, Lowestoft, Suffolk NR33 0HT, UK

Fine R.

(rfine@rsmas.miami.edu)

RSMAS, University of Miami, Miami, FL 33149-1098, USA

Firing E.

(efiring@soest.hawaii.edu)

JIMAR, University of Hawaii at Manoa, Honolulu, HI 96822, USA

Fu Lee-Lueng

(llf@pacific.jpl.nasa.gov)

Jet Propulsion Laboratory 300-323, 4800 Oak Grove Drive, Pasadena, CA 91109-8099, USA

Fukumori Ichiro

(if@pacific.jpl.nasa.gov)

Jet Propulsion Laboratory, California Institute of Technology, Pasadena, CA 91109-8099, USA

Godfrey J. S.

(godfrey@ml.csiro.au)

CSIRO Marine Research, Hobart, Tasmania 7001, Australia

- Gordon Arnold L.**
(agordon@ldeo.columbia.edu)
Lamont-Doherty Earth Observatory of Columbia University, Palisades, NY 10964, USA
- Gould John**
(john.gould@soc.soton.ac.uk)
Southampton Oceanography Centre, Empress Dock, Southampton SO14 3ZH, UK
- Grassl Hartmut**
(grassl@dkrz.de)
Max-Planck-Institut für Meteorologie, Bundesstr. 55, D-20146 Hamburg, Germany
- Haidvogel D. B.**
(dale@ahab.rutgers.edu)
Department of Marine & Coastal Sciences, Rutgers University, New Brunswick, NJ 08903-0231, USA
- Hanawa Kimio**
(hanawa@pol.geophys.tohoku.ac.jp)
Department of Geophysics, Graduate School of Science, Tohoku University, Aoba, Sendai 980-8578, Japan
- Hogg Nelson G.**
(nhogg@whoi.edu)
MS 21, Woods Hole Oceanographic Institution, Woods Hole, MA 02543, USA
- Hughes Chris W.**
(c.hughes@ccms.ac.uk)
Proudman Oceanographic Laboratory, Bidston Observatory, Bidston Hill, Prenton, CH43 7RA, UK
- Hurrell Jim**
(jhurrell@ucar.edu)
Climate and Global Dynamics, National Center for Atmospheric Research, PO Box 3000, Boulder, CO 80307-3000, USA
- Imawaki Shiro**
(imawaki@riam.kyushu-u.ac.jp)
Research Institute for Applied Mechanics, Kyushu University, Kasuga, Fukuoka 816-8580, Japan
- Jenkins W. J.**
(wjj@soc.soton.ac.uk)
Southampton Oceanography Centre, Empress Dock, Southampton SO14 3ZH, UK
- Johnson G. C.**
(gjohnson@pmel.noaa.gov)
NOAA/Pacific Marine Environmental Laboratory, Seattle, WA 98115-0070, USA
- Joyce T. M.**
(tjoyce@whoi.edu)
MS 21, Woods Hole Oceanographic Institution, Woods Hole, MA 02543, USA
- Katsaros Kristina B.**
(katsaros@aoml.noaa.gov)
NOAA/Atlantic Oceanographic and Meteorological Laboratory, 4301 Rickenbacker Causeway, Miami, FL 33149, USA
- Key R.**
(key@geo.princeton.edu)
Princeton University, Guyot Hall, Princeton, NJ 08544-1003, USA
- King B. A.**
(brian.king@soc.soton.ac.uk)
Southampton Oceanography Centre, Empress Dock, Southampton SO14 3ZH, UK
- Large William G.**
(wily@ucar.edu)
National Center for Atmospheric Research, Boulder, CO 80307, USA
- Lazier John**
(lazierj@mar.dfo-mpo.gc.ca)
Fisheries and Oceans Canada, Bedford Institute of Oceanography, Dartmouth NS, Canada B2Y 4A2
- Legler David M.**
(legler@usclivar.org)
COAPS, Florida State University, Tallahassee, FL 32306-2840, USA, presently at US CLIVAR Office, 400 Virginia Avenue, Suite 750, Washington, DC 20024, USA
- Lindstrom Eric J.**
(elindstrom@mail.hq.nasa.gov)
NASA Headquarterns Code YS, Washington, DC 20546, USA
- Liu W. Timothy**
(liu@pacific.jpl.nasa.gov)
Jet Propulsion Laboratory 300-323, 4800 Oak Grove Drive, Pasadena, CA 91109-8099, USA

Liu Zhengyu
(zliu3@facstaff.wisc.edu)
Center for Climatic Research and Department of
Atmospheric and Oceanic Sciences,
University of Wisconsin-Madison,
1225 W. Dayton Street, Madison,
WI 53706-1695, USA

Lupton J.
(lupton@pmel.noaa.gov)
NOAA/PMEL, Hatfield Marine Science Center,
Newport, OR 97365, USA

McDougall Trevor J.
(Trevor.McDougall@marine.csiro.au)
CSIRO Marine Research, Hobart, Tasmania 7001,
Australia

McPhaden M. J.
(mcphaden@pmel.noaa.gov)
NOAA/Pacific Marine Environmental
Laboratory, Seattle, WA 98115-0070,
USA

Niiler Peter
(pniiler@ucsd.edu)
Physical Oceanography Research Division,
Scripps Institution of Oceanography, La Jolla,
CA 92093-0213, USA

Nurser A. J. George
(george.nurser@soc.soton.ac.uk)
Southampton Oceanography Centre, Empress
Dock, Southampton SO14 3ZH, UK

Olbers Dirk
(dolbers@awi-bremerhaven.de)
Alfred-Wegener-Institut für Polar- und
Meeresforschung, Postfach 12 0161,
D27515 Bremerhaven, Germany

Owens Breck
(bowens@whoi.edu)
MS21, Woods Hole Oceanographic Institution,
Woods Hole, MA 02543, USA

Philander S. G. H.
(gphlder@splash.princeton.edu)
Department of Geosciences, Princeton University,
Princeton, NJ 08540, USA

Pickart Robert
(rpickart@whoi.edu)
MS21, Woods Hole Oceanographic Institution,
Woods Hole, MA 02543, USA

Price James F.
(jprice@whoi.edu)
MS21, Woods Hole Oceanographic Institution,
Woods Hole, MA 02543, USA

Reverdin G.
(reverdin@lodyc.jussieu.fr)
GRGS, 14 Avenue Edouard Belin, 31055 Toulouse
Cedex, France

Rhines Peter
(prhines@ocean.washington.edu)
University of Washington, Seattle, WA 98195, USA

Rintoul Stephen R.
(steve.rintoul@marine.csiro.au)
CSIRO Marine Research, Hobart, Tasmania 7001,
Australia, and Antarctic CRC, Hobart,
Tasmania 7001, Australia

Roether W.
(wroether@physik.uni-bremen.de)
Abteilung Tracer-Ozeanographie, Institut für
Umweltphysik, FB1, Universität Bremen, Postfach
33 04 40, 28334 Bremen, Germany

Saunders Peter M.
(peter.saunders@soc.soton.ac.uk)
Southampton Oceanography Centre, Empress
Dock, Southampton SO14 3ZH, UK

Schlosser P.
(peters@ldeo.columbia.edu)
Lamont-Doherty Earth Observatory, Columbia
University, Palisades, NY 10964-8000, USA

Sembtner A. J.
(sbert@oc.nps.navy.mil)
Naval Postgraduate School, Monterey,
CA 93943-5000, USA

Siedler Gerold
(gsiedler@ifm.uni-kiel.de)
Institut für Meereskunde, Universität Kiel, 24105
Kiel, Germany, and Instituto Canario de Ciencias
Marinas, 35200 Telde, Spain

Smethie Jr W. M.
(bsmeth@ldeo.columbia.edu)
Lamont-Doherty Earth Observatory, Columbia
University, Palisades, NY 10964-8000, USA

Smith Neville
(nrs@bom.gov.au)
Bureau of Meteorology Research Centre, Box
1289K, Melbourne, Victoria 3001, Australia

- Stammer Detlef**
(dstammer@ucsd.edu)
Physical Oceanography Research Division,
Scripps Institution of Oceanography, La Jolla,
CA 92093-0230, USA
- Suginohara Nobuo**
(nobuo@ccsr.u-tokyo.ac.jp)
Center for Climate System Research,
University of Tokyo, Tokyo 153-8904,
Japan
- Talley Lynne D.**
(ltalley@ucsd.edu)
Scripps Institution of Oceanography,
University of California San Diego, La Jolla,
CA 92093-0230, USA
- Thompson B.J.**
(thompson@diu.cms.udel.edu)
College of Marine Studies,
University of Delaware, Lewes,
DE 19958-1298, USA
- Toole John M.**
(jtoole@whoi.edu)
Department of Physical Oceanography,
MS 21, Woods Hole Oceanographic
Institution, Woods Hole, MA 02543, USA
- Wallace Douglas W. R.**
(dwallace@ifm.uni-kiel.de)
Institut für Meereskunde, Universität Kiel,
24105 Kiel, Germany
- Webb D. J.**
(david.webb@soc.soton.ac.uk)
Southampton Oceanography Centre, Empress
Dock, Southampton SO14 3ZH, UK
- Wijffels Susan E.**
(wijffels@marine.csiro.au)
CSIRO Marine Research, GPO Box 1538,
Hobart, Tasmania 7001, Australia
- Willebrand J.**
(jwillebrand@ifm.uni-kiel.de)
Institut für Meereskunde, Universität Kiel,
24105 Kiel, Germany
- Wong Annie**
(awong@pmel.noaa.gov)
Joint Institute for the Study of the Atmosphere
and Ocean (JISAO), University of
Washington, Seattle, WA 98195, USA
- Wood Richard A.**
(rwood@meto.gov.uk)
Oceans Application Branch, Hadley Centre
for Climate Prediction & Research,
Met Office, Bracknell RG12 2SY, UK
- Wunsch Carl**
(cwunsch@pond.mit.edu)
Massachusetts Institute of Technology,
Department of Earth, Atmosphere &
Planetary Sciences, Cambridge,
MA 02139-4307, USA
- Yashayaev Igor**
(yashayaev@mar.dfo.mpo.gc.ca)
Ocean Sciences Division, Bedford Institute of
Oceanography, PO Box 1006, Dartmouth,
NS B2Y 4A2, Canada
- Zenk Walter**
(wzenk@ifm.uni-kiel.de)
Institut für Meereskunde, Universität Kiel,
24105 Kiel, Germany

Foreword

I am proud to join with my colleagues in celebrating the World Ocean Circulation Experiment (WOCE), one of the largest and most successful ocean endeavours ever undertaken by the international community. In 1988 I was Chairman of the WOCE Scientific Steering Group at the time of the International WOCE Conference in Paris. Scientific discussions throughout the 1980s had resulted in first a WOCE Science Plan and finally an Implementation Plan. At the International Conference, chaired by Gerold Siedler, countries made commitments to implementation.

Now, some 13 years later, it gives me great pleasure to introduce this book. It encapsulates the enormous strides that have been made during the 1990s in understanding ocean circulation and its role in climate. This progress would not have been possible without the advances in technology (satellite and *in-situ* measurement, global high-accuracy navigation, supercomputing, the Internet) that we now take for granted. But WOCE provided the stimulus and the framework for addressing the oceans' role in climate on a global scale.

The obvious success of WOCE provides an object lesson in selfless international collaboration. Almost all WOCE data are already publicly available and will provide a unique resource for researchers to use for many years to come. WOCE also provides a sound scientific and technological foundation on which to build future research and operational ocean activities.

Finally, this foreword should pay tribute both to the small group of far-sighted individuals who embarked on this project and to the many others who over the years have guided WOCE to the success it has now achieved.

D. James Baker

*Under Secretary for Oceans and Atmosphere
Administrator, National Oceanic and Atmospheric Administration
US Department of Commerce
Washington, DC, USA*

October 2000

Preface

As a moderator and initiator of climate variability and change, and as an economic resource, the global ocean is vital to life on earth. Quantifying the ocean's role in climate has become a matter of urgency as society attempts to gauge how growing greenhouse gas concentrations will affect climate. The intergovernmental agreements of the Kyoto Protocol of 1997 indicate that policy-makers are aware of the need to act on the basis of climate projections reported by the Intergovernmental Panel on Climate Change. Determining how to improve, extend and use these projections is an enormous challenge.

The World Ocean Circulation Experiment (WOCE) is at the heart of this challenge. It predates the World Climate Research Programme, of which it is now a part. WOCE was the brainchild of a small group of scientists who, in the early 1980s, saw the prospects for instituting the first truly global ocean study, using new satellite technology and global ocean models made possible by increasing computer power. WOCE also needed unstinting international collaboration to collect a previously unobtainable *in-situ* global data set for validating and improving ocean circulation models. The satellite remote sensing, navigation and computer advances in the 1990s, coupled with developing electronic communication and the World Wide Web, made such an enterprise possible. In the process, WOCE revolutionized oceanography.

From 1990, ship-based physical and chemical measurements and satellite remote sensing together resulted in a data set of unprecedented scope and precision. New observational techniques were also developed, maturing to form the basis of an operational observing system (Argo) for the interior of the global ocean. WOCE has resulted in a much closer interaction of observers and modellers. It also gave us the first generation of global data-assimilating models, which are immensely more powerful than the techniques previously available. The new data set and techniques are a key ingredient in decadal climate prediction and the results of WOCE have reinforced the evidence that the ocean plays a key role in the earth's climate.

Ocean Circulation and Climate – Observing and Modelling the Global Ocean presents the state of knowledge of the ocean and its role in climate change at the end of the twentieth century. The idea for the book originated from the 'Ocean Circulation and Climate' conference held in Halifax, Canada, in 1998. The conference marked the end of the observational phase of WOCE and the beginning of the Analysis, Interpretation, Modelling and Synthesis (AIMS) phase that is tackling many aspects of the ocean's role in climate. After the conference, we approached the plenary speakers and other distinguished scientists to contribute to this book. We were delighted that so many agreed to join us in this project.

The book chapters draw mainly from recent WOCE results, and naturally the contributors identify a number of outstanding questions and uncertainties. However, this book is not a final summary of WOCE's achievements; WOCE researchers continue to publish a steady stream of new results in the refereed literature. Many of these results are based on the exploitation and synthesis of the unique WOCE basin- and global-scale observations and on the latest generation of ocean and climate models.

The Ocean and Climate (Section 1) discusses the importance of the ocean in the climate system, describes the main ocean processes and reviews the history of WOCE. In Observations and Models (Section 2) some fundamental aspects of ocean observations and models are discussed. New Ways in Observing the Ocean (Section 3) introduces the new observational methods and instruments and the challenge of data and information management. The Global Flow Field (Section 4) discusses the state of knowledge of the global oceanic circulation from the surface to the deep ocean and from the Arctic to the tropical and Antarctic regions, as well as interocean

exchanges. The Formation and Transport of Water Masses (Section 5) covers air-sea fluxes leading to the formation of surface water properties, the transport of these water masses into the ocean interior and the impact of ocean stirring and mixing. Large-Scale Ocean Transports (Section 6) describes the air-sea exchange, the storage and horizontal transport of heat, fresh water and carbon. Finally, The Future (Section 7) discusses the prospects for ongoing ocean and climate research and monitoring.

The book is structured to guide the reader through the wide range of WOCE science in a consistent way. Cross-references between contributions have been added, and the book has a comprehensive index and unified reference list. Individual chapters can, however, stand alone. Indeed, where subject matter is duplicated, differences in approach and interpretation are evident. All chapters have been reviewed anonymously by specialists in the field; the editors thank the referees most warmly for their critical advice and guidance.

Our hope is that this book will be read not only by oceanographers, meteorologists and climate scientists, but also by the wider scientific community of researchers, science managers and graduate students.

A book of this size and complexity requires the hard work of many people. Notable among these are Lynne Hardwick and Julie Husin at CSIRO Hobart, Australia; Roberta Boscolo and Jean Haynes in the WOCE International Project Office in Southampton; and Serena Bureau and Gioia Ghezzi of Academic Press.

Above all, this book should be regarded as a tribute to the originators of WOCE and to all the researchers, students and technicians who have transformed that early vision into a reality of which they can all feel justly proud.

Gerold Siedler
Kiel, Germany
and Telde, Spain

John Church
Hobart, Australia

John Gould
Southampton, UK

Acknowledgment

The success of WOCE was dependent upon the collaboration of hundreds of researchers worldwide and the availability of technical and financial support to provide staff, equipment, ship resources, major facilities, satellites and supercomputers. On behalf of the WOCE scientific community, we as editors gratefully acknowledge the contributions from the many funding agencies that provided these resources and supported WOCE's international planning and data management activities.

GS acknowledges the support of the Deutsche Forschungsgemeinschaft and the German Federal Ministry of Research and Technology. JC acknowledges the support of the Australian Antarctic Cooperative Research Centre and CSIRO. This article is a contribution to the CSIRO Climate Change Program. JG acknowledges the UK Natural Environment Research Council for supporting the WOCE International Project Office contribution to this book.

SECTION

1

THE OCEAN AND CLIMATE

Chapter 1.1

CLIMATE AND OCEANS

Hartmut Grassl

3

Chapter 1.2

OCEAN PROCESSES AND CLIMATE PHENOMENA

Allyn Clarke, John Church and John Gould

11

Chapter 1.3

THE ORIGINS, DEVELOPMENT AND CONDUCT OF WOCE

B.J. Thompson, J. Crease and John Gould

31

This Page Intentionally Left Blank

1.1

Climate and Oceans

Hartmut Grassl

1.1.1 WOCE and The World Climate Research Programme

The earth is mainly an ocean planet with 71% of the surface covered by water, including up to 6% coverage by sea ice. In total, perhaps as much as 85% of the earth's surface is covered by either liquid water (oceans, lakes, rivers, wet vegetation) or solid water (snow, land-ice, sea-ice). Therefore, absorption of solar energy, which drives the earth's climate system, and evapotranspiration of water at the surface, are dominated by the oceans. In addition, the global mean values of other energy fluxes, such as sensible and latent heat flux and net long-wave radiation flux, at the surface are predominantly a result of ocean-atmosphere interaction. The heat capacity of only three metres of the ocean corresponds to the heat capacity of the entire atmospheric column above. Thus, even if the horizontal ocean currents were much smaller, climate variability would still be to a large extent an ocean-related phenomenon.

Both the atmosphere and the oceans exhibit a complicated circulation pattern and their interaction determines much of the climate variability on time scales from several hours (e.g. sea breezes) to seasons, years, decades, centuries and millennia. Understanding this variability is the essence of the World Climate Research Programme (WCRP), whose single and demanding goal has been formulated as follows:

To understand and predict, to the extent possible, climate variability and climate change, including human influence on climate.

Only if climate variability is at least partially understood will it be possible to detect and predict

climate change arising from external forcing, be it by earth orbital parameter changes, solar irradiance variations, volcanic eruptions (the latter counted as external forcing despite belonging to the earth system) and/or human activities.

Given the importance of the oceans to climate, it is not surprising to find the first two projects of WCRP, the World Ocean Circulation Experiment (WOCE) and the Tropical Ocean-Global Atmosphere (TOGA) study, were ocean related. Early discussions and the formulation of science plans for WOCE and TOGA were initiated by the Committee on Climate Changes and the Oceans (CCCO; Thompson *et al.*, Chapter 1.3), jointly sponsored by the Scientific Committee for Oceanic Research (SCOR) of the International Council for Scientific Unions (ICSU), and by the Intergovernmental Oceanographic Commission (IOC) of UNESCO. The first decision on WOCE was made in 1978, before WCRP was initiated by WMO and ICSU in 1980. TOGA, which had been stimulated by the 1982-83 El Niño event, the most intense of the twentieth century until that date, was the first formally implemented WCRP project lasting from 1985 to 1994. In 1982, WOCE, focused on building models necessary for predicting climate change, became a central element of WCRP and effectively complemented the atmospheric projects within the broader scope of WCRP. Implementation of the field programme of WOCE commenced formally in 1990, at about the same time IOC became a sponsor of WCRP.

Now, in 2001, we can look back to two very successful projects of WCRP. First, TOGA has made possible physically based predictions of

climate variability on time scales of seasons to a year for those areas affected by the El Niño-Southern Oscillation (ENSO) events. Second, the field phase of WOCE has produced, for the first time, a global three-dimensional view of ocean structure as well as of the trace substance distribution of the global ocean (excluding the Arctic Basin and – due to operational constraints – parts of the Southern Ocean). At the same time there has been a significant improvement in the quality of ocean models and the WOCE data have become the basis for testing the ocean modules of climate (coupled ocean-atmosphere-land surface) models.

This book is devoted to evaluation of ocean circulation as determined from the WOCE (and other) data, to the development of ocean models and to the understanding of the ocean's circulation as a component of the climate system. Therefore I will concentrate on the role of the ocean as a component of the climate system.

1.1.2 The scientific approach to the complex climate system

Complex systems are characterized by their ability to develop transient organized structures when reacting to internal or external forcing as a result of their internal non-linear dynamics. Examples are galaxies, stars, planets, the atmosphere, the ocean, ecosystems, our body and a single cell. The preferred scientific approach to complex systems is via experiments under controlled conditions for simpler subsystems, leading to models that approach reality and thus can be used for practical applications.

In the geosciences, however, where deliberate experiments are impossible, the approach is via long-term, nearly global observations that may lead to a degree of understanding that allows numerical prediction for restricted time scales. The most successful application of this method is deterministic weather forecasting. In principle, weather forecasting can only be successful up to about 2 weeks and, at present, mostly does not incorporate more from the ocean than surface temperature as a starting field for deterministic predictions up to 1 week ahead. The climate system shows some statistical stability in its long-term behaviour despite reacting with deterministic instability to changed initial fields. Thus, climate predictions are probabilistic predictions that go beyond the predictability barrier for deterministic weather forecasts.

Since there were, until recently, no routine observations of large parts of the oceans' interior, the barrier to climate variability predictions on monthly to seasonal time scales could not be surmounted. An exception was the application of very simple empirical rules to certain regions where persistent sea surface temperature anomalies allowed some extrapolation in time. Long-term observations on nearly global scale are needed. The highest priority for seasonal forecasts was for upper ocean observations in areas with especially strong seasonal to interannual variability. This, together with developing coupled ocean-atmosphere models, was exactly the strategy pursued by TOGA scientists. They were able to implement the TOGA observing system, including the Tropical Atmosphere/Ocean (TAO) Array, a set of up to 64 moored buoys across the tropical Pacific, measuring surface meteorological variables and upper ocean structure and expendable bathythermograph measurements from Voluntary Observing Ships (VOS).

This observing system brought the breakthrough to physically based climate anomaly predictions for ENSO-affected areas by using coupled ocean-atmosphere models assimilating near-real-time observations. The success is due to the intrinsic time scales of ocean-atmosphere interaction of up to a year in the Pacific caused by the travel time of equatorial ocean Kelvin and Rossby waves across the Pacific basin.

To understand and predict the full spectrum of climate variability, long-term global ocean observations are required (for a fuller discussion see Wunsch, Chapter 2.1 and Smith, Chapter 7.4). However, prior to WOCE no such system was considered feasible. Thus a major challenge for WOCE was to demonstrate that feasibility. Given the complexity of the oceans and the limited resources available, this required a range of different techniques (observations from research ships and merchant vessels, surface drifters, subsurface floats, moored instruments and, of course, satellites). All of these observing systems required some degree of development.

WOCE's main task was to observe for the first time (largely on a basin-by-basin manner) the three-dimensional structure of the global ocean as the basis for ocean model improvement needed for more reliable climate models. This required a commitment by the research community to the

implementation of an internationally agreed plan, internationally agreed standards and the international management and sharing of data. Significant technical developments achieved during WOCE have now opened the door for an ongoing global ocean observing system. Two of the most significant technical developments are:

- accurate ocean surface topography measurements by satellite sensors, first of all by TOPEX/POSEIDON, but also by ERS-1 and -2 altimeters (Fu, Chapter 3.3);
- development of profiling autonomous Lagrangian floats determining upper ocean structure and mean current on a prescribed pressure surface about every 2 weeks and with typical survival times of about 4 years (Davis and Zenk, Chapter 3.2).

Developing the new technologies and demonstrating the feasibility of a global observing system are only the first steps to building a truly global observing system. Applications like ocean weather forecasting, global seasonal climate variability predictions, better guidance for fisheries, etc., require the operational implementation of a global array of such floats and the continuation of altimeter measurements beyond the endorsed experimental phase. Sustained observations of the ocean interior and its surface have not only been recognized as prerequisites for progress in prediction of climate variability on seasonal time scales, but also for the understanding of decadal to century time-scale climate variability, a major challenge for climate science.

Now that a near-real-time ocean observing system has been shown to be feasible and cost-effective, both CLIVAR (Climate Variability and Predictability study of WCRP) and GODAE (Global Ocean Data Assimilation Experiment) are implementing within the Integrated Global Observing Strategy (IGOS) a pilot project to demonstrate the value of a global float array in combination with satellite altimetry. Besides operational ocean observations for climate research and predictions, we still lack certain types of observations in the atmosphere, namely, the three-dimensional distribution of liquid water and ice, vertical profiles of minor constituents like ozone, and wind profiles in the lower troposphere. Since cloud-radiation interaction is a source of major uncertainty in the response of the climate system

to an external forcing (by the sun or by human activities), I wrote, in 1996, on behalf of the Joint Scientific Committee for WCRP, to the major space agencies, asking for the development of an active sensor combination for the measurement of cloud water and ice. At the same time, I also pointed to the need for a better geoid determination in order to be able to exploit fully ongoing altimeter measurements for oceanography and climate research.

To implement operational observing systems, it is necessary to start first with a research network and to demonstrate the benefit of the network for society as a whole. Only then will the resources for an ongoing operational commitment be provided. Scientists within WCRP are working to repeat these steps for as yet unobserved parts of the climate system, such as the deep ocean, sea-ice thickness, and the isotopic composition of precipitation, river water and snow. However, operational implementation will only follow if it is demonstrated to be a prerequisite for further progress and if cost-effective observational strategies are available or can be developed.

1.1.3 Ocean-atmosphere interaction and climate

The ocean and atmosphere transport on average roughly the same amount of heat from low to high latitudes. However, this is achieved in remarkably different manners. The atmosphere does it mainly by transient eddies in the middle and high latitudes; the ocean does it mainly by boundary currents, large gyres (wind-driven to a large extent) and the vertical overturning of the ocean. Although the sun delivers more energy to the southern hemisphere since we are at present nearest to the sun in January, the northern hemisphere nevertheless contains the thermal equator at all seasons over the Atlantic and the Pacific. In the Atlantic, this is due to the shape of South America and Africa and to the Atlantic transporting – as WOCE studies have made clearer – about 10^{15} W of heat across the equator into the northern hemisphere (Bryden and Imawaki, Chapter 6.1). While the ocean is influenced by the atmosphere through fluxes of momentum, fresh water, incoming solar irradiance (Fig. 1.1.1, see Plate 1.1.1, p. 44) and atmospheric thermal radiation, sea surface temperature is the main parameter influencing the heat

fluxes from the ocean to the atmosphere. The results of these ocean influences are reduced seasonal variation in maritime areas compared with continental regions, weaker meridional gradients over ocean areas and strong longitudinal dependence of yearly average temperature, especially in the northern North Atlantic (Fig. 1.1.2, see Plate 1.1.2, p. 44). Here the deviation from the zonal mean temperature exceeds 10°C off Norway. A major reason for these high temperatures (besides transport of heat from the subtropical Atlantic Ocean) is the high salinity in the northern latitude Atlantic leading to intermittent deep convection events either near to the sea-ice edge (Greenland Sea) or in the open ocean regions such as the Labrador Sea.

Long-term mean ocean–atmosphere interaction is responsible for the mean differences between marine and continental climates. Internal variability of the atmosphere–ocean–cryosphere climate system on all time scales, supplemented by external forcing (volcanic eruptions and solar cycles), produces the observed climate variability. On very long time scales, the forcing by the changed orbit of the earth around the sun (Milankovich cycles) becomes dominant.

We have good statistical descriptions of climate variability, at least for the last few decades, for many places and large continental areas. However, we lack even the basic understanding of the causes for some of the multiyear to decadal time scale ocean-focused phenomena like the Antarctic Circumpolar Wave in the Southern Ocean and the North Atlantic Oscillation. Only the ENSO and the QuasiBiennial Oscillation (QBO) stand out as being partly understood. Since ENSO is the cause of a large part of interannual variability in at least the tropics, the next breakthrough concerning the understanding of climate variability may well be related to mid-latitude variability. As well as ocean–atmosphere interaction, it is likely also to involve land ice–atmosphere, vegetation–atmosphere and sea ice–atmosphere interaction since all these interactions lead to interannual and decadal time scale variability. For example, understanding the variability of monsoons will need cooperation between two WCRP projects – the Climate Variability and Predictability (CLIVAR) study and the Global Energy and Water Cycle Experiment (GEWEX) – in coordinated enhanced observing periods.

1.1.4 Rapid changes related to the oceans

The tendency of the climate system to react strongly and rapidly to minor changes is now well established, both from direct observations and palaeoclimate reconstructions. An example (not related to the ocean) is the Antarctic ozone hole. Less than a billionth of all air molecules, the chlorofluorocarbons (CFCs) and halons, have caused through their chlorine- and bromine-containing decay products, the complete disappearance of the ozone in areas with polar stratospheric clouds (12–20 km height) in the Antarctic during early spring since the mid-1980s. (Ozone acts as a UV-B filter and is the third most important greenhouse gas after water vapour and CO₂.) This has led through mixing with mid-latitude air to the weakening of the strong latitudinal gradient of UV-B radiation. Now the daily UV-B dose reaching the surface during a sunny day in late spring and early summer is sometimes as high in New Zealand and on the Antarctic Peninsula as it is in Darwin, tropical North Australia (Seckmeyer *et al.*, 1995).

Palaeo-evidence on the instability of the global ocean conveyer belt stimulated by increased freshwater input from melting ice sheets into the Atlantic is now abundant (Keigwin *et al.*, 1994). Also model studies (e.g. Rahmstorf and Willebrand, 1995) have suggested that this may happen for comparatively slight changes in the freshwater budget of the Atlantic, north of about 30°S. It is suggested that addition of 0.1 Sverdrup (1 Sverdrup = 10⁶ m³ s⁻¹) of fresh water could completely stop deep convection in the northern North Atlantic and remove the 4°C positive sea surface temperature anomaly (compared with the Eastern Pacific at a latitude of about 50°N). In addition, coupled ocean–atmosphere GCMs (General Circulation Models) run under steadily increasing greenhouse gas concentrations show a spin-down of the strength of the meridional overturning in the Atlantic (e.g. Manabe and Stouffer, 1993) and in the Southern Ocean (Hirst, 1998). It is therefore urgent that the monitoring of the flow over the sills from the Nordic Seas into the North Atlantic and of the oceanic overturning itself, as conducted during WOCE, be continued in order to validate the models' ability to represent adequately realistic large-scale ocean circulation and its variability.

Another potential rapid change related to the ocean would be the disappearance of multiyear sea

ice in the Arctic Basin, since it would alter air-sea fluxes and especially precipitation (snowfall) strongly in high altitudes. This would certainly have a hemispheric impact. Whether the recent decline of the multiyear sea-ice area in the Arctic Basin by 18% from 1978 to 1998 reported by Johannessen *et al.* (1999) is related to a natural recent intensification of the North Atlantic Oscillation or is an effect of anthropogenic climate change is not yet clear. In order to establish reliable data sets on sea-ice thickness (the multiyear sea-ice decline is related to shrinking sea-ice thickness), an extension of the small networks of upward-looking sonars established within WCRP's Arctic Climate System Study (ACSYS), both in the Arctic and in the sea-ice area around Antarctica, is required. The free access to earlier classified data from submarines in combination with these networks would be a validation data set for the upcoming altimeter data sets, that could give estimates of sea-ice thickness.

It was one of the roles of WOCE to develop models that would allow the assessment of the sensitivity of the climate system to these types of changes.

1.1.5 Cryosphere and the oceans

Ice-ocean interactions are an important part of the climate system. Mountain glaciers, small ice caps and ice sheets influence global sea level. Deep convection in the Arctic and Southern Oceans is largely related to sea-ice formation on continental shelves or in coastal polynyas (slope convection) and open ocean deep convection is often caused by atmospheric forcing at the sea-ice edge. Sea ice is treated interactively in most coupled ocean-atmosphere models and improved parameterizations for dynamical sea-ice behaviour have been selected by the Sea Ice Modelling Intercomparison Project within ACSYS (Lemke *et al.*, 1997). However, although meltwater runoff from land-ice and the melting of tabular icebergs in the Antarctic sea-ice zone influence the thermohaline circulation, as yet no adequate parameterizations exist for these processes.

The positive freshwater balance of the Arctic Ocean creates a thin and cold, less saline layer on top of a much warmer and more saline intermediate layer of Atlantic origin. The heat content of this deeper layer is sufficient to melt the entire multiyear sea ice. Therefore, changes in the salinity

of the top layer through changes in Arctic river runoff, snow-depth on sea ice and evaporation could have a strong impact on Arctic sea ice, and in turn on Arctic Ocean circulation and at least regional climate. However, the observation of solid precipitation is at present not adequate to detect changes. This is because earlier observations (for example, snow depth on sea ice measured regularly in spring at many stations where ocean profiling took place) have largely ceased following the collapse of the Soviet Union. As yet, remote sensing methods of sufficient accuracy to detect these precipitation changes have not been developed.

1.1.6 Anthropogenic climate change and the oceans

The ocean as a key component of the climate system also plays a major role in anthropogenic climate change. First, ocean heat absorption delays the full global warming. Second, the oceans, particularly their regional pattern of heat transport and absorption, lead to significant changes in regional climate and thus rainfall and temperature change. Third, the oceans are a major sink for anthropogenic CO₂. Fourth, ocean heat absorption leads to thermal expansion of the oceans and sea-level rise and as a result to coastal erosion and flooding. Fifth, as already mentioned, changes in the formation of deep water masses at high latitudes in the North Atlantic and the Southern Ocean could lead to abrupt changes in the global ocean thermohaline circulation and a major rearrangement of global climate.

As indicated by Kattenberg *et al.* (1996), the warming response is dependent on the rate of increase of greenhouse gases because of uptake of heat by the oceans. In coupled models, a slow increase in greenhouse gas concentrations of 0.25% yr⁻¹ to doubled preindustrial levels results in 70% of the full equilibrium warming at the time of doubling. For a more rapid increase of 4% yr⁻¹, only about 40% of the equilibrium warming is achieved at the time of doubling. The present rate of increase of greenhouse gas concentrations is below 1% yr⁻¹, accounting for the combined effect of all greenhouse gases. Thus only about 60% of the warming we are committed to because of increases in past greenhouse gas concentrations should have been realized to date. In addition to slowing the rate of warming, changes in precipitation patterns

will depend strongly on the warming pattern of the ocean.

The ocean water contains about 50 times the carbon stored in the atmosphere. On average about 90 billion tons of carbon (GtC) are released from the ocean and about 92 GtC are absorbed by the ocean each year. Carbon models indicate a net uptake of 2 ± 0.8 GtC released from anthropogenic sources during the 1980s. Colleagues from the Joint Global Ocean Flux Study (JGOFS) used the WOCE Hydrographic Programme to collect a global ocean carbon data set, which is being used to improve our understanding of the carbon cycle within the ocean (Wallace, Chapter 6.3). JGOFS process studies have examined how different marine ecosystems take up carbon in different parts of the oceans from the tropics to the poles. Changes in the temperature, vertical stability, circulation and marine ecosystems will change how and where the ocean will take up carbon in the future (Sarmiento *et al.*, 1998; Matear and Hirst, 1999). Ocean colour satellite systems offer a way to monitor the biological component of this carbon uptake into the future. It will be important to include ocean carbon chemistry and biology in future ocean climate models.

Mean sea-level rise is one of the major consequences of anthropogenic climate change. While the further melting of land ice (glaciers, small ice caps, ice sheets) will certainly lead to sea-level rise, thermal expansion of seawater will be the dominant contribution during the twenty-first century (Clarke *et al.*, Chapter 1.2). Model calculations indicate sea-level rise will have large regional variations but as yet there is little confidence in these regional patterns (Clarke *et al.*, Chapter 1.2). Sea-level rise threatens the coastal zone where most of the world population lives, especially those zones where there may be concomitant increases in storm surges. Thus, sea-level rise is a major argument in the political debates on anthropogenic climate change. Here again, WOCE has led to a breakthrough by the advent of precise altimeter measurements of local, regional and global sea level (Fu, Chapter 3.3) and observations of ocean warming and thus thermal expansion (Church *et al.*, 2001). If altimeters on TOPEX/POSEIDON are continued on Jason, we will soon have more than a decade of precise global sea-level observations from space that – if calibrated by reliable coastal tide gauges – will remove the large uncertainties associated with present estimates of sea-level rise.

Although the contribution of the melting ice from mountain glaciers, small ice caps and ice sheets to sea-level changes can only be roughly estimated because of the lack of sufficiently accurate mass budgets for most glaciers, present understanding of sea-level rise does not point to potential major surprises. Furthermore, the long debate on the instability of the West Antarctic Ice Sheet has recently been less intense, but there is still no firm conclusion. As stated in Warrick *et al.* (1996, p. 389): ‘Estimating the likelihood of a collapse during the next century is not yet possible. If collapse occurs it will probably be caused more by climate changes of the last 10 000 years rather than greenhouse induced warming. Nonetheless, such a collapse, once initiated, would be irreversible.’

1.1.7 Future climate research and ocean observing systems

WOCE has revealed large-scale patterns of decadal change in the ocean whereas previously there was a tacit assumption of a steady-state ocean. It is also revealing significant horizontal and vertical variations in small-scale mixing compared with the uniform pattern assumed in earlier climate models. Thus, WOCE’s Analysis Interpretation Modelling and Synthesis (AIMS) phase is in a more challenging position than anticipated at the conception of WOCE. Will it be possible to get a consistent picture of ocean structure and circulation if one only has – taking a comparison to a meteorological case – a few radiosonde ascents at different times over different continents? A partial answer is already given in the new projects that WOCE and TOGA have stimulated: CLIVAR and GODAE. These programmes will build on the understanding gained and the techniques developed through the assimilation of the WOCE data set into global ocean models (Talley *et al.*, Chapter 7.1). While significant progress has been made, much remains to be done and continued observations are essential.

Ocean observations are more difficult to obtain than atmospheric observations because the ocean is virtually opaque to electromagnetic radiation. Remote sensing from space is thus restricted to the ocean surface and the upper parts of the euphotic zone for visible radiation. Thus, the full understanding of decadal time scale climate variability requires – as mentioned earlier – sustained observation *in* the ocean on a full global scale.

As operational oceanographic near-real-time data collection is in its infancy, an infrastructure like that existing for meteorology needs to be established by the national oceanographic services coordinated through the new IOC/WMO Joint Commission for Oceanography and Marine Meteorology (JCOMM). This should take advantage of the strong push of the scientific community in CLIVAR and GODAE for an upper ocean observing system. In other words: We need a strong Global Ocean Observing System (GOOS) as a component of the Global Climate Observing System (GCOS). As major changes in the global thermohaline ocean circulation cannot be ruled out for the twenty-first century, deep ocean conditions need to be monitored as a matter of urgency.

Many of the goals of WOCE have already been reached, and many more answers will be found during the AIMS phase. As well as achieving many of their scientific goals, WOCE and TOGA have also achieved another very important goal – they have demonstrated the feasibility and urgency of a global ocean observing system. If implemented, it will see several new applications: ocean weather forecasting, global seasonal to interannual climate variability predictions, and the understanding of decadal time scale climate variability that leads to easier detection, attribution and projection of climate change. What is now required is the will – the national and international commitments – to implement the needed observational programme.

This Page Intentionally Left Blank

1.2

Ocean Processes and Climate Phenomena

Allyn Clarke, John Church and John Gould

In this chapter, we summarize oceanic processes and features that are important in defining the ocean's role in climate. We also introduce climate phenomena in which the ocean is known to play a significant role. The chapter is intended as an overview of the entire subject matter of the book. The reader is referred to the individual book chapters and to other recent literature for more detail.

1.2.1 A global perspective

The climate system is driven by energy from the sun, with nearly half of the solar radiation absorbed at the earth's surface. Almost one third is reflected back to space by the atmosphere and from the surface and about 20% directly absorbed in the atmosphere (Fig. 1.2.1, from Kiehl and Trenberth, 1997). Both radiative processes and ocean and atmosphere circulations transfer this energy from the low latitude surface where it is initially absorbed, to higher latitudes and into the global upper atmosphere from whence it is radiated back to space. This is achieved through long-wave thermal radiation originating mostly from the atmosphere. To first order, the earth radiates back to space all the energy that it receives.

The ocean's vital role in the climate system results from its great capacity to store and transport heat, water and radiatively active gases around the globe and exchange these with the atmosphere. Many oceanic and coupled ocean-atmosphere processes, occurring on a wide range of space and time scales, are involved.

While the annual average energy received by the earth at the top of the atmosphere is a function

only of latitude, the distribution of climatic conditions at the bottom of the atmosphere is far from zonal. A striking example of the oceans' influence is that the surface temperature of northwestern Europe is about 10°C warmer than the zonal average (Fig. 1.1.2) because of the heat transported northeastward in the Atlantic. Furthermore, because of the ocean's high heat capacity, the seasonal temperature range of maritime climates is smaller (a few °C) than that of continental climates (several tens of °C, see Gill, 1982, his Fig. 2.1). Maritime climates also exhibit a delay in their summer maximum and winter minimum temperatures compared with the cycle of solar radiation (see Large and Nurser, Chapter 5.1).

Generally, only the surface mixed layer (typically tens to several hundreds of metres thick) participates directly in the seasonal cycle of heat accumulation and release. However, a small-amplitude, seasonal temperature cycle penetrates to depths as great as 1500 m in certain high-latitude regions. On time scales of years to centuries, even the deepest ocean layers exchange heat and other properties (e.g. salt, nutrients and dissolved gases) with the surface layer by vertical and horizontal advection and mixing.

The oceans contain 50 times more CO₂ than does the atmosphere. They presently sequester about one third of the 6 Gt of carbon released annually through human activities. Future uptake of CO₂ by the oceans will depend on the evolution of ocean conditions influenced by, and influencing, a changing atmosphere. The surface ocean exchanges CO₂ with the atmosphere seasonally in a similar manner to the exchange of heat and thus

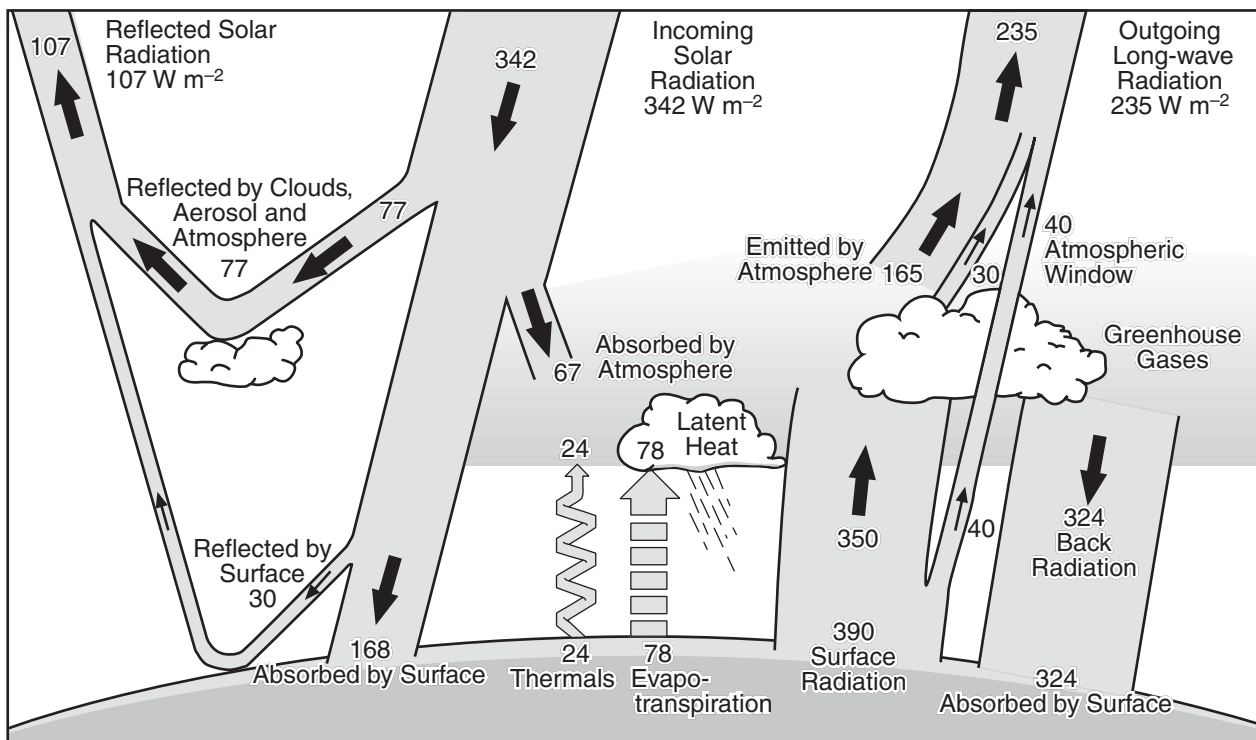


Fig. 1.2.1 Schematic showing the atmospheric and surface processes determining the earth's annual global mean energy budget (from Kiehl and Trenberth, 1997). Units are W m^{-2} .

the deeper layers are coupled to the atmosphere with respect to carbon storage on longer time scales.

The full three-dimensional ocean circulation needs to be adequately represented in global atmosphere–ocean general circulation models if realistic projections of climate on decadal and longer time scales are to be completed, including projections of abrupt climate change. This level of ocean complexity is also required for realistic projections of greenhouse gas concentrations in the atmosphere to be made and for the simulation of the timing and regional impact of anthropogenic climate change.

Although the first full-depth observations of the oceans' physical properties were made at the end of the nineteenth century, it was not until the late 1950s that significant numbers of observations of appropriate precision and accuracy became available. Only recently, with the advent of satellite observations, has there been a means of routinely observing the global ocean. Of particular importance has been the availability over the last decade of satellite altimetry of sufficient accuracy to provide the first quasynchronous global estimates of the oceans' near-surface circulation. It was against this background that the World Ocean Circulation

Experiment (WOCE) was designed. An essential task for WOCE was to produce the first quasi-synoptic set of full-depth observations of the global oceans for quantitatively defining the global ocean circulation, and thus the oceans' role in storing and transporting climatically important properties. These measurements would also be used to develop and test ocean models and to provide a standard against which past and future changes might be measured.

The ocean not only plays a fundamental role in moderating and modifying the atmospheric climate, but it is also the environment within which marine organisms live, and it strongly influences the ocean boundaries. Thus it can be said to have a climate itself that has a direct and important impact on society's use of the oceans, their living resources and their coastal boundaries.

1.2.2 Air–sea fluxes

Transfers of properties between the 'transient' atmosphere and the 'sluggish' oceans lie at the very heart of the climate system. The accurate modelling of these transfers demands a detailed understanding of the dynamics of both the upper ocean and

the marine atmospheric boundary layer. These fluxes are the ocean's principal source of momentum and energy. Together with the redistribution of heat by ocean currents and mixing, they define the temperature and salinity (and thus the density) of the ocean surface. They also determine the oceans' three-dimensional current structure and thus the temperature, salinity, density and tracer distributions from surface to seabed. Conversely, the lower atmosphere receives most of its energy from the ocean via these energy fluxes rather than directly from the sun. The ocean and the atmosphere also exchange gases and chemical compounds. Our climate arises through the interplay of these two dynamic systems.

1.2.2.1 Momentum transfer

Surface winds are the principal driver of the upper ocean circulation through wind stress (the product of a drag coefficient and the square of the surface wind speed). The drag coefficient is itself a function of wind speed, atmospheric stability and wave conditions (WGASF, 2000). To first order the pattern (Fig. 1.2.2) is of westward stress from the easterly trade winds at low latitudes and eastward stress from the high-latitude westerlies. The strongest mean wind stresses occur in the Southern Ocean. Wind stress variations both determine and are determined by climate variability. For example, El Niño events occur when the equatorial Pacific trade winds weaken and are replaced by westerly

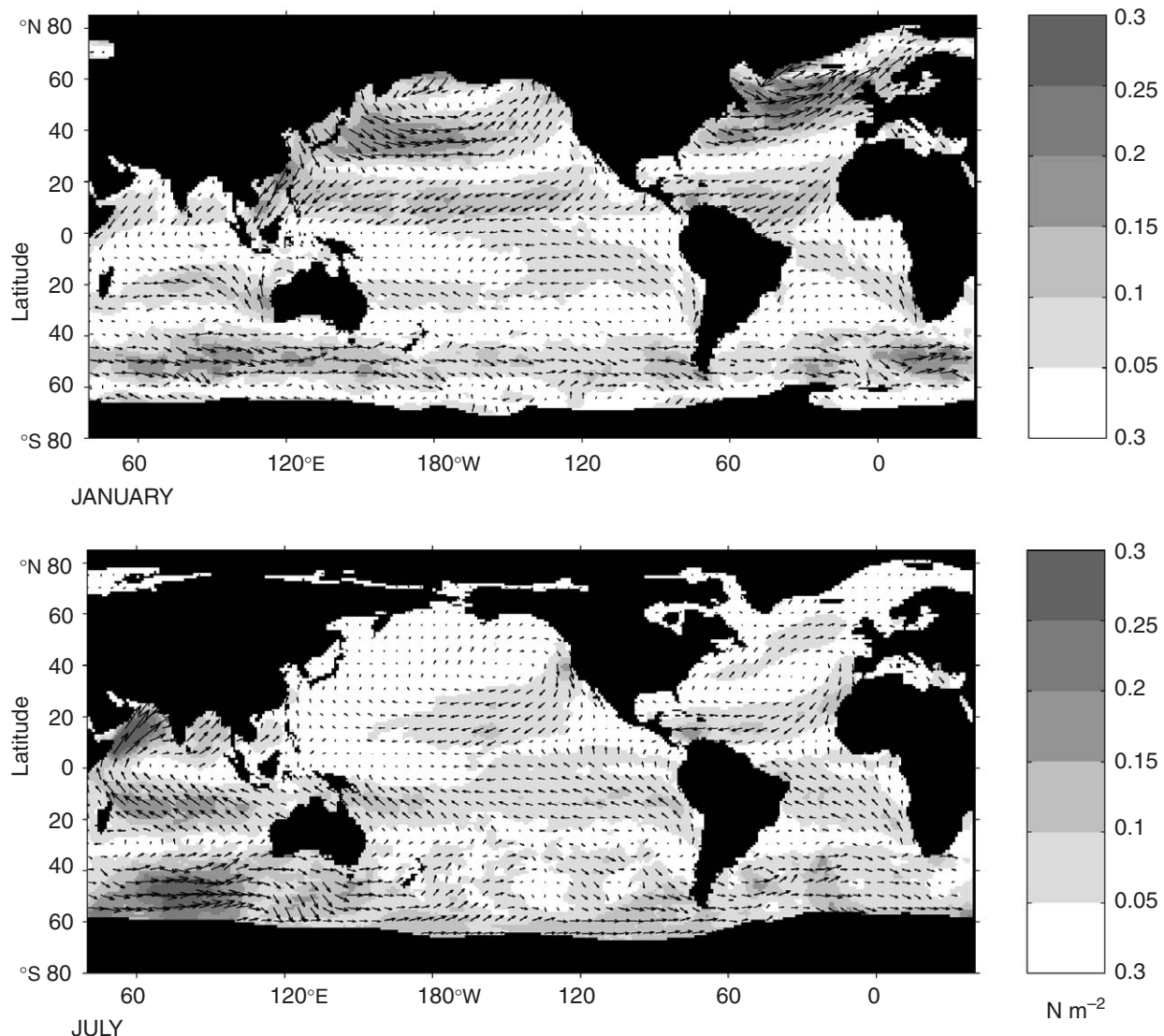


Fig. 1.2.2 The global mean wind stress patterns for January and July from Josey *et al.* (2000). Shading indicates wind stress magnitude and arrows the direction.

wind bursts driving warm water eastward along the equator, which then influence the wind system.

Quantitative descriptions of the wind stress fields have been obtained from ship observations (Hellermann and Rosenstein, 1983; Josey *et al.*, 2000), from the outputs of operational atmospheric analyses (e.g. Trenberth *et al.*, 1990) and most recently from satellite remote sensing (Liu and Katsaros, Chapter 3.4). A comprehensive review of the various products is given by WGASF (2000).

Winds directly drive the near-surface ocean layer. The rotation of the earth causes a depth-integrated Ekman transport to the right (left) of the wind in the northern (southern) hemisphere (Ekman, 1905). A large-scale confirmation of this Ekman transport, a fundamental tenet of oceanography, has come from surface drifter observations (Niiler, Chapter 4.1, Figs 4.1.6–4.1.8) obtained during WOCE and the Tropical Ocean-Global Atmosphere (TOGA) programme. The dominant wind stress pattern produces a convergence of the Ekman transport in mid-latitudes and a divergence poleward of the peak in the westerly winds. This generates the major ocean circulation gyres (Section 1.2.4.1). The continuing inability to adequately describe the wind field over the oceans significantly limits our ability to simulate and model ocean circulation.

1.2.2.2 Heat transfer

The net flux of heat at the ocean surface results from the balance between incoming short- and long-wave radiation, the loss of heat by outgoing long-wave radiation and through evaporation, and to some extent by the surface turbulent fluxes of sensible heat. There is a heat flux associated with precipitation but on the large-scale this is generally small (Curry and Webster, 1999). Each component of the surface heat budget depends on a variety of oceanic and atmospheric parameters (Liu and Katsaros, Chapter 3.4; Curry and Webster, 1999). The heat budgets of ocean and atmosphere are coupled through these air-sea fluxes.

Radiation

The incoming (short-wave) solar radiation flux at the top of the atmosphere is a function of latitude, season and time of day. Averaged globally it has a value of approximately 342 W m^{-2} (Fig. 1.2.1). There have been only small variations in the solar flux over the last millennia. Over the last two

million years, the radiation changes due to the cycles of precession, obliquity and eccentricity in the earth's orbit around the sun (the Milankovich cycles, with periods of tens to hundreds of thousands of years) have triggered long-term climate variations.

Solar radiation passes through a clear atmosphere with little absorption. However atmospheric water vapour, clouds and aerosols reflect, scatter and absorb solar radiation, significantly reducing the amount of heat reaching the surface (Fig. 1.2.1; Curry and Webster, 1999). At the sea surface, a fraction (the surface albedo – typically 5–8% when the sun is nearly overhead) of the incoming solar radiation is reflected or backscattered from the ocean (Curry and Webster, 1999). Conditions within the ocean determine where the remainder of the radiation is absorbed. Waters with heavy sediment loads or experiencing strong phytoplankton blooms absorb the solar radiation over a few metres whereas in clear water the short-wave radiation can penetrate tens of metres below the surface mixed layer. This relatively deep penetration is important in understanding the heat balance of the western equatorial Pacific Ocean and thus in simulating interannual climate variability associated with El Niño-Southern Oscillation events (see e.g. Section 4.2 of Godfrey *et al.*, 1998).

The ocean also radiates energy upwards to the atmosphere at long wavelengths. The flux is a function of the surface temperature (Curry and Webster, 1999). Long-wave radiation is strongly absorbed in water and consequently the outgoing flux originates from the topmost millimetre of the ocean. The temperature of this surface skin is slightly different (typically cooler by about 0.2–0.3°C) from that of the mixed layer immediately below. Long-wave radiation is absorbed by the atmosphere and by clouds and these in turn radiate long-wave energy out to space and back to the ocean where it is absorbed (again in the top millimetre).

Clouds, in their many forms, are the most important factor regulating both the incoming solar and the long-wave radiation. For more than a century ships' officers have documented marine clouds and over recent decades clouds have also been observed using satellites. Unfortunately, neither set of observations provides sufficient information to assess the clouds' optical thickness to either the short- or long-wave radiation.

Latent and sensible heat

The ocean also transfers heat to the atmosphere by the turbulent processes of conduction (sensible heat flux) and evaporation (latent heat flux). The sensible heat flux (Curry and Webster, 1999) is a function of the temperature difference between the ocean surface and the atmosphere immediately above and is also limited by the rate at which heat can be transferred to the air-sea interface by processes within the atmospheric boundary layer.

Latent heat flux (Curry and Webster, 1999) results from evaporation at the ocean surface. As water changes from liquid in the ocean to vapour in the atmosphere, the ocean loses energy in the form of the latent heat of vaporization and the atmosphere gains heat when the vapour condenses. Since water vapour pressure depends on temperature, sea surface temperature is an important parameter in determining the latent heat flux. As with the sensible heat flux, characteristics of the atmospheric boundary layer (water vapour content, wind speed, atmospheric stability) control the latent heat flux.

Net heat flux

The upper atmosphere receives more solar radiation at low than at high latitudes but the outgoing radiation is more spatially uniform (Bryden and Imawaki, Fig. 6.1.2). This requires a redistribution of energy by the atmosphere and ocean. As a result, there is a net heat flux into the ocean in the equatorial regions and from the oceans at high latitudes. On the western side of ocean basins, where swift western boundary currents carry warm water polewards beneath a cooler atmosphere, there is also a net heat loss by the ocean (Bryden and Imawaki, Fig. 6.1.4). As with the surface wind stress, quantitative descriptions of the air-sea heat flux have been made using ship observations, operational atmospheric analyses and satellite observations. A comprehensive review of the available products is given by WGASF (2000). The determination of heat (and fresh-water) transports, which is a central objective of WOCE, will provide constraints on the net air-sea heat (and fresh-water) fluxes. Since these determinations will require the availability of many key data sets, they will only be able to be carried out in the later stages of the WOCE project. Examples of earlier determinations from both single zonal hydrographic sections and from global inversions are given in Chapter 6.1.

1.2.2.3 Water exchange and surface salinity

Evaporation and precipitation move both heat and fresh water between the ocean and the atmosphere. The rate of evaporation is directly proportional to the oceans' latent heat loss and is controlled by the ocean-atmosphere temperature difference. Therefore the ocean influences evaporation through its surface temperature.

The difference between evaporation and precipitation (the evaporation minus precipitation ($E - P$) flux, Wijffels, Fig. 6.2.1) changes the upper ocean salinity. The highest rates of precipitation occur in the tropics with secondary maxima at latitudes of 40 to 60° (Wijffels, Fig. 6.2.3). The main evaporative regions of the ocean are at about 20°N and S (Wijffels, Fig. 6.2.2). Together with the addition of fresh water through river discharge, spring runoff from snow melt on land and through the melting of sea ice, this results in a low-salinity surface ocean in the equatorial and high-latitude regions and high salinity near 20°N and S (Gordon, Fig. 4.7.1b).

Neither evaporation nor precipitation is directly affected by the surface salinity. With no direct feedback, it is therefore a challenge to run coupled atmosphere-ocean models that maintain upper ocean salinity fields within climatological limits.

1.2.2.4 Particle exchanges

The formation of marine clouds and hence of precipitation depends on the presence of small particles to serve as condensation nuclei. Some of these nuclei are provided by aerosols originating from land-based natural and anthropogenic sources. However, most are thought to arise from the ocean when breaking waves release tiny subdroplets of seawater into the atmospheric boundary layer. The water content of these droplets rapidly evaporates, leaving salt crystals that are carried aloft where they can serve as condensation nuclei (Hudson *et al.*, 1998). In addition, some species of oceanic phytoplankton produce organic sulphur compounds in the upper water column which are then exchanged with the atmosphere. In the atmosphere they are converted into small particles of dimethylsulphide, DMS, which also serve as condensation nuclei. This exchange provides a potential climate feedback if changes in ocean productivity lead to changes in cloud cover and thus to changes in the solar radiation reaching the ocean (Charlson *et al.*, 1987).

Over large areas of the surface ocean, the levels of the nutrients needed for phytoplankton growth remain high throughout the year. One of the reasons that these nutrients are not exhausted by primary production is lack of micronutrients (such as iron) for which a source is dust carried from the continents by winds. Recent iron-enrichment experiments in the Pacific and Southern Oceans have demonstrated that phytoplankton growth can be stimulated by small additions of iron (Coale *et al.*, 1996; Boyd *et al.*, 2000).

1.2.2.5 Carbon dioxide exchanges

The ocean is a major reservoir of carbon dioxide. In spite of the fact that it already contains 50 times the mass of CO₂ in the atmosphere, the ocean has the capacity for storing much more. The surface ocean exchanges CO₂ with the atmosphere at a rate proportional to the difference in the partial pressure of the gas in the two media, with the ocean able to take up more CO₂ at lower temperatures. The factors limiting the exchange are the rate at which the gas can be transferred across the air-sea interface and the rate at which carbon is exchanged between the surface layer and the deep ocean. Since ocean currents can transport CO₂ over large distances, the location of storage of carbon may be distant from the site of air-sea exchange (Wallace, Chapter 6.3).

Photosynthesis by phytoplankton converts CO₂ within the upper ocean to organic compounds. This lowers the partial pressure of CO₂ in the surface waters, encouraging greater exchange from the atmosphere. Part of this 'fixed' carbon is converted to dissolved inorganic carbon within the surface layer through respiration and grazing as well as death and decay. Some of this fixed carbon leaves the surface layer by particle sinking and by advection. A small percentage reaches the ocean floor and is sequestered within ocean sediments for geological time scales. These issues have been explored in the Joint Global Ocean Flux Study (JGOFS) (<http://ads.smr.uib.no/jgofs/jgofs.htm>).

Annually about 2 Gt of the 6 GtC released by burning fossil fuels, is sequestered in the ocean (Prentice *et al.*, 2001). However, different approaches reveal different spatial distributions of this uptake (Wallace, Chapter 6.3). While the rate at which the ocean stores CO₂ should increase as the atmospheric concentration rises, changes in ocean circulation, temperature and/or biological

processes could have significant, but as yet poorly understood, impacts on the ocean uptake (Sarmiento *et al.*, 1998; Matear and Hirst, 1999).

1.2.2.6 Effects of sea ice cover

All air-sea exchange processes are greatly modified in the presence of sea ice, especially when that sea ice is snow covered. The many roughness elements on the surface of sea ice transfer more momentum from the atmosphere to the ice than would occur between atmosphere and ocean. Roughness elements on the underside of moving sea ice lead to large transfers of momentum between ice and ocean. These two factors mean that the net momentum transfer for atmosphere-ice-ocean coupling is generally greater than for direct atmosphere-ocean coupling. Sea ice is, however, seldom free to move and, under a convergent wind stress, much of the momentum imparted to an ice field is taken up by internal ice processes, including the formation of ice ridges and the grounding of ice floes on shorelines.

Ice is a poor conductor of heat; snow is even poorer. The rate of heat loss from an ice-covered ocean is limited by the rate at which heat can be conducted through the ice/snow layer. In winter, the presence of ice cover greatly reduces the total cooling of the water column. However, gaps in the ice (leads and polynyas) can allow large exchanges of heat when air-sea temperature differences are large. Offshore winds can rapidly remove sea ice between the shore-fast ice and the offshore pack. Intense ocean cooling and sea ice formation occurs in these latent heat polynyas (Kaempf and Backhaus, 1998; Worby *et al.*, 1998).

Newly formed sea ice has a salinity of 6 to 10, depending on the rate at which it forms. Salts are concentrated in small pockets of brine that gradually drain into the water column, increasing its density. Thus the process of sea ice formation releases salt through brine rejection and creates deep winter mixed layers through salinity-driven convection. When the ice melts in the spring, a low-salinity surface layer is formed, restratifying the water column (Tang, 1991).

Ice is a good reflector of solar radiation, particularly when the sun's elevation is low and the ice is snow covered. During spring at high latitudes, the long days have the potential to deliver heat to the surface but the greater part is reflected by ice and snow cover. When solar elevations are high

enough to reduce reflection and there is no snow cover, solar radiation is able to penetrate into and through sea ice. In doing so it heats both the interior of the ice and the water column below (Holland *et al.*, 1997). Leads are also important in allowing radiation to penetrate into the ocean thus heating the water column. The sea ice is then melted from below.

1.2.3 Ocean storage of heat and fresh water

The ocean's central role in the climate system comes from its ability to store and transport heat, fresh water (and carbon) over a wide range of time and space scales. A simple indication of the ocean's importance is that 3 m of seawater has about the same heat capacity as the whole atmospheric column above it (Gill, 1982). On the diurnal time scale, the ocean stores heat during the day and releases it to the atmosphere at night. Under calm conditions, solar heating can warm the upper few metres by about a degree, provided the water column is not too clear. Heat loss during the following night will cool the surface, making the water denser. The resulting convection will develop a shallow diurnal mixed layer a few metres to tens of metres thick.

Beyond the diurnal time scale, kinetic energy from wind and waves together with current shear at the base of the surface layer sustains an upper mixed layer a few tens of metres in thickness. The daily net heating (or cooling) of the ocean is averaged over such a mixed layer. In summer, net heating adds buoyancy to the surface waters, increasing the stratification. This, coupled with generally weaker winds in summer, makes for shallower mixed layers. The stability of the water column can be further increased by the addition of fresh water to the surface ocean through rainfall, river discharge, spring runoff from snow melt on land and through the melting of sea ice. Because these salinity-stabilized surface mixed layers are very shallow, they are able to warm up quicker in spring than they would if they were stabilized by thermal effects alone.

The depth of the winter mixed layer represents the water depth that participates directly in the seasonal cycle of storage and release of heat, fresh water and gases. The depth of this layer can reach a few hundred metres in parts of the subtropical

and higher-latitude ocean (Fig. 5.4.2, Hanawa and Talley, Chapter 5.4), greatly slowing the daily, weekly and monthly change in temperature. These deep layers are formed on the equatorward (or warm) side of major currents such as the eastward extension of western boundary currents and the Antarctic Circumpolar Current, particularly where frequent outbreaks of cold continental air masses result in large heat loss to the atmosphere. These sites are the locations for the formation of Mode waters (Fig. 5.4.3, Hanawa and Talley, Chapter 5.4), which are subsequently advected into the ocean interior. Anomalies in the heat content of these Mode waters may persist for several years despite being exposed to the atmosphere each winter when the shallow seasonal thermocline is removed (Sutton and Allen, 1997). Such ocean anomalies may be important in determining the predictability of inter-annual climate anomalies (Rodwell *et al.*, 1999).

Heat loss in a few special regions (e.g. the Labrador Sea, the Golfe de Lyon in the western Mediterranean Sea and in the high-latitude Southern Ocean) can be intense, reaching several hundred watts per square metre over areas a few hundred kilometres across during particularly intense winters. The winter mixed layers so formed extend to over a thousand metres and sometimes to the seafloor (Lazier *et al.*, Chapter 5.5). Once water enters this deep layer, it remains there for centuries before returning to the surface and contact with the atmosphere. The volume of this layer is some three to four times the volume of the thermocline. It is through these regions that the deep ocean is ventilated and renewed.

1.2.4 Ocean circulation

The ocean circulation is driven by air-sea fluxes of momentum (wind stress), heat and fresh water. The resulting circulation is thus intimately coupled to the atmosphere. Here we introduce first the upper ocean circulation, which is often thought of as being dominated by the wind forcing, and then the global thermohaline circulation. The two are intimately linked and are only described separately here for the sake of clarity.

1.2.4.1 The wind-driven circulation

The upper layer circulation in each ocean basin is driven by the large-scale distribution of wind stress or, more exactly, by the curl of the wind stress.

The wind stress curl is determined by the juxtaposition of the zonal tradewinds in the subtropics and the mid-latitude westerlies (Fig. 1.2.2). It forces anticyclonic subtropical and cyclonic subpolar gyres in each ocean basin (Fig. 1.2.3, see Plate 1.2.3, p. 44, and Niiler, Fig. 4.1.4). On the rotating earth, the wind stress curl acts to force water into (out of) the interior of the subtropical (subpolar) gyre. To conserve potential vorticity the water column moves equatorward (poleward) in the subtropical (subpolar) gyre. This Sverdrup balance is one of the main building blocks of ocean circulation theory (Webb and Sugihara, Chapter 4.2). In the subtropical gyres, it generates an equatorward transport of several tens of millions of cubic metres per second.

Volume and vorticity conservation require that water moved meridionally by the gyres circulates back to its initial latitude within western boundary currents. These currents are narrow (~ 100 km), intense ($\sim 1 \text{ m s}^{-1}$) and deep (> 1000 m) baroclinic jets carrying warm water to higher latitudes (see below). The resulting warm sea surface temperatures and the sharp horizontal gradients generate intense atmospheric low pressure systems in the western boundary current regions (e.g. Cione *et al.*, 1993).

In the absence of a continent to provide a meridional boundary in the Southern Ocean, the strong westerlies drive the energetic eastward flow of the Antarctic Circumpolar Current, resulting in large interbasin transfers of heat and mass (Fig. 1.2.3, see Plate 1.2.3, p. 44). This circulation feature is central in the oceans' role in climate (Rintoul *et al.*, Chapter 4.6).

Near the equator, the Coriolis force reduces to zero. The increasing contribution of non-geostrophic dynamics in both the ocean and atmosphere results in a complex system of zonal equatorial currents (Godfrey *et al.*, Chapter 4.3) which play an important role in interhemispheric exchanges (Frantoni and Richardson, 1999). The only direct low-latitude ocean basin interconnection is between the Pacific and Indian Oceans via the Indonesian Throughflow. This warm, westward-flowing low-salinity transport plays a central role in determining the oceanic heat and freshwater budgets of both the Pacific and Indian Oceans and in closing the global ocean thermohaline circulation (Gordon, Chapter 4.7). There is evidence that the strength of the exchange is linked to the phase

of El Niño-Southern Oscillation (ENSO); (Godfrey, 1989; Gordon, Chapter 4.7).

As the wind-driven circulation moves water around the subtropical gyres, it also moves it vertically from the surface into the main thermocline and then back into the surface. Surface density (determined by the combination of ocean circulation and air-sea exchange, Nurser and Large, Chapter 5.1) increases with increasing latitude. In those parts of the gyre where the water is moved equatorward, it moves into regions of lighter surface water and hence it descends or is subducted into the ocean interior as it flows along surfaces of constant density (Price, Chapter 5.3). Once subducted, these waters are transported around the gyres at depth within the main thermocline. When they return to their original latitude 10–50 years later (the longer times being for the denser and deeper waters), they will again enter the surface layer through their participation in winter convection. Heat, salt and other properties carried into the main thermocline through this mechanism remain isolated from the atmosphere for several decades. The volume of this reservoir is five to ten times greater than the layer that participates directly in the seasonal cycle.

Using low values of diapycnal mixing as measured in the main thermocline (Toole and McDougall, Chapter 5.2), and specified wind stress and surface density fields, the subduction process, or thermocline theory (Price, Chapter 5.3; Pedlosky, 1996), has successfully explained many of the major features of the density field of the upper 1000 m of the main gyres. Examples include the tongues of low-salinity Antarctic Intermediate Water penetrating northward near the base of the subtropical gyres at depths of 800–1000 m in the Atlantic and Pacific Oceans (Figs 1.2.4 and 1.2.5, see Plate 1.2.4, p. 44, and Plate 1.2.5, p. 44) and the tongue of low-salinity North Pacific Intermediate Water penetrating southward in the North Pacific at depths of about 500 m (Fig. 1.2.5, see Plate 1.2.5, p. 44). The subduction process also operates in the subtropics and sets the properties of the equatorial thermocline (Liu and Philander, Chapter 4.4). Correctly simulating these processes will be important for reliable projections of possible changes in ENSO events as reported in recent studies (e.g. Timmermann *et al.*, 1999a).

Boundary currents

Western boundary currents are necessary to satisfy volume and vorticity conservation. Intense western

boundary currents, like other frontal features, spawn meanders, rings and eddies that transfer momentum, vorticity, heat and other properties between the current and the surrounding ocean. These transfers create and sustain recirculation gyres that may extend over the full ocean depth, creating an expression of the boundary current within the deep and bottom waters beneath the main current. The recirculation gyres increase the transports of the boundary currents by factors of three to four.

Within WOCE, the measurement of boundary currents was an essential element of the determination of oceanic transports of heat and fresh water in each ocean gyre. The measurements were also sustained over periods of at least 20 months in order to deal with ocean variability associated with eddies and boundary current instabilities (Rossby and Gottlieb, 1998). Since boundary currents are not described explicitly in any single chapter, we provide some detail here.

The most comprehensive western boundary current measurement programme during the WOCE period was that in the Kuroshio, in which a combination of *in-situ* current measurements, geostrophy and satellite altimetry provided (due to the close linear relationship between sea surface slope and transport) a multiyear transport record (Imawaki *et al.*, 1997). The transport was estimated at $63 \pm 13 \times 10^6 \text{ m}^3 \text{ s}^{-1}$ over a 3-year period and revealed no clear annual cycle (Fig. 1.2.6). This estimate is larger than the likely transport of the Kuroshio alone because of the presence of a warm anticyclonic eddy on the offshore side of the Kuroshio (Dickson *et al.*, Chapter 7.3).

Mata *et al.* (2000) analysed data from a 2-year array of current meters in the East Australian Current (Fig. 1.2.6). The strongest variability was centred on periods between 144 and 45 days but again no annual cycle was evident. The high variability results in periodic reversals of the current direction. The estimated mean southward transport was $22 \pm 5 \times 10^6 \text{ m}^3 \text{ s}^{-1}$. The measurements also reveal a persistent equatorward deep undercurrent. The Agulhas measurements by Beal and Bryden (1999) also gave direct confirmation of the presence of an undercurrent previously postulated on the basis of water mass properties. Beal and Bryden's Agulhas transport estimate gives a value of $73 \times 10^6 \text{ m}^3 \text{ s}^{-1}$ (Fig. 1.2.6). The clearest evidence of the wind-driven response of a boundary

current is the seasonal reversal of the Somali current under the influence of the monsoonal wind regime. Logistical problems precluded sustained measurements of the Somali current during WOCE but our present understanding of this current and its relationship to the Indian Ocean equatorial current system are described in Chapter 4.3.

In the Atlantic, monitoring of the Gulf Stream system in the Florida Strait (Larsen, 1992) and between Bermuda and the US mainland (Rossby and Gottlieb, 1998) continued during WOCE. A current meter and inverted echo sounder array plus hydrographic surveys measured the Gulf Stream/North Atlantic Current transport off Newfoundland (Fig. 1.2.6, Clarke *et al.*, 1998) over 640 days during 1993–95. The median poleward transport of $140 \times 10^6 \text{ m}^3 \text{ s}^{-1}$ included a substantial contribution from a strong recirculation gyre within the Newfoundland Basin. Gulf Stream transports and their relationship to the wider Atlantic circulation are well summarized in Schmitz (1996a) but this does not include most estimates made during WOCE.

In the South Atlantic, Maamaatuaiahutapu *et al.* (1998) made measurements in the confluence region of the Brazil and Falklands/Malvinas currents. This is an area of high spatial and temporal variability and while consistent values of the Falklands/Malvinas current transport ($40 \pm 7 \text{ m}^3 \text{ s}^{-1}$) were obtained from inversions of hydrographic data constrained by current meter measurements, values for the Brazil current ranged between 30 ± 7 and $56 \pm 8 \times 10^6 \text{ m}^3 \text{ s}^{-1}$.

Coarse-resolution ocean and coupled atmosphere–ocean models (Wood, Chapter 2.3) are able to capture the direct response of subtropical gyres and their western boundary currents to the large-scale forcing of the wind. However, such models are unable to reproduce either the recirculation gyres and underestimate the transports of the boundary currents. Finer-resolution ocean models (Böning and Semtner, Chapter 2.2) are better able to reproduce the eddy dynamics and hence provide more realistic boundary current mass, heat and property transports.

The eastern boundaries of ocean basins exhibit equatorward flow linked to the subtropical gyres (e.g. California Current, Canary Current, Peru Current) and are generally regions of intense upwelling. A notable exception in the South Indian Ocean is the Leeuwin Current, which flows poleward. There

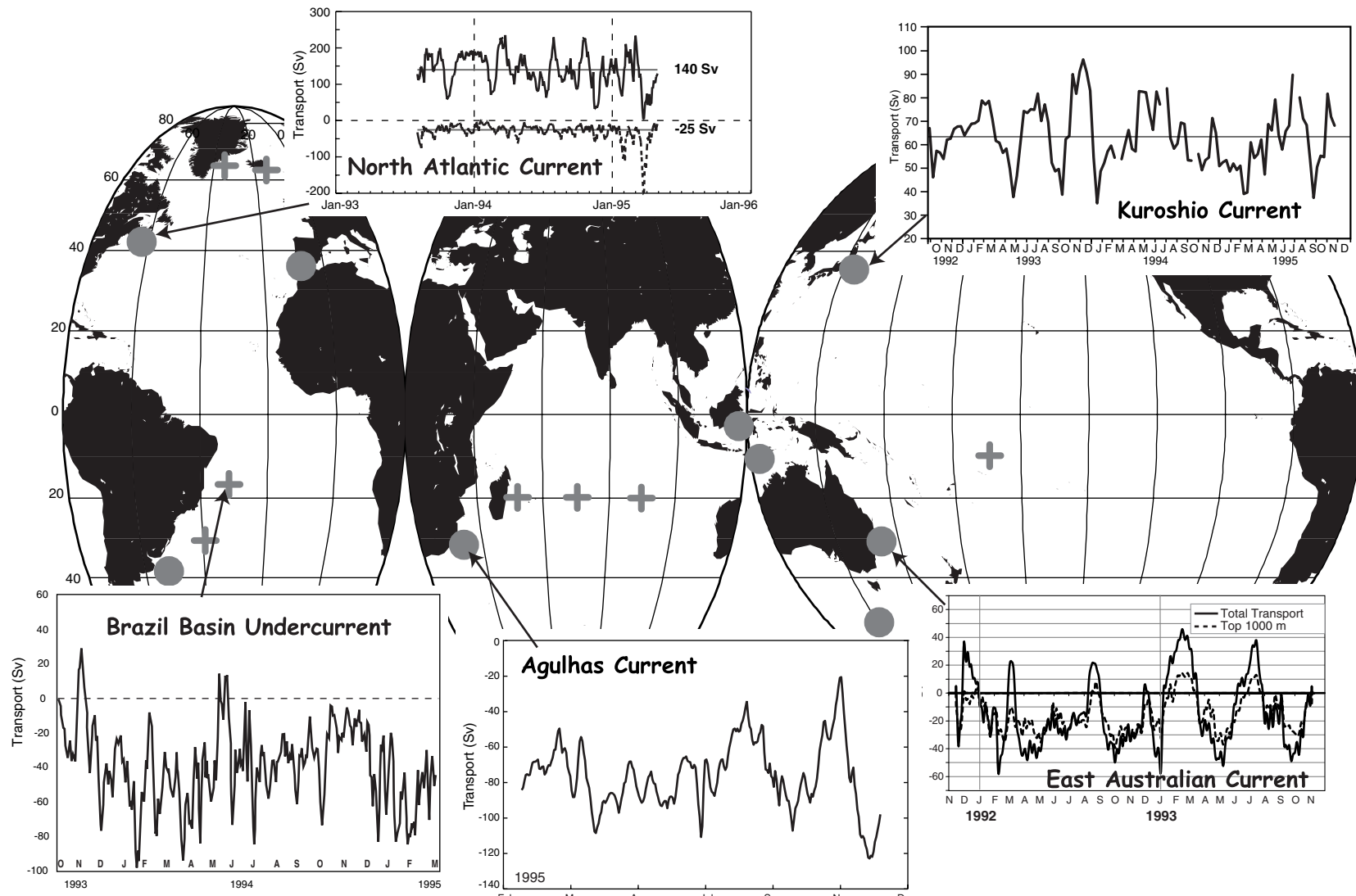


Fig. 1.2.6 Examples of boundary current measurements made during WOCE. Circles show approximate locations of upper ocean measurements; crosses are deep arrays. **North Atlantic Current:** unpublished data from Clarke *et al.* (WOCE NL No. 33, December 1998) (solid line poleward transport, dotted equatorward). **Brazil Basin Undercurrent:** unpublished data from Weatherly *et al.* (2000). **Kuroshio Current:** unpublished data from Imawaki *et al.* (WOCE NL No. 25, 1997). **East Australia Current:** from Mata *et al.* (2000). **Agulhas Current:** Beal and Bryden (1999).

are also poleward eastern boundary currents associated with the northern hemisphere subpolar gyres. In the North Atlantic, a poleward undercurrent helps to transport Mediterranean water northwards (Candela, Chapter 5.7). In the North Pacific, there is a continuous subsurface current jet carrying $0.8 \times 10^6 \text{ m}^3 \text{ s}^{-1}$ poleward just offshore of the shelf break between 33 and 51°N (Pierce *et al.*, 2000). Issues concerning eastern boundary currents, and particularly those flowing poleward, were summarized by Neshyba *et al.* (1989).

Many eastern boundary currents were instrumented during the WOCE period, thus enabling their transports to be estimated. These observations include the Benguela Current (Garzoli *et al.*, 1996), the Leeuwin Current (Domingues *et al.*, 1999), the California Current (Strub *et al.*, 1997) and the poleward eastern boundary current in the North Atlantic (Fiúza *et al.*, 1998).

1.2.4.2 The thermohaline circulation

In addition to the wind-driven circulation, the ocean exhibits a large meridional overturning circulation referred to as the thermohaline circulation. More than 60% of the surface ocean has temperatures warmer than 20°C. Below the main thermocline, the deep ocean is cold and weakly stratified (Figs 1.2.4 and 1.2.5, see Plates 1.2.4 and 1.2.5, p. 44). More than 80% of the ocean volume is colder than 4°C (calculation based on Levitus, 1982). In fact, 25% of the ocean volume has a temperature between 0.5 and 1.7°C and a salinity between 34.65 and 34.74 (Worthington, 1981).

The properties of these cold, deep watermasses are set in the winter mixed layers in the high-latitude North Atlantic and Southern Oceans. There, intense ocean heat loss to the atmosphere combined with salt rejection from the formation of sea ice, produces cold dense water that convects to form the deep and bottom waters of the global ocean (Lazier *et al.*, Chapter 5.5). These water masses then spread to fill the deep ocean. Volume conservation requires surface waters to flow poleward into these regions to replace this spreading deep water.

This coupling of the surface and deep ocean within a global circulation system has been expressed by the greatly simplified ‘icon’ of the global conveyor belt (Broecker, 1991). While this ‘icon’ has captured the public’s and politicians’ attention, it greatly oversimplifies a complex but vital component of the climate system.

Deep and intermediate water mass formation

Deep and intermediate water masses are formed through convective processes both in the open ocean and on continental shelves.

In the open ocean, deep convection occurs within localized regions of less than 200 km diameter which have very special characteristics. Each of these locations is within a cyclonic circulation that reduces the stability of the water column; all are subject to intense air–sea exchange; and contain warmer and saltier subsurface water masses. These conditions are set by the large-scale gyre circulation and by the previous winter’s cooling cycle that will have already removed most of the buoyancy from the water column as the water is advected towards these special convection regions. Open-ocean deep convection has been directly observed in both the Mediterranean and Labrador Seas; indirect evidence indicates that it also occurs in the Greenland (Schott *et al.*, 1993b; Rudels *et al.*, 1989; Watson *et al.*, 1999) and Weddell Seas (e.g. the Weddell Sea polynya; Gordon, 1982). Marshall and Schott (1999) have published a comprehensive review of open-ocean deep convection from a North Atlantic perspective.

Deep-water formation also occurs through convection over the Antarctic and Arctic continental shelves. Very intense air–sea–ice interaction in coastal polynyas again leads to large oceanic heat loss and to an increase of salinity through the formation of sea ice and the rejection of salt. Because this takes place in shallow water, these exchanges result in the formation of very dense waters that flow along the sea bed to the edge of the shelf and descend the continental slopes into the ocean depths. The major site for formation of Antarctic Bottom Water (AABW) is the Weddell Sea but there is also significant AABW formation elsewhere around Antarctica. For example, recent observations have revealed the presence of cold, dense plumes (with high concentrations of chlorofluorocarbons, CFCs) cascading down the slope (Rintoul *et al.*, Chapter 4.6). This type of convection also occurs at low latitudes where evaporation in inshore bays produces dense saline brines that drain to deeper water.

Circulation of water masses

From their high-latitude source regions, the dense waters sink into the ocean interior and participate in the global-scale overturning (the thermohaline)

circulation. Our present theoretical understanding of the deep ocean circulation is based on the work of Stommel and Arons (1960a,b). They assumed that the deep water left the abyssal layer through a spatially uniform upwelling (this implies spatially uniform vertical mixing). Vorticity balance would then require that the abyssal circulation would consist of a series of narrow western boundary currents (Fig. 4.5.1, Hogg, Chapter 4.5) feeding interior gyres.

Based on this understanding and the observational evidence, Fig. 1.2.7 (see Plate 1.2.7, p. 44) from Schmitz (1996b) shows a schematic representation of the three-dimensional circulation of deep water masses. In the Atlantic, the southward-flowing western boundary current transports NADW to the Southern Ocean. This flow is reflected in the tongue of high-salinity NADW (centred at depths of 2–3 km in the South Atlantic) in a meridional section through the Atlantic (Fig. 1.2.4, see Plate 1.2.4, p. 44). Below this there is a northward flow of low-salinity Antarctic Bottom Water (AABW) originating from the Weddell Sea. The NADW joins lower Circumpolar Deep Water (CDW) in the Southern Ocean where it is transported eastward as part of the Antarctic Circumpolar Current, and then northward along with AABW into the Pacific Ocean (Fig. 1.2.5, see Plate 1.2.5, p. 44) and Indian Ocean. Part of the CDW is upwelled south of the ACC where it undergoes transformation to lighter Antarctic Intermediate Water (AAIW) or denser Antarctic Bottom Water. In the North Pacific, no deep water is formed at the surface. Rather, part of the northward flow of deep and bottom water is returned southward as North Pacific Deep Water, with the high-silicate (and low-oxygen – not shown) tongue centred at a depth of about 3 km (Fig. 1.2.5, see Plate 1.2.5, p. 44). The high silicate and low oxygen concentrations of this water indicate it has not been in contact with the atmosphere for centuries.

The flow of NADW from the Atlantic to the rest of the world ocean must be replaced by waters entering the Atlantic through its southern boundary. Antarctic Intermediate Water enters through Drake Passage (Rintoul *et al.*, Chapter 4.6). This is referred to as the ‘cold water route’ in contrast to the ‘warm water route’ by which Agulhas Current water enters around southern Africa (Gordon, Chapter 4.7). Water also passes from the North Pacific to the Atlantic through the Arctic Ocean. The balance

between these three exchanges is thought to determine the salinity of the North Atlantic. The Indonesian Throughflow carrying warm water from the Pacific to the Indian Ocean (Fig. 1.2.7, see Plate 1.2.7, p. 44, Gordon, Chapter 4.7) is another important part of this global circulation.

The deep circulation is strongly influenced by bathymetry. The deep basins are separated from one another by oceanic ridges whose sill depth will determine the maximum density of the waters that move from one basin to another. The deepest passages between ocean basins are often relatively narrow (~ 10 km) and long (~ 100 km) and the transport through such passages is governed by stratified hydraulic conditions. At the time WOCE was being planned, many of the connections between basins had not been surveyed. Rather, their location and sill depths had been inferred by the differences between water properties between the basins. WOCE has made a significant contribution by quantifying the transport of these deep currents by the deployment of current meter moorings and repeat hydrographic sections and bathymetric surveys (Figs 4.5.3 and 4.5.4, Hogg, Chapter 4.5).

The main source regions of North Atlantic Deep Water (NADW) are separated from the rest of the North Atlantic and hence from the global ocean by the Shetland–Faroe–Iceland–Greenland ridge system. The water mass transformations that take place poleward of this ridge create water that, at the sill depths of 500 to 800 m, is denser than any other water found equatorward of the ridges. The water passes across the sill, cascades down the slope while undergoing intense mixing and entrainment (Saunders, Chapter 5.6). Through this descent, the volume transport of the current increases while the density of the water decreases.

These same intense flows and entrainment processes take place at the exits of the Mediterranean (Candela, Chapter 5.7) and Red Seas. In both cases, evaporation within the nearly enclosed basins produces salty and dense deep water. When this water exits the sea and begins its descent, the mixing and entrainment are so great that the descending water’s density is reduced to intermediate values and the newly produced water mass spreads into the ocean interior at depths of approximately 1000–1500 m.

Producing models that adequately represent the processes governing the thermohaline circulation is

a challenge to the ocean and climate modelling communities. Water mass transformations are dependent on correctly simulating buoyancy loss through heat and freshwater exchanges over several seasonal cycles as they participate in the gyre circulation. Flows over sills and the related entrainment and mixing involve processes that take place over horizontal scales of a few kilometres and vertical scale of order 100 metres. We are only just beginning to understand the complex spatial structure of deep-ocean mixing and its implications for the deep circulation. Finally, it must be remembered that the ocean actually produces its mean property transports as a summation of significant variability in both the wind-driven and thermohaline circulations on time scales of days to decades and longer.

1.2.4.3 Other buoyancy-driven flows

The North Atlantic is the saltiest of the world's oceans and the North Pacific is the freshest. This results in a change in sea surface elevation across the Arctic Ocean from the Pacific to the Atlantic. In addition to the low-salinity water that enters the Arctic from the Pacific through Bering Strait (Gordon, Chapter 4.7), the considerable input from the Siberian rivers, as well as from the MacKenzie River in North America, creates a low-salinity Arctic surface layer. This water exits the Arctic through Fram Strait and the various channels of the Canadian Archipelago and flows into the North Atlantic as the East Greenland and Labrador Currents, respectively. Both these currents are trapped along the shelf break and are driven in large part by their excess buoyancy compared with the waters found further offshore.

River runoff at mid to high latitudes produces low-salinity waters on continental shelves, and this drives equatorward flows over the continental shelves on the western sides of ocean basins, and poleward flows on the eastern side. Global ocean models and coupled ocean–atmosphere models do not presently have the vertical or horizontal resolution to resolve the shelf circulations and so their effect is usually crudely included through the various mechanism used to control the air–sea freshwater exchanges. The simulation of these circulations is important for the assessment of the potential impacts of climate change on near-coastal marine systems.

1.2.4.4 The role of sea ice in heat and freshwater transports

A significant element of the transfer of fresh water (and buoyancy) between the North Pacific and the North Atlantic via the Arctic Ocean occurs in the form of sea ice export out of Fram Strait. Sea ice fields are heterogeneous with ice thickness varying from zero in leads to 10 metres or more in ice ridges. Martin and Wadhams (1999) used satellite estimates of sea ice extent, concentration and drift rates to estimate the ice export through Fram Strait as $1530 \text{ km}^3 \text{ yr}^{-1}$ for 1994. They estimated the ice thickness through empirical relations between ice thickness, ice type and geographic location. Vinje *et al.* (1998) estimated the ice flux through Fram Strait from an upward-looking sonar over 6 years from August 1990 to August 1996. Their annual fluxes ranged from $2050 \text{ km}^3 \text{ yr}^{-1}$ in 1990–91 to a maximum of $4700 \text{ km}^3 \text{ yr}^{-1}$ in 1994–95 with a mean of $2850 \text{ km}^3 \text{ yr}^{-1}$. This mean value is close to the classical estimate of $2790 \text{ km}^3 \text{ yr}^{-1}$ based on ice production in the Arctic Ocean (Aagaard and Carmack, 1989). The export of low-salinity Arctic Surface waters through Fram Strait into the East Greenland Current and through the Arctic Archipelago into the Labrador Current are also significant contributors to this freshwater flux. The issues involved and particularly the response of these fluxes to the Arctic Oscillation are discussed by Dickson *et al.* (Chapter 7.3).

1.2.5 Ocean transport of heat, fresh water and carbon

The globe is heated by short-wave solar radiation and cooled by the emission of long wave radiation. However, the solar input exceeds the long-wave radiation at low latitudes and vice versa at high latitudes, requiring a global scale redistribution of energy. The atmosphere and the ocean together transport about 5 PW (1 PW is $1 \times 10^{15} \text{ W}$) of energy poleward. Bryden and Imawaki (Chapter 6.1, Fig. 6.1.3) indicate that this is approximately equipartitioned between the oceanic transport, the dry static atmospheric transport and the latent heat transport of fresh water (involving both ocean and atmosphere). Thus, understanding and quantifying the ocean heat and freshwater transport is critical to building reliable models of the climate system.

We generally think of three principal mechanisms by which heat and fresh water are transported by

the ocean. First, there is the overturning (or thermohaline) circulation. Cold deep and bottom waters generally flow equatorward and are balanced by an equal and opposite transport of warm surface waters. The Ekman transport associated with the direct wind forcing is an important component of this surface transport. Second, there are the gyre circulations operating in the horizontal plane. The intense western boundary currents of the subtropical gyres carry warm water poleward. After loss of heat to the atmosphere, the cooled water returns equatorward in the broad eastern return flows. Finally, time-variable ocean eddies can carry heat poleward.

As usual in ocean circulation, these three mechanisms are not independent and estimating the amount of heat carried by each depends on the definitions chosen. While all of the mechanisms operate simultaneously, the vertical overturning is dominant in the North Atlantic Ocean (Hall and Bryden, 1982). Indeed, the southward flow of deep cold water in the Atlantic results in a northward ocean heat transport at all latitudes in this ocean (Fig. 6.1.7, see Plate 6.1.7, p. 492, Bryden and Imawaki). In the North Pacific, where there is no deep water formation, the heat transport by the subtropical gyre is relatively more important (Bryden *et al.*, 1991). In the Southern Ocean, ocean eddies are thought to be the prime mechanism for the poleward heat transport (overcoming an equatorward transport associated with the northward advection of near-surface water; Rintoul *et al.*, Chapter 4.6).

In coarse-resolution coupled atmosphere–ocean climate models, the ocean modules have generally poorly simulated the observed ocean heat transport because they underestimate the strength of the gyres and do not model the eddy transports. As a result, large ‘unphysical’ flux corrections at the air–sea interface have been needed to maintain a ‘realistic’ climate. Improvements in the simulation of both the atmosphere and ocean heat transports in some recent models have reduced or even eliminated the need for flux corrections. This progress has resulted from several improvements in the ocean models as well as from increased resolution (see Wood, Chapter 2.3).

The ocean also stores significant quantities of carbon with about a third of the carbon dioxide released by the burning of fossil fuels sequestered in the ocean. The same mechanisms that store and transport heat and fresh water also store and

transport carbon. Wallace (Chapter 6.3) differentiates between the ocean transport of anthropogenic (or excess) carbon and the transport of natural (preindustrial) carbon. In preindustrial times the Atlantic Ocean is thought to have transported carbon southwards, whereas recent calculations indicate there is now a northward transport of anthropogenic carbon in the Atlantic.

1.2.6 Climatic and oceanic variability

In the previous sections, we have introduced the main physical processes important for understanding the ocean’s role in climate. We now briefly introduce a number of climate phenomena in which the ocean plays a significant role. For a more detailed description the reader is referred to other chapters in this book and the references cited.

1.2.6.1 El Niño–Southern Oscillation (ENSO)

This energetic coupled ocean–atmosphere phenomenon is perhaps the best-known example of inter-annual climate variability (Philander, 1990). Under normal conditions the trade winds maintain a pool of high-temperature water in the western equatorial Pacific. This warm reservoir drives intense atmospheric convection that provides abundant rainfall in such areas as Papua New Guinea and Indonesia. In simplest terms, El Niño occurs when a relaxation of the trade winds allows warm water to dominate the normally cool eastern equatorial Pacific, taking with it the zone of intense convection. El Niño’s local influences include increased rainfall and suppression of the coastal upwelling and marine productivity off the coast of Peru and dry conditions in the western equatorial Pacific. Because this equatorial Pacific convection is the principal driver of the large-scale meridional overturning circulation of the global atmosphere, ENSO has a near-global impact through changes in this atmospheric circulation.

ENSO events typically have a 2-year duration encompassing the warm El Niño and following cold La Niña phase, but they occur irregularly with repeat cycles as short as 2 years or as long as 10. The early 1990s were an unusually long period of moderately warm El Niño-like conditions in the eastern and central tropical Pacific (Trenberth and Hoar, 1996) followed by what was considered by some measures to be the largest El Niño event ever documented (Trenberth and Coughlan, 1998; Coughlan, 1999). This peaked at the end of 1998

with surface temperatures in the central equatorial Pacific some 3°C above the 1961–90 base level.

An operational system based on the TAO (Tropical Ocean Atmosphere)–Triton moored buoy array and upper ocean temperature measurements from volunteer observing ships is now in place to provide real-time monitoring of the state of the surface and subsurface equatorial Pacific Ocean and atmosphere (McPhaden *et al.*, 1998). Models developed over the past decade and using this data have demonstrated useful skill in predicting the evolution of the most recent (1997–98) event. For a more detailed description of ENSO, see Philander (1990) and the special issue of *Journal of Geophysical Research* (The TOGA Decade, June 1998).

A concern in interpreting the WOCE data set is the extent to which the evolution of the tropical Pacific during the 1990s imposed biases on the largely extratropical observations. Most of the one-time hydrographic sections in the Pacific were occupied between 1990 and 1994 whereas in the North Atlantic observations were spread throughout the 1990–98 period. The evaluation of such biases as may exist has yet to be made.

1.2.6.2 Other tropical sea surface temperature anomalies

Similar coherent responses of the equatorial oceans to atmospheric forcing (and related feedbacks) have been documented in the Atlantic (Mehta and Delworth, 1995) and Indian Oceans (Saji *et al.*, 1999; Webster *et al.*, 1999). In the Atlantic there are two competing hypotheses for the causes of the variability of the meridional temperature gradient (the Atlantic dipole). One view is that it is caused by regional ocean–atmosphere positive feedbacks (Chang *et al.*, 1997); the other that the anomalies on either side of the equator are due to independent processes in each hemisphere (Enfield and Mayer, 1997). Just as with El Niño, these equatorial anomalies have important impacts on the climate of the adjacent land masses (Birkett *et al.*, 1999; Markam and McLain, 1977; Bertacchi *et al.*, 1998). Thus both the development of *in-situ* observing systems and of predictive models are presently receiving considerable attention.

1.2.6.3 Extratropical anomalies – decadal and longer-term variability

Over both the North Pacific and North Atlantic there are clearly defined patterns of atmospheric

variability that show persistence over multiyear time scales. The most prominent of these are the Pacific Decadal Oscillation (PDO) and the North Atlantic Oscillation (NAO). Each can be regarded as a regional manifestation of the wider Arctic Oscillation (AO). The status of knowledge of these matters is summarized in the CLIVAR Implementation Plan (World Climate Research Programme, 1998).

In the North Pacific, there has been a general decrease in winter Sea Level Pressure (SLP) accompanied by increases in air and Sea Surface Temperature (SST) since the mid-1970s. When the variability within the ENSO frequency band is removed, the decadal variability within surface and subsurface temperature fields is an anomaly pattern that rotates clockwise around the North Pacific Gyre (Zhang and Levitus, 1997). The oceanic impacts arising from this variability has been discussed by Polovina *et al.* (1995).

For the NAO, the accepted index of its state is the normalized December–March atmospheric pressure difference between Lisbon and Reykjavik and this can be analysed in the instrumental record back to *c.* 1870. High values indicate a large pressure gradient and consequent enhanced westerly airflow carrying heat and moisture lost from the ocean across western Europe. During the period of WOCE observations the NAO has remained in a persistently high state. The oceanic impacts of the NAO are discussed at length in Dickson *et al.* (Chapter 7.3).

1.2.6.4 Changes in properties of deep and intermediate waters

Small changes in air–sea heat fluxes, such as might result from decadal climate variability and anthropogenic climate change, are difficult to observe. However, because the ocean is an integrator of short-term variability, these air–sea flux changes are manifested as changes in ocean temperatures and salinities. The WOCE data set serves as an important baseline against which past and future changes can be assessed. Comparison of WOCE sections with earlier International Geophysical Year (IGY) sections has revealed widespread and significant changes in water mass properties over decadal time scales. These are comprehensively summarized by Dickson *et al.* (Chapter 7.3) and indicate very large changes in the ocean heat storage. The maintenance of long time series, whether of hydrographic time series stations or of multiyear deployments of

current meter arrays (often with temperature sensors), have revealed both long-term trends (e.g. Joyce and Robbins, 1996) and abrupt changes in properties (e.g. Hogg and Zenk, 1997). However, a major challenge remains to link this long-period subsurface variability to changes in air-sea fluxes and to produce coupled atmosphere-ocean models that are capable of reproducing it.

1.2.6.5 Anthropogenic climate change

The oceans are crucial to simulating correctly the timing and regional impact of anthropogenic climate change. Because of their large heat capacity, the oceans are able to accumulate heat at rates that are comparable with the radiation imbalance resulting from the increasing concentrations of greenhouse gases. This accumulation of heat in the oceans will delay the impact of the warming in the atmosphere. Recent observations (and model simulations) have confirmed that large quantities of heat are being sequestered in the ocean (Sections 1.2.6.4 and 1.2.7.1; Dickson *et al.*, Chapter 7.3; Levitus *et al.*, 2000). Indeed, the observations of Levitus *et al.* (2000); (Fig. 1.2.8, see Plate 1.2.8, p. 44) indicate that the ocean warming represents a significant fraction of the enhanced greenhouse forcing over recent decades but is substantially larger than variations in solar forcing over this period.

Detection of changes in ocean properties are now beginning to be used to assess climate change simulations and to detect (and attribute) anthropogenic climate change in the ocean. For example, Wong *et al.* (1999, 2001) observe a freshening of the Intermediate Waters of the Pacific and Indian Oceans and an increased salinity in the shallower thermocline waters (Fig. 1.2.9, see Plate 1.2.9, p. 44). They attribute these changes to increased (decreased) precipitation minus evaporation at high (low) latitudes and suggest there may be an increase in the hydrological cycle as in simulations of climate change. Using coupled climate models, Banks *et al.* (2000) find similar water mass changes first emerge above the background variability in the south Indian and Pacific Oceans. On time scales of hundreds of years, the oceans will not be in balance with the changed radiative forcing and this will lead to regional changes in precipitation and possibly changes in climate variability such as ENSO (Timmermann *et al.*, 1999a). Coupled models do not yet agree in the detail of these changes but do reveal their sensitivity to the

representation of ocean processes (Hirst, 1998; Cubasch *et al.*, 2001).

1.2.6.6 Sudden climate change

Palaeoclimate records have demonstrated that the present equitable climate state under which civilization has developed alternates with prolonged glacial periods during which much of the landmasses poleward of 40–50° have been covered by continental ice sheets several kilometres thick. Modern methods have allowed finer and finer resolution of these palaeorecords; these higher resolutions have shown that the changes from glacial to interglacial conditions take place rapidly over decades to centuries.

The passage of ice ages and interglacial periods can be linked to the small changes in the solar energy received by the earth due to orbital changes (the Milankovich cycles). However, the solar energy only changes by a few per cent over millennia while the climate system changes from one state to the other over a few decades to a century. In addition, the palaeorecords have revealed rapid transitions during both glacial and interglacial periods. Surprisingly these transitions with temperature changes in Greenland of about 10°C occurred in the period of only a few decades (Fig. 1.2.10). The events have been categorized into two types. Dansgaard/Oescher events are sudden warmings of about 10°C over Greenland during glacial conditions. Heinrich events are linked to sudden surges

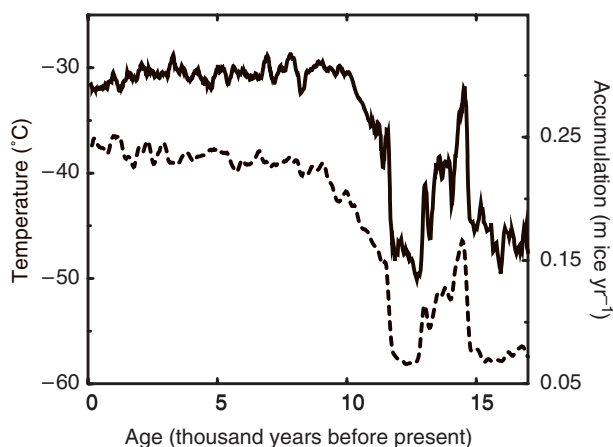


Fig. 1.2.10 Greenland temperatures (solid line) and accumulated precipitation (dashed line) showing the rapid (decade long) transition 11.6 thousand years ago at the end of the Younger Dryas event. Precipitation data from Alley *et al.* (1993).

of the Laurentide ice sheet into the North Atlantic, the extent of which are indicated by drop-stones in the ocean sediments. At the end of the last ice age when conditions had warmed to near-interglacial levels, the climate of the north Atlantic suddenly switched back to near-glacial conditions for more than a thousand years (the Younger Dryas event).

The challenge to climate scientists is to find a mechanism by which the climate system can move so quickly between two climate states. Studies of deep ocean sediments and ice cores as well as coupled climate model simulations have identified changes in the thermohaline circulation in the North Atlantic as the probable mechanism. The warm events are thought to have occurred when the thermohaline circulation penetrated further into the Nordic Seas, whereas the cold events coincided with times at which the thermohaline circulation has slackened, reducing the transport of warm water to the North Atlantic (Dansgaard *et al.*, 1993; Bond *et al.*, 1997; Alverson and Oldfield, 2000; Rahmstorf, 2001). The strength of the thermohaline circulation is related to the strength of the winter convection in the northern North Atlantic. This, in turn, is related to the degree of stratification of these northern waters through their accumulation of fresh water.

Model simulations by Manabe and Stouffer (1988) first demonstrated the existence of two stable states for the Atlantic thermohaline circulation. Similar results have since been obtained from a number of different climate models, most recently by Rahmstorf and Ganopolski (1999) and Ganopolski *et al.* (1998). The models used for such climate runs have coarse resolution and thus do not adequately (for an oceanographer at least) represent many key ocean processes. It is therefore difficult to determine whether our present climate system is close to the critical conditions for the switch to glacial conditions or distant. What is indisputable, however, is that on palaeo time scales the earth's climate has made such switches.

There have been major changes in the patterns of wintertime convection, in water mass properties and in sea ice thickness and extent in the northern hemisphere during recent decades (Dickson *et al.*, Chapter 7.3). Concerns have been raised that such changes may be a precursor of a rapid change in the thermohaline overturning of the North Atlantic Ocean.

1.2.7 Impacts of ocean climate

The distribution of the oceans' physical (and other) properties – the oceans' climate – is important in its own right as well as being central to the broader climate system. For example, ocean climate determines the productivity of the oceans (and hence impacts on fisheries), and ocean currents are important for both commercial and recreational use of the oceans. Here we introduce two important components of ocean climate – sea-level change and the impact of the ocean on inshore and shelf conditions.

1.2.7.1 Sea-level change

Climate variations over periods of decades to centuries produce changes in both globally averaged and regional sea level. Global-average sea-level change results from changes in the volume of the world's ocean as a result of changes in both the density and the total mass of the ocean.

On time scales of millennia, sea level has fluctuated by over a hundred metres as the volume of large ice sheets has varied. For example, sea level at the time of the last glacial maximum (about 20 000 years ago) was about 120 m lower than today (Fleming *et al.*, 1998). Most of the storage was in ice sheets over North America and Europe with lesser amounts in Greenland, Antarctica and elsewhere. While most of the melting occurred between 18 000 and 6000 years ago, there are indications that sea level has continued to rise slowly over the last several thousand years (Fleming *et al.*, 1998). The massive transfer of water from the ice sheets to the oceans at the end of the last ice age has resulted in ongoing isostatic land movements (post-glacial rebound) at rates of up to several mm yr^{-1} (e.g. Peltier, 1998). Changing density of the ocean as a result of warming of the ocean also changes global average sea level.

Sea-level variations over the last 200 years

Estimates of global-average sea-level change during the twentieth century are based principally upon the tide gauge data set of the Permanent Service for Mean Sea Level (PSMSL); (Spencer and Woodworth, 1993). A recent assessment is that globally averaged sea level has risen at the rate of between 1 and 2 mm yr^{-1} during the twentieth century (Church *et al.*, 2001). Douglas (1992) and Woodworth (1990) find no evidence for an

acceleration of sea-level rise during the twentieth century. However, an analysis of the few multi-century records indicate an acceleration of $0.3 \text{ mm yr}^{-1} \text{ century}^{-1}$ to $0.9 \text{ mm yr}^{-1} \text{ century}^{-1}$ (Woodworth, 1999).

One of the difficulties in establishing the global-average rate of sea-level change is the poor spatial distribution of tide gauges. However, satellite altimetry (Fu, Chapter 3.3) now provides near global and homogeneous measurements of sea level with respect to the centre of mass of the earth every 10 days. The most recent estimates of global average sea-level rise are $2.6 \pm 0.2 \text{ mm yr}^{-1}$ (Cazenave *et al.*, 1998), $3.1 \pm 1.3 \text{ mm yr}^{-1}$ and $2.5 \pm 1.3 \text{ mm yr}^{-1}$ (Nerem, 1999). These estimates used tide gauge data to remove small time-variable biases in the TOPEX/POSEIDON altimeter data, and made allowance for drifts in the water vapour corrections. The uncertainty of $\pm 0.2 \text{ mm yr}^{-1}$ for the Cazenave *et al.* estimate does not include allowance for uncertainty in instrumental drift but only reflects the temporal variations in measured global sea level. These variations correlate with global-average sea surface temperature, perhaps indicating the importance of steric effects through upper ocean heat storage (Cazenave *et al.*, 1998; Nerem *et al.*, 1999). The altimeter data suggest a rate of sea-level rise during the 1990s greater than the mean rate of rise for much of the twentieth century. Whether this indicates a recent acceleration, is the result of systematic differences between the two measurement techniques, or is merely the result of the short record is not yet clear. With high-quality *in-situ* data to support the altimeter observations, satellite altimeters will in the future be the prime means of determining global sea-level change.

Components of twentieth and twenty-first century sea-level rise

One of the major contributors to sea-level change during the twentieth and twenty-first centuries is ocean thermal expansion. Warmed surface waters are advected (subducted) into the ocean interior (Price, Chapter 5.3) such that the upper part of the water column is warmed (Sections 1.2.6.4 and 1.2.6.5; Dickson *et al.*, Chapter 7.3). As the ocean warms, the density decreases and thus the volume of the ocean increases. Salinity changes within the ocean have a significant impact on the local density and thus local sea level, but have little effect on the global-average sea level.

Evidence of large-scale ocean warming and thus thermal expansion at rates of order 1 mm yr^{-1} has come from comparing recent WOCE sections with historical data and time series stations. The evidence is most convincing for the North Atlantic, for which the longest records (up to 73 years) and most complete oceanographic data sets are available (e.g. Parrilla *et al.*, 1994; Joyce and Robbins, 1996; Arhan *et al.*, 1998; Joyce *et al.*, 1999) (Fig. 1.2.11, see Plate 1.2.11, p. 44). The warming also extends into the South Atlantic (Fig. 7.3.4, Dickson *et al.*, Chapter 7.3). The only area of substantial cooling is in the subpolar North Atlantic (Read and Gould, 1992; Dickson *et al.*, Chapter 7.3).

Observations from the Pacific and Indian Oceans cover a shorter period and thus estimates of change are less certain and may result from decadal variability rather than indicating a long-term trend. However, water mass properties indicate that these basin-scale changes are not solely a result of vertical thermocline heave but are consistent with surface warming and the resultant subduction of this water into the main thermocline (Wong *et al.*, 2001). The warming in the Pacific and Indian Oceans (Bindoff and McDougall, 2000) is confined to the main thermocline (mostly the upper 1 km) of the subtropical gyres. This contrasts with the North Atlantic, where the warming is seen at depths of 1000–2000 m. This is consistent with our understanding of the different basins described earlier – deep convection and larger meridional overturning in the North Atlantic contrasting with much shallower gyres in the Pacific. Most recently Levitus *et al.* (2000) and Antonov *et al.* (2001) have estimated global ocean heat uptake of 10^{22} J over the period 1955 to 1995 and a consequent global average rate of thermal expansion of 0.55 mm yr^{-1} .

Realistic simulation of ocean thermal expansion requires coupled Atmosphere–Ocean General Circulation Models (AOGCMs) of the climate system (Wood and Bryan, Chapter 2.3). A number of model simulations of the twentieth century have recently been completed using realistic greenhouse gas and aerosol forcings starting in 1900 or earlier. The results indicate that the average rate of change due to thermal expansion over the last hundred years was of the order of $0.3\text{–}0.8 \text{ mm yr}^{-1}$, and $0.6\text{–}1.1 \text{ mm yr}^{-1}$ in recent decades, similar to the observational estimates (Church *et al.*, 2001; Gregory *et al.*, 2001).

Additional factors contributing to recent changes in sea level include the melting of non-polar glaciers, changes in terrestrial water storage, and changes in the mass of the Greenland and Antarctic ice sheets, all stemming from climate change during the twentieth century and the aftermath of the last ice age.

The geographical distribution of sea-level change is principally determined by modified surface momentum, heat and freshwater fluxes with consequent alterations to the ocean density structure and ocean circulation. However, confidence in the regional distribution of sea-level rise is low as there is little similarity between results from different models (Church *et al.*, 2001; Gregory *et al.*, 2001).

1.2.7.2 Regional impacts of climate variability and change – links to shelf and inshore circulations

Properties of shelf waters and shelf circulation patterns have a rich spectrum of variability. This results from the multiplicity of forcing mechanisms for the shelf and coastal region. First, there is often a coastal discharge of water carrying nutrients and contaminants. This discharge is most often of fresh (light) water from rivers but can also be of dense water. Examples of the latter are the high-salinity water flowing out of the Mediterranean Sea (Candela, Chapter 5.7) and cold/saline water formed by air-sea-ice interaction on the Arctic and Antarctic shelves.

Second, atmospheric forcing of the coastal wave guide, primarily through along-shore wind stress, but also through across-shelf winds and surface heat and freshwater fluxes, is also an important driver of shelf circulation. Understanding the mechanisms of wind-induced circulation on the shelf, particularly through coastal trapped wave theory (see for example Brink *et al.*, 1987), has progressed significantly over the last two decades. The combined impacts of wind-induced upwelling and buoyancy effects can lead to complex three-dimensional, time-variable patterns both on and off the shelf. These circulations lead to considerable shelf/deep ocean exchange and remain a challenge to both observers and modellers (Hickey, 1998). Variability in both the coastal and atmospheric forcing is itself related to seasonal, interannual and decadal variability in climate.

Third, offshore ocean phenomena are a significant driver of circulation patterns on the shelf

and in the near-coastal region. These phenomena include ocean swell, tides (including the generation of baroclinic tides over topographic features), deep ocean eddies impacting the shelf, seasonal, inter-annual and decadal variability in the offshore region and, of course, the mean offshore conditions. Often the water properties on the shelf (temperatures, salinities, nutrient concentrations) are largely determined by the offshore conditions, but the processes of exchange between the deep ocean, the shelf and the near-shore region are poorly understood. The offshore influence is especially strong when the shelf is narrow and/or there is an energetic offshore current such as a western boundary current. An overview of the dynamics of offshore forcing of shelf regions is given by Brink (1998) and a number of examples of offshore forcing of shelf conditions can be found in the volume on the Global Coastal Ocean (Brink and Robinson, 1998).

One of the classic examples of offshore forcing of shelf circulation is the generation of instabilities on the inshore edge of the Gulf Stream (Boicourt *et al.*, 1998; Brink, 1998). These instabilities are the dominant source of variability on the outer shelf and reach 40 km inshore from the shelf break. They also drive nutrient-rich cold water, upwelled from below the Gulf Stream, onto the shelf. These vigorous motions are a major contributor to the exchange of oceanic and shelf waters and provide the main nutrient supply for the continental shelf (Lee *et al.*, 1991). Similarly, the East Australian Current is sometimes the dominant factor driving shelf circulation off eastern Australia. This can be through a rapid flushing of the shelf as the current spills onto the shelf when the East Australian Current or one of its eddies impinges on the shelf (Huyer *et al.*, 1988).

Another example of offshore forcing comes from the west coast of North and South America. Kelvin waves travelling eastwards in the equatorial wave-guide encounter the shelf, refracting energy into northward and southward travelling disturbances in the coastal wave guide. These disturbances are observed to travel thousands of kilometres (Brink, 1998) directly impacting ecosystems.

There are a number of documented examples where higher trophic level shelf productivity appears to be influenced by offshore conditions. For example, Pierce and Phillips (1988) demonstrated that there is a strong link between coastal sea level at Freemantle (western Australia) and the

rock lobster fishery. During non-El Niño years, they found that coastal sea level is high and that recruitment of lobster *pueruli* to the near-shore nursery grounds is high. They suggest that in non-El Niño years high coastal sea levels are indicative of a large cross-shelf sea-level slope and a strong Leeuwin Current over the continental slope. During El Niño years, coastal sea level falls and the inferred transport of the Leeuwin Current is less. Hydrographic data indicate that during these periods of low sea level, shelf waters are cooler and more saline, consistent with a weaker southward transport of tropical waters by the Leeuwin Current. The exact mechanism linking oceanographic conditions to recruitment is unclear but the origin appears to be in the physical environment. In European waters there has been a demonstrated link between the offshore transports in the Northeast Atlantic since 1975 and changes in the distribution and abundance of zooplankton species in the North Sea as revealed by the continuous plankton recorder surveys (Reid *et al.*, 1998; Holliday and Reid, 2001). A link with large-scale offshore temperature changes has also been deduced.

As a result of multiple forcing factors in the shelf region, interannual/decadal variability is often obscured by high-frequency events. Thus, determining the impact of climatic variability or change on the shelf (where much of our use of the marine environment and where most marine environmental degradation occurs) is a challenging task given our generally sparse ocean data sets. Understanding the response of the shelf circulation and its productivity to climate variability and change will require coupled models of the shelf, at the appropriate vertical and horizontal resolution, and the open ocean, as proposed by Smith (Chapter 7.4).

1.2.8 Conclusion

During the planning phase of WOCE, many of the features of the ocean circulation were known only qualitatively. Despite the ocean's profound importance for predicting long-term climate variability

and change, we are only now gaining a quantitative understanding of the oceans' mean state and of several aspects of ocean variability. This quantitative understanding has come about through coordinated high-quality *in-situ* observational efforts (e.g. King *et al.*, Chapter 3.1), development of new *in-situ* (e.g. Davis and Zenk, Chapter 3.2; Schlosser *et al.*, Chapter 5.8) and satellite (Fu, Chapter 3.3; Liu and Katsaros, Chapter 3.4) observational techniques, the widespread distribution of this data (Lindstrom and Legler, Chapter 3.5) and rapid development of computer models (Boening and Semtner, Chapter 2.2; Wood and Bryan, Chapter 2.3).

At present our quantitative understanding of ocean variability is strongest for the relatively short-lived ENSO events in the heavily sampled equatorial Pacific and for these we have developed a predictive skill. We now are beginning to explore other, longer-period, aspects of ocean variability (Dickson, Chapter 7.3) and establish sustained observing systems (Smith, Chapter 7.4). Through analyses of these data we might reasonably expect to discover other modes of ocean variability and understand their links to the atmosphere. Better climate predictions will require our understanding of ocean variability and its interaction with the atmosphere on a broad range of spatial and temporal scales to improve. Overcoming the predictability barrier will require the continued development of *in-situ* and satellite observing systems (Smith, Chapter 7.4), improved numerical models (Willebrand and Haidvogel, Chapter 7.2) and the assimilation of the data in models (Talley *et al.*, Chapter 7.1), and the closer linking of the physical system to the important biogeochemical aspects of the ocean and climate.

Acknowledgements

JC acknowledges the support of the Australian Antarctic Cooperative Research Centre and CSIRO. This article is a contribution to the CSIRO Climate Change Research Program.

1.3

The Origins, Development and Conduct of WOCE

B. J. Thompson, J. Crease and John Gould

1.3.1 Introduction

The late 1970s saw the end of a decade or more of experimental and analytical studies of the eddy field in limited parts of the deep ocean (Robinson, 1983). Numerical models, bounded by the power of available computers, were probing in similarly limited regions of the ocean basins. We were excited about what was being learnt and could see all manner of questions that needed to be addressed about the physical processes. Satellite altimetry was beginning to make an impact. There were more than enough questions of importance to keep us going in our traditional individualistic way, interspersed with the occasional grand expedition. However, there was a groundswell in the 1970s, both within and outside the community, that we should be paying more attention to the relevance of our work to the world at large. (Smaller-scale processes such as surface wave research had made this transition much earlier, supported by an already perceived practical need and by largely classical fluid dynamics.) Though there were other important strands of enquiry of practical interest, a growing concern for the global impact of climate change presented a remarkable opportunity for a refocusing of large-scale research towards global scientific problems.

In this chapter we attempt to describe in a personal, partial and informal way the evolution of a great experiment that, through a haze of (necessary) acronyms and some bureaucracy, emerges as it was started, as a sustained and we believe

successful joint endeavour by many laboratories and individual scientists from many nations.

1.3.2 Large-scale oceanography in the 1960s and 1970s

At the start of the 1960s, the evidence for an active dynamical deep ocean was just emerging following the year-long observations made by the *Aries* expedition in 1959–60 in a small area of the western Atlantic. Previously the notion of a sluggish deep ocean had prevailed, primarily through the lack of direct current observations. Indeed, the original plans for the expedition, by Swallow and Stommel, envisaged the tracking of the newly developed Swallow floats individually for up to a year in the very local area.

Analytical studies of linear large-scale ocean circulation problems (gyre circulation, westward intensification, thermohaline circulation) had perhaps proceeded faster, uninhibited by observational knowledge of the pervasive eddy field.

In the 1960s, the community was gearing itself up with the new instrumentation needed to explore the picture tentatively being revealed of an eddy-populated deep ocean. Moored long-term current meters were designed in Europe and North America. Conductivity-Temperature-Depth (CTD) probes of potentially high accuracy were also being tried at sea. At the 1969 Joint Oceanographic Assembly in Moscow, there was a prediction that we were entering a decade of ‘automated unreliability’ as

new technologies replaced the tried-and-tested traditional methods. There turned out to be some truth in this, but confidence was building sufficiently for some in the community to embark on a series of experiments in the 1970s, which eventually led to WOCE.

In 1970, Soviet scientists carried out POLY-GON-70 (POLYGON meaning 'Training Field') in the subtropical northeastern Atlantic using arrays of moored current meters and CTDs. In 1971–74, the Mid-Ocean Dynamics Experiment (MODE) was a concerted attack on the dynamical description of the full-depth open ocean at the mesoscale. MODE (MODE Group, 1978) was an important stepping stone scientifically, technically and managerially.

Scientifically, the MODE core experiment over several months in spring 1973 concentrated on a patch of the Atlantic. It was centred on 28°N 71°W, measured 4° on the side, and was partly over rough and partly over smooth topography. It was not far from the *Aries* site. The experimental area was big enough that within the duration of the experiment the velocity and density fields could be intensively studied during the passage and evolution of an eddy.

Technically, new observational tools were available. Deep-drifting neutrally buoyant SOFAR (SOund Fixing And Ranging) floats, CTDs and moored current meter arrays, while still subject to frustrating failure, were matched in accuracy to the nature and scale of the phenomenon. The ships were fitted with the new, rapidly improving Transit satellite navigation system. (Oceanographers have been, and continue to be, among the leaders in exploiting the last iota of available accuracy from navigational systems.)

Managerially, MODE was a largely successful experiment in giving the responsibility for detailed planning to a scientific council of investigators from the participating institutions. The International Geophysical Year (IGY) in 1957–58 had been a major collaborative programme but had not required the extraordinarily close working relationship that developed on a day-to-day basis between the participating laboratories. MODE, US-led but with participation also from the UK, was a foretaste of new ways of working. For the first time modellers participated actively in a field programme's design and execution, and also studied the impact of equipment failure on the value of the results. This dialogue between observers and

modellers, though sometimes fraught, has had a lasting and beneficial impact on the way large-scale oceanographic studies have developed.

Following MODE, a series of POLYMODE experiments in the North Atlantic by US and Soviet scientists established the pervasiveness, spatial variability and probable importance of the eddy field in the transfer of properties (Collins and Heinmiller, 1989).

1.3.3 Ocean research and climate

The meteorological community, under International Council of Scientific Unions (ICSU) and World Meteorological Organization (WMO) auspices, had established in 1966 the Global Atmospheric Research Programme (GARP) with two basic objectives:

- to improve the predictability of weather out to several weeks; and
- to understand better the physical basis of climate.

The first of these objectives dominated the planning and fieldwork in the 1970s. In consequence, the meteorological interest in the ocean in the First GARP Global Experiment (FGGE) was in large part limited to the reporting of sea surface temperature and pressure, these being the parameters of greatest importance for work on weather prediction. A positive outcome, which greatly influenced later WOCE planning, was increased interest in the use of drifting buoys as sensor platforms. Drogues on the buoys slowed their wind-induced drift and thus allowed, as an oceanographic bonus, estimates to be made of surface currents. The French *EOLE* satellite system was used in early experiments and later drifters used in the Southern Ocean during FGGE were the earliest large-scale operational use of random access satellite telemetry and buoy location techniques through the TIROS-n satellite. They provided essential surface meteorological coverage in an otherwise data-sparse region. The technique is now embodied in the commercial ARGOS location and data transmission system used today. The use of the ARGOS system with the profiling Autonomous Lagrangian Circulation Explorer (P-ALACE) floats (Davis and Zenk, Chapter 3.3) in the later years of WOCE is transforming the ability of oceanographers to collect synoptic subsurface data on the large scale.

1.3.3.1 The build-up to WOCE – Scientific Committee on Oceanic Research (SCOR) initiatives

Although the emphasis at the time of FGGE was on the first objective of GARP, oceanographers were starting to draw attention to the role that the oceans have in climate prediction. Interaction between oceanographers and the Joint Organizing Committee (JOC) of GARP intensified in early 1973. They saw the opportunities that the global network being developed for FGGE presented for extending knowledge, at least of the near-surface layers of the ocean. The Scientific Committee on Oceanographic Research (SCOR), through its Working Groups, played a key role in these international developments. One in particular, Working Group 43, chaired by Gerold Siedler, on 'Oceanography Related to GATE' (GARP Atlantic Tropical Experiment, our first encounter in oceanography with a second-order acronym!) was the first to develop and oversee an international oceanographic field programme within a major meteorological experiment. The scales of the design broadly spanned the synoptic scales in the atmosphere and the ocean. The oceanographic component (Düing, 1980; Siedler and Woods, 1980) was importantly the first significant step towards cooperative studies of the effect of ocean processes on climate. A meeting of the SCOR Executive Committee in 1974 in Canberra led to a significant rearrangement of SCOR's Working Groups that reflected the developing importance of climate questions. WG34 under Allan Robinson became 'Internal Dynamics of the Ocean', which was to become the focus of general ocean circulation modelling concerns. WG47 under Henry Stommel on 'Oceanographic Activities in FGGE' exploited the opportunities for oceanographic research, and WG48 directly addressed 'The Influence of Ocean on Climate'.

Discussions in Stommel's group led to the establishment in 1976 of the Committee on Oceanography and GARP (COG), which was to 'identify, stimulate and coordinate international programmes linked to the activities of GARP'. COG recognized immediately that the breadth of the problems related to climate change and variability included time scales longer than those with which GARP was concerned. Also at this time, WG48 (consisting de facto of the Chairman, Henry Charnock, and the JOC past Chairman, Bob Stewart) was also expressing the view that the problem

of climate research went well beyond the objectives of GARP and that 'perhaps a major new initiative by ICSU was required'.

By 1977, the President of SCOR was writing to the Secretary-General of WMO, drawing attention to the need to consider the impact of ocean variability on climate as well as the atmosphere's impact on the ocean. With such an expanded horizon, it was appropriate for SCOR to join in the planning of the proposed 1979 World Conference on Climate Change and Variability. At this time, SCOR WG47 was proposing to COG a major field experiment in equatorial dynamics over at least 2 years, and also suggesting that it might be an opportunity for oceanographers to invite meteorologists to take part in a predominately oceanographic experiment.

By the mid-1970s, sufficient momentum existed within both the scientific community and the international organizations that sponsored and promoted their activities to launch an investigation of the ocean's impact on climate. Studies began of the observational systems that would be required for monitoring and prediction of climate variability on time scales from weeks to decades. SCOR, JOC, the Intergovernmental Oceanographic Commission (IOC) and WMO were all involved through the creation of panels and task teams and the holding of conferences to study various aspects of the problem.

1.3.3.2 The planning for WOCE – Committee on Climatic Changes and the Ocean (CCCO) initiatives

In 1978, WMO and IOC asked their scientific advisory bodies JOC and SCOR to convene a specialist meeting on the 'Role of the Ocean in the Global Heat Budget' to consider:

- a USSR proposal for a research programme looking into the processes of air-sea interaction for the purpose of developing long-term weather and climate theory. The programme would focus on Energetically Active Zones (EAZOs); and
- scientific problems related to extended range forecasting and climate.

The meeting, chaired by Bob Stewart, and held in Kiel, actually discussed four main topics:

- ocean circulation and heat transport;
- the USSR proposal (also known as SECTIONS);

- a Pilot Ocean Monitoring Study (POMS); and
- a proposed conference on the impact of climate on global change.

The latter eventually became the JSC/CCCO Study Conference on Large Scale Oceanographic Experiments in the WCRP, which was held in Tokyo in May 1982, with Allan Robinson in the chair.

Taking its lead from COG and adopting an even wider view, SCOR decided, in November 1978, to establish an interdisciplinary Committee on Climatic Change and the Oceans with Roger Revelle as chairman and invited the IOC to co-sponsor the committee. This the IOC agreed to do early in 1979. Meanwhile, WMO and JOC were reaching a similar conclusion; that an international mechanism was needed to determine to what extent climate could be predicted and the extent of anthropogenic influence on climate. The mechanism was to be the World Climate Research Programme (WCRP), co-sponsored by WMO and ICSU and dealing with time scales from several weeks to decades. The agreement to establish the WCRP was signed by WMO and ICSU in October and November 1979, and included the establishment of the Joint Scientific Committee (JSC) to oversee the programme. This, in effect, metamorphosed GARP into the WCRP.

By the end of 1979, the ocean community considered the situation very promising for the development of the oceanographic aspects of the WCRP. There was widespread interest in the large-scale circulation of the ocean. At a critical meeting in Miami in November to consider a Pilot Ocean Monitoring Study, Carl Wunsch made a convincing scientific case for a global ocean circulation experiment. The meeting proposed moving forward with the development of observational techniques and the design of networks, while simultaneously considering the feasibility and design of global experiments. This was a bold decision, relying on significant improvements in satellite sensors. The recently flown (1978) SEASAT mission gave grounds for optimism since in its short life it had demonstrated a much-improved precision in altimeter measurement of sea surface topography. The year-on-year trend of increasing computer power provided justification for expectation that the very large computer resources needed for eddy-resolving ocean models would soon be available.

The first meeting of CCCO was held immediately following the POMS meeting, also in Miami. That meeting asked the CCCO panel on 'Theory and Modelling of Ocean Dynamics Relating to Problems of Climate Research' and the CCCO/JSC Liaison Panel to take the lead on a global ocean circulation experiment (soon to be dubbed WOCE). It was the latter that moved the WOCE concept through the international scientific coordination bodies during 1980 and early 1981.

As well as paving the way for the development of WOCE, the Panel, following suggestions from the POMS meeting, instituted the CAGE feasibility study under the leadership of Fred Dobson (Dobson *et al.*, 1982). This was to consider the feasibility of a detailed study of the heat budget in a 'cage' over and in the North Atlantic ocean on a climatological time scale aiming for an estimate of oceanic meridional heat transport with an accuracy of 20%. The report provides valuable insights into the problems involved in the direct measurement of the transport, in estimates made through combination of inward radiation and flux divergence in the atmosphere, and those from area integrals of the sea surface heat flux.

Over the period 1979–81 CCCO had before it proposals for CAGE, WOCE and the Soviet SECTIONS Programme. Each would, if they could be implemented in full, entrain the resource of many laboratories. SECTIONS, though strongly pressed by Soviet scientists at meetings, did not find favour with the rest of the community. The programme assumed a concentration on a number of areas known as 'energetically active zones' such as the Gulf Stream and Greenland–Iceland–UK Gap. Other scientists believed that this intensive study of specific areas was unlikely to yield the scientific return to match the effort needed. CAGE, in the end, fell short of its overall goal through the inability to measure the horizontal fluxes across the atmospheric boundaries. Therefore, as a combined oceanographic and meteorological experiment it was felt to be premature. WOCE, on the other hand, subsumed much of the oceanographic thinking of CAGE and moved for the first time from a regional to a global view of ocean dynamics.

The significance of the POMS deliberations for the study and prediction of climate variability can be clearly recognized in the subsequent programmes that benefited from new and improved methods for measuring the ocean. WOCE and

TOGA (WCRP's Tropical Ocean Global Atmosphere Study) were the early beneficiaries but POMS also led to the Ocean Observing System Development Programme (OOSDP), organized for CCCO by Francis Bretherton, which addressed the wide range of oceanographic and atmospheric measurement systems that needed either reinforcement or design and development. The OOSDP (Intergovernmental Oceanographic Commission, 1984) was later turned into the JSC/CCCO OOSD Panel led by Worth Nowlin. The Panel produced a valuable series of scientific reports that led to a design for an ocean observing system for climate, more specifically the climate component of the Global Ocean Observing System (GOOS). Most recently, the Climate Variability and Predictability Study (CLIVAR) Implementation Plan (World Climate Research Programme, 1998) to some extent builds on the observing systems that became prominent during WOCE and TOGA and the proposals emanating from the OOSD Panel's report.

The expectation that new information over all (or large parts) of the ocean from satellites would be available by the late 1980s, meant that coordination of satellite missions was desirable and that the requirements of the oceanographic and meteorological communities should be taken into account. JSC and CCCO called a meeting in Chilton, UK, in January 1981 to identify how (with some adjustment to schedules, orbits and sensing capabilities) projected satellites could form an essential and complementary set of observing systems to the planned *in-situ* oceanographic experiments (World Climate Research Programme, 1981). The NASA, ESA and NASDA space agency participation (from the USA, Europe and Japan) ensured that they were aware of the scientific needs. The recommendations of the meeting were addressed immediately by the JSC and CCCO. Both gave priority to an altimeter with sub-decimetre accuracy, to determination of the geoid, and to scatterometer measurements of the surface wind field as well as identifying a host of other critical satellite coordination issues. CCCO considered that the 5-year mission duration suggested by the meeting was barely adequate to define the annual cycle in many parts of the ocean. They also noted that many important oceanographic phenomena had return intervals longer than 5 years. Hence they requested extended satellite coverage.

Michel Lefebvre (personal communication) recalls that, at Chilton, the US proposal was discussed for TOPEX, a satellite carrying an optimized sub-decimetre precision altimeter. Moreover, in January 1978, a European group meeting in Schloss-Elmau (European Space Agency, 1978) had proposed an altimeter mission to ESA. Neither proposal gained immediate acceptance from the agencies. The European proposal eventually became incorporated in the successful but less-optimized multisensor ERS missions, while TOPEX was in competition with wind measuring and to a lesser extent, geodetic missions. Both these missions would contribute valuably but TOPEX was pivotal to WOCE's success.

Later in 1981, French scientists won the approval of Centre National d'Études Spatiales (CNES), and strong ministerial support, for POSEIDON, an altimeter to be flown on the French SPOT satellite. SPOT also carried a new global tracking system DORIS dedicated to, and optimized for, altimetry using an onboard receiver and a worldwide network of 50 stations. It is extensively used also for gravity field improvement. The case for a dedicated altimeter mission to make a unique and vital contribution to WOCE was immensely strengthened as France and the USA in the succeeding years developed a joint proposal for a TOPEX/POSEIDON (T/P) satellite to be launched on a French Ariane rocket. It would carry US and French altimeters and tracking systems in an orbit precisely optimized for WOCE. The Memorandum of Understanding between the two countries, signed in 1987, envisaged laying the foundation for a follow-on after T/P (Michel Lefebvre, personal communication; Ratier, 1988).

In May 1981, CCCO established a WOCE Design Options Study Group chaired by Francis Bretherton. It was charged with reporting to JSC and CCCO (after presenting the preliminary plans to the Tokyo Conference on Large-Scale Oceanographic Experiments in the WCRP, in May 1982). Some significant points raised by CCCO were that:

- altimetry with simultaneous scatterometry was essential;
- variability of sea surface topography should be easier to measure and be of more significance for climate variability than the mean;
- many areas of the oceans needed to be covered with a network of surface to near-bottom

- high-quality, complete modern hydrographic stations including temperature, salinity and nutrients; and
- appropriate methods for obtaining *in-situ* measurements of deep currents, needed for verification purposes, should be looked into.

Having heard the basic strategy for WOCE as formulated by the Design Options group, the 3rd meeting of CCCO in March 1982 offered these further observations:

- the importance of direct current measurements at the equator and over continental slopes;
- the importance of including global wind stress data;
- the advantage of combining satellite altimeter data with tide gauge data; and
- that deep-sea pressure gauges would be needed to support altimeter measurements.

The stage was now set for presentation of WOCE to a wider scientific community at the Tokyo conference (World Climate Research Programme, 1983).

The conference concluded that WOCE would be crucial for understanding the role of ocean circulation in the behaviour of the physical climate system and would be a major contribution to meeting the objectives of the WCRP. The conference recommended that the WCRP, JSC and CCCO create a Steering Group to review and guide the development of WOCE as a major activity within the WCRP. It was also recommended that the Steering Group, as a matter of priority, carry out detailed studies of such matters as:

- the appropriate mix of observing and assimilation systems needed to achieve the WOCE objectives;
- evaluation of the critical gaps of existing knowledge; and
- the actions needed to fill such gaps.

The conference pointed out that further specification of the required satellite systems (precision altimeters and scatterometers) was of particular urgency. Explicit requirements needed to be developed for forwarding to the various satellite agencies explaining:

- the desired and minimum accuracy needed;
- the desired orbital (sampling) parameters;
- the possible compromises stemming from a multinational but coordinated programme; and

- the value that would be gained by WOCE of having accuracy or sampling beyond the minimum levels needed (and up to the levels that were seen as desirable).

Finally, the notion of an experiment aimed at both the general circulation of the ocean and water mass transformation was welcomed by the conference and emphasized in the conference report. In particular, the list of observational foci of WOCE specifically refers to the determination of ventilation times and rate of water mass conversion. The discussions in Tokyo added to the list the need to make observations of the large-scale aspects of the seasonal cycle. This included the depth of the late-winter convective overturning and the study of broadband inherent variability.

In late 1982, the CCCO and JSC officers agreed, based on the Bretherton group report and the Tokyo conference conclusions and recommendations, to collaborate in establishing a WOCE Scientific Steering Group (SSG). Early in 1983, CCCO and JSC established the WOCE SSG and appointed Carl Wunsch as its chairman. WOCE had now become the principal oceanographic contribution to WCRP stream 3 on the prediction of decadal variations of climate.

1.3.4 Implementation of WOCE (SSG initiatives)

The first informal meeting of the WOCE SSG took place appropriately during a meeting on satellites at San Miniato, Italy, in April 1983, but the first formal meeting of the SSG was at Woods Hole in August that year. This immediately followed a US National Academy of Sciences Workshop on 'Global Observations and Understanding of the General Circulation of the Ocean' (National Academy of Sciences, 1983) at which Carl Wunsch presented an outline of WOCE (Wunsch, 1983).

The next 5 years were a period of intense activity, refining the scientific objectives through a series of workshops, and entraining the enthusiasm of both national funding authorities and scientists and producing both a Science Plan (World Climate Research Programme, 1986) and an Implementation Plan (World Climate Research Programme, 1988a,b). This planning phase culminated in the International WOCE Scientific Conference at the end of 1988 (World Climate

Research Programme, 1989a). Its purpose and achievement was to present the Implementation Plan to national authorities, to gain their interest, and to gauge their commitment. Thirty-one countries announced their intention to commit resources. By the end of the field phase, we could count the actual involvement of 22 countries, the contributions from which varied from more than 50% by the USA to small but valuable local contributions by small countries.

In this review we have chosen to pick out some highlights in the planning process that at the time were seen to be important, or in retrospect have become so.

The first three meetings of the SSG through early 1985 were critical in firmly establishing the objectives of the experiment and concluding that these could not be achieved by a generalized expansion of large-scale oceanography. This view was encapsulated eventually in the now much-repeated statement of the two goals of WOCE:

- To develop models useful for predicting climate change and to collect the data necessary to test them; and
- To determine the representativeness of the specific WOCE data sets for the long-term behaviour of the ocean, and to find methods for determining long-term changes in the ocean circulation.

This emphasis was not particularly limiting on the scope of the field programmes that would emerge. Indeed the initial WOCE working groups on surface forcing, reference level velocity, critical aspects of temperature/salinity distribution, tracer distributions and inputs, variations in diapycnal mixing, and depth of winter mixing read like a catalogue of problems in physical oceanography at the time. A careful reading of the WGs' terms of reference (SSG-1) is necessary to understand the focus provided by the WOCE goals. The working groups' reports contributed to a further refinement of goal 1 of WOCE to become:

To determine and understand:

- the large-scale fluxes of heat and fresh water and their divergences;
- the dynamic balance of the circulation and its response to changing surface fluxes;
- components of variability on months to years and megametres to global scale; and

- volume and location of water masses with ventilation times of 10–100 years.

The working groups were all, in one way or another, asked to pay close attention to the ability of existing measurement systems to meet the defined accuracy requirements. If such requirements could not be met, they were asked to consider if they could realistically be met by developing technology during the period of WOCE. The absolute priority for the success of the experiment was, to have at least one dedicated altimetric satellite mission, coincident with a global hydrographic survey of higher accuracy than ever before, of sufficient along-track resolution to avoid aliasing of the eddy field.

The TOPEX/POSEIDON satellite, while ultimately highly successful, provided anxious moments up to the time of launch when the durability of some of its batteries came into question. The SSG encouraged the launch of a geodetic satellite that would provide a greatly enhanced reference geoid to allow inference of the absolute topography of the sea surface. Coincidence in time was not a requirement, but the SSG foresaw the possibility of 'data decay' if the geoid and altimetry observations were too far separated in time. That satellite has yet to be launched. On the other hand, technical developments, some driven directly by the requirements of the programme, added greatly to the success of the experiment. The *in-situ* development with potentially the greatest direct impact on a global scale was the Autonomous Lagrangian Circulation Explorer (ALACE) programme of floats to measure the deep reference velocities and described elsewhere in this book (Davis and Zenk, Chapter 3.2). While RAFOS (reversed SOFAR) was building on the established SOFAR acoustic navigation technology for floats and would contribute greatly to the dynamical studies in the North and South Atlantic, ALACE was a developing technique. For ship-based velocity measurements, Global Positioning System (GPS) navigation and differential techniques permitted the hoped for, but in 1985 uncertain, development of Acoustic Doppler Current Profilers (ADCPs) as a valuable underway and on-station tool for the measurement of deep velocity profiles (King *et al.*, Chapter 3.1).

The Numerical Experimentation Group (NEG), befitting the central role of models in the project's goals, became the first of WOCE's 'permanent'

working groups. From the beginning, a strategy was adopted that explored both inverse and direct models. At the time, in the mid-1980s, eddy-resolving models were evolving only at the basin scale though the NEG was predicting the availability of global eddy-resolving models soon after the end of the twentieth century. The wish for a detailed input by modellers into experimental design, first stated in MODE and reiterated in NEG's first report, remained elusive.

With the reports of the working groups available, the SSG identified three major components (Core Projects – CP) of the programme:

- CP1, the Global Description, provided the unified framework for a global set of *in-situ* and satellite observations to meet the first and last of the Goal 1 objectives;
- CP2, on Intercean exchanges (later limited to exchanges with the Southern Ocean), was set up in recognition of the distinct scientific and logistic problems of the Southern Ocean; and
- CP3, in which dynamical models would be built and tested against an intensive set of observations on a basin scale before applying the models to the global data set.

Week-long workshops were held during 1986 to complete the initial planning of the CPs. The workshops were well attended (about 50 scientists from 13 nations at CPs 1 and 2, and from nine nations at CP3).

The CP1 workshop reached a consensus as to what should be included in the global programme of measurements to meet WOCE objectives. Although they expected changes to details, they felt the scope of CP1 would remain unchanged throughout WOCE's lifetime. This has generally been proven true.

The CP2 workshop took advantage of earlier Southern Ocean studies and reviews such as SCOR's Working Group 74 report on 'The General Circulation of the Southern Ocean: Status and Recommendations for Research'. The Workshop focused on:

- Antarctic Circumpolar Current (ACC) dynamical balance and heat and mass transport;
- meridional transports through and out of the Southern Ocean; and air-sea-ice interaction.

The outcome of the discussions of these processes became the basis for the initial CP2 implementation plan.

The CP3 workshop was unable to complete many aspects of the planning. With the exception of studies of the deep circulation in the Brazil Basin, it was clear that there were many reasons for locating most of CP3 in the North Atlantic. The workshop examined processes in the surface layer, interior and within the deep circulation needing consideration and suggested some experiments. However, a problem existed with resources and with coordination that would last until the mid-1990s and the advent of the predominantly US Atlantic Climate Change Program (ACCP) (Whitburn, 1994).

The scope of the hydrographic programme as envisaged in CP1 and CP2, with their long transoceanic meridional and zonal sections and requirement for tracer observations, was clearly going to stretch the capabilities of existing research ships. Typically these ships were limited to cruises of 4 weeks duration and a scientific party of 20. The WOCE SSG for some time worked on the idea of a Research Vessel (RV) WOCE, a dedicated and internationally managed shipboard operation to accomplish these major sections. Eventually a less centralized approach prevailed by exploiting existing individual nationally managed resources coordinated by a WOCE Hydrographic Programme Planning Office (WHPO). Even so, major refits and lengthening of research ships took place to accommodate the scientific crews of 30 or more and cruise duration of 6 weeks that the WHP required. The Indian Ocean component of the WOCE programme in 1995 came closest to the RV WOCE concept with the successful use of a single US funded ship, RV *Knorr*, and technical support from a single group for the bulk of the sections.

WOCE took the integration of observations started with MODE and POLYMODE into a new era by drawing on a very wide range of techniques. Their great scope led to some important decisions, sometimes preceded by heated debate. This is typified by the decision to use a range of geochemical tracers, particularly those with time-dependent characteristics derived from radioactive decay or the variability of their source function. It was based on their expected utility in clarifying the pathways and circulation rates in the interior of the ocean. They were expected to extend greatly the level of understanding beyond that possible using only the traditional base of temperature,

salinity and nutrient data. The resulting programme was perhaps less than a geochemist would have wished for but was an example of concentrating on the specific goals of WOCE. In the event, a major survey of CO₂ in the oceans was developed under the International Geosphere-Biosphere Programme's (IGBP) Joint Global Ocean Flux Study (JGOFS) with measurements on WOCE cruises (Wallace, Chapter 6.3).

From the start, it was recognized that the scale of the experiment and the likely level of resources would leave little room for redundancy in the observations if the objectives were to be achieved. This fact in itself led to a continuous critical evaluation of the data requirements of each component of the experiment. In retrospect this can be most clearly seen in Volume 2 of the Implementation Plan, in which the achievement of the scientific plans was linked to a series of largely non-redundant observations. At the time, there was some discussion whether Volume 2 was a useful part of the implementation plan, but it has served as a valuable tool in identifying critical observations.

George Needler, Director of the WOCE International Planning Office (IPO) for the important initial 4 years from 1985, led the writing of the Implementation Plan. The Plan was prepared over several months in early 1987 and engaged the resources of the IPO, SSG members (and other colleagues drafted in). Volume 1 gave the detailed description of the observations to be made, parameter by parameter, while Volume 2 linked the observations to the scientific objectives. An advantage of the presentation adopted in the Plan is that it is easier to identify the critical observations and to classify others, which, though important in some regional or other scientific context, as less important.

1.3.4.1 The Intergovernmental WOCE Panel (IWP)

During the planning phase, CCCO was a constant source of support, taking on much of the responsibility for keeping WMO, IOC and ICSU in touch with the experiment and resolving bureaucratic issues that arose. The implementation of the Law of the Sea and, in particular, the components of it relating to access to the Exclusive Economic Zones (EEZ), was of concern. Dynamically important boundary currents lay within such regions and there were a number of instances where access was difficult to negotiate or in some cases refused.

It remains to be seen what impact this lack of access had on the data set and whether future programmes need be concerned.

Soon after the 1988 WOCE Conference, the IOC established the Intergovernmental WOCE Panel (IWP) to assist the WOCE community in meeting the scientific, managerial, implementation and resource needs of WOCE as defined by the SSG. The IWP's objectives were similar to those of the Panel that had been established by WMO for TOGA. At its three sessions between 1990 and 1995, IWP provided nations with another opportunity to make commitments to WOCE. Even though the scientific community through the efforts of CCCO and JSC and their sponsors and subsidiary bodies worked diligently to accommodate all potential WOCE participants, some nations still wanted coordination of their WOCE activities at the intergovernmental level. Each IWP meeting 'uncovered' some new resources and tended to force nations to be specific about their participation. Access to EEZs was discussed and, in at least one case, the IOC was successful in providing the mechanism through which rights were obtained. The IWP still exists and could be utilized if needed during the final phase of WOCE.

1.3.4.2 The data-sharing model developed by WOCE

Prior to WOCE, the principal international mechanism in place for exchange of data from research activities was that through the World Data Centre system. This had been created, in support of the International Geophysical Year (IGY), in 1958. Oceanography in particular had benefited through a long-term collaboration between national data centres to the extent that there was at least a major archive of hydrographic data. However there were, and are, major problems with that system when applied to specific programmes:

- submissions to the archive were delayed by many years;
- data were of varied and often unknown quality;
- only a small number of, mainly hydrographic, parameters were collected systematically; and
- national centres, with only a few exceptions, had not been committed to active data management for a project.

Roger Revelle (personal communication, 1982) commented that data management was one of the

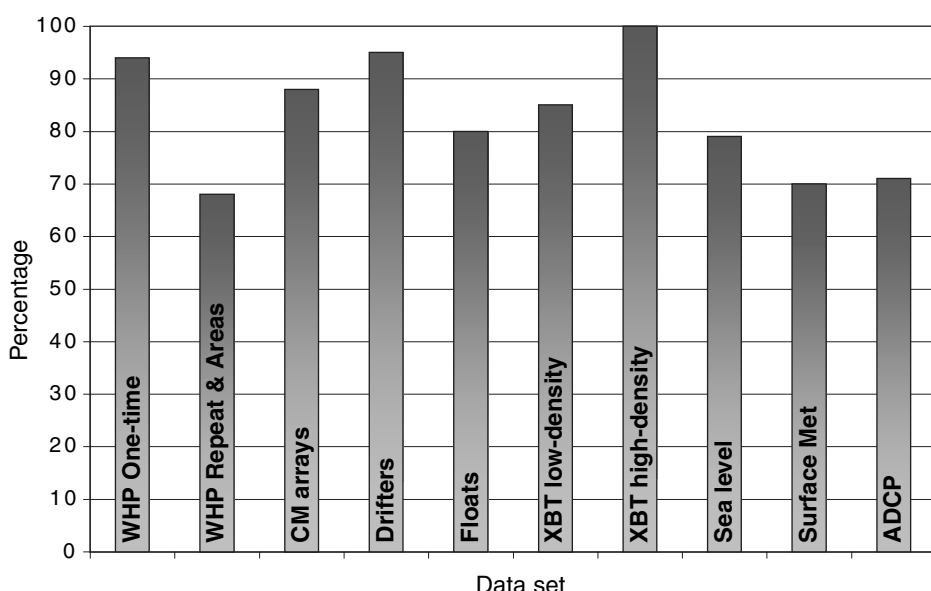


Fig. 1.3.1 Percentage of total data sets submitted to WOCE Data Assembly Centres, February 2000. WHP, WOCE Hydrographic Programme; CM, Current Meter; XBT, Expendable BathyThermograph; Surface Met, Surface Meteorology; ADCP, Acoustic Doppler Current Profilers.

most important problems facing both WOCE and TOGA and that researchers needed to ensure that it was done properly, even though the topic bored him to tears! So, in 1984 CCCO sponsored a meeting jointly with the IOC's Committees on International Oceanographic Data Exchange (IODE) and the Integrated Global Ocean Services System (IGOSS) to review and recommend the way forward. Shortly before, the US National Academy of Sciences, Space Studies Board, Committee on Data Management and Computation (National Research Council, 1982) had extensively reviewed the successes and failings of present and past satellite data management systems. It had identified some very general principles for success. The meeting felt these principles could easily be adapted to handle WCRP scientific data. They included active end-to-end involvement of scientists in the data acquisition and distribution process, peer review by the user community of the data management activities, data formats designed for ease of use by scientists, and metadata (ancillary information) to be available with each data set.

For WOCE, there was the added challenge of bringing together the data from three sources; satellite systems, ship-based research systems, and operational networks, each with its own mode of operation and time scale of data delivery. By 1986

the WOCE SSG had developed a plan based on these principles, which was to stand the test of time. Now (2000) it has demonstrably delivered (Fig. 1.3.1) to the scientific community an unprecedented set of high-quality data in a time frame not too different from that originally planned.

The WOCE Plan proposed seven Data Assembly Centres (or DACs) servicing separate primary data sets and supervised for the most part by scientists in research laboratories that were intimately concerned with the field programme. They covered the hydrographic programme, current meters, floats, surface drifters, sea level, expendable bathythermographs (XBTs), and surface meteorology. ADCP, bathymetry and sea surface salinity centres were added some years later. In addition, further scientific involvement was envisaged through Special Analysis Centres (SACs), essentially a mechanism that would serve to disseminate and preserve the derived data products from research. Although two were established (surface fluxes and hydrography) it is only now, with the advent of operational programmes such as the Global Ocean Observing System (GOOS), that interest in similar centres is developing.

The supervision of WOCE data involved scientific as well as technical quality control by independent review. This was for the most part readily

accepted and welcomed by the originating Principal Investigators (PIs) as part of a peer review process. For their part, PIs were asked to submit their data within the unprecedently short period of 2 years following the fieldwork. In some cases even a 6-month period was suggested – unrealistic perhaps at the time but now at the end of WOCE and the beginning of new field programmes not at all so. Such is the change of attitude that has been fostered.

The validity of the system is supported by three observations about the present situation:

- the unprecedented cooperation of scientists in submitting the data;
- most DACs are still largely run by the same scientists who established them; and
- the fact that the DACs have scrupulously safeguarded data submitted to them early while still allowing their use by agreement with co-workers.

‘Data sharing’ of new data has now gained widespread acceptability and hopefully will be the norm in future experiments. One finds in the WOCE bibliography, for example, no evidence of the plagiarism that some feared might result from early submissions of data to the DACs. The WOCE data system is described more fully by Lindstrom and Legler (Chapter 3.5).

There is a strong tendency in such a system for each component to go its own way so, in addition to the DACs, a Data Information Unit (DIU) was formed. Its function was to provide a single summary source on the progress of the experiment, the data and products available at the DACs, agreed standards and procedures, a bibliography, and generally to facilitate communications in WOCE. The system adapted well to the changing technology. Electronic mail was used from the very earliest planning phase of WOCE and indeed, it is hard to see how the planning process could have progressed so rapidly without it. By early 1994 the DIU was one of the first few hundred sites offering a world wide web connection, with the DACs following shortly after. The DIU’s functions, too, have changed significantly from being an online source of the national and international plans for the experiment, to being a summary source for the progress of the experiment and for links to the data sets and DACs, and now support of the final phase of the experiment.

1.3.5 Implementation and oversight

The prospect of truly global oceanography was exciting and in consequence entrained the collaboration of a large proportion of scientists engaged in deep sea physical oceanography. Although the planning was carried out during the economic boom-years of the late 1980s, the start of WOCE observations in 1990 coincided with a global economic downturn followed shortly by the dissolution of the Soviet Union. This led to the curtailment of many of the repeated hydrographic sections. The first official WOCE cruise in January 1990 was the occupation of a section across the Drake Passage on F.S. *Meteor*.

As is often the case with satellites, the launch dates of the two that would provide the altimeter and scatterometer coverage required by WOCE slipped from their original dates. TOPEX/POSEIDON was launched in August 1992 (and remarkably continues 8 years later to provide excellent data well beyond its design life; Fu, Chapter 3.3). ERS-1 had been launched in July 1991 on a more general-purpose earth observation mission that included altimetry and scatterometry. ERS-1 has now been succeeded (in 1995) by an almost identical ERS-2.

The delay in satellite launches meant that the 5-year observational phase starting in 1990 would not allow a full 5 years of coincident high-precision satellite altimeter coverage. The SSG at its 15th meeting in Toulouse in October 1990 therefore agreed to ‘extend the Global Survey over the period 1990–1997 (but no longer)’. In fact some WOCE hydrography continued into 1998.

A key new element in the WOCE observational strategy was the Autonomous Lagrangian Circulation Explorer (ALACE) float programme. The first significant deployment of ten floats was made in the Drake Passage on *Meteor*’s 1990 cruise. It was only as these floats progressed on their 2-week cycle that we learned about their performance and survival rates and found that they would indeed provide the global coverage WOCE required. These floats are described by Davis and Zenk (Chapter 3.2).

Through the observational phase, the WOCE IPO and the DIU played a key role in monitoring progress and highlighting potential problems. The International Planning Office provided

administrative backup for all WOCE Panels and WGs and regularly promulgated information about the project through the WOCE International Newsletter. The DIU, together with the IPO (which became a Project rather than Planning Office in 1990), compiled annual resource assessments of the experiment. During this time the IPO was led, in succession, by Peter Koltermann (1989–91), Nick Fofonoff (1991–93), and John Gould (1993 to present).

By 1994 (just past the mid-point of the now-extended observational phase) it was clear that WOCE would need a more detailed strategy for its post-observational phase. In consequence, the SSG and IPO drew up a plan for a phase of Analysis, Interpretation, Modelling and Synthesis (WOCE AIMS). In March 1995, the JSC, having inherited the responsibility for WOCE from CCCO, endorsed the plan and agreed that WOCE should continue in its AIMS phase to 2002 (WOCE IPO, 1995). An integral part of the strategy was the streamlining of the WOCE oversight structure. Up to this time each Core Project and many programme elements had their own oversight Panel and modelling activities were by-and-large considered separately from observations and coordinated by the WOCE Numerical Experimentation Group (NEG). The Core Project Working Groups were therefore disbanded in favour of a Synthesis and Modelling WG (SMWG), bringing together observationalists and modellers. It first met in October 1995 to start the preparation of a detailed plan for the AIMS phase (WOCE IPO, 1997).

Additionally in 1997 the Data Products Committee (this had changed in 1994 from being a Data Management Committee) assumed oversight of the WOCE Hydrographic Programme.

An essential element of the WOCE AIMS strategy was a series of regional and subject-based workshops that would (in the case of the regional meetings) stimulate basin-wide syntheses of WOCE data sets and foster collaboration between research groups. The first of these workshops was held in 1996 on the Pacific Ocean. The complete sequence and locations is shown in Table 1.3.1.

A significant number of papers based on science presented at the regional workshops were published in special issues of the *Journal of Geophysical Research*. The reports of the workshops have been published by the IPO and in a number of

Table 1.3.1 Sequence of WOCE AIMS phase workshops

| Subject | Venue | Date |
|---|-----------|----------------|
| Pacific Ocean | USA | August 1996 |
| South Atlantic | France | June 1997 |
| Southern Ocean | Australia | July 1997 |
| Ocean state estimation (with GODAE ^a) | USA | March 1998 |
| Ocean modelling (with CLIVAR) | USA | August 1998 |
| Indian Ocean | USA | September 1998 |
| Tracer AIMS | Germany | February 1999 |
| North Atlantic | Germany | August 1999 |
| Ocean variability (with CLIVAR) | Japan | October 2000 |
| Global transports (with JGOFS) | UK | Summer 2001 |

^aGODAE – Global Ocean Data Assimilation Experiment

cases these reports contain recommendations that are of long-term consequence. For instance the Ocean Moelling workshop led to the re-formation of a group charged with stimulating ocean model development within the wider framework of the WCRP. The 2001 workshop on Global Transports will address a central objective of WOCE – that of determining the oceanic transports of heat and fresh water. The JGOFS CO₂ measurements made on the WOCE one-time sections will provide estimates of the CO₂ fluxes and a key inventory of CO₂ in the oceans (Wallace, Chapter 6.3).

A further activity of the AIMS phase will be the publication of a series of atlases of WOCE Hydrographic Programme One-Time Survey data in a common format embodying profiles of all the WHP parameters.

WOCE held a conference on 'Ocean Circulation and Climate' in Halifax, Nova Scotia, Canada, in May 1998 to mark the end of the observational phase, to review the state of WOCE science and to give the large WOCE community an opportunity to make poster presentations of their latest results. The attendance of almost 400 ranging in age from the founders of WOCE to students who had barely started school in the late 1970s was gratifying and the keynote presentations were the starting point for this book. The 1998 conference was also the occasion of the distribution of the first set of WOCE Global Data on CD-ROMs. Preliminary planning is now underway for a final WOCE Science Conference to be held in the USA in 2002.

1.3.6 Was WOCE a success and what is its legacy?

WOCE achieved much of what it set out to do in terms of making ocean observations and, of those data, a large proportion are already available to the scientific community. WOCE required an unprecedented level of international collaboration that was readily forthcoming, perhaps because of the remarkable challenge that WOCE presented and the unique opportunity that it provided. It was helped by the fact that by-and-large it involved a single discipline, physical oceanography of the open ocean. It did require a close interaction of seagoing oceanographers, scientists concerned with the ocean–atmosphere interface, ocean modellers and satellite remote-sensing scientists. One might argue that it took a while for each subgroup to appreciate the others' abilities. In the mid-1990s modellers were often being asked for guidance by the observationalists as to what measurements and fields were required to critically test the models. Only in 1998 at the Ocean Modelling workshop were the modellers sufficiently confident to start to address these questions. The advances in computer power have meant that while in 1980, when WOCE planning started, global ocean models were running at a resolution of 2° , 20 years later global models are running at $1/8^\circ$ resolution and their representation of the ocean is becoming increasingly realistic. However, progress towards the objective of the four-dimensional data assimilation of ocean data into such models to provide ocean state estimations remains computer resource limited.

Some aspects of WOCE proved too complex and required too much coordination to be achieved. This was notably true of the CP3, the Gyre Dynamics Experiment. As originally planned it sought to observe the response of the gyre-scale circulation to the changing forcing field by means of repeated occupations of so-called Control Volumes (arrays of eddy-resolving hydro stations covering significant sectors of the Northern Atlantic Gyre), following the example set by the analysis of the beta triangle (Armi and Stommel, 1983). These proved too complex and required too heavy a ship commitment to be achieved by WOCE. However, the conclusion of the field programme in 1998 was marked by a gyre-scale programme in the North Atlantic in which ship-based hydrography was complemented with extensive deployments of profiling ALACE floats.

Satellite remote sensing has demonstrated, through WOCE, its crucial role in almost all aspects of present-day marine science. Comparison of computer models with ocean data is now starting to reveal hitherto undetected aspects of the oceans' behaviour. The global synthesis and the assimilation of the data into models to provide an ocean state estimate for the 1990s is underway and it is only when this has been carried out that we will really know whether our sampling strategy was appropriate to address WOCE's goals. Undoubtedly the WOCE data set is one of unprecedented accuracy, geographical extent and comprehensiveness.

A measure of success for any scientific programme is the number of papers based on its results that appear in the refereed literature. The WOCE IPO maintains a bibliography and to date, even though systematic analysis of WOCE data has barely started, over 1200 refereed papers are indexed as being associated with WOCE results at the end of 2000; this number is now increasing at the rate of around 200 papers per annum.

WOCE leaves an important legacy to future programmes, whether they be associated with climate research, as is the case of CLIVAR; need a basic physical underpinning, as with the IGBP's GLOBEC (Global Ocean Ecosystem Dynamics) programme; or are part of the developing movement towards operational programmes, such as GOOS and GCOS (Global Climate Observing System). One might justifiably claim that through WOCE the study of the global ocean 'came of age' and that through WOCE we have (or will have) both the tools and the understanding to address global ocean issues such as climate change that are of huge socioeconomic importance.

Acknowledgement and sources

We are most grateful to Bob Stewart for making available the typescript of his talk at the WOCE Conference, Halifax 1998, and also for additional critical comments.

Some detailed references are included but the majority of our sources are from the meeting reports and serial publications of the organizations referred to in the text. Specific meetings are referenced as, for example, WOCE-1 for the first meeting of the WOCE SSG. For an early discussion of the scientific basis of the Experiment, see Woods (1985a).

This Page Intentionally Left Blank

SECTION

2

OBSERVATIONS AND MODELS

Chapter 2.1

GLOBAL PROBLEMS AND GLOBAL OBSERVATIONS

Carl Wunsch

47

Chapter 2.2

HIGH-RESOLUTION MODELLING OF THE THERMOHALINE AND WIND-DRIVEN CIRCULATION

Claus W. Böning and Albert J. Semtner

59

Chapter 2.3

COUPLED OCEAN-ATMOSPHERE MODELS

Richard A. Wood and Frank O. Bryan

79

This Page Intentionally Left Blank

2.1

Global Problems and Global Observations

Carl Wunsch

2.1.1 Different views of the ocean

Some readers of the wider literature on the general circulation of the ocean come to recognize that the writing suffers from a kind of multiple personality disorder. As with the actual psychiatric situation, the different personalities do not always recognize the existence of the other individuals. One can identify several of these personalities:

1 *The descriptive oceanographers' classical ocean.* This ocean circulation is large scale, steady and laminar. Its origins lie with the technology of the mid-nineteenth to late-twentieth century, which was almost entirely ship-based. To obtain a description of the ocean, one had to lump together observations spanning many decades and treat them as though they were simultaneous. Out of 100 years of observations arose the many attempts to depict 'the' oceanic general circulation as in the diagrams of Defant (1941), Wüst (1935), Sverdrup *et al.* (1942) and many, many others. A recent example is Schmitz and McCartney (1993). The extreme version of this approach is the Broecker (1991) 'global conveyor belt', in which the caricature of the circulation renders it as a geological structure. It is an important corollary of this view that there is a unique general circulation – usually given in terms of mass fluxes – with all other property fluxes such as temperature or nutrients computed as the product of the mean flows and the local, supposed smoothly varying, property distributions.

2 *The analytical theorists' ocean.* The beginnings are often traced to Sverdrup (1947), Stommel

(1948) and the large literature that followed. A recent depiction of this ocean is in Pedlosky (1996). This impressive theoretical construct is very similar in its framework to the classical descriptive one. The ocean is thought of as essentially quasi-steady, in which features such as the Gulf Stream have nearly fixed paths. Any time variability is, as in **1**, thought of as 'noise'. There are many similarities between the pictures derived from **1** and the theory as it emerged in **2**, although the resemblance is rarely made quantitative; usually appeal is made only to pictorial similarity. (For a crude example of a quantitative test, that of the Sverdrup relationship, see Wunsch and Roemmich, 1985; Hautala *et al.*, 1994.)

There is an important field called 'geophysical fluid dynamics', whose goal might be described as the reduction of geophysical systems to terms sufficiently simple so as to produce a deep understanding of the various dynamical processes. To some degree, the analytical theorists' ocean (**2**) is that of geophysical fluid dynamics. Sometimes, however, the original simplifications are forgotten and the reduced models are then confused with the real system.

3 *The observers' highly variable ocean.* Here the focus is on elements of the ocean circulation that are time variable and that often also exhibit very strong spatial structures over very short distances (the lowest baroclinic Rossby radius of order 30 km or less). The emphasis, again for reasons of technological capability, has until very recently been on regionally varying elements. This view of the ocean emerged during

the early 1970s with programmes such as the Mid-Ocean Dynamics Experiment (MODE), the Coastal Upwelling Experiment (CUEA), POLY-MODE (an amalgam of the Russian POLYGON with the Mid-Ocean Dynamics Experiment) and International Southern Ocean Studies (ISOS). In this view, there are multiple, local, general circulations. Mean mass fluxes are perceived to be complex spatially varying fields $\langle \rho(x, y, z)\mathbf{v}(x, y, z) \rangle$ where x, y, z are three space coordinates, $\mathbf{v} = [u, v, w]$, ρ is the fluid density, and the brackets $\langle \cdot \rangle$ denote the true time average. But the circulation of any scalar field, C (e.g. temperature, carbon, or potential vorticity), must be computed as $\langle \rho(x, y, z, t)\mathbf{v}(x, y, z, t)C(x, y, z, t) \rangle$, where t is time. Unfortunately,

$$\begin{aligned} \langle \rho(x, y, z)\mathbf{v}(x, y, z) \rangle & \langle C(x, y, z) \rangle \\ \neq \langle \rho(x, y, z, t)\mathbf{v}(x, y, z, t)C(x, y, z, t) \rangle & \end{aligned} \quad (2.1.1)$$

where the failure of the equality can be at zero-order. An extreme case of such a failure would be the attempt to calculate the time-average temperature transport of the Gulf Stream by multiplying the time-average mass transport (a slow, broad flow) by the time-average temperature field, also a broad, slowly varying field. The true temperature transport involves averaging the product of a very narrow intense jet with a field having a narrow, very large instantaneous temperature maximum. In such a situation, the two sides of inequality (2.1.1) can and do differ by an order of magnitude. Because the covariances between the mass flux fields and C will be different for differing fields C , the circulation of each will be different, and often radically so.

Because of the regional focus, these differing general circulations are not usually pieced together into any sort of global picture. They remain rather, as isolated sub-basin scale, stand-alone pictures.

- 4** *The high-resolution numerical modellers' ocean.* Beginning in about 1990, basin-to-global scale models emerged that contained variability resembling the oceanic mesoscale eddy field. The character of this newly emergent view of the ocean can be seen, e.g. in the results of Semtner and Chervin (1992), Böning *et al.* (1991), Cox (1985), Smith *et al.* (2000) and others. These results, when heavily averaged,

have a qualitative resemblance to some elements of all of **1–3**, but differ quantitatively from all of them. The general circulation property fluxes differ, as in **3**, from those of mass alone, because as in **3**, the mass flux/property covariances are all different, but the scope is global.

Little communication between the apostles of these different personalities appears to exist; nearly disjoint literatures continue to flourish.

2.1.2 The origins of WOCE

By the late 1970s, a few scientists had begun to recognize that the various circulation personalities listed above could be thought of as originating in two conflicting paradigms (to use the terminology of Kuhn, 1962), although no one seems to have described it that way at the time. The two paradigms are:

- 1** The ocean is a quasi-steady, large-scale equilibrium system. I will refer to this as the 'historical' paradigm.
- 2** The ocean is a fundamentally turbulent, constantly changing, non-equilibrium system in which no element is actually fully steady. I will call this the 'WOCE' paradigm, although it would be wrong to claim that all those who formulated and carried out WOCE were subscribers to it.

2.1.2.1 The historical paradigm

The ocean is opaque to all forms of electromagnetic radiation at usable wavelengths, hence modern oceanography, from its beginnings in the late nineteenth century, has been built upon an observational base acquired by physically placing an instrument at particular positions and depths of interest. For other technical reasons, most such measurements have been not of the velocity field in the ocean, but rather of scalar quantities such as temperature, salinity, oxygen content, etc. Because ships provided the only platform for reaching mid-ocean locations, it took many decades to acquire observations adequate to delineate the bulk scalar properties of the ocean.

By great good fortune, the ocean was early on perceived to display large-scale, temporally stable, contourable fields of these tracers ('tongues', etc.; see particularly Wüst, 1935; some of these pictures are reproduced in Wunsch, 1996). It was thus possible to combine the scalar observations spanning

multiple decades into a qualitatively consistent picture. This distribution of properties was interpreted in terms of a corresponding large-scale, steady, flow pattern. Theories (wind-driven, thermocline, etc.) were then constructed that produced flows resembling the required circulation patterns.

It was inferred from this picture of very slow, creeping or ‘spreading’ flows, that the relevant time scales for serious change in the ocean circulation had to be of order 1000 years and longer, with the abyssal ocean acting only as a passive reservoir responding to the divergences of the upper ocean.

Until about 1975, available computing power permitted only coarse-resolution, extremely viscous numerical models of the ocean. These models qualitatively mimicked the available analytical solutions and this close agreement tended to confirm the historical paradigm. Almost all textbooks – oceanographic, meteorological and climate – as well as many current research papers, still reflect this view of the ocean circulation.

2.1.2.2 The WOCE paradigm

At the time WOCE was conceived, in the late 1970s, use of the new technologies, especially those able to produce time series, such as moored current meters and drifting floats, had begun to make it clear that the flow field in the ocean was very different from the steady, large-scale simple flow fields that had emerged out of the tongue depiction by Wüst and others, and from the analytical and numerical models. Rather it showed a flow field dominated by what has come to be called ‘mesoscale eddies’, but which is actually much more complex than any single, mesoscale¹ phenomenon. The kinetic energy of the variability was seen to be roughly two orders of magnitude larger than that associated with the quasi-steady basin scales. Indeed, a major supposition behind much of the WOCE design was that the ocean changed on all space scales from the sub-Rossby radius to the entire global circulation, and on all time scales out to the oceanic lifetime.

The presence of an intense variability does not necessarily mean that it has any dynamical or kinematical consequences: it could be a purely passive ‘noise’ phenomenon, causing sampling (aliasing) difficulties, but of no further consequence. But it is also true that it could be of enormous kinematical and dynamical consequence with, for example, the

tongues being nothing but the integrated fields obtained from an extremely complex small-scale structure, rather than implying large-scale steady mean flows (for an example, see Hogg and Owens, 1999, or any of the high-resolution model calculations, such as that of Smith *et al.*, 2000).

Within the group that designed WOCE there were two other overlapping, but nonetheless conflicting, views as to how best to understand the oceanic role in climate. These two views were that ultimate insight would be best obtained by:

- 1 regional and process-focused studies; or
- 2 observing where and how the ocean is changing globally.

Finally, of course, WOCE followed both these strategies to some degree. Regional programmes such as the Subduction Experiment, Brazil Basin Experiment and the Purposeful Tracer Experiment were central to what came to be called WOCE ‘Core Project 3 – Gyre Dynamics’.

In the end, however, the major activities in WOCE were on the global scale. Achieving this global strategy was not so easy. The decade of the 1970s, beginning with, among others, the Mid-Ocean Dynamics Experiment (MODE Group, 1978), can be called the ‘decade of the mesoscale’. Classical hydrographic work, which was often used to depict the global-scale ocean of the steady paradigm, had come to many to seem less ‘scientific’ than did the study of physical processes. The latter became accessible through powerful new technologies, including moored current meters, neutrally buoyant floats, Current-Temperature-Depth probes (CTDs), bottom pressure gauges, etc. In particular, the occupation of long hydrographic lines had almost ceased. Figure 2.1.1 shows most of the trans-oceanic hydrographic lines that had been obtained following the last International Geophysical Year (IGY) lines of 1959, and prior to the first WOCE discussions of 1979. The Eltanin Survey (see Gordon and Molinelli, 1982) was an exceptional large-scale survey of the Southern Ocean. Furthermore, numerical models (e.g. Holland, 1978) were beginning to show intense variability that seemed to confirm an entire physical realm of oceanography previously completely unexplored. There was a clear sense that the scientific future lay with regional studies: much of the community was focused on processes and the ‘physics’ of internal waves, the mesoscale, upwelling, tropical waves and the like.

¹ ‘Synoptic’ scale to a meteorologist.

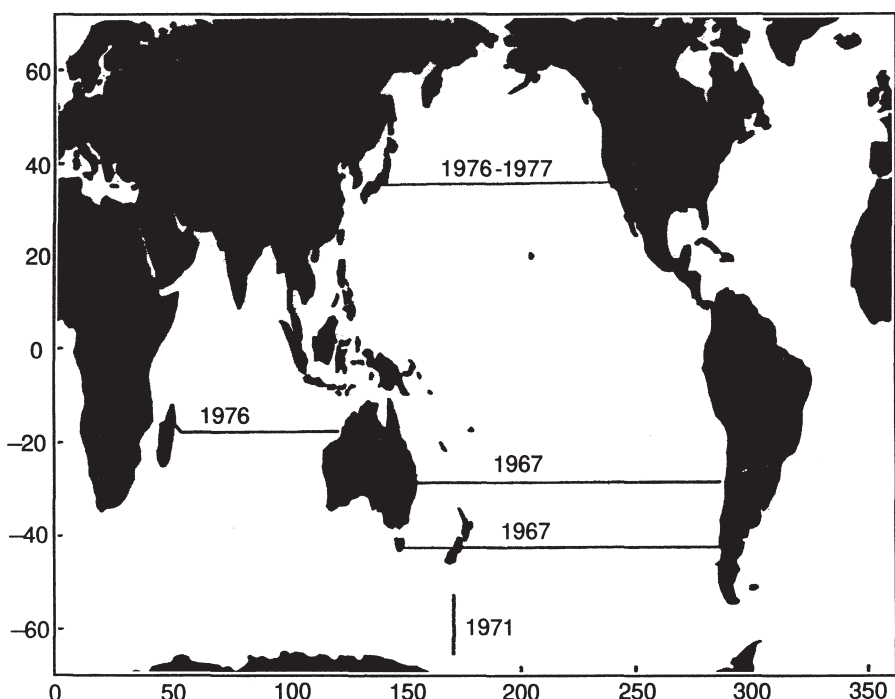


Fig. 2.1.1 The very few trans-oceanic hydrographic sections obtained during the period following the IGY (1958–59) and preceding the WOCE design period. This latter coincided with the resurvey of the North Atlantic (early 1980s), which to some extent marked a return to large-scale physical oceanography following the mesoscale, and other process programmes that dominated the 1960s and 1970s.

Much of the debate that took place in the WOCE formulation dealt with the desirability, and feasibility, of obtaining global coverage, not only by hydrography, but also with satellites, expendable bathythermographs (XBTs), etc., and the extent to which these were possible (the satellite technologies were very new; see, e.g. Born *et al.*, 1979).

As we finish WOCE, I am concerned that we are emerging with the same two paradigms (and the various conflicting personalities) largely intact and almost undisussed. Ocean science following WOCE is emerging as having a major focus on climate problems, including those involving time scales of decades and longer. WOCE was intended to provide a mechanism by which this transition to climate programmes could take place. But given the long time scales of climate change, the possibilities for self-delusion grow abundantly, and the question of what observations are required so that we come to understand the system are of very great importance.

It is the import of this chapter that more than ever one requires an adequate, long-term observational system: there is a tendency to think that models will come to substitute for observations. The basis of the hope is the understandable wish that one can evade the necessity of waiting the decades required to observe the actual climate system by modelling it instead.² Although models are extremely important elements of the arsenal for understanding climate change, and will become increasingly so, the entire history of fluid mechanics (and it is worth recalling that physical oceanography is a branch of fluid dynamics) shows that without observations one generally goes seriously astray. A famous example in classical fluid dynamics is the discrepancy between the Stokes solution for flow around a sphere and the flow actually observed in the laboratory.

2.1.2.3 Consequences

For anyone attempting to understand climate, the consequences of the application of the two views is

² A reviewer thinks I am beating a dead horse here: that no one believes models are a substitute for observations. But at least one very influential meteorologist has publicly and repeatedly asserted that because there is no ‘physics’ in the ocean (in the peculiar meteorological sense of that term), one can model everything adequately without data.

Table 2.1.1 Frameworks (paradigms) of the ocean circulation

| Historical | WOCE |
|---|--|
| Ocean is nearly steady, fundamentally large-scale, and laminar | Ocean is unsteady on all space and time scales and fundamentally turbulent |
| Modelling consequences | |
| <ul style="list-style-type: none"> • Coarse resolution adequate • Quasi-steady adequate • Integration over very long periods is accurate | <ul style="list-style-type: none"> • Extremely high resolution probably required ($<1/12^\circ$ in boundary currents) • Highly non-steady (turbulent fluid flow) • Systemic errors in physics may well accumulate over long periods of time and swamp the results |
| Observation consequences | |
| <ul style="list-style-type: none"> • Greatly simplified: keep coarse track of upper branch of 'global conveyor belt' | <ul style="list-style-type: none"> • Very serious and demanding problem • Small spatial scales and long temporal scales must be observed • Not possible to rule out any oceanic depth or region as irrelevant |
| <p>Schematic of the consequences of the two different views of the ocean circulation – ranging from the 'historical' one of a basically steady, laminar system, and the view that one is dealing with a constantly changing intrinsically turbulent fluid flow. If either view were completely correct, the modelling and observational consequences would be quite extreme. In practice, both are partially valid, but the existence of any turbulent component forces one towards the consequences of the fully turbulent system.</p> | |

very important. A 'telegraphic' summary would be as listed in Table 2.1.1.

I am acutely aware that the debate as to the oceanographic future is ongoing, and that many organizational developments are taking place. Here I run the risk of preaching to the choir; perhaps by the time this book appears, the community will regard what I say here as obvious, and will have moved to accommodate these views. I hope that this will be true.

2.1.3 What do we know?

WOCE has completed its field phase, and the serious analysis of the data has only begun. It is nonetheless possible to draw some immediate conclusions. Much of the data, but especially the TOPEX/POSEIDON altimetric data, now 7+ years long (as of early 2000), shows the extremely active time dependence of the oceanic circulation. (Wunsch and Stammer (1998) review the altimetric results.) Other widespread data sets, e.g. the neutrally buoyant floats (Davis, 1998a,b; Hogg and Owens, 1999), current meter records, surface drifters (e.g. Niiler and Paduan, 1995), etc., all confirm the turbulent nature of the flow. This extreme variability is confirmed by the high-resolution general circulation models that have been developed as part of and alongside WOCE (Semtner and Chervin, 1992;

Stammer *et al.*, 1996; Smith *et al.*, 2000). In parallel with WOCE and its preparations, it was shown that tracers such as tritium and chlorofluorocarbons penetrated to the abyssal seafloor from the surface, on time scales of 10 years, rather than the hundreds to thousands of years (e.g. Östlund and Rooth, 1990) suggested by the 'historical' view. The palaeoceanography core records show that major climate shifts occurred in the ocean on time scales of order a decade and even less (e.g. Boyle, 1990). Furthermore, even the coarse-resolution models were suggesting that the ocean circulation could undergo dramatic shifts on very short time scales (e.g. Manabe and Stouffer, 1994; Marotzke and Willebrand, 1991; Weaver *et al.*, 1993), much shorter than the historical view would lead one to expect.

A major component of the climate role of the ocean involves its transports in three dimensions of the scalar fields of heat (temperature), fresh water (salt), carbon, etc., whose large-scale structures have pervaded the discussion of the ocean circulation for more than a century. It is too soon in the WOCE analysis phase to quantify the degree to which these property transports and their variability through space and time, seasonally to inter-annually to decadal and beyond, are the result of (a) a simple time-dependent version of a laminar conveyor belt; (b) the result of a complex integration

over fully turbulent elements; or as seems likely, (c) some complex combination of both. (A particularly striking example of the complexity of the processes that maintain the tongue-like features can be seen in the Brazil Basin float and tracer results of Hogg and Owens (1999), where some large-scale, laminar flow may well coexist, but which is almost imperceptible in the data.)

But given what we see in the WOCE data and elsewhere, and what the high-resolution models are telling us, it seems a vast leap of faith to assert that one can simply integrate coarse, laminar, representations of the ocean circulation for hundreds to thousands of years and to expect that the Lagrangian property transports of heat, fresh water, carbon, etc., are being computed with useful skill. If one can do so, it is either a result of extraordinary good fortune that for this particular fluid, the turbulent fields are purely passive, or that the General Circulation Model (GCM) builders are so clever they have solved the problem of fully parameterizing the turbulent elements, boundary jets and other unresolved elements of a three-dimensional rotating, stratified fluid in a complex geometry. If the latter is actually true, it is a remarkable achievement of computational skills, a landmark in the history of fluid dynamics.

2.1.4 The need for global-scale observations

2.1.4.1 Unobserved regions

When adequate observations have been unavailable to depict the world, the human race has generally reacted in one of two extreme forms. The first form is represented by the map of New Guinea shown in Fig. 2.1.2. With no observations, the cartographer felt the need to show non-existent mountains and monsters, providing an exciting metaphor for the general unknown. The opposite extreme is to assume that ‘the absence of evidence is evidence of absence’ and to infer that nothing interesting exists where nothing has been observed. Examples are the nineteenth century inference of a biological desert in the abyss (Mills, 1983), the modern (until about 1965) assumption that the deep Pacific Ocean was devoid of any significant flow, and the inference of the existence of oceanic abyssal plains in the absence of sounding data. It is easy to make a list of phenomena that were so widely and plausibly believed to be absent

or irrelevant that little effort was made to test the hypothesis by observation:

- *Things everyone ‘knew’:*

- No interesting currents at depth on the equator (1950)
- Vertical temperature and salinity profiles are smooth (1965)
- No interesting abyssal flow structures in the Pacific Ocean (1965)
- Ocean heat transport is negligible compared to the atmosphere (1970)
- The deep interior ocean moves at climatological speeds (1958)
- Ocean mixing is geographically uniform (1970).

The date given is (very approximately) when the hypothesis started to become untenable because someone became convinced it didn’t have to be correct, and set out to test it.

There is a parallel problem in the inference of overly simplified depictions of the ocean circulation, a depiction with its roots in personality 1 described in Section 2.1.1 above. Broecker’s (1991) well-known ‘conveyor belt’ has often been used to describe the role of the ocean in climate. The picture is a visually powerful metaphor for the circulation; trouble occurs, however, when scientists begin to take it literally, forgetting its metaphoric origin. The conveyor belt has been invoked to claim that observing the ocean climate state is cheap and easy – because observations can be confined to a few upper ocean XBTs in the northern North Atlantic. As one eminent meteorologist once insisted to me, one ‘need only keep track of the upper branch to know what the whole ocean is doing’. The picture has also been invoked frequently to confirm the old prejudice that the deep ocean does nothing of interest; it has kept alive the completely incorrect view that water flowing through the Indonesian Passages connects immediately and directly across the Indian Ocean to flow around the Cape of Good Hope, among other myths.

Schematic pictures of the circulation are of course, very helpful, both as mnemonics and as aids in conveying to the non-scientific community how the system ‘works’. But when employed out of context, they can be extremely misleading. Consider the schematic in Fig. 2.1.3a (see Plate 2.1.3a, p. 76) of communication links between the



Fig. 2.1.2 Map (de Jode, 1593) showing the interesting fauna and non-existent landscape (an entire mountain range) on the coast of New Guinea and Australia placed there by mapmakers who felt compelled to show something where nothing was known. Modern scientists would leave blank such unexplored areas; sometimes these blanks are reinterpreted to imply that nothing of interest lies there – an equally unfounded hypothesis.

US and Europe. Information flows along the lines indicated and the picture would make a sensible cartoon for a public discussion of volume and fluctuations of information traffic. The picture has the great virtue of extreme simplicity. But if one looks at one indicator of the routes of information flow on modern computer links (Fig. 2.1.3b, see Plate 2.1.3b, p. 76), one's understanding of the situation, and consequent policy decisions, are likely to be quite different.

Gradually it has become clear that climate is a global phenomenon. Nonetheless, in parallel with the listing above of historical failure of some

simplifying hypotheses, there exist today a number of hypotheses that are often invoked in discussions of the ocean observation problem. They include:

- *Things many (some?) people 'know' now:*
 - There is a global conveyor belt whose strength controls the climate state through thousands of years.
 - Only the upper ocean is relevant to 'climate'.
 - Coarse resolution ocean models can be run for 1000+ years with climate forecast skill.
 - The strength of the oceanic heat transport is controlled by the surface density gradient alone.

- Only the upper tropical ocean influences the El Niño-Southern Oscillation phenomenon (ENSO).
- All changes in the circulation have deterministic causes.
- The ocean is in equilibrium with the atmosphere (the present-day ocean state is caused by interaction with the present-day atmosphere).

Few meteorologists would argue that large regions of the atmosphere can be omitted from their models without degrading them: there is no argument known to me that any part of the atmosphere is decoupled, laterally, from the rest on time scales exceeding a day or two. Similarly, it seems unlikely that any part of the ocean can safely be assumed to be unchanging, and passive, in attempts to model the system over periods from a few to thousands of years. Thus ocean modellers have gravitated towards making their models truly global. But the more sophisticated a model is, the higher is the data quality required to test it (a crude model only requires crude tests). Such models have to be tested and calibrated everywhere – an error in high latitudes will eventually ‘bite’ one in the tropics after the fluid has carried that erroneous information through the system. That transmission may take a long time, but eventually, on some climate time scale, it will probably happen. One must have observations everywhere capable of delineating all space and time scales.

2.1.4.2 Too short records

We know from the geological record that climate has been changing ever since the time when it makes sense to speak of such a phenomenon, i.e. since about 3 billion years ago. Within this enormous span of time, changes have been taking place on every time scale definable as ‘climate’, i.e. from a year or two, to millions and billions of years.

There is an enormous temptation to interpret the record of change as seen in one’s lifetime, or even in human history, as being representative of the climate system as a whole. Such a temptation is fraught with grave dangers. Systems with memory, and the climate system, particularly the ocean (and cryosphere), have long-lived and multiple time-scale memories, undergo often highly unintuitive random walks. This type of behaviour is too readily converted into interesting deterministic stories. The tendency to long random walks is the

central element of Hasselmann’s (1976) stochastic theory of climate. It is easy to give examples where one’s intuition can fail very badly in these circumstances, and I have written about this phenomenon elsewhere (Wunsch, 1992, 1999a). Consider by way of example, the ‘temperature’ record in Fig. 2.1.4a (Wunsch, 1992). Taken by itself, it resembles many oceanographic time series. One might be tempted to think of the maximum near time 2500 as representing a climate extreme. But this record was generated simply as the accumulating sum of that shown in Fig. 2.1.4b – which is pure white noise. The existence of a maximum near 2500, a strong minimum near 1800, and the apparent long-term trend in between, has no ‘cause’ other than the stochastic accumulation of a few excess positive or negative values in a long run of a purely random sequence.

Another example can be seen in Fig. 2.1.5; here the transport of a western boundary current and its spectral density are displayed. Again, the variability is not visually very different from that seen in practice (e.g. Schott *et al.*, 1988). In this particular case, however, the variability was generated in a theoretical Stommel-gyre by a purely stochastic variability (white noise in both space and time) in the interior wind forcing.

It is often argued (as in the WOCE design period), that large-scale observation systems are not required – that it suffices to instrument so-called choke points of the system and to monitor the behaviour of the flow through them. The most commonly described choke points include the Drake Passage and the Florida Straits, as well as the Indonesian Passages, and sometimes the region south of the Cape of Good Hope. But Fig. 2.1.5, and others like it, show this type of strategy to be fallacious: choke points are regions where any stochastic forcing and response for the entirety of the ocean sum together, and where one *expects* to see large-scale positive and negative excursions like that in the figure. The temptation to ascribe such fluctuations to large-scale deterministic changes, e.g. in the wind field, has not often been resisted (see the literature particularly on the Florida Current). The circulation certainly contains *both* stochastic and deterministic elements. Separating them can be quite challenging, requiring adequate observations to depict the response of the complete ocean interior. Often, the random walk explanation will prove the simplest

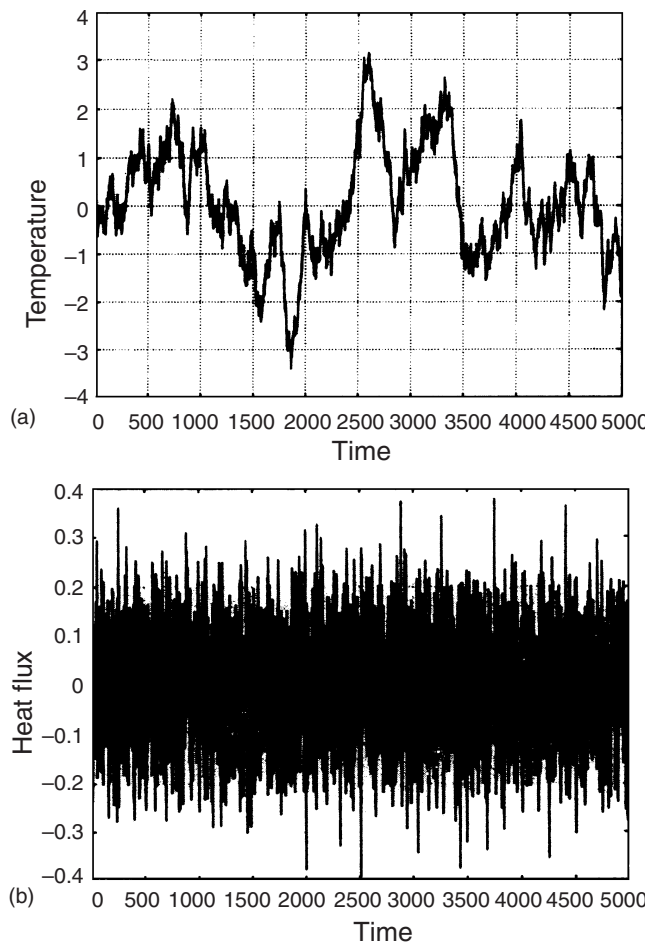


Fig. 2.1.4 (a) A pseudo-temperature record whose visual structure is much like many real oceanographic time series (it is a ‘red noise’ process). The extreme values, and apparent trends between them, lend themselves readily to rationalizations in terms of deterministic causes (Wunsch, 1992), but the record was generated from the ‘forcing’ in part (b).

(b) A pseudo-random number generator was used to generate this white noise sequence, whose running (accumulating sum) is depicted in (a). Excursions in (a) are nothing but chance runs of excess numbers of negative or positive values (see discussions in Feller, 1957; or Vanmarcke, 1983).

and could be regarded as the most compelling null hypothesis, although it is the deterministic cause that is usually assumed to be correct.

A third example is perhaps even more troubling: Fig. 2.1.6a shows Brooks’s (1923) demonstration that central African lake levels appear to follow the 11-year sunspot cycle. Figure 2.1.6b shows what happened subsequently. The reader is referred to Pittock (1978) for this and many other examples where short-record visual correlations suggested a non-existent causal relationship. Similar published examples of misleading short-record correlations can be replicated indefinitely. The problem is greatly compounded when

investigators start to shift in time the relative positions of two or more records so as to determine time lags. The probability of ‘false positives’ then grows enormously.

None of these examples just cited can be used to refute the possibility that climate change is simply causal, and so simply interpretable, and possibly even predictable. All they do is suggest that, for some purposes, there is no substitute for very long records over the entire global ocean. Climate will never be properly understood until the records encompass many realizations of the time scales one is examining (as scientific history seems to show to be true for all physical phenomena).

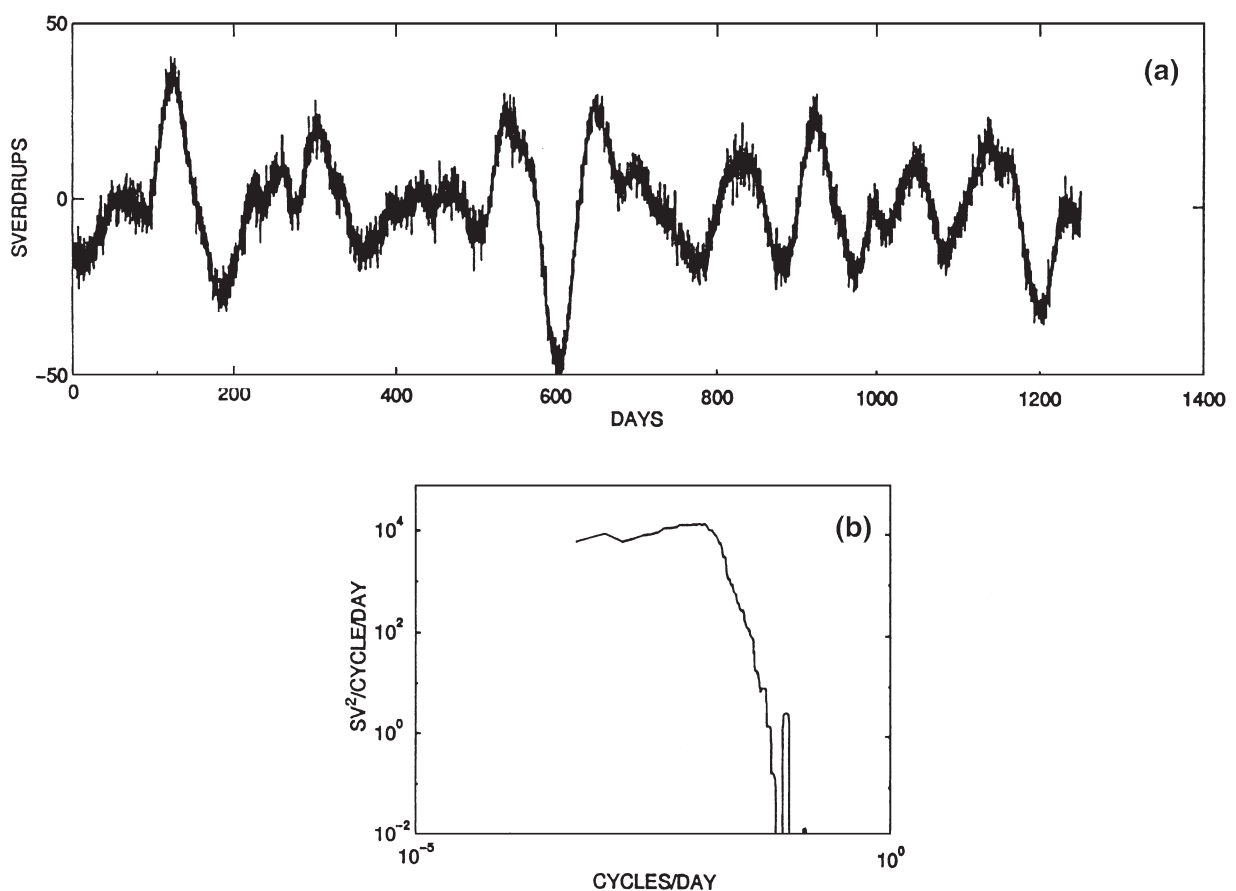


Fig. 2.1.5 (a) 'Transport' of the Stommel Gulf Stream when the interior wind field has a purely white noise (space and time) curl. The transport excursions are the result of the random summations of the responses over the entire domain of the model ocean.

(b) Power density spectrum of the record in (a) – a result similar to spectral estimates of real time series (the too rapid drop at high frequencies does not occur in the natural world – the model contains no internal waves or other noise processes).

2.1.5 Where do we go from here?

History tells us that conflicting ideas about the nature of a fluid flow can only be finally resolved by observations. We already have adequate data to demonstrate that we are dealing with a flow that has powerful turbulent elements, and that the historical picture must be abandoned as an adequate description. Something like it could conceivably ultimately re-emerge as the result of multi-decadal averaging, but such an outcome is far from assured.

The major issue for us concerns understanding the ocean as it pertains to climate prediction. Only an adequate observation base will permit us to determine the present state of the ocean, to understand which elements are undergoing secular shifts, the extent to which the ocean is predictable

beyond a year or two and, to the extent that we find predictability, to actually make forecasts.

A rational observing system is inevitably a series of compromises and tradeoffs. There is insufficient space here to discuss all of the various issues, but a few simple points are perhaps worthwhile. Our only extant true global-scale observations come from space. These, however, are currently restricted to surface properties; this restriction in turn means that only a small number of the possible measurements are really of interest, including altimetry and roughness (for the wind field). It is difficult to imagine any future ocean observations not requiring spacecraft of these types. One also needs global *in-situ* measurements. Here the trade-offs tend to be of accuracy and precision versus the need for large numbers of measurements.

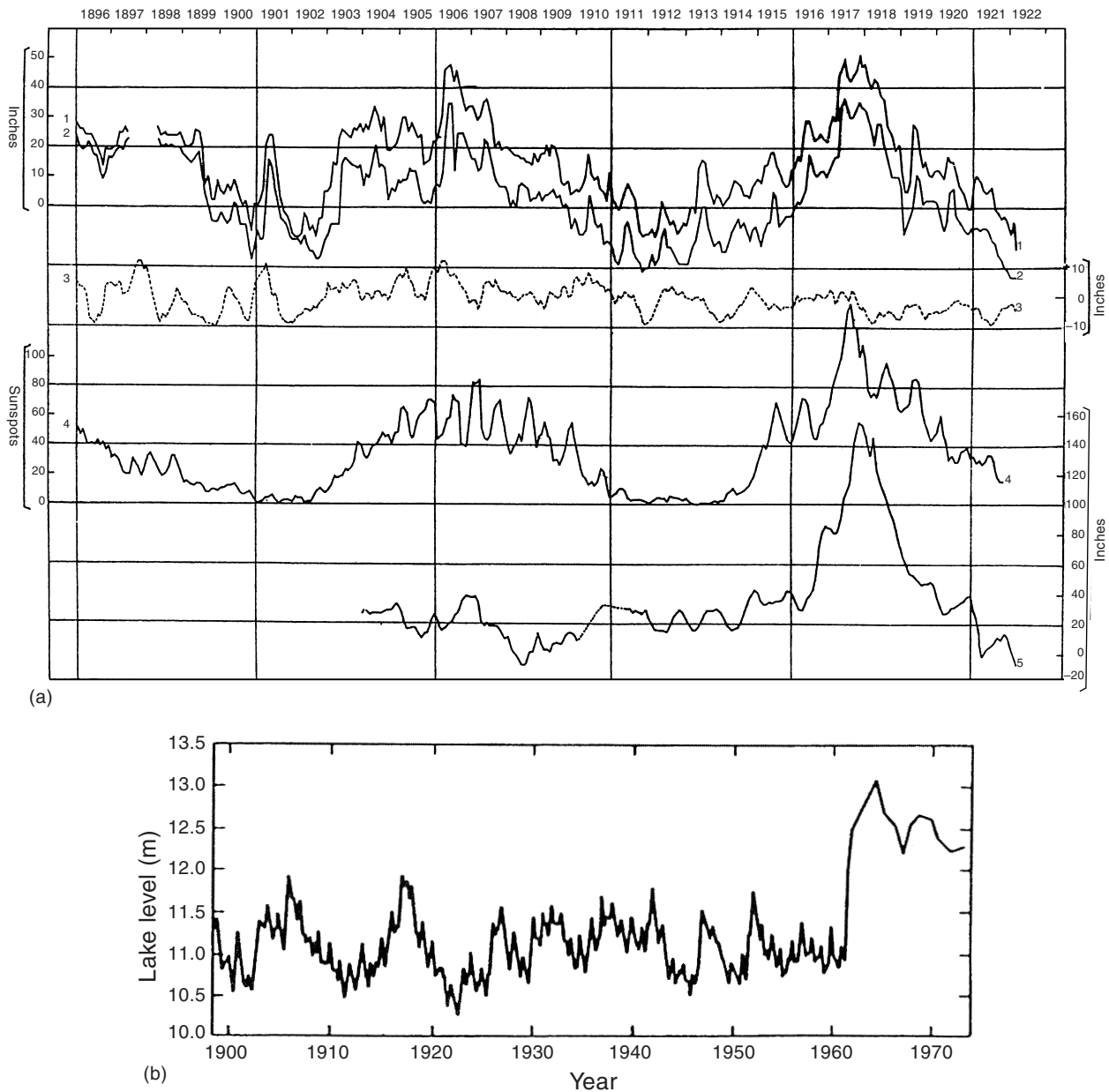


Fig. 2.1.6 (a) Brooks's (1923) graph of water levels in Central African lakes together with the simultaneous record of solar activity, which he suggested showed a possible cause and effect. Curves labelled 1 and 2 are the maximum and minimum values observed (in inches) in Lake Victoria. Curve 3 is a rainfall estimate as an anomaly from a climatology. Curve 4 denotes the monthly sunspot numbers and curve 5 is the mean level of Lake Albert.
 (b) Much longer record (from Pittock, 1978) showing the subsequent evolution of the Central African lakes in which the apparent relationship to the solar cycles has broken down completely (noticed already in the mid-1930s) and would now be regarded as specious. The abrupt change in character toward the end apparently has historical precedents prior to Brooks's record.

The Argo programme (to deploy several thousand profiling floats) is an outstanding example of what needs to be done: the production of thousands of adequate (not perfect or even the best one can do) measurements worldwide for long periods of time. A comparatively minor investment in technology

could produce a new generation of such expendable instruments of a variety of types (e.g. of long-duration expendable moorings and accompanying instruments). These and other possibilities (e.g. the entire panoply of acoustically based measurements), desperately call out for a systematic

programme of observational method tradeoffs, experimental trials, technological investment, and then sustained system evolution. No organization has emerged capable of doing these things.

WOCE itself has shown that, through the coalition of the academics, government laboratories, etc. that make up the worldwide oceanographic community, combined with modern oceanic observation and modelling technologies, the elements of a practical system already exist. This system could provide what is required, if it can be sustained and ultimately augmented. The existing system involves measurements from satellites, *in-situ* unmanned instruments such as profiling drifters, tomographic integrals, and long Eulerian time series, plus a judicious mix of shipboard measurements, all carefully carried out so as to evade the dominant aliasing effects of the variability. The modelling advances that have taken place over the past 15 years suggest that the combination of clever fluid dynamics and numerical methods, increased computing power, and the comparatively modest resources required to sustain such efforts would over the next 10–20 years become consistent with the need for fully describing the changing fluid.

But the community that put together the WOCE coalition is too small, too dependent upon year-to-year funding, too focused upon basic scientific issues, to sustain the required observations in the necessary open-ended fashion. If one seeks seriously to account properly for the ocean and its role in climate, special consideration must be given to maintaining the observation programme without destroying the underlying scientific community. Probably the central issue is that there are no operational agencies anywhere in the world that carry out large-scale systematic oceanic observations

analogous to those represented in the World Weather Watch.³ If oceanic climate issues are to be understood, the small oceanographic community will need resources, and probably the active assistance, of some operational agency or agencies to marshall the resources for an ongoing system capable of addressing the major issues.

This last statement is not a trivial one. Perhaps the greatest climate puzzle is whether one can find a way to study its ‘slow physics’ (and chemistry and biology) within funding systems based upon year-to-year budgets, high-frequency elections, short tenure deadlines, and the general wish for scientific results in the short term. Understanding the ocean in climate is surely a multi-decadal problem, at best. The observations and science required to solve it are fairly clear. What is less clear is whether we have the collective will, internationally, to produce the necessary effort.

It is, of course, possible to proceed by simply asserting that the historical paradigm remains valid. This assumption is enormously simplifying, and greatly reduces the costs and complexity of future climate programmes (see Table 2.1.1). Such a course is very appealing from many points of view, but seems dangerous to the ultimate understanding of climate should the assumption prove, as seems likely, false.

Acknowledgements

The comments of the reviewers and editors were very helpful. This work was supported in part by the National Science Foundation under Grant 9525945 and the National Aeronautics and Space Administration under Grant NAG5-2734. Contribution to the World Ocean Circulation Experiment.

³ Space agencies sometimes give the impression of being ‘operational’ agencies, simply because the planning and flight of spacecraft takes so long. But one of the great ironies of the US/France TOPEX/POSEIDON mission is that it has led the US National Aeronautics and Space Administration to declare its role in satellite altimetry to be near its end, and to seek actively to cease any further such measurements. The argument continues.

2.2

High-Resolution Modelling of the Thermohaline and Wind-Driven Circulation

Claus W. Böning and Albert J. Semtner

2.2.1 The improving realism of ocean models

The influence of numerical ocean modelling has grown dramatically over the last few decades. The use of ocean general circulation models during the 1970s and 1980s contributed to our fundamental understanding of the physical mechanisms governing ocean dynamics by extending theory beyond the limits of analytical methods. However, with the exception of certain phenomena mainly associated with wind-driven variations at low latitudes, the models were notoriously limited in their ability to simulate the observed intricacies of the global ocean circulation, rendering any quantitative confrontation with data sets beyond gross climatologies premature. In fact, the lingering disparity between the early ocean models and the high-precision, deep ocean data sets meticulously gathered by individual oceanographic expeditions may be regarded as a characteristic of pre-WOCE (World Ocean Circulation Experiment) oceanography. This distinguished oceanography from the situation in atmospheric research where models must routinely stand the test of a wealth of synoptic data and provide a primary means of obtaining dynamical insight into physical processes.

Due to significant improvements in numerical methods, advances in computer capabilities, and better data sets for initialization and forcing, ocean circulation models have become much more realistic in recent years. Simulations with realistic forcing, basin geometry, and resolutions fine enough to retain the energetic flow features with

horizontal scales of the first mode Rossby radius of deformation have been ground-breaking in the sense that they provided, for the first time, solutions of planetary scale that permitted direct and quantitative comparison with ocean observations. Having fine resolution also allows the numerical diffusion coefficients in a model to be chosen small enough to avoid fictitious non-physical damping; it also facilitates the correct transport of properties such as heat and salt by adequately representing the correlation of property maxima with the core velocities of strong narrow currents. With models improving in so many respects, an ensuing, more effective interaction between the observational and modelling communities during the WOCE decade has ultimately led to a significant expansion in the utilization of numerical models, not only for applications in physical oceanography, but increasingly also in related fields such as biogeochemistry and palaeoceanography.

As a consequence, ocean modelling activities have acquired a role in WOCE that goes much beyond the primary aim ‘to develop models useful for predicting climate change and to collect the data necessary to test them’. Irrespective of the continuing need of critical testing against observed ocean behaviours, there is a growing appreciation of the critical importance of ocean models as a key means for an understanding of a natural fluid system that, given its vast spectrum of variability, can never be comprehensible on the basis of observations alone. In particular, the great challenge of ‘state estimation’ (Talley *et al.*, Chapter 7.1), of

synthesizing diverse ocean observations scattered in space and time into a dynamically consistent picture, can be tackled successfully only on the basis of models that faithfully represent the essential mechanisms of the circulation and its response to atmospheric flux variations.

It is beyond the scope of this chapter to give a comprehensive discussion of the host of issues important in ocean model development or to attempt an assessment of the state of ocean modelling of relevance for the spectrum of applications. We feel it important, however, to reflect upon the motivations and implications of one of the most basic modelling choices – integration time – and the associated distinction between solutions in equilibrium and non-equilibrium with the thermo-haline forcing (Section 2.2.3). Our main interest here is on the dynamical aspects of the wind- and thermohaline-driven circulation in high-resolution model studies, i.e. on the forced and spontaneous variations obtained under realistic forcing, in comparison to actual (WOCE) observations. We feel it particularly instructive to contrast the behaviour and simulation capability of present ocean circulation models in different dynamical categories: variability in response to wind forcing on intra-seasonal to interannual time scales (Section 2.2.4.1); eddy variability (Section 2.2.4.2); and aspects of the decadal-scale response to variations in high-latitude buoyancy forcing (Section 2.2.4.3). Since other chapters in this volume specifically deal with dynamical and modelling issues relating to the Southern (Rintoul *et al.*, Chapter 4.6) and Tropical (Godfrey *et al.*, Chapter 4.3; Liu and Philander, Chapter 4.4) Oceans, the discussion here will mainly draw from examples from the northern mid-latitude oceans.

Discussions of many questions of model formulation, including numerical model concepts, sub-grid-scale parameterization and the forcing of ocean circulation models, are covered in Chassignet and Verron (1998). A review of developments and the quasi-equilibrium solution behaviour of global ocean models has been given by McWilliams (1996, 1998).

2.2.2 Historical perspective

The development of numerical models able to describe faithfully the dynamical behaviour of the complex, non-linear and turbulent system of the

ocean's general circulation inextricably faces a number of obstacles. One reason why the development of realistic ocean models has considerably lagged behind that of their atmospheric counterparts has certainly been the societal need for weather prediction, which focused attention on the latter. However, a key impediment in ocean model development has also been in the small-scale nature of many of the essential features of the general ocean circulation. The demands for both computing power and storage capacity from including energetic, Rossby radius-scale features in ocean models exceed the demands of comparable atmospheric models by two orders of magnitude. This is compounded by the need for much longer integration periods due to the slow adjustment of deep ocean properties in response to surface fluxes.

As demonstrated with the first near-equilibrium solution for a three-dimensional model with wind and thermal forcing, obtained for an idealized box ocean by Bryan and Cox (1968), the adjustment of the deep density fields to the imposed surface flux conditions is governed by the long time scales associated with the weak vertical diffusion and weak advective flushing of the deep ocean basins. Hence, due to the need of extremely long integration times, modelling aimed at the goal of simulating the global circulation in equilibrium with the surface fluxes has to compromise in the spatial, particularly horizontal, resolution, and hence in the representation of the actual structure of ocean current features.

The development of three-dimensional models in which both density and velocity are predicted simultaneously received its primary incentive from the need to include an interactive dynamical ocean component into climate simulation (see also Wood and Bryan, Chapter 2.3). Incorporation of oceanic feedbacks in model simulations of climate change had gone through a number of stages. Early attempts to study the CO₂-induced climate change by the use of a general circulation model of the atmosphere included the ocean merely as a saturated surface interacting with the atmosphere (e.g. Manabe and Wetherald, 1975). In a next step, the ocean's capacity for seasonal heat storage was taken into account, by including a shallow mixed-layer ocean with constant thickness of about 50 m (Manabe and Stouffer, 1979, 1980; Washington and Meehl, 1984). Up to this stage the discussion of climate change focused upon the difference

between the equilibrium climates with normal and above-normal atmospheric CO₂ concentrations. Incorporation of ocean circulation dynamics in model simulations of anthropogenic increase of atmospheric trace gases was first accomplished in the 1980s, initially by studies of the climate system response to a step function increase in idealized (Bryan *et al.*, 1982; Bryan and Spelman, 1985) and more realistic domains (Schlesinger *et al.*, 1985), followed by first investigations of gradual increase scenarios (Washington and Meehl, 1989).

While coarse-resolution models of the global ocean circulation became a standard for coupled, climate system studies, their typical application in oceanic research was not that of realistic simulation, but directed primarily at investigations of principal mechanisms. For example, a host of global model studies helped to elucidate how wind and buoyancy fluxes at the sea surface conspire to maintain the ocean's water-mass properties and tracer distributions, and how these distributions depend on model assumptions and parameters (Bryan and Lewis, 1979; Cox, 1989; Toggweiler *et al.*, 1989; England and Hirst, 1997).

Following the intensive field programmes in the 1970s (POLYGON, MODE, POLYMODE), much of the interest in ocean model development and application shifted towards the dynamics of mesoscale current features and variability that became recognized as the prime signal in direct current measurements and satellite observations. The subsequent development of eddy-resolving models of ocean circulation, pioneered by Holland and Lin (1975), Semtner and Mintz (1977), and Robinson *et al.* (1977), progressed effectively separate from the ocean climate models. The heavy demands of computing power necessary to represent mesoscale variability in large-scale models often required compromises in potentially important physics, e.g. by adopting simplified (adiabatic, quasigeostrophic) dynamical equations, and by limiting the computational domain to idealized basins.

Some significant strides in ocean model development in the second half of the 1980s can be identified that helped to blur the distinction between the two, hitherto non-interactive lines of ocean modelling. A pioneering step towards explicit representation of mesoscale processes in a wind- and buoyancy-driven, geophysically sized ocean basin was taken by Cox (1985): a grid size of 1/3° in latitudinal and 2/5° in longitudinal direction permitted

a resolution of the first mode Rossby radius in the subtropics, and thus inclusion of parts of the eddy spectrum. Shortly thereafter, the investigation of the role of mesoscale processes in the thermohaline circulation of realistic ocean basins, under realistic atmospheric forcing, was taken up by a collection of ambitious efforts. The model domains considered in these first planetary-sized, 'eddy-permitting' calculations (i.e. with grid sizes enabling representation of the upper range of mesoscale eddies) included the Southern Ocean (FRAM Group, 1991), the North and Equatorial Atlantic (Bryan and Holland, 1989), and the World Ocean without the Arctic (Semtner and Chervin, 1988, 1992). All of the computations induced a considerable number of studies, often in collaboration with observational oceanographers, probing the models' validity across a host of phenomena. The model configurations gradually evolved in subsequent years, building on the experience from the initial experiments and capitalizing on advance in computing capabilities, numerical methods, and forcing data sets. Especially for the Atlantic configuration, a large number of experiments performed by several groups as a collective 'Community Modelling Effort' (CME) added to an exploration of the influence of forcing functions, resolution and sub-grid-scale parameterization (for an overview, see Böning and Bryan, 1996). Developments in global models by three groups included substantial reductions in horizontal grid sizes: to a (latitudinal) average of 1/4° (Stammer *et al.*, 1996), 1/6° (Maltrud *et al.*, 1998), and 1/4° and 1/8° (Webb *et al.*, 1997; Saunders *et al.*, 1999).

An important contribution towards the model refinements, eventually realized during the last several years, was the formulation of numerical model concepts and algorithms that provided alternatives to the early paradigm of Bryan (1969). The model formulation based on coordinate surfaces coinciding with geopotential levels proved to be a convenient and versatile concept for a wide range of applications, but had to deal with some inherent difficulties associated with a staircase representation of topography and spurious diapycnic mixing. New model developments had in particular focused on a different representation of the vertical coordinate and, associated with that, bottom topography. Isopycnic coordinates (Bleck *et al.*, 1992; Oberhuber, 1993) appear optimally suited for a representation of advective transports in the

ocean. Terrain-following (or sigma) coordinates (Haidvogel *et al.*, 1991; Ezer and Mellor, 1997; de Miranda *et al.*, 1999) attempt to avoid spurious effects associated with stepwise representation of bathymetry. A systematic evaluation of the diverse models available today, including an assessment of the robustness of solution features and an identification of model idiosyncrasies, has only begun in recent years. Following a few basin-scale model-model comparisons in relatively coarse resolution (Chassignet *et al.*, 1996; Roberts *et al.*, 1996; Marsh *et al.*, 1996), a systematic investigation of the performance of higher-resolution models (at an average grid size of $1/5^\circ$) based on the different vertical coordinate treatments was made in the DYNAMO project (DYNAMO Group, 1997; Willebrand *et al.*, 2001).

The bulk of global model simulations and basin-scale model sensitivity and intercomparison studies have been performed on horizontal grids that still fall short in the simulation of important mesoscale current features at higher latitudes. Typical deficits in these ‘eddy-permitting’ models include the intensity and spectral distribution of eddy variability (Beckmann *et al.*, 1994a,b; McClean *et al.*, 1997; Maltrud *et al.*, 1998) and the regional distortions in intense western boundary currents such as in the pathway of the Gulf Stream near Cape Hatteras (Dengg *et al.*, 1996; Chao *et al.*, 1996) and the Grand Banks off Newfoundland (Stammer *et al.*, 1996; Willebrand *et al.*, 2001). Recently, a few very ambitious North Atlantic simulations using grid refinements to $1/12^\circ$ at the equator, based on both isopycnic (E. Chassignet, personal communication) and geopotential coordinate models (Smith *et al.*, 2000), have begun to examine systematically the impact of resolving the oceanic flow spectrum up to the first mode deformation radius over the whole North Atlantic; an illustration of the richness in flow structures emerging here is given in Fig. 2.2.1 (see Plate 2.2.1, p. 76).

By now, the reader may be concerned about the diversity of methods used to characterize model grid size. Various grid metrics have included the approximate square grid size in spherical models at middle or high latitudes, the latitudinal average grid size in square-grid Mercator models, and the equatorial grid size in square-grid Mercator models. It helps to invoke a specific metric, namely the average over valid ocean gridpoints of the effective

grid size in km, expressed in degrees using a conversion factor of 110 km per $^\circ$. Under this method, which was proposed by R. Smith, the various spherical coordinate models are close to their original designations, the ‘ $1/4^\circ$ ’ and ‘ $1/6^\circ$ ’ global models in Stammer *et al.* (1996) and Maltrud *et al.* (1998) become about $1/3^\circ$ and $1/5^\circ$, respectively; and the ‘ $1/12^\circ$ ’ and ‘ $1/10^\circ$ ’ North Atlantic models of Chassignet (personal communication) and Smith *et al.* (2000) become approximately $1/17^\circ$ and $1/14^\circ$, respectively.

Despite the remarkable progress in the computational domains realized in recent years as a result of the increase in computing capabilities available to the ocean modelling community, it has to be emphasized that the gap between those models developed and used primarily for oceanographic applications, and those used as components in climate system models, has not yet been closed. Common to all high-resolution model studies of ocean circulation, up to the present, has been a limitation of integration periods to, typically, 20–30 years (only a few eddy-permitting model experiments have been run for periods of 50–100 years). The nature of the dynamical balances realized in such model solutions and what this implies for their interpretation, for example in comparison with actual oceanic measurements, will be discussed in the next section.

2.2.3 Basic model design considerations: equilibrium versus non-equilibrium solutions

Since it is impossible to embrace, in a single model calculation, the vast range of space and time scales governing a natural, geophysical fluid system, any model construction involves a number of critical choices. The most basic choice in ocean general circulation modelling concerns integration time, and had led to a rather sharp distinction of two model categories: models aiming at solutions in thermodynamic equilibrium that require a compromise in spatial resolution; and models aiming at an accurate depiction of the actually observed, energetic flow scales that require a compromise in the adjustment to a full equilibrium state.

Despite significant strides in computer capabilities, the distinction between the two main lines characterizing ocean model development over the last couple of decades has not yet faded, nor is

likely to happen in the next few years. The horizontal resolution anticipated for the ocean component of the next generation of climate system models is of the order of 1°; while further decrease in grid size for single experiments may be possible, this has to be balanced against the need (and associated costs) for including more components of the climate system, and for ensembles of experiments integrated over long time spans (WOCE International Project Office, 1999; see also Wood and Bryan, Chapter 2.3). Obviously, the critical issue that continues to separate coarse-resolution and fine-resolution ocean modelling is integration period: in order to remove transients in the deep interior temperature and salinity fields and to achieve a state of near-thermodynamic equilibrium between the field variables and the surface fluxes, global models need to be run over time spans of several thousand years, a time scale effectively set by the pace of the weak advective and diffusive processes in the abyssal ocean.

There is little doubt that in order to be useful in coupled climate studies ocean models need to demonstrate sufficient realism in equilibrium solutions. Obviously, it is only through long-term integrations that the effect of parameterizations of sub-grid-scale mixing processes on water mass structure and thermohaline circulation will become apparent. As has been demonstrated by a number of authors, the diffusion across isopycnal surfaces not only governs pycnocline structure and dynamics (Salmon and Hollerbach, 1991), but also latitudinal property fluxes associated with the thermohaline overturning circulation (Bryan, 1987). Accordingly, comparison of simulated property distributions with the mean hydrographic state of the ocean represents a prime means of assessing model mixing parameterizations. (It should be noted, however, that although this means of testing equilibrium solutions utilizes the prime source of information gathered in the history of oceanographic field work, it is built on the implicit assumption that the observed state of the ocean is in near-thermodynamic equilibrium: as discussed, e.g. in Chapter 7.3 (Dickson *et al.*), the WOCE period appears unusual enough that this has to be regarded with some caution.) For example, some of the typical deficiencies of ocean climate models with respect to pycnocline sharpness and meridional heat transport have been attributed to either spurious mixing associated with the parameterization scheme (Danabasoglu

et al., 1994; England and Hirst, 1997; England and Rahmstorf, 1999) or the chosen profiles of vertical diffusivity (Cummins *et al.*, 1990; Tsujino *et al.*, 2000). In the last few years there has been considerable success in eliminating spurious diapycnic mixing in z -coordinate models by adopting improved parameterization schemes for eddy transports, building on the method of Gent and McWilliams (1990) (see also Section 2.2.4.2); there have also been first attempts to assess the effect on global circulation patterns of enhanced vertical diffusivity over rough bathymetry (Hasumi and Sugino, 1999a).

However, while controlling the secular behaviour of the water mass properties and thermohaline circulation, the slow small-scale interior mixing processes have little influence on the response of the flow field to atmospheric forcing anomalies at shorter time scales, a situation analogous to the spin-up of an ocean circulation model from given hydrographic conditions. It has been shown in both idealized (Kawase, 1987) and full general circulation models (Döschner *et al.*, 1994; Gerdes and Köberle, 1995) that an initial dynamic adjustment to thermohaline forcing is effectively obtained on the same time scale as for a wind-driven circulation (Anderson and Killworth, 1977), set by the travel time of baroclinic Rossby waves through the basin. Specifically, changes in the properties of Denmark Strait Overflow Water (DSOW), in the northern Irminger Basin, are communicated rapidly towards the equator via continental shelf waves along the western boundary, leaving a signature in both deep and upper western boundary currents, meridional overturning and poleward heat transport on time scales of 1–2 years; through the interior baroclinic adjustment process it then takes 10–15 years before a new quasi-equilibrium is established in the mid-latitude North Atlantic (Fig. 2.2.2). During the course of the initial, dynamic adjustment phase – that is, the first few decades of an ocean model spin-up – the large-scale water mass properties below the thermocline remain close to the initial conditions, except for regions of strong currents or near the deep water formation sites.

The differences in the governing mechanisms and dynamical balances between a long-term equilibrium state of the system and its response to changes in the surface fluxes have some important implications. First, it is the large difference in the

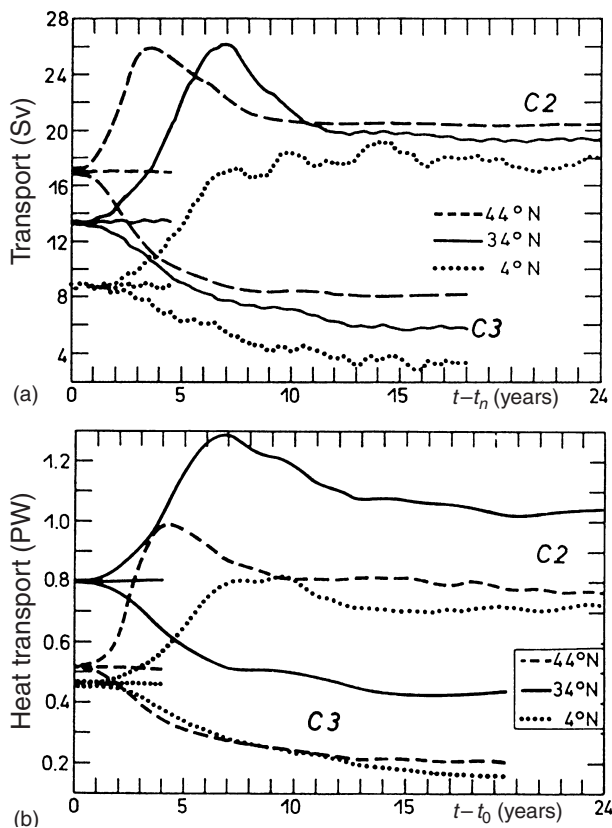


Fig. 2.2.2 Response of large-scale transport in the North Atlantic to a sudden change in the prescribed hydrographic properties of the Denmark Strait Overflow Water, from the model study of Döscher *et al.* (1994). (a) Zonally integrated transport of the NADW-overturning cell and (b) of poleward heat transport, at selected latitudes. Two model cases (C2, C3) are shown, both initialized ($t=0$) with the equilibrated state of a reference case. In C2 a denser outflow was imposed, while in C3 no outflow effect was included.

pace of the two stages in the adjustment process that provides the main rationale for model integration times of a few decades, and motivation for the analyses of model solutions in dynamic quasi-equilibrium in relation to observed ocean behaviours. While simulations of thermodynamic equilibrium are faced with the difficulty of an inaccurate knowledge of the history of surface fluxes over the secular time scales of required integration periods, simulations of the dynamical quasi-equilibrium stage can increasingly capitalize on improvements in both initial conditions (i.e. through the synthesis of the WOCE hydrographic database) and atmospheric fluxes (e.g. through the re-analysis projects in the major meteorological forecasting centres).

Accordingly, a quantitative comparison with observed time series of dynamical aspects of ocean circulation, such as surface height and boundary current transports, is rapidly gaining importance as a most powerful tool for an evaluation of model performance. It should be noted, however, that all such model analyses and confrontation of solutions with data have to account for the fact that the hydrographic (property) values in the deep ocean interior, away from intense currents, are to a large degree reflecting the initial conditions: for those areas a direct comparison with subthermocline WOCE section data is of little use. Nevertheless, the thermocline properties of WOCE sections and XBT (Expendable bathythermograph) lines allow valuable comparisons with the simulated vertical structures in models; and deep drifters provide intriguing zonal flows against which to evaluate model velocities and investigate dynamical mechanisms. In any event, the drift in the deep water mass properties, albeit weak, is not zero, implying a continuing, although very slow, evolution of the associated circulation and property fluxes. (For example, due to the ongoing storing of heat after the initial, dynamic adjustment phase, it requires integration times of several more decades to reduce local imbalances between the surface flux and the oceanic transport of heat below 0.1 PW.) The presence of the slow drift means that model property fluxes after a few decades of integration have to be interpreted with due caution.

2.2.4 Examples of model behaviour in different dynamical regimes

2.2.4.1 Wind-driven circulation and its variability on intraseasonal to interannual time scales

Model runs forced with a history of realistic time-varying atmospheric fluxes have shown increasing success in recent years in quantitatively reproducing time series from altimetric data, tide gauges, and *in-situ* station data such as western boundary current transport variability. The major forcing field for ocean current variability on intraseasonal, seasonal, and, to some extent, interannual time scales is the wind stress. Earlier ocean models typically relied on seasonal climatologies of surface fluxes estimated from historical marine observations and bulk aerodynamic formulae. In recent

years, model simulations have increasingly made use of synoptic analyses (both operational fields and re-analysis products) of global meteorological data produced by the major weather forecasting centres.

The improvements in wind stress fields by meteorological analyses have derived rather directly from higher atmospheric resolution and, in the case of re-analyses, from the application of a consistent algorithm over several decades. Improvements in the fluxes of heat and moisture have been slow and uneven; thus, there has been a continuing need for ocean modellers to scrutinize and sometimes correct the atmospheric fields available for computing these fluxes. Another important difference between the wind and thermohaline forcing functions of ocean circulation models concerns the physics of the air-sea exchange: due to the local feedback of the ocean on the heat and freshwater fluxes, the formulation of the thermohaline forcing must include a parameterization that accounts for this retroaction. For a more comprehensive discussion of both the accuracy of available air-sea flux estimates and the definition of consistent parameterizations, the reader is referred to Barnier (1998).

The distribution of large-scale, seasonal and intraseasonal sea level variability and its relation to changes in ocean circulation, were elucidated in coarse resolution (1° by 2°) global model experiments (Chao and Fu, 1995; Fukumori *et al.*, 1998). Steric changes of sea level, primarily due to seasonal changes in short-wave radiation, were in general smaller than the wind-driven variability, except for the mid-latitudes around 30°N and 30°S (see also Stammer, 1997a). Wind-driven changes were largely baroclinic in the tropics, and dominated by the annual harmonic. Large-scale sea-level variability at higher latitudes was associated with barotropic motions, and dominated by high frequencies that reflect the general frequency spectra of the wind stress curl. The reliability of the coarse resolution simulations was demonstrated by a significant correlation with altimetric data (spatially smoothed to suppress mesoscale energy) (Chao and Fu, 1995), and qualitative similarity of frequency spectra with altimetric and tide gauge measurements (Fukumori *et al.*, 1998).

The simulation of local ocean variability is complicated due to the presence of mesoscale eddies and potential effects of small-scale topographic features. Insight into the realism of the forced

upper-ocean variability in a high-resolution, global model has been obtained by comparing its sea surface height variations with both tide gauge data and altimetric data (Tokmakian, 1996). The model is the $1/4^\circ$ Parallel Ocean Climate Model (POCM) that had been built on the near-global model of Semtner and Chervin (1988, 1992). It is forced here with a time series of European Centre for Medium Range Weather Forecasting (ECMWF) fields from 1979 to the present. Figure 2.2.3 compares simulated time series of Sea Surface Height (SSH) with a suite of tide gauges from Pacific coastal and island sites. There is a qualitative agreement for many of the stations. However, median correlation for all gauges after removal of the seasonal cycle is only 0.4, indicating that much of the variance is not related to the local atmospheric forcing. There are, however, regional differences; e.g. correlation is higher (0.7) for areas dominated by ENSO signals. There is an indication that ENSO signals at middle to high latitudes along the coast of the Americas are more attenuated in the simulation than in reality – this may indicate that the model grid is still too coarse to allow the model's biharmonic damping coefficients to be small enough not to interfere with propagation of Kelvin and shelf waves. The long-term information at individual sites is complemented by the temporally more restricted (5 years) but global perspective from altimeter data. It indicates highest correlations between the model's SSH variations and the observed fields for the tropical oceans and throughout those regions of the (northern) hemisphere outside of the Kuroshio and Gulf Stream extensions, which are dominated by internally generated, mesoscale variability. The correlations in the southern hemisphere are generally lower, possibly an indication of less accurate wind forcing fields due to fewer observations (Tokmakian, 1998). A comparison of POCM results and (TOPEX/POSEIDON (T/P) variability using Hovmöller diagrams for various latitudes in the Pacific also showed excellent tracking of phenomena, especially in the lower latitudes (Stammer, 1997a). Global comparisons of $1/4^\circ$ and $1/6^\circ$ models against T/P have been made to show large-scale anomaly patterns on intraseasonal, annual and interannual time scales (Stammer *et al.*, 1996; Fu and Smith, 1996). As in the case of the coarse-resolution model simulations mentioned above, there was a generally good agreement with respect to the large-scale

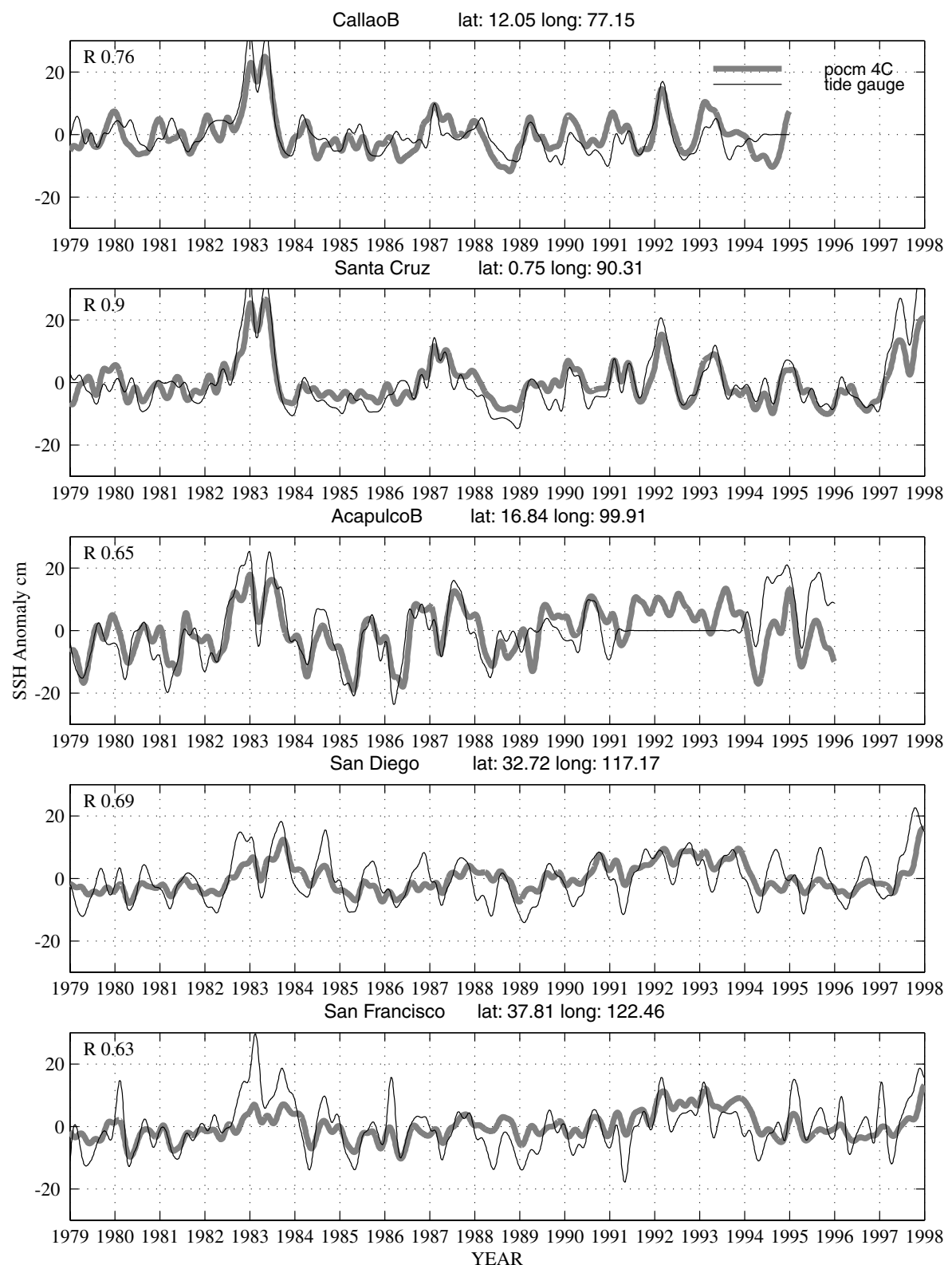


Fig. 2.2.3 SSH anomalies in the eastern Pacific Ocean: comparison of tide gauge records (from the Joint Archive for Sea Level of NODC and University of Hawaii Sea Level Center) to a global model (POCM) simulation spanning 20 years (1979–98), forced with variable wind, heat, and freshwater flux analyses from the ECMWF (Tokmakian, 1998). The time series for both data sets have had a 3-month filter applied for display purposes. Courtesy of R. Tokmakian.

patterns of intraseasonal and seasonal variability, and it included also significant extratropical aspects of ENSO.

A focal point for a host of modelling studies has been the seasonal cycle in the wind-driven gyre circulation, manifested primarily in a variability of meridional volume transports at the western boundary. It had been noted by Gill and Niiler (1973) that, in mid-latitudes, the seasonal and mean responses to the large-scale wind stress cannot be the same since the time scale for establishing the mean fields is much longer than a year. The various processes affecting the annual variation of boundary current transport were elucidated by Anderson and Corry (1985a) within the context of an idealized model. Unless forcing adjacent to the western boundary is considered, baroclinic Rossby waves had only little effect on transport variations in mid-latitudes. The seasonal response to large-scale forcing is essentially barotropic, and thus strongly influenced by topography; the phase lag is roughly zero. The particular situation in the western boundary regime of the subtropical North Atlantic was first investigated by Anderson and Corry (1985b) with a linear, two-layer model, forced with monthly wind stress anomalies of Hellerman and Rosenstein (1983). The simple model demonstrated the important role of the Bahamian Archipelago which, due to an effective blocking of the primarily barotropic response to large-scale forcing variations, leads to a seasonal cycle in the Florida Current different in origin and phase from large-scale Sverdrup dynamics, with a transport maximum in July–August and minimum in October–November. Since it is well measured in the Straits of Florida, the seasonal cycle has been used repeatedly for model–data comparisons, usually indicating a good reproduction of the phase, but discrepancies in the amplitude. However, due to the local generation it can neither serve as an indicator of variability in the ocean’s interior nor as an ideal test for large-scale models; in fact, the most critical model factor for simulations of the seasonal variation in the Straits is the (local) wind forcing: the difference between solutions of different models, forced by the same wind stress, are usually much smaller than the changes obtained by using alternative wind stress climatologies (Böning *et al.*, 1991, 2001).

A conspicuous, common feature of early model studies (e.g. Anderson and Corry, 1985b; Sarmiento,

1986; Greatbach and Goulding, 1989; Smith *et al.*, 1990) was a strong annual variation of $\pm 10\text{--}15\text{ Sv}$ east of the Bahamas which, for a long time, stood in sharp contrast to the observational evidence. In fact, a first analysis of direct current meter observations by Lee *et al.* (1990), obtained at 26.5°N over a 14-month period, gave no indication of an annual signal; instead, they showed a surprisingly large (up to about 90 Sv) variation of the volume transport on a time scale of 70–100 days. An explanation for the apparent discrepancy was offered by solutions of the high-resolution CME model experiments, which also showed the transports at that site to be governed by strong, weakly depth-dependent fluctuations arising from local instabilities of the upper-layer flow field. However, a seasonal signal very similar to that of the earlier model solutions was present also, but could be revealed only after a multiyear averaging (Böning *et al.*, 1991). The model results were confirmed when a similar averaging became possible after a multiyear continuation of the current meter measurements (Lee *et al.*, 1996). Figure 2.2.4 shows the remarkable agreement in both phase and amplitude between model results and measurements averaged over a 5.8-year span. A recent evaluation of the suite of different models used in the DYNAMO programme showed the annual cycle in the boundary regime east of the Bahamas to be a very robust feature of the solutions, suggesting that model issues such as vertical coordinate schemes and corresponding representation of local topography representation, or parameterization of sub-grid-scale mixing effects, are of minor importance for the simulation of wind-driven variations (Böning *et al.*, 2000). Obviously, the single most important factor for a realistic simulation of transport variations at seasonal time scales is the wind stress; indeed, while similar to each other, the DYNAMO simulations gave an annual range of less than half of that obtained by Lee *et al.* (1996), implying that the annual variation of the curl of the ECMWF-based wind stresses at this latitude was too weak.

The capability of high-resolution ocean models to aid in the interpretation of the sparse observations of current fluctuations on interannual and shorter time scales has also been utilized to explain the fragmented information on wind-driven changes in the North Pacific. For example, time series of absolute volume transport across a single section of the Kuroshio estimated from T/P altimeter data

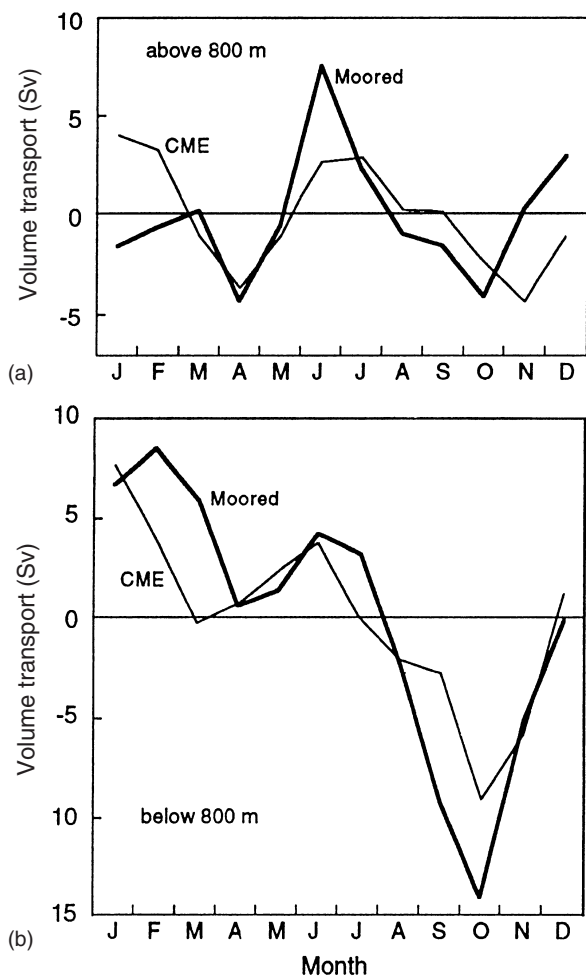


Fig. 2.2.4 Annual cycle of volume transports in the western North Atlantic at 26.5°N, east of the Bahamas, from a 5.8-year record of moored transports (heavy solid), and 5 years of a CME-model run. (a) Transports in the upper 800 m, (b) transports below 800 m. From Lee *et al.* (1996).

suggest strong fluctuations on time scales of a few months (Imawaki *et al.*, 1997). Similar to the case of the North Atlantic, the measurements appear at odds with previous model suggestions of a winter-time maximum in response to the basin-scale wind forcing (Sekine and Kutsuwada, 1994). Chelton and Mestas-Nunez (1997) analyse results from a version of the global model described by Dukowicz and Smith (1994) at a mean resolution of 1/6°, forced by ECMWF wind stress fields, and demonstrate that the low-frequency variability of the barotropic streamfunction is dominated by simple time-varying Sverdrup response over large parts of the basin. A stringent test of the model behaviour is provided by comparison with SSH time series

from T/P observations (corrected for a steric response to heating and cooling, and averaged spatially to remove effects of energetic Rossby wave signals). Time series of model transport for areal averages over the Oyashio, Kuroshio and Kuroshio Extension are similar to those estimated from the T/P data (Fig. 2.2.5). Higher correlations between model and data than between model and simple Sverdrup dynamics indicate the importance of added model dynamics not considered in linear Sverdrup dynamics.

The example again shows that quantitative tests of model simulations concerning the response to atmospheric fluctuations tend to be complicated by the presence of stochastic fluctuations of large amplitude. Because of the need for an averaging in time or space to unravel the deterministic signals, stringent tests comparable to the possibilities offered by altimeter data are usually more difficult if based on local time series, e.g. of boundary current transports. However, present evidence suggests that the high levels of model skill with respect to wind-driven variability are not restricted to near-surface phenomena. For example, the annual and semiannual variation in the transport of the Deep Western Boundary Current in the equatorial Atlantic, revealed by a synthesis of several year-long current meter time series (Fischer and Schott, 1997), are quantitatively well reproduced in the DYNAMO model simulations using wind stresses based on ECMWF analyses (Fig. 2.2.6).

The recent demonstrations of model skill concerning wind-driven variations in observable quantities, such as boundary current transports, obviously bear some implications for the models' usefulness in understanding phenomena and mechanisms less accessible to observations. A particularly important question is that of the representativeness of single hydrographic sections for estimating 'mean' fluxes, e.g. of heat transport in the ocean. Model studies have generally found an annual cycle of heat transport with a similar phase as obtained in observational estimates (e.g. Hsiung *et al.*, 1989). Inspection of various North Atlantic models, including a suite of sensitivity experiments carried out in the CME, indicated the wind forcing to be the most decisive factor for the annual range in the subtropics (Böning and Herrmann, 1994). Very small model-to-model differences were also found in the DYNAMO model intercomparison (Fig. 2.2.7), in strong contrast to the large

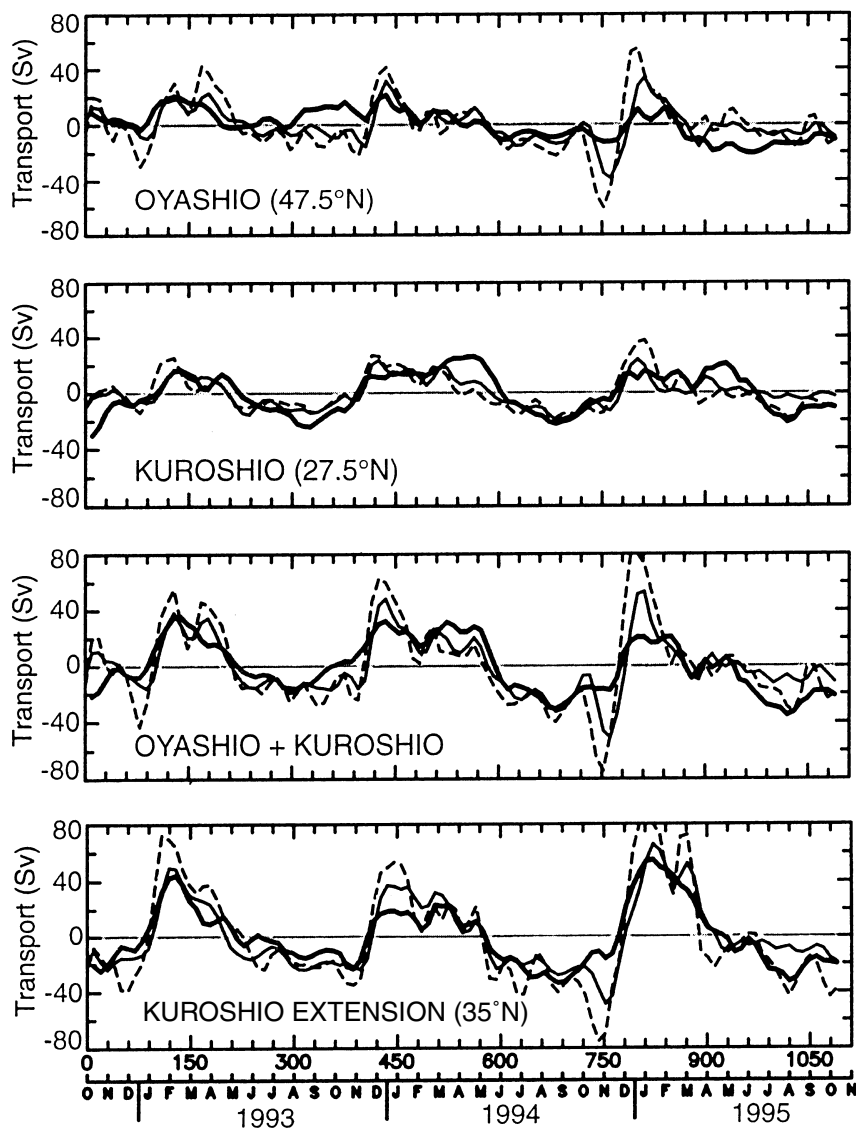


Fig. 2.2.5 Transport time series estimated from T/P SSH (thick solid lines), from a global model simulation (thin solid lines), and from the flat-bottom Sverdrup balance (dashed lines). From Chelton and Mestas-Nunez (1997).

differences in the annual mean behaviour (Willebrand *et al.*, 2001; see also Section 2.2.4.3). The similarity of model solutions with rather different mean flow patterns is suggestive of an essentially linear mechanism governing the atmospherically forced variability of ocean fluxes on seasonal time scales, adding to a remarkable consistency in model results concerning the underlying mechanism. As originally suggested by Bryan (1982), it can be understood in terms of wind-driven mass transport variations in the meridional–vertical plane: transport variations induced in the surface Ekman layer are compensated by nearly depth-independent return flows, i.e. without any

significant baroclinic adjustment except for a narrow equatorial belt. In contrast to observational studies (Molinari *et al.*, 1990b; Fillenbaum *et al.*, 1997) using the seasonal hydrographic climatology of Levitus (1982), the model results unanimously negate the significance of seasonal baroclinic flows in the interior, and suggest that the geostrophic shear observed in one-time hydrographic sections should still reflect the longer-term mean conditions.

2.2.4.2 Simulation of mesoscale variability

Investigation of the mechanisms of mesoscale ocean variability has been a ‘classical’ application

of high-resolution models since the first successful studies for idealized basins in the mid-1970s. A particular focus has been on the questions of the generation mechanisms of the observed eddy

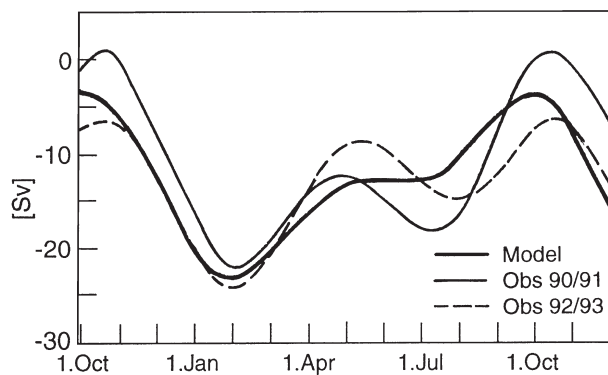


Fig. 2.2.6 Transport of the DWBC between 1000 m and 3100 m depth in the equatorial Atlantic, from several year-long time series of moored current meters (Fischer and Schott, 1997) and a DYNAMO model simulation with daily wind fields from ECMWF. Moored results shown are the combined annual and semiannual harmonics of transport variability for two different observational periods. Model curves show the mean seasonal cycle as obtained by averaging over 5 years of integration and a harmonical analysis similar to the observations. The annual mean southward transports are 13.0 Sv for the model, $12.4 \pm 6.8 \text{ Sv}$ and $13.5 \pm 5.3 \text{ Sv}$ for the two measurement periods.

spectrum and its role in the time-mean transports of heat and other properties.

High-resolution global and basin-scale models have had growing success in reproducing the eddy variability that accounts for most of the signal in SSH variability maps from T/P. Early WOCE studies with spherical-coordinate models qualitatively reproduced the localized regions of strong variability in the North Atlantic at $1/3^\circ$, in the Southern Ocean at $1/4^\circ$, and in the World Ocean at $1/2^\circ$ (Semtner and Chervin, 1988; Bryan and Holland, 1989; FRAM Group, 1991). Grid refinements have been made by switching to Mercator and/or finer grids to obtain an average of $1/6^\circ$ or $1/8^\circ$ globally and below $1/10^\circ$ in the North Atlantic. Results show that the magnitudes of variability converge toward the observed values as grid size is decreased. Figure 2.2.8 is an example from an evaluation of the circulation in the Pacific Ocean seen in two versions ($1/4^\circ$ and $1/8^\circ$ mean grids) of a global model (Saunders *et al.*, 1999). As in similar comparisons made by McClean *et al.* (1997), all model cases roughly reproduce the distribution of SSH variability as derived from the T/P altimeter. Increased resolution yields an enhanced realism in regions of strong currents in mid-latitudes, but the models tend to underestimate the T/P variability in the subtropical oceans, away from the strong currents. The reader is referred to various maps of

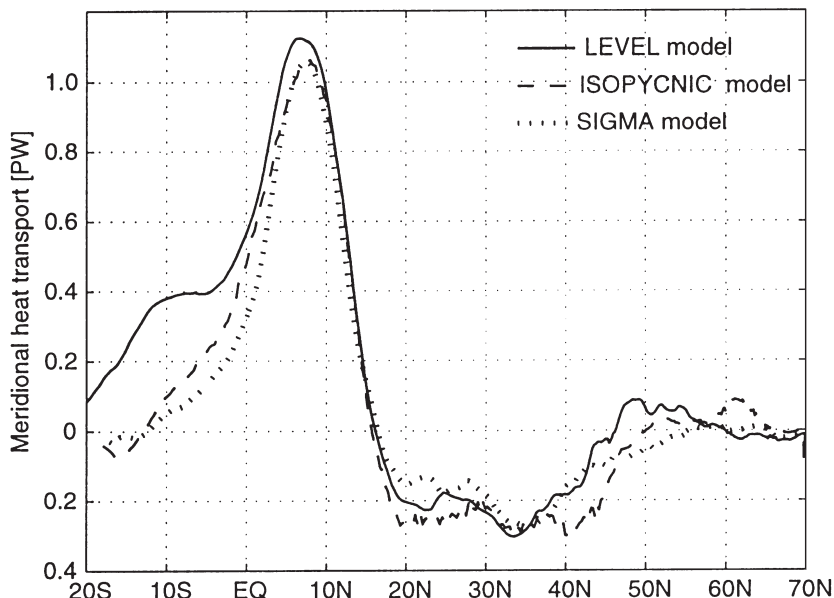


Fig. 2.2.7 Difference in 5-year mean northward heat transport between winter (Jan–Feb–Mar) and summer (Jul–Aug–Sep) for three models based on different vertical coordinate schemes and, associated with that, different representations of topography and sub-grid-scale mixing (Böning *et al.*, 2000).

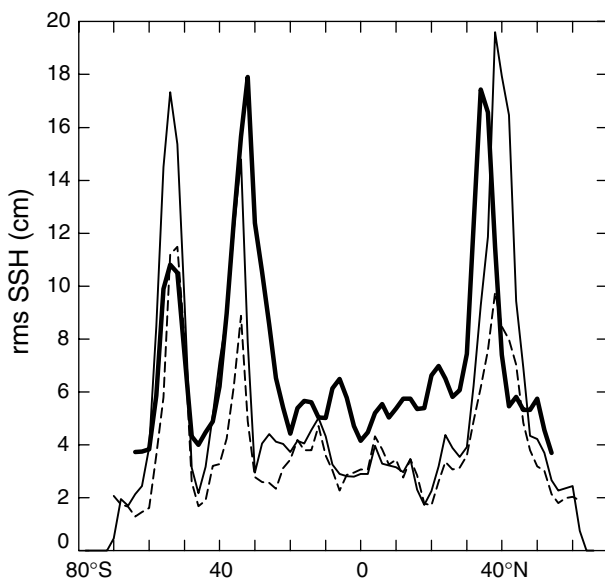


Fig. 2.2.8 Meridional profiles of the variance of SSH in the western Pacific (averaged between 150°E and 160°E). The bold solid lines are from T/P, the dashed lines are from a global model run (OCCAM) at 1/4° resolution, and the thin solid lines from a run at 1/8° resolution. From Saunders *et al.* (1999).

eddy variability (e.g. Fu and Smith, 1996) to see the improvements. One feature that remains to be reproduced effectively in the global models is the high variability near the African coast south of Madagascar, where a significant underestimate of variability may be related to inadequate meridional overturning as a result of poor initial conditions or surface forcing in the Southern Ocean. Additional analyses of the global simulations, including comparison with drifter data and discussion of eddy length scales, are found in Fu and Smith (1996), Stammer *et al.* (1996), McClean *et al.* (1997), Maltrud *et al.* (1998) and Saunders *et al.* (1999).

Figure 2.2.9, from Smith *et al.* (2000), depicts frequency-wavenumber spectra for the Gulf Stream region for an Atlantic model with 0.1° equatorial grid spacing, a model with 28 km equatorial grid spacing (i.e. the '1/6°' global model), and the same fields from T/P; another plot of the same quantity with 44 km equatorial grid spacing (i.e. from the '1/4°' global model) is given in Stammer *et al.* (1996). These clearly show the overall improvement obtained. In addition, typical deficits of previous Atlantic simulations, such as a failure to reproduce the variability in the eastern basin associated with the Azores Current (e.g. Beckmann *et al.*, 1994a,b), troublesome aspects of separation

of the Gulf Stream (e.g. Chao *et al.*, 1996) and incorrect pathways of the North Atlantic Current in the Newfoundland Basin (e.g. Willebrand *et al.*, 2000), are remedied as grid size reaches 1/10°. In each of these areas the improvement in the simulation of variability accompanies an improvement in the simulation of the mean flow, suggesting a significant regime transition in capturing ocean dynamics between 0.1° and 0.2° resolution.

The close correspondence between eddy kinetic energy distributions and mean baroclinic currents seen in both altimeter data and model results, and also the estimates of energy conversion rates from intensive field programmes, for example the SYNOP (Synoptic Ocean Prediction) study for the Gulf Stream (Cronin and Watts, 1996), strongly suggest baroclinic instability to be a main generation mechanism of mesoscale eddies. Another mechanism contributing to the spectrum of intraseasonal variability of ocean currents is wind forcing. Theory suggests that the extratropical ocean's response to forcing by wind fluctuations of annual period or less should mainly be barotropic (Willebrand *et al.*, 1980). A significant excitation of large-scale, barotropic variability at higher latitudes, notably for the eastern South Pacific and northern North Pacific, has been demonstrated by various altimeter and model analyses, e.g. Chao and Fu (1995), Fu and Smith (1996) and Fukumori *et al.* (1998). The question of a direct contribution of variable wind forcing to the observed distribution of mesoscale eddy energy has long been under debate, with some support coming from indications of a seasonal modulation of energy levels in some regions of the northeastern North Atlantic (Dickson *et al.*, 1982; White and Heywood, 1995). Recent model results show a similar seasonal cycle, with a winter maximum in eddy energy, as a result of forcing by high-frequency wind fields (Stammer *et al.*, 2000a). However, a significant wind impact on the generation of eddy energy appears to be confined to areas with very low values in their background eddy variability, i.e. away from the major frontal zones.

As noted above, for the foreseeable future it will not be possible to undertake extensive climate simulations with explicitly resolving ocean eddies. Representation of eddy effects in coarse-resolution, z -coordinate models has traditionally been rather crude, using simple downgradient diffusion terms for momentum and tracers. In the last few years,

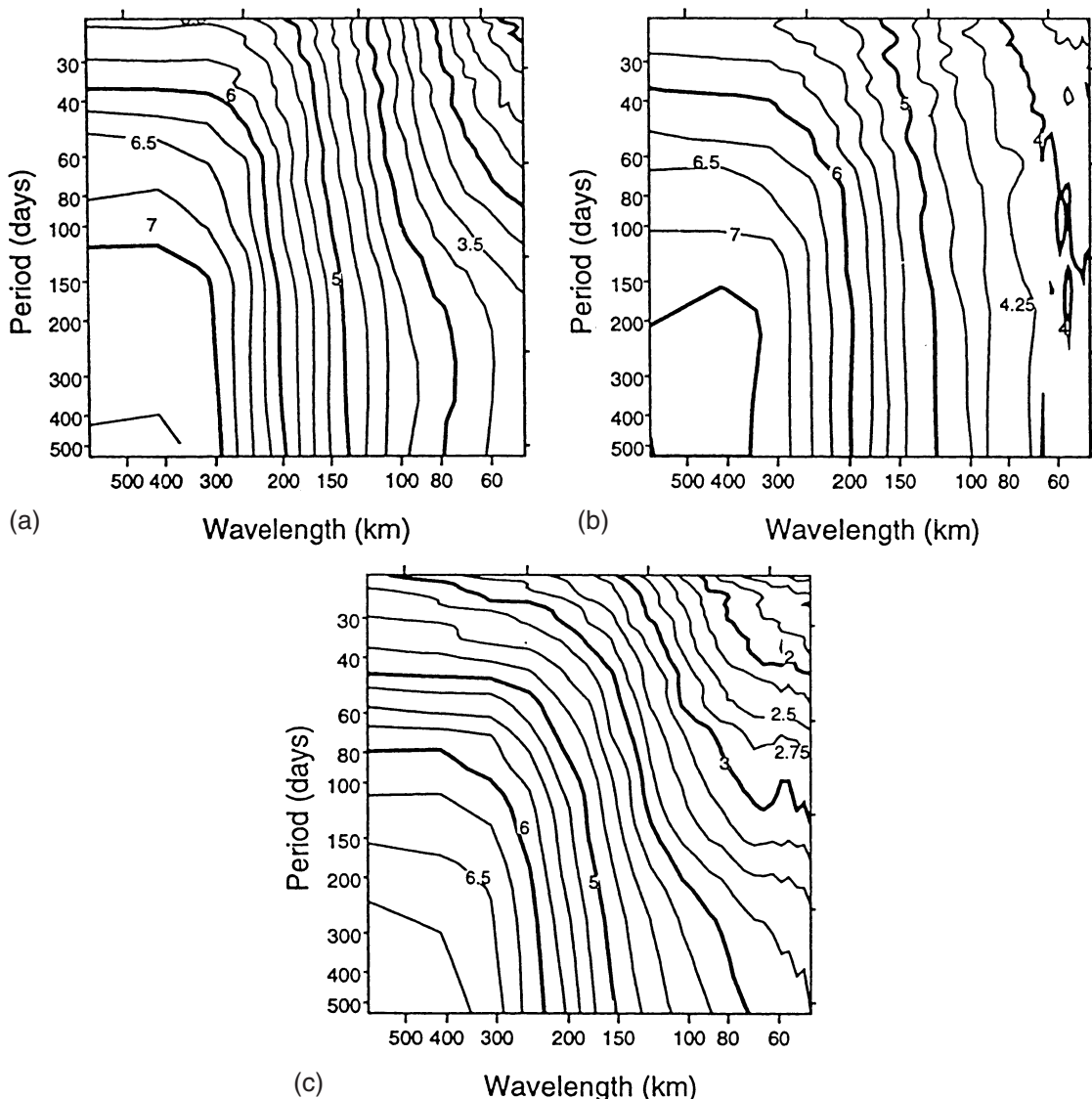


Fig. 2.2.9 Wavenumber–frequency spectra of SSH for an Atlantic model run at 0.1° (a), from T/P (b), and a model run at 0.28° (c). Data were sampled along the satellite ground tracks in the region bounded by $32\text{--}42^\circ\text{N}$ and $75\text{--}50^\circ\text{W}$ for both observations and models. The contours shown are negative logarithms to base 10 of the power spectra. From Smith *et al.* (2000).

however, there have been significant advances in parameterizing the effect of eddy fluxes, largely building on the concept of isopycnal layer mixing proposed by Gent and McWilliams (1990; hereafter GM). The important step taken by GM was to include dynamic effects of mesoscale eddies, such as the flattening of fronts (Gent *et al.*, 1995). The use of this scheme has been found of considerable success in level-coordinate models of low and intermediate resolution: improvements were noted with respect to thermocline sharpness, confinement of deep convection regimes, and elimination of spurious diapycnic mixing in frontal zones

(e.g. Danabasoglu *et al.*, 1994; England and Hirst, 1997).

Since a direct validation of eddy-mixing parameterizations is virtually impossible owing to the sparsity of measured eddy-induced fluxes in the ocean, eddy-resolving circulation models have been of critical importance to test and guide refinements of proposed schemes. A pioneering comparison of simulated eddy fluxes with the GM closure was performed by Rix and Willebrand (1996) based on CME experiments, proving a general consistency for the main thermocline of the subtropical North Atlantic. A recent analysis of a near-global,

eddy-permitting model by Bryan *et al.* (1999) lends support to the use of non-uniform mixing coefficients as proposed by Visbeck *et al.* (1997), and discussed also by Treguier *et al.* (1997). It is clear that the statistical output of the recent generation of eddy ‘resolving’ models will be of tremendous importance to further test and refine the parameterization of eddy effects in coarse-grid climate models.

2.2.4.3 Thermohaline circulation: Response to perturbations in deep water formation

There are two principal issues related to the response of large-scale ocean flows to high-latitude buoyancy forcing that have to be taken into account in all model studies of thermohaline circulation. One is the time scale for a near-dynamic equilibration of ocean currents, as discussed in Section 2.2.3. The effective adjustment within $O(10\text{--}20\text{ years})$ of major aspects of the general circulation in ocean basins (an exception to this time scale is the ACC (Antarctic Circumpolar Current) transport, which appears to take several more decades to equilibrate; see Chapter 4.6 for a discussion of ACC dynamics), justifies the use of high-resolution models with decadal-scale integration spans. An obvious appeal of relatively short model integrations is that the deep water mass properties remain close to climatology while the three-dimensional flow field has undergone dynamical adjustment to a balanced state and developed a considerable fraction of the observed energetic scales, facilitating their use in investigations of dynamical mechanisms that would not be possible using observations alone. Hence beyond the ‘classical’ application of eddy-resolving models, i.e. investigations into the role of mesoscale flow features as discussed in the previous section, these models have increasingly been utilized for a quantification of large-scale aspects of the thermohaline circulation such as the global, three-dimensional pathways of deep water and its conversion to surface water (e.g. Semtner and Chervin, 1992; Döös and Coward, 1997; Bleck, 1998), or to obtain insight into the role of conspicuous phenomena such as exchanges with marginal seas and between deep ocean basins divided by ridges and gaps.

The second, more problematic issue is that the simulation of important aspects of the ‘mean’ circulation critically depends on the representation of

small-scale ocean processes that are sub-grid-scale even for ‘eddy-resolving’ models. Accordingly, there is a strong sensitivity of model solutions to a host of model factors, including numerical formulation, resolution, and parameterization of sub-grid-scale physics, whose relative effects have only partially been unravelled to date. Model sensitivity studies over the last decade have focused mainly on the circulation of the North Atlantic. Since the subarctic Atlantic is the region where a substantial fraction of the world ocean’s deep water is formed, the ability to reproduce the essential features of that water mass conversion and the associated thermohaline overturning obviously represents a fundamental aspect of a model’s performance. Systematic model studies have especially been conducted in the framework of the CME, i.e. using a domain bounded at 15°S and 65°N , with boundary conditions aiming to mimic the water mass transformations outside the domain (Bryan and Holland, 1989).

A particular aspect of this model configuration was that the complex processes involved in the water mass transformations in the Nordic Seas, and the exchange of water across the sill of the Denmark Strait, were not part of the simulation. (The Iceland–Scotland Ridge was part of the CME domain; effects of the Faeroe Bank Channel throughflow were investigated in Redler and Böning, 1997.) Instead, the effect of the Denmark Strait outflow on the hydrographic properties south of the sill was included by a damping of T and S towards prescribed data, allowing an assessment of its role on the large-scale circulation. A suite of case studies using both medium-resolution (1°) and eddy-permitting CME model versions revealed the local density profile in the outflow regime to be a key factor for both the maximum strength and the vertical structure of the meridional overturning circulation in the North Atlantic (Dösscher *et al.*, 1994; Böning and Bryan, 1996). In the example shown in Figs 2.2.10a and b, a specification of conditions that aim at capturing the conditions of the narrow core of Denmark Strait Overflow Water (DSOW), i.e. with a minimum temperature of about 1°C , leads to an enhanced transport and downward shift in the southward flowing (North Atlantic Deep Water, NADW) branch compared with a model case using conditions as given by Levitus (1982) (i.e. with a minimum temperature of about 3°C . (Note,

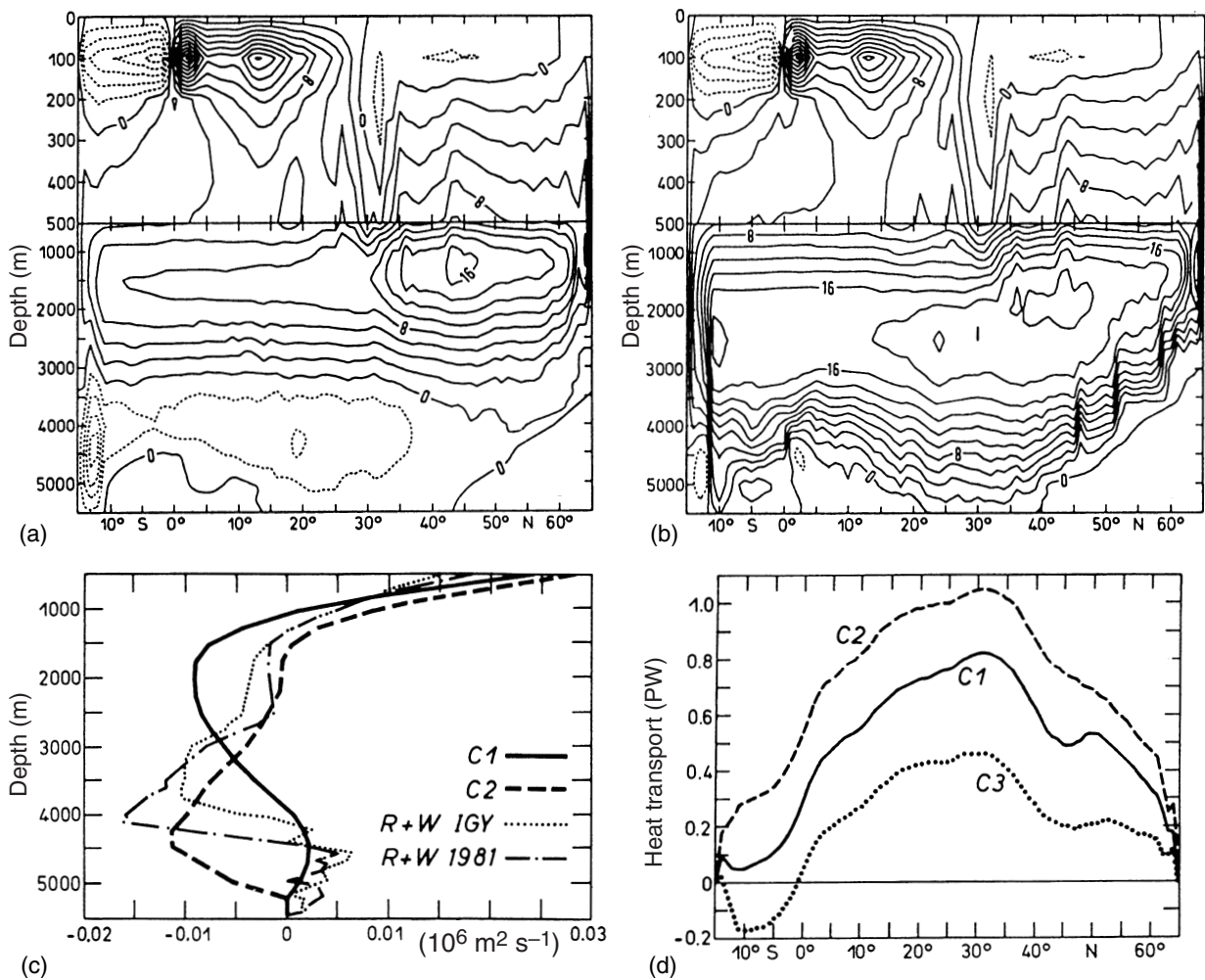


Fig. 2.2.10 Streamfunction of zonally integrated volume transport in the Atlantic for two CME model cases differing in the prescribed properties of the Denmark Strait Overflow Water near the northern model boundary at 65°N. Panel (a) shows smooth climatological data based on Levitus (1982) (model case C1); in (b) data based on an actual hydrographic section were used (case C2). Panel (c) shows a comparison of meridional transport per unit depth at 36°N of the two model cases with observational estimates (Roemmich and Wunsch, 1985; RW) based on transoceanic sections taken in 1958 (IGY) and 1981. Panel (d) shows the northward heat transport for the two cases, complemented by case C3 where an overflow effect was not included. From Döscher *et al.* (1994).

however, that the zonal grid spacing of about 60 km in this model case was not capable of resolving the narrow outflow plume, implying some exaggeration of the volume of dense water in this experiment.)

While the latitudinal pattern of meridional overturning still appears difficult to quantify observationally, the vertical profiles of the meridional transport per unit depth, obtained for individual transoceanic sections, have provided an important means of assessing model solutions. Model evaluations have mainly utilized profiles based on analyses of the repeatedly occupied sections along 24°N and 36°N (Hall and Bryden,

1982; Roemmich and Wunsch, 1985; Lavin *et al.*, 1998). Figure 2.2.10c demonstrates, for the example of the two prototype CME cases, that the changes in the relative strengths of the upper and lower NADW transports produced by the local differences in the water mass characteristics of the northern Irminger Basin can be well in excess of the range of interannual variability estimated from repeated sections.

Whereas in the CME configuration the characteristics of the outflow were prescribed as part of the northern boundary condition, their simulation in models extending into the Nordic Seas becomes dependent on a suite of delicate modelling issues,

including the representations of the subtle processes governing water mass transformation in the Norwegian and Greenland seas, and of the sill overflows across the narrow passages of the Greenland–Scotland ridge system. Some insight was provided by careful assessments of the behaviour of different model formulations, beginning with geopotential and isopycnic models in non-eddy-resolving North Atlantic configurations (Chassignet *et al.*, 1996; Marsh *et al.*, 1996; Roberts *et al.*, 1996), followed by the systematic evaluation of three comprehensive eddy-permitting models in the framework of the DYNAMO project (DYNAMO Group, 1997; Willebrand *et al.*, 2001). In addition to the difficulty in accurately depicting the passage geometries in models of moderate resolution, leading to a strong impact of minor changes in the chosen model topography (Roberts and Wood, 1997), the simulation of the dynamics of the narrow downslope flow of the dense overflow plumes (see Saunders, Chapter 5.6) has been identified as particularly critical. While in the real ocean, the density of the outflow product is governed by localized mixing with ambient waters caused by entrainment (Price and Baringer, 1994) and eddies (Krauss and Käse, 1998), the mixing rate in models has typically been affected primarily by numerical choices. In the case of DYNAMO, either too little or too strong diapycnic mixing in the outflow regime were identified as main causes for differences in the strength and vertical structure of the NADW cell akin to the CME cases discussed in Fig. 2.2.10.

In order to limit spurious numerical mixing effects and account for the impact of near-bottom dynamics in outflow regimes, the development of improved parameterization schemes has received increasing attention recently (Beckmann and Döscher, 1997; Killworth and Edwards, 1999). Inclusion of such schemes, particularly in the case of level coordinate models, has contributed to substantial improvements in the deep water formation and overturning circulation. These improvements are manifested, for example, in the simulation of the uptake and spreading of anthropogenic tracers such as CFCs (Redler and Dengg, 1999).

The subtleties in the behaviour of deep water formation and meridional overturning have important implications for the simulation of meridional heat transport in the ocean. In contrast to the primarily wind-driven variations on subseasonal to

interannual time scales (Section 2.2.4.1), model realizations of annual mean heat transports obtained under nearly identical forcing conditions have often shown substantial differences.

The overriding impact of the thermohaline overturning circulation for the poleward heat transport in the subtropical North Atlantic is illustrated in Fig. 2.2.11: the heat transport at 25°N, for a host of CME cases differing in thermohaline boundary conditions, resolution and mixing parameterizations (Böning *et al.*, 1996) and the suite of DYNAMO models (Willebrand *et al.*, 2000), approximately covaries with the local strength of the NADW cell; it increases by roughly 0.2 PW for a 4 Sv gain in the meridional mass transport. Differences in the wind forcing data used in these model cases (a diversity of marine wind climatologies and analyses from weather forecasting centres) are responsible for deviations of up to a factor of 2 in the subtropical gyre transports. However, these differences in the wind-driven vertically integrated transport make a negligible contribution to differences in heat transport: the net effect of the wind-driven circulation at this latitude is in the range of 0.2–0.3 PW.

As exemplified by the DYNAMO cases included in Fig. 2.2.11, the simulation of large-scale property transports is strongly affected by model choices of topographic details and local effects of (spurious) mixing. The potential dependency on a host of model factors very much complicates the interpretation of single model realizations or the assessment of the role of individual

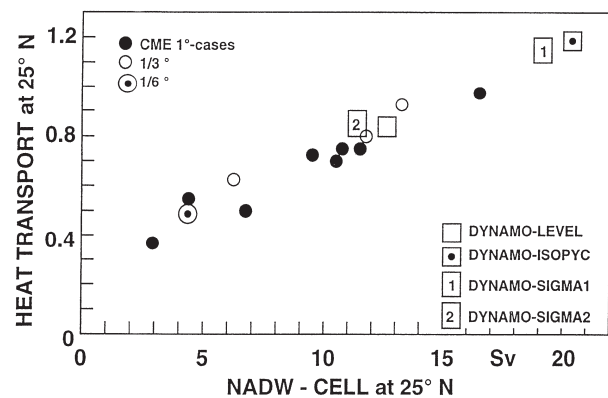


Fig. 2.2.11 Northward transport of heat versus overturning of NADW at 25°N for a host of CME model cases differing in resolution, buoyancy forcing and mixing parameterization (Böning *et al.*, 1996), and four different DYNAMO models (Willebrand *et al.*, 2001).

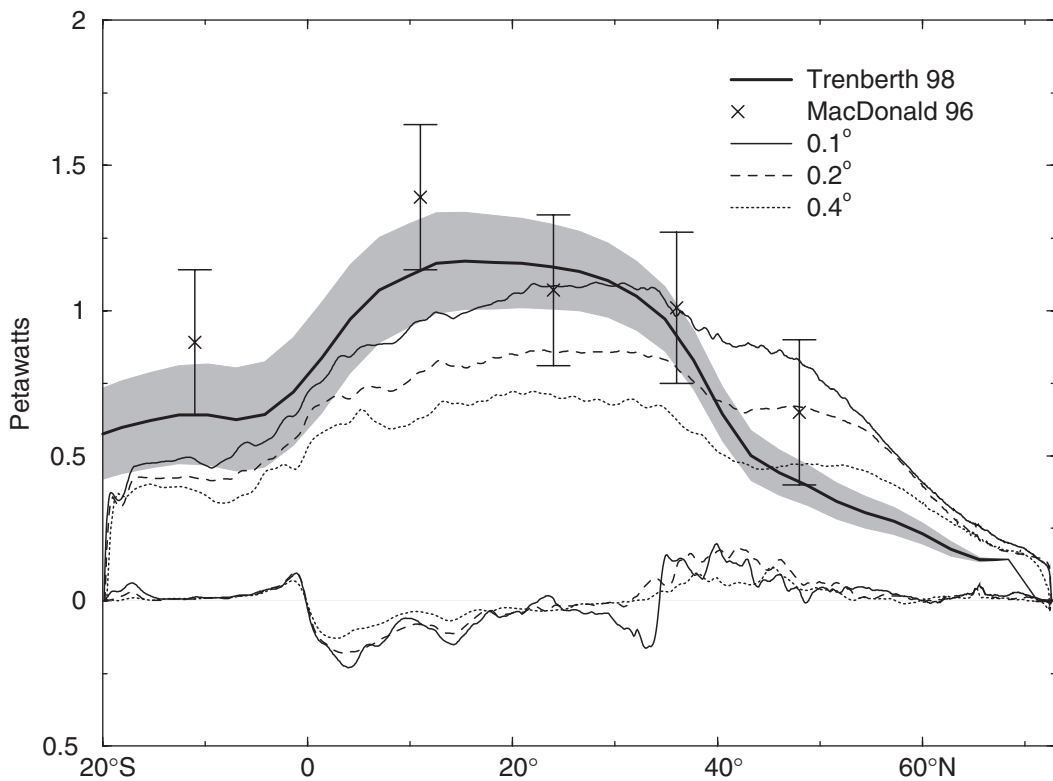


Fig. 2.2.12 Net meridional heat transport (upper curves) and transport of heat by the time-varying flow (lower curves) for North Atlantic models at 0.1° (solid), 0.2° (dashed) and 0.4° (dotted) resolution. The uncertainty range based on an atmospheric residual calculation (Trenberth, 1998a) is indicated by the shaded region; inverse model results based on ocean observations of MacDonald and Wunsch (1996) are indicated by multiplication signs. From Smith *et al.* (2000).

model factors. A particular example is the question of how model simulations of the meridional transport of heat are affected by the grid resolution. Evaluation of CME model cases using 1° , $1/3^\circ$, and $1/6^\circ$ resolution were rendered inconclusive because possible effects due to an improved resolution of (boundary) currents were outweighed by inevitable changes in the efficiency of boundary zones; e.g. Beckmann *et al.* (1994b) obtained a decrease in maximum poleward heat transport when going from $1/3^\circ$ to $1/6^\circ$ resolution, possibly caused by a less effective water mass transformation in the northern Irminger Basin. In a relevant study, Fanning and Weaver (1997a) showed in a series of idealized mid-latitude simulations with increasing resolution that an important mechanism of meridional heat transport at grid sizes below $1/2^\circ$ is that of baroclinic gyre transport, which comes to rival the heat transport of the zonally invariant meridional overturning and leads to an increase in total meridional heat transport. The

resolution issue was revisited recently in a very ambitious model study by Smith *et al.* (2000). Using a model configuration extending into the Nordic Seas similar to that in DYNAMO, each grid refinement, from $2/5^\circ$ to $1/5^\circ$, and finally to $1/10^\circ$, yielded a significant increase in meridional heat transport (Fig. 2.2.12). Interestingly, even the leap to an eddy-resolving simulation closely conforms with the behaviour of the previous eddy-permitting cases, i.e. closely falls on the regression line of Fig. 2.2.11. Hence, understanding the causes of the resolution dependence of heat transport in these cases is again complicated because of potential local effects such as differences in the simulation of transport and mixing processes in the overflow regime. It also remains to be seen whether the linear relation between heat transport and meridional overturning breaks down when fully global ocean models are used and when the imposed surface fluxes are determined by two-way interaction with an atmospheric model.

2.2.5 Concluding remarks

The primary aim of the WOCE modelling effort is the development of ocean component models for coupled ocean–atmosphere models that can be used to predict accurately climate change. The focus is hence on time scales from a few years to hundreds of years, covering both the decadal–interdecadal natural variability in climate and the long-term anthropogenic changes. Obviously, the testing of models suitable for predicting future evolution cannot be based on evaluations of equilibrium behaviours alone, but must extend also to the system's response to variations or perturbations in the external forcing, that is, it must aim at the physics of processes governing ocean dynamics at the time scales of interest.

The results of ocean modelling efforts of the past decade show that in assessing the performance of large-scale circulation models one needs to distinguish between different classes of phenomena:

- 1 Models are increasingly successful in reproducing observed aspects of large-scale circulation, including, in particular, the major characteristics of near-surface currents and mesoscale variability, and the atmospherically induced (especially wind-driven) variability on intraseasonal to interannual time scales.
- 2 In contrast, modelling of longer-term (decadal to secular) aspects, which include the dynamics of the thermohaline circulation, has been found to depend very critically on a number of local processes that are either not sufficiently well understood to allow suitable parameterization (as in the case of passage throughflows) or are (e.g. in the case of sill overflows and associated entrainment processes) dependent on a host of model factors that present modelling efforts have just begun to unravel.

In retrospect, one may note that the basic deficits of general ocean circulation models with

respect to long-term behaviours were obvious in the mid-1980s even on the basis of the crude climatological data sets available, and the principal requirements for model improvement were quite clear even without the need to collect more (WOCE) data; however, the goal of WOCE 'to collect the data to test' models, while then premature, has led to acquisition of data sets that now appear indispensable for the refinement of the present generation of models. Ocean model development for climate studies has to account for the fact that the anticipated development of computational resources will not allow resolutions finer than about 1° in the immediate future. However, the recent success in parameterizing the effects of mesoscale eddies allows smaller-scale mixing parameterizations to be tested in long simulations without the need for eddy resolution.

The characteristics of model behaviour in the different dynamical regimes have important implications for the utilization of ocean circulation models for interpretation of oceanographic measurements or observation systems design. Since the analysis of 'mean' or low-frequency current patterns and fluxes of mass, heat and other properties in any single model realization has to account for possible strong model sensitivities, the prime goal of modelling in this regime has continued to be on a principal understanding of dynamical mechanisms, e.g. of the role of individual phenomena in the global circulation. In contrast, the robustness of solutions with respect to the dynamical response to wind-driven changes, and the increasing number of examples where model predictions of phenomena have eventually been confirmed in dedicated measurement programmes, strongly suggest that the practice of ocean modelling is rapidly acquiring a more prominent role in oceanographic studies of phenomena on intraseasonal, seasonal and, to some extent, interannual time scales.

This Page Intentionally Left Blank

2.3

Coupled Ocean–Atmosphere Models

Richard A. Wood and Frank O. Bryan

2.3.1 Why coupled models?

Numerical weather prediction is now a well-established process that provides us with information of great practical value on a daily basis. But the limits of deterministic predictability of the atmospheric flow and weather are no more than a few days. Ensemble integrations of atmospheric models are now being used to try to extend this predictability, at least in a statistical sense. However, to understand, or even forecast, processes with time scales longer than a month or so we must incorporate into prediction models components of the climate system that adjust on these longer time scales. The ocean provides such time scales, and coupled ocean–atmosphere processes are likely to be fundamental to climate variability and change on all time scales from seasonal upwards. Coupled ocean–atmosphere models have been developed to address such issues.

Much of the early progress in coupled modelling was motivated by the desire to understand, and eventually forecast, the El Niño–Southern Oscillation phenomenon (ENSO), and great progress has been made in this area under the Tropical Ocean Global Atmosphere (TOGA) programme and its successor, CLIVAR-GOALS (see Delecluse *et al.*, 1998, for a review). However, in this chapter we focus on the decadal and longer time scales that are the main interest of WOCE. Coupled modelling work in this area has largely been motivated by the need to project the effects on climate of man-made emissions of greenhouse gases such as CO₂, over a time scale of 100–200 years, and one of the primary goals of WOCE was ‘to develop ocean

models suitable for predicting climate change, and to collect the data to test them’.

In this chapter we concentrate on global General Circulation Models (GCMs), which are the most comprehensive models used in modern climate research. Four possible applications can be identified:

- 1 estimation of the present climate state;
- 2 study of internal modes of variability of the climate system (e.g. ENSO, North Atlantic Oscillation);
- 3 forecasting or hindcasting such internal variability; and
- 4 longer-term, forced climate change (e.g. through solar variability or anthropogenic forcing).

Work on 1 to date has largely been done with models of individual subsystems (atmosphere or ocean), and work on 3 is in its infancy. Coupled models have been extensively used for 2 and 4. Rather than attempt a comprehensive review of this work, this chapter concentrates on the formulation and performance of modern coupled models, from an oceanographic perspective. References into the coupled modelling literature are provided to allow the reader to follow up particular topics in more depth.

2.3.2 Formulation of coupled models

A model capable of simulating climate variations on time scales of decades to centuries requires several components. At the very least, the atmosphere, land surface, ocean and sea ice, and their

interactions, must be included. While our focus here is on the ocean, we include brief descriptions of the representation of the other components in coupled models. A more detailed discussion of the fundamentals of climate models can be found in Trenberth (1992), although the models have developed since this reference was written.

2.3.2.1 Atmosphere

Atmospheric GCMs are conceptually very similar to oceanic GCMs (and of course are their historical forebears). They typically consist of a dynamical ‘core’ that time-steps the equations of motion in discretized form, linked to a number of parameterizations of processes that are unresolved at the scale of the discretization. One difference between atmospheric and oceanic GCMs is that for the atmosphere, the lack of side boundaries makes spectral discretization methods attractive in the horizontal, although finite difference methods are also widely used (see the article by J. J. Hack in Trenberth, 1992, for a fuller discussion of both spectral and finite difference methods). Typical resolution for a modern atmospheric model is T42 spectral truncation or about 3° . Since a typical first baroclinic Rossby radius in the atmosphere is around 700 km, this means that such models are what in ocean modelling terms would be called ‘eddy permitting’; the models develop synoptic scale mid-latitude weather systems, which are known to play an important part in the general circulation, but these systems cannot be said to be fully resolved.

The vertical coordinate is usually pressure, height or a terrain following (sigma) coordinate. Sometimes a generalized coordinate combining two or more of these is used. Typically around 20–30 levels are used, unequally spaced to concentrate attention in the regions of particular interest. Resolution is often enhanced in the surface boundary layer, and many models have only a few levels above the tropopause.

The sub-grid-scale processes which must be parameterized in atmospheric models (often referred to as the ‘physics’ of the model) are perhaps more numerous than in oceanic models (at least at the present stage of model development). First, many important dynamical processes are unresolved, yet produce significant vertical transports of heat, water vapour and momentum. Particular processes that must be parameterized are convective plumes,

gravity waves and turbulent boundary layer eddies. (See the chapter by J. T. Kiehl in Trenberth (1992) for a more complete exposition of the fundamentals of parameterization of physical processes in atmospheric climate GCMs.)

The water cycle is an important element of atmospheric climate. Water exists in gaseous, liquid and solid phases in the atmosphere, and its transports and phase transformations (e.g. the formation of clouds and precipitation) must be accurately represented. Many of the key processes take place at micrometre to millimetre scales and so could not be resolved in the foreseeable future.

Clouds and water vapour have important radiative effects, absorbing, emitting, scattering and reflecting the incoming solar and outgoing long-wave radiation (see Bryden and Imawaki, Chapter 6.1). The representation of clouds and their radiative properties is one of the largest areas of uncertainty in climate modelling at present. Other trace gases such as CO_2 and methane, and aerosols (small airborne particles) from natural and anthropogenic sources, have important radiative effects, which must be included in models. In current coupled models, concentrations of most of these trace substances are prescribed, although simple representations of the physics and chemistry of sulfate aerosols are now being developed (e.g. Jones *et al.*, 1999a).

Because of the greater complexity of sub-grid-scale parameterizations in atmospheric models, compared with the current generation of ocean models, atmospheric GCMs typically require considerably more computing resources per gridpoint than oceanic GCMs. Yet many of the longer time scales in the climate system are set by oceanic processes. This means that for certain long-time scale problems the use of ocean models coupled to simplified or ‘intermediate complexity’ atmospheric models is attractive. These may be dynamical atmospheric GCMs that are highly truncated in one or more directions (e.g. Saravanan *et al.*, 2000), or models in which the atmospheric dynamics and associated transports of heat and water are completely parameterized or specified. Transports due to baroclinic waves are known to be fundamental to the atmospheric heat and water balances, whereas the role of their oceanic counterparts (mesoscale eddies) is still under debate (see, e.g. Wunsch, 1999b). These highly parameterized atmospheric models vary in complexity from models with

specified or diffusive meridional transports (e.g. Rahmstorf and Willebrand, 1995; Wang *et al.*, 1999) to more complex energy and moisture balance models, sometimes including simple parameterizations of clouds and land surface processes (e.g. Fanning and Weaver, 1996). Sometimes such models are coupled to simplified (e.g. zonally averaged) ocean models rather than full ocean GCMs (Schmittner and Stocker, 1999; Petoukhov *et al.*, 2000). These simplified model configurations have the advantage of allowing long integrations, or multiple sensitivity studies, to be run efficiently in order to understand particular processes at work in the climate system. However, the simplifications inherent in such models mean that they must be used with caution for quantitative simulation and prediction. See Section 2.3.6.2 for an example of a problem where uncertainty over the magnitudes of a number of competing processes produces significant uncertainty in modelled climate response, even among complex GCMs. Also see Stocker and Schmittner (1997) and Rahmstorf and Ganopolski (1999) for examples of how the ability to perform many runs of the simplified models allows them to be used to explore the consequences of such uncertainties in a way that would be impractical with the GCMs themselves. In this sense the simplified climate models are complementary to GCMs.

2.3.2.2 Land surface

The land surface plays an important role in the global budgets of heat and water. Elements of the system that are usually represented in some way in coupled models include soil, permafrost, vegetation, snow cover and land ice (ice sheets and glaciers), and model climate simulations are sensitive to details of these parameterizations (Crossley *et al.*, 2000). Some features, for example ice sheet extents and vegetation types, are typically fixed, but models are being developed in which the vegetation responds to climate variations, allowing for additional feedbacks that may be important on decadal time scales (Wang and Eltahir, 2000; Cox *et al.*, 2000). The role of land surface elements in the fresh water budget is discussed in Section 2.3.2.6.

2.3.2.3 Ocean

A variety of ocean models have been used in coupled modelling. The z -coordinate models remain the most popular type, including the Bryan–Cox/MOM (Manabe *et al.*, 1991), LSG (Voss *et al.*,

1998), HOPE (Wolff *et al.*, 1997) and OPA (Guilyardi and Madec, 1997) models. However, the quasi-isopycnic OPYC model has also been used (Roeckner *et al.*, 1996) (see the Appendix for definitions of the acronyms for institutions and models used in this chapter). The computational cost of long runs restricts the resolution used, so that most coupled models have horizontal ocean resolution in the range 1–4°. The finest ocean resolution used to date in a global, coupled model is slightly less than 1° (Washington *et al.*, 2000), although some models use enhanced resolution in the tropics to resolve the equatorial waveguide (Roeckner *et al.*, 1996; Guilyardi and Madec, 1997; Barthelet *et al.*, 1998).

Typical models have 20–30 levels or layers in the vertical. In some cases an attempt is made to resolve the surface boundary layer and to parameterize near-surface turbulent mixing processes using the K-profile method (Large *et al.*, 1994; Gent *et al.*, 1998), turbulent kinetic energy schemes (Blanke and Delecluse, 1993; Barthelet *et al.*, 1998) and hybrid schemes (Johns *et al.*, 1997b). In other cases a bulk mixed-layer model (Roeckner *et al.*, 1996), or no specific near-surface mixing parameterization at all (Manabe *et al.*, 1991), is used. The latter may be justified as much of the thermohaline structure of the thermocline and deep ocean is determined by deep winter convection; however, summer Sea Surface Temperatures (SSTs) are sensitive to shallow wind- and shear-induced mixing.

Diapycnal mixing is known to be of fundamental importance in the meridional overturning circulation. In climate models, it is usually parameterized through vertical or diapycnal diffusion, but the strength and structure of the overturning are known to be highly sensitive to the value chosen for the diffusivity (Bryan, 1987). In practice, most coupled models impose a fixed profile of vertical diffusivity below the surface mixed layer, with deep ocean values close to the ‘canonical’ value of $1.0 \times 10^{-4} \text{ m}^2 \text{ s}^{-1}$ (e.g. Johns *et al.*, 1997b). In the various coupled models that incorporate the OPA ocean model (Guilyardi and Madec, 1997; Barthelet *et al.*, 1998), diffusivities are calculated using a turbulent kinetic energy closure scheme, leading to considerable horizontal as well as vertical variations of diffusivity (Blanke and Delecluse, 1993); however, the impact and importance of the large horizontal variations of mixing that have

been observed (see Toole and McDougall, Chapter 5.2) for the large-scale circulation has only just begun to be explored (e.g. Webb and Suginohara, Chapter 4.2; Marotzke, 1997; Hasumi and Suginohara, 1999a).

Since mesoscale eddies cannot at present be resolved in the ocean components of coupled models, their effects on the large-scale circulation must be parameterized. Considerable advances have been made in this area during the WOCE period with the development of a parameterization (Gent and McWilliams, 1990) that has two desirable properties: first, it mimics the release of available potential energy by baroclinic instability, and second, it removes grid-scale enstrophy in a way that does not introduce spurious diapycnal mixing. The latter property has been shown to be particularly important in allowing coarse-resolution models to maintain a realistically sharp thermocline and in improving meridional heat transports in both hemispheres (Danabasoglu *et al.*, 1994; Böning *et al.*, 1995). For model resolution of order 1° , a further refinement has been found useful. In order to simulate eddy transports across the Antarctic Circumpolar Current, eddy thickness diffusivities of order $2000 \text{ m}^2 \text{s}^{-1}$ are appropriate (Treguier *et al.*, 1997; Visbeck *et al.*, 1997). However, the use of such a large value is less appropriate in other parts of the ocean, and leads to weakening of narrow current systems such as the North Atlantic Current and Kuroshio. In the HadCM3 model, the parameterization of Visbeck *et al.* (1997) was therefore used, in which the thickness diffusivity is determined as a function of the local baroclinic structure (Gordon *et al.*, 2000). This issue appears less important in coarse-resolution models, where the structure of the narrow currents is presumably determined more by the larger eddy viscosity required.

2.3.2.4 Sea ice

A variety of sea ice models has been used in coupled models. Models range from simply assuming ice cover of fixed properties at ocean gridpoints where the SST falls below freezing point (Guilyardi and Madec, 1997), through single or multi-layer thermodynamic-only models (Murphy and Mitchell, 1995; Barthelet *et al.*, 1998; Voss *et al.*, 1998), to models with simple ice dynamics (e.g. Manabe *et al.*, 1991; Johns *et al.*, 1997b; Gordon *et al.*, 2000), and more sophisticated dynamics with

non-trivial ice rheologies (e.g. Roeckner *et al.*, 1996; Gordon and O'Farrell, 1997; Weatherly *et al.*, 1998; Washington *et al.*, 2000).

2.3.2.5 Coupling of component models

The atmosphere, ocean and sea ice are coupled through exchanges of heat, water, momentum and turbulent kinetic energy at their interfaces. Coupled models are typically built from component submodels that may have different resolution, time-steps, etc. The models are run quasi-independently, but exchange information at regular intervals (e.g. once per day). Care is needed to ensure that conservation properties are maintained, particularly in models that are used to study climate on decadal or longer time scales.

Surface exchanges must also reflect the different boundary layer processes going on over land, sea and sea ice. This is a particular issue when the atmosphere and ocean model horizontal grids and coastlines do not match. In this case it is possible, for example, that part of an atmosphere grid box can cover part open ocean, part sea ice and part land. Separate surface exchanges must be calculated for each component. If one component model has much finer resolution than another (e.g. the ocean is run at finer resolution than the atmosphere), the surface exchanges must be calculated at the finer resolution, since the non-linearity of the bulk formulae that are used to calculate surface fluxes means that averaging the ocean surface properties onto the atmospheric grid would not provide the correct mean surface flux. Examples of software solutions to these problems are the NCAR flux coupler (Boville and Gent, 1998) and the OASIS (Ocean Atmosphere Sea Ice Soil) coupler (Cassou *et al.*, 1998).

2.3.2.6 Closing the freshwater budget

Water vapour is lost from the ocean to the atmosphere by evaporation and sublimation from water and sea ice/snow surfaces. Water is resupplied to the ocean through direct precipitation onto the ocean and sea ice surfaces, through river runoff and through iceberg calving from the Greenland and Antarctic ice sheets. The runoff and icebergs are a residual of the many processes contributing to the land surface water budget, including accumulation and evaporation of soil moisture, evapotranspiration by vegetation, and accumulation of snow on forest canopies and ice sheets. All coupled

GCMs explicitly include parameterizations of clouds, precipitation, surface evaporation and soil moisture accumulation. However, the runoff is often transported instantaneously from the accumulation region to its river outflow point. This can lead to errors in the seasonal timing of the freshwater input to the ocean, and schemes are now being developed that take account of the time delay from the river catchment to the outflow (Hagemann and Dümenil, 1998). Iceberg calving is modelled at best as a fixed water flux into the ocean (e.g. Gordon *et al.*, 2000). Since the ice sheet dynamics by which the iceberg flux responds to variations in snow accumulation and surface temperature are not well understood, a more sophisticated parameterization seems inappropriate at this stage.

The water budget of marginal seas such as the Mediterranean, which may be enclosed at the model grid scale, presents a particular challenge to coupled models. Unlike the heat budget, there is no strong atmospheric feedback to stabilize the salinity if a small water imbalance causes it to drift from realistic values. Such imbalances can accumulate over a period to give very large salinity errors. Most models allow some form of exchange between the Mediterranean and the Atlantic, either through a simple mixing parameterization (e.g. Manabe *et al.*, 1991; Gordon *et al.*, 2000) or by opening an artificially wide ‘Gibraltar Straits’ in the model grid (e.g. Gent *et al.*, 1998; Voss *et al.*, 1998), but seas with no link to the ocean (e.g. the Caspian Sea, whose water source is runoff and whose sink is evaporation) present a particular challenge.

An additional technical issue arises in the specification of the surface boundary condition for fresh water. Most ocean GCMs in current use, both rigid lid (Bryan, 1969) and ‘dynamic free surface’ (Killworth *et al.*, 1991), are formulated to conserve ocean volume rather than mass, and require the natural boundary condition on fresh water to be converted to a boundary condition that represents a virtual salt flux (Huang, 1993). The response of the surface salinity to a surface freshwater flux Q_s (in m s^{-1}) is

$$dS/dt = -(S \times Q_s)/d \quad (2.3.1)$$

where Q_s is the water flux into the ocean and d is the depth of the mixed layer (or top model grid box). Where there is net precipitation ($Q > 0$), the

sea surface rises, resulting in lower salinity, and where there is net evaporation ($Q < 0$), the surface falls, resulting in higher salinity. However, in a rigid lid model the surface is fixed (d is constant). If (2.3.1) is applied, the model’s local salinity responds correctly to the flux Q_s , but because globally S and Q_s are anticorrelated (high salinity tends to occur in regions of net evaporation, and vice versa), the global mean salinity will tend to increase when the model is given a Q_s field whose global mean is zero. This effect has been found to be significant in practice, and can only be ‘cured’ by replacing S on the right-hand side of (2.3.1) with a fixed reference salinity S_0 , at the cost of a local inaccuracy in the salinity response (Gordon *et al.*, 2000). Formulations of the natural boundary condition are available for both rigid lid (Huang, 1993) and free surface (Roulet and Madec, 2000) models; however, there is little experience to date with their use in long coupled model runs.

The careful accounting of water discussed in this subsection is of special importance for non-flux-adjusted models (see Section 2.3.3 below). Where flux adjustments are used, they are usually chosen in such a way as to compensate for the slight imbalances described above.

2.3.2.7 Forcing

The issue of forcing of coupled models is less complex than that of forcing ocean-only GCMs, because the climate system as a whole is more self-contained than the ocean. The following fields typically need to be prescribed for a coupled model: top of the atmosphere incoming solar radiation, atmospheric composition of those radiatively active species that are not explicitly calculated in the model (see Section 2.3.2.1), and distribution of vegetation types (see Section 2.3.2.2). Most of these quantities are relatively well observed for the present climate state, and estimates exist for past climates, allowing relatively easy interpretation of model simulations of a particular climate state (but see Section 2.3.4 below). However, for long-time scale climate variability and change there is a potential for feedbacks of the biogeochemical cycles on climate (Charlson *et al.*, 1987; IPCC, 1995 (Chapter 9); Maier-Reimer *et al.*, 1996; Levis *et al.*, 1999), and development of models that include such feedbacks is still at an early stage (Cox *et al.*, 2000).

2.3.3 Model drift and flux adjustment

Large-scale general circulation models of both the atmosphere and the ocean have been developed over a number of years. One might think that, given a ‘good’ model of each subsystem, it would be a relatively simple matter to exchange surface fluxes and boundary layer properties between the two, as described in Section 2.3.2 above, and obtain a ‘good’ model of the coupled system. The history of the development of coupled models has shown this task to be harder than might be imagined, partly because it has only recently become clear what is meant by a ‘good’ model in this context. In one of the pioneering coupled models (Manabe *et al.*, 1979), little of the model’s ocean surface temperature was within 2°C of the observed values, and the whole of the Southern Ocean circumpolar region was 6–10°C too warm. Because of the fundamental importance of surface energy exchanges in the climate system, studies of long-term climate variability or anthropogenic climate change using such a model would be subject to considerable uncertainty, because the incorrect surface temperatures would distort the highly nonlinear atmospheric feedbacks that determine the response of the system to a given perturbation.

A way around this problem was developed by Sausen *et al.* (1988). The method is known as ‘flux correction’ or ‘flux adjustment,’ and involves simply adding in an additional, prescribed term to the surface fluxes of heat, fresh water and (sometimes) momentum that drive the ocean component of the coupled model. The ‘flux adjustments’ are chosen in such a way as to ensure that the sea surface temperature and salinity remain reasonably close to observed values. They may be fixed in time or seasonally varying, but never vary on longer than annual time scales. Usually they are prescribed as two-dimensional surface fields, but sometimes zonal-mean values (dependent on latitude only) have been used. It is important to understand that the flux adjustments are *prescribed*, and do not change in response to changing surface conditions. A common way of choosing the flux adjustments (e.g. Manabe *et al.*, 1991; Johns *et al.*, 1997b) is to make a preliminary run of the model to near equilibrium, with the addition of a relaxation term on the surface temperature and salinity that ensures that they remain close to the desired climatology:

$$\text{Surface flux} = q + \lambda(T_0 - T_{\text{model}})$$

where q is the surface flux computed from the model’s surface fields, T_0 is the climatological surface temperature or salinity, T_{model} is the model surface temperature or salinity, and λ is a relaxation constant chosen to keep T_{model} ‘suitably’ close to T_0 . At the end of the preliminary run the relaxation fluxes are diagnosed, and these are applied as fixed flux-adjustment terms in the main model run:

$$\text{Surface flux} = q + q_{\text{FA}}$$

where q_{FA} is simply the (suitably time averaged) value of $\lambda(T_0 - T_{\text{model}})$ from the preliminary run. Because the preliminary run was in near equilibrium (no long-term drifts), the expectation is that the main run will simply continue on this equilibrium. This can indeed be achieved in practice.

During the 1990s a number of coupled models were developed that were able to maintain stable climatologies over many centuries, using flux adjustments. The advantage of flux adjustment is that it allows such long runs to be made, with surface climatologies that are (by definition) close to reality. For some applications, this may be preferable to a model without flux adjustments that has a poorer surface climatology. For example, in order to obtain realistic ENSO-like variability in a coupled model, it may be important that the model maintains the strong zonal SST gradient in the tropical Pacific. A flux-adjusted model that maintained this gradient might show better ENSO variability than a parallel non-flux-adjusted model in which the SST gradient was too weak.

On the other hand, the flux adjustments have no physical basis, and are ‘correcting’ for a model error, which may originate in the interior dynamics of the atmosphere or ocean model, by adjusting the surface fluxes. For typical models, flux adjustments can locally be as large as the model fluxes themselves. This clearly leads to uncertainty in interpreting any experiments with the model, and by masking the model errors makes it harder for the modeller to diagnose the causes of those errors (especially when they are of an inherently ‘coupled’ nature).

During the late 1990s coupled models began to emerge that maintained acceptable surface climatologies without flux adjustments. A key element in achieving this appears to be a correct and consistent simulation of the large-scale heat budget of the atmosphere and ocean. The fundamentals of

the heat budget are described by Bryden and Imawaki (Chapter 6.1). Figure 2.3.1 shows the northward ocean heat transport in a typical flux-adjusted model (the Hadley Centre's HadCM2 model, Johns *et al.*, 1997b) and its successor, HadCM3, which is run without flux adjustments (Gordon *et al.*, 2000). The solid curve shows one observational estimate of this quantity, derived from the surface flux climatology of da Silva *et al.* (1994) (see Bryden and Imawaki, Chapter 6.1). The dotted curves show the equilibrium ocean heat transports implied by the model surface fluxes, for the two coupled models and for a run of the atmosphere component only of HadCM3, forced by observed SSTs. In all three cases, the models agree well with the observational estimate in the northern hemisphere, with more variation in the southern hemisphere (where observational estimates are also more uncertain). Estimates of the zonal mean heat flux at the top of the atmosphere

(not shown) also agree well with satellite estimates from the Earth Radiation Budget Experiment in all three cases (see Johns *et al.*, 1997b; Gordon *et al.*, 2000), suggesting that the atmosphere models are performing well in this respect. The dashed curves show the actual heat transport by the ocean model. In the case of HadCM2 this is about half what is required to balance the surface fluxes. The difference is accounted for by the flux adjustment, which puts heat into the ocean at high latitudes and removes it at low latitudes. In HadCM3, the ocean heat transport is able to come into balance with the surface fluxes (at a level not too far removed from the observations), and this allows the model to equilibrate without entailing a large drift of the SST from observed values. Figure 2.3.2 (see Plate 2.3.2, p. 76) shows the mean SST errors in HadCM3, HadCM2 and a version of HadCM2 run without flux adjustments (Gregory and Mitchell, 1997). The errors are smallest in the

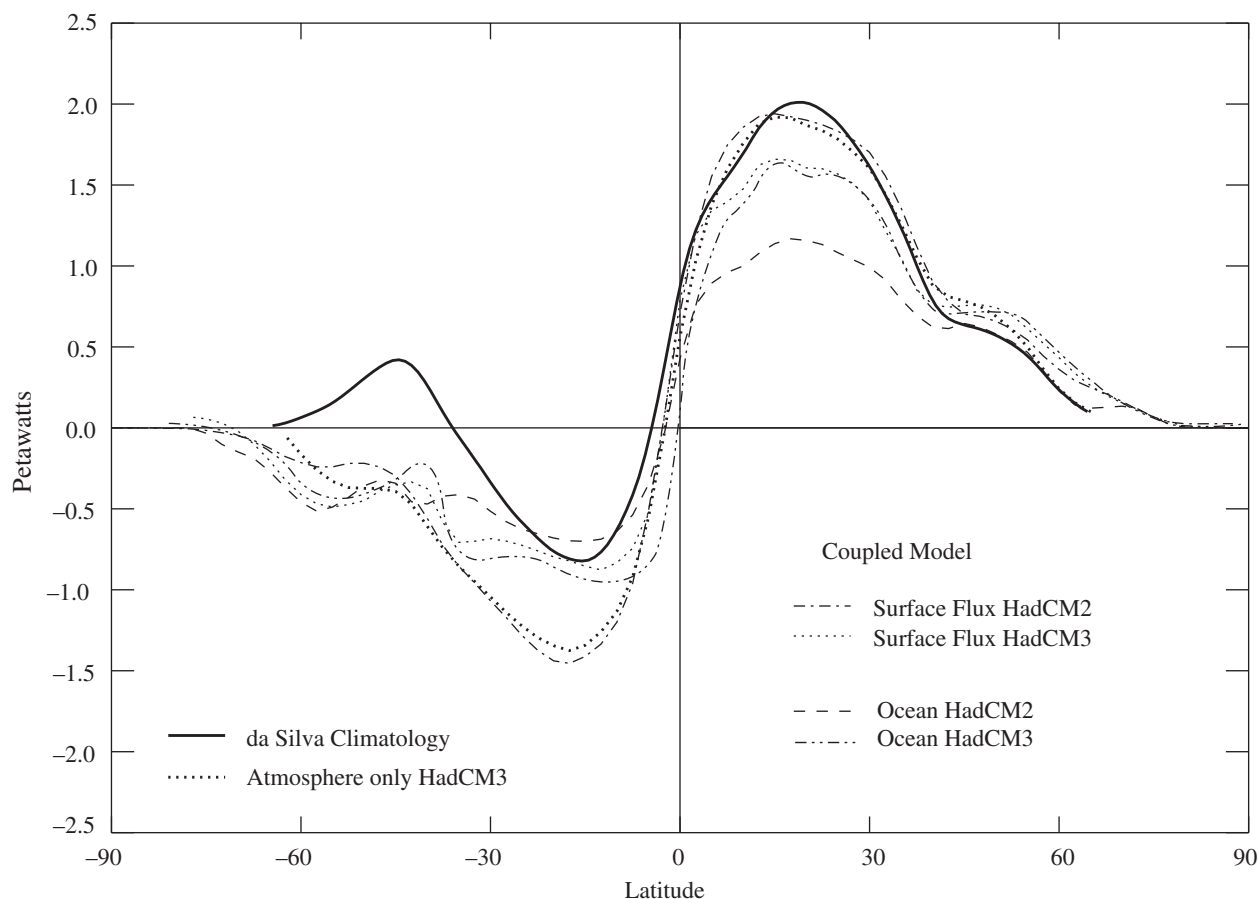


Fig. 2.3.1 Northward ocean heat transports implied by the da Silva *et al.*, (1994) surface heat flux climatology, and by the surface fluxes from the HadCM2, HadCM3 and HadCM3 models, and actual ocean heat transports in the HadCM2 and HadCM3 models. The HadCM3 results consist of the atmosphere component of HadCM3, forced by observed SSTs.

flux-adjusted model, as expected. In the non-flux-adjusted HadCM2 case the near-global cool bias is a result of a positive feedback between excess stratocumulus cloud and insufficient short-wave radiation reaching the surface (J. M. Gregory, personal communication).

Similar considerations to the above apply to the freshwater budget, which is more complex than the heat budget because of its many elements, described in Section 2.3.2 and by Wijffels (Chapter 6.2). Since there is no direct feedback of surface salinity anomalies on the surface freshwater flux, even small imbalances can potentially accumulate over decades or centuries leading to errors in elements of the large-scale circulation such as the North Atlantic meridional overturning. These imbalances can again be compensated for by appropriately chosen flux adjustments, but more recent models can maintain a stable and realistic circulation over many centuries without water flux adjustments. The water budget of coupled models remains something that is relatively poorly studied, and given its importance for topics such as the stability of the thermohaline circulation (Manabe and Stouffer, 1993, 1997; Rahmstorf, 1996; Rahmstorf *et al.*, 1996; Rahmstorf and Ganopolski, 1999; Wang *et al.*, 1999; Wood *et al.*, 1999) requires further study.

It is not clear whether the use of flux adjustments biases the variability or climate change response of a model. Fanning and Weaver (1997b) and Gregory and Mitchell (1997) see differences in the climate change response of equivalent models when run with and without flux adjustment. But since the basic states of the flux-adjusted and non-flux-adjusted models are different, it is not clear that the different responses can be attributed directly to the flux adjustments. Marotzke and Stone (1995) point out that use of flux adjustment to correct the surface climate of a control run does not necessarily correct the processes that control the climate change response of the model. In simple coupled models, flux adjustments can introduce spurious multiple equilibria of the tropical circulation (Neelin and Dijkstra, 1995), and distort the multiple equilibria of the thermohaline overturning (Dijkstra and Neelin, 1999). It has been argued that flux adjustments, being tuned to keep the model close to the present mean climate, may suppress natural climate variability. However, Duffy *et al.* (2000) show that on time scales from 1 to 20

years the flux-adjusted models in the CMIP1 study show no less variability in surface air temperature than the non-flux-adjusted models.

2.3.4 Initialization of coupled models

2.3.4.1 Categories of initialization

Since most of the ‘memory’ of the climate system on decadal and longer time scales is believed to reside in the ocean, initialization methods for coupled models focus on the ocean component. The techniques used to initialize coupled models depend on what the model is to be used for. Four categories of use were identified in Section 2.3.1 above, and we consider each of these separately:

- 1 *Estimation of the present climate state.* In the GCM context, this amounts to assimilation of observations into a model, or, to the extent that the present state is determined by the system’s memory of past conditions, integration of the model through a known history of climate forcing. The former is discussed in 3 below, the latter in Section 2.3.5.7. There is little experience to date in this area using global coupled models (see Talley *et al.*, Chapter 7.1).
- 2 *Study of internal modes of variability.* Long integrations are needed in order to characterize the statistics of such modes. Therefore it is important to minimize any long-term trends in the integration. The techniques discussed in Section 2.3.4.2 below have been used to achieve this.
- 3 *Forecasting or hindcasting of internal climate variations.* A number of coupled models have been used to hindcast (Ishii *et al.*, 1998; Barnston *et al.*, 1999) and forecast (Stockdale *et al.*, 1998) climate variations such as ENSO on seasonal to annual time scales. In this case there is evidence that the climate state is strongly controlled by the recent history of wind stress in the tropical Pacific, and a feasible approach is to initialize the ocean model by forcing it for a few years with observed wind stresses. However, model systematic errors are often of a similar magnitude to the climate variations being forecast. In this case if observed winds are used, the model forecast will drift back towards climatology, making interpretation of the forecast difficult (although Stockdale *et al.*, 1998, argue that this drift can meaningfully be subtracted out of their ENSO forecast). To avoid this difficulty,

observed wind stress *anomalies* are often added to the model's own mean wind stress climatology in the initialization phase. Similar considerations apply if ocean data such as XBT profiles or satellite SSTs are assimilated during the initialization. There is little experience here on decadal or longer time scales (for example hindcasting of North Atlantic Oscillation variability).

- 4** *Forced climate change.* Similar considerations apply as in **2** and **3** above. At the stage where any forcing is applied to the model, the 'control' (unforced) run will ideally not contain any climate drift. At the very least the rate of drift needs to be smaller than the rate of climate change due to the forcing. Again, the methods of Section 2.3.4.2 are used in practice.

2.3.4.2 Practical techniques

For applications **2** and **4** above, the primary requirement of a model initialization procedure is that the model drift should be acceptably small (small compared with the signals that are being studied). A wide variety of methods have been used (see Stouffer and Dixon, 1998, for a review). However, the methods can be split into two classes:

- a** Initialize the model from an estimate of the present climate (particularly ocean) state, and simply run the model forward in time until the drift is considered acceptably small (e.g. Guilyardi and Madec, 1997; Johns *et al.*, 1997b; Barthelet *et al.*, 1998; Gordon *et al.*, 2000). This has the advantage of being conceptually and technically simple, and by studying the processes by which the model adjusts from its (realistic) initial state to its own preferred climatology, insight can be gained into the model's systematic errors.
- b** Use separate spin-up integrations of the atmospheric and oceanic components to bring the ocean model as close as possible to a quasi-equilibrium state (no long-term drift), followed by a final recoupled phase (e.g. Manabe *et al.*, 1991; Bryan, 1998). The acceleration technique of Bryan (1984) can often be used to reduce the computing requirement of the ocean-only phase. This technique has the advantage that it may result in a smaller residual drift than method **a** (though this is not guaranteed because important atmospheric feedbacks may be missing from the ocean-only phase, leading to large drifts when the model is recoupled).

Either method has been used with both flux-adjusted and non-flux-adjusted models. However, for flux-adjusted models experience has shown that a long (multicentury) 'calibration' run is required to define the flux-adjustment terms (see Section 2.3.3), whereas shorter spin-up runs may be sufficient in the non-flux-adjusted case.

2.3.5 Coupled model simulation of present and past climates

2.3.5.1 Sea surface temperature

The ocean influences atmospheric climate largely through the SST, so for climate studies, those ocean processes that influence SST on the time scale of interest are the most important. Thus it may be that for, say, study of interannual climate variability a model with a poor representation of North Pacific Deep Water may do an adequate job. However, on the decadal to century time scales for which global coupled models are most widely used, a large number of ocean processes are potentially important. Some of these are discussed in this section.

Because of the importance of SST much attention is given by coupled modellers to the SST field simulated by the models. As discussed in Section 2.3.3 and (Fig. 2.3.2, see Plate 2.3.2, p. 76), the choice of a suitable flux-adjustment field enables any model to produce a realistic SST field, at the cost of unphysical terms (often large) in the global heat balance. The SST error field from the HadCM3 model (Fig. 2.3.2a, see Plate 2.3.2a, p. 76) shows an error pattern that appears to be common among non-flux-adjusted models: the cool errors in the North and Equatorial Pacific, and the warm errors in the Southern Ocean and in the eastern tropical Atlantic and Pacific, can also be seen (with various amplitudes) in the NCAR CSM (Boville and Gent, 1998) and in the OPA/ARPEGE model (Madec and Delecluse, 1997), and have been the subject of much diagnostic effort.

2.3.5.2 Heat and freshwater transports

The importance of a good representation of the large-scale heat transports through the atmosphere–ocean system was discussed in Section 2.3.3. More detailed comparison of ocean model heat transports with estimates from hydrographic sections has also given useful insights into model performance. For example, Banks (2000) compares

observed transports across the WOCE A11 section (Saunders and King, 1995b) with the corresponding section in the HadCM3 model. She finds that insufficient transport of Antarctic Bottom Water in the model leads to an overestimate (by $O(0.1 \text{ PW})$) of the northward heat transport across the section. Such detailed comparison against observations provides valuable guidance to model development.

Freshwater transports are less well studied in models and less well constrained by observations (see Section 2.3.2.6; see also Wijffels, Chapter 6.2). Figure 2.3.3 shows the annual mean freshwater flux into the ocean in the NCAR CSM (Doney *et al.*, 1998b), compared with the same quantity in a parallel ocean-only run, and two observational estimates. The coupled model reproduces the broad qualitative structure of the observed fluxes over most of the ocean, with some quantitative differences (the secondary maximum in the coupled model flux at about 10°S , absent in the observations and in the ocean-only run, is due to a ‘double intertropical convergence zone’, a fairly common problem in atmosphere and coupled models). Despite the broad agreement between the model and the observations, the lack of a strong local feedback between surface salinity and the

freshwater flux (Section 2.3.3) means that small freshwater imbalances may lead to long-term drifts (Bryan, 1998) or eventually even to major reorganization of the circulation such as a collapse of the thermohaline overturning (Rahmstorf, 1996; see also Section 2.3.6).

2.3.5.3 Thermohaline overturning circulation

The meridional overturning circulation is believed to carry most of the poleward heat transport of the mid-latitude North Atlantic Ocean (Hall and Bryden, 1982; see also Bryden and Imawaki, Chapter 6.1). There is strong evidence from both modelling (Manabe and Stouffer, 1988) and palaeoclimatic (Broecker, 1997) studies that this heat transport substantially warms the climate of Northwest Europe. The stability of the thermohaline overturning circulation (hereafter THC) has been the subject of much speculation and research (see Section 2.3.6). For these reasons a good representation of the North Atlantic THC is seen as an important test of climate models.

Figure 2.3.4 shows the zonally averaged overturning circulation in the HadCM3 model, about 100 years after initialization with climatological potential temperature and salinity fields. The northward flow of near-surface water, sinking in

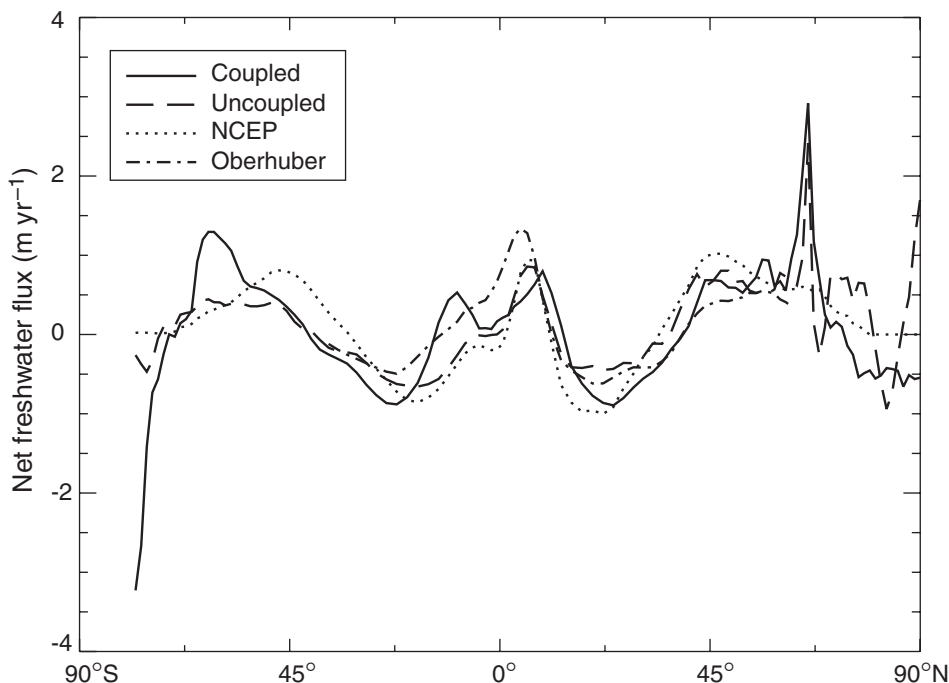


Fig. 2.3.3 Zonally averaged freshwater flux into the ocean in the NCAR CSM coupled model, in an ocean-only version of the model (uncoupled), and from an observational estimate (Doney *et al.*, 1998). Oberhuber refers to the climatology developed by Oberhuber.

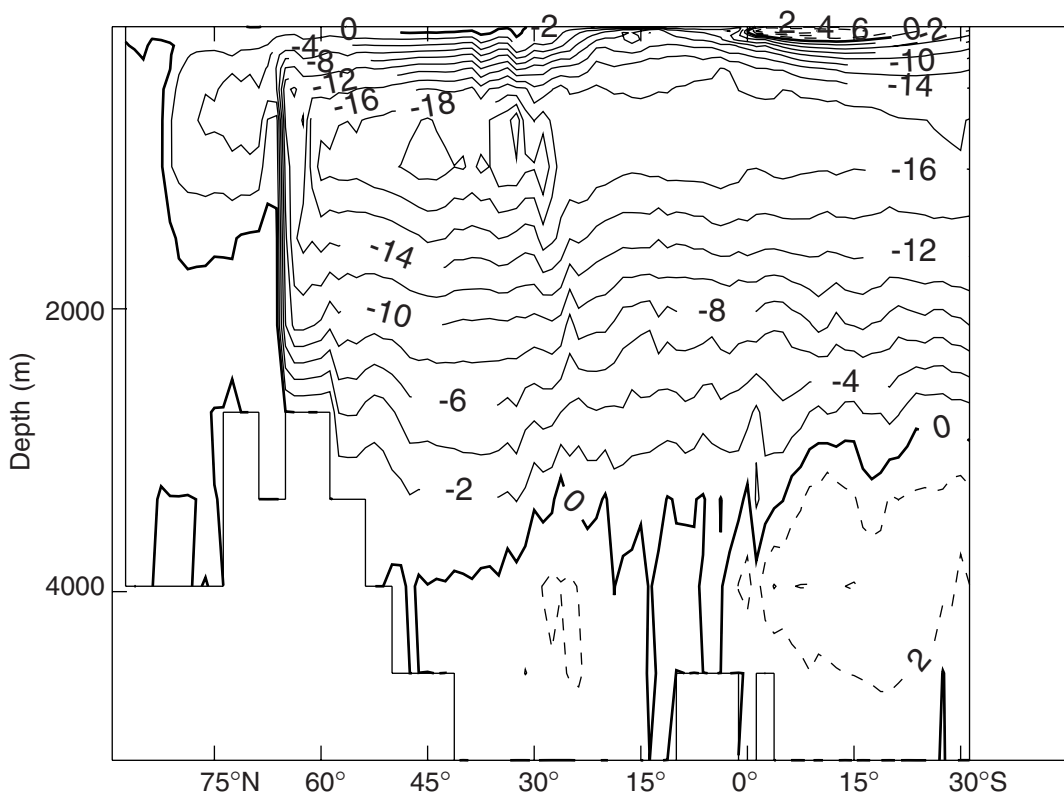


Fig. 2.3.4 Zonally integrated meridional overturning streamfunction (Sv) for the Atlantic in the HadCM3 coupled model (decadal mean from 100 to 110 years after initialization with the climatological fields of Levitus and Boyer, 1994b). Circulation is anticlockwise around negative centres (solid contours), clockwise around positive centres (dashed contours).

the subpolar Atlantic and Nordic Seas, and southward flow of North Atlantic Deep Water (NADW) can be clearly seen. There is also a weak inflow of Antarctic Bottom Water (AABW) from the Southern Ocean at 32°S. The maximum of the NADW cell (in this case about 22 Sv) is a commonly used diagnostic of the strength of a model's THC. However, since this quantity is not observable in practice, it may be preferable to diagnose the overturning at a fixed latitude where observations are available. In this model the amount of southward NADW flow at 24°N is 17.4 Sv, in good agreement with the observational estimate of 19.3 Sv (Hall and Bryden, 1982). This flow remains stable over several centuries (Fig. 2.3.7), although over the same period there is an increase in the AABW inflow that pushes the NADW higher up in the water column, leading to a less realistic vertical profile for the flow (Gordon *et al.*, 2000).

Lazier *et al.* (Chapter 5.5) describes the detailed formation sites and pathways of NADW formation, including the important role of the Nordic Sea overflows. Model studies (Dööscher and Redler,

1997; Roberts and Wood, 1997) have shown how these overflows are an important control on the strength of the THC and heat transport. Because the real overflows take place through very narrow channels (widths of order 20 km), some models include artificially wide channels at the model grid scale, with the correct sill depth. This may be justified if the overflows are hydraulically controlled (e.g. Wadley and Bigg, 1996), and realistic amounts of overflow water can result (Fig. 2.3.7). However, uncertainty must remain when this critical process is only represented at the grid scale, and further theoretical and fine-resolution model studies are necessary to establish whether the approach taken in the coarse-resolution models accurately captures the overflow physics.

The broad agreement of some models with the observed structure of the THC is encouraging, but some of the details such as the partition of overflow water between the Denmark Straits and the Faroe Bank Channel (Saunders, Chapter 5.6; Redler and Böning, 1997), and the subtropical recirculations of the deep western boundary current may

play an important role in climate variability. This topic is largely unexplored at present. The downstream behaviour of the overflow water is also important. Downslope flows are currently rather poorly represented in z -coordinate models, often resulting in excessive mixing of dense overflow waters, with significant downstream effects in the subpolar gyre. Isopycnic coordinate models represent these downslope flows more naturally (see, e.g., Roberts *et al.*, 1996; DYNAMO Group, 1997; Winton *et al.*, 1998). Implementation of bottom boundary layer models in z -coordinate models (e.g. Beckmann and Döschner, 1997; Killworth and Edwards, 1999) may alleviate this problem in future.

The formation processes of AABW are complex (Rintoul *et al.*, Chapter 4.6), and many of the relevant processes (e.g. flow under ice shelves) are not represented in the current generation of coupled models. The importance of AABW in the climate system is not as clear as for NADW, because the heat transports involved are much less, but AABW errors can still lead to heat transport errors of $O(0.1 \text{ PW})$ (see Section 2.3.5.2). Furthermore, excessive AABW formation (associated with excess northward transport of sea ice away from Antarctica) has been shown to result in century time scale model drifts and excessive transport of the Antarctic Circumpolar Current (Gent *et al.*, 2000; see also Rintoul *et al.*, Chapter 4.6).

2.3.5.4 Ventilation and water mass formation

The transfer of heat, water and passive tracers from the mixed layer to the ocean interior determines the time scale on which the mixed layer (and hence the sea surface properties) responds to a change in atmospheric forcing. For example, the ventilation of the deep and intermediate water masses provides a potential ‘heat sink’ that could slow the rate of the climate’s response to increasing greenhouse gases. So correct modelling of water mass formation processes is an important feature of a climate model.

Figure 2.3.5 shows water mass transformation rates (based on the framework of Speer and Tziperman, 1992) for the Indian and Pacific Oceans, in the NCAR CSM and derived from an observational estimate of the surface buoyancy flux (Doney *et al.*, 1998b). The qualitative structure of the transformations is well captured in the model, with surface fluxes tending to lighten the

light water masses and make dense water masses denser, but the model transformation rates are somewhat higher than those observed. This would require higher rates of interior mixing in the model, to balance the net destruction of the intermediate densities by the surface fluxes.

Another view of water mass formation and ventilation is provided by the use of natural and anthropogenic tracers such as ^{14}C and CFCs (Chlorofluorocarbons – see England, 1999; England and Maier-Reimer, 2000, for reviews). A technical issue arises here that is peculiar to coupled models (England, 2000). The concentration of a transient tracer in the ocean at a particular time is a convolution of the history of the surface flux with the ocean circulation and ventilation processes. Errors in a simulated tracer field could result from either errors in the fluxes or errors in the circulation. If the primary aim of a coupled model CFC simulation is to test the model’s ocean circulation, use of observed winds to derive the surface CFC flux may be more appropriate than use of the model’s own winds (Dixon *et al.*, 1996).

Figure 2.3.6a (see Plate 2.3.6a, p. 76) shows the Atlantic zonal mean concentration of CFC-11 in 1982, from HadCM3 (observed winds were used to calculate the surface flux in this case). The ventilation of deep waters in the North Atlantic is clear, and a number of features of the North Atlantic CFC distribution are similar to those seen in the 1988 section reported by Doney and Bullister (1992), for example the downward spreading of the low concentration isolines ($<1 \text{ pmol l}^{-1}$) between 25°N and 50°N , while the higher concentration isolines remain flat in this latitude band. The overall pattern of CFC penetration (measured, for example, by the depths of the 0.5 , 1 and 2 pmol l^{-1} contours) agrees well with the observed section (Fig. 2 of Doney and Bullister, 1992). In the southern hemisphere, rather too much deep penetration is seen when compared with the 1983 AJAX section (Warner and Weiss, 1992, Fig. 7), probably due to excessive mixing in the model.

Simulated CFC fields are known to be sensitive both to the surface flux formulation (England *et al.*, 1994; Dixon *et al.*, 1996) and to sub-grid-scale mixing parameterization (Robitaille and Weaver, 1995; England and Hirst, 1997).

Finding a way of synthesizing the large amount of transient tracer data collected during WOCE and before into a form easily used by modellers is

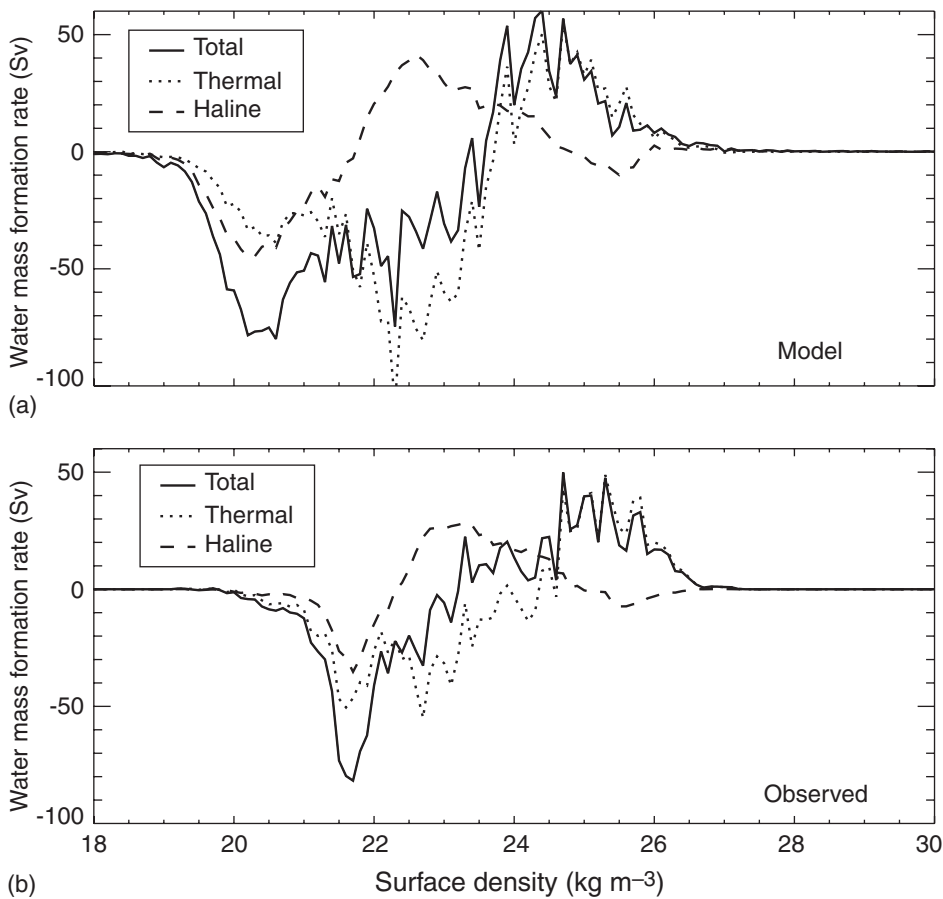


Fig. 2.3.5 Equilibrium water mass transformation rates (derived from surface buoyancy flux following Speer and Tziperman, 1992) in the Indian and Pacific Oceans, as a function of potential density, in (a) the NCAR CSM coupled model, and (b) derived from a surface flux climatology based on observations and re-analysis (NCEP-STR). Details of the model calculation and the climatology can be found in Doney *et al.* (1998b).

a challenging task, since the different sections have been sampled at different times during the past 20 years (see Schlosser *et al.*, Chapter 5.8). Nonetheless, the tracer data set provides a valuable resource for evaluating model ventilation rates over decadal time scales, and increasing use of it is likely to be made in the future. The implications of such evaluations for future climate projections are discussed in Section 2.3.6.1.

2.3.5.5 Interannual variability

The El Niño–Southern Oscillation (ENSO) phenomenon is the strongest mode of variability of the modern climate, on time scales longer than seasonal, and is believed to result from coupled interaction of the atmosphere and ocean (Philander, 1990; Neelin *et al.*, 1998). Correct reproduction of ENSO is therefore a strong test of coupled models. Many coupled models were developed as part of the TOGA programme, specifically to study the

ENSO problem (see Delecluse *et al.*, 1998), but these often involved simplifications (limited ocean domain, flat bottom) that made them inappropriate for longer-time-scale, global phenomena. Nonetheless, a number of fully global models produce ENSO-like variability in SST with realistic spatial patterns and time scales. Some models (e.g. Roeckner *et al.*, 1996; Guilyardi and Madec, 1997; Barthelet *et al.*, 1998) include enhanced resolution in order to resolve the equatorial waveguide. It is perhaps surprising that even some models with very coarse resolution still produce quite realistic-looking SST variability (e.g. Tett, 1995; Knutson *et al.*, 1997; Timmerman *et al.*, 1999b; Collins, 2000), despite the absence of equatorial waves. Physical mechanisms other than equatorial waves may be at play in ENSO, and such mechanisms appear to be present in the coarse-resolution models (see Neelin *et al.*, 1998, for a review).

The Southern Ocean exhibits more than one mode of interannual variability. Specifically, a quasi-standing wave, zonal wavenumber 3 pattern and a propagating, zonal wavenumber 2 pattern, have been identified (see Cai *et al.*, 1999, for a brief review). The propagating pattern has been named the Antarctic Circumpolar Wave (ACW), and has signatures in SST, sea ice extent and atmospheric and oceanic circulation (White and Petersen, 1996; Jacobs and Mitchell, 1996). Variability with some of the observed characteristics has been seen in a number of coupled model studies (Christoph *et al.*, 1998; Motoi *et al.*, 1998; Cai *et al.*, 1999). However, the dominant length scale of the variability is not always as observed (e.g. Cai *et al.* find ACW-like variability with wavenumber 3), and the mechanisms that drive this variability remain a subject of debate.

2.3.5.6 Decadal variability

On interannual time scales, the dominant mode of Pacific SST variability is ENSO. On interdecadal time scales the centre of action moves to the North Pacific (see, e.g., Yukimoto, 1999). This variability, which appears to be a coupled mode involving wind stress and temperature advection anomalies in the subtropical gyre, is reproduced in several models (Latif and Barnett, 1996; Robertson, 1996; Yukimoto *et al.*, 1996; Knutson and Manabe, 1998; Saravanan, 1998). Decadal modulation of the interannual ENSO signal is also seen in both observations and models (Zhang *et al.*, 1997; Lau and Weng, 1999).

The North Atlantic and Arctic Oscillations (NAO and AO) dominate the decadal variability of the Atlantic sector. A number of models produce NAO-like (e.g. Delworth, 1996; Saravanan, 1998) and AO-like (e.g. Broccoli *et al.*, 1998; Fyfe *et al.*, 1999; Shindell *et al.*, 1999) variability.

It is known that the ocean responds to atmospheric variability on decadal time scales (Dickson *et al.*, Chapter 7.3; Dickson *et al.*, 1996). An important question is whether the ocean has a significant role in driving the atmospheric variability through SST anomalies, producing a fully coupled mode and opening up the possibility of some level of climate predictability on decadal time scales. Diagnosis of CSM model heat fluxes suggests that over much of the ocean there is a strong local negative feedback of the surface heat flux on SST (e.g. Saravanan, 1998). Ocean-only model runs

have been used to show that in the GFDL model decadal THC variability can be explained as a largely passive response to surface heat flux variations (Delworth and Greatbatch, 1999). However, this does not preclude predictable oceanic forcing of the atmosphere if the ocean dynamics produces SST anomalies in regions where the atmosphere is particularly sensitive to SST. The results of Rodwell *et al.* (1999) suggest that mid-latitude SST anomalies are playing some role in driving NAO variations on decadal time scales. This is a topic of much current research.

2.3.5.7 Simulation of past climates

Palaeoclimatic evidence suggests that changes in ocean circulation have played an important role in past climate change and variability (Broecker, 1997). Coupled models are therefore likely to have an important part to play in the study of past climates. Further, coupled models are widely used to make projections of possible future climate, but most model evaluation is done by testing the models' ability to simulate present climate (as in Sections 2.3.5.1–2.3.5.6 above). How do we know that the models have not simply been 'tuned' to give a good simulation of present climate? A valuable, orthogonal test of the models is to ask whether, without 'retuning' they can simulate past climate states.

One test that has been applied to models is to ask whether, given the history of forcing over the last century or so from solar variability, volcanic and anthropogenic aerosols and greenhouse gases, they can reproduce the observed evolution of the global mean surface air temperature over that time. Since the climate (and the models) contains considerable natural variability, one would not expect the model response to be determined entirely by the forcing, and ensembles of several integrations are usually used in these studies. Several models have shown that encouraging agreement can be obtained with the observed record (Hasselmann *et al.*, 1995; Mitchell *et al.*, 1995; Haywood *et al.*, 1997; Boer *et al.*, 1999). By running the models with different combinations of forcings, insight can be gained into the attribution of observed climate variations to natural or anthropogenic causes (e.g. Hegerl *et al.*, 1997; Barnett *et al.*, 1999; Tett *et al.*, 1999).

Moving further back into time, much work has been done on the simulation of the climatic

optimum of the mid-Holocene (6000 years BP) and the last glacial maximum (LGM, 20 000 years BP). Most of this work to date has been with atmosphere-only models, but a coupled simulation of the mid-Holocene has been performed (Hewitt and Mitchell, 1998). This suggested that ocean dynamics and mixed-layer processes played a role in the enhanced monsoon rainfall shown by palaeodata. No coupled model simulations of the LGM have yet been performed, largely because of the long time scales required for the ocean circulation to adjust to the very different state at that time (including lower sea level and extensive ice sheets).

2.3.6 Coupled model simulation of future climates

One of the main uses of global coupled models is for projection of possible future climate change due to anthropogenic emissions of CO₂ and other greenhouse gases. This is a vast subject and we only touch here on a few topics. For a comprehensive review the reader is referred to recent assessment reports of the Intergovernmental Panel on Climate Change (IPCC, 1995; a new assessment report (IPCC, 2001) is in preparation at the time of writing and due for publication in mid-2001).

2.3.6.1 Climate sensitivity and transient response

The response of the atmosphere to changes in radiatively active species is determined by a number of complex feedbacks, especially those involving water vapour and clouds. The net result of these feedbacks in a model is often expressed as the ‘climate sensitivity’ of the model, defined as the change in global mean surface temperature *at equilibrium*, in response to a doubling of atmospheric CO₂ concentration. The equilibrium response is usually determined by running the atmosphere model coupled to a ‘slab’ ocean mixed layer. There is considerable variation in the climate sensitivity between models, with the current generation of models having sensitivities between 1.5 and 4.5°C (IPCC, 1995). This reflects uncertainty in the water vapour and cloud feedbacks. Although the equilibrium climate response is an important benchmark of models, it does not necessarily give a good guide to the transient response of climate over the next century to a particular scenario of greenhouse gas increase. To understand the transient response, the uptake of

heat by the ocean must be taken into account (Section 2.3.5.4), and coupled models are necessary.

Figure 2.3.6b (see Plate 2.3.6b, p. 76) shows the zonal mean temperature difference between the decade around 2050 and the decade around 2000, when the HadCM3 model is forced with a scenario of increasing greenhouse gases. The broad pattern of deeper penetration of heat at high latitudes is as expected, and similar to the CFC-11 uptake in Fig. 2.3.6a (see Plate 2.3.6a, p. 76), but beyond this the similarity between the two fields ends. Not only are the surface flux fields driving the CFC and temperature changes very different, but in the greenhouse gas run the ventilation process changes in response to the changing climate. For example, by 2050 the Labrador Sea convection would have collapsed in the greenhouse gas run (Wood *et al.*, 1999), and this would contribute to the relatively shallow penetration of heat anomalies when compared with the CFC. Thus transient tracer observations give us a valuable constraint on models by telling us about ventilation processes in the present climate, but they cannot tell us about ventilation in a changed climate. This means it would be difficult to tune a ‘slab’ mixed-layer model to give reliable projections of transient climate change.

2.3.6.2 Stability of the thermohaline circulation

Most climate models suggest that the climate response to increasing greenhouse gases includes a warming of surface air temperature and an increase in high-latitude precipitation. Both these effects might be expected to inhibit subpolar convection and so weaken the THC, and indeed most models show a THC weakening when forced with increasing greenhouse gases. This weakening probably has an important effect in moderating the climate response, particularly over northern and western Europe. However, there is great uncertainty over the magnitude of the response. For example, in experiments where CO₂ was increased to four times preindustrial values, the THC weakened by about 25% in HadCM3 (Wood *et al.*, 1999), but collapsed completely in the GFDL model (Manabe and Stouffer, 1993). Further uncertainty arises because of the possibility of hysteresis behaviour of the THC, which could lead to sudden (decadal time scale) state transitions similar to that which is believed to have occurred in the Younger Dryas

cold event of 11 000 years BP (Broecker, 1997). Such behaviour has been shown in the GFDL GCM (Manabe and Stouffer, 1988, 1997) as well as in the intermediate complexity CLIMBER model (Rahmstorf and Ganopolski, 1999 – see Section 2.3.2.1). Much of the modelling uncertainty arises because the THC response is controlled by the sum of a number of positive and negative feedbacks. These feedbacks have been extensively studied in simple models but have not as yet been systematically quantified in GCMs (see Rahmstorf *et al.*, 1996, for a review).

Figure 2.3.7 shows the response of three components of the THC to increasing greenhouse gases in the HadCM3 model: the dense flows across the Greenland–Iceland–Scotland ridge and across a section south of Cape Farewell, and the NADW flow at 24°N. These sections were chosen as there are observations against which to test the model, and in the control run the transports compare fairly well with the observational estimates.

In the greenhouse gas run, the Greenland–Scotland transport remains remarkably constant, while the flow at Cape Farewell collapses and there is a modest weakening of the flow at 24°N. These model changes represent a pattern that is not seen in the natural variability of the model. If such patterns prove to be robust, they will suggest how future observational campaigns might be targeted to detect any signal of anthropogenic climate change in the ocean.

2.3.7 Climate models, WOCE and future observations

Observational oceanographers and climate modelers are working towards the same WOCE goal of developing and testing models suitable to predict (at least in a probabilistic sense) future climate. However, the nature of observing and modelling means that the two communities have traditionally begun from different (almost opposite) starting

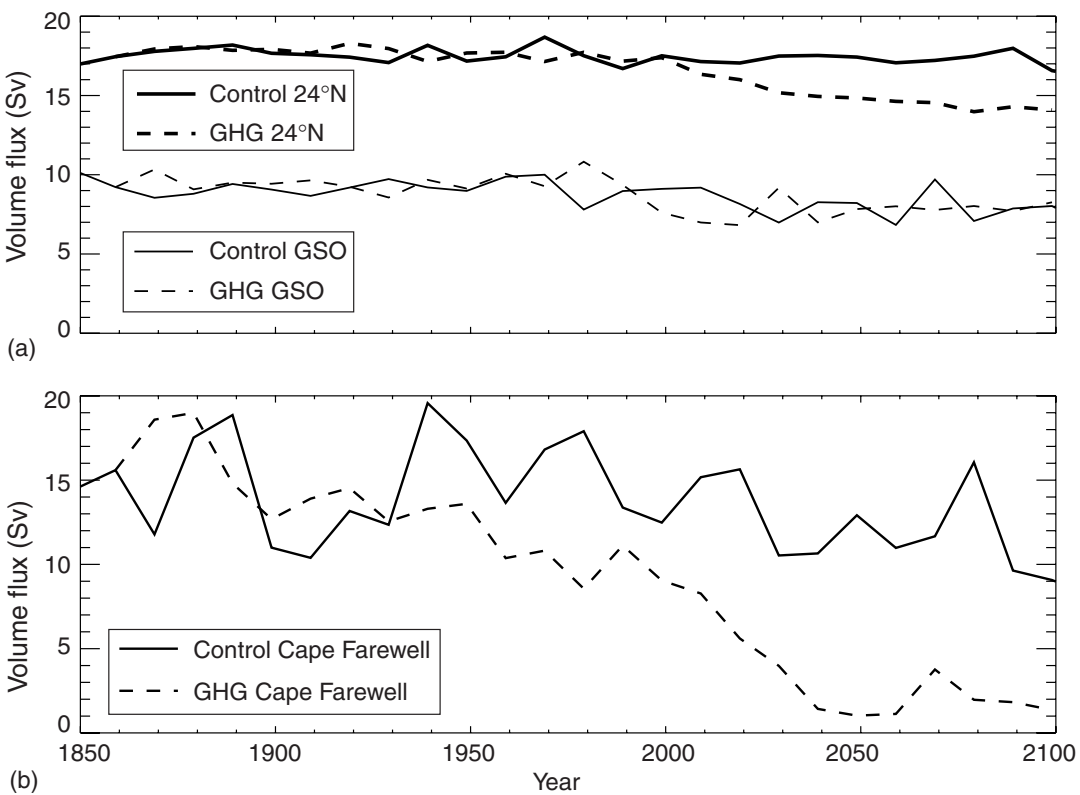


Fig. 2.3.7 Time-series of the flow of water denser than σ_θ 28.5 across (a) the Greenland–Iceland–Scotland ridge (Greenland–Scotland Overflow, GSO) and (b) a section south of Cape Farewell. Part (a) also shows the total southward NADW flow across the 24°N Atlantic section. Data are from a run of the HadCM3 coupled model forced by increasing greenhouse gases ('GHG') and from a control run with fixed greenhouse gases (Wood *et al.*, 1999). Observational estimates of the three transports, for comparison with the control values, are: Greenland–Scotland, 5.6 Sv (Dickson and Brown, 1994); Cape Farewell, 13.3 Sv (Clarke, 1984); and 24°N, 19.3 Sv (Hall and Bryden, 1982).

points. Traditional *in-situ* observations require the deployment of instruments at sea, a process that requires enormous logistical planning and is subject to all the uncertainties and difficulty of work in a hostile environment. Each ocean data set, therefore, represents a considerable investment of time and effort on the part of the investigators involved, and to extract the maximum value from the data set much work is required after the observations have been made. A single research cruise provides a detailed view of the state of the ocean at a particular place and time.

Climate modellers, on the other hand, begin with a global view. As discussed in Section 2.3.3, the large-scale, long-term mean transports of heat and water by the ocean and atmosphere are a fundamental feature of the climate system that models must attempt to reproduce. This means that climate modellers have a particular interest in the development of integrated, consistent global syntheses of a large number of individual data sets, to produce estimates of these quantities. The use of the vast WOCE data set to produce such a global picture for the 1990s, with reduced uncertainties compared with our previous knowledge, will be an important test of the success of WOCE (see especially Chapters 6.1, 6.2 and 7.1).

The above does not mean that climate modellers are interested *only* in large-scale, basin mean transports; climate change and variability are effected by many smaller-scale mechanisms. For example, the response of the thermohaline circulation to changes in surface forcing is likely to be carried from the deep convection regions to the rest of the ocean via sill overflows and boundary processes (Böning and Semtner, Chapter 2.2). Improved knowledge of the dynamical and thermodynamical processes by which the ocean achieves its large-scale transports is needed so that we can both diagnose any deficiencies in model transports and increase confidence that our models will respond correctly to any applied perturbations (e.g. greenhouse gas increase).

The nature of decadal climate variability and change means that the representativeness of the existing ocean database (especially the WOCE ‘snapshot’) of the long-term mean state of the ocean is an important question. Ultimately this can only be addressed by a long-term programme of repeated observations (see Chapters 7.3 and 7.4). In the meantime, we must rely on models, combined

with judicious use of the historical database, in order to increase our understanding of decadal changes in the ocean. For example, Wong *et al.* (1999) interpret a large amount of historical hydrographic data to show changes in the properties of intermediate water masses during the second half of the twentieth century. Quantitatively similar changes are seen in the HadCM3 model by Banks *et al.* (2000), who suggest that the observed freshening of Subantarctic Mode Water is most likely a result of anthropogenic climate change, whereas changes seen in other water masses may be due to internal climate variability. While such results must be treated cautiously, as the models still have many deficiencies, studies such as these have the potential to provide useful input to the design of long-term observing networks.

2.3.8 Summary and future developments

Considerable progress has been made in the development of coupled climate models during the WOCE period. In 1990, at the start of WOCE, only a few coupled models were in existence, and only a few runs had been made. During the intervening decade, in parallel with the WOCE observational programme, many groups have developed models; in 1996, control runs from 18 coupled models were contributed to the first phase of the Coupled Model Intercomparison Project (CMIP). Model performance has improved, and models are now emerging that produce stable, credible simulations of many aspects of present climate. A particular success is that some models can now reproduce the observed large-scale heat balances of the climate system, without the need for unphysical flux adjustments.

There remain many aspects of the model simulations that are inconsistent with or untested against observations, and the ocean components of coupled models still suffer from rather coarse resolution. However, it must be remembered that the models are largely used to study climate variability and change, and that a large error in, say, the properties of a particular deep water mass, may not have a large impact on atmospheric climate on the decadal to century time scale. In fact the extent and mechanisms by which the ocean is playing an active role in climate on these time scales is an active area of current research.

Future model developments are likely to include a move to higher resolution (including eddy-permitting

ocean models), and developments to sub-grid-scale parameterizations, in both atmosphere and ocean. For the ocean, sill overflows and their mixing in bottom boundary layers, mesoscale eddy fluxes and the spatially inhomogeneous nature of diapycnal mixing are areas where developments are likely (through improved resolution, parameterization or both). Many of these issues were discussed at the WOCE/CLIVAR workshop on ocean climate modelling held in Boulder in August 1998, and the report of that workshop (WOCE International Project Office, 1999) summarizes the state of the art and research directions envisaged at that time. Biogeochemical cycles, especially the carbon and sulfur cycles, will probably be incorporated into climate models over the next few years. While there is clearly much still to be done, the ocean components of climate models are reaching a state of maturity where serious comparison with observations is now possible, and model projections of climate variability and change can be used to help in the design of the ocean observing and monitoring systems of the future.

Acknowledgements

We thank Claire Cooper, Scott Doney, Jonathan Gregory and James Penman for help in producing the figures, and Matthew Collins, Peter Cox, Chris Gordon, Jonathan Gregory, Chris Hewitt, Colin Johnson and Catherine Senior for valuable discussions. RAW is supported by the UK Department of the Environment, Transport and the Regions. FOB is supported by the US National Science Foundation, through its sponsorship of NCAR.

Appendix: Acronyms for models and institutions

The following model names and other acronyms are used within this chapter. Note that this is not a full list of coupled models in use at the time of writing. The interested reader is referred to the CMIP project (see below), and to the assessment reports of the Intergovernmental Panel on Climate Change, e.g. IPCC, 1995, for more complete listings.

| | |
|------|---|
| CSM | Climate System Model (coupled) (NCAR; Boville and Gent, 1998) |
| CMIP | Coupled Model Intercomparison Project. A systematic intercomparison |

of a number of coupled models, co-ordinated by the Program for Climate Model Diagnosis and Intercomparison, Lawrence Livermore National Laboratory, Livermore, California, USA. CMIP1 includes model 'control' runs only, CMIP2 also includes model response to an idealized scenario of atmospheric carbon dioxide increase (see <http://www.pcmdi.llnl.gov>)

DKRZ Deutsche Klimarechnungszentrum, Hamburg, Germany

GFDL Geophysical Fluid Dynamics Laboratory, Princeton, New Jersey, USA

HadCM2/3 Coupled models of the Hadley Centre for Climate Prediction and Research, Meteorological Office, Bracknell, UK

HOPE Hamburg Ocean Primitive Equation Model (DKRZ; Wolff *et al.*, 1997)

LODYC Laboratoire d'Oceanologie Dynamique et de Climatologie, Paris, France

LSG Large-Scale Geostrophic model (MPI/DKRZ; Maier Reimer *et al.*, 1993)

MOM Modular Ocean Model (GFDL), developed originally from the model of Bryan (1969)

MPI Max Planck Institut für Meteorologie, Hamburg, Germany

NCAR National Center for Atmospheric Research, Boulder, Colorado, USA

OPA Ocean model of LODYC (Madec *et al.*, 1998)

OPA/ARPEGE OPA coupled to the atmospheric model of Meteo France/European Centre for Medium Range Weather Forecasts (Madec and Delecluse, 1997)

OPA/LMD OPA coupled to the atmospheric model of the Laboratoire de Meteorologie Dynamique (Madec and Delecluse, 1997)

OPYC Ocean isopycnic model (MPI; Oberhuber, 1993)

SECTION

3

NEW WAYS OF OBSERVING THE OCEAN

Chapter 3.1

SHIPBOARD OBSERVATIONS DURING WOCE

B. A. King, E. Firing and T. M. Joyce
99

Chapter 3.2

SUBSURFACE LAGRANGIAN OBSERVATIONS DURING THE 1990s

Russ E. Davis and Walter Zenk
123

Chapter 3.3

OCEAN CIRCULATION AND VARIABILITY FROM SATELLITE ALTIMETRY

Lee-Lueng Fu
141

Chapter 3.4

AIR-SEA FLUXES FROM SATELLITE DATA

W. Timothy Liu and Kristina B. Katsaros
173

Chapter 3.5

DEVELOPING THE WOCE GLOBAL DATA SYSTEM

Eric J. Lindstrom and David M. Legler
181

This Page Intentionally Left Blank

3.1

Shipboard Observations during WOCE

B. A. King, E. Firing and T. M. Joyce

3.1.1 The role of hydrographic measurements

Such was the transformation in shipboard hydrographic work during WOCE, that it is difficult to think back to the pre-WOCE era, and to recall what then represented the state-of-the-art in knowledge, expectation and procedures. Indeed, a generation of oceanographers has been trained whose only experience has been of the demanding standards achieved by the WOCE programme. There had been high-quality campaigns on a smaller scale before, but these depended on the expertise of a relatively small number of Principal Investigators (PIs). Standards and protocols adopted and promoted during WOCE have now become the target for many groups outside the WOCE community. The Scientific Plan for WOCE (WCRP, 1986) is a valuable reminder of the background against which these standards were set, and we make no apology for leaning heavily on that document for this introduction. Volumes I and II of the WOCE Implementation Plan (WCRP, 1988a,b) are a source of further details.

The earliest information about ocean currents came from measurements of ship drift – the difference between the average velocity of the ship determined by celestial navigation and the average velocity that would have been expected (from dead-reckoning) in the absence of currents. Compilation of ship-drift estimates provided navigational charts of the world's mean surface currents, but no information about the flow beneath the surface, and hence little idea of current transports and the general three-dimensional circulation.

Direct measurements of subsurface currents have always been few and far between, so ocean circulation has been inferred primarily from measurements of water properties: temperature, salinity, and the concentrations of oxygen and nutrients, and other tracers (Sverdrup *et al.*, 1942). The classical mode of inference was based on the intuitive notion that flow must be from the source of a water property towards the sink, hence along 'tongues' of extreme values of the property. A variation of this idea is that in the limit of weak diffusion, flow should be along lines of constant value of a conservative property such as salinity. With improved understanding of ocean dynamics, these qualitative modes of inference became increasingly supplemented, and often supplanted, by quantitative calculations of the vertical structure of horizontal currents. Except in the top 100 m and over full depth near the equator, the slowly changing components of ocean circulation are almost perfectly in geostrophic balance: that is, horizontal components of the pressure gradient are balanced by the Coriolis force, which is to the right of the velocity in the northern hemisphere and to the left in the southern. The horizontal pressure gradient cannot be measured directly, but its rate of change in the vertical is proportional to the horizontal gradient of density, and this can be estimated from a hydrographic section – a line of vertical profiles of temperature and salinity.

Hydrographic sections, then, provide estimates of the velocity component perpendicular to the section at any depth, relative to the unknown velocity at a single reference depth. Most quantitative estimates of ocean circulation come from these

geostrophic calculations, together with an estimate of the reference velocity based on any or all of several considerations: *a priori* assumptions; classical water property analysis; conservation of mass and other conservative properties within a fixed volume; and direct measurements of velocity. Methods of applying these considerations have become more sophisticated and systematic in recent years, but the conceptual basis for estimating ocean circulation in WOCE has been essentially unchanged for perhaps 75 years since the Atlantic Expedition of the *Meteor*.

Even the best hydrographic section is unable to resolve all the ocean variability. Geostrophic calculations implicitly average the currents between stations; WOCE sections were not generally eddy-resolving. The section is sampled once only, so time variation is not resolved. Section analyses generally assume that the observed section is representative of the mean circulation, although some information about temporal variability over parts of the section may be known from moored subsurface measurements, floats and drifters or space-borne measurements.

3.1.1.1 The need for a global programme

At the start of WOCE, far more was known about the North Atlantic than any other basin. There were a number of reasons for this. First, its accessibility to the oceanographic institutions of western Europe and eastern North America. Second, its size, compared with the Pacific for example, made trans-oceanic sections practical. Third, in comparison with the Indian Ocean and the Pacific, the Atlantic has the greatest variety of water types and the most vigorous water mass formation regions, so it has been the natural first target for surveys of water properties. During the International Geophysical Year (IGY) only the Atlantic was covered with a systematic, high-quality, top-to-bottom, continent-to-continent grid of hydrographic stations (Fuglister, 1960).

In the other oceans, the database was largely the result of uncoordinated surveys, leaving large gaps in coverage in one or more of the essential fields. Any substantial progress in understanding the global circulation would require a description of the distributions of heat, fresh water, chemical tracers, relative geostrophic currents and surface forcing in the other basins that would permit their discussion with the same confidence that existed for the North Atlantic.

WOCE planning defined three Core Projects. Core Project 1 – ‘The Global Description’ – was to include a hydrographic and chemical tracer survey, measurements of sea surface height, especially from altimeters, wind stress and direct current measurements.

The shipboard hydrographic programme of WOCE, known as the WOCE Hydrographic Programme, or WHP, was one of the central elements of Core Project 1. The WHP consisted of a network of trans-oceanic sections, occupied with high-quality CTD (Conductivity-Temperature-Depth) and bottle sample measurements, with a nominal along-track spacing of 50 km. Direct measurements of upper ocean currents were made continuously along the ship track with shipboard Acoustic Doppler Current Profilers (ADCPs). In the latter stages, these were supplemented with Lowered ADCPs (LADCPs): self-contained ADCPs lowered with the CTD package, which provide top-to-bottom profiles of ocean current at the station. The fundamental purpose of the WHP was to provide a complete global map of property distributions, and to enable the calculation of fluxes of those properties across sections. At the start of WOCE, shipboard ADCP data were not required observations, though many research ships were fitted with the instruments. But as the technology and data quality developed, high-quality data returns became routine.

This chapter describes the organization and success of the WHP. Section 3.1.2 covers CTD and the basic sample measurements: salinity, oxygen and nutrients. Shipboard and lowered ADCP are discussed in Section 3.1.3. Shipboard meteorology measurements are discussed in Section 3.1.4. A summary of XBT (Expendable Bathythermograph) measurements from research ships and Voluntary Observing Ships is given by Lindstrom and Legler (Chapter 3.5). Transient tracers measured from bottle samples are beyond the scope of this chapter, and are discussed by Schlosser *et al.* (Chapter 5.8). Measurements of parameters in the inorganic carbon system are described by Wallace (Chapter 6.3).

While it has been pointed out that the WHP was a central element of Core Project 1, it also underpinned the other core projects. The overall WOCE Goals and Core Projects are described by Thompson *et al.* (Chapter 1.3). Hydrography provides the dynamical link between the surface and

the ocean interior; between the surface pressure field and velocity measurements from drifters, floats and current meters. The ocean temperature and salinity fields are arguably the most fundamental of all ocean measurements.

3.1.1.2 The basis of support for the WHP

The number of different PIs who supported and participated in the work of the WHP was surely greater than for any other element of WOCE. With each cruise requiring a wide range of physical and chemical measurements, literally hundreds of PIs were involved in writing proposals, organizing cruises and cooperating in the exchange and reporting of data.

The task of completing the WHP was beyond any single nation. The programme could not have achieved the success it did if it had not been adopted and endorsed by international collaboration. Figure 3.1.1 shows the distribution, by nationality of Chief Scientist, of contributions to the one-time survey.

One reason why the deep-water observational community embraced the WHP so enthusiastically was simply to expand the knowledge of ocean water properties, circulation patterns, variability and relevant time scales, which had been so piecemeal before. While the principal motivation for the planners of WOCE was climate research, it presented oceanographers with an unprecedented

opportunity to explore some rarely or never-before sampled regions. The WHP was therefore able to tap the expertise of PIs whose enthusiasm did not extend so wholeheartedly to the overall goals of WOCE.

Other communities combined with observationists to support the programme and to capitalize on the WHP data. Scientists who make flux calculations were justifiably excited about the chance to analyse a basic global set of trans-oceanic sections, complete with a range of tracers. Previously, studies that attempted to combine several sections from a single basin had needed to use historical sections, sometimes separated in time by decades.

Another group was of scientists who analyse water properties to infer the basic water mass distributions and circulation patterns. Some regions of the ocean were still relatively unknown, so from this viewpoint the WHP was completing a general survey of the oceans.

The tracer community was as strong a champion for the WHP as any group. Tracer scientists had long worked closely with physical oceanographers, for example in the programmes GEOSECS (Geochemical Oceans Sections Study), TTO (Transient Tracers in the Ocean) and SAVE (South Atlantic Ventilation Experiment). Where such programmes were not available, they carried out their measurements on compatible long sections, and so were able to proceed on a piecemeal basis. The WHP provided the ideal vehicle to continue their work, and the tracer programme can therefore be regarded as one of a series of high-quality campaigns. Similarly, the carbon research community became a strong supporter of WOCE. The global CO₂ survey of the Joint Global Ocean Flux Study (JGOFS) could rely heavily on WOCE hydrographic observations, and many JGOFS carbon measurements were obtained simultaneously with WHP observations.

Without such a broad range of supporters and participating communities, it is unlikely that the WHP would have attracted so much investment. It may not be too fanciful to argue that outside of the polar regions and marginal seas that WOCE did not cover, the WHP will be seen as the last big experiment that includes basic shipboard exploration and survey of the distributions, modifications and exchanges of the principal water masses of the world ocean. While it will certainly be necessary to repeat a large fraction of it for a variety

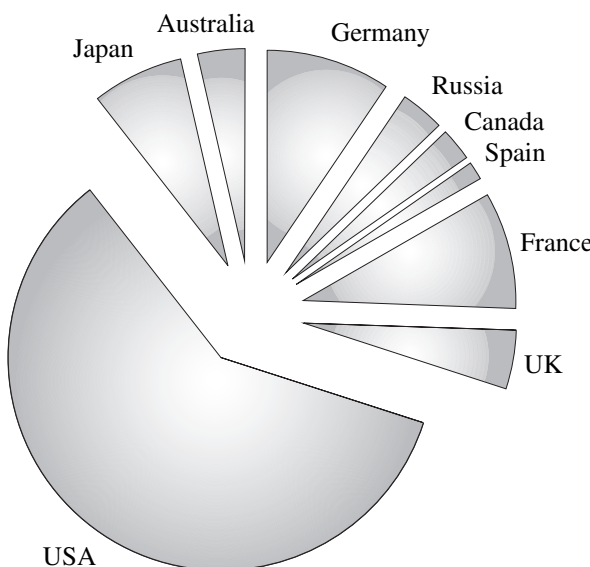


Fig. 3.1.1 Distribution of national contributions to the one-time survey, based on number of stations and nationality of cruise chief scientist. Prepared by N.P. Holliday (WOCE IPO).

of purposes, a rapid resurvey on the scale completed in the WHP is not anticipated in the immediate future. Indeed, such a resurvey would not constitute such basic global exploration as was the case in WOCE. It is difficult to imagine that a significantly more detailed global survey could be undertaken without fundamental advances in technology, especially in the use of autonomous platforms and sensors.

In the era following the WOCE observational phase, global observations are now focused on strategies for sustained observations, and determining variability and change.

3.1.2 CTD and sample measurements

3.1.2.1 Development and planning of the WOCE Hydrographic Programme

The planning for the WOCE Hydrographic Programme (WHP) officially started with the establishment and first meeting of the WHP Planning Committee in April 1987. The committee began thinking of requirements for variables to be measured and their accuracy. Three kinds of hydrography were envisioned for WOCE: one-time survey, repeat hydrography and time-series stations. The one-time survey would sample the ocean on a regular grid of lines spaced so as to cover all the major ocean sub-basins. Repeat hydrography would include two types of sampling: selected one-time lines would be repeated to check the representativeness of the one-time survey; and additional individual sections, not necessarily parts of the one-time survey, would be repeated once or twice yearly

throughout WOCE. Time-series stations were envisioned to be regular reoccupations of particular sites that were to continue from pre-WOCE measurements or to be new sites under the aegis of WOCE and JGOFS; temporal sampling at time-series sites would be sufficient to resolve the seasonal signal. Another contribution to observing the ocean variability was the high-density XBT programme conducted from Voluntary Observing Ships. Figure 3.1.2 shows lines occupied in this programme.

In terms of magnitude of effort, the initial estimates (WCRP, 1988a) indicated that the WHP was to exceed by more than an order of magnitude all previous large-scale ocean 'surveys' going back to the *Challenger* Expedition (Fig. 3.1.3). The plan called for 7700 small volume stations in the one-time survey and a further 15 000 for repeat hydrography: this would require 10 years' ship-time for the one-time and a further 15 years for repeat work.

The WHP, which officially began field work in 1990, evolved into a programme in which the bulk of the one-time survey in the Pacific Ocean was carried out during 1991–94, the Indian Ocean in 1995 and the South Atlantic in 1992–95. The one-time survey of the North Atlantic, however, had a distributed sampling throughout the WOCE period and was not concentrated in time. Documented changes in the North Atlantic during WOCE have shown a significant change in properties of Labrador Sea Water to have occurred during the North Atlantic one-time survey. The sheer size of the Pacific Basin mitigated against any

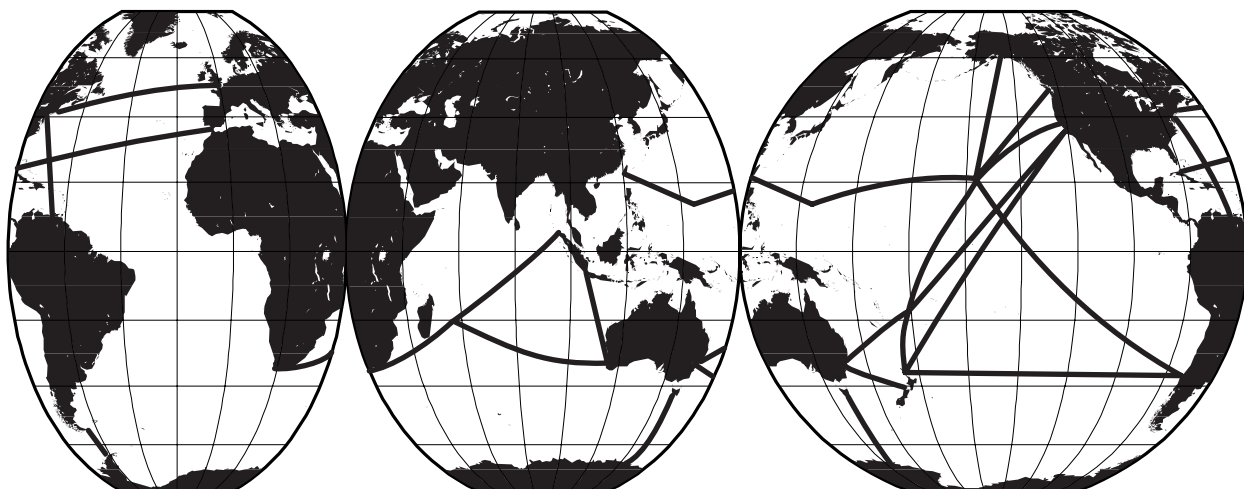


Fig. 3.1.2 Schematic location of high-density XBT lines. Prepared by N. P. Holliday (WOCE IPO).

quick survey, say during a single phase of ENSO (El Niño-Southern Oscillation). Because several lines in the pre-WOCE period (of demonstrable high quality and including the requisite tracers)

were not reoccupied in WOCE, the starting time for the Pacific survey was in effect 1985, including the pre-WOCE lines. Hence one must rely on independent data such as repeat hydrography or time-series stations to determine the degree to which the WHP one-time survey ‘snapshot’ in any one ocean basin was blurred by the motions of those being ‘photographed’.

It was recognized that the one-time survey would be more inclusive of variables measured than repeat hydrography, and have the strictest requirements for accuracy. In the minutes of the first meeting of the Planning Committee, the recommendations for CTD and water sample requirements were first stated and later (WCRP, 1988a) published: they are reproduced in the attached tables (Table 3.1.1 for CTDs and Table 3.1.2 for water samples). Original plans were that the one-time suite of water samples would include all of the tracers down to and including CFCs in Table 3.1.2. At the start of WOCE, accurate radiocarbon measurements using beta counting techniques needed large volumes (>100 litres) of water. Less accurate Accelerator Mass Spectrometer (AMS) measurements of radiocarbon were to be confined to the upper ocean where the signal was larger. However, Key (1996) has shown that with improvements in AMS methodology, the AMS facility constructed at the Woods Hole Oceanographic Institution for the WHP measurements could routinely achieve comparable accuracy from small volume samples; large-volume sampling for radiocarbon became obsolete during WOCE.

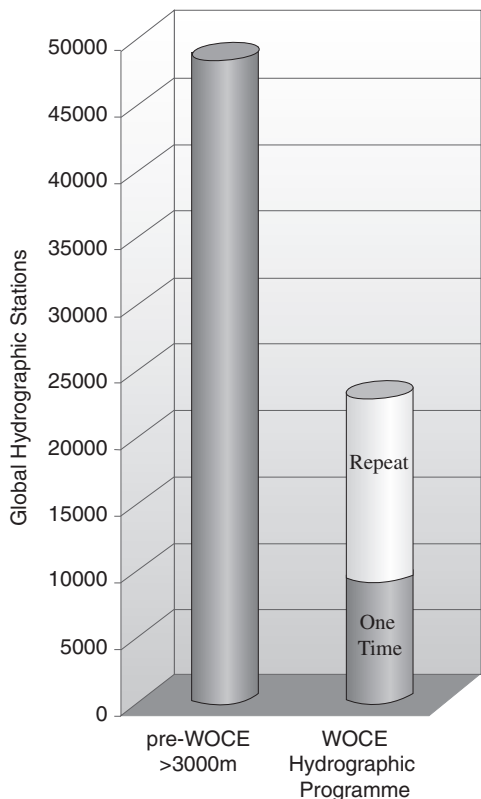


Fig. 3.1.3 Number of deep (>3000 m) stations taken before WOCE (data from NODC profile database) and in the WHP one-time and repeat surveys. Prepared by N. P. Holliday (WOCE IPO).

Table 3.1.1 One-time WHP standards for CTD sensors. The data quality goals given here and in Table 3.1.2 are regarded as attainable in low-gradient oceanic domains. They represent an ideal that can be achieved by appropriate methodologies such as those specified in the WHP Operations and Methods manual (WHPO, 1994a)

| Parameter | Standard |
|----------------|--|
| T | Accuracy of 0.002°C ; precision 0.0005°C (ITS ₉₀) |
| S | Accuracy of 0.002 PSS-78, depending on frequency and technique of calibration; precision 0.001 PSS-78, depending on processing techniques ^a |
| P | Accuracy 3 decibar (dbar) with careful laboratory calibration; precision 0.5 dbar, dependent on processing ^b |
| O ₂ | Reproducibility* 1%; same for precision ^c |

* If no absolute standards are available for a measurement, then accuracy should be taken to mean the reproducibility presently obtainable in the better laboratories.

^a Although conductivity is measured, data analyses require it to be expressed as salinity. Conversion and calibration techniques from conductivity to salinity should be stated.

^b Difficulties in CTD salinity data processing occasionally attributed to conductivity sensor problems or shortcomings in processing may actually be due to difficulties in accounting for pressure sensor limitations.

^c Existing polarographic sensors have been found to meet these requirements but better sensors need to be developed, particularly for use in high latitudes.

Table 3.1.2 One-time WHP standards for water samples

| Parameter | Standard |
|-----------------------|--|
| T | High-resolution Deep-Sea Reversing Thermometers (DSRTs) are available and with careful calibration and reading may be capable of 0.004–0.005°C accuracy and 0.002°C precision. Digital DSRTs do not require long soaking times and, potentially, can serve as a means for calibration and performance checks. Their development, and in particular their long-term stability, will be closely monitored. Carefully documented and monitored use of multiple CTD sensors have the potential to eliminate the standard use of DSRTs |
| P | Accuracy 3 decibar (dbar) with careful laboratory calibration of the CTD; precision 0.5 dbar, dependent on processing |
| S | 0.002 accuracy is possible with Autosal™ salinometers and concomitant attention to methodology, e.g. monitoring Standard Sea Water. Accuracy with respect to one particular batch of Standard Sea Water can be achieved at 0.001 PSS-78. Autosal™ precision is better than 0.001 PSS-78, but great care and experience are needed to achieve these limits on a routine basis as required for WOCE. For example, laboratories with air temperature stability of $\pm 1^\circ\text{C}$ are necessary for optimum Autosal™ performance ^a |
| O_2 | Reproducibility* <1%; precision 0.1%. Some laboratories presently achieve 0.5% accuracy*, which is recommended for WOCE measurements ^b |
| NO_3 | Approximately 1% reproducibility* and 0.2% precision, full scale (this standard is probably appropriate to WHP) |
| PO_4 | Approximately 1–2% reproducibility* and 0.4% precision, full scale |
| SiO_2 | Approximately 1–3% reproducibility* and 0.2% precision, full-scale ^c |
| ${}^3\text{H}$ | Reproducibility* 1%; precision 0.5% with a detection limit of 0.05 tritium unit (TU) in the upper ocean of the northern hemisphere and 0.005 TU elsewhere |
| $\delta^3\text{He}$ | Reproducibility*/precision 1.5 per mille (‰) in isotopic ratio; absolute total He of 0.5% with less stringent requirements for use as a tracer (e.g. He plume near East Pacific Rise) |
| CFCs | Approximately 1–2% reproducibility* and 1% precision, blanks at $0.005 \text{ pmol kg}^{-1}$ with best technique. |
| $\delta^{14}\text{C}$ | Reproducibility* and precision 2–4 per mille (‰) via beta counting on 200-litre samples; 5–10 per mille with Accelerator Mass Spectrometer (AMS) |
| ${}^{85}\text{Kr}$ | Detection limit of 1% of surface concentration; precision of 4% decreasing to 25% for samples near the detection limit |
| ${}^{39}\text{Ar}$ | Minimum detectable amount about 5% of surface value; precision of 5% of surface value |
| ${}^{228}\text{Ra}$ | 5% accuracy* and precision |
| $\delta^{18}\text{O}$ | May be used in high latitudes; these should be measured with reproducibility* of 0.02 per mille (‰) |

*Where no absolute standards are available for a measurement then the obtainable limits for the measurement are taken to mean the reproducibility presently obtainable in the better laboratories.

^aKeeping constant temperature in the room where salinities are determined greatly increases their quality. Also, room temperature during the salinity measurement should be noted for later interpretation, if queries occur. The frequent use of IAPSO Standard Seawater is endorsed. To avoid the changes that occur in Standard Seawater, the use of the most recent batches is recommended. The ampoules should also be used in an interleaving fashion as a consistency check within a batch and between batches.

^bImprovements due to new techniques make such accuracy possible. Further development of these techniques and subsequent adoption is highly recommended.

^cStrong opinion exists that with some methodologies laboratory temperature fluctuations cause significant errors, because 1°C laboratory fluctuation yields approximately 1% change in SiO_2 .

The WHP was designed to provide a relatively uniform but coarse global grid of hydrographic sections on zonal and meridional lines, resolving the density field at intermediate and large scales but not at the mesoscale ($O(10\text{--}100 \text{ km})$). The nominal station spacing of 50 km would at best marginally resolve parts of the ubiquitous mesoscale eddy field. In boundary regions and in other selected areas, closer spacing was used.

In addition to providing a basic survey of ocean parameters in unsampled regions and enabling the

calculation of geostrophic current estimates, the WHP data set was intended to be used for estimating fluxes of heat, salt and other tracers. It had been shown that with a full-depth coast-to-coast section it is feasible to estimate heat and freshwater fluxes through an ocean basin; Bryden and Hall (1980) provide an example of one such calculation. Flux calculations using this technique require the same high-quality temperature and salinity data as for dynamical calculations. Certain zonal lines were designated as ‘heat flux lines’.

These were chosen at mid-latitudes where heat flux is expected to be greatest, for example at about 30°S in the southern hemisphere basins.

Apart from requiring temperature and salinity measurements, the conclusions from such calculations are strongly dependent on the estimates of current in the boundary regions, where column-averaged properties (especially temperature) depart significantly from section-mean properties. It was intended that the heat flux lines would be supported by current meter arrays in the boundary currents. This strategy of hydrography coupled with boundary current arrays was only partially implemented: the lack of a complete trans-Indian section at 30°S during the WOCE period was a notable omission. Heavy reliance is still being placed on the 1987 pre-WOCE section described by Toole and Warren (1993). In the Pacific, the 30°N line (WOCE P2) was occupied in a number of segments, at various degrees of resolution, in 1993 and 1994. The nearest single section is the 24°N line completed in two legs on RV *Thomas Thompson* by Swift and Roemmich in 1985.

3.1.2.2 The achievements of the one-time survey in WOCE

The global array of sections designed by the WHP Planning Committee (WCRP, 1988a) contained 64 sections proposed for single occupation, but excluded the Arctic and ice-covered Southern Oceans. The principal justification for the exclusion of the high latitudes was that the design of WOCE was linked to the availability of satellite altimeter data. The TOPEX/POSEIDON ground track turns at a latitude of 66°, although ERS-1 and ERS-2 turn at 82°. Practical considerations of the resources required for high-latitude work also played a part, and, further, the Arctic was the subject of another WCRP programme: the Arctic Climate System Study (ACSYS).

Figure 3.1.4 (see Plate 3.1.4, p. 172) shows the location of one-time stations reported to the WHP Office. The figure shows the unprecedented global nature of the sampling in the WHP, as well as some of the 'holes' in the survey. Some of the holes in the Pacific and Indian basins are considered to have been filled with high-quality pre-WOCE data from the late 1980s; these are included in Figure 3.1.4 (see Plate 3.1.4, p. 172). But gaps remain where no suitable data are available, such as a meridional line at about 50°E in the Southwest Indian Ocean.

In June 2000 the WHP Office (D. Muus, personal communication) had received details of 9215 one-time stations, which exceeds the number originally planned. All stations shown in the figure include CTD and bottle temperature, salinity, oxygen and nutrients; CFCs would have been measured on most stations. Not all will have ^{3}H , ^{3}He , ^{14}C or other tracers. Many stations also have CO_2 parameters ($t\text{CO}_2$ (total dissolved inorganic carbon), $p\text{CO}_2$ (partial pressure of CO_2 in the atmosphere), pH, total alkalinity). A map showing distribution of CO_2 measurements can be found in Chapter 6.3. At the time of writing, a count of the exact number of stations on which each parameter was measured is not available, because not all tracer data have been reported to the WHP Office. Figure 3.1.5 shows the percentage of one-time cruises for which the WHP Office has been notified that a tracer was measured. For the more costly shore-based analyses, PIs are likely to have sampled a subset of the stations completed during the cruise.

In early 2000, the WHP Office online listings included 101 one-time cruises completed, of which all but one had at least the CTD temperature and salinity data submitted, and only one cruise was listed as not having bottle salinity, oxygen and nutrient data submitted to the Office. Tracers requiring shore-based laboratory analysis take longer to reach the Data Assembly Centre. (The WHP Office, described in Section 3.1.2.4, is the WOCE Data Assembly Centre for hydrographic data.)

3.1.2.3 Variability and repeat hydrography

Temporal variability is the major issue for WOCE Goal 2: determining the representativeness of WOCE data and its usefulness as a baseline for determining long-term changes. It is also a problem when combining one-time sections that are not strictly synoptic. The water mass or property transport budget for an enclosed region, for example, can be expected to balance only to the extent that all sections bounding the box are sampling the same flow and property fields; temporal changes from one part of the survey to another must be small compared with the average signal.

A total of 51 sections or geographical areas were identified for which repeat observations were desirable or likely to happen anyway. It was expected that these would produce 15 000 stations. By late 1999 the WHP Office was aware of or had received

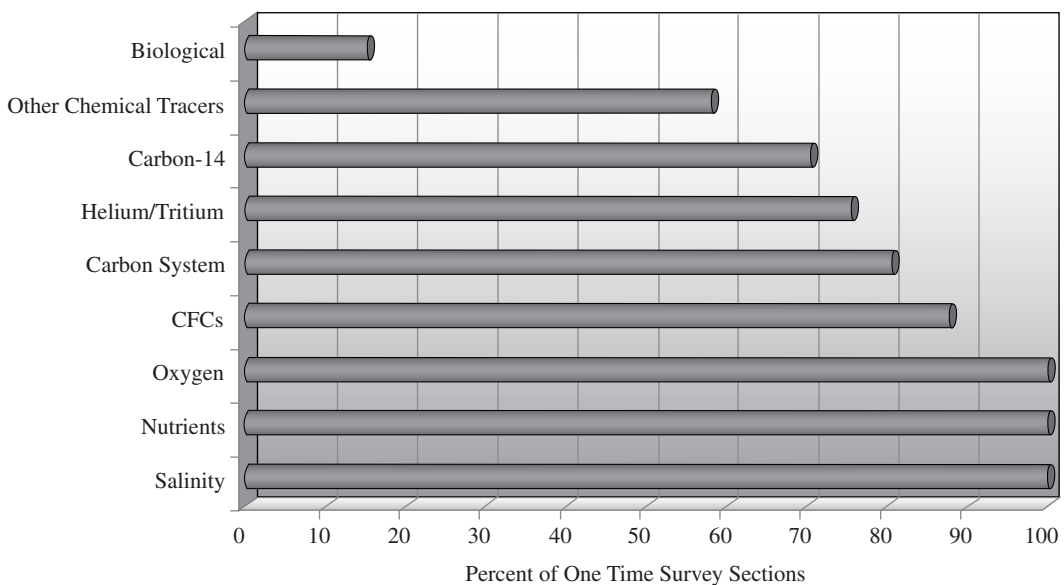


Fig. 3.1.5 Percentage of one-time cruises on which each set of tracers was measured. Prepared by N. P. Holliday (WOCE IPO).

data for 12 197 repeat hydrography stations. Their locations are shown in Fig. 3.1.6 (see Plate 3.1.6, p. 172).

The repeat hydrography programme has had some notable successes. The 48°N line in the Atlantic was occupied six times from 1993 to 1999, including twice to the standards of a one-time survey with full tracer suite, and continues to be occupied by Germany as part of a CLIVAR programme. In the Southern Ocean, the choke-points at Drake Passage and South of Australia were occupied ten and six times, respectively, by the combined efforts of several countries. Here, too, repeat measurements triggered by WOCE will continue as part of national CLIVAR plans.

However, much remains to be done in the analysis and interpretation of the repeat hydrography before the variability is appropriately quantified and the knowledge used in the analysis and interpretation of the one-time survey.

3.1.2.4 How the WHP defined standards for data and methods of measurement

The measurement techniques required for WOCE had been built up over a long period of time. But at the start of WOCE there were many parameters for which only a few groups in the world had the expertise to measure them to the required standard.

Never before had a single coordinated hydrographic survey planned to draw on contributions

from so many different institutions, investigators and countries. The question therefore arose of how to ensure that data were of a uniformly high standard, remembering that for many of the parameters the WHP Planning Committee deliberately defined a standard that before WOCE was the best achievable by an experienced investigator with access to the best analytical equipment. The scale of the WHP necessarily required a rapid growth in the capacity of the community, which implied many new investigators taking a leading role. The ambition in WOCE was not only to provide a data set of unprecedented coverage, but also of unprecedented quality.

The amounts of data and the international scope of the experiment required the establishment of a centre to coordinate the programme. The WHP Office, initially located at the Woods Hole Oceanographic Institution and later at the Scripps Institution of Oceanography, was a central facility established to oversee the global effort, to receive and evaluate incoming data, to make provisional and final data available to the WOCE community in a uniform format as quickly as possible, and to ensure a final archive was submitted to a World Data Centre. The issue of what metadata (information describing the data) would be required was addressed by a detailed description (WHPO, 1994b) of information and data requirements, including a timetable for data submission to the WHP Office.

WOCE established a group of 13 Data Assembly Centres (DACs), each of which would be responsible for one or more of the WOCE data types: hydrographic data, meteorology, current meter data, and so on. Once the bulk of the early planning for the WHP had been completed, the main function of the WHP Office was to be the DAC for CTD and bottle data.

For some measurements, the requirements for accuracy/reproducibility demanded revision of sea-going methodology in order to meet the high standards. Experts in each of the WHP measurements were invited to set down in detail the techniques they used and which were known to work. The expert knowledge thus became available to anyone wishing to participate in the programme, and was also translated into Spanish. The Spanish version was printed and distributed by the US WOCE Office at Texas A&M University. This material (WHPO, 1994a), often called the WHP 'cookbook', was produced in order to document methods that had previously not been widely disseminated. Unfortunately some techniques remained under-described, in that they did not allow an experienced technician, who followed the technique but without any specific prior knowledge, to consistently produce the desired result. However, the exercise did help propagate certain types of technical knowledge into the community. Also, the fact that standards for accuracy had been published and techniques and equipment recommended provided PIs with important leverage to help secure investment in equipment and staff.

Temperature has been measured well enough for many purposes related to inferring ocean circulation for nearly a century. Carefully used, deep-sea reversing thermometers had the potential to be accurate to 0.01°C . While platinum resistance thermometers provided the advantage of continuous measurement, there are few regions where the improvement in accuracy to order 0.002°C is crucial. However, the calibration stability of platinum thermometers means that with a well-maintained instrument the acquisition of high-quality fine-resolution temperature data can be routine.

Salinity measurements of equivalent accuracy (i.e. contributing equivalent uncertainty to density in the equation of state) were not feasible in a routine way until the development of a laboratory salinometer. With the improvement in routine determinations of sample conductivity, the equation of state itself

becomes a limiting factor, because of differences in ionic composition in the Atlantic and Pacific. While CTDs provide continuous measurement of conductivity, it is still the case at the end of WOCE that shipboard calibration of the data is required. Conductivity cells drift, and the required accuracy of 0.002 in salinity can only be recovered by adjustment of the data to agree with salinometer analyses of bottle samples. The availability of bottle samples during WOCE meant that there was little requirement to develop improved conductivity cells for the WHP. But in the post-WOCE era, increasing use of autonomous platforms, where samples for analysis are not available, has made this an urgent problem. Several manufacturers are bringing out new products with improved stability. There is now a requirement for stability of unattended salinity measurements at the level of 0.01 for up to 5 years.

At the onset of WOCE, dissolved oxygen was a difficult parameter to measure with the required accuracy. However, many laboratories took advantage of developments in equipment and techniques, notably with the widespread introduction of automatic endpoint determination of titrations. With suitable equipment an experienced analyst could make repeat measurements with a precision of $0.01 \mu\text{mol kg}^{-1}$. Nutrient measurements did not see such a significant improvement: the techniques are essentially the same as those in use during GEOSECS. The lack of standard reference materials for both nutrient and oxygen measurements remains a significant limitation.

Data quality assurance

A system of Data Quality Experts (DQEs), also overseen by the WHP Office, was conceived to ensure that the final WOCE data set was of a uniformly high quality and consistency. The idea was that all data submitted to the WHP Office would be sent to a scientist familiar with the oceanography of the region, and experienced in making and interpreting the observations in question. The DQE would examine the data for internal consistency and reproducibility. In addition, the DQE would be provided with relevant historical data from the region, and might receive data from several adjacent or intersecting WOCE cruises at once so that discrepancies could be identified and suggestions made for their resolution. Difficulties or queries identified by the DQE would be referred

back to the data originator, and the data set improved by iteration. Eventually, data-quality flags would be added to the data set to identify suspect or bad data.

By mid-way through the WHP, it was apparent that there were not enough scientists willing to act as DQEs to enable all the data to be examined in detail. Accordingly, the WHP Planning Committee decided that DQE effort should be concentrated on the one-time data. It is expected that all one-time bottle data will have been through the DQE process and all one-time CTD data will have been checked at the DAC by the time the final WOCE data archive is written to CD-ROM in 2003.

Where the DQE process has taken place, it is not clear at the time of writing what the long-term benefits will be. What becomes of the DQE comments and suggestions? They can be archived, and some changes are made after the DQE process, although the number is actually rather small: the data reported by PIs are generally of a very high quality. Because of the time lag, changes made to files held at the WHP DAC and subsequently archived may well diverge from versions held by originating PIs or in a national archive. Original versions may have been published by a PI and be in widespread circulation without the DQE modifications. Another drawback of the DQE delay is that many scientists have found it impossible to respond adequately to DQE questions. Critical personnel may have moved on to other projects and be unavailable to sort out queries. It has been suggested that the mere concept of the DQE process made it less necessary: knowing that their data submissions would be scrutinized by colleagues, PIs may have taken extra care to submit carefully checked data sets.

For repeat hydrography, the formal DQE process has been abandoned; the majority of repeat stations will be archived as reported by the investigators. Some of the repeated sections were carried out with the same personnel, facilities, and standards as the one-time surveys, and are likely to be of correspondingly high quality. Other sections may be of lesser quality for a variety of reasons. Whatever the origin of the measurements, final quality assessment of the repeat hydrography is left to the data users.

One of the effective data-quality checks emerging during the AIMS phase is the various atlas exercises: small teams have been funded to produce

basin-wide atlases of WOCE data, with the Pacific and Southern Oceans the most advanced at present. The requirement to examine every section of data in the course of atlas production has already highlighted some errors or inconsistencies in the data sets, with the information being passed back to the WHP DAC for investigation.

Documentation, data reporting and formats

The level of documentation stored with the WHP data is not as great as originally conceived. Prior to WOCE, many laboratories would routinely produce printed data reports for all major cruises. These would include detailed accounts by data processors and analysts of procedures used, calibrations applied and problems encountered. The original intention was to include this information in cruise reports, made available alongside the data in electronic form. However, the wide range of word processing packages in which PIs prepare the documentation was incompatible with the need to make the information available in a universally readable format. The task of converting the PI's version was beyond available personnel resources. A compromise was therefore reached in which the WHP Office produced minimal summaries of cruise documentation: ship, dates, personnel, PIs and so on. The WHP Office store any further documentation supplied by the PIs, but the level of detail is variable. Wherever possible, the WHPO has obtained supplementary cruise and data documentation and made it available as PDF files, including scanning in paper copies of older material if necessary.

Furthermore, the ease of access to electronic forms of the data means that many laboratories now no longer produce printed data reports. As a result, the link to the original analyst's records is now rather weaker, with possible consequences for the accuracy of data reporting. Details of blank corrections may be lost, as may formulae used for corrections and conversions. In the requirements for data reporting, the WHP was careful to specify names and units of variables to be reported. This proved to be a mixed blessing, because it gave rise to the possibility that data will be reported as having been converted to the approved units when in fact no conversion has taken place: concentration per unit volume (as commonly measured by analysts) instead of per unit mass (as requested by WHP reporting protocols) is probably the most

common error. This is a hazard of specifying the units to be used in the data format instead of requiring/allowing the data originator to supply the units.

The lack of a community standard CTD/hydrographic/tracer data exchange format prior to WOCE was recognized as a problem. WHP planners attempted to rectify this with the WHP data formats described in WHPO (1994b) for CTD and bottle data. The intention was to specify a format that included all the relevant WOCE parameters and supporting information thought desirable, and which an inexperienced user could write and read reasonably easily. Unfortunately, the WHP format definitions were not sufficiently rigorous, and so many users had trouble writing and reading files in a consistent manner. Many files submitted by PIs contain small or large discrepancies that make them hard to read, although some of them are technically legal within the specification. This was a liability throughout the WOCE observational phase, hindering exchange of data. When PIs started submitting large numbers of data files, the WHP DAC was unable to keep up with the task of fixing the format problems in the data files. Only during the WOCE AIMS phase, when the rate of new data submissions slowed, has the DAC been able to address the task of converting the data files to a more consistent interpretation of the formats. The increasing use of NetCDF may provide a format that can be widely read with a minimum of user effort.

So what recommendation can be made for the future? In order for a format to be easily and reliably read, it must be strictly defined and adhered to when the data files are written. This is difficult for inexperienced data originators. If the burden is too great they may be unwilling or even unable to cooperate. Indeed, it is difficult to imagine a community of hundreds of PIs all managing to do this flawlessly. Conversely, data will only be widely used if they are available in a common format. Data centres will have to continue to accept data in somewhat flexible formats, working with data originators to resolve ambiguities, and making the data available back to the community in a single format that each user need only learn to read once. Data centres need to be provided with resources on the assumption that every file provided to them will need to be read in, debugged and written out before the data can be made available to users.

Accuracy of data in the WHP

There is no single conclusive method for determining the accuracy of the WHP water property measurements. Instead, the overall quality evaluation relies heavily on a consistency check. The WHP sampling grid (Fig. 3.1.4, see Plate 3.1.4, p. 172) includes many cross-overs, where nearby measurements were made at different times. Above the main thermocline, the differences in water properties at these cross-overs are expected to be large; the upper ocean is highly variable due to the annual cycle, eddies, and other short-term phenomena. In and below the thermocline, however, temporal variability is expected to be much weaker, and to be manifest primarily as vertical displacements of the stratification. As a function of density, deep water properties are expected to have been approximately constant during the WHP; indeed, this is a fundamental assumption in the design of the one-time survey. Comparison of water properties at cross-overs as a function of density is therefore a check of this assumption – the ability of a one-time survey to represent a mean circulation – and also a check of measurement accuracy. The results presented need to be read with some caution since there is not universal agreement on how such comparisons should be performed or interpreted. But they remain a useful guide to the quality and consistency of the measurements.

Because density is a function of temperature, salinity and pressure, these three quantities cannot be compared independently on density surfaces. Temperature and pressure measurements are relatively direct, stable and well calibrated. Their uncertainties, typically 0.002°C for temperature and 3 dbar for pressure, are believed to be fairly well known *a priori*. Attention is therefore focused primarily on salinity, which is measured indirectly via electrical conductivity, temperature and pressure. *In-situ* CTD salinity measurements are calibrated by comparison with shipboard laboratory measurements on water samples from the hydrographic cast, which are in turn compared with measurements on standard seawater samples that are prepared in large batches.

Accuracy of the WHP one-time salinity measurements

In the Pacific Basin, WHP cross-overs were examined for salinity differences by Aoyama *et al.* (2000). Reported bottle salinities having potential temperatures between 1.0°C and 1.6°C were used

for the comparisons. A total of 42 cross-overs were available and the salinity differences ranged from 0 to 7.8×10^{-3} in magnitude with a mean difference of 2.4×10^{-3} . (Note that salinity has no dimensions. It is measured on the Practical Salinity Scale 1978.) Aoyama *et al.* went further, trying to account for systematic differences between standard seawater batches. This methodology follows Mantyla (1980), and attempts to identify and correct for differences between the label conductivity and actual conductivity ratio in batches of International Association for the Physical Sciences of the Ocean (IAPSO) Standard SeaWater (SSW). This issue is complicated by the fact that given batches have been observed to change their salinities with time (Culkin and Ridout, 1998; Bacon *et al.*, 2000). Bacon *et al.* report that the effect of ageing on SSW leads to salinity changes of up to ± 0.002 after 24–36 months. To be within 0.001 of the label value, SSW should be used within one year of production. Without specific knowledge of the systematic time-dependent changes in the SSW batches used, this effect could contribute a standard deviation of order 0.001 to deep properties. Having applied adjustments for the authors' best estimates of SSW differences, the cross-over differences in the analysis by Aoyama *et al.* were reduced to a mean of 1.8×10^{-3} . So while the cross-over differences were reduced, the change was small, suggesting that the dominant cause for the differences was not variations in SSW. The cause could be real variations in salinity due to slow changes in time over the course of the Pacific WOCE sampling, or simply a noise residue reflecting measurement error of the many different groups doing the sampling. We note that according to the WHP plan, salinity measurements were required to be accurate to 2×10^{-3} . Since the above comparisons would amplify an accuracy in the difference by a factor of $2^{1/2}$, one can say that the WHP salinity measurements in the Pacific Basin meet the requirements set out for the one-time survey.

In the Indian Ocean, Key (personal communication; also at <http://geoweb.princeton.edu/staff/Key/key.cross/crossover.html>) analyses data from 18 cross-overs after fitting to a smoothed potential density for waters deeper than 2500 dbar. The mean salinity difference (uncorrected for possible variations in SSW) is 0.8×10^{-3} . That this difference is smaller than the Pacific may be due to the short

time in which the Indian Ocean was sampled or the smaller number of measuring groups.

In the Atlantic Gouretski and Jancke (1998) have used cross-overs going back in time to pre-WOCE measurements (SAVE in 1987) and up to A22 (1997). They have examined the salinity variation on potential temperature surfaces for depths exceeding 1000 m and potential temperatures below 3°C. Mean absolute cruise–cruise differences are 2.29×10^{-3} . These are reduced to 1.86×10^{-3} if the SSW batch adjustments proposed by Aoyama *et al.* are applied. Thus in all WHP one-time survey measurements reported at the times of the above analyses, salinity has been measured to the expected high accuracy required.

Individual sections might be considered for further correction if they have exceptionally high or low systematic offsets relative to their crossing lines. Bacon *et al.* (2000) point out that the time variability of SSW is critical. A bias between cruises of size greater than 0.003 is probably environmental change, or could be caused by measurement error during a cruise. Differences smaller than 0.003 could be attributed to differences between label and actual salinity of SSW. Some of the cross-over differences identified by Gouretski and Jancke, for example, could reflect temporal changes in deep water properties. However, the Atlantic cross-over differences reported above do not show any systematic change with time.

Consistency of the WHP one-time oxygen and nutrient measurements

The nutrient and oxygen data have not yet been examined as systematically as salinity, but there have been enough initial results to warrant mention. Accuracy requirements for these parameters (see Table 3.1.2) were expressed in per cent of ocean basin full-scale values. For the Atlantic Ocean Gouretski and Jancke have expressed these (we here use WHP supported units of $\mu\text{mol kg}^{-1}$) as 3, 2.5, 0.5 and 0.06 for oxygen, silicate, nitrate and phosphate, respectively. Given that observational differences are amplified by a factor of $2^{1/2}$, it is found that Atlantic data satisfy the published requirements. In the Indian Ocean, Key examines silica cross-overs and finds a similar result. In the Pacific Ocean, Gordon, Mordy, Wilson and Ross (personal communication, 1999) find that 93% of the silica cross-overs fall within the specifications, while 87% of the nitrate and 70% of the

phosphate do as well. Since the WHP specifications refer to a standard error, one would expect that 68% of any experimental values would fall within the specifications. Thus, we again see that nutrient measurements in the one-time WHP survey meet the overall requirements. It remains to be seen whether oxygen comparisons follow this trend since these have not yet been made for the Pacific and Indian Oceans. As with salinity measurements, one should be able to identify particular sections with relatively high or low nutrient or oxygen values. The WHP specifications for these variables represent reproducibility constraints, since no standard reference materials were available for an absolute calibration of dissolved oxygen or nutrients in the WHP, in contrast to salinity.

3.1.3 Current measurements in the shipboard hydrographic programme

3.1.3.1 The nature of Acoustic Doppler Current Profilers

An Acoustic Doppler Current Profiler (ADCP) is a high-frequency multibeam sonar. A short pulse of sound is transmitted along each beam, and the Doppler shift of the sound scattered back is estimated as a function of time since the transmission, or equivalently, range to the scatterers. The Doppler shift is proportional to the relative velocity component along the beam between the transducer and the scatterers. There are typically four beams, all at the same elevation (angle from the vertical), and at 90° intervals of azimuth. If we assume the scatterers are moving with the water, and the water velocity is roughly uniform in any horizontal plane intersected by the four ADCP beams, then the four radial velocity components at any given range yield estimates of both horizontal velocity components, and two independent estimates of the vertical velocity component. Estimates from successive range cells provide a vertical profile of the water velocity relative to the instrument. If the orientation and velocity of the instrument relative to the earth are known, the profile of water velocity relative to the earth can be calculated. Range, resolution, and accuracy depend on the sonar's frequency and on other instrumental and environmental factors; typical values for common 150 kHz instruments are 300 m vertical range, 8 m vertical resolution, and 11 cm s^{-1} standard deviation of single-ping horizontal velocity

component estimates. Ensembles of successive single-ping profiles are normally vector-averaged to reduce the variance of the velocity estimate. ADCPs have been deployed in many ways and locations: on the seafloor, looking upward; looking up or down from a mooring, or downward from a moored buoy; on the bottom of a ship; and lowered from a ship, usually as part of a standard profiling instrument package including a CTD and a water sampler. We are concerned here only with the latter two: shipboard (SADCP) and lowered (LADCP).

In calculating absolute (earth-relative) velocity profiles from an ADCP mounted on a ship that is underway, say at 5 m s^{-1} , the desired signal – the ocean current – is the small difference between two large numbers: the velocity of the ship relative to the earth and the velocity of the ship relative to the water. Both numbers therefore must be measured with high accuracy, and with particular attention to minimizing bias – any systematic errors that persist longer than a few minutes. Two navigational measurements are crucial: the position fixes that are first-differenced to calculate the ship's velocity over the ground, and the heading measurements used to transform the ADCP velocity vectors from the instrument coordinate system into the geographical coordinate system: east, north and up. Prior to 1991, uncertainty in transducer heading was the primary factor limiting shipboard ADCP accuracy for most applications. The Global Positioning System (GPS) revolutionized shipboard ADCP profiling by providing not only excellent position fixes, but unprecedented heading accuracy. We will return to this topic.

Shipboard ADCPs measure upper ocean currents with effective horizontal resolution as fine as 1–2 km, but are blind to currents below a few hundred metres depth. Lowering a self-contained, internally recording, ADCP on a wire extends the profiling range to the ocean bottom, but with horizontal resolution limited to the station spacing. The method is in many ways similar to shipboard profiling, but there is a crucial difference: over most of the depth range, the velocity of the instrument cannot be determined directly by navigation. The horizontal position of the instrument relative to the ship is known only at the times of launch and recovery. As the instrument descends, the ADCP records a large number of overlapping velocity profiles, each with a range of only

100–200 m from the instrument, and each relative to the unknown velocity of the instrument. These unknown velocities are removed by differentiating the profiles in the vertical. The resulting overlapping shear profiles are then interpolated to a uniform depth grid and averaged to give a composite shear profile. Integrating this shear profile in depth gives a velocity profile relative to a single unknown constant of integration. If the vertical mean of the relative velocity profile is subtracted out, then the constant that remains to be determined is just the depth-averaged velocity. This can be calculated by a method closely analogous to that used in shipboard ADCP work (Fischer and Visbeck, 1993). The depth-averaged absolute water velocity is the time-average of the velocity of the water relative to the instrument, plus the time-average of the ship velocity as calculated from the position difference between the start and end of the cast, minus a small correction (usually less than 1 cm s^{-1}), calculated from the time-integral of the relative velocity profile. If the vertical velocity were a constant during the downcast, and another constant during the upcast, then the time-integral would be equivalent to a depth-integral – which is of course zero for the de-meaned relative velocity profile. Hence the calculation of the depth-averaged velocity is very insensitive to the accuracy of the relative velocity profile.

At the start of the WOCE Hydrographic Programme (WHP) in 1990, shipboard ADCP installations were common but the technique was not yet entrenched in the mainstream of physical oceanography. Shipboard ADCP data were not archived by the US National Oceanographic Data Center (NODC). The shipboard ADCP was generally viewed as an ancillary tool for the WHP, of secondary priority; but it was cheap and readily available, so it survived – and eventually thrived. By the end of the WHP, good shipboard ADCP installations were almost universal on blue-water research ships, the data were archived at the US NODC and the Japanese Oceanographic Data Center (JODC), and the shipboard ADCP was widely viewed as a standard and highly valuable tool. Most WHP cruises resulted in shipboard ADCP data sets (Fig. 3.1.4b, see Plate 3.1.4b, p. 172); many non-WHP cruises did also, yielding an extensive global data set available for the WOCE analysis phase.

Lowered ADCP profiling was in its infancy at the start of the WHP: the method was developed

in 1989 (Firing and Gordon, 1990; Fischer and Visbeck, 1993). Early LADCP hardware was cumbersome, and its use on WHP cruises was initially restricted to regions where it was expected to be particularly valuable. A prime example is the near-equatorial band, where the complex current structure is poorly estimated by geostrophic calculations from typical synoptic sections (Moum *et al.*, 1987). With hardware improvements making the LADCP easier to use during the Pacific phase of the WHP, current profiling on complete CTD sections became routine; coverage was particularly good in the Indian Ocean and reasonable in the Atlantic (Fig. 3.1.4c, see Plate 3.1.4c, p. 172).

3.1.3.2 Evolution and status of shipboard ADCP systems and the impact of GPS

Shipboard and lowered ADCP systems critically depend on more than the Doppler sonar itself; equally important are the attitude and position sensors. During the WHP, shipboard system improvement was almost entirely in the navigational component: Global Positioning System (GPS) measurement of position and heading.

Although it did not officially reach Initial Operational Capability until December 1993 (Standard Positioning Service) and Full Operational Capability until April 1995 (fully tested military functionality), research ships started to obtain fixes from GPS receivers much earlier. The first satellite was launched as early as 1978, but numbers grew slowly at first, with 10 satellites launched up until 1985, followed by a 4-year gap. In the mid- to late-1980s, many research ships were fitted with a GPS receiver to enable them to obtain fixes during the few hours per day when sufficient satellites were visible above the horizon. With the aid of a rubidium or caesium standard clock, a two-dimensional position fix could be obtained with just two satellites. Fixes obtained in this way gave useful relative positions for the calculation of ship speed, but were susceptible to large apparent jumps in position (sometimes several hundred metres) when there was a change in the combination of satellites used to calculate the fix.

The main operational series of so-called Block-II satellites were launched at the rate of about five per year from early 1989 onwards, and a complete constellation of 24 satellites was reached for the first time in mid-1993. In favourable locations, coverage for position fixes had already grown to

nearly 100% by mid-1991. Thus availability grew rapidly during the early stages of the WHP, but the earliest cruises still had gaps in coverage.

The importance of improved position measurement

Accuracy during the WHP has varied depending on the status of 'Selective Availability' (SA), on the type of receiver, and on the availability of a differential correction, either in real time or in delayed reprocessing. SA is the deliberate reduction of accuracy for civilian users by the US Department of Defense. It was first activated in July 1991, and was continuous after November 1991. The error level was set to zero on 2 May 2000. Under SA, position uncertainty (approximately 2 standard deviations) is of the order of 100 m, equivalent to velocity uncertainty of 47 cm s^{-1} for a 5-minute average, or 4 cm s^{-1} for a one-hour average. This was the best that was available with a standard single-frequency civilian receiver using the Coarse Acquisition or C/A code. This level of accuracy is also known as the Standard Positioning Service, or SPS.

By the time the WHP was concentrated in the Indian Ocean in 1995, most US ships had military GPS receivers. These could receive signals on both the L1 and L2 frequencies, and could decode the encrypted P/Y code, with about 10 m position accuracy, and a corresponding 10-fold improvement in velocity accuracy.

An alternative method of improving accuracy with just a C/A code receiver is Differential GPS. In this technique, signals are received at a fixed antenna of known location, as well as the mobile antenna. At the fixed location, an estimate can then be made of the error introduced by SA for each satellite in common view of both antennas, and a correction made at the mobile antenna. The technique assumes a similar satellite geometry at both locations. Since the GPS satellites orbit at an altitude of approximately 20 000 km, DGPS provides useful corrections over baselines of several thousand kilometres. Differential methods, when available either in real time or in a delayed processing mode, provide P/Y code accuracy, or better, with C/A receivers. Uncertainty of as little as 4 m (one standard deviation) on a 2000 km baseline has been observed (King *et al.*, 1996; Pierce *et al.*, 1999). As early as 1993 there were commercial systems for receiving DGPS corrections in real time, but they were charged at a very expensive

daily rate that put them out of reach of research budgets. Delayed-mode was the only feasible option for research ships. In 1996 a commercial receiver became available (the Ashtech GG24), which was capable of receiving signals from both GPS and the Russian GLONASS system; the latter was by then not subject to SA or encryption. However, this potentially useful advance was overtaken by the routine commercial availability of affordable real-time DGPS corrections via telecommunications satellites. Many non-US research ships were equipped with continuous real-time DGPS, providing effective high-quality positions over most of the global ocean. On 2 May 2000, the level of SA error on C/A code was set to zero, immediately providing accuracy comparable to P/Y code; the US government has declared its intention not to reintroduce it. For precise applications, however, DGPS is still generally superior to uncorrected GPS.

Even when degraded by SA, position fix accuracy usually is not the limiting factor for SADCP applications; the error in section-averaged velocity caused by fix error varies inversely with the length of the section, and is usually below the ocean signal (and internal wave 'noise') level for scales larger than about 10 km. Fix accuracy is most important for smaller horizontal scales and in regions of weak currents. It is also important for evaluating and calibrating the sonar system; we will return to this point.

GPS heading measurements

In 1990, a far more serious problem than position uncertainty was heading uncertainty. The error characteristics of gyrocompasses were poorly known and unmeasurable until the advent of GPS attitude measurement methods early in the decade. The sensitivity of shipboard ADCP measurements to heading error, however, was always clear: a 1° error on a ship underway at 5 m s^{-1} causes a 9 cm s^{-1} cross-track velocity error. Heading error can be viewed as the sum of a constant error in angular offset between the transducer axis and the axis of the gyrocompass or other heading source, and a zero-mean but time-variable error in the heading measurement itself. The angular offset is usually estimated in either or both of two ways: (1) in shallow water, by comparing the velocity of the ship over the ground as measured by GPS with the velocity measured by the ADCP tracking the

bottom, and (2) in deep water, for each major ship acceleration such as stopping on station, by comparing the acceleration measured by GPS with the acceleration relative to a water layer (assumed to be spatially uniform) measured by the ADCP (Joyce, 1989; Pollard and Read, 1989). Individual estimates by each of these methods is noisy, particularly when SA is in effect, so many estimates must be averaged to get a usable calibration factor. It is possible to see slow (week-to-week) changes in compass error, but no more than a very crude correction for the time-variable heading error can be made.

An opportunity to measure and therefore compensate for this error was again provided by GPS. Signals are encoded on a carrier wave of approximately 20 cm wavelength. By examining the relative phase of the carrier at a pair of antennas, it is possible to determine their relative position with an accuracy of a few millimetres after resolving the integer wavelength ambiguities.

The first attempt to measure heading using this technique on a WHP cruise was in the Pacific in May 1991 on RV *Thomas Washington*. Developed by Ramon Cabrera and Eric Firing, the system used two commercial GPS receivers with antennas mounted 1–2 m apart. Gyrocompass heading helped to resolve the ambiguity inherent in the phase measurements. This system was used on several ships and other WHP cruises until it was supplanted by the commercially available Ashtech GPS 3DF, a four-antenna GPS attitude sensor (King and Cooper, 1993; Griffiths, 1994). The 3DF could track six satellites on each antenna. Changing constellations, multipath interference, and occasional shading of an antenna by superstructure meant coverage was far from continuous, and varied between ships depending on the detailed geometry of the installation. Poor choice of setup parameters in the receiver (too strict or too slack settings for internal quality checks) could also have disastrous effects. A data return of 70% was typical, leaving significant gaps, sometimes several hours, without a heading determination. The successor to the 3DF was the ADU2. This had improved algorithms and the ability to track up to 12 satellites simultaneously. With the arrival of the ADU2, coverage became routinely near 100%.

The 3DF and ADU2 revolutionized shipboard ADCP data quality by solving the single biggest instrumental problem: the uncertainty in heading.

With a well-functioning GPS attitude sensor, the total heading uncertainty can be reduced to 0.1° or less, bringing the corresponding velocity uncertainty below 1 cm s^{-1} . 3DF installations on research vessels have shown that gyrocompass errors are typically $\pm 1\text{--}2^\circ$ in low and middle latitudes, and transient errors can reach 5–10° peak-to-peak in high latitudes. Without correction from a GPS attitude sensor, the high-latitude errors are doubly crippling – they are very large, and the ocean currents are often weak (e.g. Heywood *et al.*, 1999). Errors include damped oscillations at the Schuler period, 84 minutes, excited by accelerations of the ship; an offset proportional to the northward velocity component of the ship, for which the built-in compensation is not always effective; and other short- and long-term drifts for which we know of no model.

Other sources of error in SADCP velocities

Now that the problem of heading error has been solved, and position fixes accurate to 10 m or better are widely available, other sources of error in SADCP-measured currents gain attention and significance. Alderson and Cunningham (1999) show that the hitherto ignored errors caused by pitch and roll bias (most systems do not use any pitch or roll estimates in vector-averaging the single-ping velocity profiles) are significant in applications such as the calculation of transport through Drake Passage. They also note that errors due to correlations among pitch, roll and heave (Kosro, 1985) may now be detectable. Firing (unpublished data), using pitch and roll measured by a 3DF and heave from the single-ping vertical velocity component measured by the ADCP, has estimated such errors as occasionally reaching 5 cm s^{-1} during rough weather on a North Atlantic WHP cruise of the RV *Knorr*. Another rough-weather error, a much larger bias in the direction of motion of the ship, was identified more than a decade ago, but remains a problem on most ships. There has been a variety of speculation about the explanation, but none that the present authors find convincing. A major source of small-scale shear error is the presence of strong scattering layers. As the sound from a forward-looking beam, for example, encounters a scattering layer (or the bottom), the part of the beam with the shortest range and earliest return is closer to vertical than the nominal beam angle; the angle of encounter increases with time to a larger

than nominal value as the beam passes through the scattering layer. The Doppler shift due to the forward motion of the ship is therefore first biased low, then high, resulting in a characteristic 'S' in the forward velocity component. The height of the 'S' is typically a few tens of metres, and the amplitude may be $10\text{--}20\text{ cm s}^{-1}$ (E. Firing, unpublished data). Localized biases due to coherent swimming of scattering layers have also been identified near topography (Wilson and Firing, 1992) and in the open ocean.

It is perhaps remarkable that the main sources of SADCP error are almost all due to factors other than the sonar instrument itself. The exceptions are the skew errors caused by the tracking algorithm in an early version of the firmware (Chereskin and Harding, 1993), and the scattering layer 'S', which is a function of beam width.

3.1.3.3 Lowered ADCP systems

Although the LADCP and SADCP systems and algorithms are similar in many ways, there are some important differences relevant to LADCP profile errors; the LADCP depends much more critically on the inherent accuracy of the sonar. It is important to distinguish between the accuracy of the relative velocity profile as a function of vertical wavenumber, and the accuracy of the depth-averaged velocity – their error sources and characteristics are nearly independent. One must also distinguish instrumental errors, caused by the fundamental limitations of the hardware and software, from errors or shortcomings associated with the way the LADCP samples the ocean.

To avoid confusion in the subsequent discussion, we will use the word 'profile' to refer to the composite profile measured over the whole water column. Each segment of profile stored by the instrument will be referred to as an 'ensemble'. Generally, an ensemble will result from just one or two pings.

Because the relative velocity profile is calculated as the depth-integral of a composite shear profile, relative velocity errors between two depths tend to grow as the square root of the separation, as in a random walk (Fischer and Visbeck, 1993). The velocity error wavenumber spectrum is red for scales larger than the depth range of each individual ADCP ensemble, and white for smaller scales (Firing and Gordon, 1990). The magnitude of the error increases with uncertainty in the raw ADCP

velocity estimates, and decreases with increasing range of the individual ensembles and with increasing numbers of ensembles. This analysis assumes unbiased ADCP ensembles. Unfortunately, the composite relative velocity profile is extremely sensitive to small shear biases in the individual ensembles; fortunately, such bias has been dominant only in a small fraction of the profiles that have been made. The reason for these occasional episodes of bias, which cause the downcast and upcast profiles to cross in a characteristic 'X' on plots of velocity versus depth, has not yet been determined. Sometimes the problem can be reduced by rejecting data from the most distant bins in each of the single-ping ensembles; sometimes it can be eliminated by rejecting shears from the top few bins of each ping on the upcast where a beam intersects the wake of the package. Sometimes none of these is effective and the poor profile remains unexplained.

Because the relative velocity profile accuracy depends on the accuracy and the range of the single-ping ADCP ensembles, it decreases with reduced acoustic backscattering strength. Backscattering at the 150–300 kHz frequencies typical of LADCPs varies widely with depth and location. It generally decreases from the upper ocean to the abyss, often with a sharp change near 1000 m. Typical differences exceed 20 db. At all depths, scattering tends to be weak in the tropics and subtropics, increasing slightly at the equator (particularly in the eastern Pacific) and increasing greatly in subpolar regions. Consequently, it tends to be easiest to get good LADCP profiles at high latitudes; conversely, in some low-latitude regions, the relative velocity profiles have been rendered useless below about 1000 m. (An estimate of the global distribution of backscattering strength is an interesting side effect of WOCE LADCP measurements that is being pursued, but we will not discuss it further here.)

Until recently, relative velocity profiles were subject to major interference from sound reflected from the ocean bottom. For each individual ping in the affected depth range, the bottom reflection of the previous ping overwhelms the signal scattered from the water. With a 1-Hz ping rate, for example, the interference would be centred at about 650 m off the bottom, and could contaminate a depth band up to 200 m thick. The velocity signature of this interference depends on the

velocity of the package over the ground. When the velocity is small, the bottom-contaminated velocity estimates are similar to the surrounding uncontaminated estimates, and the interference is not visually evident in the calculated velocity profile. When the package velocity is larger than 10 cm s^{-1} or so, the interference shows up as a velocity spike and/or offset in the processed LADCP profile, if no special editing is done. Editing out the contaminated depth range leaves a gap in the composite shear profile and therefore an uncertain offset between the parts of the velocity profile on either side of the gap. The problem can be avoided entirely by using a staggered ping sequence, so that the interference appears in two non-overlapping depth ranges on alternate pings. Editing out the interference then leaves no gap in the composite shear profile. The use of two ADCPs, one looking up and the other down is described on a web site by Visbeck (<http://www.ideo.columbia.edu/~visbeck/ladcp>). This also solves the problem: the upward-looking profiler's data remains uncontaminated.

The accuracy of the depth-averaged velocity depends almost entirely on the accuracy of the position fixes at the start and end of the cast, and on the accuracy of the time-integrated velocity of the water relative to the package. Fix accuracy is not a major concern, given that SA now has been turned off, and that P/Y code fixes and DGPS (real-time or post-processed) were widely available during the WHP. Even when only C/A code fixes with SA were available, the resulting uncertainty in velocity is less than 1.6 cm s^{-1} for 95% of all casts lasting 2.5 h or longer. Of greater concern is the velocity integral, for which there are two types of error: that of the velocity measurement itself, and that due to gaps in the sampling. Long gaps, as opposed to occasional ping dropouts and the normal interval between pings, are caused primarily by interference from sound reflecting off the ocean bottom instead of the water. Although such gaps can last several minutes, this interval is short compared with the entire profile, and can be filled by interpolating a low-pass filtered time series of the water velocity relative to the package. Even if the interpolated velocity is in error by 10 cm s^{-1} on average, and the gap is 5 min, the contribution to the depth-averaged velocity error will be only 0.3 cm s^{-1} for a 2.5-h profile. Therefore the most worrying type of error is that which contributes a bias to the velocity measurement. Of the possible

causes, we will mention two here: compass error and ambiguity error.

Velocity errors arising from LADCP magnetic compass errors

Self-contained ADCPs use magnetic flux-gate compasses. These can fail to measure the true orientation of the package, either because of inherent instrument error, or because the presence of other magnetic materials on the package (e.g. mounting hardware or pressure cases) can generate their own local magnetic fields or distort the earth's magnetic field. Compass errors can vary with tilt as well as heading.

Compass error affects both the relative velocity profile and the depth-averaged velocity calculation. The LADCP is much less sensitive to compass error than a shipboard ADCP because the magnitude of the velocity error is proportional to the speed of the water relative to the instrument, which is usually smaller for the LADCP by a factor of 10 or more. For example, if the horizontal speed of the water relative to the LADCP is 20 cm s^{-1} , a 5° compass error will cause a 1.7 cm s^{-1} velocity error perpendicular to the mean velocity. Compass accuracy varies with geographic position and instrument tilt, becoming increasingly problematic near the magnetic poles. Systematic errors exceeding $5\text{--}10^\circ$ sometimes can be detected by comparing simultaneous LADCP and SADCP profiles in their common depth range; errors up to 60° were identified on one high-latitude cruise, but the cause was not found (Hummon and Firing: Post-cruise compass calibrations for North Atlantic WOCE LADCP, unpublished document); errors were much smaller on other cruises in the same region. With respect to compass error, the LADCP at the end of WOCE is at the same stage the SADCP was prior to WOCE: the error can be large, and it is very difficult to measure. Unfortunately, no technical solution analogous to a GPS heading sensor is presently known.

Ambiguity error

Much of the WHP LADCP data set was obtained using 150 kHz broadband sonars (BB-150) from RD Instruments. Unlike the narrow-bandwidth sonars with which most of the WHP shipboard ADCP data were collected, the BB-150 transmits pulses modulated with repeated pseudorandom codes to estimate Doppler phase shift in the range $\pm 180^\circ$ (Pinkel and Smith, 1992). The velocity

corresponding to a 180° phase shift is therefore called the ambiguity velocity; a larger velocity magnitude will wrap around, reversing its sign. Decreasing the code length increases the ambiguity velocity at the cost of accuracy. Broader bandwidth increases accuracy and reduces the minimum available code length, but at the cost of profiling range, which is critical for the LADCP. The usual compromise is a medium-bandwidth setting, for which the maximum ambiguity velocity for the BB-150 is about 3.3 m s^{-1} (along the beam axis), and lower ambiguity velocities have been used on occasion. Although the maximum ambiguity velocity is large compared with average LADCP lowering rates and relative currents, it can be exceeded instantaneously as the package is lifted and dropped with the pitch and roll of the ship. Ambiguity errors can occur in any or all of the four beams on a given ping. Some but not all of the errors can be found using consistency checks and glitch detection algorithms; editing is much more effective when applied to single pings rather than to multi-ping averages. After editing out the detectable errors, bias may still result from the undetected errors and from the selective removal of samples with the largest velocities. Bias is largest in the vertical velocity component but may be significant in the horizontal component also. We are not aware of any quantitative estimates of the ambiguity error biases remaining in processed WHP LADCP data sets.

Accuracy of LADCP data

This brings up an important question: how do we evaluate LADCP performance in practice? And, how good or bad is it? There have been only a few comparisons between LADCP profiles and independent velocity profile measurements. Fischer and Visbeck (1993) showed the result of comparison with Pegasus (an acoustically tracked free-fall probe) profiles: rms differences of about 5 cm s^{-1} in each component, up to a factor of two larger than the rms difference between Pegasus up and down casts. Hacker *et al.* (1996) made a similar comparison, but compared only the depth-averaged velocity estimates from the two methods. (Poor Pegasus profile quality, particularly at high vertical wavenumbers, discouraged comparison of the relative velocity profiles.) Rms differences of the depth-averages were about 1.5 cm s^{-1} on a cruise in 1992, and under 1 cm s^{-1} on a 1993 cruise using a better LADCP.

Given that direct comparisons between LADCP and other profiling methods are rare, and clouded by uncertainties in the alternative methods and by spatial and temporal differences in sampling, we are led to rely on other consistency checks. The most general one is the comparison between up and down casts. As noted above, this comparison sometimes shows obvious problems. A second useful comparison is between the top of the LADCP profile and simultaneous shipboard ADCP data. This comparison is made separately for LADCP up and down casts; temporal differences are often substantial, as verified by on-station shipboard ADCP time series. Similarly, Send (1994) has shown that Pegasus up-down differences are roughly consistent with a Garrett-Munk type internal wave spectrum. A third type of comparison is between the bottom of the LADCP profile and the near-bottom velocity calculated by tracking the bottom in addition to the water. Cunningham *et al.* (1997) have shown cases where this method, together with the shipboard ADCP comparison, reveal a disturbing lack of consistency; the cause of the error is not yet clear.

As this discussion of error sources should suggest, there is no good easy answer to the question, 'What is the error in an LADCP profile?' A reasonable but vague answer would be, 'A few cm s^{-1} , except when backscattering is very low, or something else goes wrong.' A better answer would point out that accuracy tends to be highest for the depth average, but lowest for the lowest non-zero vertical wavenumbers; that relative velocity profile errors are larger for deep profiles than for shallow ones, but the reverse may be true for the depth-averaged velocity; etc. More precisely quantifying the errors in existing LADCP profiles, and finding ways of reducing errors in future profiles, is an ongoing project.

3.1.3.4 Applications: how are SADCP and LADCP measurements changing our view of ocean currents and physics?

The scientific role of ADCP observations is a function of their strengths and weaknesses relative to other types of observations. The main strengths are:

- 1 measurement of absolute current profiles, in contrast with geostrophic profiles, which are always relative to an unknown reference;
- 2 high horizontal and vertical resolution;

- 3 measurement of both velocity components, also in contrast to geostrophic sections;
- 4 low marginal cost, leading to a large data set.

The weaknesses are:

- 1 accuracy limitations, particularly with respect to transport integrated over long sections (SADCP and LADCP), and with respect to the large-scale structure of the LADCP profile;
- 2 sensitivity to adverse environmental conditions: bad weather or inadequate populations of scatterers.

Another crucial characteristic is a strength for some applications and a weakness for others: the measurement of ageostrophic as well as geostrophic velocity components. The barotropic tidal currents, for example, are usually viewed as noise in open ocean current measurements. To reduce this source of noise in shipboard or lowered ADCP profiles, one may subtract the tidal currents estimated from

a model based on satellite altimetry (e.g. Egbert, 1997), as done by Donohue *et al.* (2000a). Baroclinic tides are usually a larger noise source in SADCP measurements than barotropic tides, but they cannot generally be modelled well enough to be removed. Given a suitable repeated survey pattern, however, they can be estimated from the measurements themselves, and thus partially removed (Feng *et al.*, 1998a).

The most straightforward application of ADCP measurements, and one that takes advantage of all of the method's strengths, is the synoptic imaging of currents along sections. We are still discovering currents such as the Agulhas Undercurrent (Beal and Bryden, 1997; see also Fig. 3.1.7), and exploring the spatial and temporal structure of previously known currents (e.g. Schott *et al.*, 1997; Rossby and Gottlieb, 1998; Beal and Bryden, 1999). As expected at the start of the WHP, ADCP measurements have been particularly revealing at

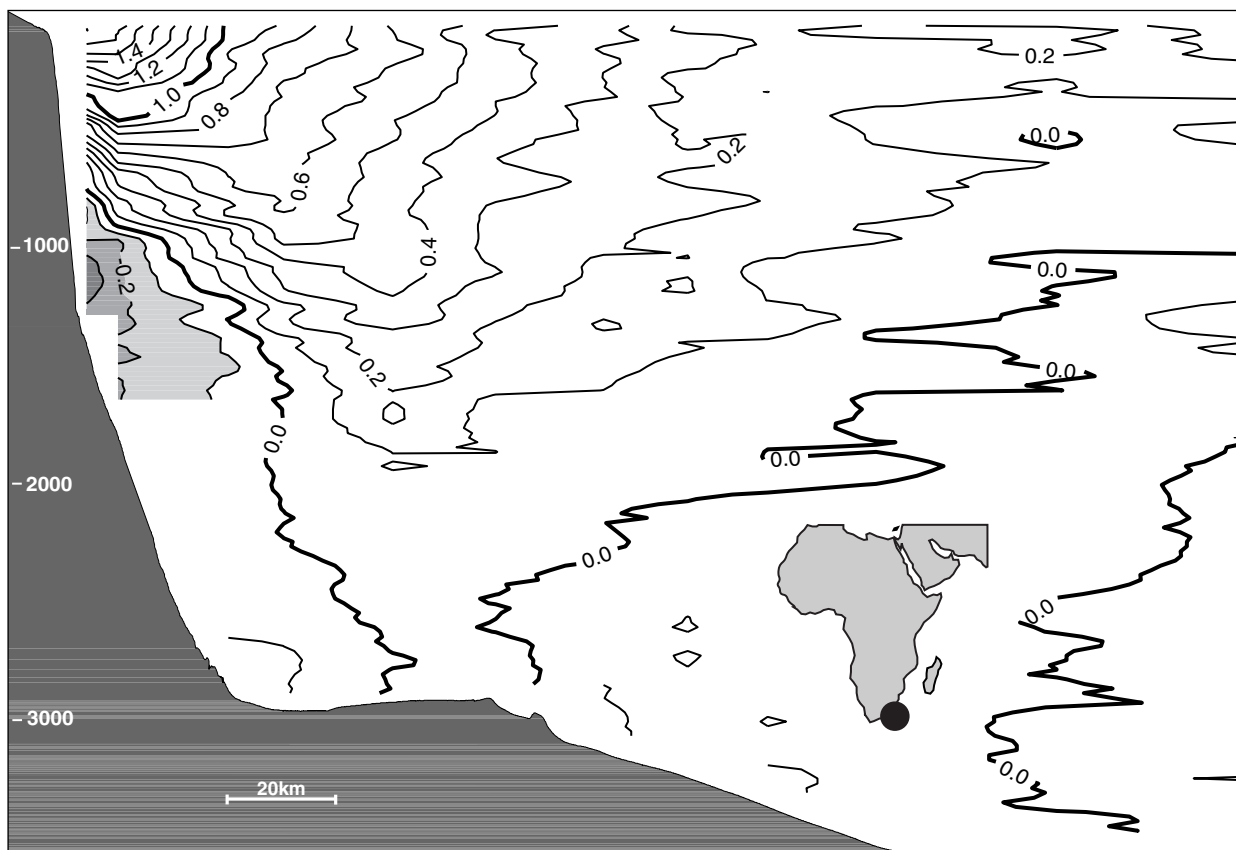


Fig 3.1.7 LADCP vertical section showing the Agulhas Undercurrent. The contour interval is 10 cm s^{-1} . Contour annotation in m s^{-1} . Positive values denote the Agulhas Current, flowing towards the southwest. Area shaded grey highlights the Agulhas Undercurrent, flowing towards the northeast. Offshore distance is indicated by the 20 km scale bar. Redrawn from Beal and Bryden (1997).

low latitudes (Firing *et al.*, 1998), where geostrophic calculations from synoptic sections are poor. Perhaps less expected has been their utility in high latitudes, where they have shown narrow currents and eddies extending to the bottom – features that would be misrepresented by typical geostrophic sections. King *et al.* (1996) show the Antarctic Circumpolar Current at Drake Passage resolved at 3 km resolution along track. An eddy with a strong barotropic component was encountered at 60°S on that section: the top-to-bottom geostrophic shear from CTD data was no more than 30 cm s^{-1} (King and Alderson, 1994), while the ADCP revealed surface speeds up to 60 cm s^{-1} .

SADCP and LADCP measurements can be blended with geostrophic shear calculated from CTD profiles for improved estimates of geostrophic currents and transports. The simplest method is to use SADCP velocities as the reference for the geostrophic shear profiles. The ageostrophic velocity component is usually the largest source of error. Saunders and King (1995a,b) reduced the error by smoothing along track, then estimated a noise threshold below which the ADCP-referenced bottom velocities were considered negligible and set to zero. The ageostrophic noise can also be reduced by averaging in the vertical over the thickest layer with consistently good measurements, but excluding the mixed layer (Bacon, 1994). Wijffels *et al.* (1998) found the problem of ageostrophic ‘noise’ in the ADCP velocities to be an insurmountable problem for referencing. Instead, they used deep portions of LADCP profiles to reference geostrophic profiles in the Kuroshio and its recirculation region, and the full LADCP profiles inshore of the Kuroshio. Compared with the SADCP, LADCP profiles have the advantage of sampling the full water column, most of which we expect to have lower levels of ageostrophic noise, but the disadvantage of providing only point measurements in the horizontal rather than a genuine average between stations. Close station spacing is therefore crucial.

A more complex method of blending ADCP and geostrophic current estimates is via an inverse model. Joyce *et al.* (1986) set up a system with conservation in 13 layers, and investigated the impact of using ADCP currents as additional constraints in the box inverse, compared with using hydrographic data only. Bingham and Talley (1991) compared two methods of using the

SADCP velocities in the inverse, as additional constraints or as initial values, and found the latter preferable. These studies are based on pre-WOCE data sets; inversions using the much higher-quality WOCE ADCP data are in progress, and it is too early to say how much (or how little) the velocity measurements will contribute to the end result. Some hints are provided by an intriguing study in which inversions were performed on the output of a numerical model, FRAM. First, McIntosh and Rintoul (1997) showed that an initial estimate of the section-averaged reference velocity differing greatly from the correct value could bias the inversion under some conditions; in such a case, if the section-averaged ADCP velocities are sufficiently accurate, they would improve the solution. Second, the small-scale structure of the actual reference layer velocity was not strongly constrained by the geostrophic shear and water property distributions, so that good flux estimates could be produced with highly smoothed reference-layer velocity estimates. This implies that when the section-averaged ADCP-derived reference velocity is not significantly different from the default of zero, it may have little effect on the net fluxes from the inversion; but the inversion without any direct velocity input will misrepresent the horizontal structure of the velocity field at the reference level.

SADCP data from 44 cruises combined with CTD data from 29 of these have been used to elucidate the current and potential vorticity structure of subsurface currents near the equator in the Pacific. Averaging in density coordinates in the vertical, and in stream coordinates meridionally centred on the eastward-flowing North and South Subsurface Countercurrents, Rowe *et al.* (2000) showed that the mean zonal velocity at the core of each current is sharply peaked as a function of latitude; the corresponding relative vorticity reversal contributes to a potential vorticity front at the core no wider than 40 km. The high horizontal resolution of the ADCP measurements was critical in resolving this structure.

SADCP data have been used in the Atlantic (Chereskin and Roemmich, 1991), the Pacific (Wijffels *et al.*, 1994), and the Indian Ocean (Chereskin *et al.*, 1997) to measure the surface Ekman layer transport across a low-latitude zonal section, and its distribution in the vertical. The cross-track Ekman velocity was estimated as the

difference between the geostrophic velocity and the ADCP velocity. In each case the measured Ekman transport was in reasonable agreement with the theoretical transport calculated from the wind stress, and extended below the mixed layer to the top of the pycnocline. As Chereskin *et al.* (1997) note, 'the Ekman contribution to the heat and salt fluxes must be measured; it can not be determined merely by inferring the volume transport from the wind and using the surface temperature and salinity.'

The ageostrophic part of LADCP profiles is also turning out to be valuable. Using a parameterization based on the fine-scale internal wave shear variance, Polzin and Firing (1997b) inferred a factor of 10 elevation of turbulent kinetic energy dissipation and diapycnal mixing rates in a region of the Southern Ocean with strong near-bottom currents relative to a nearby region with weaker deep flow. A comparison between 18 simultaneous eXpendable Current Profiler (XCP) and LADCP profiles in the North Atlantic has shown that, after spectral correction for their inherent high wavenumber rolloff, LADCP profiles can yield such parameterized estimates within a factor of two of those based on the higher-resolution XCP profiles (Polzin *et al.*, 2000a).

3.1.4 Shipboard meteorology

In this section we will discuss underway meteorology measurements made during WHP cruises. The Voluntary Observing Ship (VOS) programme is beyond the scope of this chapter.

WOCE planners recognized that meteorological data from research ships would have a number of uses; these included: initialization of atmospheric models (especially in data-sparse regions); provision of accurate estimates of basic meteorological variables for comparison with ships of opportunity; comparison with model output; comparison with satellite-derived quantities (Liu and Katsaros, Chapter 3.4); validation of climatologies and model-derived fluxes. The relevant chapter in the WOCE operations and methods manual (Taylor and Weller, 1991) gives further explanation.

The greatest requirement was for meteorological measurements that would enable the definition of surface fluxes of heat, water and momentum (Large and Nurser, Chapter 5.1). The objective (WCRP, 1988b) was to obtain estimates (averaged

over monthly or longer time scales) of the four components of heat flux to an uncertainty of 10 W m^{-2} , of evaporation and precipitation to 1 mm per day and wind stress to within 10%.

The basic observables are sea surface temperature, air temperature, wind velocity, barometric pressure, incoming short- and long-wave radiation and humidity. Ships in the WOCE programme were valuable platforms from which to make accurate *in-situ* measurements. The chief advantages of WOCE ships were: they travelled through data-sparse areas; they were manned by crews and scientists with an interest in obtaining good meteorological data; and their operating schedules permitted sensors and electronics to be returned to laboratories periodically for calibration.

3.1.4.1 Developments for and during WOCE

Prior to WOCE, acquisition of meteorological data was somewhat uneven, even on research ships. Many, indeed most, of the research ships that would take part in the WHP did not have automated systems, so the only meteorological data returned were the manual observations made by the bridge officers and transmitted by radio or in delayed mode from bridge Meteorological Logbooks. In the late 1980s, several countries were developing automated systems to ensure that their research ships routinely acquired and reported high-quality meteorological data. In the UK, for example, the Institute of Oceanographic Sciences Deacon Laboratory (IOSDL) was developing a system called MultiMet, and in the USA the IMET (Improved Meteorological Measurements) system was being developed at WHOI. Other countries were undertaking similar developments. A careful test of the ability of different systems and platforms to make the measurements was carried out as part of the TOGA-COARE experiment in November 1992–March 1993 (Bradley and Weller, 1995a,b, 1997).

The minimum suite of measurements required on an automated system included wind velocity, air temperature, air humidity, sea surface temperature, downward radiative fluxes and air pressure. Other parameters of value included wind stress measured using the dissipation technique, ocean skin temperature (by downward-looking radiometer) and other radiative flux measurements. The latter quantities are required specifically for satellite data validation.

The main challenge to automated systems was the selection, siting around the ship and maintenance of the sensor suite. In order to achieve good exposure for any relative wind direction, two or three sensors for each variable are required. Calibration and maintenance of the sensors is required at frequent intervals.

The introduction of high-quality automated data systems meant that many ships were now acquiring and reporting meteorological data for the first time: IMET systems were installed on numerous (six to eight) US research vessels, and are now being installed on some US Voluntary Observing Ships. A comprehensive account of the status of shipboard meteorology measurements and the associated surface flux calculations at the end of the 1990s can be found in the Final Report of the Joint WCRP/SCOR Working Group on Air-Sea Fluxes (WGASF, 2000).

3.1.4.2 Data assembly and quality control

The Data Assembly Centre for surface meteorology is at the Center for Ocean-Atmosphere Prediction Studies (COAPS) in Florida State University. Data are assembled, reviewed for quality using an automatic system, have quality flags attached, and are made available to the user community (Smith *et al.*, 1996). (Note in passing that while QC flags are set, data are not changed. Thus the end user is responsible for determining the action taken with flagged data.) Data assembled via this route are particularly valuable because of the quality of the instrumentation, continuous data collection and documentation efforts. At the time of writing, the DAC has data from 454 WOCE cruises, which they estimate to be 74% of the completed total. The distribution of data held at the DAC is shown in Fig. 3.1.8 (see Plate 3.1.8, p. 172).

3.1.4.3 Uses for shipboard meteorological data

In addition to the high quality, there are a number of other characteristics that make these data particularly valuable:

- Coverage is obtained from data-sparse regions, particularly the Southern Ocean, which is rarely visited by ships of opportunity.
- Many of the automated data are not reported via the GTS. This means they are not included in Numerical Weather Prediction products and can be used as an independent check.

- Some ships report standard bridge observations at synoptic hours, but also have independent automated systems. This allows an intercomparison between the two data streams.

The high quality of research vessel data also makes them suitable for evaluating flux products. While this can be done on short time scales, i.e. synoptic rather than climatological or other longer-averaged time scales, spatial and temporal coverage is limited. Cruises are not typically repeated to a particular region, and coincidence of ships with, for example, satellite overpasses may not be exact.

3.1.5 Summary and conclusions

The one-time survey was a success in achieving global coverage, meeting its requirements on sampling accuracy of the basic hydrography, documenting methods used at sea and ashore and educating a generation of hydrographers to achieve the above in the face of a heavy seagoing schedule, which strained personnel and logistics.

Advances in the use and exploitation of ADCPs during the WOCE observational period were enormous. Data quality from shipboard ADCPs improved by an order of magnitude, although this was due to improvements in external navigation rather than enhancements to the instrument itself. Lowering of self-contained ADCPs with CTD packages progressed from being an innovative development to a routine exercise wherever the hardware could be made available. While the deployment of LADCPs is now routine, there remains much to be done in understanding and reducing the errors and uncertainties associated with LADCP data. Although the WHP has been an obvious beneficiary of ADCP developments, it is likely that they would have taken place even without the existence of the programme.

The full scientific payoff of the programme remains to be realized as up until now, few attempts have been made to incorporate these measurements (including transient tracers) with other data (for example from float trajectories and ADCPs) or models of the circulation.

While not all taken at the same instant of time, sufficient WHP measurements were repeats of earlier (e.g. IGY) sections or have been made multiple times (24°N in the Atlantic has been re-occupied now four times since the IGY) to begin

to understand the effects of water mass variability during the 'WOCE era' in major parts of the world ocean. We are confident the WHP global effort will remain one of the major achievements of WOCE when viewed by future generations of oceanographers.

Another challenge for the analysis phase of WOCE is to determine, in some sense, how the ocean should be surveyed in future. The emphasis so far has mainly been on quantitative analysis of ocean circulation, and such strategic questions have largely been deferred. By the time WOCE formally comes to an end, we should be in a position to answer such questions as 'Did we do the right sections, and in sufficient detail, to address the WOCE goals?'. Presented with a question such as 'How much anthropogenic CO₂ does the ocean contain, and how is that changing?', the community must design a sampling strategy that states how and when the key regions of the ocean should be sampled. If that strategy is more effective because of lessons learnt from the WOCE global survey, then we will continue to reap benefit from the investment in the WHP for decades to come.

The question arises of what has been achieved that would not have been achieved without WOCE? What is the legacy of the shipboard programme? There are two unarguable benefits.

First, the near-global coverage. Obviously the major institutions of the world would have carried out a considerable amount of hydrographic work during the WOCE observational period, 1990–97. But the work would almost certainly have been concentrated in the same regions of interest that had prevailed for the previous hundred years. Portions of the main ocean basins would remain poorly sampled, or maybe even unsampled with modern methods and tracers. The opportunity and achievability of a global survey, not synoptic but at least concentrated in a few-year period, led investigators to propose and undertake cruises that they would not otherwise have contemplated.

Second, the widespread improvement in data quality. The insistence of WHP planners on setting the highest standards and publishing them provided an incentive for data gatherers to rethink their activities and improve their performance where necessary. Institutions were persuaded to release the necessary capital resources. Suddenly no-one wished to fall below what became the recognized standard. The substantial investment has provided a lasting benefit. The WOCE requirements for measurement accuracy are still considered to be the standard to meet. They have been widely adopted by oceanographers outside the community of the WHP. Many groups engaged in deep-water oceanography for other purposes, such as fisheries and biochemistry, aspire to meet WOCE standards at least for CTD data.

The ambitions of a high-quality global hydrographic survey have therefore been largely realized. A global survey has been completed that bears a remarkable likeness to the one envisaged in 1988. The requirements on data quality have been fulfilled. Neither the completeness nor the uniformly high quality would have occurred without the planning and stimulus of the coordinated shipboard programme.

Acknowledgements

The authors are pleased to acknowledge the additional comments and suggestions contributed by the editors and two anonymous referees. In particular one of the referees contributed a number of observations on the background to the WHP, which are included in Sections 3.1.1 and 3.1.2. Jerry Kappa and Dave Muus (WHPO, SIO), Pat Caldwell (University of Hawaii), Kathy Donohue (University of Hawaii) and S. Smith (COAPS) provided station positions for Figs 3.1.4, 3.1.6 and 3.1.8, and Penny Holliday (WOCE International Project Office) prepared many of the figures at SOC. Roberta Boscolo redrew Fig. 3.1.7.

3.2

Subsurface Lagrangian Observations during the 1990s

Russ E. Davis and Walter Zenk

3.2.1 Determining currents in the ocean

Because the ocean is practically opaque to all but acoustic radiation, knowledge of its motion below the surface is sporadic and gained at great effort. Most of what we know about the ocean's circulation is based not on actual velocity observations but rather on hydrographic measurements. These measurements of water properties are used in two ways. Temperature and salinity are used to calculate density that, according to the geostrophic relation, determines the vertical variations (shear) of horizontal flow. These properties and others are used as tracers to infer absolute flow.

Ever since the basis for the 'dynamic method' was laid out by Sandström and Helland-Hansen (1903), geostrophic shear has been used to interpret hydrographic sections and develop atlases of the large-scale ocean circulation. Numerous methods have been advanced for converting geostrophic shears into absolute velocities including using other hydrographic tracers to infer levels or surfaces of no motion (e.g. Defant, 1941). Two of the advances that provided impetus for the World Ocean Circulation Experiment (WOCE) were the related 'beta-spiral' and 'inverse' methods developed, respectively, by Stommel and Schott (1977) and Wunsch (1977). In these methods potential density surfaces are taken as material surfaces, allowing conservation equations for potential vorticity, and perhaps other tracers, to provide additional constraints on absolute velocity. To a considerable extent, the WOCE Hydrographic

Programme was designed with the intent of using these methods and other forms of data assimilation in which dynamical and/or tracer evolution laws are used to establish the absolute velocity of the general circulation.

WOCE also included observations to measure directly the velocities of the general circulation. Current meter arrays were particularly important in determining the structure and transport of concentrated currents along boundaries and in passages. Such measurements at a point are called Eulerian in recognition of Euler's use, in his theory of dynamics, of coordinates that are fixed in space. Of concern here, WOCE also included an unprecedented international project to use neutrally buoyant floats to measure mid-depth absolute velocity, in part to establish a level of known motion with which to reference geostrophic shears. Measurements by current-followers are often called Lagrangian in honour of the founder of dynamical analysis in a coordinate system that moves with the material. The purpose of this chapter is to provide the historical context for the WOCE float programme, to discuss the methods and limitations of analysing Lagrangian measurements, and to present some of the results gained.

3.2.2 Historical aspects: Stommel's vision to the WOCE Float Programme

Some 45 years ago Bowden (1954) initiated a serious scientific dispute by his thorough review of contemporary knowledge and methodology of

in-situ current measurements. At the time, direct current observations in the deep ocean were very limited, being restricted to about 20 locations in the Atlantic. Most were made by recording instruments suspended from anchored ships for durations between several hours and a few days. Bowden concluded there was great 'need for continuing the measurements at one station for a period of the order of a week ... to derive a satisfactory value for the mean current'.

In a Letter to the Editor, Henry Stommel (1955) suggested the visionary construction of Lagrangian alternatives to the Eulerian current measurements favoured by Bowden. Two devices came to Stommel's mind: (1) floats that sink to a predetermined depth where they 'keep in "trim" in the manner of a submarine' and (2) the more elegant species of 'buoyant floats of a material less compressible than water ... without any power-driven control'. Stommel imagined locating his freely drifting floats a single time using the time of arrival of explosive sound waves at three shore-based SOFAR (Sound Fixing And Ranging) stations. By expecting that 'currents as slow as $10^{-2} \text{ cm s}^{-1}$ could be detected' he rated these current observations to be much more precise than the state-of-the-art vessel-based measurements.

Stommel's plea for Lagrangian *in-situ* observations marks the birth date of a completely new

generation of oceanic instruments. Practically all elements of Stommel's vision have become reality since his $1\frac{1}{2}$ -page paper appeared in 1955: floats with active depth control and passive pre-ballasting have been constructed; oceanographers have learnt to utilize the acoustical transparency of the SOFAR channel for locating and data transmission; floats have been used in quantity to map ocean circulation and its fluctuations. The only thing missing is that Stommel's 'SOFAR time bombs' have been replaced by more peaceful and long-lived piezoelectric devices and sophisticated electronic instrumentation.

The first report of a functional neutrally buoyant float appeared only a few months after Stommel's note when John Swallow (1955) introduced his ingenious invention of what later became known as a Swallow float (Fig. 3.2.1). This pioneering instrument represents the first passively ballasted drifter according to Stommel's second specification. At the surface these floats are slightly negatively buoyant but, owing to the choice of material that make them less compressible than the ambient water, gain buoyancy while sinking. Swallow's first test missions in the Iberian Basin lasted about 3 days and revealed deep clockwise M_2 -tidal currents superimposed on a steady drift. In contrast to Stommel's suggestion, Swallow's floats were located by a dual-hydrophone array



Fig. 3.2.1 John C. Swallow preparing an early neutrally buoyant float on the RRS *Discovery II* in spring 1955. These 'Swallow' floats were constructed from readily available scaffolding tubing, whose physical properties were well established, and the wall thickness was reduced by etching in a solution of caustic soda (cf. Charnock, 1997). Courtesy J. Gould, Soc, Southampton, UK.

under the keel of a research vessel within a range of about 200 m.

Five years later Swallow and Hamon (1960) summarized their first experiences during the International Geophysical Year (IGY). They had observed deep currents of order $0\text{--}5 \text{ cm s}^{-1}$ with time scales of weeks and spatial scales of a few tens of miles. It was explicitly noted that a 'level of no motion' could not be detected in the eastern North Atlantic. Swallow and Hamon's observations of the wide range of variability, including the lack of a reference layer for geostrophic current calculation, were confirmed and extended later by joint British/US (*Aries*) observations 350 km west of Bermuda (Crease, 1962). In this frequently referenced article, Crease comes to two basic observational results:

- 1 float trajectories are 'contrary to the widely held view that the deep ocean is relatively quiescent with velocities of order 1 cm s^{-1} ; and
- 2 the new observations 'raise the question of just how important the...mean circulation is...compared with the eddy transport of properties...'

The discovery that the interior ocean was not quiescent led to the internationally coordinated Mid-Ocean Dynamics Experiment (MODE) during the early 1970s (MODE Gap, 1978). MODE, and its successor POLYMODE, gave impetus to development of a new float technology that fulfilled Stommel's dream of long-range tracking. Rossby and Webb (1970) developed a new generation employing large low-frequency sound projectors capable of being tracked in the SOFAR channel at ranges beyond 1500 km. The remarkable increase in size over a Swallow float of these instruments, which became known as SOFAR floats, is shown in Fig. 3.2.2. SOFAR floats were first tracked in the western North Atlantic by military facilities and later by self-recording moored sound receivers. By offering a multiyear life and a long tracking range, these floats made possible the first identification of mesoscale structures (Riser and Rossby, 1983) and their statistics (Freeland *et al.*, 1975) and the discovery by McDowell and Rossby (1978) of tight coherent eddies in the North Atlantic, called Meddies because their water properties disclosed their Mediterranean source. Over the years substantial improvements for tracking Swallow floats were made (Swallow *et al.*, 1974) and their utility for observing small-scale processes continues.

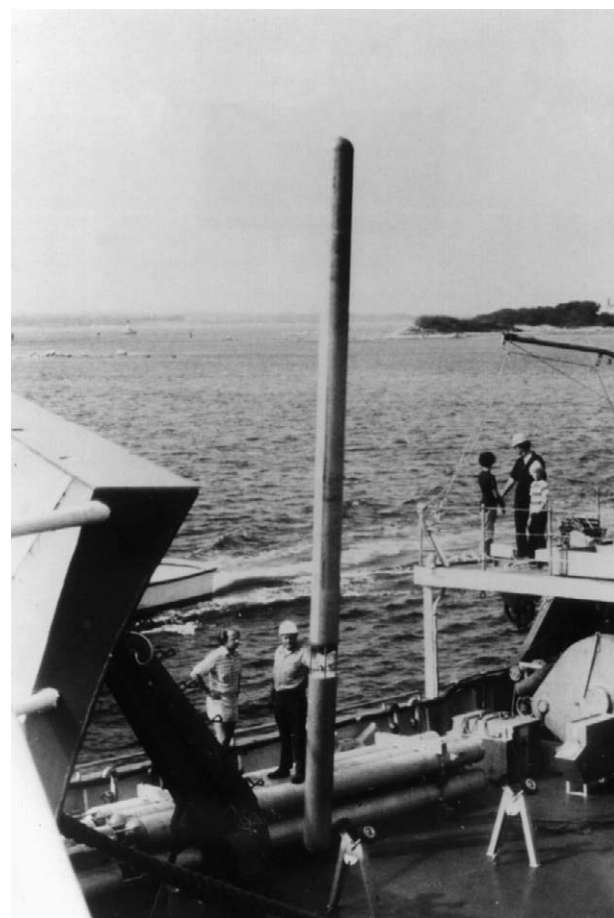


Fig. 3.2.2 The first neutrally buoyant float that could be tracked for long distances was the SOFAR float developed by Tom Rossby (left) and Doug Webb (right), who watch one being loaded for deployment in the Mid-Ocean Dynamics Experiment (MODE).

Rossby *et al.* (1986) introduced a fundamentally new step by reversing the principle of the SOFAR tracking and exchanging the location of sound sources and receivers. The principle of the reversed SOFAR technology, using roving receivers and fixed sound sources, was expressed by the acronym RAFOS, i.e. SOFAR spelled backwards. Former SOFAR floats were converted into moored sound sources and replaced by low-cost and lightweight RAFOS floats with acoustical receivers. These expendable instruments record times of sound arrival from moored sources, drop a ballast weight at the end of their mission and upload their data via satellite after surfacing. They are typically used on missions for 6–24 months to deliver eddy-resolving submerged trajectories and time series of temperature and pressure. Studies that depended on the relatively low-cost and

well-resolved trajectories of RAFOS floats include the description of the transport of water across the axis of the Gulf Stream by Bower and Rossby (1989) and many studies discussed below.

In some studies a high premium is placed on using floats to represent fluid-parcel trajectories. This dictated the uninterrupted current following that can be achieved only with acoustic tracking. It also requires a float with approximately the same compressibility as seawater, which can follow water parcels as they change depth. A technique for increasing a float's compressibility to approximate that of seawater by adding a spring-backed piston was developed by Rossby *et al.* (1985) and is used in many studies where quasi-Lagrangian properties are primary.

In a sense the idea of autonomous (i.e. not requiring an acoustic tracking network) floats traces to Stommel's idea of current-followers that are located only occasionally. The first autonomous float (Davis *et al.*, 1992), shown in Fig. 3.2.3, was the Autonomous LAgrangian Circulation Explorer



Fig. 3.2.3 Jim Dufour holding the ALACE that his engineering improvements made into a reliable autonomous float.

(ALACE). A hydraulic pump enables this instrument, with a mass near 25 kg, to change its volume by moving oil between external and interior bladders. On an interval between a few days and a month, an ALACE cycles from depth to the surface, where it is located by satellite and uplinks collected data. Because autonomous floats operate independently of sound-source arrays, provide hundreds of cycles over a time up to 7 years and are easily deployed, they can operate economically on a truly global scale to provide the long records needed to isolate the general circulation from mesoscale variability. The autonomous mode of operation also allows data to be received continuously through multiyear missions, alleviating the difficulty with RAFOS floats that data is received only at a mission's end.

The penalty for autonomous operation is a long time interval between known positions, which precludes resolving eddies unless cycling is rapid, and periodic surfacing that interrupts the quasi-Lagrangian trajectory. In addition to errors in positioning, a float's vertical motion through sheared currents introduces error into the estimates of the end positions of the at-depth period over which subsurface currents are measured. While descent and ascent velocities vary widely with depth, a float operating at 800 m passes through the upper 400 m in approximately an hour. In a uniform shear with 50 cm s^{-1} difference across 400 m this corresponds to a position change during ascent/descent of less than 1 km (less than the error in long-range acoustic tracking) and on a 20-day cycle time contributes an error of 1 mm s^{-1} to the mean current measurement. Outside western boundary currents, shears are generally smaller than this and variable, so the main effect of shear is to add velocity noise that adds little to the noise coming from mesoscale variability and is easily suppressed by averaging over time or multiple floats.

During WOCE, the family of Lagrangian current-followers grew substantially. In France, Ollitrault *et al.* (1994) developed a hybrid of RAFOS and ALACE technology called MARVOR after the Celtic word for seahorse. It blends the vertical cycling and repeated data transmission functions of ALACE with the eddy-resolving properties of RAFOS floats. For the study of potential vorticity conservation, Sundermeyer and Price (1998) used

a SOFAR float that included ALACE technology to cycle between a pair of isotherms in the main thermocline. While ALACEs are pre-ballasted to drift approximately at a selected depth, the more modern autonomous floats used toward the end of WOCE, such as the SOLO (Davis *et al.*, 2000) and APEX, have full buoyancy control and can be programmed to follow the flow at a different depth than the bottom of their profiles, or even to track isotherms. These floats correspond exactly to the category of floats that ‘keep in trim in the manner of a submarine’ that Stommel had in mind in 1955.

The aspect of float development that made possible the bold WOCE attempt to directly measure velocity fields on basin scales was the cost reduction made possible by the development of RAFOS and vertical cycling technologies that make it possible to measure velocity at a cost near two thousand dollars per year. A RAFOS float costs about \$4500, autonomous floats twice this, and MARVOR floats about three times as much. RAFOS floats typically operate for 1–2 years, autonomous floats can report every 10 days for over 5 years, and Ollitrault (1999) has shown that 50% of his MARVOR floats were still alive after 5 years. Sound sources (approximately \$22 000 each) and costs of analysis of acoustic time delays add to the cost of RAFOS and MARVOR operations.

The scientific utility of ALACE floats has been significantly increased by adding temperature and conductivity sensors so that temperature and salinity profiles from transits between the surface and the target depth can be reported (cf. Davis *et al.*, 2000). Because a Profiling ALACE (P-ALACE) executes 200 depth cycles, the per-profile cost is competitive with expendable probes so long as the conductivity sensor remains stable enough to yield good salinities. Even if the float’s entire construction and communication cost is charged to profiling (neglecting the value of velocity observations), the full operational cost of a temperature profile is about \$50, with \$25 to add a salinity profile.

To complete this historical perspective, let us note that the community is now implementing Henry Stommel’s last vision for observing the ocean. He was aware that early autonomous floats could, in addition to tracking currents, be adept at

measuring profiles, but that there were many reasons for wanting to control where these profiles were taken. A simple solution was to fit wings to a buoyancy-changing float to produce a simple autonomous underwater glider. In a visionary article, Stommel (1989) combined this with the revolutionary idea of generating the necessary buoyancy forcing from the ocean’s thermal stratification to propose a new observational tool, which he called ‘Slocum’ in honour of the first global circumnavigator, Captain Joshua Slocum (1900) and enjoyed demonstrating a prototype thermal buoyancy engine in the workshop behind his Falmouth home. Technologists from University of Washington, Scripps Institution of Oceanography and Woods Hole Oceanographic Institution are adapting autonomous float technology to develop simple electric-powered underwater gliders, while Webb Research Corporation is implementing Stommel’s full vision of thermal-powered gliders. In each implementation, wings are used to efficiently convert buoyancy into forward motion of the $O(30 \text{ cm s}^{-1})$ as the vehicle cycles between shallow and deep levels. This forward motion can be used to hold station to gather a time series of profiles (a virtual mooring) or to sample autonomously a hydrographic section of several thousand kilometres in length.

3.2.3 The WOCE Float Programme

There was, at the start of WOCE, great optimism that inverse analyses based on conserving transport of tracer water properties measured in the WOCE Hydrographic Programme could accurately estimate the absolute mean velocity of the general circulation. But for two reasons it was felt that direct observations of absolute subsurface flow should be included in the measurement programme. First, the precision that could be achieved by inverse analysis procedures was uncertain, but it was clear that their accuracy would be improved by including direct velocity observations. Second, these inverse methods, like their more traditional predecessors, use the distribution of tracers to infer absolute flow and therefore depend on knowing how well tracers are conserved along streamlines. Since absolute velocities and mixing are both linked to tracer distributions (cf. Toole and McDougall, Chapter 5.2), if absolute mean velocities were measured,

then inverse analyses could be used to infer tracer-mixing rates.

This reasoning led to a programme of direct velocity observations in WOCE. Moored arrays were used to measure the transport of selected, usually concentrated, currents, and the Surface Velocity Programme (see Niiler, Chapter 4.1) used current-following drifters to measure directly global flow at 15 m depth. A loosely coordinated WOCE Float Programme was undertaken with the bold objective, made possible by the new technology discussed above, of establishing over the global ocean a level of well-measured absolute mean velocity with which to reference geostrophic shear measurements from WOCE hydrographic sampling and historical data. Additional objectives were characterizing eddy variability and providing visualization of transport processes such as intergyre or inter-basin transport. In addition to the relatively low sampling resolution of the global programme, it was understood from the outset that there would be special regional foci where higher-resolution regional deployments would be required. The Deep Basin Experiment (see Hogg, Chapter 4.5) made particularly powerful use of Lagrangian methods to measure deep flow in the Brazil Basin and from that to infer the mixing processes so critical to the deep circulation.

Design of the global array was based on an assessment that by the end of WOCE it would be possible to map global geostrophic shear with a lateral resolution near 500 km, which dictated the target resolution for the float-based reference field. Measurements could be at any depth but, since errors in the reference field are added to velocities at all depths, the velocity measurements must be accurate. The main limitation to accurate determination of average velocity (say over the WOCE decade) was identified as temporal variability, which was thought to result primarily from mesoscale eddies. The velocity accuracy necessary to provide significant assistance in synthesizing the combined hydrographic and float data set was deemed to vary from $O(3 \text{ mm s}^{-1})$ across most of the interior ocean to $O(1 \text{ cm s}^{-1})$ in strong western boundary currents and the Antarctic Circumpolar Current.

From elementary sampling theory, error ε_U in the average \mathbf{U} of velocity \mathbf{u} calculated from N independent measurements is

$$\varepsilon_U = \sigma_U / N^{1/2} \quad (3.2.1)$$

and from a continuous time series it is

$$\varepsilon_U = \sigma_U (T_{\text{INT}} / T)^{1/2} = (2K/T)^{1/2} \quad (3.2.2)$$

where σ_U is the standard deviation of \mathbf{u} variability, T is the length of the record from which the average is computed, T_{INT} is the integral time scale of the variable part of \mathbf{u} , and K is the asymptotic lateral Taylor particle diffusivity. The integral time scale is related to the velocity time-lagged covariance, $\langle \mathbf{u}(s)\mathbf{u}(s+t) \rangle$, and the velocity frequency spectrum, $\Phi(\omega)$, by the following relations (simplified to one-dimensional flow)

$$\begin{aligned} T_{\text{INT}} &= \sigma_U^{-2} \int_{-\infty}^{\infty} \langle \mathbf{u}(s)\mathbf{u}(s+t) \rangle dt \\ &= \sigma_U^{-2} 2K = \sigma_U^{-2} 2\pi\Phi(\omega=0) \end{aligned} \quad (3.2.3)$$

showing the source of sampling error is the lowest frequency variability. Although (3.2.2) strictly applies to a single time series, Davis (1991) argued it also applies to a collection of time series of total length T so long as they are statistically independent and long compared to T_{INT} .

The WOCE sampling for a 'level of known motion' was focused near 1000 m depth. This reflected considerations of acoustic propagation range, the energy for autonomous floats to complete a cycle and a desire to minimize contact with bathymetry. It also reflected the demand to minimize sampling errors in the measured velocity field. According to equations (3.2.1) and (3.2.2), this recommends a depth where velocity variability is minimum and, because the evidence is that eddy energy decreases with depth in the upper 1 or 2 km, the upper ocean was avoided. This was a bold decision because, rather than focusing on levels with the greatest intrinsic interest, it made success of the global array dependent on its ability to assist in interpreting post-WOCE hydrography.

At intermediate depths in the North Pacific Schmitz (1988) found that eddy speeds decreased from about 10 cm s^{-1} near the Kuroshio to 3 cm s^{-1} some 2000 km to the east and that they decreased with depth above 1500 m. Rossby *et al.* (1983) found from analysis of SOFAR float trajectories that the integral time scale was a relatively constant 10 days, while Böning (1988) analysed a larger body of float data to find that T_{INT} varies inversely as σ_U and is approximately 8 days when σ_U is 10 cm s^{-1} . These estimates essentially agree

for western boundary currents and lead to a 4-year record being required to reduce the sampling error to 1 cm s^{-1} in strong 10 cm s^{-1} variability. In the interior the two empirical laws diverge and predict a range between 2.5 and 7.5 years of record to achieve 3 mm s^{-1} accuracy. Thus the sampling requirements for a global array to determine a level of known motion on the 500 km scale boils down to obtaining a 5-year record in every 500 km by 500 km region, which translates to 1000 floats with 5-year lives distributed over the ice-free ocean.

An aspect of the WOCE Float Programme's design that deserves comment is the goal of deploying floats uniformly, rather than concentrating them in special regions such as western boundary currents. In part this design reflects the fact that concentrated deployments in strong currents are not very effective because the floats are quickly swept through the region of interest. When long-term averages are sought at reasonable cost it is necessary to rely on new floats being recruited into the region of interest as fast as others exit it, and this requires that floats be deployed into the source waters of the current as well as the current itself. Another, more subtle reason for seeking a uniform sampling array is the bias of the mean velocity measured by non-uniform Lagrangian arrays in an eddy field. Just as tracers diffuse down their concentration gradient, there is an average transport of floats from a region where, on average, there is a high concentration of floats to regions with low average concentration. If C is the float concentration averaged over the time used to find the mean velocity U , then the mean float velocity will be in error by

$$\delta U = -K \text{grad} \ln C \quad (3.2.4)$$

(Davis, 1991). Imagine floats deployed preferentially into a strong current so that the average concentration of floats roughly doubled over 200 km. A typical boundary current K of $O(4 \times 10^3 \text{ m}^2 \text{ s}^{-1})$ would lead to a significant 2 cm s^{-1} cross-stream error in the float-measured mean flow.

Diffusion bias is an example of a characteristic of quasi-Lagrangian float sampling: because the velocity being measured determines the location at which samples are taken, the velocities observed may not be typical of the field as a whole. The classical Stokes drift of particles on a material surface in a surface wave field is an example of this

phenomenon. Because the time- or area-averaged velocity on the measured surface differs from the average velocity at the average depth of that surface, and because floats tend to stay longer in the forward flow under crests than in the reverse flow under troughs, the average velocity of floats can differ from the Eulerian mean velocity. Indeed recent theoretical discussions (e.g. Gent and McWilliams, 1990) indicate that the appropriate advection velocity for passive tracers in a layer of thickness h is

$$U_{\text{ADV}} = U + \langle u' h' \rangle / \langle h \rangle \quad (3.2.5)$$

where U is the Eulerian mean velocity and primes represent fluctuations around the mean. Floats that follow the vertical fluid flow (which are then non-diffusive tracers) move at U_{ADV} while isobaric floats, which respond to part of the Stokes drift process but not all of it, will follow neither U nor U_{ADV} exactly. In most of today's float arrays sampling noise probably masks these relatively small effects but a comparison of Lagrangian and Eulerian mean velocities may ultimately be the most direct way to test theories parameterizing $U_{\text{ADV}} - U$.

In addition to their sampling biases, pseudo-Lagrangian observations can be more difficult to interpret than an equivalent number of fixed-position time series. Because time and space changes cannot be separated along a single float trajectory, successful analysis of variability from float data depends critically on having high enough sampling density to determine both space and time structure. In regions with large temporal variability a few Eulerian measurements (like moorings) are much more effective in determining temporal variability than are a few floats. On the other hand, the wandering nature of float trajectories eliminates the topographic biases that can confuse moored observations and floats are quite effective in mapping spatial structures if temporal variability is small.

3.2.4 WOCE float observations

3.2.4.1 Implementation and instrumentation

The WOCE Float Programme was undertaken by scientists from many different nations. Generally a nation, or a few collaborating nations, took responsibility for observations in a selected region. Not all the planned deployments were funded and,

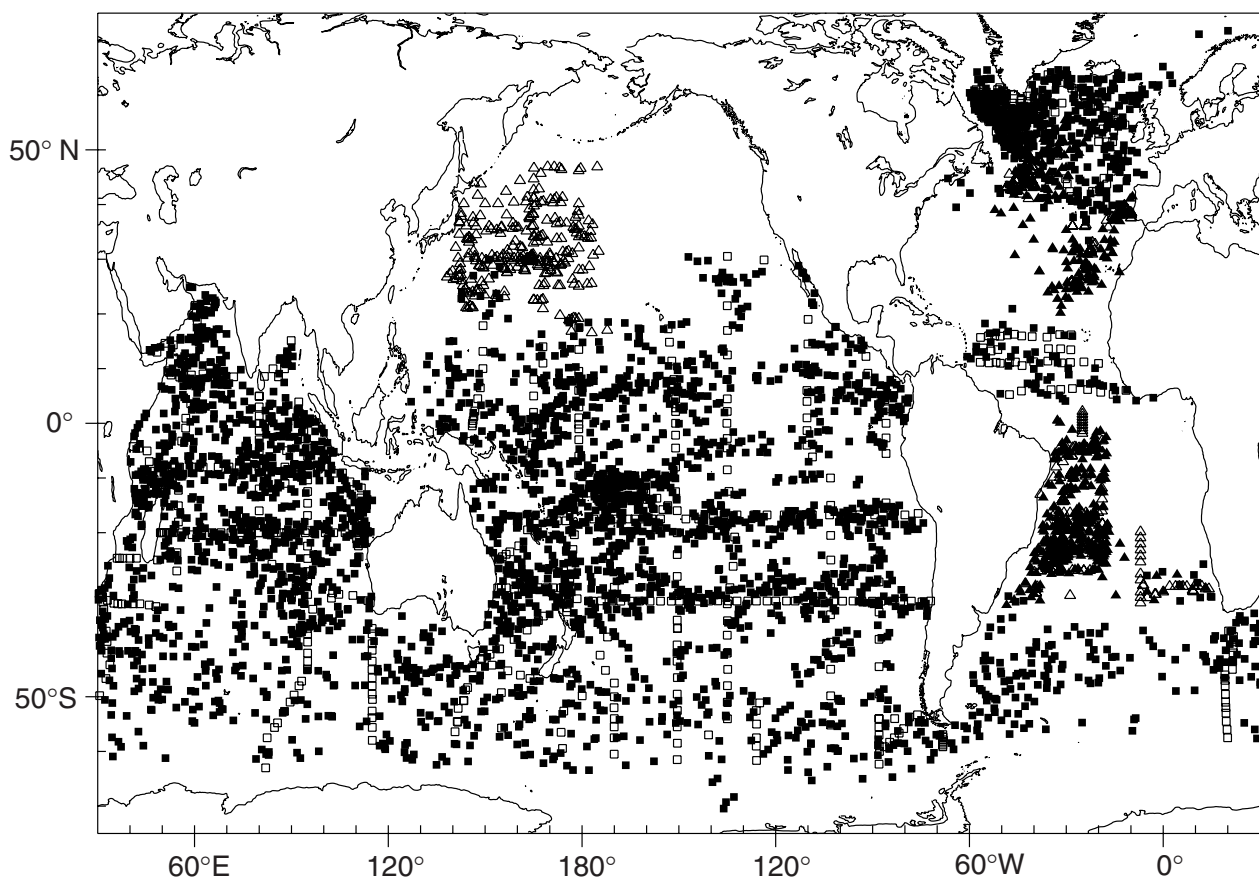


Fig. 3.2.4 A global plot of WOCE-era data in the archives of the WOCE Float Data Assembly Center. Each float trajectory contributes an open symbol at its deployment position and a solid symbol every 200 days of operation. Squares denote ALACEs while triangles indicate RAFOS or MARVOR floats. There are approximately 2100 autonomous float-years and 450 acoustically tracked float-years of data represented. Courtesy C. Wooding, Woods Hole Float Data Assembly Center.

consequently, some regions were not sampled as planned. Partially compensating for this were local deployments by scientists outside WOCE. Since the WOCE float sampling density was matched to the density of hydrographic observations, it was feasible to deploy many of the floats from the WOCE Hydrographic Programme (WHP) cruises and the scientists of the WHP deserve much of the credit for the efficiency of the float programme.

While initial analyses of WOCE floats are expected to be done by those who deployed them, ultimately the complete data set will be collected and made public. To begin this process, a Float Data Assembly Center established at the Woods Hole Oceanographic Institution is gathering all available float data, both from the WOCE era and before. On its web site <http://www.whoi.edu/science/PO/WFDAC/table.htm> one can see visual data summaries and download available data sets. Figure

3.2.4 shows the distribution of data available at the Float DAC in mid-1999. WOCE float data will be gathered through 2001 or later. The pattern of float distribution in Fig. 3.2.4 describes what will be available when all WOCE float data have been assembled.

Usage of the three main float types – RAFOS, ALACE and MARVOR – during WOCE was unevenly distributed. In general, where a high density of velocity mapping was required or pseudo-Lagrangian trajectories were desired (rather than the sequence of mean velocity measurements provided by autonomous floats) acoustically tracked floats were employed. For example, in the South Atlantic, the Deep Basin Experiment sought to measure deep-ocean flows and tracer fields well enough that rates of diapycnal mixing, and its putative role in the dynamics of the deep circulation, could be measured. This required observing

absolute velocity close to the bottom and resolving the small scales that bathymetry introduces (Hogg *et al.*, 1996) and led to using RAFOS and MARVOR floats. The necessary acoustic network was maintained by institutions in the US, Germany and France covering the tropical and subtropical South Atlantic. Similarly, toward the end of WOCE observations, scientists from Germany, France, the US and UK, observing the complex flow in and around the eastern boundary currents and convoluted topography of the eastern North Atlantic, chose to employ RAFOS and MARVOR floats as part of the European initiative EUROFLOAT (Speer *et al.*, 1999) and of ACCE (Atlantic Circulation and Climate Experiment in the US and Atlantic Climate Change Experiment in Europe).

3.2.4.2 Basin-wide studies

The float observations needed to carry out the ambitious WOCE plan to accurately map flow globally would have been prohibitively expensive using relatively short-lived acoustically tracked floats needing an array of sound sources. Thus over much of the global ocean WOCE sampling fell to autonomous floats with the consequent loss of continuous tracking. Figure 3.2.5 (see Plate 3.2.5, p. 172) is an example of raw ALACE data from near 1000 m depth in the southwestern Indian Ocean. The very rapid flow in the Agulhas is an extreme example of a region where the higher spatial resolution of acoustic tracking would be desirable. At the same time, the vigorous chaotic motion where the Agulhas loses its coherence is a clear example of the need for the massive sampling that is made possible by autonomous operation.

The first large-scale WOCE deployment was in the South Pacific, the largest of ocean basins, where between 1991 and 1995 over 300 ALACEs, some reporting temperature profiles, were deployed, mainly from WOCE hydrographic cruises, to map mean flow near 1000 m depth. Over half of these floats were still reporting at the end of 1999, but a preliminary analysis (Davis, 1998b) hints at what can be expected when WOCE Float Programme sampling is complete. Design of the WOCE array assumed a Lagrangian velocity time scale of $O(10)$ days so that successive ALACE velocities, most of which were averages over 25 days, should be serially uncorrelated. This was confirmed for all South Pacific velocities except zonal flow within $O(10^\circ)$

of the equator where variability on a seasonal time scale dominates and confirms the design estimate that more than 5 years of data are required to achieve the desired accuracy for mean flows. Remarkably, the spatial structure and evolution of the low-frequency equatorial variability was well predicted by the data-assimilating NCEP (National Center for Environmental Prediction) model (Behringer *et al.*, 1998) and could, therefore, be coherently subtracted from the observations before incoherent averaging was carried out.

Perhaps the most visually striking feature of the raw South Pacific data is how within about 15° of the equator velocities are dominantly zonal with remarkably short meridional scales manifested in zonal trajectories that reverse and return in the opposite direction within a few degrees of latitude. Outside this equatorial band raw data is chaotic, presumably because of mesoscale variability.

Simple time-area averages of the float data show the main features of the South Pacific circulation but the most accurate results are obtained from objective maps that take account of the horizontal continuity relation implied by geostrophy. Figure 3.2.6 portrays the mean flow at 900 m obtained from the 840 float-years of data available in 1997 (1200 float-years were available at the end of 1999). This map of geostrophic pressure roughly corresponds with the scheme devised by Reid (1997) from a combination of geostrophic shear and tracer distributions. The dominant feature is the South Equatorial Current cutting northwestward across the gyre connecting the South Pacific's southeast corner off Chile to the low-latitude western boundary currents along the northeastern coast of Australia and along New Guinea. The ends of this current, evident in the floats and Reid's analysis, are likely spots for transgyre transport between the Southern Ocean and subtropics in the southeast and between the subtropical and tropical circulation in the northwest.

Also evident in both float data and Reid's analysis are an intermediate depth East Australia Current, westward flow south of Australia, and the confluence of the polar limb of the subtropical circulation and the polar circulation east of New Zealand. Differences between the float data and Reid's analysis are found in speeds of the Antarctic Circumpolar Current and the South Equatorial Current, in the double-gyre subtropical circulation (with western boundary currents along the coasts

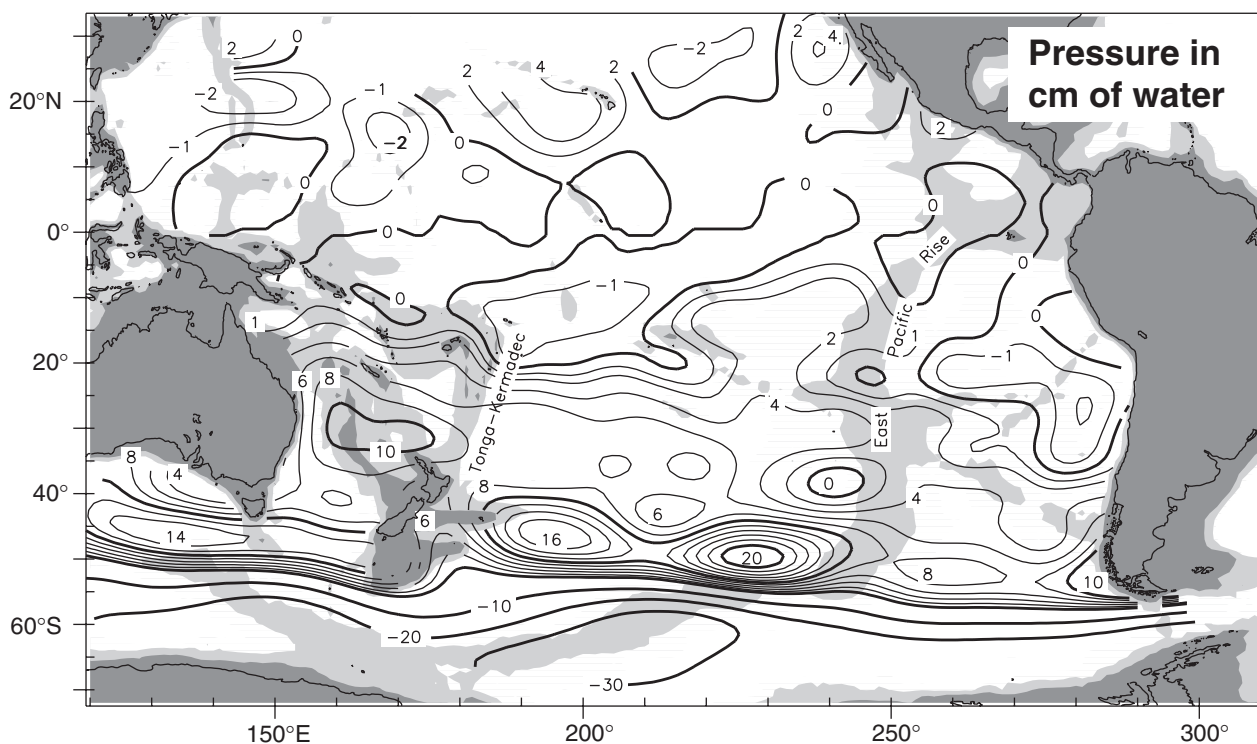


Fig. 3.2.6 The general circulation of the South Pacific at 900 m as determined by ALACEs (Davis, 1998b). Mean velocity from an objective mapping is depicted as geostrophic pressure in cm of water. Note the double-gyre structure of the subtropical circulation, with western boundaries along Australia and New Zealand, which is bounded on the north by a concentrated deep South Equatorial Current. Westward flow south of Australia is fed from the Tasman Sea. Note confused patterns of flow in the equatorial zone and over the tropical East Pacific Rise.

of Australia and New Zealand) found with floats but not by Reid, and in the absence in the float data of the tropical gyre found by Reid. While analysis of the South Pacific must await the complete data set, and the integration with basin-wide hydrographic data is yet to begin, Wijffels *et al.* (2000) have used an inverse analysis to infer absolute velocity across the P6 section near 32°S from hydrographic and float data. They found the float data to significantly improve their analysis over what could be obtained from hydrographic data alone.

The North Pacific was not sampled as completely as the South Pacific but Riser (personal communication) explored mid-depth flow in the western North Pacific using 57 RAFOS floats deployed at 1000 m roughly between 20°N and 40°N and west of the dateline. Except near the western boundary, the motion of these floats is remarkably zonal, much more so than comparable large-area deployments in other subtropical regions. The ratio of eddy variability to large-scale signal is also smaller than is generally found at

these latitudes in other basins. The large-scale flow is eastward everywhere outside the boundary region and, unlike schemes derived from hydrography, there is no westward return flow in the region. Flow over the Izu-Ogasawara Ridge, in both the large-scale field and individual trajectories, is normal to bathymetric contours, showing that barotropic potential vorticity is far from conserved. The Emperor Seamounts do, however, appear to steer the flow.

In 1994 and 1995 the WHP turned to the Indian Ocean and these cruises supported basin-wide deployments of over 225 ALACE floats. Over half of these were temperature profilers deployed mainly in the tropics, where seasonal thermal variability is poorly known, and in subpolar latitudes where even the mean thermal structure had been poorly sampled. Most of these floats are still reporting and no basin-scale analysis has yet been completed.

Float coverage in the South Atlantic has been through a number of loosely coordinated regional studies including substantial deployments in the

Brazil Basin Experiment. Boebel *et al.* (1999) developed the first basin-wide description of intermediate depth flow in the South Atlantic between the equator and 55°S by combining autonomous float data from the subpolar region, RAFOS data from the subtropics and MARVOR data from the tropics to map average flow near 1000 m. The result, based on over 165 float-years of data from

186 trajectories, is shown in Fig. 3.2.7. While the absence of data from the eastern basin hinders interpretation of how Antarctic Intermediate Water passes northward, the results show its interjection into the subtropical circulation east of the Malvinas Confluence near 45°S, two excursions across the South Atlantic between 45° and 25°S, a quasi-stationary western-boundary bifurcation

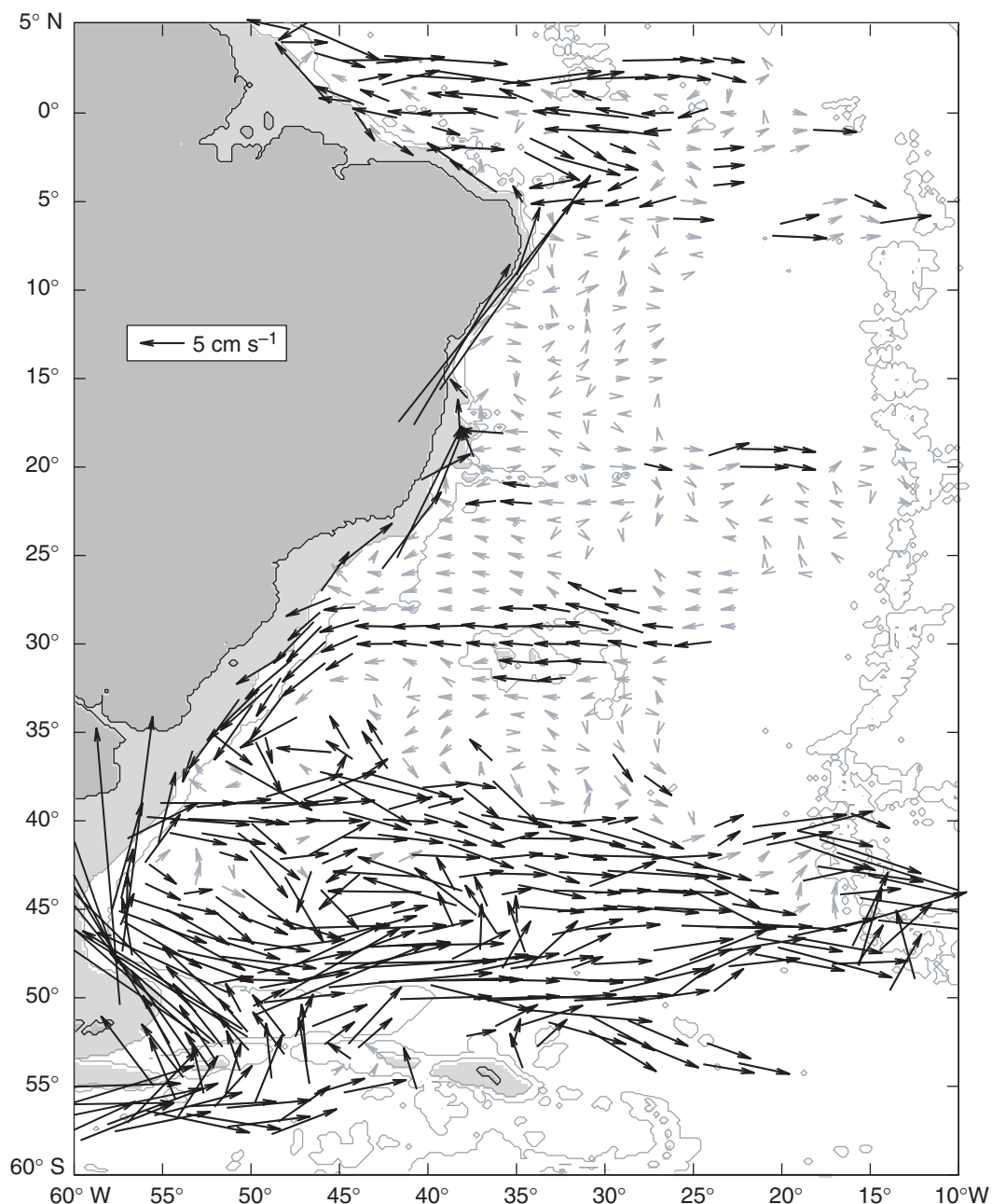


Fig. 3.2.7 The mean circulation of the western South Atlantic near 1000 m depth as determined from RAFOS, MARVOR, ALACE and SOLO floats by Boebel *et al.* (1999). Arrows are averages over $2^\circ \times 4^\circ$ boxes. Light arrows indicate speeds less than 3 cm s^{-1} . East of the Malvinas Confluence the South Atlantic Current and Antarctic Circumpolar Current form separate high-speed flows. A bifurcation near 30°S ends a developed westward flow. Circulation in the equatorial zone exhibits thin zonal flows of alternating direction.

near 30°S at the southern edge of the Brazil Basin, strong (30 cm s^{-1}) northward flow in the North Brazil Undercurrent, and strong zonal flows with little organized meridional motion in the equatorial zone.

The last WOCE observations examined the North Atlantic beginning in 1997. The float work included extensive deployments of temperature and salinity profiling autonomous floats from the subpolar gyre to the tropics. These were supplemented by intermediate-depth RAFOS floats in the North Atlantic Current and the northeastern North Atlantic. This was an internationally coordinated effort by groups from France, Germany, the UK and the US. In the subpolar gyre the scientific goal was to follow the warm-to-cold water transformation from the North Atlantic Current through the subpolar gyre, the process of intermediate-water formation and the subsequent spreading of Labrador Sea Water throughout the North Atlantic. Other scientific foci were formation of 18°C water in the western subtropical gyre as well as pathways of cross-equatorial flow and water-property variability in the tropics.

To date the densest gyre-scale float coverage anywhere was in the subpolar gyre. Over 200 autonomous profiling floats were deployed, mainly in the western two-thirds of the gyre. The North Atlantic Current and eastern basin were populated mainly with acoustic floats, as summarized by Bower *et al.* (2000). The results from the various surveys in different regions have not been fully integrated, but already a new, and in several ways surprising, picture of the mean intermediate-depth flow has emerged.

Lavender *et al.* (2000a) used a very dense array of 180 autonomous floats to construct the map of mean flow near 700 m shown in Fig. 3.2.8 (see Plate 3.2.8, p. 172) covering the Labrador and Irminger Basins (see Lazier *et al.*, Chapter 5.5; Saunders, Chapter 5.6). In addition to the expected peripheral current under the East and West Greenland Currents and the Labrador Current, this discloses some surprises. First, the plot and trajectories of individual floats indicate that most of the flow in the deep Labrador Current turns back into the subpolar gyre rather than joining the deep western boundary current as it flows southwest. Hydrographic tracers make it clear that Labrador Sea Water does continue south of Flemish Cap and the Grand Banks but the float observations raise

the question of how this pathway is maintained. Equally surprising, offshore of the peripheral current there is a countercurrent that flows anticyclonically around both the Labrador and Irminger Basins and provides a short, direct path for newly formed Labrador Sea Water to reach the Irminger Basin. These same observations show that 40% of newly formed intermediate water leaves the Labrador Basin within 1 year and that this water can reach the eastern basin in 2–3 years by either the pathway southward in the Labrador Current and then east, or in the countercurrent and then out of the Irminger Basin. By averaging float velocity along isobaths, Fischer and Schott (2000) inferred, from 15 profiling floats injected into the deep western boundary current, the structure and the variability of the deep Labrador Current at 1500 m depth. They found this current to be about 100 km wide with an averaged core of 18 cm s^{-1} . These floats also confirmed elements of the two basic pathways by which freshly ventilated Labrador Sea Water is advected away from its formation zone.

WOCE activities in the North Atlantic also represented the first widespread use of profiling autonomous floats to report repeated profiles of temperature and salinity. Profiling floats were deployed in the western subtropical gyre to examine formation and circulation of 18°C water and in the tropical Atlantic to examine the hydrological cycle, pathways of cross-equatorial flow and the generation of tropical sea surface temperature anomalies. Autonomous CTD (Conductivity-Temperature-Depth) profilers from these deployments and the subpolar array now regularly deliver time series of temperature and salinity from most of the North and tropical Atlantic. This is extending regular profiling into regions not visited by shipping, like the Labrador Sea, and into severe winter conditions when ocean processes are particularly vigorous but there are few other observations.

An example of the profile data now routinely available is the 2-year time series of salinity in Fig. 3.2.9. This is from a float that spent most of its life in the interior of the Labrador Sea, not far from Weather Station B (57°N, 53°W), where Labrador Sea Water is formed by deep convection. The figure shows winter cooling overcoming salinity stratification to drive deep convection followed by rapid spring restratification by fresh water. Models suggest that convective plumes mainly mix

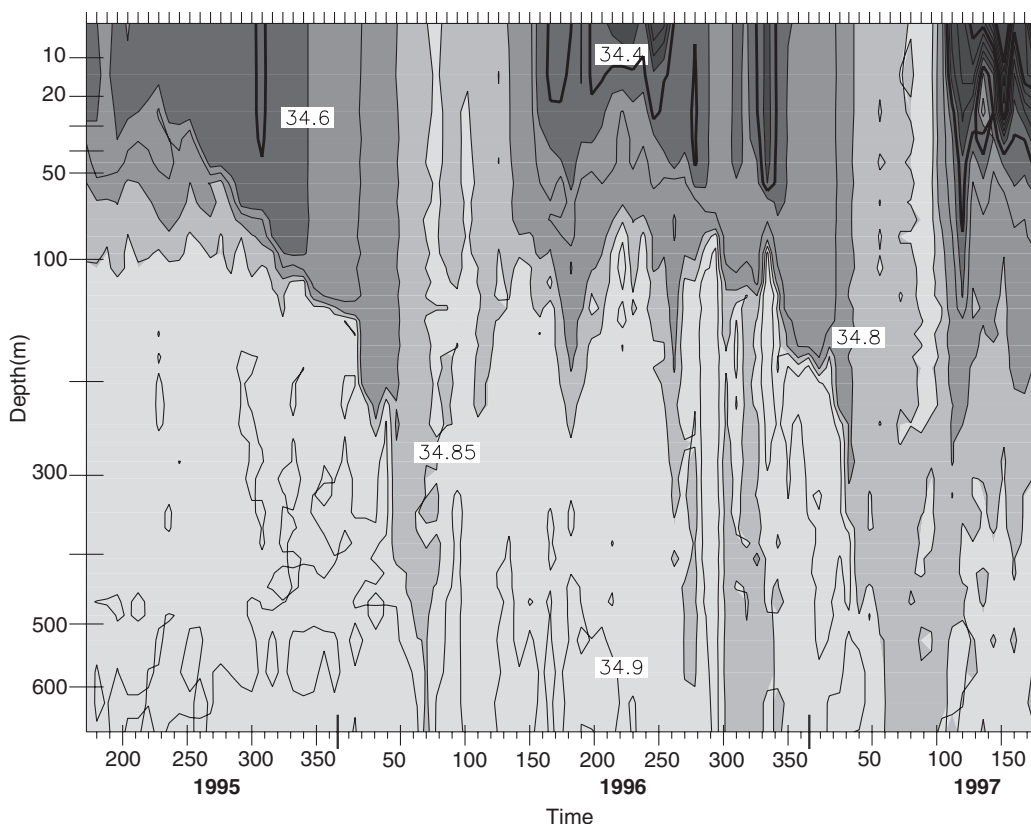


Fig. 3.2.9 Time series of salinity profiles from a P-ALACE that operated in the Labrador Sea for over 2 years reporting T and S profiles every 8 days. The depth scale is stretched. Note how a near-surface fresh layer builds rapidly in the early spring and is destroyed by convection each winter.

the upper ocean and it is the downward motion during restratification that injects the new water into the intermediate depth circulation. The source waters for the rapid spring capping are uncertain. Profiles like those in the figure show that during early 1996 and 1997 there was convection to about 1200 m while there was little deep convection in 1998. They can also show, by the location of deep mixed layers, where convection occurs. Figure 3.2.10 (see Plate 3.2.10, p. 172) shows that deep mixed layers were concentrated near a mid-depth recirculation gyre in the western Labrador Sea, a centre of convection already identified from hydrographic data. Convection also occurred in the far northern Labrador Sea and southwest of the tip of Greenland where it was not anticipated.

3.2.4.3 Regional studies

In addition to broad-scale measurement of mean flow to augment the WOCE hydrographic sampling, the 1990s included a number of regional float experiments to look at key processes, concentrated currents or intergyre exchanges. A desire to

track water parcels and examine small-scale features generally dictated use of acoustically tracked floats. In addition to giving a high-resolution quasi-Lagrangian view of specific regions and phenomena, these regional experiments provide the sampling needed for broad-scale mapping in their region and contribute floats to neighbouring regions. Particularly in the Atlantic, the overall float programme is made up of several individual experiments with specific scientific objectives that were also coordinated to contribute to the basin-scale programme.

A regional RAFOS study in the western equatorial Pacific (Zenk *et al.*, 1999b) amplified the South Pacific ALACE picture by examining how intermediate water crosses the equator along the western boundary. Figure 3.2.6 shows this water to be carried from the southeastern South Pacific to the western tropical Pacific by the South Equatorial Current but is ambiguous about exchange with the North Pacific. Some of the RAFOS floats were entrained into the New Guinea Coastal Undercurrent, running northwestward along that island's

continental slope, near 3°S, and then flowed across the equator to about 2°N before separating from the slope. Like similar ALACE trajectories shown by Davis (1998b), these floats crossed the equator without notable flow perturbations like one might expect from the zonal flows generally felt to dominate equatorial flow system.

The largest regional float experiment was in the South Atlantic as part of the Deep Basin Experiment and used RAFOS floats from several nations. Most of these floats drifted at intermediate depths (600–1100 m) but Hogg and Owens (1999) concentrated their seedings on two deeper levels of the Basin. Their preliminary findings were based on complete tracks for only about one-half of their returning floats. They had launch and surfacing positions for the floats that had not yet been tracked and these produced a set of net displacement vectors over a mission length of 800 days. Several features were clearly evident. First, the Deep Western Boundary Current (DWBC) at 2000 m was observed advecting North Atlantic Deep Water southward along the Brazilian continental rise down to about 20°S. Second, the steadily southward flow of the DWBC is interrupted by the Vitória-Trindade Seamount Chain deflecting all deep floats to the east with a westward return flow to the south of the seamount chain. This seems to confirm an advective balance of the DWBC tongue as argued by Zangenber and Siedler (1998) on potential-vorticity and mass-conservation grounds. Third, away from the boundary, floats at 2500 m and within the Antarctic Bottom Water (4000 m) reveal a primarily zonal pattern with astonishingly short space- and long time-scales, as shown graphically in Fig. 4.5.7 (see Plate 4.5.7, p. 300) of this volume. Variance-preserving spectra from simultaneous deep Eulerian observations show energy to be concentrated at periods shorter than 100 days for the meridional component while spectra of zonal flow continue to increase with time scale.

Meddies have been the subject of various float studies, summarized by Käse and Zenk (1996), with emphasis on Lagrangian behaviour. These intermediate-depth anticyclonic eddies have azimuthal speeds up to 30 cm s^{-1} and translation speeds of $2.5\text{--}5 \text{ cm s}^{-1}$. They carry warm salty water of Mediterranean origin deep into the North Atlantic and are implicated in the formation of the Mediterranean salt tongue. Indeed, the longevity

and long distance travelled by these floats raises again Crease's question of the relative importance of mean flow and eddies in determining ocean transport. Bower *et al.* (1997) examined the formation, near the Strait of Gibraltar, of these small coherent eddies by seeding the Mediterranean undercurrent with 49 RAFOS floats. They found that Meddies are formed along the continental slope south of Spain and west of Portugal at a rate of 15–20 per year in a process that apparently involves roll-up of the boundary layer along the slope. Richardson *et al.* (2000) re-analysed all RAFOS data from the Iberian and Canary Basins in the early 1990s for evidence of Meddies. They found approximately 29 coexisting eddies that seem to decay primarily through collision with seamounts. Remarkably, it appears that in February of 1994 (toward the end of the Bower *et al.* study) about 50% of the Meddies in the northeastern Atlantic were tagged by floats.

In an example of how regional experiments can clarify processes lost to the global-scale coverage, an international consortium mounted the Cape of Good Hope Experiment (KAPEX) to examine inter-basin communication at the tip of Africa. Using a combination of hydrography, surface drifters and RAFOS floats (Boebel *et al.*, 1998), KAPEX focused on the processes by which intermediate-depth water is exchanged between the Indian and South Atlantic Oceans. Analysis of the 1996–99 observations, plus ALACE data described below, will provide new insights into the complex flow and mixing patterns in this region and address the hypothesis that there is a significant transport from the Indian to Atlantic Oceans carried by Agulhas eddies.

An extensive study with RAFOS floats with tuned compressibility addressed the Lagrangian behaviour of the North Atlantic Current (NAC) using nearly 100 quasi-isopycnal RAFOS floats (Rossby, 1996; Dutkiewicz *et al.*, 1999; Zhang *et al.*, 1999a). The mean velocity of the NAC in the Newfoundland Basin was seen to consist of a sequence of large-amplitude meanders with wavelength near 400 km (not dissimilar to those in the deeper flow shown in Fig. 3.2.8 – see Plate 3.2.8, p. 172). While the NAC front was found to approximate a material stream-tube, eddy transport with the surrounding waters was quantified and found to be asymmetric, favouring transport from the subpolar gyre to the subtropical side. Rossby *et al.* (2000) have expanded their studies of the NAC

into the central basin and new descriptions of Lagrangian pattern in this region are expected.

With a similar focus on gathering a Lagrangian description of an important transport process, the pathway of the North Atlantic's deep western boundary current and its interaction with the Gulf Stream were examined by Bower and Hunt (2000a,b) using RAFOS floats. They found only a small amount of intermediate water from the Labrador Sea to cross under the Gulf Stream into the subtropical circulation while Nordic Seas overflow waters bifurcate, one branch following the Gulf Stream offshore while the other remains attached to the western boundary. The clarity of these results suggests a similar acoustic-float study to resolve the question, raised in the subsection above, of how Labrador Sea Water enters the subtropical gyre.

A number of regional float experiments in the North Atlantic have examined different elements of the complex circulation there, both elucidating specific processes and collectively forming the backbone of that part of the global array. For example, Fig. 3.2.11 (see Plate 3.2.11, p. 172), adopted from Zenk (2000), shows daily-resolved trajectories of RAFOS floats just east of the Mid-Atlantic Ridge. These isobaric floats were deployed after June 1997 at the depth of the Labrador Sea Water, i.e. roughly at 1500 m. They demonstrate the transport of this water mass eastward through Charlie-Gibbs Fracture Zone at about 53°N in more detail. After passing this gap the pathways bifurcate, one approaching the western extent of the European continental rise while the other feeds the Iceland Basin. The Icelandic branch meets Iceland–Scotland Overflow Water at the northern tip of the Iceland Basin and then advects the floats southwestward along the flanks of the Reykjanes Ridge. Particularly along the Icelandic branch, these continuously tracked trajectories give a quasi-Lagrangian view of the mean flow patterns in Fig. 3.2.8 (see Plate 3.2.8, p. 172) that are based on an entirely independent data set.

In another example of regional experiments giving a closer view of patterns smoothed over in basin-scale coverage, Rossby *et al.* (2000) present case studies of selected trajectories from the Irminger and the Iceland Basins. Despite the apparent eddy motion they see a rather robust pattern of float pathways emerging. Rossby's isopycnal-following instruments provide explicit

information on advection and mixing along their pathways. The authors expect particularly challenging results that will include estimates of cross-frontal fluxes of heat and oxygen between the subpolar and the subtropical gyres.

Finally, Lavender *et al.* (2000b) present results from a regional deployment of autonomous Vertical Current Meter floats to explore the vertical motion associated with deep convection. One interesting question addressed was whether a region of convection is one of general downwelling. Although the floats (cf. Davis *et al.*, 2000) can measure vertical motion down to $O(3 \text{ m day}^{-1})$, the way they are entrained into, and detrained from, convecting plumes causes them to give a biased measure of the mean vertical motion, so the results are equivocal. A perplexing paradox is that the vertical temperature flux $\langle w' T' \rangle$ apparently carried by the plume scale (quasi-Lagrangian time scales of less than 88 h) is insufficient to explain the observed cooling below 400 m depth.

3.2.5 The future

It is clear that the Swallow float has become an observational tool capable of charting the world ocean's subsurface general circulation and providing numerous and economical profiles of ocean properties. Even though the analysis of WOCE-era floats has only begun, it is clear that they will have significant impacts on the field. Floats have provided visualization of basin-scale flows including intergyre and interbasin transport. In many regions enough observations have been accumulated to produce statistically reliable descriptions of absolute flow from which hydrographic shears can be referenced. While many float data sets have yet to be combined and the integration of mapped mean flow and hydrography has so far been accomplished only on one hydrographic section, bringing all these data together to produce consistent analysis will produce a significant increase in what is known about the general circulation.

While this analysis is going on, oceanography will be undergoing a significant change made possible, in part, by a new global array of 3000 profiling floats reporting profiles of temperature and salinity over the upper 2000 m as well as absolute velocity observations. This international programme Argo, began implementation in 2000 with a goal of providing real-time observations

with 10-day and 3° resolution. These data will allow us to establish accurately the transports and seasonal cycle of the ocean's heat engine and hydrological cycle and to track climatic variations on time scales from years to decades. Because Argo data will be made publicly available within hours of collection, it will be possible to watch the El Niño-Southern Oscillation (ENSO) develop, see the upper ocean changes produced by tropical storms, and know almost immediately how strongly convection is ventilating the ocean in any winter. These data will not only support new areas of research but, through data assimilating modelling, will make possible now-casts and forecasts of the ocean on a regular basis. Details on Argo can be found on the web at <http://www.argo.ucsd.edu>.

The fast evolution of observational technology over the 1990s makes it foolhardy to guess what the next decade will bring, but a hint of what is ahead can be obtained by extrapolation of activities already underway. For observation of subsurface velocity, it is likely that both continuously tracked neutrally buoyant RAFOS floats and autonomous floats will be needed. For acoustic floats a major limitation to economical sampling can be overcome by widespread deployment of high-energy sound sources. It is, for example, entirely feasible today to install enough sound sources that a float could be continuously tracked anywhere in the tropical or North Atlantic. Since sound sources, like radio stations, can serve different users, the presently rather simply structured network of moored sound sources will require greater international coordination in the future. The benefits of an organized RAFOS network will be linked with the responsibility of contributing parties to maintain such arrays of sound sources over an extended period of time on a basin-wide scale. Miniaturization of receiver electronics and production in great numbers could result in a significant decline in float prices. This, and development of new sensors, could open other fields of research and even commercial opportunities such as fish tracking with high spatial resolution (Rossby, personal communication). Biogeochemical sensors now under development may be suitable for Lagrangian instruments and an operational oxygen sensor on RAFOS floats has been successfully demonstrated by Rossby *et al.* (2000) in the North Atlantic.

For autonomous floats the availability of Global Positioning System (GPS) navigation and polar

orbiting satellites supporting two-way communication will reduce the length of on-surface periods, making trajectories more nearly Lagrangian. This will also allow float missions to be adjusted after deployment by, for example, allowing cycle times to be reduced as a float approaches concentrated boundary currents or regions where small-scale structure is of interest. The new satellite communication will increase the amount of data that is feasibly relayed, allowing floats to report measurements of more variables, at higher precision and higher depth resolution. The same satellite developments make feasible autonomous gliders that can be used to gather time series of profiles or sections at predetermined locations. Use of the ocean's thermal gradient to supply power to both profiling floats and gliders might greatly extend float life in the well-stratified parts of the ocean.

Techniques for deploying floats are also expanding. Repeated deployments from one location are made possible by the 'float park' concept (Zenk *et al.*, 2000) in which floats are inexpensively moored until they are deployed on a schedule. Seeding autonomous floats from commercial shipping vessels and their air deployment will likely increase as the use of floats moves from specific deployments to the maintenance of observing arrays.

Success of the Argo programme depends on stable salinity sensors and several different sensors have been used on profiling floats. Long-term stability has been a problem with some so that early autonomous profiling has been most useful in the upper ocean where salinity changes are large enough that salinity uncertainties do not cloud the picture. Progress is being made and recent results suggest that long-term stability to $O(0.01)$ in salinity is feasible. The T versus S plot in Fig. 3.2.12 (see Plate 3.2.12, p. 172), from an 18-month record from a P-ALACE deployed in the subtropical North Atlantic by S. Riser, shows that recent long-term salinity profiling has reached the point where relatively subtle climatic variations of salinity can be reliably observed autonomously. This figure shows that observed salinity variations near 700 m depth are $O(0.01)$, substantially smaller than the $O(0.1)$ climatic variations already seen in the historical record.

The full power of neutrally buoyant devices to observe ocean properties will be realized only when accurate, long-lived sensors become available to

measure a broad suite of parameters. Drifts and biofouling must be overcome to achieve long-term accuracy and the full economy float platforms. Biofouling may be significantly reduced when new cellular satellite communication reduces the time during which floats must stay at the surface, but

one suspects much work lies ahead to both increase the longevity of existing sensors and to expand the variables that can be sensed with low-power, long-lived sensors. This may well be the next frontier for float technology.

This Page Intentionally Left Blank

3.3

Ocean Circulation and Variability from Satellite Altimetry

Lee-Lueng Fu

3.3.1 Altimeter observations

Space-age technologies have made satellite remote sensing a powerful new tool with which to study the earth on a global scale. The only truly global observations made with regular sampling in space and time during WOCE (the World Ocean Circulation Experiment) were obtained from space-borne sensors. However, the opacity of the ocean to electromagnetic sensing has limited most space-borne measurements to the properties of the very top surface layer of the ocean (such as sea surface temperature and colour). The promise of measuring the height of sea surface using radar altimetry (Chelton *et al.*, 2000) emerged in the 1970s and provided a tantalizing opportunity to oceanographers for obtaining information about the dynamics of the ocean at greater depths. This is because the sea surface height relative to the geoid is the dynamic topography of the ocean surface (referred to as the ocean topography hereafter), which is related to the circulation and density field of the entire water column. Without being able to measure the ocean topography directly, oceanographers have constructed it using density measurement to compute the dynamic height of the sea surface in the past. Despite the great potential value of satellite altimetry, the challenge has been the required measurement accuracy. A simple analysis (e.g. Wunsch and Stammer, 1998) shows that a 1 cm tilt in the ocean topography is associated with a mass transport of 7 Sv ($1 \text{ Sv} = 10^6 \text{ m}^3 \text{ s}^{-1}$) in an ocean of 4000 m depth at 24° latitude, if the

entire water column moves at the same velocity. The actual transport varies with latitude and the vertical distribution of current velocity, but this value provides a rough estimate. Such a magnitude is an appreciable fraction of the transport of the Florida Current ($\sim 30 \text{ Sv}$), for example. Therefore the tall order for satellite altimetry is to make measurement of the sea surface height from space with an accuracy on the order of 1 cm.

Shown in Fig. 3.3.1 is the geometry of satellite altimetry. There are three components in the determination of ocean topography, η : the altimeter range measurement, h ; the radial height of the orbit, H ; and the geoid height, N . They are related as follows:

$$\eta = H - h - N \quad (3.3.1)$$

Determination of all three with an accuracy of 1 cm is extremely challenging (see Chelton *et al.*, 2000 for a review). The measurement of h is affected by uncertainties from sources including imperfect knowledge of the interaction of electromagnetic waves with the rough seas, the delay in the propagation of electromagnetic waves through the atmosphere and the ionosphere, as well as the calibration of the instrument's electronics. The determination of H is made by computations that rely on a precise knowledge of the earth's gravity field, the ability to model the non-gravitational forces such as radiation pressure and atmospheric drag, and the ability to track the location of the spacecraft precisely. The knowledge of N has to be obtained from

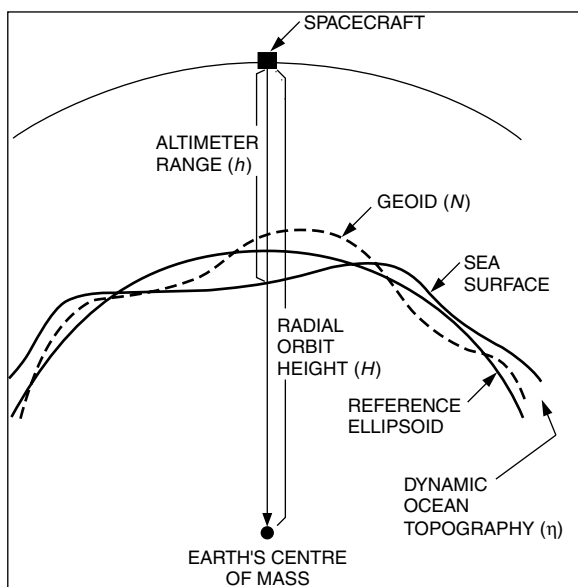


Fig. 3.3.1 Measurement geometry of satellite altimetry.

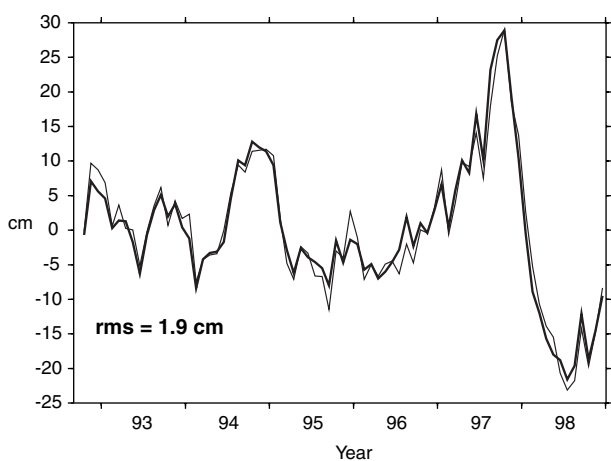


Fig. 3.3.2 Comparison of T/P measured sea level (thin line) to the observation made by the tide gauge at the Christmas Island (thick line). Courtesy of R. Cheney of NOAA.

independent approach and its accuracy is a major issue in using altimetry for studying ocean circulation (National Research Council, 1997).

The concept of satellite altimetry was demonstrated in the 1970s. A variety of missions with different emphases were conducted in the past two decades – Skylab (1973), GEOS-3 (1975), SEASAT (1978), GEOSAT (1985), ERS-1 (1991), TOPEX/POSEIDON (1992), ERS-2 (1995), GEOSAT Follow-on (1998). Among these, TOPEX/POSEIDON (denoted by T/P hereafter) is the only altimetric satellite specifically designed for studying the global ocean circulation (Fu *et al.*, 1994). The

effort includes an instrument package for measuring signal delay in the media as well as precision satellite tracking, an optimal choice of orbit configuration for orbit determination and tidal sampling, and a long-lead programme in improving the knowledge of the earth's gravity field. A recent review of the results from the mission has been provided by Wunsch and Stammer (1998).

The evolution of the accuracy in sea surface height measurement has spanned more than two orders of magnitude from Skylab to T/P. The root-mean-square (rms) uncertainty in the T/P sea surface height measurement ($[H-h]$ in equation (3.3.1)) made over a distance of 6.2 km (made within approximately 1 second flight time) along the satellite's ground tracks was 4.7 cm after the completion of the mission's calibration phase (including errors in both orbit determination and altimeter measurement) (Fu *et al.*, 1994). The accuracy in orbit determination has been improved since the launch of T/P primarily as a result of improved gravity models based on the T/P data (Tapley *et al.*, 1996). The sea surface height measurement uncertainty is approaching 4 cm based on the new gravity models (Chelton *et al.*, 2000). A significant portion of the measurement errors is random in space and time and can be reduced by filtering. For example, Cheney *et al.* (1994) showed agreement between the T/P data and tide gauge data in the tropical Pacific within 2 cm (rms) when the data were averaged over 1° latitude by 4° longitude cells on a monthly time scale. Figure 3.3.2 shows such a comparison with the tide gauge data at the Christmas Island based on 6 years of data. Ocean tides have been removed from both the altimetry and tide gauge data.

The largest variability of sea surface height is due to the ocean tides with a global rms amplitude of about 32 cm (Le Provost *et al.*, 1995; Chelton *et al.*, 2000). The signals of tides must be removed before using the data for studying ocean circulation. Due to the relatively long repeat periods (often longer than a few days) of a satellite altimeter, the short-period tides are often aliased to much longer periods. For example, a sun-synchronous orbit, in which many earth-observing satellites have been flown, would alias solar tides into a period of infinity and make them become indistinguishable from the ocean topography of the mean circulation. T/P is the first altimeter flown in a well-chosen orbit that avoids aliasing tidal periods to

those of oceanographic interests (Parke *et al.*, 1987). The best ocean tide models derived from the T/P data are accurate with an rms error of 2–3 cm (Le Provost, 2000) in the open ocean. This is by itself a major accomplishment. For the first time the knowledge of ocean tides, a major component of the fluctuating ocean currents, is available everywhere in the open ocean. On the other hand, this knowledge allows the removal of tidal signals from altimetry data with an accuracy comparable to the altimeter measurement accuracy. The residual tidal signals appear in the corresponding aliased periods such as 62 days for the M_2 component, and 173 days for the K_1 component in the T/P data. Because the aliased tidal periods are precisely known (Le Provost, 2000), these residual errors will not affect the study of ocean circulation in a significant way if the aliased periods do not coincide with those of strong ocean variability. However, the aliased period of K_1 , 173 days, is very close to the semi-annual period and could be problematic in regions where the semiannual variability is strong, such as the South Atlantic and the central tropical Pacific (Jacobs *et al.*, 1992). In the tropical regions, especially in the Indian Ocean where the ocean has substantial variability at periods near 60 days (Luyten and Roemmich, 1982; Kindle and Thompson, 1989), the M_2 tidal aliasing also presents a problem. Because the phase of the tides are sampled differently by adjacent satellite tracks, aliased tidal signals may appear as travelling waves and create confusions for interpretation (e.g. Chelton *et al.*, 2000).

With the performance of T/P, we are able to determine the first two terms of equation (3.3.1) within a few centimetres over the global ocean every 10 days. We still need accurate geoid models to derive ocean topography from altimetric observations. The accuracy of the present geoid models, however, has not yet matched the accuracy of satellite altimetry, making the derived ocean topography not sufficiently accurate for determining the details of the absolute ocean circulation. This deficiency has long been recognized by the geodynamics community (National Research Council, 1997). New missions such as GRACE (Gravity Recovery and Climate Experiment) (Wahr *et al.*, 1998; Davis *et al.*, 1999) and GOCE (Gravity Field and Steady-State Ocean Circulation Explorer) (LeGrand and Minster, 1999) have been planned to obtain more accurate measurement of the earth's gravity field

and hence the knowledge of the geoid. However, at wavelengths longer than 3000 km, the errors of the geoid models presently available are below the level of oceanographic signals. At these large scales, satellite altimetry has provided the first direct measurement of the ocean topography. The utility of such measurement for the determination of the oceanic general circulation is discussed in Section 3.3.2.

Without detailed knowledge of the geoid, satellite altimetry data have primarily been used to study the temporal variability of the ocean. Because the temporal variability of the geoid is negligibly small when compared to that of the ocean, sea surface height measured along precisely repeating ground tracks or at ground-track cross-overs is used to compute the temporal change of the ocean. Studies based on early altimetry missions have to deal with a host of errors from orbit uncertainties, poor corrections for the atmospheric effects, and inaccurate knowledge of the tides (e.g. Wunsch and Gaposchkin, 1980; Fu, 1983; Fu and Cheney, 1995). These errors have often limited the utility of altimetry to the study of the energetic mesoscale eddies and boundary currents. T/P is the first altimetry mission that produces data sufficiently accurate for studying variabilities on scales larger than the mesoscale without the need for correcting large-scale errors at the expense of distorting signals. This data set has led to many new discoveries at the large scales where conventional *in-situ* measurements suffer from inadequate sampling. Results from studies focused on the large scales (larger than the mesoscale, whose upper bound is loosely defined as 500 km) are discussed in Section 3.3.3. Results on smaller-scale variabilities, including mesoscale eddies and ocean currents whose cross-current scales are less than 500 km, are discussed in Section 3.3.4. Concluding discussions and future perspectives are given in Section 3.3.5. The reader should note that a substantial portion of Sections 3.3.2 and 3.3.3 is adapted from Fu and Chelton (2000).

3.3.2 The ocean general circulation

In the open ocean a few hundred km away from the equator, the large-scale oceanic flows are nearly in geostrophic and hydrostatic balance, leading to the integral form of the 'thermal wind' equation for the horizontal velocity at depth z :

$$v(z) = \frac{g}{\rho f} \int_{z_0}^z \frac{\partial \rho}{\partial x} dz + v_0 \quad (3.3.2)$$

where z_0 is a reference level for the integration and v_0 is the velocity at the reference level, ρ is the density of seawater, g is the earth's gravity acceleration, f is the Coriolis parameter defined as $f=2\Omega \sin\phi$, where Ω is the earth's rotation rate (7.292×10^{-5} rad s $^{-1}$), and ϕ is the latitude. Historically, the reference level was chosen to be at great depths where the velocity was assumed to be zero, or at least close to zero. Therefore the velocity of the ocean could be determined from the knowledge of the ocean's density field. However, the choice of a 'level of no motion' for the reference level has been controversial and problematic. The reader is referred to Wunsch (1996) for a full discussion. Determination of the absolute velocity at a given level over the global ocean is one of the most challenging tasks facing physical oceanographers.

The ocean topography derived from altimetry in principle is a straightforward approach to the reference level velocity problem. The surface geostrophic velocity can be obtained directly from the gradients of the topography:

$$v = \frac{g}{f} \frac{\partial \eta}{\partial x}, \quad u = -\frac{g}{f} \frac{\partial \eta}{\partial y} \quad (3.3.3)$$

The ocean topography derived from early altimetry missions was only marginal for detecting absolute circulation because its uncertainty was larger than the oceanic signal at all scales. The uncertainty is dominated by the satellite orbit errors at large scales and by the geoid errors at small scales. For instance, the first map of the absolute circulation derived from the SEASAT altimeter showed only a marginal resemblance to the basin-scale (>6000 km) circulation of the Pacific (Tai and Wunsch, 1983). In preparation for T/P, a systematic gravity model improvement project was conducted in the 1980s, leading to progressively improved gravity and geoid models. These models were first applied to the GEOSAT data as well as the re-analysis of the SEASAT data. The ocean topography was solved as a solution to an inverse problem involving simultaneous adjustments of orbit, geoid, and ocean topography. The resulting ocean topography solutions were extended to spherical harmonics of degree and order 6–10, with wavelengths of 4000–6000 km (Tapley *et al.*, 1988; Denker and Rapp, 1990; Marsh *et al.*, 1990; Nerem *et al.*, 1990; Visser *et al.*, 1993). The

formal estimate of the error in these solutions was about 15 cm.

Despite the progress in deriving realistic ocean topography from altimetry, the result would not be useful scientifically if it does not provide new insight of the circulation and improve the estimate of important quantities such as mass and heat transports. Wunsch (1981) suggested that the ocean topography based on historical hydrographic data and a conventional mid-depth level of no motion had an accuracy of 10–25 cm. The altimetric ocean topography must be more accurate than this level to be useful. In fact the results from inverse models based on extensive *in-situ* data are much more accurate and place a more stringent test on the utility of altimetry (e.g. Martel and Wunsch, 1993a). Trying to incorporate the GEOSAT result of Nerem *et al.* (1990) into their North Atlantic model for an improved estimation of the circulation, Martel and Wunsch (1993b) found that the GEOSAT result was not compatible with the conventional data, and that the error in the altimetry-derived ocean topography was too large by at least a factor of two to contribute anything new about the circulation.

The gravity model improvement activities supported by the T/P project culminated in a series of the so-called Joint Gravity Models (JGM) (Tapley and Kim, 2000). The geoid derived from the most recent one, called JGM-3 (Tapley *et al.*, 1996), has an accuracy about a factor-of-two better than the one obtained by Nerem *et al.* (1990). The formal error of the JGM-3 geoid model in terms of a set of functions that are orthonormal over the oceans is shown in Fig. 3.3.3 (after Rapp *et al.*, 1996). Displayed in Fig. 3.3.4a is the ocean topography computed as the difference between a 2-year averaged T/P mean sea surface (1993–94) and the JGM-3 geoid, up to degree 14 of the orthonormal expansion. The error in JGM-3 becomes larger than oceanographic signals beyond degree 14, as discussed below. This ocean topography is compared with the simulation of a numerical ocean general circulation model (Fig. 3.3.4b). The model denoted as POCM-4B, has a spatial resolution of 1/4° and 20 vertical levels. The basic formulation of the model was described in Semtner and Chervin (1992). The model was run from 1987 to 1994 and driven by daily winds and monthly heat flux. The simulation of the global ocean circulation produced by the model has been used by

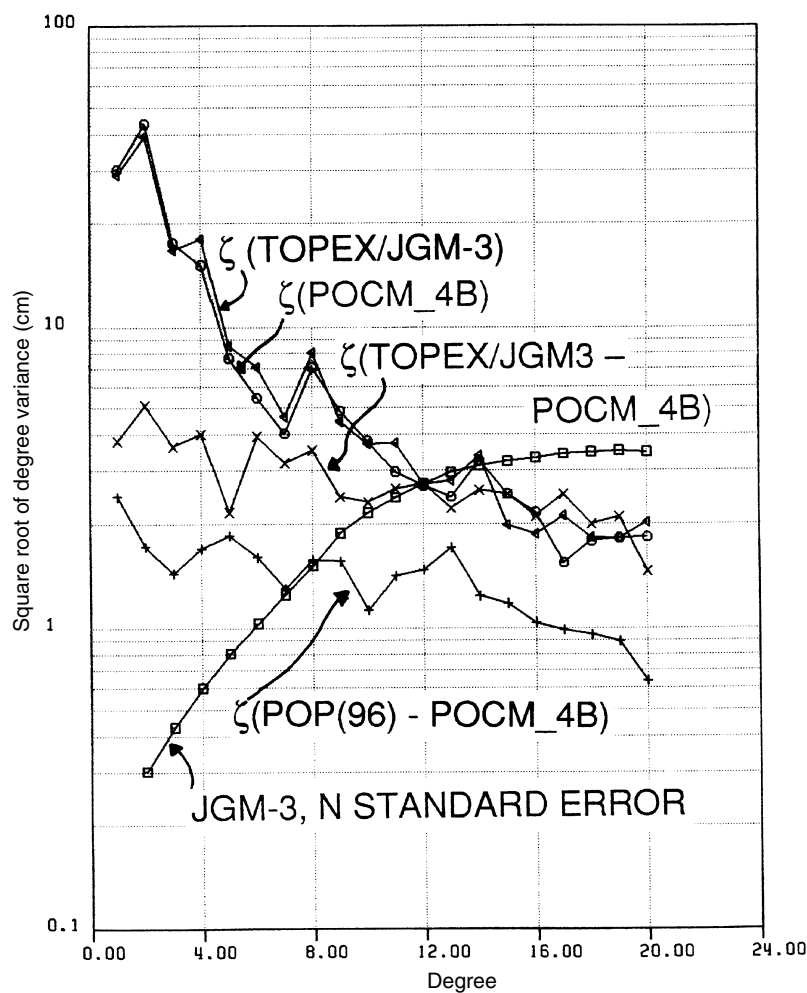


Fig. 3.3.3 The square root of variance in cm as a function of degrees of the orthonormal ocean functions for the following: the JGM-3 geoid undulation standard error, the ocean topography determined from T/P (based on the JGM-3 geoid) and from an ocean model (POCM_4B), the difference between the T/P ocean topography and POCM_4B, as well as the difference in ocean topography between two different ocean models (POCM_4B and POP96). The degrees in the abscissa refer to those of a set of expansion functions similar to the spherical harmonics, but they are orthonormal over the global oceans. From Rapp *et al.* (1996).

many studies as a benchmark for comparison with observations (Rapp *et al.*, 1996; Stammer *et al.*, 1996).

The visual resemblance between the T/P observation and the model is quite encouraging. Rapp *et al.* (1996) performed a quantitative evaluation of the comparison. The rms difference between the T/P topography and the model up to degree 14 is 12.4 cm. The corresponding rms difference in geostrophic velocity speed is 2.5 cm s^{-1} , about 50% of the signal. If the correlation between the model error and the observation error is small, which is not an unreasonable assumption, then the difference can be interpreted in terms of the magnitudes of the observation error and the model

error. Since the systematic orbit error (geographically correlated) based on the JGM-3 gravity model is less than 1 cm in the T/P data (Tapley *et al.*, 1996) and other altimetry systematic errors also at the 1 cm level (Fu *et al.*, 1994), the observation error at the large scales is dominated by the geoid error. Up to degree 14 the JGM-3 geoid model has an rms error of 6.8 cm (Table 1, Rapp *et al.*, 1996). The inferred rms error for the ocean model is then about 10 cm. Fu and Smith (1996) compared the T/P ocean topography with the model of Smith *et al.* (1992a), which is similar to the model of Semtner and Chervin (1992) but with a $1/6^\circ$ spatial resolution. They found that the large-scale error of this model was about 10 cm as

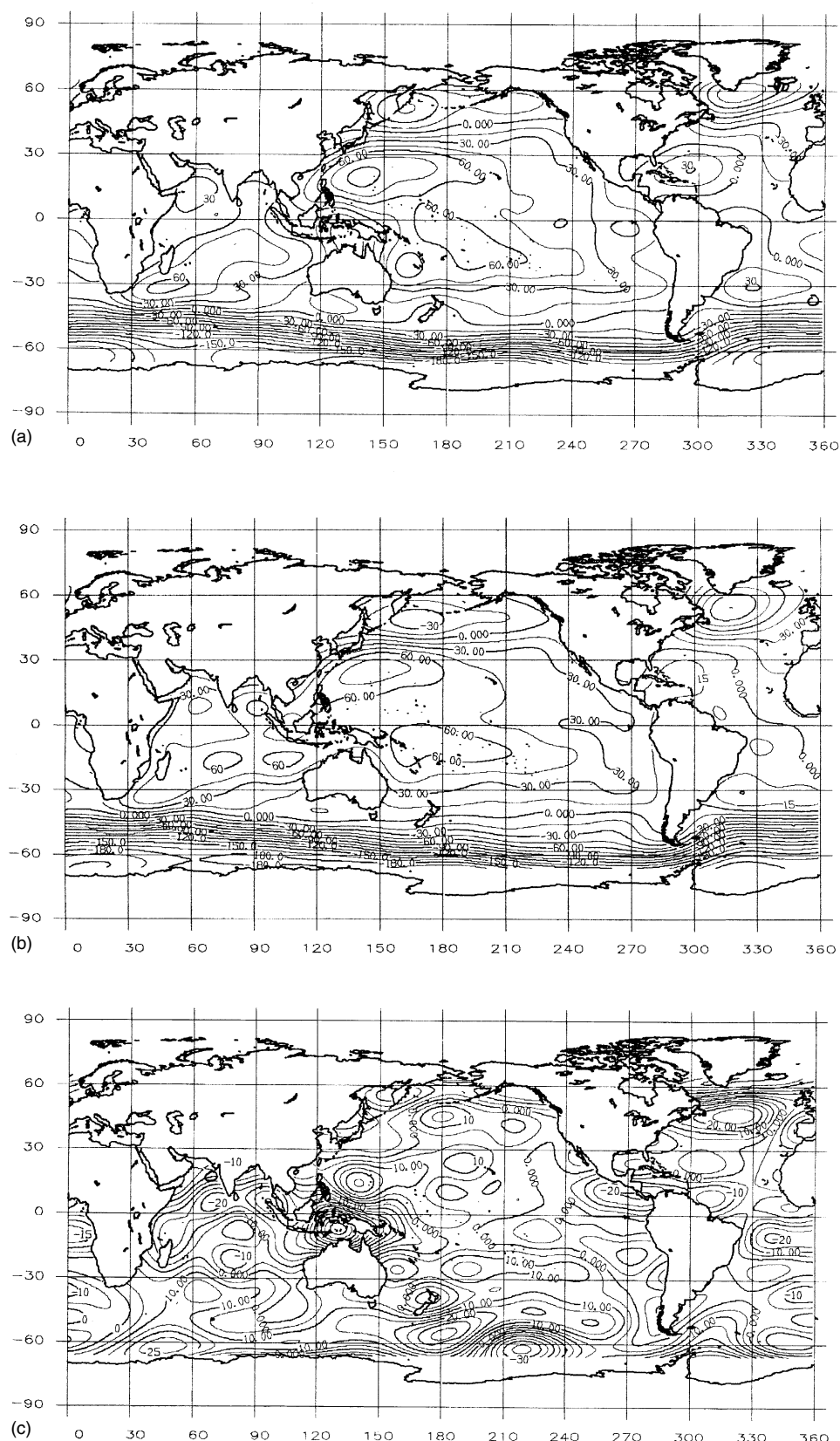


Fig. 3.3.4 (a) Ocean topography estimated from the T/P data from 1993–94 and the JGM-3 geoid. (b) Ocean topography simulated by an ocean general circulation model (POCM_4B) for the same time period. (c) The difference between the top and middle panels ($T/P - POCM_4B$). Contour interval is 10 cm. Adapted from Rapp et al. (1996).

well. For the first time the errors of global ocean models have been assessed against a global data set with a specified error estimate. One should note, however, that the error estimates are approximate and heavily dependent on the geoid errors, which are often not well determined.

The map of the difference between the T/P topography and the model (T/P-model) (Fig. 3.3.4c) reveals a few large discrepancies: -62 cm in the Banda Sea (between Australia and Indonesia and to the east of the Timor Sea); from 36 cm to -37 cm in the South Pacific sector of the Antarctic Circumpolar Current. The large discrepancy in the Banda Sea is puzzling, because the estimated geoid error in the area is only about 8 cm to degree 14. However, there are large high-wavenumber geoid features in the region that are not well modelled and might have aliasing effects on the low-degree representations of the ocean topography (Rapp *et al.*, 1996).

There are indications suggesting that the discrepancies in the Southern Ocean might be caused by problems in the ocean model. The difference between the Semtner and Chervin's model and the model of Smith *et al.* (1992a) denoted as POP (96) in Fig. 3.3.3, shows large values ($20\text{--}30\text{ cm}$) in the same region of the Southern Ocean (Rapp *et al.*, 1996; their Fig. 3.3.2). The rms difference by degree between the two models is also shown in Figure 3.3.3. Although the two models are not totally independent, their difference perhaps reflects a lower bound for the errors in both models. The reader is also referred to Park and Gambéroni (1995) for a regional study of the Indian Ocean sector of the Southern Ocean. They reported agreement between the T/P ocean topography and the simulations by the Fine Resolution Antarctic Model (FRAM Group, 1991) in revealing several gyre-scale circulation patterns that were absent in historical hydrographic data.

The error of the JGM-3 geoid becomes larger than the signal in ocean topography (Fig. 3.3.3) at degrees higher than 14 (corresponding to a wavelength of about 3000 km), where the rms difference between the T/P topography and the model becomes comparable to the signal magnitude. The correlation between the T/P topography and the model drops from the high values of $0.8\text{--}0.9$ at low degrees to below 0.5 at degrees higher than 14. The utility of the JGM-3 model is thus limited to degrees lower than 14. Another slightly more

recent model, called EGM96 (Lemoine *et al.*, 1998), was constructed using a more extensive database than JGM-3. Preliminary assessment suggests that EGM96 has about a-factor-of-two improvement over JGM-3 up to degree 20. With this increased accuracy, the utility of altimetry-derived ocean topography may be extended to degree 18 (Lemoine *et al.*, 1998).

Ganachaud *et al.* (1997) conducted a linear inverse calculation to evaluate whether the T/P ocean topography is useful for improving the estimate of the oceanic general circulation relative to a previous estimate based on historical hydrographic data (Macdonald and Wunsch, 1996). They first found that after certain spatial smoothing (excluding wavelengths shorter than 1600 km), altimetrically determined velocities were consistent with hydrographic estimates within the error bars of each. After this consistency check, they further combined the two estimates using a recursive inverse procedure and obtained a new solution that is fully consistent with both altimetry and hydrography. However, the resulting solution did not reduce the error in the circulation and its associated heat transport in any significant way because the geoid (JGM-3) error was still too large. They further concluded that in order to obtain a geoid model sufficiently accurate to improve upon the hydrographic estimate of ocean topography, specifically designed gravity missions meeting very demanding requirements would be required (also see National Research Council, 1997; Tapley and Kim, 2000). The planned missions such as GRACE and GOCE mentioned in Section 3.3.1 are designed to fulfil these roles.

The study of Ganachaud *et al.* (1997) has provided a particular view of the utility of altimetry through the perspective of a linear inverse calculation based on hydrographic data and geostrophic dynamics (also see LeGrand *et al.*, 1998). One could argue that the prior error estimates assigned to the hydrographic solution might be too optimistic. Given the difference in the sampling (in both space and time) of the circulation between hydrography and altimetry, the combination of the two data sets using a linear inverse model is quite tricky. It is expected that when the continuous global altimetry data are combined with a state-of-the-art general circulation model, one should be able to obtain an optimal estimate of the time-evolving global circulation, from which a

well-sampled, time-averaged general circulation should emerge. As discussed earlier, the errors in the ocean models are generally larger than the altimetric ocean topography at large scales. The combined solution through data assimilation should produce an optimal estimate that is better than the one based on either data or model alone. Such an approach was taken by Stammer *et al.* (1997). Some preliminary results from the study can be found in Wunsch and Stammer (1998). The effects of altimetry on the model simulation are clearly identified. However, it is not yet clear whether such estimates are consistent with the hydrographic estimates as well as other types of observations. The difficulty lies in the determination of the error covariance of the estimates resulting from complex calculations involving highly non-linear general circulation models.

3.3.3 Large-scale sea-level variability

After the tidal signals are removed (including the effects of the solid earth tides), the sea-level variability has a total amplitude of 12 cm (global rms). After making the inverted barometer correction (see discussions below), the amplitude is reduced to about 10 cm (Wunsch and Stammer, 1997). The large scales (wavelength larger than about 500 km) account for about 6–7 cm (Wunsch and Stammer, 1998), while the mesoscales account for about 7–8 cm. As noted in 3.3.1, the large-scale variability was often partly removed in the analysis of altimetry data in order to reduce the large orbit errors present in the data collected by missions flown before T/P. Therefore, the large-scale sea-level variability has not been fully accessible to satellite altimetry until the advent of T/P. The sampling of T/P is particularly suited for resolving large-scale variability. Its 10-day repeat period is able to sample fast-moving equatorial waves as well as barotropic variabilities. The time separation between adjacent tracks, whose longitudinal separation is 315 km at the equator and 220 km at 45° latitude, is only 3 days. Therefore, T/P is able to sample partially large-scale signals even at periods shorter than its 20-day Nyquist period.

Kuragano and Kamachi (2000) investigated the characteristics of spatial and temporal scales of sea-level variability using T/P data. They fitted a

three-dimensional Gaussian model to the observed covariance as a joint function (as opposed to separate functions) in latitudinal, longitudinal and temporal lags. They found that in areas where the mesoscale energy is low, the dominant scales are generally larger than 500 km. At mid- and low latitudes, the large-scale variability is generally anisotropic with larger zonal scales and westward phase propagation, exhibiting the presence of Rossby waves (see Sections 3.3.3.2 and 3.3.3.3). At high latitudes, the large-scale variability becomes more isotropic, perhaps reflecting locally forced response. In areas where the mesoscale energy is high, the large-scale variability becomes obscured without some space-time filtering.

The large-scale variability of sea level is basically caused by the ocean's response to the forcing by the atmosphere. The primary forcing mechanisms include wind stress, pressure, and air-sea exchange of heat and fresh water (Section 3.3.3.1). These are part of the air-sea interaction processes. Large-scale sea-level variability is in fact a key indicator of climate variability. Mostly driven by wind, the large-scale, baroclinic waves are observed extensively by altimetry. They are discussed in terms of the extratropical and tropical regions in Sections 3.3.3.2 and 3.3.3.3, respectively. The relation between large-scale sea-level variability and subsurface fields and motions is discussed in Section 3.3.3.4. The global annual cycle, interannual variability, and global mean-sea-level changes are discussed in Sections 3.3.3.5, 3.3.3.6 and 3.3.3.7, respectively.

3.3.3.1 The ocean's response to the atmosphere

Atmospheric pressure forcing

The response of the ocean to atmospheric pressure forcing has not received the same attention as the response to wind and buoyancy forcing. This is because pressure forcing is a much less effective mechanism for generating oceanic motions. The conventional wisdom is that, to first order, the ocean responds to pressure forcing in a static manner. An increase (decrease) in atmospheric pressure by 1 mbar would depress (raise) sea level by nearly 1 cm. The ocean acts like an 'inverted barometer'. The horizontal gradient of the atmospheric pressure is completely compensated by the adjustment of sea level, leaving no pressure gradient just below the

sea surface. Therefore, there is no geostrophic movement of water associated with the ocean's response. If not corrected for such static response, sea-level data would be very difficult to analyse for studying the variability caused by ocean circulation. The variability of atmospheric pressure has a global rms magnitude of about 7 mbar with a high degree of spatial variability. The resulting inverted barometer (IB) sea-level variations can be as large as 15 cm (rms) in the Southern Ocean where the atmospheric pressure variability is the largest. The 'inverted barometer' correction is thus a very important issue in analysing altimeter data.

How well can the ocean's response be represented by the IB approximation? This subject has recently been reviewed by Wunsch and Stammer (1997). Their conclusion is that an IB response is expected at all frequencies and wavenumbers except those falling on certain dispersion curves, where dynamic response occurs. The dynamic response assumes various forms of gravity and Rossby waves. Resonance is possible depending on the reflecting properties of the ocean bottom and specific geometry of the ocean basin. Analysis of the T/P altimeter data has indeed shown a near IB response in most of the non-tropical regions. Fu and Pihos (1994) performed a regression analysis between T/P sea-level anomalies (computed as deviations from the time mean) and pressure fluctuations. They found that the sea-level response over regions poleward of 30° latitude was weaker than IB with a regression coefficient of -0.84 ± 0.29 (1 standard deviation) cm mbar $^{-1}$. (The minus sign indicates an inverse relationship.) They also performed a multivariate regression analysis to remove the effects of wind forcing, which is correlated to pressure. The result indicated a response much closer to IB at -0.96 ± 0.32 cm mbar $^{-1}$. Their results in the tropics showed a complete breakdown of the IB effect. However, after the removal of the wind effects by using the simulation of a tropical ocean model driven by wind, the sea-level response became IB-like even in the tropics where the pressure forcing is particularly weak.

Gaspar and Ponte (1997) and Ponte and Gaspar (1999) used the T/P cross-over differences within 10-day repeat cycles to investigate the IB effects at high frequencies (primarily at periods of 3–4 days). Outside the tropics, their results were

similar to those of Fu and Pihos (1994), whose study, based on repeat-track analysis, did not filter out any particular frequencies. The high-frequency sea-level response is generally weaker than IB with a regression coefficient about -0.9 cm mbar $^{-1}$. The coefficient dropped to -0.7 cm mbar $^{-1}$ in a number of regions in the Southern Ocean. They were able to simulate the observed relation between sea level and pressure using a numerical model of a homogeneous ocean driven by both wind and pressure. They found that the extratropical sea-level response became much closer to IB if the model was driven only by pressure. Most of the apparent non-IB response in the extratropical regions was due to the wind effects, consistent with the multivariate regression analysis of Fu and Pihos (1994) and the modelling study of Ponte (1994). However, the pressure-driven simulations still revealed significant non-IB response (~ -0.9 cm mbar $^{-1}$) in the Southern Ocean where semi-closed f/H contours occurred and hence provided conditions favourable for resonant response. Another extensive region of pressure-driven non-IB response (from -0.7 to -0.8 cm mbar $^{-1}$) is in the tropics, where the frequency band of free waves is wider than that in the extratropics and is thus more prone to resonant response. However, the atmospheric pressure variability is very small (rms value less than 2 mb) in the tropics and hence the magnitude of the ocean's non-IB response is also extremely small there.

Steric sea-level variability and the heat budget of the ocean

The effects of the ocean's exchange of heat (heating/cooling) and fresh water (evaporation/precipitation) with the atmosphere change the density of the ocean and hence the sea level (the 'steric' effect). The steric variability of sea level is to first order due to the change of the heat content in the ocean on seasonal time scales, with the effects of freshwater exchange (via salinity) playing a secondary role (Gill and Niiler, 1973). Therefore sea-level variability has been used to infer the heat storage in the upper ocean and the rate of heat exchange between the ocean and the atmosphere. Leuliette and Wahr (1999) showed global patterns of the thermal effects on sea level using a coupled-pattern analysis of simultaneous altimeter data and sea-surface-temperature data. However, the

salinity effects on sea level are important in certain regions (Maes, 1998; Sato *et al.*, 2000). On global scales, the contribution of freshwater exchange between the ocean and the atmosphere is discernible in the seasonal variations of the global mean sea level after the thermal effects are removed (Minster *et al.*, 1999).

Steric sea-level variability occurs over the scales of air-sea heat and freshwater exchange, typically on the order of 1000 km and larger. To study the mechanisms of sea-level variability at these scales, it is essential to be able to separate the steric effects from others. To the extent that the steric effect is dominated by temperature, steric sea level, η_s , is simply related to thermal expansion and its change can be computed from air-sea heat flux as follows (Chambers *et al.*, 1997; Stammer, 1997a; Wang and Koblinsky, 1997):

$$\frac{\partial \eta_s}{\partial t} = \frac{\alpha Q}{\rho_0 c_p} \quad (3.3.4)$$

where α is the coefficient of thermal expansion of seawater, c_p is the specific heat, and Q is the net air-sea heat flux anomaly. The knowledge of Q is primarily based on climatology compiled from observations of its various components. Time-varying Q is available only from simulations made by models run by meteorological centres. Using the Q provided by the ECMWF (European Centre for Medium Range Weather Forecasts), Stammer made estimates of the steric component of sea level and compared them with T/P observations. At mid-latitudes the steric sea level accounts for a major portion of the observed sea-level variations (also see Vivier *et al.*, 1999; Ferry *et al.*, 2000). Significant discrepancies are primarily confined to the tropics and subtropics, where the temporal variability of heat flux diminishes and the wind-induced sea-level variability dominates. The steric variability at mid-latitudes is larger in the northern hemisphere than the southern hemisphere by a factor of two, reflecting the contrast between the two hemispheres in the distribution of land mass. The cold air blown from the continents to the warm oceans during winter time is a major contributor to the air-sea heat flux. The lack of land mass in the southern hemisphere leads to less steric variability.

Errors in the model simulation of Q are difficult to estimate. The study of Siefridt (1994) indicates that the errors in the ECMWF heat flux are roughly 20–40 W m^{-2} (also see Ferry *et al.*, 2000),

larger than the signals of heat flux variability in many regions. The errors in the southern hemisphere are probably worse because of the lack of data for constraining the models. In many studies, altimetric observations of sea level have actually been used to estimate the heat flux. White and Tai (1995) computed the correlation between sea-level anomalies (relative to an annual cycle) from T/P and the upper ocean heat storage anomalies from XBTs. The correlation obtained over the globe was 0.5–0.8. Based on the regression analysis, they were able to estimate the interannual changes in heat storage over the global upper ocean (above 400 m) using the T/P data. Although the inferred estimates from altimetry are not as accurate as direct estimates from XBTs, the uniform and frequent global coverage of altimetry leads to globally gridded estimates of heat storage anomalies with sampling errors less than those obtained from the XBT data by a factor of two. When the estimated heat storage anomalies were used to compute the rate of heat storage change integrated over large ocean basins, the errors in the estimated basin-wide air-sea heat flux are only about 2 W m^{-2} , about half those obtained from the XBT analysis. Such errors are comparable to the signals of the seasonal-to-interannual variability of basin-wide air-sea heat flux (e.g. integrated over the entire Pacific), a quantity extremely difficult to measure.

Chambers *et al.* (1997) also made estimates of heat storage and its rate of change using equation (3.3.4) with T/P altimeter data. At interannual time scales, the inferred rates of heat storage change have an error of about $5\text{--}10 \text{ W m}^{-2}$ when compared with the TOGA (the Tropical Ocean and Global Atmosphere Programme) results. When integrated over an ocean basin, the error in the estimate of interannual heat flux change is essentially dictated by the error in estimating the mean-sea-level trends. Based on an error of $2\text{--}3 \text{ mm yr}^{-1}$ for the mean-sea-level trends (Nerem and Mitchum, 2000), their estimates of the error in basin-wide heat flux change determined from T/P altimetry are $1\text{--}1.5 \text{ W m}^{-2}$, comparable to the estimate of White and Tai (1995). Given this uncertainty, Chambers *et al.* (1997) reported that the North Atlantic and the oceans in the southern hemisphere gained heat from the atmosphere at an average rate $0\text{--}3 \text{ W m}^{-2}$ from 1993 to 1995. However, it is difficult to verify this conclusion from independent sources because of the sparse distribution of *in-situ* observations.

When the altimetric estimates of heat storage change are averaged over large ocean basins, the errors caused by non-thermally related sea-level signals tend to be averaged out, leading to a fairly accurate estimate of basin-wide heat flux change. However, such error reduction does not apply to regional analysis. For instance, the effects of heat advection by ocean currents become important in the regions of the Kuroshio Extension and the Gulf Stream. In an effort to investigate the utility of altimetry data for diagnosing the heat budget of the ocean, Qiu and Kelly (1993) used a numerical model of the ocean's mixed layer driven by wind and heat flux with the geostrophic current velocity estimated from GEOSAT observations for estimating the mixed-layer depth and temperature of the Kuroshio Extension region. They found that the advection of heat by the surface flows made a substantial contribution to the local heat balance. The advection warms the upstream region of the Kuroshio Extension while it cools the downstream region due to the presence of the recirculation gyre. Using a similar approach, Kelly and Qiu (1995a,b) ran the mixed-layer model with assimilation of altimeter data and sea surface temperature data for studying the heat balance of the Gulf Stream gyre. Rather than forcing the model with heat flux produced by weather centres, heat flux was estimated as the residual of the heat budget that involved horizontal advection, vertical entrainment, and eddy diffusion. The error in the heat flux estimate ranges from 20 to 100 W m⁻². Based on the heat budget analysis, the seasonal variability of the heat content of the gyre to the south of the Gulf Stream is primarily forced by the air-sea heat flux (also see Wang and Koblinsky, 1996). Within the Gulf Stream and to the north of it, the cooling by the southward Ekman advection of cold water has a tendency to be balanced by the warming of the Gulf Stream. A very complex pattern of air-sea interaction was present in the region, showing coupling between the air-sea heat flux and the wind-driven circulation (also see Kelly *et al.*, 1999).

Wind-forced variability

Wind stress exerts forcing on the ocean over a wide range of spatial and temporal scales. The ocean's response is complicated, involving both local adjustment and propagating waves from remote forcing. The vertical structure of the ocean's

response is a function of the spatial and temporal scales of the forcing. The relation between wind-forced sea-level variability and the internal structure of the oceanic variability is thus scale-dependent.

Outside the tropics, the ocean's response to time-varying wind forcing at large scales is primarily through the vertical motion caused by the convergence/divergence of the Ekman flow in the surface layer driven by the curl of wind stress, the Ekman pumping (e.g. Pedlosky, 1987b). Depending on the spatial and temporal scales of the forcing, the ocean's response has different vertical structures. At spatial scales larger than 1000 km and time scales shorter than 300 days, the ocean's response is primarily barotropic, or depth independent (Willebrand *et al.*, 1980; Koblinsky *et al.*, 1989; Fukumori *et al.*, 1998). Sea level is then a good indicator of the motion of the entire water column and can be described to a large extent by the linear barotropic vorticity equation:

$$\begin{aligned} \frac{\partial}{\partial t} \nabla^2 \eta + \beta \frac{\partial \eta}{\partial x} - \frac{f}{H} \left(\frac{\partial \eta}{\partial x} \frac{\partial H}{\partial y} - \frac{\partial \eta}{\partial y} \frac{\partial H}{\partial x} \right) \\ = \frac{f}{\rho g} \left[\nabla \times \left(\frac{\tau}{H} \right) \right]_z \end{aligned} \quad (3.3.5)$$

where η is the sea-level anomaly, β is the meridional derivative of f ($\beta = 2\Omega \cos \phi / R$, where R is the earth's radius), H is the depth of the ocean bottom, and τ is the wind stress. Fu and Davidson (1995) made an attempt to describe the T/P sea-level observation at periods shorter than one year using equation (3.3.5). They divided the ocean into $10^\circ \times 10^\circ$ boxes and computed the box averages of each term of equation (3.3.5). Small-scale variabilities were averaged out to focus on the large scales. They found that over most of the ocean such computation was too noisy, and that a dynamic balance described by equation (3.3.5) was revealed only in a few regions where the signal-to-noise ratio was significant. These regions are primarily in the central and northeast Pacific and southeast Pacific. Freely propagating barotropic Rossby waves are homogeneous solutions to equation (3.3.5). According to the dispersion relation, the periods of these waves for wavelength larger than 1000 km are generally less than 30 days. These waves are not well resolved by the data and can be a source of the noise in the calculation. Fu *et al.* (2001) presented an example of such waves with a period of 25 days in the Argentine Basin

of the South Atlantic Ocean. These waves are marginally resolved by T/P. At periods longer than 60 days, Vivier *et al.* (1999) showed that a time-dependent Sverdrup relation, represented by equation (3.3.5) without the first term on the right-hand side, was valid in most of the subtropical and subpolar regions of the Pacific Ocean. They filtered out all propagating waves from altimeter data before the analysis.

Large-scale variability in the T/P data at periods less than 100 days was investigated by Fu and Smith (1996) and Chao and Fu (1995) using ocean general circulation models. Geographic distribution of sea-level variance in the period band of 20–100 days is in excellent agreement between model and data (Fig. 3.3.5, see Plate 3.3.5, p. 172). Most of the variance is in the high latitudes and the tropics. While the variance in the tropics is mostly due to baroclinic motion (Fukumori *et al.*, 1998), the variance at the high latitudes is caused

by barotropic motion, as suggested by the high degree of coherence between the model-simulated sea level and barotropic stream function in the period band at high latitudes (Chao and Fu, 1995).

Comparisons of the T/P observation with model simulation in these regions show that the model is able to simulate the sea-level variations with respect to the individual high-frequency events, especially in the North Pacific (Fig. 3.3.6). This indicates that wind is the primary forcing for sea level at these scales, because only wind forcing, as opposed to thermal forcing, which is also applied to the model, can create such variabilities; it takes an accurate wind field to produce faithful simulations of the real events. The relatively poor correlation in the Southern Ocean is probably due to the poor accuracy in the wind forcing due to the scarce data used in the ECMWF analysis. Although the analysis of the observations using a simplified barotropic vorticity equation leads to mixed results,

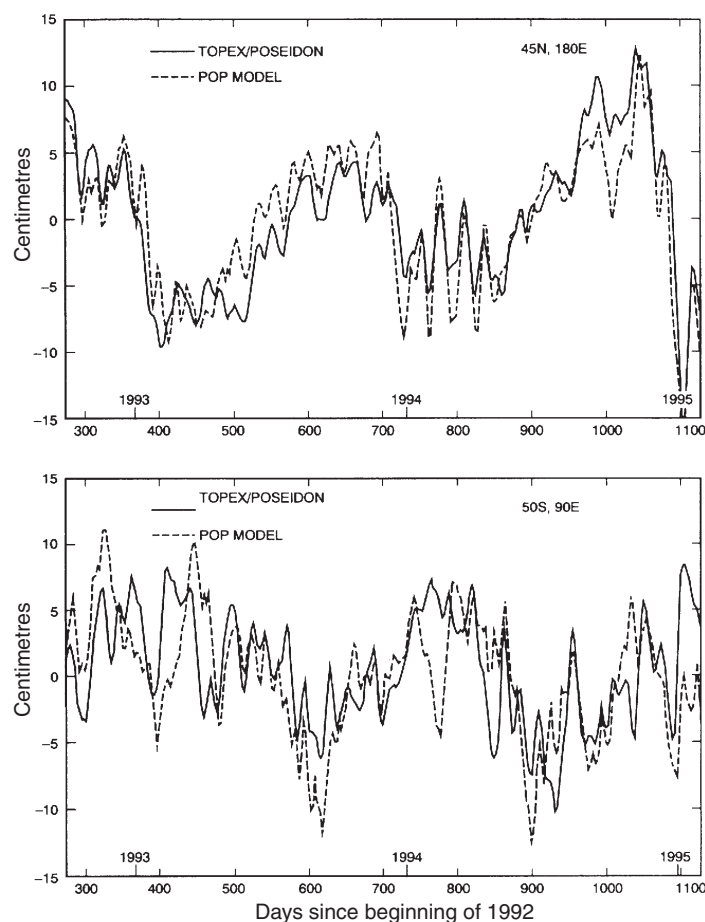


Fig. 3.3.6 Large-scale (> 1000 km) sea-level variations in the central North Pacific ($45^{\circ}\text{N}, 180^{\circ}\text{E}$; top panel) and the South Indian Ocean ($50^{\circ}\text{S}, 90^{\circ}\text{E}$; bottom panel). T/P observations are shown as solid lines and the model simulations (from the same model as in Fig. 3.3.5) as dashed lines. From Fu and Smith (1996).

the general circulation model simulations provide convincing evidence that the large-scale, intraseasonal sea-level variability is largely due to wind-forced barotropic motion of the ocean.

Sea-level variability has significant amount of energy at periods shorter than the repeat period of altimetry (e.g. 10 days for T/P, 17 days for GEOSAT, 35 days for ERS). Fukumori *et al.* (1998) demonstrated that model simulations driven by wind could partially account for these high-frequency barotropic variabilities in the T/P data. Although the 10-day repeat period of T/P was not adequate for resolving the variabilities, Fukumori showed that 12-h sampled model simulations were able to explain more variance of T/P data than 3-day sampled simulations. These high-frequency variabilities, if not removed, would create aliasing problems for studying low-frequency variability using altimetry data. Recent studies of Stammer *et al.* (2000a) and Tierney *et al.* (2000) have suggested that de-aliasing of this kind can be performed using ocean general circulation models forced by accurate wind and atmospheric pressure.

As time scale increases, the ocean's response to wind becomes increasingly baroclinic. This is because the wavelength of barotropic Rossby waves decreases with increasing period. For example, the wavelength is about 100 km for a wave period of 300 days at 45° latitude. The wind forcing has relatively little energy in this frequency/wavenumber band to generate barotropic waves. The minimum period of baroclinic Rossby waves is basically a function of latitude (Gill, 1982). Such period is on the order of 500 days and longer poleward of the 50° latitude, where there is not sufficient wind energy at such long periods (Fukumori *et al.*, 1998, their Fig. 13) to force the baroclinic waves. However, due to the limited duration of available observations, we are not able to address the baroclinic energy at decadal scales when the basin-wide baroclinic adjustment processes become important. On the other hand, the minimum wave period becomes shorter at low latitudes (e.g. 100 days equatorward of 20°), where the wind has substantial energy available in the period band to force the baroclinic waves. Therefore the ocean's baroclinic response to wind forcing is primarily originated at mid- and low latitudes. This response is discussed below in terms of baroclinic waves in the extratropical and tropical regions separately.

3.3.3.2 Extratropical Rossby waves

Westward propagation is a ubiquitous characteristic in a display of sea-level anomalies with a time-longitude section except within the vicinity of the equator (Fig. 3.3.7, see Plate 3.3.7, p. 172). Its interpretation in terms of Rossby waves has been documented in a large body of literature (Fu and Chelton, 2000). Identification of the source of these waves is not easy, but they are to a large extent forced by wind remotely. Because of the variability of the sea surface temperature associated with the waves, local wind could be affected by the waves and becomes coupled to them, leading to an ocean-atmosphere-coupled system (White *et al.*, 1998b).

Many studies were focused on regional analyses in which evidence of Rossby waves was documented and standard theories were invoked to interpret the observations (White *et al.*, 1990a; Kelly *et al.*, 1993; Le Traon and Minster, 1993; van Woert and Price, 1993). A systematic search for Rossby waves was conducted by Jacobs *et al.* (1993) in the Pacific Ocean. They fitted the GEOSAT sea surface height anomalies to a set of waves with wavenumbers and frequencies obeying a quasigeostrophic Rossby wave dispersion relation. Such fitting was performed using a least-squares technique in $10^\circ \times 10^\circ$ boxes. They found evidence for the generation of baroclinic waves along the eastern boundaries and the so-called β refraction along the path of westward propagation into the ocean interior. The β refraction is caused by the fact that the wave's zonal phase speed is faster at low latitudes than at high latitudes due to the latitudinal dependence of β ($\equiv df/dy$). The propagation direction of the waves is thus changing with latitude.

Polito and Cornillon (1997) conducted a basin-wide survey in the North Atlantic using T/P data. They estimated the phase speed of Rossby wave propagation in two period bands centred on the annual and semiannual periods. The westward phase speeds were found to increase equatorward as predicted by theory (also see Nerem *et al.*, 1994). The wavelengths range from 400 to 4600 km for the annual band and 270 to 2500 km for the semiannual band. The wave amplitudes in the annual band (2–12 cm) are larger than those in the semiannual band (1–4 cm). They also reported evidence for remote generation of the waves at the eastern boundary by fluctuating wind stress curl and the interaction of the waves with the Mid Atlantic Ridge.

Chelton and Schlax (1996) conducted a global analysis of the properties of Rossby waves detected by T/P. They also showed evidence of the β refraction: after leaving the eastern boundary, wavefronts travel faster at low latitudes than at high latitudes due to the latitudinal dependence of β , creating an arc of wavefront with the leading edge at low latitudes and the trailing edge at high latitudes. The waves are apparently amplified when passing over mid-ocean topographic features. The westward phase speeds in the extratropical regions poleward of 10° latitude were found to be systematically higher than the prediction of standard theory (Pedlosky, 1987b). The deviation from standard theory increases with latitude (Fig. 3.3.8). Such findings are consistent with simulations by the state-of-the-art ocean general circulation models (Fu and Chelton, 2000). Killworth *et al.* (1997) showed analytically that the discrepancy is mainly due to the modification of the mean potential vorticity field by a vertically sheared mean flow. Qiu *et al.* (1997) reported that the apparent increase in the westward phase speed could also be explained as the simultaneous existence of locally forced waves and remotely forced waves that were subject to eddy dissipation. However, the analysis methods of Chelton and Schlax (1996) have ruled out the theory of Qiu *et al.* (1997) as a plausible explanation for the observed fast Rossby wave phase speeds (Fu and Chelton, 2000).

By analysing the frequency-wavenumber spectrum computed from the T/P data, Zang and Wunsch (1999) compared the wavenumbers of the peak energy in each frequency band with the dispersion relation of linear Rossby waves. They found that at the lowest wavenumbers (wavelengths longer than 1000 km) and frequencies (periods longer than 200 days), the dispersion relation is not distinguishable from that of the linear first mode baroclinic Rossby waves. At larger wavenumbers, however, the corresponding frequencies are generally higher than the dispersion relation allows, thus leading to a phase speed larger than the prediction of the standard linear theory. Such energy might be a combination of free waves, forced waves and non-linear eddies. If all these components are lumped together, one would obtain an apparent phase speed that is larger than the prediction of the standard linear theory.

White *et al.* (1998b) investigated the properties of Rossby waves with a biannual period in the

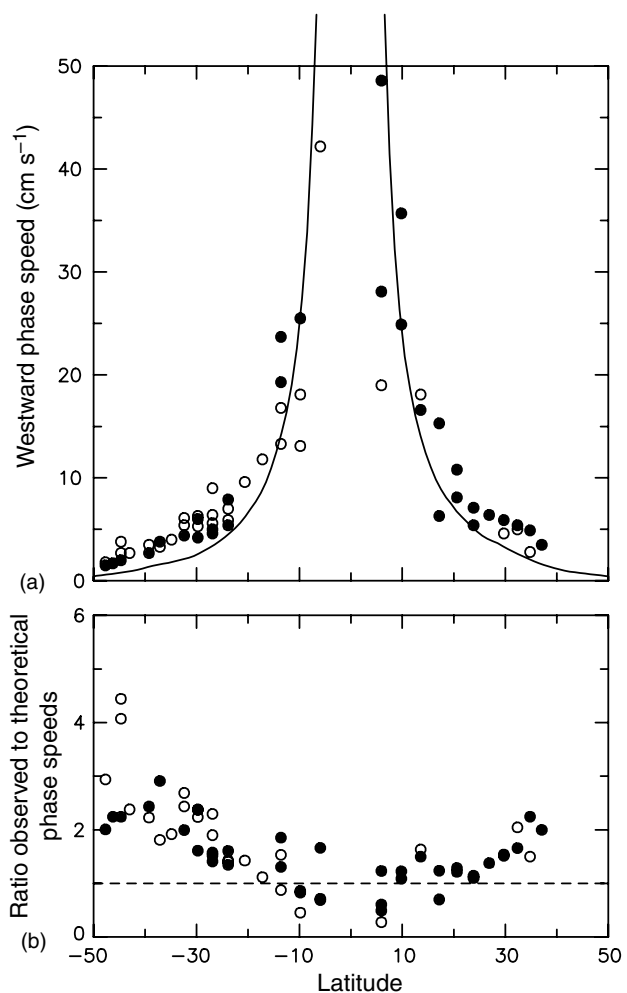


Fig. 3.3.8 (a) Globally distributed estimates of the phase speeds (versus latitude) of westward-propagating sea-level signals estimated from T/P data. The solid circles correspond to Pacific estimates, and the open circles correspond to Atlantic and Indian Ocean estimates. The solid line represents the prediction of the standard theory for linear, non-dispersive, freely propagating, first mode baroclinic Rossby waves. (b) Ratio of the observed phase speeds to the phase speeds predicted by the theory. From Chelton and Schlax (1996).

Pacific Ocean. They analysed simultaneous observations of sea surface height, temperature, and wind and found that the evolution of these fields can be described by a theory of ocean-atmosphere-coupled waves. The phase relationships among these observations are consistent with the following scenario: the meridional advection of heat by the oceanic flows associated with the waves is balanced by the heat exchange with the atmosphere; the meridional wind anomalies are induced by a balance of the advection of the atmospheric planetary vorticity by the wind and the low-level

convergence induced by the sea surface temperature anomalies. Such waves are self-sustaining and propagating westward with a phase speed higher than that of standard linear free Rossby waves. The discrepancy between the observed phase speed from the standard Rossby wave theory can be largely accounted for by the coupled theory. The results of White *et al.* (1998b) should be viewed with the caveat that only 2 years of data were used to study a biannual phenomenon. The theory needs to be re-examined using longer data records, which are now readily available.

An interesting scenario for the generation of mid-latitude Rossby waves was demonstrated by Jacobs *et al.* (1994). By using GEOSAT data and an ocean general circulation model, they showed that ENSO-induced perturbations in the tropics could propagate poleward along the ocean's eastern boundaries as coastal trapped waves. These waves tend to evolve into Rossby waves and transmit the effects of ENSO into the mid-latitude oceanic interiors. Such tropics-extratropics connection is an important factor affecting the long-term climate variability.

3.3.3.3 Tropical Kelvin and Rossby waves

Large-scale low-frequency oceanic waves play a key role in the dynamics of the tropical ocean and its interaction with the atmosphere. These waves are essentially driven by winds, but the overlying winds are also affected by the waves through air-sea coupling mechanisms. The interplay of baroclinic Kelvin waves and Rossby waves has been proposed to be an important mechanism for sustaining the semioscillatory behaviour of ENSO in the delayed-action-oscillator theory (Battisti, 1988; Schopf and Suarez, 1988). Altimetry data provide a basin-wide perspective to test the validity of the theory. The early studies with the GEOSAT data (Delcroix *et al.*, 1991; du Penhoat *et al.*, 1992) clearly showed the important roles of the Kelvin and Rossby waves in the 1986–87 El Niño and the 1988–89 La Niña. White *et al.* (1990b) reported evidence for the reflection of equatorial Rossby waves into eastward Kelvin waves at the western boundary of the tropical Pacific, a key requirement for the delayed-action-oscillator theory. By projecting sea-level anomalies into Kelvin and Rossby wave components, Boulanger and Fu (1996) showed persistent reflection of Kelvin waves into Rossby waves at the eastern boundary of the Pacific in

1993–95, while the reflection of Rossby waves at the western boundary was relatively intermittent. They also suggested that the reflection of Rossby waves played a role in the onset of the warming of 1994–95.

Using a longer record of T/P data, Boulanger and Menkes (1999) repeated the calculation of Boulanger and Fu (1996) to study the properties of the equatorial Rossby and Kelvin waves from October 1992 to May 1998. Shown in Fig. 3.3.9 are longitude–time plots of the Kelvin and the first mode Rossby wave coefficients. Near the western boundary, the Kelvin waves generated by the reflection of Rossby waves were highly damped and rarely propagated past the dateline. Most of the Kelvin waves east of the dateline were forced by west wind bursts west of the dateline. In late 1997 during the peak of the 1997–98 El Niño, however, the strong upwelling Rossby waves (negative sea-level anomalies) originated east of the dateline created strong reflected Kelvin waves at the western boundary. These reflected upwelling Kelvin waves worked against the locally forced downwelling Kelvin waves and eventually passed the dateline and reversed the sea-level anomalies all the way to about 100°W, leading to the demise of El Niño in May 1998. The Rossby wave reflection into Kelvin waves seems to have played a significant role in the termination of El Niño, consistent with the delayed-action-oscillator theory. Near the eastern boundary, reflection of Kelvin waves into the first mode Rossby waves is quite persistent. The reflected Rossby waves produce anomalously westward surface currents that tend to slow down the eastward progression of the eastern edge of the warm pool of El Niño. These waves are thus an impediment to the growth of El Niño, consistent with the conceptual model of Picaut *et al.* (1997).

3.3.3.4 The relation between sea level and subsurface variability

As noted earlier, a major advantage of altimetry over other ocean remote sensing is the relation between observed sea level and subsurface fields. From the discussions in the preceding sections on the various mechanisms of sea-level variations, it is clear that sea-level variations reflect changes in subsurface fields due to thermal and mechanical processes. Except for steric change of sea level due to buoyancy forcing, large-scale sea-level variability

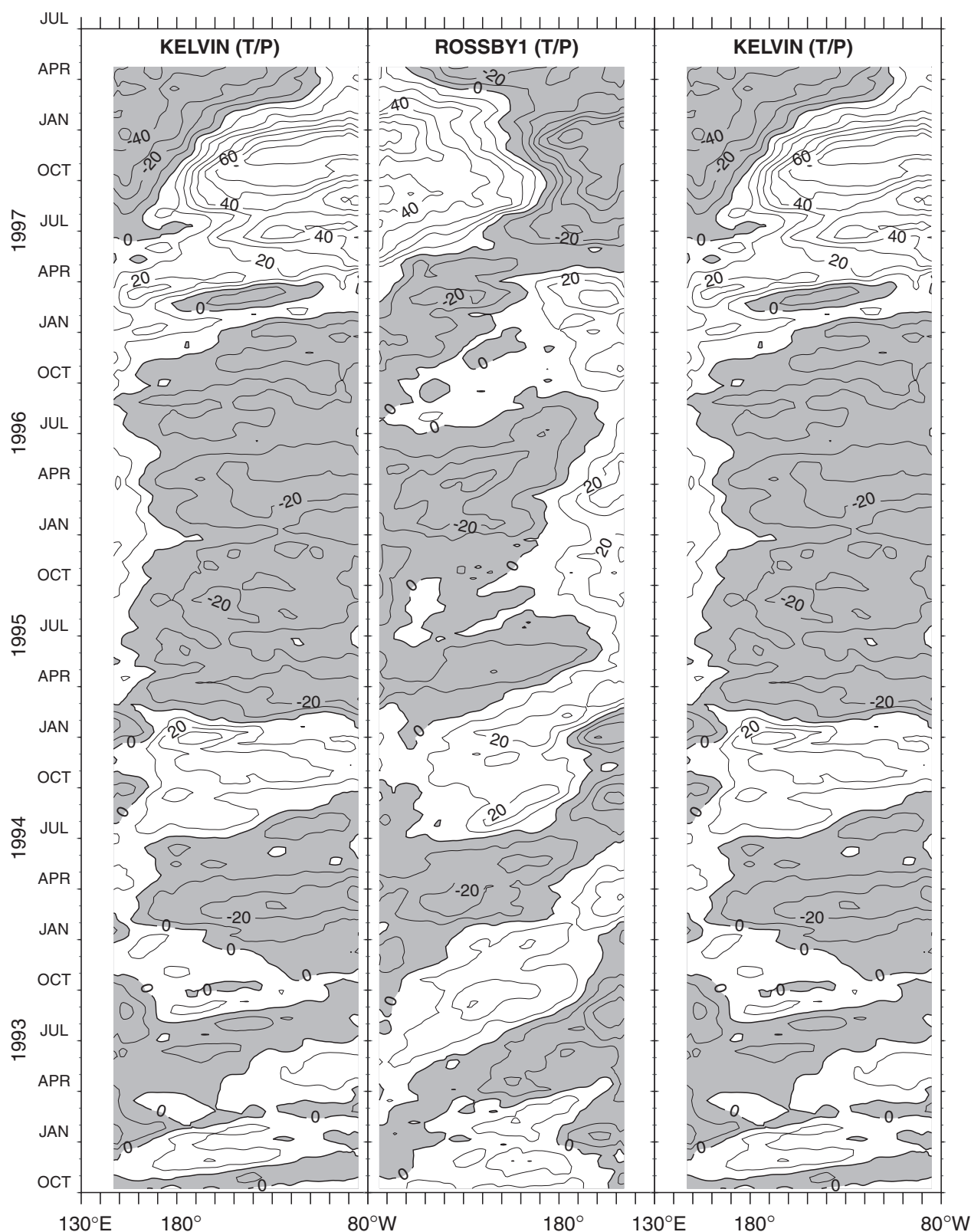


Fig. 3.3.9 Longitude-time sections of the projections of T/P observed sea-level anomalies onto Kelvin waves (left panel), and the first meridional mode Rossby waves (middle panel; the direction of longitude is reversed to facilitate the visualization of wave reflections at the eastern boundary of the ocean). The Kelvin wave component is repeated in the right panel for visualizing the wave reflections at the western boundary. The units are arbitrary. Negative anomalies are shaded. From Boulanger and Menkes (1999).

is predominantly caused by adiabatic, mechanical forcing and thus has a tight relation with subsurface variability as part of an organized motion field of the water column. For the barotropic mode, the surface geostrophic velocity determined from sea-level variability through equation (3.3.3) represents the uniform horizontal velocity of the entire water column. For the baroclinic mode, sea-level change is related to the change in the height of the subsurface constant-density surfaces, the isopycnals. Therefore, sea level has been used to estimate subsurface density field, from which horizontal geostrophic velocity at depths has also been estimated.

Carnes *et al.* (1990) used GEOSAT altimeter data to estimate the subsurface temperature field in the Gulf Stream area. They applied statistical regression analysis to a set of AXBT (Air-dropped expendable bathythermograph) data deployed along the GEOSAT ground tracks and derived an empirical relation between subsurface temperature and surface dynamic height. They then applied the empirical relation to the GEOSAT altimeter data for estimating the subsurface temperature field. They used the ocean topography derived from the altimeter data relative to a geoid model as a surrogate for the dynamic height. The rms difference between the GEOSAT-derived ocean topography and the dynamic height is 15–19 cm, mostly reflecting the geoid errors and the GEOSAT altimeter measurement errors. The resulting temperature estimates have an rms error of about 1°C below 200 m. The error increases to 2°C near the surface, where there is significant change in temperature due to the annual cycle of heat exchange with the atmosphere. The thermally driven variability of temperature as a function of depth does not have a tight relation with the sea-level variability.

Using T/P data with a series of repeating transects (repeat every 3 months) of XBT and XCTD (Expendable Conductivity and Temperature profiler) across the North Pacific Ocean (from Taiwan through Guam to San Francisco), Gilson *et al.* (1998) studied the relationship between altimetric sea-level measurements and the subsurface temperature and currents. A total of 5 years of simultaneous *in-situ* and satellite data were analysed, allowing the relation between the two data sets to be examined over a wide range of spatial and temporal scales. The anomalies of the altimetric sea level relative to a 5-year mean were compared

with the anomalies of the dynamic height computed from the *in-situ* data relative to the same 5-year mean. The altimeter data were interpolated to the times and locations of the *in-situ* observations using an objective analysis scheme. The overall rms difference between the two anomaly fields is 5.2 cm. At wavelengths longer than 500 km, where lies 65% of the variance of the dynamic height, the two are highly coherent (0.89) with an rms difference of 3.5 cm. This difference is consistent with the measurement errors of T/P (Chelton *et al.*, 2000) and the errors in the dynamic height estimates, plus the residual dynamic height variability below 800 m, which is the deepest level of the XBT observations. At wavelengths shorter than 500 km, the coarse spacing of the T/P ground tracks led to the underestimation of the mesoscale variability, which, however, was well sampled by the *in-situ* data. The correlation between the two decreased to 0.56 at these scales.

From analysing the XBT/XCTD data, Gilson *et al.* (1998) found that, except for the annual variations, the dynamic height anomalies were largely caused by the vertical motion of the thermocline. The entire thermocline moved coherently in the vertical, causing the temperature at the thermocline depths to be highly correlated with the surface dynamic height but with an opposite sign. The high correlation between the altimetric sea-level anomaly and the surface dynamic height anomaly discussed above thus allows the use of the former to make estimates of the subsurface temperature anomaly. The correlation between the dynamic height and the subsurface temperature was derived after the annual cycle was removed from both fields. This is because the annual temperature change in the extratropical regions is primarily caused by the heat exchange with the atmosphere instead of the vertical motion of the isopycnals. The vertical distribution of the temperature change at the annual period is thus not highly correlated with the surface dynamic height, except for the tropics where the annual cycle is wind-driven (see Section 3.3.3.5) and hence the correlation between dynamic height and temperature is high. Therefore, Gilson *et al.* (1998) used the altimeter data only to estimate the subsurface temperature anomaly at non-annual time scales. The temperature anomalies derived from the altimeter data were added to the mean and the annual cycle determined from the *in-situ* data to obtain

the absolute temperature field. Such temperature estimates were able to account for 53% of the total variance, with a maximum rms error of 0.7°C at depths of 80–160 m in the central basin. The error increases to 1°C in the thermocline at both the eastern and western ends of the basin. Improvement of such estimates is expected from a longer data set that will allow increased signal-to-noise ratio and more accurate regression analysis.

Gilson *et al.* (1998) also estimated the specific volume anomaly at depths from the altimetric sea-level anomaly. With the vertical profiles of specific volume anomaly determined, they then computed the basin-wide meridional volume and temperature transports of the upper 800 m. They compared the altimetrically determined transports with those computed from the *in-situ* data and found reasonable agreement. The study of Gilson *et al.* (1998) has thus demonstrated the utility of combined use of altimeter data with *in-situ* data for making estimates of basin-wide subsurface fields and transports that are of importance to the study of climate. The potential of this combination has motivated plans for deploying a network of floats in the ocean to complement future altimetry missions (The programme is called Argo, see Wilson, 2000.) More discussions on the use of altimeter data for estimating the transports of ocean currents will be given in Section 3.3.4.3. The correlation between sea-level variability and subsurface variability makes satellite altimetry a powerful tool for a global observing system. A more effective approach to the estimation of subsurface variability from altimeter data has been provided by the use of an ocean general circulation model through the techniques of data assimilation (Fukumori, 2000). Stammer *et al.* (1997b) applied an adjoint method to a coarse-resolution ocean general circulation model ($2^\circ \times 2^\circ$, 20 vertical levels) for assimilation of T/P data along with other observations in the determination of the entire state of the ocean. They showed the impact of altimeter data on improving the meridional heat transport of the ocean. Fukumori *et al.* (1999) applied an approximate Kalman filter to a similar coarse-resolution model and showed improved estimates of subsurface temperature and velocity.

3.3.3.5 The annual cycle

The annual cycle is a major component of the large-scale variability over most of the ocean. It is

caused by a combination of many different processes and hence exhibits a very complicated geographic pattern in its amplitude and phase. Owing to its dense spatial coverage, satellite altimetry provides the first detailed description of this complicated pattern. Jacobs *et al.* (1992) presented the first results of the global ocean annual cycle from altimetry using the GEOSAT data. The analysis was complicated by large tidal and orbital errors in the data. Although ingenious methods were applied to remove these errors, the results inevitably suffer from the residual errors because both the signals and errors have similar large scales. Using the more accurate data from T/P, Stammer (1997a) computed the amplitude and phase of an annual harmonic fit to 3 years of data (1993–95, Fig. 3.3.10, see Plate 3.3.10, p. 172). Also shown are the steric component and the residual sea level. As discussed in Section 3.3.3.1, p. 148, a major portion of the annual cycle at mid-latitudes is due to steric effect with opposite phase between the two hemispheres. The larger amplitude in the northern hemisphere is clearly revealed. However, this hemispheric asymmetry was not shown in the GEOSAT result, probably due to the effect of the orbit-error-removal procedure applied to the data. In fact, the annual cycle at mid-latitudes away from the western boundary currents was mostly absent in Jacobs *et al.* (1992).

At high latitudes, where air-sea heat flux has the largest annual variability, the sea-level annual cycle is actually less than that at mid-latitudes. This is because the coefficient of heat expansion becomes smaller when the water gets colder. The coefficient at high latitudes is about only 1/3 of its value at low latitudes. In the high-latitude Southern Ocean, there is a sharp change in the phase of the annual cycle, roughly within 50–60°S where the Antarctic Circumpolar Current (ACC) flows. The annual sea-level maximum occurs in March–April to the north and in August–September to the south. This front of phase change is consistent with the GEOSAT study of Chelton *et al.* (1990) in which the annual cycle accounts for the first empirical orthogonal mode. After the steric component is removed, the phase of the wind-forced residual variability in the Southern Ocean (Fig. 3.3.10f, see Plate 3.3.10f, p. 172) has a maximum in August–October when the wind is the strongest. It is therefore apparent that the annual cycle to the north of the ACC is dominated by the

buoyancy forcing (with a maximum in March–April, see Fig. 3.3.10c; Plate 3.3.10c, p. 172), whereas to the south of the ACC, it is dominated by the wind forcing.

After the removal of the steric component, the residual annual cycle is prominent in the tropics, where the seasonal wind forcing is the main driver of the annual cycle. The annual cycle in the Pacific has two bands of high amplitude: one along 5–7°N and the other along 12–15°N. The former is associated with the annual variation of the North Equatorial Countercurrent which reaches its maximum around September–November. A westward phase propagation is observed across the current; the month of maximum sea level changes from September in the eastern part of the current to November in the western part. This phase pattern is consistent with the explanations of Meyers (1979) in terms of wind-driven Rossby waves. The variability along 12–15°N is indicative of the annual variations of the North Equatorial Current. Westward phase propagation is observed only in the eastern part of the current. There is little phase propagation in the western part, where Meyers' study suggested the existence of a near in-phase relationship between sea level and wind stress curl (also see Vivier *et al.*, 1999). The maximum in the Atlantic (along 5–7°N) is associated with the Atlantic North Equatorial Countercurrent with a phase similar to its Pacific counterpart (Richardson and Reverdin, 1987). Previous studies of the Indian Ocean (Woodbury *et al.*, 1989; Perigaud and Delecluse, 1992) suggested that the annual cycle in the southern tropical Indian Ocean was associated with Rossby waves driven by the annual cycle of trade winds (also see Masumoto and Meyers, 1998). It is also interesting to note the 180° phase change across the Arabian Sea, representing the ocean's response to the annual monsoon wind cycle during its two opposite phases (Bruce *et al.*, 1994). Significant semiannual signals are found in the Indian Ocean (Jacobs *et al.*, 1992; Basu *et al.*, 2000), as well as the central equatorial Pacific and the southwest Atlantic.

The ability of numerical models to simulate the oceanic annual cycle is an important test of the usefulness of the model for climate studies, because the annual cycle is the result of the complicated interaction between the ocean and the atmosphere. Comparisons of ocean general circulation models with the T/P altimeter data have revealed the

strengths and weaknesses of the models (Fu and Smith, 1996; Jacobs *et al.*, 1996; Stammer *et al.*, 1996). In general the models have good skills in reproducing the wind-driven component of the variability, but not the steric component. The model-simulated amplitude at mid-latitudes where the steric component dominates the annual cycle is generally too weak (by as much as 3 cm), reflecting possible problems in the model's mixing mechanism and/or the poor quality of heat flux data driving the model. Although the error in the ECMWF heat flux could cause an error of 2 cm in the annual cycle (Stammer *et al.*, 1996), there is no evidence for a systematic low bias in the ECMWF heat flux. The major culprit should be the model's lack of a good mixed layer. Li *et al.* (2000) demonstrated that the use of a state-of-the-art mixing scheme significantly improved the simulation of the annual cycle by an ocean model.

3.3.3.6 Interannual variability

It is well known that the oceanic frequency spectrum is 'red' with the background spectral level ever increasing with decreasing frequency, except for peaks such as the annual cycle. There is substantial variability at periods longer than the annual period. The relatively short record of altimetry allows one to study only the interannual scales (between a year and a decade). Shown in Fig. 3.3.11 (see Plate 3.3.11, p. 172) are the yearly-averaged sea-level anomalies computed from the T/P data for 1996–99. The anomalies were relative to a 4-year mean computed from the data covering 1993–96. The 4-year period of 1993–96 has a weak warm event (1994–95) and a weak cold event (1996) and is thus considered a reasonable period for computing a mean somewhat close to the norm. The yearly averaging has filtered out the annual cycle and other high-frequency signals. The resulting yearly anomalies thus reveal primarily the variability on time scales longer than a year. However, the mesoscale variability is still visible in many places after the averaging, especially along the Indian Ocean sector of the ACC as well as in the Brazil/Malvinas Confluence region of the South Atlantic. The large-scale features clearly illustrate the effects of the dramatic 1997–98 El Niño and its transition into La Niña in 1998–99. The high sea levels in the western Pacific and the eastern Indian Ocean in 1996 set the build-up stage for El Niño, during which the tropical Pacific Ocean and

the Indian Ocean exhibit large-scale changes, with elevated sea levels in the eastern Pacific Ocean (the maximum reached over 30 cm in December 1997) and the western Indian Ocean.

Chambers *et al.* (1999) computed the empirical orthogonal functions for the T/P data during 1992–98 after removing an annual and a semi-annual sinusoid as well as a linear trend. They found that the ENSO-related variability (appearing as the leading mode) in the Indian and Pacific Oceans are highly correlated with no significant phase lags. They also demonstrated that the wind anomalies in the western tropical Pacific and the eastern Indian Ocean were significantly correlated with each other and opposite in direction. As the wind anomalies (westerly anomaly in the western Pacific and easterly anomaly in the eastern Indian Ocean) became intensified during the initial phase of the 1997–98 El Niño, downwelling (thermocline depressed/sea level elevated) Kelvin waves started propagating eastward in the Pacific, whereas downwelling Rossby waves started propagating westward in the Indian Ocean. Such processes led to the buildup of the high sea levels in the western Indian Ocean and the eastern Pacific Ocean during the peak of El Niño. Refer to Section 3.3.3.3 for the roles of the Kelvin and Rossby waves in the formation of El Niño in the Pacific.

After El Niño evolved into La Niña in mid-1998, the entire North Pacific Ocean became progressively abnormal. In 1999, the western part of the basin was characterized by a large pool of high sea level north of New Guinea and west of the Philippines, as well as by a series of bands of high sea level extending from the western boundary of the basin to the central basin from subtropical to high latitudes. The two bands of high sea level emanating from east of Japan are most notable. The eastern part of the basin exhibits low sea levels from the Gulf of Alaska to the southern tip of Baja California. This strip of low sea level connects to the huge pool of low sea level associated with La Niña in the central equatorial Pacific. This pattern of sea-level change has drawn significant attention from the climate research community, because it bears a strong resemblance to a phase of ENSO-like, long-term variability of the Pacific Ocean (Zhang *et al.*, 1997). The record is obviously too short to lead to any conclusions, but something apparently very interesting has been occurring in the Pacific Ocean.

The 1997–99 ENSO event is probably the most intensively observed to date in comparison with previous events. Satellite altimetry has played a significant role in providing a unique global perspective to complement *in-situ* observations, which are mostly concentrated in the equatorial regions. In fact, T/P data have been incorporated into the data stream used by NOAA's National Center for Environment Prediction for short-term climate forecast. The merits of altimeter data in improving the skills of prediction models have been demonstrated in hindcast experiments and reported in Ji *et al.* (2000).

There is evidence that ENSO also affects the remote Southern Ocean (Peterson and White, 1998) via the so-called Antarctic Circumpolar Wave, which is an eastward ocean–atmosphere-coupled wave circling around Antarctica. This wave is originated in the western subtropical South Pacific Ocean due to ENSO activities. This wave creates a slow oceanic teleconnection mechanism that spreads the influence of ENSO to other ocean basins 6–8 years later. Jacobs and Mitchell (1996) showed earlier evidence of such a wave in the relatively short GEOSAT altimeter data. Using the much longer record of T/P data, W. White (personal communication) found clear evidence of this wave pattern.

The long duration and high accuracy of the T/P data record have created opportunities to study the interaction of variabilities of different spatial and temporal scales. A number of studies have showed evidence of transfer of energy between eddy and gyre scales. The seasonal and interannual variability of gyres, boundary currents, and their associated eddy fields is apparently linked to the exchange of energy among them. The readers are referred to Sections 3.3.4.4 and 3.3.4.6 for a discussion.

3.3.3.7 Global mean-sea-level change

Sea-level variability at the largest scale is the variation of the global mean sea level. There is a high level of interest in mean-sea-level change because it is a clear indicator of the consequence of global warming through the melting of polar ice and mountain glaciers as well as the thermal expansion of seawater. Estimation of mean-sea-level change in the past was based on tide gauge observations (Douglas, 1991). However, the sparse distribution of tide gauges presents a serious sampling problem that requires long averaging time to reduce the sampling errors. The global coverage of altimetry

thus provides an attractive approach to measuring the mean-sea-level change. However, the small signal ($\sim 1 \text{ mm yr}^{-1}$) presents a formidable challenge to the capability of altimetry measurement system. All the attempts at estimating mean sea level using altimetry data collected before T/P basically testified the degree of difficulty of the problem (Born *et al.*, 1986; Wagner and Cheney, 1992).

After the demonstration of the much improved measurement accuracy of T/P, it became tantalizing to tackle the problem of mean sea level using the T/P data. The first attempt (Nerem, 1995) actually triggered the discovery of a software error in the data processing system, which had caused an erroneous large sea-level rise in the calculation. This problem was first revealed by comparison with tide gauge observations (Nerem *et al.*, 1997; Mitchum, 1998), as well as intercomparison between the two altimeters onboard T/P. This experience has further demonstrated the importance of independent calibration of altimetry measurement. Mitchum (1998) calculated the difference in sea-level measurements between T/P and nearby tide gauges. Such calculation was performed at nearly 100 tide gauges and a global mean of the differences was then obtained and used to calibrate out any drifts in the altimetry measurement of global mean sea level. Shown in Fig. 3.3.12 is the time series of the mean sea level estimated from the tide-gauge calibrated T/P data (with the record mean, the annual and semiannual

components removed), along with a time series of the global mean sea surface temperature since 1982 (from Nerem and Mitchum, 2000). The agreement in the pattern of variability during the overlap of the two records is quite good. The linear trend in sea level is estimated to be $2.5 \pm 1.3 \text{ mm yr}^{-1}$, with the error being dominated by the calibration error due to land motions of the tide gauges.

Mitchum (1997) demonstrated that a carefully selected network of about 30 tide gauges equipped with precision GPS receivers for detecting land motions would provide calibration for altimetry with a similar accuracy (1 mm yr^{-1} for a 3-year record; 0.2 mm yr^{-1} for a 10-year record) compared with the 100 gauges with poorly known land motions. However, as illustrated by Fig. 3.3.12, mean sea-level variations have significant interannual components. Both sea level and sea surface temperature show the effects of the 1997–98 ENSO event. Nerem and Mitchum (2000) conducted simulations that took into account the interannual variabilities and showed that it would take a 10-year record from T/P-class altimetry to detect a linear trend in sea level with an accuracy of 0.5 mm yr^{-1} , and a 30-year record to detect an acceleration in sea level with an accuracy of 0.02 mm yr^{-2} .

Returning to Fig. 3.3.12, the agreement between mean sea level and mean sea surface temperature suggests that the sea-level change is to a large extent due to the thermal expansion of seawater at

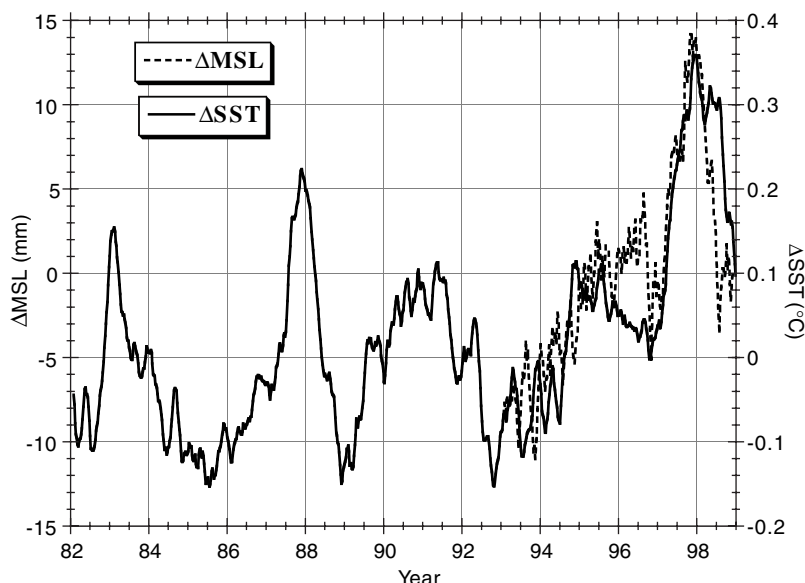


Fig. 3.3.12 Comparison of variations in global mean sea level (dashed) with global mean sea surface temperature (solid), after removing the annual and semiannual variations. From Nerem and Mitchum (2000).

interannual time scales (also see Leuliette and Wahr, 1999). The figure indicates that the ocean's heat storage increased during the 1997–98 El Niño. Nerem and Mitchum (2000) also computed the global mean total water vapour content using the radiometer measurement from T/P. They found that the water vapour content was highly correlated with the mean sea level (correlation coefficient of 0.9 with zero lag). This finding, coupled with the observation of decreased outgoing long-wave radiation during El Niño (Wong *et al.*, 1998), provides supporting evidence for the extra heat storage of the ocean during El Niño. Nerem *et al.* (1999) also showed the simulation of mean-sea-level change during the 1997–98 El Niño by an ocean general circulation model forced by wind and sea surface temperature. Their results indicated that most of the extra heat was stored in the upper 200 m of the ocean.

Using T/P and ERS-1 data, Minster *et al.* (1999) studied the effects of the earth's hydrological cycle on the annual variation of the global mean sea level. They removed steric effects estimated from climatology and found that the remaining signal had an amplitude close to 1 cm with a maximum in mid-September. This signal is due to the annual change of the mass of the ocean. This finding is consistent with the annual variation of water mass in the atmosphere and the land. On seasonal time scales, the hydrological cycle actually has a larger effect on global mean sea level than the steric effect, which is responsible for an amplitude of only 0.5 cm with a maximum in early March.

3.3.4 Currents and eddies

The sampling capability of a single altimeter is a tradeoff between spatial and temporal resolutions. Although the instrument makes high-resolution (6–7 km) sampling along its ground tracks, the spacing between adjacent ground tracks is hundreds of kilometres, depending on the orbit repeat period. The two-dimensional structures of currents and eddies are thus often not well mapped by satellite altimetry (Greenslade *et al.*, 1997; Le Traon and Dibarboire, 1999). However, the systematic along-track sampling of the global mesoscale variability by satellite altimetry has made a profound impact on the understanding of the dynamics of currents and eddies. The first demonstration of the potential of satellite altimetry was due to Cheney

et al. (1983). The qualitative features of the distribution of global mesoscale variability was revealed by using only 24 days' worth of SEASAT data. The cross-track resolution of SEASAT was very coarse (longitudinal cross-track spacing of 930 km at the equator) due to its short 3-day repeat period. With a longer repeat period (17 days) GEOSAT produced much denser tracks (164 km equatorial cross-track spacing) at the expense of temporal sampling. More detailed maps of the global mesoscale variability were produced (Zlotnicki *et al.*, 1989; Shum *et al.*, 1990). The 35-day repeat orbit of ERS-1 and -2 has undersampled the temporal variability but provided very good spatial coverage (78 km equatorial cross-track spacing). The sampling of the 10-day repeat orbit of T/P is a compromise, leading to fairly good coverage in both space and time at high latitudes. The spatial coverage at low latitudes (315 km equatorial cross-track spacing) is certainly too coarse for mapping eddies. The combination of observations from T/P and ERS, however, has led to improved mapping of mesoscale eddies (Le Traon *et al.*, 1998; Le Traon and Ogor, 1998).

The study of currents and eddies is the most productive application of satellite altimetry. First of all, eddies and currents represent the most energetic component of ocean circulation. Their large signals stood out first in the background of the substantial measurement errors in the early altimetric measurements. Second, the scales of eddies and currents are sufficiently smaller than those of orbit errors, which have to be filtered out from the poorly determined orbits of early altimetry missions. Therefore, eddies and currents are not significantly affected by the filtering. A large body of literature has been produced on the subject. It is beyond the scope of this chapter to present a comprehensive review (see Le Traon and Morrow, 2000). In this section I will focus on topics that are illustrative of the utility of altimetry of interests to WOCE.

3.3.4.1 Global sea surface height variability

The geographic distribution of the mesoscale variability derived from satellite altimetry provides a first-order test of the validity of eddy-resolving ocean general circulation models. Although these models are able to simulate the basic features of the distribution of mesoscale energy, there have been significant discrepancies in both energy level

and details of geographic pattern in comparison with observations (Fu and Smith, 1996; Stammer *et al.*, 1996; McClean *et al.*, 1997). The most notable examples include the regions of the Gulf Stream and Kuroshio, where the models are not able to simulate the energetic zonal extensions of these currents after leaving the coasts. Suspecting that the model's spatial resolution might be an important factor causing these discrepancies, Smith *et al.* (2000) have recently conducted a simulation of the North Atlantic circulation at $1/10^\circ$ (the previous highest resolution was $1/6^\circ$). Comparison of this new model simulation with combined T/P and ERS observations is shown in Fig. 3.3.13 (see Plate 3.3.13, p. 172; after Smith *et al.*, 2000). The agreement represents a significant improvement over previous simulations based on $1/6^\circ$ resolution (Fu and Smith, 1996). The highest rms variability reaches 50 cm in both the simulation and observation, whereas the previous simulation reached only 30 cm. The geographic pattern of simulated distribution of energy has correctly reflected the Gulf Stream extension current for the first time. The along-track repeated observations from T/P also allow comparison of wavenumber-frequency spectrum of the variability. Figure 3.3.14 shows that the increased model resolution has resulted in a more realistic simulation of the spectrum. This new $1/10^\circ$ simulation represents probably the most realistic simulation of the Gulf Stream system to date. Satellite altimetry has provided the motivation and validation for such efforts.

3.3.4.2 Geostrophic velocity variability

Geostrophic velocity has been estimated from the sea surface height slope computed from altimetry measurement. The cross-track component of the velocity can be computed from the along-track slope. Since the computation of a slope is a high-pass operation and thus sensitive to the measurement noise, along-track smoothing has to be performed to obtain a reliable estimate of current speed. Smoothing over a distance on the order of 100 km has been a standard practice for analysing GEOSAT data (Le Traon *et al.*, 1990; Shum *et al.*, 1990; Zlotnicki *et al.*, 1993). The smoothing scales required for T/P are somewhat shorter due to the improved measurement noise. Strub *et al.* (1997) made comparisons between T/P and AVHRR observations in the California Current region and found that T/P was able to resolve spatial scales of 50–80 km in the velocity estimation. They also made direct comparison of the velocity estimates from T/P with ADCP observations below the mixed layer and obtained an error estimate of $3\text{--}5\text{ cm s}^{-1}$ for the altimetric velocities. They also concluded that T/P had captured the dominant time scales of the current variability.

Stammer (1997b) made an attempt to retain signals in the T/P data at scales as small as possible. He extracted energy in various wavenumber bands by applying the Lanczos filter with cutoff scales varying from 18 to 100 km. A noise model was applied to wavelengths smaller than 30 km to correct for the noise contributions. This noise model was based on the assumption that all the energy

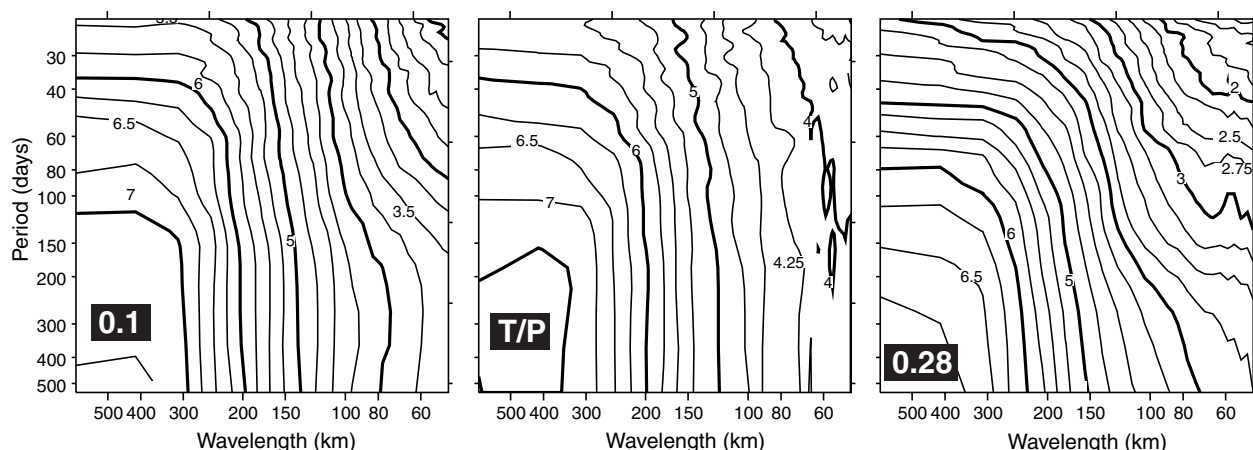


Fig. 3.3.14 Wavenumber–frequency spectrum of sea surface height variability in the Gulf Stream region ($32\text{--}42^\circ\text{N}$, $75\text{--}50^\circ\text{W}$) computed from the same ocean model as in Fig. 3.3.13 (left), the T/P data (middle), and the same ocean model with a resolution of 0.28° (right). The plots show contours of \log_{10} of the power density. The data were sampled along the T/P ground tracks. From Smith *et al.* (2000).

at wavelengths shorter than 60 km in the large expanse of extremely low data variance is entirely due to noise. He then showed that the eddy kinetic energy at high latitudes (e.g. the Labrador Sea) was dominated by scales less than 60 km. His results also indicated that the distribution of energy with scales as small as 20 km was still correlated with oceanic structures instead of being spatially homogeneous as expected for measurement noise.

The kinetic energy of the surface geostrophic current estimated from T/P by Stammer (1997b) was compared with a global set of sparsely populated current meter observations (Wunsch, 1997). There is a general agreement between the two estimates. Based on the current meter observations, Wunsch (1997) found that the eddy kinetic energy is mostly dominated by the barotropic and first baroclinic modes. Because the baroclinic mode is intensified

near the surface, the altimeter observations reflect primarily the baroclinic mode, and thus the motion of the main thermocline.

At the cross-over points where ascending and descending tracks intersect, geostrophic velocity vectors have been computed from the two cross-track velocity components. The accuracy of the estimate is dependent on the magnitude of the crossing angle. If the angle is significantly different from 90°, the errors in one of the components will become large. For instance, the tracks are more meridional than zonal in the equatorial regions, making the meridional velocity component poorly determined. The situation is reversed at high latitudes where the satellite tracks become more zonal than meridional and hence the zonal component is poorly determined. Current ellipse and Reynolds stress tensors of ocean currents have

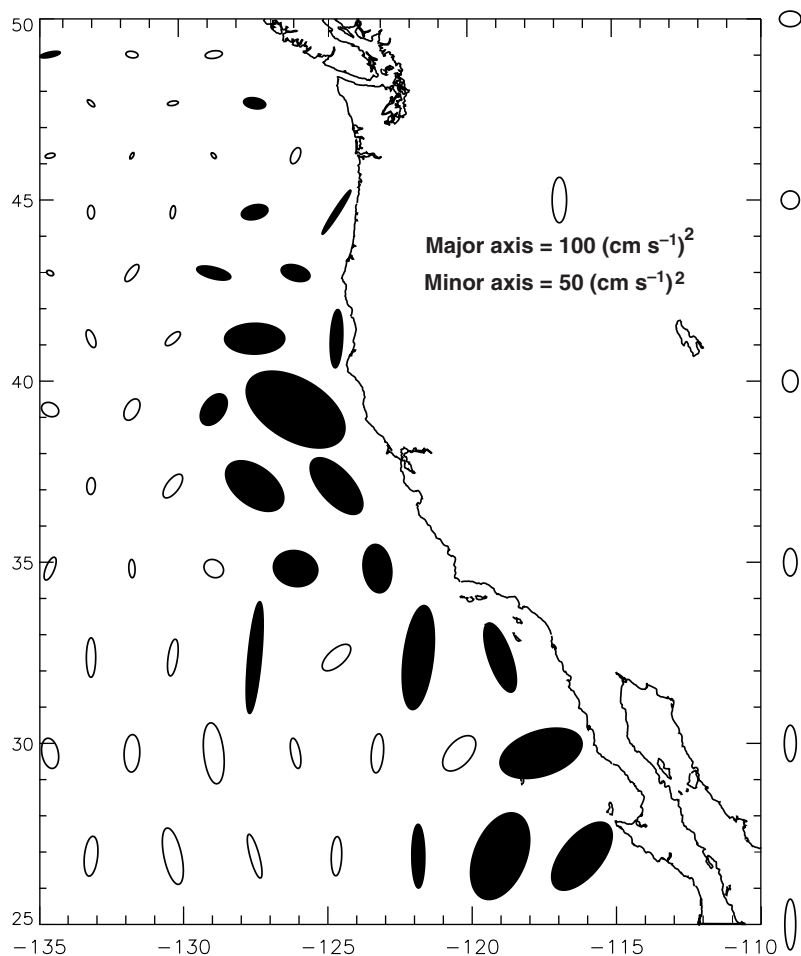


Fig. 3.3.15 Current ellipses for the surface geostrophic velocity determined from the T/P data at cross-over points for the period September 1992–September 1995. Uncertainty in the estimates is shown along the right axis. The scale of the ellipse is indicated on the plot. Ellipses with major axes greater than the uncertainty are shown darkened. From Strub *et al.* (1997).

been computed using satellite altimetry data (e.g. Johnson *et al.*, 1992; Morrow *et al.*, 1992). An example of current ellipses estimated from the T/P data in the California Current region is shown in Fig. 3.3.15 (after Strub *et al.*, 1997), along with the uncertainty in the estimates. Notable features in the core of the current are the high eddy kinetic energy and the tendency of along-shore orientation of the velocity variability. The error estimates might be too large for the region north of 45°N, where the size of the ellipses is smaller than that of the errors.

3.3.4.3 Estimation of current transport and variability

The temporal variability of the transport of surface currents can be readily determined from the difference in altimetric sea-surface-height anomalies (with temporal mean removed) across the domain of the current (Zlotnicki, 1991). Determination of the absolute velocity and transport of currents and eddies is problematic because the knowledge of the geoid at the mesoscale is not sufficiently accurate for oceanographic applications. Significant effort has been made to construct local geoid models based on oceanographic and geodetic data for altimetric studies of ocean currents. The accuracy of these geoids is highly inhomogeneous, varying from 5 to 40 cm (e.g. Rapp and Wang, 1994; Hwang, 1996). Their utility is thus mixed. However, oceanographic measurements made simultaneously with altimetry can be used to estimate the local geoid without the use of any geodetic data.

Using *in-situ* hydrographic observations made by AXBTs along GEOSAT ground tracks at times close to a satellite overpass, Mitchell *et al.* (1990) estimated the along-track geoid in the Gulf Stream region by subtracting the dynamic height computed from the *in-situ* data from the altimetric sea surface height. Such a ‘synthetic geoid’ was then used for estimating dynamic heights and hence absolute cross-track geostrophic velocities from other altimeter measurements along the same track. Among many sources of errors, the unknown contribution of barotropic current to the sea surface height is an outstanding one. Kelly *et al.* (1991) used direct measurements of ocean current velocity made by ADCP under a GEOSAT track from Bermuda to Cape Cod to estimate the sea surface dynamic topography for determining the geoid. However, the ageostrophic component of velocity

becomes a source of error, among others. Nevertheless, these synthetic geoid models are more accurate than most of the gravimetric geoids along the specific satellite tracks where the synthetic geoids are derived.

Howden *et al.* (2000) used the gravimetric geoid of Rapp and Wang (1994) with T/P data to study the transport of the Gulf Stream. They derived a relation between sea surface dynamic height and baroclinic transport at various depths. This relation was then used to estimate the baroclinic transport from the height difference across the Gulf Stream measured by altimetry. The cross-stream sea surface height profile was derived in a stream coordinate (relative to the moving stream axis) rather than an Eulerian coordinate. The results based on the stream coordinate were much more stable than those based on an Eulerian coordinate. The results, showing very little interannual variability over the 5-year study period, were compared favourably with estimates based on XBT and ADCP observations made by a ship periodically sailing between New Jersey and Bermuda.

The relationship between the volume transport of the Kuroshio and ocean topography was investigated by an effort of repeated hydrographic surveys and deployment of moored instruments along a line underneath a T/P ground track south of Japan (Imawaki *et al.*, 1997). Absolute ocean topography was estimated from hydrographic and current meter data during a 2-year period. The difference in the topography across the Kuroshio was found to be highly correlated with the volume transport of the upper 1000 m. The standard deviation of a linear fit between the directly measured transport and the transport estimated from the ocean topography is only 4.3 Sv over a range of 34–91 Sv. Using the mean ocean topography thus obtained as a reference for the T/P sea surface height anomalies (relative to the mean calculated over the same period as the *in-situ* data), Imawaki *et al.* (1997) estimated the variability of the Kuroshio volume transport from the T/P data over longer time spans than the *in-situ* measurement (Fig. 3.3.16). There is no apparent annual cycle in the variability, which is dominated by interannual and intraseasonal time scales. The variability of the Kuroshio transport is greater than that of the Gulf Stream by about a factor of two in terms of the ratio of standard deviation to the mean (Howden *et al.*, 2000).

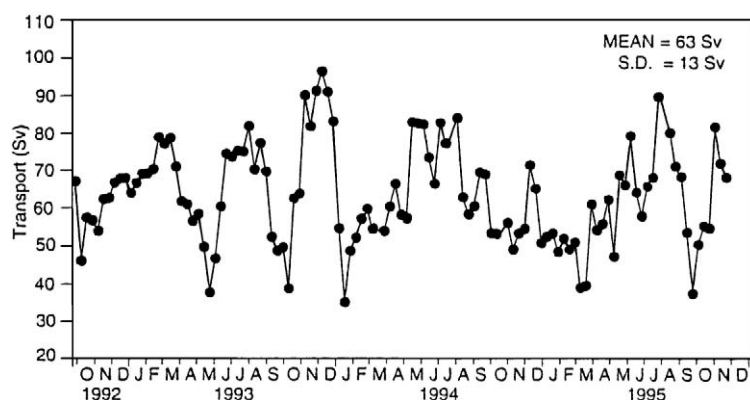


Fig. 3.3.16 Absolute volume transport of the Kuroshio determined from the T/P observations based on regression analysis of altimetry and *in-situ* data. From Imawaki *et al.* (1997).

Garzoli *et al.* (1997) investigated the utility of altimeter data in making inference on the sub-surface flow fields in a region of the southeastern Atlantic covering the path of the migration of the Agulhas eddies and the Benguela Current. Based on data from inverted echo sounders and current meters deployed during the T/P mission, they obtained a linear relationship between the sea-level anomalies from T/P and the depth of the 10°C isotherm (representative of the depth of the main thermocline) as well as the surface dynamic height (relative to 1000 m). They then used the altimeter data to estimate the isotherm depth and dynamic height, which in turn allowed the estimate of the mass transport of the upper 1000 m to be made. The altimeter-derived transports were compared favourably with the estimates from the *in-situ* data. The altimeter data were then used to study the seasonal and interannual variability of the transports beyond the 1-year period of *in-situ* data coverage. The northward baroclinic transport of the Benguela Current ranges from 12 to 15 Sv, with fluctuations of up to 25 Sv. The source of the current is mainly from the South Atlantic with contributions from the Indian Ocean varying from year to year.

The flow of the Pacific Ocean water into the Indian Ocean through the Indonesian seas, the so-called Indonesian Throughflow, has a profound impact on the global circulation and climate. Based on simulations of an ocean general circulation model, Potemra *et al.* (1997) developed a technique for relating the sea levels at four locations (south of Java, northwest of Australia, in the Pacific warm pool, and off the Philippines) to the transport of the throughflow. They applied the

techniques to the T/P data for estimating the variations of the throughflow. The performance of the approach needs to be tested by comparison with direct observations.

In the absence of a systematic deployment of *in-situ* observations in coordination with satellites, it is not possible to construct accurate synthetic geoid or mean ocean topography over a large domain to study the absolute circulation of a current system. However, one can always use climatological mean ocean topography as an approximation. For example, Lagerloef *et al.* (1999) obtained reasonably accurate estimates of the equatorial current velocity in the Pacific Ocean using T/P data in combination with the hydrographic database of Levitus and Boyer (1994b). In addition to the geostrophic component (including a beta-plane version at the equator), they also used a model for the wind-driven Ekman flow with parameters tuned to a surface drifter data set and a wind stress field. The estimated total velocity field compares reasonably well with the TOGA observations.

Without using climatology, Kelly and Gille (1990) developed a rather ingenious technique for estimating the absolute ocean topography across strong currents from their temporal variabilities. An analytical model is used to describe the ocean topography of an isolated jet in terms of its kinematic parameters (i.e. location, width and amplitude) determined from the observed temporal sea-level changes as an inverse problem (also see Tai, 1990). Comparison of the altimetry-derived velocities with simultaneous *in-situ* velocity measurements demonstrated the validity of the technique (Joyce *et al.*, 1990). The technique was

applied to the Gulf Stream and the Kuroshio for studying their spatial and temporal characteristics with results consistent with *in-situ* data (Kelly, 1991; Qiu *et al.*, 1991). The technique was extended to study the recirculation flanking the main current of the Kuroshio (Qiu, 1992) and the Gulf Stream (Qiu, 1994). By combining the altimetric estimate of the ocean topography with historical hydrographic data, Qiu (1994) estimated the deep circulation of the Gulf Stream region with results consistent with *in-situ* observations.

Gille (1994) applied the kinematic jet model technique of Kelly and Gille (1990) to the ACC using GEOSAT data. She obtained estimates of the mean path and ocean topography of the Polar Front and Subantarctic Front of the ACC. Her results are in fair agreement with other estimates obtained from *in-situ* and satellite sea surface temperature observations (Belkin and Gordon, 1996; Moore *et al.*, 1999). She also analysed the spatial and temporal variability of the surface transport of the ACC calculated from the sea surface height difference across the two fronts (Gille and Kelly, 1996). Shown in Fig. 3.3.17 is a wavenumber-frequency spectrum of the ACC surface transport variability. Three peaks are present at the annual period: the main peak is located at zero wavenumber, indicating an along-stream in-phase annual variation; the other two have a wavenumber of 3 cycles around the ACC with westward and eastward phase propagation, respectively. Another peak is present at a period of 1/3 cycle per year with a wavenumber of 3 cycles around the ACC with eastward phase propagation. Fruitful research is anticipated from applying the technique to the multiyear T/P data.

3.3.4.4 Interaction between eddies and mean flow

Spatial variability of the eddy Reynolds stress allows the study of the interaction between eddies and mean flow. Using only 1 year's worth of GEOSAT data, Tai and White (1990) showed some very interesting patterns of Reynolds stress convergence that suggested that the Kuroshio Extension was accelerated by a convergence of eddy momentum flux, while the mean flow was decelerated by a divergence to the north and south of the current. This finding is consistent with theoretical ideas of the growth of meanders of an eastward zonal jet

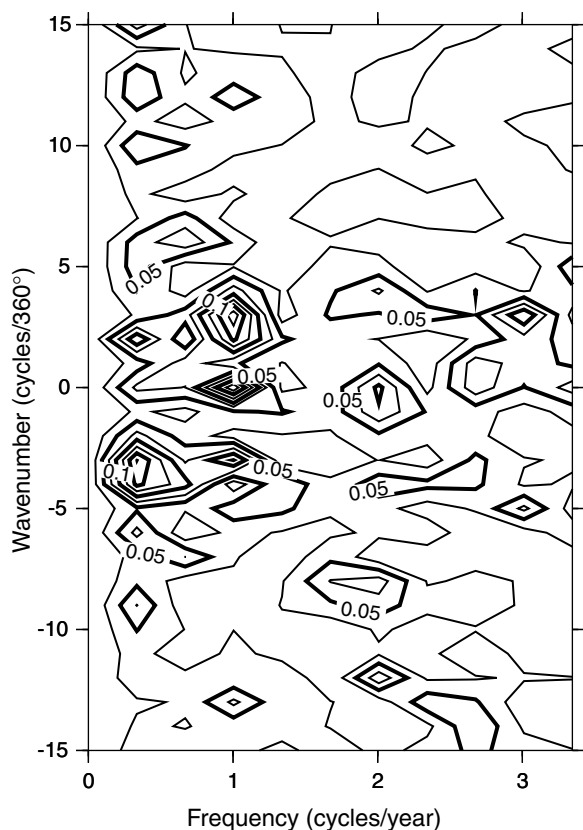


Fig. 3.3.17 Frequency-wavenumber spectrum of the surface transport variability of the Antarctic Circumpolar Current estimated from GEOSAT data. Values shown are power density in square metres per spectral band. Amplitudes exceeding 0.05 m^2 (those enclosed by bold lines) are statistically significant at 95% level. From Gille and Kelly (1996).

due to baroclinic instability and the westward propagation of Rossby waves to the north and south of the jet (Wood, 1988; Hogg, 1988). Similar patterns of eddy-mean flow interactions were observed in the northeastern Atlantic (Beckman *et al.*, 1994a; Le Traon and De Mey, 1994).

The variability of the Kuroshio Extension in relation to eddy field was further studied using T/P data. Qiu (1995) found that the eddy kinetic energy in the Kuroshio Extension and its southern recirculation gyre had undergone significant variations. The eddy energy in the recirculation region steadily increased in 1993–94, while the flow strengths of the Kuroshio Extension and the recirculation were steadily decreasing in 1993–94. Analysis of the energetics suggested that there was a transfer of energy from the mean flow to the eddy field of the recirculation region via barotropic instability.

Adamec (1998) noted that the eddy kinetic energy in the Kuroshio Extension region was particularly weak in 1994 until early 1995. Simultaneous sea surface temperature observations showed a weakening of the north–south temperature gradient across the current during the summer of 1994, implying a weaker front and hence less energy source for the eddies. This sea surface temperature change was consistent with the eddy heat flux estimate using both altimetry and sea surface temperature data. The implication of the study is that the eddies are playing a convoluted role in the overall energetics of the Kuroshio current system.

The eddy Reynolds stress underlying all the aforementioned studies was computed from gridded altimeter data through spatial interpolations. Because Reynolds stress is a second-order quantity, it is particularly sensitive to interpolation errors. The direct estimation of the quantity at cross-over points discussed in Section 3.3.4.2 is probably a more robust approach. Using GEOSAT data, Morrow *et al.* (1994) computed the Reynolds stress tensor at the cross-over points in the Southern Ocean to diagnose the momentum balance of the ACC. They found that the zonally averaged meridional flux of zonal momentum is too small by at least two orders of magnitude to balance the momentum input by wind. This conclusion confirms the importance of the stress generated by bottom pressure against topography (Munk and Palmén, 1951; Treguier and McWilliams, 1990). Wilkin and Morrow (1994) applied the Reynolds stress determined from altimetry to estimating the rate of kinetic energy transfer between eddy and mean flow. The results were compared favourably with the simulation of an ocean general circulation model.

3.3.4.5 Eddy scales and dynamics

The statistical information provided by altimetry on the sea surface currents and eddies is unique and unavailable from any other observational techniques. It allows us to survey the spatial and temporal scales with a regular sampling over the global oceans for years. Stammer (1997b) conducted a comprehensive analysis of frequency and wavenumber spectra of the eddy variability using T/P data. His study has revised the conclusions from previous studies based on less accurate and much shorter data records. While he found that the frequency spectrum has different forms in

dynamically different regions (tropics, low- and high-energy regions), a universal form exists for the wavenumber spectrum in extratropical regions. The universal wavenumber spectrum assumes the following form:

$$\begin{aligned}\Gamma_0(\tilde{k}) = & 135\tilde{k}^{-0.7}, & 0.18 \leq \tilde{k} \leq 1.006, \\ & 135\tilde{k}^{-2.8}, & 1.006 \leq \tilde{k} \leq 2.057, \\ & 501\tilde{k}^{-4.6}, & 2.057 \leq \tilde{k} \leq 4.54\end{aligned}\quad (3.3.6)$$

where $\tilde{k} = k/k_0$, and k_0 is the wavenumber for the dominant local eddy scale. The important role of the Rossby radius of deformation in determining the eddy scales in extratropical regions is clearly demonstrated in the study. Stammer (1997b) also found that the geographic distribution of eddy kinetic energy is to a large extent correlated to that of the vertical shear of horizontal geostrophic velocity over the upper 1000 m (the thermal wind). These findings suggest that the baroclinic instability is a major source of eddy energy over most of the open ocean outside the tropics. However, Le Traon and Morrow (2000) considered that the eddy dynamics in the areas of low eddy energy might be more linear and subject to wind forcing.

Shown in Fig. 3.3.18 (see Plate 3.3.18, p. 172) are the geographic distributions of the eddy temporal and spatial scales computed by Stammer (1998) from the T/P data as follows:

$$T = C_\eta^{-1}(0) \int_0^{T_0} C_\eta(\tau) d\tau \quad (3.3.7)$$

where T_0 is the first zero-crossing of the autocorrelation function of the sea surface height, C_η . The spatial scales range from 180 km in the tropics to 60 km at high latitudes. The temporal scales are longest in the subtropical gyres and shortest at high latitudes with a factor of five difference. Stammer (1998) demonstrated that these eddy scales derived from T/P were related to those derived from the theory of baroclinic instability. These findings led him to carry the analysis further to address the eddy diffusion and transport processes using the statistical information from T/P.

Based on dimensional arguments, the eddy diffusion coefficient, κ , should be proportional to $v' l'$, where v' and l' are the eddy velocity and length scales, respectively. Since $v' \sim (K_E)^{1/2}$, $l' \sim (K_E)^{1/2} T_{bc}$,

we have $\kappa = aK_E T_{bc}$, where K_E is the eddy kinetic energy, T_{bc} is an eddy-mixing time scale, and a is a constant. Stammer (1998) showed that the T/P-derived eddy time scale (T_{alt}) is approximately $0.5 T_{bc}$, leading to $\kappa = 2aK_E T_{alt}$. The constant a is a correlation coefficient that determines the efficiency of individual eddies to mix tracer particles. Based on the theory of Stone (1972), $a = 0.7 \times (L_r/L)^2$, where L_r is the Rossby radius of deformation of the first baroclinic mode and L an eddy mixing length scale. Using T/P results, $a \sim 0.05$. Another factor of 0.1 was further applied to a to scale K_E to represent the average kinetic energy of the upper 1000 m, resulting in $a = 0.005$. With this value and the T/P results for K_E and T_{alt} , Stammer (1998) created a global map of eddy diffusion coefficient (Fig. 3.3.19). The field is highly inhomogeneous with values close to $1000 \text{ m}^2 \text{ s}^{-1}$ in the western boundary currents and greater than $3500 \text{ m}^2 \text{ s}^{-1}$ in the tropics. The lowest values are found in the eastern basins where the eddy energy is low. The large values in the tropics are least reliable, but they partly reflect the vigorous eddy mixing resulting from the tropical instability waves (Perigaud, 1990). Despite the various assumptions underlying the foregoing analysis, the eddy-diffusion coefficients derived from altimetry are compared well with the values estimated from *in-situ* observations (e.g. Krauss and Böning, 1987).

By applying the eddy-diffusion coefficient to the meridional temperature and salinity gradients, Stammer (1998) estimated the meridional eddy transport of heat and salt. Shown in Fig. 3.3.20 is the zonally integrated meridional eddy transports of heat and salt. The eddy heat transport varies between $\pm 0.3 \text{ PW}$ with a maximum at mid-latitudes and the tropics. At mid-latitudes where there are adequate *in-situ* observations, Wunsch (1999b) found that the altimetric estimates were consistent with the estimates obtained from current meter data. The values in the Southern Ocean are also consistent with independent estimates (e.g. Gordon and Owens, 1987). The pattern of salt transport is basically similar to heat transport except that the salt transport in the North Pacific is significantly weaker than in the North Atlantic.

3.3.4.6 Temporal variation of mesoscale energy

The energy source for mesoscale eddies, being either the instability of the mean flow or the wind, is varying with time. The energy level of eddies is thus expected to change with time. Long-term altimetry measurement provides an excellent opportunity to examine the subject. Results from the relatively short GEOSAT data are not conclusive. Zlotnicki *et al.* (1989) indicated that the eddy variability in the northeast Pacific and northeast Atlantic was

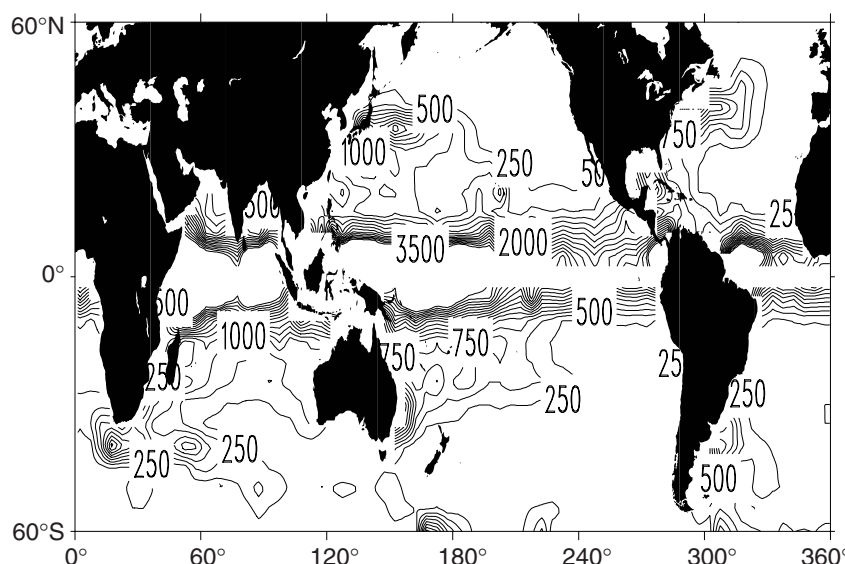


Fig. 3.3.19 Eddy-mixing coefficient in $\text{m}^2 \text{ s}^{-1}$ determined from T/P data. The contour interval is $250 \text{ m}^2 \text{ s}^{-1}$. From Stammer (1998).

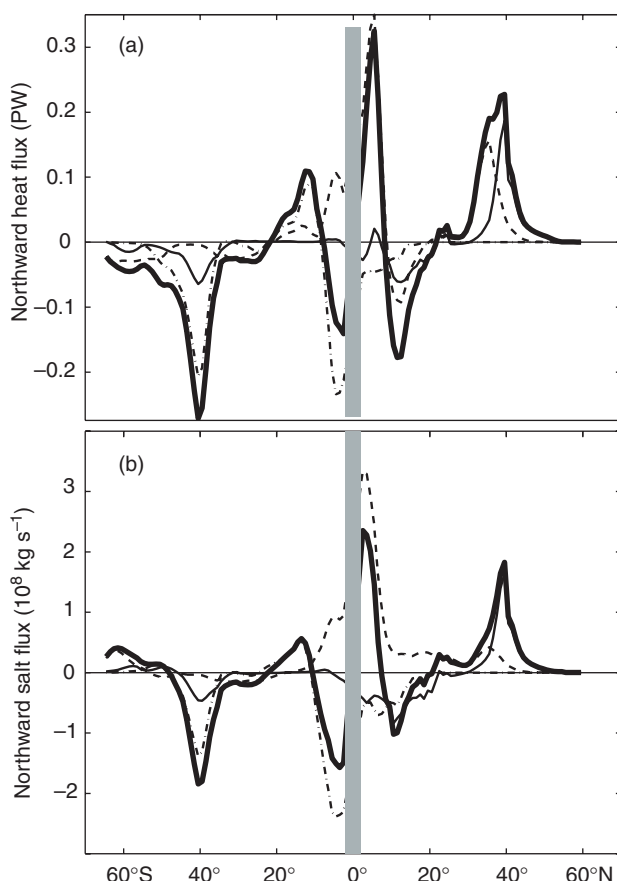


Fig. 3.3.20 Zonally integrated meridional eddy transport of heat (a) and salt (b). Bold solid lines are for global integrals, thin solid lines are for the Atlantic Ocean, dashed lines are for the Pacific Ocean, and the dashed-dotted lines are for the Indian Ocean. Adapted from Stammer (1998).

higher in winter than summer. A recent analysis of 4 years of T/P data indicated that these two regions were in fact the only regions where a significant impact of wind on the variation of eddy energy can be determined (Stammer and Wunsch, 1999). They suggested that the low-frequency fluctuations of the degree of baroclinic and barotropic instabilities were important mechanisms in modulating the eddy energy in most other regions.

Qiu (1999) discovered a pronounced annual cycle in the eddy energy level in the Subtropical Countercurrent in the North Pacific Ocean. This current is located between 20°N and 25°N from 135°E to 185°E. The eddy kinetic energy in the region reaches maximum in April–May and minimum in December–January. Using a 2.5-layer reduced-gravity model, Qiu (1999) was able to demonstrate that the annual variation of eddy

energy was primarily caused by the annual variation of the degree of baroclinic instability of the Subtropical Countercurrent and the North Equatorial Current to its south. In spring the current system has a large vertical shear and a weak vertical stratification, leading to a strong baroclinic instability. In fall, the reverse happens and hence the instability is reduced. The theoretical time scale of the instability is about 60 days, matching the observed lag of the eddy energy cycle from the instability cycle.

Wang and Koblinsky (1999) reported that the mesoscale sea surface height variance in the Kuroshio Extension region varies by more than a factor of two over 6 years based on T/P data. They found that the temporal variation of the eddy energy is correlated with the sea-surface-temperature difference across the Kuroshio Extension. If the surface temperature gradient is a reflection of the baroclinicity (or the available potential energy) of the current, this finding is suggestive of the baroclinic instability as a source of the eddy-energy variability.

Witter and Gordon (1999) analysed 4 years of T/P data and discovered that the path and area extent of the migration of the Agulhas eddies from the Indian Ocean to the Atlantic was affected by a basin mode of interannual variability of the South Atlantic, which underwent a transition from a state of enhanced gyre-scale circulation in 1993–94 to a state of weaker circulation in 1996. The migration path of the Agulhas eddies became more constricted and narrower in 1996 than in 1993–94. The dynamic interpretation of the observation is yet to be explored.

3.3.5 Concluding discussions

As discussed in Section 3.3.1, a unique aspect of satellite altimetry is its global observation of a dynamic boundary condition of the ocean. This boundary condition allows inference to be made about the circulation and density field at depths, giving altimetric observations an important role in providing a global perspective for integrating the various pieces of WOCE observations to achieve a synthetic description of the ocean circulation. A powerful approach to achieving such a synthesis is through the use of an ocean general circulation model to assimilate observations for making an estimate of the entire state of the ocean. In fact,

oceanographic data assimilation has been motivated to a large extent by the advent of high-quality altimeter data, whose large-scale regular sampling has made data assimilation a fruitful approach to exploiting the utility of the data. A large body of literature exists on model assimilation of altimeter data (see Fukumori, 2000, for a review). Most of the progress to date has been focused on methodologies and their demonstration. The challenge is the quantification of the skill of a numerical model for optimizing the prediction of subsurface fields from altimeter data. Ultimately the framework provided by altimetry with an assimilating model will be used to incorporate other WOCE observations in a dynamically and statistically consistent manner to create a description of the entire state of the ocean during the WOCE period. Some preliminary progress has been reported in Stammer *et al.* (1997) and Fukumori *et al.* (1999). Preliminary results showing the utility of assimilating altimeter data in improving the prediction of ENSO have been reported by Ji *et al.* (2000).

The utility of altimetry for global ocean synthesis underscores the importance of keeping precision satellite altimetry missions continuous in time for climate studies. Strategies for such sustained observing systems were discussed in Nowlin (1999). In the near term, T/P will be succeeded in the year 2001 by its follow-on mission called Jason-1, which will make observations in the same orbit as T/P with expected performance exceeding that of T/P. Jason-1 is a continuing collaboration between the USA and France. While Jason-1 will demonstrate the operational applications of altimetry, strategies for making altimetry become part of a long-term ocean observing system are a pressing issue. Also of importance is the deployment of *in-situ* observation network complementary to altimetry observations such as the array of Argo floats (Wilson, 2000).

A Jason series has been proposed to maintain long-term precision altimetric observations of the global ocean topography. The concept is to forge a long-term collaboration between the USA and France in ocean altimetry and its operational implementation and application. The performance goal is to progress from the T/P standard systematically to an accuracy of 1 cm through dedicated effort and new technologies. While other ocean topography observing systems will continue or emerge (tide gauge network, other altimetry missions, new

remote sensing techniques), the Jason series will provide a benchmark for calibrating and integrating other measurements to achieve a globally consistent data set.

As noted in Section 3.3.1 and several other sections, a single altimeter suffers from a compromise in sampling the spatial and temporal scales of ocean variability. Multiple conventional nadir-looking altimeters are needed to map the ocean mesoscale eddies (Greenslade *et al.*, 1997; Le Traon and Dibarboure, 1999). During the Jason-1 time frame, the European ENVISAT will make altimetric measurement in the ERS orbit, providing a dual-altimeter coverage of the global ocean. New technologies have provided a promising approach to low-cost altimeters for multiple deployments in the future (e.g. Raney, 1998). In the mean time, new techniques are being developed for mapping ocean topography with two-dimensional spatial resolutions. Interferometric techniques are a promising approach to wide-swathe altimetry by measuring the interference between signals received by two altimeters flown on the same spacecraft with a slight off-nadir pointing (Rodriguez *et al.*, 2000). The reflections of GPS signals off the ocean surface are being analysed for detecting ocean topographic features (LaBrecque *et al.*, 1998). Such developments of new techniques and technologies should be an integral part of the strategy for a long-term observing system.

A substantial improvement of the knowledge of the geoid is expected in the next 5–10 years. GRACE, a USA/Germany joint mission, will utilize a pair of low-earth-orbiting satellites whose relative distance is precisely determined (Wahr *et al.*, 1998; Davis *et al.*, 1999). The measurement of the distance plus onboard accelerometer measurements will be analysed to improve the geoid accuracy to less than 1 cm at spatial scales greater than 200 km (half wavelength). GRACE is planned for launch in 2001. The GOCE mission, currently planned by the European Space Agency, will fly a system based on gradiometry and GPS precision tracking in a low orbit. GOCE is expected to extend the 1 cm geoid accuracy to a scale of 100 km. With such accurate knowledge of the geoid, absolute surface geostrophic current velocity and its variability will be determined from altimeter data with details including the swift boundary currents and mesoscale eddies (LeGrand and Minster, 1999). Such information will provide

a powerful constraint for ocean models as well as ocean-atmosphere-coupled models for simulation and prediction of the global environment.

Institute of Technology, under contract with the National Aeronautics and Space Administration. Support from the TOPEX/POSEIDON Project is acknowledged.

Acknowledgements

The research described in the paper was carried out by the Jet Propulsion Laboratory, California

3.4

Air–Sea Fluxes from Satellite Data

W.Timothy Liu and Kristina B. Katsaros

3.4.1 Forcing the ocean

The ocean circulation is forced at the surface through exchanges with the atmosphere of momentum, heat and water. The wind exerts a stress on the surface, which alone can produce many features of ocean currents in observations and in numerical model analyses. The buoyancy due to cooling and heating at the surface, and salt concentration or dilution due to evaporation or precipitation, likewise can also generate much of the observed circulation pattern. The real ocean combines these varying forces in non-linear ways with the tidally driven motions to produce a complex and varying circulation pattern. Understanding the fundamentals of these processes lies behind the World Ocean Circulation Experiment (WOCE). The variability and predictability of the consequences of varying forcing, natural or due to anthropogenic effects and the resulting feedback on the atmospheric circulation are central to the Climate Variability and Predictability (CLIVAR) programme.

The oceanic storage of radiatively active (greenhouse) gases depends on surface wind and upper ocean temperature, so is intimately connected to all the other air–sea interaction processes and their consequences. Joanne Malkus once lamented that the observations at large scales and the interactions on all scales were almost impossible ever to achieve and take account of (Malkus, 1962). However, that was before the advent of satellite meteorology and oceanography. Today, adequate observations at significant temporal and spatial scales can be achieved from the vantage point of space; however, strong support from *in-situ*

measurements is required, particularly from sensors such as the Argo depth-profiling array (Wilson, 2000). An illustration of the coverage of the global ocean today by three operating surface wind-sensing satellites is found in Fig. 3.4.1 (see Plate 3.4.1, p. 172). Advances in satellite technologies, better algorithms, and detailed sampling in time and space promises that sufficient measurements to understand climate variability and predictability can be obtained in the near future. In this chapter, we discuss current methods to evaluate the air–sea fluxes from space and point to some promising trends.

The momentum flux is the result of wind shear. Heat flux can be divided into four components:

- 1 sensible heat resulting from thermal gradient;
- 2 latent heat carried by evaporation;
- 3 short-wave radiation from the sun; and
- 4 long-wave radiation from the atmosphere and the ocean.

Hydrologic forcing is the difference between precipitation (rain) and evaporation. Momentum flux, sensible heat flux and evaporation are turbulence transports (Liu, 1990). The turbulence fluxes are not measured routinely over the global oceans. They are parameterized, through bulk aerodynamic formulae, in terms of the mean measurements provided in ship reports or by space-based sensors.

3.4.2 Bulk parameterization

The bulk formulae relate the fluxes of momentum (surface stress τ), sensible heat (SH), and latent

heat (LH) to the mean parameters measured in the atmospheric surface layer.

$$\tau = \rho C_d (u - u_s) \quad (3.4.1)$$

$$SH = \rho C_h (T - T_s) \quad (3.4.2)$$

$$LH = LE = \rho C_e u (q - q_s) \quad (3.4.3)$$

where ρ is the surface air density, L is the latent heat of vaporization, and E is evaporation. u , T and q are the equivalent neutral wind speed, temperature and specific humidity at a reference height (usually taken to be 10 m). The subscript 's' indicates the values at the ocean surface. The transfer coefficients of momentum, heat and moisture under neutral stability, C_d , C_h and C_e , have been determined through fitting field measurements or solving flux-profile relations (e.g. Liu *et al.*, 1979; Large and Pond, 1982; Bradley *et al.*, 1991; Smith *et al.*, 1992; DeCosmo *et al.*, 1996; Fairall *et al.*, 1996). Charnock (1955) postulated that C_d is a function of wind stress in a well-developed sea and Donelan *et al.* (1997) and others have found that C_d depends on sea state. Wind, temperature and specific humidity at any height in the atmospheric surface layer under any stratification can be converted to u , T and q , using the flux-profile relations (e.g. Liu and Tang, 1996). In general, u_s is assumed to be zero and q_s is the saturation humidity at T_s multiplied by 0.98, to account for the reduced-saturation specific humidity over salt water.

Atmospheric stratification is difficult to estimate from space, but the enterprise is saved by the roughness of the sea being a function of the wind stress. As long as the original satellite calibration for wind speed is done for neutral atmospheric stratification, our stress estimates from satellite measurements (equivalent neutral wind) will be correct using the bulk formulae. This fortuitous advantage is to some extent carried over to the sensible and latent heat flux estimates. In any case, over most of the ocean, the atmospheric temperature is closely adjusted to the sea surface temperature, which implies near-neutral stratification. In addition, whenever the wind speed is greater than 10 m s^{-1} , the atmosphere approaches neutrality since the mechanical turbulence dominates over the buoyancy forced turbulence (e.g. Kraus and Businger, 1994).

3.4.3 Wind forcing

There are several sets of space-based global wind fields available now and for the future. The Special Sensor Microwave/Imager (SSM/I) operates at 19, 22, 37 and 85 GHz in dual polarization (except for 22 GHz, which has only vertical polarization), on the polar-orbiting operational spacecraft of the Defense Meteorological Space Program (DMSP). It has provided continuous wind speed measurements over the global ocean since July 1987. Recently, several DMSP satellites have been in orbit at the same time, providing complete daily coverage with ever better algorithms based on the long data record (e.g. Wentz, 1996; Krasnopolsky *et al.*, 1999). SSM/I has a wide scan and, therefore, good coverage (1400 km) (Fig. 3.4.1, see Plate 3.4.1, p. 172), but does not provide information on the surface wind direction. The wind speed from SSM/I has been combined with surface wind data from a numerical model through a variational method to produce wind vector fields at 6-hour intervals and at 2° by 2.5° resolution (Atlas *et al.*, 1996). These large-scale wind fields over the tropical Pacific were evaluated by Busalacchi *et al.* (1993) by comparison with operational Numerical Weather Prediction (NWP) products and interpolated wind fields from ship measurements and cloud motions. They found large-scale similarity between SSM/I and other wind fields, but suggested that the dense space-time coverage of SSM/I offers a distinct advantage in forcing ocean circulation models. The SSM/I wind fields were found by Liu *et al.* (1996) to generate more realistic anomalous ocean cooling in an ocean general circulation when compared with the results simulated by the same model but forced by NWP winds. The SSM/I wind fields have more structure and energy than NWP winds but have the same directional characteristics as the NWP winds. SSM/I is an operational sensor that will be operated well into the twenty-first century. The production of wind vector data from these assimilated microwave radiometer measurements, however, is a research effort.

Scatterometers send microwave pulses to the earth's surface and measure the backscattered power (so-called radar cross-section) from the surface roughness. Over the ocean, the backscatter depends on ocean surface roughness due to small (centimetre scale) waves. The idea of remote sensing of ocean surface winds was based on the belief

that these surface ripples are in equilibrium with the local wind stress. The backscatter depends not only on the magnitude of the wind stress, but also the wind direction relative to the direction of the radar beam (the azimuth angle) (e.g. Jones *et al.*, 1978). Space-based scatterometers, operating on polar-orbiting satellites, provide both wind speed and direction through multiple looks at any one pixel in the swathe. Two wavelength bands, at frequencies of approximately 5 and 14 GHz, have been used with satellite scatterometers. The higher frequencies of the Ku-band allow greater sensitivity at low wind speeds to wind direction, but also exhibit stronger influence from atmospheric precipitation, as compared with the lower frequencies of the C-band. The geophysical model function, from which ocean surface wind vectors are retrieved from the radar cross-section, are largely based on empirical fits of data (e.g. Jones *et al.*, 1978; Freilich and Dunbar, 1993; Thiria *et al.*, 1993; Stoffelen and Anderson, 1997; Wentz and Smith, 1999).

The European Remote Sensing (ERS) satellites ERS-1 and 2 (Attema, 1991), launched in 1991 and 1996, respectively, carry the Advanced Microwave Instrument (AMI). This operates at the C-band (5.3 GHz) frequency and provides wind vectors at 50 km resolution over a 500 km swathe to the right of the satellite subtrack (Fig. 3.4.1b, see Plate 3.4.1, p. 172). This narrow swathe limits the daily coverage to 40% of the global ocean, and it requires 3 days to provide almost full coverage, but the ERS-2 continues to provide data in 2000. Bentamy *et al.* (1998) found good agreement between the interpolated wind fields derived from ERS-1 data and weekly and monthly averaged NWP wind fields. Liu *et al.* (1995) simulated Kelvin waves and anomalous ocean warming in the equatorial Pacific by forcing an ocean general circulation model with ERS-1 scatterometer winds. Weekly wind fields derived from ERS scatterometers were shown by Grima *et al.* (1999) to be superior to wind fields from a climate model in simulating tropical ocean circulation in that the observed upper ocean structure agreed better with buoy-measured ocean structure and currents.

The National Aeronautics and Space Administration (NASA) launched the very first scatterometer on the SEASAT satellite in June 1978, which lived for only 3 months. It operated at the Ku-band (14.6 GHz). Four fan-beam dual-polarized antennas

illuminated two 500 km swathes, one on each side of the spacecraft, providing wind vectors at 50 km resolution. However, only one side was in operation most of the time. The US developments since have built on that experiment. In 1996, NASA Scatterometer (NSCAT) was launched on the Japanese spacecraft, Midori (ADEOS-1). Its six fan-beam antennas provided 600-km wide swathes on both sides of the spacecraft. It measured at the Ku band (14 GHz) and provided ocean surface winds at 25 km resolution, and covering 77% of the global ocean every day (Fig. 3.4.1a, see Plate 3.4.1, p. 172), until its early demise in June 1997, owing to loss of the solar panel on the spacecraft. The quality of data was shown to be above expectation through comparison with *in-situ* measurements (e.g. Bourassa *et al.*, 1997; Freilich and Dunbar, 1999), through comparison with winds from the analysis of NWP models (e.g. Liu *et al.*, 1998; Atlas *et al.*, 1999; Ebuchi, 1999), and through forcing of ocean circulation models (e.g. Chen *et al.*, 1999; Chu *et al.*, 1999; Milliff *et al.*, 1999; Verschell *et al.*, 1999).

A new scatterometer, SeaWinds, was launched on the NASA mission QuikSCAT in June 1999. SeaWinds uses pencil-beam antennas in a conical scan. The antennas radiate Ku-band microwaves at 46° and 54° incident angles and measure the backscattered power across a continuous 1800 km swathe. SeaWinds is capable of providing wind speed and direction at 25 km resolution over 93% of the earth's ice-free oceans every day, under both clear and cloudy conditions (Graf *et al.*, 1998). The power of synoptic global coverage and high spatial resolution by a space-based scatterometer is clearly illustrated in Fig. 3.4.2 (see Plate 3.4.2, p. 172). The impact of scatterometer winds in the analysis of Hurricane Floyd, shown in the insert of Fig. 3.4.2, is discussed by Liu *et al.* (2000). The SeaWinds data used in the insert was specially produced to have a spatial resolution of 12.5 km and for the strong wind and high precipitation conditions in tropical cyclones. Practical utility for obtaining the gale force wind radius in tropical cyclones is reported by Uhlhorn *et al.* (2000). SeaWinds was also found to detect the circulation of tropical depressions early in their development (Katsaros *et al.*, 2000). Both the scatterometers on SEASAT and NSCAT have a data gap at nadir between the two swathes. The continuous 1800-km wide swathe of SeaWinds is a tremendous technical advance.

The empirical form of the original scatterometer algorithm leads to an asymptotic decrease in the sensitivity in scatterometer-derived winds for higher wind speeds (Cavanié and Lecomte, 1987). Insufficient measurements in the past prevented significant improvement of wind retrieval for wind speeds over 25 m s^{-1} . Quilfen *et al.* (1998) illustrated with the C-band AMI data, at 25 km resolution, obtained for a special 20-orbit data set, that the backscatter cross-section continues to show sensitivity beyond 20 m s^{-1} winds in tropical cyclones. Similarly, Yueh *et al.* (2000) have shown that a Ku-band scatterometer is sensitive to both wind speed and direction under hurricane conditions, with wind speeds up to 35 m s^{-1} . Improvement of the wind-retrieval algorithm under the strong wind conditions of tropical cyclones is

being vigorously pursued (e.g. Jones *et al.*, 1999b; Liu *et al.*, 2000).

The equivalent neutral winds produced by space-borne scatterometers (Liu and Tang, 1996) are uniquely related to the surface stress by equation (3.4.1). Another valid algorithm approach relates the backscatter observation directly to measurements of surface stress instead of to the equivalent neutral wind; the feasibility was demonstrated by Liu and Large (1981), Weissman and Gruber (1999), and others.

The minimum requirements for the US scatterometer are wind speed accuracy of either 10% or 2 m s^{-1} , depending on which is larger, and directional accuracy of 20° in the speed range of $3\text{--}10 \text{ m s}^{-1}$, under all weather conditions except heavy rain. Freilich and Dunbar (1999) clearly

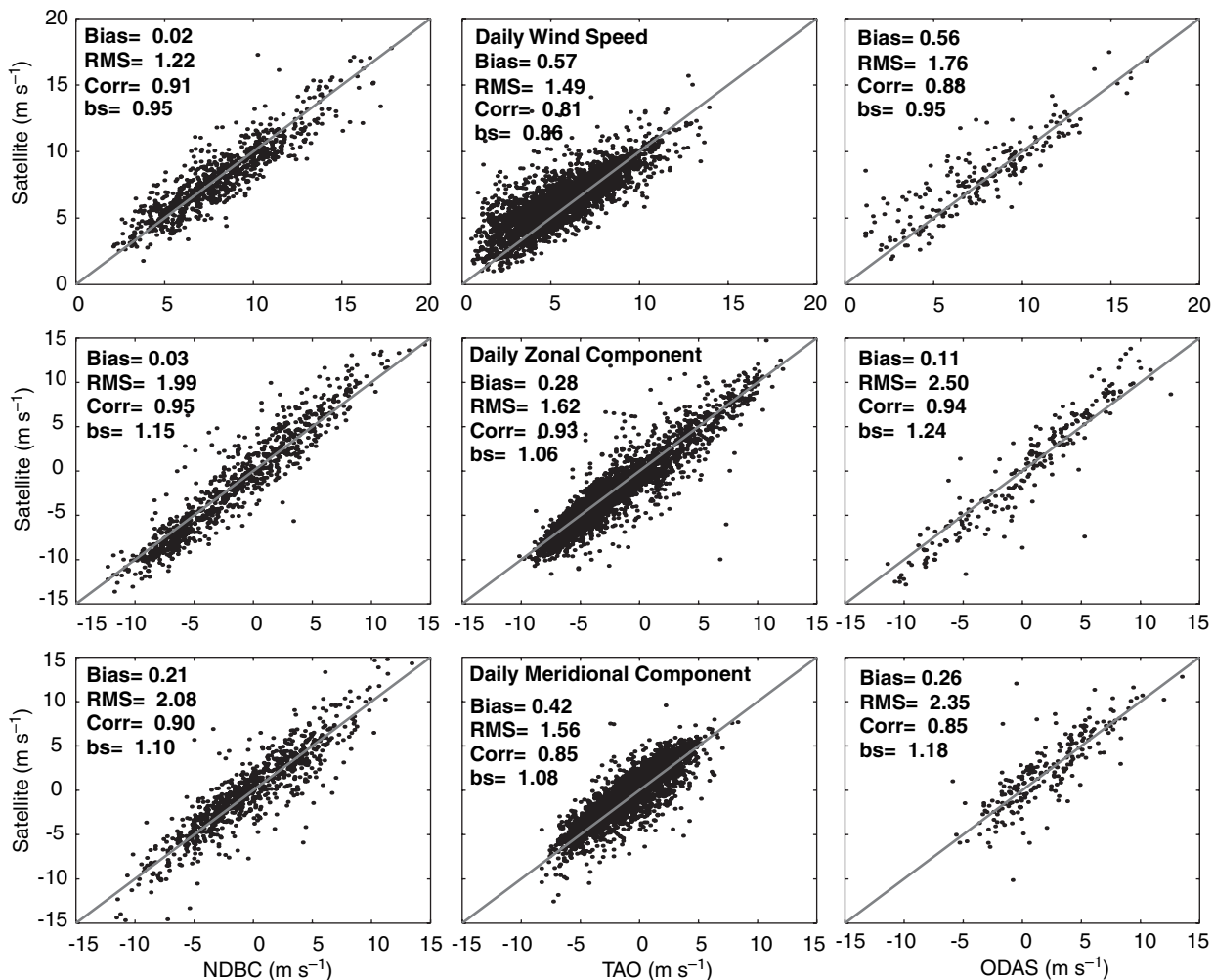


Fig. 3.4.3 Comparison of the global ocean by wind estimates from satellite instruments (SSM/I (top row), ERS-2 AMI (middle row) and QuikSCAT's SeaWinds (bottom row)) versus buoy networks (NDBC (left column), TAO (middle column) and ODAS (right column)). bs, best fit slope. After Bentamy *et al.* (2000).

showed that the accuracy of NSCAT data exceeds the requirement. The comparison in Fig. 3.4.3 shows that other data also meet the requirement. Figure 3.4.3 illustrates that the three underlying wind estimates show small biases of the order of $0\text{--}1.25\text{ m s}^{-1}$ and rms values $<2\text{ m s}^{-1}$ compared with three sets of buoys – the TOGA-TAO (Tropical Ocean and Global Atmosphere–Tropical Atmosphere and Ocean) array; the NDBC operational array, mid-latitude US coast; and ODAS, the European network (Bentamy *et al.*, 2000). Higher accuracy and spatial resolution, however, are desirable in a number of applications, including the study of hurricanes (Liu *et al.*, 2000) and eastern boundary wind stress curl (Milliff *et al.*, 2001). From these multiple data sets new climatological wind fields can be derived. A merged wind field employing data from two SSM/Is, the ERS-2 AMI, and NSCAT have been calculated on a daily basis at $1^\circ \times 1^\circ$ resolution (Bentamy *et al.*, 1999).

3.4.4 Thermal forcing

3.4.4.1 Latent heat flux

The computation of LH by the bulk aerodynamic method requires u , T_s and q as seen in equation (3.4.3). Over the ocean, u and T_s have been directly retrieved from satellite data, but not q . A method of estimating q and LH from the ocean using satellite data was proposed by Liu and Niiler (1984). It is based on an empirical relation between the integrated water vapour (W , measured by space-borne microwave radiometers) and q on a monthly time scale (Liu, 1986). The physical rationale is that the vertical distribution of water vapour through the whole depth of the atmosphere is coherent for periods longer than a week (Liu *et al.*, 1991). The relation does not work well at synoptic and shorter time scales and also fails in some regions during summer (Liu *et al.*, 1992). The relation has also been scrutinized in a number of studies (e.g. Hsu and Blanchard, 1989; Eymard *et al.*, 1989; Esbensen *et al.*, 1993; Jourdan and Gautier, 1994). Modification of this method by including additional geophysical parameters or Empirical Orthogonal Functions (EOFs) as estimators have been proposed (e.g. Wagner *et al.*, 1990; Cresswell *et al.*, 1991; Miller and Katsaros, 1991; Chou *et al.*, 1995), with some overall improvement, but the inherent limitation is the lack of information about the vertical distribution of q near the surface.

Liu (1990) suggested two possible improvements in LH retrieval. One suggestion was to obtain information on the vertical structures of humidity distribution and the other was to derive a direct relation between LH and the brightness temperatures (BT) measured by the radiometer. Liu *et al.* (1991) demonstrated that the boundary-layer water vapour is a better predictor of q . Schulz *et al.* (1993) developed an algorithm for direct retrieval of boundary-layer water vapour from radiances observed by SSM/I. However, without using any new measurements that can distinguish vertical structures, and without the knowledge of the boundary-layer (or mixed-layer) height, any significant improvement of the retrieval of LH by this method remains to be demonstrated. Information from the new microwave humidity sounders on the operational polar orbiters of DMSP and the National Oceanic and Atmospheric Administration (NOAA), as anticipated by Liu (1990), has not been optimally utilized at present.

Because all the three geophysical parameters, u , T_s and W , can be retrieved from the radiances at the frequencies measured by the Scanning Multichannel Microwave Radiometer (SMMR) on Nimbus-7 (similar to SSM/I, but with 10.6 and 6.6 GHz channels as well and no 85 GHz channels), the feasibility of retrieving LH directly from the measured radiances was also demonstrated by Liu (1990). Such a method may improve accuracy in bypassing the uncertainties related to the bulk parameterization method. Liu (1990) used coincident BT values observed by the SMMR and LH computed from ship data on monthly time scales. While SMMR measures at ten channels, only six channels were identified as significantly useful in estimating LH. SSM/I, the operational microwave radiometer that followed SMMR, lacks the low-frequency channels that are sensitive to T_s , making direct retrieval of LH from BT alone unfeasible. The microwave imager (TMI) on the Tropical Rainfall Measuring Mission (TRMM), which was launched in 1998, includes low-frequency measurements sensitive to T_s . Direct retrieval of LH has received renewed interest. Bourras and Eymard (1988) attempted to combine SSM/I radiances and T_s measurements to compute LH, and Liu *et al.* (1999) tried to do the same using TMI radiances alone, but more vigorous effort in validation is required to demonstrate any significant improvement of these more direct methods over the indirect methods.

Validation of the LH is very difficult because there are very few direct measurements. Validation data are largely computed through the bulk parameterization method, with its inherent uncertainties. The mean parameters from merchant ships have poor quality and distribution. The accuracy of LH estimated from instantaneous spacebased data is about $30\text{--}40\text{ W m}^{-2}$, and rms errors are half of that for monthly mean over 2° areas (e.g. Schulz *et al.*, 1997).

3.4.4.2 Short-wave radiation

Global surface net short-wave radiation (SR) has been computed from the Earth Radiation Budget Experiment (ERBE) data from 1985 to 1989 (Li and Leighton, 1993). The variability of SR is largely controlled by the variability of clouds, and most of the computations of SR over the ocean make use of the high resolution and high sampling of the diurnal cycle by data from geostationary satellites. The International Satellite Cloud Climatology Project (ISCCP) (Rossow and Schiffer, 1991) has provided calibrated and standardized cloud data from four geostationary satellites operated by the US, Japanese and European space agencies. A number of methods (e.g. Gautier *et al.*, 1980; Bishop and Rossow, 1991; Pinker and Laszlo, 1992) have been used to compute net SR at daily time scales and $2^\circ \times 2.5^\circ$ resolution, including the operational effort by the Surface Radiation Budget Program at Langley Research Center. The availability of ISCCP data is expected well into the future, but the data record has not yet been extended to recent years. Higher spatial resolution is also desirable and is being pursued by the above-mentioned project.

The SR estimates for the ocean are simplified compared to those over land by the known reflectance of the sea surface. Variations in reflectance due to surface roughness and white caps could be included in the formulation as a function of u (e.g. Katsaros, 1990). The multifrequency data of the new generation geostationary satellites will allow discrimination of atmospheric aerosol scattering and surface reflection, so that it will be possible to take these second-order effects into account. The role of Saharan and other mineral dust and atmospheric pollution (as from wild fires and volcanoes) is being addressed by several research groups and will improve the accuracy of net surface radiative flux estimates.

High correlation between the SR and T_s tendency (time differential of T_s) is demonstrated in Fig. 3.4.4 (see Plate 3.4.4, p. 172). This correlation is consistent with the notion that solar heating is the main driver for the seasonal changes of T_s away from the equatorial wave guide, where ocean dynamics may be more important. The relative roles of solar heating and evaporative cooling in changing the annual cycle of T_s and T_s changes during El Niño and the Southern Oscillation (ENSO) have been studied (e.g. Liu and Gautier, 1990; Liu *et al.*, 1994).

3.4.4.3 Sensible and net long-wave heat fluxes

It is much more difficult to estimate SH and surface net long-wave radiation (LR) from satellite data than SR or LE. The magnitude and variability of SH are relatively small over much of the open ocean. The weighting functions (contributions of radiance as a function of height) of space-borne atmospheric sounders are too broad to help retrieval of near-surface air temperature with sufficient accuracy for the bulk aerodynamic formula (equation 3.4.2). A relationship similar to the W versus q derived from microwave radiometers has not been found. Unlike humidity, the vertical variation of temperature is not coherent through the entire atmosphere. As suggested by Liu and Niiler (1990) and Liu (1990), SH can be estimated from LE if the Bowen ratio or the relative humidity is known. This is equivalent to deriving T from q . The accuracy of a prescribed formula for Bowen ratio and relative humidity is, however, quite uncertain (Liu and Niiler, 1990) and would vary regionally. There have been a number of attempts (e.g. Thadathil *et al.*, 1993; Kubota and Shikauchi, 1995; Konda *et al.*, 1996) to derive T (SH) from q retrieved with the method of Liu (1986). Recently, Jones *et al.* (1999b) attempted to produce T and q using a neural network approach. Currently there is nothing better to offer, but future numerical models well constrained with satellite data should be able to resolve this difficulty.

Long-wave radiation is strongly affected by atmospheric properties below cloud base, which are hidden from space-borne sensors. Methods that combine cloud information with atmospheric soundings and numerical models have been attempted (e.g. Frouin *et al.*, 1988; Gupta *et al.*, 1992). Classical LR climatologies

(e.g. Bunker, 1976a) used bulk formulae and relied on a ship's human observer for the cloud reports. The Frouin *et al.* method uses satellite-derived cloud information instead (see also review by Katsaros, 1990). Improved atmospheric temperature sounders such as the Atmospheric Infrared Sounder (AIRS) scheduled for launch early in the year 2000 might advance estimation of both of these difficult surface fluxes.

3.4.4.4 Present capability

With better than 20 W m^{-2} accuracy, we are able to discern the annual cycle and ENSO variations of the largest variable components of the ocean surface heat flux – the solar heating and the evaporative cooling. To close the net air–sea energy budget, or to estimate the meridional heat transport in the ocean, we need an absolute accuracy of the total flux of at least 10 W m^{-2} on a monthly $2^\circ \times 2^\circ$ resolution. We cannot meet this stringent requirement at present. More intense effort is needed to estimate SH and SR contributions, even if the state of the art leaves much to be desired. Since these terms are typically much smaller than SR and LH at low latitudes and in the tropics, even large percentage errors, of 20–30%, give relatively small absolute errors in the net budget (exceptions are cold, clear high-pressure situations in the subtropics). Estimates within a few W m^{-2} may be possible for the tropical oceans but we should be prepared to assess accuracy based on the region and the general pattern of the circulation.

3.4.5 Hydrologic forcing

The computation of evaporation has been described in Section 3.4.4.1. To estimate ocean surface hydrologic forcing, we also need the precipitation (P) at the surface. In the past, attempts have been made to estimate P from space-borne sensors at visible, infrared and microwave wavelengths (e.g. Arkin and Ardanuy, 1989; Wilheit *et al.*, 1991). There are visible and infrared sensors, but no microwave sensors, on geostationary satellites. Microwave sensors such as SSM/I have the advantage of being more directly related to rain but are limited by the insufficient sampling of the diurnal cycle on polar orbiters. Two or three satellites flying in tandem or a satellite in low-inclination orbit may alleviate this problem. Production and validation of space-based rain data have been

undertaken by the Global Precipitation Climatology Project (GPCP), and data at 2.5° and monthly resolutions from 1986 to 1994 are available. Precipitation for a very long period of time has also been derived from the operational Microwave Sounding Unit (Spencer, 1993).

The launching of TRMM in November 1997, with its low-inclination orbit (higher sampling rate), opened up a new era of estimating both surface rainfall and the precipitation profile (Kummerow *et al.*, 1998). There are a number of instruments on TRMM, but only TMI and the precipitation radar (PR) are directly relevant in estimating the hydrologic forcing. TMI operates at five frequencies and has a swathe width of 760 km. From these measured radiances, the integrated column precipitation over the ocean can be estimated, among a number of parameters. The spatial resolution varies with frequency, being 15 km at 10 GHz and 5 km at 85 GHz. PR sends radar pulses at 13.8 GHz and measures the backscatter, from which the three-dimensional rainfall distribution over both land and ocean can be derived. The horizontal resolution is 4.3 km, but the swathe is narrow at only 220 km.

Figure 3.4.5 (see Plate 3.4.5, p. 172) shows that a large value of precipitation is found in the Intertropical Convergence Zone and South Pacific Convergence Zone all year round. Heavy precipitation is also obvious along the storm tracks in the western North Pacific and North Atlantic during the boreal summer. The strong and steady trade winds and dry air cause strong evaporation in the subtropical oceans, except in the eastern part of the ocean basin of the summer hemisphere, where coastal upwelling produces low T_s , which reduces E .

In addition to the extreme sparsity of *in-situ* validation standards over the ocean, the problem of space-based precipitation estimates is compounded by the short period of rainfall. There is no comprehensive evaluation of precipitation over the global ocean, but many validation experiments are being conducted, and we expect useful accuracy estimates will be forthcoming in the near future.

3.4.6 Future prospects

NASA will provide another scatterometer identical to SeaWinds on QuikSCAT to fly on ADEOS-2, scheduled for launch in November 2001. QuikSCAT

will fly in tandem with ADEOS-2 in a complementary orbit to optimize the coverage by the two scatterometers, if QuikSCAT has a long life. The two SeaWinds instruments are expected to demonstrate the importance of high-wavenumber and high-frequency forcing of the ocean. The European Space Agency will fly a series of dual-swathe C-band operational scatterometers, called ASCAT, on the Meteorology Operational Platform (METOP) beginning in 2003. NASA is planning to supply an improved scatterometer to the Global Change Observation Mission (GCOM), paving the way for an operational scatterometer system. If this project is approved, global ocean winds will be monitored by at least two wide-swathe scatterometers at the same time, starting in 2001. The goal is to have decadal time series of wind stress at a resolution sufficient to resolve the inertial frequency in the mid-latitude ocean (Large and Crawford, 1995) and diurnal variation in the tropical ocean (Large and Gent, 1999).

CERES, the Multiangle Imaging Spectroradiometer (MISR), and the Moderate-Resolution Imaging Spectroradiometer (MODIS) on NASA's Terra mission, launched in December 1999, will provide estimates of the radiative forcing. Similarly, two instruments (the Spinning Enhanced Visible and Infrared Imager (SEVIRI) and the Global Earth Radiation Budget (GERB) sensor) will be available on the Meteosat Second Generation, the next European geostationary satellite. There are a number of improved atmospheric temperature and humidity sounders such as AIRS and the Advanced Microwave Sounding Units (AMSU) that have improved spectral and vertical resolutions, scheduled to be launched early in the twenty-first century. They may advance the estimation of evaporation and the sensible and long-wave net heat fluxes.

Following TMI, surface hydrologic forcing (both evaporation and precipitation) can be estimated from the Advanced Microwave Scanning Radiometer (AMSR); it is similar to TMI but has more channels. One will be launched on the NASA Mission Aqua and the other on ADEOS-2, scheduled for 2000 and 2001, respectively. A single polar orbiter may not be able to provide sufficient sampling for precipitation, but two AMSR instruments in complementary polar orbits should improve the monitoring of the hydrologic forcing.

NASA is also planning a global precipitation mission, with international partners, which would expand the tropical rain-measuring capability of TRMM to high latitudes.

Even from the vantage point of space, no single polar-orbiting instrument can monitor air-sea exchanges with sufficiently high resolution, extensive coverage, and frequent sampling, nor can any single instrument be expected to operate for the long period needed to acquire climate-relevant time series. International and interagency cooperation and coordination is required for keeping an optimal suite of sensors operational for a long period of time.

Present general circulation models are structured to be initialized by and to assimilate traditional ground-based measurements. Space-borne sensors do not measure the same parameters. For example, space-based sensors measure radiance and backscatter averaged over an area, while ground-based instruments measure wind and temperature at a single location. Space-based data are forced to imitate and are compared against ground-based standards because of historical bondage. Innovative and revolutionary approaches will be needed for optimal utilization of space-based measurements. Developments in four-dimensional assimilation of the plethora of measurements coming on line will eventually allow atmospheric models to be sufficiently constrained to provide the correct surface fluxes. An important aspect for development is that NASA has made the data freely available to scientists; the European and Japanese space agencies are following suit, with their data freely available to a large research community. Linkage to websites with data access and information can be found at <http://airsea-www.jpl.nasa.gov/seaflux>.

Acknowledgements

The research was performed at the Jet Propulsion Laboratory, California Institute of Technology, under contract with NASA, and at the NOAA Atlantic Oceanographic and Meteorological Laboratory. It was jointly supported by the Physical Oceanography Program, the Earth Observing System Interdisciplinary Science Program, the QuikSCAT Project, and the TRMM Project of NASA. Assistance by Ms Gail Derr with production of the manuscript is gratefully acknowledged.

3.5

Developing the WOCE Global Data System

Eric J. Lindstrom and David M. Legler

3.5.1 Organization and planning for WOCE data systems

Traditionally, the collection and analysis of *in-situ* oceanographic data has been the task of individual scientists. To address larger problems, such as the nature of the global ocean circulation, scientists worked together to make WOCE (World Ocean Circulation Experiment) a reality. Still, most WOCE data have been collected by individual Principal Investigators or small, specialized teams under their direction. However, the task of producing a global view of the oceans depends on assembling the contributions of all the PIs into an easily accessible composite data set of quality-reviewed data.

The various components of WOCE combine to form the biggest and most comprehensive oceanographic experiment to date. Satellite measurements, *in-situ* observations and the development of models are all contributing to this first truly global ocean experiment. Figure 3.5.1 shows how the number of WOCE oceanographic stations far exceeds previous experiments, and illustrates the high number of 'data years' of direct current measurements being accumulated. In addition there are some 60 000 XBT (eXpendablebathythermograph) profiles collected per year, and extensive sets of ADCP (Acoustic Doppler Current Profiler) and surface salinity data. The global satellite data sets provide a level of coverage previously unobtainable. The accurate and quasi-synoptic WOCE data set will be the definitive baseline of the 'state of the ocean' against which past and future changes will be measured. The

success of WOCE has relied on a new level of international cooperation that is set to continue in future climate-related projects and global ocean observational programmes.

Investigators retain data in order to conduct quality checks, to maintain the privilege of first publication, or simply because of over-commitment. Thus, the first hurdle for WOCE data management was assembling the data and associated documentation. Once assembled, the identification of data products of general use had to be completed and resources for such production identified. It was also recognized early that the organization of data (largely by measurement type) for assembly and quality control was not the most conducive to analysis and synthesis of the results obtained. The basin-scale circulation would ultimately have to be described using a mix of data and information spanning all the WOCE observing subsystems.

In this chapter we provide an overview of the data handling by WOCE. The remainder of the first section describes the objectives of the WOCE Data System, the reasoning for developing the infrastructure as it is, and the data policies and practices used. The idea of data streams and the functional elements necessary to manage them are briefly described in the second section. The third section is devoted to the future ambitions and directions for delivery of WOCE data products and transition to future programmes.

A detailed and updated summary of WOCE field programmes is not the subject of this chapter. Data status is available through the WOCE Data Information Unit (DIU) (<http://www.cms.udel.edu>).

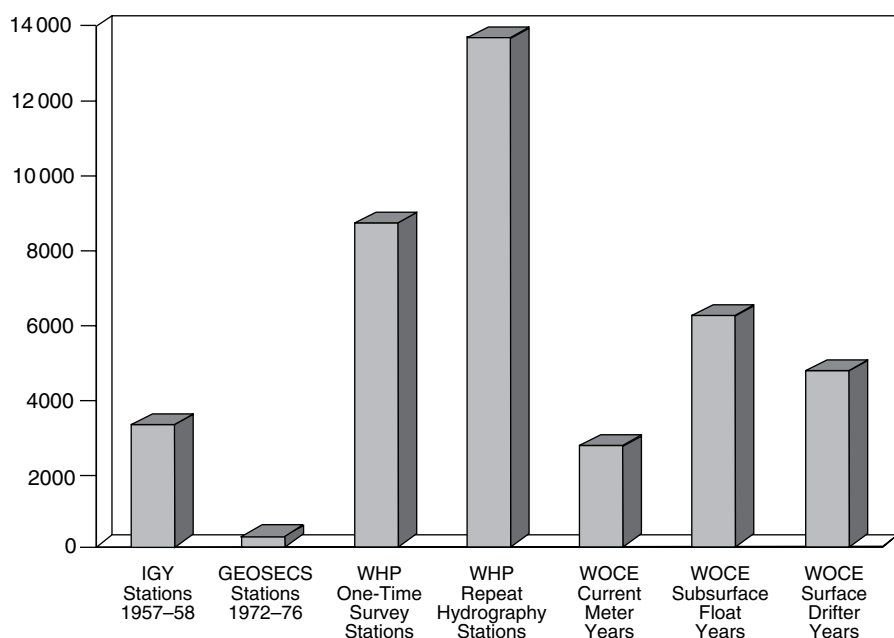


Fig. 3.5.1 Number of hydrographic stations and data-years of measurements taken by WOCE Hydrographic Programme (WHP) and previous oceanographic expeditions. Figure reproduced courtesy of WOCE International Project Office.

3.5.1.1 Primary functions of the data system

WOCE data activities fall in three areas: assembly and distribution of data, production of data products, and participation in analysis/interpretation of the data sets in order to understand ocean processes. The initial framework for a WOCE Data System was developed to assist in these functions.

At least one Data Assembly Centre (DAC) exists for each type of data. Their primary functions are to assemble data sets, subject them to quality control, and ensure distribution. The collection and quality review processes are different for each data stream; however, each DAC maintains an updated and public inventory of data received and also documents its quality control procedures. The DACs take an active role in tracking data quality, including contacting data providers to confirm suspected reasons for problematic data. This feedback leads to improved observation systems, procedures and review criteria. Providing for easy access to the data sets for WOCE and other investigators is also a necessary function of the DACs. Online access has been emphasized wherever possible.

A second function of the DACs and a Data Information Unit (DIU) is to provide information about how the data were obtained. This metadata must include origination and quality review results and should be as easily accessible in a reasonable

way as the data sets. Metadata is particularly valuable for future climate studies when biases from the observation system must be considered. Useful information in metadata also includes primary references such as journal publications and technical reports where available.

A third function of the centres is to create, compile, and/or track data products that are deemed useful for WOCE.

For two types of data – hydrographic and surface fluxes – there are also Special Analysis Centres (SAC) that perform additional functions to address science-driven objectives such as developing gridded products for analysis of water mass properties or evaluating various surface flux products for forcing ocean models.

The WOCE archive has been established to ensure a permanent home for the original and quality-reviewed WOCE data. The complete list of data streams with listings of the DACs, SACs and archive site is presented in Table 3.5.1.

The WOCE Data System is fundamentally different from anything formerly organized in oceanography. It was unprecedented in scope of data types and sources to be assembled and relatively uncompromising in the high priority it put on data quality and documentation. It attempted to place responsibility for assembly of data and

Table 3.5.1 Elements of the WOCE Data System

| Data streams ^a | Elements ^b |
|------------------------------------|------------------------|
| Metadata and programme information | |
| Data information unit | UDEL, USA |
| Hydrographic programme | |
| WHP office | SIO, USA |
| WHP special analysis centre | BSH+, FRG |
| Surface drifters | |
| Global drifter centre | AOML, USA |
| Archive | MEDS, CAN |
| Upper ocean thermal data | |
| Data assembly (GTS) | MEDS, CAN |
| Data assembly (delayed mode) | NODC, USA |
| Regional quality control centres | |
| Atlantic | AOML, USA |
| Pacific | SIO, USA |
| Indian | AODC/CSIRO, AUS |
| Global UOT data centre | IFREMER, FR |
| Sea level | |
| Fast delivery | UH, USA |
| Archive | BODC, UK |
| Subsurface floats | |
| Moored measurements | |
| Surface meteorology/air-sea flux | |
| Surface salinity | |
| Satellite altimetry and SST | |
| Bathymetry | |
| Acoustic Doppler current profiler | |
| Global data assembly centre | JODC, Japan |
| US data assembly and online access | UH, USA |
| Model results and derived products | Not established |
| WOCE data archive | WDC, Oceanography, USA |

^aAbbreviations: GTS, Global Telecommunications System; SST, Sea Surface Temperature; UOT, Upper Ocean Thermal; WHP, WOCE Hydrographic Programme.

^bAbbreviations for WOCE Data System elements:
UDEL, USA – University of Delaware; BSH, Germany – Bundesamt für Seeschiffahrt und Hydrographie; MEDS, Canada – Marine Environment Data System; UH, USA – University of Hawaii; WHOI, USA – Woods Hole Oceanographic Institution; JPL, USA – Jet Propulsion Laboratory; JODC, Japan – Japan Oceanographic Data Center; WDC-Oceanography, USA – World Data Center-Oceanography, Silver Spring (NODC); SIO, USA – Scripps Institute of Oceanography; AOML, USA – Atlantic Oceanographic and Meteorological Laboratory; NODC, USA – National Oceanographic Data Center, USA; IFREMER, FR – Institut Français de Recherche pour l'Exploitation de la Mer; BODC, UK – British Oceanographic Data Centre; FSU, USA – Florida State University; NGDC, USA – WDC-Marine Geophysics (NGDC).

quality-control oversight in the hands of experts intimately familiar with that data type. It recognized the need for centralized access to coordination and management information through the development of the WOCE Data Information Unit. It also recognized the need to develop mechanisms for improving access and integration of the data sets for ease of use by the scientific community. It has consequently evolved into a

remarkably robust data system capable of delivering needed data, information, and products to meet community needs.

3.5.1.2 WOCE data policies and practices

Role of the Data Products Committee

A forum for interaction of the scientific community and data managers was essential for the development of WOCE, as data management was one

of the most important problems it faced. WOCE set up a Data Management Committee to oversee aspects of the data system. This committee provided the needed functionality for WOCE data management and initially focused only on data management issues. Seeds of new ideas such as developing higher-level products and complete information archives were planted early, and as the field phase progressed it became apparent that the committee must nurture these forward-looking ideas to support successfully a synthesis of WOCE results. Thus the Data Management Committee was transformed into the WOCE Data Products Committee (DPC). This involved increasing direct participation by WOCE scientists while maintaining, *ex officio*, the full complement of WOCE data management leaders in its ranks. Its primary functions were as follows:

- To provide oversight and advice for the incorporation of WOCE data into a coherent representation of the global circulation and its variability, the resulting transports of heat and fresh water, and the distribution of physical and chemical properties.
- To interact with other WOCE working groups in order to advise the WOCE Scientific Steering Group (SSG) on the data products that will be required for community-wide WOCE analysis and synthesis activities.
- To be responsible to the SSG for the timely and appropriate production and delivery of WOCE data and data products to the community of WOCE researchers.
- To advise the SSG on the effectiveness of all elements of the WOCE Data System (DACs, SACs, Archive and DIU) by continuing oversight of the System's operation, and to recommend changes to the system, where appropriate, and to take advantage of technological developments.

The DPC has served as the catalyst for change and coordination among the DACs and SACs. Openly sharing data sources, as well as quality-control and data management technologies and experiences is a common tenet of DPC members. The advent of network and CD-ROM based information technologies encouraged creation of archive-ready data products. Invited science presentations at annual DPC meetings led to improved products, enhanced collaboration with WOCE

researchers, and served as a compass for evolutionary development of the integrated WOCE Data resource.

WOCE data-sharing policy

WOCE has developed a data-sharing policy that strikes a balance between the requirements of the experiment as a whole and the intellectual rights of the individuals who contribute to the programme. The trade-off between these different interests has resulted in a policy that expects data to be made publicly available within 2 years of the data set being complete. Investigators are thus allowed a reasonable period to complete their own analysis and publications, while ensuring the global data set is accumulated and made accessible for wider examination. Data may be assembled at centres soon after collection but for some data types will not be released by DACs without the consent of the originator. WOCE encourages investigators to share data with others and to authorize general release as soon as possible. If investigators demand exclusive rights to data more than 2 years old, then WOCE encourages peer pressure and funding agencies to persuade the originator to give consent for its general availability.

Evolution of the WOCE Data System

A number of changes and adaptations had to be made to the data system as it developed during the field phase of WOCE. The difficulty in assembling data in a timely manner was not fully appreciated during the planning of WOCE. The more time that passes between the time of data collection and the assembly of the data and metadata at a DAC, the more likely it is that problems or questions about the data will remain undocumented or unresolved. Because investigators delayed submission of data to assembly centres, the WOCE data-sharing policy received much attention. The data-sharing policy was refined to recognize that the need for data assembly in a timely manner is an issue independent of the investigators' consent to make data publicly available.

As originally envisioned, there would have been many SACs in WOCE – perhaps as many as one for each data type. However, the concept of centralized analysis centres, under data management oversight, charged with developing and circulating data products and analyses was not popular. Instead it became apparent that production of any special

products of great utility to the community should be produced on the basis of proposals for specific data (or model) products. DACs were eventually charged with tracking such product generation initiatives and to broaden their scope to accommodate their own involvement in these activities.

Technology developments impacted the WOCE Data System in a number of ways. Observational technologies developed during the experiment, necessitating new responsibilities (e.g. profile capability on floats, lowered ADCPs) for data assembly and quality control. Perhaps most profound was the change resulting from the advent of the World Wide Web and browser software. The web capability brought the disparate functional elements together virtually and stimulated online access to many heretofore hidden resources.

Providing for easy access to the data sets for WOCE and other investigators is also a necessary function of the WOCE Data System. Online access has been emphasized wherever possible. The widespread use of the World Wide Web and public Internet sites for data files has revolutionized online data distribution in just the past few years. Likewise, inexpensive CD-ROM technology has allowed mass distribution of data for immediate local accessibility. Data availability for WOCE has changed dramatically as a result of these developments.

The concept of a single WOCE Data Resource

One aim of WOCE data facilities and WOCE Data Products Committee is to provide better and more comprehensive access to WOCE data of all kinds. One concept that is assisting in this direction is that of a WOCE 'Data Resource' (Fig. 3.5.2). The idea is that the seeker of WOCE data should begin to see the highly distributed WOCE data system more as a single entity (despite the fact that the data assembly, quality control, distribution and documentation functions will remain highly distributed). The distributed system continues to allow the value-adding processes of quality control, collation of metadata, and establishment of common data formats for each data type. However, the Data Resource is a rubric for more natural arrangement of the WOCE data for analysis, modelling, data assimilation and interpretation. The development of a 'virtual' WOCE Data Resource (that logically organizes access to all of the WOCE data streams including metadata, modelling results and data

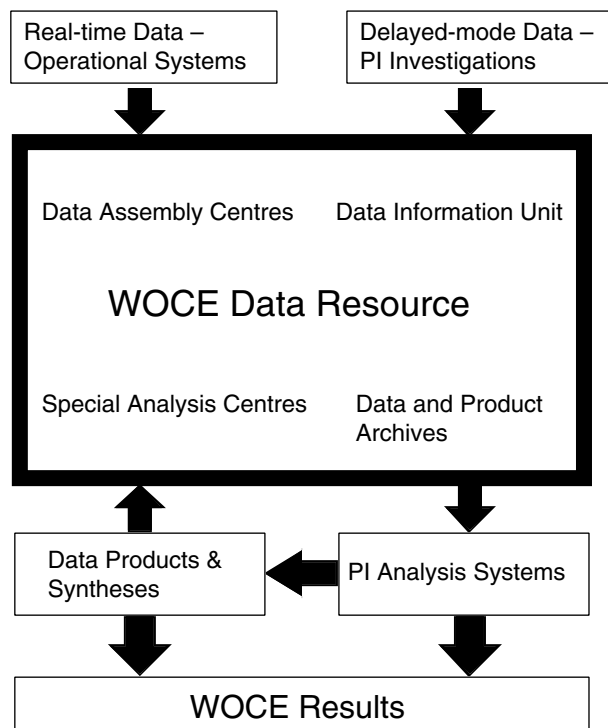


Fig. 3.5.2 Conceptual schematic of the WOCE Data Resource.

products) better satisfies a range of generic user needs during the WOCE Analysis, Interpretation, Modelling and Synthesis (AIMS) phase.

The aim of the Data Resource is to provide researchers with an interface through which a wide range of WOCE data and data products may be accessed without concern for the complex internal structure and distributed nature of the WOCE data infrastructure. The WOCE Data Resource allows integrated data products to be developed more easily and transparently from available data.

3.5.2 Elements of the WOCE Data System

3.5.2.1 Data streams in WOCE

The WOCE Data Resource is composed of a number of data streams. Data streams were identified based on types of data that were naturally grouped together during collection and/or processing. Thirteen data streams were identified (see Table 3.5.1). The purpose of defining data streams was to prescribe the boundaries of WOCE data management and data policies. A few WOCE data sets (e.g. lowered ADCP, deep pressure gauges and inverted echo sounders) were not initially identified as fitting into any regular data streams and

were identified as ‘orphan’ data sets requiring special treatment by data managers in WOCE.

Data streams have the following properties that need to be managed, monitored, or developed:

- source of data;
- means of communicating data;
- one or more points of assembly;
- quality control gating with feedback to users;
- data distribution mechanism;
- scientific analysis with feedback to quality control;
- value-added products;
- some level of integration into single data resource;
- delivery of data to the permanent archive.

Functional elements to manage, monitor or develop these properties are peculiar to each specific data stream identified in WOCE.

3.5.2.2 Elements of the WOCE Data System

Thirteen data streams are identified in WOCE. Together they constitute the WOCE Data Resource. It is through these streams that qualified data and information are made available to the final WOCE Data Archive.

There are 22 functional units in the WOCE Data System spread across seven countries (USA, Canada, UK, France, Germany, Australia and Japan, see Fig. 3.5.3). These are listed in Table 3.5.1.

Metadata and programme information

The WOCE Data Information Unit (DIU) is a comprehensive guide to the WOCE programme and is the gateway to the online WOCE Data Resource. The DIU actively involved science expertise as well as database and information specialists to maintain this dynamic resource. Links to WOCE data and products, information about data status, and details of all the field activities can be found at the DIU. The centre supports a bibliography of WOCE publications and links to online abstracts relating to WOCE.

Hydrographic programme

The WOCE hydrographic data are the core measurements of the observational programme (see King *et al.*, Chapter 3.1), and include CTD (Conductivity-Temperature-Depth) and discrete bottle data from one-time and repeated sections and time series stations. Almost all WOCE Hydrographic Programme (WHP) data sets include discrete

salinity sampling, and those from the one-time survey also include oxygen, nutrients and a range of other tracers including chlorofluorocarbons, tritium, helium-3, carbon-14 and several CO₂ parameters.

Processing of CTD data requires application of laboratory calibration data, vertical averaging of bottle/CTD data at scales not exceeding 1–2 dbar, correction using bottle values collected simultaneously, and quality control. The data originators carry out these functions, with subsequent assembly and quality control by the WHP Office (WHPD).

Almost all WHP data sets include water samples for shipboard or later analysis. Each data type carries its own set of processing and quality control procedures to ensure the highest, consistent quality across all WOCE data. These procedures are carried out by the originators and overseen by the DAC based on standards and WOCE procedures specific to each measured quantity.

A Special Analysis Centre for WOCE hydrography was established in Germany early in the programme. Its mission is to provide a globally consistent data set and to generate gridded products for use in models and other analyses. Specialized visualization programs and historical (pre-WOCE) hydrographic data are also available from the SAC.

Surface drifters

The drifter data are assembled by the NOAA AOML Drifting Buoy Data Assembly Center and by the Marine Environmental Data Service in Canada. The WOCE drifter data set includes positions, times, temperature and drogue depth and status; for some records atmospheric pressure and salinity are also measured. The DAC generates regularly updated position and velocity products (interpolated to 6-h intervals) from the raw data.

Upper ocean thermal

Upper ocean thermal data are collected mainly from XBTs deployed by voluntary observing ships in two modes; broad-scale with relatively low along-track resolution, and a limited number of sections with high along-track resolution. The temperature profiles are sent to data centres in real time (with relatively low vertical resolution) and most are eventually replaced by their high-vertical-resolution equivalents in delayed mode. The profiles are managed such that users have access to

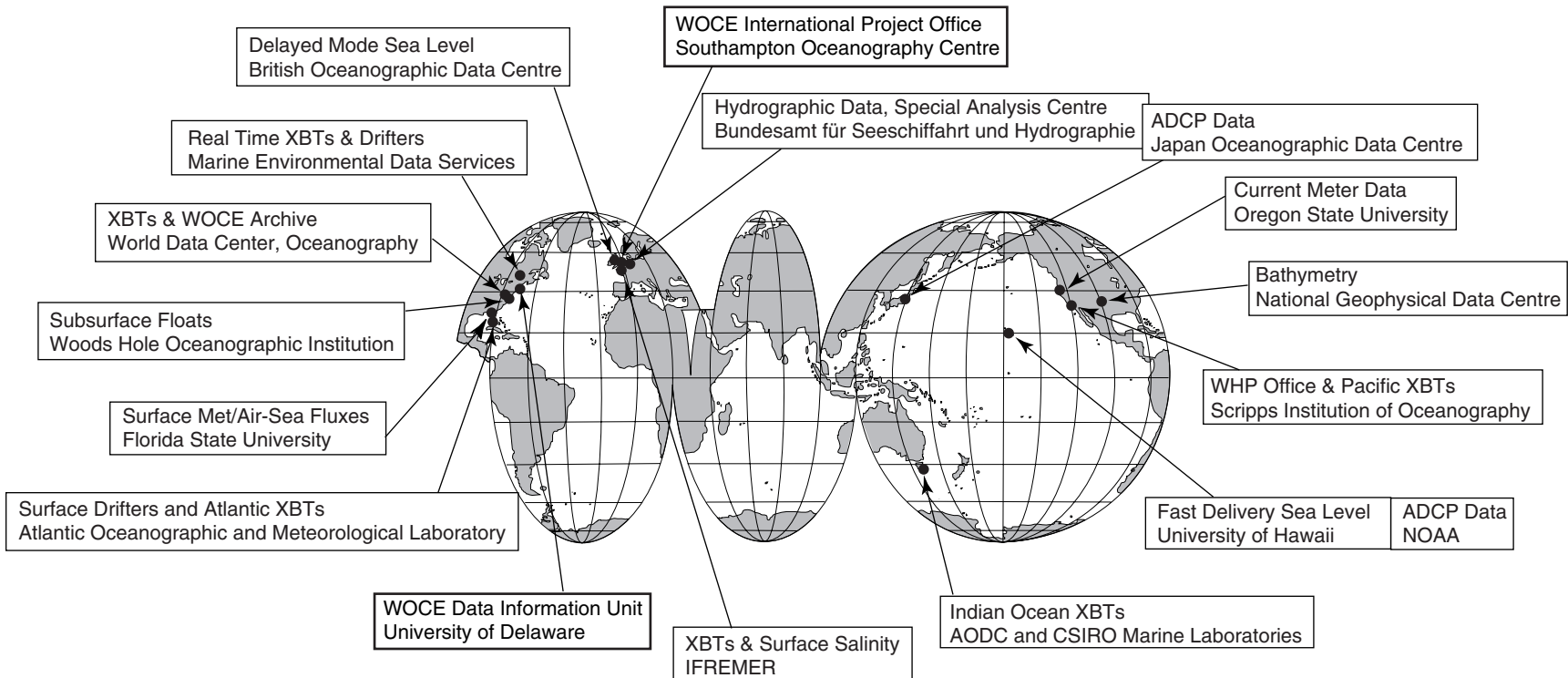


Fig. 3.5.3 Locations of distributed WOCE Data System (see Table 3.5.1). Figure reproduced courtesy of WOCE International Project Office.

the highest vertical resolution and most rigorously quality-controlled profiles available. The quality control of the data occurs in two stages; the DACs perform initial screenings and three Regional Quality Control centres perform a more rigorous scientific quality control. All these centres coordinate the collection and monitor data receipts to ensure maximum data recovery to the WOCE Data Resource.

Sea level

WOCE *in-situ* sea-level data are received from a global network of tide gauges and the data are treated in two different modes. The fast delivery DAC obtains data in real time from over 100 stations globally and provides hourly, daily and monthly data sets within a month of collection. The delayed-mode centre assembles and quality controls data from 160 stations, and provides original resolution and hourly data, station metadata, summary statistics as well as plots of low-frequency variations, and analysis of tidal constants.

Floats

Prior to WOCE there was no mechanism to assemble or archive data from neutrally buoyant floats. The WOCE DAC first assembled historical float data and made this available on CD-ROM. The WOCE float data are assembled by the WOCE subsurface float DAC in Woods Hole. Visual images of float tracks are made available as a regular product.

Moored measurements

Moored current meter arrays have been deployed for WOCE in narrow passages and in regions of strong currents. The data set consists of velocity, time and position for each current meter, and may also include temperature, salinity and pressure. The Current Meter DAC has generated mean flow statistics for each array, and has acquired and quality controlled a large set of relevant historical data. The QC system and product generation capabilities developed by the DAC provide unprecedented ability for PIs to generate data reports.

Surface meteorology/air-sea flux

During the WOCE observation period research vessels and moored buoys collected high-frequency

marine meteorology data including surface winds, air and sea temperature, humidity, atmospheric pressure, precipitation and other variables. The Surface Meteorology DAC assembles, extensively quality controls and documents these data. Air-sea flux values for momentum, turbulent heat and moisture can be estimated from the data using bulk formulae. The Air-Sea Fluxes SAC is one of a number of groups that produce near-global fields of atmospheric variables and fluxes as well as uncertainties.

Surface salinity

Surface salinity data from bottle samples and from thermostalinographs are assembled by IFREMER in France.

Satellite measurements

Satellite altimetry data have been collected from the ERS-1, ERS-2 and TOPEX/POSEIDON platforms, providing unprecedented observations of sea level variability and wave height. Also of interest to WOCE are measurements of wind velocity from scatterometers, as well as Sea Surface Temperature (SST) and water vapour content from radiometers. The satellite agencies distribute data and a variety of gridded fields and other products from their online data centres. The global products resulting from ocean observation from low earth orbit provide unprecedented information for the analysis and synthesis of sparse *in-situ* measurements.

Bathymetry

Bathymetric data from WOCE survey vessels are assembled and archived by the National Geophysical Data Center (NGDC) in the USA. Here they are merged into the central database of depth information about the ocean. Data from WOCE are separately recoverable from NGDC.

Acoustic Doppler current profiler

Direct current measurements are made by ADCPs operated as hull-mounted instruments sampling the upper 300 m and as lowered ADCPs sampling the full water column at stations. The ADCP DAC at present assembles the shipboard data and can provide the full resolution data set and an averaged set with hourly time spans and 10 m depth intervals. The DPC is working to ensure lowered ADCP data will become a part of the final

WOCE archive, but have yet to develop an effective plan.

Model results and derived products

While needed logically by the WOCE data and information structure, a specific assembly and distribution point for WOCE model results has not been established. PIs have been encouraged to make their results publicly accessible through web sites and the DIU has attempted some compilation of these web sites. Other products that may derive from the WOCE Synthesis (e.g. atlases, gridded products, etc.) would also benefit from assembly and documentation at a central site. However, it is most likely that they will also be made available through PI web sites or as part of WOCE Global Data Set on CD-ROM.

WOCE Data Archive

The US National Oceanographic Data Center (NODC) serves as the host for the World Data Center, Oceanography, in Silver Spring. That centre archives the records of WOCE observations. The NODC provides a focal point that brings WOCE data streams to a common end point. The archive assures the safekeeping of the data and necessary transition to alternative media of the future. It is expected that this will ultimately serve as the online source for all WOCE data long after DACs have evolved and grown into other projects. NODC has ensured mass production and wide distribution of the WOCE Global Data Set.

3.5.3 The WOCE Global Data Set and future developments

3.5.3.1 WOCE Global Data version 1.0

The WOCE data resource is being built upon the already existing data streams. All DACs have established interfaces that allow the selection and search of their own individual data streams. These data streams will be linked in a more systematic way to create one cross-linked searchable data set. This is being accomplished in several stages, the initial phase of which has already been achieved. The World Wide Web has enabled the creation of an embryonic virtual data resource through which the DACs offer access to data and products.

A major step towards the WOCE Data Resource has been the recent production of version 1.0 of the WOCE Global Data on CD-ROMs. These

platform-independent CD-ROMs can be read with free software (Web browsers) and contain all available data, metadata and products at the DACs in February 1998. However, the CD-ROMs do not represent the complete WOCE Data Resource since it is continually expanding as more data become available through completion of quality control or public release by investigators. Data products are evolving as scientific issues are addressed and as synthesis proceeds. Many initial products could become redundant as new data are added and new ideas for forming products are developed.

3.5.3.2 Future versions and directions

The penultimate phase of implementation of the WOCE Data Resource will be the integration of the data sets, documentation and products from the individual data streams into a single logical virtual site or volume. To achieve this level of integration, the WOCE Data System will develop and adopt a set of conventions for data formats and data/metadata content. This level of uniformity should be evident in WOCE Global Data V2.0, scheduled for publication in September 2000. It will facilitate searching, gathering, and synthesis actions across the entire WOCE data system. WOCE Global Data V3.0 represents the integration of the *complete* WOCE Data Resource, thereby becoming the legacy of the WOCE field programme. It may include gridded or self-gridding products suitable for forward models as well as products suitable for data-assimilation and inverse models. For example one can envision that queries to produce three-dimensional gridded temperature fields will result in tagged analyses based on data from multiple instruments (e.g. XBT, CTD, profilers) within the user-defined spatial and temporal domains.

3.5.3.3 Evaluation and transition to future programmes

The WOCE data system has developed into a distributed resource providing quality-controlled oceanographic data. While other attempts to create distributed data systems have met with mixed success, the WOCE system has proven successful and could serve as a model for other elements within WCRP (World Climate Research Programme) and IGBP (International Geosphere–Biosphere Programme). The WOCE DACs and

SACs have assembled and reviewed millions of oceanographic observations. In creating this growing resource they have learned much about the process of adding value to observations made in support of oceanography. Undoubtedly, through this process they have contributed to the improvement of the design, implementation and utilization of ocean observation systems.

WOCE was begun with the understanding (WOCE Goal 2) that a long-term ocean observation programme would evolve from it, designed on the basis of the scientific conclusions of the Experiment. As a WOCE successor programme, CLIVAR (Climate Variability and Predictability) requires a scientific underpinning and plan that reflects present understanding of oceanic behaviour and which utilizes new technical capabilities that have become available since the inception of WOCE. The CLIVAR field programme will necessarily have strong elements that are experimental in nature – because ocean science has not yet evolved to the stage where long-duration, useful measurements can be regarded as either routine or as based upon frozen technologies. The CLIVAR programme, following-on from WOCE, has now developed momentum and is preparing for implementation

planning. Its requirements for ocean observations are large and it may usefully assimilate expertise and infrastructure from the WOCE Data System.

The emphasis of data systems envisioned for future programmes have a few key features in common. For CLIVAR, the first is the need for real-time data delivery for climate prediction purposes. During WOCE several centres operated successfully with this as an objective. Another feature is the end-to-end management of data streams with overarching principles of data quality and consistency. They will require close synergistic relationships between data providers, data assembly/quality review efforts and data users. This philosophy is necessary to generate long time series for climate change detection and attribution.

Other major programmes such as the Global Ocean Data Assimilation Experiment (GODAE), Global Ocean Observing System (GOOS) and Global Climate Observing System (GCOS) will also require more near-real-time reporting of oceanographic data for its inclusion in time-sensitive data ocean products. It is obvious that such requirements will necessitate end-to-end management of data streams as has been pioneered in WOCE.

SECTION

4

THE GLOBAL FLOW FIELD

Chapter 4.1

THE WORLD OCEAN SURFACE CIRCULATION

Peter Niiler

193

Chapter 4.2

THE INTERIOR CIRCULATION OF THE OCEAN

D. J. Webb and N. Sugino

205

Chapter 4.3

THE TROPICAL OCEAN CIRCULATION

J. S. Godfrey, G. C. Johnson, M. J. McPhaden, G. Reverdin and Susan E. Wijffels

215

Chapter 4.4

TROPICAL-EXTRATROPICAL OCEANIC EXCHANGE PATHWAYS

Zhengyu Liu and S. G. H. Philander

247

Chapter 4.5

QUANTIFICATION OF THE DEEP CIRCULATION

Nelson G. Hogg

259

Chapter 4.6

THE ANTARCTIC CIRCUMPOLAR CURRENT SYSTEM

Stephen R. Rintoul, Chris W. Hughes and Dirk Olbers

271

Chapter 4.7

INTEROCEAN EXCHANGE

Arnold L. Gordon

303

This Page Intentionally Left Blank

4.1

The World Ocean Surface Circulation

Peter Niiler

4.1.1 Background

Through many centuries mariners have observed ocean surface currents by noting how their vessels drift, and cartographers have prepared maps on the basis of these ship-drift reports. Instrumental observations of ocean currents on a global basis began about 115 years ago during the voyage of HMS *Challenger*. She left Portsmouth, England, on 21 December 1872, on an ocean expedition that was to navigate the globe in three and a half years. The measurements of the state of the ocean at 354 stations already included ocean current observations with drifting buoys (Thompson, 1877). Aboard were drifters consisting of 4×4 feet cross-shaped canvas sea anchors, attached with various lengths of cod line to 1 foot \times 5 feet spindle-shaped iron watch buoys that were used as surface floats (Fig. 4.1.1). The drifters were deployed from a skiff when the *Challenger* was firmly anchored at an ocean station, with the bottom dredge over the fantail and the skiff lowered over the side. The sea anchors, or drogues, were at various depths, sometimes as deep as 600 fathoms. At 1- to 2-h intervals, the displacements of the watch buoys were obtained by triangulation from the anchored *Challenger*.

The scientists aboard the *Challenger* interpreted the displacement of the watch buoy, divided by the time between observations, as an ocean current at the depth of the sea anchor. They admitted that they did not know how to correct these observations for the effects of the forces of the winds on the watch buoy or the relative water motion between the buoy and the drogues on the cod line. Additionally, they could not obtain data in rough weather.

The instrumental technique of observing ocean currents by following drifters in the open sea captured the imagination of oceanographers and has held it to this day. With the advent in the early 1970s of a cost-effective technique of locating radio transmitters from the TIROS weather satellites, scores of drifting objects could be followed as they moved across the ocean surface of the entire globe (Garrett, 1980). But the problem of interpreting the drift of objects on the ocean surface as a current at some depth was a problem that challenged oceanographers for a hundred years after the *Challenger*. Significant action for its solution was taken in the early 1980s when scientists began planning the World Climate Research Programme (WCRP). They recognized that large arrays of satellite-tracked drifters could be used economically to observe the entire global ocean near-surface circulation, provided the following technical problems were solved (McWilliams and Masterson, 1982).

The water-following capability of drifters had to be determined so that a rational hydrodynamic design could be developed. Over a dozen designs of drifters were in use, but no field-verified engineering formulae were available for choosing the shapes or relative sizes of the surface float, the tether line or the drogue. Could the effects of wind and vertical shear on the slip of drogues through water be measured and corrected? A calibration at sea of the water-following capability of drifting buoys was needed, and that was the first task.

The existing drifters were large, unwieldy and costly to deploy in large numbers. For a century

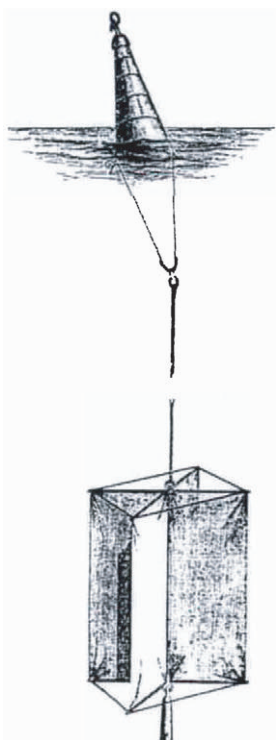


Fig. 4.1.1 The *Challenger* expedition drifter.

oceanographers had carefully lowered drifters into the water by cranes from stationary research vessels. These devices usually weighed several hundred pounds, and they could not easily be shipped or deployed into remote areas on a routine basis. A rugged miniaturization of the drifters was required so they could be easily deployed by one deck hand from the fantail of a Volunteer Observing Ship (VOS). These drifters would have to survive a free-fall of 30 feet (~ 10 m) to the water surface into the wake of a large cargo ship that was travelling at 20–30 knots.

Oceanographers had to extend the operational life of a drifter at sea several times over what was commonly the case in the early 1980s. The wave-tossed ocean surface is a corrosive and stressful environment where drifters would usually break within several months. Why drifters were failing was a question that could only be answered by recovering significant numbers after they had been at sea for periods of time.

The costs of returning data from the ARGOS satellite location system and distributing it to users had to be reduced by a large factor. The management costs of the satellite data system for locating drifters could not be afforded by a programme of the scope contemplated by the WCRP planners. And a centre had to be established for quickly

distributing the data to both the research and the operational communities of scientists.

In 1987, a small team of scientists, supported by the Tropical Ocean and Global Atmosphere Programme (TOGA) of WCRP, set out to obtain an instrumental record of the world's ocean surface circulation. They embarked upon the ambitious programme to design, calibrate, deploy and distribute data from a global array of lightweight, low-cost drifters (WCRP, 1988c). The first objective, to measure the currents of the tropical Pacific Ocean, was accomplished (Niiler, 1995). A Drifter Data Center was established at the Atlantic Oceanographic and Meteorological Laboratory (AOML in Miami, USA). Then the project was expanded to a global scale under the sponsorship of the World Ocean Circulation Experiment (WOCE) and other scientific programmes, and between 1991 and 1999, an accurate instrumental circulation record of the greater part of the global ocean surface was obtained.

The WOCE scientific plan (WCRP, 1988a) called for the observations of the annual average global surface circulation and its variance on a nominal 5° latitude $\times 5^\circ$ longitude space resolution with data gathered over a 3- to 5-year time period in each ocean basin. Wind-driven currents were to be separated from geostrophic currents. Oceanographers estimated that a minimum of 4500 drifters would be required to achieve these goals. Since 1988, over 45 scientific projects in 18 countries contributed resources to this Global Drifter Programme. By the close of the twentieth century, over 4800 calibrated drifters were deployed, achieving and exceeding the objectives of WOCE. From 1993 onward, an average global array of 700–900 drifters were in the ocean providing data on ocean currents and sea surface temperature. The raw data from these drifters is gathered on the ARGOS system and is distributed with about a 2-h delay on the Global Telecommunication System (GTS). The processed data, and the extensive list of scientific papers that have been published using these data, can be viewed on the Drifter Data Center web site: <http://www.aoml.noaa.gov/>. The Data Buoy Cooperation Panel (DBCP) of the Intergovernmental Oceanographic Commission (IOC) and the World Meteorological Organization (WMO) now sponsor the Global Drifter Programme.

This chapter describes the new drifters and summarizes the global data set of near-surface current

observations and the calculations with that data that were the objectives of WOCE. In particular, the mean circulation, the eddy energy distribution and the wind-driven, or Ekman currents are discussed. The richness of this global data set is revealed in the extensive literature listed at the aforementioned web site.

Section 4.1.2 discusses how low-cost, rugged, satellite-fixed drifters were made and the methods of deriving a map of ocean currents from drifter data in a wind- and wave-tossed ocean. Besides the data obtained during the observational period of WOCE, in the period 1978–94 meteorologists deployed over 800 drifting buoys of the First Global GARP Experiment design (FGGE-type) into the Southern Oceans for the purpose of measuring sea level atmospheric pressure. These FGGE drifters usually did not have drogues attached and their motion was corrected for the effects of wind relative to the drifters deployed in the Global Drifter Programme. Section 4.1.3 presents the maps of the mean circulation, its uncertainty and the eddy energy on the spatial resolution set out in WOCE plans. Section 4.1.4 discusses the interpretation of the observed circulation in terms of the local wind-driven or Ekman currents. In Section 4.1.5, the future of the drifter observations is briefly discussed. The Global Drifter Programme,

or Surface Velocity Programme (SVP) drifters, now serve as platforms to which sensors are attached for observing winds, salinity, temperature, ocean colour and atmospheric pressure.

4.1.2 Methodology

Since the WOCE surface circulation data were obtained with a new instrumental methodology, it is essential to discuss it at length. It represents an important development in the instrumental technology of ocean current observations. A number of different drifter designs were used in the Global Drifter Programme. A complete description of each drifter is maintained in a 'meta' file at the Global Drifter Data Center. Since 1991, nearly all of the drifters were configured with a spherical surface float, a plastic-impregnated wire tether and a drogue in the shape of a cloth cylinder with circular holes on its sides – the 'SVP drifter' (Sybrandy and Niiler, 1991; Figs 4.1.2 and 4.1.3). The surface float contained a radio transmitter, digital controller, batteries, antenna and several ocean sensors. The controller was programmed to sample the sensors, format the data and periodically turn on the transmitter. A Sea Surface Temperature (SST) sensor was mounted on the lower portion of the surface float and a submergence sensor was

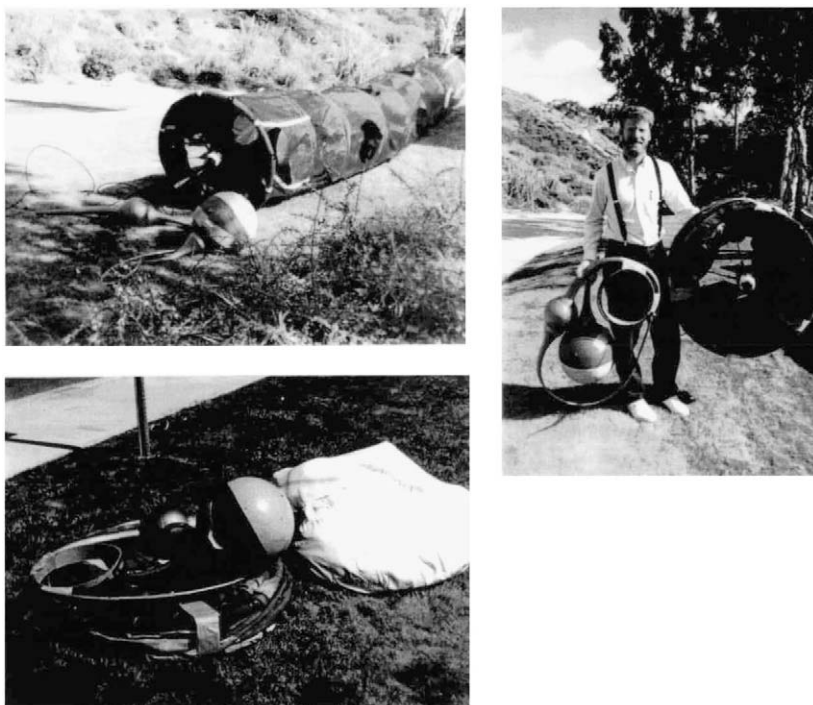


Fig. 4.1.2 The WOCE/TOGA Lagrangian drifter.

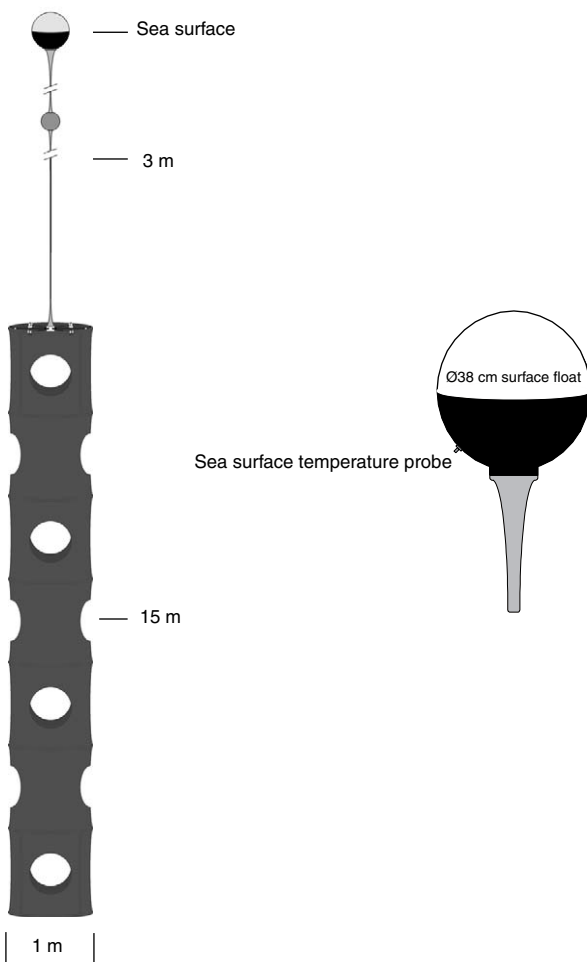


Fig. 4.1.3 Schematic of SVP drifter.

mounted on the upper portion. When the drogue was attached the surface float submerged often; no submergence was observed when the drogue was detached. These drifters weighed about 24 kg when packed into biodegradable cardboard boxes that served also as deployment packages.

When the drifters were deployed at sea, the transmitter emitted a 0.5-watt signal at 401.65 MHz, approximately every minute. This broadcast contained a 252-bit message with the identification number of the drifter and the sensor data. When the TIROS satellite passed over the drifter, the ARGOS system on board received a sequence of messages from the drifter. This sequence of messages was used to locate the drifter under the satellite track by Doppler ranging, with a maximum accuracy of about 300 m. A more typical rms error of 600 m was found off the coast of California (Poulain *et al.*, 1987). The number of observations per day depended upon the number of times a TIROS satellite passed overhead, ranging from six

times in equatorial latitudes to 15 times at 60°N latitude. The data from TIROS was received by Service Argos facilities and distributed to the GTS and the Global Drifter Center. The Marine Environmental Data Service (MEDS) of Canada collects and stores all the drifter data picked up by the GTS. To minimize the costs of Service Argos distributing the data, the drifters usually broadcast one day out of every three.

The ARGOS location data was interpolated to regular time intervals by kriging (Hansen and Poulain, 1996). A velocity was computed from the rate of change of the interpolated displacement with time. This velocity is the sum of the average velocity of the water over the vertical extent of the drogue and the 'slip' of the drogue through the water. This slip can be caused by the effects of the waves and wind on the surface and subsurface elements of the drifter and the relative motion of the water between the drogue and the float and tether assembly (Niiler *et al.*, 1987). Using a variety of drogue sizes and in a variety of wind conditions, field observations of the slip were made with current meters attached to the top and bottom of the drogue. These demonstrated that the slip of the drogue through the water was directly proportional to wind speed and inversely proportional to the ratio of the drag area of the drogue and the sum of the drag areas of the float and the tether (Niiler *et al.*, 1995). The drag area is the product of the total frontal cross-sectional area of a component multiplied by its drag coefficient. The drifters in the Global Drifter Programme had a drag area ratio in excess of 40 so that the wind-produced slip through the water was less than 1 cm s^{-1} in winds of 10 m s^{-1} . The velocity data were corrected for the effects of the wind slip using the NCEP re-analyzed winds, which were interpolated to the 6-hourly drifter locations, and the wind-produced slip current was removed from the velocity.

In the course of the Global Drifter Programme a number of drifters whose submergence sensors indicated that the drogues had become detached were recovered at sea. All had tether failures at points where the fish bite was coincident with a stress concentration point above the subsurface float. With design changes since 1995, the tethers remain intact for an average of 550 days (Kennan *et al.*, 1998). Drifters appear to sink over a period of several years in biologically rich waters as barnacles accumulate on the surface float. This sinking

was indicated by an increase of surface float submergence with time. Some were also picked up by fishermen or went ashore, especially around the islands of the western tropical Pacific and the northwest coast of North America.

If the drifters lose their drogue, the surface float usually will continue to operate. On 32% of the drifter data on file the submergence switch indicated severed tethers. The motion of the float, with a 3 m segment of tether attached, was still valuable data on water motion, provided the velocity difference between the floats with drogues attached and those without drogues could be rationalized in terms of other observable parameters, such as wind and waves. A second valuable data set came from drifters that meteorologists deployed for measuring atmospheric pressure. Commencing in FGGE in 1978, meteorologists deployed a large number of drifters in the Southern Oceans that typically had cylindrical floats of 2 m length. These FGGE-type drifters usually had no drogues or the drogues became detached within 60 days (Garrett, 1980). After 1983 no drogues were attached; 842 FGGE-type drifter records on file at MEDS had usable position data. By comparing the average velocity obtained by drifters with drogues and those without drogues or the FGGE-type drifters, it was found that the latter slip downwind relative to

drifters with drogues by 0.88 cm s^{-1} per 1 m s^{-1} of wind (Pazan and Niiler, 2000). Again, the NCEP Reanalyzed winds were interpolated to the 6-hourly drifter locations and this wind-produced bias current was removed. The data presented here also includes the wind-slip-corrected data from WOCE/TOGA Lagrangian drifters without drogues and the FGGE-type drifters.

After the wind-slip corrections were applied, the velocity data were averaged over a specified number of days and segregated into geographical bins of specified degrees of latitude and longitude. If the bin was too small, not many observations were contained therein; if too large, the space scale of the ocean circulation would be obscured. The bin size of 2° latitude by 6° longitude, when coupled with over 100, 2-day average observations per bin, gave stable statistics of the mid-basin ocean current systems (Fig. 4.1.4). The data density distribution of Fig. 4.1.4 is based on a total of 962 672 2-day average, wind-slip-corrected velocity observations.

To resolve the western boundary currents, such as the Kuroshio and the Gulf Stream, the bin size should be 20 km across the current and several 100 km along the current. It was not possible to draw sensible maps of the circulation where both mid-ocean spatial scales and western boundary spatial scales of averaging are displayed on the

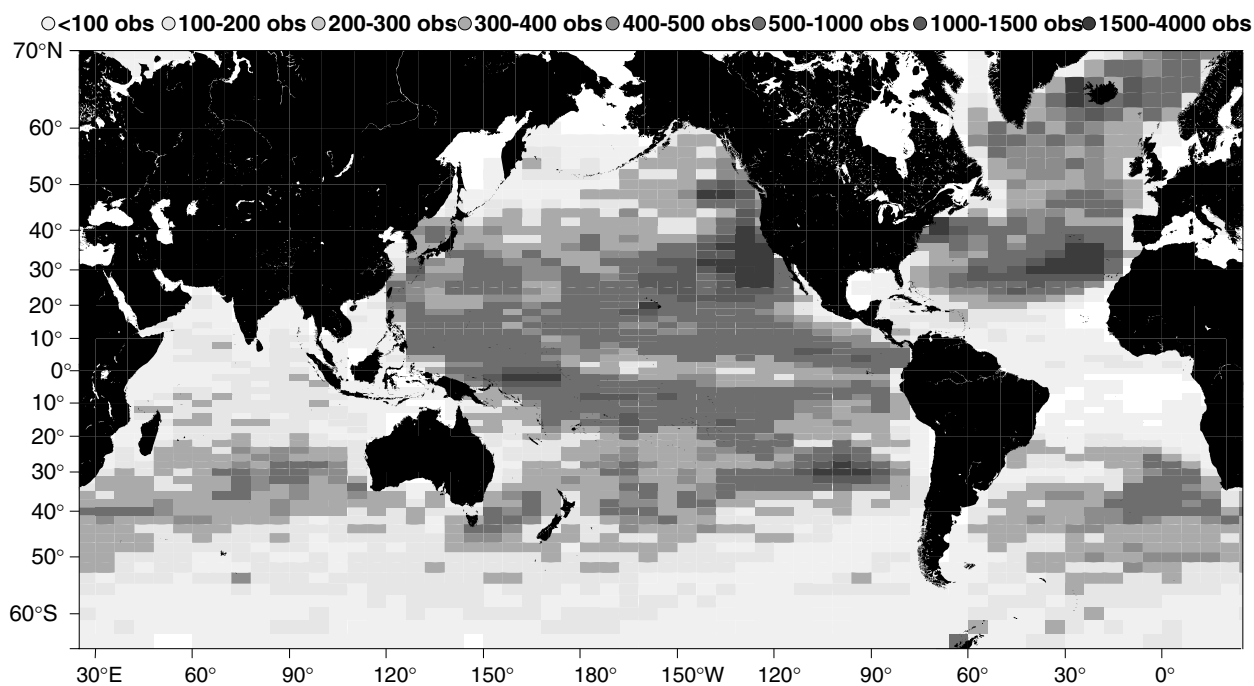


Fig. 4.1.4 Number of 2-day average drifter observations from combined Global Drifter Programme and FGGE-type drifters, January 1978–June 1999.

same map. The western boundary current systems were averaged on the same scales as mid-ocean circulation, but with full awareness that this $2^\circ \times 6^\circ$ average, as originally specified in the WOCE plan, cannot capture the true spatial scale or the velocity amplitude of the western boundary circulation features. Each boundary current requires a binning strategy that is unique and is not presented in this overview for every boundary current system. An example of the effects of reducing the averaging scale in the western North Pacific is discussed below. Also, bin size affects the computation of the scale-dependent dynamical quantities such as divergence (Poulain, 1993) and the relative vorticity. A more sophisticated binning routine would have to be used if stable gradients of the mean velocity are desired, an objective not in the WOCE plan.

Finally, the drifters followed the two-dimensional circulation at 15 m depth and this velocity field could be strongly convergent or divergent due to the sinking or rising of water vertically. Drifters were usually released in large-scale divergent areas along merchant shipping lines in the tropics or regions near coasts from where they travelled to the mid-gyres that were typically convergent. The resulting sampling of the velocity field thus could occur in a biased fashion if the tendency to remain in a convergent region was greater than the wind-produced slip to transit the region. Regions of strong convergence could, thus, be sampled more often than regions of divergence, and if the velocity in either region were stronger, then a bias would result from the ensemble mean. Within the Kuroshio, south of Kyushu, this biased sampling led to the result that the ensemble mean drifter current was about 30 cm s^{-1} larger than the average current derived from a combination of current meters, hydrography and satellite altimeter sea-level observations (Uchida *et al.*, 1998). Apparently, drifters converged towards the velocity axis of the Kuroshio. This is another reason why the detailed structures of each of the strong western boundary current regions were not discussed; each boundary current would require a different velocity data set to assess the potential biases of drifter sampling.

Satellite altimeter data offer a technique for testing the sampling characteristics of the variance of the velocity also in the open ocean, although they cannot provide a test for the mean. This test was carried out in the North Pacific in a comparison of the variance of geostrophic currents normal to

the TOPEX/POSEIDON altimeter track. The geostrophic component of the drifter velocity was computed by subtracting the Ekman component according to the formulae specified in Section 4.1.4 (Ralph and Niiler, 1999). The geostrophic velocity normal to the satellite track from drifter data was binned on a nominal $2^\circ \times 3^\circ$ spatial scale. Then bins were chosen with more than 33, 5-day average observations and where more than five drifters produced the data. If data from only one or two drifters existed in a bin, the data could not be representative of average conditions, as these drifters could have resided in very special features such as a single cold or warm eddy. This sampling is equivalent to 164, 2-day average observations on a $2^\circ \times 6^\circ$ resolution, as displayed on Fig. 4.1.4. Using the above criteria, the ensemble average variance from drifters was within the standard error of the track normal geostrophic velocity variance computed from the TOPEX/POSEIDON satellite altimeters from the period 1992–98 (Barth *et al.*, 2001). This comparison was important for testing the scheme of averaging both drifter and altimeter data and for the future considerations of merging of two global circulation data sets in such a way that biases between the two data sets would be minimized.

4.1.3 The global mean velocity and velocity variance

The principal objective of WOCE was to observe the world ocean circulation. The 15-m depth ensemble average drifter velocity of the world shows the major surface current systems (Fig. 4.1.5a, see Plate 4.1.5, p. 300). Apparent on Fig. 4.1.5a are the strong poleward-flowing western boundary currents in each ocean and the strong zonal currents in the tropics that flow in the direction of the winds. In the Norwegian Sea, there is a strong poleward current along the eastern boundary (Poulain *et al.*, 1996). The North Pacific Equatorial Countercurrent, flowing counter to the wind, is evident in the $5\text{--}10^\circ\text{N}$ latitude band, spanning the entire North Pacific basin. Mariners could approximately locate most of these currents a century ago from the ship-drift charts (Bowditch, 1966; Richardson, 1989). The observations used in Fig. 4.1.5a were made with calibrated instruments, providing a nearly 10-fold improvement in accuracy of individual observations over those of ship

drift (Richardson, 1997), and the drifter observations were also made over broad ocean areas where ships do not go. New current patterns were discovered; several of these are discussed below.

The mean velocity vector map on Fig. 4.1.5a (see Plate 4.1.5a, p. 300) includes an ellipse at the tip of each vector. This is the standard error of the mean, or uncertainty, ellipse at each location. To compute this ellipse, let $\langle u \rangle$, $\langle v \rangle$ be the ensemble mean velocity components within each bin in the latitude (x), longitude (y) directions, respectively. The symbol $\langle \rangle$ is the arithmetic average of the ensemble of observations within each bin. Let u' , v' be the corresponding deviations from these means. Rotate the x , y coordinate system into the principal variance axes so that in the rotated coordinate system $\langle u'v' \rangle = 0$. In the rotated coordinate system the equation for the variance ellipse is $\{x^2 \langle u'^2 \rangle^{-1} + y^2 \langle v'^2 \rangle^{-1}\} = 1$. If N is the number of 'independent' velocity observations within each bin, then the equation for the standard error ellipse is $\{x^2 \langle u'^2/N \rangle^{-1} + y^2 \langle v'^2/N \rangle^{-1}\} = 1$. The number of independent observations depends upon the Lagrangian auto-decorrelation time scale in each bin. Here it was chosen to be 6 days, or an average of the many estimates computed at various locations in the Pacific (Poulain and Niiler, 1989; Paduan and Niiler, 1993; Bi, 1995). Thus every third observation in a bin was considered independent. For a normal distribution of variability, there is an 18% probability that a mean vector computed from a different large and random sample of data within the bin will fall outside the ellipses drawn on Fig. 4.1.5a.

The most completely sampled distribution of circulation was in the tropical Pacific where, commencing in 1978, small numbers of FGGE-type drifters were deployed over a 10-year period. The basin-scale observations with the WOCE/TOGA Lagrangian Drifters have been continuous since 1988. From these data, Reverdin *et al.* (1994) calculated the seasonal cycle of currents and Frankignoul *et al.* (1996) computed the anomalous currents. During the 1986–87, 1992–93 and 1997–98 El Niños, the surface circulation of the entire Pacific within 6°S of the equator was to the east (NOAA, 1997–1998). A comparison of the observed and modelled circulation was made with coupled models of tropical Pacific circulation at the end of TOGA (WCRP, 1995b). The least sampled basin was the tropical Atlantic, where

observations began on a systematic basis in 1998 and will continue as part of ongoing WCRP-sponsored programmes.

The surface geostrophic currents, relative to 1000 m or 3000 m depth, inferred from hydrographic data in the tropical and subtropical Pacific Ocean basin are toward the equator (e.g. Wyrtki, 1975). The observed currents from drifters within the 25° latitude belt around the equator, however, were toward the pole. Thus, a most striking difference was found between the observed meridional component of velocity and that computed from hydrographic data. This phenomenon had been documented from a comparison of the ship-borne Acoustic Doppler Current Profiler (ADCP) observations of currents and those computed from hydrographic data from an 11°N section across the Atlantic (Chereskin and Roemmich, 1991) and 10°N section across the Pacific (Wijffels *et al.*, 1994). These direct observations of circulation implied that generally in the subtropics, the locally wind-driven meridional circulation was much stronger and in the opposite direction from that derived from the geostrophic balance alone. Within the winds of the Northeast Trades, both the meridional and the zonal components of the Ekman velocity were stronger than the surface geostrophic velocity (Niiler and Barth, 2001). The meridional velocity plays an important role in the transport of heat from the equator toward the poles. Its strength and its depth distribution are a function of the vertical turbulent processes, which are not well known in the upper ocean and thus heavily parameterized in ocean circulation models. In Section 4.1.4, the Ekman velocity component is further discussed with a view toward improving this parameterization.

On Fig. 4.1.5a (see Plate 4.1.5a, p. 300), two different scales of velocity vectors were used in order to display the boundary currents and the mid-ocean circulation, with their respective standard error ellipses. Mean surface circulation in the centre of gyres was not known before the large number of drifter observations became available, as ship drift was not accurate enough to resolve the mean surface velocity and hydrographic methods did not include the strong, local wind-driven component. A discovery in the mid-Pacific was that of a 'gyral' current system north and east of the Hawaiian Islands, whose existence was predicted by Sverdrup *et al.* (1942), but had remained

unconfirmed until now (Niiler and Barth, 2001). There was no significant mean current system within 1° of the equator, contrary to every existing mean ocean current chart now in use. The South Equatorial Current vanished on the equator and had a maximum on either side of the equator. The remarkable steadiness of the Pacific North Equatorial Current, west of the dateline, and the South Equatorial Current in the eastern Pacific, were neither anticipated nor demonstrated by the ship drift charts of those regions (Wyrtki *et al.*, 1976).

As an example of how the picture of circulation on Fig. 4.1.5a changes with changing spatial resolution, a chart using $1^\circ \times 1^\circ$ binned data was made for the western North Pacific (Fig. 4.1.5b, see Plate 4.1.5b, p. 300) and western North Atlantic (Fig. 4.1.5c, see Plate 4.1.5c, p. 300). In both oceans, a countercurrent can be discerned at $21\text{--}23^\circ$ latitude. These subtropical countercurrents were predicted to exist from the high-resolution hydrographic data, for example as shown by White and Walker (1985), but had not been evident in ship-drift charts. Along the western North Pacific boundary, a significant flow was found from the North Equatorial Current to the South China Sea between Taiwan and Mindanao. This latter pathway of water exchange between the Pacific and the Indian Oceans has not been explored as carefully as the

pathways through the Indonesian archipelago. The steadiness of the North Equatorial Current is further in evidence in the spatial ‘smoothness’ of the vectors at this high resolution. There were a number of features of the continuity and discontinuity of the surface flow between the major current systems that require an examination of the detailed tracks of the drifters, a task that requires even higher resolution in space and time than has been done here. The data similar to those displayed on Figs 4.1.5a and 4.1.5b,c will continue to be examined with more scrutiny for discoveries of circulation features than can be done in this treatise. It suffices here to state that the calibrated instrumental observations of ocean circulation on a global basis will continue not only to discover circulation patterns not seen before, but also to map these and those familiar to mariners with great accuracy.

The second WOCE observational programme objective was to document the eddy energy distribution of the global ocean. Drifter data were used to construct such a map. The eddy energy, which is defined as $\{\langle u'^2 \rangle + \langle v'^2 \rangle\}/2$, varies by two orders of magnitude over the globe and therefore it cannot be well graphed on a linear scale on one chart. The distribution of the square root of the eddy energy or variance, $\{\langle u'^2 \rangle + \langle v'^2 \rangle\}/2\}^{1/2}$, is displayed instead (Fig. 4.1.6). It is independent

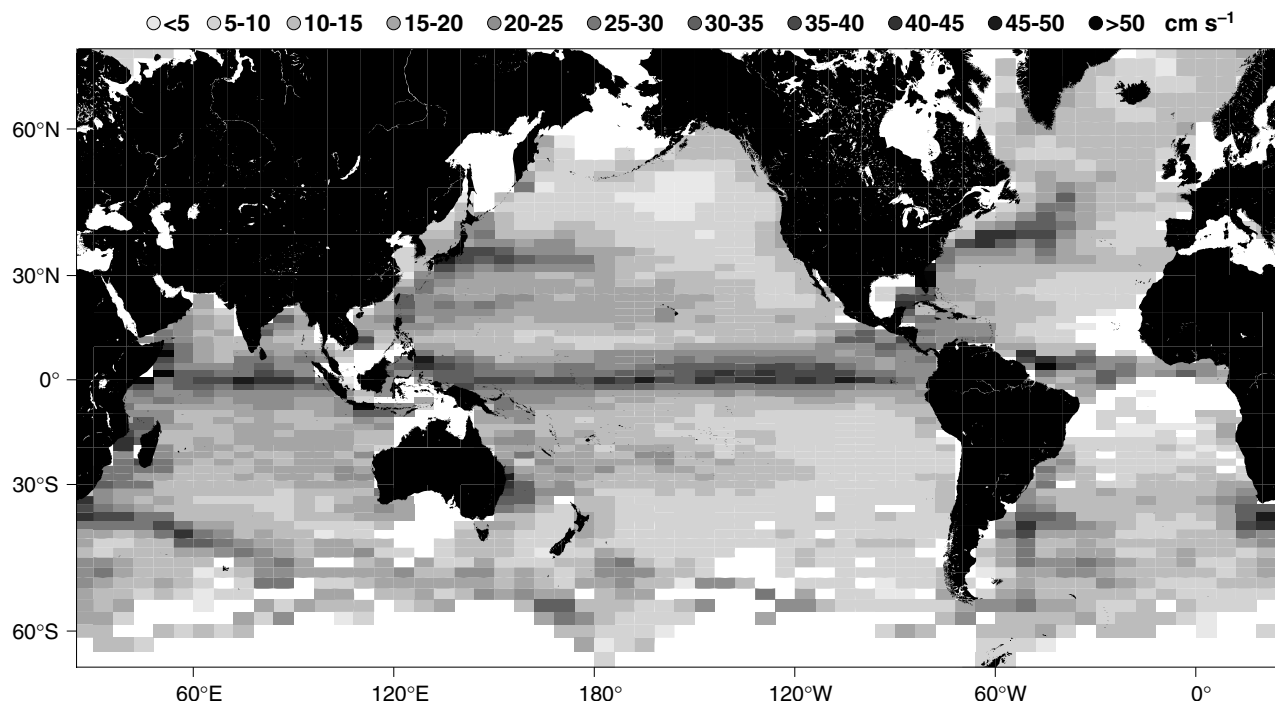


Fig. 4.1.6 Square root of 15-m depth eddy energy based on data from Fig. 4.1.5 (see Plate 4.1.5, p. 300).

of the coordinate system in which the velocity components were computed.

The large eddy energy regions were: along ocean western boundaries and their seaward extensions; the equatorial zones of the Tropical Instability Waves (Baturin and Niiler, 1997); and wind-driven jets (Ralph *et al.*, 1997). The subtropical frontal zones in the western Pacific and Atlantic displayed relative maxima, as did the Canary Current system in the North Atlantic. The Circumpolar Current system displayed regions of high energy, both due to the eastward extensions of Malvinas/Brazil Confluence and the Aghulas Current and the effects of the topographic ridges southeast of New Zealand and the central South Indian Ocean. The lowest eddy energy regions were in the northeastern North Pacific, the region north of Iceland and the central tropical South Atlantic. The South Atlantic minimum is based on a small number of observations. Figure 4.1.6 presents a challenge to eddy-resolving ocean models, as these should be able to duplicate the observed regions of both high and low eddy energy.

The eddy energy distribution obtained by drifters can differ from those developed by ship drift or from satellite altimeters in several important ways. Direct observations of velocity with drifters have the capability to resolve very low levels of currents with a variance of about $2\text{ cm}^2\text{ s}^{-2}$, or the sum of the squares of the instrumental errors due to ARGOS fixes (1 cm s^{-1} , averaged over a day) and unknown slip through the water due to the shear of currents between the drogue and the float (1 cm s^{-1}). This estimate is a lower bound, because the drifter eddy energy uncertainty is also a function of the number of independent samples within the resolving grid and the biases due to over-sampling convergent regions. Unknown scales of the mean circulation, on scales smaller than a bin, can alias the mean shear within a bin into eddy energy. When comparing the ship-drift-observed eddy energy to drifter observations in the northeast Pacific, the ship-drift observations show a very large area of nearly constant eddy energy of about $400\text{ cm}^2\text{ s}^{-2}$ (Wyrki *et al.*, 1976), while the drifter data show that region to contain an eddy minimum of less than $25\text{ cm}^2\text{ s}^{-2}$. Thus, ship-drift random error of about $\pm 20\text{ cm s}^{-1}$ appeared to have produced large regions of constant eddy energy that have been interpreted as ocean current variability. The eddy energy computed from

altimeters can miss the $100\text{--}300\text{ cm}^2\text{ s}^{-2}$ variability due to wind-driven currents. The uncertainty of eddy energy computed from satellite altimeter data is restricted to the geostrophic part of the currents. This uncertainty should be a function of latitude, the filtering length along the satellite track, the number of independent estimates of sea-level slope at the track cross-over, and the angle of that cross-over (Strub *et al.*, 1997).

The quantitative comparisons of drifter and satellite altimeter-derived eddy distributions of the world are ongoing areas of fruitful research. Comparisons of individual satellite altimeter-derived currents with drifter-observed currents from the Gulf of Mexico demonstrate an 85% coherence between the two observations, provided an appropriate spatial scale of smoothing (110 km) is adopted for the satellite data processing (Ohlmann *et al.*, 2001). This spatial scale of smoothing is different in different latitude bands, increasing from 55 km at 50°N to 120 km at 5°N (Barth *et al.*, 2001). The combined satellite sea-level observations and the direct observations of circulation can now produce truly global, accurate maps of ocean eddy energy.

4.1.4 The wind-driven Ekman currents

Ekman (1905) presented the first modern fluid mechanical theory of wind-driven ocean currents on the rotating globe. His calculations showed that the large spatial scale, steady winds drive a surface current at an angle to the right of the wind in the northern hemisphere and to the left in the southern hemisphere. The Coriolis force, coupled to ocean turbulence, restricted the currents to a shallow surface layer, now called the 'Ekman layer'. In the northern hemisphere this wind-driven current rotates progressively to the right with increasing depth through this turbulent layer. The vertical average of the horizontal velocity was precisely at right angles to the wind, independent of the depth of the Ekman layer or the nature of the turbulence therein. Observations with current meters have verified certain aspects of Ekman's theory, such as the rotation of currents with depth and the vertical average velocity to the right of the surface winds (Davis *et al.*, 1981; Price *et al.*, 1987; Chereskin, 1995). Drifter data offer further tests of Ekman's theory, especially regarding the strength of the wind-driven currents, the depth of

the Ekman layer and the nature of the turbulent mixing coefficient within that layer.

The Ekman theory applies to wind-driven currents several degrees north or south of the equator. To compute the Ekman currents, we used the conservation principles of momentum. At 15 m depth observed mean velocity should be the sum of a geostrophic velocity obtained from the pressure gradient and a direct wind-driven velocity, the 'Ekman velocity' (Pedlosky, 1987b; Bi, 1995). The 15-m depth pressure gradient, and the corresponding geostrophic velocity, was computed from the Levitus and Boyer (1994b) atlas of historical mean temperature and salinity on a 1° latitude by 1° longitude resolution and then averaged into the same 2° × 6° bins used for the drifter observations. In this latter calculation, the geostrophic velocity was assumed to vanish at 1000 m depth. No significant difference would result if the geostrophic velocity were assumed to vanish at 3000 m depth. An Ekman velocity was computed from the difference of the total observed velocity and the geostrophic velocity relative to 1000 m, using drifter data only where drogues were attached.

The Ekman velocity (Fig. 4.1.7), when viewed relative to the ensemble average winds observed along the drifter tracks, showed a predominant rotation to the right of the wind in the Northern Hemisphere and a predominant rotation to the left

of the wind in the Southern Hemisphere. Ekman (1905) predicted this change of direction, but observations had been lacking in the Southern Hemisphere to confirm it. Scrutiny of Fig. 4.1.7 further reveals that the Ekman velocity was not of the same magnitude at locations where the wind was the same. Ralph and Niiler (1999), using a subset of the drifter data in Fig. 4.1.7, showed that this variability could be accounted for by a model of the Ekman velocity magnitude as a function of Coriolis parameter and wind speed. Their best statistical fit was with the formula where the Ekman velocity magnitude, U , was proportional to the wind-friction velocity, u^* , and inversely proportional to the square root of the Coriolis parameter, f , i.e. $U = Au^*/f^{1/2}$. This relationship is graphically represented in Fig. 4.1.8 with data that was in the shaded regions in Fig. 4.1.7, the most robust areas of observations. This model accounts for 62% of the variance of the Ekman velocity magnitude field, with a regression coefficient, A , of $0.081 \text{ s}^{-1/2}$ (± 0.013). Though derived here from a different wind data set (NCEP Reanalysis versus European Centre for Medium Range Weather Forecasts (ECMWF) operational winds) and from the larger drifter data set (1988–99 versus 1988–96; 30° versus 20° off the equator) that was used by Ralph and Niiler (1999), the regression coefficients were marginally statistically different (0.081 ± 0.013 versus 0.065 ± 0.002).

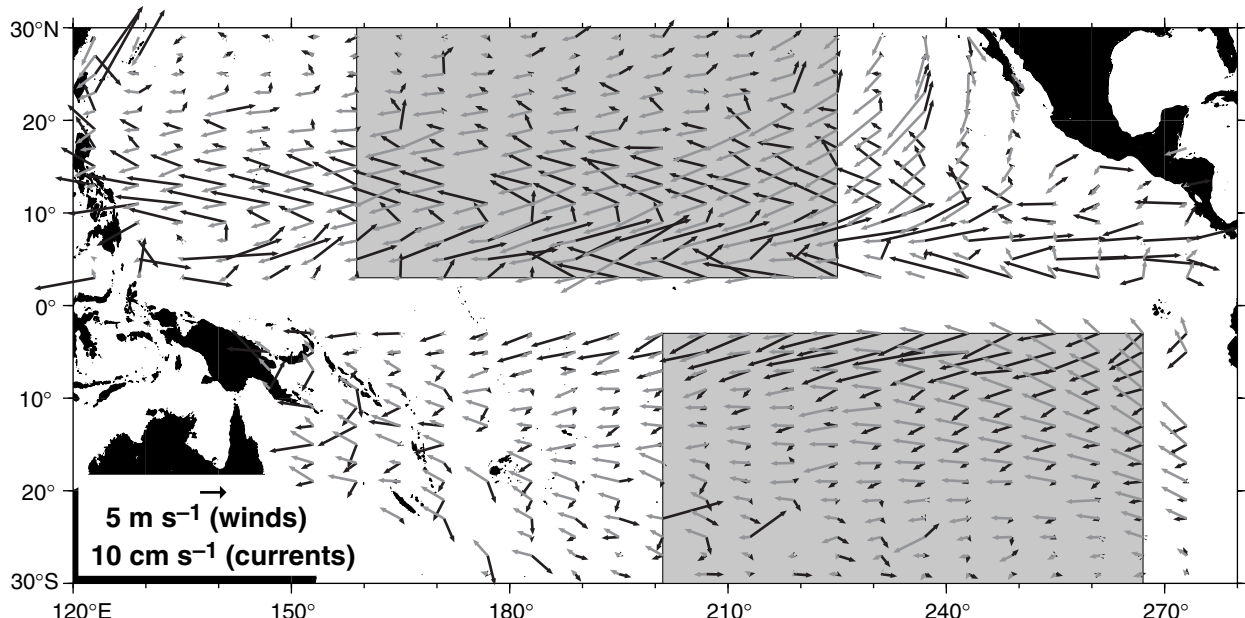


Fig. 4.1.7 Ekman velocity (black) and NCEP Reanalysis wind velocity (grey) in the subtropical Pacific on a 2° × 6° resolution computed from drogued drifter data, January 1988–June 1999, and Levitus 1994 hydrography data referenced to 1000 m. The shaded region is used in Fig. 4.1.8.

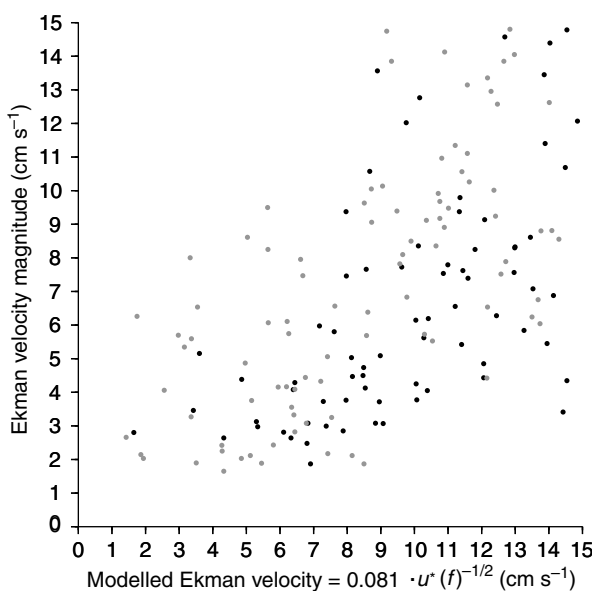


Fig. 4.1.8 Regression of observed Ekman velocity magnitude (ordinate) versus model (abscissa) from data in the shaded regions of Fig. 4.1.7. Black dots are associated with the southern hemisphere; grey dots with the northern hemisphere. For detailed explanation, see text.

Ekman (1905) also pointed out that the scaling of the momentum balance equations, with the above formula for magnitude of the Ekman velocity, implied that the depth scale of the Ekman layer was proportional to wind friction velocity and inversely proportional to the square root of the Coriolis parameter. This indicated that the observations at 15 m depth could well have been in different vertical levels of the Ekman layer. When Ekman velocity data from Ralph and Niiler (1999) was stratified according to the scale depth at which it was observed, a spiral of currents resulted, with progressively increased rotation with increasing depth of observation within the scaled Ekman layer. Figure 4.1.9 is an adaptation of the data presented by Ralph and Niiler (1999) in a form that demonstrates this rotation and the decrease of currents with depth.

In Fig. 4.1.9 the quantity D , equal to $u^*/0.065 f^{1/2}$, is the Ekman layer depth scale. The data on Fig. 4.1.9 points out that the wind-driven currents near the top of the Ekman layer can be in excess of 15 cm s^{-1} . The observations with drifters do not go all the way through the Ekman layer because the vertically averaged current in Fig. 4.1.9 is not at right angles to the wind. In this interpretation of the Ekman layer scaling, the turbulent diffusivity within the upper part of the Ekman layer was proportional

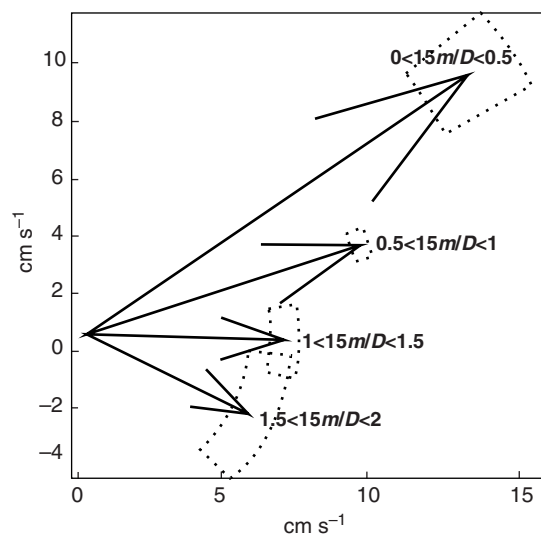


Fig. 4.1.9 The ageostrophic velocity vector relative to wind as a function of scale depth of Ekman layer. Amplitude scales are in cm s^{-1} . The wind vector is along the ordinate axis. The dotted region is 95% confidence interval.

to the friction velocity squared, or the magnitude of the wind stress. This relationship of wind to diffusivity was suggested by Ekman (1905), based on two specific observations of wind-driven ocean currents separated by 60° of latitude. Drifter data in the shaded regions of Fig. 4.1.7 confirmed it with 247266 additional observations.

4.1.5 Future global circulation observations

The WCRP provided the impetus for oceanographers to observe directly the circulation of the oceans. These observations are being used not only to make new maps of the ocean currents, as was done here, but also to test global, numerical models of the circulation (Saunders *et al.*, 1999). To date, the models that parameterize upper ocean mixing to increase dramatically as the Richardson number is lowered below a critical value agree best with the observations of the global pattern of 15-m depth currents observed by drifters (WCRP, 1995b). This mixing parameterization is also consistent with the scaling that resulted in Figs 4.1.8 and 4.1.9 (see Niiler and Kraus, 1977, for the physical model). The model tests will need to continue, as there already are a large number of ocean circulation models and climate change models in use by the scientific community that have not been tested, and new ones are being created each year.

It is the role of instrumental circulation observations to suggest which climate models most accurately replicate the circulation of the oceans and which models should be significantly improved. Surface circulation data is an important aspect of climate model testing and selection. This is because surface circulation carries ocean thermal energy over great distances from regions where it is transferred into the oceans from the atmosphere to regions where it is released back to the atmosphere. Modelling of the climate patterns of the globe and the changes of these patterns depend crucially on having realistic ocean surface currents and their long-term changes reproduced in the models to transport the thermal energy of the ocean/atmosphere system in a realistic manner.

The Global Drifter Programme continues to play a significant role in the acquisition of ocean and marine atmosphere data from the remote oceans. The DBCP encourages and organizes the additions of barometers to these drifters (DBCP, 1999). The British, Canadian, South African, French and US meteorological agencies now make use of these platforms to acquire sea-level pressure data from the Pacific, Atlantic, Indian and Southern Oceans for their operational weather prediction models. At present, most of the *in-situ* SST data in the Southern Hemisphere are acquired from SST sensors on the Global Drifter Programme drifters. These *in-situ* SST observations are used together with TIROS satellite infrared images of the ocean surface to make accurate global maps of SST for use

in climate research and long-range weather predictions (Reynolds and Smith, 1994). The ENSO Ocean Observing System of the National Oceanographic and Atmospheric Administration (NOAA) will continue to place about 250 drifters into the tropical and Southern Oceans each year. Operational science agencies and research programmes deploy an additional 200–400 drifters. There continues to be a population of 800–1000 drifters in the global ocean to date, with 920 drifters transmitting data to the GTS at the time of writing.

Acknowledgements

The following countries contributed drifters to the observations of surface circulation of the global oceans that were presented here: Argentina, Australia, Brazil, Canada, France, Great Britain, Iceland, India, Japan, Korea, Netherlands, Mexico, Portugal, Russia, South Africa, Taiwan and the USA. The principal scientists are too many to be thanked individually here for continuing to provide accurate instrumental observations of ocean currents, so the author truly thanks them collectively. The skills of Andy Sybrandy, Sharon Lukas, Norman Barth and Myra Pazos in the preparation and analysis of the data are gratefully acknowledged. During the preparation of this manuscript, the author was sponsored by grants from NOAA/OAR and NOAA/OGP through the Joint Institute of Marine Observations at the Scripps Institution of Oceanography.

4.2

The Interior Circulation of the Ocean

D.J. Webb and N. Sugino

4.2.1 Processes in the ocean interior

In this chapter we concentrate on the interior circulation of the ocean away from the equator and, for the most part, away from all boundaries. We will also generally concentrate on flows at scales larger than the Rossby radius.

Our present knowledge about such flows comes from a mixture of hard *in-situ* observations and shrewd theoretical analysis. This combination works best in the top kilometre of the ocean where current velocities are relatively large. At greater depths the mean velocity (often less than 0.5 cm s^{-1}) is usually masked by the mesoscale eddy field ($\sim 5 \text{ cm s}^{-1}$) and by tides ($\sim 5 \text{ cm s}^{-1}$). As a result our knowledge of the deep ocean is still far from complete.

Observations of tracer distributions and mixing processes in the ocean show that the transport is primarily along density surfaces. Observations and theoretical studies indicate that, away from the equator and boundaries, the currents are basically in geostrophic balance. This means that in the momentum equation, which describes the dynamical behaviour of the ocean, the main balance is between the Coriolis force and the horizontal pressure field.

Another key result from both observations and theory is that at oceanic scales the potential energy of the ocean is much larger than its kinetic energy. As a result, the processes that ultimately determine the circulation are the ones that are most effective at changing the potential energy of the ocean.

Such processes usually occur at the boundaries. Examples are the changes in sea level produced by convergences and divergences of the wind-driven

Ekman transport and by heating, cooling, precipitation and evaporation at the ocean surface. The circulation can also be driven by inflows or outflows at the boundary of a basin.

Within the ocean, the most important process is probably the deep convection normally occurring at high latitudes (Morawitz *et al.*, 1996; Schott *et al.*, 1996; see also Lazier *et al.*, Chapter 5.5). Interior vertical mixing is generally weak, but it may become important in deep ocean basins, where other processes are negligible, or in regions where there are large breaking internal tides (Egbert, 1997). The inertial terms in the momentum equation are also generally considered to be small. However, in regions of strong currents, such as the Gulf Stream and Kuroshio, there are often large recirculation regions that are almost certainly due to the effect of these terms.

4.2.1.1 The response to changes in forcing

Our understanding of how the ocean responds to a change in the forcing depends primarily on theory (Anderson and Gill, 1975; Gill, 1982) but is supported by many observations. Initially there is an imbalance between the new pressure field and the Coriolis term. This imbalance produces inertial oscillations that may last for a few days but eventually die or propagate away. Geostrophic balance then takes over, and Kelvin and Rossby waves dominate the response at large scales for periods of many months. Eventually these die away, leaving a residual steady-state circulation.

The conservation laws associated with mass, energy and angular momentum severely limit the possible steady states of the ocean circulation.

They also result in relatively simple equations for the mean ocean circulation. Thus if we consider the vertically integrated effect, we obtain Sverdrup's (1947) relation between the curl of the wind stress and the ocean meridional transport. The addition of a western boundary current then leads to the Stommel (1948, 1965), Munk (1950) and Munk and Carrier (1950) models of the gyre circulation, the Godfrey (1989) 'Island Rule' and the Stommel and Arons (1960a,b) theory for the abyssal circulation of the ocean.

The next level of understanding comes from applying the same ideas to the conservation of potential vorticity on density surfaces. The results emphasize the role of ventilation in determining the vertical structure of the subtropical gyres (Price, Chapter 5.3). They also highlight the importance of potential vorticity mixing within the ocean.

These theories often work well for the near-surface flows in the subtropics, but they tend to be less useful at high latitudes and at depth because there the effect of topography is important. Topography can both steer currents and produce isolated Taylor columns. Elsewhere divergences and convergences associated with the bottom Ekman layer can also have an effect.

In trying to understand the mean circulation we also need to consider the effect of the mesoscale eddy field, internal waves and tides. At one stage it was thought that the mesoscale eddies were so widespread that they might have an important effect on the dynamics (Warren, 1981b). However, this now appears to be true only for the regions where eddy kinetic energy is highest (Stevens and Ivchenko, 1997) or where non-linear interactions with topography generate an along-slope current (Holloway, 1992). Elsewhere the eddies are very effective at mixing properties on density surfaces, but otherwise their dynamical effect is small.

For a long time the background internal wave field was thought to be important for vertical mixing in the deep ocean (Munk, 1966). This is the field usually associated with the Garrett and Munk (1979) spectrum that has a relatively uniform amplitude throughout the ocean. However, both theory and direct measurements show that the cross-isopycnal mixing it produces is an order of magnitude too small to explain the observed properties of the ocean (Toole and McDougall, Chapter 5.2). Instead there is now evidence that topography (Polzin *et al.*, 1997; see also Hogg,

Chapter 4.5) and tides (Egbert, 1997; Munk and Wunsch, 1998) can produce large amounts of vertical mixing in localized regions of ocean. This is a new field of study and the implications have still to be fully investigated.

4.2.2 Observational evidence

As stated above, the interior flow of the ocean is difficult to measure directly with current meters because of the long integration time needed to overcome the masking effect of the mesoscale eddy field and other motions. Because of this, our knowledge about the ocean circulation has come primarily from hydrographic sections and tracer studies. In recent years, and especially during the World Ocean Circulation Experiment (WOCE), this has been complemented by high-quality data from deep floats (Autonomous Lagrangian Circulation Explorer (ALACE) floats) and surface drifters. Very long current meter data records are also becoming available.

4.2.2.1 Classical hydrography

Some of the best early descriptions of the large-scale Atlantic circulation resulted from the Meteor expedition of the 1920s. Two main approaches were used to analyse the data, one based on the distribution of tracers (Wüst, 1935) and the other on the thermal wind equation (Defant, 1941). The dynamic height method (see also Fofonoff, 1962) works well in the top few hundred metres of the ocean, where currents are strong. As a result Defant's (1941, 1961) analysis of the surface dynamic height field of the Atlantic still compares well with modern results. Defant also found that down to about 900 m the amplitude of the field slowly declined but its overall shape changed little.

Below 1000 m the method tends to fail. This is because the method only defines current shears and so it needs an absolute current to be defined at some level. Water properties can be used to estimate a level of no motion (or zero reference current) but, given the low currents in the deep ocean, it is difficult to do this to sufficient accuracy. However, where currents are strong, or the level of no motion estimates are good ones, the method may still be successful. Thus, despite the limited amount of data available, Defant's (1941) analysis of the flow at 2000 m shows a well-defined deep western boundary current in the North and South

Atlantic and a strong Antarctic Circumpolar Current.

In regions of the deep ocean where currents are small, Wüst's (1935) approach based on water properties and core layers is usually more reliable and more informative. In the Atlantic the water property method indicates both the southward flow of North Atlantic Deep Water and the northward flow of Antarctic Bottom Water. It also shows saline Mediterranean Water spreading out into the Atlantic along the southern branch of the subtropical gyre, well below depths where the traditional dynamic height method is effective.

Since their introduction, both methods have been widely used in all oceans. They also form the basis of most inverse methods used to determine ocean circulation (Wunsch, 1996). Among the traditional analyses of the large-scale circulation one might specially mention the work of Worthington (1976, 1981), Warren (1981b), and the recent results of Schmitz (1995, 1996a,b) and Schmitz and McCartney (1993). Possibly the most detailed recent large-scale analyses are those of Reid (1981, 1986, 1989, 1994, 1997). Results for part of the Pacific are shown in Fig. 4.2.1.

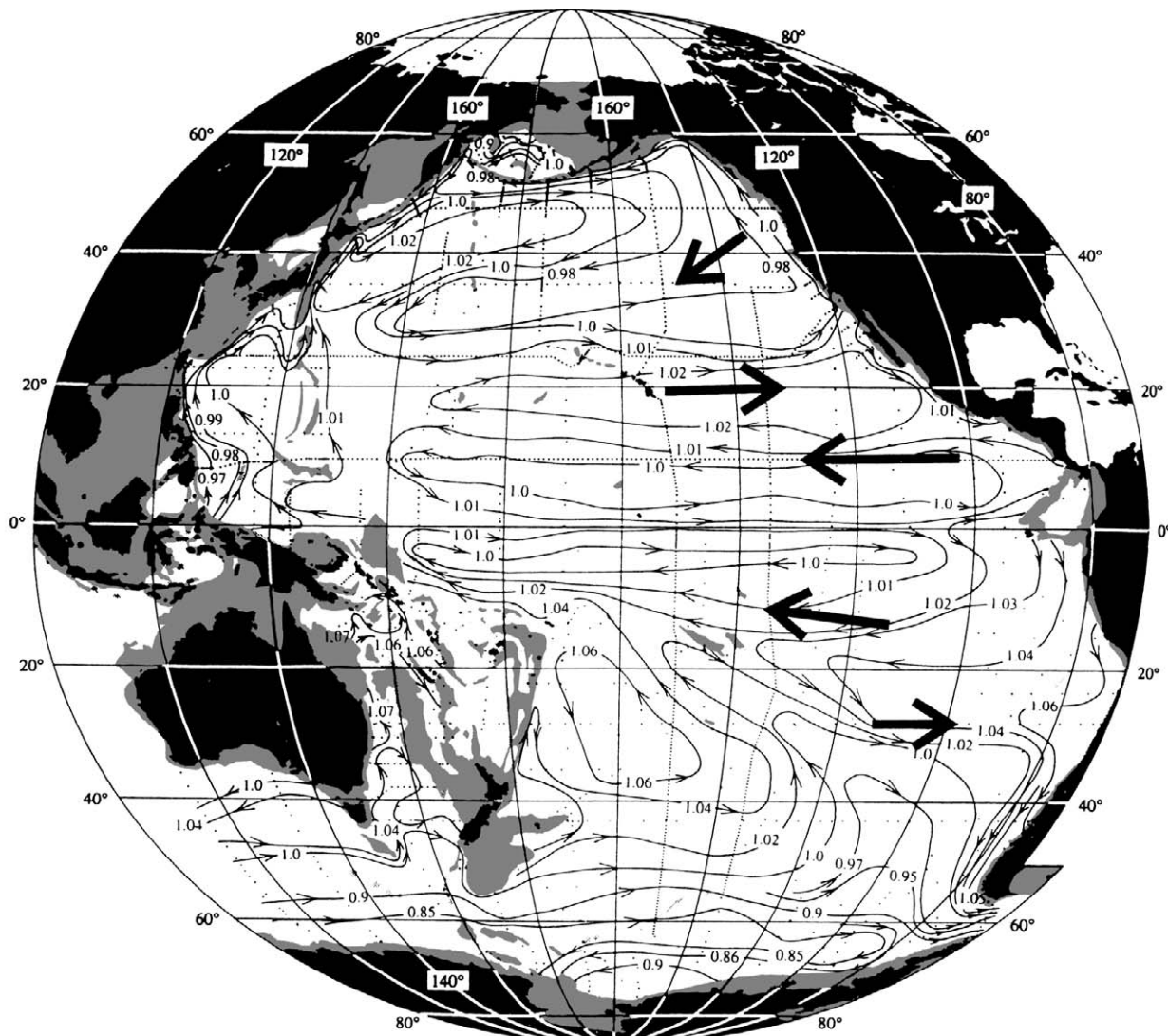


Fig. 4.2.1 Adjusted steric height at 2500 dbar in dynamic metres ($10 \text{ m}^2 \text{ s}^{-2}$ or J kg^{-1}). The arrows show the direction of geostrophic flow. Thick arrows indicate the location and direction of ^3He plumes at these depths. Adapted from Reid (1997) and Lupton (1998). Copyright by Elsevier Science and the American Geophysical Union.

4.2.2.2 Developments during WOCE

During the WOCE period there have been two important developments which can provide independent estimates of a reference current. The first makes use of Global Positioning Systems (GPS) ship navigation together with the Acoustic Doppler Current Profiler (ADCP) (King *et al.*, Chapter 3.1). The second makes use of long-term statistics from freely drifting surface floats and deep drifters (Davis and Zenk, Chapter 3.2; Niiler, Chapter 4.1). Both methods are still under development, with new techniques being developed to reduce the errors involved.

In one example of the first method, Saunders and King (1995b) used GPS and ADCP measurements, made when their ship was underway, to estimate a reference velocity for each station pair in the western boundary current region of the WOCE A11 section. Taking a slightly different approach, Beal and Bryden (1997) used GPS with a lowered ADCP to estimate the reference velocity at each station in their Agulhas Current section. In both cases the estimated errors are a few centimetres per

second, so the method is not presently suitable in the deep ocean outside the boundary current region. However, in future it may be possible to use the barotropic velocity measured from a lowered ADCP to reduce the errors further (see King *et al.*, Chapter 3.1).

The float studies during WOCE have involved the development and deployment of high-quality surface floats and deep profiling floats (Davis, 1998b; Davis and Zenk, Chapter 3.2). The float results for the flow of the Equatorial and South Pacific at 900 m are shown in Fig. 3.2.6. Overall there is good agreement with the analysis of Reid (1989, 1994, 1997). Both types of floats may be affected by the (random) noise due to the mesoscale eddy field and more systematic errors due to regions of convergence and divergence at their measurement level.

As discussed by Hogg in Chapter 4.5, the WOCE current meter arrays have also provided excellent data on the transports in deep western boundary currents and the flows between deep ocean basins. However, away from these regions,

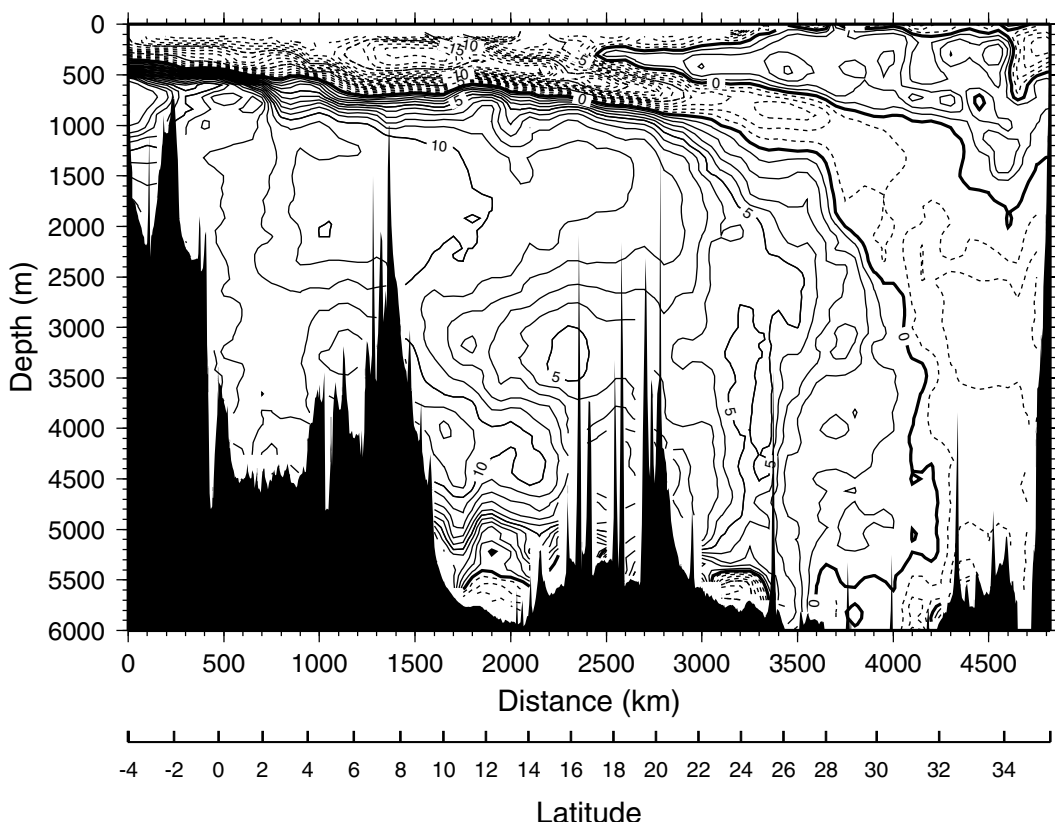


Fig. 4.2.2 Oxygen profile on WOCE Section P10 showing the deep frontal structures in the western Pacific. The section runs roughly north–south along 145°W between New Guinea and Japan. Contours in units of ml l^{-1} . Adapted from Wijffels *et al.* (1998). Copyright by the American Geophysical Union.

noise due to the natural variability of the current field tends to swamp estimates of the mean currents (even after 3 years of measurements; see Arhan *et al.*, 1989), so other methods have to be used.

4.2.2.3 Modern tracers in the Pacific

Better results are coming from modern tracer measurements (see Schlosser *et al.*, Chapter 5.8), especially in the Pacific. Talley and Joyce (1992) and Wijffels *et al.* (1998) have studied the tracer distribution in the deep North Pacific and shown the existence of a series of well-defined zonal fronts extending from 2000 m to abyssal depths (see Fig. 4.2.2). Lupton (1998) reports on the helium distribution in the Pacific. He shows that it forms a series of plumes at depths near 2500 m, indicating that the currents at such depths are primarily zonal (his main results are overlaid as arrows in Fig. 4.2.1).

Both results give strong support to Reid's (1997) description of the Pacific circulation near 2500 m, which shows a series of well-defined zonal flows. This is markedly different from model results (i.e. Obata *et al.*, 1996), which show only a westward flow with a stronger meridional circulation.

4.2.3 Theory of gyre-scale circulation

Our theoretical understanding of ocean circulation is based primarily on the conservation laws for mass and momentum. The momentum equation, relative to fixed axes on a rotating earth, is,

$$\rho \frac{\partial \mathbf{u}}{\partial t} + \rho(\mathbf{u} \cdot \nabla) \mathbf{u} - \rho \mathbf{f} \times \mathbf{u} - \rho \mathbf{g} - \nabla p + \mathbf{d} = 0 \quad (4.2.1)$$

where \mathbf{u} is velocity, t time, \mathbf{f} the Coriolis vector, \mathbf{g} gravity, p pressure and \mathbf{d} the viscous stress due to small-scale processes.

Away from the boundaries, the ocean is observed to be primarily geostrophic, that is to say the main balance is between the Coriolis term and the horizontal pressure gradient. Taking the curl of the vertical component of equation (4.2.1), integrating it vertically, dropping small non-linear and viscous terms and assuming that vertical velocities are zero at depth, we obtain Sverdrup's relation (Sverdrup, 1947),

$$\rho U_y \beta = \nabla_h \times \tau \quad (4.2.2)$$

U_y is the north-south transport, β equals $\partial f / \partial y$ and τ is the surface wind stress (see Veronis, 1981; Pedlosky, 1987b, 1996; and Müller, 1995 for more details).

Thus away from boundaries, the north-south transport of the ocean is zero unless there is a wind stress curl acting locally. Additional transports can occur at boundaries, especially western boundaries, but on the eastern boundary these are normally observed to be small. As a result it is possible to define a stream function that defines the interior flow field,

$$\Psi = \frac{1}{\rho \beta} \int_x^{x_e} \nabla_h \times \tau \quad (4.2.3)$$

where x_e lies on the eastern boundary and ∇_h is the horizontal gradient operator. Equation 4.2.3 should be valid until the western boundary current region is reached.

Many authors have used the Sverdrup relation to deduce the wind-driven interior circulation of the ocean (Welander, 1959; Evenson and Veronis, 1975; Hellerman and Rosenstein, 1983). More recently Godfrey (1989) used the Island Rule (see also de Szoeke, 1987) to generalize a solution for the full ocean including the Indonesian Throughflow.

Such calculations are well suited to the subtropics where they provide a good indication of the mean flow in the top 1000 m of the ocean. They are not suited for use at high latitudes where bottom topography is important and the assumption of zero bottom velocity is invalid. The Sverdrup relation is also not sufficient to explain the strength of the Antarctic Circumpolar Current (Webb, 1993).

4.2.3.1 Potential vorticity

The above theory considers the vertically integrated wind-generated transport. Luyten *et al.* (1983) developed the approach further by applying vorticity conservation to individual layers of the ocean. They showed that, away from boundaries,

$$\frac{d}{dt} \left(\frac{\mathbf{f} + \nabla_h \times \mathbf{u}}{H_l} \right) = 0 \quad (4.2.4)$$

A number of papers have been written on the implications of this result (Rhines and Young, 1982a,b; Pedlosky, 1996). The governing idea is

that the potential vorticity becomes fixed at the point where the water in each density layer loses contact with the surface and remains constant until either the water upwells again into the surface layer or it becomes changed in the western boundary current. The theory also predicts the existence of shadow zones, regions where the characteristics intersect solid boundaries, so there is no flow, and regions of closed characteristics. In the latter case, the mesoscale eddy field eventually homogenizes the potential vorticity.

The theory helps to explain the main features of the potential vorticity field calculated by Keffer (1985) from hydrographic data. Keffer shows that the potential vorticity is reset wherever the water returns to the surface mixed layer. He also finds regions of homogenized potential vorticity but his results show that even outside these regions diffusion has a significant effect.

de Szoeke (1987) used a three-layer version of the Luyten *et al.* (1983) model to investigate the structure of the subtropical gyre in the South Pacific. At depth the results agree well with both the float and hydrographic data discussed previously, including the southward movement of the gyre with depth. The agreement is less satisfactory at the surface, especially in the tropics.

Similarly Talley (1985) was able to use the model to explain the large-scale features of the shallow salinity minimum in the North Pacific. However, the theory could not explain many of the observed small-scale structures.

Recently Robbins *et al.* (2000) have used tracers to study the ventilated flows in the North Atlantic. In the surface layers they find good agreement with the theory but in layers that intersect the Azores Current they find that there is little advection across the current, only diffusion. This is consistent with Jia's (2000) isopycnal model study of the North Atlantic, which shows that the Azores Current entrains these water masses into the Mediterranean Outflow.

4.2.3.2 The effect of topography

In the subtropical gyres there is now general agreement between results from hydrographic data, autonomous floats and the Sverdrup and ventilation theories of gyre circulation. At high latitudes this is not so, primarily because the reduced stratification means that topographic effects can no longer be ignored.

Rotating flows in the limit of weak or zero stratification have been investigated by Taylor (1917), Hogg (1973), Huppert (1975), Huppert and Bryan (1976) and many others. When there is no stratification the flow is independent of depth. In most geophysical flows the vorticity ($\nabla \times \mathbf{u}$) is small compared with f , so from (4.2.4) the flow must follow lines of constant (f/H).

With stratification, the effect of topography drops off with height, the vertical scale distance being proportional to Lf/N , where L is the horizontal scale of the topography and N is the Brunt–Väisälä frequency ($-g\rho^{-1}\partial\rho/\partial z$) $^{1/2}$.

In the main thermocline at mid-latitudes, f is approximately $1/4\text{ h}^{-1}$ and N is 10 h^{-1} . So for features with horizontal scales of less than 100 km , the vertical scale will be less than 2.5 km . As a result, the near-surface circulation rarely sees the effect of deep topography. (The converse is also true, so in the subtropics the surface forcing has little effect at depth. However one of us, Sugihara, has found that a model ocean with a flat bottom can generate weak zonal flows at 2.5 km below the subtropical gyre.) At 60°N , the Brunt–Väisälä frequency is nearer 3 h^{-1} so features with horizontal scales of 100 km have a vertical influence of order 8 km . As this is larger than the depth of the ocean, all such features have strong effects on the surface circulation.

Hughes *et al.* (1998) recently showed that the current speed is also involved. In the Antarctic Circumpolar Current, the mean current is larger than the first mode Rossby wave speed and so density compensation never has a chance to become established.

The importance of topography at high latitudes is seen in surface dynamic height plots of the North Atlantic where the surface currents cross the Mid-Atlantic Ridge just south of Iceland. The FRAM (Fine Resolution Antarctic Model) atlas (Webb *et al.*, 1991) also shows the effect of topography on a numerical model where the Antarctic Circumpolar Current skirts Kerguelen and the Campbell Plateau.

Topography can further complicate the picture through the Sverdrup transport produced by the bottom friction due to other currents. Dewar (1998) considers this problem analytically. Deep zonal jets seen in the OCCAM (Ocean Circulation and Climate Advanced Modelling Project) model results may be due to this mechanism.

4.2.4 The abyssal circulation

At present, most theoretical studies of the deep circulation are based on the ideas of Stommel (1958) and Stommel and Arons (1960a,b). Their work incorporated a number of key ideas. The first was that surface water downwells into the deep ocean in a few localized regions near the poles. Second, they assumed that upwelling occurs fairly uniformly throughout the deep ocean as a result of the vertical mixing due to breaking internal waves. This is an important concept and is consistent with Munk's (1966) ideas on abyssal mixing, the apparent uniform nature of the internal wave field (Garrett and Munk, 1979) and observations of the sporadic breaking of internal waves (Woods, 1968).

Another key idea was the realization that uniform upwelling in the deep ocean acts like Ekman suction at the sea surface and so produces similar Sverdrup gyres. Finally, they realized that the flow could be completed by a series of deep western boundary currents with the three main oceans connected by the flows in the Antarctic Circumpolar Current. The result, taken from Stommel (1958), is shown in Fig. 4.5.1.

The pattern of deep western boundary currents has been confirmed by measurements. There is evidence of similar potential vorticity conserving systems producing flows around the deep trenches in the Pacific (Mitsuzawa and Holloway, 1998) and there have been a number of publications extending the theory to more complicated basins and topography (Pedlosky, 1996).

However although this view of the deep ocean circulation is very appealing, observational evidence indicates that something is wrong. First, the tracer observations referred to earlier indicate that the flow is much more zonal than is expected from theory. Second, Munk (1966) and Munk and Wunsch (1998) found that a diapycnal diffusivity of $10^{-4} \text{ m}^2 \text{ s}^{-1}$ was required in the deep ocean to support the thermohaline circulation. However, most observational estimates from microscale profiling (Gregg, 1989) and tracer release experiments (Ledwell *et al.*, 1998) give values near 10^{-5} m s^{-1} , an order of magnitude lower.

There have been two key observations to fill the gap. The first comes from satellite measurements of the tides (Egbert, 1997). These show that the tides in the deep ocean lose a significant amount of energy where the tidal wave crosses major topographic

features such as the mid-ocean ridges. The energy loss is almost certainly due to the generation of internal tides. These are strongly non-linear and so will eventually break, causing local vertical mixing.

This is confirmed by measurements of mixing made in the South Atlantic as part of the Deep Basin Experiment (Hogg, Chapter 4.5; Toole and McDougall, Chapter 5.2). Polzin *et al.* (1997) found values of $10^{-5} \text{ m}^2 \text{ s}^{-1}$ over much of the deep Brazil Basin but above the rough Mid-Atlantic Ridge the values were much larger, reaching $10^{-3} \text{ m}^2 \text{ s}^{-1}$ in the bottom-most 150 m (see Fig. 5.2.5, Plate 5.2.5, p. 428). The values near $10^{-5} \text{ m}^2 \text{ s}^{-1}$ were consistent with mixing due to the background isotropic internal wave field. In contrast, the high values were associated with upward-propagating internal waves generated by the interaction of tide and other currents with the rough bottom topography (J. Toole, personal communication).

Such observations imply that the upwelling in the deep ocean is not uniform and so the Stommel and Arons' hypothesis about the abyssal circulation needs revision. In fact, where we do have evidence for mean flows in the deep ocean away from the western boundary currents, the flows appear to be mainly zonal. Examples are the Pacific tracer measurements discussed earlier and the float observations in the South Atlantic Deep Basin Experiment (see Hogg, Chapter 4.5). In the Pacific, Talley and Johnson (1994) demonstrated that the zonal flows are not associated with hydrothermally driven abyssal circulation. Here and in the South Atlantic the zonal flows may be due to the enhanced vertical mixing near topography and the resulting upwelling.

If the upwelling is non-uniform, then on the basis of the theory discussed earlier, one would expect meridional or depth contour crossing flows in the regions where the vertical velocity is divergent and more zonal or contour-following flows where mixing is weak. Such behaviour is seen in numerical model studies of rectangular basins with enhanced mixing near the side wall boundaries (Marotzke, 1997; Samelson, 1998). It is also seen in a global ocean model (Hasumi and Sugihara, 1999a) that tries to represent realistically the variations in mixing due to the interaction of tides and topography.

Although this idea of inhomogeneous vertical mixing in the deep ocean helps to explain the

observed zonal flows and fronts, it still does not explain why Munk's (1966) estimate of vertical diffusion in the ocean is an order of magnitude greater than the generally observed value. Munk and Wunsch (1998) investigate how much dissipation is needed in the regions of enhanced vertical mixing to explain the discrepancy. The figure they find is near 1.9 TW, which they propose is half due to the wind and half to the tides. The figure is not impossible but it raises a number of concerns. Thus it requires most of the energy input from the wind to be dissipated in the regions of enhanced vertical mixing, it requires a mixing efficiency near Osborn's (1980) upper bound, and it requires the turbulence affecting Bottom Water in the Brazil Basin to be typical of all levels of the deep ocean.

An alternative possibility is that one of the premises is wrong. In fact this seems to be the solution of the problem. Numerical models (Döös and Webb, 1994; Döös and Coward, 1997; Toggweiler and Samuels, 1998) indicate that mixing in the deep ocean is not essential for the thermohaline circulation. Instead, as shown in Fig. 4.2.3 (see Plate 4.2.3, p. 300), the models show that over half of the North Atlantic Deep Water (NADW) may be brought up to the surface around Antarctica by Ekman suction acting in regions where the deep density layers outcrop.

This effect is also discussed by Hasumi and Suginohara (1999b). They find that the production rate of NADW and the annual mean air-sea heat flux anomalies are both proportional to the wind stress over the Southern Ocean. They also show that these effects are associated with changes in the stratification of the deep ocean, whose mechanism is detailed by Tsujino and Suginohara (1999).

Munk and Wunsch (1998) also assume that deep mixing in the ocean has to upwell approximately 30 Sv across the 3.5°C surface within the ocean and that this water eventually upwells through a significant fraction of the ocean's depth. As was discussed above, given the area and stratification of the deep ocean, this requires a vertical diffusion coefficient κ of approximately $10^{-4} \text{ m}^2 \text{ s}^{-1}$. Averaged over the whole ocean, this requires a total energy input of 2.1 TW.

In fact the value of 30 Sv, based on the inverse model results of Macdonald and Wunsch (1996) for both Deep and Bottom Water, may be an overestimate. If we take the figure of 3.5°C to roughly

coincide with the boundary between Deep Water (i.e. North Atlantic Deep Water) and Intermediate Waters, then Schmitz's (1995) estimate of the flux across this surface is 14 Sv. A related estimate comes from the Atlantic at 30°N where the southward flux of water colder than 4.0°C is of order 17 Sv (see Bryden, Chapter 6.1). To this figure we should also add an unknown amount of deep water formed from lighter waters by mixing across the Antarctic Circumpolar Current. The flux of Antarctic Bottom Water does not need to be included in the figures because it is formed at the surface from water masses in the Deep Water density class (Foster and Carmack, 1976; Olbers *et al.*, 1992; Schmitz, 1996b).

The models (Döös and Webb, 1994; Döös and Coward, 1997; Hasumi and Suginohara, 1999b) indicate that between 9 and 12 Sv of Deep Water is upwelled and converted to Intermediate Water in the Southern Ocean. This is a net value, which in the case of the eddy-resolving models (Döös and Webb, 1994; Döös and Coward, 1997) includes the flux in the opposite direction due to eddies. If this is correct, then it only leaves 5–8 Sv to be upwelled by diapycnal mixing in the deep ocean.

Using the figures of Munk and Wunsch (1998), a diapycnal diffusivity of $10^{-5} \text{ m}^2 \text{ s}^{-1}$, due to the background isotropic internal wave field, can upwell 3 Sv across the 3.5°C surface. The remaining 2–5 Sv can be upwelled by localized enhanced mixing as long as the resulting area-averaged diapycnal diffusivity affecting the deep and intermediate waters is also of order $10^{-5} \text{ m}^2 \text{ s}^{-1}$. On the basis of the earlier figures this requires around 0.2 TW from the wind or the tides. If these reduced estimates are correct, they may explain why regions of enhanced vertical mixing have not been more widely observed.

Estimates of internal tide dissipation using barotropic tidal models alone give values near 1.1 TW (Sjoberg and Stigebrandt, 1992; Morozov, 1995). Similar values have recently been obtained from satellite altimeter observations of the barotropic tides (Egbert and Ray, 2000). When satellite altimeter data is used to constrain both the barotropic and baroclinic tides, the estimate drops to 0.6 TW (Kantha and Tierney, 1997). Together with the contribution from the wind, these dissipation rates are barely sufficient to mix the 30 Sv of Macdonald and Wunsch through the full depth of the water column. However, even

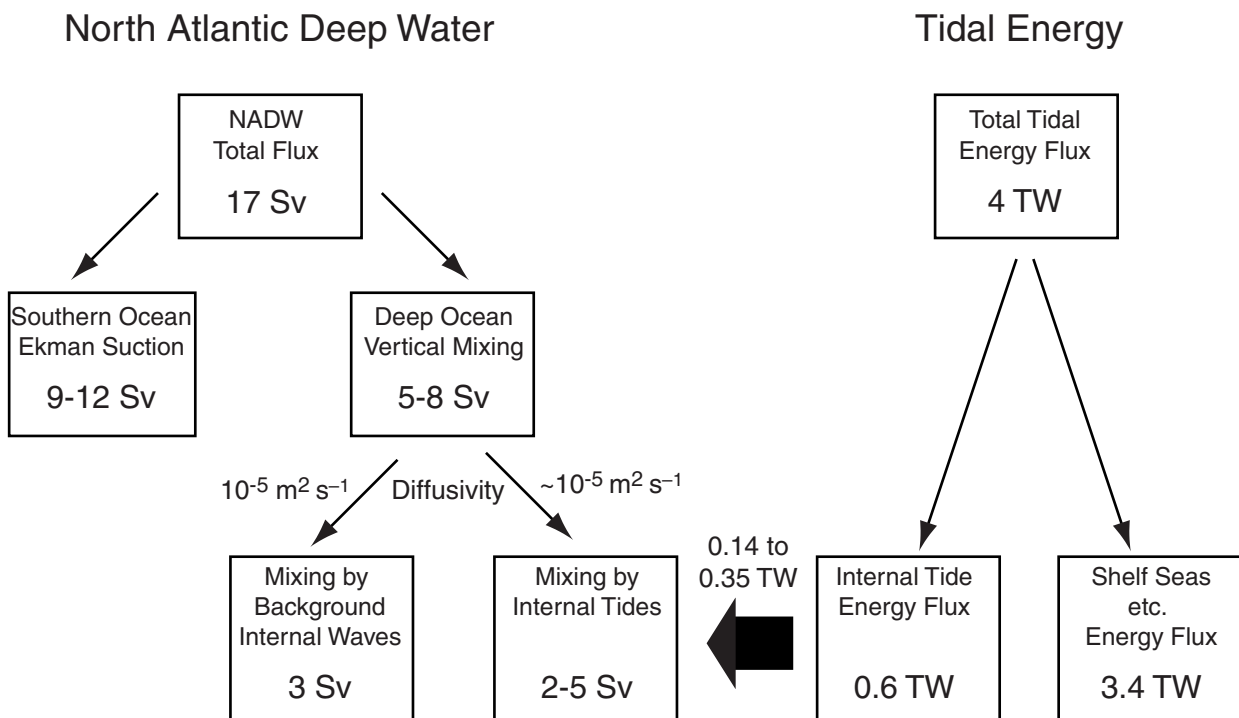


Fig. 4.2.4 Schematic of the proposed relationships between the upwelling of North Atlantic Deep Water in the present ocean, the flux of tidal energy and the diapycnal mixing coefficient.

allowing for inefficiencies in the mixing process, they are more than enough to provide the extra vertical mixing that we require.

Because of the consistency between the revised fluxes, summarized in Fig. 4.2.4, we believe that there is no longer a real discrepancy between the observed mixing coefficients in the deep ocean and the strength of the thermohaline circulation. Instead we have some confidence in this alternative picture (due originally we believe to Döös and Coward, 1997 and Toggweiler and Samuels, 1998), in which a large fraction of the water mass conversion, associated with the upwelling branch of the thermohaline circulation, occurs in the surface layers of the Southern Ocean.

The remainder of the conversion occurs in the deep ocean where there is a background mixing coefficient of about $10^{-5} \text{ m}^2 \text{ s}^{-1}$, due to the background internal wave field. There is also enhanced mixing in those parts of the deep ocean where there is strong interaction between ocean currents and topography. Such a pattern of deep mixing should produce a complex flow field, with zonal or contour-following flows in regions of weak vertical mixing and meridional or contour-crossing flows in regions of strong mixing.

4.2.5 Conclusions

When we were first contacted by the editors of this book to write this chapter, the question they posed was 'What governs the interior flow?'. At the time it seemed a bit of a poisoned chalice for, as Joe Reid wrote in 1981 at the beginning of a similar chapter,

There is a large part of the ocean circulation for which we have very little information and very vague concepts.

(J. L. Reid, 1981)

However, there are some important facts and equally important clues. As a fact we know that the circulation must conserve mass, heat, salinity and momentum. On a rapidly rotating earth, this means that away from the boundaries it must approximately conserve potential vorticity. As a result the ideas developed from Sverdrup balance, ventilation and topographic steering should hold throughout most of the ocean.

The clues come from the recent WOCE deep ocean measurements of tracers and turbulence and the satellite observations of tidal energy loss. These indicate that vertical mixing in the ocean is

likely to be very patchy. If this is true, then in the deep ocean we are likely to see a series of zonal jets, possibly steered by deeper topography, instead of the standard picture of a large gyre in each of the major ocean basins.

This new picture of the deep ocean is revolutionary and exciting. It requires a lot more study

developing both the theory and the observational database. Observations of the ocean are always expensive but they are essential for the further development of our understanding. Our picture of the deep ocean is becoming clearer but there is still a lot to do.

4.3

The Tropical Ocean Circulation

J. S. Godfrey, G. C. Johnson, M. J. McPhaden, G. Reverdin and Susan E. Wijffels

4.3.1 Flow and water mass transformation patterns

Most of the heat absorption into the global oceans, and much of the freshwater absorption, occurs in the tropics. Furthermore, Sea Surface Temperature (SST) is sufficiently high in the tropics that deep atmospheric convection can and does occur over it. Movements of deep convection patterns, which affect climate globally, depend sensitively on small changes in SST. Thus it is critically important for the improvement of global climate models that their ocean components – when driven by accurate surface fluxes – should accurately simulate water mass changes, circulation, and above all SST, not only on long-term mean but on a variety of time scales. To achieve this one must do more than simply locate where water mass conversion takes place; it is necessary also to identify and parameterize the mechanisms by which it occurs. These aims are particularly relevant in the tropics.

The top-to-bottom vertical sections obtained in the World Ocean Circulation Experiment (WOCE) provide a resource for learning how to make such model improvements. At least 21 of the meridional and 10 of the zonal WOCE one-time hydrographic sections were occupied partly or fully within the tropics throughout the Pacific, Atlantic and Indian Oceans. These WOCE sections, together with other data and models, are the subject of active study by many scientists. Their research builds on a long history of earlier work on the tropical circulation. The primary aim of this chapter is to review the present understanding of flow and water mass transformation patterns within the tropics of all three oceans.

Unfortunately, it is a very complex subject. With regard to the ‘traditional’ use of hydrographic data for evaluating transports of heat and other quantities, particular care has to be taken in analysing cross-equatorial or near-equatorial sections; geostrophy cannot be assumed for flow through such sections, unless several repeats are undertaken (e.g. Lukas and Firing, 1984). More importantly, especially in the Pacific, near-equatorial currents and temperatures have major inter-annual variability associated with the El Niño phenomenon, so that (for example) the time-averaged product (vT) of temperature and meridional velocity at a given location may have large eddy-flux contributions from variations on El Niño-Southern Oscillation (ENSO) time scales. These must be allowed for in order to achieve the WOCE goals of quantifying the long-term mean heat and fresh water transports in the global ocean. There are also significant variations due to the seasonal cycle, the Madden-Julian Oscillations of 40- to 60-day period, and Tropical Instability Waves of 20- to 30-day period. To elucidate these, it will be necessary to supplement WOCE observations with others that resolve these variations. The Tropical Ocean and Global Atmosphere (TOGA) Observing System can resolve many of them in the upper few hundred metres of the Pacific, from about 1985 onwards. It consists of the Tropical Atmosphere Ocean (TAO) mooring array, expendable bathythermograph (XBT) sections including surface salinity data, surface drifters and tide gauge data, supplemented with remotely sensed SST, wind stresses and sea level. These data, and relevant results from them, are reviewed by McPhaden *et al.*

(1998) (referred to below as TOGAObs). The output of Ocean General Circulation Models (OGCMs) driven with observed flux products, with and without the assimilation of observed ocean data, will also provide a valuable analysis tool.

The complexity does not stop here. In the tropics, much water mass formation occurs due to Kelvin–Helmholtz instability and mixing in layers with low Richardson numbers. Mixing is thus a highly non-linear function of the mean circulation, so it may vary considerably with seasonal and non-seasonal circulation changes. Tidal mixing, mixing due to flow over sills and horizontal mixing are similarly non-linear processes, and research on all of them is still at the early stages of development. All of them are probably confined to locations that are quite small compared with that of a typical WOCE ‘box’. In the following sections, we mainly describe our present understanding of flow patterns, but we also discuss water mass formation processes where appropriate. As will be seen, the variety of processes is very rich in the equatorial region; we will emphasize those we feel particularly need to be better parameterized, to create a more effective ocean component of a coupled climate model. This implies that we will discuss some near-surface processes that result in little transport of heat, but are nevertheless of importance for changing SST.

Sections 4.3.2, 4.3.3 and 4.3.4 each deal with observations and some modelling results, in the Pacific, Atlantic and Indian Oceans, respectively, relating to the main flows near the equator and their water mass sources. The presentation varies for each ocean, since the outstanding issues and available data vary among the three basins. We use the fact that the dynamics of the equatorial Atlantic and Pacific basins are similar to shorten the discussion of the former. However, the Indian Ocean is qualitatively different from the other two, so rather more discussion is devoted to it than to the Atlantic. Some conclusions are given in Section 4.3.5. We deal quite cursorily with the ENSO phenomenon and shorter-time-scale variability, referring readers wherever possible to the June 1998 issue of the *Journal of Geophysical Research* – a special issue devoted to reviews of TOGA. Similarly, we will not devote much attention to the Indonesian Throughflow, since this was the subject of another special issue of the *Journal*

of *Geophysical Research* in May 1996. Nor have we tried to deal at all comprehensively with cross-equatorial sections undertaken in WOCE, which are described (for the Pacific) in the special issue of *Journal of Geophysical Research*, June 1998. A comparable special issue for the Atlantic is *Deep-Sea Research*, January 1999; and *Geophysical Review Letters* devoted a special section to the Indian Ocean WOCE Expedition in 1997.

4.3.2 Equatorial phenomena in the Pacific Ocean

4.3.2.1 Flows within the Pacific equatorial thermocline

A schematic diagram of equatorial flows within the thermocline in the Pacific (adapted from Philander, 1990) is seen in Fig. 4.3.1, while a mid-Pacific annual mean cross-section, due to Wyrtki and Kilonsky (1984), is shown in Fig. 4.3.2. Mean easterly winds along the equator drive the South Equatorial Current (SEC) westward at the surface, piling warm water into the western Pacific. An along-equatorial pressure gradient therefore develops over the top 250 m to roughly balance the wind stress; this drives the Equatorial UnderCurrent (EUC) eastward. The EUC shoals and upwells (as can be seen in the equatorial tongue of east-flowing water reaching towards the surface in Fig. 4.3.2), supplying the bulk of the surface water that diverges from the equatorial East Pacific in meridional Ekman transports. As indicated in Fig. 4.3.1, the EUC is in turn supplied by the meridional geostrophic inflow that compensates the Ekman transports, including inflows at the western boundary. The geostrophic inflow is indicated by tongues of high-salinity water in Fig. 4.3.2 flowing equatorward from both hemispheres.

The SEC is a broad shallow current, extending from the subtropical South Pacific to 2–5°N; it mainly occurs in the top 200 m (Fig. 4.3.2). Its breadth is set by patterns of wind stress curl. Wind curls also generate the North Equatorial Counter-Current (NECC), found north of 2°N in the west, and 5°N in the east Pacific. The temperature field seen in Fig. 4.3.2 provides the main geostrophic balance for the SEC, NECC and EUC. These flows, together with the surface Ekman flows and the equatorial western boundary currents including the Indonesian Throughflow (IT), all vary seasonally and through the irregular ENSO cycle.

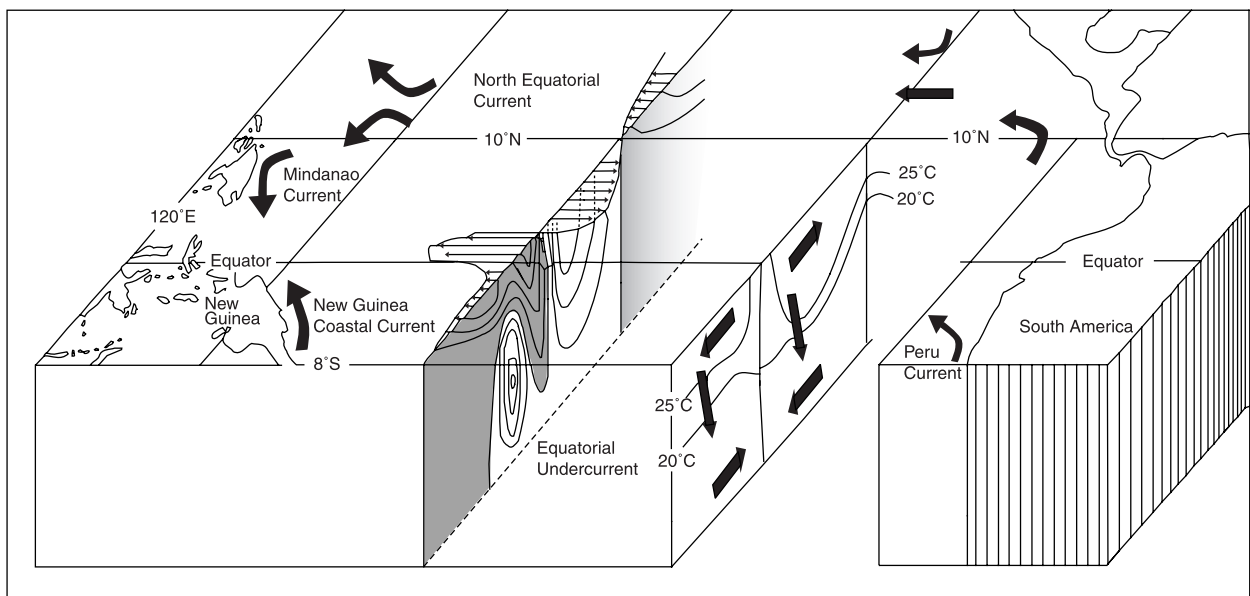


Fig. 4.3.1 Schematic of flow patterns in the equatorial Pacific, above the thermocline. Adapted from Philander (1990).

These flows combine to carry the mean heat and fresh water transports, whose elucidation is a primary objective of WOCE, out of the equatorial Pacific.

To address the complex topic of how this is achieved, this section on thermocline flows in the equatorial Pacific has six subsections. They deal in turn with flow pathways; budget studies; thermo-haline phenomena; eddy diffusion; the width and depth of the EUC; and longer-term variability, from Tropical Instability Waves to ENSO.

Upper ocean flow pathways in the equatorial Pacific

Given the nearly conservative nature of subsurface ocean flow, it is useful to delineate the pathways by which waters of various sources flow into and out of the upper equatorial Pacific, from their subduction point until they return to the surface mixed layer (Liu and Philander, Chapter 4.4). Any water mass changes due to subsurface processes along these pathways (e.g. mixing in the low Richardson number region above and below the EUC core; Toole *et al.*, 1987) also need to be accounted for. Several hypotheses for decadal variability of El Niño are predicated on assumptions regarding pathways to the EUC (e.g. Gu and Philander, 1997; Zhang *et al.*, 1998a; Schneider *et al.*, 1999b). The clarification of flow pathways is being pursued by modellers as well as observationalists, with some success, e.g. McCreary and Lu (1994),

Liu *et al.* (1994), Lu and McCreary (1995) and Lu *et al.* (1998). However, in the following we do not attempt to review the results of these models in detail, concentrating on recent observational studies.

We concentrate on flows feeding the EUC. About 25 Sv (1 Sv = $10^6 \text{ m}^3 \text{ s}^{-1}$) enter the EUC from western boundary currents, of which about half comes from the north via the Mindanao Current. The other half enters via the New Guinea Coastal Current and an analogous flow east of New Ireland (Lindstrom *et al.*, 1990; Butt and Lindstrom, 1994; Wijffels *et al.*, 1995). These flows are ultimately fed by subduction in subtropical latitudes, and are marked by high oxygen concentrations and (particularly from the south) by high salinity. Of these 25 Sv, Wijffels (1993) estimates that 17 Sv enter with EUC densities. This inflow is quite close to the EUC transport at 165°E, where estimates are all close to 16 Sv; similar EUC values are also found near 142°E (Gouriou and Toole, 1993), in agreement with the inflow being confined close to the western boundaries.

Johnson and McPhaden (1999; referred to below as JMcP) investigate equatorward geostrophic flow in the interiors of the North and South Pacific. They use averaged hydrographic data to estimate the geostrophic equatorward flow between the base of the mixed layer and a neutral surface close to the base of the thermocline (25.9 in the northern hemisphere, 26.2 in the southern – each close

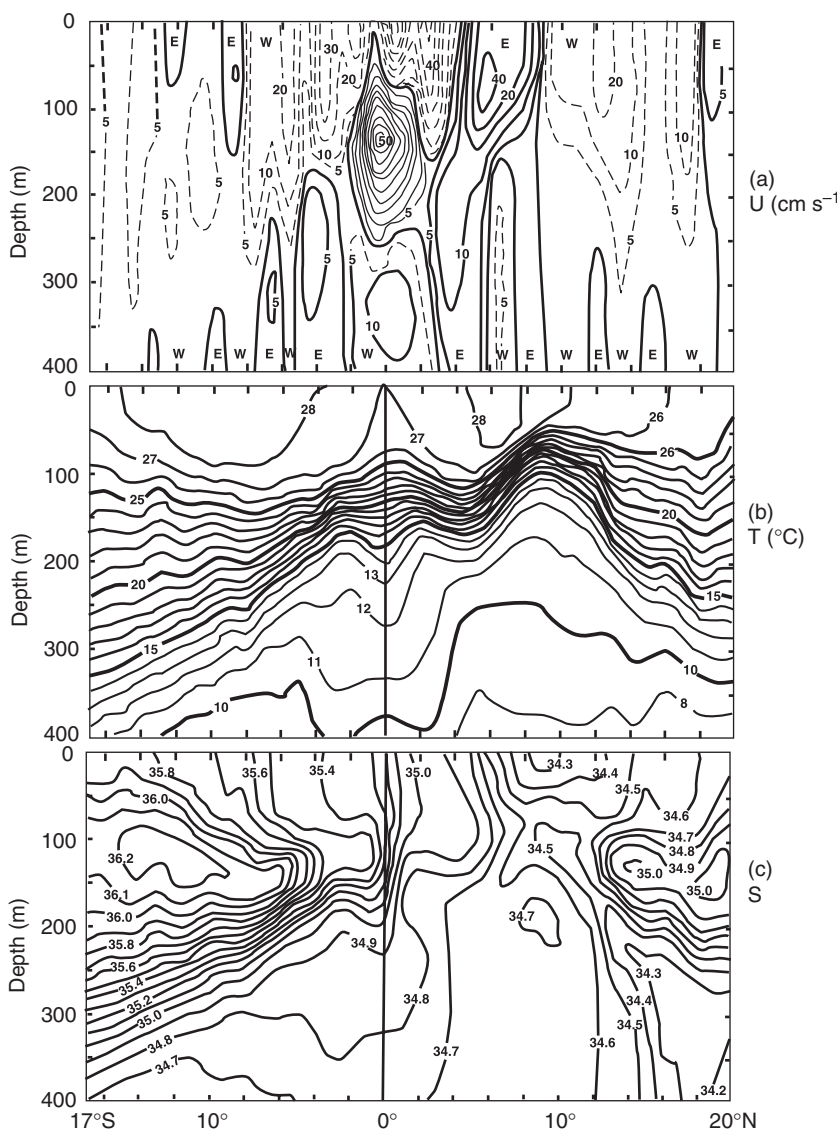


Fig. 4.3.2 Mean zonal geostrophic flow U (cm s^{-1}), temperature T ($^{\circ}\text{C}$), and salinity S between Hawaii and Tahiti and from 0–400 m, for the period April 1979–March 1980. Adapted from Wyrtki and Kilonsky (1984).

to the base of the thermocline), below which some poleward flow is found. The equatorward flow is well defined in magnitude in the South Pacific, being $15 \pm 1 \text{ Sv}$ between 17°S and 7°S , nearly all in the east and central Pacific. Nearly all this inflow has neutral density greater than 23, and thus can directly feed the EUC. In the North Pacific, JMcP also investigate earlier suggestions (Fine *et al.*, 1987; McPhaden and Fine, 1988; Liu, 1994; McCreary and Lu, 1994) that further water enters the EUC via a circuitous interior pathway. This passes west of the strong vorticity barrier of large fN^2 values at 10°N , to reach the EUC in the central Pacific. JMcP find the magnitude of this interior flow to be $5 \pm 1 \text{ Sv}$. However, half of this

has neutral density less than 23, placing it above the EUC. Thus the northern interior pathway may not be a significant fractional contributor to the EUC. The net of an EUC at 165°E of 16 Sv plus these flows is about 37 Sv – rather more than the observed magnitude of the EUC near 155°W , namely about 32 Sv (see TOGAOb for a review). Wijffels (1993) also found a net convergence of about 6 Sv in the EUC density range. The maximum transport of the EUC is believed to occur near 140°W .

This picture of rather close mass balance of flow in the EUC density range is puzzlingly different from the net thermocline picture in the western Pacific. Net Ekman and geostrophic flows out of

the Pacific west of 165°E and between 10°N and 14°S show a divergence of 6.4 Sv (Wijffels, 1993) – comparable to the Indonesian Throughflow, whose mean value in the thermocline appears to lie in the 5–10 Sv range (e.g. Meyers *et al.*, 1995; Gordon *et al.*, 1999a). But this water cannot be upwelled from the depth range of the EUC, which is in good mass balance in the west Pacific; it appears to come from further down. However, attempts to close the western Pacific volume budget are difficult due to the strong intraseasonal and interannual variability in the flows there. Using long-term averaged XBT lines, Morris *et al.* (1996) was able to balance these flows over a much larger region encompassing the whole western half of the Pacific Ocean and the Indonesian Seas.

JMcP find that geostrophic convergence towards the equator, below the surface mixed layer, increases to about 65 Sv when the limits are taken at 3°S and on the trough between the SEC and the NECC. The excess of 25 Sv over what is needed to supply the EUC is presumably warmed in the westward-flowing SEC, subducted in the east or central Pacific, and then upwelled again to flow out in the surface mixed layer further west. (This phenomenon is referred to as the ‘Tropical Cell’, as opposed to the ‘Subtropical Cell’ that supplies subtropical water to the equator, e.g. Lu *et al.*, 1998.) It should be noted that the picture of a meridionally symmetric system near the equator is not quite correct; mean meridional flow across the equator is not zero, but is given quite well by the Sverdrup relation (e.g. Joyce, 1988).

Budget studies

One means by which our ideas on equatorial dynamics can be refined is by use of budget studies, and several of these have been undertaken in the equatorial Pacific. Bryden and Brady (1985) used repeat hydrographic sections along 150°W and 110°W, from 5°N to 5°S, to determine annual mean geostrophic flows through the boundaries of this rectangle, above 500 db. This region includes the climatological mean position of the EUC maximum strength (about 140°W). After adding Ekman transports, vertical velocities (assumed to be mainly confined to 0.75°S–0.75°N) were determined by mass conservation. They find that about half the 57 W m^{-2} absorbed in the region is used to heat the zonal SEC as it traverses the region, and half heats the meridional outflows. Zonal flow in the EUC is

basically along the zonally sloping isotherms, so that upwelling through isotherms is typically only 1/3 of the net upwelling. Stress divergence can be inferred from the mean momentum budget; it implies that eddy mixing of momentum extends well below the core of the Undercurrent, consistent with Toole *et al.*’s (1987) finding that low Richardson numbers occurred below the EUC as well as above.

Wijffels (1993) examined top-to-bottom sections along 10°N and 14°S in the Pacific, and repeat meridional sections at 165°E. She used these to form mass and heat budgets for the region. Her resulting description of flow patterns at each depth is basically compatible with that given earlier. A major uncertainty is the size of the Ekman fluxes across the zonal sections. Based on an assumption of small vertical mixing through barrier layers, Godfrey and Lindstrom (1989) concluded that the heat flux into the far western equatorial Pacific is only of order $0\text{--}10 \text{ W m}^{-2}$. When Wijffels used this as an average over the whole western part of her domain, it implied that the Indonesian Throughflow must be smaller than 7 Sv if heat is to be conserved. The reason is that subthermocline inflow from south of Australia must warm enough to enter the thermocline, a temperature change of about 10°C. This in turn would imply that Gordon’s (1986; also Gordon, Chapter 4.7) warm water pathway for the ‘Conveyor Belt’ circulation is weak.

The TOGA Coupled Ocean–Atmosphere Response Experiment of 1992–93 (COARE; see Godfrey *et al.*, 1998, for a review) provided some answers to the questions Wijffels raised. Fluxes were measured over 4 months from a moored buoy (Weller and Anderson, 1996), and detailed near-surface budgets were undertaken using these fluxes in order to test closure, and thus reduce some of the uncertainties in surface heat and fresh water flux measurements. Feng *et al.* (1998b) demonstrated that the heat budgets closed to better than 10 W m^{-2} , on each of three periods of a few weeks. Both Feng *et al.* and Cronin and McPhaden (1997) found that the heat budget was primarily one-dimensional, with periods near wind bursts when advection was important. The 4-month average heat flux into the surface in COARE was nearly 25 W m^{-2} (Weller and Anderson, 1996). Climatologies show small seasonal variations of heat flux at this location, so this may be close to an

annual mean. Most annual mean heat flux climatologies show a minimum near the COARE region. Thus the average over the whole of Wijffels' western Pacific domain would probably be substantially greater than 25 W m^{-2} .

Apart from the question of the magnitude of the surface heat flux into the western equatorial Pacific, a further question is raised by Wijffels' study: how is the heat mixed down, to change South Pacific subthermocline water into the upper-layer water that flows out with the Indonesian Throughflow? Two processes can be postulated. The first involves the New Guinea Coastal Current (NGCC; Lindstrom *et al.*, 1990). On annual mean this western boundary current travels northwestward toward the equator; but in austral summer, the surface flow is downwind (southeastward), against the mean northwestward flow. A strong shear zone therefore exists at this time in the NGCC, and low Richardson numbers are observed below the mixed layer, suggesting mixing there (S. Cresswell, personal communication). Second, Ffield and Gordon (1996) suggested that tidal mixing raised vertical eddy diffusivities by a factor of about 10 throughout the Indonesian Archipelago over the usual values of about $10^{-5} \text{ m}^2 \text{s}^{-1}$. This implies that surface heat fluxes of order 40 W m^{-2} are carried through both the surface and the base of the mixed layer, to the thermocline waters below. It is quite plausible that tidally enhanced eddy diffusivities (perhaps not as large as in Indonesia) are widely distributed in the west Pacific, near reef complexes; e.g. Pinkel *et al.* (1997).

Thermohaline phenomena

In the Warm Pool regions of the western Pacific and eastern Indian Ocean, the net heat flux is not as large as in the east Pacific; but rainfall is heavy. Heat and fresh water contribute about equally to the surface buoyancy flux in this region. Under these conditions the true mixed layer is often defined by a halocline; short-wave penetration through this halocline gently warms the water just beneath (e.g. Lewis *et al.*, 1990), resulting in a nearly isothermal region below the mixed layer. This is named the 'barrier layer', because the combination of low eddy diffusivity and low temperature gradient within it imply low net turbulent heat fluxes (Godfrey and Lindstrom, 1989; Lukas and Lindstrom, 1991). Lukas (1988) suggested that the barrier layer in the central Pacific might be maintained dynamically,

by subduction of warm salty water at the eastern edge of the Warm Pool. Picaut *et al.* (1996) describe observations of a salinity front in the central equatorial Pacific, at which just such a subduction phenomenon is thought to occur. The front moves east and west by over 1000 km. This behaviour has been simulated successfully in a numerical model, and salty water does indeed subduct at the model front to continue westward a few tens of metres below the surface (Vialard and Delecluse, 1998a,b). In the model, the non-linear advective movement of the front is tightly linked to wind driving associated with the El Niño (P. Delecluse, personal communication).

The net result of these effects is that to the west of the mid-Pacific salinity front, wind-driven entrainment from the base of the mixed layer can slightly warm the mixed layer, rather than cooling it as in the eastern Pacific. This process (along with low wind speeds and evaporation) may be the reason that SST remains high in the Warm Pool region, despite the high cloud cover and low insolation in these regions. Thus there may be a new positive feedback mechanism associated with ENSO. An ENSO event spreads the fresh, Warm Pool eastward; SST warms to above 28°C , because of 'Barrier-Layer Shutoff of Entrainment' (Lukas, 1988); this SST increase permits deep convection to occur, and the resulting heavy precipitation perpetuates the barrier layer. Support for this positive feedback mechanism comes from a basin-scale analysis of interannual variations in surface layer hydrography and precipitation in the tropical Pacific (Ando and McPhaden, 1997).

Eddy diffusion

Pacanowski and Philander (1981) found that the inclusion of a strong Richardson number dependence in their parameterizations of vertical viscosity and diffusivity isolated most dissipation to the shear zone between the EUC and the surface current. This greatly improved their model's ability to reproduce observed equatorial density and current structures. Direct observations (Peters *et al.*, 1988) showed the Richardson number dependence to be still stronger than Pacanowski and Philander assumed. Kunze *et al.* (1990) developed a parameterization of dissipation rates, to be applied only in unstable conditions ($Ri < 0.25$); Peters *et al.* (1995) and Polzin (1996) found this formula agreed with their dissipation data, to within a factor of 2.

Tsuchiya and Talley (1998) in the eastern equatorial Pacific and McPhaden (1985) in the central equatorial Pacific note the possibility that salt fingering is an important mixing mechanism.

With regard to lateral mixing, tropical instability waves are the primary contributors to lateral diffusivities in the tropical Pacific (Hansen and Paul, 1984; Bryden and Brady, 1989; Flament *et al.*, 1996). The energetics of these waves are complicated, and there appears to be more than one form of instability of the major zonal currents that can give rise to the observed variability (Luther and Johnson, 1990; McCreary and Yu, 1992). Effective lateral heat and momentum diffusivities due to these waves as inferred from observational studies are generally around 10^3 to $10^4 \text{ m}^2 \text{ s}^{-1}$ (Bryden and Brady, 1989; Swenson and Hansen, 1999; Wang and McPhaden, 1999). These diffusivities are generally positive, though Lukas (1987) and Bryden and Brady (1989) found instances (from mid-Pacific mooring data) when eddy diffusivities were negative, both for momentum and heat. The implications of this result have not to the authors' knowledge been taken up yet by the modelling community. Richards and Pollard (1991) and Richards (1998) have used fine-scale hydrographic observations across the western Pacific to show that double-diffusion, combined with observed interleaving flows with vertical scales of a few tens of metres, can generate quite large 'horizontal diffusivities' in the equatorial western Pacific.

Dynamics of the Equatorial Undercurrent's width, depth and strength

Empirically, the simple balance $dP/dx = \tau^{(x)}$ holds quite well along the equatorial Pacific and Atlantic Oceans, where P is the depth-integrated pressure above an assumed depth of no motion of (say) 400 db. For reasonable choices of 'reduced gravity', this implies that the thermocline depth must be substantially greater than observed mixed-layer depths in the western Pacific, or Atlantic. Below the mixed layer, one might expect friction to be small compared to the zonal pressure gradient; since Coriolis force is zero, the balance should be inertial – water simply accelerates down the pressure gradient. Pedlosky (1987a, 1991) developed an inertial model of the EUC, matching it to the Luyten *et al.* (1983) 'ventilated thermocline' away from the equator; the model simulates Pacific EUC

width and strength quite well. Wacongne (1990) notes that an integration of $dP/dx = \tau^{(x)}$ across the Pacific and Atlantic implies greater thermocline depth in the west Pacific compared with the Atlantic, and suggested that this is the reason for the substantially greater depth of the Pacific EUC compared with the Atlantic. She compared OGCM simulations of the Atlantic and Pacific EUCs; she found an inertial acceleration zone at the western end of the model EUCs. The maximum speed of the EUC was found at the eastern end of this inertial region. Vertical friction was strongly dependent on Richardson number in this model, and therefore only became important to the east of this region, where shears became large and Richardson numbers small. Qualitatively similar behaviour occurred (in the OGCM) in the equatorial Pacific; but here the inertial region extended about 72° of longitude from the western boundary, compared with only 14° in the Atlantic. Thus the Pacific EUC reaches its maximum through the action of gentle accelerations over a very long fetch; it is this long fetch that allows the Pacific EUC to exceed the Atlantic in strength. However, McPhaden (1993) finds that similar conclusions also hold in a linear, frictional model of the EUC, and he notes that 'the exact mix of linear and nonlinear processes that leads to the observed differences between the Atlantic and Pacific Oceans remains to be determined'. The strongly non-linear nature of both lateral and vertical friction, noted in the preceding subsection, further complicates the matter.

Temporal variability: Tropical Instability Waves, Madden–Julian Oscillation, mean seasonal cycle, ENSO

As noted earlier, the task of working out the heat and fresh water budget is still further complicated by variability associated with the El Niño phenomenon, seasonal cycle, Madden–Julian Oscillations of 40- to 60-day period, and Tropical Instability Waves of 20- to 30-day period. To elucidate these, it will be necessary to supplement WOCE observations with observations from the TOGA Observing System (McPhaden *et al.*, 1998; referred to below as TOGAOb).

Currents estimated from thermal data via geostrophy match more direct observations well. For example, mean transport values for the EUC, SEC, NEC and NECC along 150 – 158°W between March 1979 and June 1980 (Wyrtki *et al.*, 1981) are

reproduced by estimates from the TOGA XBT network, within the standard deviations of both measurements. The mean EUC and SEC from the Tahiti-to-Hawaii Shuttle data of Fig. 4.3.2 are also well reproduced in XBT data at similar longitudes (Picaut and Tournier, 1991). Drifter data confirm the universally poleward mean nature of surface flow in the Pacific (TOGAObs, Reverdin *et al.*, 1994). TAO mooring data provide mean seasonal cycles of zonal flow and temperature along the equator at four longitudes, with at least 7 years of data in each average (TOGAObs). The boreal spring decrease in the SEC and associated increase in the upper parts of the EUC is particularly noteworthy at all longitudes; these are earliest and of greatest magnitude in the east Pacific. There are indications that the observed annual-cycle variations in current, SST and wind stresses may be linked through an ENSO-like feed-back mechanism, and that the annual cycle is non-stationary – e.g. annual thermocline variations were much greater in the 1990s than the 1980s. TOGAObs also reviews work on mean seasonal cycles elsewhere in the equatorial Pacific, using XBT, drifter and tide gauge data.

For a review of variability on ENSO, Madden-Julian Oscillations and Tropical Instability Wave time scales, we refer the reader to TOGAObs and the accompanying articles in the TOGA Special Issue of the *Journal of Geophysical Research*, of June 1998. However, one item of particular interest in the context of WOCE is the relation of the Indonesian Throughflow (IT) to ENSO. Clarke and Liu (1993, 1994) and Meyers (1996) showed that the strength of the IT was closely related to ENSO, using sea level and XBT data, respectively. According to Clarke and Liu, the ENSO variations of thermocline depth in the western Pacific are transmitted by Kelvin and Rossby waves along the western coast of Australasia. Thermocline behaviour at the Indonesian coast is determined by Indian Ocean wind. Both have an ENSO component of the same sign, but the latter is much smaller. As a result, the peak-to-trough variation of the IT is about ± 5 Sv – comparable to its mean value (7 Sv, from steric heights relative to 400 db).

4.3.2.2 Mean subthermocline zonal currents in the equatorial Pacific

Current structure below the thermocline has obviously received less attention than upper ocean flow.

However, Firing (1987, 1989) obtained 41 meridional sections of currents from top to bottom across the equatorial Pacific, at 159°W, over 16 months in 1982–83. The resulting long-term mean section of zonal flow (Fig. 4.3.3a) shows a remarkably complex pattern of interleaving jets. Even the nomenclature is difficult, with some significant features (e.g. the eastward current at 3000 m near 2°S and the westward flow near 4000 m) having no name as yet. The observations spanned the 1982–83 ENSO event but are nevertheless similar to earlier data sets, so Firing (1987) suggested that these flows may be permanent. This has been largely borne out by the results of Firing *et al.* (1998). They examined 12 top-to-bottom velocity sections, mostly measured on WOCE cruises, and a geostrophic current estimate based on the average of a large number of hydrographic sections at 165°E between 1984 and 1991 (Gouriou and Toole, 1993; Wijffels, 1993). The latter average (Fig. 4.3.3b) shows a remarkable similarity to Fig. 4.3.3a; the South and North Intermediate CounterCurrents (SICC, NICC) and the Lower and Southern Equatorial Intermediate Currents (LEIC, SEIC) and 3000 m current are all quite similar in magnitude and location to Fig. 4.3.3a. At 165°E the 4000 m current is located on the equator, though sample density below 2000 m decreases, making the mean less reliable at such depths. The ‘Equatorial Deep Jet’ regime, with alternating jets about 2° wide every 200–300 m between 500 and 2500 m, is just as evident in the mean geostrophic flow at 165°E as in Fig. 4.3.3a. The only large differences at 165°E from Fig. 4.3.3a lie above 300 m, where the Northern and Southern Subsurface CounterCurrents (NSCC, SSCC; also known as Tsuchiya Jets) are observed at 165°E about 2–3° from the equator near 270 m. In the far west Pacific, the Subsurface CounterCurrents (SCCs) typically form minor maxima within the general band of eastward flow that includes the EUC and the NECC; however, the SCCs diverge poleward, developing a distinct identity further east. The south edge of the NSCC is just seen in Fig. 4.3.3a. The direct velocity sections provide a spot sampling of variability with longitude, season and phase of the ENSO cycle; they, too, generally confirmed the idea that the 159°W section is representative of the mean flow, over most of the width of the Pacific. However, departures of individual sections from the mean are substantial, and they show no obvious relationship with season or with the phase of the ENSO cycle.

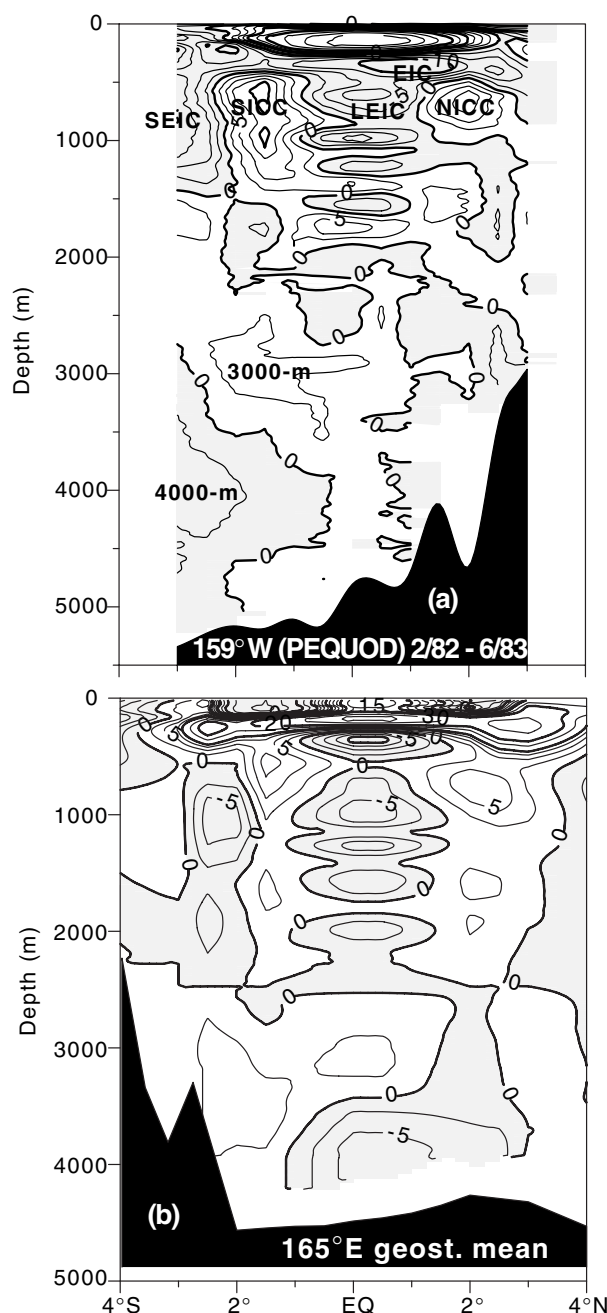


Fig. 4.3.3 (a) Mean zonal current from 41 sections along 159°W , February 1982 to June 1983, from the Pacific Equatorial Ocean Dynamics (PEQUOD) programme. Profiles were made at 0.5° intervals. Contour interval is 2.5 cm s^{-1} , with heavy contours at integral multiples of 10 cm s^{-1} . Shaded regions show westward flow. SEIC, South Equatorial Intermediate Current; SICC, South Intermediate CounterCurrent; EIC, Equatorial Intermediate Current; LEIC, Lower Equatorial Intermediate Current; NICC, Northern Intermediate CounterCurrent. Equatorial Undercurrent on the equator at 150 m is not labelled. From Firing *et al.* (1998). (b) Mean geostrophic zonal velocity on 165°E . Contours as in (a). From Firing *et al.* (1998).

The search for possible dynamical explanations and/or higher latitude origin of these features is proceeding in a rather piecemeal fashion, with different explanations offered for different features; this almost certainly reflects physical reality. In the following we briefly discuss several of the various flows (named and unnamed, and including the SCCs) in Figs 4.3.3a,b. We start from the bottom and work upwards.

4000-m current

Johnson and Toole (1993) analysed flow through a deep hydrographic section at 10°N , taken in 1989. In the East Pacific near 110°W , they deduced a southward flow of Lower Central Pacific Water (LCPW) of 4.7 Sv over the gently sloping bottom found west of the East Pacific Rise. This is quite close to the mean westward transport in the '4000-m current' of Fig. 4.3.3a (about 6 Sv). Ponte and Luyten (1989) had also found an equatorial westward jet from 138°W to 148°W below 3500 m, of similar velocities and depth distribution. Johnson and Toole concluded that the '4000-m current' of Fig. 4.3.3a originates in the eastern North Pacific. It then travels along the equator to 159°W . They attributed its presence at 2.5°S in Fig. 4.3.3a, rather than on the equator, to topographic steering around the south end of the Line Islands. They suggested that further westward, this flow rejoins the northward-flowing LCPW that crosses the equator in the central Pacific Basin. Wijffels (1993) adds a discussion of flows through 14°S to Johnson and Toole's data sources; her Fig. 5.14 summarizes the results. The flows through 14°S do not supply much of the 4000-m current, but a still deeper flow of bottom water – though confined to deep western boundary currents in trenches – upwells about 4 Sv into the equatorial strip. The overall impression is of an elongated cyclonic gyre in the north equatorial Pacific, in the LCPW depth range. It is interesting that Myers and Weaver (1997) obtained a qualitatively similar, elongated gyre in their depth-integrated model of wind-driven circulation. The Joint Effect of Baroclinicity and Relief (the JEBAR), as generated by observed long-term mean upper ocean density structure, was crucial to their result.

3000-m and 2000-m currents

Talley and Johnson (1994, referred to below as TJ) note that earlier workers had observed plumes

of high ${}^3\text{H}/{}^3\text{He}$ ratio, emitted from hydrothermal vents at the East Pacific Rise near 110°W ; the plumes drift westward near 2500 m. Stommel (1982) and Hautala and Riser (1993) developed a model in which this heat source, or the heat source in combination with broader Stommel–Arons (Stommel and Arons, 1960a,b) circulation, might explain the westward flow. To test this idea further, JT obtained a map of potential temperature on the $36.96\ \sigma_2$ surface (near 2700 m), using data from several WOCE deep hydrographic sections and earlier sources. Broad westward tongues of warm water are seen near 5°N and 10°S – but a narrower tongue of cold water suggests eastward flow along 2°S , coinciding closely with the ‘3000-m current’ seen in Fig. 4.3.3a. Similar features are also found in the Atlantic near 2000 m. In that ocean, Böning and Schott (1993) find a Kelvin wave-like eastward jet along the equator, in a numerical model. They suggest that eddy-diffusive mechanisms, associated with resolved flow and salinity components in the model, can generate the observed salinity tongue slightly south of the main flow (near 2°S in the Atlantic).

Johnson and Talley (1997) (referred to below as JT) explored the currents between about 2000 and 3000 m in more detail. They took temperature (T) and salinity (S) data from deep Conductivity–Temperature–Depth (CTD) sections at 10°N and 15°S , plus three WOCE meridional sections at increasing distance east of the East Pacific Rise. They first defined a single ‘background’ θ –S relation for all sections, against which to define anomalies. In their zonal sections of salinity anomaly (Fig. 4.3.4; see Plate 4.3.4, p. 300), plumes of salty water ‘reminiscent of smoke from a chimney’ are seen west of the East Pacific Rise, appearing to emanate off the top of the Rise. The three meridional sections also show such plumes, with greatest strengths at 2700 m near 10°S and 8°N . A cold, fresh tongue lies between them at 2°S . The two salty plumes are about 600 km across meridionally, 800 m vertically, and decay to half-strength in 2800 km westward. Consistent with the idea that these plumes are formed by geothermal heat release from the East Pacific Rise, JT also find that buoyancy frequency N^2 shows similar plumes – minimum buoyancy occurs within the salinity plume, with an underlying plume of maximum buoyancy near 3200 m. A vertical derivative of the thermal wind relation yields $f\partial^2 u/\partial z^2 = -\partial N^2/\partial y$,

so a rough estimate of velocity and transport is obtained by vertical integration using the above dimensions. The result is the prediction of two flow cells overlying one another – a cyclonic cell (eastward flow nearest the equator, i.e. between about 4° and 8° from the equator) near 3200 m, and an anticyclonic cell near 2700 m. The lower one was predicted earlier, but JT provide the first observational evidence for it. The order of magnitude and sign of the predicted flows on the equatorial side of these cells are comparable to the steady flows seen near 3000 m and 2000 m, respectively, near 2°S in Fig. 4.3.3a. JT describe three different dynamical scenarios to account for their inferred flows; the most realistic is also the most complex, and the dynamical relationship between the salty plumes and the eastward 3000 m jet in Fig. 4.3.3a remains unclear. However, JT note that the (previously unremarked) westward flow seen near 2°S , 2000 m in Fig. 4.3.3a may be related to the flow at 3000 m in a vertical couplet sense, as in the flow generated by the plumes.

Reversing jets

In the 17-month average on the equator (Fig. 4.3.3a), four wavelengths of an apparent wave can be seen between 1000 and 2200 m depth. Such reversing jets have been observed in the other oceans (e.g. Luyten and Swallow, 1976; Eriksen, 1981; Ponte and Luyten, 1989, 1990). However, the lengths of these other records are inadequate to test whether the jets have a substantial component with period of more than a year, as Fig. 4.3.3a shows to be the case in the Pacific. It seems plausible that this phenomenon may be related to enhanced vertical diffusion and upwelling along the equator. Several authors (e.g. Bryan, 1987; Weaver and Sarachik, 1990; Sugino and Aoki, 1991; Wang, 1995) obtain reversing equatorial jets in their models, associated with an enhanced overturning cell on the equator. However, Wang (1995) finds that the density stratification in these models is much too low, and that the cells disappear if a more realistic stratification is introduced.

On the other hand, Semtner and Chervin (1992) also obtained reversing jets in the equatorial Pacific, in a global model where deep temperature and salinity – and therefore stratification – was restored to observed values. A distinctive feature of their run was the use of the Pacanowski–Philander (Pacanowski and Philander, 1981)

Richardson-number-dependent parameterization of vertical eddy diffusivity and viscosity; they remark that ‘this parameterisation may give rise to enough physically-based vertical mixing for equatorial upwelling to be favored over more uniform upwelling’. Dengler and Quadfasel (2001) provide clear evidence of layers with low Richardson number between reversing jets in the Indian Ocean (see below).

Equatorial Intermediate Currents

The four Intermediate Currents seen in Fig. 4.3.3a near 800 m (SEIC, SICC, LEIC, NICC; see caption to Fig. 4.3.3a) appear to extend from 165°E to at least 135°W (Firing *et al.*, 1998). There is no obvious evidence of change in latitude at least from 165°E to 159°W, suggesting that they may basically be passive inertial jets. They occur at the depth at which Antarctic Intermediate Water crosses the equator, in the New Guinea Coastal Undercurrent (Tsuchiya, 1991), and their existence may be dynamically linked to the need for that water to reverse the sign of its vorticity; but the details have so far not been explained. The westward-flowing EIC (Delcroix and Henin, 1988) near 1.5°N, 400 m in Fig. 4.3.3a has also received little study so far. At 165°E the EIC lies directly on the equator, with quite strong vertical shears between it and the EUC above it (Fig. 4.3.3b), at the level of the SCCs (see next subsection). Low Richardson numbers have been observed in this region, suggesting that internal mixing may occur here (Toole *et al.*, 1987). Wijffels (1993) ascribes an eastern tropical Pacific origin to EIC water. Bingham and Lukas (1995) name this water mass ‘South Pacific Tropical Intermediate Water’, and note that a similar but slightly different water mass (‘North Pacific Tropical Intermediate Water’) lies just north of the eastward-flowing NECC. Both water masses have oxygen minima; Bingham and Lukas suggest they may be trapped in unventilated ‘shadow zones’ (Luyten *et al.*, 1983).

Subsurface Countercurrents – ‘Tsuchiya Jets’

These features – the off-equatorial lobes of the dumbbell-shaped region of eastward flow in Fig. 4.3.3b, near 250 m – have been extensively studied recently (Johnson and Moore, 1997; Rowe *et al.*, 2000), following on from work by Tsuchiya (1972, 1975, 1981), Tsuchiya *et al.* (1989) and McPhaden (1984). Johnson and Moore obtained

temperature, salinity and pressure averages on neutral density surfaces from CTD data available in 1997, and objectively analysed the result to form a sharper picture of the SCCs than had been obtained earlier. Confirming the earlier work, they found two jets that proceed from west to east with rather constant transport (8.5 ± 1.5 Sv for the NSCC; 5.5 ± 1.5 Sv for the SICC). Peak velocities shoaled and diverged from 240–250 m ($\pm 2.5^\circ$) at 165°E to 130–160 m ($\pm 5^\circ$) at 110°W. The northern jet was slightly shallower than the southern. The jets become ‘thicker’ with distance downstream. The transport-weighted neutral density of the SCCs also decreases from west to east. Both SCCs are marked by minima in buoyancy frequency, N^2 . The NSCC marks a strong salinity front (fresher water to the north), apparently marking the northern limit of South Pacific water carried north along the Australian and Papua New Guinea coast and across the equator at this density level. A weaker core of high salinity marks the SICC (see also Johnson and McPhaden, 1999). Tsuchiya (1981) found a southern hemisphere origin for the SICC, while Bingham and Lukas (1995) found that water from both hemispheres contribute to the NSCC.

Johnson and McPhaden (1999) show maps of depth, acceleration potential, salinity and planetary potential vorticity on the 26.5 neutral surface, which cuts through the SCCs. The SICC proceeds directly to the South American coast near 10°S, confirming Lukas’ (1986) conclusion that the SICC and EUC turn south to feed the Peru–Chile Undercurrent and Countercurrent. The NSCC fades out just before reaching central America, apparently entrained into the northernmost edge of the North Equatorial Current. It is likely to be strongly freshened in the process, and to enter the southernmost edge of the North Equatorial Current. It is thus a candidate to supply upper level water in the Indonesian Throughflow (Godfrey *et al.*, 1993; Lu *et al.*, 1998). The SCCs form the poleward boundaries of a broad equatorial region of low planetary potential vorticity.

Johnson and Moore (1997) idealized the SCCs with an inertial model, in which the jets were bounded above by a neutral surface that sloped uniformly from east to west (the base of the thermocline). They were bounded below by a surface that was flat on either side of each jet, but with a greater depth equatorward of each jet than poleward.

Geostrophy thus leads to eastward flow in the narrow sloping region between the two flat parts of the lower surface, relative to the denser, stagnant fluid beneath. Flow between the two surfaces is zero wherever the lower surface is flat, so the two sides of the sloping region are streamlines. With this geometry, the observed near-constant mass transport and increasing downstream thickness of the currents with distance east is automatically satisfied. Using conservation of vorticity and Bernoulli function, they solved for the latitude, width and flow distribution in the jet. For realistic inflow conditions, the poleward movement is well simulated, with peak jet velocity increasing 50% downstream. Rowe *et al.* (2000) explore the SCCs further, showing that in individual sections they form sharp (20 km wide) poleward boundaries of a pool of constant vorticity water. Net flow within this pool is westward, not eastward, due to strong westward transports near the equator. Horizontal convergence/divergence of these flows implies that strong diapycnal processes are involved within the constant vorticity pool. Kitamura and Sugino (1987), following McPhaden (1984), obtained SCC-like features in their model, though they were a factor of 10 too weak; their results were well captured by a linear analytic model. Ishida *et al.* (1998) obtained more realistic SCCs in an Ocean General Circulation Model (OGCM). The fine vertical resolution (55 levels) and horizontal resolution (1/4°) extending to high latitudes are considered important elements of the simulation, since SCCs are believed to mark sharp fronts that extend to quite high latitudes along eastern boundaries (P. Lu, personal communication).

The flow paths of the SCCs may also be of importance for understanding the heat budget of the upper equatorial Pacific, because of the possibility that the SCCs supply much of the Indonesian Throughflow (e.g. Wijffels, 1993; Lu *et al.*, 1998).

Rossby wave beams and the annual cycle of temperature below the thermocline

Before leaving the topic of subthermocline zonal flows along the equator, it may also be noted that McCreary (1984) combined all vertical modes with the same meridional wavenumber to form equatorial ‘beams’, which he showed were capable of carrying wind-forced energy downward to the bottom. Rothstein *et al.* (1988a) found that if realistic mean currents are included, this process is

inhibited for Kelvin waves by critical-layer absorption. On the other hand, Lukas and Firing (1985) and Kessler and McCreary (1993) report observations of annual-frequency temperatures below the thermocline that match McCreary’s (1984) model for the Rossby wave beam. Davis (1998b) finds the bulk of variability in zonal velocity at 900 m as measured by floats is accounted for by annual variability of spatial modes predicted by a model.

Evidently, the nine cross-equatorial sections undertaken as part of WOCE (e.g. Kawabe and Taira, 1998; Kaneko *et al.*, 1998; Roden, 1998; Tsuchiya and Talley, 1998; Wijffels *et al.*, 1998) will provide a powerful resource for gaining further understanding of the deep equatorial Pacific. However, it should be noted that the problem of interpreting and comparing synoptic sections is particularly difficult below the thermocline, because the TOGA array provides no guidance to non-seasonal variability at these depths.

4.3.3 Equatorial Atlantic

4.3.3.1 Introduction

In the tropical Atlantic Ocean there has been a strong interest in investigating the subsurface circulation during WOCE. Most of the observational work there in this period consisted of deep hydrographic and current sections, western boundary and equatorial mooring arrays, and subsurface floats. The seasonal response of the near-surface equatorial Atlantic Ocean was studied earlier, to a large extent during the FOCAL/SEQUAL experiment in 1983–84, which indicated the extent to which the near-surface variability in temperature and currents is forced by the seasonal variability of the wind stress. This data set presented a nice example of interannual variability, suggesting coupling mechanisms between the near-equatorial ocean and the atmosphere, reminiscent of El Niño (Philander, 1986; Delecluse *et al.*, 1994), which were investigated further by Zebiak and Cane (1987), Zebiak (1993) and Servain (1991). Renewed interest in air-sea coupling mechanisms in the equatorial Atlantic have originated from the analysis of long time series of surface parameters (in particular, SST and winds) and from modelling experiments. This has led to the identification of extra-equatorial modes of variability with a very low frequency (decadal) (Servain, 1991), and possible air-sea mechanisms with a mostly

thermodynamic feedback (Carton *et al.*, 1996a; Chang *et al.*, 1997). However, the investigation of the modes of variability associated with air-sea coupling in the equatorial Atlantic has not been sought after experimentally until recently. It is only in the last couple of years, and in particular with the PIRATA (PIlot Research Array in the Tropical Atlantic) array of upper ocean and meteorological moorings (Servain *et al.*, 1998) and other recent programmes that new experimental investigation is been carried out.

Comparisons of Pacific and Atlantic Equatorial Undercurrents were made in the previous section. The section on the tropical Atlantic will therefore be focused on what we learnt during the WOCE decade about the circulation and its variability, and about the associated heat and fresh water transports, based on repeated hydrographic sections, mooring arrays and floats. Forward modelling efforts that are most relevant are the ones at high resolution, which incorporate the average large-scale thermohaline circulation. A large part of the investigation up to now has focused on the western boundary and subsurface equatorial circulations, in order to understand how these circulations are linked and how they participate in the large-scale meridional thermohaline cells.

At the beginning of WOCE, the tropical Atlantic circulation was well known only near the surface and away from the western boundary. The upper thermocline circulation had been outlined; the presence of rings shed by the North Brazil Current retroflection had been identified, while deeper currents could only be sketched very roughly. The pathways of southern water to the subtropical Northern Hemisphere, evidenced from water mass analysis, were not clearly known. However, it was already estimated that 13 Sv of the transport of the Florida Current originated from the Southern Hemisphere, primarily in the warm surface layer and below the thermocline (Schmitz and Richardson, 1991). The ocean circulation was known to carry heat northward and fresh water southward (Roemmich, 1983; from the inversion of 8°N and 8°S hydrographic sections). This was also known to involve the thermohaline circulation with a net flow to the north in the upper 1000 m (surface, thermocline and Antarctic Intermediate Water) and near the ocean bottom (AntArctic Bottom Water, AABW). A compensating southward flow occurred in-between with waters of different

northern Atlantic origins labelled 'upper, middle and lower North Atlantic Deep Water', (uNADW, mNADW and lNADW). There was some suggestion, based on transient tracer observations in the uNADW, that the southward path of the North Atlantic water across the equatorial ocean might not be a direct one. These data revealed a tongue of higher CFC (chlorofluorocarbon) concentration in 1982 along the equator in the western equatorial Atlantic Ocean (Weiss *et al.*, 1985).

One main way in which our knowledge of the subsurface circulation and of its variability has been acquired since the mid-1980s has been through repeat hydrographic sections, particularly in the western Atlantic Ocean, both across the equator and near the western boundary. In addition, a few mooring arrays have been implemented. These have been supported by float observations, mostly near 1000 m depth, and by transient tracer observations, which have been the most instrumental for understanding the deeper circulation. High-resolution modelling efforts have contributed to the investigation of the circulation in the upper ocean and its variability. The WOCE effort has led to more precise estimates of water mass transformation, heat and freshwater transport. However, there is still considerable uncertainty, and the synthesis of these different sets of observations is far from being accomplished. Many papers describing the state of the analysis were published in *Deep-Sea Research* 46, numbers 1–2 (1999), or in *Journal of Geophysical Research* 104, number C9 (1999).

4.3.3.2 Equatorial circulation in the upper 1000 m

Meridional repeat sections have been carried out along 35°W, which can be combined to provide an average picture of the equatorial circulation and some idea of its seasonal variability (Stramma and Schott, 1996; Schott *et al.*, 1998; Bourles *et al.*, 1999b). The average circulation bears some similarities with the Pacific Ocean. An Equatorial UnderCurrent (EUC) (Fig. 4.3.5) in the equatorial thermocline (core near isopycnal 24.5) is surrounded by westward currents. This is the SEC. A seasonal surface trapped North Equatorial Countercurrent occurs north of 5°N (Fig. 4.3.6). At the equator, the EUC usually overlies a westward EIC bounded by eastward currents at 4°N (NEUC) and 3–4°S (SEUC). These have their largest velocities

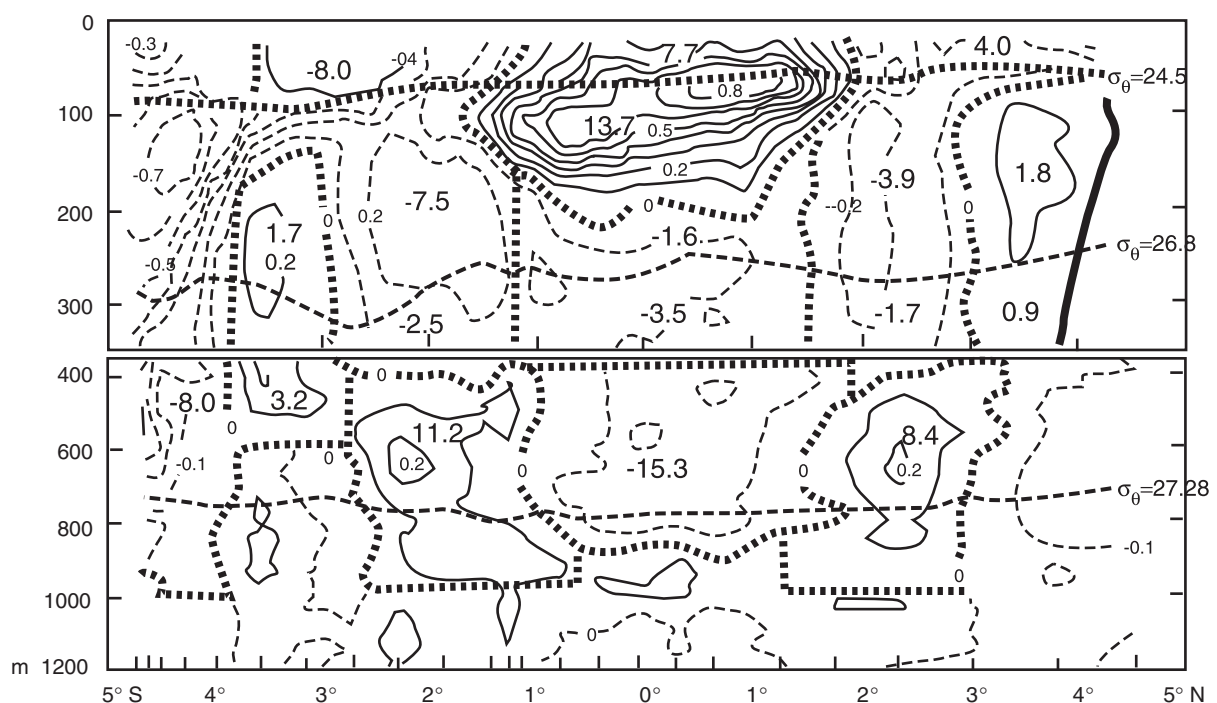


Fig. 4.3.5 Meridional section of zonal current along 35°W in March 1994 (from Schott *et al.*, 1995). Contours give velocity in m s^{-1} , positive (thin solid lines) eastward, negative (dashed lines) westward. Transport in Sverdrups of current branches are indicated in plots (large bold numbers; $1 \text{ Sv} = 10^6 \text{ m}^3 \text{ s}^{-1}$); boundaries are marked by heavy dotted lines. Heavy dashed lines indicate isopycnal surfaces.

near the isopycnal surface 26.8. The vertical and lateral domain of the EIC is quite variable, especially on seasonal time scales. The separation between the eastward NEUC or SEUC with the NECC or EUC, respectively, is not always distinguishable.

The 35°W section is located quite far west in the Atlantic, so that it is difficult to ignore direct influence of the western boundary currents, in particular south of the equator (along 35°W, the shelf break off Brazil is located near 4.5°S). For instance, in March 1994, two sections at 30°W and 35°W provide quite different estimates of the transport of the SEUC (3.7 and 1.7 Sv, according to Bourles *et al.*, 1999b and Schott *et al.*, 1995, respectively). The current is also centred at different latitudes. However, the above-named currents are known to exist at other longitudes (Arhan *et al.*, 1998).

The North and South Atlantic EUCs and the Pacific NSCC and SSCCs, or ‘Tsuchiya Jets’, have different nomenclature but seem likely to be dynamically similar. The current structure below these is more variable than in the Pacific, with suggestion of eastward currents near 2–3°S (South Intermediate Countercurrent) and 2–3°N (North

Intermediate Countercurrent) in the AntArctic Intermediate Water (AAIW) layer near the $\sigma_\theta = 27.28$ surface.

Detailed investigation of water mass characteristics indicate that the EUC and the SEUC derive their properties from the southern hemisphere via the North Brazil UnderCurrent (NBUC). The NEUC also derives the bulk of its properties from the southern hemisphere, but with a contribution from the northern hemisphere that might be seasonally dependent (larger in the northern spring: Schott *et al.*, 1995, 1998; Arhan *et al.*, 1998; Bourles *et al.*, 1999a,b). The EIC carries low-oxygen water to the western boundary, whereas the eastward currents in the AAIW layer (centred near 800 m) often carry oxygen-rich fresh water eastward (Schott *et al.*, 1995). Below the surface layer, there is relatively little evidence of seasonal variability of these currents, although XBT sections suggested a seasonal cycle in the subsurface geostrophic shear (Reverdin *et al.*, 1991; Molinari and Johns, 1994). These sections confirm the earlier understanding of the seasonal cycle in the surface layer, which is most pronounced in the NECC. Transport is largest in the boreal autumn,

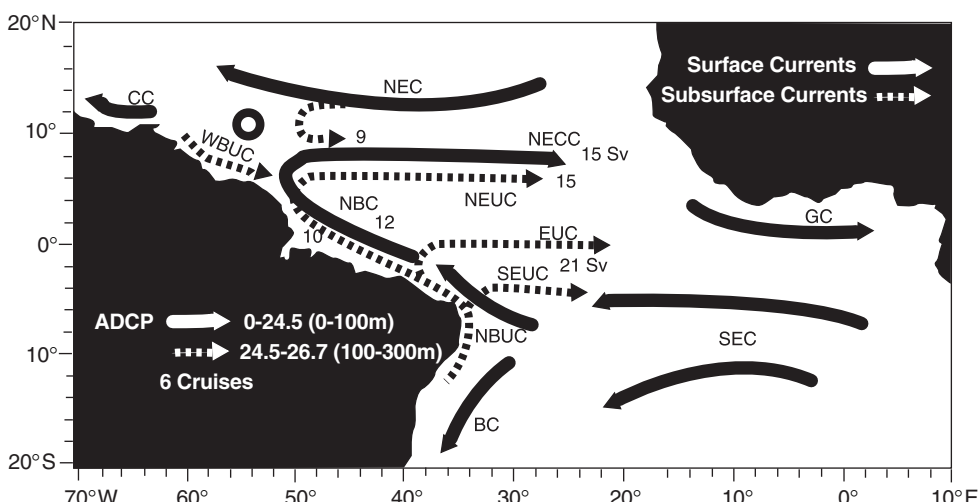


Fig. 4.3.6 Schematic of the near-surface and thermocline currents with indications of some of the transports (from Bourles *et al.*, 1999a). EUC, Equatorial UnderCurrent; SEUC and NEUC, South and North Equatorial UnderCurrents; NBUC, North Brazil Undercurrent; BC, Brazil Undercurrent; SEC, South Equatorial Current; NECC, North Equatorial CounterCurrent; NEC, North Equatorial Current; GC, Guinea Current; CC, Caribbean Current; WBUC, Western Boundary Undercurrent.

and smallest in boreal spring. (Notice, however, the presence of eastward currents during the March 1993 CITHER cruise at 7.5°N, but at a latitude further north than usual for the NECC; Arhan *et al.*, 1998; Arnault *et al.*, 1999; Bourles *et al.*, 1999b.)

Upper ocean circulation near South America

The strongest meridional transports in the tropical Atlantic occur near South America (Fig. 4.3.6). The system of boundary currents and its connection with the ocean interior, in particular near the equator, has been the subject of a particularly large effort. Recent investigations (da Silveira *et al.*, 1994; Stramma *et al.*, 1995) have suggested the permanence of the northward-flowing North Brazil UnderCurrent (NBUC) in the thermocline and below. It is already present at 10°S and continues across 5°S to the vicinity of the equator, shedding water to the SEUC along its path. The current is typically 100 km wide, trapped close to the shelf break with largest velocity in the thermocline in a core of very salty water originating from the south Atlantic subtropical gyre. There is often evidence of an offshore recirculation (Schott *et al.*, 1995, 1998).

North of 5°S, the NBUC is capped with the surface-intensified North Brazil Current (NBC), carrying water from both the South Atlantic subtropical gyre and water recently upwelled along the equator

(Schott *et al.*, 1993a). A series of mooring measurements across this current near the equator, combined with data from three sections, show a mean transport of some 23 Sv. This flow exhibits surprisingly little seasonal variability, either in the upper thermocline layer or below to 1000 m (Schott *et al.*, 1998). Other sections along 44°W in 1989–91 also suggest that the seasonal cycle is weak. This contrasts strongly with the large variability of the transport across a mooring array at 4–5°N, which presents a minimum transport of 13 Sv in April–May and a maximum of 36 Sv in July–August (Johns *et al.*, 1998). The latter result, however, is consistent with the seasonal displacement of the separation point moves equatorward until May, and then moves poleward as the NBC separates from the coast at a higher latitude to form the NECC. In April–May, the NBC often feeds a surface eastward equatorial current already observed in 1984 (Weisberg *et al.*, 1987). However, the details as to how the NBC feeds the different equatorial currents, either in the thermocline or below, are still largely not understood. The same applies to the question of how water masses and potential vorticity get modified in this process (see Schott *et al.*, 1998; Bourles *et al.*, 1999a,b for a description of these transformations).

Whether there is some direct transport of southern water along the western boundary to the

Caribbean Sea is still the subject of some debate. Schmitz and Richardson (1991) estimated, based on earlier data, that on the order of 13 Sv of southern hemisphere water was entrained into the northern subtropical gyre above 1000 m. At least half this transport can be traced through the passages of the lesser Antilles (Wilson and Johns, 1997). Sections off French Guiana (Bourlès *et al.*, 1999a,b) indicate that in the boreal spring, part of the NBC near the surface, and even in the subthermocline, continues along the continental slope. The presence of a northwestward flow was also found near 10°N in March 1996 (Schott *et al.*, 1998), but it is arguable whether this water is really of equatorial origin. The seasonal poleward continuation of the NBC along the slope has been a feature consistently present in numerical simulations of the equatorial Atlantic (Philander and Pacanowski, 1986; Schott and Böning, 1991; Böning and Schott, 1993), although probably to a larger extent than observed. There is also a flow present most of the year on the Guiana shelf going toward the northwest and carrying 3–5 Sv (Johns *et al.*, 1998; Bourlès *et al.*, personal communication). There are other means of transporting southern water to the north: by retroflection eddies spun off by the NBC in October–April, and through the interior circulation (in particular, via the NECC and around the dome of Guinea: Siedler *et al.*, 1992; Arhan *et al.*, 1998). There is also some indication of poleward flow along Africa from the thermocline down to the AAIW layer (Fratantoni and Richardson, 1999; Stramma and Schott, 1999). However, the relative importance of these different pathways is not yet known, nor understood.

The previous discussion has focused on the northward flow of southern water, the direction required to supply the Atlantic conveyor belt circulation. An interesting question is to what degree northern water penetrates into the equatorial area. Based on the water mass characteristics, this is not a dominant effect. However, there is indication of a penetration of northern water towards the equator in the thermocline. During boreal spring, some surveys identified a remnant of the NECC west of 40°W, which is directly fed by thermocline water of northern Atlantic origin (Bourlès *et al.*, 1999b). There is clearly a recirculation of part of the North Equatorial Current towards the NECC in all seasons. In the thermocline and below, at 4°N

and further north, there is an indication of a subsurface equatorward flow (the Western Boundary Undercurrent; Fig. 4.3.6) along the continental slope, which is strongest in late boreal winter and spring (Johns *et al.*, 1990, 1998; Colin and Bourlès, 1994; Wilson *et al.*, 1994; Bourlès *et al.*, 1999a). Numerical experiments (Schott and Böning, 1991) suggested that this could contribute to the EUC, although the presence of this water has not yet been identified there. This return current could fit the circulation expected from Sverdrupian budgets (Mayer and Weisberg, 1993), but these budgets do not take into account the thermohaline component of the flow and are not expected to hold for the mean (although there is more evidence for the annual variability).

4.3.3.3 Circulation below 1000 m

Transient tracers (for example CFCs) illustrate the arrival to the equatorial area of recently formed waters, in particular in the upper North Atlantic Deep Water (uNADW near 1500–2000 m: Andrié *et al.*, 1998, 1999; Fig. 4.3.7). This shows a flow path near the western boundary, with a tongue of high concentration towards the east in the vicinity of the equator. The simultaneous current measurements have indicated that this is associated with particular current directions, both near the western boundary and along the equator (usually, towards the southern hemisphere and towards the east, respectively). In particular, along 35°W, flows associated with high CFCs are consistently eastward near 2–3°S in the uNADW (Fig. 4.3.8), and near 1.5°S in the lNADW. There are also occasional eastward zonal currents in the uNADW along the equator, but with large differences from cruise to cruise (Rhein *et al.*, 1995; Fischer and Schott, 1997). Similar to what is observed in the Pacific Ocean, all the current profiles within 1° of the equator indicate the presence of jets with a short vertical scale of 400–600 m, in particular between 1000 and 2500 m depth (Gouriou *et al.*, 1999). These jets are found to last many months and have a large zonal coherence. The flow north of the equator can also be quite variable, in particular away from the slope, as has been shown from two repeat sections off French Guiana separated by 45 days (Andrié *et al.*, 1999).

The deep water flow along the continental slope is steadier than is found in the interior. Moorings near 44°W indicate a current trapped to within

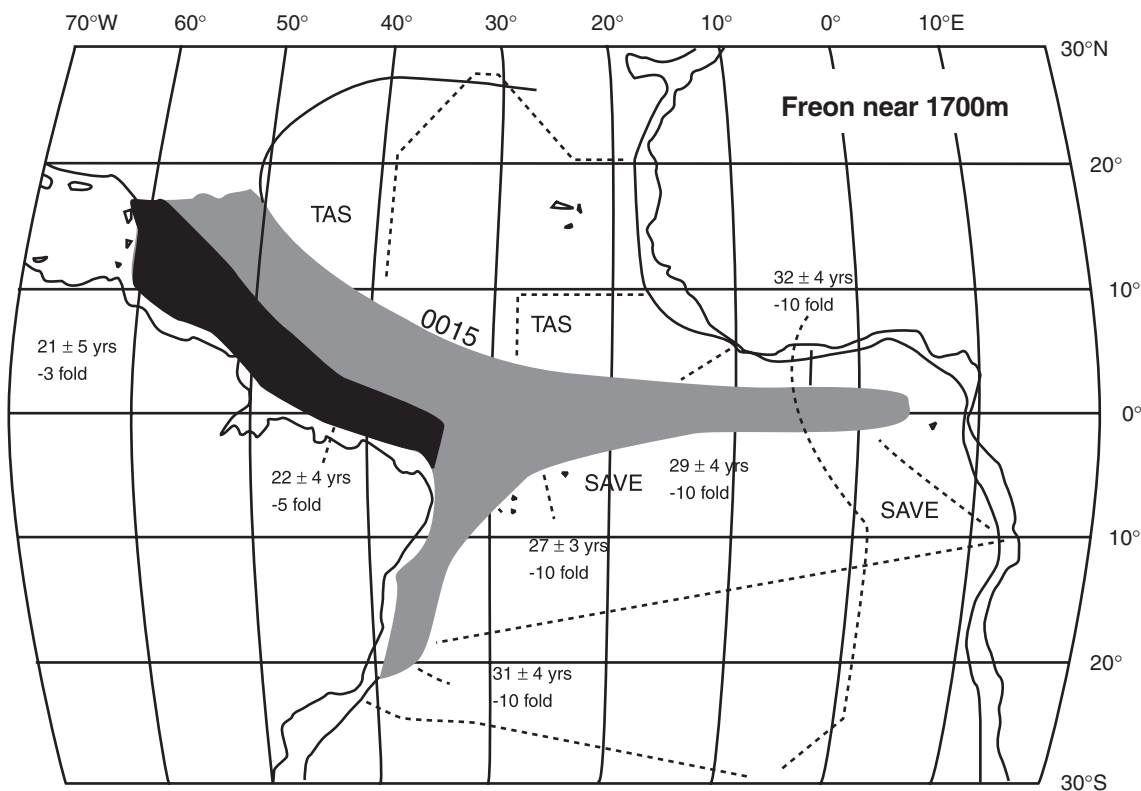


Fig. 4.3.7 Composite F-11 concentration near 1700 m based on measurements from the TAS (1983) and SAVE (1987–88) expeditions (age-corrected to 1988) (Ray Weiss, personal communication). Higher concentrations have darker shading.

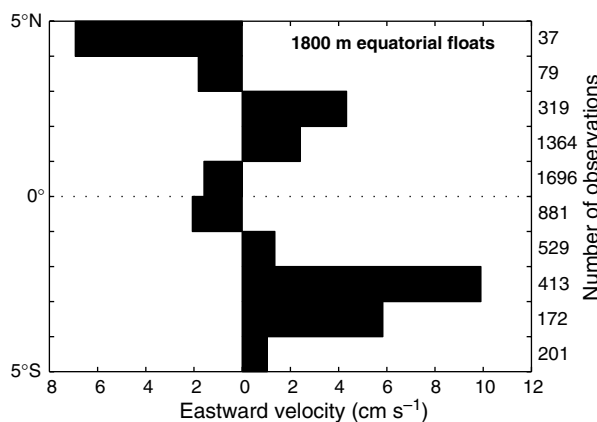


Fig. 4.3.8 Average zonal velocity at 1800 m along a 35°W section. Based on the composite of float velocities in 1989–92. From Richardson and Fratantoni (1999).

100 km of the slope with maximum velocity in the uNADW layer (the lNADW layer is not well sampled by this mooring array, and probably 5–6 Sv of this water reaches the equator east of this array). Circulation in the uNADW layer was also sampled by floats (Richardson and Schmitz, 1993;

Richardson and Fratantoni, 1999), their paths illustrating the link between the western boundary current and the equatorial circulation. How the interior equatorial flow connects with the western boundary current south of the equator is not yet clear, nor is the exact nature of the interaction with the topography. Sections along 5°S indicate a southward boundary transport on the order of 19 Sv, but somewhat off the continental slope, and not necessarily closely correlated to tracer extrema. These data have also illustrated the importance of offshore recirculation cells, some of which are probably permanent, so that the transport estimate of 19 Sv taking only southward currents into account should be viewed as an upper estimate of the southward transport in this layer.

The circulation of Antarctic bottom water in the equatorial Atlantic will be presented in another chapter, and we will not comment on it here.

The available direct current data in the deep equatorial Atlantic Ocean all suggest the presence of strong seasonal variability, both at annual and semiannual period (Fischer and Schott, 1997;

Hall *et al.*, 1997; Thierry, 2000). The mooring array at 44°W suggests that near the western boundary flow direction varies but remains parallel to the topography and that transports of the deep waters change by more than a factor of 2, whereas flow changes are mostly zonal further east along the equator. Along the equator, the phase is observed to increase from the bottom upward (Hall *et al.*, 1997; Thierry, 2000), which suggests the energy propagates downward. The large vertical-scale variability seems to be captured in high-resolution models of the tropical Atlantic (Schott and Böning, 1991; Fischer and Schott, 1997) and is reminiscent of the other tropical oceans. (The smaller scales associated with the equatorial jets are however not present in these models, even in more recent higher-resolution models; C. Böning and A.-M. Treguier, personal communications.) Evidence for a seasonal cycle at the equator near the western boundary is less pronounced in the upper layers of the ocean than at depth. This also occurs in the western equatorial Indian Ocean, where current meters (Schott *et al.*, 1989) show strong northward flow at depth in boreal summer. In the Atlantic, Fischer and Schott (1997) note that the observed annual cycle of mean deep transport is quite close to the Sverdrup estimate, in both amplitude and phase (though this does not hold for the observed large semiannual cycle). The upward phase propagation probably reflects Rossby wave activity.

Mooring arrays near the western boundary have also identified energetic higher-frequency variability in the upper ocean layers (Johns *et al.*, 1990; Colin *et al.*, 1994; Schott *et al.*, 1993a, 1998; Johns *et al.*, 1998). There is evidence of variability close to the surface at 20- to 30-day periods in the early boreal summer, similar in period to the equatorial instability waves found north of the equator that are initiated at the beginning of the upwelling season, when the meridional shear of the near-equatorial currents increases (Legeckis and Reverdin, 1987; Weisberg, 1984). During the second part of the year, large oscillations at periods of 40 to 60 days are present near the boundary and extend below the thermocline. North of 4°N, these oscillations are associated with the shedding of rings from the NBC retroflection. These rings drift to the northwest towards the Lesser Antilles, and can be identified and monitored using satellite altimetry (Didden and Schott, 1993) or ocean

colour (Johns *et al.*, 1990). They are responsible for a significant transport (up to 3 Sv) of southern water into the north Atlantic subtropical gyre (Fratantoni *et al.*, 1995). Only a few numerical models generate these eddies, for reasons that need to be examined in detail. Important variability associated often with meanders is also observed in the North Equatorial Countercurrent (Arnault *et al.*, 1999).

4.3.3.4 Meridional heat and freshwater transports

Meridional heat and freshwater transports have been investigated based on single hydrographic sections across the basin, usually several degrees away from the equator. This helps to minimize the error associated with the large variability near the equator, which is not properly sampled during the sections. The tropical Atlantic gains heat from the exchange with the atmosphere, and gains fresh water because of the presence of the ITCZ (Intra-Tropical Convergence Zone) and the outflow of rivers. The Amazon River in particular contributes 0.2 Sv. Peterson and Stramma (1991) and Speer *et al.* (1996) provide a review of earlier estimates of the meridional heat flux. MacDonald and Wunsch (1996) provide estimates at 11°S and 11°N (0.9 pW and 1.4 pW, respectively) based on single sections. Lux *et al.* (2001) also use inverse modelling to provide estimates based on a one-shot hydrographic survey 7.5°N–4.5°S (January–March 1993). Interestingly, their mass budget requires considerable conversion of intermediate and deep waters, in particular the transformation of AAIW into uNADW in the equatorial region. Analysis of high-resolution model simulations (A.-M. Treguier, personal communication) suggests that this does not result from seasonal variability of mass convergence not properly taken into account in the inverse model, although these issues remain to be thoroughly examined. The hydrographic sections also suggest that significant meridional transports occur in the eastern equatorial Atlantic, something that has been hitherto ignored in experimental analyses based mostly on measurements in the western boundary currents. At the time of the hydrographic survey, the Ekman transport contributes a significant share of the meridional heat transport at 7.5°N, illustrating how sensitive the heat and freshwater transport estimates will be to uncertainties in the wind stress and to its seasonal

and interannual variability. This was also clearly illustrated in numerical model simulations of the equatorial Atlantic seasonal cycle (Böning and Herrmann, 1994). The difficult next step will be to combine optimally the individual sections and other observations in order to separate properly the mean transports from their variability, at subseasonal, seasonal and interannual time scales.

4.3.4 Near-equatorial circulation in the Indian Ocean

4.3.4.1 Introduction

The tropical Indian Ocean has a wind system that is grossly different from those in the Atlantic and Pacific. Wind-driven upwelling, with its associate water mass conversion and cool SSTs, occurs mainly in the seasonally reversing western boundary currents rather than in the eastern equatorial region. Thus a completely different set of mechanisms control heat and freshwater absorption. The sparsity of Indian Ocean data also implies a need to use information that has been superseded by better products in the other two oceans. For these reasons the discussion here takes a somewhat different form.

The question of greatest interest for WOCE may be: how does the heat absorbed into the northern Indian Ocean (north, say, of 7°S, the southernmost latitude for which the Indian Ocean can be regarded as a closed basin) get advected southward? We now have plausible qualitative ideas on the three-dimensional pathways by which thermocline water enters across 7°S; moves (with much vacillation due to seasonal and intraseasonal variability) to upwelling sites; and is removed across 7°S, near the surface. The seasonally reversing winds play a very important role here (Fig. 4.3.9); to first approximation, their zonal component changes sign across the equator, in summer, winter and on annual mean. Consequently there is meridional Ekman transport with the same sign on both sides of the equator. It is southward on annual mean, which is believed to be a major driver of the heat absorption in the northern Indian Ocean. The small annual mean westerly component of wind along the equator (Fig. 4.3.9c) may maintain the observed annual mean pressure gradient along the equator, holding temperatures low in the western Indian Ocean as observed.

In this section we review our understanding of heat transport, water mass formation, surface heat flux and SST, in the tropical Indian Ocean. We first review the present understanding of the mean seasonal cycle of flow along and across the equator, in and above the thermocline and away from the western boundary; and also the open-ocean surface heat budget. Next we discuss the heat transport properties of the highly non-linear western boundary currents, consisting of the East African Coast Current and Somali Current (SC), plus the various recycling flows that occur a few hundred kilometres offshore; these are referred to below as the 'Somali Current System'. It is then possible to describe two mechanisms for cross-equatorial heat transport in the thermocline, which involve links between the western boundary and equatorial flows. Then we consider the relation of equatorial flows to higher-latitude flows, outside the western boundary current. Finally, we consider deeper flow patterns, including the Deep Reversing Jets found on the equator, and the deep western boundary currents; this raises questions regarding how heat penetrates through the thermocline.

4.3.4.2 Flow above the thermocline

Zonal flows along the equator

Early work by Wyrtki (1973b) showed that strong east-flowing semiannual 'Wyrtki Jets' (WJs) occur along the equator between each monsoon. They are driven by westerly winds at the monsoon transitions in the central equatorial Indian Ocean. They are associated with shoaling of the 20°C isotherm in the western Indian Ocean, and deepening in the eastern. Another striking feature of Indian Ocean zonal flows is the spasmodic occurrence of eastward undercurrents, beneath a westward surface current. Knox (1976) and McPhaden (1982a,b) showed, from weekly temperature and current data from Gan (0°41'S, 73°10'E), that at this location an undercurrent usually occurred towards the end of the winter monsoon in February–March, after a period of easterly equatorial winds. Zonal flow during the summer monsoon is relatively weak. Annual mean flow (Fig. 4.3.10c), like the annual mean wind stress, was eastward at all depths in 0–200 m at Gan, and was 0.3 m s⁻¹ at the surface. This result may be of particular significance for understanding Indian Ocean properties, since it suggests a well-defined steady pathway for

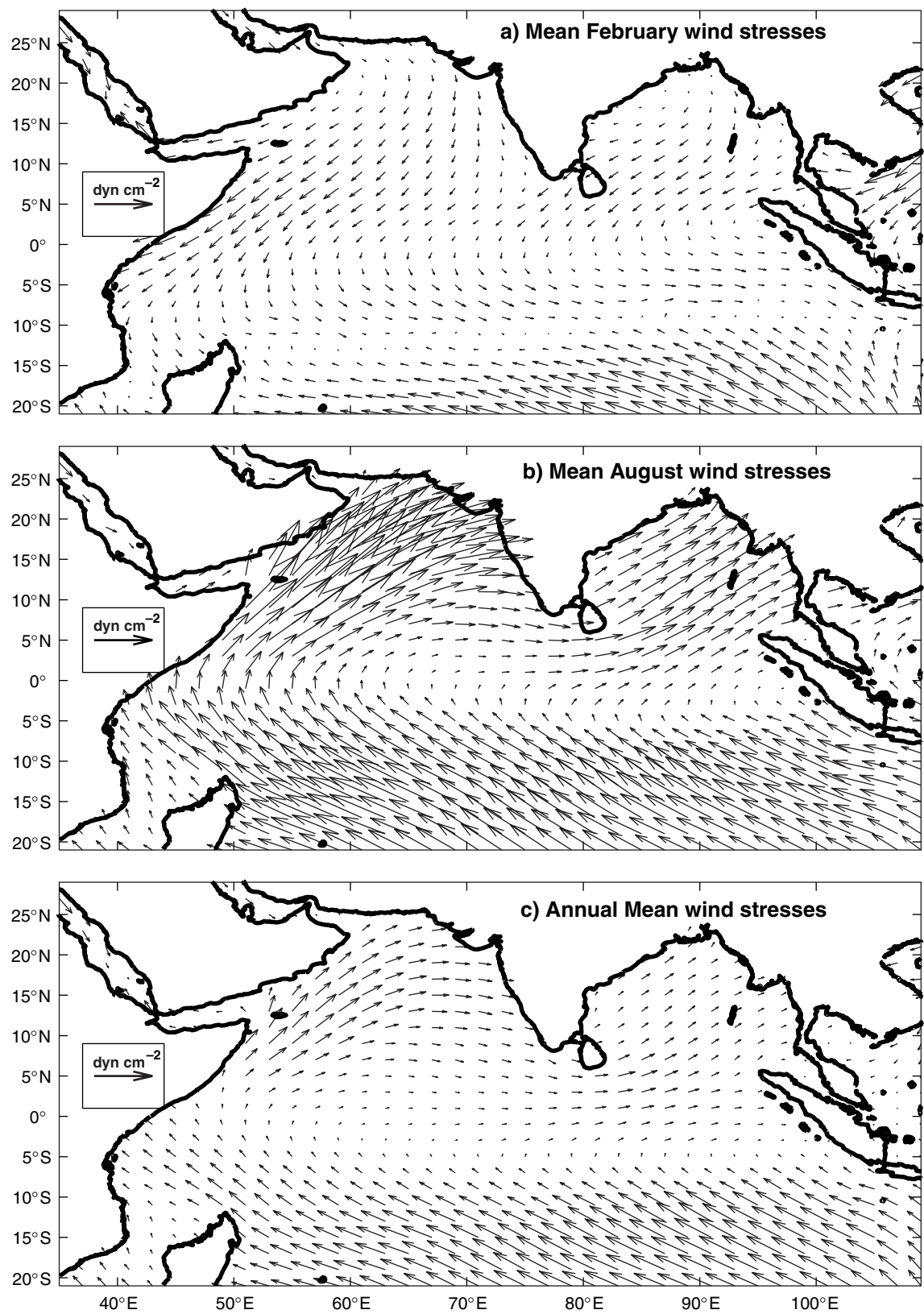


Fig. 4.3.9 Climatological wind stresses in dyn cm^{-2} in the tropical Indian Ocean: (a) February; (b) August; (c) annual mean. After Hellerman and Rosenstein (1983).

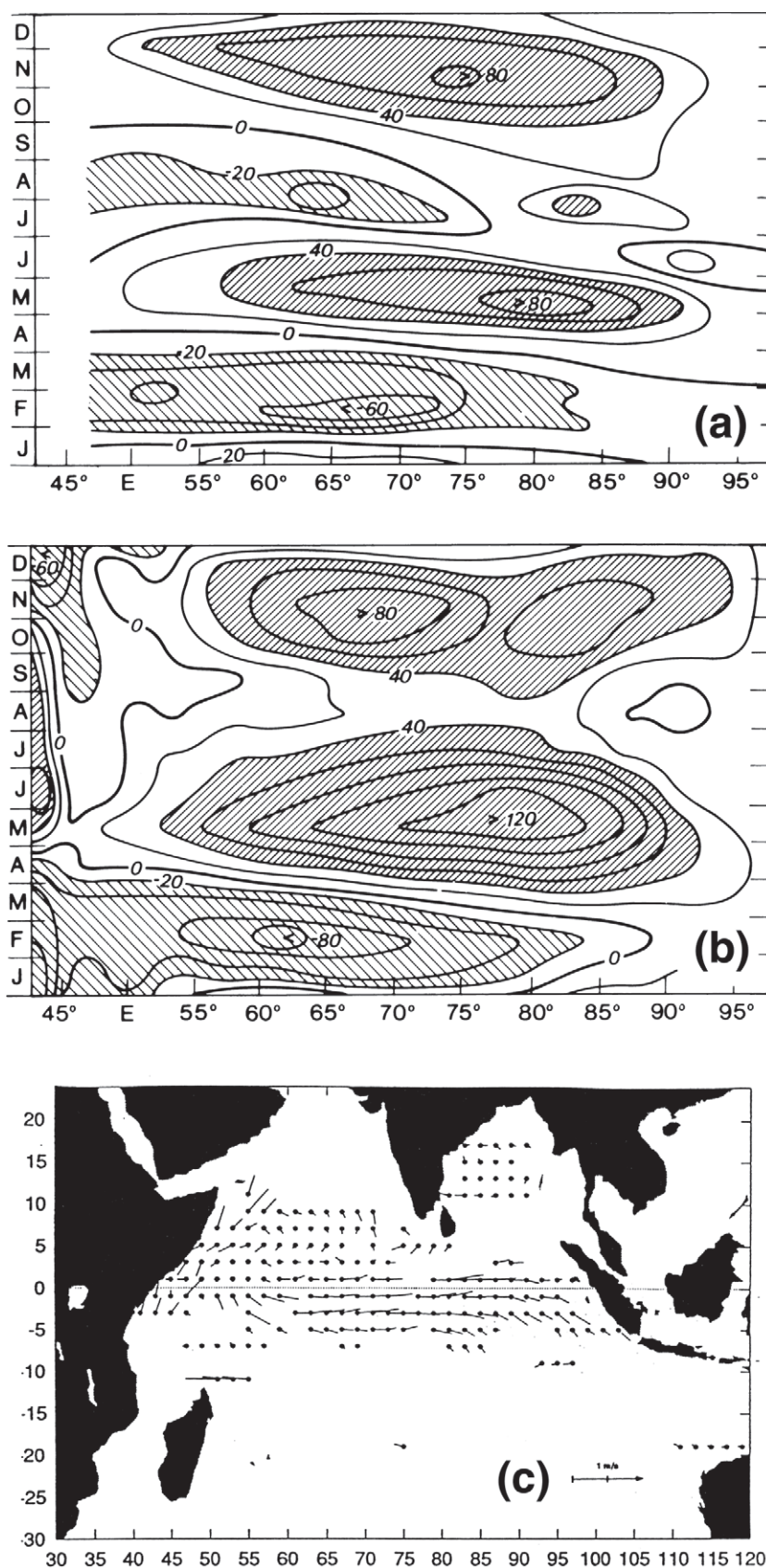


Fig. 4.3.10 (a) Annual cycle of surface zonal currents from ship drift between 1°S and 1°N in the Indian Ocean, from Reverdin (1987); (b) Surface zonal currents from the GFDL model examined by Visbeck and Schott (1992) (see text); (c) Annual mean surface flow from buoy drifts (from Molinari *et al.*, 1990a). Note that currents extend outward from the dots, so that (for example) currents along the equator are eastward.

salty west Indian Ocean water to exchange with fresh east Indian water.

Several climatologies of Indian Ocean currents and transports are available (Reverdin, 1987; Molinari *et al.*, 1990a; Rao *et al.*, 1989; Hastenrath and Greischar, 1991). The first two papers examined the equatorial region in detail. Reverdin (1987) used ship-drift observations in 1°S–1°N to generate a mean seasonal cycle of surface zonal flow along the equator (Fig. 4.3.10). The WJs are clearly visible. Molinari *et al.* (1990a) found that a climatology derived from satellite-tracked buoys was very comparable to the earlier ones from ship drifts, within the error limits of both. The WJs are moderately well represented in typical OGCMs, e.g. Fig. 4.3.10, from Visbeck and Schott (1992). One major source of discrepancy between models and observation seems to lie in uncertainties in equatorial winds, e.g. Anderson and Carrington (1993). Han *et al.* (1999) investigated the semi-annual WJs in some detail, in a numerical model; they found that wind forcing is the primary cause of the WJs. However, Rossby waves, resonance, and mixed-layer shears are all necessary to produce jets with realistic strength. Fresh water input in summer tends to make the fall WJ stronger but shallower than the spring WJ; however, dissipation around the Maldives slows the jets and tends to make them more equal.

Molinari *et al.* (1990a) compared annual mean currents from ship drift and buoys; Figure 4.3.10 shows the buoy version. Strong eastward equatorial currents are seen in most longitudes, except near the western boundary. This is one region where ship drift and buoy climatologies do not agree; marked convergence onto the equator is apparent in Fig. 4.3.10 in the western boundary, but it does not appear in the ship-drift climatology (not shown). This suggests that ships may not resolve an eddy-like feature centred on (0°, 50°E), which shows up frequently in individual buoy tracks. It is known as the ‘Southern Gyre’, and it may play a role in transporting heat and other properties eastwards and/or across the equator. However, the strong surface convergence evident in Fig. 4.3.10c at the equatorial western boundary suggests that there may be annual mean sinking here. This will be discussed further, in connection with the western boundary current system.

Compared with other oceans, data on subsurface Indian Ocean flows is very sparse. Reverdin

(1987) provided a qualitative indication of the EUC, by showing the equatorial ‘bulging’ of the layer between the mixed layer base and the 20°C isotherm depth, relative to 2.5°N, 2.5°S. He found that near 55°E the EUC is confined to the period January–June, and is strongest in March. It reaches the eastern boundary, but is weak west of 80°E. Donguy and Meyers (1995) examined XBT data from lines that crossed the equator; they found that subsurface temperature–salinity relations were sufficiently well defined for use in estimating transports along their lines. They estimated seasonal cycles of geostrophic transport relative to 400 db between 2.5°S and 0.5°S, and between 0.5°N and 2.5°N, along three lines that cross the equator near 55°E, 65°E and 80°E. These show major longitudinal differences in seasonal cycle. At 55°E, at the eastern end of the Southern Gyre, the seasonal cycle shows even larger differences between 2.5°S and 0.5°S and 0.5°N and 2.5°N.

Interannual variability of zonal currents is also a strong feature of the equatorial Indian Ocean. Reppin *et al.* (1999) examined data from six moorings along 80°30'E, between July 1993 and September 1994. Their Acoustic Doppler Current Profiler (ADCP) observations at the equator did not agree with earlier climatologies; the autumn 1993 WJ (35 Sv) was much stronger than the spring 1994 one (5 Sv). Similarly, the EUC was present in January to June 1994 as expected, but it reappeared strongly in August 1994. Reppin *et al.* related these results to strong interannual wind variations in 1994. They first compared historic ship-drift data with zonal winds and with the Southern Oscillation Index (SOI=Tahiti–Darwin pressure), showing that all three were quite strongly correlated on 6-month time scales. When they correlated their own 25-m currents with local winds and the SOI on monthly time scales, they found remarkably high correlations. The unusual features in summer 1994 were due to unseasonal winds at that time, resulting in upwelling and cool SST in the equatorial eastern Indian Ocean. However, Saji *et al.* (1999) and Webster *et al.* (1999) suggest an alternative explanation for the 1994 event, involving ENSO-like coupled air-sea interactions within the Indian Ocean, which they refer to as the ‘Indian Ocean Dipole’.

As noted earlier, the annual mean flow along the equator may contribute to zonal water exchange from the salty Arabian Sea to the fresh Bay of

Bengal. Reppin *et al.* (1999) show a cross-section of annual mean zonal velocity at 80°30'E. There is an eastward transport of about 6 Sv in the top 150 m, between 2°N and 2°S (assuming symmetry about the equator). Reppin *et al.* note that this average may not be representative, due to the unseasonal winds of 1994. McPhaden's (1982a) equatorial data at Gan imply an eastward transport of about 10 Sv in the top 200 m if they are typical of flows in 2°N–2°S. Donguy and Meyers (1995) also show an annual mean transport of about 15 Sv, between 2.5°N and 2.5°S. Thus, there is agreement on substantial mean eastward flow along the equator. McPhaden suggested that this mean flow may be partly due to non-linear effects, associated with Ekman convergence onto the equator carrying eastward momentum down, in the transition season (Cane, 1980; Philander and Pacanowski, 1980).

The WJs and related semiannual flows may be regarded as the near-surface manifestation of semiannual currents that extend to considerable depth. Luyten and Roemmich (1982) analysed current meter data at several equatorial moorings; their zonal currents at 700 m showed a narrow semiannual frequency band. They found upward phase propagation, indicative of downward group propagation, and suggested that the sharp dropoff of semiannual energy below 200 m (e.g. compared to semiannual currents at Gan, McPhaden, 1982a) is due to the fact that semiannual Kelvin waves only propagate this deep in a full crossing of the Indian Ocean. Similarly, annual period flow in both Kelvin and Rossby waves should only penetrate a few hundred metres before reflection, perhaps explaining the purity of the semiannual signal at 700 m. The velocities at that depth were primarily due to semiannual Rossby waves, as borne out by westward propagation of the semiannual signal. LR remarked that the Indian Ocean at semiannual frequency should behave like the Pacific does at annual frequency, in agreement with the later findings of Kessler and McCreary (1993).

Cross-equatorial currents

The meridional currents across the equator, away from the western boundary, are of particular interest since it is these that force oppositely directed deeper, colder flow through mass conservation, thereby transporting heat out of the Indian Ocean. The movement of surface water across the equator

in the ocean interior might at first sight be expected to take a long time to establish, because the establishment of Sverdrup balance usually takes months – the time required for Rossby waves to cross the ocean. However, a zonal wind stress $\tau^{(x)} = A(x, t)y$ that is linear in the distance y from the equator has a non-divergent meridional Ekman transport $A/\beta\rho$, with $f = \beta y$ the Coriolis parameter and ρ the water density. This Ekman transport is also identical to the Sverdrup transport, i.e. the vorticity added to the ocean through the curl of this particular wind is exactly what is needed to balance its Ekman transport, in its travel north or south. Thus, for this wind, Sverdrup cross-equatorial flow is established on the time scales of Ekman transports – i.e. only a few days or weeks. It is apparent from Fig. 4.3.9 that a wind of this form is a major contributor to the total wind stress, at least in summer and winter and on annual mean, in the near-equatorial Indian Ocean. On this argument, we would expect the Indian Ocean to respond quite quickly to seasonal variations in $A(x, t)$; this behaviour is indeed seen in numerical models.

$A(x, t)$ also varies strongly in association with Intraseasonal Oscillations (IO); as a result, cross-equatorial transport also varies on intraseasonal time scales. This may complicate analysis of WOCE sections within 15° of the equator, since the effect is seen (in one model) to dominate over seasonal or longer-term variability, as shown in Fig. 4.3.11 (from Loschnigg and Webster, 2000). Much of the heat transport on intraseasonal time scales may consist of a balance between Ekman transport and a compensating barotropic flow, with little consequence for the baroclinic flows that can be deduced from WOCE sections. Nevertheless, it may be of interest to check whether baroclinic flows do develop in deep western boundary currents on these short time scales, in models with realistic bottom topography and adequate vertical resolution.

Modelling studies often show a shallow meridional overturning cell on the equator, confined to the top 100 m or less. This model cell reverses sign with the monsoon, and is confined within about 1° of the equator. Because f is zero, the surface meridional wind $\tau^{(y)}$ drives a surface downwind flow (and subsurface mass-balancing counterflow). This surface flow is usually opposite in direction to the equatorial Ekman transport, which as shown

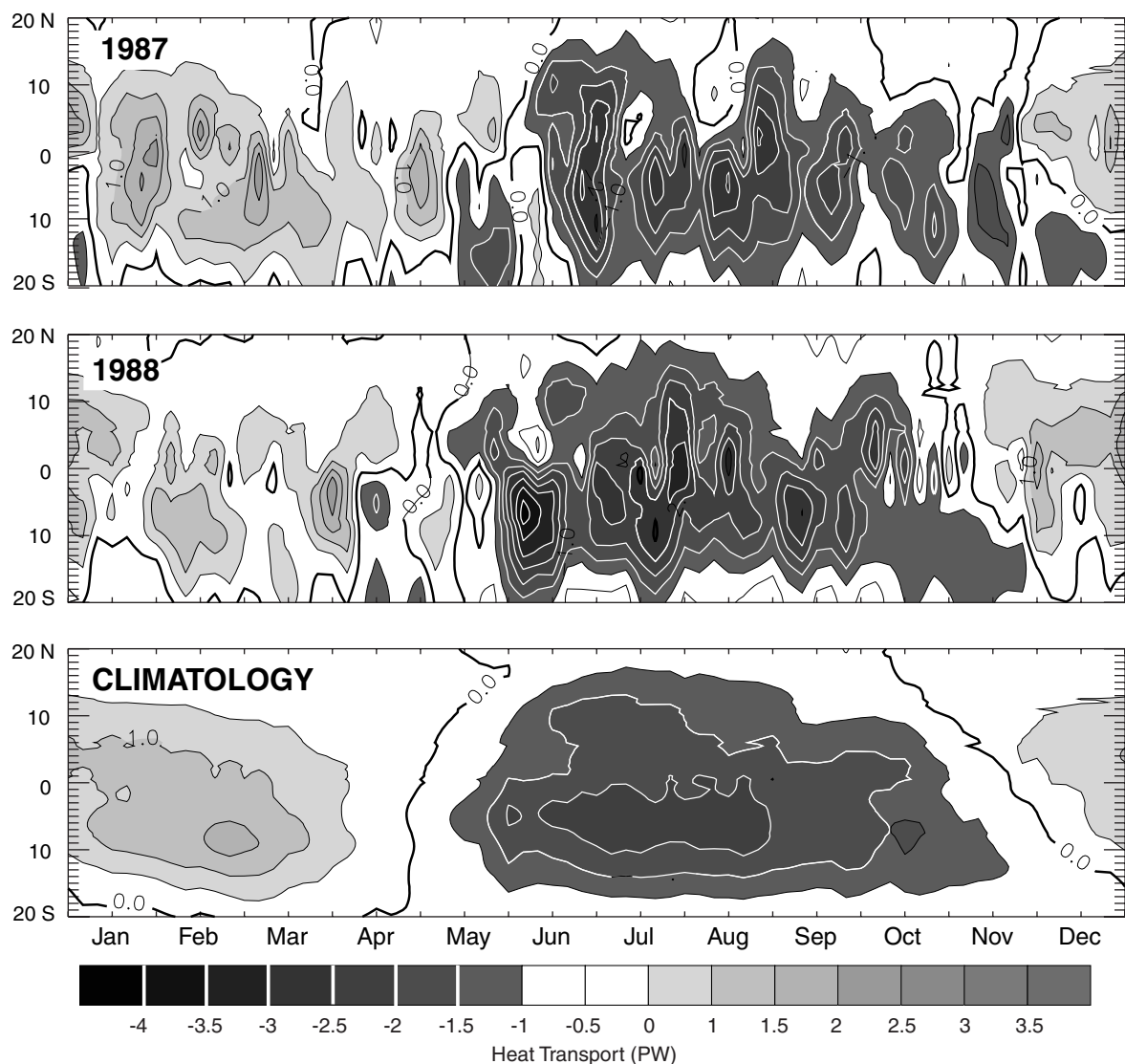


Fig. 4.3.11 Cross-equatorial heat transport in petawatts ($PW, 10^{15} W$) as a function of time and latitude, from an Indian Ocean model driven with daily wind stresses (Loschnigg and Webster, 2000).

earlier is $(\partial\tau^{(x)}/\partial y)/\beta p$. In the models, the Ekman transport augments the counterflow a few tens of metres below the surface downwind flow (Wacondgne and Pacanowski, 1996; Gartennicht and Schott, 1997). Some qualitative support for the idea that a Wacondgne–Pacanowski cell may exist in the real ocean comes from work of Hastenrath and Greischar (1989), who obtain divergences from the Cutler and Swallow (1984) ship-drift currents. They show surprisingly consistent patterns. In the transition seasons, there is equatorial divergence in the western Indian Ocean and convergence in the eastern, consistent with Wyrtki (1973b); but in June to September, there is convergence in $0\text{--}5^\circ\text{N}$, divergence in $0\text{--}5^\circ\text{S}$, more or less

uniformly across the Indian Ocean. The inverse of this pattern is seen in January–March. Thus the summer and winter surface divergence patterns are consistent with what one might expect, if the seasonal cycle of surface transport across the equator were zero, or the inverse of the higher-latitude Ekman flows. Hastenrath and Greischar find typical convergence magnitudes of $\pm 10^{-7} s^{-1}$, possibly suggesting that over the 3 months of summer or winter mixed-layer depths should roughly double (or halve) on either side of the equator. However, this is not observed. Alternatively, water may flow from the surface convergence to the divergence, just below the surface, consistent with the existence of a Wacondgne–Pacanowski cell. There is

also some support for a Wacongne–Pacanowski cell from an ADCP current meter record (Reppin *et al.*, 1999). These authors find no annual cycle in equatorial flow at the top of their record (25 m), but their Plate 1b appears to show a seasonal cycle of the correct sign just below 25 m, contaminated by substantial 16-day wave activity.

McPhaden (1982a) found almost no mean seasonal cycle in meridional flow in the Gan data. Annual mean meridional velocity had the right sign, but the magnitude was about four times too large to match the Sverdrup relation. Residual variability had a flat spectrum. These results may reflect a distortion of flow around Gan.

Equatorial surface heat budget

Adequate representation of the surface mixed-layer heat budget is crucial to representing SST variations. Despite the strong semiannual signal in equatorial currents, McPhaden (1982a) found that annual frequencies dominated the thermal structure at Gan. McPhaden (1982b) examined the surface heat budget with the Gan data, and found that a simple balance, basically equating rate of change of mixed-layer heat content to the anomaly of observed heat flux, worked surprisingly well in accounting for mixed-layer temperature changes. However, Molinari *et al.* (1986) compared surface heat fluxes with the rate of change of SST over much of the Indian Ocean, and found that such behaviour was rare. They found that net surface heat fluxes accounted for 80% or more of the observed changes in seasonal heat content of the mixed layer in only 11% of the ocean area north of the equator and west of 80°E. The comparable figure for 0–20°S was 36%. Rao and Sivakumar (1999) examined the mixed-layer heat budget for the Indian Ocean north of the equator and west of 80°E. They include horizontal advection by taking the scalar product of ship's drift current with SST gradient multiplied by the mixed-layer depth, and obtain entrainment velocity following McPhaden and Hayes (1991). Climatological salinity variations are also included. The result accounts quite well for SST change in December–May, when SST warms up to 30°C (a major factor in monsoon onset). Advective processes – and salinity effects – play important roles in most regions, though near Gan (73°E) advective terms are small, in agreement with McPhaden (1982b). Loschnigg and Webster (2000) also conclude that advection plays

an important role in SST development before monsoon onset.

Western boundary current flows

Mass balance requires that an equal and opposite subsurface flow must balance the net surface meridional Ekman flow out of the northern Indian Ocean. In order to dissipate its vorticity, this subsurface flow must cross the equator in the western boundary current. According to 2 years of current meter data, the northward annual mean thermocline flow across the equator in the western boundary current is about 10 Sv (Schott *et al.*, 1990; referred to below as SSF), which is close to the magnitude expected from this argument. It all occurs above 500 m, and has a transport-weighted mean temperature of 15.4°C. SSF note that if the compensating surface Ekman flow has a temperature of 28°C, it 'would result in a southward heat transport of -3.6×10^{14} W, which is not too far off the air-sea flux results'.

This direct, wind-driven process is an important one for carrying heat southward out of the Indian Ocean; but it may not be the only one. A special feature of the 'Somali Current System' (SCS) is that it reverses seasonally. This raises the possibility that 'eddy fluxes', on seasonal or other time scales, may also be important. SSF note that in winter (December–February) the equatorial western boundary currents themselves have almost zero cross-equatorial flow, but 5 Sv of southward flow in the top 100 m nearly compensates the 4 Sv of northward flow in 100–400 m. They find a southward heat flow of about 3×10^{14} W at this time, associated with this cell near the western boundary.

Does this observed wintertime cell near the western boundary contribute to the annual mean heat transport out of the Indian Ocean? It seems reasonable that it does. It will be argued below that, to first approximation, most of the thermocline water crosses the equator northeastwards in one winter, in the western boundary; is upwelled and warmed the following summer; and returns across the equator the next winter, at a higher, warmer level. (This level need not be the surface mixed layer.) In such a situation there will be a net southward flow of heat on annual mean, which is strictly internal to the reversing SCS and does not depend on the meridional Ekman transports.

Current meter records show that the southward winter flow across the equator does not penetrate

to 4°S, but must exit eastward. Indeed, as suggested by Fig. 4.3.10c, much of the annual mean eastward flow along the interior equatorial Indian Ocean appears to originate from the western boundary; the convergence in Fig. 4.3.10c occurs in autumn and winter. In winter, water approaching the equator from the Somali Current has an SST of 26–27°C, while SST elsewhere is more than 28°C; so some of the flow from the northeast may sink to join the eastward EUC. This may either happen directly, or by crossing the equator in the top 100 m of the western boundary current and joining the EUC shortly afterwards. If this hypothesis is correct, the details of the SCS will probably need to be accurately represented in models, in order to quantify the meridional and zonal transfers of heat in the tropical Indian Ocean. We will therefore describe the SCS in a little detail.

SSF developed the first schematic, observation-based picture of the mean seasonal flow pattern of the SCS. They first examined 2 years of current meter records at several equatorial moorings, plus earlier off-equatorial current meter records. These records are very different from one another. Equatorial longshore current profiles show much stronger vertical shears than those near 5°N and 4°S in both monsoons, and profiles for the winter

monsoon change sign between 4°S and 5°N, suggesting strong longshore convergence onto the equatorial region at this time (in agreement with Fig. 4.3.10c). Further, while surface currents reverse with the monsoon winds at the equator, the equatorial longshore flow is northward below about 100 m throughout the year, except in March–April.

Second, SSF combine available hydrographic data to display 3-monthly seasonal patterns of salinity at $\sigma_0=25$ (near a salinity maximum, 110 m on equator); of oxygen at $\sigma_0=26.6$ (an oxygen minimum, 250 m on equator); and at $\sigma_0=27.2$ (Red Sea salinity maximum, 680 m on equator). Figure 4.3.12 shows salinity on the 25.0 surface. Southern low-salinity water moves north along the boundary to about 5°N, in May–July, early in the summer monsoon. This proceeds in July–October to an intermingling of ‘southern’ water among ‘northern’, in the ‘Great Whirl’, a large eddy that develops in early summer and moves northward, covering 5–13°N before its decay in fall. At this time the $\sigma_0=25$ level breaks the surface in many near-coastal stations. This indicates that north-flowing water upwells more than 100 m in its passage from the equator to the Great Whirl. Relatively saline North Indian Water penetrates

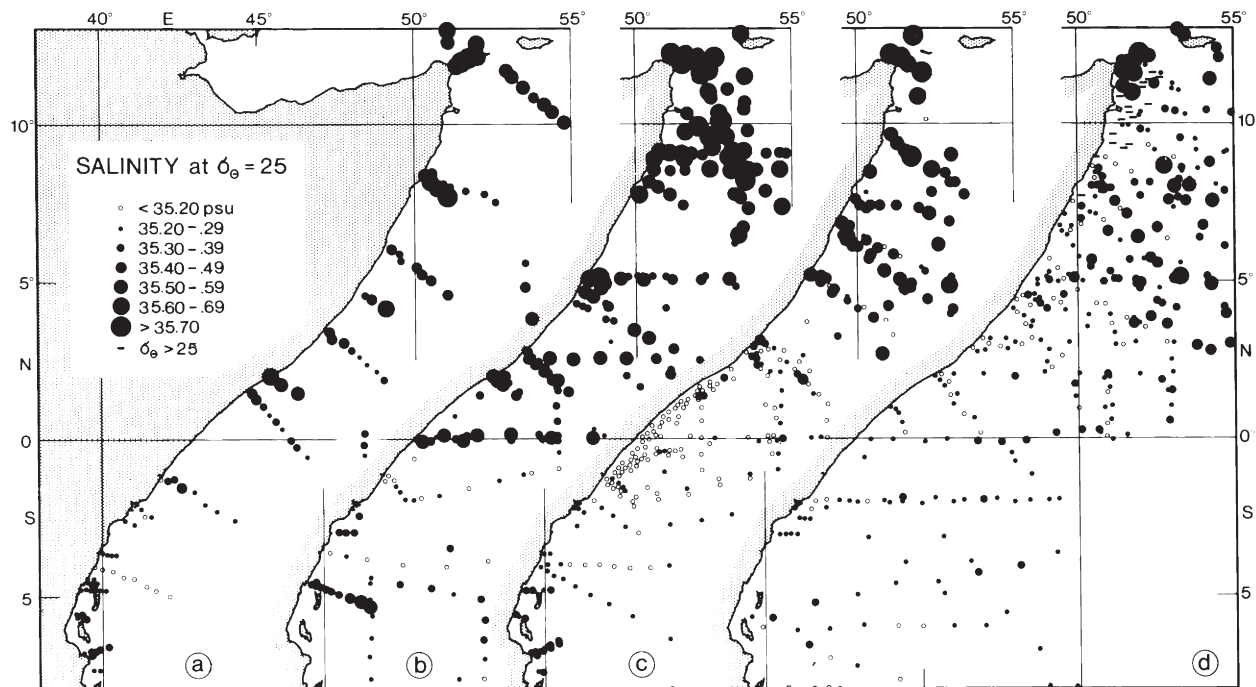


Fig. 4.3.12 Seasonal distribution of salinity on $\sigma_0=25$ (mean depth about 110 m on the equator) from historical data: (a) November–January; (b) February–April; (c) May–July; (d) August–October. From Schott *et al.* (1990).

southward again in November–January; some appears to get right across the equator in a narrow western boundary current. By February–April, saline water has penetrated southward to the equator at a wide range of longitudes. Oxygen at the middle level ($\sigma_0=26.6$; not shown) shows a similar seasonal pattern, with smaller amplitude, perhaps due to slower seasonally reversing currents at this depth; so also does the salinity at $\sigma_0=27.2$.

From these sources, and numerous previous observations (Swallow and Bruce, 1966; Warren *et al.*, 1966; Düing and Schott, 1978; Leetmaa *et al.*, 1982; Quadfasel and Schott, 1982, 1983;

Gonella *et al.*, 1983; Schott, 1983, 1986; Swallow *et al.*, 1983, 1991; Molinari *et al.*, 1990a) SSF devised the schematic shown in Fig. 4.3.13, which shows currents in the top 100 m (top panel) and in 100–400 m (bottom panel) at (generally) 2-month intervals through the year. The buoy data of Fig. 4.3.10c suggests a minor amendment to the schematic flow pattern of Fig. 4.3.13 (top): the strong winter convergence of longshore currents seen in Fig. 4.3.13 is probably in fact located closer to the equator.

We refer readers to SSF for a detailed month-by-month description of Fig. 4.3.12. However, it

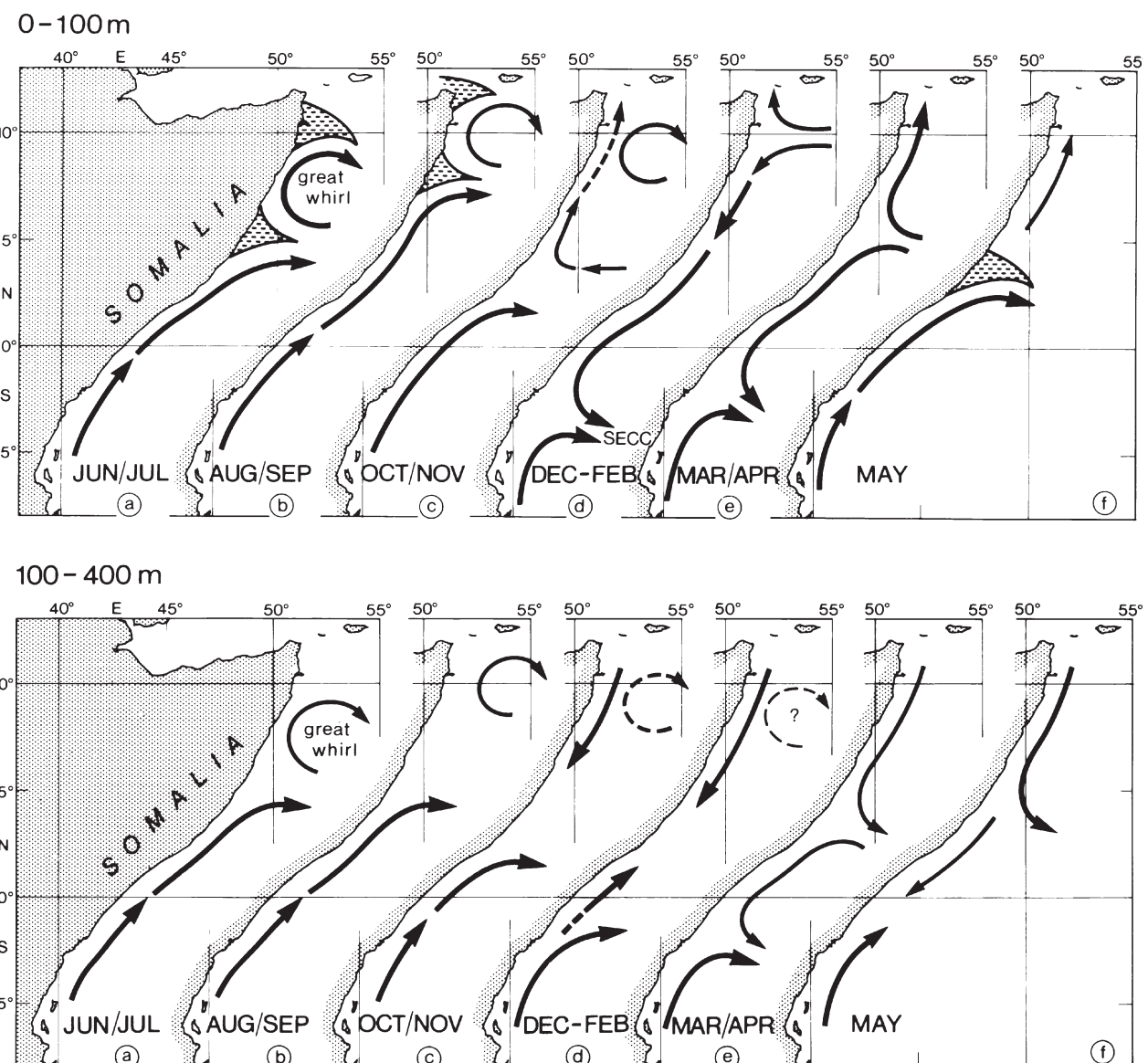


Fig. 4.3.13 Schematic representation of Somali Current circulation patterns for different seasons and for the top 100 m, and for 100–400 m. From Schott *et al.* (1990).

will be apparent that near the depth of about 100 m (Fig. 4.3.12), seasonally varying currents do seem to advect water masses northward nearly the full length from the equator to 10°N, and to mix them up in the Great Whirl. Winter advection similarly returns salty water to most of the region. Observed current magnitudes near 100 m also support this conclusion. In other words, annual flushing of the SCS is rather complete, at least in the top 100 m. It is therefore physically plausible that an ‘eddy flux’ heat transport mechanism like the one described above may contribute to heat removal from the northern Indian Ocean.

The equator-spanning Southern Gyre appears to mediate the transfer from the SCS to the equatorial flows. Schott *et al.* (1998) undertook hydrographic surveys in the offshore regions of the Somali Current in summer 1995. They showed that the Somali Current becomes disconnected from the interior Arabian Sea between 4°N and 12°N, both in currents and water masses. The Southern Gyre is clearly evident in their maps of near-surface currents. In the later map, salinity is actually higher south of the equator than north of it along 50°E, suggesting that the Southern Gyre is transporting water from the Somali Current across the equator, and then eastwards.

The qualitative picture just presented suggests that the most of the water formed in the top 100 m in summer in the SCS may escape via the south-flowing cross-equatorial western boundary current, and thence eastward via the Wyrtki Jet (in October–November) or by the EUC (in December–February). However, the quantitative details of this picture are important for assessing the contribution of SCS flushing to the net meridional heat flux out of the Indian Ocean – and to its interannual variability.

Models with only one active layer but high horizontal resolution are quite successful in simulating several features of Fig. 4.3.13; for example, Luther and O’Brien (1985, 1989) and Luther *et al.* (1985) obtained quite realistic simulations of the ‘Great Whirl’ and ‘Southern Gyre’ in their runs. A run with a fixed seasonal cycle of winds shows much less interannual variability than one with realistic, interannually varying winds. However, such models cannot resolve subtleties of the vertical circulation such as whether the SCS outflow joins the EUC. Visbeck and Schott (1992) addressed the issue of equatorial divergence, at least in the 150–800 m

depth range, by comparing available observations with the output of a Geophysical Fluid Dynamics Laboratory (GFDL) model run, driven by Hellerman and Rosenstein (1983) mean seasonal winds. This limited-area model had a zonal resolution of 0.5° in the western Indian Ocean, and a meridional resolution of 0.33° in the region of interest. Figure 4.3.10b shows the mean seasonal cycle of surface zonal currents along the equator from the model, in fair agreement with Reverdin’s (1987) climatology. A similar level of agreement is found between model and observation for vertical sections through the EUC at 55°E, due to Leetmaa and Stommel (1980). The model’s annual-frequency zonal currents along the equator have amplitudes and phases that are in reasonable accord with observations in the western boundary current and in the EUC. The model is somewhat less successful in simulating the Somali Current at the equator, but model longshore currents showed a large degree of asymmetry about the equator; longshore semiannual transport amplitude reached 5 Sv near 2°N, S.

Before leaving the topic of the western boundary current, we consider the seasonal relationship of the wind-driven overturning cell to water mass formation and SST change. Hsiung *et al.* (1989) used observed surface fluxes and heat content changes to estimate seasonal net northward cross-equatorial heat flux into the Indian. In winter, it is northward; but at this time, it may not contribute to water mass conversion. Instead the heat transport is probably balanced by adiabatic deepening of the thermocline (WP). Water mass conversion is probably primarily confined to summer – especially late summer, when the thermocline is shallowest. It is interesting also that in a typical summer intraseasonal event, SST falls by about 2°C off Somalia (Webster *et al.*, 2000), possibly due to upwelling induced by the strengthened Findlater Jet at this time. Thus the overturning cell may be linked to water mass conversion and SST change on sub-seasonal time scales; such SST changes may be of importance to our understanding of the Madden–Julian Oscillation (e.g. Madden and Julian, 1994) as a coupled ocean–atmosphere phenomenon.

Relation of equatorial flows to higher-latitude flows, outside the western boundary current

The eastward flow along the equator, mostly in the two WJs but with a substantial annual mean of

5–15 Sv (see above), must disperse northwards and southwards into the interior. Zonal surface currents estimated from buoys and ship drifts (Molinari *et al.*, 1990a) show a semiannual signal on both sides of the equator; however, annual mean surface flow is predominantly to the southeast, along the Indonesian coast. The predominantly southward movement of the equatorial flow is expected from the Sverdrup relation, as noted by McPhaden (1982a). These annual mean results are consistent with the observations of Schott *et al.* (1994), who find that the annual mean westward flow between Sri Lanka and 4°11'N, along 80°30'E (just north of the section described by Reppin *et al.*, 1999) was only 2–3 Sv. From mass conservation, one might expect it to equal the fraction of equatorial eastward flow that turns north, east of 80°30'E. The Sri Lankan westward flow was largely confined to the top 100 m, occurs mainly in winter, and is fresh (see, for example, the section near this line in March 1995, Talley and Baringer, 1997). By contrast the eastward equatorial zonal jet is about 200 m deep, and is salty. These results are consistent with summer freshening of the inflow in the Bay of Bengal (e.g. Shetye *et al.*, 1991). However, even when flow on the equator and south of Sri Lanka is westward, saline Arabian Sea water flowed east (at least in 1995) in a continuous North Equatorial Counter-Current (NECC). This flowed from 3°N at 80°E to the north end of Sumatra (Hacker *et al.*, 1998).

Semiannual flows along the Indonesian coast are evident from coastal tide gauge data (Wyrtki, 1961a), and from XBT data (Meyers *et al.*, 1995). Red Sea Water is apparent near Bali (Fieux *et al.*, 1994), indicating that flow must occur on annual mean along the south coast of Indonesia. This is in agreement with current meter data from March 1997 to March 1998 at 115 m and 175 m south of Java, despite unusually strong southeasterly winds (Sprintall *et al.*, 1999). Since the Indonesian Throughflow is southward on annual mean (e.g. Meyers *et al.*, 1995), the flow diverging southward from the equator must all join the ECC and SEC, at least in the top 400 m.

Clarke and Liu (1994) showed that on interannual time scales, sea level varies coherently by a few centimetres from Java to Bombay in India. They find that any sea level discontinuity in proceeding around the south tip of Sri Lanka does not vary greatly interannually; thus the zonal jet

emanating from this point should not vary much on interannual time scales. They ascribe this broad-scale sea level variation to interannual variations of the equatorial Kelvin wave along the equator, i.e. to interannual variations in zonal equatorial winds.

4.3.4.3 Deeper circulation and equatorial jets

A major issue for the Indian Ocean is: Is there a moderate to large conversion of Antarctic Bottom Water into Deep Water in this basin, as suggested by Toole and Warren (1993), Toole and Raymer (1985) and Robbins and Toole (1997)? If so, where does the mixing take place that feeds heat to these depths, and what physical processes are responsible for it? The equatorial region and the connecting western boundary regions are likely places for strong mixing, because strong currents are observed there (at least near the surface). Traditional analysis of top-to-bottom hydrographic sections may assist in solving such questions, though care needs to be taken with possible aliasing of high-frequency effects such as those seen in Fig. 4.3.11. However, relative to other oceans, equatorial data on deep currents (or even on the occurrence of low Richardson numbers in the thermocline, which may control downward diffusion there) is quite sparse in the Indian Ocean. In the following, we briefly consider: seasonality of deep zonal currents; deep cross-equatorial flows; abyssal flows; and deep reversing jets, and their associated shear mixing zones.

Luyten and Roemmich (1982) analysed year-long current meter records at 200 m, 500 m and 750 m, in 47–59°E; they have been discussed earlier. Reppin *et al.* (1999) give amplitudes and phases of annual and semiannual zonal currents, at or near the equator at 80°30'E. Semiannual amplitudes at 600 m are about 0.1–0.15 m s⁻¹, close to those found by Luyten and Roemmich, with smaller values near 1000 m and 2000 m. An annual cycle of order 0.05 m s⁻¹ is apparent at 600, 1000 and 2000 m.

As for deep cross-equatorial flows, these are liable to be confined to western boundary currents. Schott *et al.* (1989) reported observations of the deep Somali Current at the equator, from two moorings in October 1984 to September 1985, and two more from September 1985 to September 1986. Flows at 1000, 1500, 2000 and 3000 m show substantial variability on time scales of weeks

to months. Thus (for instance) a southward mean flow at 1000 m that falls with distance offshore from 0.08 m s^{-1} at the inshore mooring may not be significant. However, combining two years of data near the 2000 m isobath yields an alongshore component of $0.041 \pm 0.029 \text{ m s}^{-1}$ to the southwest, with an onshore flow of $0.029 \pm 0.013 \text{ m s}^{-1}$. Annual means at 1500 m, 2000 m and 3000 m are nearly zero. However, a strong seasonal flow occurs at 3000 m: $0.103 \pm 0.018 \text{ m s}^{-1}$ to the northeast in summer (June to September), $0.066 \pm 0.027 \text{ m s}^{-1}$ to the southwest in winter. Wacongne and Pacanowski (1996) compared these currents with their model results and suggested that this deep seasonal reversal may indicate a mass-conserving response to meridional Ekman transports, which are southward (northward) in summer (winter), on both sides of the equator. Marked differences in salinity patterns on the 1.8°C isotherm (about 2600 m) under the length of the Somali Current were found when data from August 1964 (Warren *et al.*, 1966) were compared with surveys in April 1985 and April 1986 (Fieux *et al.*, 1986; Schott *et al.*, 1989). These differences are consistent with the previously mentioned seasonal reversal observed at 3000 m on the equator under the Somali Current in 1984–85 (Schott *et al.*, 1989). However, regional hydrographic surveys spanning December 1986–January 1987 and repeated in July–August 1987 failed to reveal a seasonal cycle in deep salinity or dissolved oxygen distributions (Warren and Johnson, 1992). This difference may have been owing to the remarkably weak southwest monsoon in 1987, which could have been insufficiently strong to reverse a presumed prevailing southwestward flow along the western boundary.

Below 3000 m, water mass properties and geostrophy do indicate some mean flow in the equatorial regime, at least within the western deep basin system. The very narrow Amirante Passage (9°S , 52°E) admits a bottom water flow northward into the Somali Basin with transport estimates ranging from $1 \pm 0.5 \text{ Sv}$ based on two station pairs (Fieux and Swallow, 1988) to $4 \pm 1 \text{ Sv}$ based on three short sections (Barton and Hill, 1989). The most recent estimate based on an analysis of WOCE and historical hydrographic data suggests $1.0\text{--}1.7 \text{ Sv}$ (Johnson *et al.*, 1998). This flow apparently continues north to at least 3°S along the western boundary, but may turn eastward at the

equator (Johnson *et al.*, 1991a; Warren and Johnson, 1992), possibly consistent with inviscid boundary current dynamics (Johnson, 1993). The heat budget for the bottom water of the Somali Basin gives an estimate of vertical eddy diffusivity from 2.5 to $10 \times 10^{-4} \text{ m}^2 \text{ s}^{-1}$ (Fieux and Swallow, 1988; Barton and Hill, 1989) with the range mainly a result of the inflow transport estimate range. After the bottom water warms through diabatic processes, at least some of it may return southward through the Amirante Passage (Johnson *et al.*, 1998), to complete the deep meridional overturning cell, although there also is evidence for northward flow out of the Somali Basin through the Owen Fracture Zone (10°S , 57°E) to supply the bottom waters of the Arabian Basin (Johnson *et al.*, 1991b; Quadfasel *et al.*, 1997).

Luyten and Swallow (1976) were the first to discover equatorial deep jets in the Indian Ocean. They were further investigated by Ponte and Luyten (1990), who found no clear spectral peak in the zonal velocity, though visual inspection suggests a wavelength of about 500 m (in ‘stretched metres’, i.e. depth adjusted by a factor of $(N/N_0)^{1/2}$, with N the buoyancy frequency, N_0 is the depth-averaged buoyancy frequency of 1 cycle h^{-1}). Dengler and Quadfasel (2001) examined hydrographic and current profiles along the 80°S – 30°E current meter section discussed earlier, during three cruises. Once low vertical modes were removed from the data, all three sections showed largely zonal, vertically alternating jets, with speeds of up to 0.12 m s^{-1} . These jets were within a degree of the equator. Vertical length scales were about 300 m, lengthening to 1000 m at depth; relatively strong vertical shears occurred between the jets. The jets were largely reversed in July 1993 and September 1994, relative to December 1990; this is consistent with the semiannual reversals found by Luyten and Roemmich (1982) continuing to substantial depths. CTD data showed layers of low stratification, often 50 m thick, which coincided with the bands of large vertical shear. Richardson numbers within these layers were often less than 0.33, suggestive of active turbulence. This was confirmed by examining shear spectra (from the Pegasus current profiler) and strain spectra (from the CTD temperature profiles). Spectral densities were about five times greater on the equator than at 2° on either side, implying large internal wave activity with vertical

length-scales of tens to hundreds of metres. Direct estimates of dissipation rates within the unstable zones ($Ri < 0.33$) are as large as $10^{-7} \text{ W kg}^{-1}$, but the depth average is about $7.5 \times 10^{-10} \text{ W kg}^{-1}$. This dissipation rate, and the shear and strain spectral densities, are 3–5 times larger than comparable values between about 3200 m and 1000 m depth at 140°W in the Pacific (Gregg *et al.*, 1995). Muench and Kunze (1999) find that the replenishment of short wavelength internal waves can be strongly altered in the presence of jet-like structures like those observed, which may result in an energy source adequate to maintain the jets against dissipation.

Modelling issues associated with deep overturning circulation in the Indian Ocean are discussed by Warren (1994) and Lee and Marotzke (1998).

4.3.4.4 Summary: Implications for heat and fresh water transport, water mass changes, heat fluxes and SST

As stated in the introduction, we are concerned here with using WOCE and other data to help us understand the physical mechanisms relating heat and fresh water transport, the associated water mass changes, surface heat and fresh water fluxes, and SST. We need to understand these relations on all time scales (not just on long-term mean), if we are to understand and simulate the Indian Ocean SST changes that are so critical to climate variability. Section 4.3.4 has presented a qualitative picture of two possible modes of heat transport in the upper equatorial Indian Ocean. One mode involves the directly wind-driven overturning cell. A second involves an ‘eddy transport’ internal to the Somali Current System, which appears to draw deep water in from the East African Coast Current, warm it in the Somali Current, export it just across the equator in the western boundary, and thence feed annual mean zonal flow along the equator. The latter exits in the South Equatorial Countercurrent. We also briefly considered connections to deep overturning circulations.

The question of the relative sizes of the direct wind-driven and annual ‘flushing’ mechanisms is important for purposes of understanding inter-annual variability, because the first is now fairly well understood physically, but the second is not. Unfortunately it will be hard to tease the two mechanisms apart, since the main effect of the annual flushing mechanism is to change the temperature

distribution of the geostrophic inflows and outflows to the basin. However, we do not know what physically sets this distribution, either in the presence or the absence of the eddy transport mechanism.

Hopefully, traditional analyses of WOCE Indian Ocean sections may settle the question of how much heat is mixed down through the thermocline, to warm incoming Bottom Water and drive the deep overturning cell. To do so, they will need to allow for possible aliasing of ‘snapshot’ data by short time scale effects, such as the large variations in transport associated with the Intraseasonal Oscillations (Fig. 4.3.11). It will then be necessary to find the sources of the deep mixing – and of the mixing of heat through the thermocline. Equatorial mixing such as that associated with the Deep Reversing Jets is a strong candidate; but mixing within the Somali Current System is another one. Unfortunately, many issues associated with the SCS are difficult to test observationally, because they require work within the Exclusive Economic Zones of several countries.

4.3.5 Overall conclusions

The comparison between the three equatorial oceans seems to confirm that the qualitative resemblance between current systems in the Pacific and Atlantic covers a wide variety of phenomena. Both have an SEC, EUC and NECC with an annual cycle of similar phase, though the EUC display some marked quantitative differences. Furthermore, the Atlantic NEUC and SEUC seem to be somewhat similar to the NSCC and SSCC (Tsuchiya Jets) in the Pacific. If this is confirmed, the terminology should be rationalized so that similar phenomena have the same name in each ocean. Observational work has tended to take a different approach in the two oceans, resulting in complementary insights. For example, the inventory of currents feeding the Pacific EUC could usefully be examined for the Atlantic. The apparent analogies may extend to the Equatorial Intermediate Currents and to the Deep Reversing Jets. Conversely, the links of Atlantic current variability to ring formation may have Pacific analogues.

One major difference between the Atlantic and the other two oceans is, of course, that the entire equatorial Atlantic circulation from the surface to the North Atlantic Deep Water outflow is part of

an overturning cell, which transports large amounts of heat northward across the equator. In the Pacific and Indian Oceans, overturning cells are confined to the thermocline with weaker deep cells below. In the Pacific Ocean, significant northward flow across the equator is required to supply the Indonesian Throughflow.

The main mechanisms resulting in heat and freshwater transport in the equatorial Indian Ocean are completely different from those in the Pacific and Atlantic, largely because the winds – especially those along the equator – are so different. Thus the Somali Current, rather than the equatorial Indian Ocean, seems to be the major region of near-surface water mass generation. Hence Indian Ocean equatorial flows must be organized primarily to carry cold inflows and warm outflows across the equator, rather than upwelling them on the equator and distributing them to both sides as in the other two oceans. However, it is quite likely that the main transport mechanisms of each ocean are significant (if minor) contributors in the other. Thus, wind-driven upwelling in the eastern Indian Ocean plays a role in SST cooling and water mass formation during interannual ‘Indian Ocean Dipole’ events (Saji *et al.*, 1999). Conversely, seasonal fluctuations of Pacific near-surface equatorial currents, such as the New Guinea Coastal Current, could provide a mean cross-equatorial ‘flushing’ of water masses like those that flush Somali Current water south. In all three oceans, the Ekman transport across the equator, generated by zonal winds that are anti-symmetric about the equator, may be balanced (on seasonal time scales) by flows at around 3000 m or deeper. This is at least consistent with observations in the Atlantic and Indian Oceans, but less is known about deep seasonal cross-equatorial currents in the Pacific.

As noted in the Introduction, mechanisms of the mixing processes that create new water masses are highly non-linear, and mixing ‘hot spots’ are probably located quite tightly in space – and in time. (For example, tidal mixing may be concentrated

near spring tide, while that due to intraseasonal activity may be concentrated near westerly wind bursts.) A variety of qualitatively different mechanisms have emerged, including heat release from mid-ocean ridges as well as tidal mixing and Kelvin–Helmholtz instability across shear zones. The fact that (according to observed climatologies) strong mixing occurs in Indonesia, within the very high SSTs of the Warm Pool, suggests that locating the source of the mixing is not just a matter of locating low SSTs. So far, it has in fact not proved possible to locate definitely a clear source of tidal mixing in the Indonesian Seas. On the other hand, progress is being made in understanding mixing at the shear zones associated with the Deep Reversing Jets. Refraction of internal waves may sustain these jets in the presence of diffusion. Early process study work suggested that mixing (probably by Kelvin–Helmholtz instability) may extend well below the EUC, in the Pacific; but such results could well be revisited, using the much more extensive data now available. Mixing processes in several coastal regions also need direct observation.

The analysis of WOCE hydrographic section data for purposes of estimating long-term means is made more complicated by variability on inter-annual, seasonal and intraseasonal time scales, which may cause aliasing in geostrophic current estimates. The TAO/Triton mooring array can assist greatly in disentangling such effects in the upper few hundred metres of the Pacific, but model studies suggest that variability on all three time scales is important in the Indian Ocean. Intraseasonal variability is less prominent in the Atlantic, slightly simplifying the analysis task there.

Acknowledgements

We wish to thank two anonymous reviewers, and Dr J. McCreary, for their careful and constructive comments on this manuscript, which (at least to our eyes) have improved the coherence and readability of the result. Eric Firing and Roger Lukas have offered many helpful items to this review.

4.4

Tropical–Extratropical Oceanic Exchange Pathways

Zhengyu Liu and S. G. H. Philander

4.4.1 The role of diffusion and advection

The salient feature of the thermal structure of the ocean is the thermocline, which is particularly sharp and shallow in low latitudes. The processes that maintain the thermocline are presently of considerable interest because those processes appear to be of central importance to interdecadal climate variability and global climate changes (Cane *et al.*, 1997; Gu and Philander, 1997; Liu, 1998; Zhang *et al.*, 1998a).

The first studies of the thermocline were motivated by Ellis' (1751) measurements that revealed extremely cold water at depth in the tropical Atlantic. Rumford (1800) speculated that cold currents from polar regions must sustain the low temperatures in low latitudes. Lenz (1845), who first noticed that the depth of the thermocline decreases with decreasing latitude in the tropics (see Fig. 4.4.1a), inferred that there is equatorial upwelling sustained by a pair of thermohaline cells, one in each hemisphere (see Warren, 1981b, for a historical review of this topic). A century later, these ideas are quantified (Robinson and Stommel, 1959; Robinson and Welander, 1963) in a model in which the thermocline depends on a balance between the downward diffusion of heat and the upwelling of cold water.

Over the past two decades, oceanographers have found that, to account for the observed thermocline structure, diffusive thermocline models require a diffusivity much larger than that which is observed. This prompted them to explore thermocline models in which horizontal advection rather than diffusion is of primary importance (Luyten *et al.*, 1983;

Pedlosky, 1987a; Liu, 1994; McCreary and Lu, 1994). In these models, subduction of surface waters in the subtropics, which in part is maintained by poleward Ekman drift in the surface layers, feeds subsurface, equatorward geostrophic flow along isopycnals. Upwelling, especially at the equator, closes the circulation. Evidence for such a circulation comes from hydrographic sections and tracer data (Tsuchiya, 1968; Wyrtki, 1975; Fine *et al.*, 1981, 1987; Quay *et al.*, 1983; Roemmich, 1987; Tsuchiya *et al.*, 1989; Johnson and McPhaden, 1999). If it is assumed that water parcels conserve their potential vorticity $f\partial_z\rho$ as they travel equatorward, then major features of the thermocline can readily be explained. Because the Coriolis parameter f decreases with decreasing latitude, conservation of potential vorticity requires that the vertical density gradient $\partial_z\rho$ increase. The reduction of layer thickness for all the subduction layers further requires a shoaling of thermocline as the equator is approached. This tropical–extratropical oceanic exchange is a means by which a change in surface conditions in the extratropics can affect the structure of the tropical thermocline, in turn affecting tropical ocean–atmosphere interactions, and hence can contribute to climate fluctuations and climate changes at decadal and longer time scales.

This chapter is a review of recent research on tropical–extratropical exchanges in the Pacific Ocean. Section 4.4.2 concerns the relatively shallow exchange of thermocline waters between the tropics and subtropics. Section 4.4.3 focuses on the exchange of colder, intermediate waters between the tropics and subpolar regions. Section 4.4.4

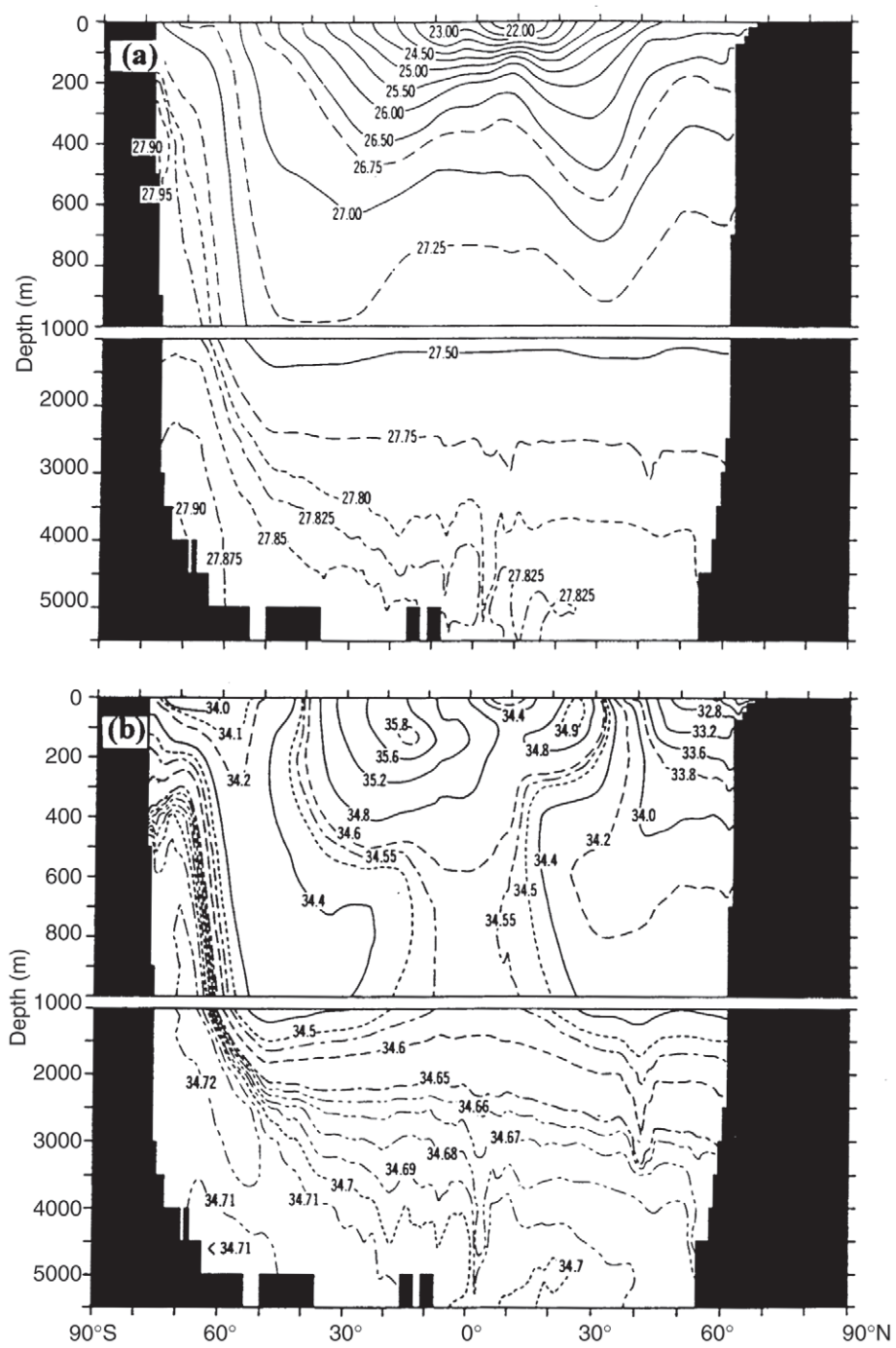


Fig. 4.4.1 Annual mean Pacific zonal average of (a) potential density and (b) salinity. After Levitus (1982).

summarizes the results and discusses questions that remain to be addressed.

4.4.2 Tropical–subtropical exchanges of thermocline waters

The general features of the tropical–subtropical water exchanges can be inferred from Fig. 4.4.1, which shows the climatological, zonal mean

density and salinity fields of the Pacific Ocean. Isopycnals are seen to descend in the mid-latitude, to reach a maximum depth at about 30° latitude, and to shoal steeply as the equator is approached. Isohalines in Fig. 4.4.1b have a similar tongue structure. Together, these pictures suggest that water subducts in the mid-latitudes and then proceeds equatorward. Figure 4.4.2 plots of the same fields as measured along the Hawaii-to-Tahiti

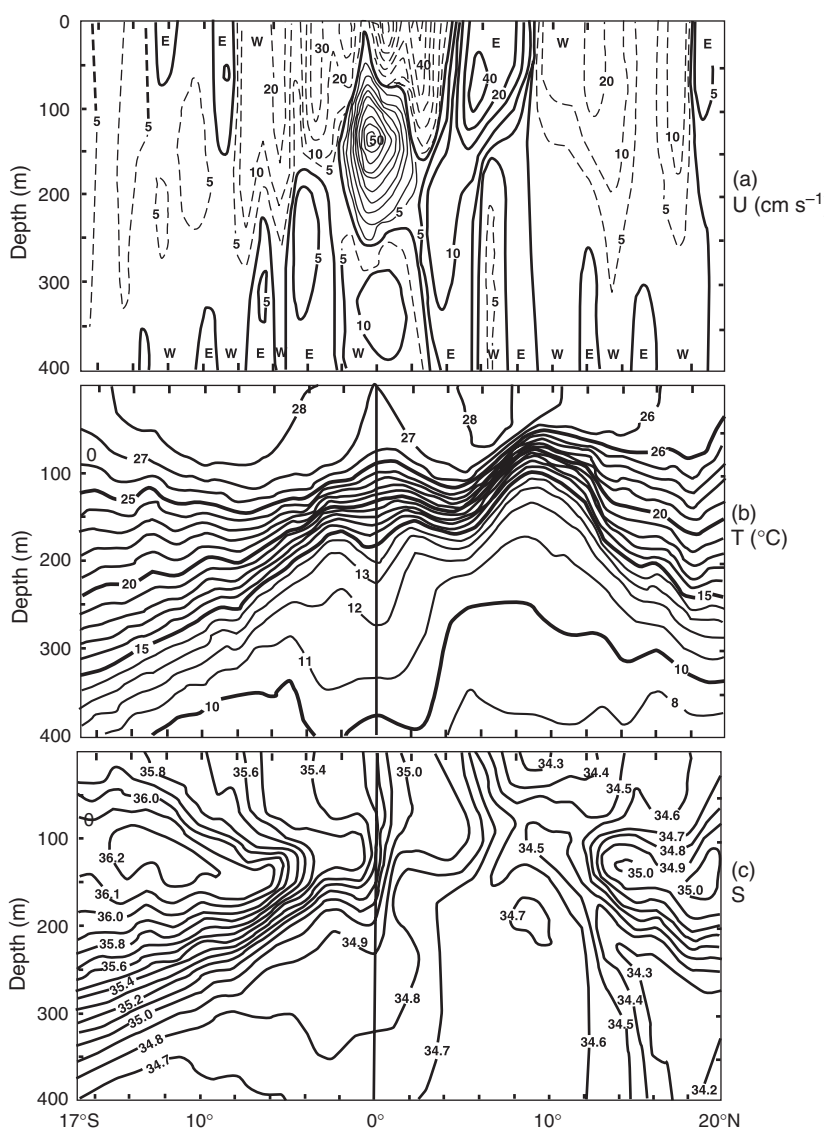


Fig. 4.4.2 Mean distributions of (a) zonal geostrophic flow $U (10^{-2} \text{ m s}^{-1})$ relative to 1000 dbar, (b) temperature $T (\text{ }^{\circ}\text{C})$, and (c) salinity between Hawaii and Tahiti (about 150°W and 160°W) and from the sea surface to 400 m. After Wyrtki and Kolonsky (1984).

transect, show a much sharper temperature gradient and tongues of high-salinity water that stretch equatorward, especially from the south. These figures also show how the currents are related to the temperature and salinity fields (the equatorial thermocline coincides with the core of the Equatorial Undercurrent) and reveal that below the Undercurrent there is a thermostad, a region of low vertical stability with temperatures between 11°C and 14°C . The figures suggest that the flow that maintains the thermocline at the equator is also involved with the source water of the Equatorial Undercurrent. This flow is asymmetrical relative to the equator in several ways. From the salinity field it appears that water reaches the equator more

readily from the southern than from the northern hemisphere. Furthermore, the flow from the north, but not that from the south, encounters a ridge in the thermocline near 10°N . This is the ridge of the North Equatorial Countercurrent, a feature forced by Ekman upwelling associated with the Intertropical Convergence Zone.

Persuasive evidence for the circulation described above comes from tracer studies, specifically of bomb tritium. Fine *et al.* (1981, 1987) infer from tritium measurements that tritium-rich surface waters subduct in the northern subtropics, then flow along isopycnals towards the equatorial thermocline of the central Pacific where it arrives some 10 years later (see Figs 4.4.3a and b). Figure 4.4.3c

suggests a ventilation pathway that starts in the eastern subtropical North Pacific, continues southwestward in the North Equatorial Current, and then proceeds southeastward in the North Equatorial Countercurrent. Observations also show additional pathways to the Equatorial Undercurrent. Some of the water in that current passes through low-latitude western boundary currents (Tsuchiya *et al.*, 1989) such as the Mindanao Current (Lukas

et al., 1991; Fine *et al.*, 1994; Bingham and Lukas, 1995), the New Guinea Coastal Undercurrent (Lindstrom *et al.*, 1987) and the New Ireland Coastal Undercurrent (Butt and Lindstrom, 1994; Fine *et al.*, 1994). The western boundary pathway can also be observed in Fig. 4.4.3c, which shows a branch of subduction water that tends to penetrate from the central Pacific towards the western boundary.

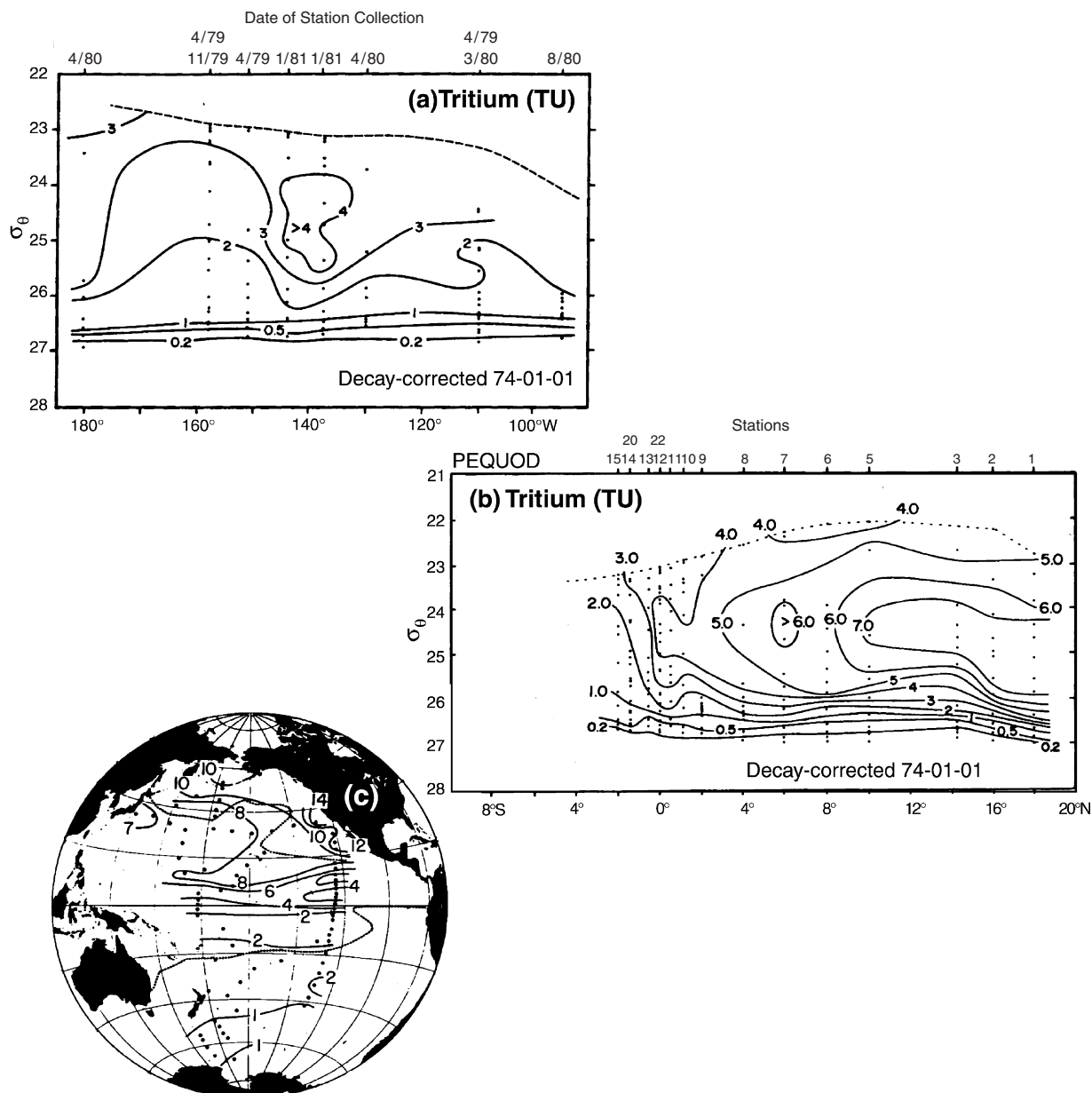


Fig. 4.4.3 Tritium (TU) distributions in the North Pacific. (a) Zonal section (versus σ_θ) along the equator; (b) north-south vertical section (versus σ_θ) along the PEQUOD track at 138°W (after Fine *et al.*, 1987); and (c) the isopycnal of 23.9 σ_θ . After Fine *et al.* (1981). Tritium decay corrected to 74-01-01 in (a) and (b), and to 72-01-01 in (c).

The dynamics of tropical–subtropical water exchanges were first explored by Pedlosky (1987a, 1988), who developed an inertial theory for the Equatorial Undercurrent in which its waters have their origin in the subduction of cold surface waters in the subtropics. Liu *et al.* (1994) and McCreary and Lu (1994) further pursued these ideas with more sophisticated models. They found that much of the water in the Equatorial Undercurrent participates in an intense recirculating *tropical cell* with water rising to the surface at the equator, drifting westward and poleward, then sinking near 3° latitude, and rejoining the Undercurrent in the upper thermocline. In the mean time, tropical–subtropical exchanges are accomplished in a latitudinally wider *subtropical cell* in two ways. After subduction in the subtropics, the subtropical cell provides waters to the equator by means of subsurface low-latitude western boundary currents (*western boundary pathway*), and also by means of a more direct pathway through the interior of the ocean basin (*interior pathway*).

Figure 4.4.4 plots the trajectories of particles subducted along 25°N and 25°S in a model that assimilates measurements (Ji *et al.*, 1995). In both

hemispheres, water that subducts relatively close to the coast of the Americas (*interior exchange window*) is seen to reach the equator through the interior pathway; water that subducts further west (*western boundary exchange window*) is seen to follow a western boundary pathway to low latitudes; water that subducts the furthest west (*recirculation window*) joins the subtropical gyre and proceeds poleward in the mid-latitude western boundary current. Figure 4.4.5 (see Plate 4.4.5, p. 300) shows representative trajectories and also indicates, in isochrons, how the time it takes (in years), to reach 5° latitude, depends on the location of subduction. Whereas interior pathways tend to take 10 years or less, are relatively shallow, and start relatively close to the equator, western boundary pathways take 10 years or longer, tend to be deeper, and start further poleward. The fact that a deeper layer tends to flow more in the western boundary pathway is consistent with the beta-spiral vertical structure of thermocline circulation (Schott and Stommel, 1978). These results are consistent with observations (Fig. 4.4.6, see Plate 4.4.6, p. 300) (Tsuchiya, 1968; Fine *et al.*, 1981, 1987; Johnson and McPhaden, 1999).

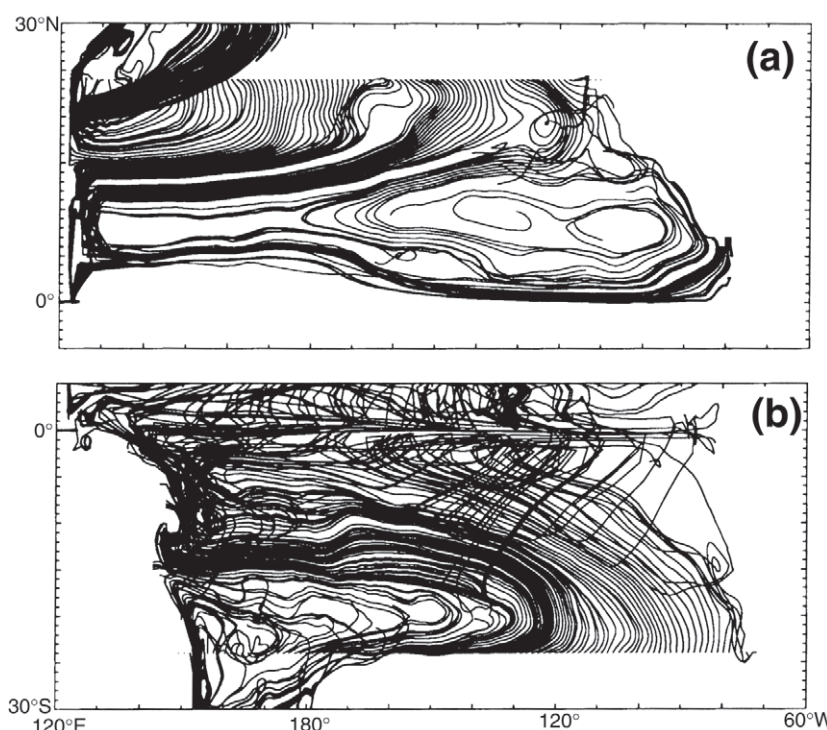


Fig. 4.4.4 Particle trajectories 19 years after subduction. The particles are initiated along 24°N and 24°S at the depth of 50 m. The velocity field is taken from the annual mean flow of the NCEP assimilated ocean data (Ji *et al.*, 1995). After Liu and Huang (1998).

The dynamics of these exchange processes can be explained in terms of simple thermocline models (Liu, 1994; McCreary and Lu, 1994; Liu and Philander, 1995). Liu (1994) describes how the boundaries of these different subduction windows depend on the structure of the windstress patterns.

The tropical–subtropical water exchange in the Pacific is strongly affected by the complex spatial pattern of the trade wind. The asymmetry of that field relative to the equator, the Intertropical Convergence Zone, where the southeast and northeast trades meet, is mostly in the northern hemisphere and causes the pathways of water parcels to be different in the two hemispheres. Routes to the equator in the southern hemisphere can be direct but the presence of the eastward North Equatorial Countercurrent in the northern hemisphere complicates matters. That current is associated with a ridge in the thermocline near 10°N (see Fig. 4.4.2). A parcel conserving potential vorticity could have difficulty negotiating that ridge, an impression that one may also have from the salinity distribution of Fig. 4.4.2c (Lu and McCreary, 1995). Nevertheless, the thermocline deepens westward and therefore it remains possible for the flow to conserve potential vorticity while crossing the thermocline ridge. Dynamically, this thermocline ridge is forced by the dominant Ekman upwelling in this region. The upwelling produces a northward geostrophic current that tends to block the interior equatorward penetration. However, in the central Pacific, the Ekman pumping is downward in the latitudes of North Equatorial Countercurrent. This generates a southward geostrophic flow and therefore enables the interior pathway to penetrate across the latitude of North Equatorial Countercurrent (McPhaden and Fine, 1988; Liu and Huang, 1998). That is why, in Fig. 4.4.5 (see Plate 4.4.5, p. 300), the northern hemisphere interior trajectory moves southwestward up to 10°N, then continues southeastward in the Countercurrent. These results are confirmed by recent modelling (Huang, 1996; Blanke and Raynaud, 1997; Gu and Philander, 1997; Lu *et al.*, 1998; Rothstein *et al.*, 1998b; Huang and Liu, 1999; Harper, 2000) and hydrographic (Fig. 4.4.6, see Plate 4.4.6, p. 300; Johnson and McPhaden, 1999) studies.

Because of the different pathways for subducted waters in the two hemispheres, the contributions to equatorial thermocline waters (lighter than $26.2\sigma_0$) by interior pathways is on the order of

14 Sv for the southern hemisphere, but only 4 Sv for the northern hemisphere. Contributions via western boundary currents amount to approximately 14 Sv for each hemisphere (see Butt and Lindstrom, 1994; Wijffels, 1993; Huang and Liu, 1999; Johnson and McPhaden, 1999).

The details of the low-latitude western boundary flows are complex and involve several coastal currents that include the Mindanao Current (Lukas *et al.*, 1991; Fine *et al.*, 1994; Bingham and Lukas, 1995), the New Guinea Coastal Undercurrent (Lindstrom *et al.*, 1987), and the New Ireland Coastal Undercurrent (Butt and Lindstrom, 1994). These currents are highly variable so that information about them is tentative. It appears that waters from the southern hemisphere penetrate into the northern hemisphere. Some of it joins the eastward North Equatorial Countercurrent, and some leaks into the Celebes Sea and eventually into the Indian Ocean because of the Indonesian Throughflow.

The salinity distribution in the Equatorial Undercurrent (Figs 4.4.1b and 4.4.2c) suggests that much of the water in that current comes *from* the saline South Pacific. However, that inference is tentative until we explore the role of entrainment of subthermocline waters into the Equatorial Undercurrent, the topic of the next section.

4.4.3 Tropical–subpolar exchange of Intermediate Waters

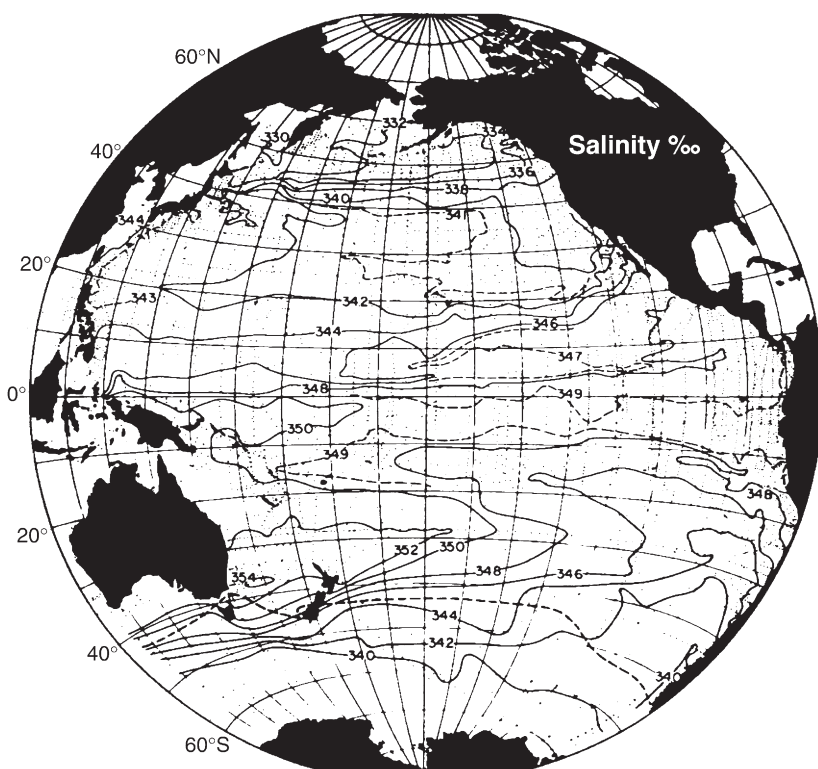
Immediately beneath the equatorial thermocline is a layer of low vertical stability, with temperatures between 11°C and 14°C, known as the thermostad (Montgomery and Stroup, 1962). The cause of this low stability has received surprisingly little attention. It probably is a consequence of vertical mixing induced by the large vertical shear of the Equatorial Undercurrent. This mixing is a means for Intermediate Waters to be entrained into shallower layers and hence is an important aspect of the maintenance of the equatorial thermocline. Clues to the origin of these Intermediate Waters come from its properties that are evident in Fig. 4.4.2: high salinity, high oxygen concentration and low nutrient concentration. On the basis of the salinity distribution along isopycnals, Tsuchiya (1981) suggested that these waters have their provenance in the surface layers of the ocean northeast of New Zealand, and in the Tasman Sea, which, according to Toggweiler *et al.* (1991), may

also be associated with the colder (7–10°C) Subantarctic Mode Water (McCartney, 1982) that is formed in the Antarctic Circumpolar Current region. The path of this water towards the equator is indicated by the salinity tongue (values of 34.9 on the thermosteric anomaly surface of $160 \times 10^{-8} \text{ m}^3 \text{ kg}^{-1}$) in Fig. 4.4.7. From its source, where the salinity exceeds 35.2, the water first flows eastward in high latitudes, then turns westward in lower latitudes, all part of the anticyclonic subtropical gyre of the South Pacific. The flow turns northward through the Coral and Solomon Seas to approach the equator through the Vitiaz Strait (Lindstrom *et al.*, 1987; Fine *et al.*, 1994). Ultimately the water joins either the deeper part of the Equatorial Undercurrent, or the deep eastward Equatorial Subsurface Countercurrents along the flanks of the thermostad (Tsuchiya, 1981). Mixing then causes its entrainment into shallower layers, including the surface layers that have poleward Ekman transport.

The northern Pacific too has Intermediate Waters, with a salinity minimum of less than 34.5.

The North Pacific Intermediate Water enters the western equatorial Pacific via the Mindanao Current at $26.5\text{--}26.6 \sigma_0$ and spreads eastward in the North Equatorial Countercurrent at about 2–3.5°N (Fig. 4.4.8) (Fine *et al.*, 1994; Bingham and Lukas, 1995). Most of the North Pacific Intermediate Water seems to leak out to the southern Celebes Sea and ultimately into the Indian Ocean, with little contribution to the equatorial currents.

In the lower part of the Intermediate Water ($>26.8 \sigma_0$), the Antarctic Intermediate Water is entrained into the subtropical gyre in the eastern Pacific as it flows eastward in the Antarctic Circumpolar Current. It moves counterclockwise around the gyre and flows westward in low latitudes ($\sim 20^\circ\text{S}$) as a tongue of low salinity extending well into the Coral Sea (Taft, 1963; Reid, 1965, 1986; Johnson, 1973). Then, it is advected by the bottom part of the New Guinea Coastal Undercurrent northward across the equator, with a characteristic salinity minimum of about 34.55 at the density of approximately $27.2 \sigma_0$ (Fig. 4.4.8). After crossing the equator, part of the water turns



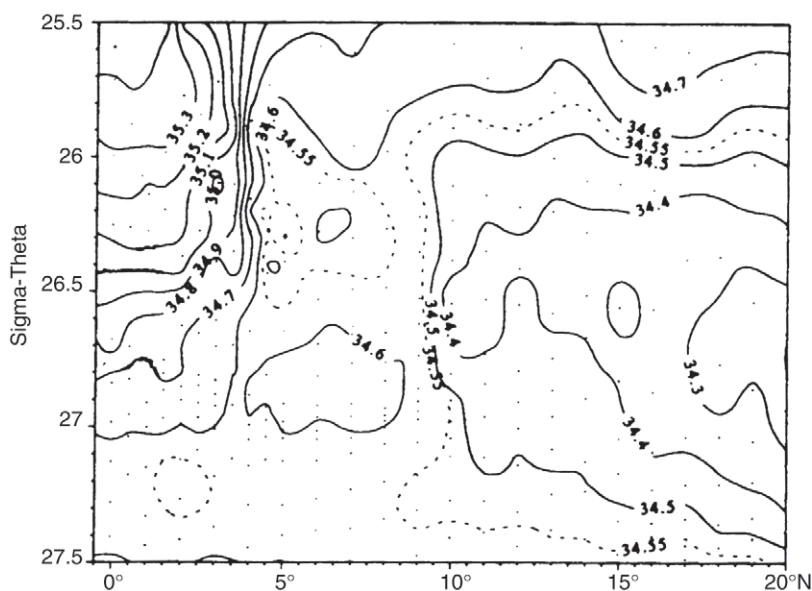


Fig. 4.4.8 Salinity along 137°E observed during the Ryofu Maru cruise. Small dots mark locations of bottle measurements. After Bingham and Lukas (1995).

eastward in the North Equatorial Subsurface Countercurrent – contributing to the equatorial Intermediate Water. The rest of the water either continues northward along the eastern Mindanao Coast (Tsuchiya, 1991; Bingham and Lukas, 1995), or leaks out to the Celebes Sea (Fine *et al.*, 1994).

Although there is at present no theory for the dynamics of the Intermediate Water, recent numerical experiments capture some of its principal features. Figure 4.4.9 shows the velocity field of these waters in the third layer of the 3.5-layer Pacific model of Lu *et al.* (1998). This model is forced with the observed winds and, in addition, imposes the transport of 10 Sv of Intermediate Water across 35°S, and the export of the same volume of water, in the thermocline and surface layers, through the Indonesian Straits. The Intermediate Water is seen to participate in a gyre: the flow is first eastward, then westward, before turning equatorward in a western boundary current. Some of the water joins the deep, eastward equatorial currents, providing one-third of the transport of the Equatorial Undercurrent. The remainder crosses the equator and either joins the North Equatorial Countercurrent, or proceeds northward in the Mindanao Coastal Current. The six-layer ocean model of Shriver and Hurlburt (1997) has similar pathways.

The Intermediate Water pathway seems to be influenced by both wind and buoyancy forcings. The effect of the wind forcing in the subtropical gyres is reflected in the anticyclonic circulation in

the interior ocean, as evident in Figs 4.4.7 and 4.4.9. This aspect is absent from the strictly buoyancy-driven abyssal flow (Stommel and Arons, 1960a,b), in which the deep convection induces waters that simply flow westward before they feed into the deep western boundary current. On the other hand, the intermediate water circulation also differs from the wind-driven thermocline circulation in the subtropics, with the formation in the subpolar region, with a much broader vertical structure and a much slower speed. In the equatorial region, unlike the thermocline water, whose eastward penetration is confined within the Equatorial Undercurrent, the Intermediate Water can flow eastward in deeper eastward currents such as the North and South Subsurface Countercurrents. During the course of their eastward penetration, these two subsurface countercurrents diverge from the equator (McPhaden, 1984; Johnson and Moore, 1997), confining the equatorward pathway in the western boundary (Johnson and McPhaden, 1999). These topics need further study, given the importance of this circulation to the maintenance of the equatorial thermocline.

4.4.4 Summary and further issues

Over the past two decades, observational and modelling studies of the exchanges of tropical and extratropical waters have shed much light on the circulations that maintain the tropical thermocline.

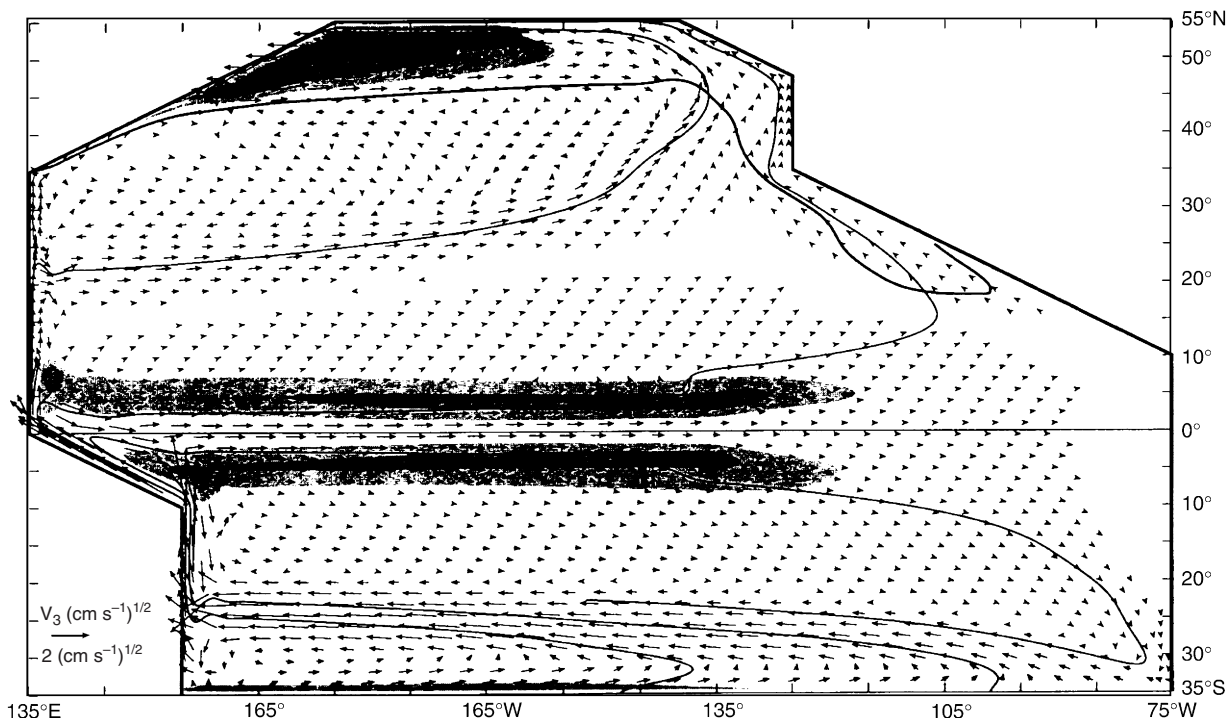


Fig. 4.4.9 The horizontal distribution of layer 3 velocity in a 3.5-layer model simulation of the Pacific (after Lu *et al.*, 1998). Regions of upward entrainment velocity are shaded and several streamlines are drawn to illustrate prominent Intermediate Water pathways.

Both interior and western boundary pathways are available for water that subducts in the subtropics to reach the equator. The journey takes on the order of a decade. Asymmetries, relative to the equator, of the surface winds (the Intertropical Convergence Zone), is mainly north of the equator; this translates into a reduction in the amount of water that follows the interior pathway in the northern Pacific. As a result, the Equatorial Undercurrent receives more thermocline waters from the south than from the north downstream. Meridional recirculation in a narrow equatorial cell that is only a few degrees latitude wide is far more intense than the tropical–extratropical exchange so that, to a first approximation, the intensity of the Equatorial Undercurrent is determined by the winds along the equator.

The waters below the equatorial thermocline originate mainly in the subantarctic region of the southern Pacific. (Intermediate Water from the northern Pacific never reaches the equator but ultimately flows into the Indian Ocean.) Tracer observations indicate, and models corroborate, that the pathways for Intermediate Water to the equator involves western boundary currents. (Weiss *et al.*, 1985, and Kawase and Sarmiento,

1986, established this for the Atlantic.) How this Intermediate Water, once it is advected in the subsurface countercurrents into the thermostatad below the equatorial thermocline (McPhaden, 1984; Johnson and Moore, 1997), gets mixed with shallower, warmer water is unclear. The matter needs attention because it could prove a crucial aspect of the processes that maintain the equatorial thermocline.

How the flow of upper ocean waters through the Indonesian Straits into the Indian Ocean affects the tropical–extratropical exchanges in the Pacific needs clarification. Gordon (1986) and Ffield and Gordon (1992) find that the thermocline waters in the Indonesian Seas come mainly from the northern Pacific. Fine (1985) reaches a similar conclusion on the basis of tritium data. However, Godfrey *et al.* (1993) argue that the southern Pacific contributes to the Indonesian throughflow. Fine *et al.* (1994) suggest that waters from both hemispheres mix in the Mindinao Current before proceeding to the Indian Ocean.

The Indian Ocean is intriguingly different from the Pacific and Atlantic Oceans because a steady westward trade wind, and in turn the equatorial upwelling, is essentially absent in the Indian Ocean.

There, the vertical mixing of waters of different temperature does occur along the Somali coast during the southwest monsoon season, and in the Arabian Sea (McCreary and Kundu, 1988). The processes that maintain the thermocline in the Indian Ocean need to be explored.

The tropical-extratropical exchanges in the Atlantic Ocean differ from those in the Pacific in being far more asymmetric relative to the equator. Water that subducts off southwestern Africa does reach the equatorial thermocline, but the water that subducts north of the equator in the Atlantic does not (Fine *et al.*, 1987, 1994; Harper, 2000). Consistent with this result is the tritium distribution, which shows a sharp front on the southern boundary of the North Atlantic subtropical gyre (Sarmiento *et al.*, 1982; Kawase and Sarmiento, 1985). This strong asymmetry relative to the equator in the Atlantic could have several reasons. One is the thermohaline circulation in which there is a net northward flow of warm surface waters across the thermocline (Schmitz and McCartney, 1993). Another possible factor is the coastal geometry, i.e. the small zonal extent of the Atlantic just north of the equator. Waters that subduct off northwestern Africa are likely to join northward-flowing western boundary currents before they can travel far south towards the equator.

The dynamics of subduction temperature variability remain to be studied. Up to now, studies of tropical-extratropical exchanges have focused on water masses that amount to passive tracers. Little attention has thus far been given to the fate of temperature anomalies that subduct in the subtropics. (These anomalies have been described in recent observations: Deser *et al.*, 1996; Zhang *et al.*, 1998a; Schneider *et al.*, 1999b.) Part of a temperature anomaly could be salinity-compensated with no density signature (Miller *et al.*, 1998). This part of a salinity-compensated temperature anomaly should behave exactly like a passive tracer, whose evolution is determined by mean subduction flow and small-scale mixing. It is possible that a temperature anomaly is generated to be accompanied by a compensation salinity. For example, an anomalous westerly wind in the mid-latitude could generate both a cold surface temperature anomaly and a low surface salinity anomaly by inducing a southward Ekman flow advection. The subtropical cold surface temperature anomaly, by reducing evaporation, could further freshen the

surface water and therefore compensate an additional part of the cold temperature anomaly. However, a sea surface temperature anomaly usually will not be completely salinity-compensated.

It is more likely that a large part of a sea surface temperature anomaly in the subtropics is not salinity-compensated. The non-compensated temperature anomaly will induce density disturbances that propagate as dynamic waves. On interannual and shorter time scales, the Rossby waves that are of primary importance are refracted equatorward (Schopf *et al.*, 1981; Chang and Philander, 1989). On longer time scales, the subduction anomalies can be understood in terms of higher baroclinic modes of planetary waves that tend to be advected by the mean current (Liu, 1999a,b). The evolution of these planetary waves are controlled by wave dynamics as well as mean advection and mixing, and therefore could differ significantly from a passive tracer. Preliminary studies suggest that, in the subtropics, the amplitude of a density anomaly could decrease along the subduction pathway due to the divergent group velocity (Liu, 1993), or increase in the far downstream of a subtropical gyre due to planetary wave instability (Liu, 1999a). Furthermore, the speed of the density anomaly is usually somewhat slower than the mean flow, because of the northward propulsion by the eastward mean potential vorticity gradient in the ventilated zone (in the northern hemisphere) (Liu, 1999b; Stephens *et al.*, 2000). A subducted temperature anomaly also has a more complex spatial structure than a subducted passive tracer anomaly (Liu and Shin, 1999). In addition, the subduction density anomaly has distinctively different dynamic responses to the surface wind stress as well as buoyancy forcing (Huang and Pedlosky, 1999; Liu, 1999b; Schneider *et al.*, 1999b). Finally, if density disturbances reach a western coast, they can generate coastal Kelvin waves that propagate to the equator (Lysne *et al.*, 1997; Liu *et al.*, 1999b; Shin and Liu, 2000).

The climate implication of tropical-extratropical water exchange remains speculative at the present stage. The exchange is recognized to be critical in affecting the mean equatorial thermocline, and in turn the surface temperature through equatorial upwelling. The influence of tropical-extratropical exchange on the ocean-atmosphere interactions and climate variability remains yet to be quantified. These resultant climate fluctuations have only recently been given attention.

Acknowledgements

We would like to thank Drs M. McPhaden and G. Johnson for helpful comments on an earlier

version of the manuscript and Dr J. Pedlosky for a helpful discussion. This work is supported by NSF and NOAA.

This Page Intentionally Left Blank

4.5

Quantification of the Deep Circulation

Nelson G. Hogg

4.5.1 Deep circulation in the framework of WOCE

During the design phase of the World Ocean Circulation Experiment (WOCE) it was recognized that various strategies were needed to 'divide and conquer' the massive problem of making a significant step forward in our understanding of the global circulation. One of these was a series of 'subject' meetings to contrast with the earlier 'sector' meetings at which different ocean basins had been the topic. One such meeting was held at Woods Hole in 1986 and concerned the subject of the deep circulation and its interaction with topography. Advice was sought on a variety of issues from the use of tracers, to the roles of diapycnal mixing, interaction with a rough bottom, the relative importance of advection and diffusion, etc. A set of objectives was formulated and further refined at the Core Project 3 meeting at the Royal Society later in the year (WCRP, 1987). Ultimately, the list of objectives for improving our knowledge of the deep circulation became:

- to explore and fill out the system of Deep Western Boundary Currents (DWBCs) and quantify their transports, on a global basis;
- to quantify the interior circulation, away from the DWBCs, including the role of mixing, deep passages, etc.;
- to quantify the time-dependent production of deep and bottom waters;
- to determine the importance of topographic form stress; and
- to study the dissipation of kinetic energy through frictional processes at the bottom.

At the writing of this chapter it is fair to say that the above list remains pretty much intact as important research areas: WOCE has made significant contributions to the first two topics, which will be outlined below; little advance has been made on the last three.

A guiding framework for the design of an experimental approach to understanding the deep circulation is provided by the circulation scheme devised by Henry Stommel (1958) and further embellished in the series of papers with Arnold Arons and others. This posits that there are a small number (two) of deep water formation areas in the polar regions of the ocean and that the water made dense there must spread equatorward in DWBCs on a rotating spherical planet (Fig. 4.5.1). Recognizing that there is a thermocline separating warm surface water from deep cold water over much of the globe, Stommel further hypothesized that this is maintained, against the downward diffusion of heat, by a uniform upwelling that supplies the upper ocean with the water needed to replace that which sinks at high latitudes. Such an upward vertical velocity at the top of the abyssal layer implies vortex stretching. Conservation of potential vorticity then demands poleward flow in the interior. With this scheme in mind researchers during WOCE sought to fulfil the first two objectives listed above. Progress toward quantifying and fleshing out the system of DWBCs on a global basis (Section 4.5.2) was achieved through strategic placement of moored arrays along the western boundaries of the world's oceans. Recognizing that quantification of the deep circulation on a global basis was well beyond our means, research on this objective was

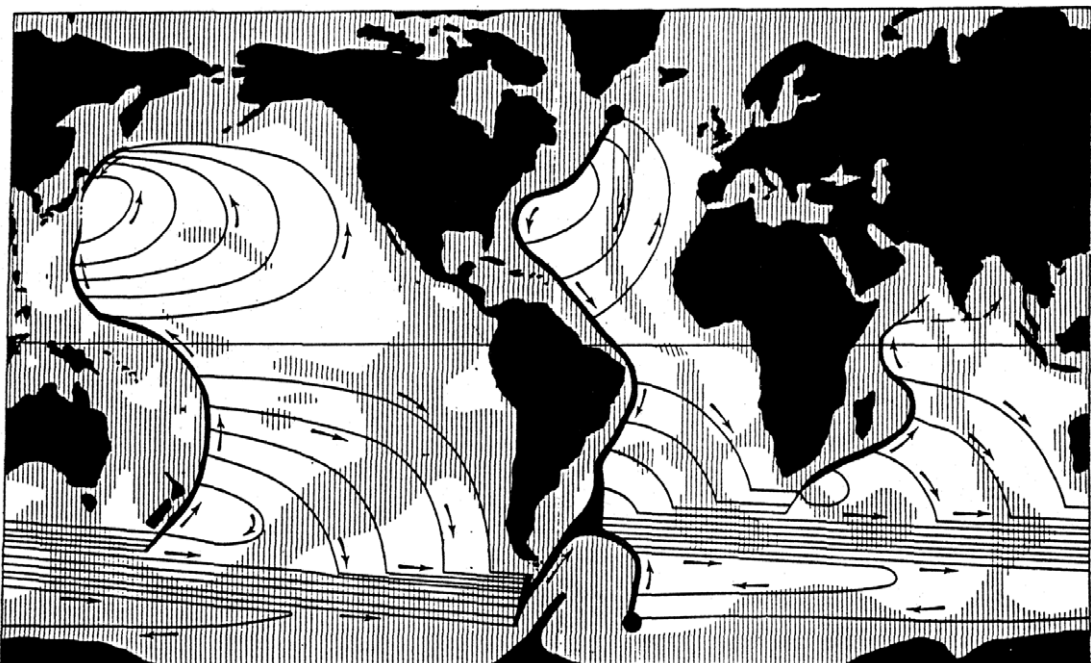


Fig. 4.5.1 The scheme for the circulation of the abyss by Stommel (1958) as driven by two isolated sinking regions at the poles and uniform upwelling over the rest of the globe.

focused, instead, on a small region of the South Atlantic – the Brazil Basin – in a programme known as the Deep Basin Experiment (DBE), results from which are described in Section 4.5.3. A brief summary ends this chapter (Section 4.5.4).

4.5.2 Deep Western Boundary Currents

After Stommel proposed his deep circulation scheme, Swallow and Worthington (1957, 1961) quickly discovered the DWBC off the east coast of the USA using traditional hydrographic measurements and the newly developed, neutrally buoyant float (the ‘Swallow float’). Although the signature of the DWBC had certainly been recognized earlier by Wüst (1935) in the *Meteor* hydrographic sections across the Atlantic, the direct velocity measurements were not subject to the usual reference level issues. But recognition that these deep boundary currents carry water that has been in recent contact with the atmosphere has allowed investigators to identify them from section data and build a fragmentary picture of their global distribution (Fig. 4.5.2). At the beginning of WOCE the deep Pacific was relatively unexplored: on the basis of a small number of hydrographic sections and measurements within the Samoan Passage (at 10°S, no. 22 on Fig. 4.5.2) it was known that Circumpolar Deep Water (CDW, more loosely called Antarctic

Bottom Water or AABW) flowed northward along the western boundary, but its entry into and circulation within the North Pacific was less well mapped out. Hence the call for four moored arrays along the western boundary, two of which did not occur – the one south of the Aleutians (no. 26, Fig. 4.5.2) and another in Wake Passage (no. 23). Two arrays were suggested for the eastern South Pacific, one to explore the possible flow northward along the eastern flank of the East Pacific Rise (no. 20) and the other to investigate the deep flow along the coast of South America at 35°S (no. 19). Neither was attempted.

Historically, the Atlantic has been much better measured. Through the systematic sampling of hydrographic programmes such as the *Meteor* Expedition of the 1920s and the International Geophysical Year of the 1950s, the network of DWBCs has been sketched out relatively well, although quantified in only a few places with moored arrays. Within the Atlantic sector it was proposed to establish new moored arrays, mainly to measure the overflows from the Greenland and Iceland Seas (nos 1 and 2) and in support of the DBE (nos 3–9, see Section 4.5.3).

The entry of AABW into the southern Indian Ocean was explored with three arrays (nos 15, 17 and 18). In this ocean there are two major meridionally oriented ridge systems that give the

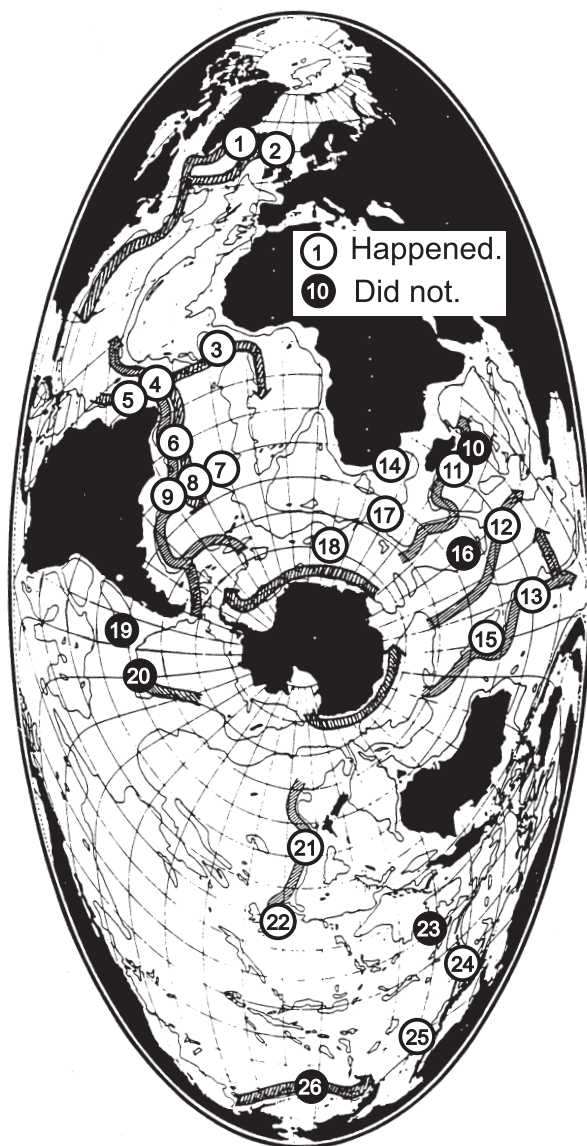


Fig. 4.5.2 The system of DWBCs as it was known in the late 1980s with sites proposed for moored current meter arrays for the study of DWBCs in WOCE: open circles are used for those that were undertaken and filled ones for those that were not. The various locations with their WOCE designations are: (1) ACM1, Denmark Straits overflow; (2) ACM1, Faroe Bank Channel; (3) ACM11, Romanche & Chain Fracture Zones; (4) ACM10, Equatorial passage; (5) ACM7, 50°W; (6) ACM24, 19°S; (7) ACM13, Hunter Channel; (8) ACM12, Vema Channel; (9) ACM3, 30°S; (10) ICM5, 8°S; (11) ICM3, Madagascar; (12) ICM3, central Indian Ridge; (13) ICM3, 90°E Ridge; (14) ICM1, deep Agulhas; (15) SCM4, Broken Plateau; (16) SCM5, Southeast Indian Ridge; (17) SCM9, Crozet Plateau; (18) SCM6, Crozet-Kerguelen Islands; (19) PCM14, 35°S; (20) PCM10, East Pacific Rise; (21) PCM9, Chatham Rise; (22) PCM11, Samoan Passage; (23) PCM12, Wake Passage; (24) PCM7, Izu-Ogasawara Ridge; (25) PCM6, Hokkaido; (26) PCM8, Aleutians. Base chart with current fragments courtesy of B. Warren.

possibility of three western boundary currents. Moored arrays were placed across each along 20°S (nos 11–13). In addition, measurements of the deep boundary currents along the African coast north of Madagascar at 10°S (no. 10) and on the Southeast Indian Ridge near 30°S (no. 16) were proposed but did not happen.

4.5.2.1 The Pacific

Deep water flows into the Pacific from the south along the Continental Rise east of New Zealand and makes its way northward through the Samoan Passage at 10°S. The WOCE period measurements have served mainly to quantify the transports in this region. An ambitious array of 60 current meters on 20 moorings was placed from the 3000 m isobath on the Tonga-Kermadec Ridge to a point more than 10° further offshore (Whitworth *et al.*, 1999; no. 21, Fig. 4.5.2). The spatially integrated and time-averaged flow of CDW over the 22-month measurement period was calculated to be 15.8 Sv while the root-mean-square (rms) variability was a large fraction of this at 9.2 Sv. This variability arose from low-frequency motions at several identifiable periods: 50 days, 20 days and 10 days. Taking the longest as the most conservative to use in calculations of degrees of freedom, the indicated zero crossing of the time-lagged correlation function would be at about 12.5 days (i.e. a quarter period) and the integral from zero to this point of order 8 days, say (it would be 6.25 days if the correlation dropped linearly from unity to zero over this interval). Thus, from 22 months of measurements there are about 40 degrees of freedom and the standard error of the mean transport is about 1.4 Sv, as shown in Fig. 4.5.3.

Some 20° to the north at the Samoan Passage, Roemmich *et al.* (1996; no. 22, Fig. 4.5.2) reported a mean northward transport of bottom water of 10.6 Sv with a standard error of 1.7 Sv from an 18-month measurement programme. Here again there is substantial variability centred on periods of 30 days, which Rudnick (1997) hypothesized results from a topographically induced resonance. Of the 10.7 Sv total transport only 7.1 Sv flows directly through the passage: the rest is through a gap in the Robbie Ridge to the west (1.1 Sv) and along the flanks of the Manihiki Plateau to the east (2.8 Sv), both estimates coming from dynamic calculations performed on single hydrographic sections. This natural variability easily encompasses the range of transport estimates

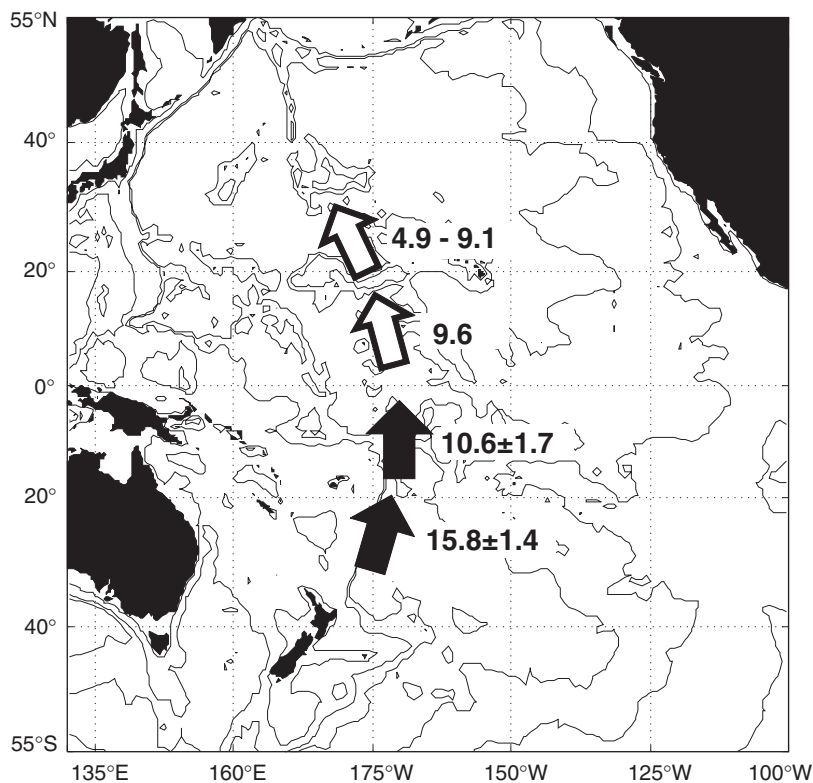


Fig. 4.5.3 Transport estimates, in Sverdrups, from the Pacific for the Circumpolar Deep Water. Filled arrows give transports and their standard errors as derived chiefly from moored array measurements. Open arrows are from dynamic computations on hydrographic section data.

computed by Johnson *et al.* (1994a) and Freeland (2001) from hydrographic section data and the application of a 1.2°C reference surface.

On the basis of the Stommel schematic (Fig. 4.5.1) one would expect the DWBC to diminish northward as water bleeds into the interior and to vanish by the time it reaches the latitude of southern Japan ($\sim 25^\circ\text{N}$). The measurements off New Zealand and in the Samoan Passage described above do indicate such a drop, which is significant at the standard error level (but not at the 95% confidence level). There are no other direct measurements of transport further north although dynamic computations by Johnson and Toole (1993) gave 9.6 Sv net northward flux of CDW across 10°N , and two separate computations (using the same data set!) gave 4.9 Sv (Bryden *et al.*, 1991) and 9.1 Sv (Roemmich and McCallister, 1989) at 24°N . This is comforting evidence for the expected drop in transport of bottom waters toward the north in the Pacific.

Two moored arrays were placed in the suspected southward-flowing boundary current regime east of Japan: one south of Hokkaido (Owens and

Warren, 2001; no. 25, Fig. 4.5.2) and the other to the east of Honshu at the point where the Kuroshio leaves the coast (Hallock and Teague, 1996). The flow, inshore of the Japan and Kuril Trench axes, was found to be southward in the mean. Further offshore it appeared to return northward in a deep circulation trapped to the sharply changing trench geometry, perhaps as might be anticipated from the Stommel–Arons theory modified to include the bottom relief (e.g. Johnson, 1998; Warren and Owens, 1988) although this is not entirely clear (Owens and Warren, 2001).

4.5.2.2 The Atlantic

NADW

The Atlantic continues to be the best measured basin and the DWBCs have been quantified by long-term measurements at a dozen or so locations stretching from the overflow regions in the north to the Scotia Arc in the south (Fig. 4.5.4). Starting in the north, where the North Atlantic Deep Water (NADW) is formed through mixing of its component parts (from the Labrador Sea, Denmark Straits and Iceland–Scotland Ridge as well as AABW),

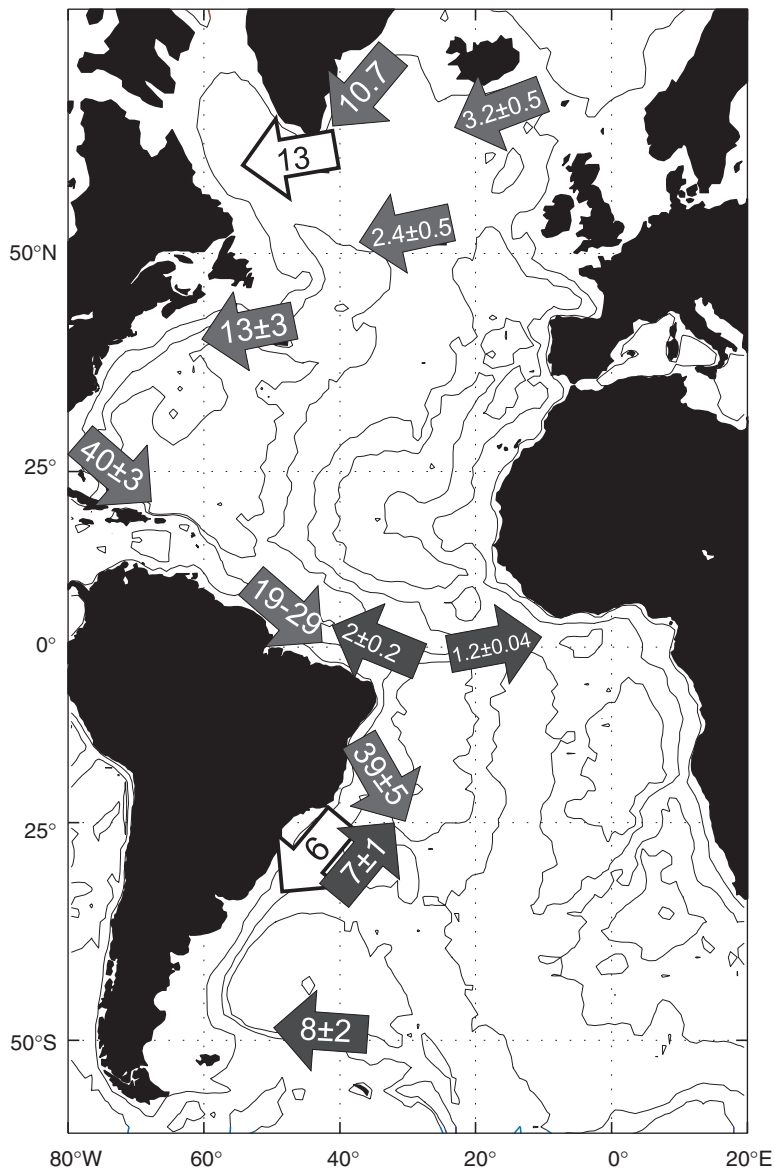


Fig. 4.5.4 Transport estimates, in Sverdrups, from the Atlantic for the NADW and AABW. Filled arrows give transports and their standard errors as derived chiefly from moored array measurements. Arrows with a northward component are for AABW while those with southward tendencies are used to distinguish the warmer NADW. Open arrows are derived mainly from dynamic computations on hydrographic section data.

Saunders (1996; no. 2, Fig. 4.5.2) estimated that 3.2 ± 0.5 Sv of water with $\sigma_0 > 27.8 \text{ kg m}^{-3}$ flows southward along the eastern flank of the Mid-Atlantic Ridge toward the Charlie-Gibbs Fracture Zone at 53°N , where he found that 2.4 ± 0.5 Sv continues westward into the western basin (Saunders, 1994). Surely the prize for the most ambitious attempt at measuring DWBC flows goes to the Dickson and Brown (1994; no. 1, Fig. 4.5.2) (see also Dickson *et al.*, 1990) effort downstream of the Denmark Straits. Here some 96 instruments were deployed on three sections across the current.

Although the maximum deployment period was about 1 year, the main ‘Angmagssalik’ array was set three times to give an almost unbroken 3-year record. Total transport of dense water (again, $\sigma_0 > 27.8 \text{ kg m}^{-3}$) was found to be 10.7 Sv at this site, a substantial increase over that believed to be coming through the Straits. Unfortunately, no estimate of error or variance was given but the authors stated that the variance was comparable to the energy in the mean and the time scales were short, of less than 10 days, so the error must be just a fraction of a Sverdrup. Summing the two northern

components, the 3 Sv from the eastern basin and the 10 Sv coming southward along the Greenland coast, gives very nearly the 13.3 Sv that Clarke (1984) reported at the southern tip of Greenland (Cape Farewell), again with unquantified errors.

The DWBC then traces the boundary of the Labrador Sea before entering the subtropics at the Grand Banks. At this point, just to the west of the southern tip of the Banks, Pickart and Smethie (1998) have calculated that 13.3 Sv of water with $\sigma_0 > 27.8 \text{ kg m}^{-3}$ flow westward. This estimate is based on the average of three hydrographic sections taken over a period of 4 years referenced with velocity profiling instruments. The reported variance is 4.2 Sv and, with just two degrees of freedom, the error in the mean is 3 Sv: by this point along the boundary there has been no significant change in transport from that observed at Cape Farewell.

Further south the next well-measured site is at 27°N, where a current meter array monitored the western boundary currents to the east of the island of Abaco in the Bahamas for a period of almost 5 years from 1987 to 1992 (Lee *et al.*, 1996). Here, the DWBC was defined on the basis of the direction of the mean flow: above 800 m depth the flow was primarily to the north (the Antilles Current) while that below was southward (the DWBC). After some judicious sampling was applied, as the core of the deep flow was often not adequately resolved by the array, the total deep transport was found to be an astonishing $40 \pm 3 \text{ Sv}$! This enhancement over that seen further north and that inferred necessary to balance the meridional overturning ($\sim 13 \text{ Sv}$) suggests that much of the 40 Sv is returned to the north in an offshore recirculation zone that was not adequately instrumented.

However, similar large southward transports within the NADW further south have been reported. At 8°N, Johns *et al.* (1993), on the basis of a single mooring, several hydrographic sections, some Pegasus velocity profiles and a heuristic model of the current structure, computed a southward transport of 22 Sv for the flow below 2500 m – the Lower NADW. Much of this is believed to be returned to the north in another recirculation when the DWBC encounters a topographic constriction near 6°N.

Closer to the equator at 44°W 2-year-long moored array measurements gave 14–17 Sv for the Upper NADW, depending on analysis method (Schott *et al.*, 1993a; Fischer and Schott, 1997; no. 5, Fig. 4.5.2). Sparse sampling of the lower

NADW gave estimates varying between 4.5 Sv and 12 Sv so the total transport of NADW across the equator has a large range: 18.5–29 Sv, consistent with the work of Rhein *et al.* (1995), who found that $26.8 \pm 7.0 \text{ Sv}$ cross 35°W between 2°N and 5°S with $19.5 \pm 5.3 \text{ Sv}$ reaching 5°S. The actual pathways for flow crossing the equator appear to be complex. Based on the trajectories of 14 SOFAR (SOund Fixing And Ranging) floats ballasted to be at 1800 m, Richardson and Fratantoni (1999) suggested a combination of meridional flow near the boundary and elongated zonal flows in the interior: eastward jets at 2°N and 2°S and a westward one on the equator, patterns that are supported by tracer distributions (e.g. Weiss *et al.*, 1985; Andrié *et al.*, 1998, 1999). Deep jets, trapped to the equator and first observed in the Atlantic by Ponte *et al.* (1990), have now been shown to reverse with the seasons by Gouriou *et al.* (1999) but to change little over a period of 5 years for the same season of the year.

At 18°S in the South Atlantic, Weatherly *et al.* (2000; no. 6, Fig. 4.5.2) reported a total southward transport of NADW of 39 Sv. The rms variance is $\sim 20 \text{ Sv}$, which, combined with a 20-day integral time scale for the area (Hogg and Owens, 1999) and the 18-month record length, gives the standard error of about 5 Sv shown on Fig. 4.5.4. Again the authors appealed to a possible recirculation further offshore to return part of this large flux, but had no measurements to support its existence. Indeed, direct measurements in the interior by floats (Hogg and Owens, 1999, see below) have shown only zonal flows. On the basis of dynamic computations from hydrographic sections at 19°S and 30°S, Zangenberg and Siedler (1998) computed a rapid decline in NADW transport from 27 Sv at 19°S to 6 Sv at 30°S and argued that this divergence is taken up by a zonal flow to the east in the latitude band 25–30°S. The float data, to be described below, are in qualitative support.

It is curious that the DWBC transports of NADW at subtropical and high latitudes are all of the order needed to balance the meridional overturning (13 Sv), while those in the tropical band are consistently higher by a factor of 2–3. Although this could well point to the existence of repeated and disconnected recirculation zones in this region (e.g. Schmitz and McCartney, 1993), finding the offshore northward return flow has been an elusive quest.

AABW

It has been conventional to call the deepest water mass in the North Atlantic ‘Antarctic Bottom Water’ and, as its name implies, its ultimate source is in the Antarctic region. Just as NADW represents a mixture between various source waters, AABW is a mixture of CDW, Weddell Sea Deep Water (WSDW) and NADW. Its upper boundary within the Atlantic is usually taken to be around 2.0°C , potential temperature, or some related potential density surface, rather than the 1.2°C surface as is used in the Pacific.

Weddell Sea Deep Water enters the South Atlantic through one or more gaps in the Falkland Ridge, which separates the Georgia and Argentine Basins. Along the northern flank of this topographic feature Whitworth *et al.* (1991) estimated that 8.2 Sv of water colder than 0.2°C (their definition of WSDW) flows westward. The standard deviation is 7 Sv and they identified a principal period for variability of 70 days, apparently resulting from a meandering of the Circumpolar Current. With a 14-month observation period this gives about 12 degrees of freedom and a standard error in the mean of 2 Sv . Whitworth *et al.* (1991) suggested that most of the 8.2 Sv is recirculated water as the pure WSDW component has a westward transport of just 2.5 Sv .

At the northern end of the Argentine Basin, the Santos Plateau–Rio Grande Rise system is a major impediment for the continued northward flow of bottom water. Here Hogg *et al.* (1999; nos 7–9, Fig. 4.5.2), through use of 2-year-long measurements, calculated that a total of 6.9 Sv of water colder than 1.9°C flows into the Brazil Basin: this is partitioned as 4 Sv through the Vema Channel (no. 8) and $2.9 \pm 1.2\text{ Sv}$ through the Hunter Channel (no. 7) further to the east, with the relatively large error resulting from poor spatial resolution of the flow by the moored array (Zenk *et al.*, 1999a). Although Hogg *et al.* (1999) failed to quantify the error in the earlier Vema Channel transport measurements, Hogg *et al.* (1982) reported a standard deviation for the transport of 1.2 Sv and Hogg and Owens (1999) computed an integral time scale for the area of about 10 days. This gives a standard error in the mean, based on a 2-year observation programme, of $\pm 0.2\text{ Sv}$. Thus the flow into the Brazil Basin is $6.9 \pm 1.2\text{ Sv}$, with the error being dominated by that in the Hunter Channel transport number.

The bottom water flowing into the Brazil Basin has just two exits and both are at the equator: the Romanche-Chain Fracture Zone complex in the Mid-Atlantic Ridge (no. 3, Fig. 4.5.2) and a deep equatorial passage that allows AABW entrance into the western North Atlantic (no. 4). Both topographic constrictions were well planted with moorings during WOCE as part of the Deep Basin Experiment (see Section 4.5.3). With respect to the first (Romanche-Chain FZ), Mercier and Speer (1998) estimated that 1.22 Sv flows to the east. This is a remarkably steady flow with a standard deviation of just $\pm 0.25\text{ Sv}$. Combined with a reportedly short time scale of 10–20 days and a 2-year record, the standard error of the mean is just $\pm 0.04\text{ Sv}$. At the western exit Hall *et al.* (1997) reported that $2.0 \pm 0.2\text{ Sv}$ of AABW flows out of the Brazil Basin.

Further north there has been little direct measurement of AABW transports. Based on property distributions it is apparent that the AABW follows the western flank of the Mid-Atlantic Ridge, rather than the western boundary of the basin where Schmitz and McCartney (1993) suggested a rather complicated set of recirculations. Some of the water progressing northward along the Mid-Atlantic Ridge does exit to the east through the Vema Fracture Zone (not to be confused with the Vema Channel) near 11°N . Fischer and Schott (1997) computed $1.8\text{--}2.0\text{ Sv}$ based on synoptic data.

Atlantic summary

The Stommel (1958) scheme (Fig. 4.5.1) was for the depth-integrated flow of the abyss below about 2000 m. The composite of the AABW and NADW transports (Fig. 4.5.4) do conform to his picture in a qualitative sense: there is, all along the western boundary, a net transport toward the south. However, in a more quantitative sense there is disagreement as the transport should steadily decrease while supplying fluid to the interior and it manifestly does not do so. The various investigators who have produced the large transport numbers in the tropics each ascribe them to possible recirculation further offshore but direct measurement, so far, has failed to reveal it in a convincing manner.

4.5.2.3 The Indian Ocean

Although the moored arrays set in the Indian Ocean had all been recovered by mid-1997 there is, as of this writing, little or no presentation of the

results in the literature. Beal and Bryden (1997) have identified a deep countercurrent beneath the Agulhas at 30°S (no. 14, Fig. 4.5.2) using a lowered acoustic Doppler profiler. This current transports approximately 6 Sv of Red Sea Water and Antarctic Intermediate Water (AAIW) toward the northeast. Read and Pollard (1997) have studied the deep flow into the Mozambique Basin (no. 17, Fig. 4.5.2). Based on sparse direct current measurements and two hydrographic sections there appears to be 1 Sv of WSDW entering below 4000 m.

4.5.2.4 Inferences for mixing

A number of the measurements described above were made in passages that constrain the flow from one basin to another. Downstream of these passages the deeper isopycnals and isotherms can be contained entirely within the basin, or may connect to other basins through narrow passages where the transport has been measured. Using simple heat and mass balances for these surfaces Whitehead and Worthington (1982) and Hogg *et al.* (1982) were able to infer basin-averaged 'vertical' (i.e. perpendicular to the property surface) mixing rates of a few square centimetres per second, well above the direct estimates made in the thermocline (see Toole and McDougall, Chapter 5.2). With the many additional arrays placed across passages these budgets were repeated to build up a sparsely sampled, global picture of abyssal, cross-isopycnal dissipation (Fig. 4.5.5). The high values reported by Whitehead and Worthington (1982) and Hogg *et al.* (1982) have been echoed in the Discovery Gap (eastern North Atlantic) by Saunders (1987) and in the Amirante Passage of the western Indian Ocean (Johnson *et al.*, 1998). Even higher values have been computed for the deepest water masses flowing through the Romanche Fracture Zone (up to $500 \text{ cm}^2 \text{ s}^{-1}$) by Ferron *et al.* (1998), for the Samoan Passage (again, up to $500 \text{ cm}^2 \text{ s}^{-1}$) by Roemmich *et al.* (1996), and for a gap at 28°S in the Ninetyeast Ridge of the Indian Ocean (up to $100 \text{ cm}^2 \text{ s}^{-1}$) by McCarthy *et al.* (1997).

4.5.3 The interior: The Deep Basin Experiment

The results we have been describing all concern the measurement of flows in places where they

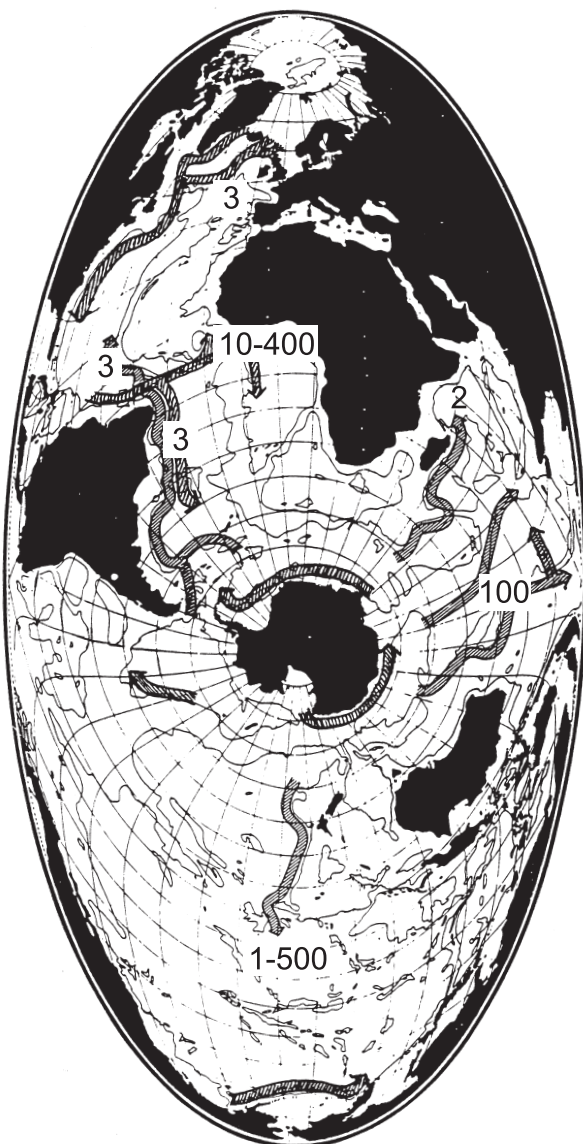


Fig. 4.5.5 Estimates of cross-isotherm diffusivity, in $\text{cm}^2 \text{ s}^{-1}$, made by balancing the inflow of mass and heat to abyssal basins downstream of passages.

are expected to be swift, namely along the deep western boundaries of ocean basins or in passages that intercept these flows. The Stommel scheme also predicts the nature of the interior circulation, albeit based on the simple assumptions of uniform upwelling at the top of the abyss and a flat-bottomed ocean. Shortly after the publication of this concept the DWBC south of Cape Romain (South Carolina) was discovered by Swallow and Worthington (1957, 1961) and this led, almost immediately, to the attempt to measure the slow poleward flow in the interior southwest of Bermuda

that, instead, revealed the mesoscale eddy phenomenon (Crease, 1962; Swallow, 1971).

Advances in technology, principally the RAFOS float (reverse of SOFAR; see Davis and Zenk, Chapter 3.2), suggested to a number of investigators during the formulation of WOCE plans that it was time to revisit the question of the deep interior circulation. Certainly, given the numbers needed to average out the eddy noise in the presence of the expectedly weak mean flow, it was not feasible to attack the global deep circulation problem. Instead, it was decided to concentrate on a sub-basin of the South Atlantic – the Brazil Basin – where sufficient background information was available to suggest that the ‘mean flow’ could be measured. Prior knowledge included the Hogg *et al.* (1982) computation of elevated mixing rates (see Section 4.5.2.4), which demanded significant upwelling and supported the Stommel notion that meridional flows should be present. Based on computations of eddy kinetic energy from satellite measurements of sea surface elevation, this basin was expected to be relatively ‘quiet’ such that the signal-to-noise ratio would be enhanced. The South Atlantic is also a crossroads of water masses. Below the thermocline there are three major ones: the AAIW and AABW with southern sources are split in the vertical by NADW from the north. A final attribute of the Brazil Basin is that its geometry is relatively simple (Fig. 4.5.6). It is bounded on all four sides by the coast or ridges through which there are only a small number of passages (four) that permit flow of the bottom water to, or from, neighbouring basins.

The bulk heat and mass balances give basin-averaged estimates for diffusivity and fluxes across constant property surfaces. As was pointed out by Munk (1966), the mixing can be accomplished in a variety of ways: intense mixing along boundaries has become a popular alternative to Stommel’s uniformly distributed hypothesis (e.g. Armi, 1978). Hence, the hydrographic programme for the DBE was designed to allow calculation of budgets on scales small enough that one might be able to discriminate between boundary and interior locations. In addition, a deliberate tracer release was performed along with associated microstructure measurements in order to observe directly the vertical mixing process at a particular location over the rough topography of the Mid-Atlantic Ridge.

4.5.3.1 Bounding arrays and budgets and mixing

Moored arrays were placed along the southern boundary of the Brazil Basin, including the Vema and Hunter Channels, and in the two equatorial passages. As was described in Section 4.5.2, the net inflow of AABW (potential temperatures less than $\sim 2^\circ\text{C}$) is $6.9 \pm 1.2 \text{ Sv}$ while that flowing out at the equator is $1.22 \pm 0.04 \text{ Sv}$ to the east through the Romanche-Chain complex and $2.0 \pm 0.2 \text{ Sv}$ to the west into the western North Atlantic. The net inflow into the Basin is, therefore, $3.7 \pm 1.2 \text{ Sv}$, which must upwell if a steady state is to be maintained. This is little different from the estimates made by Hogg *et al.* (1982): Morris *et al.* (1997) have used the DBE data set to redo the flux balance calculation: they found that the diffusivity is approximately $3 \pm 0.8 \text{ cm}^2 \text{ s}^{-1}$ and has no significant variation with property type used for the bounding surface.

An inert chemical, sulphur hexafluoride (SF_6), was released on the western flank of the Mid-Atlantic Ridge near 20°S in an attempt to observe directly and quantify the stirring of the tracer across density surfaces (Ledwell *et al.*, 2000, see also Toole and McDougall, Chapter 5.2). Implied diffusion rates vary from order $2\text{--}4 \text{ cm}^2 \text{ s}^{-1}$ over the lower segments of the Mid-Atlantic Ridge to order $10 \text{ cm}^2 \text{ s}^{-1}$ over the rougher segments. St Laurent (1999) has developed a dynamically consistent interpretation of the hydrographic, microstructure and tracer data. Bottom-enhanced mixing driven by the barotropic tide interacting with the rough topography of the Mid-Atlantic Ridge forces a secondary circulation over the various fracture zones. With large extrapolation it is possible to account for most of the mixing and upwelling that is implied by the net inflow to the basin to be occurring over the rough topography of the ridge flanks.

4.5.3.2 Lagrangian measurements

The upper water mass, AAIW, is discussed elsewhere (Davis and Zenk, Chapter 3.2; Hanawa and Talley, Chapter 5.4), so here we will concentrate on the two deepest water masses. With Stommel’s scheme in mind, as well as that of Reid (1989), it was expected that the signal (the mean flow) would be less than 1 cm s^{-1} while the rms noise from the mesoscale eddy field would be of the

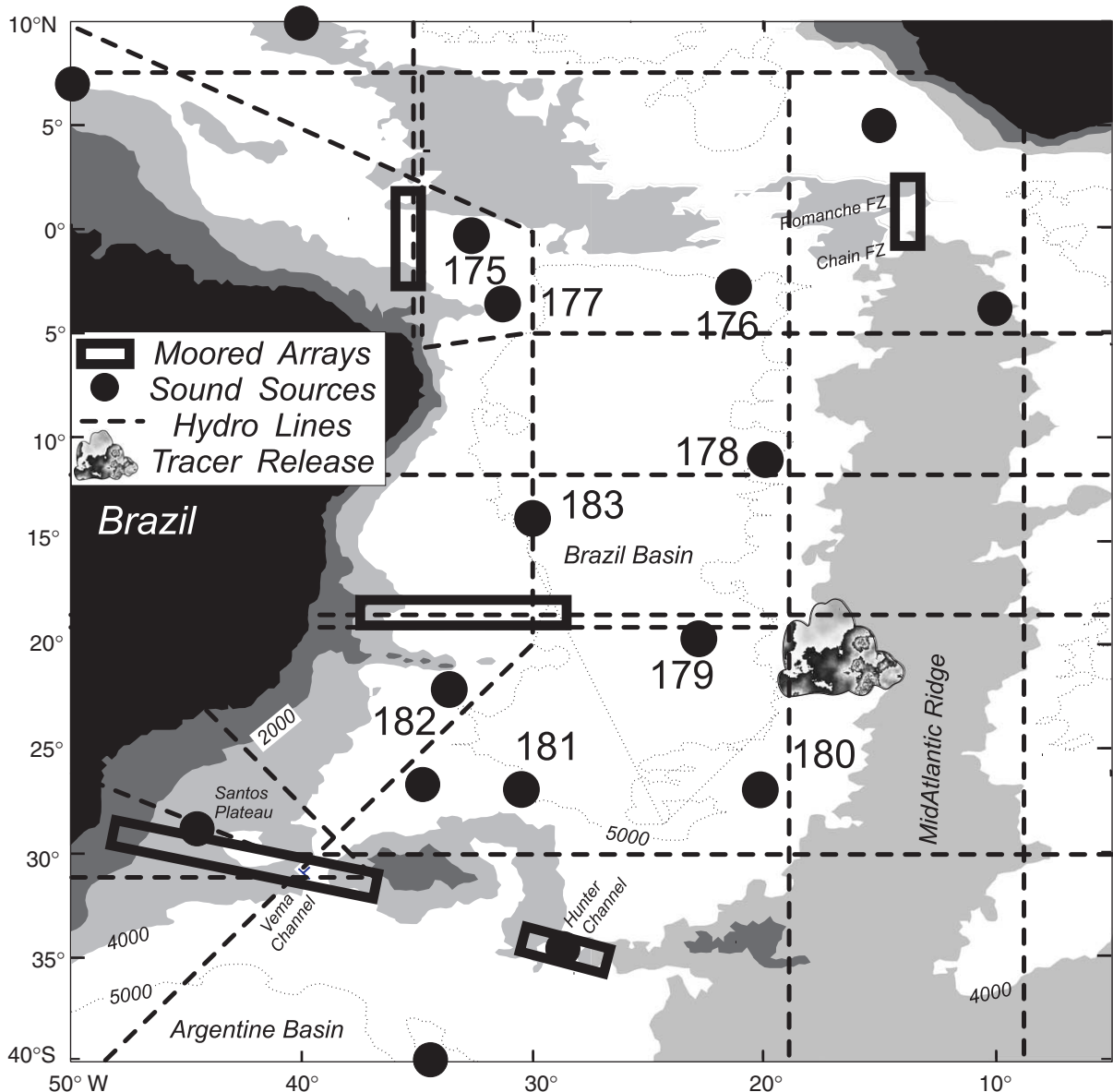


Fig. 4.5.6 The Deep Basin Experiment experimental plan. Symbols are identified in the legend. Solid circles are an array of sound sources used for locating neutrally buoyant floats placed at three levels: the AAIW (~ 800 m), NADW (~ 2500 m), and AABW (~ 4000 m). Those with numbers also contained current meters at 2500 m depth.

same order. Resolution of the mean flow on scales of 500 km then demanded more than 200 floats, with lifetimes of 2.5 years, in order to reduce the eddy error to less than 1 mm s^{-1} (see Hogg and Owens, 1999). Fiscal realities and technological problems reduced that number to approximately 70 at each of the AABW and NADW surfaces. For those floats that lasted the full 2.5 years we show in Fig. 4.5.7 (see Plate 4.5.7, p. 300) their net displacements. At neither level do they conform to the Stommel schematic. Although the DWBC is visible at both levels, interior displacements are mainly zonal and possess small meridional length

scales. The implied circulation is also quite unlike any of the modern interpretations of hydrographic data, which are all dominated by meridional flows in the interior (e.g. Reid, 1989; Zhang and Hogg, 1992; Speer and Zenk, 1993; Durrieu De Madron and Weatherly, 1994).

This zonal interior is consistent with the notion that little mixing is occurring away from the rough topography: little mixing implies little upwelling, no vortex stretching and zonal flows to conserve the planetary vorticity component (ignoring possible complications from topography).

Although the various circulation schemes that have been assembled from hydrographic data are generally in qualitative disagreement with the float data, there is some consistency to be found there. For example, we show in Fig. 4.5.8 (see Plate 4.5.8, p. 300) the oxygen distribution on six potential density surfaces within the NADW from a section along 25°W (from Talley and Johnson, 1994) along with the mean zonal flows calculated from the float and current meter data sets in the Brazil Basin (selected to be away from the western boundary). There is rough agreement between the source direction implied by the oxygen and the directly observed mean flows: the interior flow is almost Wüstian in the sense that it appears to flow down property tongues. Rüth *et al.* (2000) have recently reported that the Mid-Atlantic Ridge is a source of primordial helium to the NADW layer of the South Atlantic. Sections of terrigenic ^3He at 11°S and 30°S show plumes extending westward from the ridge crest. The first of these is coincident with generally eastward flow and oxygen-rich water (Fig. 4.5.8) while at 19°S the ^3He does not spread far from the ridge. Whether these findings are in contradiction or reflect the probably complex, zonally banded, time-varying, circulation has yet to be determined.

There is a broad band of eastward flow between 20°S and 25°S within the NADW that appears to originate in the DWBC. This could well supply the ‘Namib Col Current’ (Warren and Speer, 1991; Speer *et al.*, 1995b), which is believed to extend across the whole of the South Atlantic to the Namib Col, a break in the Walvis Ridge near 22°S. This is also the band of latitudes in the South Atlantic at which the minimum depth of the Mid-Atlantic Ridge is the deepest, reaching 2500 m on average versus 2000 m to the north (Vanicek, 1998).

4.5.3.3 Time variations

In designing the DBE an assumption was made that time scales, beyond the mesoscale, would be long enough that a quasi-steady hypothesis could be made. Indeed, the estimates of diffusion rates from bulk balances depend on this. However, this has not proven to be the case. For example, a line of floats set along 19°W between the equator and 20°S at 4000 m (Fig. 4.5.7b, see Plate 4.5.7b, p. 300) all move to the west, more or less steadily. Another line of floats set about a year later move in the

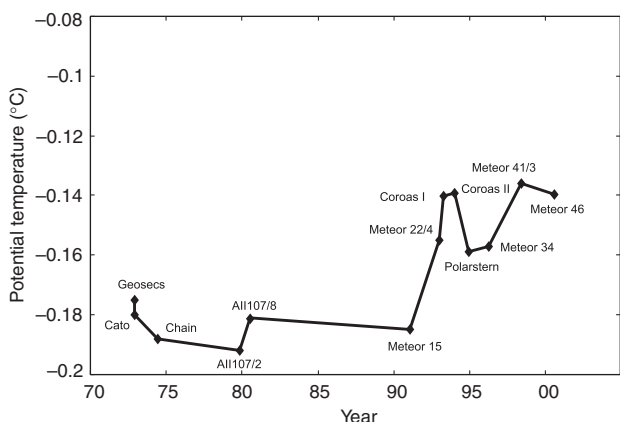


Fig. 4.5.9 Temperature of the coldest water within the Vema Channel versus time. Adapted from Hogg and Zenk (1997) with the most recent point courtesy of Walter Zenk (personal communication).

opposite direction. Low-frequency motions of inter-annual time scale are the most likely explanation.

Within the Vema Channel measurements of hydrographic properties have been made repeatedly since the first station was occupied during GEOSECS in 1972 (Fig. 4.5.9). Being careful to select stations that were within a cold lens hugging the eastern flank of the channel, Hogg and Zenk (1997) reported an abrupt warming of the bottom water in the early 1990s, at the beginning of the DBE. This warming has also been observed in the Argentine Basin by Coles *et al.* (1996) and Hall *et al.* (1997).

4.5.4 Summary

Progress has been made on quantifying the transports of DWBCs in the various ocean basins. However, the large variability in time and small spatial scales put great demands on available technology. Almost all investigators who have attempted to quantify deep transports of water masses have remarked on the surprisingly large temporal variations in their studies and the difficulties in reconciling moored array observations with those from synoptic sections. Measurements of large DWBC volume fluxes within the tropical and subtropical Atlantic point to extensive recirculation along the western boundary, but this is only inferred to account for the large computed transports in the subtropics. In the Brazil Basin, the large transport observed near 19°S seems to diverge a little further south and feed a zonal current that extends across

the whole of the South Atlantic between 20°S and 25°S.

The concept of a quasi-steady mean circulation also seems elusive. John Swallow's failed attempt to observe it off Bermuda during the *Aries* Expedition discovered, instead, the ocean mesoscale phenomenon. By choosing a location in the world's oceans where the mesoscale energy would be small, DBE investigators seem, instead, to have found an energetic, longer-period variability. As has been discovered elsewhere in the very spotty holdings that we have of long time series, the frequency spectrum is generally red, a particularly good example being the increasingly long time series from 'KIEL 276', a mooring that has been maintained for 20 years in the eastern North Atlantic (Müller and Siedler, 1992).

However, there are aspects of the deep circulation that are robust. Heat and mass transports through deep passages are quite steady, in contrast to those elsewhere along the boundaries. The consequent implications for upward diffusion of properties show mixing rates greater, indeed, in some places much greater, than $1 \text{ cm}^2 \text{ s}^{-1}$, in the deep ocean wherever such estimates have been made.

Acknowledgements

Continued support from the National Science Foundation through grants OCE 90-04396, OCE 90-04864 and OCE 94-15509 is much appreciated. Comments from two reviewers and Mindy Hall were very helpful. This is contribution number 9997 from the Woods Hole Oceanographic Institution.

4.6

The Antarctic Circumpolar Current System

Stephen R. Rintoul, Chris W. Hughes and Dirk Olbers

4.6.1 Flow in the zonally unbounded ocean

The absence of land barriers in the latitude band of Drake Passage has a profound influence on the dynamics of currents in the Southern Ocean and, more generally, on the earth's climate. Within this band, the strong eastward flow of the Antarctic Circumpolar Current (ACC) connects each of the ocean basins. Sverdrup dynamics in their usual form cannot be applied to flows within a zonally unbounded ocean, and as a consequence the dynamics of the ACC have long been a topic of debate. Eddy fluxes are believed to play a more central role in both the dynamical and thermodynamical balances of the Southern Ocean than in other areas of the world ocean. The interbasin connection provided by the ACC permits a global overturning circulation to exist; the overturning circulation, in turn, dominates the global transport of heat, fresh water and other properties that influence climate (see Gordon, Chapter 4.7; Bryden, Chapter 6.1; and Wijffels, Chapter 6.2). The vigorous interbasin exchange accomplished by the ACC also admits the possibility of oceanic teleconnections, where anomalies formed in one basin may be carried around the globe to influence climate at remote locations (e.g. White and Peterson, 1996). The fact that no net meridional geostrophic flow can exist across the unblocked latitudes isolates the Antarctic continent from the warmer waters at lower latitudes to some extent, contributing to the glacial climate of Antarctica; what heat does get carried poleward to balance the heat lost to the atmosphere must be carried by eddies.

Energetic interactions between the atmosphere, ocean and sea ice result in the formation of water masses that play an important role in the global overturning circulation, and ventilate a substantial fraction of the volume of the global ocean. As a result of these unique aspects, many characteristics of the present-day ocean circulation and climate reflect the influence of the Southern Ocean.

The major currents of the southern hemisphere oceans are shown in Fig. 4.6.1. The ACC is the dominant feature in terms of transport, carrying a mean transport of 134 ± 13 Sv through Drake Passage (Whitworth, 1983; Whitworth and Peterson, 1985). The ACC consists of a number of circumpolar fronts, which correspond to water mass boundaries as well as deep-reaching jets of eastward flow (Orsi *et al.*, 1995). The two main fronts, the Subantarctic and Polar Fronts, are shown in Fig. 4.6.1. Poleward of the ACC, cyclonic gyres are found in the embayments of the Weddell and Ross seas. Westward flow near the continental margin of Antarctica (the Antarctic Slope Front) is found at many locations around the continent (Jacobs, 1991; Whitworth *et al.*, 1998). Equatorward of the ACC, the circulation consists of westward-intensified subtropical gyres in each basin. Strong poleward flow in the western boundary currents is balanced by weaker equatorward flows in the interior of the basins. The main focus of this chapter is on the ACC itself, but exchanges between the ACC and the subtropical and subpolar regimes are also an important part of the story.

While the horizontal flows shown in Fig. 4.6.1 are the dominant circulation features, the weaker

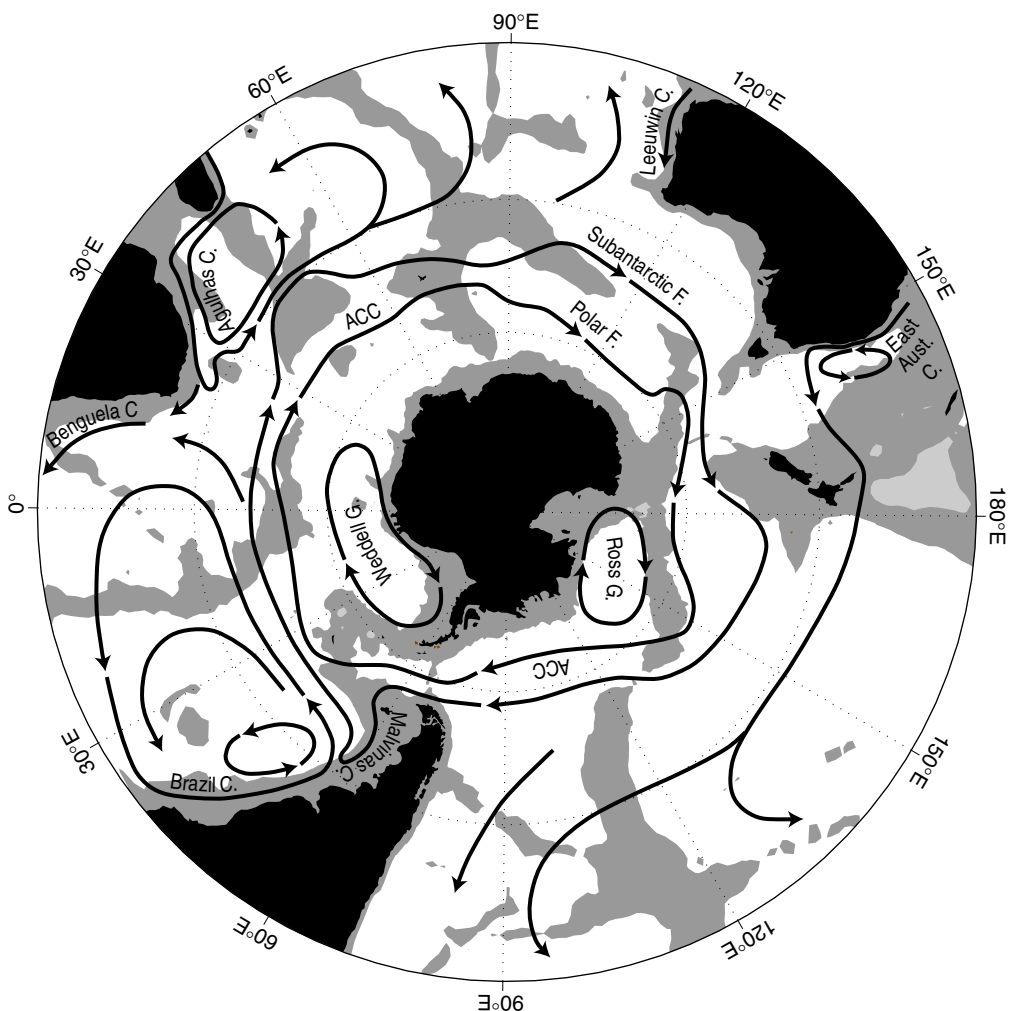


Fig. 4.6.1 Schematic map of major currents in the southern hemisphere oceans south of 20°S. Depths shallower than 3500 m are shaded. The two major cores of the Antarctic Circumpolar Current (ACC) are shown, the Subantarctic Front and Polar Front. Other abbreviations used are F for front, C for Current and G for gyre.

flows in the meridional-vertical plane are also significant. By following property extrema such as an oxygen minimum or salinity maximum, early investigators (e.g. Sverdrup, 1933) inferred the overturning circulation shown schematically in Fig. 4.6.2. Deep water spreads poleward and upward across the ACC and is balanced by equatorward flow in lighter and denser layers. This pattern is driven at least in part by the wind stress acting on the sea surface: south of the westerly wind stress maximum (which generally lies near the axis of the ACC), the Ekman transport is divergent and deep water upwells into the surface layer; north of the westerly wind maximum, the Ekman transport is convergent and surface waters are downwelled into the ocean interior. The water masses exported from the Southern Ocean to lower latitudes as part of

this overturning circulation are responsible for renewing the intermediate and abyssal depths of the southern hemisphere oceans. However, although the general pattern and significance of the meridional circulation of the Southern Ocean has been recognized for many decades, until recently no attempt had been made to quantify the flow paths and water mass conversions implied by Fig. 4.6.2.

The ACC is also unique in the extent to which eddy fluxes contribute to the dynamical and thermodynamical balances. For example, in the absence of mean meridional geostrophic flow across the Drake Passage gap, eddies must carry a significant poleward heat flux to balance the heat lost to the atmosphere at high latitudes and the heat carried equatorward in the Ekman layer (de Szoeke and Levine, 1981). A significant eddy

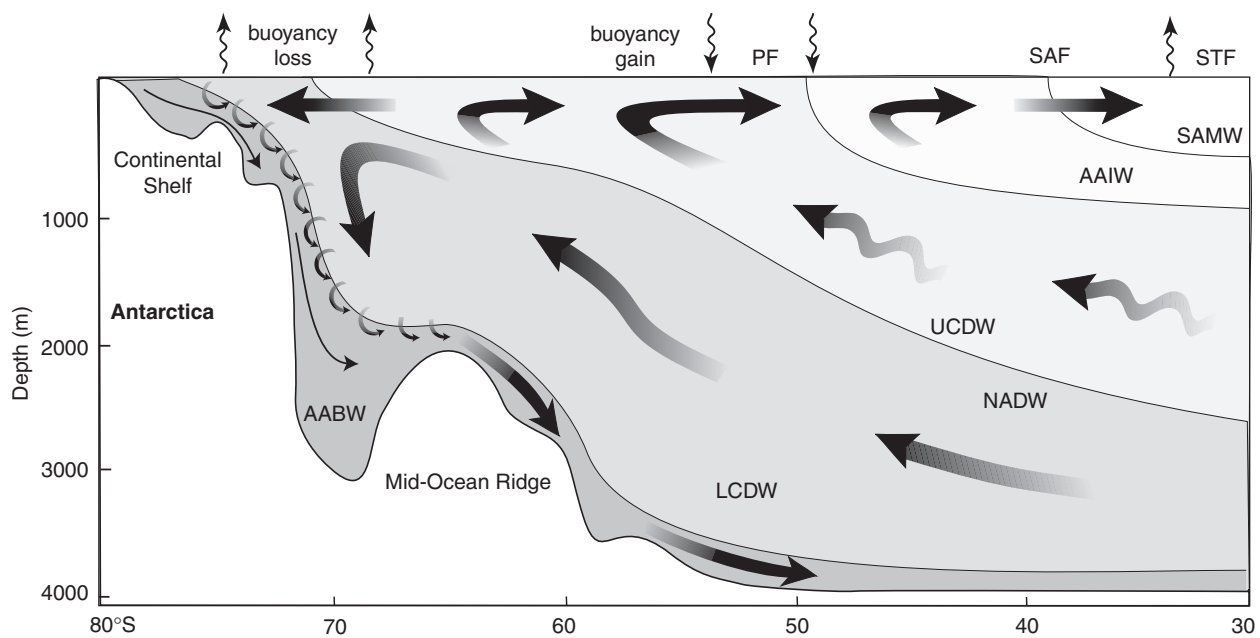


Fig. 4.6.2 A schematic view of the meridional overturning circulation in the Southern Ocean (from Speer *et al.*, 2000). An upper cell is formed primarily by northward Ekman transport beneath the strong westerly winds and southward eddy transport in the UCDW layer. A lower cell is driven primarily by formation of dense AABW near the Antarctic continent. PF, Polar Front; SAF, Subantarctic Front; STF, Subtropical Front; AAIW, Antarctic Intermediate Water; UCDW, Upper Circumpolar Deep Water; NADW, North Atlantic Deep Water; LCDW, Lower Circumpolar Deep Water; AABW, Antarctic Bottom Water.

heat flux is consistent with observations in Drake Passage that the fronts satisfy the linear criteria for baroclinic instability (Bryden, 1979; Wright, 1981). Extrapolation of eddy heat flux measurements in Drake Passage and southeast of New Zealand to the entire circumpolar belt suggested the eddy fluxes were large enough to close the heat balance (Bryden, 1979; Bryden and Heath, 1985), but concern remained that these observations were not representative of the ACC as a whole.

In terms of theory and modelling of the ACC, the state of the art prior to the WOCE (World Ocean Circulation Experiment) period can be briefly summarized as follows. Early wind-driven models of the ACC gave huge transport values unless very large friction was included. Munk and Palmén (1951) proposed that bottom form stress balanced the wind stress. High-resolution quasi-geostrophic models tended to confirm this balance (e.g. McWilliams *et al.*, 1978). At the same time, Sverdrup theory appeared to do a reasonable job of predicting the transport and path of the ACC (Stommel, 1957; Baker, 1982). However, prior to the WOCE era no high-resolution primitive equation models with realistic geometry, stratification,

and full thermodynamics had been run, and many dynamical questions remained open.

Here we review what has been learnt about the Antarctic Circumpolar Current system over the last decade, largely as a result of the WOCE programme. By the 'ACC system' we mean not only the zonal flow of the ACC itself, but also the meridional overturning circulation and water masses of the Southern Ocean. Nowlin and Klinck (1986) provide a comprehensive review of ACC physics as understood at that time, primarily on the basis of measurements in Drake Passage and earlier circumpolar hydrographic surveys. We assume the reader has some familiarity with the dynamics of ocean or atmosphere circulation. Readers interested in more background on topics such as Sverdrup balance, Ekman layers, and potential vorticity are referred to textbooks such as Gill (1982).

We first describe recent observations of the structure and transport of the ACC (Section 4.6.2). Numerical and analytical models have led to substantial advances with regard to the theory and dynamics of the ACC, and its links to the meridional circulation (Section 4.6.3). New observations

and analysis techniques have allowed the circulation, formation and modification of Southern Ocean water masses to be quantified for the first time, as discussed in Section 4.6.4. Observations, theory and modelling over the last decade have led to new insights into the meridional circulation of the Southern Ocean and its link to the global overturning circulation (Section 4.6.5). Finally, we identify a number of important questions that remain open, despite the substantial progress made during the WOCE era (Section 4.6.6). These open questions will provide the challenges for the next generation of field programmes and modelling efforts to follow WOCE.

4.6.2 Observations of the Antarctic Circumpolar Current

A decade ago our knowledge of the structure of the ACC was largely built on detailed measurements in Drake Passage and coarse-resolution hydrographic sections at other longitudes. The increase in the number of high-quality, high-resolution sections and advances in remote sensing have revealed a number of new features of the ACC.

4.6.2.1 Fronts of the ACC

An example of the high-quality sections spanning the ACC collected during WOCE is shown in Fig. 4.6.3. This winter section between Australia and Antarctica near 140°E (WOCE repeat section SR3) illustrates a number of features that are characteristic of the ACC system. As noted first by Deacon (1937), isopleths of all properties generally slope upward to the south across the ACC in a series of steps, or fronts. The locations of the major fronts are indicated above the plots in Fig. 4.6.3. (For the criteria used to define the fronts at SR3, see Rintoul and Bullister (1999).) A number of prominent property extrema in Fig. 4.6.3 define the well-known water masses of the Southern Ocean, as discussed in Section 4.6.4.

Orsi *et al.* (1995) and Belkin and Gordon (1996) have described the circumpolar path and characteristics of the major fronts of the ACC based on careful analysis of a large number of hydrographic sections across the ACC (e.g. Fig. 4.6.4, see Plate 4.6.4, p. 300). In addition to the two main fronts of the ACC, the Subantarctic Front (SAF) and Polar Front (PF), Orsi *et al.* (1995) identified two other fronts that were circumpolar

in extent, the ‘southern front’ and ‘southern boundary’ of the ACC (Fig. 4.6.4, see Plate 4.6.4, p. 300). They also showed that while in Drake Passage the fronts are almost always distinct features separating zones of quieter flow and uniform water properties, at other longitudes the fronts of the ACC merge or split. The merging of fronts is particularly dramatic in the southwest Indian Ocean (Fig. 4.6.1), where the Subantarctic and Polar Fronts of the ACC and the Subtropical Front and Agulhas Return Current are all in close proximity and together produce some of the largest temperature and salinity gradients in the world ocean (Olbers *et al.*, 1992; Park *et al.*, 1993; Read and Pollard, 1993; Belkin and Gordon, 1996; Sparrow *et al.*, 1996). The SR3 section shown in Fig. 4.6.3 provides another example of a frontal structure more complex than the classical description based on Drake Passage experience: both the SAF and PF are split into two branches, and the southern SAF and northern PF have merged near 53°S.

While studies like those above have shown that at most longitudes it is possible to identify particular fronts in hydrographic sections, and so verify their circumpolar extent, advances in remote sensing and modelling of the ACC have provided a new view of the rich structure of the current. By representing the SAF and PF as meandering Gaussian-shaped jets, Gille (1994) was able to map the full circumpolar path of the fronts from GEOSAT altimeter data and illustrate the extent to which the fronts were steered by topography. Streamfunction maps from eddy-resolving numerical models reveal a more complex, filamented structure to the ACC than that generally inferred from hydrographic climatologies (e.g. Maltrud *et al.*, 1998). Mean gradients of sea-surface temperature (Fig. 4.6.4, see Plate 4.6.4, p. 300) also show a complex, filamented structure similar to that seen in the models (Hughes and Ash, 2001).

4.6.2.2 ACC transport

The need to measure the transport of the ACC was a key motivation for the International Southern Ocean Studies (ISOS) experiment in the 1970s. Early attempts to use a small number of current meters to provide a reference for geostrophic calculations were frustrated by the banded nature of the flow: the resulting transport estimates varied dramatically depending on whether a particular instrument was in a front or not. During ISOS, the

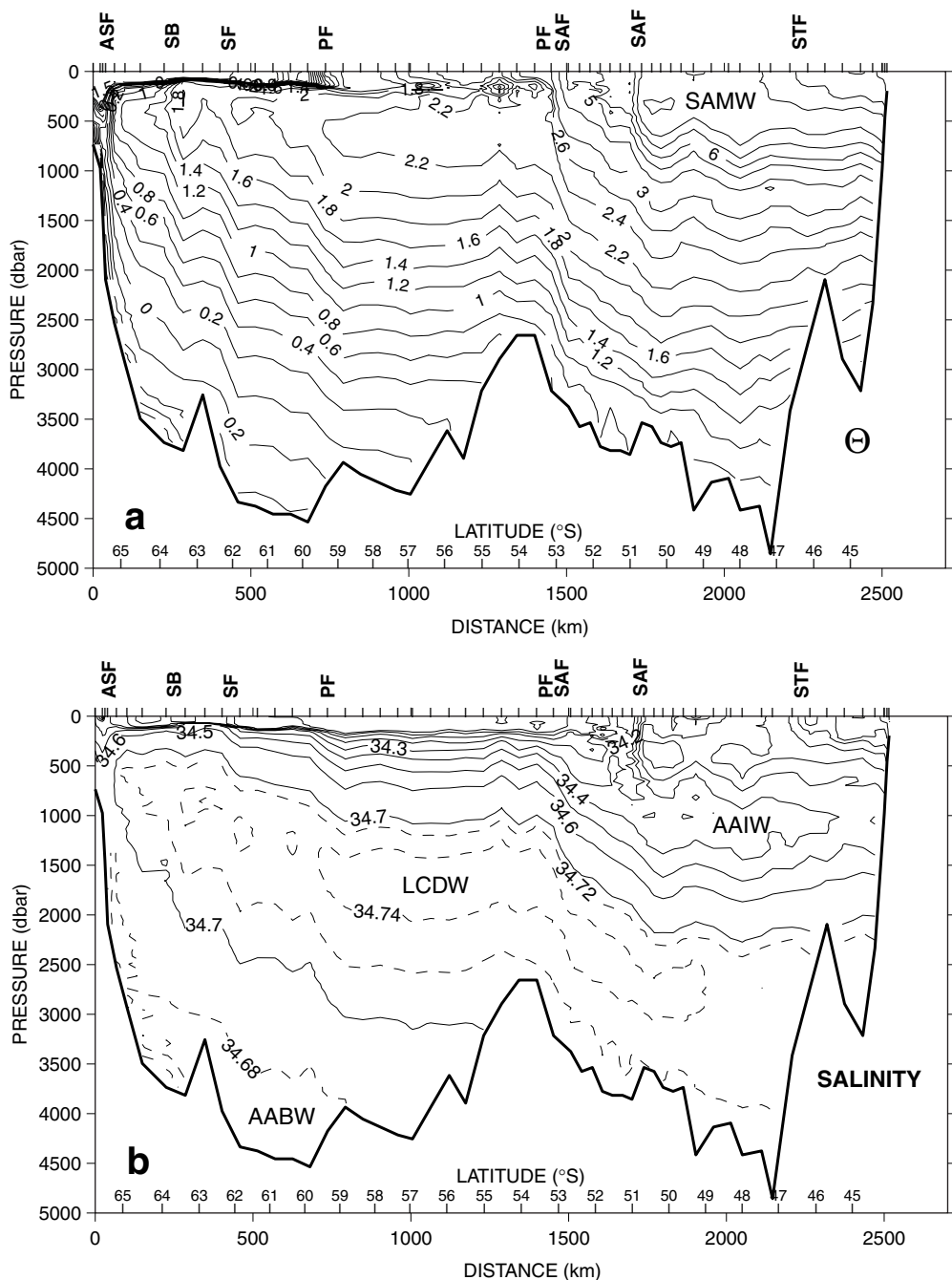


Fig. 4.6.3 Properties versus pressure along the WOCE SR3 repeat section between Australia and Antarctica ($\approx 140^\circ\text{E}$): (a) potential temperature ($^\circ\text{C}$; contour interval is 1° for $\theta > 3^\circ\text{C}$, and 0.2° for $\theta < 2.6^\circ\text{C}$); (b) salinity (on the practical salinity scale, contour interval is 0.1 for solid contours, and 0.02 for dashed contours); (c) oxygen ($\mu\text{mol kg}^{-1}$, contour interval is 20); and (d) neutral density γ_n (kg m^{-3} , contour interval is 0.1). The section was occupied in winter (September) 1996. The major fronts are indicated above the plots: STF, Subtropical Front; SAF, Subantarctic Front; PF, Polar Front; SF, southern ACC front; SB, southern boundary of the ACC; ASF, Antarctic Slope Front. The major Southern Ocean water masses are also indicated: SAMW, Subantarctic Mode Water; AAIW, Antarctic Intermediate Water; L(U)CDW, Lower (Upper) Circumpolar Deep Water; AABW, Antarctic Bottom Water (see also Section 4.6.4). Bold contours in (d) denote the isopycnals used to define the layers in Fig. 4.6.14.

mean transport of the ACC was estimated to be 134 Sv, with an uncertainty in the mean of 13 Sv, and a range of 98 to 154 Sv (Whitworth, 1983;

Whitworth and Peterson, 1985). The ISOS transport time series was based on pressure gauges at either side of the passage, with an average speed

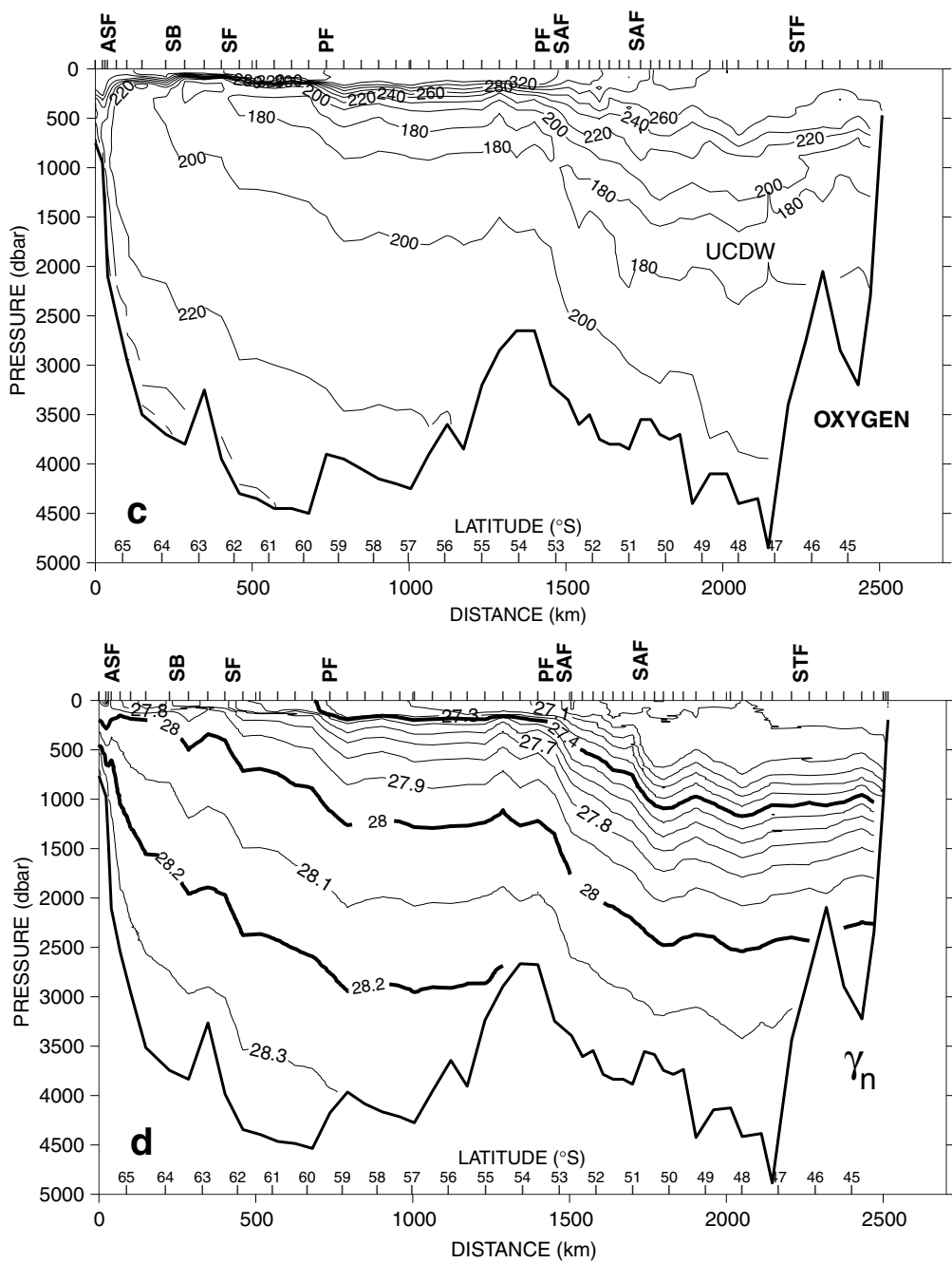


Fig 4.6.3. Continued

calculated from three hydrographic sections referenced to current meters used to 'level' the gauges and so determine the absolute transport (Whitworth *et al.*, 1982). By resolving the narrow fronts of the ACC, the ISOS measurements significantly reduced the uncertainty in transport estimates of the ACC. Nevertheless, the loss of two moorings in the vicinity of the Subantarctic and Polar Fronts, the discrepancy between direct and hydrographic estimates of the vertical shear, and the fact

that the current meter moorings were not coherent, mean that the transports may be subject to somewhat more uncertainty than the error bar quoted above would indicate.

Whitworth *et al.* (1982) and Whitworth (1983) showed from ISOS measurements that the barotropic variability was higher in frequency and larger in magnitude than the baroclinic variability. This observation, together with the similarity between repeat sections across Drake Passage

(Reid and Nowlin, 1971), has sometimes been interpreted to mean that the variability at Drake Passage is entirely barotropic. This is not supported by the ISOS measurements: the range of observed baroclinic transport in the upper 2500 m (70–100 Sv) is comparable to the range of absolute transport (105–140 Sv), and the respective standard deviations are 5.5 Sv and 8.5 Sv. The barotropic variability is larger and of higher frequency, but the baroclinic variability is also significant.

Prior to WOCE, there were no measurements of either baroclinic or barotropic variability of the ACC at other locations. Repeats of WOCE section SR3 south of Australia (140°E) show that the baroclinic variability there is similar in magnitude to that measured by dynamic height moorings deployed for 1 year in Drake Passage during ISOS. The variability is dominated by changes in dynamic height at the northern end, as also found during ISOS. The SR3 section south of Australia extends both further south (into colder water, with lower dynamic height) and north (warmer water, higher dynamic height) than the Drake Passage section, and so the dynamic height difference and baroclinic transport is larger at SR3. For example, the mean transport in Drake Passage above and relative to 2500 m is 87 Sv (Nowlin and Clifford, 1982; Whitworth, 1983); at SR3, the mean of six CTD (Conductivity-Temperature-Depth) sections is 107 Sv (Rintoul and Sokolov, 2000), while the mean based on 36 summer XBT (expendable bathythermograph) sections is 109 Sv (Rintoul *et al.*, 2001). The mean baroclinic transport south of Australia (relative to a ‘best guess’ reference level: at the bottom except near the Antarctic margin, where a shallower level is used consistent with westward flow over the continental slope and rise; see Rintoul and Sokolov, 2000) is 147 ± 10 Sv (mean ± 1 standard deviation), about 13 Sv larger than the ISOS estimate of absolute transport through Drake Passage. The transport south of Australia must be larger than that at Drake Passage to balance the Indonesian Throughflow, which is believed to be of $O(10)$ Sv (Gordon, Chapter 4.7; Cresswell *et al.*, 1993; Meyers *et al.*, 1995). However, given the large remaining uncertainty in the barotropic flow at both chokepoints, the agreement is likely to be fortuitous.

Rintoul and Sokolov’s (2000) estimates of the baroclinic transport variability south of Tasmania show that the ACC itself is surprisingly steady

with time (Fig. 4.6.5). Variations in net transport largely reflect variations in westward flow across the northern end of the section, rather than changes in transport of the ACC fronts. Because the water flowing to the west south of Tasmania is warm relative to the rest of the section, the changes in this current branch have a relatively large impact on the net interbasin exchange of heat. In other words, while the ACC is undoubtedly the primary means of interbasin exchange, *variations* in the transport between the Indian and Pacific basins are dominated by changes in the flow north of the ACC.

While our picture of the circumpolar baroclinic structure of the ACC has become more complete in recent years, progress in determining the barotropic flow, and hence improving our estimates of the absolute transport, has been slower. The WOCE strategy to determine the transport of the ACC relied on several elements: repeat hydrographic sections across each of the Southern Ocean ‘chokepoints’, pairs of deep pressure gauges spanning each chokepoint, and direct velocity measurements from shipboard and lowered ADCPs (Acoustic Doppler Current Profilers). Because of the width of the sections, directly monitoring the absolute transport with a coherent array of traditional moored instruments is not feasible.

Shipboard and lowered ADCPs combined with much more accurate navigation and heading measurements are likely to provide valuable constraints on the barotropic component of the ACC. For example, Donohue *et al.* (2000b) use ADCP observations in the Pacific to infer that the flow at the bottom beneath the SAF is significant, and in the same direction as the near-surface flow, thus enhancing the transport of the SAF over that estimated from the thermal wind alone. At least at the present time, however, both SADCP (Shipboard ADCP) and LADCP (Lowered ADCP) measurements are subject to uncertainties that are large enough to prevent their direct use as a reference velocity for estimating transports across long sections (Donohue *et al.*, 2000).

However, it is feasible to monitor a portion of the current directly, and such a strategy was adopted at the Australian chokepoint, where a 425-km-long coherent array of current meters, Inverted Echo Sounders (IESs), and seafloor electrometers (HEMs) was deployed across the main axis of the ACC to measure both absolute

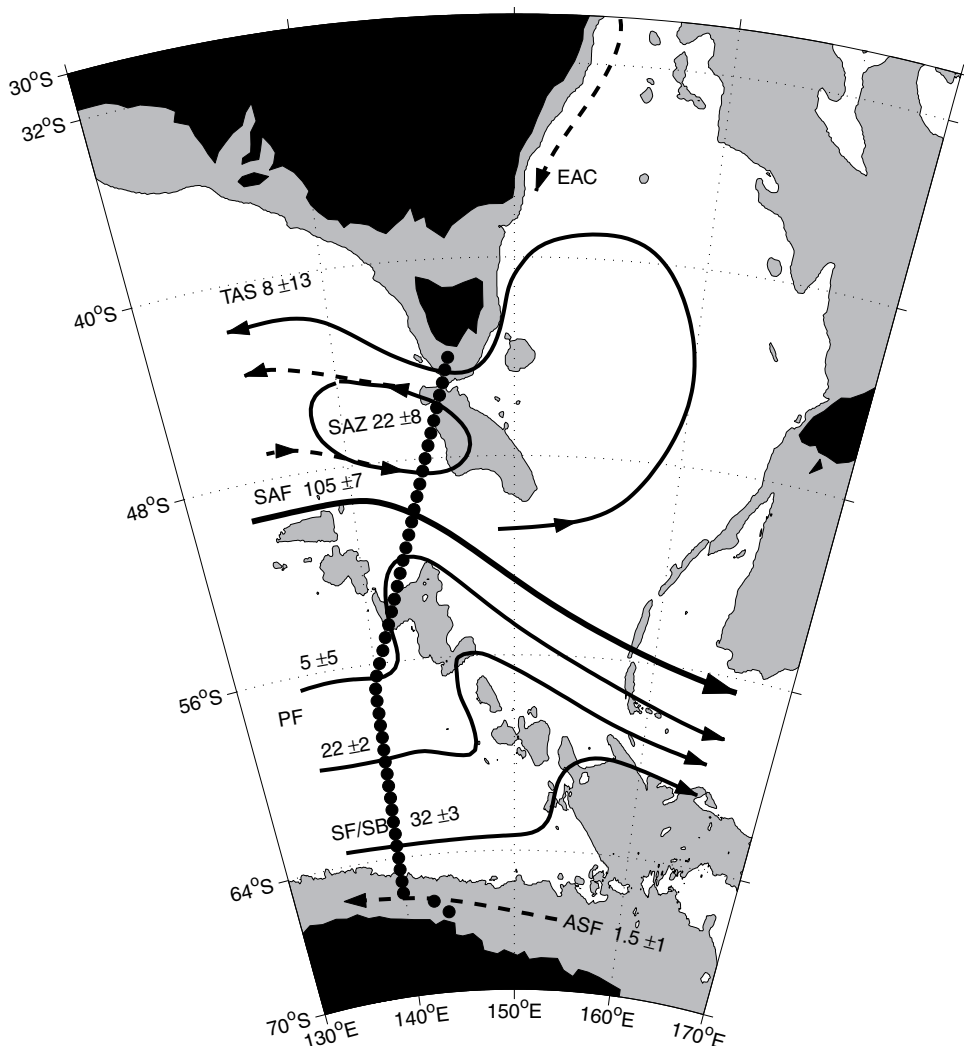


Fig. 4.6.5 Schematic summary of the main circulation features south of Tasmania, based on six repeats of WOCE repeat line SR3. The numbers represent top-to-bottom transports (mean \pm 1 standard deviation). TAS, outflow of Tasman Sea water; SAZ, anticyclonic recirculation in the Subantarctic Zone; SAF, Subantarctic Front; PF, two branches of the Polar Front; SF/SB, southern front and southern boundary of the ACC; ASF, Antarctic Slope Front. See Rintoul and Sokolov (2000) for details.

transport and dynamics of the current (the Subantarctic Flux and Dynamics Experiment, SAFDE; Luther *et al.*, 1997). The array spanned the SAF, the main core of the ACC at this longitude, along the line of WOCE repeat section SR3 (between roughly 49 and 53°S in Fig. 4.6.3). Preliminary analysis of the baroclinic (from the IESs) and absolute (from the HEMs) transport time series shows that while substantial barotropic flows occur in some parts of the array at some times, the 701-day mean baroclinic (relative to the bottom) and absolute transports through the central 200 km portion of the array are similar (54.4 ± 3.1 Sv and 50.4 ± 4.2 Sv, respectively) (Luther *et al.*, 1998).

Pairs of deep (1000 m) pressure gauges were deployed across a number of passages to monitor transport variability during WOCE. The idea, based on ISOS experience, is that pressure difference across the passage is proportional to changes in absolute transport. Meredith *et al.* (1996) found that the variability of pressure difference measured across Drake Passage for 4 years during WOCE was somewhat smaller than measured during the ISOS experiment (corresponding to a transport standard deviation of 8 Sv in WOCE compared with 10 Sv during ISOS). The greatest difference between the two records was the absence during WOCE of any events like two observed during ISOS where transport changed by 40% in a few

weeks. Hughes *et al.* (1999) used results from two eddy-permitting numerical models to show that transport correlated better with pressure measured on the south side of Drake Passage than with pressure difference across the passage. Pressure to the south was also highly coherent around the coast of Antarctica. The model transport variations were well correlated with zonally averaged wind stress (with a lag of less than 3 days) near the south of Drake Passage, and occurred in currents that are strongly steered by f/H contours, rather than following the path of the ACC. The circumpolar coherence of pressure at the Antarctic continental margin is also observed in the WOCE pressure records, as is the relationship (also noted from the ISOS measurements) between bottom pressure and wind stress, for semiannual and shorter periods. The pressure record at the northern side of the passage is dominated by local effects, resulting in the relatively weak correlation between pressure difference and transport.

While much has been learnt about the circumpolar structure of the ACC in the last decade, we have not yet made much progress in refining our estimate of the mean absolute transport of the ACC. Improved estimates of absolute transport are likely to come from inverse models capable of synthesizing the complete suite of WOCE observations (hydrography, Eulerian and Lagrangian velocity measurements, and remote sensing) with dynamical constraints. Development of such models is an active research area. Several recent models give absolute transport estimates that are similar to geostrophic estimates relative to the bottom (e.g. Macdonald, 1998; Sloyan and Rintoul, 2001a; Yaremchuk *et al.*, 2000). However, given that each of these models start with a first guess of zero barotropic flow, and no such calculations have yet included the full WOCE data set including direct velocity measurements, it is inappropriate to conclude that the barotropic contribution to the mean absolute transport of the ACC is small.

4.6.2.3 Antarctic Circumpolar Wave

The ACC is of interest in part because it allows communication between the ocean basins. One phenomenon that depends on the oceanic teleconnection provided by the ACC is the Antarctic Circumpolar Wave (ACW) identified by White and Peterson (1996). The ACW consists of anomalies

in sea-surface temperature, sea-level pressure, and sea-ice extent that propagate eastward around the Southern Ocean. The patterns have zonal wavenumber 2 and circle the globe in about 8–9 years, so the apparent period at any location is about 4 years.

The discovery of the ACW has sparked considerable interest. Part of this interest lies in the potential predictability offered by the ACW. Two recent studies suggest that the ACW has a substantial impact on rainfall in Australia and New Zealand, and may provide some predictive skill (White and Cherry, 1998; White, 2000). The physics of the ACW, in particular the extent to which it represents a coupled mode of the ocean–atmosphere system, has also been a topic of active debate. The initiation of the ACW may be the result of atmospheric teleconnections related to the El Niño–Southern Oscillation (ENSO) (Peterson and White, 1998; Baines and Cai, 2000). Other studies suggest the ACW arises from, or is at least maintained by, atmosphere–ocean coupling within the Southern Ocean (Qiu and Jin, 1997; White *et al.*, 1998a; Goodman and Marshall, 1999; Talley, 1999c; Baines and Cai, 2000). Several recent model experiments suggest, on the other hand, that the ACW is a passive ocean response to atmospheric forcing, and not a true coupled mode. These studies themselves differ as to the nature of the atmospheric forcing that drives the ACW, with ACW-like oscillations resulting from stochastic forcing (Weisse *et al.*, 1999), standing patterns in the atmosphere (Christoph *et al.*, 1998; Cai *et al.*, 1999), or ECMWF (European Centre for Medium Range Weather Forecasts) re-analysis fluxes (Bonekamp *et al.*, 1999). In summary, a variety of dynamical hypotheses have been proposed to explain the ACW, each of which succeeds in explaining at least some of the characteristics of the ACW. Longer time series of observations (including subsurface ocean measurements) and further modelling studies will likely be required to improve our understanding of the mechanism of the ACW.

4.6.2.4 Eddy fluxes of heat and momentum

The large-scale heat budget of the area south of the ACC implies a significant poleward eddy heat flux across the current (de Szoeke and Levine, 1981), and observed fluxes in Drake Passage (Bryden, 1979; Nowlin *et al.*, 1985) and southeast

of New Zealand (Bryden and Heath, 1985) are of the right sign and sufficient magnitude to close the heat budget if extrapolated around the circumpolar belt. But the reliability of such an extrapolation is obviously open to question, given the length and heterogeneity of the ACC. With regard to eddy momentum fluxes, both the Drake Passage and New Zealand measurements suggest the momentum flux carried by the lateral Reynolds stresses is small relative to the wind stress. The primary significance of eddies in the momentum budget of the Southern Ocean lies in their ability to transfer momentum downward across density surfaces, rather than horizontally, as described below.

Over the last decade, our understanding of the eddy field and its influence on the ACC has improved as a result of several advances: satellite altimeter observations of the ACC as a whole, a limited number of additional current meter measurements, and numerical models capable of resolving (or at least ‘permitting’) eddies.

Measurements of sea-surface height variability from satellite altimeters has permitted the eddy energy distribution around the entire ACC to be mapped for the first time (Wunsch and Stammer, 1995). High eddy energy is found where the ACC interacts with topography or with poleward extensions of the subtropical western boundary currents (e.g. the Malvinas–Brazil Current Confluence). Morrow *et al.* (1994) showed that the lateral Reynolds stresses were generally small, but on average tended to transfer momentum into the jets of the ACC, accelerating the mean flow, although more recent results suggest that the eddies act to decelerate some of the strongest jets (Hughes and Ash, 2001).

There have been only a few *in-situ* measurements of eddy fluxes in the ACC during WOCE. South of Australia, an array of four tall current meter moorings was maintained for 2 years (Phillips and Rintoul, 2000). The array was deployed at the Subantarctic Front along the WOCE SR3 line (centred on $\approx 50.7^\circ$ S in Fig. 4.6.3), in a region that altimetry suggests is one of moderate eddy activity, with the eddy energy increasing rapidly downstream. Although the eddy heat flux varies across the array, the mean values show poleward eddy heat fluxes at all depths between 300 and 2500 m that are significant at the 95% level. The eddy heat fluxes are larger in magnitude than the two previous such measurements, in Drake Passage

and southeast of New Zealand. If extrapolated to the circumpolar belt, the eddy heat flux south of Australia would carry 0.9 PW of heat poleward (40-h to 90-day band-passed data, ‘poleward’ defined as normal to the direction of daily shear), more than sufficient to balance the heat loss to the atmosphere and the export of heat in the Ekman layer. (Note that this estimate of the eddy heat flux contains both the divergent, dynamically active part of the eddy heat flux and the non-divergent part, see Marshall and Shutts (1981).) The eddy heat flux scaled by the mean vertical temperature gradient gives the vertical momentum flux (e.g. Johnson and Bryden, 1989). South of Australia, fluctuations in the ‘eddy band’ (40-h to 90-day periods) carry momentum downward at a rate of about 0.2 N m^{-2} (2 dyne cm^{-2}) at all depths (i.e. at about the same rate as momentum is supplied by the wind stress).

4.6.3 Dynamics of the ACC

The absence of continental barriers in the latitude band of Drake Passage makes the dynamics of the ACC distinctly different in character from those of currents at other latitudes. At levels where no topography exists to support zonal pressure gradients, there can be no mean meridional geostrophic flow. The vertically integrated vorticity balance in the Sverdrup approximation, which at least qualitatively succeeds in describing the wind-driven circulation in the interior of closed basins, cannot be used to infer zonal flows in the zonally unbounded Southern Ocean. Even the concept of a wind-driven circulation in the Southern Ocean is inappropriate, as the wind- and buoyancy-forced circulations are inextricably linked. The unique dynamics of the zonal and meridional circulation of the Southern Ocean have attracted the attention of theoreticians for many years. Recent work has led to substantial progress in understanding the heat, momentum and vorticity budgets of the ACC, although some questions remain a source of controversy.

4.6.3.1 Sverdrup balance arguments applied to the ACC

Sverdrup balance holds in the interior of the subtropical gyres because the wind-driven circulation does not penetrate deep enough to interact with bottom topography. In spin-up calculations, the deep circulation is effectively cut off (in the absence

of thermohaline forcing) by the westward propagation of baroclinic Rossby waves generated at the eastern boundary and on topographic features (Anderson and Gill, 1975; Young, 1981). In fact, as long as the mean flow is slow enough that Rossby wave propagation is minimally affected, a succession of Rossby waves of increasing vertical mode number acts to confine the circulation to an ever shallower depth. This only stops when the flow speed becomes comparable to the Rossby wave speed, for the wave mode with the same depth scale as the current.

In the Southern Ocean, observation confirms that the flow at all depths is strongly influenced by bottom topography. From the above argument, this would imply a flow speed comparable to the Rossby wave mode with a vertical scale of 2000 m: the first baroclinic mode. This is consistent with the observation that mesoscale features seen in temperature and sea-surface height propagate eastwards in the ACC, compared with westward propagation elsewhere (Hughes *et al.*, 1998). More importantly, it implies that the Sverdrup balance must be upset by interactions with bottom topography.

Nevertheless, several attempts have been made to apply Sverdrup theory to the ACC by assuming that various topographic features act as ‘effective continents’, blocking the flow. Stommel (1957), for example, suggested that the Scotia Island arc, east of Drake Passage, effectively extended the Antarctic Peninsula across the Drake Passage gap. Southward interior flow in Sverdrup balance with the wind stress curl was returned in an unusual arrangement of boundary currents: a western boundary current against South America, and an eastern boundary current along the coast of the Antarctic Peninsula and Scotia Island arc, the two currents being joined in some unspecified way by flow through Drake Passage. The transport is then given by the zonally integrated wind stress curl at the southernmost latitude of South America (which is also the northernmost latitude of the Scotia Island arc – there is no overlap; any overlap would complicate this, since it would not then be clear at which latitude the wind stress curl was relevant). Baker (1982) found some support for this argument in a comparison of wind stress curl at 55°S with baroclinic transport through Drake Passage from hydrography.

Webb (1993) suggested the Kerguelen Plateau was a sufficient barrier effectively to block the

flow. Webb’s model is a highly idealized source-sink flow in a homogeneous, flat-bottomed ocean, but it can also be recognized as an application of Godfrey’s (1989) ‘island rule’ to the geometry of Antarctica, which immediately generalizes it to the case of a stratified ocean obeying Sverdrup dynamics except in specified western boundary regions. The non-Sverdrup flow all occurs in western boundary currents off the eastern coasts of South America and Kerguelen Plateau (and possibly the Antarctic Peninsula), resulting in a flow around Antarctica that is proportional to an integral of the wind stress along a line encircling the continent. This flow becomes infinite in the limit where the northernmost latitude of Kerguelen Plateau is equal to the southernmost latitude of South America, with no overlap. With only Sverdrup balance and western boundary currents involved, Webb’s model is the most natural extension of wind-driven gyre dynamics to the Southern Ocean.

While the Sverdrup models of Stommel (1957) and Webb (1993) give reasonable values for the ACC transport (about 120 Sv) when combined with climatological wind stress estimates, the theories are incomplete. There are latitudes at which neither of the proposed ‘effective’ continental boundaries is shallower than 2000 m, so the assumption that these block the flow must at least be contingent upon some assumption of the weakness of stratification at these latitudes. The dynamics allowing the eastern and western boundary currents to join in Stommel’s model are not clear. Perhaps most importantly, these flat-bottomed Sverdrup models ignore interaction between the flow and the bottom topography.

The observation that the ACC penetrates to great depth suggests this assumption is not justified. Topographic interactions link the horizontal and meridional circulations, as can be seen most clearly from the barotropic vorticity equation:

$$\rho_0 \beta \Psi_x = \mathbf{k} \cdot \nabla p_b \times \nabla H + \mathbf{k} \cdot \nabla \times \boldsymbol{\tau} + \mathbf{k} \cdot \nabla \times \mathbf{F} \quad (4.6.1)$$

where Ψ is the barotropic streamfunction, p_b is bottom pressure, H is ocean depth, $\boldsymbol{\tau}$ is wind stress, and \mathbf{F} represents frictional and non-linear terms and \mathbf{k} is the unit vector in the local vertical (upwards). Integrating (4.6.1) over a zonal band enclosed by two latitude lines ϕ_1 and ϕ_2 , there is no net northward transport so the left-hand-side

integrates to zero, and Stokes' theorem can be applied to turn the right-hand-side into two line integrals along the bounding latitude lines, giving

$$\oint \phi_1 [p_b H_x + \tau^x + F^x] dx - \oint \phi_2 [p_b H_x + \tau^x + F^x] dx = 0 \quad (4.6.2)$$

In fact, the zonal momentum balance tells us more than this, since the integral over depth and longitude of this balance is precisely

$$\oint [p_b H_x + \tau^x + F^x] dx = 0 \quad (4.6.3)$$

at any latitude.

It has been clearly established (Gille, 1997; Stevens and Ivchenko, 1997) that this balance is dominated by the first two terms: the northward Ekman flux is balanced by a geostrophic southward return flow at depth, with a very small contribution from F^x . This means that F^x can also be neglected in equation (4.6.2). There are some complications due to the different meridional scales of terms in (4.6.2), but in practice this is true when ϕ_1 and ϕ_2 are separated by more than about 3–5 degrees of latitude.

The implication of the above is that, for the area integral between these latitudes, $\nabla \times \tau$ is almost entirely balanced by $\nabla p_b \times \nabla H$. Returning to the barotropic vorticity balance, this means that the southward flow driven by the wind stress curl (as in a flat-bottomed Sverdrup balance) returns north in a flow balanced not by viscous terms as in a Munk or Stommel boundary current, but by the bottom pressure torques. (If the two latitudes are separated by less than about 3°, the dominant balance is between bottom pressure torques and non-linear terms, as found by Wells and de Cuevas (1995).)

The role of topographic torques is graphically illustrated in Fig. 4.6.6 (see Plate 4.6.6, p. 300). This shows the barotropic streamfunction from the Southern Ocean of the global eddy-permitting model OCCAM (Ocean Circulation and Climate Advanced Modelling Project) (Coward, 1996), superimposed on the bottom pressure torque (the first term on the right-hand-side of (4.6.1)). Both quantities have been smoothed by 4.25° longitude by 3.25° latitude averaging to reduce the effect of non-linear terms. It is clear from Fig. 4.6.6 that northward flows are associated with positive torques, and southward flows with negative

torques, as in equation (4.6.1). Physically, the curvature of the earth means that a small circle drawn around a point on the earth's surface has its poleward extremity closer to the earth's axis than its centre, and its equatorward extremity further away, but not by the same amount. Water flowing into the circle from the polar side carries with it more azimuthal velocity relative to the circle's centre, as a result of planetary rotation, than water leaving the circle at the equatorial side. Hence (since f changes sign at the equator), a northward flow represents a removal of anticlockwise angular momentum from the circle, which must be balanced by a positive torque, such as bottom pressure torque or wind stress curl. For comparison with Fig. 4.6.6, a typical wind stress curl over this region gives a torque of 10^{-7} N m^{-3} . The fact that the bottom pressure torques are large relative to the wind stress curl suggests that the agreement with Sverdrup balance found by Baker (1982) was fortuitous.

4.6.3.2 Meridional circulation

Much discussion of ACC dynamics has centred on the meridional overturning circulation. In particular, with an eastward wind driving a northward Ekman flux, how does the southward return flow cross the ACC? Integrating the zonal momentum equation over depth and longitude at a particular latitude, the fact that there must be a return flow means that the integrated Coriolis force is zero, and the question can be rephrased as, what zonal force balances the zonal wind stress? This is the question addressed almost 50 years ago by Munk and Palmén (1951), who concluded that Reynolds stresses and viscous terms were probably too small, and that the wind stress is likely balanced by a bottom form stress due to pressure differences across major topographic features.

This viewpoint is now well established, with *in situ* and satellite altimeter measurements (Bryden and Heath, 1985; Morrow *et al.*, 1994; Phillips and Rintoul, 2000) confirming the smallness of lateral Reynolds stresses, and eddy-resolving primitive equation models (Gille, 1997; Stevens and Ivchenko, 1997) clearly demonstrating a balance between wind stress and bottom form stress. Eddy-resolving Quasi-Geostrophic (QG) models must (by construction) also show such a balance (McWilliams *et al.*, 1978; Treguier and McWilliams, 1990; Wolff *et al.*, 1991), but are useful for illustrating how the balance is established. A summary

of the momentum balance in the different model types is given in Olbers (1998).

In terms of the meridional overturning (the zonally integrated flow at fixed depths), this balance is equivalent to saying that the northward Ekman flux returns in a geostrophic southward flow, supported by zonal pressure differences across topography. The only difference from the situation in other oceans is that, at the latitudes of Drake Passage, the topography does not reach the surface, so the return flow must occur at depths below about 2000 m, as in Fig. 4.6.7.

At first sight, such a deep overturning cell would seem to require large diapycnal fluxes; 10–15 Sv sinking below 1000 m at around 40°S would be comparable to the effect of deep convection in the North Atlantic, but in a region where deep convection does not occur. However, there is an important difference between flows averaged at constant depth and at constant density. In the Fine Resolution Antarctic Model (FRAM), Döös and Webb (1994) have shown that a large fraction of this overturning, labelled the Deacon Cell, occurs with very little associated change in density, as in Fig. 4.6.8. Fluid at a given density flows north, just east of Drake Passage, at one depth, and

southwards elsewhere at a slightly deeper level. Seen at a given depth, denser fluid flows north, and lighter fluid flows south, with no integrated flow except at the top (the Ekman layer) and at depths blocked by topography. The flow integrated at constant depth then shows a cell penetrating to great depth, but a fluid particle will pass northward and southward across a given latitude at depths separated by only a few hundred metres, and with no appreciable change of density. The possibility of such circulations decouples the meridional overturning integrated at constant depth from that integrated at constant density. Analogous circulations are also seen in the tropospheric Ferrel cells (McIntosh and McDougall, 1996; Karoly *et al.*, 1997).

This observation means that the meridional overturning averaged on potential (or neutral) density surfaces is worth looking at in more detail. For purposes of discussion, it is useful to consider two extreme possibilities.

- *Case I.* The northward Ekman flux at some latitude is all returned to the south in density layers that do not intersect topography. The most extreme (and least realistic) version of this

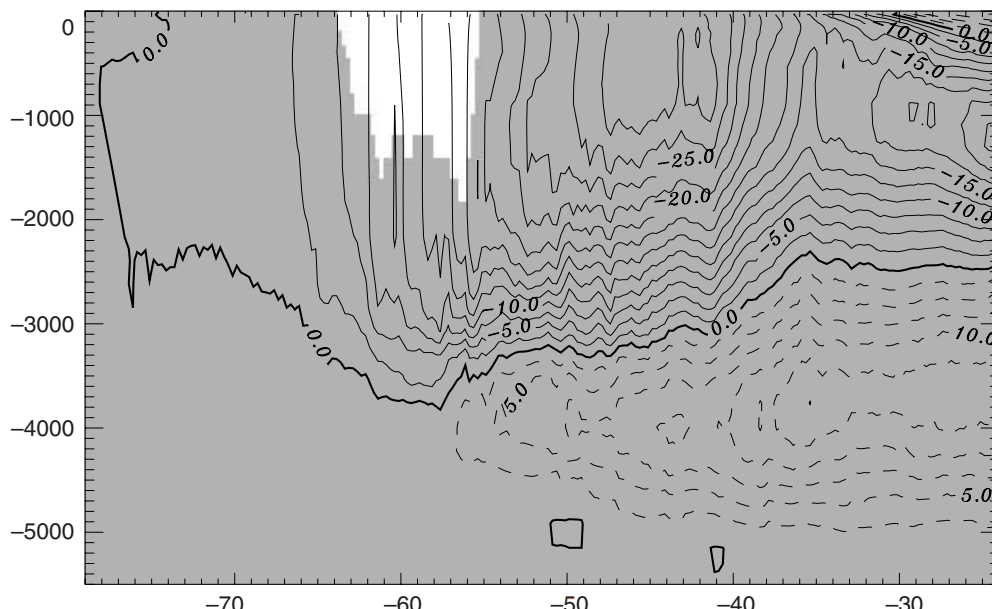


Fig. 4.6.7 The overturning streamfunction from a six-year mean of the Fine Resolution Antarctic Model, calculated by integrating meridional velocity at constant depth, and then integrating vertically. Flow is anticlockwise around highs (dashed contours) and clockwise around lows (solid contours), with a contour interval of 2.5 Sverdrups. The unshaded region shows the range of latitudes and depths (Drake Passage latitudes) which are unblocked by topography at any longitude. See FRAM (1991) and Döös and Webb (1994) for details of the FRAM model.

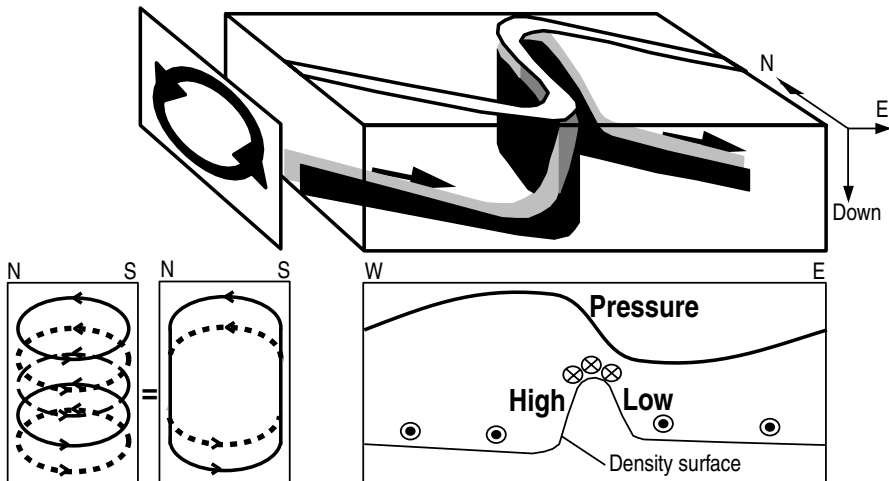


Fig. 4.6.8 Schematic showing an idealized trajectory of a water particle in the ACC moving on a density surface. The trajectory is shown in three dimensions, and projected onto the horizontal plane (top), a constant longitude plane (left), and a constant latitude plane (lower right). The resulting circulation integrated at constant latitude and depth, for this density surface, is an overturning cell with a vertical extent of a few hundred metres. Deeper density surfaces show similar overturning cells, with northward branches at the same depth as the southward branch of the cell related to lighter water, so the zonally integrated cell including all density classes represents a meridional overturning penetrating to great depth, without a need for any water particles to traverse such a large depth range (lower left). Note that this circulation implies higher pressure where the density surface is rising to the east compared with where it is deepening to the east. This results in an eastward pressure force (interfacial form stress) on the water below. This is related to the fact that the northward flow occurs where the vertical thickness of water above the density surface is small, and southward flow where the thickness is large, so there is a net southward mass flux at lighter densities due to the geostrophic flow. This partly balances the northward surface Ekman flux, since the interfacial form stress partly balances the eastward surface wind stress. The same kind of pressure force acting on the sloping bottom topography leads to the bottom form stress, which closely balances the zonally integrated zonal wind stress, since the zonal and depth integral of northward transport is very small.

scenario is the QG picture with only a few density layers, as in the models referred to above. With no flux between layers, all the Ekman flux returns to the south in the top layer, and isopycnal averaging shows no overturning, whereas level averaging shows an overturning cell reaching the bottom layer, which is the only layer containing topography.

- *Case II.* The southward return flow is all in density surfaces that intersect topography. This scenario requires a feedback mechanism between the wind stress and thermohaline forcing, so that the diapycnal flux into and out of these deep layers to the north and south of the chosen latitude can balance the northward Ekman flux.

Consider the balance of zonal momentum, integrated zonally and over two layers (which may be stratified), separated by an isopycnal. The upper layer of thickness h includes the Ekman layer, the lower one reaches from $z = -h$ to the ocean bottom. Writing the depth-integrated northward

volume flux in each layer as V_i , $i = 1, 2$, the steady-state balances read

$$-\rho_0 f \bar{V}_1 = -\bar{b}' \bar{p}'_x + \bar{\tau}^x \quad (4.6.4)$$

$$-\rho_0 f \bar{V}_2 = \bar{b}' \bar{p}'_x - \bar{H} \bar{p}_{bx} \quad (4.6.5)$$

where the overbar denotes time and zonal mean (see Fig. 4.6.9 for a schematic showing the relationship between geostrophic meridional flow and interfacial form stresses on an arbitrary layer). In case I, with the Ekman flux all returning above the isopycnal at $z = -h$, we have $\bar{V}_1 = \bar{V}_2 = 0$. Friction and Reynolds stress are generally negligible and the only remaining terms are wind stress and the pressure forces on the boundaries: interfacial form stress and bottom stress. Thus, for case I, the wind stress and bottom stress are in balance, and are equal to the interfacial form stress at any isopycnal below the Ekman return flow and above the bottom. Some dynamical mechanism, such as stationary waves excited by topography in an eastward current, or

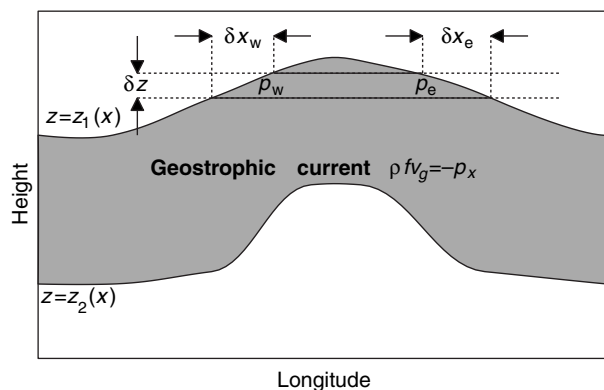


Fig. 4.6.9 Schematic demonstrating the meaning of interfacial form stress for an arbitrary (not necessarily constant density) layer of water (shaded). The net eastward force on the layer is given by $-\int p_x dx dz$, which is related to the net northward geostrophic mass transport in the layer by $f \int \rho v_g dx dz = -\int p_x dx dz$. The contribution to this area integral from the vertical portion δz is $(p_w - p_e) \delta z$, where p_w and p_e are pressures at the upper boundary of the layer. This can be written as $p_w z_{1x} \delta x_w + p_e z_{1x} \delta x_e$. Performing the vertical integral then gives $-\int p_x dx dz = \int (p_1 z_{1x} - p_2 z_{2x}) dx$, where $p_{1,2}$ is pressure at $z = z_{1,2}$. This is the difference between the eastward pressure force on the top interface from above, and that on the lower interface. The layer considered may be bounded by isopycnals, in which case these boundary forces are interfacial form stresses, or the lower interface may be the ocean floor, in which case the corresponding boundary stress is the bottom form stress. In the limit of a small density difference $\delta \rho$ between upper and lower surface, the difference in boundary stresses becomes the interfacial form stress divergence (times $\delta \rho$).

baroclinic instability (again requiring zonal flows comparable to the baroclinic Rossby wave speed), is necessary to maintain the structure of correlated pressure gradients and isopycnal heights that produces interfacial form stresses at depth (see Section 4.6.3.3).

In case II, if we identify $z = -h$ with the position of any isopycnal that does not intersect the bottom or the Ekman layer at the latitude under consideration, then the northward Ekman flow all returns to the south beneath this level, giving $\bar{V}_2 = -\bar{V}_1 = \bar{\tau}^x / \rho_0 f$. The Coriolis force in the lower layer then exactly balances the form stress, and there is no interfacial form stress on density layers above topography. The difficulty here is in supplying the lower layer with the sources and sinks of water necessary to maintain this flow, without inducing

flows in the intermediate layers. A change in wind stress, for example, would upset the balance, and cause some layers to start filling and others emptying. If this change in configuration could then change the buoyancy forcing by some mechanism such as that proposed by Gnanadesikan and Hallberg (2000) (a feedback between buoyancy forcing and interface height), then an equilibrium might be attainable. Understanding the feedback mechanism could then lead to a prediction for the density structure and therefore the baroclinic flow.

Taken together, these two cases make plain the intimate relationship between wind forcing and buoyancy forcing. Models can produce circumpolar currents when forced by wind alone or by buoyancy alone. The steady state requires a balance for both, and cannot be said to be driven by one or the other. Whether the real Southern Ocean is closer to case I or case II is discussed in detail in Section 4.6.5.

4.6.3.3 Theoretical predictions of ACC transport

A complete theory capable of predicting the absolute transport of the ACC is a formidable challenge. Such a theory would need to account for both wind and buoyancy forcing, stratification, the effect of eddy fluxes in the momentum and buoyancy budget, and for interactions between the strong deep currents and bottom topography. While a complete theory requires elaborate mathematics, some insight can be gained into the factors controlling the transport of the ACC by appealing to a variety of simpler models.

Estimates from eddy flux parameterizations

Simple estimates of the baroclinic transport can be derived from the above considerations of momentum transfer in the ACC. These estimates rest on the assumption that the transfer is mainly downward and carried by the interfacial form stress of the transient eddies. In the extreme case when the stress is transferred undiminished through the water column down to depth (and taken up there by topographic form stress) its magnitude is set by the surface wind stress $\bar{\tau}^x$. With $b' = \rho' / \rho_z$ and $p'_x = \rho_0 f v'$ the interfacial stress $\bar{b}' \bar{p}'_x$ turns into the lateral buoyancy flux and the momentum balance in the water column below the Ekman layer becomes

$$\bar{\tau}^x = \bar{b}' \bar{p}'_x \approx - \frac{fg}{N^2} \bar{v}' \bar{\rho}' . \quad (4.6.6)$$

Following Green (1970) and Stone (1972) the lateral buoyancy transport of eddies, growing in the instability process, can be parameterized in term of the gradient of the mean flow, $\overline{v'\rho'} = -\kappa\rho_y = -\kappa\rho_0 f u_z/g$. The idea to combine (4.6.6) with parameterizations of the buoyancy flux for inferring the transport in the form

$$\kappa \frac{f^2}{N^2} u_z = \tau^x / \rho_0 \quad (4.6.7)$$

was first pursued by Johnson and Bryden (1989). They used Green's form of the diffusivity $\kappa = \alpha |f|^2 / \sqrt{Ri}$, obtained for a baroclinically unstable flow, where $Ri = N^2 / (u_z)^2$ is the local Richardson number, l is a measure of the eddy transfer scale and the constant α measures the level of correlation between v' and ρ' in the buoyancy flux ($\alpha = 0.015 \pm 0.005$ according to Visbeck *et al.* (1997)). The shear of the zonal flow and wind stress are then related by

$$\alpha \frac{|f|^3}{N^3} l^2 u_z^2 = \tau^x / \rho_0 \quad (4.6.8)$$

Johnson and Bryden's results are obtained by equating the turbulence scale l with the baroclinic Rossby radius λ . For $l = \pi^2 \lambda$, with $\lambda = NH / (|f| \pi)$, we get their estimate of the shear

$$u_z = \frac{N}{|f|} \left(\frac{\tau^x / \rho_0}{\pi^3 \alpha \lambda H} \right)^{1/2} = \left(\frac{\tau^x / \rho_0}{\pi^3 \alpha H^2} \cdot \frac{N(z)}{|f|} \right)^{1/2} \quad (4.6.9)$$

The first relation was used by Johnson and Bryden (1989), with λ taken to be a measure of the bulk Rossby radius, and shows the shear is proportional to the local Brunt–Väisälä frequency $N(z)$. More importantly, the shear is proportional to the root of the wind stress amplitude τ^x . In the following we use a local Rossby radius and an exponential Brunt–Väisälä frequency profile, $N(z) = N_0 \exp(z/2d)$. With $\tau^x = 0.2 \text{ N m}^{-2}$, $H = 3500 \text{ m}$, $N_0 = 1.4 \times 10^{-3} \text{ s}^{-1}$, $d = 2500 \text{ m}$, and a width $B = 600 \text{ km}$ of the ACC, integration of (4.6.9) yields a transport of 82 Sv relative to the bottom.

Visbeck *et al.* (1997) suggest that in the presence of differential rotation the eddy transfer may be restricted by the Rhines scale $\sqrt{u/\beta}$ rather than the Rossby radius. With $l = \sqrt{u/\beta}$ we find a cubic relation between τ^x and the velocity,

$$u u_z^2 = \frac{\tau^x \beta}{\rho_0 \alpha} \frac{N^3(z)}{|f|^3} \quad (4.6.10)$$

For the exponential $N(z)$ this is easily integrated. A transport of 67 Sv relative to the bottom and a total transport of 124 Sv is obtained for the above set of parameters. In this model the transport would only mildly increase with the magnitude of the wind stress, as $(\tau^x)^{1/3}$.

The action of eddies is not only manifested in the interfacial form stress, it also implies an eddy transport of potential vorticity. A formulation of the momentum balance which is more precise than (4.6.6) is expressed as a balance between the eddy Potential Vorticity (PV) flux and the vertical divergence of the frictional stress (Marshall *et al.*, 1993b),

$$-\frac{\partial}{\partial y} \overline{u'v'} + f \frac{\partial}{\partial z} \frac{\overline{v'p'}}{\rho_z} = \overline{v'q'} = -(\tau^x / \rho_0)_z \quad (4.6.11)$$

This balance holds above the depth level where topographic blocking sets in. The eddy PV flux consists of the lateral Reynolds stress divergence and the vertical divergence of the interfacial form stress. Equation (4.6.6) is in fact the consequence of (4.6.11) if the Reynolds stress divergence is small and significant frictional effects are absent below the Ekman layer. If eddy mixing of PV is down the mean PV gradient, $\overline{v'q'} = -kq_y$, vanishing of the eddy PV flux implies homogeneous mean PV. Observations indeed show that isopycnal vorticity gradients are small in and north of the Antarctic Current regime (Marshall *et al.*, 1993b). Furthermore, a linear relation was found to exist between the large-scale PV and density, $f\rho_z = a + b\rho$, with $d = f/b$, the e-folding scale of the density field. This implies an exponential $N(z)$, as assumed before, and it also imposes a constraint on the current shear,

$$u_{zz} - \frac{u_z}{d} = \beta \frac{N^2}{f^2} \quad (4.6.12)$$

obtained by taking the meridional derivative of $f\rho_z = a + b\rho$. Vertical integration leads immediately to the velocity profile and the transport, expressed in term of the shear at some level z_0 , or the corresponding density gradient, or the parameters of Green's parameterization (Eqn 4.6.7) at the level z_0 . A more meaningful interpretation is found if (4.6.12) is reformulated as constraint on the vertical profile of the diffusivity κ by inserting (4.6.7),

$$\frac{\partial}{\partial z} \frac{N^2}{\kappa} - \frac{N^2}{\kappa d} = \beta \frac{\rho_0 N^2}{\tau^x} \quad (4.6.13)$$

Apparently, the assumption of a homogeneous PV state sets the vertical profile of the lateral diffusivity of buoyancy. Since N^2 decays exponentially with scale d in this model, we find $(1/\kappa)_z = \rho_0\beta/\tau^x = \text{constant}$, and thus

$$\kappa(z) = \frac{\kappa_0}{1 + (\rho_0\beta\kappa_0/\tau^x)(z - z_0)} \quad (4.6.14)$$

where $\kappa_0 = \kappa(z_0)$. In this model the shear consists of two parts,

$$u_z = \frac{N^2}{f^2} \left[\frac{\tau^x}{\rho_0\kappa_0} + \beta(z - z_0) \right] \quad (4.6.15)$$

The first contribution is directly wind-driven. The second contribution is driven by the eddies that homogenize the associated PV. The transport (relative to the bottom) of this latter is fairly small and westward ($\approx -2 \text{ Sv}$) whereas the first part contributes 39 Sv for our standard values and a diffusivity $\kappa_0 = 1000 \text{ m}^2 \text{ s}^{-1}$ at $z_0 = -1000 \text{ m}$. Following (4.6.14), κ then increases to $1200 \text{ m}^2 \text{ s}^{-1}$ at depth 3500 m, and (4.6.7) then implies $\rho_y(z_0)/\rho_0 \approx -2.1 \times 10^{-10} \text{ m}^{-1}$, in good agreement with observations.

Wind-driven flow in a two-layer QG channel yields very sluggish flow in the deep layer when its topography is arranged such that the geostrophic contours are blocked by the walls (see e.g. Wolff *et al.*, 1991). Straub (1993) found a regime where the baroclinic instability arrests the shear at its critical level, and with the assumption that the deep flow vanishes, the transport becomes $BH\beta\lambda^2$ (notice that this corresponds to the second term in equation (4.6.15)). This is only a few Sv, and Straub argues that this contribution would add as a ‘channel component of the Southern Ocean’ to the values obtained from Sverdrup-type estimates. Though neat as a concept, the baroclinically arrested state seems not to occur in more realistic models like FRAM, nor in the real ocean: here the current is highly supercritical with respect to the baroclinic Rossby wave propagation (Hughes *et al.*, 1998).

All these concepts determine the transport relative to the bottom velocity. Evidently, with a bottom velocity of only 1 cm s^{-1} (this is the typical size of bottom velocities obtained with inverse models, see e.g. Olbers and Wenzel, 1989) and a depth of 3500 m we gain a contribution of 21 Sv for a current width of 600 km. How good is the

assumption of zero bottom velocity? The component of the bottom velocity that is normal to the height contours is constrained by the kinematic condition of no flow through the bottom, $w + \mathbf{u} \cdot \nabla H = 0$ at $z = -H$. An estimate of the vertical velocity at the bottom may be obtained by integration of the planetary vorticity equation, $f w_z = \beta v$, from below the surface Ekman layer (with depth D) to the bottom. One finds

$$\mathbf{k} \cdot \nabla \times \mathbf{r}/(\rho_0 f) - w(-H) = \frac{\beta}{f} \int_{-H}^D v \, dz \quad (4.6.16)$$

In the zonal mean the transport below the Ekman layer is returned in the Ekman layer, then $w(-H) = -\mathbf{u}(-H) \cdot \nabla H \approx -(\partial \tau^x / \partial y) / (\rho_0 f)$ and thus $u(-H) \approx \tau^x / (\rho_0 f \delta H)$ where δH is the height of the topography. Values of the order of a few mm s^{-1} are obtained. In view of the fact that the cancellation between the geostrophic flow and the Ekman transport certainly does not occur locally, and the fact that this constraint applies only to the component of \mathbf{u} normal to the bathymetry, the estimate of the bottom velocity must be considered as a lower bound.

As is evident from (4.6.9), (4.6.10) and (4.6.15), the dependence of the baroclinic transport on the amplitude of the wind stress and the Brunt–Väisälä frequency is generally governed by the degree of non-linearity of the eddy flux parameterization. It should be kept in mind that in these parameterizations only transient eddy effects are taken into account. As shown below (and in all analyses of the zonally averaged momentum balance of numerical models), vertical transfer of momentum is also established by standing eddies.

The barotropic formstress mechanism

Estimates of the transport from a more complete theory, which includes the barotropic component of the flow, are difficult to obtain without elaborate mathematics and extreme simplifications. The flat-bottom case, with the usual frictional parameterizations of the bottom or Reynolds stress, is certainly an unrealistic oversimplification. For a flat-bottomed channel with constant wind stress, the total transport is $B\tau^x / (\rho_0 R)$ or $B^3\tau^x / (12\rho_0 A)$, where B is the channel width, R the coefficient of linear bottom friction and A the lateral eddy viscosity. But this model leads to extremely large transports for reasonable choices of the frictional parameters (Hidaka’s dilemma). This dilemma is

somewhat relieved when partial barriers are introduced representing continents and leaving smaller gaps (Drake Passage) for the current to pass through (Gill, 1968).

The flat-bottom case gives unrealistic results because it does not allow for the bottom form stress to work in the overall momentum balance (4.6.3), repeated here as

$$\tau^x - \tau_b^x - \overline{H p_{bx}} = 0 \quad (4.6.17)$$

This balance has been shown to hold in all more or less realistic numerical models (τ_b^x is the frictional bottom stress, put to the linear from $\rho_0 R H u$ below). The relevance of equation (4.6.17) to the transport becomes clear when the relation of the bottom form stress to the physical mechanisms responsible for establishment of the bottom pressure field are considered.

The simplest of such models are barotropic with simple topography. For Charney and DeVore's (1979) barotropic model of QG flow over sinusoidal terrain (with wavelength $2\pi/k$), the bottom form stress is evaluated as

$$\overline{H p_{bx}/\rho_0} = \frac{1}{2} (f\delta)^2 \frac{R H u}{R^2 + k^2(u - c_R)^2} \quad (4.6.18)$$

where $c_R = \beta/k^2$ is the speed of barotropic Rossby waves and δ is the amplitude of the topography relative to the mean depth. From the form of (4.6.18) it is obvious that the form stress is most effective if the current speed equals the speed of the Rossby wave, a situation termed 'topographic resonance'. Adapted to ACC conditions, (4.6.17) only yields the subcritical solution ($R^2 \ll (kc_R)^2$ and $u \ll c_R$) and the transport per unit width becomes

$$H u = \frac{\tau^x / (\rho_0 R)}{1 + (1/2)(\delta a k)^2} \quad (4.6.19)$$

with $a = |f|/\beta$. If the flow is constricted in a channel this relation still applies (Olbers and Wübbner, 1991), but if the topography gets sufficiently high so that blocking of the geostrophic contours by the walls occurs, i.e. $\delta > \delta_c \sim B/a$, the flow switches to a different regime with transport

$$H u = \frac{L \tau^x}{\rho_0 B \pi f} \frac{\delta_c}{\delta(\delta - \delta_c)} \quad (4.6.20)$$

as shown by Krupitsky and Cane (1994) for $R/|f| \leq O(\delta^3)$, $\delta > \delta_c$, and in similar form by Wang and Huang (1995). The barotropic pressure form stress reflected in these expressions is seen to act as a drag on the flow that considerably reduces the transport compared to the flat-bottom value $B \tau^x (\rho_0 R)$, so that transports of only 10–20 Sv are easily achieved. In the blocked state with transport (4.6.20), the current runs through the channel entirely in boundary layers at the southern and northern walls, connected by an internal boundary-layer current following the blocked geostrophic contours. Krupitsky *et al.* (1996) use a heuristic equivalent barotropic model (see also Ivchenko *et al.*, 1999) to show that stratification can relieve this unrealistic behaviour by modifying the geostrophic contours. In an unblocked channel – a Charney–DeVore model with topographic perturbations approaching zero at the walls – the current is allowed to cross the geostrophic contour by frictional processes at all values of topography height and only friction processes allow for a component of the pressure that is out-of-phase with respect to the topography.

Baroclinic mechanisms

The reaction of the zonal barotropic pressure force on the topography leads to a strong reduction in the transport in wind-driven barotropic models. In numerical General Circulation Models (GCMs), it is found that baroclinicity increases the transport from the small values of the barotropic topographic state to realistic values in the range of the observed transport of the ACC. This appears both in coarse-resolution models, for example the early experiments by Bryan and Cox (1972), Cox (1975), and more recently by Olbers and Wübbner (1991) and Cai and Baines (1996), and in models with eddy resolution, for example the FRAM experiment (FRAM Group, 1991) and Gille (1997). Analysis of the momentum balance (4.6.17) in FRAM shows that the barotropic and baroclinic bottom form stress components exceed the wind stress by two orders of magnitude (Stevens and Ivchenko, 1997), with eastward acceleration by the barotropic pressure field and a corresponding deceleration by the baroclinic pressure field largely cancelling, such that the wind stress is almost balanced by the residual and the momentum balance (4.6.17) works essentially without friction. Notice that in these baroclinic

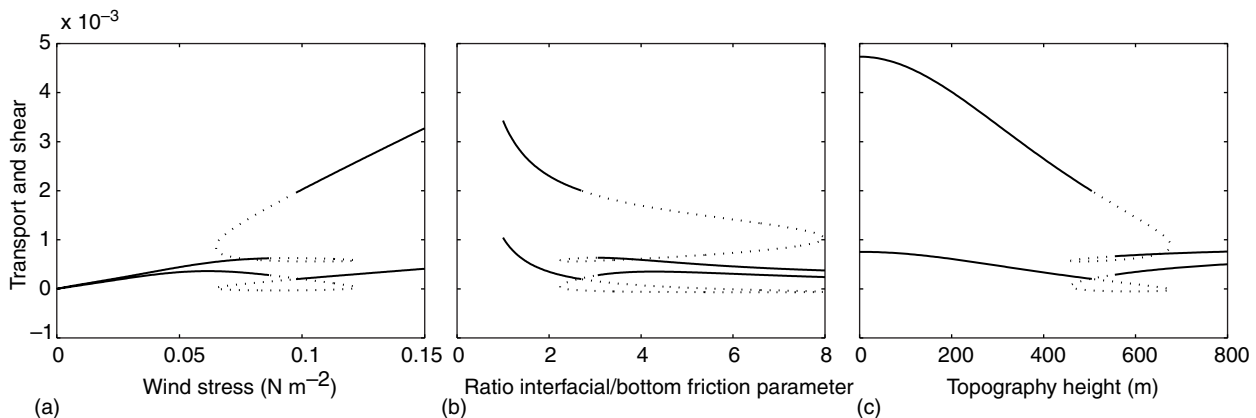


Fig. 4.6.10 Sensitivity of the zonal barotropic transport and shear in the low-order two-layer QG model of Völker (1999) to (a) wind stress amplitude, (b) interfacial and bottom friction, and (c) height of the topography. The flow is forced by sinusoidal wind stress τ^x in a zonal β -plane channel with sinusoidal topography elevation (periodic in the zonal direction, one half sine in meridional direction and vanishing on the walls), friction between the layers and at the bottom is linear. The lower curve in each panel is the shear, the upper curve the transport (both are scaled). Solid lines indicate stable solutions, dotted lines indicate unstable solutions. Notice that there is a small window in the parameter space where only unstable solutions exist. Values of the parameters (if not varied): interfacial friction parameter $2.9 \times 10^{-7} \text{ s}^{-1}$, bottom friction parameter $1.1 \times 10^{-7} \text{ s}^{-1}$, topography height 500 m, wind stress amplitude 0.1 N m^{-2} .

conditions the barotropic pressure does not act as a drag as in homogeneous models. Coarse models have an equally strong effect of the baroclinic pressure field but an unrealistically large contribution from lateral friction.

Baroclinic pressure gradients are established either by thermohaline forcing changing the stratification by water mass conversion, or simply by adiabatic rearrangement of a prescribed layering of stratified mass being lifted over the topography. The latter mechanism is operating in baroclinic adiabatic models (case I in the terminology of Section 4.6.3.2). As shown in Olbers and Völker (1996) and Völker (1999), the waves that produce the topographic resonance of Charney and DeVore (1979) are now baroclinic. These are generated in resonance with the topography and become stationary when the barotropic current speed equals the baroclinic Rossby wave speed. The transport decreases strongly with increasing topography height, starting from a frictionally controlled state at low heights with a transition to a complex resonant regime with multiple equilibria at intermediate heights, and further to a state controlled by barotropic and baroclinic bottom form stresses at high topography. The dependence of the transport and shear of this model on the topography height and other system parameters (friction and forcing) are displayed in Fig. 4.6.10. Stable solutions exist where the curves are bold. Solutions with dotted

curves are unstable (in the window of unstable solutions homoclinic orbits and chaotic behaviour is found; this disappears when increasing the number of resolved modes). Though the momentum balance (4.6.17) in this latter solution seems to operate without friction, it should be pointed out that the barotropic and baroclinic bottom stresses are due to phase shifts of the topographically induced pressure gradients with respect to the topographic undulations, which in turn are proportional to the coefficients of bottom and interfacial friction of the model, again in correspondence to the barotropic model. It is particularly interesting that eddy effects do not appear explicitly in (4.6.17), but transient eddies or bottom friction are needed to produce the phase shift in standing eddies, which is necessary to produce bottom form stress. The baroclinic topographic resonance theory determines the transport in adiabatic models in a manner similar to the barotropic Charney–DeVore mechanism: the bottom form stress is a complicated resonance function of the barotropic and baroclinic velocities and the transport follows from (4.6.17) and a corresponding balance for the baroclinic momentum. The structural properties of this low-order model are preserved when the degrees of freedom are increased from the simplest non-trivial model with 11 modes to a number representing a moderately resolved coarse model (with 75 modes).

The crucial role of transient eddies or non-ideal fluid behaviour beneath the mixed layer is also clear in realistic conditions. Consider a contour of constant time-averaged PV on some density surface beneath the mixed layer but above topography. Since PV and potential density are both materially conserved for an ideal fluid, any steady-state flow can have no component across the PV contour. Thus if there is a return flow at this density, since it must cross this PV contour (assumed to close around Antarctica), either friction or transient eddies are required to permit this.

Analytical theories of the ACC in which the baroclinic pressure field, and thus the bottom stress, is established by thermohaline forcing are still lacking. Several numerical studies (e.g. Olbers and Wübbel, 1991; Cai and Baines, 1996; Gent *et al.*, 2000; Gnanadesikan and Hallberg, 2000) with coarse-resolution models have recently investigated the dependence of transport on the buoyancy forcing at the surface. The state of the ACC in these models is generally intermediate between the extreme cases I and II described in Section 4.6.3.2. There is conversion of deep to lighter water masses to allow for a deeper (than Ekman layer) reaching meridional cell but there is also a parameterized interfacial stress of some kind. It is likely that the barotropic and baroclinic form stresses are not solely created by thermohaline processes because the topographic resonance mechanism should be operating as well.

An increase of the ACC transport by an increase of the buoyancy loss by increased brine release off the Antarctic shelf was documented in primitive equation models by Olbers and Wübbel (1991) and clearly described in Gent *et al.* (2000). Using restoring boundary conditions for heat and salt and different wind fields, Gnanadesikan and Hallberg (2000) found a similar strong increase of the ACC transport with strengthening of the overturning circulation (linked to a deeper thermocline and increased water mass transformation in the northern hemisphere). As shown by Cai and Baines (1996) and Gent *et al.* (2000), parameterizations of sub-grid mixing play an essential role: the ACC transport and the overturning transport are larger in the presence of a larger vertical diffusivity and a smaller isopycnal diffusivity. The latter is in qualitative agreement with the baroclinic transport models (4.6.7) and (4.6.15). It also

agrees with the baroclinic Charney–DeVore model described above, where the transport strongly decreases with friction between the layers (see Fig. 4.6.10b).

Topographic steering

The important role of submarine topography in the dynamics of the ACC was discussed in the preceding sections. The topography also acts to steer the current, as noted very early on by Sverdrup *et al.* (1942, pp. 468; 606–607) and described by Gordon *et al.* (1978) (see also the pressure maps in Webb *et al.*, 1991, and the steric height maps in Olbers *et al.*, 1992). Steering by bathymetry has also been detected in the sea surface topography obtained from altimeter data, as reported by Chelton *et al.* (1990) and Gille (1994). A laboratory model of homogeneous and linearly stratified flow over realistic topography is reported by Boyer *et al.* (1993). The resulting flow is in fair agreement with observations regarding steering by the major ridges and troughs, but it also shows significant discrepancies that are traced back to inadequate representation of small-scale passages and fracture zones, unrealistic forcing (which was simulated by sources and sinks of mass) and neglect of the planetary β effect. Early models of topographic effects on the ACC were homogeneous (Kamenkovich, 1962; Johnson and Hill, 1975), so that f/H contours inevitably dominated the flow pattern. The breaking of f/H or bathymetry control by stratification is demonstrated in many simple numerical models (e.g. Klinck, 1993) and the coarse- and high-resolution models of the circumpolar circulation discussed above.

Theory suggests the flow may be steered along bathymetry contours, latitude circles or the geostrophic contours f/H . The conditions under which one of these effects will dominate can be clarified by use of the balance (4.6.1) of integrated vorticity. If the deep ocean is motionless, $\rho_0 f \mathbf{k} \times \mathbf{u}_b = -(\nabla p)_b = 0$, the bottom torque term in (4.6.1) vanishes because $(\nabla p)_b = \nabla p_b - g \rho_b \nabla H$. This allows a ‘free mode’ in the transport streamfunction following f contours; in case of locally weak stress curl the flow would follow such a path. However, a motionless abyss requires strong stratification to shield the flow from the influence of topography. The ACC is far from such a state but the converse condition of a homogeneous water

column is inappropriate as well. The influence of stratification is visible in other forms of the vorticity balance

$$(\mathbf{k} \times \nabla \Psi) \cdot \nabla \frac{f}{H} + \frac{f}{H^2} \mathbf{U}^g \cdot \nabla H = \mathbf{k} \cdot \nabla \times (\boldsymbol{\tau}/(\rho_0 H)) \quad (4.6.21)$$

or

$$H^2 \mathbf{u}_b \cdot \nabla \frac{f}{H} + \mathbf{U}^g \cdot \nabla f = f \mathbf{k} \cdot \nabla \times (\boldsymbol{\tau}/\rho_0 f) = f w_E \quad (4.6.22)$$

obtained from (4.6.1) using $\mathbf{k} \times \nabla \Psi = H \mathbf{u}_b + \mathbf{U}^g - \mathbf{k} \times (\boldsymbol{\tau}/f)$ (ignoring lateral stresses and bottom friction for simplicity). Here, \mathbf{U}^g is the baroclinic (thermal wind) transport relative to the bottom. Obviously, in the case of weak stratification when the baroclinic transport term in the above balances could be ignored, the transport streamfunction and the bottom velocity both would follow f/H contours where the corresponding stress curls are weak. If, in addition, the variation of the planetary vorticity f along the path of the flow is small the bathymetry contours act as characteristics (the topographic $\beta_T = f \Delta H / (H \Delta L)$ is in fact generally larger than the planetary β).

A more detailed consideration of stratification effects in models would obviously be required to distinguish between these different possibilities. An intelligent shortcut has been pursued by Marshall (1995a,b) using the homogeneous potential vorticity model of Marshall *et al.* (1993b). With a functional dependence $f \rho_z = Q(\rho)$, the density field ρ and the baroclinic transport \mathbf{U}^g is determined by a boundary value, say $\rho(\mathbf{x}, z=0) = \rho_s(\mathbf{x})$. Also the bottom density ρ_b is determined by ρ_s . Furthermore, the bottom is a material surface and – since Montgomery potential, $M = p + g \rho z$, and density are conserved along the three-dimensional flow in adiabatic conditions – we have a functional dependence $M_b = M_b(\rho_b)$. Assuming no friction in the abyss, the bottom velocity is geostrophic, i.e. $f \mathbf{u}_b = \mathbf{k} \times (\nabla M_b + g H \nabla \rho_b)$. Inserting these relations into (4.6.22) we find (after some manipulation)

$$A(\mathbf{k} \times \nabla \rho_s) \cdot \nabla \frac{f}{H} + B(\mathbf{k} \times \nabla \rho_s) \cdot \nabla f = \frac{f^2}{g} Q_s w_E \quad (4.6.23)$$

with

$$A = H^2 (H - H_{\text{ref}}) Q_b, \quad B = \int_{-H}^0 Q z \, dz \quad (4.6.24)$$

This vorticity equation determines the surface density from the Ekman pumping w_E , provided the functional relations $H_{\text{ref}}(\rho_b) = (1/g) \partial M_b / \partial \rho_b$ and $Q(\rho)$ are specified. The extreme cases with their characteristics $f/H = \text{constant}$ and $f = \text{constant}$ appear again in (4.6.23) – corresponding to a homogeneous ocean with large A (because here $H_{\text{ref}} \gg H$) and motionless abyss with large B (because here $Q \gg Q_b$). For constant H_{ref} and linear $Q(\rho) = a + b \rho$ (as found by Marshall *et al.*, 1993b) the characteristic problem (4.6.23) is linear and characteristics are easily computed. Marshall (1995b) presents a solution for the transport streamfunction and the interior circulation for an unforced case ($w_E = 0$), prescribing a surface density section between Antarctica and Australia (Fig. 4.6.11). The solution transports 160 Sv, and streamlines are largely zonal and quite indifferent to topography in large portions of the domain. Nevertheless, topography clearly steers the current over the major topographic features such as the Atlantic Ridges, the South East Indian and Macquarie Ridges, the Pacific–Antarctic Ridge and the East Pacific Rise. These patterns are enhanced for larger values of the reference depth H_{ref} , which leads to an increase of the deep currents. Outstanding in the solution is an exaggerated northward deflection over the Kerguelen Plateau, whereas the observed equatorward displacement of the current behind Drake Passage and the gradual poleward migration in the rest of the Southern Ocean is not reproduced, presumably due to neglect of the wind forcing.

4.6.4 Water mass formation and conversion

Isopycnals shoal steeply to the south across the Southern Ocean, reflecting the baroclinicity of the ACC (Fig. 4.6.3). Water spanning a wide range of density is thus directly forced by exchange of momentum, heat and fresh water with the overlying atmosphere and sea ice. The air–sea–ice interactions strongly modify the physical and chemical properties of outcropping layers and transform water from one density class to another. The water masses formed in this way ventilate a substantial fraction of the world ocean volume and are a key link in the global overturning circulation (Section 4.6.5).

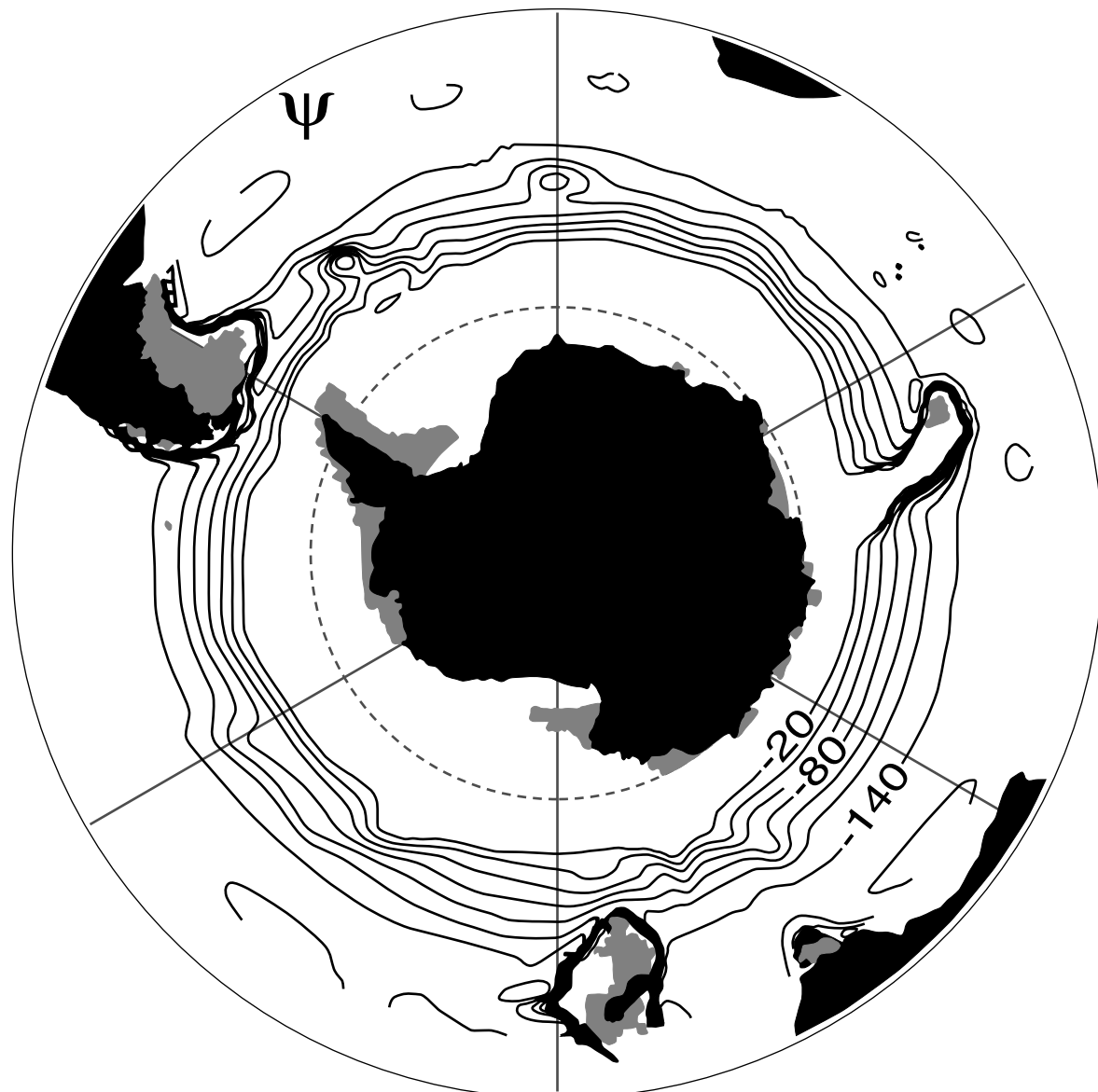


Fig. 4.6.11 Mass streamfunction in Sverdrups from the analytical model of Marshall (1995b), in which fluid parcels negotiate a variable bottom topography while conserving density and potential vorticity. The inviscid, adiabatic circulation follows characteristics which lie between the f/H contours found in a homogeneous ocean and the f contours found in a strongly stratified ocean.

4.6.4.1 Subantarctic Mode Water and Antarctic Intermediate Water

Subantarctic Mode Water (SAMW) is formed by deep winter convection on the equatorward side of the ACC (Hanawa and Talley, Chapter 5.4; McCartney, 1977). The deep convection imprints the SAMW with its characteristic properties: a vertically well-mixed (hence low potential vorticity) layer that is rich in oxygen (Fig. 4.6.3). These tracers allow the SAMWs to be tracked from their formation regions to the southern hemisphere

subtropical gyres, where they renew the waters of the lower thermocline (McCartney, 1982).

The Antarctic Intermediate Water (AAIW) is identified by a salinity minimum layer that descends near the Subantarctic Front (Fig. 4.6.3b; Hanawa and Talley, Chapter 5.4). Early authors traced the salinity minimum core layer poleward to where it outcropped in the cold, fresh Antarctic Surface Water, and inferred that circumpolar sinking along this layer renewed the AAIW tongue. The apparent spreading was thought to be driven

by either wind, buoyancy loss, or mixing along isopycnals, depending on the author. McCartney (1982) presented an alternative view, that AAIW is made up of the densest SAMW produced in the Pacific, the end-product of gradual cooling, freshening and loss of buoyancy by air-sea fluxes along the long SAMW circulation path across the Indian and Pacific Oceans. England *et al.* (1993) showed a similar mechanism operating in a GCM. From the southeast Pacific, AAIW spreads north and west in the Pacific and through Drake Passage. Further modification by air-sea fluxes and mixing in the southwest Atlantic produces a cooler and fresher variety of AAIW in the southwest Atlantic (Molinelli, 1981; Piola and Georgi, 1982; Piola and Gordon, 1989; Talley, 1996a).

High-quality hydrographic and tracer sections collected during WOCE have focused attention on the distribution and circulation of SAMW and AAIW. The SAMW becomes progressively cooler, fresher and denser across the Indian and Pacific basins (McCartney, 1982). Within each basin, the lighter SAMW varieties are injected further west, and are restricted to the southwest corner of the subtropical gyre. Dense varieties entering the subtropical gyres on their eastern sides travel around the gyres and extend to lower latitudes. While the circulation of the denser AAIW shares some similarities with that of the overlying SAMW, there are important differences as well. In contrast to the near-circumpolar formation of SAMW, the formation of 'new', well-ventilated AAIW is limited to the southeast Pacific and southwest Atlantic, as indicated by the gradual decrease in AAIW oxygen and potential vorticity across the Atlantic and Indian basins (Gordon and Molinelli, 1982; Talley, 1996a). For example, at the WOCE SR3 section south of Tasmania (the eastern limit of the Atlantic-Indian variety of AAIW), the oxygen and chlorofluorocarbon (CFC) saturations of AAIW are only 65% and 10–20%, respectively; the 'ventilation age' of AAIW based on CFC-11 is 22–26 years (Rintoul and Bullister, 1999). AAIW enters the lower thermocline of the Atlantic and Pacific subtropical gyres mainly in the southeast quadrant; in contrast, oxygen-rich AAIW enters the Indian basin preferentially in the southwest (Fine, 1993; Toole and Warren, 1993). In the western boundary currents of the subtropical gyres, modified 'older' AAIW returns to the south, resulting in multiple varieties of AAIW with similar densities

at some longitudes (e.g. 40°E, Read and Pollard, 1993; 140°E, Rintoul and Bullister, 1999), and a shift in AAIW properties between basins (Piola and Georgi, 1982).

Few estimates have been made of the formation rate of SAMW and AAIW. Even less attention has been paid to the rest of the circulation loop associated with export of SAMW/AAIW to lower latitudes: what is the fate of SAMW/AAIW exported from the Southern Ocean? What water masses are modified to supply the SAMW/AAIW, and where and how does this occur?

Sloyan and Rintoul (2000, 2001a) have used a box inverse model, which explicitly includes air-sea buoyancy fluxes and the water mass transformations they drive (e.g. Walin, 1982; Speer and Tziperman, 1992), to examine the formation and circulation of SAMW and AAIW. Comparing the transport in density layers at each Southern Ocean chokepoint shows that 18 Sv more SAMW/AAIW leaves the Indian Ocean sector south of Australia than enters the basin south of Africa (Fig. 4.6.12). This production rate represents the net effect of air-sea buoyancy fluxes, diapycnal mixing and meridional exchange with the subtropical gyre. The net production in the Indian sector is balanced by net consumption in the other basins. SAMW is formed in the Indian sector both by cooling and freshening of subtropical water carried south in the Agulhas Current and its extension, and by water flowing northward across the ACC (and gaining buoyancy) in the Ekman layer. SAMW is carried from the Indian to the Pacific by the ACC, where it is modified by mixing and air-sea exchange, and ultimately returns to the Indian basin via the Indonesian passages (Gordon, Chapter 4.7). The SAMW therefore participates in an Indian-Pacific 'throughflow gyre' in which warm throughflow water is converted to cool SAMW in the Indian Ocean, and SAMW entering the Pacific basin is converted back to water warm enough to supply the throughflow.

In the zonal integral, 34 Sv of Upper Circumpolar Deep Water (UCDW) is upwelled south of the ACC and converted to IW densities by air-sea buoyancy flux (Fig. 4.6.12; see also the discussion in Section 4.6.5 and Fig. 4.6.14). This transformation by air-sea fluxes of heat and fresh water is largely compensated by diapycnal mixing south of 40°S. However, the compensation is not immediate. While the zonally integrated export of SAMW/

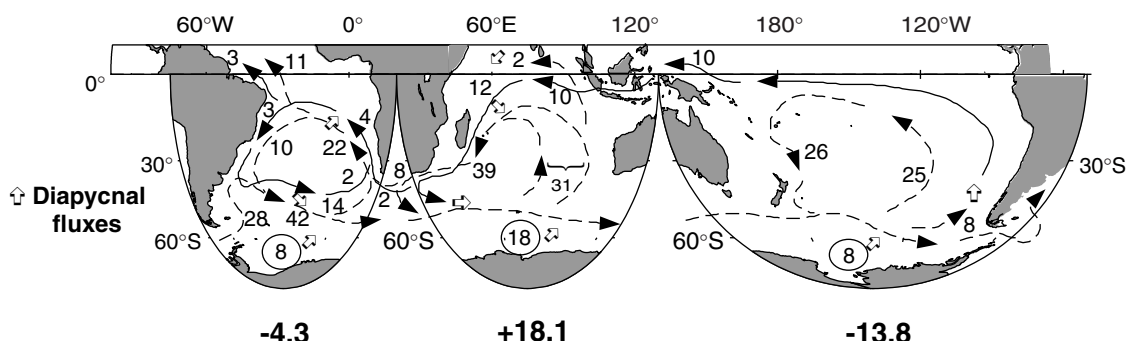


Fig. 4.6.12 A summary of the circulation and formation of SAMW and AAIW, from the inverse model of Sloyan and Rintoul (2001a). Numbers give volume fluxes in Sv of thermocline water (solid line, neutral density $<26.0 \text{ kg m}^{-3}$) and intermediate water (SAMW/AAIW, dashed line, neutral density $26.0 < \gamma_n < 27.4 \text{ kg m}^{-3}$). Open arrows represent diapycnal fluxes driven by air-sea exchange and interior mixing. Circled numbers in each of the Southern Ocean sectors represent conversion of Upper Circumpolar Deep Water to SAMW and AAIW. Bold numbers below figure are the net convergence (+ve) or divergence (-ve) of SAMW/AAIW in each sector of the Southern Ocean due to meridional and diapycnal fluxes; mass is conserved by a compensating divergence in zonal transport of the ACC.

AAIW from the Southern Ocean is small ($< 5 \text{ Sv}$), the gross exchange is large (about $\pm 80 \text{ Sv}$). The inflow of ‘new’ SAMW/AAIW to the subtropical gyres is roughly balanced by an outflow of ‘old’ SAMW/AAIW, whose properties have been modified by mixing during their transit of the gyres. Part of the returning SAMW/AAIW is then converted to denser UCDW by diapycnal mixing.

Because the SAMW and AAIW are renewed by air-sea interaction on decadal time scales, they provide a good place to look for evidence of changes in forcing over such time scales. Several recent studies have identified decadal changes in the SAMW and AAIW layers in the south Indian and Pacific oceans (e.g. Bindoff and Church, 1992; Johnson and Orsi, 1997; Bindoff and McDougall, 2000). Wong *et al.* (1999) have shown that these patterns are generally coherent throughout the Pacific. These changes are consistent with warming and freshening at the surface outcrops of these layers, as predicted to occur in coupled climate models forced by increasing greenhouse gas concentrations (Bindoff and McDougall, 1994).

4.6.4.2 Circumpolar Deep Water

Two prominent core layers underly the salinity minimum of the Antarctic Intermediate Water throughout the Southern Ocean. An oxygen minimum layer (Fig. 4.6.3c) is used to define the Upper Circumpolar Deep Water (UCDW) (Callahan, 1972). At slightly greater depth (and density) lies the salinity maximum of the Lower Circumpolar

Deep Water (LCDW) (Fig. 4.6.3b). The LCDW layer is supplied by saline North Atlantic Deep Water (NADW) exported from the Atlantic. The addition of ‘new’ NADW in the South Atlantic produces an oxygen and salinity maximum between the UCDW and LCDW entering the basin through Drake Passage (Reid *et al.*, 1977). The high-salinity signature of the NADW/LCDW can be traced to low latitudes of the abyssal Indian and Pacific basins (Reid and Lynn, 1971). LCDW enters the low-latitude basins primarily in a series of deep western boundary currents (see Hogg, Chapter 4.5). Within the subtropical basins, the LCDW is slowly modified by mixing with surrounding fresher water, and the oxygen concentrations are reduced by biological consumption. The return of the slightly less dense, low-oxygen water from the Indian and Pacific basins supplies the oxygen minimum of the UCDW (Callahan, 1972). Both types of CDW spread poleward and upward across the Southern Ocean, ultimately outcropping at the sea surface south of the ACC. As described in the previous section and in more detail in Section 4.6.5, the outcropping of CDW and the resulting water mass transformation by air-sea fluxes provides the main connection between the lower and upper limbs of the global overturning circulation.

4.6.4.3 Antarctic Bottom Water

The WOCE decade has seen substantial progress in our understanding of where, how and at what rate AABW is formed in the Southern Ocean. In the

Weddell Sea several major programmes have contributed to this advance (see Fahrbach *et al.*, 1998, for a review). The new results are broadly consistent with the picture of circulation and water mass formation in the Weddell developed by earlier investigators. Relatively warm Circumpolar Deep Water (sometimes called Warm Deep Water in the Weddell) enters the basin from the east in the Weddell gyre and is converted to Weddell Sea Deep and Bottom Water through ice–ocean–atmosphere interactions along the southern and western margin. Two mixing scenarios have been proposed for the formation of Weddell Sea Bottom Water: (1) mixing of Winter surface water, Warm Deep Water, and Western Shelf Water, whose salinity has been enriched by brine rejected during sea ice formation (Foster and Carmack, 1976); and (2) mixing of Ice Shelf Water (formed by cooling and freshening of Western Shelf Water beneath the vast ice shelves in the southern Weddell Sea) with Weddell Sea Deep Water and Warm Deep Water (Carmack and Foster, 1975; Foldvik *et al.*, 1985a).

Fahrbach *et al.* (1994a) maintained a line of current meter moorings and repeat hydrographic sections across the central Weddell Sea between 1989 and 1993. They estimate a Weddell gyre transport of 30 Sv, almost all of which is carried in narrow currents along the continental slope. Recent model results of Beckmann *et al.* (1999) indicate that Fahrbach's section does not cut through the centre of the Weddell gyre, which has a maximum transport exceeding 50 Sv, in agreement with observations along the Greenwich meridian (Schröder and Fahrbach, 1999). By considering inflow and outflow in density layers across this section, Fahrbach *et al.* (1991) infer a net conversion of 3–4 Sv of Winter and Warm Deep Water to Weddell Sea Deep and Bottom Water. Direct measurements of the outflow of bottom water (potential temperature $< -0.7^\circ\text{C}$) from moorings in the western boundary current show a mean of 1.7 Sv, and a range from 0.8 to 3.9 Sv; additional bottom water export occurs offshore of the narrow boundary current (Fahrbach *et al.*, 1994). Dense shelf water also escapes from the Weddell Sea to the Scotia Sea through gaps in the island chain separating the basins (Whitworth *et al.*, 1994).

The 700-km-long drift of Ice Station Weddell in 1992 further refined our understanding of

ice–ocean–atmosphere interactions in the western Weddell Sea (Gordon *et al.*, 1993; Gordon, 1998). Taken together, the results of recent programmes identify a number of distinct AABW sources along the southern and western rim of the Weddell Sea, each with a characteristic temperature, salinity and stable isotope signature. The relative importance of the two mixing scenarios described above varies along the rim of the Weddell. Entrainment of warmer and saltier deep water found over the slope largely determines the ultimate properties of deep and bottom water leaving the Weddell Sea. Gordon (1998) estimates the formation of Weddell Sea Bottom Water (WSBW) (potential temperature $< -0.7^\circ\text{C}$) during the period of the Ice Station drift to be 4.0–4.8 Sv. Mensch *et al.* (1998) estimate a similar formation rate (about 5 Sv of deep and bottom water) from tracer measurements obtained during the Ice Station.

Satellite observations of a large polynya in the Weddell Sea in the late 1970s, and the large changes in temperature and salinity of Weddell Sea Deep Water that resulted (Gordon, 1982), first sparked interest in the variability of Weddell waters. A number of recent studies have documented variations of deep and bottom water properties. Gordon (1998) concludes that the average salinity of the WSBW formed during the Ice Station is too low to provide the end-member required to account for the deep water of the Weddell gyre, and suggests that the bottom water forming at the present time contains more Ice Shelf Water. Nøst and Østerhus (1998) describe the impact of several large grounded icebergs north of the Filchner depression, which have caused the cessation of high-salinity shelf water formation there and led to a cooling and freshening in the depression. Further afield, Coles *et al.* (1996) and Hogg and Zenk (1997) have observed cooling and freshening (on isopycnals) of AABW spreading north in the South Atlantic, which they attribute to changes in open ocean convective events in the Weddell Sea.

Recent studies have also identified or confirmed a number of important sources of AABW outside the Weddell Sea. Rintoul (1998) shows that the Adélie coast (140–150°E) is likely to be a more significant source of bottom water than previously appreciated. The Adélie Land Bottom Water is evident in Fig. 4.6.3 as a thin layer of cold, fresh, dense, high-oxygen water found over the continental slope and rise of Antarctica. He argues on the

basis of Worthington's (1981) volumetric census, and T-S properties at the sills bounding the Australian–Antarctic Basin, that the Adélie Land Bottom Water accounts for up to 25% of the global volume of AABW. The concentration of CFC-11 in plumes of Adélie Land Bottom Water is high ($>2.9 \text{ pmol kg}^{-1}$ in 1991; Rintoul and Bullister, 1999), and the CFC saturation (35%) is similar to that in plumes observed in the southwest Weddell Sea. High CFC concentrations observed over the continental slope at 30°E in the eastern Weddell Sea (Mantisi *et al.*, 1991) indicate that a source exists along the Enderby coast or in Prydz Bay as well, as suggested earlier by Jacobs and Georgi (1977).

Recent studies have also identified regions of the Antarctic coastline where AABW is *not* formed. For example, Fahrbach *et al.* (1994b) show that AABW is not formed in the eastern Weddell Sea, primarily because of the inability to confine shelf water (and increase its salinity) over the narrow shelf there. In the Amundsen and Bellingshausen Seas, nearly undiluted warm Circumpolar Deep Water intrudes onto the shelf and melts large amounts of continental ice, preventing formation of dense saline water (Hellmer *et al.*, 1998).

Foster (1995) confirmed the observation of Carmack and Killworth (1978) that the Wilkes Land coast east of 150°E forms water that is not quite dense enough to sink to the seafloor. Sinking of Antarctic shelf waters to deep, rather than abyssal, layers is potentially of significant importance to ventilation of the deep ocean at lower latitudes, since these lighter layers are less confined by bathymetry and are free to spread northward. The formation of 'not quite bottom' water around Antarctica has so far received little attention, and the transport is unknown. Weppernig *et al.* (1996) conclude from the distribution of stable isotopes that a large fraction ($>80\%$) of the dense Ice Shelf Water leaving the continental shelf in the Weddell Sea supplies the WSDW at intermediate depth, rather than sinking to the bottom to supply WSBW.

A powerful demonstration of the utility of transient tracer measurements is the use of CFC inventories to estimate the formation rate of AABW (Orsi *et al.*, 1999). They find that about 8 Sv (4.9 Sv in the Atlantic and 3.2 Sv in the Indian–Pacific) of new bottom water (a 50:50 mix of dense shelf water and entrained deep water) must sink across the 2500 m isobath to explain the observed CFC-11 inventory in the AABW layer

(water with neutral density greater than 28.27 kg m^{-3}). Much of the 3.2 Sv formed in the Indian–Pacific sectors is likely produced by sources in the Australian Antarctic Basin (e.g. Adélie Land), since the average CFC-11 concentration there is 2.5 times as large as that of the Atlantic and Pacific basins (Fig. 4.6.13).

The CFC-11 inventory of Orsi *et al.* (1999) provides a strong integral constraint on the formation of AABW. Broecker *et al.* (1997) have noted that $\text{PO}_4^* (\text{PO}_4^* = \text{PO}_4 + \text{O}_2/175 - 1.95 \mu\text{mol kg}^{-1}$, where 175 is the average molar Redfield ratio of O_2 consumption to remineralization in the deep sea and 1.95 is an arbitrary constant.) also provides a constraint on the relative production of dense ventilated water in the Southern Ocean and the North Atlantic: roughly equal contributions from the two source regions are required to explain the PO_4^* value observed in the deep Indian and Pacific Oceans. The PO_4^* budget thus requires sinking of about 15 Sv of ventilated shelf water around Antarctica, a factor of three to four higher than implied by the CFC-11 inventory or by transport measurements near the sources. Part of this discrepancy may be explained by exchange of ventilated shelf water with deep water lighter than neutral density of 28.27 kg m^{-3} . However, given that the CFC content of the lighter deep water is so much lower than that of the dense abyssal layer it is difficult to see how this process can account for the discrepancy. Another possibility is that AABW production in recent decades is substantially smaller than the average during the last millennium (Broecker *et al.*, 1997). The conflict between estimates of ventilated deep water production based on CFC and PO_4^* remains unresolved.

WOCE sections, moored arrays, and other recent measurements have helped to map out the system of deep western boundary currents and through-passage flows that carry AABW and LCDW to lower latitudes (e.g. Mantyla and Reid, 1995; Rhein *et al.*, 1998a; Whitworth *et al.*, 1999; Zenk *et al.*, 1999a; see also Hogg, Chapter 4.5).

4.6.5 The Southern Ocean and the global overturning circulations

The global overturning circulation is often taken to be synonymous with the circulation loop formed by sinking and export of NADW from the

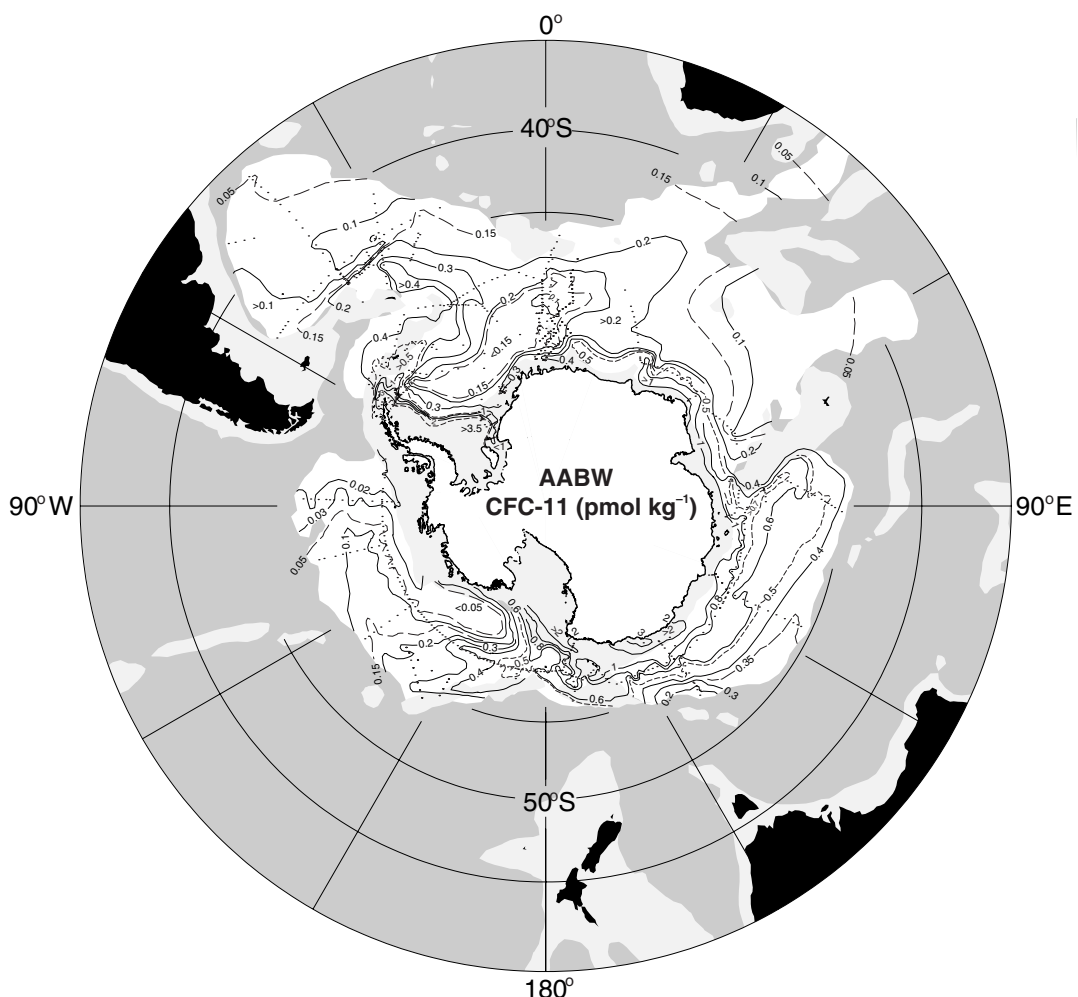


Fig. 4.6.13 Inventory of CFC-11 in the AABW layer (between neutral density 28.27 kg m^{-3} and the seafloor), from Orsi *et al.* (1999). The layer-mean CFC-11 concentrations in the Atlantic (Weddell–Enderby), Indian (Australian Antarctic), and Pacific basins are $0.17, 0.47$ and $0.18 \text{ pmol kg}^{-1}$, respectively.

North Atlantic, upwelling elsewhere in the ocean, and a return flow of lighter water. The ACC carries NADW from the Atlantic to the other ocean basins and so forms an important link in this circulation path. But the significance of the Southern Ocean to the global overturning goes beyond the passive role of redistributing NADW. Upwelling and buoyancy forcing in the Southern Ocean drive the water mass transformations required to close the NADW cell, as well as several additional overturning circulations, both shallow and deep. The nature of the overturning circulation is also intimately related to the dynamics of the ACC, as described above.

To balance the sinking of NADW in the North Atlantic, somewhere deep water must be converted to lighter water. Given that no zones of

concentrated upwelling from the abyss to the thermocline have been observed, the traditional assumption is that the upwelling is more or less broadly distributed in the ocean interior. This assumption, together with conservation of potential vorticity, has profound implications for the deep flow, as illustrated in the simple and elegant theory of the abyssal circulation of Stommel and Arons (1960a).

Direct measurements of mixing in the ocean pycnocline, however, typically find diffusivities an order of magnitude too low to support the upwelling required to balance the sources of deep water (Ledwell *et al.*, 1993; Toole *et al.*, 1994). Radiocarbon distributions also argue against widespread upwelling of deep water through the pycnocline (e.g. Toggweiler and Samuels, 1993). On the other hand, recent measurements suggest

diapycnal mixing throughout much of the water column is enhanced over rough topography (Polzin *et al.*, 1997; Ledwell *et al.*, 2000). Diapycnal mixing may also be enhanced near the boundaries of the ocean (Wunsch, 1970; Armi, 1978). To date there are few direct measurements of diapycnal mixing, and so it is not yet clear if (non-uniform) interior mixing will prove to be sufficient to balance the sinking at high latitude.

An alternative view is that the required conversion of dense to light water occurs primarily in the Southern Ocean, where deep isopycnals outcrop and are exposed to air-sea fluxes of heat and fresh water (Döös and Coward, 1997; Toggweiler and Samuels, 1998). Here we reconsider the meridional overturning in the Southern Ocean, this time from the perspective of its connection to the rest of the world ocean.

As explained in the introduction, an active overturning circulation in the Southern Ocean was inferred by early investigators on the basis of the prominent core layers (Figs 4.6.2 and 4.6.3) which extend across the ACC (e.g. Sverdrup, 1933). Deep water spreads south and upward across the ACC, and is balanced by sinking and northward flow of both lighter intermediate water and denser bottom water. This picture is broadly consistent with the requirements of closure of the NADW overturning – import of NADW to the Southern Ocean is balanced by export of IW and BW, as observed in the South Atlantic (Rintoul, 1991; Saunders and King, 1995b) – and suggests that the water mass conversions taking place in the Southern Ocean are a key element of the overall cell. The ‘intermediate’ cell (conversion of DW to IW) is consistent with northward Ekman transport driven by the strong westerly winds: divergent Ekman transport drives upwelling of deep water, which in steady state must be converted to lighter water by buoyancy input from the atmosphere as it is driven north across mean density contours (Fig. 4.6.1; Toole, 1981; Speer *et al.*, 2000).

However, in the ensuing 60 years, few attempts have been made to quantify the flow paths in Sverdrup’s diagram. One recent exception is Schmitz’s (1995, 1996a,b) attempts to synthesize global view from a large number of published estimates for individual branches of the overturning circulation. Summing his estimates for the three individual basins at about 40°S, the overturning in the Southern Ocean consists of 53 Sv of deep water

(NADW/UCDW) flowing south, balanced by 48 Sv of bottom water (AABW/LCDW) and 5 Sv of intermediate water (SAMW/AAIW) flowing north. Schmitz’s summary of ‘best guess’ values from the literature suggests that in the zonal integral the deep cell (DW to BW) is much stronger than the intermediate cell (DW to IW) of Sverdrup’s diagram.

Schmitz’s circulation scheme is derived from a number of individual estimates, which may not be internally consistent. His results are, however, very similar to estimates from a recent Southern Ocean inverse model, which provides an internally consistent solution that explicitly includes air-sea buoyancy forcing and diapycnal mixing (Sloyan and Rintoul, 2001b). In the zonal integral across roughly 30°S they find 52 Sv of deep water flowing south, balanced by 46 Sv of lower deep and bottom water and 6 Sv of intermediate water flowing north (Fig. 4.6.14; see caption for layer definitions).

These results suggest the deep overturning cell, in which dense AABW/LCDW exported to the Indian and Pacific is balanced by import of slightly less dense DW, dominates the overall Southern Ocean overturning. Note that the contribution of NADW to the zonally integrated overturning is small by comparison: for example, the 10 Sv poleward flow of lower NADW (neutral density between 28.0 and 28.2) is more than compensated by strong equatorward flow in this density class in the Indian and Pacific. The intermediate cell (conversion of DW to IW) is weak in the zonal integral at 40°S (although the gross exchanges in this density class are large, as described in Section 4.6.4.1).

The observations of flow entering and leaving the Southern Ocean across 30–40°S imply significant poleward transport in density layers shallower than the Drake Passage sill (neutral density of 27.4–28.0 kg m⁻³). In addition, the net northward transport of light water is much smaller than the Ekman transport, suggesting that much of the Ekman transport returns poleward at similar density south of 40°S. Substantial poleward transport in density layers not blocked by topography implies divergence of the interfacial form stress, or equivalently, the eddy buoyancy flux (Section 4.6.3). Speer *et al.* (2000) show that there are strong gradients in isopycnal thickness (or potential vorticity) across the ACC in the UCDW layer; eddy mixing will therefore tend to smooth out the gradient, resulting in a volume flux to the south. Meridional gradients of isopycnal thickness are

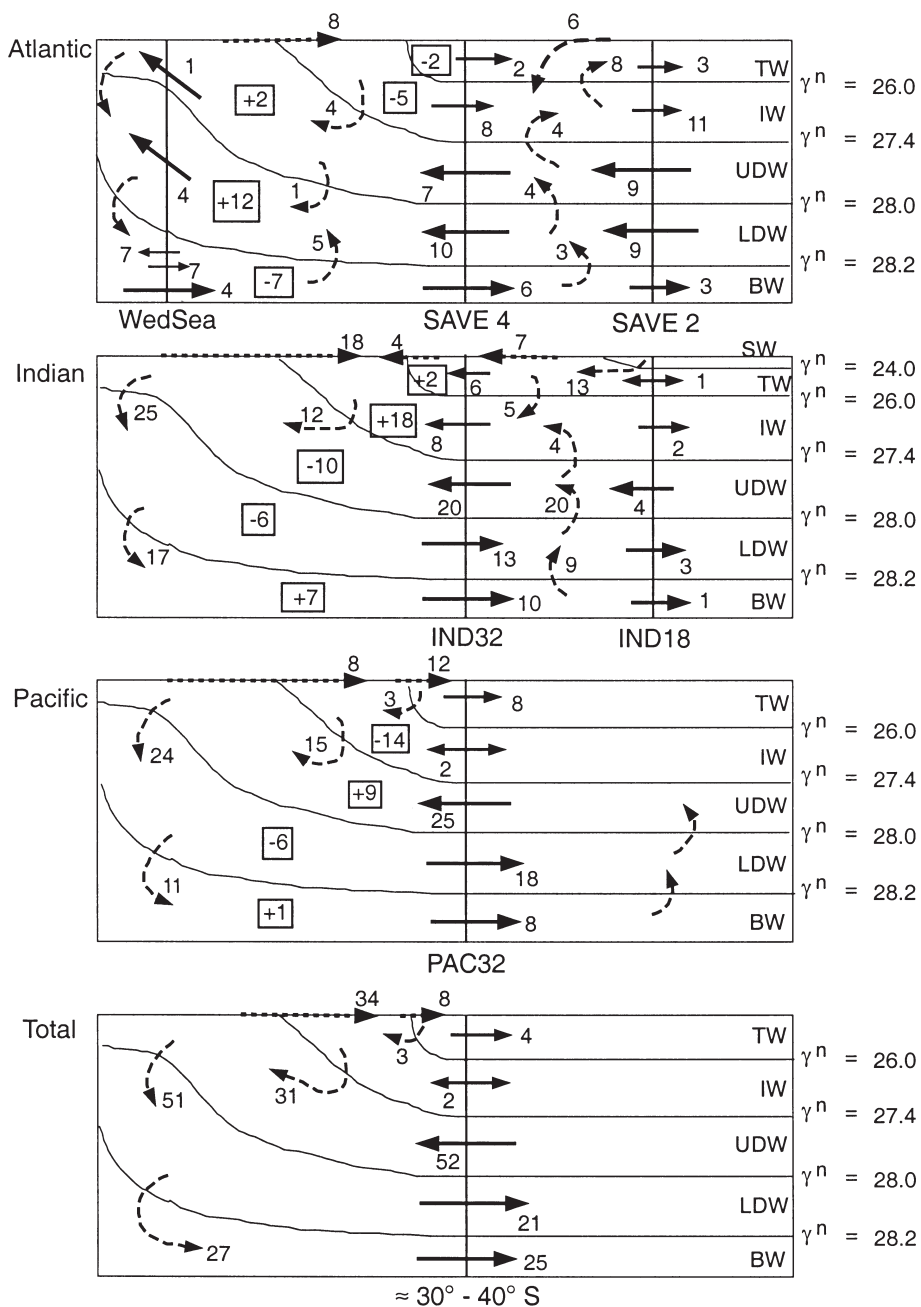


Fig. 4.6.14 A schematic five-layer view of the overturning circulation (units of $10^6 \text{ m}^3 \text{ s}^{-1}$) in each southern hemisphere basin, and the zonal sum, from the inverse model of Sloyan and Rintoul (2001b). SW, Surface Water; TW, Thermocline Water; IW, Intermediate Water; UDW, Upper Deep Water; LDW, Lower Deep Water; and BW, Bottom Water. The neutral surfaces used to define each layer are shown. Air-sea flux-driven diapycnal fluxes are shown by bold, dashed arrows at the sea surface. Net diapycnal fluxes due to interior mixing are indicated by thin dashed arrows; their location along the isopycnal is schematic only. Numbers in boxes represent the net convergence (+ve) or divergence (-ve) of a particular layer in that sector of the Southern Ocean. Two-headed arrows in intermediate water highlight that the net flux is the difference between nearly balancing northward and southward fluxes. Labels beneath each plot indicate the hydrographic sections used in the inverse model (e.g. PAC32 is a section at about $32^\circ S$ in the Pacific).

small in the LCDW layer, which lies below the topography where mean geostrophic meridional flow is possible. In the terminology of Section 4.6.3.2, these observations suggest the real ocean is closer to case I.

Because the overturning circulation in numerical models depends on how the model is forced (e.g. restoring or surface flux boundary conditions), how eddies are parameterized, and whether the model is in steady state, they do not provide conclusive evidence for or against deep versus shallow compensation of the Ekman transport. Nevertheless, a number of recent simulations, both coarse and fine resolution, support the idea that a significant fraction of the Ekman transport is balanced by a return flow shallower than the topography (case I). For example, Hirst and McDougall (1998) show that a coarse-resolution level model with the Gent and McWilliams (1990) parameterization of eddy-induced advection is consistent with case I: in density coordinates, there is very little meridional overturning associated with the Ekman transport between 40°S and 60°S. While the degree of cancellation between the eddy-induced advection and the Ekman transport (nearly complete in their model) depends on the value chosen for the diffusivity, the model improvements that result when such a parameterization is used support the notion that eddy-driven transport likely plays an important role in the overturning circulation of the Southern Ocean. (The simulation is also improved by the decrease in horizontal mixing permitted when the eddy parameterization is used.) Killworth and Nanneh's (1994) analysis of the zonal momentum budget in isopycnal layers in FRAM supports this conclusion: at the latitudes of Drake Passage, almost all (at the southern side) to about half (at the northern side) of the northward transport of light water returns south at densities that do not intersect topography.

In summary, observations suggest significant poleward flow in layers above topography, which must be driven by divergence of the eddy (standing and/or transient) interfacial form stress, in addition to a poleward flow in density layers blocked by topography. A variety of numerical simulations also suggest that the presence of eddies permits a southward flux at densities above topography, which compensates a large fraction of the northward Ekman flux. In QG simulations this compensation

must be complete, since no diabatic transport is permitted. In PE models that either resolve or adequately parameterize the effect of eddies, there is still a large degree of compensation. The time and zonal mean flow at constant depth, in which the Ekman mass transport returns at depths blocked by topography, is thus decoupled from the time and zonal mean flow at constant density, in which most of the Ekman transport returns at densities above topography.

4.6.6 Conclusions

Substantial progress has been made in understanding the circulation of the Southern Ocean during the 'WOCE decade'. This progress has relied on advances in observations, theory and modelling. Observations collected during WOCE represent a significant achievement, given the challenges posed by the remote and often hostile nature of the Southern Ocean. Highlights include a circumpolar survey of high-quality hydrographic, tracer and ADCP data (including some of the first repeat sections obtained in the region), a number of mooring arrays, float and drifter deployments, and satellite measurements of sea surface height and temperature. Analytical models have provided insight into the mechanisms responsible for setting the transport of the ACC. The last decade has also seen rapid development of numerical models of the Southern Ocean, including the first GCMs to incorporate stratification, realistic topography, and to resolve (or 'permit') eddies. The ability of coarse-resolution models to simulate the Southern Ocean has also improved significantly, in part due to more effective parameterizations of the effect of eddies. Fine-resolution models have achieved sufficient realism that we can use them to estimate the magnitude of individual terms in the momentum or vorticity budgets, to identify sites of strong topographic influence, and to describe qualitatively the circumpolar structure of the complex, filamented ACC, although it is still not clear what resolution is necessary for a truly realistic simulation.

The momentum, vorticity and buoyancy budgets – and as a consequence, the zonal and meridional circulations – are intimately linked. The dynamics of the ACC differ in character from those of strong currents in other ocean basins that are zonally blocked. The now established fact that

the zonal wind stress is balanced by bottom form stress means that the Sverdrup balance is upset by interactions with topography: meridional flows driven by the wind stress curl are returned in flows balanced by bottom pressure torques rather than in viscous boundary layers. In addition, for a significant part of the northward Ekman flux to return in density layers that do not intersect topography at some latitude (as models and observations indicate), a strong, deep-reaching ACC is needed to maintain the interfacial form stress divergence required for dynamical balance of the return flow. Without strong top-to-bottom flow, the ACC could not achieve a dynamical state that is almost non-viscous, supercritical with respect to Rossby wave propagation and meridionally constrained in narrow fronts.

It has long been recognized that eddy fluxes play an important part in the dynamics and thermodynamics of the Southern Ocean. In the last decade the central role of eddies has become even more clear. Eddies carry heat poleward and momentum downward across density surfaces; the momentum transfer helps establish the correlation between pressure and topography that provides the bottom form stress to balance the wind; and a substantial fraction of the meridional overturning circulation is dynamically balanced by the divergence of interfacial form stress. In this sense, the dynamical analogy between the ACC system and the mid-latitude troposphere is even more complete than previously appreciated.

The high-quality WOCE hydrographic and tracer sections have provided new insights into the formation and circulation of Southern Ocean water masses. Buoyancy exchange with the atmosphere drives substantial water mass transformations, converting both light water to dense water (e.g. over the extensions of the subtropical western boundary currents, and near the Antarctic margin) and dense to light (over much of the Southern Ocean, where northward Ekman transport combines with heat and freshwater input to convert deep water to intermediate water). Tracers have been used to refine estimates of the rate of Antarctic Bottom Water formation, to identify the main circulation pathways, and to quantify the ‘ventilation age’ of Southern Ocean water masses.

Many of these ideas have come together to provide a new appreciation of the significance of the Southern Ocean in the global climate system. The

ACC provides the interbasin connection required for a global thermohaline circulation to exist. Perhaps a more important link between the Southern Ocean and the global overturning circulation is the transformation of water masses driven by air-sea forcing and diapycnal mixing. Various lines of evidence suggest that diapycnal mixing rates in the main thermocline are too slow to support the traditional view that sinking of deep water is balanced by upwelling uniformly distributed over the ocean. Much of the conversion of cold to warm water that is required to close the NADW overturning circulation appears to take place in the Southern Ocean, where deep water outcrops and is exposed to air-sea buoyancy forcing. The NADW cell, however, is overwhelmed in the zonal integral by an even stronger deep overturning involving conversion of upper deep water to denser lower deep and bottom water in the Southern Ocean, and conversion of lower to upper deep water in the deep basins of the Indian and Pacific Oceans.

Analysis of WOCE data from the Southern Ocean is at an early stage. We anticipate further progress will be made as the full suite of observations collected during WOCE (e.g. hydrography and tracers, floats, altimetry, moorings) are synthesized. Advances in theory and modelling of the ACC also continue at a rapid rate. Among the important open questions to be addressed by these analyses and future observational programmes are: What is the absolute transport of the ACC, and how and why does it vary in time? How sensitive are the water mass conversions taking place in the Southern Ocean, and the overturning circulations of which they are part, to changes in atmospheric forcing? What are the relative contributions of ‘deep’ and ‘bottom’ waters produced along the Antarctic margin to the ventilation of the deep sea? How representative are the WOCE-era measurements? Can we detect and interpret changes between measurements made during WOCE and historical or future observations?

Many, but not all, of these questions will be answered as analysis of the WOCE data set continues. However, while a major step forward, the WOCE observations are still sparse in space and time. In a region as remote as the Southern Ocean, there will always be a strong reliance on remote sensing and autonomous instruments. For example, the development of profiling floats now provides

the opportunity to sample the variability of the Southern Ocean on broad spatial scales for the first time. The floats complement, but do not replace, the high-density repeat sampling along fixed cruise tracks required for transport estimates. Direct, coherent and sustained *in-situ* measurements of absolute velocity on large spatial scales, as required to improve our understanding of the barotropic flow, remain beyond our present technological capacity. However, the combination of a highly accurate and well-resolved geoid from planned satellite gravity missions and satellite altimetry will provide an unprecedented opportunity to resolve the absolute flow of individual jets in the ACC, and make possible quantitative studies of eddy-mean flow interactions in the Southern Ocean. The Southern Ocean also remains a great challenge for ocean models, which suffer their greatest difficulties where strong currents and eddies interact with bottom topography, a process central to the dynamics of the ACC. While significant progress been made in the

theory, observation and modelling of the Southern Ocean, we still do not have a realistic theoretical picture of the dynamical processes that regulate the response of the ACC to wind stress and thermohaline forcing. Only with such a picture will it be possible to place the WOCE observations into their proper context and determine their limitations. The challenge is to use and extend the WOCE data and models to help build that picture.

Acknowledgements

We thank Trevor McDougall, Peter Baines, the editors, and two anonymous reviewers for their comments on an earlier draft. We also thank Louise Bell and Jennifer Moss for preparing several figures. This work is supported in part by Environment Australia through the CSIRO Climate Change Research Program. Contribution No. 1628 from the Alfred-Wegener-Institute for Polar and Marine Research.

4.7

Interocean Exchange

Arnold L. Gordon

4.7.1 Interocean Links

Earth's climate, responding to the different thermodynamic properties of the land and ocean surfaces, is sensitive to the continental configuration and distribution of mountain ranges. This is clearly seen in the pattern of mean annual and seasonal range in such climate parameters as temperature and humidity and in the quasistationary patterns of atmospheric circulation, from small-scale sea breezes to planetary waves. Presumably because of the ocean-land configuration, each ocean basin is exposed to different atmospheric forcing, taking on correspondingly distinct property and circulation characteristics (Figs 4.7.1a,b, see Plate 4.7.1a,b, p. 300). These in turn provide feedback to the climate system through their effect on Sea Surface Temperature (SST) distribution, heat and freshwater fluxes and ocean overturning. Similarity between oceans is inhibited by their varied degrees of isolation from one another, and thus the coupled ocean-atmosphere system is influenced by the efficiency of interocean exchanges that link the ocean basins. More efficient interocean exchange leads to reduced contrast between the oceans, with each ocean closely resembling its neighbour. Interocean exchange would be expected to be balanced mainly by ocean circulation on approximately a horizontal plane. Less efficient exchange is expected to produce oceans that contrast sharply with each other, a condition more apt to induce stronger global reaching, overturning thermohaline circulation. Equilibrium states between patterns of interocean exchange and circulation on the horizontal and vertical planes may be expected for specific continental configurations.

4.7.1.1 Antarctic Circumpolar Current

The oceans of the southern hemisphere vary less from each other than do the northern hemisphere oceans. Isolation and differences grow with distance from the rapid interocean exchange afforded by the Antarctic Circumpolar Current (ACC; for detailed information of the ACC, see Rintoul *et al.*, Chapter 4.6). The ACC is the giant of interocean exchange, carrying about 134 Sv (Sverdrup, $1 \text{ Sv} = 10^6 \text{ m}^3 \text{ s}^{-1}$) of polar and subpolar water masses from west to east through the Drake Passage (Nowlin and Klinck, 1986). Variations in ACC transport through the Drake Passage amount to 20% of the mean. ACC transport is enhanced south of Australia by the Indonesian Throughflow, of about 10 Sv.

The ACC is mainly a zonally flowing current, but large quasistationary waves in the ACC, guided by bottom topography, lead to a latitudinal swing of approximately 1200 km (furthest north in the Atlantic; furthest south in the southwest Pacific – Gordon *et al.*, 1978; Orsi *et al.*, 1995). The equatorially flowing Malvinas Current, which may be considered as a branch of the ACC, carries subpolar waters well to the north, to the separation of the Brazil Current near 38°S. Transient waves in the ACC (Antarctic Circumpolar Wave; White and Peterson, 1996) may link the ACC with sea ice distribution and larger-scale climate variability (Yuan and Martinson, 2000). Mesoscale eddies within the ACC provide oceanic meridional heat and freshwater fluxes to balance much of the ocean-atmosphere exchange south of the ACC.

The Southern Ocean meridional overturning is induced by the large-scale wind and by buoyancy forcing of the very cold conditions along the margins of Antarctica. Deep water (potential temperature 1–2°C, salinity 34.7–34.9) with characteristics developed in more northern latitudes, upwells around Antarctica to be converted into Antarctic Intermediate Water (AAIW; 3–5°C, 34.2–34.4) and Antarctic Bottom Water (AABW; <–1°C, 34.65–34.75). Southern Ocean overturning induces large upward heat flux, limiting sea ice thickness (Gordon and Huber, 1990). Southern Ocean overturning is most effective in projecting Southern Ocean water mass properties to the global scale (see Sloyan and Rintoul, 2000b).

An interesting aspect of the ACC relevant to interocean heat and freshwater fluxes, the theme of this chapter, which may contribute to the saltiness of the Atlantic Ocean, was pointed out by Gordon and Piola (1983), who inspected the salinity change of the subpolar surface water within the ACC *en route* across the South Atlantic. They found that the observed freshening equals the net evaporation minus precipitation of the subtropical South Atlantic. The water vapour derived from the subtropics is carried southward, to balance excess precipitation over the ACC (see Fig. 12.10 of Peixoto and Oort, 1992). The ACC exports the fresh water across the Indian Ocean into the Pacific Ocean. This situation arises because the poleward extension of South America and the Andes limits freshwater transfer from the Pacific to the Atlantic by both ocean and atmosphere. There is no such block provided by Africa, which does not reach the position of the maximum westerlies. The same may be true of the Indian sector, as southern Australia is also well north of the maximum westerlies. Extraction of fresh water from the South Atlantic increases the salinity of the South Atlantic subtropical water, which has an extensive region of surface salinity of greater than 36.4, an attribute lacking in the other southern hemisphere subtropical gyres (Fig. 4.7.1b, see Plate 4.7.1b, p. 300). Saline South Atlantic surface water eventually spreads northward within the North Brazil current and may be a factor in the saltiness of the North Atlantic Ocean.

4.7.1.2 Northern oceans

The great ocean embayments of the northern hemisphere vary markedly from each other. Surplus

precipitation and runoff over evaporation in the North Pacific induces low surface salinity with a highly stable halocline inhibiting deep-reaching convection. The lack of deep convection in the subpolar North Pacific and associated meridional overturning circulation limits poleward spreading of warm low-latitude waters, which further suppresses evaporation (Warren, 1983). The North Atlantic Ocean, with excess evaporation over precipitation and runoff, forms a saline surface layer prone to deep convection and the formation of North Atlantic Deep Water (NADW). Sinking of surface water associated with NADW formation draws compensatory warmer surface water poleward. Warmer SST in the western subtropical North Atlantic (relative to that of the North Pacific, Fig. 4.7.1a, see Plate 4.7.1a, p. 300) may encourage further evaporation, invigorating Atlantic meridional overturning circulation. Evaporation of the subtropical North Atlantic and net precipitation over the equatorial Pacific are coupled by westward water vapour flux (about 0.3 Sv; Zaucker and Broecker, 1992) across the Isthmus of Panama, thought to be a major force behind NADW formation (Zaucker *et al.*, 1994).

The Pacific halocline abruptly developed, along with intensification of northern hemisphere glaciation, about 2.73 million years ago (Haug *et al.*, 1999). It is likely that this coincided with severing of the direct oceanic link between the North Pacific and North Atlantic Oceans with the rise of the Isthmus of Panama and, by inference, the development of a saline North Atlantic, conducive to NADW formation. Thus a change in interocean exchange 2.73 million years ago forced a different pattern of horizontal and vertical circulation that remains active in today's ocean.

The Indian Ocean north of 10°S is exposed to a strongly monsoonal climate. Convection into the thermocline and intermediate levels occurs within the evaporative, saline Arabian and Red Seas. Enormous influx of fresh water produces stratification reminiscent of an estuarine environment within the Bay of Bengal. Exchange of fresh water between the Arabian Sea and the Bay of Bengal may be viewed as a regional analogue to the Atlantic–Pacific global-scale system.

4.7.1.3 The global chain of interocean thermohaline links

Interocean exchange is suspected as being an important part of the present-day global thermohaline

circulation, particularly that which is in response to NADW formation (Gordon, 1986, 1996a,b; Broecker, 1991; Rintoul, 1991; Gordon *et al.*, 1992; Schmitz, 1995; MacDonald and Wunsch, 1996). The reader is directed to the excellent two-volume report of Schmitz (1996a,b).

NADW is exported into the Indian and Pacific Oceans by the ACC, becoming entangled in the overturning circulation of the Southern Ocean and associated AAIW and AABW formation. NADW export from the Atlantic Ocean must be balanced by import of Indian and Pacific Ocean waters within the water column shallower than NADW – but how? From the warm saline Indian Ocean thermocline and intermediate waters around the southern rim of Africa (the warm route), or from cooler, fresher subpolar Pacific water through the Drake Passage (the cold route)? Or, as more likely, both? Does the Indonesian Throughflow have anything to do with NADW formation? Do the ratio or efficiencies of these return routes vary in time? Might such variability be coupled to NADW formation and climate variability? Though there has been a plethora of papers on these subjects, some favouring the warm route (a recent example is that of Holfort and Siedler, 2001) and others the cold route (Rintoul, 1991; Schlitzer, 1996), definitive answers as to the climate importance of interocean exchange are still evolving.

MacDonald and Wunsch (1996) investigated the nature of the global thermohaline circulation pattern using a set of 23 (mostly WOCE) sections and the statistical guidelines of the inverse box model approach. Within the limits of the non-synoptic data set, two independent large-scale, global integrated circulation cells emerge. The Atlantic–Southern Ocean cell carries NADW into the Southern Ocean, where it is integrated into the Southern Ocean overturning cell and spreads into the Indian and Pacific Oceans. The second cell is confined more to a horizontal plane, linking the Pacific and Indian Oceans by westward flow within the Indonesian Seas and eastward flow (presumably within the subpolar zone) south of Australia. The two cells are linked through the highly time-dependent Agulhas Retroflection south of Africa and through upwelling of deep waters in the Pacific Ocean (Gordon, 1996b).

Interannual to decadal SST anomalies may be transferred between ocean basins by the interocean links (e.g. the ACC; Peterson and White, 1998).

Also, one can envision that SST anomalies could be generated within an ocean basin by variability in the interocean transport (e.g. variability in any of the three interocean channels discussed below: Bering Strait, Indonesian Seas and Agulhas Retroflection). Millennium-scale changes in wind and sea level associated with glacial epochs may also be expected to alter the form of the interocean exchange, which would alter global thermohaline circulation with feedback to the climate system (Seidov and Haupt, 1999).

While the ACC is by far the largest conduit for interocean exchange, water mass differences between the major ocean basins would be much larger were it not for various smaller interocean links, which may be linked into a global chain. The objective of this chapter is to present the current state of knowledge about those small but important interocean links. The regional oceanography of these areas is not developed (see Tomczak and Godfrey, 1994), but rather only those aspects directly associated with interocean fluxes. The interocean links discussed below are: the Bering Strait (Fig. 4.7.1c, see Plate 4.7.1c, p. 300) and Indonesian Seas (Fig. 4.7.1d, see Plate 4.7.1d, p. 300), which allow for the export of low-salinity North Pacific upper layer water to the Atlantic (Arctic) and Indian Oceans, respectively; and the Agulhas leakage of Indian Ocean thermocline and intermediate water into the Atlantic at the southern rim of Africa (Fig. 4.7.1e, see Plate 4.7.1e, p. 300). Before discussing these interocean links, it is worthwhile mentioning the presence of westward flow of Pacific water into the Indian Ocean immediately south of Australia.

4.7.1.4 South of Australia

Observations (Fine, 1993; Reid, 1997; Rintoul and Bullister, 1999) and models (Semtner and Chervin, 1992; Speich *et al.*, 2000) suggest flow of Pacific water into the Indian Ocean along the southern coast of Australia. While much of this may be part of a closed anticyclonic gyre in the Great Australian Bight, there is a possibility of waters from the Tasman Sea flowing into the Indian Ocean. Rintoul and Bullister (1999) find 2–3 Sv of Tasman water flowing westward south of Tasmania within the 800 and 3000 m depth interval; Speich *et al.* (2000) in their model study find 3.2 Sv of Pacific water entering the Indian Ocean in the upper 1200 m, and the model shows this

water crossing the Indian Ocean to flow south through the Mozambique Channel, Agulhas Current and into the South Atlantic. Whether the westward flow immediately south of Australia is an important, overlooked element of a global-scale interocean circulation pattern, or more of a regional, Indian Ocean gyre reaching into the Tasman Sea, is an important issue to be resolved. The basic question is, 'Is the South Pacific "climate" imprinted on the Pacific to Indian flow south of Australia?'

4.7.2 Bering Strait

4.7.2.1 Introduction

The Bering Strait, with a sill depth of 45 m within Anadyr Strait (about 200 km south of the narrowest width of Bering Strait), allows cold, low-salinity surface waters to flow from the North Pacific to the Arctic's Arctic Sea (Fig. 4.7.1b, see Plate 4.7.1b, p. 300). While the mass transport of less than 1 Sv is minor compared with other interocean flows, it is notable because of the influence of the Bering strait transport on the Arctic freshwater budget (Aagaard and Carmack, 1989, 1994; Swift *et al.*, 1997). North Pacific waters entering the Arctic Sea spreads within the Arctic upper pycnocline layer into the Canada Basin. The Bering Strait water eventually is exported from the Arctic to the northern North Atlantic Ocean via the Fram Strait and within the complex channels of the Canadian northwest territory (Rudels *et al.*, 1994; Jones *et al.*, 1998).

4.7.2.2 Transport

A 4-year time series of temperature, salinity and velocity data across the Bering Strait from 1991 to 1994 is presented by Roach *et al.* (1995). They find a mean transport of 0.83 Sv with a weekly standard deviation of 0.66 Sv. The annual cycle has a range of 1 Sv, with a maximum in summer, and a secondary maximum in January. Interannual variability of 0.5 Sv is observed. The northward transport of Pacific water is linearly linked to the meridional wind (transport = $1.06 - 0.12 V$, where V = meridional wind in $m s^{-1}$). Roach *et al.* (1995) find that the salinity of the throughflow is near 32 in autumn and about 34 in the spring, the difference reflecting summer ice melt and winter ice formation. Niebauer (1998) shows large changes in sea-level atmosphere pressure over the North Pacific as the Aleutian low shifts zonally in response to El Niño and La Niña phases (further east during

El Niño). Large interannual variability of the transport and properties of the Bering Strait Throughflow may be related to changing sea ice distribution and wind responding to the shifting Aleutian low.

4.7.2.3 Thermohaline fluxes

Aagaard and Carmack (1989) stress the importance of salinity to convective overturning within the Greenland, Iceland, Norwegian and Labrador Seas. Much of the low-salinity surface water carried into these seas by the East Greenland Current is derived from the North Pacific via the Bering Strait. Investigating the freshwater budget for the Arctic Sea (defined as the region between Fram Strait and Bering Strait) relative to 34.80, the mean salinity of the Arctic Sea, they find that the Bering Strait Throughflow of 0.8 Sv supplies $1670 \text{ km}^3 \text{ yr}^{-1}$ of fresh water to the Arctic Sea; if spread evenly over the Arctic Sea, this amounts to 18 cm yr^{-1} . This is the second largest source of fresh water for the Arctic Sea, the largest being river runoff ($3300 \text{ km}^3 \text{ yr}^{-1}$, about 0.13 Sv of fresh water, providing an Arctic freshwater cover of 35 cm yr^{-1}).

Wijffels *et al.* (1992) begin their global assessment of oceanic freshwater fluxes with the Bering Strait, using 0.8 Sv of 32.5 salinity water. In their analysis '... freshwater transport applies to that part of a seawater flux that is pure water.' As seawater is roughly 3.5% salt, the freshwater component is 96.5%. Wijffels *et al.* (1992), using the Bering Strait flux and the Baumgartner and Reichel (1975) sea-air freshwater flux values, find 0.75 Sv of fresh water enters the Arctic Sea from the Pacific. That, with the 0.18 Sv (0.05 Sv more than the Aagaard and Carmack value) of fresh water added to the Arctic by excess of runoff and precipitation minus evaporation, yields 0.93 Sv of fresh water exiting the Arctic Sea, across the latitude of Iceland.

In summer, when the Bering Strait throughflow transport is at a maximum, it injects its properties into the 50–100 m layer of the Arctic Sea, inducing a weak subsurface temperature maximum. In winter, colder and more saline Bering Strait water spreads into a deeper Arctic layer, 150–200 m, producing a temperature minimum (Tomczak and Godfrey, 1994; Rudels *et al.*, 1996). Cold, low-salinity Bering Strait water contributing to the Arctic pycnocline, acts to isolate the warmer deeper water derived from the Atlantic from the ice covered surface, reducing vertical heat flux and

promoting a thicker sea ice cover than found in the Southern Ocean, where the temperature and salinity profiles coincide.

The Bering Strait water, boosted by an additional 0.13–0.18 Sv of river inflow and excess precipitation, ultimately passes into the North Atlantic, where it provides the fresh water to offset the net evaporation over the Atlantic Ocean and input of salt from the Indian Ocean, conceivably playing a vital role in the susceptibility of the Atlantic Ocean to convection (Rahmstorf, 1995, 1996; Weijer *et al.*, 2001a; see Section 4.7.5).

4.7.3 Indonesian Seas

4.7.3.1 Introduction

A pathway for more massive export of Pacific upper ocean water to an adjacent ocean than afforded by Bering Strait occurs within the Indonesian Seas (Fig. 4.7.1d, see Plate 4.7.1d, p. 300; see also Godfrey, 1996; Lukas *et al.*, 1996). Large-scale observation-based studies (including inverse solutions) reveal significant Pacific export of fresh water and heat into the Indian Ocean (Piola and Gordon, 1984, 1986; Toole and Raymer, 1985; Wijffels *et al.*, 1992; Toole and Warren, 1993; MacDonald, 1993; MacDonald and Wunsch, 1996; Ganachaud, 1999). Shriver and Hurlburt (1997; also see Goodman, 1998) find profound effects on the Indonesian ThroughFlow (ITF) if model NADW formation is shut down, implying that even the far-off Atlantic thermohaline budgets may be related to ITF (Gordon, 1986). Increased oceanic heat and freshwater flux into the Indian Ocean at the expense of the Pacific affect atmosphere–ocean coupling with potential impacts on the ENSO and monsoon phenomena. Webster *et al.* (1998) state that the ITF heat flux ‘...is comparable to the net surface flux over the northern Indian Ocean and a substantial fraction of the heat flux into the western Pacific warm pool...it would appear that the throughflow is an integral part of the heat balances of both the Pacific and Indian Oceans.’

Model research reveals dependence of Pacific and Indian Ocean SST and upper-layer heat storage on the throughflow (Hirst and Godfrey, 1993; Verschell *et al.*, 1995; Murtugudde *et al.*, 1998). The Indian and Pacific Oceans would be very different if the ITF were zero (MacDonald, 1993). Maes (1998) finds that the effect of a zero ITF would raise sea level in the Pacific and lower sea level in

the Indian by 2–10 cm. Schneider (1998) shows that the presence of the throughflow shifts the warmest SST and associated atmospheric convective region towards the west, relative to a no-throughflow condition.

The ITF waters are drawn from the Mindanao (North Pacific thermocline) and Halmahera (South Pacific thermocline) eddies at the Pacific entrance to the Indonesian Seas, between the Philippines and New Guinea. Models show that the ITF source water (North Pacific versus South Pacific) depends upon land geometry and the tropical Pacific wind fields (Nof, 1996; Morey *et al.*, 1999; Wajsowicz, 1999). Observations show that the ITF is composed mostly of North Pacific thermocline and intermediate water flowing through Makassar Strait (Fine, 1985; Ffield and Gordon, 1992; Gordon, 1995; Gordon and Fine, 1996). Traces of what may be low-salinity Sulu Sea water are found in the Makassar Strait thermocline in the boreal winter season (Ilahude and Gordon, 1996). Wajsowicz’s (1996) model shows that the westernmost deep channel, Makassar Strait, carries the bulk of ITF. While some Makassar throughflow exits the Indonesian Sea within Lombok Channel (Murray and Arief, 1988), most turns eastward within the Flores Sea to enter the Banda Sea before entering the Indian Ocean (Gordon and Fine, 1996). In the deep channels east of Sulawesi, South Pacific water infiltrates (isopycnally) into the lower thermocline of the Banda Sea and dominates the deeper layers through density-driven overflow (Van Aken *et al.*, 1988; Gordon and Fine, 1996; Hautala *et al.*, 1996; Ilahude and Gordon, 1996).

The Indonesian Seas are not a passive channel linking the two oceans: within the seas the ITF thermal and salinity stratification and the SST are significantly modified by tidal and wind-induced mixing and by sea–air fluxes (Ffield and Gordon, 1992, 1996). The various Pacific water masses composing the ITF are altered, so that the thermohaline profile of ITF entering the Indian Ocean is quite different from that of the source Pacific water masses.

4.7.3.2 Transport

ITF transport estimates based on observations (Fig. 4.7.1d, see Plate 4.7.1d, p. 300), models and conjecture range from near zero to 30 Sv (Wyrtki, 1961a; Godfrey and Golding, 1981; Murray and Arief, 1988; Godfrey, 1989; Kindle *et al.*, 1989;

Cresswell *et al.*, 1993; Hirst and Godfrey, 1993; MacDonald, 1993; Toole and Warren, 1993; Molcard *et al.*, 1994, 1996, 2001; Miyama *et al.*, 1995; Godfrey, 1996; Gordon *et al.*, 1997, 1999a; Potemra *et al.*, 1997; Shriver and Hurlburt, 1997; Gordon and McClean, 1999; Gordon and Susanto, 1999; Potemra, 1999).

As part of the US–Indonesian Arlindo programme, velocity and temperature were measured at various depths at two moorings within a 45-km wide constriction of the Makassar Strait near 3°S between December 1996 and June 1998 (Gordon *et al.*, 1998a, 1999a; Gordon and Susanto, 1999; Ffield *et al.*, 2000). The 1997 average southward transport with Makassar Strait is 9.3 Sv, with a range of about ± 2.5 Sv depending on how the surface flow is taken into account (Gordon *et al.*, 1999a). Temperature and salinity data obtained during the Arlindo cruises (five cruises from 1991 to 1998) indicate there is no return to the Pacific Ocean of Makassar North Pacific-derived thermocline water along a route east of Sulawesi Island (Gordon and Fine, 1996; A. Gordon and R. Fine, personal communication; in fact during the La Niña condition of December 1996, a time of strong ITF, see Section 4.7.3.4, additional North Pacific thermocline water may enter the Banda Sea from the north).

Measurements in the Lombok Strait (Murray and Arief, 1988; Murray *et al.*, 1989) from January 1985 to January 1986 show an average transport of 1.7 Sv, with a maximum of 4.0 Sv towards the Indian Ocean during July and August, and less than 1 Sv from December 1985 to January 1986. The mean transport between the sea surface and 1250 m in the Timor Passage (between Timor and Australia) measured from March 1992 to April 1993 is 4.3 Sv (Molcard *et al.*, 1996). Cresswell *et al.* (1993) using CTD and ADCP sections obtained in October 1987 and March 1988 across Timor Passage find 7 Sv flowing towards the Indian Ocean. Molcard *et al.* (2001) find a range of transport within Ombai Strait (north of Timor, between Timor and Alor Island) during 1996 (December 1995 to December 1996) of 3–6 Sv, depending on the assumed cross-strait shear. While caution is urged as these time series measurements were made at different times and ENSO phases, Makassar Strait transport is comparable to the transport sum of 10.5 Sv through the passages of the Lesser Sunda Island chain.

The various streams of the ITF merge to enter the South Equatorial Current of the Indian Ocean. Within the upper 400 m passing across a section between Java and Australia, the ITF is estimated from 1983 to 1989 XBT data (Meyers *et al.*, 1995; Meyers, 1996) to be 5 Sv, with a 12 Sv August–September maximum, and near zero transport in May–June and again in October–November. Quadfasel *et al.* (1996) find that of the 22 Sv transport within the upper 470 m of the South Equatorial Current in the eastern Indian Ocean in October 1987, approximately 9 Sv is derived from the ITF. Gordon *et al.* (1997), using five meridional WOCE sections in the Indian Ocean, find that the Indian Ocean South Equatorial Current transfers on average 9 Sv of Indonesian Throughflow water westward within the Indian Ocean. Fieux *et al.* (1994, 1996) find 18 Sv passing into the Indian Ocean between Java and Australia in August 1989 and 2.6 Sv headed eastward in February 1992. The Indian Ocean South Equatorial Current estimates support an ITF transport of 10 Sv.

Inverse (and related) solutions also suggest mean values for the ITF transport. Piola and Gordon (1984) find 14 Sv, while Toole and Warren (1993) deduce a throughflow of 6.7 Sv. Robbins and Toole (1997), using the same data as Toole and Warren but with a silica constraint, find a ITF transport of 9.9 Sv. MacDonald and Wunsch (1996) arrive at a ITF of 7 Sv with a global inverse solution. de las Heras and Schlitzer (1999) calculate the ITF as 13.2 Sv. Ganachaud (1999) finds a ITF of 15 ± 3 Sv.

4.7.3.3 ITF and ENSO

Observational and model studies suggest the ITF transport sways in tune with ENSO: larger transport during La Niña condition, smaller transport during El Niño (Kindle *et al.*, 1989; Bray *et al.*, 1996; Fieux *et al.*, 1996; Gordon and Fine, 1996; Meyers, 1996; Potemra *et al.*, 1997). The high-resolution POP model (Gordon and McClean, 1999) yields a 12 Sv annual average during La Niña and 4 Sv average during El Niño. The Arlindo mooring observations within the Makassar Strait, which span the entire cycle of the strong 1997/1998 El Niño, find a correlation ($r=0.73$) between Makassar transport and ENSO (Gordon *et al.*, 1999a; though the time-series is far too short to say this with assurance). During the El Niño months December 1997 to February 1998 the transport

average is 5.1 Sv, while during the La Niña months of December 1996 to February 1997 the average is 12.5 Sv, a 2.5-fold difference. Most of the remaining variance of ITF transport once ENSO effect is removed is explained by the annual cycle, with a June maximum and December minimum (Gordon *et al.*, 1999a), and by intraseasonal events (Sprintall *et al.*, 2000; Susanto *et al.*, 2000).

As 1997 was for the most part an El Niño year, when ITF is expected to be smaller than average, the climatic ITF within the Makassar Strait is expected to be larger than the 1997 mean of 9.3 Sv. Assuming that the relationship of the Makassar ITF to ENSO is defined by the 1.6-year record (which without a longer time series is a crude approximation), a climatic mean for the ITF may be expected to be 13 Sv (from Fig. 4b of Gordon *et al.*, 1999a). An ITF transport of 10–15 Sv seems like a fair number to use, at least until observations more accurately determine the ITF mean and variability.

4.7.3.4 ITF transport profile

The Arlindo Makassar Strait measurements suggest a complex vertical profile of transport, with implications for interocean thermohaline fluxes and mass budget of the western tropical Pacific warm pool water: the most persistent and strongest ITF occurs within the thermocline and not within the warm surface layer (Gordon and Susanto, 1999; Gordon *et al.*, 1999a). The data indicate frequent occurrence of maximum southward speeds within the mid to lower thermocline. The subsurface maximum occurs during times of large transport, from April to September 1997 and again in April 1998 to the end of the record in June 1998.

An upward-looking ADCP at 150 m on the Arlindo Makassar Strait moorings provided a record of surface layer flow from 1 December 1996 to 1 March 1997. This time series shows increasing southward speeds with increasing depth, with surface flow varying from near zero to northward. This was not a local wind effect, as the NSCAT-measured winds during this period were directed towards the south. Model results suggest similar temporal dependence. Masumoto and Yamagata (1993) with the GFDL (Geophysical Fluid Dynamics Laboratory) model forced by Hellerman and Rosenstein (1983) winds show northward surface flow within Makassar during

the winter months. Using a model driven by ECMWF (European Centre for Medium Range Weather Forecasting) winds, Potemra *et al.* (1997) find that Ekman transport in the Indonesian Seas is directed towards the Pacific in the winter months, with strong Indian Ocean-bound Ekman transport in summer. The 1/6° resolution POP (Parallel Ocean Program) model display a surface (upper 100 m) flow towards the north in Makassar Strait during the winter, and towards the south in the summer months (McClean, personal communication, February 1999).

The reality and causes of seasonal oscillations of the surface flow must be further investigated. Possible candidates are: strong monsoonal zonal wind across the southern boundary of the Makassar Strait (Java and Flores Seas) relative to the weak monsoonal winds in the northern boundary of the Makassar Strait (Sulawesi Sea); Ekman pumping along the southern coast of the Sunda Islands (Potemra, 1999); or a buoyancy effect induced by the enormous amount of very-low-salinity Java Sea water injected into the Flores Sea and southern boundary of the Makassar Strait during the boreal winter.

4.7.3.5 Thermohaline fluxes

The Arlindo Makassar Strait time series reveals that the ITF transport is linked to thermocline depth: transport is smaller and thermocline shallower during El Niño (Bray *et al.*, 1996, 1997; Meyers, 1996; Ffield *et al.*, 2000). The correlation between variability in the average thermocline temperature to variability in the southward Makassar transport is $r=0.67$ (Ffield *et al.*, 2000). Using nearly 15 years of XBT data, Ffield *et al.* (2000) show that the Makassar upper thermocline temperature is highly correlated with ENSO: 0.77 for the Southern Oscillation Index; -0.80 for NINO3 SST anomaly, and -0.82 for NINO4 SST anomaly. The correlations increase when the ENSO time series are lagged a month or so. Thus the Makassar temperature field – when coupled with the throughflow – transmits equatorial Pacific El Niño and La Niña temperature fluctuations into the Indian Ocean.

An estimate of the internal energy transport (Warren, 1999) for the Makassar Strait is made by Ffield *et al.* (2000) by integrating the product of temperature, volume transport, density and specific heat in the upper 400 db of the water column.

The 0 to 150 db temperature is obtained by subtracting the depth-weighted 150 to 400 db temperature time series from the full-depth temperature time series estimated from the travel time measured by Inverted Echo Sounders. The 1997 Makassar Strait internal energy transport is 0.50 PW (petawatts). If the Makassar temperatures are referenced to 3.72°C, as in Schiller *et al.* (1998), the 1997 internal energy transport is reduced to 0.39 PW. The ENSO influence on the internal energy transport may be estimated: 0.63 PW during the La Niña months of December 1996 through February 1997, and 0.39 PW during the El Niño months of December 1997 through February 1998.

The average transport-weighted temperature determined by the Arlindo moorings is approximately 11.5°C with an average salinity of 34.45 (K. Vranes, Columbia graduate student). This is cooler and saltier than the ITF characteristics envisioned by Piola and Gordon (1984; ITF of 33.6) and Toole and Warren (1993; ITF temperature of 24°C). Toole and Warren (1993) deduce a throughflow of 6.7 Sv with salinity of 34.5. They assign it with a temperature of 24°C, which yields a heat-flux divergence between Indonesia and 32°S of 0.98 PW. The heat and freshwater divergence within the Indian Ocean north of 32°S depends on the temperature and salinity of the net poleward flow across 32°S. Using the Toole and Raymer (1985) Fig. 3 and their mean temperature and salinity along 32°S across the Indian Ocean of 5.71°C and 34.80, together with the ITF characteristics found by the Arlindo moorings, yields an ITF heat flux of roughly 0.27 PW and a net precipitation minus evaporation plus runoff over the Indian Ocean (north of 32°S) of nearly -0.3 Sv. As the ITF water is not likely to be cooled to 5.71°C, this value represents a maximum heat flux. An estimate of minimum heat flux may be calculated by assuming the ITF water eventually passing poleward within the Agulhas Current across 32°S confined to roughly the same density interval as the ITF in the Indonesian passages. This yields a value statistically equal to zero. This means that the ITF heat may be eventually lost south of 32°S, consistent with the model results of Hirst and Godfrey (1993) and of Allan *et al.* (1995), who find much enhanced ocean-to-atmosphere heat flux along 40°S when the ITF is included.

4.7.4 The Agulhas Retroflection

4.7.4.1 Introduction

A third interocean exchange route considered as important to larger-scale thermohaline circulation lies not within the confines of a channel, but rather in the gap between the southern shores of Africa and the ACC, a gap occupied by the Agulhas Retroflection (see Lutjeharms, 1996, Fig. 1d). The Agulhas Current flows westward along the southern rim of Africa, with a transport approaching 100 Sv. Rather than continuing into the South Atlantic, Agulhas water curls back to the Indian Ocean, feeding the eastward-flowing Agulhas Return Current near 40°S, the ACC main axis falling further south, near 48°S (Read and Pollard, 1993). However, not all of the Agulhas water turns back to the Indian Ocean. That part that does not turn back passes into the South Atlantic, in what is often called Agulhas leakage. Of all of the interocean exchanges, the Agulhas leakage into the Atlantic has drawn the most attention (and controversy) in terms of its role in NADW formation (Gordon, 1996a).

Recent WOCE-generated advances in our understanding of the Indian–South Atlantic exchanges are reported in two recent collections: Wefer *et al.* (1996) and a special section of the *Journal of Geophysical Research* (Gordon *et al.*, 1999b). The articles by de Ruijter *et al.* (1999), Witter and Gordon (1999), Garzoli *et al.* (1999), Arhan *et al.* (1999) and McDonagh and Heywood (1999) are particularly relevant to the topic of invasion of Indian Ocean water into the Atlantic. Also see Rintoul *et al.*, Chapter 4.6 and the model results of Semtner and Chervin (1992), Boddem and Schlitzer (1995), Cai and Greatbatch (1995), Döös (1995), Lutjeharms and Webb (1995) and Florenchie and Verron (1998). How models ‘handle’ the Agulhas leakage depends very much on their eddy-resolving characteristics (Marsh *et al.*, 2000). The de Ruijter *et al.* (1999) paper provides an excellent review of interocean exchange afforded by the Agulhas Retroflection.

4.7.4.2 Transport

Benguela Current

Gordon *et al.* (1992), using oxygen and CFC data collected during the South Atlantic Ventilation Experiment cruise no. 4 (SAVE-4) from 7 December 1988 to 15 January 1989 (not 1989 and 1990, as stated in Gordon *et al.*, 1992), find that of the

25 Sv Benguela Current geostrophic transport, 15 Sv are drawn from the Indian Ocean. Nine Sv (2 Sv of thermocline water warmer than 9°C and 7 Sv of lower thermocline and Antarctic Intermediate Water) of this Indian Ocean water pass into the North Atlantic within the North Brazil Coastal Current. The rest of the Indian Ocean water entering the South Atlantic follows the subtropical gyre, eventually to return along the horizontal plane to the Indian Ocean along a path just south of the Agulhas Return Current. As the Indian Ocean thermocline and intermediate layers are saltier than the other major provider of the Benguela Current water (the South Atlantic Current defining the polar limb of the subtropical gyre), the Agulhas leakage also adds salt to the South Atlantic. The leakage is also warmer than the waters of the South Atlantic Current, and hence also adds heat to the Atlantic Ocean.

Saunders and King (1995b), using WHP section A11 (roughly along 40°S, ending at 30°S at Africa), find a northward transport of 10 Sv of thermocline water ($<\sigma_0$ of 26.8) drawn from the Agulhas Retroflection and 5 Sv of AAIW. Garzoli *et al.* (1996) estimate the Benguela Current transport, based on a 16-month (1992–93) time series of Pressure and Inverted Echo Sounder (PIES) and current meter data at 30°S, as 16 Sv. Applying the property-based estimate of the percentage of Indian Ocean water found by Gordon *et al.* (1992), the Indian Ocean influx would be on average 10 Sv, 6 Sv of which enter into the upper limb of the Atlantic meridional overturning circulation. During the mooring deployment discussed by Garzoli *et al.* (1996), three oceanographic sections were obtained across the Benguela Current near 30°S. While the sample number is small, higher transport is associated with a more saline thermocline and intermediate layer, suggesting that variable Benguela Current transport is due to a variable Agulhas leakage.

Holfort and Siedler (2001) in an inverse solution find 9 Sv of warm surface water (Agulhas leakage) and 6 Sv of cold AAIW pass northward across 30°S in the South Atlantic. This is close to the values found by Saunders and King (1995b). Their partitioning between warm and cold route contrasts with that of Schlitzer (1996) of 2 Sv of Agulhas leakage to 11.9 Sv of AAIW. Stutzer and Krauss (1998) assimilate drifter trajectories into a model for the South Atlantic. They find that the Benguela Current, with its Indian Ocean component, directly

feeds the South Equatorial Current, with bifurcation near 10°S along the Brazilian coast. Clearly some Indian Ocean water is deflected into the North Brazil Current and northern hemisphere.

Agulhas eddies

The primary means by which the Agulhas injects Indian Ocean water into the Benguela Current occurs within large anticyclonic eddies. These energetic eddies of Agulhas (Indian Ocean) water can be traced across the South Atlantic Ocean (Byrne *et al.*, 1995). Interannual variability of the width and latitude of the transoceanic corridor occurs, with expansion and contraction of the South Atlantic subtropical gyre (Witter and Gordon, 1999). Effects of seafloor topography on the eddy propagation is clearly evident in observations and models (Byrne *et al.*, 1995; Kamenkovich *et al.*, 1996; Florenchie and Verron, 1998). On average six Agulhas eddies enter the South Atlantic each year, injecting from 3 to 9 Sv into the South Atlantic Ocean. In transit they dissipate, losing their core of Indian Ocean water (Byrne *et al.*, 1995) into the Benguela Current and South Equatorial Current.

4.7.4.3 Heat and freshwater fluxes

The South Atlantic contributes to the overall high thermocline salinity of the Atlantic Ocean in two ways: the ACC exports fresh water from the South Atlantic subtropics (Gordon and Piola, 1983); warm saline Indian Ocean thermocline water is injected into the Benguela Current (Gordon *et al.*, 1992). Agulhas leakage occurs in the form of Agulhas rings shed from the Agulhas Current's retroflection and surface water filaments (Lutjeharms, 1996). In addition, branches of the Agulhas Current may flow directly into the Benguela Current between the Africa and the main offshore corridor that carries the eddies towards the northwest (Gordon *et al.*, 1992; Garzoli *et al.*, 1996). These branches of Indian Ocean water lost from the core of the eddies are carried into the South Equatorial Current of the South Atlantic, part of which passes into the northern hemisphere.

Byrne *et al.* (1995) estimate that the average Agulhas eddy sampled within the southeastern South Atlantic transfers at least 0.8 Sv of Indian Ocean water into the South Atlantic. Two newly formed Agulhas eddies found near the retroflection each contributed 1.4 and 1.8 Sv, respectively, of Indian Ocean water (Byrne *et al.*, 1995). Clement

and Gordon (1995) find that three Agulhas eddies found within the Cape Basin (east of Walvis Ridge) each transferred between 0.45 and 0.90 Sv of Indian Ocean thermocline and intermediate water. As there are on average six such eddies per year, the total flux of Indian Ocean water above 1000 m introduced into the Atlantic by the eddy mechanism may be from 5 to 10 Sv. Van Ballegooyen *et al.* (1994) finds that Agulhas eddies contribute salt and heat to the South Atlantic thermocline waters at a rate of up to $2.5 \times 10^6 \text{ kg s}^{-1}$ (salt) and 0.045 PW (heat), assuming a yearly total of six eddies. Agulhas filaments may provide only 13% of the total interocean salt flux, the heat being lost quickly to the atmosphere (Lutjeharms and Cooper, 1996). Garzoli *et al.* (1996) and Duncombe Rae *et al.* (1996) find that the eddies measured during the BEST experiment (1992–93) contributed 0.007 PW, $4.5\text{--}6.7 \times 10^5 \text{ kg s}^{-1}$ and 2.6–3.8 Sv of heat, salt and volume flux, respectively, into the South Atlantic Ocean.

Garzoli *et al.* (1999) concluded from a detailed survey of three Agulhas eddies that a reasonable estimate for mass and heat flux from the Indian Ocean to the Atlantic is 6–10 Sv and 0.006 PW. The decrease of Indian Ocean core water observed as an Agulhas eddy dissipates indicate a slow transfer of Indian Ocean water from the confines of the eddy to the Benguela Current. In this way Indian Ocean water injected into the South Atlantic within an eddy may not accompany the dynamic feature of the eddy across the South Atlantic near 30°S (Byrne *et al.*, 1995; Witter and Gordon, 1999), but rather may be advected to the northwest within the general circulation of the Benguela Current and South Equatorial Current, as shown schematically by Gordon *et al.* (1992). The interaction of an Agulhas eddy with the atmosphere, seafloor topography (Kamenkovich *et al.*, 1996) and surrounding South Atlantic water strongly control its trajectory and modification (Arhan *et al.*, 1999).

Weijer *et al.* (1999) find that heat and salt flux associated with South Atlantic interocean exchanges, and in particular the ratio of thermocline to intermediate components (lateral boundary buoyancy profile), has a strong influence on the Atlantic meridional overturning circulation. An important aspect of the injection of Indian Ocean salt into the South Atlantic at the Agulhas Retroflection may be related to the ‘... shape of the salt flux profile...’, but the more important impact of Agulhas leakage

to Atlantic meridional overturning circulation may be due to the Indian Ocean heat flux, which will drive further evaporation in the South Atlantic.

There is ambiguity in the heat flux calculations associated with Agulhas leakage, as authors use different reference temperatures. To determine interocean heat flux one needs to identify the temperature of the water that leaves the Atlantic Ocean, balancing the mass injection of the Agulhas leakage. There are two reasonable options (Gordon, 1985): on the horizontal plane, with the transfer of cooler South Atlantic Current upper-layer water into the Indian Ocean south of the Agulhas Return Current; or on the vertical plane, by export of (2°C) NADW into the Indian and Pacific Oceans. Transport-weighted temperature (relative to 1500 m) was estimated from the SAVE-4 section across the South Atlantic Current crossing 10°W (used by Gordon *et al.*, 1992) as 10°C. The transport-weighted Agulhas transport (relative to 1500 m) taken between the station pair 49 and 50 in Gordon *et al.*, (1987) is calculated as 15°C. The heat flux from the Indian Ocean to the Atlantic for an Agulhas leakage of 15 Sv (upper 1500 m, Gordon *et al.*, 1992) for closure within the upper 1500 m is 0.3 PW (this is a larger value than calculated by Gordon (1985), where the smaller temperatures difference from opposing sides of a detached Agulhas eddy was used). For closure by the colder NADW the heat flux is 0.8 PW. The corresponding values for 5 Sv and 10 Sv Agulhas leakage, respectively are 0.1, 0.3 PW and 0.2, 0.6 PW. Estimates of the northward heat flux across the South Atlantic subtropics (18°S to 30°S) ranges from 0.1 to 0.9 PW, with error estimated in excess of 0.2 PW (MacDonald and Wunsch, 1996; Ganachaud, 1999; Holfort and Siedler, 2001). Heat flux values of less than 0.3 PW indicate that Agulhas leakage is predominately balanced by export of Atlantic water within the upper 1500 m, while heat flux values greater than 0.3 PW suggest significant involvement with the Atlantic meridional overturning circulation. The two methods for closure are not mutually exclusive and their relative importance may be time variable.

Within 50 km of the coast the Agulhas Current intermediate water, in the 4–8°C interval, is more saline than at points further offshore (Beal and Bryden, 1999). Remnants of Red Sea water flow southward are observed hugging the continental

slope to at least the southern coast of Africa (Gordon, 1986; Beal *et al.*, 2000), whereas offshore of the Agulhas axis, within the anticyclonic zone, the intermediate depths are dominated by lower-salinity AAIW coming from the subtropical Indian Ocean. Beal *et al.* (2000) conclude that all of the Red Sea overflow into the Indian Ocean is eventually exported by the western boundary current. As Red Sea water is not observed within the Agulhas Return Current, either its signature is removed by mixing or it fully contributes to the Agulhas leakage. Possibly the inshore component of the Agulhas preferentially contributes to the interocean exchange, and to the Atlantic's high salinity.

4.7.5 Discussion

Interocean exchanges have been subject to much attention in recent years (Schmitz, 1995, 1996a,b). The ACC, Bering Strait, Indonesian Seas and Agulhas Retroflection (and perhaps the westward flow immediately south of Australia) offer pathways for interocean exchange. Interocean fluxes of mass, heat and fresh water are expected to vary across the full range of temporal scales in concert with climate variability. As they vary, heat and freshwater budgets of neighbouring oceans change; temperature and salinity anomalies from long-term means can develop. These anomalies may play a role in the climate phenomena (oscillations) associated with each ocean basin. Peterson and White (1998) find that heat and freshwater anomalies forming in the western subtropical South Pacific Ocean spread eastward within the ACC entering the subtropical gyres of the Southern Hemisphere. The migration of these anomalies is linked to the 3- to 5-year Antarctic Circumpolar Wave (White and Peterson, 1996).

Transport of Pacific waters entering the Indian Ocean via the Indonesian Seas displays strong dependence of the phase of ENSO. During El Niño the Indonesian Throughflow is greatly reduced, delivering less heat and fresh water into the Indian Ocean. Might these variations introduce heat and freshwater anomalies into the Indian Ocean thermocline, linking ENSO and monsoon climate phenomena? The transfer of subtropical Indian Ocean water into the South Atlantic also displays variability. The transport of the Benguela Current may be modulated by Agulhas leakage (Garzoli *et al.*, 1996). The pathway of Agulhas eddies across the

South Atlantic varies interannually, along with pulsations in the form of the subtropical gyre (Witter and Gordon, 1999), influencing the distribution of heat and fresh water within the South Atlantic, and perhaps altering the access of the Agulhas leakage to the pathways along the Brazilian coast leading into the northern hemisphere (Stramma and Schott, 1996; Schott *et al.*, 1998).

Roach *et al.* (1995) find that there can be interannual variations of up to 1 ppt in salinity of the Bering Strait throughflow. Niebauer (1998) discusses the variability of wind over the Bering Sea to ENSO and how this relationship changed in the 'regime shift' of the later 1970s. Changing wind fields and sea ice distribution in the Bering Strait region may have a downstream effect on the Arctic freshwater budget and the flux of fresh water through Fram Strait, affecting NADW formation within the Greenland, Norwegian and Labrador Seas. As the Bering Strait did not exist during the lowered sea level of the glacial epochs, a vital freshwater source for the Arctic was severed. While other parts of the Arctic hydrological cycle would be greatly altered by the glacial condition, reduced inflow of Pacific fresh water into the Arctic pycnocline may be expected to reduce its stability and allow greater vertical heat flux from the warmer deep water to the sea ice cover.

The Atlantic Ocean receives low-salinity water from the Arctic and saline water from the Indian Ocean in association with Agulhas leakage (Gordon *et al.*, 1992; De Ruijter *et al.*, 1999). The former acts to attenuate convection in the northern North Atlantic (Zaucker *et al.*, 1994), while the latter has the opposite effect. On entering the South Atlantic a density anomaly of Indian Ocean water is only small, due to the counteracting effects of the heat and salt anomalies on the density. However, the heat is quickly lost to the atmosphere while the salt remains in the water column (Gordon *et al.*, 1992). According to modelling studies the effect of the warm and salty Indian Ocean source is to strengthen and stabilize the northern meridional overturning of the Atlantic (Weijer *et al.*, 1999; Weijer, 2000; Weijer *et al.*, 2001a,b), while the effect of the Bering Strait (Arctic source) freshwater flux is to weaken the northern overturning. In the present-day climate state the Indian Ocean source effect dominates over the northern freshwater fluxes. Shutting down the source of Indian Ocean water brings the ocean circulation close to a state where

it can switch between two equilibrium conditions: one with the northern-driven overturning, the other with southern-driven overturning (see Rahmstorf, 1995, 1996). With the Agulhas leakage reduced to near zero, the Bering Strait takes on greater significance, with relatively small variations in Bering Strait inflow (or other freshwater sources in the north) initiating switches from one state to the other, perhaps triggering large climate fluctuations.

It is clear that distribution of heat and fresh water associated with NADW formation has a major impact on North Atlantic (and points beyond?) climate. The process is very robust, as even massive introductions of fresh water do not permanently shut down the North Atlantic thermohaline overturning circulation: it's a salty ocean and it wants to stay that way. Why? Is it locally maintained (certainly there is a lot of positive feedback), or might there be a global factor such as the pattern of interocean exchange (export of fresh water from the Atlantic by the ACC and by introduction of Indian Ocean salt through Agulhas leakage)? NADW spreads into the ACC, entering the southern ocean thermohaline overturning cell, eventually contributing to AAIW, spreading into each ocean. Most of the AAIW upwells into the thermocline of the major oceans. Its NADW-derived component must weave its way back to the North Atlantic. Much of AAIW directly enters the South Atlantic upwells, mostly in the tropics (You, 1999), to enter the North Atlantic thermo-

cline. Some AAIW no doubt upwells in the Pacific and Indian Oceans, to be converted to thermocline water, which then passes, with increasing salinity, through the Indonesian Seas and around the rim of southern Africa. Strong transients overshadowed by other elements of the regional circulation complicate the pathway, but on the decadal and longer scales, its impact on climate is felt.

Climate models, in their quest to simulate the variability, must not only get mass and thermohaline fluxes correct within the major ocean basins, but they must also simulate the fluxes in the constricted pathways connecting these oceans (see, for example, Ribbe and Tomczak, 1997a). This is a very challenging task because of the complex boundary conditions within the passages, temporal variability and lack the observational base to enable evaluation of the model results.

Acknowledgements

The most relevant grants covering the task of preparing this chapter are: NSF grants OCE 97-29322 and OCE 95-29648, Office of Naval Research, N00014-98-1-0270 and NASA grant NAG5-8297. I am grateful to Will deRuijter for pointing out his recent research with Weijer and others, concerning the large-scale influence of Agulhas leakage on Atlantic overturning. Comments of the editors of this volume and of two reviewers have also greatly improved this presentation. Lamont-Doherty Earth Observatory contribution number 6053.

SECTION

5

FORMATION AND TRANSPORT OF WATER MASSES

Chapter 5.1

OCEAN SURFACE WATER MASS TRANSFORMATION

William G. Large and A. J. George Nurser

317

Chapter 5.2

MIXING AND STIRRING IN THE OCEAN INTERIOR

John M. Toole and Trevor J. McDougall

337

Chapter 5.3

SUBDUCTION

James F. Price

357

Chapter 5.4

MODE WATERS

Kimio Hanawa and Lynne D. Talley

373

Chapter 5.5

DEEP CONVECTION

John Lazier, Robert Pickart and Peter Rhines

387

Chapter 5.6

THE DENSE NORTHERN OVERFLOWS

Peter M. Saunders

401

Chapter 5.7

MEDITERRANEAN WATER AND GLOBAL CIRCULATION

Julio Candela

419

Chapter 5.8

TRANSFORMATION AND AGE OF WATER MASSES

P. Schlosser, J. L. Bullister, R. Fine, W. J. Jenkins, R. Key, J. Lupton,

W. Roether and W. M. Smethie, Jr

431

5.1

Ocean Surface Water Mass Transformation

William G. Large and A.J. George Nurser

5.1.1 The problem

Ocean water mass characteristics are set by direct contact with the atmosphere and subsequent transport and mixing in the ocean interior. Section 5 deals with these interior processes, including the conservative mixing of heat and salt to produce water masses of intermediate densities. Lazier *et al.* (Chapter 5.5) discuss changes in surface water mass properties that influence the deeper layers, which become an essential part of the global thermohaline overturning. In the absence of significant mixing, surface water mass properties can be transported to the ocean interior, where they influence the structure of the ocean interior and thus further influence climate variability and change. (For example, in Chapter 4.4 Liu and Philander demonstrate how water mass properties set in the extratropics affect the structure of the tropical thermocline, thus affecting tropical ocean–atmosphere interactions, and hence climate fluctuations and change at decadal and longer time scales.)

The focus of this chapter is air–sea interaction, which creates new density classes at the surface, and in particular extrema of both light and dense water. Such surface water mass transformation depends both on the surface density and the surface flux of density (Speer and Tziperman, 1992; Walin, 1982). As such, it is not easily measured or modelled. A direct determination requires better observations of the ocean’s near-surface temperature and salinity than are commonly available. Even more problematic is the measurement of the

surface heat and freshwater fluxes that make up the density flux. This complicated subject is comprehensively covered by the WCRP/SCOR Working Group on Air-Sea Fluxes (WGASF, 2000).

In ocean modelling a common practice has been to restore surface temperature and salinity to observed values (Cox and Bryan, 1984), which strongly limits surface density errors. However, to do so often requires very erroneous fluxes (Killworth *et al.*, 2000), especially of fresh water, and hence water mass transformation (Large *et al.*, 1997). Conversely, forcing with observed fluxes has resulted in poor representation of surface temperature and salinity (Rosati and Miyakoda, 1988) and hence water mass transformation. The two approaches can be combined so that relaxation terms are added to climatological heat and salt fluxes (Barnier *et al.*, 1995). However, Nurser *et al.* (1999) find that the relaxation substantially modifies the surface density flux of a North Atlantic model. Large *et al.* (1997) use more physical surface boundary conditions, where in particular, the freshwater and heat fluxes are coupled through an explicit evaporation/latent heat flux. The global result is an improved equilibrium water mass distribution, because the combined effect of surface density and surface flux errors on water mass transformation is reduced (Doney *et al.*, 1998b).

In this chapter, we first set out Walin’s theory of water mass transformation, focusing on how surface fluxes drive diapycnal flow in the surface mixed layer. We briefly discuss how lateral mixing within the mixed layer and entrainment at the

base of the mixed layer modify the properties of the waters that are released into the thermocline (subducted). We then present our best description of ocean surface density from post-WOCE knowledge of the global Sea Surface Temperature (SST) and Sea Surface Salinity (SSS). A new set of surface fluxes appropriate for the WOCE period is then compiled. Finally, we apply the water mass transformation formalism to these data sets, and produce estimates of water mass transformation in various oceans and subregions of the oceans. We will compare our results with those of Speer *et al.* (1995a), who used different flux and density fields.

5.1.2 Theory of surface water mass transformation

5.1.2.1 The diapycnal circulation

In a pioneering work, Walin (1982) presented a view of the circulation in terms of the flow of water across isotherms being driven by heating and cooling. This work can be generalized to link the diapycnal flow to diabatic forcing of (potential) density (Speer and Tziperman, 1992; Tziperman, 1986), and indeed to link flow across surfaces of any property to forcing of that property (Viudez, 2000). In principle, the water mass formation rate – the convergence of the diapycnic flow – may be diagnosed from only the diabatic forcing without requiring any additional information about the circulation or dynamics.

The total globally integrated diapycnal flow across any isopycnal must be zero in the time mean. Diapycnal flow in the mixed layer driven by surface forcing, lateral mixing, and entrainment must be balanced by diapycnal flow in the thermocline driven by diffusion, or possibly by opposite diapycnal flow in the mixed layer in different parts of the global ocean.

In this section we focus on the *surface* water mass transformation: that is the diapycnal flow in the surface mixed layer, which creates the water masses that are mixed by the diffusive processes in the thermocline. Model diagnostics (Marshall *et al.*, 1999; Nurser *et al.*, 1999) and scaling analysis (Garrett and Tandon, 1997; Nurser *et al.*, 1999; Tandon and Zahariev, 2000) seem to show that the surface fluxes dominate the entrainment and lateral mixing in setting this diapycnal flow, at least for the denser waters.

The formation rate of water masses of various densities in the North Atlantic was estimated from climatological surface heat and freshwater fluxes by Speer and Tziperman (1992), while Speer *et al.* (1995a) considered global formation rates. Garrett *et al.* (1995) considered transformation rates in a simple model of the Red Sea, while Tziperman and Speer (1994) studied transformation rates in the Mediterranean. Recently, Marsh (2000) has looked at the year-to-year variability of surface water mass transformation in the North Atlantic. Speer extended Walin's theory to consider formation rates in T - S space, and found (Speer, 1993; Speer *et al.*, 1995a) that the surface fluxes implied core water mass properties consistent with observations of mode waters revealed in Worthington's volumetric census of T and S (Worthington, 1976, 1981).

5.1.2.2 Water mass formation and diapycnal volume fluxes

Consider the volume sandwiched between the isopycnal surfaces with potential densities ρ and $\rho + \Delta\rho$. We consider a limited area of the ocean, such as the North Atlantic, with an open boundary (Fig. 5.1.1a).

Strictly speaking, it is mass rather than volume that is conserved (Viudez, 2000). However, if the Boussinesq approximation is made and the ocean is assumed to be incompressible, we can consider volume rather than mass budgets, and define water mass formation using a volume budget of a density layer. We write ΔV as the volume of fluid with density between ρ and $\rho + \Delta\rho$, $\Delta\psi$ the volume flux of fluid with density between ρ and $\rho + \Delta\rho$ out of the domain, and $G(\rho)$, $G(\rho + \Delta\rho)$ the diapycnal volume flux of fluid crossing the ρ and $\rho + \Delta\rho$ isopycnals respectively. Note that Garrett *et al.* (1995) and Speer *et al.* (1995a) denote this term by A . The sign convention is (Fig. 5.1.1a) that G is positive if directed towards increasing ρ .

By incompressibility, the volume budget of the control volume bounded by ρ and $\rho + \Delta\rho$ isopycnals, the ocean surface, and the open boundary is

$$\left(\frac{\partial \Delta V}{\partial t} + \Delta\psi \right) = G(\rho) - G(\rho + \Delta\rho) + \int_{\text{outcrop}} \rho_0^{-1} \mathcal{F}_{\text{in}} \, dA \quad (5.1.1)$$

where $\int_{\text{outcrop}} \rho_0^{-1} \mathcal{F}_{\text{in}} \, dA$ is the net surface influx (of volume) at the surface over the outcrop, with ρ_0

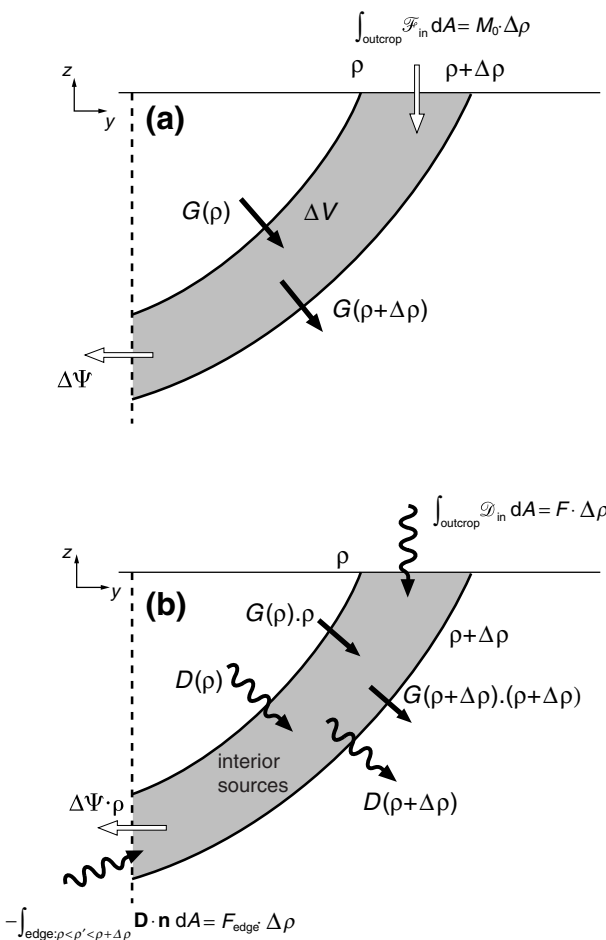


Fig. 5.1.1 Schematic vertical sections showing the volume and mass balances for a volume element bounded by the density surfaces ρ and $\rho + \Delta\rho$ that outcrop at the sea surface. (a) The volume of the layer depends on the divergence of the diapycnal volume flux G , crossing the density surfaces, the volume flux exiting the domain $\Delta\Psi$, and the surface influx of fresh water \mathcal{F}_{in} integrated over the outcrop, $M_0 \cdot \Delta\rho$. (b) The mass content of the layer depends on the advective change from the diapycnal volume flux, ρG and the mass exiting the domain, $\rho \Delta\Psi$, as well as the divergence of the diffusive mass fluxes, D_{diff} , the surface influx of density \mathcal{D}_{in} integrated over the outcrop, the density flux through the edges of the control volume into the layer, $F_{\text{edge}}(\rho) \Delta\rho$, and the interior density source.

mean density and \mathcal{F}_{in} the net freshwater input (mass per unit area per unit time). Summing the volume inflation and the outflow terms gives the water mass formation

$$M\Delta\rho = \frac{\partial\Delta V}{\partial t} + \Delta\Psi \quad (5.1.2)$$

where the water mass formation per unit of density, M , is given by

$$M = -\frac{\partial G}{\partial \rho} + M_0 \quad (5.1.3)$$

This formation rate M is thus the convergence of the diapycnal volume flux plus the surface volume flux per unit of density

$$M_0(\rho) = \lim_{\Delta\rho \rightarrow 0} \frac{1}{\Delta\rho} \int_{\text{outcrop}} \rho_0^{-1} \mathcal{F}_{\text{in}} \, dA$$

$$= \int_{\rho_0}^{-1} \mathcal{F}_{\text{in}} \delta(\rho_{\text{surf}}(\mathbf{x}) - \rho) \, dA.$$

This surface volume flux M_0 is generally small in comparison with $\partial G / \partial \rho$, and so is neglected in applications of (5.1.3).

Equation (5.1.3) above can be applied to an arbitrary control volume. In particular, the lower bounding surface in Fig. 5.1.1 can be the deepest depth of the mixed layer, so that the volume is made up of those waters with density between ρ and $\rho + \Delta\rho$ that lie within the mixed layer and seasonal thermocline. If this volume has closed boundaries that block any lateral export or import of waters of density ρ , across into other regions of the mixed layer and seasonal thermocline, then M defined as in (5.1.3) is the net rate at which water, of density ρ , passes into the main thermocline (Marshall *et al.*, 1999; Tandon and Garrett, 1997).

Care must be taken in relating the formation rate M to 'subduction' rates however. For example, the outcrop region of a typical mid-thermocline isopycnal in the North Atlantic (e.g. with density anomaly 26.5 kg m^{-3}) includes regions of strong subduction (to the east, over the subtropical gyre) and intense entrainment (to the west, over the Gulf Stream region) (Marshall *et al.*, 1999). The entrainment and subduction largely cancel out, leaving a *net* formation rate considerably smaller than the total subduction of fluid from that outcrop. On the other hand, if we consider only the eastern part of this outcrop, where there is only subduction, then M is *not* simply the fluid subducted into the thermocline over the eastern Atlantic, but the *difference* between the fluid subducted and the input of mixed layer and seasonal thermocline waters across the western, open, boundary of the domain.

5.1.2.3 Diapycnal volume fluxes and density sources

We now consider the potential density budget for the same layer (see Fig. 5.1.1b). We write D as the

area-integrated density flux across an isopycnal, defined to be positive in the direction of increasing density. Then $D_{\text{diff}}(\rho)$, $D_{\text{diff}}(\rho + \Delta\rho)$ are the integrated diapycnal density fluxes across the ρ and $\rho + \Delta\rho$ isopycnals, $\int_{\text{outcrop}} \mathcal{D}_{\text{in}} dA$ is the total density flux into the ocean where the surface density lies between ρ and $\rho + \Delta\rho$ (\mathcal{D}_{in} is the density influx per unit area) and $\int_{\text{edges}} \mathbf{D} \cdot \mathbf{n} dA$ is the total density flux across the edge of the control volume (here \mathbf{D} is the vector diffusive density flux).

The density budget of the control volume between the ρ and $\rho + \Delta\rho$ isopycnals is a balance between advective and diffusive density fluxes, and interior sources:

$$\begin{aligned}
 & \underbrace{\left(\frac{\partial(\Delta V)}{\partial t} + \Delta\psi \right) \rho + G(\rho + \Delta\rho)(\rho + \Delta\rho) - \rho G(\rho)}_{\text{outward advective density fluxes}} \\
 & = -(D_{\text{diff}}(\rho + \Delta\rho) - D_{\text{diff}}(\rho)) \\
 & \quad + \underbrace{\int_{\text{outcrop}} \mathcal{D}_{\text{in}} dA - \int_{\text{edges}} \mathbf{D} \cdot \mathbf{n} dA}_{\text{diffusive influx of density}} \quad (5.1.4) \\
 & \quad + \underbrace{M_0 \rho \cdot \Delta\rho}_{\text{surface advective influx of density}} \\
 & \quad + \text{interior sources of density}
 \end{aligned}$$

or more concisely

$$\begin{aligned}
 & M\rho + \frac{\partial}{\partial\rho}(\rho G) \\
 & = -\frac{\partial D_{\text{diff}}}{\partial\rho} + F + C + F_{\text{edge}} + M_0 \cdot \rho \quad (5.1.5)
 \end{aligned}$$

where we have introduced $F(\rho)$, the surface density influx per unit of density (Fig. 5.1.1b):

$$\begin{aligned}
 F(\rho) &= \lim_{\Delta\rho \rightarrow 0} \frac{1}{\Delta\rho} \int_{\text{outcrop}} \mathcal{D}_{\text{in}} dA \\
 &= \int_{\text{outcrop}} \mathcal{D}_{\text{in}} \delta(\rho_{\text{surf}}(\mathbf{x}) - \rho) dA \quad (5.1.6)
 \end{aligned}$$

This F is Speer and Tziperman's (1992) transformation driven by air-sea fluxes.

We have similarly introduced $F_{\text{edge}}(\rho)$, the diffusive influx through the control-volume edge into the layer per unit of ρ , and $C(\rho)$, the interior source of density arising from cabling – ‘densification’ through mixing (e.g. McDougall, 1984, 1987).

But by volume conservation (5.1.3) $M = -\partial G/\partial\rho + M_0$, so the density content gain implicit in volume inflation and lateral outflow may be eliminated in (5.1.5), leaving

$$G(\rho) = -\frac{\partial D_{\text{diff}}}{\partial\rho} + F + F_{\text{edge}} + C \quad (5.1.7)$$

The edge flux $F_{\text{edge}}(\rho)$ is relatively small if the control volume is chosen to have a vertical edge, since isopycnal slopes in the thermocline are small and the horizontal diffusive flux is therefore weak. It can, however, be important where the control volume is chosen with an almost horizontal lower boundary, e.g. the base of the winter mixed layer (Marshall *et al.*, 1999). Although the cabling term C is generally relatively small in the mixed layer, because it is always positive it has a systematic effect over large time and space scales.

Thus, a cross-isopycnal volume flux directed from light to dense, $G(\rho) > 0$, requires a density supply either from a convergence of diapycnal density fluxes, $-\partial D_{\text{diff}}/\partial\rho > 0$, or from the surface, $F > 0$ (or possibly from the edge flux $F_{\text{edge}} > 0$ or cabling $C > 0$). This relation for water mass formation holds for both steady and time-varying cases.

5.1.2.4 Mixing in the seasonal thermocline and mixed layer

We would like to relate the formation rates, M , derived from differentiation of the surface transformation rate, to ‘subduction’ and the production of water masses passing into the main thermocline. One problem, discussed above, is that a domain containing the outcrop region of a given isopycnal will in general include regions both of subduction and entrainment, while M only gives the *net* production. The other problem is that mixing processes within the mixed layer and seasonal thermocline may change the transformation G (and hence the M supplied to the permanent thermocline).

So let us (Marshall *et al.*, 1999; Tandon and Garrett, 1997) take the lower bounding surface of our control volume as the maximum (late winter) mixed-layer depth (Fig. 5.1.2). There will be lateral diffusive fluxes within the mixed layer (denoted by D_{lat}), entrainment fluxes through the base of the mixed layer (denoted by D_{ent}), and diapycnal fluxes within the seasonal thermocline (denoted by D_{dia}). Also there will be a diffusive flux F_{edge} up through the lower bounding surface, the position of the base of the winter mixed layer.

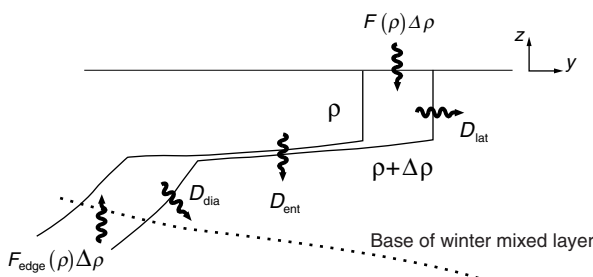


Fig. 5.1.2 The domain (seasonal thermocline and mixed layer) above the deepest winter mixed-layer base (dotted line). The diffusive density flux across the isopycnals is broken up into contributions D_{dia} of flow across isopycnals in the seasonal thermocline, entrainment fluxes D_{ent} , and lateral fluxes within the mixed layer, D_{lat} . The diffusive flux through the base of the mixed layer up between the two isopycnals is $F_{\text{edge}}(\rho)\Delta\rho$, and that into the surface is $F(\rho)\Delta\rho$.

The lateral fluxes within the mixed layer are driven by eddies in baroclinically unstable regions. This mixing is most likely to be important where the mixed layer is both deep and has strong gradients, such as in the winter subpolar North Atlantic and in parts of the Antarctic Circumpolar Current (ACC). Model runs (Marshall *et al.*, 1999; Nurser *et al.*, 1999) suggest that the derivative $\partial D_{\text{lat}}/\partial\rho$, which drives G , can reach 6–8 Sv over the North Atlantic ($1 \text{ Sv} = 10^6 \text{ m}^3 \text{ s}^{-1}$) for the denser waters $>\sim 27.5 \text{ kg m}^{-3}$. Compare this with typical transformation rates of 20 Sv (see Section 5.1.5) driven by the surface forcing.

The entrainment fluxes D_{ent} , which lighten fluid as it is entrained into the mixed layer, appear in two guises. First, in equatorial regions there is systematic upwelling into fairly shallow mixed layers. This flux is indeed important (McWilliams *et al.*, 1996; Nurser *et al.*, 1999), but should probably be regarded as part of the ‘return’ circulation of fluid from the permanent thermocline into the upper ocean. Second, there are the entrainment fluxes at mid-latitudes associated with wind-driven deepening of the mixed layer in autumn. Such fluxes can reach annual-average values of up to 25 W m^{-2} (for heat) giving density fluxes of $\sim 1.5 \times 10^{-6} \text{ kg s}^{-1} \text{ m}^{-2}$ (Nurser *et al.*, 1999). However, in the model diagnosis they were found not to make a great impact on G , with $\partial D_{\text{ent}}/\partial\rho$ typically 2–3 Sv, in agreement with the scale analysis of Garrett and Tandon (1997).

The diapycnal fluxes within the seasonal thermocline are less clear. The numerical results of

Marshall *et al.* (1999) for the North Atlantic found diapycnal flow driven by $\partial D_{\text{dia}}/\partial\rho$ reaching 8–10 Sv both at lighter densities $\sim 23 \text{ kg m}^{-3}$ and at mid-densities $\sim 26 \text{ kg m}^{-3}$. This may include some entrainment flux, as the model had no explicit wind-driven mixed layer. The flux F_{edge} through the surface defined by the winter mixed-layer base was found by Marshall *et al.* (1999) to be significant at lighter densities, reaching 8–10 Sv at $\sim 23\text{--}24 \text{ kg m}^{-3}$. At such densities the winter mixed-layer base lies at shallow depths where stratification is strong. These fluxes are of course sensitive to the model diffusivities for T and S ; here the vertical diffusivity $K_v = 3 \times 10^{-5} \text{ m}^2 \text{ s}^{-1}$ and the lateral diffusivity $K_H = 1000 \text{ m}^2 \text{ s}^{-1}$.

The net effect is that diffusive processes within the mixed layer and seasonal thermocline, while less important at higher densities, do profoundly change the transformation rates at lighter densities $<\sim 25.5 \text{ kg m}^{-3}$. For these lighter waters G calculated over the mixed-layer and seasonal thermocline can be very different from F , even having the opposite sign (Marshall *et al.*, 1999; Rhines, 1993; Tandon and Garrett, 1997).

We now describe surface temperature, salinity and density fields together with the surface density flux field for three years (1991–93) of the WOCE period. We use these surface property and flux fields to perform water mass diagnostics for the three-year period.

5.1.3 Ocean surface temperature, salinity and density

5.1.3.1 Sea surface temperature, SST

With the advent of satellite radiometer measurements at the end of the 1970s, SST has become a relatively well-known ocean parameter. In the procedure implemented by Reynolds and Smith (1994), the frequent, near-global sampling of the satellites provides consistency and coverage, while *in-situ* data is used to remove biases. In areas where the satellite measurements indicate the presence of sea ice, the SST algorithms fail, but it is possible to assume that the true averaged SST is not very different from the freezing point ($\sim -1.8^\circ\text{C}$). Throughout the WOCE years, 1991–97, these SST fields are available weekly. However, some flux data are only available monthly, so we use $\langle \text{SST} \rangle_{m,y}$, where $\langle \rangle$ denotes a monthly mean: $m=1$ to 12 is the month of the year, and $y=1991$

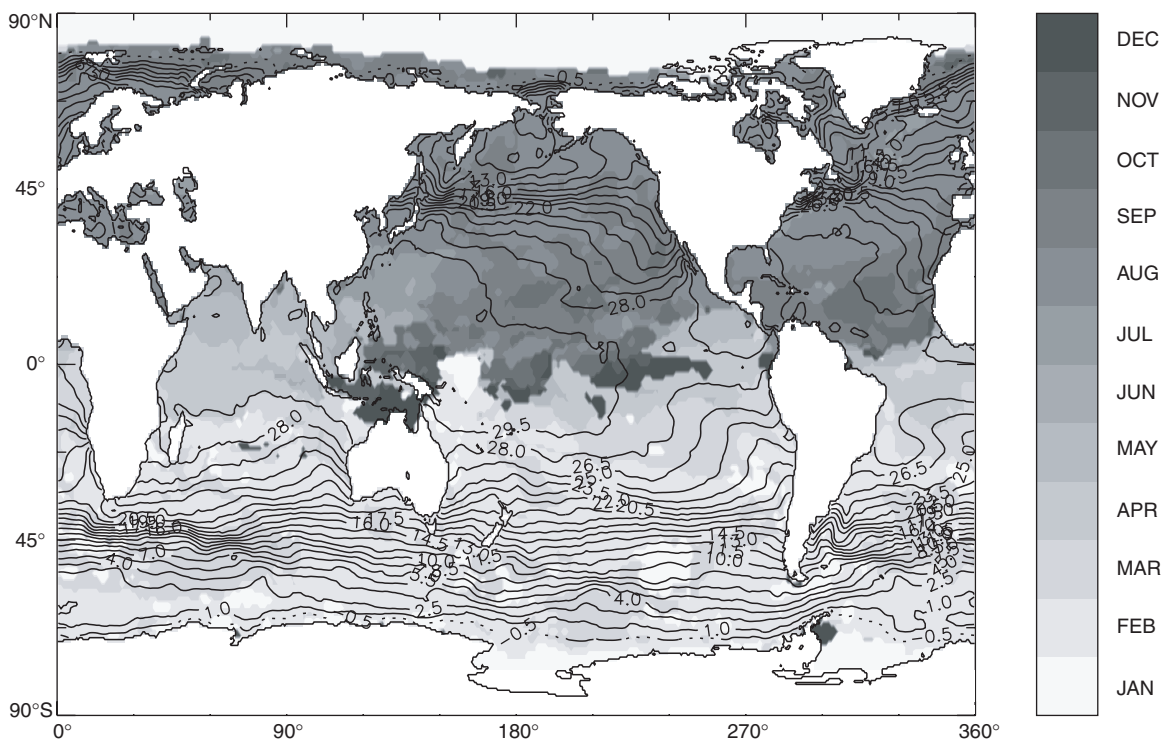


Fig. 5.1.3 Maximum monthly sea surface temperature, $\langle \text{SST} \rangle_{\text{max}}$, with a contour interval of 1.5°C , overlaid on the month of the maximum, M_{SSTmax} .

to 1997 is the year. There are 84 such values at each point of on $2^{\circ} \times 2^{\circ}$ global grid.

We are interested in extrema in sea surface density (SSD), and whether or not these result from corresponding extrema in sea surface temperature (SST) and/or sea surface salinity (SSS). Therefore, monthly data sets are searched for the months and years of maxima and minima of SST, SSS and SSD. Note that the months of extrema may not correspond to the phase of the annual harmonic in regions where there is higher frequency variability, such as a significant semiannual harmonic. In particular a maximum and minimum need not be separated by exactly 6 months. From the 84 values of $\langle \text{SST} \rangle_{\text{m,y}}$ the maximum, $\langle \text{SST} \rangle_{\text{max}}$, as well as the month, M_{SSTmax} and year Y_{SSTmax} , of the maximum were determined. The month, M_{SSTmin} , year, Y_{SSTmin} , and minimum, $\langle \text{SST} \rangle_{\text{min}}$ were found similarly.

In Figure 5.1.3 contours of $\langle \text{SST} \rangle_{\text{max}}$ are superimposed on a greyscale plot of M_{SSTmax} . The dominant feature is the equatorial warm pool of $\langle \text{SST} \rangle_{\text{max}} > 29.5^{\circ}\text{C}$, which extends across all the Indian Ocean and half the Pacific. It is found as far poleward as 30°N and 20°S . Equally large values

are found on either side of Central America and off the west coast of tropical Africa. The extreme warm temperatures in the tropics were formed in every month of the year, though the areas of M_{SSTmax} corresponding to January, February and March are all very small and near Australia. In the Indian Ocean the phase of $\langle \text{SST} \rangle_{\text{max}}$ appears to follow the northward overhead passage of the sun; April south of about 10°N , May further north and finally June and July in the Arabian Sea. In the equatorial western Pacific the maximum SST generally did not occur when the sun was directly overhead. As expected, poleward of the tropics the maximum SST almost always occurs in late summer (August–September in the Northern Hemisphere and February–March in the Southern).

In Figure 5.1.4 contours of $\langle \text{SST} \rangle_{\text{min}}$ are superimposed on a greyscale plot of M_{SSTmin} . Nowhere is $\langle \text{SST} \rangle_{\text{min}}$ greater than 29.5°C . Equatorial cold tongues extend westward from the eastern boundaries of all basins, but this feature is strongest and most extensive in the Pacific. Elsewhere there are sharp gradients (fronts) associated with western boundary currents (Gulf Stream, Kuroshio and Brazil), and the ACC. Over large areas of polar

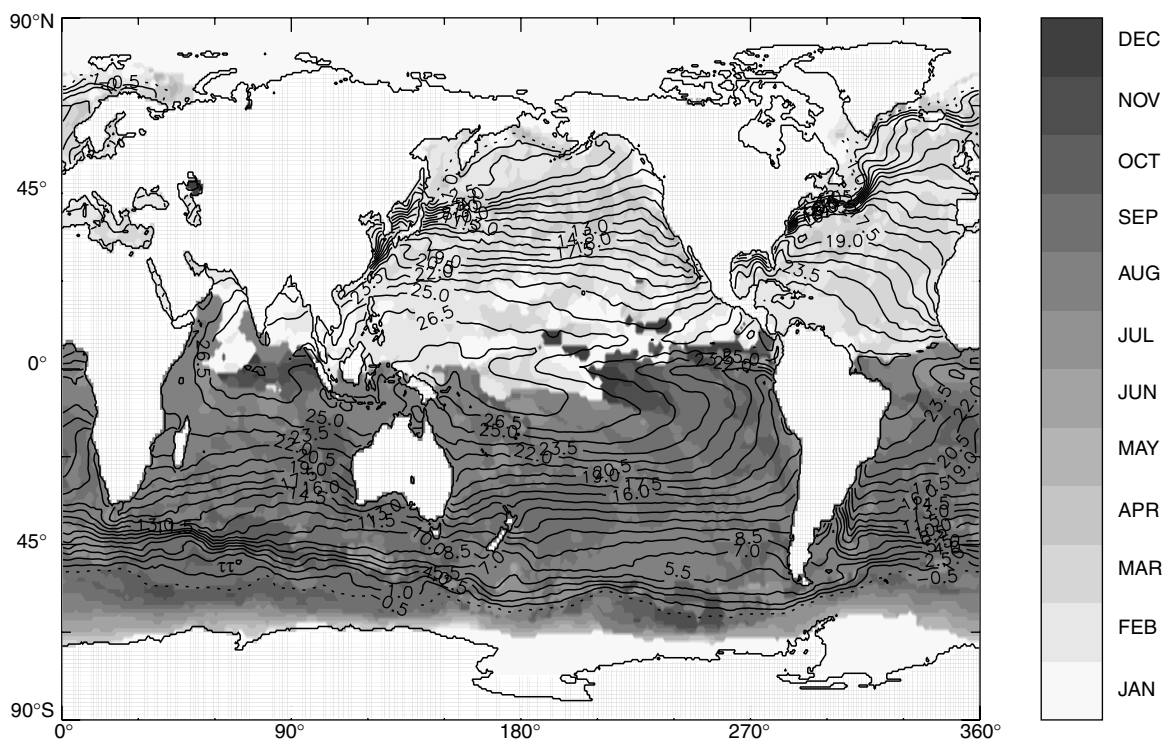


Fig. 5.1.4 Minimum monthly sea surface temperature, $\langle \text{SST} \rangle_{\text{min}}$, with a contour interval of 1.5°C , overlaid on the month of the minimum, M_{SSTmin} .

seas $\langle \text{SST} \rangle_{\text{min}}$ is less than -0.5°C . At most points in the northern hemisphere the minimum SST is in February or March, but it occurs as early as January in the tropical Pacific and Indian Oceans, and as late as April in the North Atlantic and Pacific Oceans. Conversely, most minima in the southern hemisphere occur in August and September, with some in June and July. Along the equatorial Pacific the minimum occurs systematically later in the year from September at 250°E to April at 170°E . This progression marks the development of the cold tongue.

There is no significant correlation between the years of maximum SST, Y_{SSTmax} , and of minimum SST, Y_{SSTmin} , indicating that the year in which a point has its maximum SST is unlikely to be the year in which it has its minimum. The year 1997 appears to have been relatively warm in that there are large areas of $Y_{\text{SSTmax}}=1997$, but few with $Y_{\text{SSTmin}}=1997$. The coldest years in the central equatorial Pacific were 1995 and 1996. There does not appear to be any systematic propagation of either $\langle \text{SST} \rangle_{\text{min}}$ or $\langle \text{SST} \rangle_{\text{max}}$ along the routes of the major current systems. For example, in the Pacific sector of the ACC, Y_{SSTmax} following

the flow direction is 1992 ($180\text{--}250^{\circ}\text{E}$), 1995 ($250\text{--}275^{\circ}\text{E}$), 1993 ($275\text{--}290^{\circ}\text{E}$), and 1997 ($290\text{--}300^{\circ}\text{E}$).

5.1.3.2 Sea surface salinity, SSS

Unlike SST, near surface salinity has never been measured monthly on basin scales. However, there are mean monthly climatologies of $\langle \text{SSS} \rangle_m$. We use that of Levitus *et al.* (1994) updated to 1998 (Levitus *et al.*, 1998), which gives global maps for each month of salinity at standard depths. We are forced to assume that the surface climatologies, $\langle \text{SSS} \rangle_m$, are representative of the monthly average SSS for month m in each of the seven WOCE years. This assumption may be more valid in some regions than others, but is clearly a weakness in the WOCE data set and this study. Nevertheless, the global distributions of both the maximum, $\langle \text{SSS} \rangle_{\text{max}}$, and minimum, $\langle \text{SSS} \rangle_{\text{min}}$, are shown in Figure 5.1.5. Values less than 30 are usually associated with river runoff into coastal regions or enclosed seas, and/or with melting sea ice and are not contoured, nor are values greater than 38, which are found in enclosed regions of high evaporation, such as the Mediterranean and Red Seas.

Apart from rivers and ice melt, low-salinity surface water is produced by rainfall. Accordingly, the Intertropical Convergence Zones tend to be areas of low $\langle \text{SSS} \rangle_{\min}$, most notably in the Pacific between 5°N and 15°N , where these low values are found from September through to November. Conversely the deserts of the subtropical highs can be identified as regions of high

$\langle \text{SSS} \rangle_{\max}$. The Indian Ocean is anomalous, with greater east–west variations in both $\langle \text{SSS} \rangle_{\max}$, and $\langle \text{SSS} \rangle_{\min}$.

As with temperature, there are SSS gradients (fronts) associated with the major ocean currents. The ACC is characterized by $\langle \text{SSS} \rangle_{\max} = 35 \pm 0.5$ and $\langle \text{SSS} \rangle_{\min} = 34.5 \pm 0.5$ between South America and the Pacific; the Kuroshio by

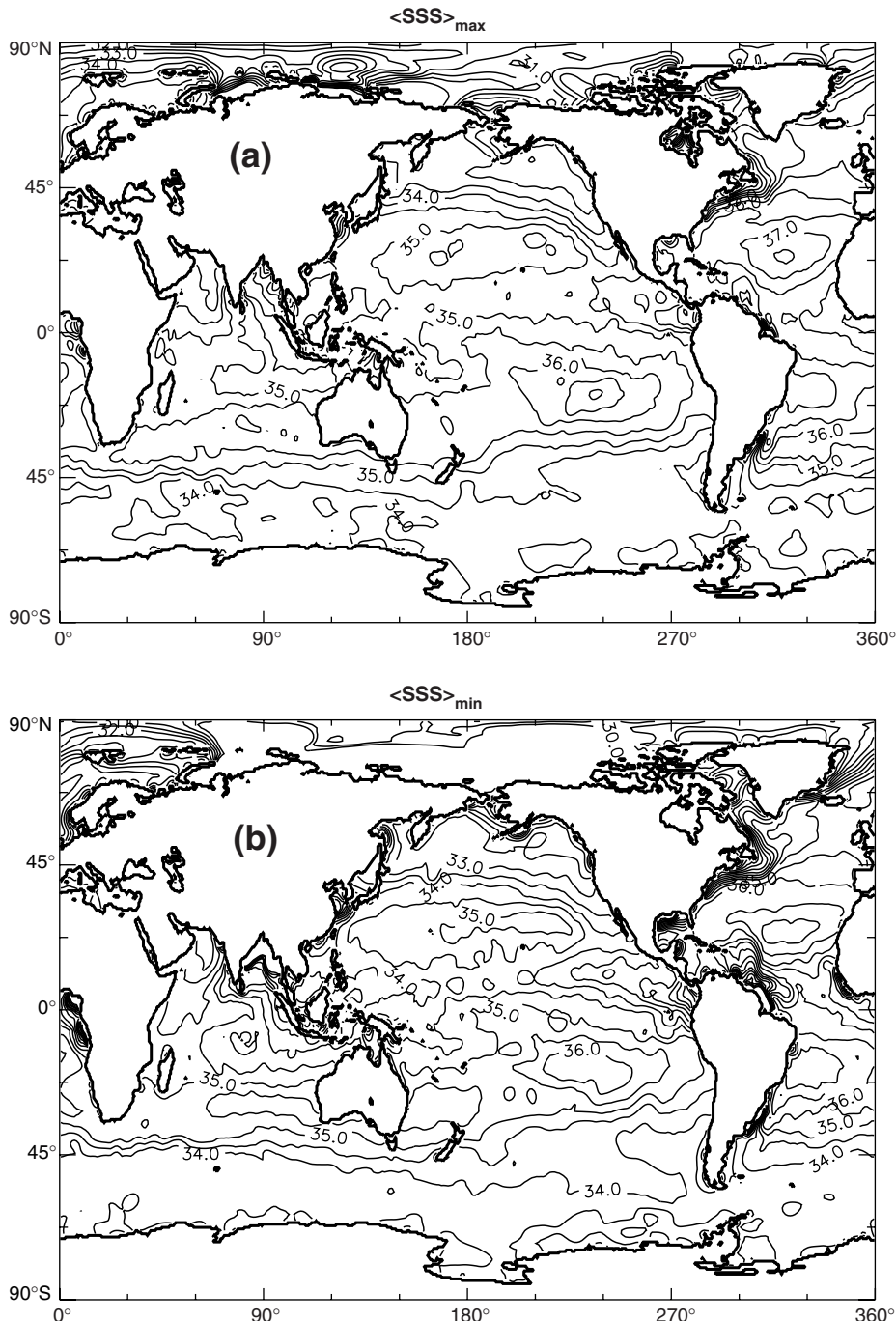


Fig. 5.1.5 (a) Maximum mean monthly sea surface salinity, $\langle \text{SSS} \rangle_{\max}$, with a contour interval of 0.5. (b) Minimum mean monthly sea surface salinity, $\langle \text{SSS} \rangle_{\min}$, with a contour interval of 0.5.

$\langle SSS \rangle_{\max} = 34 \pm 0.5$ and $\langle SSS \rangle_{\min} = 33.5 \pm 0.5$; and the Gulf Stream by both $\langle SSS \rangle_{\max}$ and $\langle SSS \rangle_{\min}$ between about 33 and 36.

5.1.3.3 Sea surface density, SSD

A monthly mean sea surface density is computed from the equation of state, $\rho = \rho(T, S)$, as

$$\langle SSD \rangle_{m,y} = \rho(\langle SST \rangle_{m,y}, \langle SSS \rangle_m) \quad (5.1.8)$$

Since in general this is not equal to the mean of the density, this is another weakness of this study imposed by the limits of the WOCE data sets. However, use of equation (5.1.8) is equivalent to linearization about the monthly mean SST and SSS at each point with appropriate thermal and haline expansion coefficients. This is preferred over the common oceanographic practice of linearizing about fixed reference SST and SSS with invariant coefficients.

The minimum of these 84 monthly values at each point, $\langle SSD \rangle_{\min}$, is superimposed on a greyscale map of the month, $M_{SSD\min}$, in Figure 5.1.6. In Figure 5.1.7 contours of $\langle SSD \rangle_{\max}$ are superimposed on a greyscale plot of its month, $M_{SSD\max}$.

Very light surface water $\langle SSD \rangle_{\min}$ (with density anomaly $< 21 \text{ kg m}^{-3}$) is found in small tropical regions where SST is highest, but its distribution more closely resembles that of $\langle SSS \rangle_{\min}$, rather than $\langle SST \rangle_{\max}$, in all three basins. This similarity suggests that low salinity is the controlling factor in producing the lightest surface water in these regions. In contrast, in the tropics and the subtropics, the features of $\langle SSD \rangle_{\max}$ appear closely related to those of $\langle SST \rangle_{\min}$, but these densities are not extremes. The densest southern hemisphere surface water, $\langle SSD \rangle_{\max} > 28 \text{ kg m}^{-3}$, is found in April over a small region of the Weddell Sea. It corresponds to a relative maximum in $\langle SSS \rangle_{\max} \sim 35$ (Fig. 5.1.5), which is also found in April (not shown).

At high northern latitudes the salinity resulting from river runoff and ice melt is sufficiently low to overcome the cold temperatures and produce light surface water, $\langle SSD \rangle_{\min} < 20 \text{ kg m}^{-3}$. These latitudes also produce some of the heaviest surface waters $\langle SSD \rangle_{\max} > 28 \text{ kg m}^{-3}$. Such waters are found north of Norway at a point where the warm saline North Atlantic water has cooled sufficiently, but before it mixes with fresher Arctic waters, and

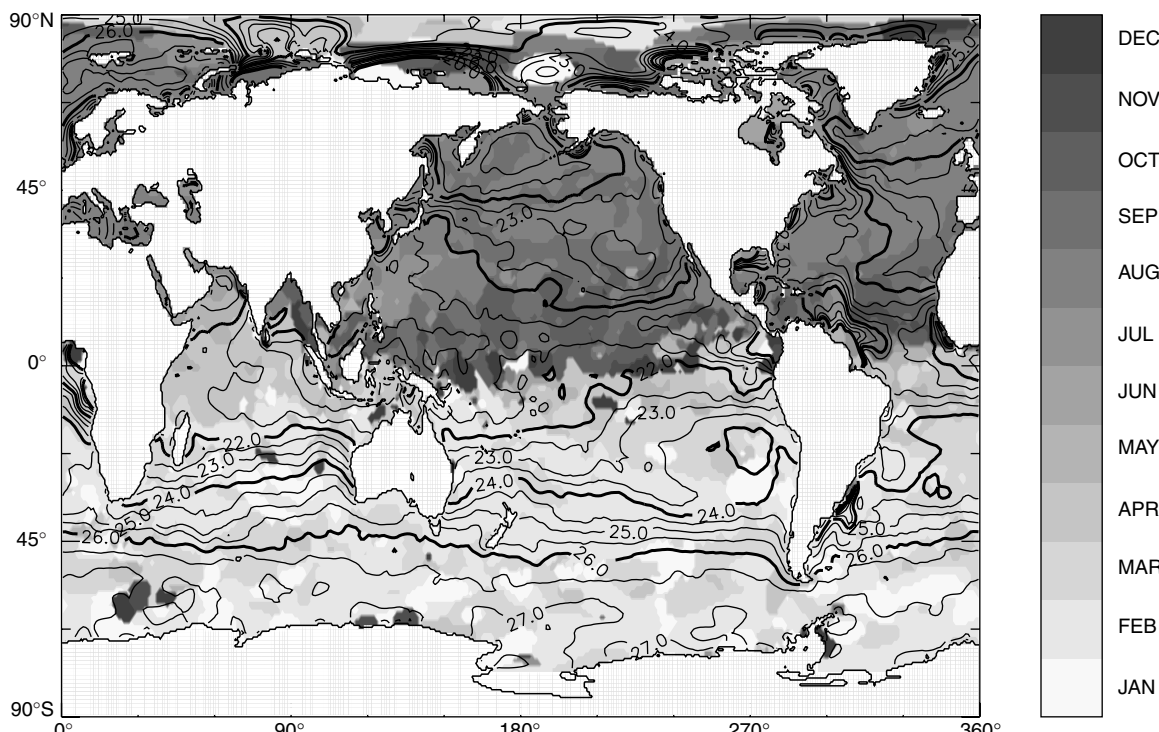


Fig. 5.1.6 Minimum monthly sea surface density, $\langle SSD \rangle_{\min}$, with a contour interval of 0.5 kg m^{-3} , overlaid on the month of the minimum, $M_{SSD\min}$. Even valued contours are bold, including the 26.0 contour encircling Iceland.

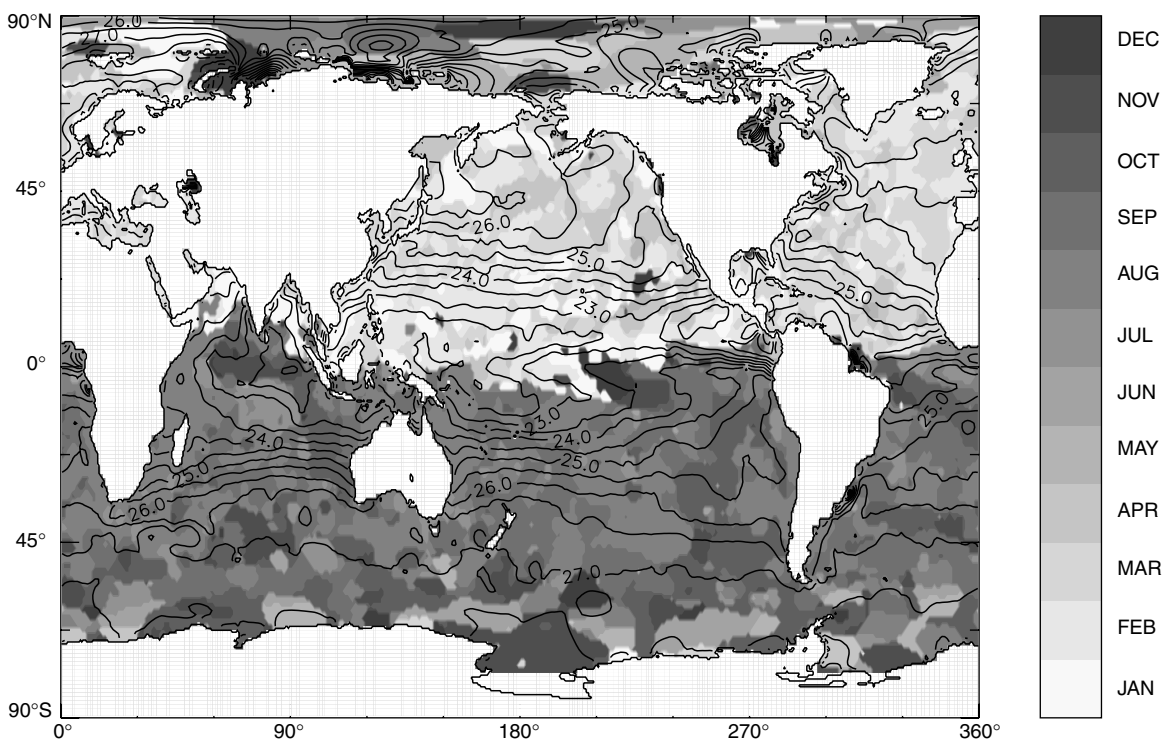


Fig. 5.1.7 Maximum monthly sea surface density, $\langle \text{SSD} \rangle_{\text{max}}$, with a contour interval of 0.5 kg m^{-3} , overlaid on the month of the maximum, M_{SSDmax} .

southeast of Greenland where there is a small region of moderately saline surface water, $\langle \text{SSS} \rangle_{\text{max}} > 35$, combined with cold $\langle \text{SST} \rangle_{\text{min}}$ along the coast. However, in Baffin Bay such dense water results from a relative maximum in $\langle \text{SSS} \rangle_{\text{max}}$ found in January–February, presumably due to ice formation. At mid-latitudes temperature is the primary control of the intermediate surface densities. Accordingly, $\langle \text{SSD} \rangle_{\text{min}}$ is found in late summer to early autumn and $\langle \text{SSD} \rangle_{\text{max}}$ occurs in late winter to early spring. In winter strong meridional gradients in $\langle \text{SSD} \rangle_{\text{max}}$ are confined to latitudes between about 20° and 40°N , where there are corresponding gradients in SST, and little variation in SSS. At higher latitudes, however, the decreasing salinity towards the poles tends to compensate for the decreasing temperature and weak gradients in $\langle \text{SSD} \rangle_{\text{max}}$ are the result. This compensation is particularly apparent in the Gulf Stream, Kuroshio and ACC regions, where the associated gradients evident in both $\langle \text{SST} \rangle_{\text{min}}$ and $\langle \text{SSS} \rangle_{\text{max}}$ are much less obvious in $\langle \text{SSD} \rangle_{\text{max}}$. In contrast, the seasonal thermocline established in summer effectively isolates the surface water from the wintertime salinity field, so that the spatial variability of $\langle \text{SSD} \rangle_{\text{min}}$ is

much like that of $\langle \text{SST} \rangle_{\text{max}}$. However, at the higher southern latitudes seasonal thermoclines are weaker because of the stronger winds, and salinity compensation again results in little variation in $\langle \text{SSD} \rangle_{\text{min}}$.

5.1.4 Surface fluxes of heat, fresh water and density

Here we describe the construction of global fields of ocean surface heat flux, \mathcal{H}_{in} , and freshwater flux, \mathcal{F}_{in} , that are used to compute the monthly mean surface density flux,

$$\langle \mathcal{D}_{\text{in}} \rangle_{m,y} = \langle \alpha / C_p \rangle_{m,y} \langle \mathcal{H}_{\text{in}} \rangle_{m,y} + \frac{\langle \text{SSS} \rangle_{m,y} \langle \mathcal{B} \rangle_{m,y} \langle \mathcal{F}_{\text{in}} \rangle_{m,y}}{(1-S)} \quad (5.1.9)$$

Here \mathcal{D}_{in} , \mathcal{H}_{in} and \mathcal{F}_{in} are positive when they act to increase, respectively, surface density, temperature and freshwater content (i.e. lower salinity). Consistent with equation (5.1.8), the values of α , β and specific heat, C_p , are allowed to vary spatially and monthly with $\langle \text{SST} \rangle_{m,y}$ and $\langle \text{SSS} \rangle_{m,y}$. Under sea ice these fluxes will be assumed to be zero, because

we do not know how to estimate reasonable values; this is another shortcoming of the analysis.

There are four components of the open ocean heat flux; the net short-wave (solar, Q_{sw}) and long-wave (Q_{lw}) radiative fluxes and the latent (Q_{lat}) and sensible (Q_{sen}) turbulent fluxes:

$$\mathcal{H}_{\text{in}} = Q_{\text{sw}} + Q_{\text{lw}} + Q_{\text{lat}} + Q_{\text{sen}} \quad (5.1.10)$$

The latter three are generally negative, cooling terms, and Q_{sw} is always positive. The freshwater flux is the sum of precipitation, P , and evaporation $E = Q_{\text{lat}}/L$:

$$\mathcal{F}_{\text{in}} = P + E \quad (5.1.11)$$

where the latent heat of evaporation remains constant at $L = 2.5 \times 10^6 \text{ J kg}^{-1}$ and E is generally negative, like Q_{lat} .

Direct measurements of heat and freshwater fluxes are difficult, expensive, and hence much too rare for our purposes. However, some of these measurements have been used to develop bulk formulae by which the fluxes can be estimated more frequently and over larger areas from more readily available data. Attempts have been made to develop algorithms to produce surface wind stress and heat flux directly from satellite observations. More commonly, satellite data are converted first to the intermediate parameters required by the bulk formula (Liu and Katsaros, Chapter 3.4), but not everything is amenable to remote sensing across the global oceans (WGASF, 2000). Unfortunately, it is apparent that no single data set is entirely satisfactory for our purposes. Therefore, we use different data sources for different components of the problem, as recommended by the WGASF (2000). Our choices reflect the priority of sampling frequency and global coverage during the WOCE years, so as to obtain the monthly means needed for input into equation (5.1.9), as well as ready availability. Other justifiable choices could have been made, and most are discussed at length by the WGASF (2000).

First, we utilize the satellite radiation data as processed by the International Satellite Cloud Climatology Project (ISCCP) to produce monthly estimates of solar insolation $\langle I \rangle_{\text{m},y}$ (Bishop *et al.*, 1997) and cloud fraction $\langle C \rangle_{\text{m},y}$ (Rossow and Schiffer, 1991). From coincident data, cloud cover is regressed against the ratio of insolation to

predicted clear sky radiation. Missing cloud cover, especially at high latitudes, is filled by inverting this regression with the more extensive insolation data set then used as input. At present, we have these products only for the years $y = 1983$ to 1993. The insolation and a constant surface albedo of 0.07 directly give

$$\langle Q_{\text{sw}} \rangle_{\text{m},y} = f_s (1 - 0.07) \langle I \rangle_{\text{m},y} \quad (5.1.12)$$

where the factor, $0.85 < f_s < 1.0$, allows the solar radiation to be reduced, as suggested by some empirical evidence (Large *et al.*, 1997; WGASF, 2000).

Another important data set is the Xie and Arkin (1996) merged precipitation. It contains global, monthly mean precipitation estimates ($\langle P_{\text{xa}} \rangle_{\text{m},y}$) from $y = 1979$ to the present. There are a blend of satellite microwave sounding unit (MSU) data, *in-situ* observations and atmospheric model output. It is our subjective impression that these are at least as good as any other precipitation estimate in middle and high latitudes, but perhaps overestimate the tropical precipitation. A problem may be that the influence of coastal or island rain gauge observations extends too far out to sea. In the tropics the MSU data (Spencer, 1993) give systematically lower values. Such differences argue against Wijffels's (Chapter 6.2) ensemble averaging of precipitation from diverse sources, assuming equal validity of each data set. Instead we choose to use MSU data in the tropical Indian (18°S to 5°N) and Pacific (18°S to 18°N) oceans and in a small region off the Alaskan panhandle, with a linear blend over 10° latitude and/or longitude to full $\langle P_{\text{xa}} \rangle$ elsewhere. This blended data set $\langle P_{\text{mxa}} \rangle_{\text{m},y}$ has been produced for the years $y = 1979$ to 1993 only.

The bulk formulae that we utilize require SST, the cloud fraction and the near-surface atmospheric state, namely wind speed U_{air} , temperature, T_{air} , specific humidity, q_{air} and density, ρ_{air} . Although there are areas of the ocean where these are directly observed (WGASF, 2000), the areas of insufficient sampling (including virtually all of the southern hemisphere) are too large for our present requirement of monthly means during specific WOCE years. Therefore, our SST is $\langle \text{SST} \rangle_{\text{m},y}$ from Reynolds and Smith (1994). The atmospheric state is taken from the 6-hourly NCEP/NCAR re-analysis (Kalnay *et al.*, 1996). Apparent biases

in these fields include weak equatorial trade winds (Milliff *et al.*, 1999), which we ignore, and too much low level moisture (relative humidity always above 80%), which is corrected by reducing q_{air} by a factor $f_q=0.94$. We then compute 6-hourly values of:

$$\begin{aligned} E &= \rho_{\text{air}} C_E \left(q_{\text{sat}} (\langle \text{SST} \rangle_{m,y}) - f_q q_{\text{air}} \right) \\ Q_{\text{lat}} &= LE \\ Q_{\text{sen}} &= \rho_{\text{air}} C_{\rho_{\text{air}}} C_H U_{\text{air}} (\langle \text{SST} \rangle_{m,y} - T_{\text{air}}) \\ Q_{\text{lw}} &= \varepsilon \sigma T_{\text{air}}^4 [0.39 - 0.05 e_{\text{air}}^{1/2}] F(\langle C \rangle_{m,y}) \\ &\quad + 4 \varepsilon \sigma T_{\text{air}}^3 (\langle \text{SST} \rangle_{m,y} - T_{\text{air}}) \end{aligned} \quad (5.1.13)$$

Here σ is the Stefan–Boltzman constant and an emissivity $\varepsilon=1$ is used to account for some reflection of downwelling long-wave radiation; e_{air} is the vapour pressure (a function of the corrected humidity, $f_q q_{\text{air}}$) and q_{sat} gives the saturation humidity above sea water as a function of SST. This Q_{lw} formula (Berliand and Berliand, 1952) with latitudinally varying cloud correction factor, $F(\langle C \rangle_{m,y})$ (Bunker, 1976a), has been evaluated by Fung *et al.* (1984).

The bulk transfer coefficients for evaporation, C_E , and sensible heat, C_H , are found by adjusting specified neutral, 10-m values for the heights and stability of the atmospheric state data. These neutral, 10-m values are given by:

$$\begin{aligned} 1000C_D &= 2.70(\text{m s}^{-1})/U_{\text{N10}} \\ &\quad + 0.142 + 0.0764(\text{m}^{-1}\text{s})U_{\text{N10}} \\ 1000C_E &= 32.7C_D^{1/2} \\ 1000C_H &= \begin{cases} 18.0C_D^{1/2}, & \text{stable} \\ 34.6C_D^{1/2}, & \text{unstable} \end{cases} \end{aligned} \quad (5.1.14)$$

These are plotted as a function of neutral 10-m wind speed, U_{N10} , in Fig. 5.1.8, so they can be compared to the many variations shown and discussed by WGASF (2000). The C_D formulation is within 10% of at least one of the five examples shown in WGASF (2000) for all winds between 3 and 25 m s^{-1} . It is a fit to a compilation of observations from 1 m s^{-1} to more than 25 m s^{-1} , and its infinite value at zero wind is consistent

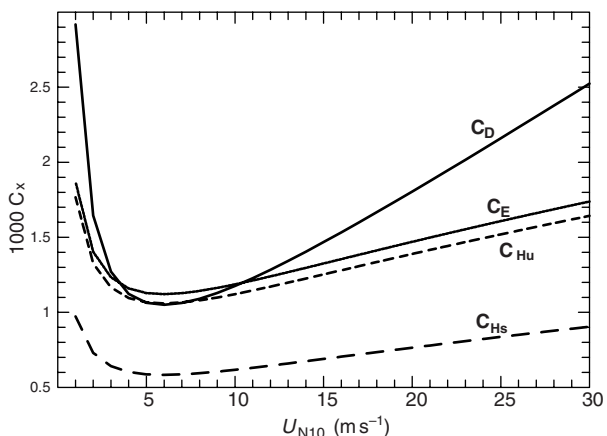


Fig. 5.1.8 Neutral 10-m transfer coefficients as a function of the neutral 10-m wind speed, U_{N10} . The drag coefficient is C_D , C_E is the Dalton number, and C_{Hu} and C_{Hs} are the neutral Stanton numbers in unstable and stable atmospheric conditions, respectively.

with the theoretical behaviour of wind over a smooth plate. The dependence of C_E and C_H on the square root of C_D is also theoretical, while the stability dependence of C_H is observed (WGASF, 2000). The complete set of transfer coefficients (5.1.14) has been used to produce flux climatologies that are consistent with alternatives (Doney *et al.*, 1998b).

Note that because ISCCP provides both $\langle C \rangle_{m,y}$ used in the Q_{lw} formula (5.1.13) and $\langle I \rangle_{m,y}$, there can be considerable cancellation of error; a satellite retrieval that gives too much cloud underestimates $\langle I \rangle_{m,y}$ but makes Q_{lw} less negative, often by about the same amount. This benefit would not be expected if solar radiation and cloud were derived from independent data sources. Although the NCEP/NCAR re-analysis covers the years 1958 to the present, we restrict the computation of monthly means $\langle \mathcal{H}_{\text{in}} \rangle_{m,y}$, $\langle \mathcal{F}_{\text{in}} \rangle_{m,y}$ and $\langle \mathcal{D}_{\text{in}} \rangle_{m,y}$ to the first three WOCE years, $y=1991$ to 1993. Extension to the end of WOCE awaits the acquisition of ISCCP data for later years.

5.1.4.1 The surface heat flux

Levitus *et al.* (2000) show that the temperature of the world ocean increased from the 1950s to the 1990s at a rate equivalent to a surface heat imbalance of only 0.3 W m^{-2} . They also find that the upper 300 m cooled between 1990 and 1995. It is, therefore, inconsistent that even with the $\sim 17\text{ W m}^{-2}$ more cooling due to the drying factor,

f_q , the average of $\langle \mathcal{H}_{in} \rangle$ is nearly 17 W m^{-2} , with $f_s=1.0$. It is not clear how best to correct the surface flux estimates to reconcile this inconsistency, but something needs to be done. We prefer to keep $f_q=0.94$, so that the annual cycle of Q_{lat} in the North Atlantic then closely matches the observed climatology from Kent and Taylor (1995). There is little to be gained by adjusting the under-sea-ice flux, because the insulation provided by snow and ice cover makes the flux small, and because the area is only about 10% of the ocean surface. The simplest adjustment is to reduce uniformly the ice-free surface flux by 16.4 W m^{-2} . Alternatively, the solar radiation can be suitably reduced with $f_s=0.90$. The three-year global average of this corrected flux is 154 W m^{-2} . The average latent, sensible and long-wave components remain at -95 , -22 and -37 W m^{-2} , respectively, and the corrected net flux, $\langle \mathcal{H}_{in} \rangle$, is near zero.

The global distribution of the adjusted net heat flux ($\langle \mathcal{H}_{in} \rangle_{m,y} - 16.4 \text{ W m}^{-2}$), averaged over the 36 months, is shown in Figure 5.1.9 (see Plate 5.1.9, p. 428), which can be compared to climatological estimates shown by the WGASF (2000) and the atlas of Beranger *et al.* (1999). All the features of this three-year average are expected; equatorial heating with peaks in the western Indian, eastern Pacific and central Atlantic; strong heating in the upwelling regions off the west coasts of continents; weak heating over much of the Southern Ocean and northeast Pacific; strong cooling of western boundary currents (the Gulf Stream, Kuroshio and Aghulas in particular); and pockets of strong cooling in northern high latitudes (Labrador Sea and off Iceland). The strength of these features varies widely between climatologies, but none in Figure 5.1.9 appear to be outliers. In particular, the region of the eastern equatorial Pacific with more than 100 W m^{-2} heating is similar to that of da Silva *et al.* (1994). However, our adjustment in this region may be compensating for a lack of latent and sensible heat loss because of the weak equatorial winds. There probably should be net cooling along much of the Antarctic coast to represent the cooling of exposed surface water to the freezing point. Further cooling is balanced by ice formation, a form of ocean heating that should be balanced primarily by additional ocean cooling offshore where the Antarctic ice melts. Quantifying these sea-ice processes is beyond the scope of

this work, but clearly important, even though they do not affect the global heat budget, only the meridional distribution of heating.

The latitudinal variation of zonal averages (not shown) from Figure 5.1.9 is very much like that of the COADS (Comprehensive Ocean-Atmosphere Data Set) climatology based on ship and buoy observations (da Silva *et al.*, 1994), but the amplitudes (cooling and heating maxima) tend to be smaller. Between about 20°S and 60°N , where the observations are most plentiful, the zonal averages differ by at most $\pm 10 \text{ W m}^{-2}$. Such differences are not large given the uncertainties in both (WGASF, 2000). The zonal averages are not so similar to climatologies extracted directly from re-analysis projects, including the NCEP (Beranger *et al.*, 1999). Differences with the latter are due to different radiation, the f_q drying factor, different transfer coefficients (Fig. 5.1.8), and the time interval.

Included in the Beranger *et al.* (1999) atlas is the Josey *et al.* (1999) COADS-based calculation shown by Bryden and Imawaki (Chapter 6.1), who discuss in more detail the issue of correcting for global heat flux imbalance, and in particular the 30 W m^{-2} bias of this climatology. Compared with Figure 5.1.9, it has generally greater heat flux everywhere, but by less than the 30 W m^{-2} bias, except in the Indian Ocean where the difference is typically greater than 50 W m^{-2} . The atlas also shows that differences between the zonal means of the Josey *et al.* (1999) heat fluxes and other climatologies, including Figure 5.1.9, are nearly symmetrical about the equator. This result suggests that poorer sampling in the southern hemisphere is not the only source of the global imbalance.

Of more interest to WOCE, and oceanography in general, are the meridional heat transports implied by the mean surface heat flux. Since this inference assumes no ocean heat storage it becomes less robust for short time intervals such as our three WOCE years. Also, Bryden and Imawaki (Chapter 6.1) argue convincingly that the error that accumulates in the integration of surface heat flux over large areas becomes greater than the uncertainty in direct estimates of ocean heat transport. If true, estimates can be used to constrain the heat flux estimates, and in particular to judge between Figure 5.1.9 ($f_s=1.0$) and the alternative $f_s=0.9$. The global and Atlantic implied heat transports for both cases are shown in Figure 5.1.10.

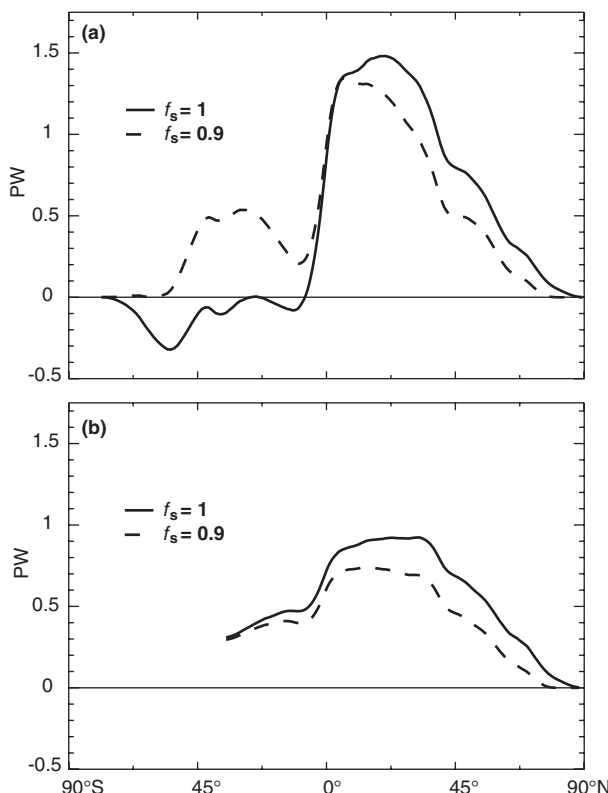


Fig. 5.1.10 The implied northward heat transport from the fluxes in Figure 5.1.9 (see Plate 5.1.9, p. 428) ($f_s=1.0$) and from the case with reduced solar heating ($f_s=0.9$), for (a) the globe, and (b) the Atlantic Ocean.

In the Atlantic, the differences in the northward transport across 25°N and 14°S are about 0.48 and 0.30 Sv, respectively. This difference in the direct estimates shown in Bryden and Imawaki (Chapter 6.1) is 0.7 ± 0.4 Sv, which supports the choice of Figure 5.1.9 ($f_q=1.0$), as do comparisons over other Atlantic regions. We note that significant sea-ice melting can occur as far north as 50°S and as far south as 50°N . The neglect of this process and the excess cooling in regions of ice formation means that the behaviour of Figure 5.1.10 at high latitudes is not reliable.

5.1.4.2 The surface freshwater flux

The three-year average evaporation is $-38.1 \text{ mg m}^{-2} \text{ s}^{-1}$ of fresh water, which includes the effects of the drying factor, f_q , and cannot be adjusted without changing the latent heat flux and upsetting the heat budget. The corresponding average precipitation is $33.1 \text{ mg m}^{-2} \text{ s}^{-1}$, which does not include any excess of precipitation over evaporation in ice-covered regions that eventually enters the

ocean as meltwater. The imbalance of $5 \text{ mg m}^{-2} \text{ s}^{-1}$ is 13% of the evaporation and can be reasonably accounted for by the above melt, the total runoff from all land masses, including Antarctica, and a possible increase in ocean salinity over the three years. Such an increase is more likely than a change in heat content, because SSS, where differences are most likely to appear first, does not directly feedback on the freshwater flux, unlike SST and the heat flux. The imbalance could be reduced to include only runoff ($\sim 10\%$ of evaporation), by increasing the precipitation by a few per cent. Such an adjustment would not be unreasonable, given the very large uncertainty in monthly precipitation estimates at individual points; perhaps a factor of two. However, it is likely that biases in the blended precipitation vary geographically, so we choose not to correct and take

$$\langle P \rangle_{m,y} = \langle P_{\text{mxa}} \rangle_{m,y}$$

The resulting global distribution of $\langle \mathcal{F}_{\text{in}} \rangle_{m,y}$ averaged over the 36 months is shown in Figure 5.1.11 (see Plate 5.1.11, p. 428). Again, all the expected features are present in this three-year average. In the northern hemisphere Atlantic and Pacific there is net precipitation associated with the mid-latitude storm tracks and the intertropical convergence zones ($2\text{--}10^\circ\text{N}$), with excess evaporation between. The Indian Ocean is anomalous, with net precipitation in the east and evaporation in the west. In the southern hemisphere there is a small excess of precipitation over most of the Southern Ocean and in the South Pacific Convergence Zone and the South Atlantic Convergence Zone, with significant excess evaporation in most other locations. In the North Atlantic there is a very high spatial correlation with the freshwater flux shown by Schmitt *et al.* (1989). The magnitudes are very similar everywhere except in the region of the Gulf Stream and its extension, where Figure 5.1.12 shows more precipitation relative to evaporation. However, Figure 5.1.12 does differ significantly in the tropics from computations that use the precipitation from Numerical Weather Prediction models, including the tropical $\langle P_{\text{xa}} \rangle$. An example is the operational analysis from ECMWF evaluated by Beranger *et al.* (1999). The 1991–96 mean shows much greater tropical rainfall than used for Figure 5.1.12, including an excess of precipitation over evaporation extending eastward to 160°W along 15°S in the Pacific.

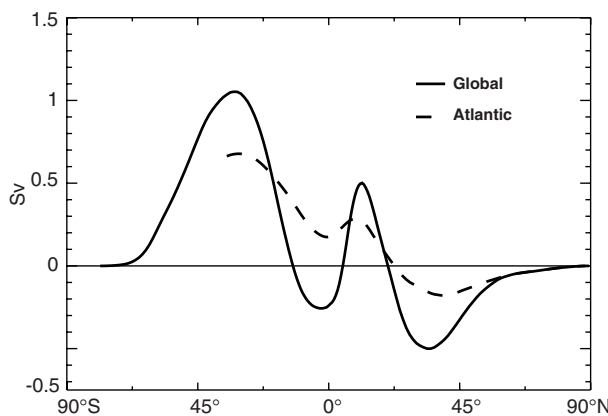


Fig. 5.1.12 The implied northward transport of fresh water from the fluxes of Figure 5.1.11 (see Plate 5.1.11, p. 428) for the globe and for the Atlantic Ocean.

This feature is typical of atmospheric numerical models, is due to an erroneous ITCZ south of the equator, and is one major difficulty in using such analyses. This artefact is also evident in the ensemble average of Wijffels (Chapter 6.2), which also shows more net freshwater flux in the western tropical Pacific and eastern tropical Indian Ocean. Otherwise, the two fields are not significantly different.

There is nothing unexpected in the zonal average freshwater flux (not shown) from Figure 5.1.11. There are maxima at 52°N, 6°N and between 45 and 60°S at 20, 37 and 15 $\text{mg m}^{-2} \text{s}^{-1}$, respectively. The minima at 20°S and 22°N are both about $-26 \text{ mg m}^{-2} \text{s}^{-1}$. The northward freshwater transport implied by these flux averages is shown in Figure 5.1.12. The differences from Wijffels *et al.* (1992) are surprisingly small, considering the time period, the uncertainties, particularly in precipitation, and the accumulation of error as the fluxes are integrated. At 35°S, the northward transport into the Atlantic is nearly identical. Comparison with the results compiled by Wijffels (Chapter 6.2) shows a consensus in the northern hemisphere and divergence in the southern hemisphere, which reflects the growth of error as the integration proceeds southward across the large areas of the tropics where precipitation is uncertain. Direct hydrographic estimates suggest that the freshwater influxes in the tropical Atlantic of Figure 5.1.11 are too small.

5.1.4.3 The surface density flux

The contribution to \mathcal{D}_{in} from 1 $\text{mg m}^{-2} \text{s}^{-1}$ of fresh water flux varies only slightly with salinity between 0.023 $\text{mg m}^{-2} \text{s}^{-1}$ (30) and 0.030 $\text{mg m}^{-2} \text{s}^{-1}$ (37).

This is about equal to the contribution of 1 W m^{-2} of heat flux at temperature of 5°C ($0.025 \text{ mg m}^{-2} \text{s}^{-1}$). However, the effect of 1 W m^{-2} is about three times greater at 29°C ($0.08 \text{ mg m}^{-2} \text{s}^{-1}$), but about a factor of two smaller at 0°C ($0.015 \text{ mg m}^{-2} \text{s}^{-1}$), because of the decrease in expansion coefficient α with temperature.

The 36-month average of $\langle \mathcal{D}_{\text{in}} \rangle_{\text{m},y}$ computed from (5.1.9) and the fluxes of Figures 5.1.9 and 5.1.11 is shown in Figure 5.1.13 (see Plate 5.1.13, p. 428). This flux is most negative in the tropical Atlantic and Pacific Oceans, where the heat and freshwater contributions have the same sign. It is most positive in regions of the western boundary currents, where the cooling is sufficient to overcome the net precipitation. Farther poleward, as α decreases, there is a tendency for the two effects to cancel. In the Indian Ocean there is cancellation both in the west (heating and evaporation) and in the east (cooling and precipitation), so that the meridional structure of the heat and freshwater fluxes is lost. There is little density flux in the Southern Ocean, where fluxes are small with a tendency to cancel in many regions. Over much of the subtropical gyres evaporation is reinforced by cooling to give a net positive density flux.

Overall, the three-year averages of Figure 5.1.13 (see Plate 5.1.13, p. 428) are very much like the climatological density flux (north of 30–40°S) computed from revised COADS heat and freshwater fluxes (Speer *et al.*, 1995a), both in features and magnitude. There are no unreasonable differences given the different time intervals and the uncertainties in the surface heat and freshwater fluxes (WGASF, 2000). However, positive density flux does cover more of the Indian Ocean in Figure 5.1.13 (see Plate 5.1.13, p. 428). The advantages of the present data are that they are monthly and include the Southern Ocean to the limit of Antarctic ice.

The annual cycle of density flux (not shown) is much as expected; positive in the winter hemisphere and negative in the summer, even in the western boundary current regions. The flux is negative throughout the year in the equatorial Atlantic and Pacific. In the Indian Ocean and far eastern equatorial Pacific there is a strong monsoonal variation with considerable spatial structure and large amplitudes in the density flux fields in both the June–July–August and the December–January–February seasons.

5.1.5 Surface water mass transformation and formation

The surface densities of Section 5.1.3 and the air-sea density flux of Section 5.1.4 allow the surface water mass transformation, $F(\rho)$ to be calculated from equation (5.1.6). In order to estimate long-term transformation, we want the time average of F : that is, the time-averaged density flux that passes through the ocean surface where the density equals ρ , following the movement of the outcrop over time. We calculate the three-year time average from 1991 up to 1993, $\langle F(\rho) \rangle_{3\text{-year}}$, as a simple sum of monthly values.

Note that from equations (5.1.3) and (5.1.7), where we consider only the surface forcing,

$$M = -\frac{\partial G}{\partial \rho} = -\frac{\partial F}{\partial \rho} \quad (5.1.15)$$

The water mass that accumulates or is destroyed as a result of surface fluxes between two isopycnals that differ by $d\rho$ is $M(\rho)d\rho = G(\rho) - G(\rho + d\rho)$.

The surface fluxes of heat and fresh water play a dual role in surface water mass transformation and formation. First, through (5.1.9), they determine the surface density flux, \mathcal{D}_{in} , equation (5.1.6). Second, they influence surface temperature and salinity, and hence ρ , in (5.1.6) and (5.1.15). However, the two fluxes differ in an important way. Consider a positive (negative) heat flux trying to create an extreme light (heavy) density class. To do so, it must warm (cool) the surface water, but in doing so the heat flux itself becomes less positive (negative), which tends to shut the process down. There is no such direct negative feedback involved when a positive (negative) freshwater flux tries to create extreme density classes, because \mathcal{F}_{in} does not depend on SSS. This difference is consistent with the observation (Section 5.1.3) that extreme densities $\langle \text{SSD} \rangle_{\text{max}}$ and $\langle \text{SSD} \rangle_{\text{min}}$ appear to be more closely associated with extremes in salinity, $\langle \text{SSS} \rangle_{\text{max}}$ and $\langle \text{SSS} \rangle_{\text{min}}$.

Figure 5.1.14 shows the 1991–93 water mass transformation rates in three ocean basins: Arctic plus Atlantic, Pacific plus Indian, and Southern. The rates for some smaller ocean regions are shown in Figure 5.1.15. Negative transformation rates indicate that the surface fluxes act to transform the surface water to lower density classes; positive transformation rates indicate transformation to greater density. From equation (5.1.15), a negative

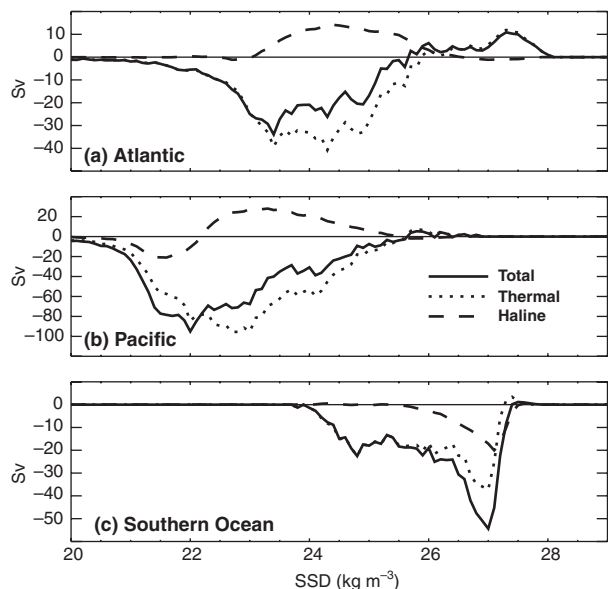


Fig. 5.1.14 Water mass transformation rates in Sverdrups ($1 \text{ Sv} = 10^6 \text{ m}^3 \text{ s}^{-1}$) as a function of sea surface density anomaly (SSD) in kg m^{-3} , for the global ocean partitioned into (a) the Arctic–Atlantic basin (north of the Cape of Good Hope and excluding the Mediterranean); (b) the Indian–Pacific basin, and (c) the Southern Ocean. The total (solid traces) is decomposed into its thermal and haline parts.

slope indicates water mass formation, and a positive slope represents destruction of a water mass by surface exchange. All the basins show the same general features. Using the Arctic–Atlantic basin as an example, there is little surface water below some low density, here 22 kg m^{-3} . Since surface fluxes are creating waters of these extreme light densities from heavier waters, F is negative for waters $\approx 22\text{--}23 \text{ kg m}^{-3}$. Similarly, there is no water denser than some upper limit, here about 28 kg m^{-3} , and water passes from lighter to heavier densities with $F > 0$ at $27.5\text{--}28 \text{ kg m}^{-3}$. Creation of these extreme water masses is balanced by loss of intermediate waters, where $M = -\partial F / \partial \rho < 0$. This is the archetypal behaviour (Nurser *et al.*, 1999), since over the long term surface forcing and thermocline diffusion must cancel out so that there is no net change in water mass structure. Since diffusion creates waters of intermediate densities from those of extreme densities, surface fluxes *must* do the reverse.

Note that the integral over all ρ of F gives the time-averaged net density input into the ocean over the region being considered. Even though the Atlantic loses fresh water (Fig. 5.1.12) and heat

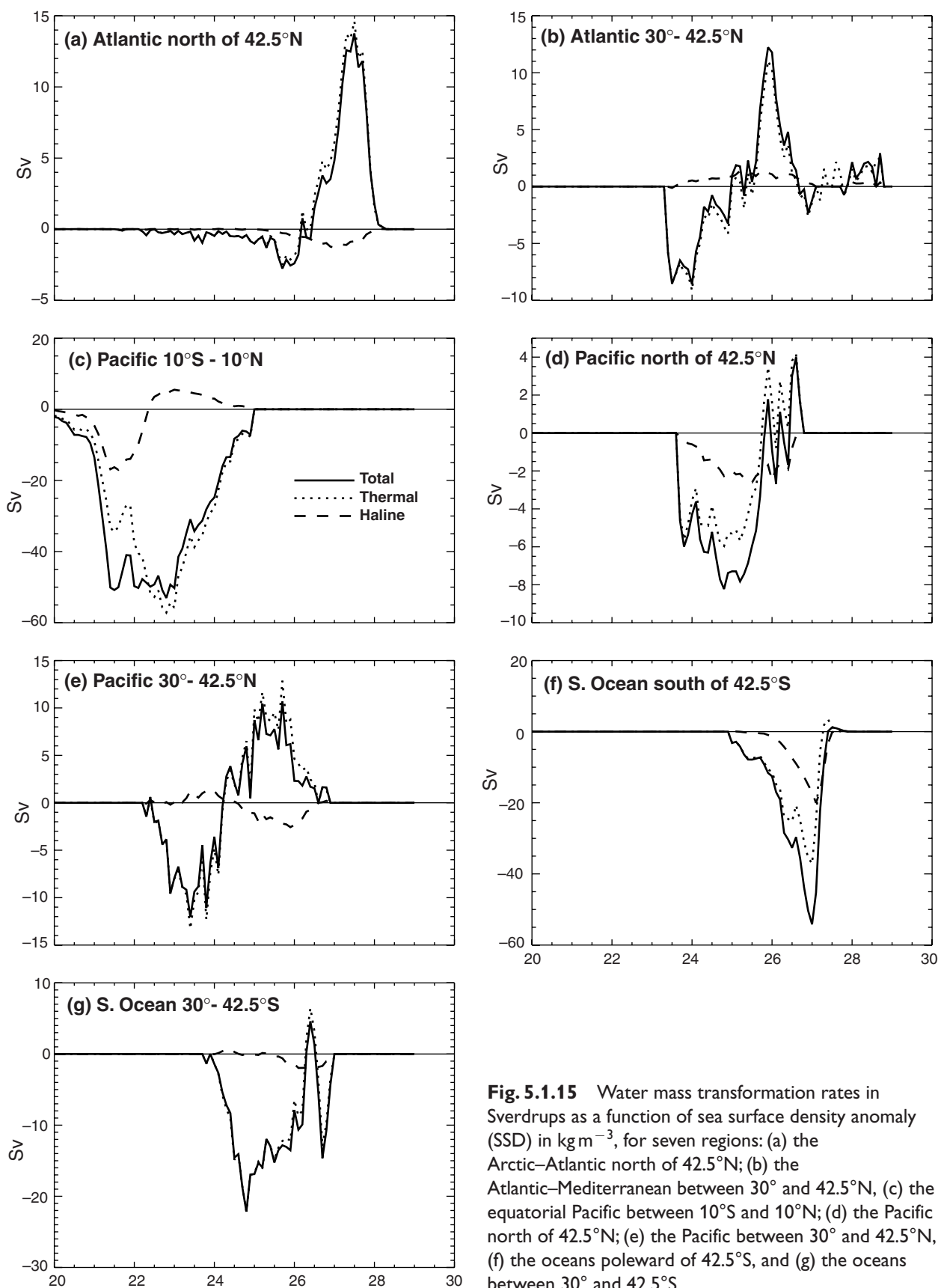


Fig. 5.1.15 Water mass transformation rates in Sverdrups as a function of sea surface density anomaly (SSD) in kg m^{-3} , for seven regions: (a) the Arctic–Atlantic north of 42.5°N ; (b) the Atlantic–Mediterranean between 30° and 42.5°N , (c) the equatorial Pacific between 10°S and 10°N ; (d) the Pacific north of 42.5°N ; (e) the Pacific between 30° and 42.5°N , (f) the oceans poleward of 42.5°S , and (g) the oceans between 30° and 42.5°S .

(Fig. 5.1.10b), it also loses density (Fig. 5.1.14a), since the warming acts on warmer waters where the coefficient of expansion α is large, and the cooling acts on cool waters where α is small. A similar effect was noted over the seasonal cycle by Zahariev and Garrett (1997). This effect is balanced by cabbeling in the interior (e.g. Davis, 1994).

Comparison of Figures 5.1.15a and 5.1.15b with 5.1.14a of the Atlantic–Arctic basin indicates that the large haline transformation in the latter between 23 kg m^{-3} and 26 kg m^{-3} occurs south of 30°N . Between 23 and 25 kg m^{-3} it is largely compensated by the thermal component (Fig. 5.1.14a). Further north, thermal transformation dominates and in the density range of subtropical mode water 26.3 – 26.7 kg m^{-3} the negative slope gives 5 Sv as the average rate at which this water mass formed at the surface (Fig. 5.1.15b). A similar rate of subpolar mode water formation (27.5 – 28 kg m^{-3}) north of 42.5°N is evident in Figure 5.1.15a. Note the formation of very dense waters with densities 28 – 29 kg m^{-3} in the Mediterranean (included in Figure 5.1.15b but not in Figure 5.1.14a).

The overall picture in the Pacific–Indian basin is broadly similar, though skewed towards lighter densities. Again there is large haline transformation at lighter densities, thermally compensated in the range 21 – 24 kg m^{-3} . However, in contrast to the North Atlantic, there is little formation of dense waters in the subpolar North Pacific (Fig. 5.1.15d). Air–sea fluxes in the subtropical North Pacific, however, generate $\sim 10\text{ Sv}$ of thermocline waters (Fig. 5.1.15e), comparable to the production in the subtropical North Atlantic (Fig. 5.1.15b). Figure 5.1.15c indicates that almost all the global transformation below about 22 kg m^{-3} occurs in the tropical Pacific between 10°N and 10°S . In this region about 20 Sv of light surface water is formed at densities below 21.3 kg m^{-3} .

The plot of transformation in the Southern Ocean, Figure 5.1.14c, shows less than 2 Sv of dense water (27.5 – 28 kg m^{-3}) being formed, mostly thermally. It is unrealistic, given the poor fluxes and temperature and salinity fields, to expect this data set to show creation of the extreme water types such as Weddell Sea Bottom water that mix to form Antarctic Bottom water (Rintoul *et al.*, Chapter 4.6). The formation of Antarctic Intermediate water of density 27 – 27.3 kg m^{-3} is only evident as a negative slope in the haline transformation, giving about 5 Sv . Even the more limited

area of Figure 5.1.15f is too large to produce a clear signature in the total transformation. However, there is a clear signal of the 30 Sv of Subantarctic Mode Water formation between 26.5 and 27 kg m^{-3} , which Speer *et al.* (1997) show is mostly formed in the Indian Ocean sector. Over the whole Southern Ocean (Fig. 5.1.14c) the creation by surface fluxes of about 30 Sv of mode waters with densities between 26 and 27 kg m^{-3} is consistent with the formation of 26 Sv of such waters in the scheme shown in Chapter 4.6, Figure 4.6.12.

Our results show some differences from those presented by Speer *et al.* (1995a) who used (i) fluxes and (sometimes) SST from the COADS data set as analysed by Oberhuber (1988) and Wright (1988), together with Levitus SST/SSS, and also (ii) fluxes from Isemer and Hasse (1987) for the North Atlantic as a comparison. They of course did not have fluxes for the Southern Ocean (south of 30 – 40°S). They found water mass transformation peaking at $\sim 30\text{ Sv}$ at densities of 26.5 kg m^{-3} in the North Atlantic, rather than our values of $\sim 15\text{ Sv}$ (Fig. 5.1.15a,b). Our values are closer to those found by Marsh (2000) for the North Atlantic, who used the Southampton Oceanography Centre (SOC) climatology (Josey *et al.*, 1998, 1999), which covers the period 1980–97. Using the unadjusted climatology, he found a peak transformation rate of $\sim 14\text{ Sv}$ at 27.5 kg m^{-3} , and $\sim 9\text{ Sv}$ at 26.3 kg m^{-3} . If he corrected the SOC fluxes so as to balance the net global heat balance (reducing short-wave by 8% and increasing latent heat loss by 13%, following da Silva *et al.* (1994)), he found instead peak rates of $\sim 15\text{ Sv}$ at 27.5 kg m^{-3} , and $\sim 19\text{ Sv}$ at 26.3 kg m^{-3} . Ours and Marsh's values are in fact more similar to the maxima obtained in the model diagnoses of Nurser *et al.* (1999) and Marshall *et al.* (1999) of 15 – 20 Sv , which were forced by climatology (Esbensen and Kushnir, 1981) and by 1992 NMC fluxes respectively, plus relaxation.

These discrepancies emphasize the sensitivity of the properties and formation rates of oceanic water masses to the surface flux field (and indeed to the SST and SSS fields). They may arise from interannual variability rather than simply from uncertainties in the fields. Using the unadjusted SOC climatology, Marsh (2000) found very considerable interannual variability in the transformation in the North Atlantic. For instance, the peak transformation at $\sim 26.3\text{ kg m}^{-3}$ ranged from as little as 1 Sv in 1980 to 16 Sv in 1987, compared

with the average ~ 9 Sv. Our average is only over a three-year period and so may not be representative of the long term.

This issue of interannual variability in the fluxes is addressed in Figure 5.1.16 (see Plate 5.1.16, p. 428). It shows annual flux anomalies between 1982 and 1997. Note that the radiative forcing everywhere and the precipitation in the tropical Pacific and Indian Oceans after 1993 are climatological. Our three-year analysis period of 1991–93 was most unrepresentative of the later WOCE years, 1994–97, in the following respects: the positive freshwater flux anomalies in the equatorial Indian and Pacific, the negative freshwater flux anomaly in the equatorial Atlantic, and the greater ocean heating throughout the Atlantic, extratropical Indian and the Pacific south of about 30°N . The WOCE years (1991–97) differ from the earlier years (1982–90) in several ways. There are generally negative heat flux anomalies at all latitudes of the Indian Ocean. The equatorial Pacific heat and freshwater flux anomalies are smaller in amplitude. There is heating over most of the South Atlantic. The amplitude of the heat flux anomalies associated with the North Atlantic Oscillation (NAO) (north of 45°N in the Atlantic) is smaller. In Figure 5.1.16 (see Plate 5.1.16, p. 428) an ‘average’ year would be characterized by a vertical zero contour in all six panels. No such year exists, with 1992 perhaps the closest. No short period (e.g. our analysis period, or the WOCE period) appears to be ‘typical’ of either another short period, or of a longer period. Prime contributors to this observation are the irregular variability of the El Niño-Southern Oscillation (ENSO) and the NAO.

5.1.6 Summary

In this chapter we have set out Walin’s (1982) formal theory of water mass transformation. We have diagnosed transformation driven by surface fluxes across density classes in various regions of the World Ocean, over three years of the WOCE period. Our results cover almost all the World Ocean. They are broadly similar to, but show distinct differences from, other diagnoses using different climatologies. These differences arise partly from uncertainties in the flux fields, but also from their substantial (Marsh, 2000) temporal variability. Our results are derived from observations over a three-year period, which may not be representative of the long term.

The sensitivity of these transformation rates to the surface fluxes emphasizes just how important accurate knowledge of the surface fluxes is. Numerical ocean models that are driven by incorrect fluxes acting on incorrect surface temperature and density distributions will not contain the correct water masses. Models forced by relaxation and/or climatological fluxes can easily develop regions of ‘mismatch’ between surface fluxes and surface properties. The strong spurious fluxes acting on fluid that is too warm and saline over an incorrectly separated Gulf Stream are a classic example of this problem. Coupled models, e.g. by Doney *et al.* (1998b), which take into account the finite heat capacity of the atmosphere offer more hope in this regard.

Care must be taken in relating the formation rates, M , derived from differentiation of the transformation rate driven by surface fluxes, F , to ‘subduction’ and the injection of water masses into the main thermocline. In the first instance, scaling analysis and numerical model runs (Garrett and Tandon, 1997; Marshall *et al.*, 1999; Nurser *et al.*, 1999; Tandon and Zahariev, 2000) suggest that diffusive processes within the mixed layer and seasonal thermocline, while relatively unimportant at higher densities, do profoundly change the transformation rates at lighter densities $<\sim 25.5\text{ m}^{-3}$. For these lighter waters the total transformation G calculated over the mixed layer and seasonal thermocline can be very different from F , even having the opposite sign (Marshall *et al.*, 1999; Rhines, 1993; Tandon and Garrett, 1997). Second, the domains over which we integrate to find G may include regions of entrainment as well as subduction. The entrainment and subduction will tend to cancel out, leaving a *net* formation rate considerably smaller than the total subduction of fluid from that outcrop. Over an open domain, however, M is now the difference between the fluid subducted down into the thermocline, and the input of mixed layer and seasonal thermocline waters of that density across the open boundary of the domain. This may give something different from the subduction or ventilation rate.

Despite these caveats, these water mass diagnostics are particularly useful in understanding the generation of denser mode and intermediate waters, where diffusive and recirculatory processes are not such an issue. They are powerful tools for understanding the diabatic circulation, offering the

possibility of relating changes in properties to change in surface forcing.

The separation of waters into masses with various properties is one of the key tools of classical hydrography. The extension of the analysis to T - S classes gave good agreement between the T - S properties of the observed major 'mode' water

masses and the T - S classes being formed by surface processes (Speer, 1993; Speer *et al.*, 1995a). Quantitative diagnosis on these lines will be a demanding test of the ability of ocean and climate models to simulate both the mean state and variability and long-term change in the real ocean.

5.2

Mixing and Stirring in the Ocean Interior

John M. Toole and Trevor J. McDougall

5.2.1 Scales of mixing and stirring

One of the intriguing concepts in physical oceanography is the cascade of energy and scalar variance from global scales, at which the ocean is forced, to sub-centimetre scales, where molecular dissipation reigns. Between these exist a variety of dynamical regimes governing flows that both transport energy through physical space and eventually flux it to smaller scales. A beautiful and often vexing aspect of fluid dynamics involves the relationships between these disparate scales of motion. Simple scaling arguments even suggest that microstructure controls the intensity of the global-scale thermohaline circulation. This chapter will focus on the tail of the ocean energy cascade: the stirring role of mesoscale eddies and smaller-scale motions and the mixing by turbulence and double diffusion. A background theme will be how stirring and mixing impact the general circulation: the principal focus of the World Ocean Circulation Experiment (WOCE). Basic to our presentation will be the differentiation between mixing and stirring. The former we define as the irreversible action of molecular viscosity, heat conduction and solvent diffusion responsible for the destruction of velocity and water property gradients. Owing to seawater's relatively small coefficient of molecular viscosity ($\nu = O(10^{-6} \text{ m}^2 \text{ s}^{-1})$), the frictional dissipation of kinetic energy in the ocean interior is only effective at centimetre scale. Interactions and instabilities of larger-scale motions act to flux kinetic energy to sub-metre scales where viscous dissipation acts. Similarly, with the molecular diffusivity of heat, D_T , of order $10^{-7} \text{ m}^2 \text{ s}^{-1}$ and that

for salt, D_S (and most other solutes), of order $10^{-9} \text{ m}^2 \text{ s}^{-1}$, it is only by successive straining of scalar property distributions (stirring) by mesoscale flows, internal waves and ultimately, turbulent eddies that water property gradients at millimetre scale are enhanced to where molecular diffusion is effective. Importantly, the sub-metre sized motions responsible for the actual mixing clearly lie well beyond the reach of global- or even basin-scale numerical simulations. Indeed, not even mesoscale eddies are resolved in today's climate simulations. Therefore, in addition to summarizing recent experimental findings and ideas, we will also address the parameterization question of how to express stirring and mixing in terms of larger-scale (model-resolved) motions.

To place our story in context, we will begin by reviewing in Section 5.2.2 some of the scaling arguments that relate mixing to the ocean's general circulation. Though developed for highly idealized domains, the scaling (supported by numerical simulations) suggests a dynamical connection between the mean global-scale overturning circulation and mixing supported by turbulent eddies: a horizontal length scale range of order 10^9 . Our background discussion continues with a summary of indirect estimates of diapycnal ocean mixing inferred from large-scale circulation studies, water property distributions and simple ocean dynamics. Subsequent sections highlight some of the physical processes involved in the energy cascade between the gyre and dissipation scales.

Mesoscale eddies near the Rossby radius of deformation are the principal stirring agents within the

energy and scalar variance cascades at scales of order 100 km. Eddies of these diameters, principally formed by baroclinic instability at large-scale oceanic fronts, act to stir fluid parcels in a way that is highly constrained by the stratified nature of the fluid. Theoretical understanding of this issue has progressed since the pioneering paper of Gent and McWilliams (1990). One promising approach for understanding how the effects of mesoscale eddies should be parameterized is the Temporal-Residual-Mean (TRM) formalism (McDougall and McIntosh, 1996, 2000), which provides the link between the different views that are apparent from averaging these turbulent flow fields in height coordinates and in density coordinates. The TRM framework reduces the flux parameterization problem from three dimensions to two and shows how the divergent part of the density flux is skew-symmetric so that the total advection velocity can be adiabatic. These ideas are reviewed in Section 5.2.3.

Moving towards smaller scales, shear dispersion involving internal waves (e.g. Young *et al.*, 1982) and possibly vortical mode motions (Polzin *et al.*, 2000b) appear active at horizontal scales of 1 to a few km. And at thermohaline fronts, intrusions with similar lateral scales supporting (and possibly driven by) double diffusive mixing are commonly observed. Section 5.2.4 gives a brief overview of research on these motions.

Diapycnal mixing is a broad topic; we will restrict attention here to the mechanisms and intensity of mixing below the surface boundary layer. The reader is referred to Large and Nurser (Chapter 5.1), Price (Chapter 5.3), Hanawa and Talley (Chapter 5.4) and Lazier *et al.* (Chapter 5.5) for a discussion of the very significant and important mixing and resultant water mass modification that occurs in and about the ocean's surface layer. Our presentation on diapycnal mixing is organized by depth: thermocline processes are discussed in Section 5.2.5 and abyssal processes in 5.2.6. Mechanistically, two classes of diapycnal mixing have been defined: turbulent and double diffusive. In the former, mechanical energy is expended as 1-to-100+ cm-scale eddies strain scalar variance to small scales where it is destroyed by molecular diffusion (see recent reviews by Gregg, 1987, 1998; Caldwell and Moum, 1995; and Gargett, 1989). Energetic turbulence mixes heat, salt and other scalar fields at similar rates. In the ocean interior, a principal energy source for the turbulence is the

internal wave field, and so our presentation contains extensive discussion of waves. Double diffusive processes (salt fingering and diffusive layering) become relevant when the vertical gradients of temperature or salinity have the same sign, and thus contribute oppositely to the vertical density gradient (see review by Schmitt, 1994). Due to the dissimilar molecular diffusivities of heat and salt, convective motions develop and release the potential energy associated with the unstably-stratified component. The associated vertical buoyancy flux is up-gradient. As discussed below, the relative importance of turbulent and double-diffusive mixing varies within the oceans depending on the background stratification and internal wave energy level. Though we don't pursue the idea further, it should be remembered that heat and salt fluxes associated with weak turbulence (that does not completely homogenize water properties) may also result in up-gradient buoyancy fluxes, again a consequence of the dissimilar molecular diffusivities for temperature and salinity (Gargett, 1988; Merryfield *et al.*, 1998).

5.2.2 Background

Basic energy arguments applied to an idealized, steady ocean suggest a direct connection between the large-scale flows and mixing. To overcome friction in a steady ocean circulation, there must be an input of mechanical energy over each closed streamline. This concept led Sandström (1916) to postulate that a closed, steady, buoyancy-driven circulation can be maintained only if the heating source is positioned at a lower geopotential than the cooling source (Huang, 1999). Sandström carried out simple laboratory experiments that appeared to confirm this idea, but application to the real ocean circulation is problematic. Sea level in the tropics where the oceans are heated is some 1 m higher (relative to a geopotential surface) than it is in the polar oceans where cooling occurs. Why then does a substantial mean thermohaline circulation exist in the ocean? Jeffreys (1925) proposed that mixing is capable of redistributing density, leading to a pressure field of the sense to sustain an overturning circulation in the face of frictional damping. Huang's (1999) closed-tube model for the thermohaline circulation, which demonstrates how the flow is controlled principally by diffusion of density when heating occurs at a higher potential than

cooling, suggests that both Sandström and Jeffreys were right. When the heating source lies above the cooling source, an overturning circulation is still possible because of mixing; but when that mixing is solely the result of molecular diffusion (as would virtually be the case in a careful laboratory experiment), the flow is very slow (and so difficult to observe.)

Scaling arguments by Welander (1971), Bryan (1987) and others for the steady overturning circulation in a simplified ocean basin (e.g. pie-shaped, single-hemisphere) also imply a strong dependence of the overturning circulation on buoyancy diffusion. The Sverdrup vorticity balance, thermal wind equation and vertical advective–diffusive balance for the density yield the scalings:

$$VD \sim WL, \quad \Delta p/p_0 \sim fVL/gD, \quad D \sim K/W$$

which, when combined into an expression for the meridional overturning transport, $M = VHL$, gives

$$M \sim [gf^{-1}(\Delta p p_0^{-1})L^4]^{1/3}K^{2/3}$$

With the density scale ($\Delta p p_0^{-1}$) set by a surface relaxation boundary condition, we arrive at the scaling:

$$M \sim GK^{2/3}$$

where G depends on the surface buoyancy forcing and the basin width. A slightly weaker dependence $M \sim K^{1/2}$ is obtained with surface flux boundary conditions (Huang and Chou, 1994; Zhang *et al.*, 1999b). Here V and W are the horizontal and vertical velocity scales, respectively, with L and D the corresponding length scales. The (assumed uniform) diapycnal diffusivity is K ; g and f are the gravitational acceleration and Coriolis parameter. Numerical box-model experiments using the GFDL MOM2 code (Bryan, 1969; Pacanowski, 1995) with the Gent and McWilliams (1990) eddy transport parameterization (see below) carried out by Zhang *et al.* (1999b) exhibited this scaling with little dependence on the strength of the wind driving for diffusivity values in the oceanographically relevant range between 10^{-5} and $10^{-3} \text{ m}^2 \text{ s}^{-1}$. Interestingly, Bryan's (1987) earlier study using a model with relaxation boundary conditions developed with horizontal and vertical diffusion (as opposed to epi- and diapycnal) showed a weaker dependence than $M \sim K^{2/3}$, possibly due to cross-isopycnal mixing by horizontal

diffusion in regions of sloping isopycnals (Veronis, 1975; McDougall, 1988), and/or because the model was not run sufficiently long to achieve steady state.

But the connection between diapycnal mixing and the overturning circulation is less straightforward in more realistic ocean geometries, in particular those including the zonally unbounded Southern Ocean. The sloping isopycnals of the Antarctic Circumpolar Current (ACC) allow an upward flow of deep water, even in the absence of interior mixing, with meridional Ekman transport and atmospheric modification of the mixed-layer waters closing the circulation. But such a meridional flow is in part opposed by the actions of mesoscale eddies driven by instabilities of the ACC. When these ideas are introduced in scaling arguments and energy budgets for an ocean with an ACC, it is found that the Southern Ocean circulations (large-scale and eddy) may exert more control on the intensity of the meridional overturning circulation and the depth of the main pycnocline north of the ACC than does diapycnal mixing (Toggweiler and Samuels, 1998; Gnanadesikan, 1999).

Relationships between mixing and circulation are perhaps clearest in the extratropical deep oceans where waters are isolated from local atmospheric forcing. Circulation schemes for the Pacific and Indian Oceans deduced using pre-WOCE and WOCE hydrographic section data have implicit need for significant diapycnal mixing in the abyss. The meridional overturning circulations for these basins involve net northward flow of Circumpolar Deep Water at the bottom and a mid-depth southward return of Indian/Pacific Deep Water (e.g. Wunsch *et al.*, 1983; Roemmich and McCalister, 1989; Wijffels *et al.*, 1996a; Robbins and Toole, 1997; Macdonald, 1998; Ganachaud, 1999). As the isopycnals associated with these deep water masses do not outcrop anywhere in these oceans (north of the Southern Ocean), these circulations imply diapycnal flow and hence interior mixing. Stommel and Arons (1960a,b) explored the dynamical implications of the vertical velocity field associated with such deep overturning circulations. Their schematics (which, for clarity, were derived for a flat bottom and spatially uniform upwelling from the abyss to the main thermocline) have poleward-directed abyssal flow in the interior with a series of deep western boundary currents and

zonal jets to close the circulation. In parallel, Wyrtki (1961b) and Munk (1966) looked at the scalar balance equations, and derived relationships between vertical advection and diffusion. These ideas that link mixing, the vertical velocity, and the horizontal circulation have guided thinking about the abyssal flow field for the past 40 years.

Munk's (1966) seminal paper (revisited by Munk and Wunsch, 1998) inferred the ocean mixing rate from a simple vertical advective–diffusive balance for the main thermocline: $w\Theta_z = (K\Theta_z)_z$. The model, fitted to observations of the typical 1-km e-folding scale for the potential temperature profile ($\Theta(z)$) and a guess at the average vertical upwelling rate (10^{-7} m s^{-1} : equivalent to a global bottom water formation rate of some 25 Sv uniformly upwelling into the thermocline), gives $K \sim 10^{-4} \text{ m}^2 \text{ s}^{-1}$. Admittedly, this is a greatly simplified model; the ocean obviously has a fully three-dimensional, time-varying circulation. Munk certainly acknowledged this in his original paper, suggesting that enhanced mixing in a (relatively thin) layer above the (sloping) bottom followed by lateral exchange with the interior might be the actual mechanism sustaining the thermocline. (This process has come to be known as boundary mixing: see Armi, 1978; Garrett, 1991.) Comparably sized average diffusivity estimates have also been derived from hydrographic box inverse models (e.g. Wijffels, 1993; Ganachaud, 1999) and extended beta-spiral calculations (e.g. Olbers *et al.*, 1985; Olbers and Wenzel, 1989). But as Wunsch (1996) notes, small errors in the coefficient matrices of these models ‘can easily produce spurious apparent mixing.’ (Indeed, an inverse model developed by St Laurent (1999) that includes both hydrographic and microstructure data finds that skill in diagnosing the diapycnal velocity comes largely from the latter.) Additionally, Davis (1994) discusses how time dependence can introduce error into K estimates inferred from a steady model.

Estimates of diathermal and diapycnal heat fluxes in the abyssal ocean have also been derived from heat budgets for semi-enclosed deep basins (e.g. Hogg *et al.*, 1982; Whitehead and Worthington, 1982; Saunders, 1987; Roemmich *et al.*, 1996; Morris *et al.*, 1997). These analyses derive mass and heat conservation statements for control volumes bounded by an interior isotherm (or isopycnal) and the bottom to relate estimates of the mean temperature transport through an inlet strait

to the turbulent heat flux across the bounding surfaces of the control volumes. When these turbulent fluxes are expressed in terms of an average diathermal/diapycnal diffusivity, values of order $10^{-4} \text{ m}^2 \text{ s}^{-1}$ are again obtained. Interestingly, related analyses for upper-ocean layers bounded by isotherms (isopycnals) and the free surface find similar need for significant diathermal fluxes (e.g. Speer, 1997; Zhang and Talley, 1998). (Note that the upper-ocean-layer analyses are far more complicated than their abyssal counterparts because of the significant and time-variable exchanges of heat and buoyancy at the air–sea interface (Garrett and Tandon, 1997). In contrast, geothermal heat flux generally makes negligible contribution to abyssal-layer heat budgets.)

These indirect and budget calculations, while valuable for setting bounds on the diapycnal mass transports and property fluxes, do not shed light on the possible mechanisms supporting the mixing, or where within each control volume it occurs. Indeed, the ocean mixing community has been engaged in a 30-year effort to find processes capable of supporting diapycnal fluxes consistent with $O(10^{-4} \text{ m}^2 \text{ s}^{-1})$ diffusivities. As discussed below, some progress has been achieved in the last decade.

5.2.3 The Temporal-Residual-Mean circulation

In this section we examine turbulence at the horizontal scale of tens of kilometres and we use our basic knowledge of these mesoscale flows to deduce something about how the fluxes achieved by these motions should be parameterized in coarse-resolution ocean models. Mesoscale eddies cause significant lateral fluxes of density and tracer, particularly in the Southern Ocean. Yet the effects of mesoscale eddies still need to be parameterized in climate models because of the present and foreseeable limitations of computer power that constrain model resolution. The mixing achieved by mesoscale eddies was traditionally parameterized as horizontal diffusion, but we have learnt in the past decade what damage this horizontal mixing had been doing to the model results. Specifically, horizontal mixing implies an uncontrolled amount of diapycnal property flux in regions of sloping isopycnals, often dominating the parameterized diapycnal mixing in the model. What was needed was a formulation for mesoscale mixing

that is the three-dimensional extension of the successful zonal-residual-mean theory of atmospheric science. The landmark paper of Gent and McWilliams (1990) marked the beginning of the oceanic work on this topic and since that time oceanographers have accepted that scalar properties should be advected by a velocity other than the Eulerian-mean velocity.

Mesoscale eddies act to mix fluid parcels in a way that is highly constrained by the stratified nature of the fluid. The residual-mean theory provides the link between the different views that are apparent from averaging these turbulent flow fields in height coordinates and in density coordinates. It reduces the parameterization problem from three dimensions to two dimensions and it shows how the eddy fluxes are skew-symmetric in height coordinates so that the total advection velocity can be adiabatic. While mesoscale eddies cause a very significant southward flux of heat in the Southern Ocean, should this flux be regarded as a mixing or a stirring of heat? To the extent that there are balancing gradients of potential temperature and salinity along isopycnals, this component of the heat flux will eventually lead to mixing of heat at the very smallest scales of motion and hence we might call this aspect of the mesoscale heat flux 'mixing'. The rest of the heat flux that is observed in Cartesian coordinates does not appear as a heat flux in density coordinates, but rather is associated with an extra horizontal velocity that advects all fluid properties along isopycnals. This part of the mesoscale eddy heat flux might more properly be labelled 'stirring'.

To understand how an eddy flux in Cartesian coordinates might induce an extra fluid velocity, we appeal to residual-mean flow theory, which was originally developed in the atmospheric literature where the averaging operator was a zonal average. In developing the three-dimensional residual-mean theory it is convenient to first deal with the density conservation equation and to ignore any non-linearity in the equation of state. The Eulerian-mean density conservation equation reads (the overbar operator describes a low-pass temporal average)

$$\bar{\gamma}_t + \nabla_H \cdot (\bar{V} \bar{\gamma}) + (\bar{w} \bar{\gamma})_z = \bar{Q} - \nabla_H \cdot (\bar{V}' \bar{\gamma}') - (\bar{w}' \bar{\gamma}')_z \quad (5.2.1)$$

where Q is the instantaneous diapycnal source term and γ is a form of density that excludes the

effects of the compressible nature of seawater. Our quest is to gain an understanding of the three-dimensional turbulent density flux and its divergence that appears in this equation. Less than a decade ago it was commonplace in ocean modelling to assume that the horizontal density flux, $\bar{V}' \bar{\gamma}'$, could be parameterized as a down-gradient Fickian flux, while the vertical turbulent density flux was ignored except for the part attributed to small-scale diapycnal mixing. This exactly horizontal mixing led to fictitious diapycnal fluxes of density (the Veronis effect) and caused serious problems such as spurious vertical motion in western boundary currents. The temporal-residual-mean theory demonstrated the inadequacy of this prior approach and provided a route forward that avoided such fictitious diapycnal density fluxes.

In order to develop a residual-mean conservation equation for, say, density, we need to realize that the Eulerian-mean density is not the most appropriate mean density to appear in the mean density conservation equation that is carried by an ocean model. The Eulerian-mean density, $\bar{\gamma}(x, y, z, t)$, describes a density surface whose average height is not that of the original Eulerian averaging, namely z . The appropriate mean density for our purposes is the one whose surface is, on average, at the height of the averaging. This density can be expressed in terms of $\bar{\gamma}$ by $\tilde{\gamma} = \bar{\gamma} - (\bar{\phi}/\bar{\gamma}_z)_z + O(\alpha^3)$, where $\bar{\phi} = \frac{1}{2}\bar{\gamma}'^2$, is half the density variance measured at a fixed point in space and the terminology $O(\alpha^3)$ indicates terms that are of cubic or higher order in perturbation amplitude.

McDougall and McIntosh (2000) rewrote the mean density conservation equation (5.2.1), in terms of the modified mean density, $\tilde{\gamma}$, as

$$\begin{aligned} \tilde{\gamma}_t + \nabla_H \cdot (\bar{V} \tilde{\gamma}) + (\bar{w} \tilde{\gamma})_z \\ = \bar{Q}^{\#} - \nabla \cdot F^M + O(\alpha^3) \end{aligned} \quad (5.2.2)$$

and showed that the modified density flux, F^M can be expressed as

$$\begin{aligned} F^M = \tilde{\gamma} U^+ + M + O(\alpha^3) \\ = -A \nabla \tilde{\gamma} + N + O(\alpha^3) \end{aligned} \quad (5.2.3)$$

where M and N are both non-divergent density fluxes and the antisymmetric matrix A (see McDougall, 1998) is defined in terms of the two components of the quasi-Stokes streamfunction,

$\Psi = (\Psi^x, \Psi^y)$, which is expressed in terms of velocity and density perturbations at fixed height by

$$\Psi \equiv -\frac{\bar{V}'\bar{\gamma}'}{\bar{\gamma}_z} + \frac{\bar{V}_z}{\bar{\gamma}_z} \left(\frac{\bar{\phi}}{\bar{\gamma}_z} \right) + O(\alpha^3) \quad (5.2.4)$$

This quasi-Stokes streamfunction is the two dimensional streamfunction for an extra three-dimensional velocity, $\mathbf{U}^+ \equiv \nabla \times (\Psi \times \mathbf{k}) = \Psi_z - \mathbf{k}(\nabla_H \cdot \Psi)$. The mean density conservation equation, (5.2.2), can also be written in the form

$$\bar{\gamma}_t + \nabla \cdot (\bar{U}^\# \bar{\gamma}) = \bar{Q}^\# + O(\alpha^3) \quad (5.2.5)$$

where the total advection velocity is $\bar{U}^\# \equiv \bar{U} + \mathbf{U}^+$, and the modified diapycnal source term in (5.2.2) and (5.2.5) is

$$\bar{Q}^\# \equiv \bar{Q} + \left[-\frac{\bar{Q}'\bar{\gamma}'}{\bar{\gamma}_z} + \frac{\bar{Q}_z}{\bar{\gamma}_z} \left(\frac{\bar{\phi}}{\bar{\gamma}_z} \right) \right]_z \quad (5.2.6)$$

The essential feature of this Temporal-Residual-Mean (TRM) approach to the density equation is that it shows that the relevant three-dimensional density flux, namely the modified density flux, \mathbf{F}^M , can be decomposed into a non-divergent flux and a flux that is directed along the density surfaces, $-\mathbf{A}\nabla\bar{\gamma}$. Moreover, this skew flux can be represented in the conservation equation as an extra advecting velocity (together with a different non-divergent flux). It can be shown that this same extra advecting velocity is at work in the passive tracer equation, and that there is a flux of tracer along isopycnals due to the symmetric part of the diffusion tensor.

In the original Reynolds-averaged mean density equation, equation (5.2.1), the task of parameterizing the eddy density flux is daunting and has never been done successfully because each of the three components of the eddy flux, $\bar{U}'\bar{\gamma}'$, needs to be parameterized. We have little or no intuition about how much of this flux should be divergent, how much should be diapycnal, or what form the non-gradient terms might take. The TRM approach has greatly simplified the parameterization task because rather than having to parameterize the three-dimensional eddy density flux, all one needs to parameterize is the two-dimensional quasi-Stokes streamfunction, given in equation (5.2.4).

Another achievement of TRM theory (and equally of the Gent and McWilliams, 1990, eddy-parameterization scheme) is that even if the parameterization of Ψ is imperfect, because the

parameterized term enters the density conservation equation as a skew flux that is equivalent to an extra advection of density, the total velocity, the TRM velocity, $\bar{U}^\# \equiv \bar{U} + \Psi_z - \mathbf{k}(\nabla_H \cdot \Psi)$, will have a diapycnal component only if the diabatic source term, $\bar{Q}^\#$, is non-zero (see equation (5.2.5)). That is, uncertainty in the parameterization of the quasi-Stokes streamfunction will not cause spurious changes in water masses. This is in direct contrast to the fictitious density fluxes that arise when the mesoscale eddy mixing is parameterized as being down the horizontal density gradient. These fictitious density fluxes caused unwanted water mass conversion.

With errors that are cubic in perturbation quantities, it is possible to show that the TRM approach of forming averaged quantities for use in height coordinates corresponds to averaging temporally the instantaneous conservation equations in density coordinates. The quasi-Stokes streamfunction, Ψ , defined by equation (5.2.4), is the contribution of perturbations to the horizontal transport of fluid that is denser than $\bar{\gamma}(z)$, the density of the density surface whose average height is z . It is this horizontal transport of fluid that must be added to the volume transport found by using the Eulerian-averaged velocity in order to represent correctly the transport of water of each density class.

This physical interpretation of the quasi-Stokes streamfunction provides guidance on the boundary conditions that should be imposed at the top and bottom of the ocean. Figure 5.2.1 displays the temporal variations in the heights of three different $\bar{\gamma}$ surfaces (panels (a) to (c)) when the ocean's density field displays harmonic temporal variations. Any density surface that is less dense than any in the ocean at a particular time is assumed to reside at the sea surface. The modified density, $\bar{\gamma}$, appropriate to each height has the property (by definition) that the height of this $\bar{\gamma}$ surface averages to zero, as is indicated by the shading in Figure 5.2.1 (the shaded area appearing below the mean height is equal to the shaded area above the mean height). As the sea surface (or the ocean floor) is approached, the shaded area reduces to zero and so the correlation of velocity and thickness in this shaded region must also tend to zero. That is, the contribution of eddies to the transport of water that is more dense than $\bar{\gamma}$ reduces to zero as the sea surface (or ocean floor) is approached.

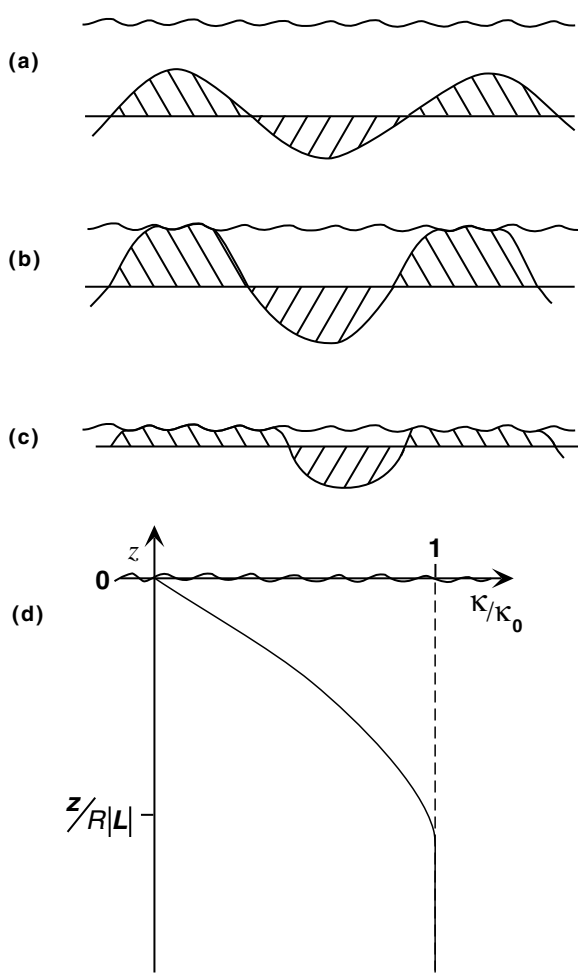


Fig. 5.2.1 Sketch of the temporal variation of the heights of three different density surfaces as the sea surface is approached. Panel (d) sketches the implication for the vertical tapering of the diffusivity. Here R is the Rossby radius and $|L|$ is the magnitude of the slope of a density surface. Further details can be found in McDougall (1998).

By definition, this transport is the quasi-Stokes streamfunction and so it must approach zero smoothly at the top and bottom boundary, even when the bottom boundary is sloped. Note that this behaviour is in contrast to the theory of Killworth (1997), which has delta functions of transport against the top and bottom oceanic boundaries. We believe that the physical interpretation of the quasi-Stokes streamfunction, and the interpretation of the density of a coarse-resolution model as being the modified density, $\tilde{\gamma}$, precludes these delta functions.

A Taylor series approach also shows that the thickness-weighted horizontal velocity, \hat{V} , obtained

by averaging V between a pair of closely spaced $\tilde{\gamma}$ surfaces is

$$\begin{aligned}\hat{V} &\equiv \tilde{V} + V^B = \bar{V} + \Psi_z + O(\alpha^3) \\ &= \bar{V}^{\#} + O(\alpha^3)\end{aligned}\quad (5.2.7)$$

where \tilde{V} is the value averaged on the density surface (that is, \tilde{V} is not thickness-weighted) and $V^B = \bar{V}'|_{\tilde{\gamma}} z'_z$ is the horizontal bolus velocity due to the correlation between the horizontal velocity perturbations evaluated on the density surface and the perturbations of the thickness between density surfaces. Hence the thickness-weighted horizontal velocity, \hat{V} , obtained by averaging in density coordinates, is equal to the horizontal TRM velocity, $\bar{V}^{\#}$, up to error terms of cubic order in perturbation quantities.

In a similar fashion, it can be shown that the modified diapycnal source term, $\bar{Q}^{\#}$, given by equation (5.2.6), is equal to the thickness-weighted source term that is obtained by averaging Q between a pair of closely spaced $\tilde{\gamma}$ surfaces. To date, $\bar{Q}^{\#}$ has been parameterized using the small values of the diapycnal diffusivity that are observed in the thermocline (see below). As Tandon and Garrett (1996) have pointed out, this implies that the eddy kinetic energy of mesoscale eddies cannot be dissipated in the ocean interior but rather must be dissipated near the upper and/or lower boundaries.

When the tracer equations are examined in the light of this TRM approach one finds that there is only one interpretation for the tracers that are carried by eddyless coarse-resolution models: they are the thickness-weighted mean tracer values that would be found by averaging the tracer between density surfaces. This dictates the way in which ocean observations should be compared with the output of coarse-resolution ocean models and also the way in which ocean observations should be averaged before performing inverse calculations.

Ocean GCM (General Circulation Model) simulations using the Gent and McWilliams (1990) scheme have found large diapycnal transports in the Southern Ocean for both the Eulerian-mean flow and the quasi-Stokes circulation. Hirst and McDougall (1998) specifically plotted the zonally averaged streamfunctions of both the Eulerian-mean flow and the quasi-Stokes flow in density coordinates to illustrate the diapycnal nature of both circulations (their Fig. 6). They found about

14 Sv of zonally averaged diapycnal transport in the Southern Ocean in both the Eulerian-mean and the quasi-Stokes circulations. The Gent and McWilliams (1990) scheme is often described as being a parameterization of ‘bolus transport’, but this is not the case since, by definition, the bolus transport occurs along isopycnals and has no diapycnal component. There is another compelling reason why the eddy-induced velocity of Gent *et al.* (1995) is not the down-gradient thickness flux or bolus velocity: namely that the quasi-Stokes velocity is three-dimensionally non-divergent whereas the bolus velocity is three-dimensionally divergent (McDougall and McIntosh, 2000). Rather, the Gent *et al.* (1995) scheme is the community’s first attempt at parameterizing the quasi-Stokes streamfunction of the TRM theory.

Under the assumption that the horizontal flux of density is directed down the horizontal density gradient, the quasi-Stokes streamfunction, equation (5.2.4), of the TRM theory is virtually the same as is used in the Gent *et al.* (1995) scheme. While this down-gradient assumption on density is a common assumption, several authors have recently made the point that there may be better theoretical support for the flux of potential vorticity along neutral density surfaces being directed down the epineutral gradient of potential vorticity. This naturally leads to a parameterization for the bolus velocity and then one has to address the questions of applying boundary conditions at the top and bottom of the ocean and of avoiding a singularity at the equator. The theory of Killworth (1997) and other parameterization schemes based on the down-epineutral-gradient of potential vorticity are, by construction, applicable to the parameterization of eddies in eddyless, density-coordinate models. In such density-coordinate models, the additional velocity that is required is the bolus velocity and this velocity is three-dimensionally divergent and adiabatic. It is not obvious *a priori* that such a parameterization scheme should be applied to a z -coordinate model where the use of the continuity equation ensures that whatever choice is made for its horizontal components, the extra velocity is three-dimensionally non-divergent and, most importantly, diabatic at leading order. The down-gradient potential vorticity parameterization can also lead to a fictitious torque that spontaneously generates angular momentum (Cummins, 2000). In any event, this chapter does

not address in detail the various options that have been proposed for parameterizing the quasi-Stokes streamfunction, but instead we have concentrated on describing the theoretical framework in which such a parameterization will be used.

Treguier (1998) has analysed a high-resolution primitive equation model for the zonally averaged bolus velocity and has found a small diffusivity for use in the Gent *et al.* (1995) scheme (the quasi-Stokes diffusivity). If it can be shown that it is appropriate to use such a small diffusivity for the quasi-Stokes streamfunction, then this should have some benefits so long as the models remain stable with these smaller diffusivities. The two benefits that come to mind are avoiding the slowing of the horizontal circulation of the subtropical gyres that occurs with the larger values of the quasi-Stokes diffusivity, and reducing the intrusion of Antarctic Bottom Water into the North Atlantic, which is too strong with present values of the quasi-Stokes diffusivity (Hirst and McDougall, 1998).

At the large horizontal scales appropriate to global circulation problems, the TRM flow can be parameterized independently of the interaction of the flow with bottom topography as described by, for example, Holloway’s (1997) Neptune Effect. This is because at these scales the Neptune Effect forces a barotropic flow whereas the quasi-Stokes circulation of the TRM theory is baroclinic, having no depth-averaged component at each location. There is also the interesting issue of whether the present implementation of the TRM circulation in ocean models is displaying improvements for the correct reasons. Several authors have described substantial improvements including more realistic deep water properties, less unwanted deep convection and less drift in coupled atmosphere–ocean models (see Hirst *et al.*, 1996). An important common element of these improvements is that the Bottom Water of the world’s oceans has been able to sink from the surface to the ocean bottom with very little dilution. In fact, in the work of Hirst and McDougall (1996) it was found that there was insufficient diapycnal mixing occurring in the overflow regions. Previously such a result had only been possible using a density-coordinate model. In this way, a coarse-resolution height-coordinate model has been shown to be sufficiently ‘adiabatic’ for the purposes of climate modelling.

In practice, the sinking of Deep and Bottom Water frequently occurs in continental slope

canyons and across sills, bathymetric features not well represented in coarse-resolution models. The TRM advection scheme achieves this ‘adiabatic’ sinking motion because of two almost equal effects, as demonstrated by Hirst and McDougall (1996). First, the unwanted horizontal diffusion is eliminated, and second, an extra advection (or skew diffusion) is added that assists in the transport of water from the surface to the deep. The elimination of horizontal diffusion is thought to be physically required, but the extra advection at the bottom of the ocean seems to be more an artefact of the bottom boundary condition on the quasi-Stokes streamfunction than a representation of the actual boundary-current mechanisms that achieve the transport of bottom water. In this way it may be that half of the benefits that we are seeing to date have been obtained by stealth: obtaining the right results for the wrong reasons. It is not at all clear that such cancellation of error will hold for circulations in alternate climate states as, for example, might result from global warming.

We concentrated here on the density equation with the implicit assumption that the Eulerian-mean velocity is available as model output of the momentum equations. This is usually a good assumption because of the dominance of the geostrophic balance at the large scales relevant to the global ocean circulation. There is, however, an alternative way of implementing a TRM parameterization: one can apply the TRM averaging approach to the horizontal momentum equations, thereby obtaining a forcing term on the right of these equations that looks somewhat similar to the Eliassen–Palm flux of the zonal-averaging literature. The key result of that literature is that while the Eliassen–Palm flux is of second order in perturbation quantities, its divergence is one order higher and so can often be ignored, or at least assumed to be equal to the northward flux of potential vorticity. No such result has been proven for the three-dimensional problem under temporal or ensemble averaging. Indeed, it seems very likely that the divergence of this flux is still of second order in perturbation quantities. Nevertheless, if one boldly assumes this result by a crude analogy with the zonal averaging literature, the parameterization would effectively be a form drag in the horizontal momentum equations and the tracer equations would not need any extra skew flux term. The results of this approach are expected to be very similar to the more

conventional method of implementing the TRM scheme in the tracer equations.

In summary, the TRM approach tells us how we should interpret the variables that are carried in an eddyless ocean model, it reduces the eddy-parameterization task from a three-dimensional to a two-dimensional task, and it provides physical insight that dictates that the quasi-Stokes streamfunction should be smoothly tapered to zero as the sea surface and the ocean floor are approached. The parameterization task is now quite specific: we must learn how to parameterize the quasi-Stokes streamfunction, equation (5.2.4), and we now know that this is not the same as parameterizing the bolus velocity. If we are successful in parameterizing equation (5.2.4) we will be able to run an eddyless height-coordinate model knowing that it is equivalent to first running a density-coordinate model at high resolution and then averaging over the mesoscale eddies.

5.2.4 Lateral dispersion between the mesoscale and the microscale

Eddy motions also strain passive tracers on isopycnals, cascading variance towards smaller spatial scales where it is eventually dissipated by molecular diffusion. Recent studies are beginning to illuminate the connections between the mesoscale and microscale. Ledwell *et al.* (1998) inferred lateral diffusivities as a function of spatial scale from the lateral spread of the WOCE North Atlantic Tracer Release Experiment (NATRE) tracer patch with time. Initially, when the bands of SF₆ had horizontal scales of 100–1000 m, the tracer appeared to spread with a lateral diffusivity of $\sim 0.07 \text{ m}^2 \text{ s}^{-1}$. This rate is consistent with shear dispersion due to near-inertial internal waves (Young *et al.*, 1982). After about 6 months, the tracer had been drawn into much longer streaks with horizontal widths of 1–30 km. The width-to-length ratio of the streaks suggested lateral diffusion on these scales was $\sim 2 \text{ m}^2 \text{ s}^{-1}$, far stronger than can be accounted for by internal wave shear dispersion (Sundermeyer and Price, 1998). Polzin *et al.* (2000b) proposed that vortical mode motions (fine-scale structures with non-zero Ertel potential vorticity) might be responsible for the dispersion on these scales. For the period when the tracer patch was 30–300 km in width and thus had comparable size to individual mesoscale eddies, Ledwell *et al.* felt an eddy

parameterization of dispersion was inappropriate. Eventually though, as the patch broadened still further to scales of 300–1000 km, expression of dispersion in terms of an apparent eddy diffusivity was again deemed sensible, and Ledwell *et al.* estimated a zonal diffusivity of 2300 (1000–4000) $\text{m}^2 \text{s}^{-1}$ and a meridional diffusivity of 650 (200–1200) $\text{m}^2 \text{s}^{-1}$. This N–S/E–W difference may reflect strain by the mean anticyclonic gyre flow and/or manifestation of the planetary potential vorticity gradient restricting meridional dispersion (e.g. Bartello and Holloway, 1991).

For completeness, we also note a special form of lateral diffusion possible at water mass fronts: thermohaline intrusions. Joyce (1977) discussed how interleaving of water masses at fronts can greatly increase the surface area and property gradients between waters and thus enhance lateral mixing (a form of shear dispersion; Taylor, 1953). In addition to turbulent mixing acting on the enhanced gradients that result from vertical interleaving, intrusions also support double diffusion. The vertical fluxes resulting from the latter may create horizontal pressure gradients that drive intrusions across fronts (Stern, 1967; Toole and Georgi, 1981; McDougall, 1985a,b), giving rise to epipygcnal as well as diapycnal property fluxes. Armi *et al.* (1989) discussed a beautiful ‘natural laboratory’ study of thermohaline intrusive mixing in which the decay of a Mediterranean water lens was followed over 2 years. During this period, intrusions advanced from the periphery of the lens towards its centre at a rate of about 30 km yr^{-1} , eventually reaching the core. Ruddick and Hebert (1988) went on to infer a horizontal diffusivity for salt due to the intrusive motions of $0.4 \text{ m}^2 \text{s}^{-1}$, nearly as large as what Ledwell *et al.* derived at their 6-month point in NATRE.

5.2.5 Diapycnal mixing in and above the main thermocline

5.2.5.1 Ocean interior

Ocean microstructure studies conducted over the past 30 years, chiefly sampling the main thermoclines of the North Atlantic and Pacific Oceans, routinely returned scalar diapycnal diffusivity estimates that were of order $10^{-5} \text{ m}^2 \text{s}^{-1}$ (Fig. 5.2.2) (see also Gregg, 1987, 1998; Gargett, 1989; Toole *et al.*, 1994; Caldwell and Moum, 1995). The bulk of these studies inferred diapycnal fluxes through

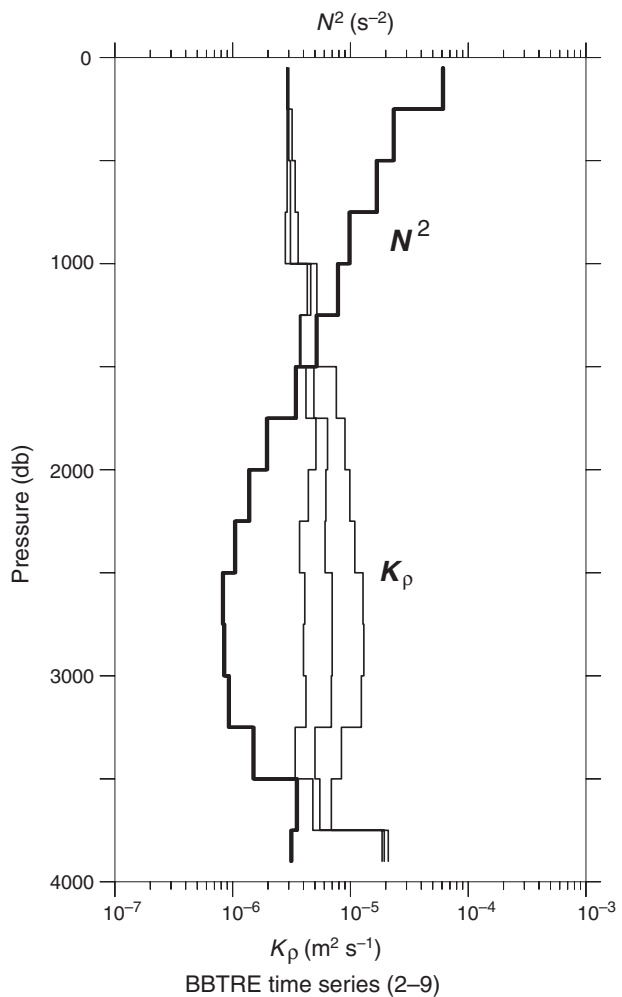


Fig. 5.2.2 Estimates of diapycnal eddy diffusivity (K_p) derived from velocity microstructure data using the expression of Osborn (1980), and the squared buoyancy frequency N^2 . The data shown represent an average of eight profiles made on the South American continental slope in the eastern Brazil Basin. Assumed dissipation noise levels of $(3, 2, 0) \times 10^{-10} \text{ W kg}^{-1}$ were subtracted from the observations resulting in the three K_p curves shown. Statistical uncertainty in the diffusivity values are less than ± 2 times the given values (95% confidence interval). Diffusivity values of order $10^{-5} \text{ m}^2 \text{s}^{-1}$, as found at this site, are characteristic of ocean regions with background-intensity internal waves.

models of the turbulent kinetic energy (Osborn, 1980) and temperature variance (Osborn and Cox, 1972) budgets that assume statistical balance between turbulent production and dissipation. The seeming discrepancy between these microstructure-based diffusivity estimates for the main thermocline and the inferred values reviewed in Section 5.2.2 (largely derived for the abyssal ocean) caused

some to question the Osborn–Cox and Osborn interpretation of ocean observations (e.g. Gibson, 1982; Baker and Gibson, 1987). But, as discussed below, recent microstructure studies that sampled the abyssal ocean found significant mixing there. Moreover, weak diapycnal mixing at thermocline depth in the ocean interior was confirmed during the WOCE programme by Ledwell *et al.*'s (1993, 1998) North Atlantic Tracer Release Experiment. NATRE focused on diapycnal dispersion across a density surface at about 300 m depth in the eastern subtropical Atlantic, an environment characterized by a near-climatological (see below) internal wave field (Duda and Jacobs, 1995). Ledwell and colleagues fitted simple models to the tracer distribution evolution with time (Fig. 5.2.3) to estimate a time-mean diapycnal diffusivity of

$0.12 \pm 0.02 \times 10^{-4} \text{ m}^2 \text{ s}^{-1}$ for the first 6 months of the experiment and $0.17 \pm 0.02 \times 10^{-4} \text{ m}^2 \text{ s}^{-1}$ for the following 24 months. Temperature and velocity microstructure measurements taken in the vicinity of the tracer cloud (but over a far more limited time interval) implied comparable magnitude (but slightly smaller) diffusivity values (Sherman and Davis, 1995; Ruddick *et al.*, 1997; St Laurent and Schmitt, 1999).

Mixing in the ocean interior is often the result of internal wave superpositions leading to intermittent episodes of shear and/or advective instability (e.g. Thorpe, 1978, 1979; Munk, 1981; Kunze *et al.*, 1990). Gradient Richardson numbers for major ocean currents like the Gulf Stream are invariably subcritical (i.e. larger than 1/4, the chief exceptions to this being the equatorial undercurrents and

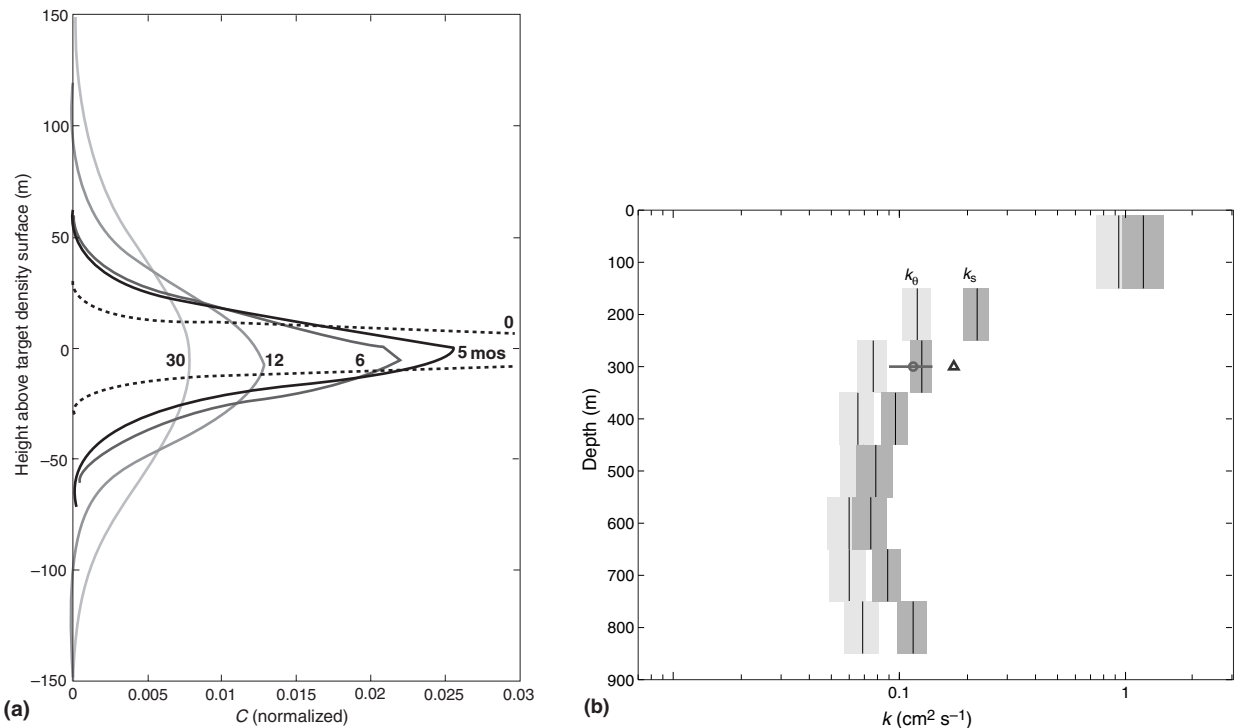


Fig. 5.2.3 The diapycnal dispersion of the inert tracer SF_6 with time during the North Atlantic Tracer Release Experiment (Ledwell *et al.*, 1993, 1998). In panel (a), normalized tracer concentration data sampled at various times (in months) after injection and averaged laterally on isopycnals are displayed relative to the mean density profile of the study region along with the estimated initial condition (dotted line). This figure is reprinted from Watson and Ledwell (2000). Fits of these profiles to a one-dimensional advection/diffusion model yielded estimates of diapycnal diffusivity. The diffusivity deduced for the first 6 months of the experiment was $0.12 \pm 0.02 \times 10^{-4} \text{ m}^2 \text{ s}^{-1}$, increasing to $0.17 \pm 0.02 \times 10^{-4} \text{ m}^2 \text{ s}^{-1}$ for the remainder of the experiment. Panel (b) reprints St Laurent and Schmitt's (1999) profiles of effective diffusivity for temperature and salinity based on velocity and temperature microstructure measurements, fine-scale Richardson number and density ratio estimates, and a model of salt-finger fluxes. Their estimates are reported in a series of depth bins with statistical uncertainties based on the observed sampling distributions. The data supporting these diffusivity estimates were collected in the month prior to the tracer release. Ledwell *et al.*'s diffusivity estimates for the two time periods noted above are also displayed.

marginal sea overflows: see below). Knowledge of mixing in the ocean interior is thus intimately linked to an understanding of the flow field associated with internal waves. In the 1970s, a spectral model of the canonical internal wave field was developed by Garrett and Munk (1972a, commonly referred to as the GM prescription). With updates (Garrett and Munk, 1975; Cairns and Williams, 1976; Gregg and Kunze, 1991), this model remains a valid baseline description of the climatological wave field. One of the first applications of GM was a statistical prediction for the amount of mixing supported by shear instability within the wave field (Garrett and Munk, 1972b). Pinkel and Anderson (1997a,b) recently revisited this topic with application to the upper ocean. Wave-wave interaction models were subsequently developed to build dynamical understanding of the observed internal wave spectrum (McComas and Bretherton, 1977; McComas and Müller, 1981; Henyey and Pompfrey, 1983; Müller *et al.*, 1986). These also led to estimates of the turbulent mixing rate in terms of the rate at which energy in the internal wave field moves through wavenumber space towards vertical scales of order 10 m (where shear and advective instabilities are presumably active and the energy is ultimately dissipated). With statements about the mixing efficiency (Γ), these models yield predictions for the turbulent buoyancy flux, ($\Gamma \varepsilon$), associated with a given internal wave field, or if preferred, the diapycnal eddy diffusivity: $K_p = \Gamma \varepsilon N^{-2}$. (Here, ε is the dissipation rate of turbulent kinetic energy per unit mass.) Polzin *et al.* (1995) investigated several of the wave-wave interaction models and found that Henyey *et al.*'s (1986) predictions had greatest consistency with observed dissipation rates, as was previously observed by Gregg (1989), although the robustness of this model derivation can be debated (in particular, the heavy reliance on interactions between motions of similar scale that violates basic model assumption: C. Garrett, personal communication, 1999). Importantly, the Henyey *et al.* model suggests a small diffusivity associated with the canonical GM wave field: $K_p^{\text{GM}} = 7 \times 10^{-6} \text{ m}^2 \text{ s}^{-1}$, independent of depth and stratification (as suggested by Figure 5.2.2).

The somewhat greater diapycnal dispersion of the NATRE tracer as compared with the temperature- and velocity-microstructure-based estimates appears to be due to an additional mixing

mechanism: double diffusion. Ruddick *et al.* (1997) and St Laurent and Schmitt (1999) found evidence of salt fingering in the relative sizes of the turbulent kinetic energy and thermal dissipation rate estimates, most notable when the latter investigators conditionally sampled for low density ratio and high Richardson number. Based on data collected in the month prior to the tracer injection and using a salt-finger flux model together with an estimate of the turbulent mixing that was occurring, St Laurent and Schmitt derived an average effective salt diffusivity of $0.13 \pm 0.01 \times 10^{-4} \text{ m}^2 \text{ s}^{-1}$ at the isopycnal where the tracer was injected (Fig. 5.2.3b). Their estimate is consistent with the diapycnal diffusivity deduced from the tracer dispersion during the first 6 months of Ledwell *et al.*'s experiment. (SF_6 should mix in a similar fashion as salt in this ocean environment.) Additionally, their estimate of the diapycnal buoyancy flux convergence caused by salt fingers and the occasional turbulent mixing event was consistent with Ledwell *et al.*'s observation that the tracer sank relative to the density field over the course of the experiment.

The intensity of double-diffusive mixing is a strong function of the density ratio. Although the salt-finger fluxes were relatively weak in the NATRE region where the density ratio approached 1.6, there are extensive ocean regions characterized by ratios closer to 1.0 (Schmitt, 1981). Here we might expect average diapycnal fluxes to exceed those associated with the background GM internal wave field, with the added complication that the effective heat and salt diffusivities may differ substantially. Using laboratory-based flux laws and measurements in the salt-fingering-favourable thermohaline staircase southeast of Barbados in the tropical Atlantic Ocean, Schmitt (1988) and Kunze (1990) estimated the vertical diffusivity for salt to be $1-2 \times 10^{-4} \text{ m}^2 \text{ s}^{-1}$. As the staircase region encompasses approximately one-quarter of the area of the Atlantic between 10 and 15°N, salt fingering may dominate the diapycnal salt flux at these latitudes (Schmitt, 1998). Fingering may also be important for removing mixed-layer density-compensated thermohaline variability soon after subduction (Rudnick and Ferrari, 1999; Schmitt, 1999). At high latitudes, the characteristic thermohaline stratification of cold, fresh above warmer, more saline waters supports the diffusive layering mode of double diffusion (e.g. Padman

and Dillon, 1987; Muench *et al.*, 1990). Microstructure measurements (e.g. Larson and Gregg, 1983; Osborn, 1988; Padman and Dillon, 1987) have lent credence to laboratory-derived laws for fluxes through the diffusive interfaces characteristic of this instability. Kelley (1984, 1990) in turn derived expressions for the effective diapycnal heat and salt diffusivities by this double-diffusive process that approach $10^{-4} \text{ m}^2 \text{ s}^{-1}$ as the density ratio approaches 1.0. Thus far unclear are the potential interactions between diffusive layers, internal waves, shear and turbulence.

More intense mixing also appears to occur in ocean regions characterized by an energized internal wave field (more energetic than the GM background). The Henyey *et al.* (1986) model suggests that the energy flux through the wave field (and thus the dissipation rate) increases quadratically with the fine-scale shear spectral level of the internal waves (equivalently as the fourth power of the fine-scale velocity gradient in the spatial domain; Gregg, 1989). A weak dependence on the frequency content of the wave field is also suggested (Henyey, 1991; Polzin *et al.*, 1995). Thus, to identify areas of enhanced mixing in the ocean interior one might equivalently search for regions of energetic internal waves. These might include sites of internal wave generation, and/or distortion by, for example, bottom reflection or the effects of larger-scale flows. More on these below.

5.2.5.2 Role of ocean currents

In addition to the shears associated with the ubiquitous internal waves, there are a handful of open-ocean current systems that develop internal instabilities leading to turbulent mixing. Most notable in this regard are the Equatorial Undercurrent–South Equatorial Current (EUC/SEC) systems of the tropical Pacific and Atlantic Oceans. Frictional damping and diapycnal heat and buoyancy fluxes are believed to be of first order importance in the momentum budget of these currents and the heat budget of the equatorial waters, respectively. A series of cruises to the equatorial Pacific conducted in the 1980s examined the turbulence in this low-latitude environment (e.g. Gregg *et al.*, 1985; Moum *et al.*, 1989; Lien *et al.*, 1995). These studies report intense turbulent dissipation above the undercurrent core, diurnally modulated with the cycle of air–sea buoyancy exchange. The causal agent responsible for the diurnal signal in mixing

below the surface layer appears to be high-frequency internal waves that radiate down from the surface layer (see Wang *et al.*, 1998; Wang and Muller, 1999). On longer time scales, these research teams found mixing in the EUC varies with the strength of the wind stress and the ambient shear between the SEC and EUC. Averaging over the diurnal and longer-period fluctuations, mean diapycnal diffusivities in excess of $10^{-3} \text{ m}^2 \text{ s}^{-1}$ were obtained. Mean eddy viscosities also estimated in the EUC/SEC shear flow were comparably large.

At greater depths, remarkable arrays of zonal jets about the equator have been observed in all three oceans (Luyten and Swallow, 1976; Firing, 1987, 1988; Ponte *et al.*, 1990). These flows have been interpreted as long-period, high-mode, equatorially trapped planetary waves (see Muench *et al.*, 1994). Superimposed on these ‘equatorial deep jets’ is a spectrum of Kelvin, Rossby, mixed Rossby–gravity and inertial gravity waves down to periods of a few days, melding with an internal wave field of approximate GM shape but enhanced energy (Eriksen, 1980, 1981; Blumenthal, 1987; Gregg *et al.*, 1995). Of relevance to our discussion, Pacific and Atlantic microstructure data from the equator appears to be modulated by the vertical shears associated with the equatorial deep jets (Gregg *et al.*, 1995; K. Polzin, personal communication, 1999). But the long jet time scales imply that the turbulence does not erode them. These findings motivated Muench and Kunze (1999) to investigate wave-mean flow interaction wherein the jets might be sustained by transfer of energy from the internal wave field at critical layers. Their model predicts peak dissipation rates on the jet flanks of comparable magnitude to what is observed and significant momentum flux divergences of the sense to sustain jets (though the study begs the question of the jets’ origin). The peak dissipations at the jet flanks are not excessively large however, corresponding to diapycnal diffusivities around $10^{-4} \text{ m}^2 \text{ s}^{-1}$, with values about the jet cores typically an order of magnitude smaller. The lower-thermocline tropical waters are thus characterized by somewhat enhanced diapycnal exchange as compared with mid-latitudes, largely due to the equatorial deep jets. (On its own, the equatorial internal wave field, though more energetic than GM, does not seem to equate with enhanced mixing, leading Gregg *et al.* (1995)

to suggest that wave–wave interactions were weaker at low relative to mid-latitudes.)

In contrast, the Gulf Stream, one of the most significant ocean currents on the globe, does not appear to support significant turbulent diapycnal mixing. Gregg and Sanford (1980) and Osborn (1980) inferred diffusivity values from microstructure profiles in the Stream that average much less than $10^{-4} \text{ m}^2 \text{ s}^{-1}$. And Winkel *et al.* (1992) report an average diffusivity value of $4.1 \times 10^{-5} \text{ m}^2 \text{ s}^{-1}$ across the Florida Current outside the 10- to 50-m-thick surface and bottom boundary layers. One attribute of these large-scale currents that is thought important to mixing is their horizontal shear. Ocean areas characterized by negative relative vorticity are often sites of enhanced internal wave energy density. As discussed by Kunze (1985) and Kunze and Boss (1998), low-frequency internal waves sense an effective inertial period that depends on the relative vorticity of the large-scale flow in which they are imbedded. Flows with negative relative vorticity are capable of forming wave-trapping zones in the horizontal and critical layers in the vertical. At the latter, wave energy accumulates and eventually dissipates. Kunze *et al.* (1995) and Kunze and Toole (1997) offer examples of this process within a warm core ring of the Gulf Stream and within a rectified anticyclonic flow atop a mid-latitude seamount, respectively. In the latter case, the diapycnal buoyancy flux above the seamount was some 200 times that of the background interior value (on a per unit area basis). But this enhanced mixing above the seamount may be due as much to the abrupt bathymetry being a strong source of internal wave energy (see below) as to the over-lying vortex that traps that energy.

5.2.5.3 Near-bottom mixing

Isopycnals characteristically found in the main thermocline of the ocean interior approach, and commonly intersect, the bottom over the continental slopes and shelves, mid-ocean ridges and seamounts. In those regions where the bottom doesn't slope too steeply, a (virtually) homogeneous layer some 10 or (sometimes many) more metres thick is often observed: the bottom boundary layer (e.g. Caldwell, 1976; Lentz and Trowbridge, 1991). These layers are sometimes believed to be the manifestation of turbulent mixing driven by bottom stresses associated with the overlying flow,

but exceptional levels of turbulent kinetic energy dissipation don't always span the depth of the homogeneous layers. This is, consequently, a rather inefficient mixing mechanism as the bulk of the turbulence lies in previously mixed water (see discussions by Armi, 1978, 1979 and Garrett, 1979, 1991). Indeed, thick bottom-layer formation can also be the result of lateral convergence in the boundary layer flow and involve little or no mixing.

Breaking of boundary-reflected internal waves in the stratified water column above the bottom layer is believed to be a far more efficient mixing mechanism. Linear bottom-reflection kinematics for sloping bathymetry predicts a range of incident waves that reflect with smaller vertical scale and greater energy density (Phillips, 1977; Eriksen, 1982). The effect is greatest about the critical wave frequency: $\omega_c = [N^2 \sin^2(\alpha) + f^2 \cos^2(\alpha)]^{1/2}$, where α is the angle of the bottom from horizontal. Incident waves at this frequency reflect with a group velocity vector parallel to the bottom (and so are not able to carry energy away from the slope. Linear theory in fact breaks down at this point.) It is surmised that subsequent breaking of the reflected waves may in turn support enhanced turbulent mixing above slopes (Eriksen, 1985; Garrett and Gilbert, 1988; Slinn and Riley, 1999), although destructive interference of bottom-reflected waves above concave bathymetry and generation of along-isobath mean flows may limit or distort the effect (Gilbert and Garrett, 1989; Slinn, 1999, respectively). A key point with this mixing mechanism relates to the waves' ability to propagate vertically; wave breaking and associated turbulent dissipation can occur remote from the bottom (and any homogenized bottom layer) and thus support mixing of water properties. But as is the case for bottom-boundary-layer mixing, the ability of secondary and tertiary circulations to remove the products of wave breaking and thus sustain the stratification is central to the effectiveness of these near-boundary mixing processes (Garrett, 1991; Garrett *et al.*, 1993a).

In support of these ideas, enhanced internal wave energy density has been reported about the estimated critical wave frequencies in moored current meter records obtained above sloping bathymetry (Eriksen, 1985, 1998), though the evidence is not universal (e.g. Gilbert, 1993). And Toole *et al.* (1997) found enhanced dissipation supporting diffusivities of around $5 \times 10^{-4} \text{ m}^2 \text{ s}^{-1}$

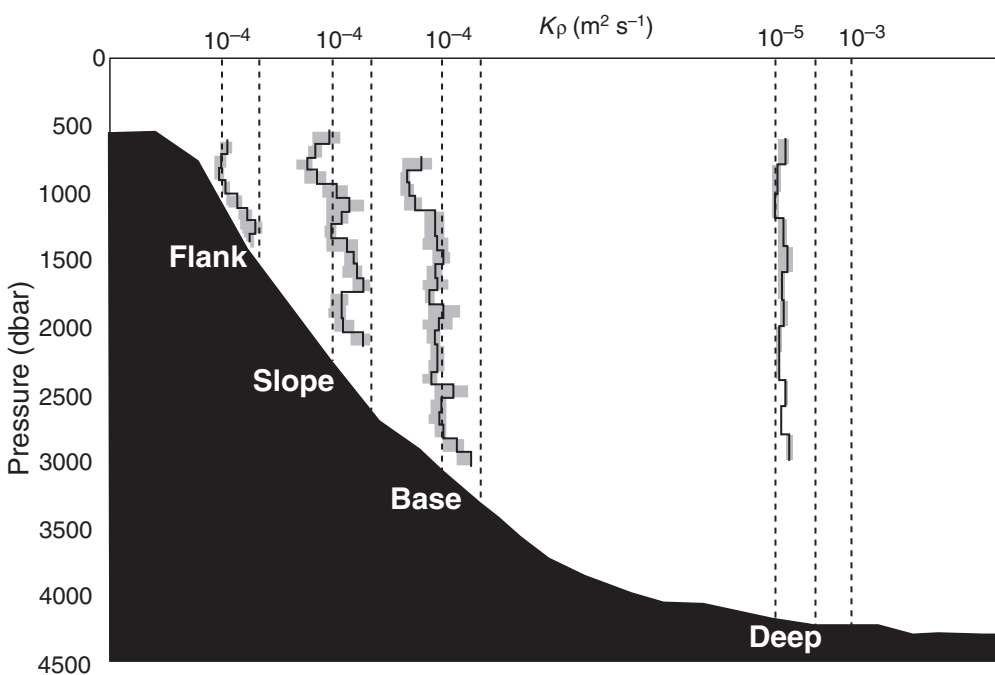


Fig. 5.2.4 Estimates of diapycnal diffusivity based on velocity microstructure at sites about a seamount in the northeast Pacific Ocean (reprinted from Toole *et al.*, 1997). Profile data were grouped by local water depth and averaged in 100-m vertical bins. Shown are the estimated mean diffusivities and their statistical uncertainties (95% confidence intervals) as a function of position relative to the seamount.

in the bottom-most 500 m above the sloping flanks of Fieberling Guyot (Fig. 5.2.4). The specific role of the near critically reflected waves in the heightened dissipations was not clear, however. Somewhat more suggestive was Lueck and Mudge's (1997) discovery of an intense mixing patch that extended away from the summit rim of Cobb Seamount (where the baroclinic tide is critical) with slope consistent with an internal wave beam at M_2 frequency.

Significant near-bottom mixing is also observed within dense overflows from marginal seas; examples include the Mediterranean outflow (Price *et al.*, 1993; Wesson and Gregg, 1994) and that through Denmark Strait (Oakey and Elliott, 1980). These bottom-intensified currents commonly accelerate downslope, achieving supercritical Froude and Richardson numbers. Kelvin–Helmholtz instabilities and hydraulic jumps have been observed, resulting in significant entrainment and dilution of the source overflow waters (Price and Baringer, 1994). The waters that ultimately ventilate the ocean interior thus differ greatly from those created by air–sea exchange in the marginal seas. Indeed, the most critical element distinguishing the models

examined in a recent North Atlantic intercomparison was their treatment of the northern overflows (DYNAMO Group, 1997).

5.2.5.4 Thermocline-depth summary

Diapycnal mixing across thermocline-depth isopycnals appears to vary widely in space. A baseline level of mixing is sustained by the background internal wave field, but that level is low, supporting a diffusivity of around $1 \times 10^{-5} \text{ m}^2 \text{ s}^{-1}$. Regions certainly exist with greatly enhanced mixing, but these are rare and/or localized. Though not the focus of our discussion, we would be remiss here not to reiterate the critical role of the mixing in and about the surface boundary layer. Indeed, Nurser *et al.* (1999) and Marshall *et al.* (1999) suggest that a significant fraction of the inferred mixing across upper-ocean control volume surfaces actually occurs about the base of the time-varying surface mixed layer. Also of great importance at these densities is the mixing and entrainment within descending plumes from marginal seas. In contrast, the interior-ocean diapycnal turbulent fluxes at thermocline depth appear of secondary importance.

5.2.6 Mixing in the abyss

5.2.6.1 The Brazil Basin tracer release experiment

Understanding mixing in the abyssal oceans, where isopycnals do not outcrop locally, is perhaps a simpler problem as the issues relating to time-variable air-sea exchanges are absent. However, progress here has been slowed by the logistical difficulties of working at great depth, but that is starting to change. Motivated by the large diapycnal diffusivities inferred from abyssal heat budgets for semi-enclosed basins, WHOI (Woods Hole Oceanographic Institution) investigators recently conducted a joint finestructure/microstructure and tracer study in the Brazil Basin in conjunction with the WOCE Deep Basin Experiment. Full water column profiles of temperature, salinity and horizontal velocity along with turbulent dissipation rate information were obtained on two cruises spanning the zonal interval between the 3800 m isobath on the continental slope east of Brazil and the Mid-Atlantic Ridge crest (Polzin *et al.*, 1997; Fig. 5.2.5, see Plate 5.2.5, p. 428). Those stations occupied in the western part of the Basin, including those taken over the smoothly sloping South American continental rise where a deep western boundary current is located (see Durrieu De Madron and Weatherly, 1994), were characterized by background-intensity internal waves and weak turbulent mixing. Kunze and Sanford (1996) also found background-intensity internal wave shears in the deep Sargasso Sea (a region characterized by smooth bathymetry). In contrast, above the rough flanks of the Mid-Atlantic Ridge in the Brazil Basin, internal wave energy was much enhanced and accompanied by energetic microstructure that implied diffusivity values of order $10^{-3} \text{ m}^2 \text{ s}^{-1}$. Rough areal averaging of these microstructure data suggest there may be sufficient mixing in the abyssal Brazil Basin to close the heat budget reported by Hogg *et al.* (1982).

Polzin *et al.* (1997) postulated that the enhanced internal wave energy (and ultimately the energy source of the strong turbulence) is the product of internal wave generation by flow over the rough bathymetry of the mid-ocean ridge. In particular, barotropic tidal currents were implicated, mean and mesoscale flows being thought too weak in the eastern Brazil Basin. Critical bottom reflection of waves radiating down from the thermocline

might have also contributed, but it is unlikely they caused the observed fortnightly modulation in depth-integrated kinetic energy dissipation that motivated a tidal explanation (Ledwell *et al.*, 2000). Building on the idea of bottom wave generation, Polzin (2000) went on to take a locally generated wave field as a bottom boundary condition in a model that predicts the dissipation profile in terms of vertical wave propagation and wave-wave interaction. The model predictions for the turbulent dissipation rate magnitude and vertical structure are in good agreement with the observations. Interestingly, Munk and Wunsch (1998) independently explored the ideas of internal tide generation and mixing from an astronomical viewpoint. The decay rate of the moon's orbit sets the global energy dissipation rate; the difficult part is quantifying what (possibly small) fraction of this energy supports mixing in the deep ocean. Indeed, a large fraction of the barotropic tidal dissipation may happen in shallow seas within bottom boundary layers. Though very uncertain, Munk and Wunsch indicate that perhaps as much as 10^{12} W of energy is supplied to open-ocean tides that, in turn, dissipates and supports diapycnal mixing in the ocean interior. This amount of energy could support an order $10^{-4} \text{ m}^2 \text{ s}^{-1}$ globally averaged deep ocean diffusivity. Recent work by Egbert and Ray (2000) gives supporting evidence for barotropic tidal energy scattering into baroclinic motions at ocean ridge systems (that in turn presumably dissipates and supports diapycnal mixing). They estimate an M_2 barotropic-to-baroclinic tidal energy conversion rate in the deep ocean of $0.7 \pm 0.15 \text{ TW}$, and by extrapolation for all tidal constituents, a deep-ocean tidal conversion rate of $1 \pm 0.25 \text{ TW}$.

5.2.6.2 Other abyssal mixing mechanisms

Enhanced deep-ocean internal wave shears have also been observed in the Southern Ocean south of Australia by Polzin and Firing (1997). Rather than the tides, as were implicated in the Brazil Basin, Polzin and Firing suggest internal wave generation in the deep Southern Ocean is associated with mean and mesoscale eddy currents responding to bottom roughness. Based on the extended Henyey *et al.* (1986) internal-wave-energy parameterization, they inferred $K_p \sim 5 \times 10^{-4} \text{ m}^2 \text{ s}^{-1}$ below 1000 m within the Antarctic Circumpolar Current (see also Polzin, 1999). In addition to supporting

enhanced mixing through much of the water column, the surmised bottom-generated internal waves must also carry momentum upwards and thus re-distribute the bottom stress up into the water column. If so, an Ekman-type balance might support net meridional flow above the height of the bathymetric sills of the zonal flow in the Southern Ocean.

The observed bottom-intensified profiles of K_p over rough topography have an interesting consequence for the diapycnal velocity. Neglecting (demonstratively small) consequences of the non-linear equation of state and curvature effects, the steady-state density equation in a coordinate system aligned with the isopycnals is $w^* \rho_z = (K_p \rho_z)_z \sim (\Gamma \varepsilon)_z$ (St Laurent *et al.*, 2000). In the Brazil Basin above the Mid-Atlantic Ridge flank, ε is observed to increase with depth below about 2500 m, implying that $w^* < 0$. Moreover, w^* is increasingly negative with depth, indicating water column stretching. Vorticity considerations in turn imply poleward flow at these levels; possibly consistent with the southward displacement experienced by the centre of mass of the tracer injected at this site (Ledwell *et al.*, 2000; St Laurent *et al.*, 2000). But mass conservation for the bottom waters, in light of the flow entering the Brazil Basin through the Vema Channel, requires net upwelling across deep isopycnals (a positive average w^*). Mass balance may be achieved by strong ‘upward’-directed flow across isopycnals within the many fracture zones of the ridge driven by mixing immediately above the (insulating) bottom.

Before departing the deep ocean, it is important to call attention to other potentially significant mixing processes: those associated with enhanced abyssal currents. Under some conditions, Deep and Bottom waters may be locally accelerated, the resulting strong shears supporting enhanced mixing. For example, significant turbulent dissipation was observed near the bottom at the Blake Bahama Outer Rise where the deep western boundary current is enhanced by local recirculation and topographic effects (Stahr and Sanford, 1999). Flow acceleration is also observed in narrow ocean passages, particularly those that include a vertical sill that can result in downstream flow acceleration by gravity. Such flows may internally produce low Richardson number and develop shear instability. Internal lee waves and hydraulic jumps might also play a mixing role within such

currents. An example here is provided by the flow through the Romanche Fracture Zone in the equatorial Atlantic (Polzin *et al.*, 1996; Ferron *et al.*, 1998). Mixing in the Romanche Fracture Zone warms the coldest waters passing over this Mid-Atlantic Ridge sill from about 0.9°C to nearly 1.5°C. Thus turbulence acting at centimetre scale appears as important as the depths of the sills in the Romanche Fracture Zone in defining the bottom water properties of the Eastern Atlantic basins.

5.2.6.3 Abyssal summary

While deep-ocean dissipation estimates are too few to attempt a quantitative global estimate of abyssal mixing intensity and diapycnal transport, recent results motivate speculation. The Brazil Basin study re-emphasizes that not all baroclinic tides and internal lee waves link directly to enhanced turbulent dissipation and mixing. The connection is most direct for waves at high vertical wavenumber ($>\sim 0.01 \text{ cycles m}^{-1}$). Although energy at these fine scales can come from larger motions via wave-wave interactions, such small-vertical-scale waves are directly generated by flow over bottom irregularities with 1–5 km horizontal scale. Existence of this near-direct energy source suggests that it is small-scale bottom roughness, as opposed to broad slopes or step-change-like bathymetric structures, that is key to mixing in the abyss. Unfortunately, bathymetric information at these small spatial scales is today limited to localized regions surveyed with specialized acoustic sounders. If, however, the bottom roughness is self-similar (areas of 1 km scale roughness correspond to areas that are rough at 10 km scales), the global bathymetric map inferred by Smith and Sandwell (1994) provides some guidance. The map suggests that perhaps half of the seafloor can be characterized as rough, which implies that significant diapycnal transport is widespread at depth. But these rough areas are distributed in a complex fashion around the globe; the field of diapycnal velocity that drives the abyssal circulation is thus likely to be equally complicated. Although their theory does not require uniform upwelling, the Stommel and Arons (1960b) schematics, which for clarity were based on this simplification, are impressed on our subconscious. It is time to revisit the venerable Stommel–Arons abyssal flow patterns with an eye towards developing new paradigms. In regions of

intense turbulent mixing we might even need to question the basic Sverdrup vorticity balance.

5.2.7 Discussion

This chapter has summarized recent developments in the fields of diapycnal mixing in the ocean interior and aspects of dispersion by mesoscale eddies and smaller scale motions. While these oceanic stirring and mixing mechanisms operate at quite disparate horizontal length scales, they are linked through the scale cascade that ultimately reaches the dissipative end of the spectrum. Given limitations in computer power, eddy processes must be parameterized in coarse-resolution ocean and coupled ocean–atmosphere climate models; mixing processes require parameterization in all models (apart from direct numerical simulations that are viable only for very limited spatial domains). Given the relationships between scales, care must be taken that parameterizations for one class of motion don't adversely impact what occurs on other scales. The now classic example of this problem was the contamination of diapycnal diffusive fluxes in simulations resulting from a horizontal (as opposed to isopycnal) stirring parameterization.

A major advance in the field of ocean interior stirring came about by the realization of Gent and McWilliams (1990) that oceanic properties should not be advected in an ocean model by the Eulerian-mean flow but rather by some appropriate approximation of the Lagrangian velocity. From this early work it took several years before the importance of this idea on coarse-resolution ocean models was realized. The theoretical aspect of this work has progressed by making connections to the zonally averaged residual-mean theory of the atmospheric scientists, and the three-dimensional version of this approach, the temporal-residual-mean has been summarized in this chapter. The realization of the need for this type of extra advection (or equivalently, an extra skew diffusion) has allowed many modellers to achieve substantial improvements in ocean simulations including, for example, the deep ocean temperature field. The parameterizations used for this skew-diffusion to date are rather crude and are clearly in need of refinement.

Great progress has been made over the last 15 years documenting the pattern and intensity of diapycnal mixing in the ocean. Perhaps the most

significant turbulent mixing occurs in and about the surface layer where water properties are modified by air–sea exchange as well as by internal mechanisms. Clearly a first step in building a realistic ocean model is to parameterize accurately surface-layer processes. We direct the reader to Large and Nurser (Chapter 5.1), Lazier *et al.* (Chapter 5.5), Price (Chapter 5.3) and Hanawa and Talley (Chapter 5.4) for detailed discussion. Large (1998) also presents an excellent discussion of surface boundary-layer processes and their parameterization. Below the surface-layer environment, a background level of diapycnal flux is sustained by the canonical GM internal wave field via wave breaking. This level is relatively weak, however – equivalent to a diapycnal diffusivity of about $10^{-5} \text{ m}^2 \text{ s}^{-1}$. Thus to first order, the circulation in and above the main thermocline might be thought of as a turbulent surface layer above a stratified, near-ideal-fluid interior.

On closer inspection of course, one finds ocean-interior regions with diapycnal fluxes above the background level parameterized by $K \sim 10^{-5} \text{ m}^2 \text{ s}^{-1}$ background. One subset involves ocean currents that directly support turbulent mixing. Marginal sea overflows and flows through straits are examples here, as perhaps are the equatorial undercurrents (though the turbulent dissipation there is modulated by diurnally generated high-frequency internal waves). Getting the mixing in these flows ‘right’ appears key to synthesizing realistic abyssal stratifications and water properties and sensible low-latitude circulations. Adoption of critical Froude- or Richardson-number-based parameterization schemes for mixing in these flows has shown promise (e.g., Schudlich and Price, 1992; Price and Baringer, 1994; Price and Yang, 1998). Enhanced diapycnal flux has also been inferred where the internal waves are more energetic than the GM background. Recent parameterizations of mixing by internal wave instability and breaking exhibit skill in relating wave field characteristics to dissipation rates. For example, the Henyey *et al.* (1986) model with extensions (see Polzin *et al.*, 1995) yields dissipation estimates within a factor of two of observations for wave fields ranging to seven times more energetic than GM. Underlying this success, however, is a somewhat shaky theoretical foundation (particularly for wave fields significantly different than GM) that would benefit from further study. This aside, the relationships between

waves and dissipation move this part of the mixing parameterization problem to one of internal wave prediction. Showing the most promise here is the abyssal mixing topic where flow over irregular bathymetry has been linked to the profile of diapycnal diffusivity via baroclinic tide and internal lee wave generation, propagation and interaction (Polzin, 1999, 2000). One of the weak links in this modelling is the wave generation at the bottom; work to date builds on models that assume small-amplitude bathymetry or neglect of non-linear advection effects. Mid-ocean ridges, continental slopes and seamounts (where much of the deep-ocean mixing is found) are certainly not small-amplitude structures. It also remains to sort out the relative roles of bottom-generated and bottom-reflected internal waves in heightened abyssal mixing.

Over sizeable ocean areas, the thermohaline stratification supports double diffusion and here we also anticipate enhanced diapycnal fluxes. Double-diffusive flux laws based on laboratory work have been developed that predict the diapycnal heat and solute diffusivities in terms of the thermohaline stratification (e.g. Schmitt, 1988; Kelley, 1984, 1990), and initial efforts to explore these in ocean circulation models have been made. Yet to be made are definitive ocean observations to verify these laws at low density ratio where the fluxes are believed large to complement those acquired in the North Atlantic Tracer Release Experiment at moderate density ratio.

Last we come to mixing in and about the bottom boundary layer, a topic we admittedly gave limited attention to here. Albeit often inefficient with turbulence acting on previously homogenized water, we are loath to discount completely the bottom boundary layer from an account of ocean-mixing processes. Often more problematic than

parameterizing physical bottom-boundary-layer processes in ocean models is the elimination of spurious mixing deriving from the model formulation. Beckmann (1998) gives a nice review of these issues.

Although there has been headway developing understanding of ocean stirring and mixing, fundamental questions remain. In what ways does stirring and mixing (mesoscale, turbulent, double-diffusive) control the mean meridional overturning circulation and its associated redistribution of heat and fresh water? What is the interplay here between mixing in the surface boundary layer and that in the interior? Is there need for significant mixing across thermocline-depth isopycnals beyond that occurring in and about the time-varying surface mixed layer? If yes, is near-boundary mixing above continental slopes and seamounts sufficient in addition to the $O(10^{-5} \text{ m}^2 \text{ s}^{-1})$ diffusivity supported by the background internal wave field? How representative are the Brazil Basin deep mixing results to the global ocean? What does a global abyssal circulation driven by spatially varying mixing over rough bathymetry look like, and is it consistent with the distribution of abyssal water properties and the handful of transport estimates that are available? Though daunting, these are all approachable questions that define an active research area today. Growth in understanding ocean mixing and stirring will continue.

Acknowledgements

JMT wishes to acknowledge support from the US National Science Foundation and Office of Naval Research for his own research efforts on ocean mixing and for the preparation of this chapter. This article is a contribution to the CSIRO Climate Change Program.

This Page Intentionally Left Blank

5.3

Subduction

James F. Price

5.3.1 A little of the background on oceanic subduction

The formation and circulation of thermocline water masses is a central theme of large-scale, physical oceanography. The formation half of the phenomenon usually involves a combination of horizontal and downward flow that has a resemblance to the relative movement of tectonic plates. The formation of thermocline water masses by combined vertical and horizontal flow has come to be termed 'subduction' (Luyten *et al.*, 1983). This chapter reviews the progress made toward understanding the oceanic subduction process and its consequences, with some emphasis upon contributions made during the 1990s.

Though the intent here is to highlight recent progress, it is fitting to point out that the roots of our modern ideas are clearly found in the first basin-scale surveys of the Atlantic Ocean conducted during the 1920s and 1930s. The *Meteor* expedition, described in the monograph by Wüst (1935), revealed the large-scale, three-dimensional patterns of temperature, salinity and oxygen concentration over the Atlantic Ocean. These patterns were highly suggestive of water mass formation at the sea surface in specific and rather confined regions, followed by downward and horizontal flow into the thermocline or abyssal ocean. Regarding the Subantarctic Intermediate Water, Wüst (1935, p. 3) noted that 'The vertical structure of the Subantarctic Intermediate Water, with its horizontal spreading at depth, is analogous to a vertical figure of the horizontal arrangement of temperature and salinity at the surface of the

formation region. The upper portions of the Intermediate Water conform to the northern while the lower ones conform to the southern parts of the formation area.' Wüst (1935, p. 60) noted an effort by Wattenberg during the mid-1920s to infer the current speed along the spreading path of intermediate water by observing the distance between salinity and oxygen anomalies that were presumed to be annual pulses imposed by seasonality at the sea surface. The data available at that time were probably not adequate to this demanding task, in part because the subduction process works as a 'demon' that admits mainly winter waters to the main thermocline (the demon is described further below). Iselin (1939) was performing a similar analysis of North Atlantic properties at about the same time, and his famous Temperature/Salinity (T/S) diagram (Fig. 5.3.1), in which vertical and horizontal profiles were superposed, reveals what seems to be a distributed source of thermocline water at the sea surface, and a downward and southward flow of water over at least a portion of the North Atlantic subtropical gyre. Iselin noted that the best correlation between surface and thermocline T/S properties was with winter surface conditions (as if water at the surface in summer did not contribute significantly to thermocline properties). A second and perhaps more fundamental point is that the T/S properties of subducted waters are evidently not grossly altered by vertical or horizontal mixing after thermocline waters leave the surface layer, i.e. after they are subducted into the thermocline. This implies a crucial idealization for thermocline models, namely,

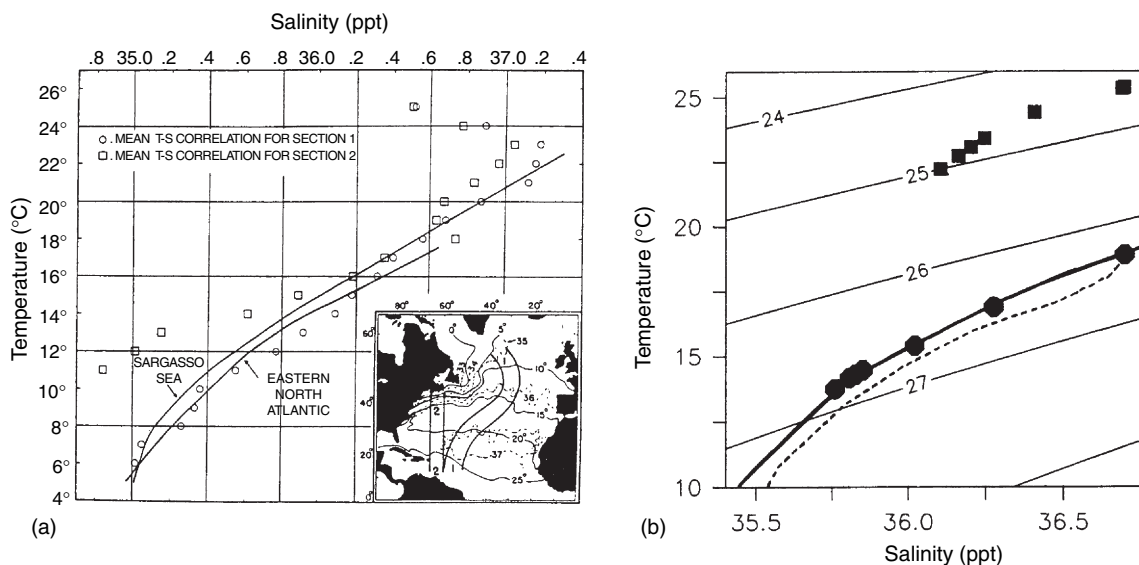


Fig. 5.3.1 (a) T/S diagram from Iselin (1939) showing the T/S relationship along the sea surface in winter in the western North Atlantic (open squares) and at depth (the solid line labelled Sargasso Sea) and along the sea surface in winter in the central North Atlantic (open circles) and at depth (the solid line labelled Eastern North Atlantic). Note that the surface and subsurface T/S relationships are similar over only a small portion of the total temperature range shown. (b) T/S diagram from a seasonally varying model of the North Atlantic (heavy solid line and symbols) by Williams *et al.* (1995). The squares are summer surface data, and the circles are winter surface data; the latter lie directly upon a vertical T/S profile from the same region (solid line). The similar dashed line is a T/S vertical profile from an ocean climatology. From Williams *et al.* (1995), Fig. 9.

that atmospheric forcing (and mixing) is confined to within a relatively thin surface layer of the ocean, and vanishes in the stratified water below.

One of the first successful attempts to estimate the three-dimensional mass flux through the thermocline was by Montgomery (1938), who constructed a streamtube model whose lateral boundaries were observed isohalines, and whose upper and lower boundaries were observed density surfaces. This streamtube had an open mouth at the base of the upper ocean Ekman layer, and then followed a path defined by the observed salinity and density fields downward and equatorward into the North Atlantic main thermocline. The mass flux through such a streamtube was found to be roughly consistent with the convergence of the Ekman transport over the streamtube mouth. Montgomery's streamtube model was regional in scope and diagnostic in that it required detailed information on the distribution of the tracers (salinity and density) that are themselves the result of the circulation. Though far from a complete model, Montgomery's streamtube analysis was nevertheless a crucial step in establishing a quantitative connection between wind forcing, tracer fields and the three-dimensional circulation.

Another, and crucial, connection between the thermocline circulation and the wind fields is given by the Sverdrup theory that relates the vertical integral of the meridional current (sea surface to seafloor) directly to the wind stress curl. The Sverdrup relation makes no distinction between the directly wind-driven surface layer and the geostrophic (unforced) flow below. The seminal circulation model of Luyten, Pedlosky and Stommel (1983, hereafter, LPS) might be viewed as a model that makes explicit the distinction between the ocean surface layer, which is in direct contact with the atmosphere and thus subject to a stress curl, and the nearly unforced (or adiabatic) thermocline below. The Sverdrup relation for transport was assumed to hold within the thermocline alone, and the thermocline water (represented by a few discrete layers) was assumed to be in contact with the atmosphere at appropriate, specified latitudes. The result was a three-dimensional circulation and thermocline structure that gave remarkable insight into major features of the subtropical thermocline. In particular, the LPS model showed that the thermocline circulation could be envisioned as made up of domains having quite distinct dynamics and characteristic paths through the thermocline by

virtue of their connection (or not) to the sea surface. In regions that are directly connected to the surface, i.e. that are within a Montgomery streamtube, the flow can be said to be wind-forced and the regions swept out by such a streamtube are ‘ventilated’, in the sense that the water along one of these paths was at the sea surface a definite, advective, time in the past. The LPS theory makes detailed predictions for these ventilated portions of the thermocline, and is often referred to as the ventilated thermocline model. There are other extensive regions of the thermocline that are not within a Montgomery streamtube and that are not connected to the sea surface by way of an advective path. These ‘unventilated’ regions may or may not be at rest; along the eastern boundary of a gyre there are extensive unventilated regions that abut the eastern boundary and extend well out into the basin (Fig. 5.3.2 is from a continuous model of the ventilated thermocline developed by Huang and Russell (1995) and having the same

dynamics). These eastern regions, called ‘shadow zones’, have potential vorticity contours that terminate on the boundary, and so are at rest in these models. These eastern shadow zones of the LPS model appear to be analogues of the low-oxygen regions found along the eastern boundaries of most subtropical gyres, and the explanation that the LPS model provides of these regions is one of the most compelling results of the subduction theory.

Along the western boundary of the gyre there is another extensive unventilated region that may be in vigorous circulation, though not directly in contact with the atmosphere (Huang and Russell, 1995, and references therein). Within these so-called ‘pool’ regions the circulation is closed through the western boundary current, the details of which are not specified. The potential vorticity distribution within the western pool region is presumed to be horizontally uniform as a result of horizontal mixing, again the details of which need

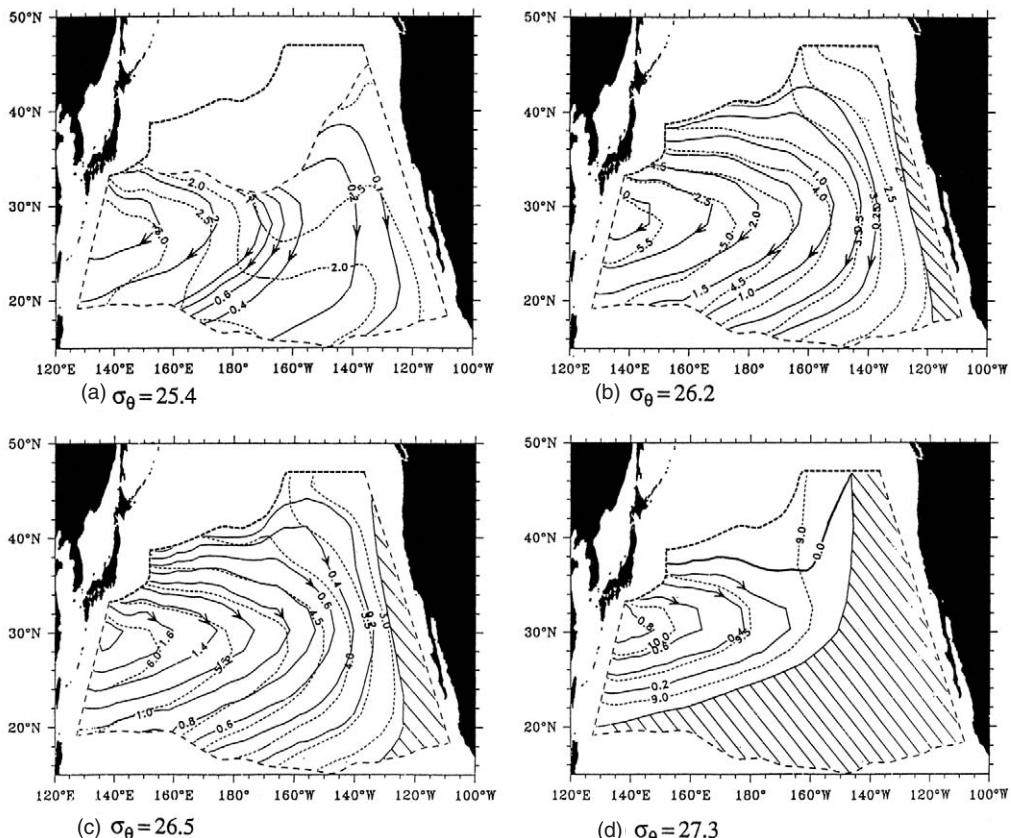


Fig. 5.3.2 Flow patterns on four isopycnal surfaces in the North Pacific computed by a continuous model of the ventilated thermocline due to Huang and Russell (1995). The thin dotted lines are the layer depth in 100s of m. The solid lines with arrows are the volumetric streamfunction. Shaded areas on the eastern edges are shadow zones. From Huang and Russell (1995), Fig. 7.

not be specified (so long as it is not zero and the flux is down gradient).

At given latitude, Sverdrup transport occurs within both the central ventilated region and the western, unventilated pool region. The width of the western pool region and the ratio of the meridional transports in the two regions depends upon a number of parameters, including the stratification and the ratio of the meridional scale of the wind stress (the half width of the subtropical wind cell, roughly) and the scale of the variation of the Coriolis parameter, proportional to the earth's radius but dependent upon latitude. This ratio can be rather small, and thus on a given isopycnal layer only a small fraction of the Sverdrup transport occurs within the directly ventilated region of the thermocline, the rest being within the western pool region. Thus only a fraction of the sea surface is within the 'mouth' of a Montgomery streamtube, typically the central and eastern half of a subtropical gyre. This may be evident in Iselin's subduction diagram (Fig. 5.3.1a). Notice that the central profiles (in depth and along the sea surface) are closely similar over a substantial range of temperatures, roughly 8°C to 16°C. By comparison, the western profiles are not closely similar, and indeed the best match is over the range 15°C to 18°C where the western profile overlaps the central profile. That is, the western profile in depth is more like the central (surface or depth) profiles than the western surface profile. This suggests that to the extent that western thermocline water has an origin at the sea surface in the North Atlantic, then that origin is in the central or eastern subtropical surface layer. This eastward bias of subduction has observable consequences in the evolution of interannual Sea Surface Temperature (SST) anomalies (discussed in Section 5.3.4).

Subduction theory has been extended and applied in many directions since the seminal LPS contribution. This chapter attempts a summary of the progress toward three main questions:

- 1 What are the surface layer dynamics of the subduction process? (Section 5.3.2)
- 2 What are the predictions of a continuous (as opposed to a layered) model? And how applicable is the LPS adiabatic dynamics to the ocean and to numerical model results? (Section 5.3.3)
- 3 What is the thermocline response to interannual variability of surface forcing? (Section 5.3.4).

An excellent review of subduction theory up until about 1990 is by Huang (1991). The monograph by Pedlosky (1996) is a masterful treatment of many aspects of large-scale ocean circulation theory, including especially tropical–subtropical connections associated with subduction that are not much discussed here (and see also Liu and Philander, Chapter 4.4).

5.3.2 Surface-layer dynamics and thermodynamics of the subduction process

The first steady models of the ventilated thermocline took subduction as an observed fact and then proceeded to find the consequences for the Sverdrup flow of the thermocline. It was clear, though, that the subduction process (the passage of water from the surface layer to the main thermocline) must involve the combined effects of upper ocean dynamics, which are highly diabatic, and the gyre circulation. It was expected, too, that the details of where and how much water is subducted must be of consequence to the resulting circulation, and would certainly affect tracer distributions. Indeed, some of the first comparisons of observed, large-scale tracer inventories and tracer ages with the Ekman pumping rate (Sarmiento, 1983; Jenkins, 1987) disclosed that the subduction rate on some isopycnal layers was well in excess of the Ekman pumping rate onto those surfaces, implying a subduction process beyond that envisioned by Montgomery (1938).

The subduction rate may be defined as the rate at which water flows downward across a surface defined by the depth of the late winter mixed layer (Cushman-Roisin, 1987; Williams, 1991; Marshall and Nurser, 1992; Marshall *et al.*, 1993a). If that surface were level, then only a vertical velocity would support a flux, and at depths close to the sea surface, the vertical velocity would be due mainly to Ekman pumping. However, in some regions, especially near western boundary currents, the winter mixed-layer depth has a significant horizontal gradient, and in that case a purely horizontal velocity will also carry water from the surface layer into the main thermocline, i.e. cause subduction. This process has been termed 'lateral induction' (Huang, 1991). Over the region just south and east of the Gulf Stream, lateral induction has been estimated to produce about as much

subduction as does Ekman pumping alone (Huang, 1990). Lateral induction is slightly less important over the North Pacific because the slope of the winter mixed-layer depth is less than that in the North Atlantic, but nevertheless makes a significant contribution (Huang and Russell, 1995).

The basin-scale tilt of the late winter mixed-layer depth must itself be a reflection of the pattern of heat (or buoyancy) exchange between the ocean and atmosphere combined with the large-scale circulation. For example, imagine a water column circulating in a subtropical gyre. In regions where the column receives annual-average surface heating (say in the generally southward flow in the eastern subtropical gyres of the North Atlantic or North Pacific), then the late winter mixed-layer depth will tend to shoal from year-to-year as heat is accumulated above the main thermocline (Fig. 5.3.3; Woods, 1985b; Paillet and Arhan, 1996). This important thermodynamic aspect of the subduction process has been investigated by Marshall and Marshall (1995), Garrett *et al.* (1995), Speer and Tziperman (1992) and Speer *et al.* (1995a), and related to kinematic aspects by Marshall *et al.* (1999).

An intriguing feature of the subduction process noted by Iselin (1939) is that the subduction process evidently selects mainly late winter water

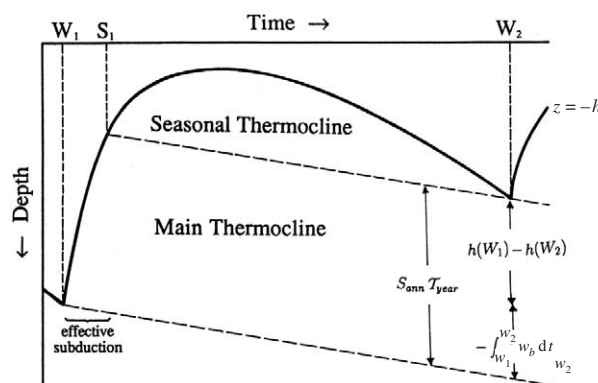


Fig. 5.3.3 A schematic of an upper ocean water column undergoing seasonal cycling and subject to downward Ekman pumping. Subduction is said to occur when water moves from the seasonally affected layer into the main thermocline. During the second winter, the mixed-layer depth is much less than in the first winter, causing significant subduction of water into the main thermocline. If this were a water column circulating within a steady gyre, we might term this subduction process lateral induction. From Williams *et al.* (1995), Fig. 6.

for subduction. Stommel (1979) provided an explanation of winter selection by describing the effects of seasonal cycling and downward Ekman pumping. In a region of large amplitude seasonal cycling there will be a temporary subduction of water within the lower seasonal thermocline as the seasonal thermocline builds in spring and early summer (Fig. 5.3.3). During the following winter, most of this water will be entrained again into the deepening winter mixed layer. However, the deepest portion of the winter mixed layer, the amount given roughly by the Ekman pumping displacement (if other non-local effects are omitted), will be pushed downward below the deepest extent of the winter mixed layer, and is thereby subducted into the main thermocline. Thus the combined effects of seasonal cycling of the upper ocean density and steady, downward Ekman pumping will select water from the deepest part of the seasonal thermocline (a water mass formed in late winter) for subduction into the main thermocline. This 'Stommel demon' selection process has been shown by Williams *et al.* (1995) to operate within a seasonally varying numerical ocean model in very much the way Stommel anticipated (Fig. 5.3.1). Seasonal signals within thermocline tracer fields are thus greatly attenuated when compared with the seasonal cycle at the sea surface. Interannual variations within the thermocline have been detected, however, and interpreted within the light of time-dependent subduction theory (discussed in Section 5.3.4).

5.3.3 Development of steady, continuous models: Application to numerical model analysis and observations

The thermocline of the LPS theory was represented by only a few discrete layers. While this idealized representation is sufficient to portray qualitative features of the circulation, more realistic continuous models are preferable for close comparison with observations (Williams, 1989, 1991; Huang and Qiu, 1994; Huang and Russell, 1995). Huang and Russell (1995) developed analytic solutions from a continuous model built upon the ideal fluid thermocline balances that assume conservation of density, linearized Bernoulli function, and a linearized potential vorticity within the main thermocline (after subduction). The Sverdrup relation on integrated transport was presumed to hold within

the thermocline, and unventilated thermocline waters (the pool region of Section 5.3.1) were presumed to have horizontally uniform potential vorticity equal to that of the adjacent streamline within the ventilated region. Surface-layer data included the surface density and the Ekman pumping rate. With this, and a few other detailed assumptions, the problem reduces to solving a free boundary value problem for the Bernoulli function in density coordinates. The resulting solutions hold a rather remarkable resemblance to the North Pacific thermocline (Fig. 5.3.2) and can be used to diagnose several interesting properties. First, the depth of the wind-driven subtropical gyre of the North Pacific is found to be no more than about 1.4 km (and is typically much less), compared with about 1.7 km in the North Atlantic. Huang and Russell (1995) attributed the difference to the comparatively strong thermohaline forcing and circulation of the North Atlantic, and the shallow and strong halocline found over much of the North Pacific (see also Talley, 1985, for an analysis of salinity over the North Pacific). Second, the renewal time for subtropical thermocline water masses can be estimated from their volume and advective ventilation rate, and is found to be about 3 years for the lightest density classes ($\sigma = 24.1\text{--}24.7$), and about 10–15 years for the subtropical mode waters ($\sigma = 25.3\text{--}25.7$). The mass flux from the ventilated thermocline is exported mainly to the tropics, where it must, on average, have a significant influence on the thermocline properties of the tropics (Gu and Philander, 1997; Kleeman *et al.*, 1999). Whether interannual *anomalies* produced over the subtropics are important for the tropics is less clear. Third, the model yields a compact description of the mass balance of the main thermocline (Fig. 5.3.4). Within the North Pacific, the ventilated portion of the thermocline receives about 21 Sv from the seasonal layer as a result of Ekman pumping, and about 10 Sv due to lateral induction. The same figures for the North Atlantic are about 12 Sv and 12 Sv. Thus, Ekman pumping accounts for a somewhat larger fraction of the North Pacific total of subduction, a consequence of the shallow (and not strongly tilted) winter mixed-layer depth topography of the North Pacific. The meridional mass flux within the unventilated portion of the North Pacific thermocline was estimated by Huang and Russell (1995) to be about 28 Sv,

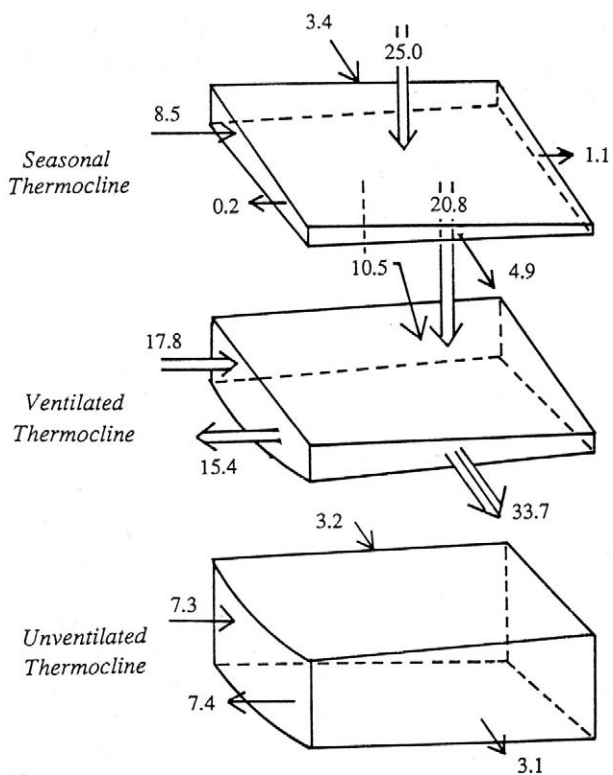


Fig. 5.3.4 Mass fluxes (units of Sverdrups) between layers of the North Pacific thermocline indicated. The northern boundary is to the top, and the Ekman pumping is shown as the downward-directed double arrow. From Huang and Russell (1995), Fig. 12.

which is about 59% of the Sverdrup transport. Over the North Atlantic, the same figure was about 42%. From these results, Huang and Russell (1995) concluded that the North Pacific thermocline is less strongly ventilated than is the North Atlantic thermocline, largely a consequence of the smaller lateral induction over the North Pacific.

Subduction theory provides a language and a conceptual framework useful for describing the thermocline-depth distribution of tracers and circulation seen in numerical models and in ocean data sets. An especially clear and extensive description of the subduction process and consequences in a numerical model is by New *et al.* (1995), who used the Miami isopycnic model to simulate the thermocline-depth circulation within the North Atlantic. The simulations were forced with seasonally varying surface fields, and after 30 years of integration the thermocline circulation had settled into a nearly steady state. Isopycnal layers that came to the sea surface (outcropped) in winter (Fig. 5.3.5) over the central basin exhibited

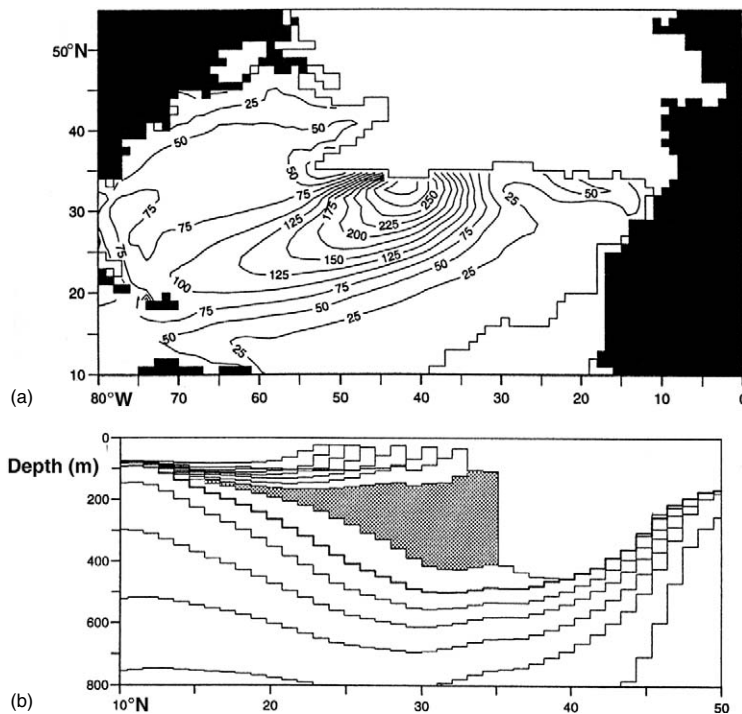


Fig. 5.3.5 (a) Thickness of an isopycnal layer having density 26.7 from the Miami isopycnic model. This is year 30 of an integration having steady wind and surface fluxes. This layer outcrops to the north of the thin line. (b) A vertical section along 45°W in winter showing the 26.7 layer as the shaded region. Note the pronounced thinning of the layer to the south of its subduction latitude (roughly 37°N at this longitude). Partly this results from the section not being aligned with the core of the subducted layer, and partly it results from diffusion of water with lesser thickness into this layer. From New *et al.* (1995), Figs 10 and 11.

many of the consequences of subduction expected from the LPS theory. Fluid on the $\sigma=26.7$ layer is drawn southwards and westwards into the main thermocline as a part of the Sverdrup flow. Along its northern extent the $\sigma=26.7$ layer has a fairly large thickness compared with other layers above and below having the same density difference, and in that regard is like a mode water (McCartney, 1982; Siedler *et al.*, 1987; Hazeleger and Drijfhout, 1998; Schmid *et al.*, 2000; and see also Hanawa and Talley, Chapter 5.4) having low potential vorticity (Fig. 5.3.6). For a substantial distance downstream of the subduction region this low Potential Vorticity (PV) forms a tongue that serves to mark the subducted water mass. (In the real North Atlantic there is no strictly comparable mode water formed at this density and general location.) An interesting question is whether the water within this layer conserves potential vorticity, as assumed in the idealized LPS theory. Since the low PV tongue is surrounded by higher PV waters on all sides, there is bound to be some diffusion of (higher) PV into the subducted water

mass. This significantly erodes the low PV tongue, which, 5–10 years after subduction, begins to lose its identity. The low potential vorticity is spread by diffusion into the surrounding waters, which thus have a negative potential vorticity diffusion tendency (balanced in this near steady state by horizontal advection). The change of PV within the subducted water is not small, and horizontal diffusion clearly influences the basin-scale distribution of PV (see Toole and McDougall, Chapter 5.2 for a review of mixing in the ocean). Nevertheless, the overall pattern of thermocline circulation in the numerical model solution is qualitatively as expected from the purely advective (adiabatic) theory of LPS.

In numerical models that admit mesoscale eddy variability, the subduction rate is liable to be affected by eddy variability (Marshall, 1997), especially in high eddy energy regions, e.g. the formation site of western subtropical model water near the Gulf Stream. Hazeleger and Drijfhout (2000) showed comparable eddy-resolving and non-eddy-resolving simulations of the Gulf Stream region to illustrate this process. The net subduction rate was

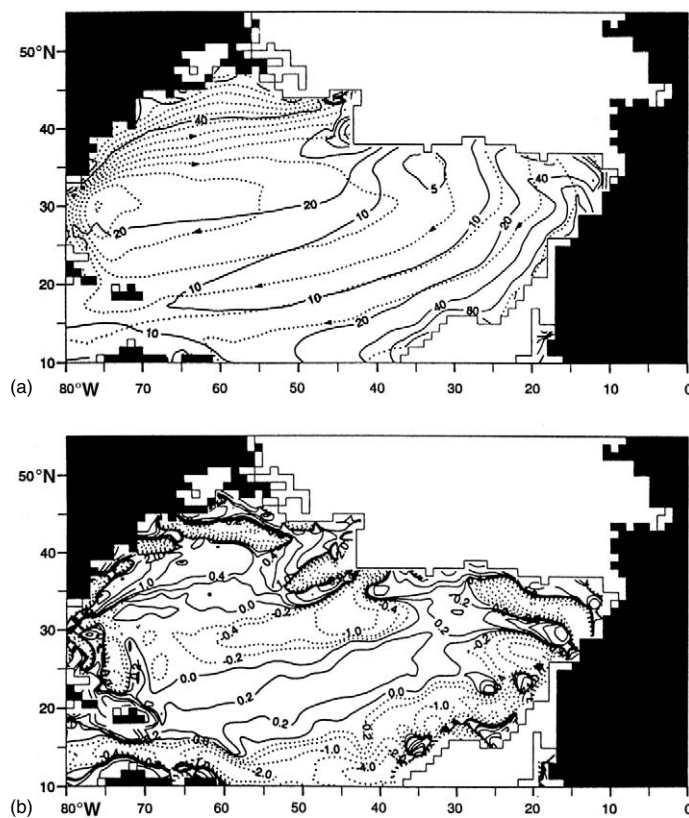


Fig. 5.3.6 (a) Montgomery potential (dashed lines with arrowheads, contour interval $0.5 \text{ m}^2 \text{ s}^{-2}$) and isolines of linearized potential vorticity (units are $10^{-11} \text{ m}^{-1} \text{ s}^{-1}$) for a layer having density 26.85. (b) The field of potential vorticity diffusion tendency for this layer (diffusion is here all in the horizontal). The positive tongue along the core of the subduction pathway is consistent with the increase of potential vorticity within the core of the subducted water. Outside of this core, the diffusion tendency is of the opposite sign, and the effect of diffusion is to decrease the potential vorticity. From New *et al.* (1995), Figs 17 and 18.

not dramatically altered by eddy variability. Nevertheless, in the former case the subduction process, especially within the western basin, occurred mainly by a divergence of the eddy thickness flux, and thus could be termed eddy subduction. In some localized regions this eddy subduction reached amplitudes of 100 m yr^{-1} . Spall (1995) and Follows and Marshall (1994) examined subduction processes near oceanic fronts. There, too, the subduction process occurs mainly in conjunction with eddy formation (baroclinic instability), and thus could be said to be eddy subduction.

Another view of eddy effects and subduction has been developed by Robbins and Jenkins (1998), and Jenkins (1998), who have analysed 15 years of tritium and ${}^3\text{He}$ observations from the eastern subtropical North Atlantic with the aim of characterizing the circulation and ventilation rates. Within shallow layers of the thermocline ($\sigma = 26.5$), the tritium- ${}^3\text{He}$ -inferred age was found

to be nearly steady and consistent with the notion of direct advective flux from surface outcrops within the gyre. At deeper levels in the thermocline, the tracer-inferred age has shown a significant increase over the period analysed, and has only recently begun to approach a steady state. A time-changing tracer-inferred age could perhaps result from a time-changing circulation, or, on the balance of evidence (Robbins *et al.*, 2000), more likely from a transient tracer balance due to horizontal diffusion (which is ignored in straightforward age estimates). Robbins *et al.* (2000) showed that horizontal diffusion into the lower thermocline from a convective ventilation region north of the gyre boundary would yield the observed horizontal structure of the tracer fields; it also yielded roughly the observed temporal increase of tritium- ${}^3\text{He}$ ages, all assuming a steady circulation. For the tritium- ${}^3\text{He}$ tracer pair, diffusion is thus of great importance, especially within the

deeper thermocline where mean flows are weakest (see also Joyce and Jenkins, 1993; Joyce *et al.*, 1998).

The DYNAMO Group (DYNAMO Group, 1997) examined the ventilated thermocline and subduction dynamics in three high-resolution models of the North Atlantic, each forced by the same surface fluxes. The models differed with respect to their vertical discretization and representation of surface layer processes. Despite the similar surface forcing, the models each developed a unique pattern of subduction in the subtropics, and a corresponding, unique potential vorticity distribution in the upper thermocline. The overall patterns were not unrealistic, but the interesting question to consider here is – How could we make these numerical models better? By better we could mean either more consistent with North Atlantic observations, or even just more consistent with one another. An attempt to answer this question reveals something significant about the subduction process, namely, that it is not a simple, direct outcome of a single process or parameterization. Instead, subduction and ventilation in these comprehensive models are an outcome of the

combined effects of surface layer processes, especially those that determine the depth of the late winter mixed layer, and the underlying circulation. Thus, subduction and thermocline ventilation cannot be tuned or improved in a direct and straightforward way, as might be possible with, say, a parameterization of surface wind stress. Some examples of model changes that improve aspects of the circulation are given by Jia (2000), who showed that inclusion of an entraining Mediterranean outflow greatly improved the simulated Azores Current in a high-resolution numerical model (see also New *et al.*, 2000b). Similarly for upper ocean dynamics, Spall *et al.* (2000) showed that gyre-scale advection improved upper ocean predictions. These improvements may, in addition, have beneficial consequences for subduction and thus for the thermocline circulation and ventilation.

5.3.4 Transient response of the thermocline to decadal variability

The first attempts by Wattenberg (Wüst, 1935) to find the signal of subducting seasonal SST

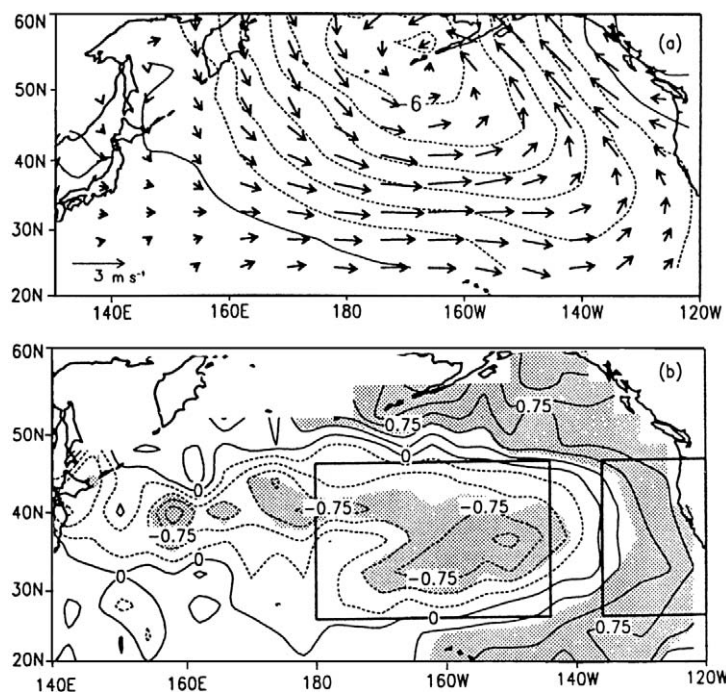


Fig. 5.3.7 (a) Winter surface wind and pressure differences between 1977–88 and 1971–76 (from Deser *et al.*, 1996, Fig. 1). The Aleutian Low and associated westerly winds were stronger during the period 1977–88. (b) Annual average of SST difference between 1977–88 and 1970–76 (nearly the same period as above). Note that the central North Pacific was cooler by about 0.75°C during the period of stronger Aleutian Low, while the eastern and northeastern North Pacific were warmer by about the same amount. From Deser *et al.* (1996), Fig. 6.

variations were well ahead of the ocean observations available at that early stage of ocean science. Modern data compilations, and most notably the extensive climatology of upper ocean temperatures made by Levitus and Boyer (1994b) and by White (1995) from *in-situ* sources, are sufficient to reveal the complex time-dependent response of the North Pacific Ocean to interdecadal variations of wind stress and surface heat flux. Deser *et al.* (1996) used the former climatology to examine the interannual response of the upper North Pacific (upper 400 m) over the period 1970 to 1991, which included a significant shift of atmosphere and ocean climate beginning at around 1976. During the decadal period from 1977 to 1988 the Aleutian low was deepened, compared with the period 1971–76 (Fig. 5.3.7a). North Pacific SST was cooled by about 0.75°C in the western and central subtropical regions and warmed by about the same amount along the west coast of North America (Fig. 5.3.7b). The analysis of this event by Miller *et al.* (1994), Deser *et al.* (1996) and Schneider *et al.* (1999b) provides a remarkable view of the interaction between surface layer anomalies imposed by the atmosphere and gyre-scale circulation. Theories of subduction have had a central role in developing the description and understanding of this important climate phenomenon.

The pattern and the amplitude of the SST anomalies appear to be caused by direct air-sea interaction (Miller *et al.*, 1994; Inui *et al.*, 1999). Winters with stronger than normal westerly winds (the period from 1977 to 1989) produce a cool SST anomaly, and there is a strong visual correlation between the wind anomaly amplitude and the SST anomaly amplitude. The surface layer processes that contribute to the cooling include enhanced surface heat loss associated with higher winds, increased vertical mixing associated with higher winds (and deeper winter mixed-layer depths), and increased advection by Ekman transport, with stronger westerlies leading to enhanced cool advection. Whether there is positive or negative feedback between the atmosphere and ocean as a consequence of this anomaly formation process is an important question for the future.

The subsurface signature of the cold surface anomaly is a series of cold pulses that appear to move downward through the upper 400 m (central region) or 200 m (eastern region) at a rate of about 100 m yr^{-1} . Averaged over several years, the

annual pulses appeared to form an envelope that descended much less rapidly, about 15 m yr^{-1} within the central North Pacific. Within the eastern North Pacific, there is little penetration of this anomaly below about 200 m, and no evidence of the slow envelope found in the central region (Fig. 5.3.8). This significant difference in the vertical propagation of the thermal anomalies between the central and eastern regions might be attributed in part to the shallow and relatively intense thermocline in the eastern region, and it is also consistent with expectations from subduction theory that depicts the eastern thermocline as a shadow zone,

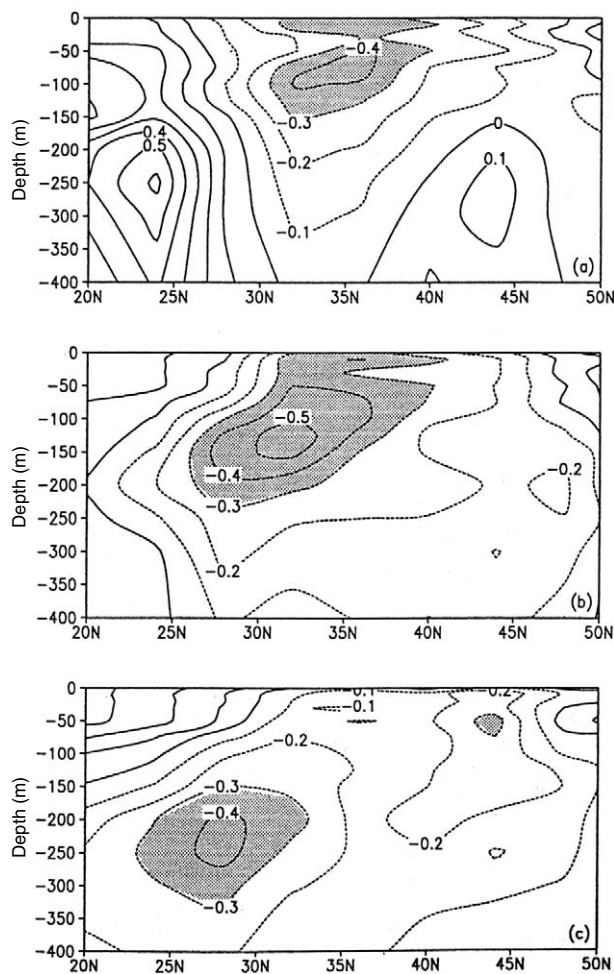


Fig. 5.3.8 Annual subsurface temperature anomalies shown as a function of depth and latitude for the central North Pacific region (the central box of Fig. 5.3.7). The time periods are (a) 1977–81, (b) 1982–86 and (c) 1987–91. Anomalies cooler than 0.3°C are shaded. Note that the cool anomaly found at the surface in 1977–81 (compare with Fig. 5.3.7b) moved downward and southward, and that it slowly decreased in amplitude. From Deser *et al.* (1996), Fig. 10.

with levels below about 200 m not directly connected to the sea surface by an advective path.

An important extension of this analysis was performed by Schneider *et al.* (1999b) utilizing a climatology prepared by White (1995) that covered the period 1955 to 1996. This data set showed the late 1970s' central North Pacific cold anomaly described in detail by Deser *et al.* (1996), as well as a warm anomaly during the period 1973–76 that moved along a similar path and speed (Fig. 5.3.9). Schneider *et al.* (1999b) made direct comparisons of the observed anomaly movement with the predictions for the mean flow from a three-layer model of a thermocline driven by subduction. They found that the thermocline model gave a realistic depiction of the potential vorticity distribution in the ventilated portion of

the subtropical gyre, and moreover, anomalies that had an origin in the central North Pacific appeared to move southward and westward along the path expected of a potential vorticity conserving flow. Anomalies generated at the surface in the eastern North Pacific appeared to rise and fall in place, i.e. without obvious movement, as did anomalies occurring in the Kuroshio region of the western North Pacific. The average meridional translation speed of the central North Pacific anomalies was about 0.007 m s^{-1} , and consistent with the Sverdrup flow predicted by the ventilated thermocline model (and with the geostrophic velocity referenced to 1500 m) (Fig. 5.3.10). The central North Pacific anomalies moved southwestward from their apparent origin north of Hawaii and reached 18°N along the western boundary within about

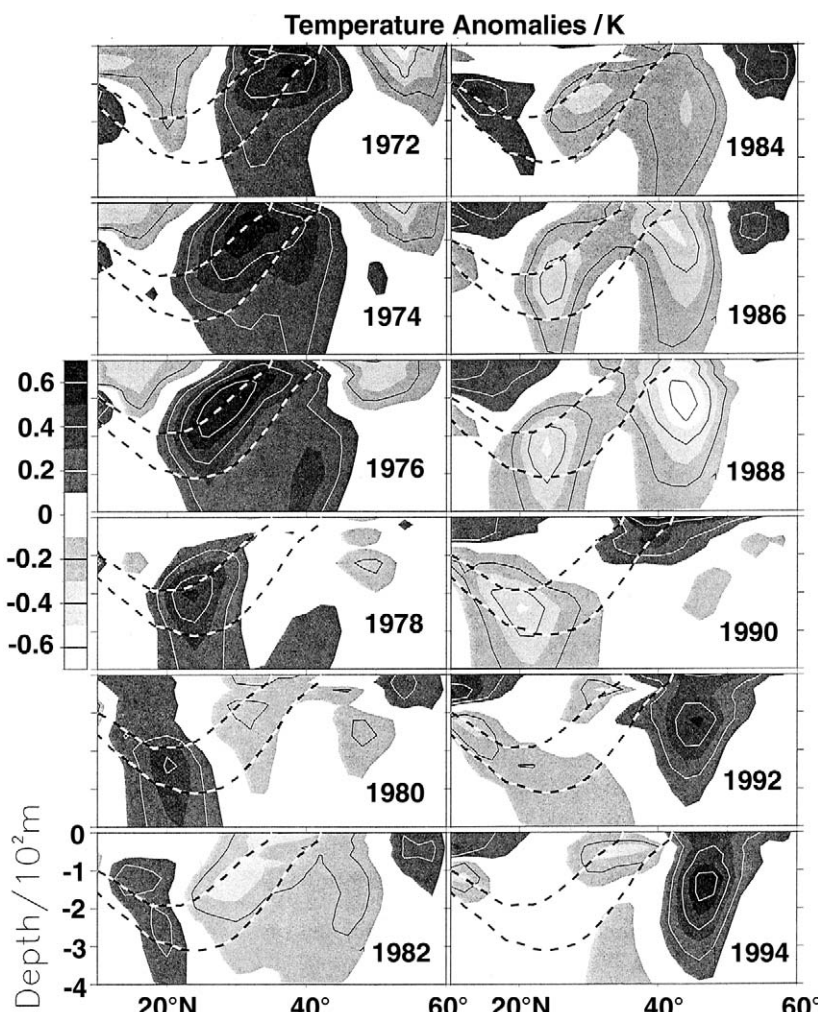


Fig. 5.3.9 Annual temperature anomalies from the White (1995) climatology smoothed with a five point triangular taper. These data are from the central North Pacific (145°W to 170°W). The mean positions of the 12°C and 18°C isotherms are shown by dashed lines. From Schneider *et al.* (1999b), Fig. 1.

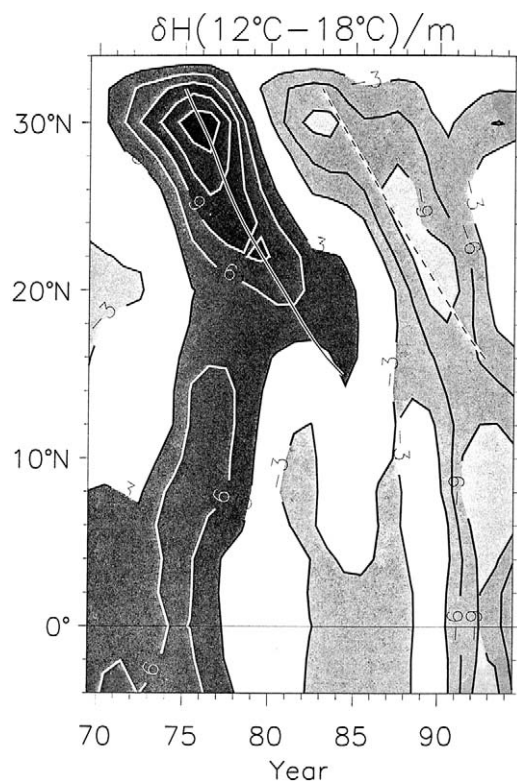


Fig. 5.3.10 Depth anomaly of the layer defined by the 12°C and 18°C isotherms averaged zonally along a path of constant mean potential vorticity starting in the central North Pacific. Note the southward displacement of anomalies, as in Fig. 5.3.9. The corresponding advection speed given by the ventilated thermocline model is the solid line; and the geostrophic mean speed is the dashed line; both are about 0.007 m s^{-1} . The height anomaly appears to move as if it were a nearly passive tracer riding on the Sverdrupian, geostrophic flow of the thermocline. From Schneider *et al.* (1999b), Fig. 6.

8 years. The anomaly amplitude was then reduced to about 5 m, which is not large compared with other thermocline variability in the tropics. The cold anomaly then appeared to spread eastwards along the equator, and increased in amplitude somewhat. Schneider *et al.* (1999a) concluded that the subduction process provides a time-delayed connection between the subtropical and tropical oceans, but that the amplitude of the subtropical signal is probably not significant when compared with other thermocline variability generated locally by wind forcing within the tropics. The phenomenology of tropical–subtropical connections is the subject of very active research (Liu and Philander, Chapter 4.4) and the last word on subtropical–tropical connections is undoubtedly not in.

The anomalies seen in the climatologies are most evident in the height of isotherms. Thickness anomalies, i.e. potential vorticity anomalies, had an amplitude of only a few per cent of the mean potential vorticity, and were by comparison much harder to map. The most extensive climatologies do not include salinity with the same time and space extent, and so the dynamic height associated with the height anomalies is not known from direct observation. Thus their generation mechanism and their intrinsic dynamics, whether they are passive scalars or baroclinic waves is not evident from the thermal climatology alone. Schneider *et al.* (1999b) used COADS-based surface forcing fields to make a detailed study of the history of the upper ocean heat and momentum balance for the period noted. The upper ocean heat budget included terms for air–sea heat exchange, entrainment, and horizontal advection by the Ekman transport. All three terms would tend to be increased (or decreased) by stronger (or weaker) than average westerly winds. During the period 1973–76 westerly winds were slightly weakened over the central North Pacific, and the result was sea surface warming, most evident in the winters. Following 1976 there was a period of stronger than average westerly winds causing enhanced cooling and the eventual appearance of the late 1970s and early 1980s warm anomaly.

Thermocline-depth thermal anomalies might also be generated by anomalous Ekman pumping, which exhibits large year-to-year variability. However, there is no clear correlation with decadal time scale thermal anomalies and thus Schneider *et al.* (1999b) concluded that the central North Pacific sea surface thermal anomalies appeared to be generated by local, diabatic surface forcing associated with variations in the strength of the westerlies. The occurrence of anomalous westerly winds in the central North Pacific appeared to be correlated somewhat with El Niño events. Thus tropical–subtropical connections through the atmosphere and ocean may be indirect, multi-faceted, and by no means easily sorted out from observations or models.

These and other observational studies of inter-annual variability have stimulated theoretical and experimental research aimed at understanding the generation and propagation of decadal time scale thermocline anomalies (Liu and Zhang, 1999; Huang and Pedlosky, 1999; Inui and Liu, 2001;

Huang, 2001a). Liu and Shin (1999) calculated the response of the Miami isopycnic model to a cooling anomaly imposed over the central North Pacific (Fig. 5.3.11). The response was diagnosed by tracking a passive tracer and discrete particles for 15 years. The resulting cool oceanic anomaly (a lifted isopycnal surface; the maximum amplitude is about 30 m, or somewhat more than the observed anomalies noted above) moved to the southwest, roughly along the path followed by the passive tracer and the particles. Thus, a surface-forced (diabatic) thermal anomaly of moderate amplitude appears to behave, to a first approximation, much like a passive tracer injected into the undisturbed circulation (Fig. 5.3.12). To the same approximation, these results are consistent with the observations and conclusions of Schneider *et al.* (1999b). A careful, quantitative analysis of the motion of the centre of mass of the cold anomaly

showed that it moved slightly less rapidly to the west and south than did a truly passive tracer. Moreover, while the diabatic forcing was spatially confined, the ocean thermal anomaly appears to disperse, and warm anomalies (considerably weaker in amplitude) appear in distant parts of the basin. Thus, the characterization of the thermal anomaly motion by a single speed is not the entire story, at least not within these numerical experiments.

Similar model experiments have elucidated the decadal response to anomalous Ekman pumping. Liu and Zhang (1999) find that anomalous Ekman pumping produces a thermocline-depth anomaly that has the approximate vertical structure of a first mode baroclinic wave. These anomalies propagate westward with very little apparent Doppler shifting or other effect of the mean wind-driven circulation. This first mode response has a prominent

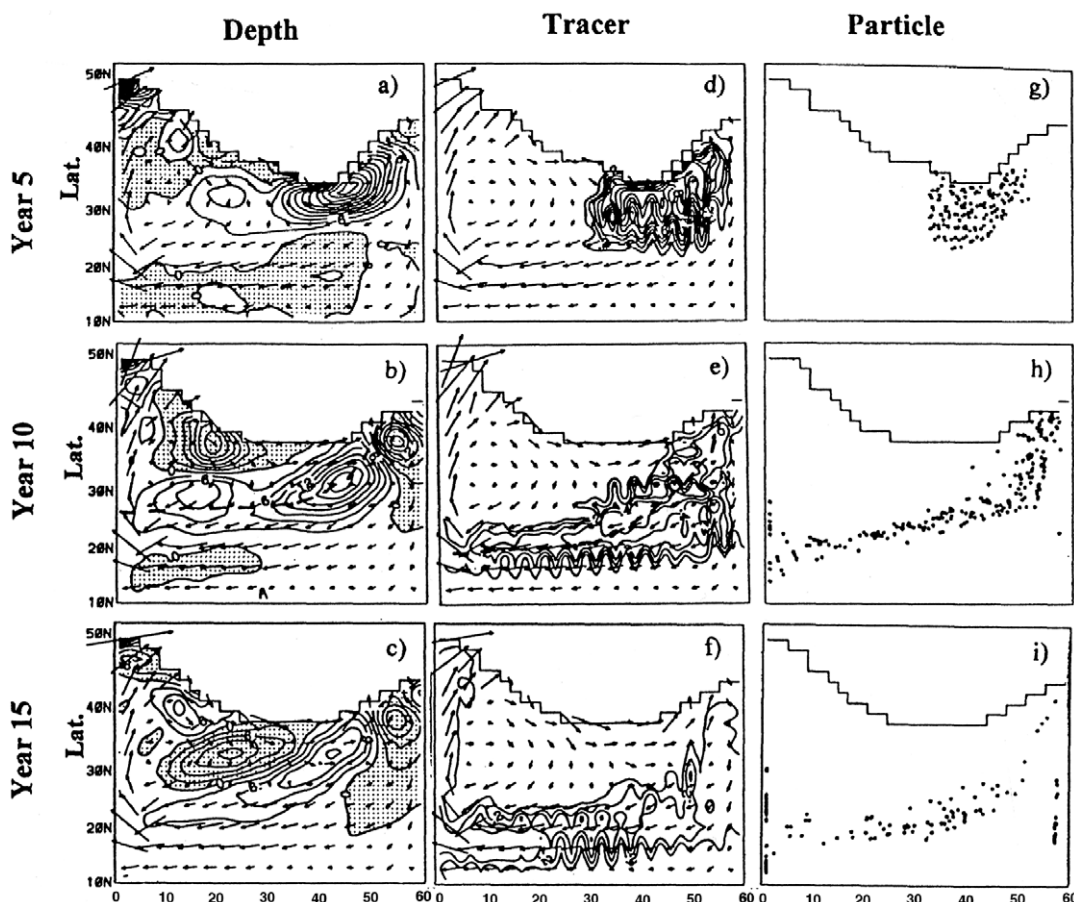


Fig. 5.3.11 Five-year sampled sequence of layer depth (left column), tracer concentration (centre column) and particle positions (right column) from two integrations of the Miami isopycnic model by Liu and Shin (1999). In the left column, an otherwise steady circulation was perturbed by 5 years of anomalous surface cooling in a confined region (near the tracer patch in year 5). The tracer and particles were injected into the unperturbed circulation. Note that the thermal anomaly moves like the passive tracers, to a first approximation. From Liu and Shin (1999), Fig. 1.

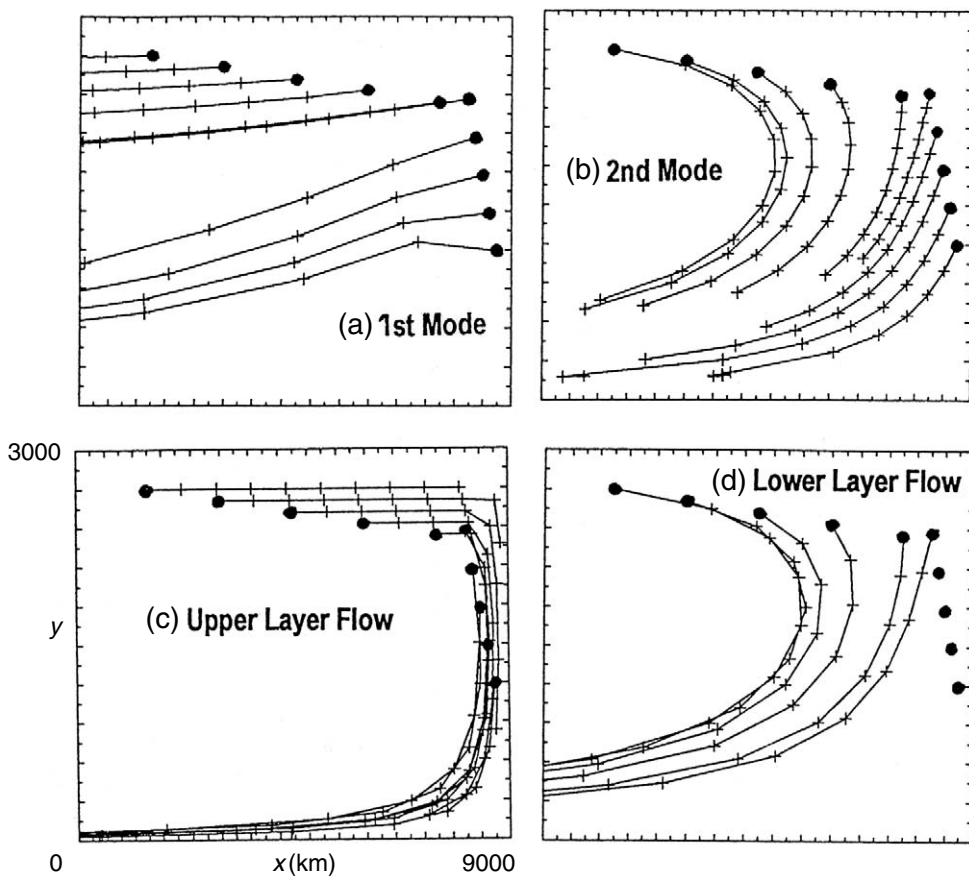


Fig. 5.3.12 (a and b) Wave ray paths at 2-year intervals computed by WKB approximation within a QG model of the ventilated thermocline. The waves are first and second baroclinic modes (a and b, respectively). The lower row (c and d) shows the paths of passive particles advected by the mean flow in layer one (c) and layer two (d) of the model. Note that first mode waves propagate almost westward and are termed the non-Doppler-shifted mode, while second mode waves are very strongly affected by the mean flow. From Liu and Zhang (1999), Fig. 4.

signature in sea surface height. Diabatic surface forcing, on the other hand, tends to produce a forced response that changes sign with depth once within the lower thermocline, and thus has a strong projection upon the second or higher baroclinic modes (Huang, 2001a). These higher baroclinic mode waves propagate very slowly, and are so strongly advected by the mean flow that they move almost as if a passive tracer. Thus a crucial difference between (anomalous) buoyancy forcing and anomalous Ekman pumping forcing thus appears to be that the former produces second (or higher) baroclinic mode structure, while the latter produces mainly a first baroclinic mode response.

5.3.5 Summary and outlook

It is easier to supply the proof when we have previously acquired by the method some

knowledge of the question than it is to find it without any previous knowledge.

[Archimedes, c.287–212 BC]

Archimedes was the earliest known fluid dynamicist and perhaps even the first physical scientist whose work has survived down to the present more or less intact. Archimedes' envisioned that research was a cycle – observation, experimentation and analysis – that is remarkably like the method of modern ocean circulation studies. A difference may be that today these stages are not always completed by one investigator, nor even in one era. The painstaking observations and insightful descriptions of the North Atlantic thermocline made by Wüst, Iselin, Montgomery and their colleagues during the 1920s and 1930s were compelling evidence for a three-dimensional circulation of the thermocline, and yet the analysis or 'proof'

of this circulation, the construction of the LPS subduction theory, required many decades of concerted effort. The subduction theory has been remarkably fruitful for almost 20 years now and, if anything, the pace of research on time-dependent phenomenon has quickened with the availability of comprehensive air and sea climatologies.

The new WOCE data sets, and particularly the basin-scale surveys that are strongly reminiscent of the *Meteor* expedition, will undoubtedly help us to define the shortcomings of present, idealized thermocline models. In this respect the WOCE field effort may some day appear to have been the observational stage that began only the second (or third?) major cycle of ocean science research. The analysis stage of this new cycle is only beginning

and no one could foretell what new proof may emerge in the next 10–20 years. More comprehensive and more realistic models of the thermocline and upper ocean circulation seem bound to follow, if only because present models are so lean.

Acknowledgements

The author was supported by the US Office of Naval Research and by the National Science Foundation Grant No. OCE94-01300 during the time of manuscript preparation. Thanks to Zhengyu Liu, Rui Xin Huang and Mike Spall and for allowing the use of their unpublished manuscripts, and to the editors and referees for helpful comments on the draft manuscript.

This Page Intentionally Left Blank

5.4

Mode Waters

Kimio Hanawa and Lynne D. Talley

5.4.1 Ventilation and mode water generation

‘Mode Water’ is the name given to a layer of nearly vertically homogeneous water found over a relatively large geographical area. Mode waters usually occur within or near the top of the permanent pycnocline, and hence are apparent through the contrast in stratification with the pycnocline waters. Therefore, in a volumetric census in, for instance, a temperature–salinity diagram, this homogeneity in comparison with surrounding higher stratification produces a maximum inventory. Masuzawa (1969) first introduced the term ‘Subtropical Mode Water’ (STMW) in reference to the thick layer of temperature 16–18°C in the northwestern North Pacific subtropical gyre, on the southern side of the Kuroshio Extension. This STMW is the counterpart of the previously identified Eighteen Degree Water associated with the Gulf Stream Extension in the North Atlantic (Worthington, 1959). The terminology ‘Mode Water’ was extended to the thick near-surface layer north of the Subantarctic Front by McCartney (1977), who identified and mapped the properties of the Subantarctic Mode Water (SAMW). McCartney and Talley (1982) then applied the term ‘Subpolar Mode Water’ (SPMW) to the thick near-surface mixed layers in the North Atlantic’s subpolar gyre. The term ‘Mode Water’ now is nearly ubiquitous for describing any thick, broadly distributed, near-surface layer. To distinguish it from other mode waters, the Subtropical Mode Water described by Masuzawa (1969, 1972) is now usually referred to as North Pacific Subtropical

Mode Water (NPSTMW) and the North Atlantic’s Eighteen Degree Water is sometimes called North Atlantic Subtropical Mode Water (NASTMW).

Mode waters have been identified in every ocean basin, always on the warm side of a current or front. Subtropical mode waters are associated with every separated western boundary current of subtropical gyres. Mode waters have been identified recently in the northeastern portions of several subtropical gyres – this identification is extended herein to all basins. In the southern hemisphere, the Subantarctic Front is the southern boundary of the subtropical gyres. Because isopycnals plunge so rapidly towards the north across the front, a very thick mode water is found to the north of the front.

Mode waters are generally distributed below the surface far beyond their formation areas. Ventilation of the ocean interior occurs when fluid is subducted, or pushed down, from the ocean surface. The initial view of how this occurs dates back to Iselin (1939), who proposed that water would be pushed downwards along sloping isopycnals from the base of the Ekman layer by the wind-induced vertical Ekman pumping velocity. Stommel (1979) recognized that only the fluid leaving the deep winter mixed layer irreversibly enters the permanent pycnocline (the ‘mixed-layer demon’ hypothesis), and this biases the temperature and salinity properties of the main thermocline toward those of the deep winter mixed layer. Consequently, it is actually the flow through the base of the winter mixed layer (rather than the Ekman layer) that ventilates the underlying ocean,

and, as pointed out by Woods (1985b), the absence of a mixed layer in idealized models precludes lateral induction (by horizontal advection) across the sloping base of the mixed layer. Williams (1989) therefore included a spatially varying mixed layer in the model of Luyten *et al.* (1983), and found that the volume of ventilated fluid within the subtropical gyre was indeed much increased due to lateral induction. In fact, several studies have now shown that the subduction rate in the North Atlantic subtropical gyre due to lateral induction is about two to four times greater than that resulting from Ekman pumping alone (Jenkins, 1982; Sarmiento, 1983; Marshall *et al.*, 1993a; New *et al.*, 1995). The readers may refer to Chapter 5.3 of this book by Jim Price for more detailed discussion of subduction.

Mode water studies are useful from various viewpoints. First, mode water reflects temporal variations of oceanic and hence climatic conditions. Variations in mode water properties, distribution and circulation are manifestations of variations in wintertime air-sea interaction (surface cooling) in the formation area, oceanic heat transport to the formation area, eddy activity in the formation area and spin-up/spin-down of the gyre. Second, mode water simulation is a good target for numerical models, particularly those with mixed layers. In order to model mode waters and their variations accurately various processes must be correctly simulated, including: plausible separation of western boundary currents and their extensions, frontal systems, mixed-layer processes given proper surface forcing, eddy activity in the formation area, advection/ventilation/subduction processes and isopycnal/diapycnal mixing. Numerical simulations of NASTMW (Marsh and New, 1996; Hazeleger and Drifhout, 1998, 1999) and SAMW (Ribbe and Tomczak, 1997b) have been carried out. Reproducing mode water distribution, circulation and variability in numerical models will assist mode water studies as well as improvement of the numerical models themselves. Third, mode water in the sense of its potential vorticity signal is a good tracer of subtropical ventilation, as useful as chemical tracers of ventilation (Sarmiento *et al.*, 1982; Talley, 1988; Joyce *et al.*, 1998; Schneider *et al.*, 1999b). This could be particularly useful in the case of the eastern subtropical mode waters and the SAMW, which are subducted in the eastern parts of the gyres.

In this chapter, we describe the distribution and water properties of mode waters in the world's oceans. Mode waters are defined and their general characteristics presented in Section 5.4.2. The global distributions and basin descriptions of mode waters are presented in Section 5.4.3. Intermediate waters are discussed in several chapters (see Davis and Zenk, Chapter 3.2; Rintoul *et al.*, Chapter 4.6; Gordon, Chapter 4.7; and Schlosser *et al.*, Chapter 5.8). Here in Section 5.4.3 a brief discussion is presented of the low-salinity intermediate waters as they relate to mode waters. In Section 5.4.4, temporal variations of subtropical mode water properties in the North Pacific and North Atlantic are reviewed, and some information about variation of SPMW properties is presented.

5.4.2 Definition, detection and general characteristics of mode waters

Mode waters are characterized by homogeneity of water properties in the vertical as well as the horizontal. Thickening of isopycnal layers occurs in many places, so the following several characteristics are generally used to identify mode waters. (1) In a volumetric sense, a mode water has a substantial volume in some region, in comparison with surrounding water masses. (2) Water properties such as temperature, salinity and oxygen are highly homogeneous in the horizontal and vertical. (3) At a given station, that is, in a single vertical profile, mode water appears as a pycnostad (low vertical density gradient) between the seasonal and main (or lower) pycnoclines (high vertical density gradient). (4) Mode water is found well beyond its outcropping area as a result of advection. (5) Mode water formation or maintenance is usually associated with wintertime convective mixing due to buoyancy loss from the ocean surface, in a much more limited region than the total area occupied by the mode water. (6) Mode water formation areas occur in conjunction with permanent fronts, on the low-density side of the front, where the isopycnal slopes precondition the region for a thicker layer than occurs on the high-density side of the front.

A minimum in the vertical gradient of potential density (σ_0), or equivalently in the Brunt–Väisälä frequency, is often used to identify mode water (Fig. 5.4.1). Isopycnic potential vorticity is a related quantity that is useful as well, since it is a

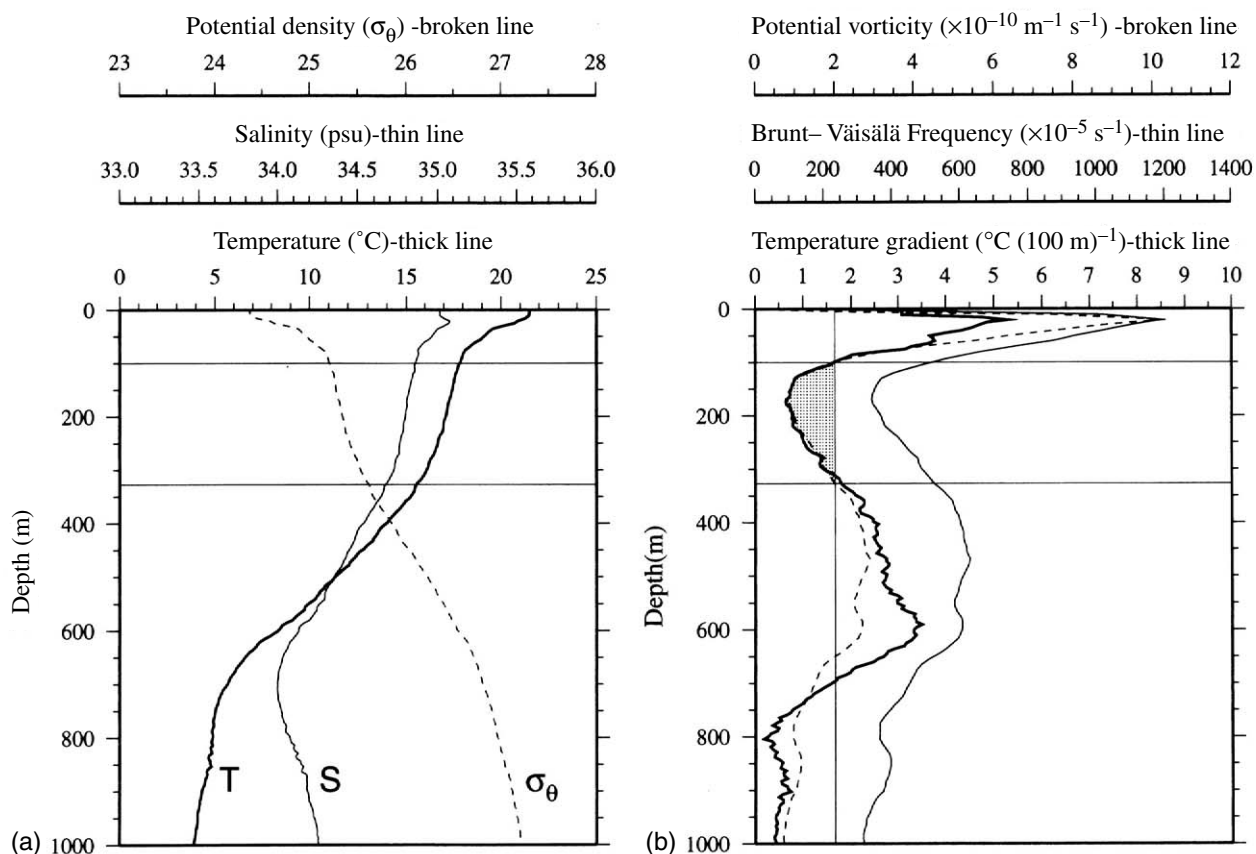


Fig. 5.4.1 Example of a single vertical profile with mode water. This CTD profile was taken at $29^{\circ}5' \text{N}$, $158^{\circ}33' \text{E}$ on May 16, 1993 during KH-93-2 *Hakuho-Maru* cruise. (a) Profiles of potential temperature, salinity and potential density and (b) those of Brunt–Väisälä frequency, potential vorticity (PV) and temperature gradient (sign reversed). The vertical line in the right panel denotes $2 \times 10^{-10} \text{ m}^{-1} \text{ s}^{-1}$ of PV which is approximately equivalent to $1.5^{\circ}\text{C (100 m)}^{-1}$ of temperature gradient (sign reversed) to be used as threshold to identify North Pacific subtropical mode water (NPSTMW). Shaded layer (bounded by two horizontal lines) with PV less than this value can be regarded as NPSTMW.

dynamically conserved property. Potential vorticity depends on the Coriolis parameter (planetary component), the vertical density gradient (stretching component) and local vorticity of the flow (relative vorticity). The last is demonstrably small compared with the stretching component in most regions, and is also difficult to compute from hydrographic data. When relative vorticity is ignored, the potential vorticity quantity (PV) is

$$PV = \frac{f}{\rho} \frac{\partial \rho}{\partial z} \quad (5.4.1)$$

where f is the Coriolis parameter and ρ is the potential density. This is sometimes referred to as isopycnic potential vorticity.

Temperature profiles are more abundant than profiles that include salinity, particularly for studies of variability of mode waters in the North

Pacific. Since both salinity and temperature are relatively homogeneous in mode water, vertical temperature gradients are sometimes used instead of potential vorticity or the vertical gradient of potential density to identify the core of the mode water.

The specific values of potential vorticity or temperature gradient that have been used to define the boundaries of a given mode water are empirical. Values that have been used to trace NPSTMW in space and time are potential vorticity less than $2.0 \times 10^{-10} \text{ m}^{-1} \text{ s}^{-1}$ (Suga *et al.*, 1989) or temperature gradient less than $1.5^{\circ}\text{C (100 m)}^{-1}$ (Hanawa *et al.*, 1988a).

Mode waters have been mapped on isopycnal or core layer surfaces. A core layer is the locus of a vertical extremum of a property (Wüst, 1935). For mode waters, the core layer is the vertical

minimum of potential vorticity, potential density or temperature (e.g. McCartney, 1982).

The low-salinity intermediate waters in the North Atlantic and Southern Ocean are closely associated with mode waters; this association is described in more detail in the next section. The low-salinity intermediate water of the North Pacific on the other hand has not been shown to be associated with mode waters. All three major intermediate waters have some regions of low potential vorticity resulting from convective formation at the sea surface, and in this sense there are similarities to mode waters. The Labrador Sea Water of the North Atlantic is formed from mode waters of the subpolar gyre (Talley and McCartney, 1982). The Antarctic Intermediate Water of the Pacific is a subducted mode water associated with the Antarctic Circumpolar Current. The Antarctic Intermediate Water of the Atlantic and Indian Oceans also arises from this circumpolar mode water, but through advection and modification of the Pacific mode water in Drake Passage (McCartney, 1977).

5.4.3 Geographical distribution of mixed-layer depth and mode waters in the world's oceans

Mode water formation areas are generally characterized by wintertime mixed layers that are relatively thick compared with other mixed layers in the same geographical region. Talley (1999a) mapped the global winter mixed-layer thicknesses, using Reid's (1982) approach employing the depth of high oxygen saturation. This map is reproduced here as Figure 5.4.2 (see Plate 5.4.2, p. 428).

Globally the thickest mixed layers are in the northern North Atlantic and around the northern region of the Southern Ocean in the Pacific and eastern Indian Oceans. These thick layers are associated with the North Atlantic's Subpolar Mode Water and the Southern Ocean's Subantarctic Mode Water, described below. Relatively thick mixed layers are also found in the subtropical mode water areas near the separated western boundary currents.

Mode waters originate as thick winter mixed layers, but are then subducted and advected away from the formation areas. They are usually defined as mode waters after they are capped by either a seasonal pycnocline or the permanent pycnocline

under which they are subducted. The global distribution of mode waters as it was understood in the late 1970s was mapped by McCartney (1982). Talley (1999a) used the global hydrographic data sets compiled by J. Reid and A. Mantyla (personal communication) as well as numerous World Ocean Circulation Experiment (WOCE) stations to produce a new schematic map of mode waters, including the same features as McCartney (1982) and adding newly defined eastern subtropical mode waters and central mode waters (see below). Figure 5.4.3a (see Plate 5.4.3a, p. 428) is a slightly updated version of Talley's (1999a) map, including here more information regarding the density of the mode waters.

Subtropical mode waters associated with western boundary current extensions of subtropical gyres, Type I, are found in all basins (associated with the Kuroshio, Gulf Stream, East Australian Current, Brazil Current and Agulhas Current). These arise from convection in the thickened layers on the south (north) side of the current axes in the northern (southern) hemisphere, where a natural bowl in isopycnal surfaces occurs between the separated current and its recirculation. STMWs, especially in the northern hemisphere, are associated with large surface heat loss from the ocean as a result of cold, dry air outbreaks in winter from the nearby continents. Low potential vorticity (weak stratification or thick mixed layer in winter) associated with these mode waters arises as a result of convection near the axis of the separated western boundary currents, and possibly also from the origin of some of the source water from the equatorward, negative relative vorticity side of the separated current. Equatorward Ekman transport into the STMW formation area may also modify STMW properties, particularly in making them fresher to the east, as is observed in the North Pacific (Suga and Hanawa, 1990). Eddy exchange across the separated boundary current could also accomplish a freshening (Talley, 1997).

A second type of subtropical mode water, of density not very different from STMWs associated with the western boundary current, Type II, is found in the eastern part of the subtropical gyres (light pink in Figure 5.4.3a, see Plate 5.4.3a, p. 428). The Madeira Mode Water (Käse *et al.*, 1985; Siedler *et al.*, 1987) is the archetype of this mode water. Hautala and Roemmich (1998) have described this mode water for the North Pacific. A similar

low-density mode water is evident in the south-eastern South Pacific (mapped in Talley, 1999a, but not fully described anywhere yet). The mechanism for the existence of eastern STMWs, however, has not been elucidated. They appear in the subtropical gyre regions bounded by the equatorward side of permanent zonal fronts (such as the Azores Front in the North Atlantic and the subtropical fronts in the North and South Pacific) and the western side of eastern boundary current fronts (such as the Canary, California and Peru Currents). These eastern mode waters are much weaker than the western STMWs in terms of thickness and area of extent. The North Atlantic and North Pacific eastern STMWs have been studied through the seasons and show major seasonal variability associated with advection and seasonal outcropping. These mode waters are in the primary subduction areas of the gyres and thus provide a useful tracer for ventilation studies within the subtropical gyre.

A third, denser, type of subtropical mode water, Type III, is associated with the subpolar fronts on the poleward boundaries of the subtropical gyres (dark in Fig. 5.4.3a, see Plate 5.4.3a, p. 428). The densities of these mode waters are considerably higher than for the first two types just described. The archetype is the Subantarctic Mode Water, found just north of the Subantarctic Front (McCartney, 1977). A similar mode water is found in the North Pacific (North Pacific Central Mode Water; Nakamura, 1996a; Suga *et al.*, 1997), just south of the Subarctic Front. In the North Atlantic, the Subpolar Mode Water of density near 26.9 to $27.0 \sigma_0$ on the south side of the North Atlantic Current should be identified as this denser type of subtropical mode water, circulating southward into the subtropical gyre, as described by McCartney (1982).

Mode waters are also found around the outside of the cyclonic subpolar circulations (Type IV). The North Atlantic Subpolar Mode Water (SPMW; McCartney and Talley, 1982) is the most obvious of these mode waters, since it is associated with very thick mixed layers (see Figure 5.4.2 (see Plate 5.4.2, p. 428) and description below). A weak version of sub-polar mode water is found around the periphery of the North Pacific subpolar gyre, although it has not been singled out and named. Thick layers occur in the Nordic Seas but have not been singled out as mode waters. Finally, although mode waters have not been reported around the

periphery of the cyclonic gyres south of the Antarctic Circumpolar Current, it is possible that they exist as a result of the downward slope of isopycnals towards the outer side of cyclonic circulations. This could be explored further.

A weak mode water, Type V, has been described in the high evaporation region of the South Atlantic, in conjunction with the high-salinity water observed in the subsurface layer of the subtropical gyre (Tsuchiya *et al.*, 1994), as described below. A feature like this has also been found in the North Pacific, assumed to be due to subduction of high-salinity surface water (Shuto, 1996). High-evaporation, high-salinity surface waters and subducted saline subsurface layers occur in every subtropical ocean. Thus a subsurface potential vorticity minimum (mode water) might be associated with the subtropical underwater in every ocean. These shallow salinity extrema have been given various names in different oceans. We follow the name 'Subtropical Underwater' used by Worthington (1976) for the feature in the North Atlantic. These water masses are described in numerous publications (for the North Atlantic, e.g. Worthington, 1976; for the South Pacific, e.g. Tsuchiya and Talley, 1996; and for the Indian Ocean, e.g. Wyrtki, 1973a; Toole and Warren, 1993).

The mode waters of each basin are described now in more detail. The two northern hemisphere oceans are described first, as they have many features in common, both with limited subtropical and subpolar gyres. The subtropical mode waters of the southern hemisphere subtropical oceans are then treated together since they share similar features. The circumpolar Subantarctic Mode Water, which as mentioned above is actually a type of subtropical mode water, is then described in a section on the Southern Ocean. Table 5.4.1 is the summary of mode waters in the world's ocean, in which acronym, full name, type of mode waters, characteristic temperature ($^{\circ}\text{C}$), salinity, potential density (σ_0) and references are given.

Here note that in the following description, terminology is based on original references as much as possible: Eighteen Degree Water and North Atlantic Subtropical Mode Water (NASTMW) are synonymous.

5.4.3.1 North Atlantic Ocean

The North Atlantic subtropical mode water (Eighteen Degree Water; Worthington, 1959) has

Table 5.4.1 Mode waters of the world's oceans. Acronym, full name, type, characteristic temperature (°C), salinity, potential density (σ_0) and references are given. Types of mode waters are those associated with separated western boundary current (I), those found in the eastern region of the subtropical gyre (II), those associated with the subpolar front (III) and those associated with the outer side of cyclonic circulation (IV). See the text for details. Type V mode waters ('Subtropical Underwaters', e.g. shallow subtropical salinity maxima) are not included in the list but are present in each ocean.

| Acronym | Full name | Type | Temperature (°C) | Salinity | Potential density σ_0 | References |
|-----------------------|-------------------------------------|---------|------------------|-----------|------------------------------|---|
| <i>Atlantic Ocean</i> | | | | | | |
| NASTMW ^a | North Atlantic STMW | I | 18 | 36.5 | 26.5 | Worthington (1959) |
| MMW | Madeira Mode Water | II | 16–18 | 36.5–36.8 | 26.5–26.8 | Käse <i>et al.</i> (1985), Siedler <i>et al.</i> (1987) |
| SPMW ^b | Subpolar Mode Water | III, IV | 8–15 | 35.5–36.2 | 26.9–27.75 | McCartney (1982), McCartney & Talley (1982) |
| SASTMW | South Atlantic STMW | I | 12–18 | 35.2–36.2 | 26.2–26.6 | Provost <i>et al.</i> (1999) |
| SAESTMW | South Atlantic Eastern STMW | II | 15–16 | 35.4 | 26.2–26.3 | Provost <i>et al.</i> (1999) |
| <i>Pacific Ocean</i> | | | | | | |
| NPSTMW | North Pacific STMW | I | 16.5 | 34.85 | 25.2 | Masuzawa (1969, 1972) |
| NPESTMW | North Pacific Eastern STMW | II | 16–22 | 34.5 | 24–25.4 | Hautala & Roemmich (1998) |
| NPCMW | North Pacific Central Mode Water | III | 9–12 | 34.1–34.4 | 26.2 | Nakamura (1996a), Suga <i>et al.</i> (1997) |
| SPSTMW | South Pacific STMW | I | 15–19 | 35.5 | 26.0 | Roemmich & Cornuelle (1992) |
| SPESTMW ^c | South Pacific Eastern STMW | II | 13–20 | 34.4–35.5 | 25.5 | Tsuchiya & Talley (1996) |
| <i>Indian Ocean</i> | | | | | | |
| IOSTMW | Indian Ocean STMW | I | 17–18 | 35.6 | 26.0 | Gordon <i>et al.</i> (1987), Toole & Warren (1993) |
| <i>Southern Ocean</i> | | | | | | |
| SAMW | Subantarctic Mode Water | III | 4–15 | 34.2–35.8 | 26.5–27.1 | McCartney (1977) |
| SEISAMW ^d | Southwest Indian SAMW | III | 8 | 34.55 | 26.8 | Thompson & Edwards (1981), McCarthy & Talley (1999) |

^a Eighteen Degree (18°) Water.

^b There are various varieties of SPMW. See the text for details.

^c This terminology is tentative and no formal name is given yet.

^d SEISAMW is a variety of SAMW.

properties centred at 18°C, 36.5 psu and 26.5 σ_0 (this form will be used in the present chapter to indicate characteristic temperatures, salinities and densities). It is found throughout the northwestern part of the subtropical gyre. Its formation area is just south of the Gulf Stream Extension, most likely associated with the wall and meanders of the current (Talley and Raymer, 1982), and in an area of very high surface heat loss to the atmosphere. In winter the mixed layer where Eighteen

Degree Water is formed is as deep as 350 to 400 m (Worthington, 1959). The temperature of the core is lower to the east, suggesting that advection and cooling along the Gulf Stream are part of the formation process. The Eighteen Degree Water is advected southward out of the Gulf Stream Extension region, filling the western subtropical gyre (Worthington, 1976).

The stability of Eighteen Degree Water properties was demonstrated by Schroeder *et al.* (1959)

using data near Bermuda dating back to the *Challenger* voyage in 1873 and including the then 4-year time series at the Panulirus station (1954–58). Ebbesmeyer and Lindstrom (1986) showed that newly formed NASTMW may persist for several years within the Gulf Stream recirculation. On the other hand, within the relative stability of Eighteen Degree Water existence and properties, variations are clear (Talley and Rayner, 1982; Talley, 1996) – thickness changes reflect variations in formation rate while temperature and salinity changes also reflect changes in surface forcing and possibly exchange with other regions, as reviewed below (Section 5.4.4).

The Madeira Mode Water (MMW; Siedler *et al.*, 1987; earlier observations by Käse *et al.*, 1985) is the archetype of the relatively low-density subtropical mode waters of the eastern subtropical gyres. Using hydrographic and historical XBT (eXpendable BathyThermograph) data, Siedler *et al.* documented the existence of this mode water, which is clearly distinct from the Eighteen Degree Water of the western subtropical gyre. It is associated with the warm side of the Azores Front and is offshore of the coastal upwelling area. The MMW has temperature and potential density ranges of 16–18°C and 26.5–26.8 σ_0 . Winter mixed layers in its formation region are about 200 m thick (Käse *et al.*, 1985). Although the MMW almost disappears as a thick mode by the end of summer (Siedler *et al.*, 1987), it is advected southwestward from its formation and joins the thermocline as part of the North Atlantic Central Water. This layer has been the focus of intensive investigations into the subduction process, in which the water was observed from winter outcrop to restratification, deepening and potential vorticity homogenization (Joyce *et al.*, 1998).

Mode waters of higher density in the northern subtropical gyre and the subpolar gyre of the North Atlantic were documented by McCartney and Talley (1982), and called Subpolar Mode Water (SPMW), with a density range of 26.9 σ_0 east of Newfoundland to 27.75, in the Labrador Sea. The very smooth, broad-scale description of the SPMW in that first paper suggested that SPMW originates as thick layers at 14–15°C in the North Atlantic Current loop. The concept was that these layers are advected eastward south of the North Atlantic Current to the eastern Atlantic, becoming cooler and denser along the path. These

11–12°C SPMWs were then thought to split to the south and north, with the southward flow entering the subtropical gyre thermocline (McCartney, 1982). These southward flowing SPMWs are often called Eastern North Atlantic Water (e.g. Harvey, 1982; Pollard *et al.*, 1996). The northward flow becomes the inflowing warm surface water of the subpolar gyre. These northward-flowing SPMWs continue to cool and increase in density, with 8°C water found east of Iceland. This SPMW then splits, with a portion entering the Norwegian Sea as the main part of the warm Atlantic inflow to the Arctic, and hence the precursor to North Atlantic Deep Water formation. The remainder was thought to circulate westward past Iceland into the Irminger Sea and then on into the Labrador Sea, eventually cooling enough to become Labrador Sea Water (Talley and McCartney, 1982).

There is a reason however to consider major modifications to this picture of the SPMW formation, transformation and circulation. The portion of the SPMW that is south of the North Atlantic Current and the 11–12°C water of the northeastern subtropical gyre are really mode waters of the northern subtropical gyre, located south of the wind-stress curl gyre boundary. In this sense, these waters are similar to the North Pacific Central Mode Water described by Nakamura (1996a) and Suga *et al.* (1997). The relative amount of the SPMW that turns northward to continue transformation to higher density has not yet been quantified well. Other modifications to the large-scale picture of SPMW transformation are emerging as well (Talley, 1999b): the Subarctic Front, which is the extension of the North Atlantic current, turns northeastward between the Reykjanes Ridge and Rockall Plateau. It separates SPMWs of the eastern and western subpolar gyre. A connection between the eastern and western SPMWs is not clear since strong, permanent westward surface flow just south of Iceland is not apparent in the climatological circulation. The warmer SPMWs of the eastern subpolar gyre feed the Norwegian Sea. The origin of the colder SPMWs of the western subpolar gyre, which feed the Labrador Sea convection, are not as clear, but may come from a different part of the North Atlantic Current/Subarctic Front. This region is under intensive study as one of the last WOCE process studies, leading into a CLIVAR (Climate Variability and Predictability) study of decadal and centennial change.

The fresh intermediate water of the North Atlantic, the Labrador Sea Water (LSW), arises from convection in the western Labrador Sea (Clarke and Gascard, 1983; Pickart *et al.*, 1997; Lazier *et al.*, Chapter 5.5) and is advected throughout the subpolar Atlantic and into the subtropical Atlantic (Figure 5.4.3b, see Plate 5.4.3b, p. 428; from Talley, 1999a). The source waters of LSW are the Subpolar Mode Waters – LSW can be considered the densest of the SPMWs. It is characterized in the subpolar North Atlantic as a pycnostad, a salinity minimum and an oxygen maximum (Talley and McCartney, 1982). It is a salinity minimum in the subpolar region because of the large inflow of saline subtropical surface waters (that become the SPMW). LSWs signature in the subtropical North Atlantic is not as clear because it is opposed by the saline Mediterranean Outflow Water, which occupies a similar density range and which mixes with LSW. In the tropical and South Atlantic, LSW and Mediterranean Outflow Water are considered to be part of the southward-flowing North Atlantic Deep Water. Here LSW contributes the high-oxygen core known as Middle North Atlantic Deep Water (Wüst, 1935).

5.4.3.2 North Pacific Ocean

North Pacific Subtropical Mode Water (NPSTMW) is found throughout the northwestern part of the subtropical gyre (Hanawa, 1987; Bingham, 1992). Hanawa and Suga (1995) provided a thorough review of NPSTMW studies.

The core of NPSTMW is 16.5°C, 34.85 psu and 25.2 σ_0 . The approximate outcrop area is the zonal band from the Izu Ridge to the international date-line in longitude and from 28°N to the Kuroshio Extension (Hanawa and Hoshino, 1988; Yasuda and Hanawa, 1997, 1999; Hanawa and Yoritaka, 2000). In late winter, a well-developed mixed layer thicker than 300 m is formed in this area. In the formation area, temperature and salinity decrease from west to east (Suga and Hanawa, 1990; Bingham, 1992). This decrease of salinity to the east reflects the input of northern surface water with lower salinity through Ekman transport.

The source water of NPSTMW is apparently the Kuroshio Extension (Bingham, 1992). The surface temperature of the Kuroshio Extension decreases eastward, corresponding to a local heat loss of more than 800 W m^{-2} in winter. Maps of acceleration potential, which yield the geostrophic

flow on isopycnals (Montgomery, 1938), suggest that the Kuroshio water detrains southward into the thick layers in the formation area of NPSTMW. Thus the eastward decrease in NPSTMW temperature is more a function of the Kuroshio Extension temperature than an indication of eastward advection of the NPSTMW itself. The NPSTMW formation area lies dynamically between the Kuroshio Extension and a westward recirculation south of the Kuroshio Extension. Winter convection in the narrow region just south of the Kuroshio, perhaps accentuated in anticyclonic meander regions, thickens the NPSTMW layer further. Using maps of potential vorticity on isopycnals, Suga and Hanawa (1995b) showed the seasonal movement of NPSTMW formed in the western part of the formation region. Based on synoptic surveys in 1987 and 1888, Suga and Hanawa (1995a) described the substantial advection of NPSTMW by anticyclonic eddies propagating westward in the region south of Japan. During Kuroshio large meander periods, the intrusion of NPSTMW into the region just south of Japan is blocked and the NPSTMW path is shifted further south (Suga and Hanawa, 1995b).

A denser type of subtropical mode water was described by Nakamura (1996a) and Suga *et al.* (1997), who named it North Pacific Central Mode Water (NPCMW). This mode water is distributed in the central North Pacific (approximately 170°E to 150°W) between the Kuroshio Extension Front (approx. 33°N) and the Kuroshio Bifurcation Front (approx. 40°N). NPCMW has a temperature of 9–12°C and potential density around 26.2 σ_0 . This water is synonymous with the ‘stability gap’ described by Roden (1970), by which was meant the lowered stability region south of the Subarctic Front. Southward Ekman transport of cool, fresh water may play a role in decreasing the stability of this region. Reid (1982) showed that winter mixed layers in this region are thicker than anywhere else in the North Pacific, including the NPSTMW region. Very thick mixed layers ($>500 \text{ m}$) are found locally in Kuroshio warm core rings just east of Honshu, which may precondition the central region to have particularly thick winter mixed layers, and hence be a precursor to the NPCMW.

The third, low-density, mode water of the subtropical gyre is found in the eastern North Pacific. Using the WOCE high-density XBT data between Honolulu and San Francisco as well as historical

XBT data in this well-observed region, Hautala and Roemmich (1998) described this mode water (NPESTMW), whose low potential vorticity influence was documented by Talley (1988). This water is analogous to the Madeira Mode Water of the North Atlantic (Siedler *et al.*, 1987). NPESTMW has temperatures from 12 to 22°C and potential density $24\text{--}25.4\sigma_0$. As with the Madeira Mode Water, NPESTMW is subducted and advected southward, mixing along its path. Hautala and Roemmich showed the formation of NPESTMW in each winter. The temperature of the potential vorticity minimum was similar in the periods 1970–79 and 1991–97 (with inadequate data for the intervening period). This eastern region of the North Pacific has received some attention as a possible source for decadal changes that might propagate to the tropics and influence El Niño. Schneider *et al.* (1999b) used depths of isopycnal surfaces and its variations as a primary tracer of subduction/advection changes in the eastern subtropical Pacific, finding that the tropical influence of the subtropical waters was minimal.

Unlike the North Atlantic and Southern Ocean, the North Pacific does not have a distinct subpolar mode water, in the sense of thick layers that are maintained by winter convection. However, relatively thick layers, marked by lower potential vorticity, are found around the rim of the subpolar gyre, particularly in the Gulf of Alaska (Talley, 1988). These layers lie above the strong and relatively shallow pycnocline, which is maintained in part by freshwater input at the sea surface. It might, however, be misleading to call the thick layers mode waters, except insofar as they are dynamically similar to the much more dramatic Subpolar Mode Water of the North Atlantic.

The low-salinity intermediate water of the North Pacific, North Pacific Intermediate Water (NPIW), is not closely associated with mode waters, unlike the LSW of the North Atlantic. The ventilation source of NPIW is the Okhotsk Sea and Oyashio region (Reid, 1965; Talley, 1993). In the Okhotsk Sea, brine rejection during sea-ice formation on the broad shelves ventilates the intermediate densities (Kitani, 1973; Talley, 1991). Convection in the southern Okhotsk Sea creates a low potential vorticity signature in the upper portion of the ventilated layer (Yasuda, 1997), and could be considered an indicator of mode water. The newly ventilated waters enter the North

Pacific and are advected into both the subpolar and subtropical gyres. NPIW is not apparent as a core layer in the subpolar gyre because the overlying surface waters are even fresher than NPIW (unlike the situation in the North Atlantic), and because the potential vorticity signature of NPIW is weak. NPIW is characterized by a salinity minimum in the evaporative subtropical gyre because there are no other sources of water at this density, unlike the North Atlantic, which has saline subsurface input from the Mediterranean.

5.4.3.3 Subtropical South Atlantic Ocean

The South Atlantic subtropical gyre has several prominent fronts, each with its own subtropical mode water (Tsuchiya *et al.*, 1994; Provost *et al.*, 1999). Tsuchiya *et al.* documented three mode waters along 25°W, plus a weak pycnostad at the Antarctic Intermediate Water density. Provost *et al.* showed the geographical distribution of these mode waters and provided details regarding their formation regions. These include two types of Subantarctic Mode Water (SAMW; McCartney, 1977, 1982) and a type of subtropical mode water that is associated with the surface salinity maximum of the central subtropical gyre. The SAMWs are clearly part of the subtropical gyre rather than of a high-latitude cyclonic gyre, and should perhaps be best identified as subtropical mode waters, which is how Provost *et al.* identify them. The southernmost SAMW lies between the Subtropical Front and the separated Brazil Current Front, with approximate properties of 12°C, 35.1 psu and $26.7\sigma_0$. North of the Brazil Current Front is found a less dense SAMW, at about 13.5°C, 35.3 psu and $26.6\sigma_0$. McCartney (1982) mapped these two modes as a single mode water at about $26.5\sigma_0$, showing the limited geographical area and weakness of the mode compared with those of other oceans.

Provost *et al.* also describe a lighter STMW, at $26.2\sigma_0$, in the Brazil Current recirculation region and restricted to a smaller western region than the mode waters they identified at 26.5 and $26.6\sigma_0$ (corresponding to the mode waters identified by Tsuchiya *et al.*, 1994). They mapped the winter outcrop windows and extent of influence of all three of these mode waters, showing that all originate primarily in the western South Atlantic, in the overshoot and recirculation area of the Brazil Current, i.e. the southwestern corner of the Brazil Current. The dominant mode water has properties

of 14–16°C, 35.5–35.9 psu and $26.5\sigma_0$. They also showed a qualitative correlation between the observed variations of SASTMW and interannual atmospheric forcing using National Centers for Environmental Prediction (NCEP) re-analysis data. Provost *et al.* also note mode waters associated with Agulhas Rings containing Indian Ocean waters.

A fourth subtropical gyre mode water shown by Tsuchiya *et al.* (1994) is in the region between 24°30'S and 11°30'S. It is associated with the subtropical high-salinity water, with properties of 21°C, 36.5 psu and $25.6\sigma_0$. This salinity maximum water, which is also known as Subtropical Underwater, apparently achieves its thickness from the buoyancy loss associated with evaporation, and is considered a mode water here since it retains its thickness after subduction.

5.4.3.4 Subtropical South Pacific Ocean

The subtropical gyre of the South Pacific has a weak subtropical mode water between New Zealand and Fiji, as shown by Roemmich and Cornuelle (1992) using WOCE high-density XBT lines. This South Pacific STMW lies north of the Tasman Front and East Auckland Current, which originate as the separated East Australian Current. Perhaps in accord with the weakness of the East Australian Current itself, the SPSTMW is relatively poorly developed (thin) compared with NASTMW and NPSTMW. The STMW properties are 15–19°C with a typical salinity of 35.5 psu and core density around $26.0\sigma_0$. Roemmich and Cornuelle showed that the SPSTMW volume (inventory in the cross-section) decreased dramatically between 1986 and 1991. They speculated that this decrease might be due either to long-period change in air-sea heat exchange or to fluctuations in heat transport by ocean currents.

A shallow, low-density subtropical mode water, similar to the Madeira Mode Water (MMW) of the North Atlantic and the northeastern subtropical mode water of the North Pacific (NPESTMW), is found in the southeastern Pacific. Its core density is $25.5\sigma_0$, with a temperature range of 13–20°C and salinity of 34.3–35.5 psu. This feature is evident in WOCE sections (e.g. Tsuchiya and Talley, 1996), and has not yet been described in a separate publication.

5.4.3.5 Subtropical Indian Ocean

Subtropical mode water is found in the southwest Indian subgyre (Gordon *et al.*, 1987; Olson *et al.*,

1992; Stramma and Lutjeharms, 1997). Indian Ocean STMW properties are 17–18°C and 35.6 psu. Toole and Warren (1993) found this STMW (at 17°C and $26.0\sigma_0$) west of about 45°E on their hydrographic section at 32°S. They remarked on the relative weakness of this pycnostad compared with its northern hemisphere counterparts, suggesting that surface heat loss in the Agulhas region is likely much lower than in the northern hemisphere regions. Colder, fresher mode water is found within the Agulhas rings that detach from the retroflection and propagate westward into the South Atlantic (Olson *et al.*, 1992). The data used in these studies are from synoptic surveys. The distribution area, water properties and temporal variability of this STMW have not been mapped.

The eastern South Indian Ocean is dominated by the local type of Subantarctic Mode Water, called the Southeast Indian Subantarctic Mode Water (SEISAMW), which is discussed in the next section.

5.4.3.6 Southern Ocean

The Southern Ocean is dominated by the major fronts of the Antarctic Circumpolar Current. The northernmost front is the Subantarctic Front (SAF), which lies close to the zero wind-stress curl line and hence is the southern boundary of the subtropical gyres (see also Rintoul *et al.*, Chapter 4.6, Fig. 4.6.2). The SAF is furthest north in the western South Atlantic, where it is identical with the Falkland Current front. The SAF moves southward as it rounds Antarctica, and is furthest south in the southeastern Pacific where it enters Drake Passage. North of the SAF, the winter mixed layers reach to more than 700 m thickness (Fig. 5.4.2, see Plate 5.4.2, p. 428). McCartney (1977, 1982) first described the totality of these thick mixed layers, giving them the name Subantarctic Mode Water (SAMW). The SAMW water properties vary in relation to the southward spiralling of the SAF around Antarctica. The warmest SAMW (15°C, 35.8 psu, $26.5\sigma_0$), which is the same as the main Subtropical Mode Water discussed by Provost *et al.* (1999), occurs where the SAF is furthest north, in the western Atlantic. The coldest SAMW (4–5°C, 34.2 psu, $27.1\sigma_0$) occurs just west of Drake Passage.

It is not clear how continuous the SAMW is around the whole of the Subantarctic Front. McCartney's (1977) hypothesis was that the warmest, least dense SAMW in the western Atlantic smoothly transforms to the coldest, densest SAMW

and hence Antarctic Intermediate Water (AAIW) west of Chile. On the other hand, McCartney (1982) showed substantial northward circulation of the SAMW in each ocean basin. The thick SAMW in the southeast Indian Ocean is singled out and called the SEISAMW because of its major impact on ventilation of the Indian Ocean's subtropical gyre thermocline through subduction and northward advection. The SEISAMW advection leads to a thick layer of high oxygen that persists even into the tropics (McCarthy and Talley, 1999). A less dense SAMW is subducted and advected northwards in the western Indian Ocean (McCartney, 1982). Likewise, the northward circulation of the densest SAMW in the east, near Chile, provides a major ventilation signal of high oxygen for the South Pacific, associated with the low salinity. This subducted SAMW is the Antarctic Intermediate Water (AAIW) of the Pacific. SAMW subducted and advected northward in the western South Pacific is less dense than the AAIW and provides an oxygen-rich layer in the western South Pacific.

It is likely that, as with the North Atlantic SPMW, both hypotheses – of continuous eastward flow and of substantial equatorward advection – are correct. Thus the SAMW ventilates the Indian as SEISAMW and the Pacific as both SAMW and AAIW through subduction, while at the same time a portion of the SAMW continues eastward and is gradually transformed into colder, denser SAMW, with the final portion flowing through Drake Passage to become the main core of the AAIW in the Atlantic and Indian Oceans (Talley, 1997). The SAMW is modified somewhat during this passage, and then at the confluence of the Falkland and Brazil Currents enters the South Atlantic and Indian gyres as a salinity minimum (Atlantic/Indian Antarctic Intermediate Water; Talley, 1996a).

There is a wide variation in the thickness of SAMW (reflected in mixed-layer thickness in Figure 5.4.2, see Plate 5.4.2, p. 428), with the thickest layers being found in the eastern Indian Ocean (SEISAMW) and across the South Pacific, with somewhat shallower layers in the South Atlantic and western Indian Ocean (Piola and Georgi, 1982). The transition to thick layers in the central Indian Ocean is sudden and occurs just east of Kerguelen Plateau; a cause has not been established. Thompson and Edwards (1981) observed winter formation of SEISAMW with approximate properties of 8°C and 34.55 psu, confirming

McCartney's (1977) finding for SAMW properties in this region. They pointed out, as did McCartney, that unlike in the South Atlantic, SAMW in this area cannot contribute locally to the formation of AAIW.

A major open question regarding SAMW is the role of northward Ekman transport across the SAF in maintaining the volume and thickness of the SAMW. The SAF lies near the maximum westerly wind stress (and hence zero wind-stress curl), and so northward Ekman transport is largest there. Various estimates place the net northward Ekman transport at about 10 Sv ($1\text{ Sv} = 10^6 \text{ m}^3 \text{ s}^{-1}$) around the circumpolar belt. This is a good fraction of the net 5 Sv and 14 Sv of SEISAMW and AAIW, respectively, that move northward into the subtropical gyres (Talley, 1999a for SEISAMW, and Schmitz, 1995 for AAIW). The remaining subducted transport would then originate in the subtropical gyres. Using a high-resolution numerical model, Ribbe and Tomczak (1997b) and Ribbe (1997) examined the effect of northward Ekman transport of the Antarctic surface water on water properties of SAMW. They noted that this cold and fresh water might also drive mid-latitude convection itself to form SAMW. Using air-sea fluxes, Speer *et al.* (1997) estimated a formation rate of 25 Sv of SAMW in the Indian Ocean in the density range $26.5-27.2 \sigma_0$, with a peak formation rate at $26.9 \sigma_0$; geostrophic estimates from their inverse model suggest that half remains in the Indian and half is exported to the Pacific. This large SAMW formation rate is reflected in the proxy mixed-layer map of Figure 5.4.2 (see Plate 5.4.2, p. 428) where an abrupt change in mixed-layer depths is apparent in the central Indian Ocean.

Antarctic Intermediate Water (AAIW) is the low-salinity intermediate-depth layer of the southern hemisphere (distribution in Figure 5.4.3b, see Plate 5.4.3b, p. 428). As noted above, it is very closely associated with SAMW. AAIW in the Pacific Ocean originates in the southeast near Chile, where it is identical with the local SAMW (McCartney, 1977). Convection in this region reaches to about 600 m based on oxygen profiles (Tsuchiya and Talley, 1998). SAMW/AAIW is subducted northward into the South Pacific subtropical gyre. The resulting low-salinity layer is apparent throughout the Pacific up to the southern boundary of the North Pacific's subtropical gyre. Part of the convected water near Chile flows

through Drake Passage on the northern side of the Subantarctic Front. Some modification of properties occurs in this region. When the thick layer reaches the confluence of the Brazil and Malvinas Currents, it plunges down and spreads out into the South Atlantic/Indian subtropical gyre as a salinity minimum (McCartney, 1977; Talley, 1996a). An oxygen maximum is associated with the AAIW through much of the South Atlantic. A pycnostad is also associated with this new AAIW in the southwestern South Atlantic, but is much weaker and more geographically restricted than in the South Pacific, presumably because of vigorous mixing at the western boundary as it enters the Atlantic. There are no sources of AAIW elsewhere in the Atlantic and Indian Oceans, as is apparent from the changes in salinity, oxygen and potential vorticity away from the Brazil/Malvinas confluence. Major modification of AAIW occurs through mixing, and the various AAIWs referred to in the literature reflect these regional mixings rather than new ventilation.

5.4.4 Temporal variability of mode water properties and distribution

A marked characteristic of mode waters is their apparent stability in properties and location (Schroeder *et al.*, 1959; Warren, 1972). Thus mode water distributions, such as shown in Figure 5.4.3a (see Plate 5.4.3a, p. 428), and approximate core properties can be mapped using data sets from all decades. The stability of properties and, indeed, the interbasin similarity in temperature (although not density because of interbasin salinity differences) are remarkable and clearly associated with the largest scale, longest time-scale wind and buoyancy forcing. Of course, however, there is some variation in properties of the mode waters, which has been studied in areas where time series are adequate. These variations in these near-surface water masses, in temperature, salinity, density and thickness, are linked to surface forcing changes, although in some cases the connection is not yet obvious. In this section, we briefly review the temporal variability of mode waters where it has been documented.

5.4.4.1 Seasonal variation

After the formation of mode water in late winter, it is capped by the seasonal thermocline, due to incident solar radiation. As the seasons progress, mode water is advected away from the formation area

and sometimes becomes permanently capped. In order to trace the seasonal evolution of North Pacific STMW, Suga and Hanawa (1995b) mapped potential vorticity and deduced that the main body of NPSTMW formed in the western part of the formation area is advected westward by the Kuroshio recirculation. During this movement, the NPSTMW is subject to substantial diapycnal mixing.

The seasonality of NASTMW has not been investigated to the same degree as NPSTMW. At Bermuda, which is well downstream of the formation area, seasonality of the mixed layer depths is clear, with a sudden shoaling of near-surface isopycnals during late winter followed by a gradual deepening of the isopycnals through the rest of the year (Talley and Rayner, 1982). However, a seasonal cycle in mode water properties at this site, which is some distance from the mode water outcrop, is not easily apparent.

In the South Pacific STMW, Roemmich and Cornuelle (1992) showed a large seasonal change in mode water inventory and properties using seasonal XBT sampling.

The eastern Subtropical Mode Waters of the North Atlantic and North Pacific have both been studied at the seasonal cycle. Siedler *et al.* (1987) and Hautala and Roemmich (1998) both show the seasonal outcropping of the Madeira Mode Water (MMW) and eastern North Pacific STMW (NPESTMW). Siedler *et al.* show the advection of the MMW downstream after capping in late winter and the near disappearance of the mode in late fall after heating from above and possibly diapycnal mixing. Likewise Hautala and Roemmich show the strength of the eastern North Pacific mode just after it is capped at the end of winter, and its decline in strength as the surface layer restratifies further through the summer and fall.

The seasonality of other mode waters has not been documented to our knowledge.

5.4.4.2 Interannual variations

Interannual variability is roughly defined as variability on time scales of 2 to about 7 years, encompassing the El Niño time scale, but not extending to the decadal time scale.

In the North Pacific STMW, large year-to-year variabilities in temperature and its distribution have been described, especially in relation to the strength of interannual Wintertime East Asian Monsoon. Monsoon strength is well represented

by the Monsoon Index (MOI), which can be defined as the sea-level pressures between Nemuro, Japan, and Irkutsk, Russia (Hanawa *et al.*, 1988b; Watanabe, 1990). Suga and Hanawa (1995c) demonstrated a good correlation between the MOI and the potential vorticity and apparent oxygen utilization of NPSTMW along the repeated 137°E section. This means that severe wintertime cooling in the formation region causes the high formation rate of colder and oxygen-rich NPSTMW. Hanawa and Yoritaka (2000) described the year-to-year variation of NPSTMW core layer temperatures using XBT data taken along 32°30'N once a year from 1990 to 1993. Over the data period of 4 years, core layer temperatures in the western part of the formation area between 140°E and 160°E substantially changed, with a range of 0.7°C, apparently associated with the MOI. These changes were confirmed by Taneda *et al.* (2000) using data taken around the Ogasawara Islands, which is the downstream site of the Kuroshio recirculation. Yasuda and Hanawa (1999) clarified the above change in temperature and area distribution by making composites of water properties with respect to the MOI.

A local interannual signal of NPSTMW in the region south of Honshu is due to the existence or disappearance of the large meander of the Kuroshio (Suga and Hanawa, 1995a). When the Kuroshio large meander is present, NPSTMW is blocked from advecting westward by the Kuroshio recirculation into the region south of Japan. This is also confirmed by the repeat hydrographic observations at 137°E (Suga and Hanawa, 1995c).

For the South Pacific STMW, as mentioned in the previous subsection, Roemmich and Cornuelle (1992) described variations over 5 years using the first WOCE high-density XBT survey. However, the time series was too short to determine if the time scale of the variations was actually interannual or longer.

An interannual signal for the North Atlantic STMW (Eighteen Degree Water) has not been sought using long time series, since the record appears to be dominated by decadal variation (see below). Klein and Hogg (1996) described the variation of water properties and formation rate from 1987 to 1990 using moored data as well as XBT data in the eastern part of the recirculation region of the Gulf Stream. They found that the severe winter of 1988 led to the formation of a colder

type of mode water, followed by increasing temperature after the mild winter of 1989. They also pointed out that since the relationship between winter forcing and water properties was qualitative, advection could strongly influence the water properties.

5.4.4.3 Decadal variations and abrupt shifts

The North Atlantic Eighteen Degree Water has demonstrable decadal variations, possibly associated with variations in the North Atlantic Oscillation. Using Sea Surface Temperature (SST) records in the Eighteen Degree Water formation area and at Bermuda and Ocean Weather Station E, Fieux and Stommel (1975) described a warming of late winter SST from 1910–20 to a maximum in 1950–60, and thereafter cooling. Talley and Raymer (1982), Jenkins (1982) and Talley (1996b) documented the variability of Eighteen Degree Water core and isopycnal properties using the hydrographic time series at Bermuda, which was started in 1954 (Figure 5.4.4, see Plate 5.4.4, p. 428; from Talley, 1996b). Joyce and Robbins (1996) and Talley (1996b) continued the Bermuda time series analysis, showing that salinity changes on isopycnals in the upper ocean at Bermuda, including through the Eighteen Degree Water core, correlate well with the North Atlantic Oscillation (NAO) index. The Eighteen Degree Water was strong in three periods – 1956–57, the late 1960s and the early 1980s – coinciding with low NAO. The mode water was weakest from 1975 to 1978, just following a year with high NAO and low surface salinity. Looking at potential vorticity as a marker of the core of Eighteen Degree Water, it appears that the core density, rather than being somewhat cyclic like isopycnic salinity, changes discretely. Such changes occurred around 1965, 1975, 1980 and 1985–87. During the intervening periods, the density was rather stable, with the exception of the very weak STMW period of 1975–78. The density of the core for these periods has ranged from 26.4 to 26.55 σ_0 .

Dickson *et al.* (1996) showed that SST in the Sargasso Sea (Eighteen Degree Water formation area) is out of phase on a decadal scale with SST in the Labrador Sea and in phase with SST in the Greenland Sea (see also Dickson *et al.*, Chapter 7.3, in particular Fig. 7.3.5). Thus formation of Eighteen Degree Water is out of phase with convective formation of intermediate water in the

Labrador Sea. Dickson *et al.* attributed this large-scale pattern to the NAO, in which Labrador Sea Water formation is vigorous when the westerlies take a northern path, and in which Eighteen Degree Water formation is vigorous when the westerlies shift towards the south and west.

In the North Pacific subtropical gyre, Bingham *et al.* (1992) compared surface temperature structures of the western North Pacific in two pentads, 1938–42 and 1978–82, using hydrographic data for the former and mostly XBT data for the latter. They found that NPSTMW during the former period was thicker, more uniform in temperature and more confined geographically. They speculated that the greater thickness during the former pentad resulted from stronger wintertime cooling, and that the difference in geographic extent between the two pentads might be caused by reduced advection of the Kuroshio, which was in a large meander state for a larger fraction of the former pentad.

In the mid-1970s, all environmental variables for the North Pacific showed a shift into a state dominated by a deep Aleutian Low (Nitta and Yamada, 1989; Trenberth, 1990; Tanimoto *et al.*, 1993). Yasuda and Hanawa (1997) compared temperature fields for the decades before and after the shift: 1966–75 and 1976–85. In the latter decade, North Pacific Central Mode Water (NPCMW) was widely distributed and its temperature was much colder than before. In the western subtropical gyre, in the North Pacific STMW (NPSTMW) formation area, the water in the southwest was warmer in the latter decade, while colder water occupied the eastern part. These decadal changes in temperature for NPSTMW and NPCMW were attributed partly to the enhancement of heat loss at the sea surface and from enhanced Ekman heat divergence and partly to the larger heat advection by the Kuroshio, which was spun-up during the latter decade.

5.4.4.4 **Comments on temporal variability of mode waters**

As mentioned in the beginning of Section 5.4.4, the existence of substantial temporal variability on various time scales is expected since mode water formation reflects late winter conditions, which

have interannual and decadal variability. Variability in circulation strength, which is related to wind-field strength, also affects mode water properties, for instance in the effect of a strengthened Kuroshio on NPSTMW temperature, or the effect of the Kuroshio large meander on NPSTMW distribution. The variability of NASTMW and NPSTMW have been documented to some degree, although the mechanisms for their variations have not been fully explored. Unfortunately at present data are lacking to undertake such studies for the rest of the mode waters. It is expected that the accumulation of monitoring data like XBT/XCTD measurements, among others, will make the description of variability possible in the near future and that these results will provide new insight to ocean climatic variations and changes.

5.4.5 **Summary**

Mode waters are part of the continuous stratification of the upper oceans, where they are prominent because of their volumetric significance. Thus they are likely to have a disproportionate influence on surface water and surface temperature evolution, which are central to ocean–atmosphere climate interactions. As a community, we have not yet fully documented the properties and distribution of mode waters, which must be the first step. This work is in progress by a number of investigators, including the authors and collaborators. Second, fluxes, formation rates and mechanisms are far from elucidated, including for instance basic questions about the reason for the existence of the eastern subtropical mode waters, the role of eddies in formation, and even the role of topography and local mixing for some mode waters such as Subpolar Mode Water that are close to boundaries.

The authors hope that in the WOCE-AIMS (Analysis, Interpretation, Modelling and Synthesis) period, using various kinds of observations taken during WOCE, including hydrography, XBTs, surface temperatures and fluxes, every mode water in the world's oceans will be fully described, with major progress in understanding mechanisms for formation and feedback of mode waters on the atmosphere.

5.5

Deep Convection

John Lazier, Robert Pickart and Peter Rhines

5.5.1 Convection and spreading

Density of ocean water generally increases with depth. At the surface, however, stirring by waves and convection creates a well-mixed homogeneous layer. Waves alone can mix the upper ≈ 50 –100 m. But convection, forced by an increase in density at the surface via heat loss or evaporation, can greatly increase the mixed-layer depth. During winter, heat loss from the surface of the ocean is high and convectively mixed surface layers are the norm in the extratropical oceans. The deepest (> 1500 m) are found in the Labrador Sea (Fig. 5.5.1), the Greenland Sea (see Dickson *et al.*, Chapter 7.3) and the Golfe du Lion in the Mediterranean Sea (see Candela, Chapter 5.7), because of two unique features. First, they are near land where cold air flows over the water to create the necessary high heat loss. And second, they have weak cyclonic circulations, which keeps the convecting water confined and relatively stationary where the high heat loss occurs. This combination provides the persistent heat loss from the same body of water that is needed to force convection to reach great depths.

An example of a layer mixed by convection is illustrated in Figure 5.5.2 by a plot of $\sigma_{1.5}$ ($\sigma_{1.5} + 1000$ = potential density in kg m^{-3} referenced to 1500 decibars (1 decibar corresponding to about 1 m)) versus depth, on 25 February and 8 March, in the Labrador Sea. The convective layer is the approximately homogeneous layer next to the surface about 750 m deep with a $\sigma_{1.5}$ of 34.652 kg m^{-3} on 25 February (Station 66) and 1150 m deep and 34.673 kg m^{-3} 11 days later

(Station 118). In the potential temperature versus salinity plots of these two stations (Fig. 5.5.3) the homogeneous layer is identified by the concentrations of temperature and salinity values next to the station labels. Beneath this upper layer temperature and salinity both increase well above the values observed in the mixed layer. At Station 66, for instance, the temperature and salinity in the mixed layer are 2.82°C and 34.806 down to ≈ 700 m but 3.02°C and 34.845 at 750 m. As deepening of the mixed layer continues it mixes into and incorporates this warmer, saltier water, which increases the salinity of the mixing layer. This explains why the salinity in the mixing layer is higher at Station 118 than at Station 66 (Fig. 5.5.3). The heat added from the warm water below also increases the temperature of the mixing layer. In this case the value at Station 118 is not above that at Station 66, but it is above the value it would have been without the extra heat from below.

A common relationship studied in deep convection regions is that between heat loss from the surface and the resulting depth of convection. A simple way of estimating this is to integrate the buoyancy between the existing and final conditions and convert the integrated buoyancy loss to a heat loss. For example, in the situation shown in Fig. 5.5.2, it is of interest to know how much heat loss is required to increase the density of the mixed layer to $1034.694 \text{ kg m}^{-3}$ ($\sigma_{1.5} = 34.694$) which occurs at ≈ 2000 m. The change of slope at this depth in the curve in Fig. 5.5.2 indicates the greatest depth reached by convection during the severe winters of 1993 and 1994. Starting with

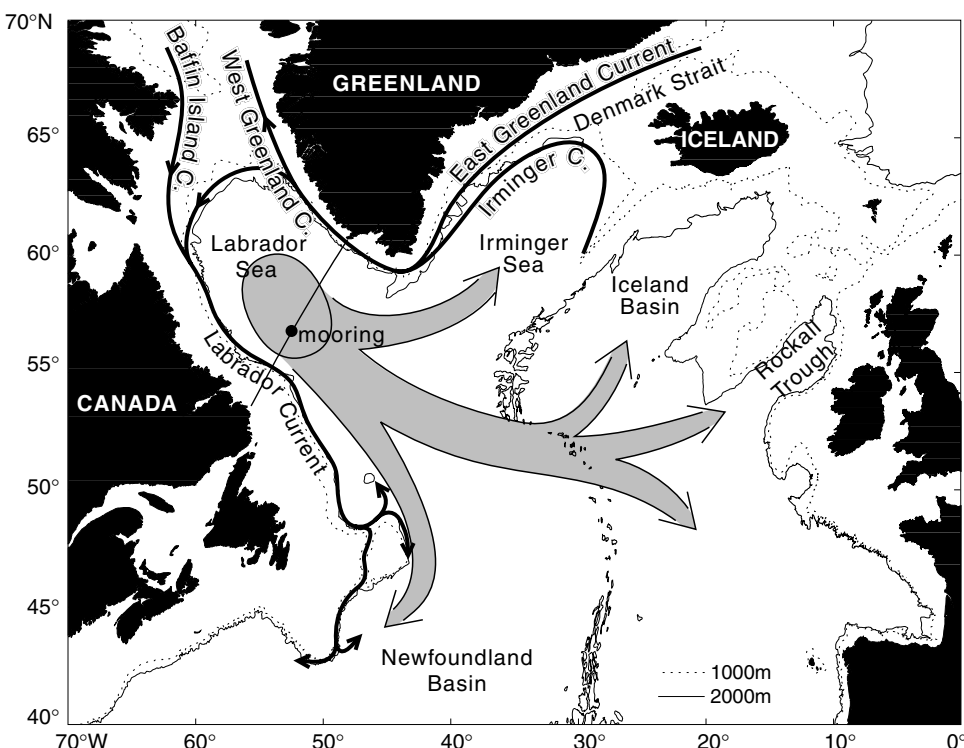


Fig. 5.5.1 Map of the northern North Atlantic showing the Labrador, Greenland and Irminger Currents, which border or influence the Labrador Sea. The WOCE AR7W CTD line across the Labrador Sea and the Bravo mooring on the line are indicated by a line and dot. The flows of the intermediate depth Labrador Sea Water (LSW) away from the Labrador Sea eastward to the Irminger Sea and the eastern North Atlantic, and southward to Newfoundland Basin are indicated by the broad open arrows. Adapted from Sy *et al.* (1997).

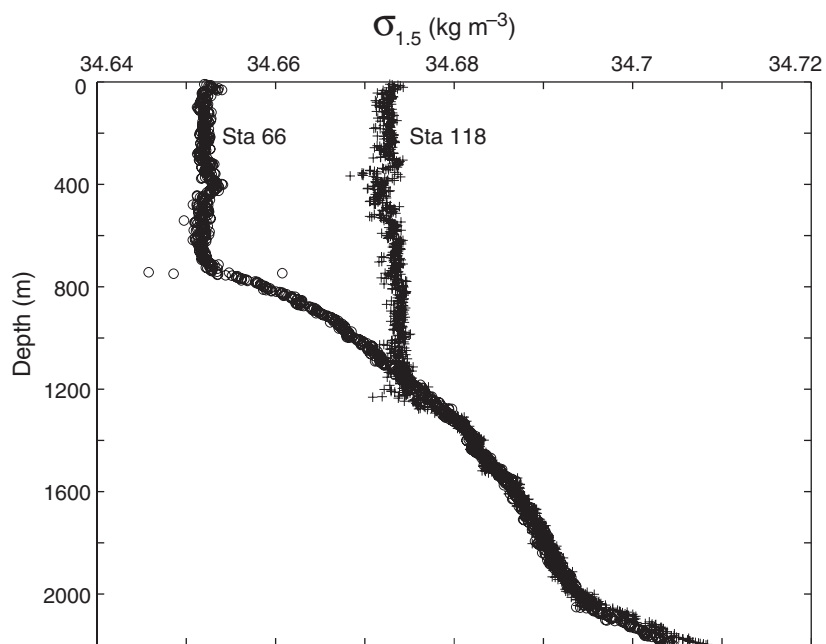


Fig. 5.5.2 Vertical distribution of $\sigma_{1.5}$ obtained from Research Vessel (RV) *Knorr* at 56.8°N 54.2°W in the Labrador Sea on 25 February (Station 66) and 8 March 1997 (Station 118).

the observations at Station 66 the required buoyancy loss is found by calculating

$$g/\rho_0 \int \Delta \rho \, dz$$

where g (10 m s^{-2}) is the acceleration due to gravity, ρ_0 ($\approx 1034 \text{ kg m}^{-3}$) is the reference density, z is the depth and $\Delta \rho$ is the difference in density between Station 66 and a density of $1034.694 \text{ kg m}^{-3}$. This yields a buoyancy loss of $0.47 \text{ m}^2 \text{s}^{-2}$, which can be converted to joules by dividing by $g\alpha/\rho_0 c$ where g and ρ_0 are as before, α ($10^{-4} \text{ }^{\circ}\text{C}^{-1}$) is the thermal expansion of water and c ($4.2 \text{ kJ kg}^{-1} \text{ }^{\circ}\text{C}^{-1}$) is the specific heat capacity of seawater. The conversion suggests a heat loss of $\approx 2 \times 10^9 \text{ J m}^{-2}$ will create a mixed layer to 2000 m and density of $1034.694 \text{ kg m}^{-3}$. Since Station 66 was obtained on 25 February, only 35 days before the usual end of the cooling season on 1 April, it would require a heat flux of about 630 W m^{-2} over the 35 days. Although such high heat fluxes have been observed in the area (see The Lab Sea Group, 1998), they are relatively rare and only sustained for significant periods in exceptionally severe winters.

A similar buoyancy calculation starting with data obtained near the end of summer in 1996 yields $\approx 4 \times 10^9 \text{ J m}^{-2}$ as the heat loss required to create a convection layer to 2000 m or $1034.694 \text{ kg m}^{-3}$. Over the approximately 180 days of cooling between 1 October and 1 April this

would require an average heat flux of $\approx 250 \text{ W m}^{-2}$. Smith and Dobson (1984) calculated that between October and April the average heat loss from the central Labrador Sea, based on meteorological observations at Ocean Weather Ship *Bravo* (56.5°N 51°W) between 1946 and 1974, is $\approx 150 \pm 60 \text{ W m}^{-2}$. These values imply that a winter severe enough to produce convection to 2000 m, i.e. $\approx 250 \text{ W m}^{-2}$ for 180 days, would occur when the heat loss over the winter was larger than the average by ≈ 1.5 standard deviations or roughly once in 10 years; this is about what is observed.

The buoyancy calculation is also useful because it is dependent only on the density profile. If the density profile remains unchanged, the heat loss required to produce a mixed layer to a given depth remains the same; independent of changes in the temperature and salinity profiles. In the Labrador Sea this point arises with the warmer, saltier water evident beneath the mixed layer in Figure 5.5.3. This water originates in the North Atlantic Current and is carried into the Labrador Sea from the Irminger Sea by the Greenland Currents. Its temperature and salinity vary with time but the density tends to remain roughly constant as the temperature effect on density is largely compensated by an opposite salinity effect. Thus in a given year the temperature and salinity in this layer may be higher than average, but if the density profile is

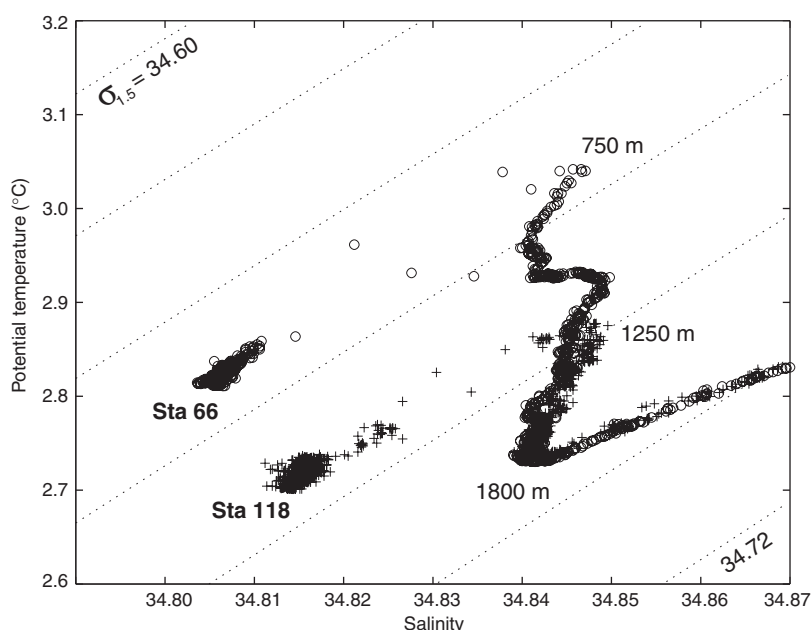


Fig. 5.5.3 Temperature versus salinity distributions at the same stations plotted in Figure 5.5.2. The observations in the mixed surface layers are clustered near the station labels. The sloping dotted lines indicate surfaces of constant $\sigma_{1.5}$.

not changed, the buoyancy is not changed and the depth of convection, for a given heat loss, will not be altered.

The foregoing one-dimensional view of convection is expanded to two dimensions in the contour plot of salinity (Fig. 5.5.4, see Plate 5.5.4, p. 428) obtained in the Labrador Sea in July following the exceptionally cold winter of 1992–93. The water mass resulting from convection is the large volume of homogeneous water lying between 360 and 800 km on the horizontal scale and 500 and 2300 m in the vertical. Because of its large volume and unique temperature and salinity properties that are renewed in the Labrador Sea, the water mass has its own name; the Labrador Sea Water (LSW).

The newly formed Labrador Sea Water is a mixture of all the water down to 2300 m including the water in contact with the atmosphere at the surface. In these uppermost layers the concentration of gases such as oxygen, carbon dioxide, tritium and chlorofluorocarbons (CFCs) are at or near equilibrium with the atmosphere. By transporting these gases down from the upper layers of the ocean to intermediate depths, convection provides a mechanism to ventilate the deeper layers, which is one of the most important consequences of deep convection. Dissolved oxygen, for example, is slowly used up in the deep ocean by biological processes and would eventually vanish without the renewal via convection. Also most of the carbon dioxide ever put in the atmosphere by volcanoes since the formation of the earth became dissolved in the ocean and is now contained in sediments in the bottom of the ocean. As combustion of fossil fuels over the earth raises the carbon dioxide content of the atmosphere it is important to understand the rate this gas is entering the deeper layers of the ocean through processes such as deep convection.

The upper layer (0–500 m) in the central part of the salinity section in Figure 5.5.4 (see Plate 5.5.4, p. 428) is clearly not as well mixed as the layer between 500 and 2300 m. This is because the observations were obtained in July about 3 months after deep convection ceased at the end of the cooling season about 1 April. Since that time the surface layer has been flooded with fresh water derived from melting ice and river runoff. As well, the layer below this low-salinity surface layer, to about 500 m, has been invaded by higher-salinity water from the right, that is, the northeast. This more saline water is the water found under the

convection layer in Figure 5.5.3 and is known as the Irminger Water (IW) because it is transported into the Labrador Sea from the Irminger Sea in the East and West Greenland Currents that lie over the continental shelf and slope (Fig. 5.5.1). On the left or southwest part of the section there is again a salinity maximum at about 300 m over the Labrador continental slope, which also tends to invade the central region. This is again Irminger Water, which has been transported around the Labrador Sea in the West Greenland and Labrador Currents. Beneath the LSW, between 2300 and 3300 m, lies a water mass identified by the salinity maximum at about 2800 m. This is the North East Atlantic Deep Water (NEADW). It originates in the eastern basin of the North Atlantic and flows into the western basin through gaps in the Mid-Atlantic Ridge. At the bottom of the section is the Denmark Strait Overflow Water (DSOW) with a slightly lower salinity than in the NEADW above. DSOW is the densest water in the northern North Atlantic; it originates in the seas north of Iceland and comes to the Labrador Sea after flowing over the sill in Denmark Strait between Greenland and Iceland (see Saunders, Chapter 5.6). The last water mass of note in the section is the low-salinity water over the Labrador continental shelf that flows south out of Baffin Bay in the Baffin Island Current and the Labrador Current. A similar band of low-salinity water of Arctic origin lies over the Greenland continental shelf but it was covered by heavy ice in July 1993 and not sampled when the rest of these data were collected. The rapid transition between the low-salinity waters over the shelves and the higher-salinity waters of the sea's interior mark the baroclinic currents lying over the upper part of the continental slopes, i.e. the Labrador and West Greenland Currents.

In the Atlantic Ocean, ventilation of the intermediate layers by deep convection occurs only in the Labrador Sea. The historical notion has been that the overturning occurs primarily in the western interior of the basin. Indeed, this is where it has been observed the most (Clarke and Gascard, 1983; Wallace and Lazier, 1988; Lilly *et al.*, 1999). Recent evidence has demonstrated, however, that convection can (at least on occasion) occur closer to the western boundary, directly into the rim current system (Pickart *et al.*, 2000a). Not surprisingly, this boundary current water mass product is less dense than the interior water mass, and

becomes restratified more quickly. Theoretical considerations suggest that convection adjacent to a sloping boundary should result in a greater net vertical sinking of water than overturning in the interior (Hallberg and Rhines, 1996; Spall and Pickart, 2000).

Subsequent to formation, the new LSW spreads to other regions of the ocean at intermediate depths. Our knowledge of the speed of this flow and its influence increased during the World Ocean Circulation Experiment (WOCE) due to the widespread high quality observations of temperature, salinity and CFCs across the North Atlantic. One study by Sy *et al.* (1997) suggested that the newly ventilated water formed in the Labrador Sea during the severe winters of the early 1990s moved into the Irminger Sea within months, to the Iceland Basin within a year, and to Rockall Trough on the eastern boundary in approximately 5 years, yielding a trans-Atlantic speed of approximately 2 cm s^{-1} . This speed is about three to four times greater than the previous estimate, and one conclusion is that the intermediate flows are much faster than previously thought. An alternative explanation, however, is that convection occurred over a far greater extent of the Labrador Basin during this high NAO (North Atlantic Oscillation) period. This would allow for more direct (and much faster) contact of the new water with both the North Atlantic Current, and Deep Western Boundary Current (including convection directly into the latter as noted above). In this scenario, the ‘initial condition’ for escape from the Labrador Sea is greatly enhanced. Regarding the surprisingly short time lag to the Irminger Basin (6 months according to Sy *et al.*, 1997), yet another scenario is possible: that deep convection occurred within the Irminger Basin itself. This possibility is raised by Pickart *et al.* (2000b).

The far-field influence of LSW in the subtropical gyre was examined by Curry *et al.* (1998) in a comparison of six decades of data from the Labrador Sea and from the ocean near Bermuda. A correlation between these two regions suggests the products of deep convection in the Labrador Sea impact the waters off Bermuda after about 6 years. These studies along with others such as those by Cunningham and Haine (1995a,b) confirm the LSW flow patterns mapped by Talley and McCartney (1982) and sketched in Figure 5.5.1.

For the reader wishing a more thorough review of deep convection, Marshall and Schott (1999)

provide an excellent summary of studies of observations, laboratory experiments, theory and modelling. Also the Labrador Sea is the focus of two recent descriptions. The first, by the Lab Sea Group (1998), concentrates on the observations obtained in conjunction with the cruise of the *Knorr* to the Labrador Sea in January and February 1997. This includes high-resolution numerical simulations and data from meteorological measurements, CTD surveys and neutrally buoyant floats. The second by Lilly *et al.* (1999) concentrates on the observations obtained from a mooring placed in the central part of the sea between 1994 and 1995, and by drifting, profiling P-ALACE (Profiling-Autonomous Lagrangian Circulation Explorer) floats.

In the next section some features of plumes, the convective mixing agents, are reviewed. This is followed in Sections 5.5.3 and 5.5.4 by discussions of two phenomena associated with the convection. The first is the increase in the amplitude of temperature and salinity variability during convection observed in moored records. The second is the restratification of the density field following the cessation of convection.

5.5.2 Plumes – the mixing agent

Convection begins to increase the depth of the mixed layer in the Labrador Sea near the end of September when the surface net buoyancy flux from the surface turns from positive to negative. Deepening continues until about the end of March, when the buoyancy flux again becomes positive. The effect of this deepening on the density structure is illustrated, for part of the water column, by the year-long time series of $\sigma_{1.5}$ at five depths between 260 m and 2000 m plotted in Figure 5.5.5 (see Plate 5.5.5, p. 428). The deepening mixed layer is indicated to have reached the instrument at 260 m by the rapid increase in $\sigma_{1.5}$ in the first week in February. This is followed a week or so later by a similar increase at 510 m as the mixed layer reaches that instrument. The fact that the $\sigma_{1.5}$ at these two depths continues to increase until the end of the first week in March suggests the mixed layer continues to increase in depth and density during this interval. After the first week in March, $\sigma_{1.5}$ at 260 and 510 m remain relatively constant for about 3 weeks. This likely indicates convection is continuing but that the buoyancy

flux is now not great enough to increase noticeably the density and depth of the mixing layer. The end of convection is indicated in these data by the sudden decrease in $\sigma_{1.5}$ at 260 and 510m at the end of March. This change indicates the beginning of the restratification process, which is discussed more fully in Section 5.5.3.

When convection is active, water at the surface becomes denser than the underlying water and descends in plumes. This water is replaced by slightly lighter water rising toward the surface. The physical features of the convecting water including the plumes and the water between has been the subject of a number of investigations, most notably by the group of scientists at Kiel working in the Golfe du Lion in the Mediterranean Sea with moored Acoustic Doppler Current Profilers (ADCPs) and current meters. The cartoon in Figure 5.5.6 summarizes some of the main features of plumes and the

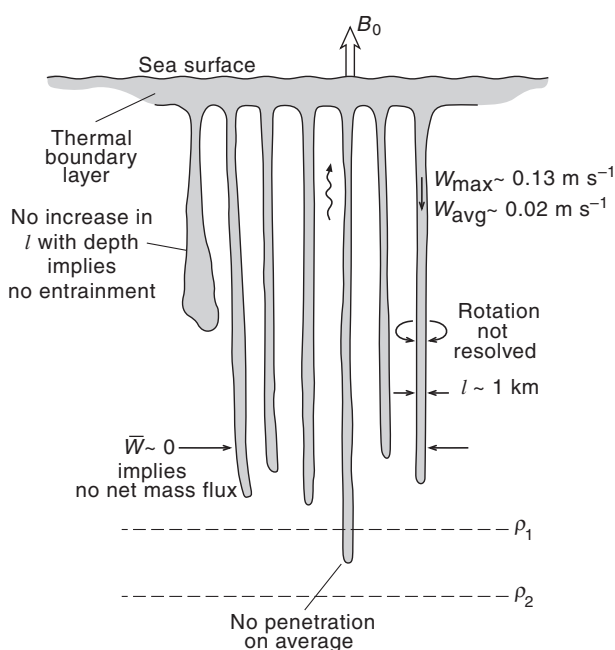


Fig. 5.5.6 Schematic diagram of a convecting layer indicating approximate values for features of individual plumes, including the horizontal scale, vertical downward velocity, rotation and entrainment. Across the patch of convecting water there is no net vertical mass flux and no significant penetration into the layers of denser water beneath the convecting layer. Buoyancy (B_0) lost from the surface creates the thermal boundary layer in the upper $\approx 100\text{m}$ where the denser water that sinks within the plumes is formed. The wiggly up arrow indicates the upward flow (slow) that replaces the downward flow (fast) within the plumes.

mixing layer as described by Schott and Leaman (1991), Schott *et al.* (1993b, 1996) and Send and Marshall (1995).

At the surface in this picture is the thermal boundary layer where the water is losing heat/buoyancy to the atmosphere. Water in this layer is, on average, slightly denser than in the mixed layer beneath and descends into the mixing layer within plumes that have a horizontal dimension of $\approx 1\text{ km}$; i.e. an aspect ratio of ≈ 1 . The average rate of descent within the plumes is $\approx 0.02 \text{ m s}^{-1}$ while the maximum is $\approx 0.13 \text{ m s}^{-1}$. Rotation of the plumes, due to the horizontal component of the Coriolis force, is expected because water must converge into the plume at its top and presumably diverge out of it near the bottom. However, this effect has not yet been conclusively observed in the field, although it has been observed in laboratory experiments, e.g. by Helfrich (1994) and Maxworthy and Narimousa (1994), and in numerical simulations, e.g. by Jones and Marshall (1993). Another effect that has not been observed is an increasing horizontal dimension with depth that is expected if water is entrained into the plumes as they descend.

These investigators have also concluded there is no net vertical mass flux within a convecting region or patch. This appears to have solved the long-standing puzzle of whether the descending water was replaced by rising water between the plumes or by converging flow in the upper layer and diverging flow in the deep layer. Finally, they suggest that on average the plumes are not penetrative, that is, the plumes do not have the energy to descend into water that is denser than the water within the plume. One consequence of this is illustrated in Figure 5.5.2 by the fact that the bottom of the mixing layer at Station 118 lies on the $\sigma_{1.5}$ versus depth curve observed earlier at Station 66. If convection were penetrative the bottom of the mixed layer would lie below this curve and the $\sigma_{1.5}$ versus depth gradient below the mixing layer would be greater than observed earlier, as has been described by Deardorff *et al.* (1969) in tank experiments.

A new and direct view of the motion within convecting plumes has recently been obtained from freely drifting floats (Lab Sea Group, 1998). When a float is launched it immediately sinks to a predetermined depth below the convecting layer where it remains for 7 days while its buoyancy adjusts. At the end of this period its buoyancy decreases slightly and it rises into the convecting

layer. A large attached drogue then pulls the float up and down with the convecting water. In the Labrador Sea over 25 days in February and March 1997 the maximum vertical velocity observed by the floats was downward at 0.2 m s^{-1} with a rms value for all the observations of 0.02 m s^{-1} , suggesting an average round trip for a parcel of 1 day. On a number of occasions the floats were seen to penetrate below the average bottom of the mixing layer. This suggests that, contrary to the conclusions mentioned above that the convection is not penetrative, a certain amount of plume penetration into denser layers does occur. As these floats also record temperature to within 0.001°C it is possible to calculate the vertical heat flux through the mixing layer from the difference in the temperature of the descending water and the ascending water.

5.5.3 Temperature and salinity variability

The previous section discussed some features of convection that are now better understood because of time series records obtained during convection. An additional feature noted in these records is an increase, during convection, in the amplitude of temperature and salinity variability. This was noted by Lilly *et al.* (1999) in records obtained from a mooring in the Labrador Sea (Fig. 5.5.5,

see Plate 5.5.5, p. 428). An example of this phenomenon is evident in the temperature record at 510 m in Figure 5.5.7, where the variations in temperature suddenly increase in the middle of February when the deepening mixed layer reaches this depth. Spectra calculated from 85-day pieces of this record before and after the arrival of the convection layer, Figure 5.5.8, show a broadband four-fold increase in the energy of the variability after the sensor is immersed in the mixed layer. A time series (not shown) of this energy, between 0.32 and 0.06 cph, calculated from sequential 256-h blocks of data, shows a peak in February shortly after the mixed layer arrives, followed by a decline to 1/30th of the peak value by the end of the record in June. The minimum energy in the record is in November at a value 1/60th of the peak, which arrives 3 months later. The decline from the beginning of the record to the minimum in November is presumably due to higher energy levels created during convection in the winter prior to the setting of the mooring.

Lilly *et al.* (1999) also demonstrated that the effect of the temperature fluctuations on density were largely compensated by fluctuations in salinity, suggesting that much of the fluctuations are along density surfaces rather than across them. This observation is illustrated in Figure 5.5.9 in

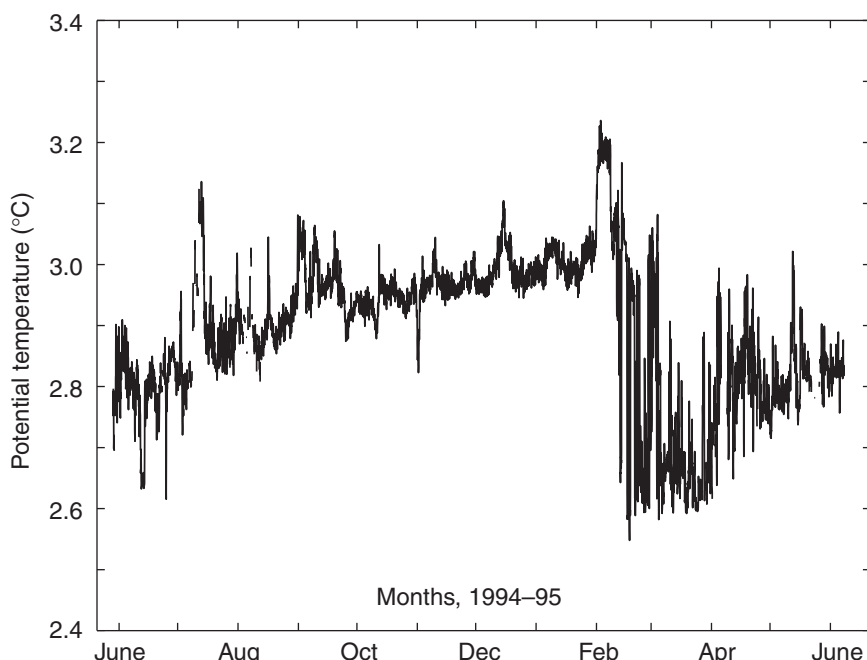


Fig. 5.5.7 A 1-year record of temperature at 510 m illustrating the increase in variance during and after the mixed layer reaches the depth of the instrument in early February 1995.

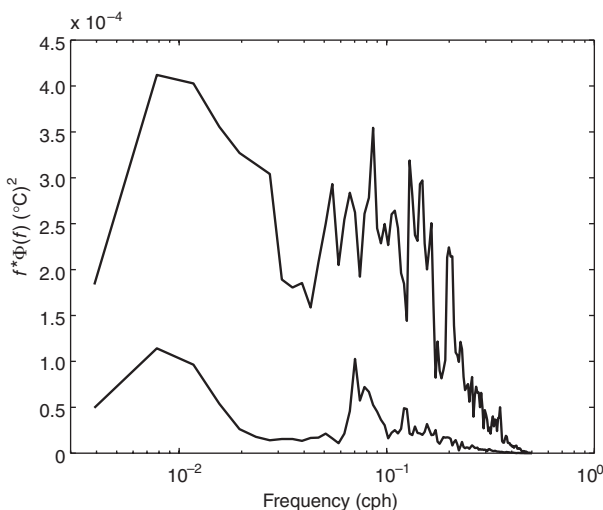


Fig. 5.5.8 Two variance-preserving spectra based on 2048 1-h blocks of data from the 510 m temperature record illustrated in Figure 5.5.7. The lower-energy block occurs between 30 September and 25 December 1994, before the mixed layer reaches the instrument. The more energetic block occurs between 8 March and 1 June 1995 during convection and after it ceases.

temperature versus salinity plots at four depths during 21 days in March when convection was at its full extent and the density at these levels was relatively constant in time (Fig. 5.5.5, see Plate 5.5.5, p. 428). At each depth the hourly observations show the extent of the fluctuations and the fact that they are largely parallel to the constant density surfaces.

The likely cause of the fluctuations (Lilly *et al.*, 1999) is that they are horizontal variations in temperature and salinity being swept past the mooring by the current. These authors showed that the necessary horizontal variability was indeed observed in data from P-ALACE float records. Recent work by Rudnick and Ferrari (1999) suggests that these compensating horizontal variations in temperature and salinity may be ubiquitous features of the mixed layer whether it is convecting or not. They carefully studied such variations in the upper mixed layer of the Pacific Ocean. Using data obtained from a Conductivity-Temperature-Depth (CTD) profiler towed over 10° of latitude at 50 ± 0.3 m the authors establish that horizontal gradients in temperature and salinity over scales of 20 to 10 000 m

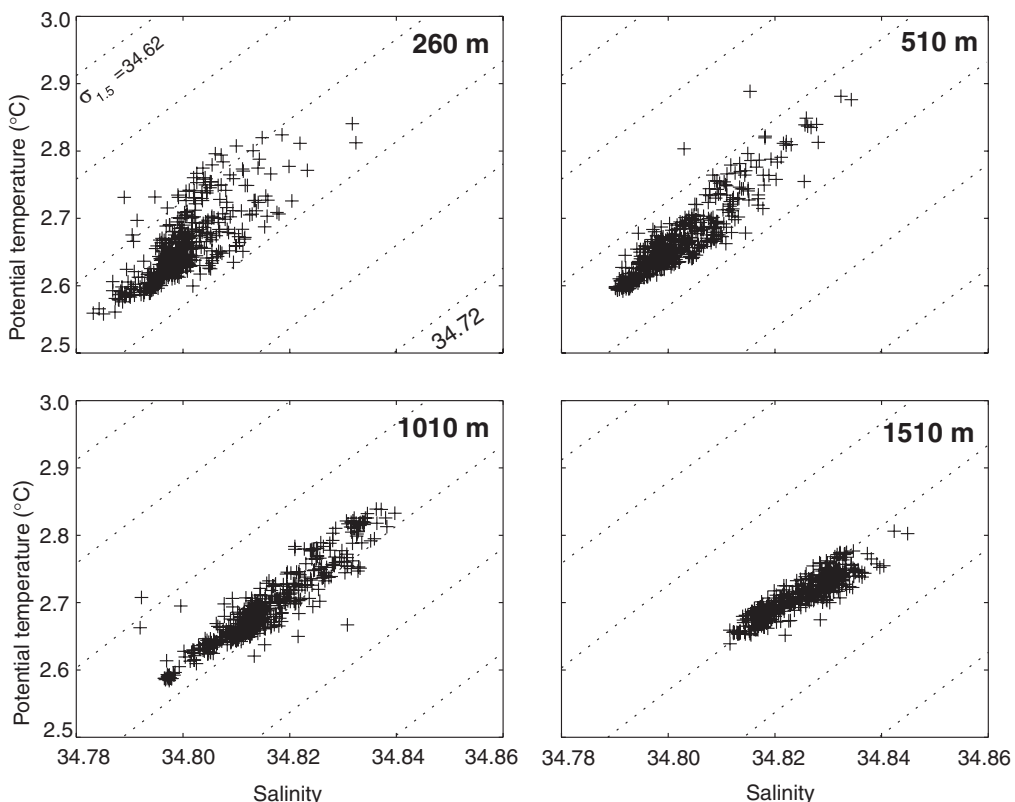


Fig. 5.5.9 Temperature versus salinity diagrams based on data obtained at 260, 510, 1010 and 1510 m, between 12 March and 2 April 1995, during the final stage of convection when the density at these depths remained relatively constant.

'tend to compensate in their effect on density'. From these results we tentatively conclude that the compensating temperature and salinity variations originate in the surface layer and are propagated to intermediate depths during convection.

Data equivalent to that obtained by Rudnick and Ferrari (1999) has not been collected in the Labrador Sea. However, CTD profiles collected in February and March 1997 suggest a similar situation exists there, even during deep convection. Temperature and salinity data collected in the upper 600 m at four locations, separated by 30 km, on 25–26 February and 8–11 March, are plotted in Figure 5.5.10 with similar symbols denoting similar locations. The range in $\sigma_{1.5}$ in both groups of stations is $\approx 0.01 \text{ kg m}^{-3}$ while the temperature and salinity variations are 0.1°C and 0.02, respectively. In their effects on density the horizontal gradients in temperature largely compensate the gradients in salinity, just as observed by Rudnick and Ferrari (1999). Figure 5.5.10 also demonstrates that the magnitudes of the gradients remain roughly constant with time as the mixed layer deepens from 700 to 1100 m (Fig. 5.5.2). From this we conclude that the temperature and salinity gradients propagate down to intermediate depths,

with the deepening mixed layer, where they are carried along in the current to be observed as fluctuations by moored instruments.

Currents at the Labrador Sea mooring are, according to Lilly *et al.* (1999), variable and predominantly barotropic. The variability in direction is readily apparent in the progressive vector plot of the 750 m record shown in Figure 5.5.11. Subsequent data from 5 years' deployment of the *Bravo* mooring show the Eulerian mean horizontal velocity at this site to be rather unpredictable from year to year. The speed of the flow is $\approx 0.15 \text{ m s}^{-1}$ from the beginning of the record to the end of August and from the beginning of March to the end of the record. For the months of October through February the speed is $\approx 0.07 \text{ m s}^{-1}$, or half the value over the other months. Neither these changes, nor the changes in direction seen in Figure 5.5.11, appear to be related to the arrival of the convection layer that reaches to the depth of the instrument throughout March. The large-scale flow, it seems, is not altered by the presence of convection. However, the study of eddies in the region by Lilly and Rhines (2000) shows that intense, sub-mesoscale and mesoscale eddies, overwhelmingly anticyclonic, populate this site. Kinks in the progressive vector diagram

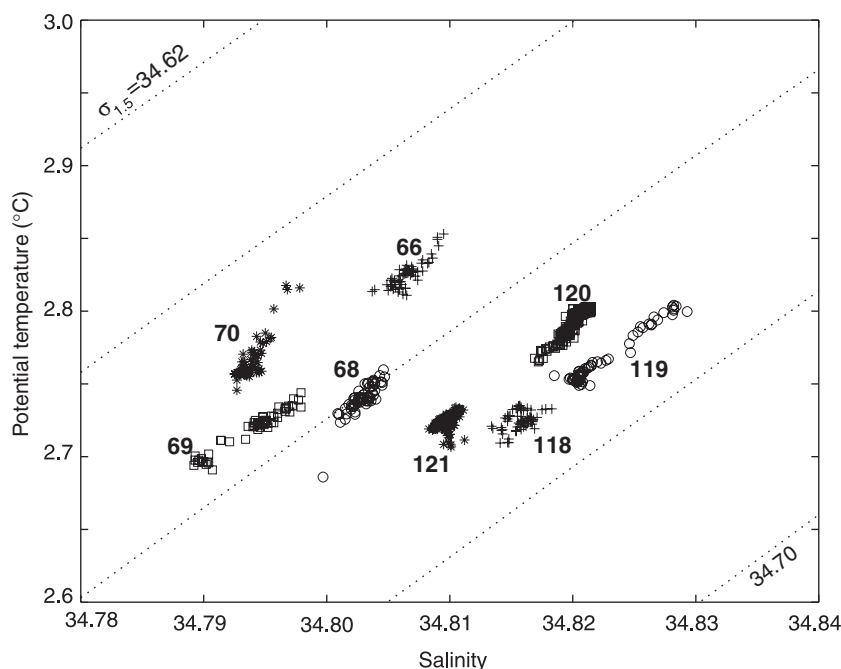


Fig. 5.5.10 Temperature and salinity values from the mixed layers of four pairs of RV *Knorr* CTD stations obtained in the mid-Labrador Sea during convection in early 1997. Stations 66 and 118 (56.8°N 54.2°W) were obtained on 25 February and 8 March; Stations 68 and 119 (57.0°N 53.9°W) on 25 February and 10 March; Stations 69 and 120 (57.3°N 53.7°W) on 26 February and 10 March; and Stations 70 and 121 (57.5°N 53.4°W) on 26 February and 11 March.

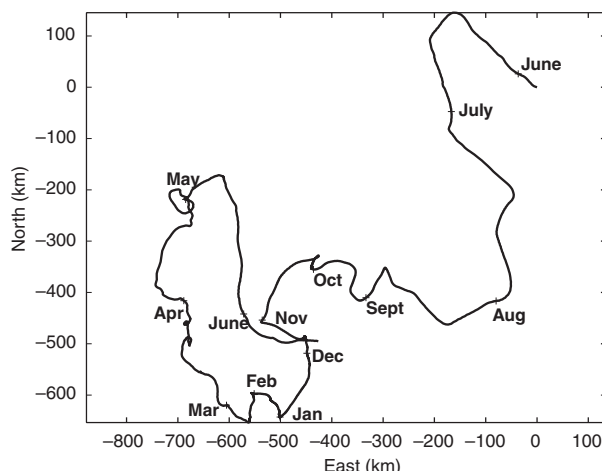


Fig. 5.5.11 Progressive vector diagram from hourly observations at 760 m on the *Bravo* mooring between 29 May 1994 and 13 June 1995. Labels indicate the first observation in each month.

correspond to passage of such eddies. In cold years, active with wintertime convection, many of these eddies have an identifiable core of relatively pure, cold, convected water and hence are associated with convection. Their origins are not yet known, but the dynamically active boundary currents on both Greenland and Labrador continental rises are two known sources, and their generation purely by convection has been documented in model studies (Jones and Marshall, 1993; Maxworthy and Narimousa, 1994; Rhines, 1998).

As noted, the speed of the current from October through February is $\approx 0.07 \text{ m s}^{-1}$ and roughly twice that after 1 March. Long-lived sub-mesoscale and mesoscale eddies have, in subsequent years altered this simple picture of a late-winter maximum in kinetic energy. The first of the two pieces of data used to calculate the spectral estimates shown in Figure 5.5.8 is therefore in the slow regime, while the later one is in the fast regime. If horizontal gradients being swept past the mooring are the cause of the temperature and salinity variability in the moored records, the doubling of the current speed would cause a doubling of the frequency of features with fixed horizontal scales. This effect is not obvious between the two spectra because the horizontal scales of the gradients are distributed broadly over the spectrum. Thus no clearly defined spectral peaks are created to be traced from one period to another except possibly the peak in the early spectrum at $\approx 0.07 \text{ cph}$ (cycles per hour). This broad peak includes two maxima; one at the

inertial frequency (0.067 cph) and one for the semi-diurnal tides (0.08 cph) but it can't be identified in the later spectrum because of the large scatter.

When convection stops, the vertical density stratification is re-established and the horizontal gradients that were brought to intermediate depths in the mixed layer are no longer renewed. Those existing when convection ends are slowly mixed away by horizontal eddy diffusion. Assuming a horizontal scale L of 100 km for the region of convection with its small-scale horizontal variations, then the time scale of eddy mixing will be about L^2/K_H , where K_H , the horizontal eddy diffusivity, is $\approx 10^3 \text{ m}^2 \text{ s}^{-1}$ (Sundermeyer and Price, 1998). This gives a time scale for the horizontal mixing of ≈ 4 months, which is about the decay time observed in the records.

5.5.4 Restratification

At the end of the cooling season, vertical mixing due to convection ceases and its dominant influence on mid-depth water properties ends. This also marks the beginning of the restratification process, during which the vertical stratification that existed prior to the homogenization is re-established. As mentioned earlier, the end of convection is indicated by the rapid decrease in $\sigma_{1.5}$ at 260 and 510 m over the first 20 days in April indicated in Figure 5.5.5 (see Plate 5.5.5, p. 428). There are no data for this year after early June 1995 but there is a decreasing trend in $\sigma_{1.5}$ at 260, 510 and 1010 m between June 1994 and the arrival of convection in February 1995. This, we assume, is due to a continuation of the restratification process following deep convection in the winter of 1993–94, which suggests to us that there are two restratification time scales: an initial rapid change that takes place over the month immediately after the cessation of convection, and a multimonth adjustment that continues until it is interrupted by the next convection event. Presumably a steady-state vertical density profile would eventually be reached if convection did not intervene.

Considering the initial stage of restratification evident in Figure 5.5.5 (see Plate 5.5.5, p. 428), it is not clear if this indicates an end to convection over a large area, or the advection of a stratified non-convecting water column to the observation site. However, the first option seems more likely as the end of convection appears in other records as a

rather rapid event marked by a rapid increase in stratification, especially in the upper layers. One of the best observations of restratification over a larger area was obtained from a tomographic array that integrates the water properties over the array to give a larger-scale picture than a single mooring can. This was obtained in the Golfe du Lion by Send *et al.* (1995), who found a period of restratification after the end of convection lasting ≈ 40 days. Another example is the salinity record from P-ALACE float 392 in the Labrador Sea (Davis, 1998a; see also Davis and Zenk, Chapter 3.2). This shows, in early 1996 and 1997 in the central Labrador Sea, a sudden transition between the low stratification associated with convection and a stratified water column. This record is admittedly like a mooring, from a single point, but it does give a consistent picture in the 2 years.

The restratification process has been modelled numerically by Jones and Marshall (1997), who envisage a homogeneous cylinder of water floating in an ocean of constant stratification. The density gradient between the cylinder and the surrounding ocean gives rise to a narrow cyclonic current that breaks up via baroclinic instability into baroclinic eddies. These horizontally mix the homogeneous water with the stratified waters, dissipating the homogeneous cylinder in time scale, τ . For the special case where the stratification in the water surrounding the homogeneous cylinder is concentrated in the upper layer, h ,

$$\tau \approx 56r/(h\Delta b)^{1/2}$$

where r is the radius of the homogeneous cylinder, h is the depth of the upper stratified water bounding the homogeneous cylinder and Δb is the difference in density between the homogeneous water and the surrounding water in buoyancy units. For the Labrador Sea where $h \approx 500$ m, $\Delta b \approx 2 \times 10^{-3}$ m s $^{-2}$ and $r \approx 100$ km, $\tau \approx 65$ days. This result is about twice the 1-month time scale for the rapid restratification but one-fifth of the 10-month time scale for the slow restratification suggested in Figure 5.5.5 (see Plate 5.5.5, p. 428). This suggests the modelling result is more applicable to the rapid phase of restratification.

Additional evidence of the long period restratification has been obtained from CTD data collected in May and October of 1996. An example of the changes in isopycnal depth during this 5-month interval is shown in Figure 5.5.12, in which are

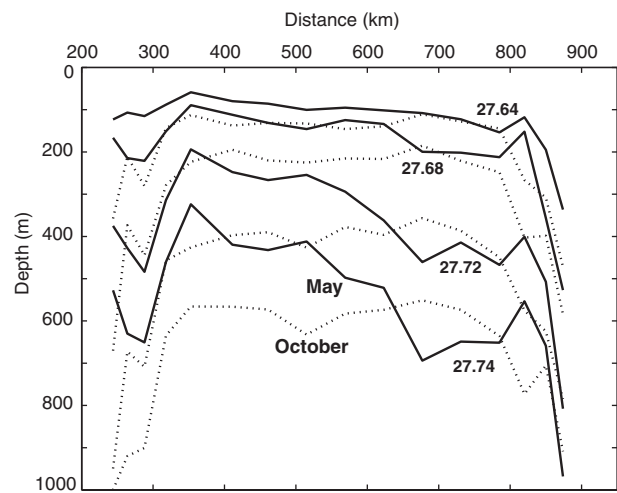


Fig. 5.5.12 Four surfaces of constant σ_0 (potential density anomaly relative to 0 m) across the Labrador Sea based on CTD data collected in May 1996 (solid lines) and October 1996 (dotted lines).

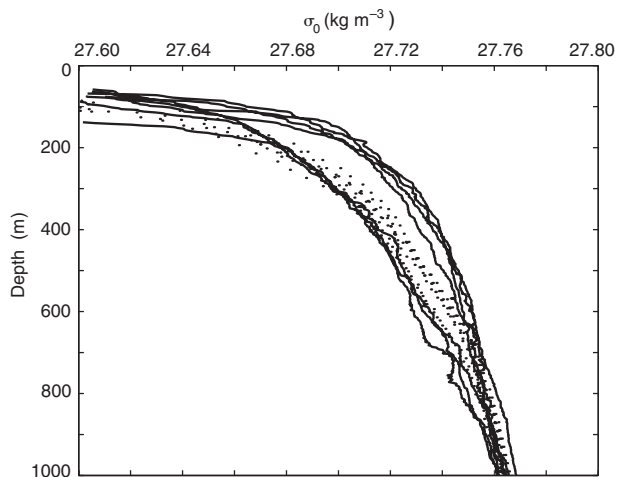


Fig. 5.5.13 Vertical profiles of σ_0 across the Labrador Sea in May (solid) and October 1996 (dotted).

plotted the depths of four isopycnals across the Labrador Sea during the two cruises. At the stations between 400 and 600 km the isopycnal depths increase significantly between May and October, while the 27.72 and 27.74 kg m $^{-3}$ surfaces between 650 and 790 km show a decrease in depth. Vertical profiles from this data set, presented in Figure 5.5.13, illustrate a different aspect of the same phenomenon. The solid curves in this figure are from the May cruise, the shallowest four from between 400 and 600 km and the deeper three from 650 to 790 km. October profiles from the same locations are dotted. As in Figure 5.5.12, the shallower isopycnal surfaces between 400 and 600 km descend, during the 5 months between cruises, while the deeper surfaces between 650 and 800 km rise.

The region between 400 and 600 km region is where convection has been observed to reach its greatest depth in winter. This was most recently observed during the February 1997 *Knorr* survey of the Labrador Sea, when the deepest mixed layer along the CTD line across the Labrador Sea, shown in Figure 5.5.1, was 1100 m at the 3000 m isobath on the Labrador side, 700 m in the centre of the basin, and 200 m at the 3000 m isobath on the Greenland side (Lab Sea Group, 1998, Fig. 16). These observed isopycnal depth changes reflect a slow adjustment following convection. Lighter water, from beyond the region of deepest convection, moves into the upper water column in the region of deepest convection, while denser water in the region of deepest convection moves outward at mid-depth. Eddy diffusion appears to be the primary reason for these changes.

Another view of restratification is obtained in the temperature and salinity time series obtained on a mooring over the 1994–95 winter in the middle of the Labrador Sea. When these values are plotted against each other as in Figure 5.5.14, it is clear that temperature and salinity at these depths slowly increase between periods of convection and that density slowly decreases. The decrease in density is the same decrease observed in the two previous figures while the temperature and salinity increases are signatures of the Irminger Water invading the central region.

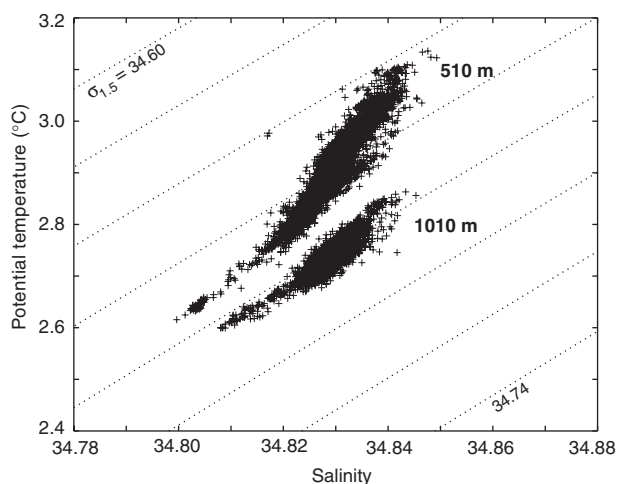


Fig. 5.5.14 Temperature versus salinity at 510 and 1010 m from the Bravo mooring during the period of restratification between June 1994 and January 1995, i.e. before the mixed layer reached these sensors in February 1995.

5.5.5 Summary and discussion

Our purpose in this chapter has been to present a short review of deep convection concentrating on advances made during the WOCE observing period. Using mostly examples from the Labrador Sea we began with a discussion of the depth, homogeneity and energy changes of the deepening mixed layer, as well as some interactions between the mixed layer and the underlying stratified water based on observations obtained during the winter of 1997. Data obtained in July 1993, following a series of severe winters, demonstrated that the convectively mixed water (Labrador Sea Water) represents $\approx 40\%$ of the cross-sectional area of the deep Labrador Sea and is the dominant water mass of the region. The work of Sy *et al.* (1997) demonstrated the flow of this water away from the Labrador Sea at intermediate depths toward the east to be more rapid than previously thought and the work of Curry *et al.* (1998) revealed a 5-year delay between the volume of LSW in the Labrador Sea and water properties at intermediate water in the subtropical gyre.

Details of convecting plumes such as their diameter (≈ 1 km), rate of descent (maximum $\approx 0.13 \text{ m s}^{-1}$, mean $\approx 0.02 \text{ m s}^{-1}$), rotation (not yet resolved), and the net downward mass flux in a convecting region (≈ 0) were presented following the work of Schott *et al.* (1993b, 1996). The ideas of Lilly *et al.* (1999) with respect to the increase in temperature and salinity variability observed at mid-depth during and following convection in moored time series records was revisited with the addition of the work of Rudnick and Ferrari (1999). Their work suggests that density-compensating temperature and salinity gradients are ubiquitous in the mixed layer, which led us to suggest that the observed increased variability is due to these pre-existing gradients being swept past the sensors after they have been propagated to intermediate depths by deep convection.

Our discussion of restratification following convection suggested a two-stage process. First is a rapid change lasting a month or so, possibly related to baroclinic eddies generated from baroclinic instability in a current at the edge of the convecting region, as suggested by Jones and Marshall (1997). The second stage, a multi-month process, involves the slow decrease in the mixed water as it flows away from the region and its replacement at

lower densities by water inflowing from the boundaries.

While the focus of this chapter has been on the Labrador Sea, numerous aspects of the convective processes discussed here apply as well to the other two locations of open-ocean convection in the North Atlantic: the Greenland Sea and the Mediterranean Sea. For example, all three regions are subject to strong wintertime winds blowing off the adjacent continental boundaries. These seasonal winds bring cold, dry air over the relatively warm ocean (the air-sea temperature contrast is especially large in the Mediterranean Sea), leading to the high buoyancy loss that drives the overturning. A second common factor among the regions is the 'layering' of *in-situ* water masses within the water column. Each sea is characterized by a relatively cold and fresh upper layer, warmer and saltier water beneath this, and a larger body of weakly stratified water occupying the middle of the water column (i.e. the remnant of the convective product from earlier years). The relative volumes and properties of these layers can modulate the occurrence of convection. For example, a large abundance of water remaining from an earlier period of convection predisposes the water column to further overturning. On the other hand, enhanced flux of the highly buoyant surface water to the convection region can help inhibit the overturning. This effect appeared to be important during the late 1960s when the Great Salinity Anomaly invaded the Labrador Sea (Lazier, 1980).

A third important similarity between the three areas of convection is the regional circulation; each of them is characterized by a cyclonic flow regime. This is undoubtedly a crucial aspect of the preconditioning for convection. The isopycnal doming in the centre of each of the 'gyres' allows the more weakly stratified subsurface waters to reside closer to the sea surface and hence be more readily subject to the atmospheric buoyancy forcing. Furthermore, in each sea, part of the cyclonic flow regime involves boundary currents (e.g. in the Mediterranean Sea it is the westward flowing Northern Mediterranean Current). This has several ramifications. It enhances the ability for newly formed water masses to exit the region, and influences the restratification process since the boundary currents contain more highly stratified water. Additionally, there is increasing evidence that convection may at times occur directly within the boundary currents

(Mauritzen, 1996a; Schott *et al.*, 1996; Pickart *et al.*, 2000a), since after all this is where the heat loss is greatest.

But as there are common threads to the overturning in the Labrador, Greenland, and Mediterranean Seas, there are also significant regional differences. The Greenland Sea is unique in that ice plays a significant role in the preconditioning phase. As discussed in Marshall and Schott (1999), the deepest overturning occurs in late-winter just after the ice-free 'Nord Bukta' region opens up. In the Mediterranean the winds are more localized in space than in the other two regions (Candela, Chapter 5.7). This clearly impacts the convection, as the region of deepest mixed layers generally lies in the path of the Mistral winds. Furthermore, these winds are not cold enough to cause convection during daylight hours, so the Mediterranean has a daily cycle of overturning that is not present in the other two seas. Also, the impact of the basin-scale NAO wind pattern impacts the Labrador and Greenland Seas to a much greater extent than it does the Mediterranean. Finally, the respective sizes of the convection zones and convected water masses differ greatly. In the Mediterranean, the convecting patch is of order 50 km wide; in the Greenland Sea it is of order 100 km wide; and in the Labrador Sea the zone of convection approaches 500 km width, and includes the boundary currents.

Convection at each of these three Atlantic sites contributes to the global meridional overturning circulation, although the quantitative measures are not yet known. In the Greenland Sea particularly, the deep convection into the cyclonic gyre seems rather isolated from the processes that produce the dense overflows (Mauritzen, 1996a). Mediterranean water and Labrador Sea water both make an obvious contribution to the Upper North Atlantic Deep Water, respectively, as very high- and low-salinity end points. Distant identification of Labrador Sea Water follows its low salinity, potential vorticity, and low nutrient concentration, high dissolved oxygen, tritium and CFCs. The rate of efflux of Labrador Sea Water into the open Atlantic is known to vary greatly, with the intensity of wintertime forcing. Johns *et al.* (1997a) observe velocity and CFC maxima associated with both deep and shallow NADW near Abaco, some 5000 km south of the Labrador Sea. A striking increase in CFCs (even after adjusting for time-dependence of the

source) was seen in 1995–96, subsequent to the intensely cold winters of 1988–94, and before this a path change was observed by their current meter array. The 8- to 10-year transit time is slower than the core-current speeds would suggest, yet faster than earlier estimates. For the era ending 1977, Jenkins and Rhines (1980) observed dilution of the tritium maxima of the deep western boundary currents by factors of order 10, from the subpolar gyre to the Blake–Bahama Outer Ridge; this indicated dilution and delay (by recirculation) mechanisms *en route*, which were later explored in model studies by Pickart (1988).

Model studies (Hallberg and Rhines, 1996) suggest that when convection is initiated or increased at the high-latitude source, a pressure wave propagates down the western boundary, as a topographic Rossby wave, well before the arrival of tracer-tainted, identifiable water mass. Such model studies (also that of Winton, 1997, and Spall and Pickart, 2000) point out that sloping continental rise topography acts as a waveguide, and rather gently leads dense water masses equatorward from high latitude, as they gently sink. Thus, ‘sinking’ is minimal in the near-field of the convection, but occurs downstream. Production of kinetic energy of the overturning circulation by potential energy created by buoyancy forcing requires that dense water sink and less dense water rise, but the sites of sinking and rising are, at least in model studies, often distant from the convection. In a diapycnal/epipyccnal coordinate system, however, convection is more locally associated with time-averaged diapycnal transport (‘water mass conversion’). Such analyses are beginning to be carried out with models and are an insightful way to approach the link between convection, sinking and global meridional overturning.

Thus we are still seeking to quantify production rates of the constituent water masses of the global meridional overturning. Outward transport of Labrador Sea Water is even difficult to define, because of extensive recirculation within the

subpolar gyre and entrainment once the water mass has left the subpolar gyre. Estimates have ranged from less than 1 Sv to more than 10 Sv. By using the relaxation rate of the central Labrador Sea Water after cessation of convection (either annually or, through periods of negative NAO index, interannually), we estimate that renewal of that mass occurs at a rate that decreases with depth from the surface and residence times ranging from roughly 2 years above, to greater than 5 years at 2000 m (Lilly *et al.*, 1999). Much remains unknown about the detailed geography of deep convection and circulation. In the Labrador Sea, both interior and boundary currents are known to participate in the deep convection (Spall and Pickart, 2000, estimate 1–2 Sv of boundary current production). The boundary current, however, is shielded from deep convection by low-salinity shelf waters at some sites. Where the circulation crosses from Greenland to Labrador, the boundary currents broaden and slow, and are generally exposed to some of the most intense air–sea heat flux in the Sea; here and over the wide continental slope near Labrador, convection may be particularly deep (Cuny *et al.*, 2000).

Direct velocity and transport measurements are needed to augment water mass observations. Unfortunately the Lagrangian movement of water masses is difficult to observe, even with modern ‘quasi-Lagrangian’ floats and drifters. Lavender *et al.* (2000c) describe the Labrador/Irminger Sea circulation as observed with P-ALACE floats. They concentrate on the Eulerian ensemble mean velocity field, and remark that ‘no floats travelled southward to the subtropical gyre in the deep western boundary current, the putative main pathway of dense water in the meridional overturning circulation.’ If the boundary current is concentrated to a narrow width, for example at the Flemish Cap, then these profiling floats may have difficulty staying within it; tracer observations assure us that the transport does take place.

5.6

The Dense Northern Overflows

Peter M. Saunders

5.6.1 The sources

The deep and abyssal waters of the global ocean are produced at near-polar latitudes by the intense cooling of winter storms. The waters convect downwards and spread slowly equatorward, renewing the deepest and most distant layers of the global ocean on a time scale of several hundred years. In the south convection carries such water from the fringes of the Antarctic continent directly to great depths, particularly in the Weddell and Ross Seas. In the north, because of the topography of the seabed, the cold dense waters are dammed up behind the Greenland–Iceland–Scotland ridge (Fig. 5.6.1) and enter the world ocean at shallow levels. They are known as the northern overflows of the Atlantic Ocean and form the deepest component of North Atlantic Deep Water (NADW), whose course can be traced into the Southern, Indian and Pacific Oceans. In the Atlantic this water mass forms the deep component of the overturning circulation, southward at depth, northward at shallower levels, which give rise to the transports discussed in Section 6 of this volume.

The goals of this chapter are to review what is currently known about the northern overflows on the basis of observations, models and theory providing, as project WOCE (World Ocean Circulation Experiment) has done, a baseline of knowledge for future research. Special emphasis will be given to the assembly of a coherent body of observations in one location in order to simplify the evaluation of the increasingly sophisticated numerical models expected in the future. In the following pages we review the sources of the overflows and their paths

(north of 60°N), the measurements of their transport, and of the estimates of errors, uncertainties and variability. The successes and failures of modelling the overflows to date will also be considered, along with the topics of hydraulic control (at the sills) and the nature and magnitude of mixing.

5.6.1.1 Sources of the overflow

The nature of the barrier separating the North Atlantic from the Nordic seas is revealed in Figure 5.6.1. The principal channels for the overflows are the Denmark Strait in the west and the Faroe Bank Channel in the east. Their sill depths are at 620 m and 840 m, respectively, whereas between them the maximum barrier depth is about 480 m. Minor episodic overflows occur principally just west of the Faroe Islands and on the Wyville–Thomson ridge where the maximum depth is 625 m. Here we will concentrate on the two major overflows that principally determine both the properties and flux of NADW. A detailed discussion of the minor overflow components can be found in the recent review by Hansen and Østerhus (2000).

The outflow of cold water from the region north of the ridge is approximately balanced by the inflow of warm Atlantic water, the imbalance arising from the net inflow to the Arctic through the Bering Strait and the excess of fresh water from runoff and precipitation at polar latitudes. The inflowing waters are saline and because of the surplus of fresh water the outflowing waters are cold and fresh. Mauritzen (1996a) describes the conversion between these two types as follows.

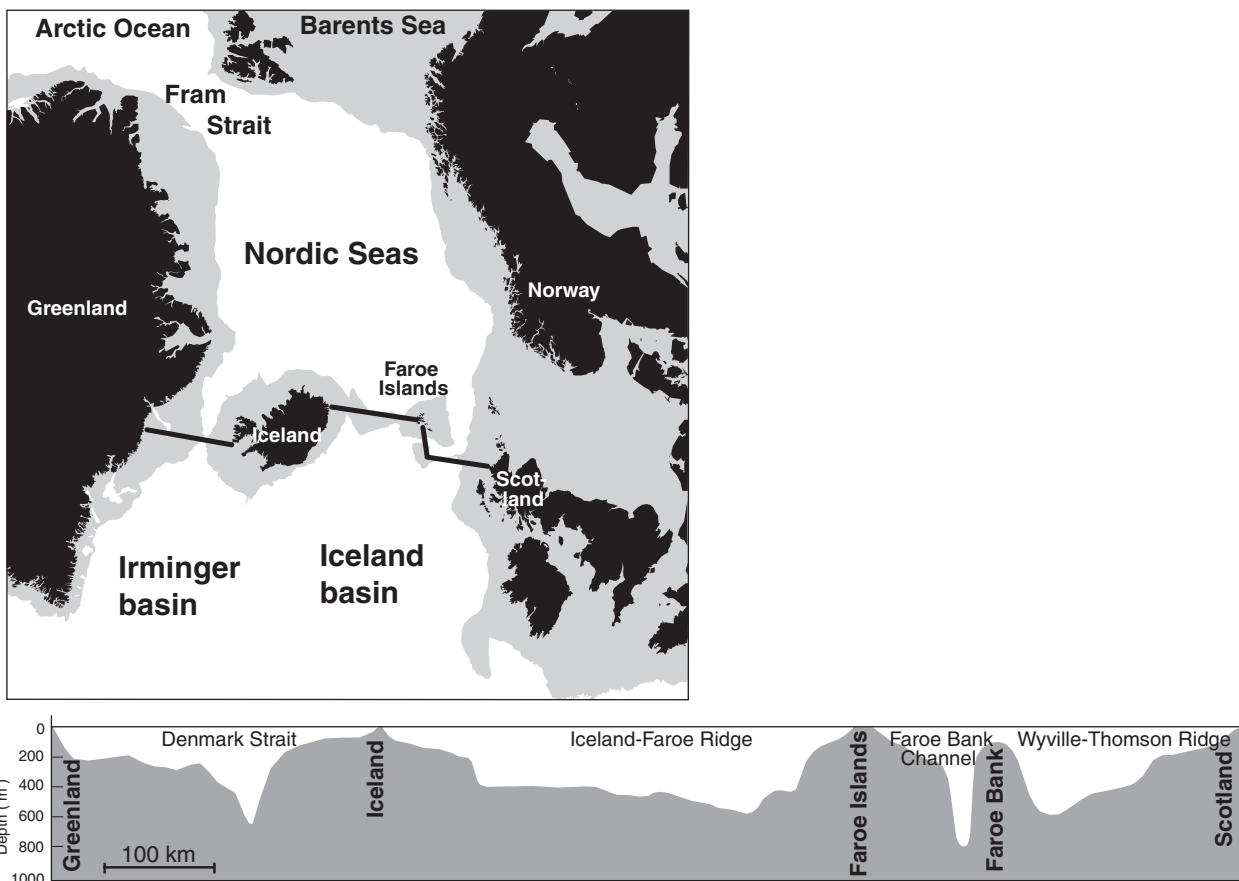


Fig. 5.6.1 Cross section of the Greenland–Iceland–Scotland Ridge (lower), and its context (upper). Slightly modified from Østerhus *et al.* (2000).

The inflowing water is resolved into three distinct branches: ‘flow westward (and then southward) at Fram Strait; flow northward through the Fram Strait and then around the Arctic Ocean; and flow passing through the Barents Sea and then through the Arctic Ocean. These branches, with modified hydrographic properties, return southward as distinct layers of the East Greenland Current, the former two to supply the Denmark Strait overflow, the latter to supply the Iceland–Scotland overflow’ (through the Faroe Bank Channel). ‘The principal water mass product of the Iceland and Greenland Seas is an intermediate water mass that (also) supplies the Iceland–Scotland overflow.’ In a second paper Mauritzen (1996b) quantifies the transports and associated air–sea exchanges. Earlier work by Swift and Agaard (1981) and subsequent researchers emphasized the role of conversions within the Nordic Seas and just north of Iceland, but Mauritzen (1996a,b) showed that in the former case the air–sea fluxes could not sustain the required conversion rate.

Sections showing property distributions at the two major sills are found in Figures 5.6.2 and 5.6.3.

5.6.2 Overflow paths

The topography of the Iceland and Irminger basins determines the overall paths of the dense northern overflows, with the steepness and roughness of the margins significant controlling factors. Building on investigations over the previous 50 years, Swift (1984) produced the first comprehensive description of their paths south of the Greenland–Scotland ridge and north of about 55°N. He demonstrated how the downstream properties of the overflow change by entrainment and mixing, with the Iceland–Scotland component traversing in an anti-clockwise sense the northern and western perimeters of the Iceland Basin before exiting through the Charlie–Gibbs Fracture Zone into the Irminger Basin. Here the overflow crosses from east to west before becoming incorporated into the deep western boundary current formed from the Denmark Strait

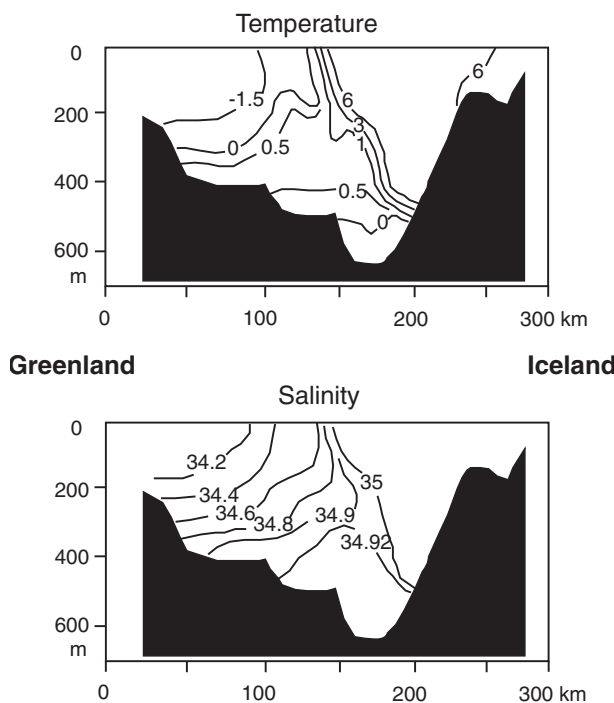


Fig. 5.6.2 Temperature and salinity sections near the sill of the Denmark Strait. Redrawn from Mann (1969); data from a Hudson cruise, January 1967.

overflow. This picture was elaborated by Dickson and Brown (1994), who 10 years after Swift quantified the transports (discussed in Section 5.6.3). Our own version of the path of the overflows shows the same picture (Fig. 5.6.4) and despite the last several years effort both within and without WOCE, there are still a number of questions remaining.

- It has long been recognized that the deepest levels of the Iceland Basin are filled with very cold water that descends steeply downslope near the exit of the Faroe Bank Channel (Crease, 1965). How and why? Most of the overflows for most of their path cross the slope at very shallow angles but evidently details of the terrain play a crucial role.
- What is the path of the overflow on the eastern flanks of the Reykjanes Ridge? In particular what is the relation of the overflow waters to the prominent depositional drifts present in the Iceland basin and sketched on Figure 5.6.4?
- What fraction of the Iceland–Scotland overflow does *not* pass through the Charlie–Gibbs

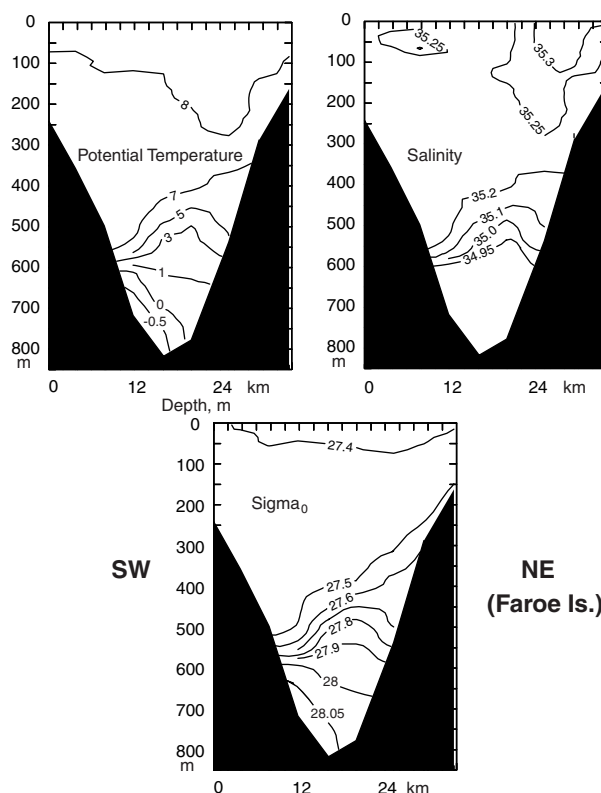


Fig. 5.6.3 A hydrographic section near the sill of the Faroe Bank Channel. Stations 48–56 of Challenger cruise 15/87, May 1987 (Saunders and Gould, 1988).

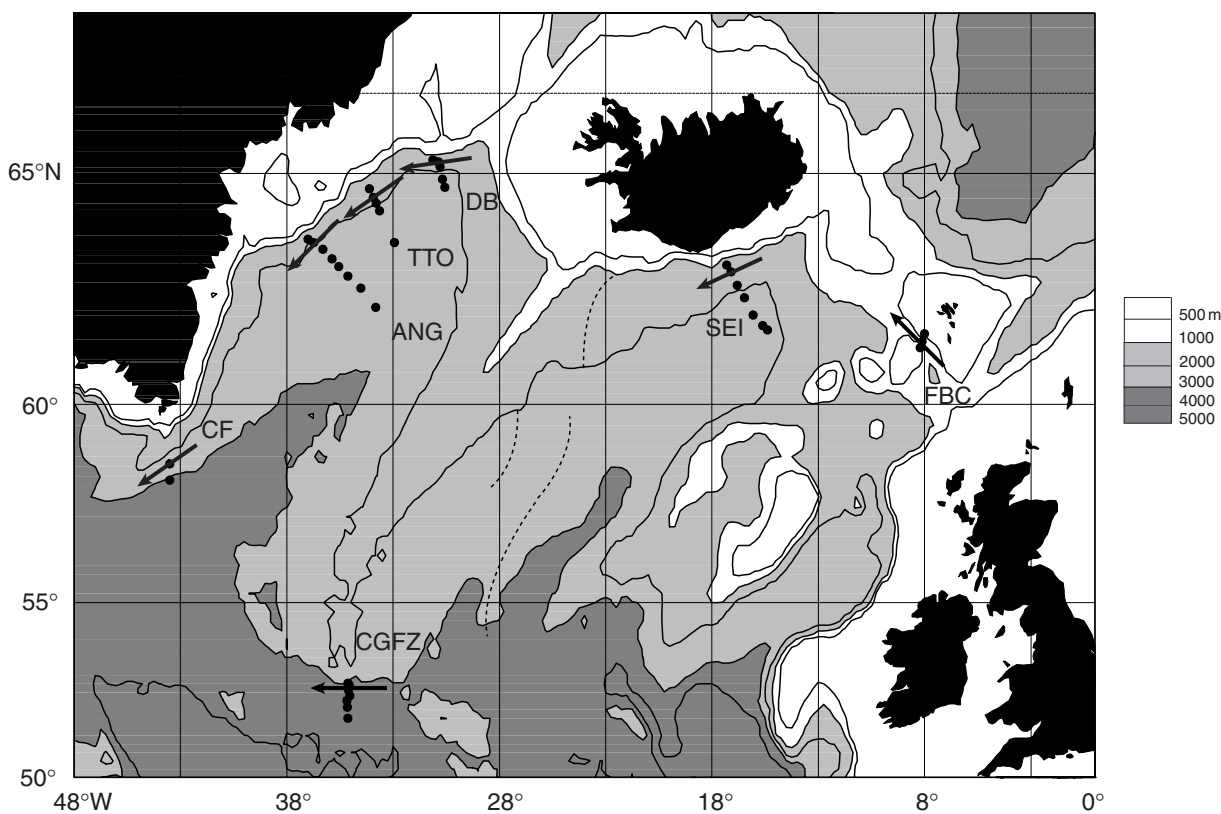


Fig. 5.6.4 The location of seven moored arrays described in this section superimposed on the bathymetry of the North Atlantic. The arrows represent the direction of the overflow and the location of its core (maximum speed). The broken lines in the Iceland basin represent the crest of sedimentary drifts formed by persistent bottom currents. FBC, Faroe Bank Channel; SEI, Southeast Iceland; CGFZ, Charlie–Gibbs Fracture Zone; DB, Dohrn Bank; ANG, Angmagssalik; CF, Cape Farewell.

Fracture Zone (CGFZ) and instead passes south along the east flank of the mid-Atlantic ridge? (Tracer data confirms that overflow water can be seen at 48°N, and even estimates of its transport have been made (Fleischmann and Rhein, 2000).)

- What is the path of the eastern overflow when it exits the CGFZ into the Irminger basin? On exit it occupies a depth range 2000–3500 m, is separated from the bottom and has its core near 2500 m. The overflow is believed to turn northward along the western flanks of the Reykjanes Ridge before crossing the gently upsloping floor of the Irminger basin from east to west. But is the crossing concentrated or diffuse? And in what range of latitudes does it occur?

The above questions may be answered in part by detailed hydrographic and tracer studies supported by lowered ADCP (Acoustic Doppler Current Profiler) measurements, but to proceed from snapshots to means will require arrays of moored

instruments of the kind which have already furnished the crucial information concerning the overflow fluxes. The locations of such major arrays are shown in Figure 5.6.4. Neither single nor pairs of moorings provide the quantitative information on transports which will be presented in the following section, so that many other data sets are not shown here. Information concerning the key array measurements are given in Table 5.6.1: it will be noted that most originate in the run-up to, rather than during the WOCE period.

5.6.3 Observed transport means and variability

All of the array measurements to be discussed have been described in the literature, so no space will be given over to describing instrumentation, deployment and calibration procedures. Nevertheless, it is noteworthy that with the exception of one three-mooring deployment, all measurements were made

Table 5.6.1 Long-term transport measurement sites along the overflow paths

| Site | Year | Duration | Instruments/ moorings ^a | Reference | Location (approx.) |
|----------------|---------|----------|---------------------------------------|-------------------------------|-----------------------|
| Faroe Bank | | | | | |
| Channel | 1987–88 | 6 months | 9/4 | Saunders (1990) | 62°N, 8°W |
| | 1998 | 3 months | 3/3* | Østerhus <i>et al.</i> (1999) | |
| SE Iceland | 1990–91 | 1 year | 13/7 | Saunders (1996) | 63°N, 16°W |
| CGFZ | 1988–89 | 1 year | 16/8 | Saunders (1994) | 52°N, 35°W |
| Denmark Strait | 1973 | 36 days | 12/4 | Ross (1976) | 66°N, 28°W |
| Dohrn Bank | 1990 | 100 days | 14/5 | Dickson and Brown (1994) | 65°N, 31°W |
| TTO | 1990–91 | 1 year | 15/5 | Dickson and Brown (1994) | 64°N, 33°W |
| Angmagssalik | 1987–88 | 1 year | 14/7 | Dickson and Brown (1994) | 63°N, 35°W |
| | 1988–89 | 1 year | 21/8 | | |
| | 1989–90 | 200 days | 16/6 | | |
| Cape Farewell | 1978 | 60 days | 6/3 | Clarke (1984) | 59°N, 44°W |

^aInstruments are Aanderaa current meters except for upward-looking moored ADCPs.*

Table 5.6.2 Characteristics of the overflow at selected sites

| Site | Distance downstream (km) | Potential temperature (°C) | Salinity | Depth (m) – top/core/bottom |
|----------------|--------------------------|----------------------------|--------------|-----------------------------|
| Faroe Bank | | | | |
| Channel | 0 | –0.7–+3.0 | 34.9–35.1 | 500/700/850 |
| SE Iceland | 500 | 1.4–3.0 | 34.95–35.02 | 1200/1300/2300 |
| CGFZ | 2000 | 2.4–3.35 | 34.94–34.975 | 1600/2000/3500 |
| Denmark Strait | 55 | –1–+2.0 | 34.7–35.0 | 250/700/900 |
| Dohrn Bank | 215 | –0.45–+3.0 | | 700/1500/2200 |
| TTO | 380 | 0–3.0 | 34.83–34.90 | 1000/1700/2600 |
| Angmagssalik | 550 | 0.35–3.0 | | 1200/1800/2800 |
| Cape Farewell | 1300 | 1.4–3.0 | 34.9–34.93 | 2000/2500/3400 |

with rotor-vane recording current meters manufactured by Aanderaa. The exception is the Faroe Bank Channel deployment reported by Østerhus *et al.* (1999), who employed upward-looking ADCP instruments. So far only provisional results have been reported from this experiment.

From the reported measurement I have summarized some characteristics of the overflow hydrology in Table 5.6.2, along with the depth range over which the overflow current is found and the approximate depth of the velocity core. Together with the transport estimates, these quantities are the zero order characteristics that analytical and numerical models (discussed in Section 5.6.5) should predict.

5.6.3.1 Re-analyses

Dickson and Brown (1994) and their co-workers made a significant contribution to the quantification of the overflow transports in a 5-year period of investigation (1987–91), deploying more than 80 current meters in the overflow downstream from the Denmark Strait. Their data sets have been made publicly available and have been re-analysed by me in order to extract information not presented in their original work. This has also allowed a uniform treatment of the majority of the data sets described in these sections.

To explain the re-analysis procedures, we focus attention on the 3 years of measurements from the Angmagssalik site approximately 550 km

downstream from the Denmark Strait sill. Our aim is to construct a transport time series from each deployment and to look for seasonal and interannual signals. Not all of the individual current meter records are complete, of course. To fill such gaps we have made use of the strong correlation between instruments on the same mooring, often separated by no more than 300 m. A prediction of a current component for a missing period is then made utilizing linear regression derived from the data-present period. The direction normal to the array is selected (for Angmagssalik 225°) and subsequently designated downstream.

In defining the cross-sectional area of an overflow it is commonplace to make use of a snapshot or climatological distribution of a property (density, potential temperature or salinity) to define the overflow boundary. We have constructed a time-varying estimate of this quantity using the temperature recorded on all the instruments. Potential temperature time series were calculated at each instrument using the measured temperature, instrument depth and contemporary CTD (Conductivity-Temperature-Depth) measurements. Linear interpolation or extrapolation between instruments on the same mooring then yields the height of a selected potential temperature value. We have restricted such a calculation to the 3°C isotherm, which invariably lies very close to the upper instrument. As we have verified, the likely error introduced there by *linear* interpolation is small. By combining the two or three downstream flow

measurements on each mooring we have constructed the transport time series of that mooring colder than 3°C and per unit cross-stream distance, along with its mean value, variance and error of the mean. The squared error ε^2 is derived from the integral time scale of the series I , the variance σ^2 and the record length T according to the expression

$$\varepsilon^2 = 2\sigma^2 I/T$$

The integral time scale increases with distance downslope, inshore equal to about 1 day, increasing to about 4 days at 200 km distance. The mean value together with the error estimate are plotted for each of the moorings for each of the three deployments in Figure 5.6.5.

We have examined the different deployments and can find no systematic difference among them. Consequently we can confirm that the mean transport cannot be distinguished over the 3-year period – a conclusion that Dickson and Brown already reached. The total transport of the overflow is obtained by integration with distance; by eye we have utilized the triangular area shown and obtained a 3-year average of 9.0 ± 0.5 Sv (colder than 3°C). Note that on the 1988 deployment the most distant mooring indicated a NE or recirculating flow. The integration we quote extends only to the location of reversal of the transport. Similar re-analyses have been undertaken at the Dohrn Bank and TTO (Transient Tracers in the Ocean) sites.

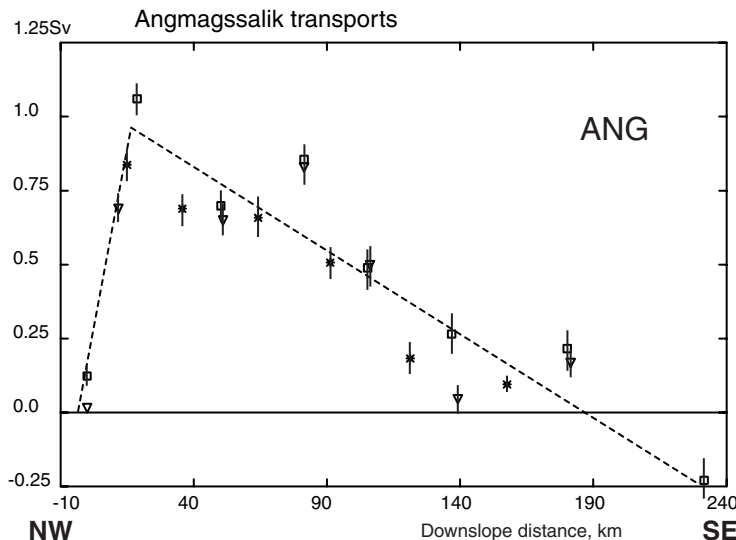


Fig. 5.6.5 Transport colder than a potential temperature of 3°C for each of the moorings and for a strip of width 10 km for the three deployment years, 1987–89, as a function of downslope distance.

5.6.3.2 Transport statistics

All of the re-analysed records along with the earlier data sets of the author's have been averaged over a 12-hour period utilizing a simple top-hat filter. From these data sets the transport time series have been constructed, first the time series of the downstream transport per mooring and then by integrating cross-stream the time series of the overflow transport. In Table 5.6.3 we tabulate these results for seven sites including means, variance and estimated errors. Mean values shown here are similar to values previously reported by Dickson and Brown (1994), but we are able to include new information about the transport variability and uncertainty. In Figure 5.6.6 we show the time series for five transport time series (two published previously) and in Figure 5.6.7 spectra of the transports.

5.6.3.3 The Iceland–Scotland Overflow

Missing from this figure is a time series for the Faroe Bank Channel transport. Two attempts were made by the author to measure this. On the first attempt, year-long deployments were made commencing in spring 1987, but only two of five moorings were recovered. On the second attempt 8-week deployments were made in the fall of 1989 and although four of five moorings were successfully recovered (in a channel in which the overflow width is less than 16 km) the fifth was key to the construction of a time series. Since those studies Østerhus *et al.* (1999) have reported provisional results from an array of three bottom-moored

upward-looking ADCP (Acoustic Doppler Current Profiler) instruments (1.9 Sv colder than 3.0°C, agreeing with earlier estimates) and their full analysis is awaited with interest. The mean speeds, in excess of 1 m s^{-1} , are extreme for any bottom currents. Based on our own records from the channel it seems unlikely that there are transport reversals there, and the energetic periods are quite short, only 3–6 days (Saunders, 1990).

The array measurements southeast of Iceland are approximately 500 km downstream and are also virtually free of transport reversals (Fig. 5.6.6). No seasonal signal is seen in the transport with a mean of 3.2 ± 0.5 Sv and a mean potential temperature of 2.8°C. The energetic periods are 4–10 days (Fig. 5.6.7). An analysis of the potential temperature–salinity (or θ–S) characteristics reveals that the overflow at this site consists of Faroe Bank Channel water (1.6 Sv) mixed in equal parts with modified North Atlantic water (7–8.5°C, 35.1–35.3, 0.8 Sv) and Modified East Icelandic water (1–3°C, 34.7–34.9, 0.8 Sv). The latter component can only have crossed the Iceland Faroes ridge, a conclusion at variance with that (incorrectly) reached earlier by the author (Saunders, 1996).

At the southeast Iceland site the overflow occupies the depth range of the Labrador Sea Water (LSW) with a core near 1500 m and θ–S of about 4°C and 34.92. It is with this water that the overflow initially mixes as it continues south on the flanks of the Reykjanes Ridge. The detailed descent path of the overflow is unknown but eventually

Table 5.6.3 Statistics of overflow transports at selected sites

| Site | Flow direction (°) | Mean transport (Sv) | Variance (Sv ²) | Integral time scale (days) | Transport error (Sv) | Mean potential temperature (°C) |
|--------------------|--------------------|---------------------|-----------------------------|----------------------------|----------------------|---------------------------------|
| Faroe Bank Channel | 315 | 1.9 ^a | | | 0.5 | 0.40 |
| | 304 | 1.9 ^a | | | | |
| SE Iceland | 240 | 3.2 ^a | 2.0 | 2.5 | 0.5 | 2.77 |
| CGFZ | 270 | 2.4 ^c | 9.0 | 5 | 0.5 | 2.90 |
| Denmark Strait | 250 | 2.5 ^b | 2.25 | (2) | (0.5) | |
| Dohrn Bank | 251 | 4.25 ^a | 2.25 | 2.5 | 0.3 | 1.22 |
| TTO | 245 | 5.7 ^a | 9.9 | 4.4 | 1.0 | 1.59 |
| Angmagssalik | 225 | 9.0 ^a | 9.0 | 3.0 | 0.25 | 1.78 |

^aWater colder than 3.0°C.
^bWater colder than 2.0°C.
^cWater more saline than 34.94.

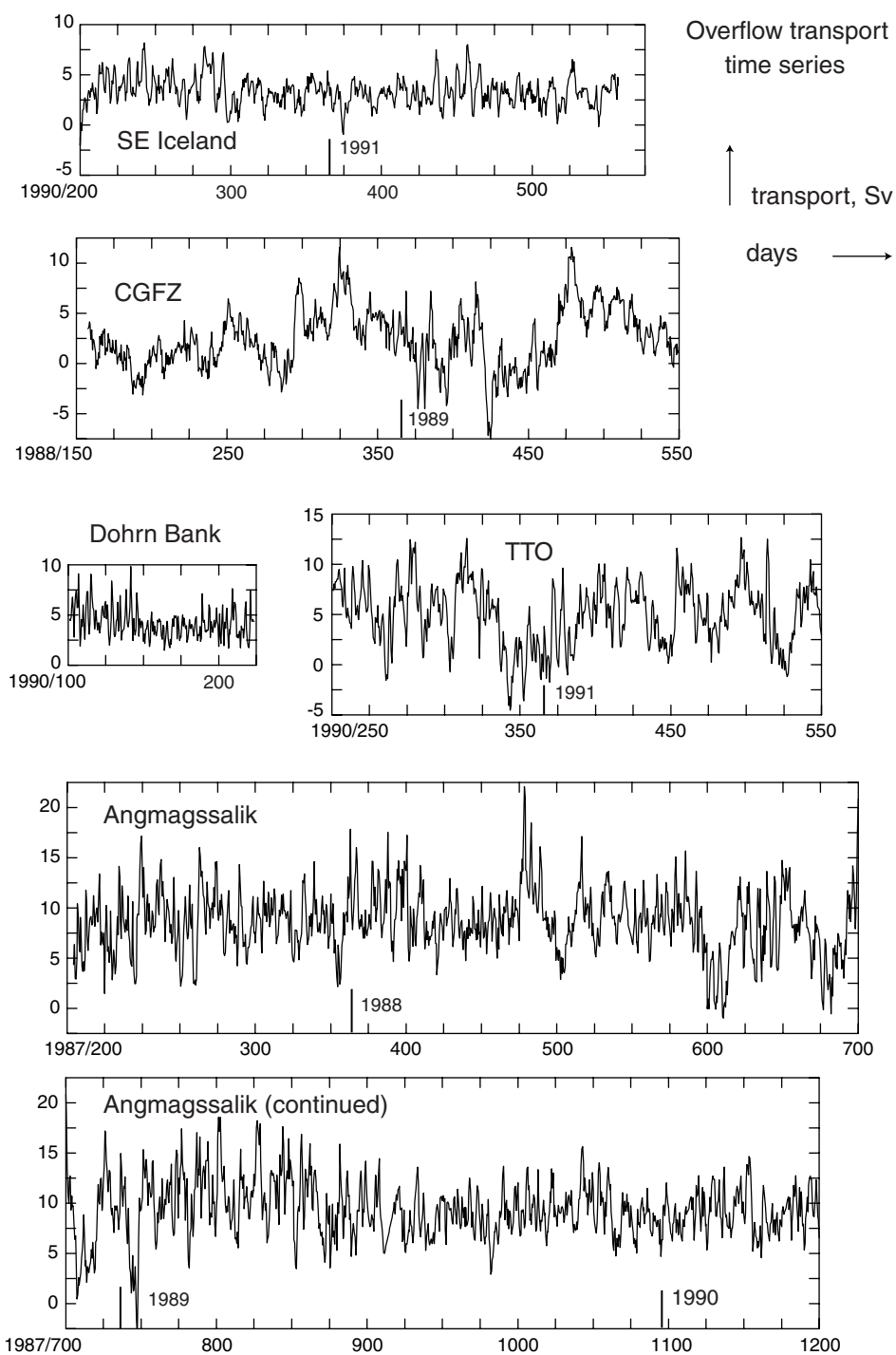


Fig. 5.6.6 Overflow transport time series at the locations shown in Figure 5.6.4. Transport is measured in $10^6 \text{ m}^3 \text{s}^{-1}$ (Sv) and year boundaries are indicated on each abscissa.

about 2000 km from the Faroe Bank Channel sill it reaches the complex region of the CGFZ and threads its way through the two east–west transform valleys.

The topographic complexity of the region is such that the author elected to place the transport array

within both valleys at its western end (Saunders, 1994). Here the overflow is seen as a salinity maximum (*c.* 34.98) with a potential temperature of about 2.9°C but now occupying the deeper levels of 1600 m to 3500 m. The mean transport determined was $2.4 \pm 0.5 \text{ Sv}$ (Table 5.6.3) and shows

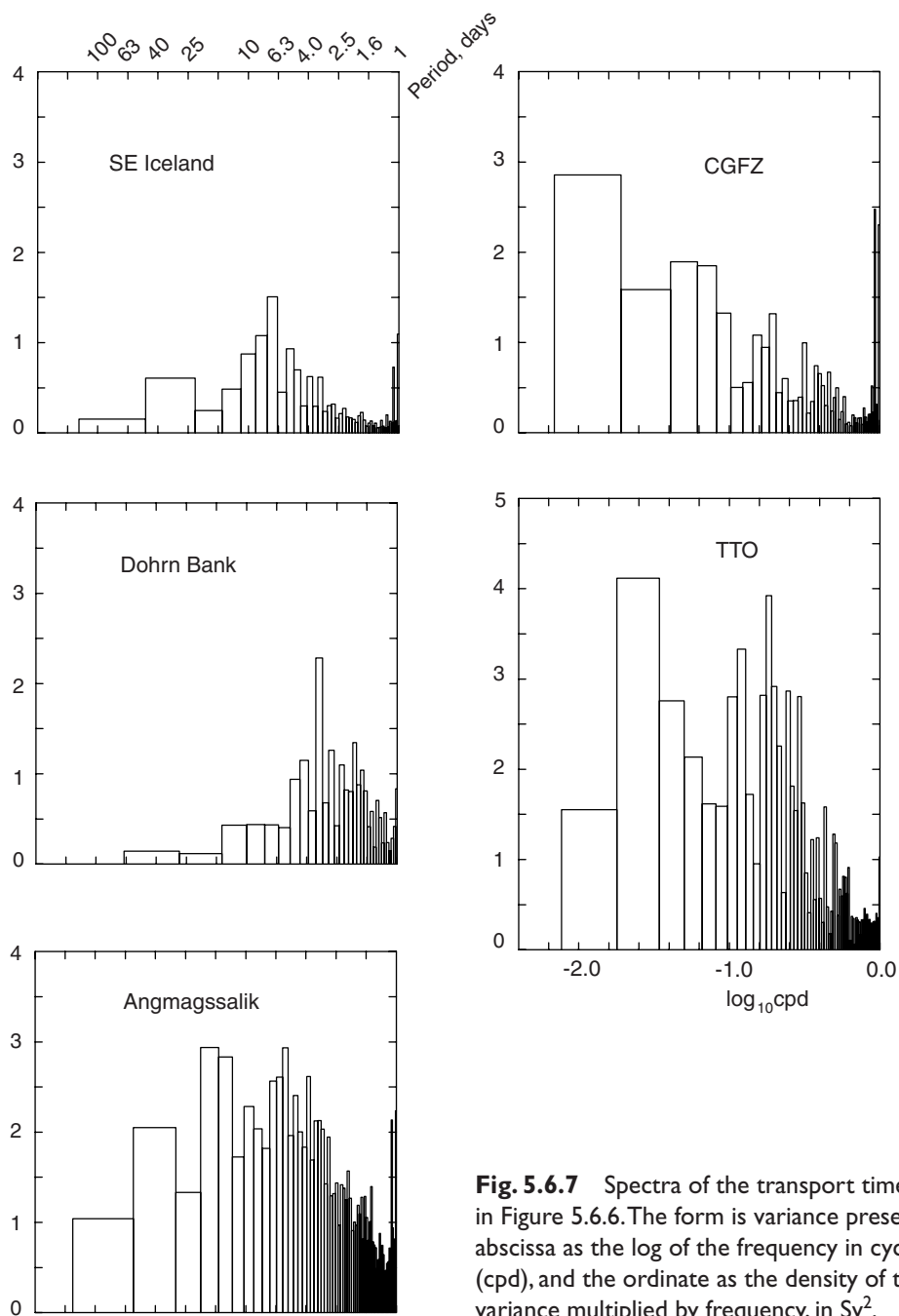


Fig. 5.6.7 Spectra of the transport time series shown in Figure 5.6.6. The form is variance preserving with the abscissa as the log of the frequency in cycles per day (cpd), and the ordinate as the density of transport variance multiplied by frequency, in Sv^2 .

frequent and long-lived reversals (Fig. 5.6.6). The energetic variability is broad-band with periods from 10 to 100 days (Fig. 5.6.7) and no seasonal signal can be seen. At levels below a depth of 3500 m the water is of western basin origin and is periodically flushed to the west in strong overflow events and returns as the overflow weakens or reverses. The author (Saunders, 1994) speculated that the overflow reversals might be related to northward migrations of the North Atlantic

Current; subsequent observations by Schott *et al.* (1999) have confirmed this.

Because the estimate of the overflow transport in the CGFZ is less than that at the southeast Iceland site a second branch of overflow water must exist. The excess may circulate cyclonically within the Iceland basin, as suggested by Harvey and Theodorou (1986), or may escape to the south along the eastern flanks of the mid-Atlantic ridge. The latter overflow path was rejected by

Worthington and Volkmann (1965) but an analysis of recent observations of nutrients and tracers (U. Fleischmann *et al.*, personal communication) suggests otherwise.

Just west of 35°W the CGFZ overflow turns northward and flows along the western margin of the Reykjanes Ridge (Worthington and Volkmann, 1965). The transport has not been measured there and, as was indicated in Section 5.6.1, the location of the crossing of the overflow to the western margin is unknown. Dickson and Brown (1994), by virtue of the near doubling of transport in the Denmark Strait overflow between the TTO and Angmagssalik arrays (Table 5.6.3), argue that the merging must occur between them, near 63.5°N. Independent evidence for this conclusion, for example in the form of a tracer signal, is strongly desirable.

5.6.3.4 The Denmark Strait Overflow

Ross (1976) constructed a 36-day-long overflow time series for a section 55 km south of the sill of the Denmark Strait (not reproduced in Fig. 5.6.6). This brief record showed no reversals, a mean of 2.5 ± 0.5 Sv towards 250° (for water colder than 2°C), a standard deviation of 1.5 Sv and bursts of 1-day duration every few days. Remarkably, these observations have not been repeated, although isolated year-long records nearby (Aagard and Malmberg, 1978) confirmed the persistence of the core of the flow and demonstrated the absence of a seasonal signal – just as in the Faroe Bank Channel.

About 160 km downstream from this site was the first of three arrays deployed by Dickson and Brown (1994), which they named Dohrn Bank. The transport record is 120 days in length, has a mean of 4.25 ± 0.3 Sv (for water colder than 3°C) and a mean potential temperature of 1.22°C. The flow shows no reversals but is energetic at periods 2–5 days (Fig. 5.6.7).

The TTO current meter site, 380 km downstream from the sill, was chosen to lie along a hydrographic section conducted during the TTO experiment. The transport record is 11 months in length, has a mean of 5.7 ± 1.0 Sv (for water colder than 3°C) and a mean potential temperature of 1.59°C. The large uncertainty in the mean transport is due to loss of data, not only on a lost mooring, which lay in the outer parts of strong flow (see Fig. 5.6.4), but also incomplete records from the adjacent inshore mooring. Figure 5.6.6

shows a period of very weak transport across the 1990–91 boundary, and surprisingly long period variability (from 4 to 60 days, see Fig. 5.6.7). The uncertainty in the mean transport makes model validation (Section 5.6.5) an unreliable activity here.

At a distance of about 550 km from the Denmark Strait sill lies the Angmagssalik site at which three year-long arrays were deployed. These have been described in the section on re-analysis and the value of the mean transport of 9.0 ± 0.5 Sv reported. The mean potential temperature is 1.78°C and the periods of energetic variability range from 4 to 60 days (Fig. 5.6.7). Monthly averaged transports (not shown) have only a small range, namely from 5 to 11 Sv, but in the last $4\frac{1}{2}$ months of 1988 and the first month of 1989 (days 600–750) some very low persistent values were achieved. These were not reported by Dickson and Brown. Before these measurements were made, a conjecture that the overflow would show such overall steadiness would have been met with derision. The absence of a seasonal signal was also unexpected in light of the seasonal fluctuation seen in the inflow of North Atlantic water hugging the shelf edge east of the Faroe Islands (Gould *et al.*, 1985). However, neither the inflow on the North side of the Faroe Islands nor the East Greenland current have been observed sufficiently well to exclude the possibility of seasonal compensation. In both 1995 and 1997 moorings were deployed at depths of 1950 m and 2325 m at the Angmagssalik site (corresponding to distances of 50 and 80 km, respectively, on Fig. 5.6.5). Dickson *et al.* (1999) find that for the months of January and February 1997 the mean speed of the flow at the deeper mooring is much weaker than measured at all previous months, although afterwards the speed recovers to more nearly normal values. However, from these measurements alone, quantitative changes in overflow transport cannot be derived.

Although the Angmagssalik and southeast Iceland sites are the same distance downstream from their respective sills, namely 500 km, their overflow characteristics differ (Table 5.6.3). In the Iceland basin the mean flow is weaker than in the Irminger basin (3.2 Sv versus 9.0 Sv) and its variability is less energetic (2.0 Sv^2 versus 9.0 Sv^2). Compared with the transport at the sills, the flux has increased by factors of 1.7 and 3.5, respectively, and the core of the flow has descended 600 m

(to 1300 m from 700 m) and 1200 m (to 1800 m from ~ 600 m), respectively. The stronger entrainment in the western basin may also be responsible for the longer period variability seen at the Angmagssalik site (2.5–60 days) compared with that at the southeast Iceland site (4–10 days).

At Cape Farewell, the southernmost tip of Greenland, a 60-day deployment of three moorings has also furnished a transport estimate (Clarke, 1984). However, only three current meter records (on two moorings) were involved in calculating the dense water overflow. These measurements were combined with a hydrographic survey to yield a transport of overflow water in the range 13–16 Sv. However, the offshore limit of flow was arbitrary and it is quite impossible to associate any kind of uncertainty with the estimate. This figure is widely quoted in the literature and has been, unfortunately I believe, linked with those estimates for which error bounds can be derived. Nevertheless, the site is so well defined geographically that estimates there are almost inevitable (see Section 5.6.6). Clearly array measurements targeting the overflow should be made at Cape Farewell – if possible soon.

To summarize this section: the principal observed characteristics of the overflows in the Iceland and Irminger basins are presented in Tables 5.6.1–5.6.3. Nowhere has a seasonal signal been seen and variability (energy and period) generally increases downstream. Questions remain concerning steep downslope flows, the southward penetration of the overflow in the Iceland basin, and the merging of the two overflows in the Irminger basin.

5.6.4 Processes in the overflows

Currently the subjects of the location, intensity and impact of mixing within the northern overflows are active fields of research and it is likely that when this chapter is in print new results will already be appearing. All this information will be used to test and improve the parameterization of mixing in both analytical and numerical models; the latter are of particular importance in describing the overflows and hence the meridional overturning of the North Atlantic.

The vertical structure of overflows using expendable current profilers has been studied by Johnson and Sanford (1992) in the Faroe Bank Channel, in the region downstream of the Denmark Strait, as

well as in the Mediterranean outflow. Based on all these studies a turbulent planetary boundary layer (Ekman layer and logarithmic layer) is found to exist below the current maximum. A bottom mixed layer is also found, often considerably thicker than the planetary boundary layer. In the interface between the cold overflow and overlying warm water the shear is sufficiently strong to overcome the stratification and generate Kelvin-Helmholtz billows and mixing. As a result a cross-stream flow occurs opposite in sign and in terms of transport roughly equal in magnitude to that found near the bottom.

The author's unpublished observations from a 35-day deployment of moored instrumentation made in October 1989 near the sill of the Faroe Bank Channel support this picture (see Fig. 5.6.8). Assuming the downstream flow is in the direction 308–310°, the turning of the flow to the left 10 m above the bottom ($\sim 20^\circ$), and the turning to the right 300 m above the bottom (~ 5 – 7°) is shown in the mean flow: note that the warm water 400 m above the bottom has the direction 128°, i.e. in opposition to 308°. The thickness of the bottom mixed layer exceeds 100 m about 60% of the time and about 10% of the time it exceeds 200 m. Given the existence of a well-defined temperature–salinity relation, we can calculate the bulk Richardson numbers over a depth interval of 100 m centred about 350 m above the bottom. A time series from this calculation is shown in Figure 5.6.9. Richardson numbers are seen to be strongly modulated by semidiurnal tides and inertial oscillations and critical values are frequently achieved, the latter arising almost entirely from maxima in the shear (not shown here).

The impact of mixing is seen most clearly where the overflow is in contact with only warmer (lighter) water; then the warming that results can be quantitatively linked via mass flux divergence to average diapycnic diffusivity. Over a 75-km path within and beyond the exit of the Faroe Bank Channel a diffusivity across the 3°C isotherm has been estimated as $100 \pm 50 \text{ cm}^2 \text{ s}^{-2}$ (Saunders, 1990).

Although to date no detailed profile observations and study of mixing processes have been reported from either the Denmark Strait Overflow or the Faroe Bank Overflow, we are aware that some have been made and await their publication with interest. An unexpected discovery of the flow

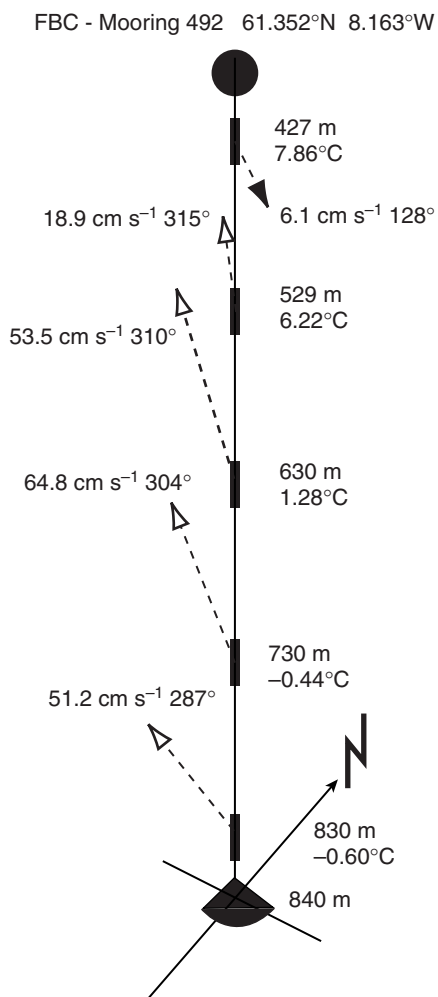


Fig. 5.6.8 Schematic representation of mooring 492 deployed for 37 days near the sill in the Faroe Bank Channel during Autumn 1989. Mean temperature, current speed and direction and depth is given for each instrument (Saunders, unpublished).

in the Irminger basin is the existence of mesoscale vortices seen in near surface drifter tracks (Krauss, 1996), anticyclonic on the inshore side of the overflow path and cyclonic on the offshore side. The vortices are surface-intensified and decay with depth, as seen in a hydrographic survey of the density field (Krauss and Käse, 1998). Spall and Price (1998) explain the cyclones as the result of potential vorticity (PV) conservation in the Intermediate Water crossing the sill, but leave the anticyclones unexplained. The existence of rotary flow at the depth of the overflow can be deduced from the Dickson and Brown moored current meter data via rotary spectral analysis, Figure 5.6.10. Note how the vortex energy decays with distance downstream. Inshore of the overflow, and especially at shallow depth, the anticyclonic circulations may accelerate the overflow, but otherwise the significance of the phenomenon is unknown. Similar behaviour was detected in flow through a deep channel in the northeast Atlantic called Discovery Gap (Saunders, 1987), although there the swirling flow was interpreted as travelling waves of subinertial frequency.

5.6.5 Analytical models of the overflow

In this section I consider what controls the discharge of the overflow, and the attempts of analytical models to predict the subsequent path and properties of the overflow. Determinations of the discharge through the Faroe Bank Channel and the Denmark Strait have principally used the concept of rotating hydraulic control in which the flow is limited by the speed of the fastest internal waves.

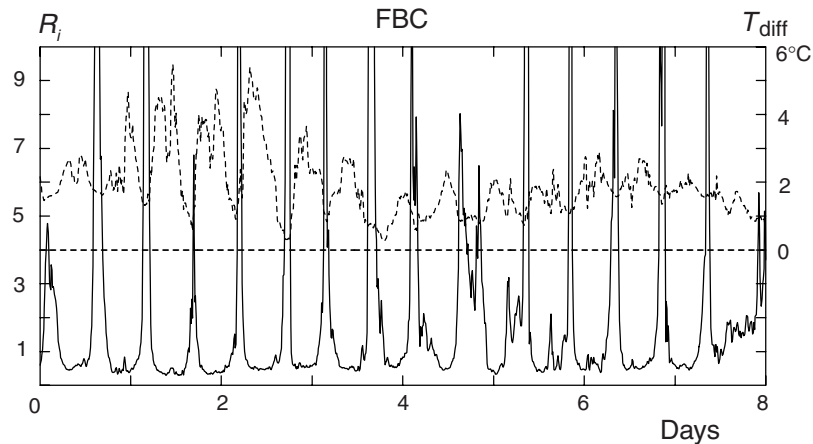


Fig. 5.6.9 The Richardson number derived from mooring 492 utilizing temperature and currents at depths of 427 m and 529 m (continuous line) recorded at 15-minute intervals. The temperature difference between the same pair of depths (dashed line) is also shown. The record is for 8 days commencing on 27 October 1989 and the minimum values of the Richardson number suggest frequent mixing events.

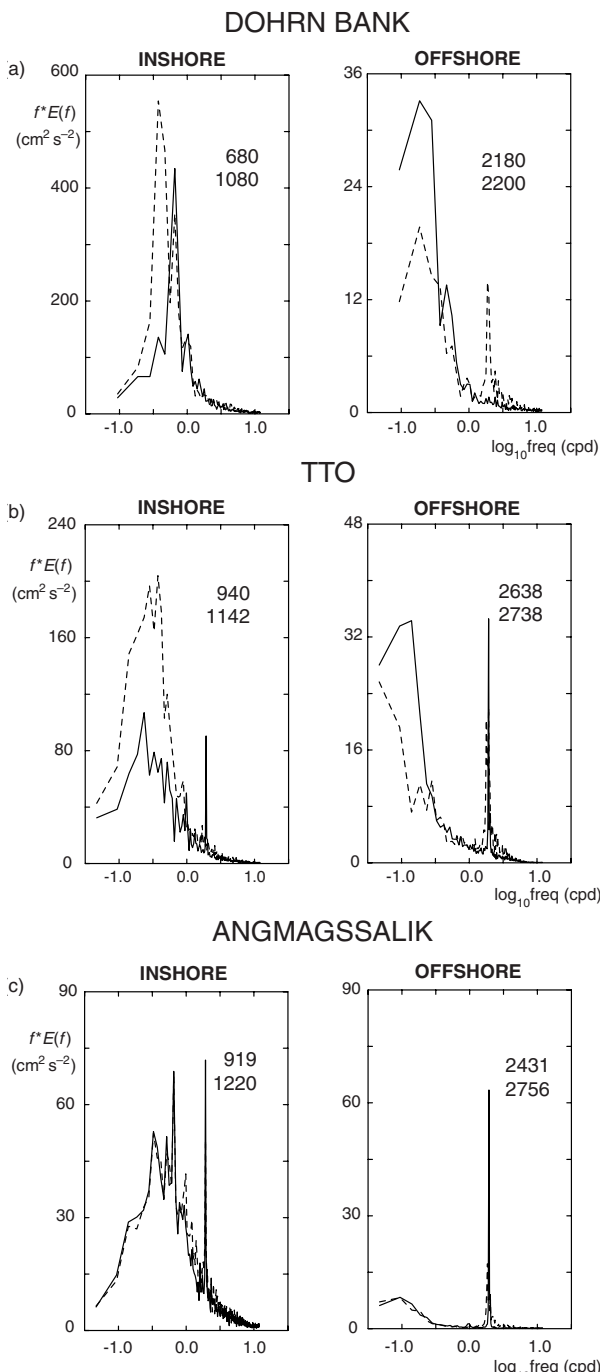


Fig. 5.6.10 Rotary spectra from current meters on the flanks of the overflow at the named sites in the Irminger Sea. For the two sites nearer to the sill, the variance of the anticyclonic flow (dashed) exceeds that of the cyclonic flow (solid); offshore the reverse holds. For the lower, more distant site no polarization is found. Two depths are indicated in each panel, that of the instrument and that of the bottom, both in m.

The subject has been reviewed by Pratt and Lundberg (1991) and by Whitehead (1998) and is complex, with solutions only found for a stratified

ocean that is represented by reduced gravity or two-layered models. Utilizing the simplest of these solutions, which assumes zero upstream potential vorticity, Whitehead (1998) has predicted the discharge through straits, over sills and through deep gaps. The results depend on four parameters: $g\Delta\rho/\rho$, reduced gravity; b , the upstream height over the sill; W , the width of the channel at the sill; and f , the Coriolis parameter. For both the northern overflows the width is greater than the Rossby radius, given by the expression $R^2 = 2g\Delta\rho b/\rho f^2$, and the discharge is

$$Q = g\Delta\rho b^2/2\rho f$$

The upstream height, measured above the sill, is that at which the ocean no longer appears to participate in the overflow process; the isopycnals are horizontal above this height. The values selected for all the parameters along with the resulting predicted discharges are seen in Table 5.6.4. Overprediction is found and is expected, since the theory is an upper limit on the flow and ignores turbulent mixing, friction and assumes a rectangular shape to the channel. Borenäs and Lundberg (1988) showed that for the Faroe Bank Channel a more reasonable shape, namely parabolic, led to a reduction of the discharge by about 30%.

Because of conservation of potential vorticity, in the heart of the channel the cross-stream shear becomes comparable to f , say 1.25 m s^{-1} per 10 km at 60°N , and observations show this to be unrealistically large. If non-zero potential vorticity is assumed the upstream flow may become confined to a boundary layer and its details may dominate the solution (Killworth, 1995). Yet another difficulty is that b , the effective depth of the sill, is a property of the observed flow, i.e. the solution itself, and is not an external parameter. The way forward is not clear.

Analytical models have also been used to predict the path of the overflow, notably those of Smith (1975) and Baringer and Price (1990). These termed 'streamtube' or 'plume' models describe integral properties of the flow and employ momentum, continuity and density conservation equations. Smith (1975) found solutions for the Denmark Strait Overflow that depended on two parameters, a bottom drag coefficient and an entrainment parameter, both of which were assumed constant. Values of bottom slope, gravitational acceleration, Coriolis parameter and overflow initial conditions were also

Table 5.6.4 Predicted discharges for the North Atlantic overflows (Whitehead, 1998)

| Site | g' (10^{-3} m s^{-2}) | h (m) | f (10^{-4} s^{-1}) | W, (km) | R (km) | Discharge (Sv) |
|--------------------|--|------------|-------------------------------------|------------|-----------|-------------------|
| Faroe Bank Channel | 5 | 400 | 1.3 | 20 | 15 | 3.0 |
| Denmark Strait | 3 | 580 | 1.3 | 350 | 14 | 3.8 |

required and path, mean buoyancy and transport derived. But hydrographic data alone and that collected over a 2-month period does not allow a critical evaluation of the model.

Baringer and Price (1997b) employed similar equations for the Mediterranean outflow but allowed both the bottom drag coefficient and interfacial drag, assumed determined by the Richardson number, to be observable quantities. The along-stream momentum equation was shown to yield the following balance:

along stream change of kinetic energy and internal potential energy of plume PLUS the change in external potential energy EQUALS the drag of the bottom and surrounding fluid.¹

The first two terms represent the slowing and flattening of the plume, the third the descent across contours. Based on observations made in the Mediterranean outflow (Johnson *et al.*, 1994b) and on the Blake outer ridge (Stahr and Sanford, 1999) it seems likely that, except very close to the sill, the principal balance is between descent and bottom drag. However, no detailed study of either of the northern overflows has yet been reported.

A development of the streamtube concept, a hybrid between analytical and fully numerical models (the latter considered in the next section), has been developed by Jungclaus and Backhaus (1994). Its integrated properties are similar to the Smith model, but it resolves the plume horizontally identifying the location of the core. The impact of topographic irregularities can also be studied, and in this respect it offers the potential to answer questions about steeply draining flow (see Section 5.6.2).

5.6.6 Numerical models of the overflow

For numerical ocean models that are global in character, there are two difficulties with the

representation of the overflows. The first is concerned with the horizontal resolution of the channels through which the overflows emerge, and the second with the vertical resolution with which overflows are described. For regional models (say covering the North Atlantic), in addition to the above difficulties experience has shown that it is essential to place the northern boundary well north of the Greenland–Iceland–Scotland Ridge (Willebrand *et al.*, 2000).

For coarse-resolution models ($>1^\circ$), such as are employed in climate modelling, the first difficulty is the most severe. In order to allow access between ocean basins it will be essential to widen channels unrealistically. For coarse vertical resolution it may also be necessary to deepen them excessively, too. Roberts and Wood (1997) illustrated these problems using a level model.

For fine-resolution models ($<1/4^\circ$ and as fine as $1/10^\circ$) the former difficulty is less severe, although ideally several gridpoints should span the channel. But even where there is good model vertical resolution at shallow depths, say 50 m intervals at 500 m, as the overflow descends the model vertical resolution coarsens, to something like 200-m intervals in excess of 2000 m in current models, which results in only one or two grid levels describing the vertical extent of the overflow.

The DYNAMO project (DYNAMO Group, 1997) was designed to compare the performance of level, isopycnal and sigma coordinate (terrain-following) eddy-permitting models with near identical initial conditions and forcing (Willebrand *et al.*, 2000). Their experience with respect to the overflow may be summarized as follows. The level model by virtue of its stepped seabed gives rise to unrealistic downslope spillage and consequent vertical convection, which mix away the overflow properties too rapidly. The sigma model has a similar defect with its excessive mixing also enhanced

¹ Mathematical expression for each of the terms can be found in Baringer and Price (1997) and also Stahr and Sanford (1999).

by horizontal diffusion across sloping isopycnals. In contrast, in the isopycnic model the diapycnic mixing is too weak and consequently the overflow properties are retained over unrealistically long distances. Some of these characteristics are shown in Figure 5.6.11 where the density distribution of a WOCE one-time section is compared with the output from

an isopycnal model, which was a component of the DYNAMO project, and a global level model (OCCAM, Webb *et al.*, 1997), which was not.

Fixes are available for some of these and other known defects, such as the coupling of a terrain-following boundary layer with a level model (Beckmann and Döscher, 1997), and on the

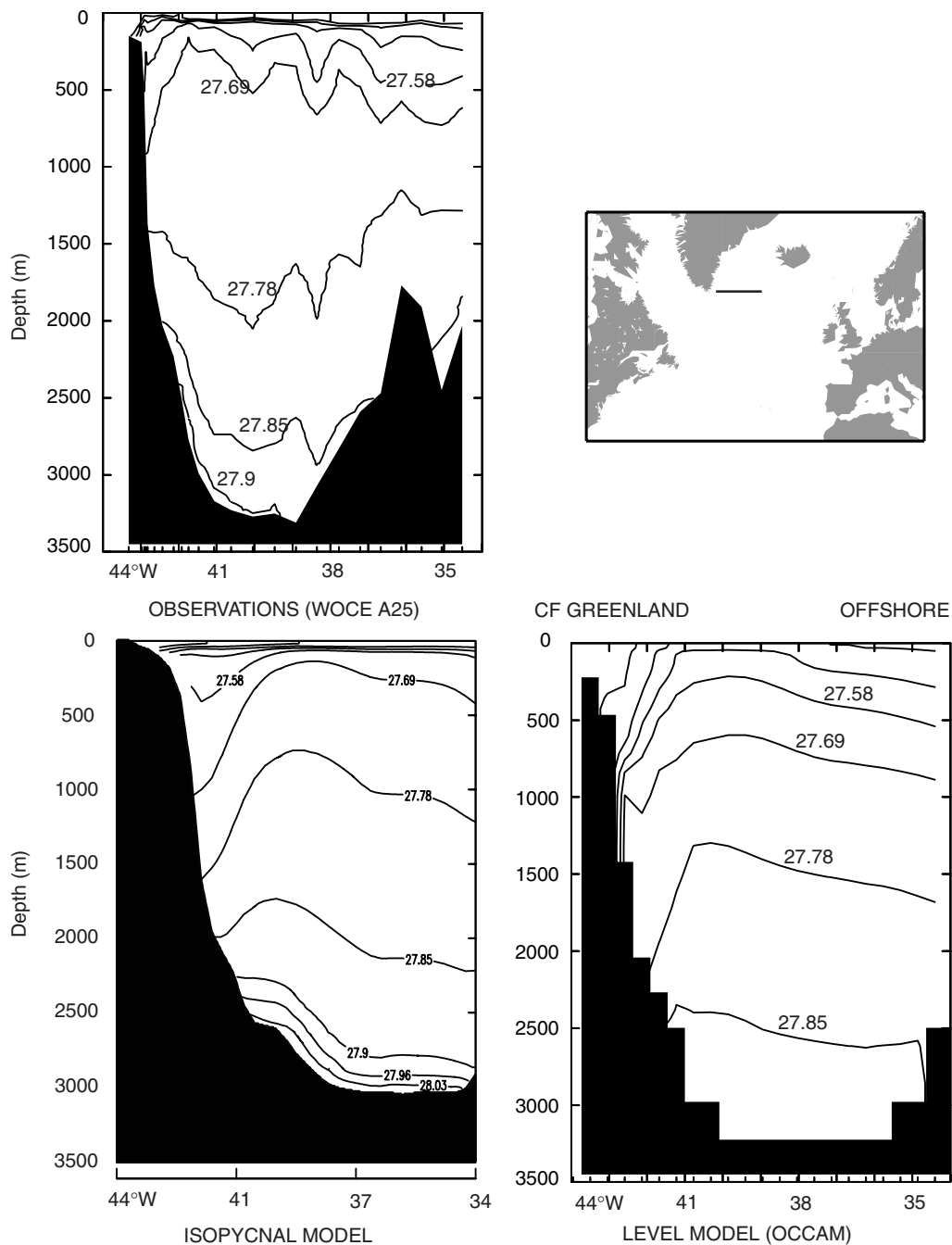


Fig. 5.6.11 The distribution of density on 60°N east of Cape Farewell (location, top right), seen in an isopycnal model (DYNAMO) and in a global level model (OCCAM, Webb *et al.*, 1997). Data from the WOCE one-time section A25, running SW to NE into Cape Farewell, is also shown.

margins an enhanced diapycnic mixing in the isopycnal model. But results from these upgrades are not yet available.

One important result from several studies of the North Atlantic has been the sensitivity of the resulting meridional overturning to the details of the overflow process (reviewed in Willebrand *et al.*, 2000; see also Böning and Semtner, Chapter 2.2). They show that the downstream development of the overflow affects both the strength and structure of the meridional overturning. Realism in modelling the overflow is thus a prerequisite for credible climate modelling.

5.6.7 Overflow variability

Because the current meter records cover only a few years, we must appeal to hydrographic observations for estimates of decadal variability. Bacon (1998) has assembled and analysed section data for the Cape Farewell data for the period 1955 to the present. Assuming the velocity field is geostrophic and is zero at 1000 m ('as other authors have done') the baroclinic transport for densities $\sigma_0 > 27.8 \text{ kg m}^{-3}$ has been calculated. The range of values is from about 2.5 to 8.5 Sv southward and is shown to be predominantly of low frequency (groups of closely spaced sections have small variance compared with that of the 42-year record). Bacon argues that while the Clarke value of 13 Sv measured in 1978 (discussed in Section 5.6.3) contains a barotropic component of 5 Sv, his own observations made in 1991, for which he estimated a combined barotropic and baroclinic estimate of 6 Sv, is quite inconsistent with such a large barotropic value. He concludes that on decadal time scales the overflow is variable, with low values in the 1950s and 1960s, high in the 1970s and 1980s and low in the 1990s. Because the causes of the barotropic velocity components (those hidden to hydrography) are unknown, Bacon's assertions are not universally accepted and their confirmation will perhaps only be demonstrated by a repetition of some of the transport measurements described in Section 5.6.3, or by coupled or ocean models with credible time-dependent overflow components.

On very much longer time scales fluctuations in the overflow has been investigated using palaeographic data. The sedimentary drifts that are a conspicuous feature of the Iceland basin (three are

sketched in Fig. 5.6.4) have been utilized for this purpose (Bianchi and McCave, 1999). These authors have constructed a time series of sediment grain size on the Gardar drift at 56°22'N and 27°49'W from the termination of the last glaciation (13 000–11 500 years BP) to the present. They argue that the sortable silt size (in the range 10–63 μm diameter) derived from a core is a qualitative measure of the near-bottom current speed and, on the assumption that the Iceland–Scotland overflow path remains close to the site sampled throughout their record, derive variations in the overflow strength. They find fluctuations that correspond to the 'little ice age' (AD~1550) when the flow slowed, and 'the medieval warm period' (AD~900–1250) when the flow speed intensified, and find the principal variability at a period of 1500 years. The information palaeographic data provides cannot be obtained by any other method and the verification of the conclusions derived from it can probably only be established and quantified by climate theory or climate modelling.

The concept of multiple equilibria for the global thermohaline circulation was first proposed by Broecker *et al.* (1985a) although Stommel (1961) had demonstrated such behaviour in a simple reservoir model. It was argued that sufficient freshening of the waters in the Nordic seas would prevent the production of dense water and shut off the saline upper inflow, leaving dense water production to the Antarctic region and/or the Pacific. Such a phenomenon occurred during the last glaciation when the overflows were believed shifted south, weakened or entirely absent. Such a change in the nature and strength of the meridional overturning in the North Atlantic appears to be confirmed in the pioneer modelling work of Bryan (1986) and Manabe and Stouffer (1988).

5.6.8 What have we learnt in WOCE?

In project WOCE the sustained experimental study of the northern North Atlantic (the subpolar gyre) was in 1997–98 and most of the *in-situ* observations, hydrography and float tracks, have yet to be reported. Via inverse analysis or via model assimilation the strength of the overturning circulation and in particular the contribution from the overflow may thus be re-assesed. Much of the science on which this review was based thus predated the WOCE programme and in particular on the work

of the author and of Dickson and Brown (1994) in which the overflow transports in both the Iceland and Irminger basins were quantified. The advances reported here are modest but I have sought to extract new information from the older measurements, information which should prove of value to modellers. Initially the overflows were observed to be surprisingly steady but more recent observations have suggested variability on time scales of months to millennia. There is ongoing effort into

investigating detailed processes within the overflow plume that will undoubtedly benefit future modelling, because parameterizing the mixing has been shown to be critically important. While current state-of-art ocean general circulation models represent the overflows poorly, the prospects are encouraging. Unfortunately the same cannot yet be said for the ocean component of coupled models, which are needed for credible climate modelling and prediction.

This Page Intentionally Left Blank

5.7

Mediterranean Water and Global Circulation

Julio Candela

5.7.1 Marginal seas

Marginal seas bordering the world's oceans make important contributions to the global thermohaline ocean circulation through their exchange of water with the major oceanic basins. Their principal effect is related to processes of water mass formation that occur within these bordering seas where heat and/or net freshwater losses are intensified due to their confined nature. It is well known that some of the intermediate and all of the deep water masses of the world's oceans are produced as the result of intense air-sea exchange in marginal seas (Warren, 1981a). The water masses formed in the marginal sea typically enter the open ocean as a dense outflow through a restricted channel or strait. One of the best known outflows is that from the Mediterranean Sea, which enters the North Atlantic through the Strait of Gibraltar as the lower layer of a two-way exchange flow (Bryden *et al.*, 1994; Bower *et al.*, 1997). After rounding Cape St Vincent, at the southwestern corner of the Iberian Peninsula, the outflow water begins to spread into the eastern North Atlantic to form a warm and salty tongue that extends westward from Portugal across the eastern Atlantic (Wüst and Defant, 1936; Worthington, 1976; Lozier *et al.*, 1995). This tongue is one of the most prominent features of the North Atlantic hydrography at intermediate depths, and its high-salinity water has been implicated in the preconditioning of the North Atlantic Deep Water formation (Reid, 1978).

This chapter deals with the Mediterranean Sea and its influence on the world's ocean thermohaline circulation and therefore on climate. It

describes water formation processes within the Mediterranean Sea, outlining the characteristics of well-known water formation sites and the evidence of recent shifts in water formation locations within the sea. Then it focuses on the characteristics of the exchange flows between the Mediterranean and the North Atlantic Ocean through the Strait of Gibraltar based on historical as well as recent (1994–96) flow measurements that reveal significant seasonal and interannual variability of the exchange flows, and in particular of the Mediterranean outflow into the North Atlantic. This outflow is then the subject of a detailed description since it determines the way the Mediterranean Water mixes with the surrounding waters in the North Atlantic, creating a warm and saline tongue of water that can be identified throughout the whole North Atlantic at a depth of about 1100 m (Fig. 5.7.1). It is fundamental for numerical models investigating the influence of the Mediterranean Water on the thermohaline circulation of the World Ocean to reproduce or parameterize the mixing processes in the outflow accurately, since they determine the properties and the depth of penetration of the Mediterranean Water in the North Atlantic. The chapter ends with a discussion of observational hydrographic evidence, mainly put forth in Reid's (1994) study, which supports the hypothesis that the Mediterranean contribution to the Nordic and Labrador Seas allows the formation of deep waters in the North Atlantic, or at least that without this contribution the waters formed would not be dense enough to penetrate to the depths they presently do.

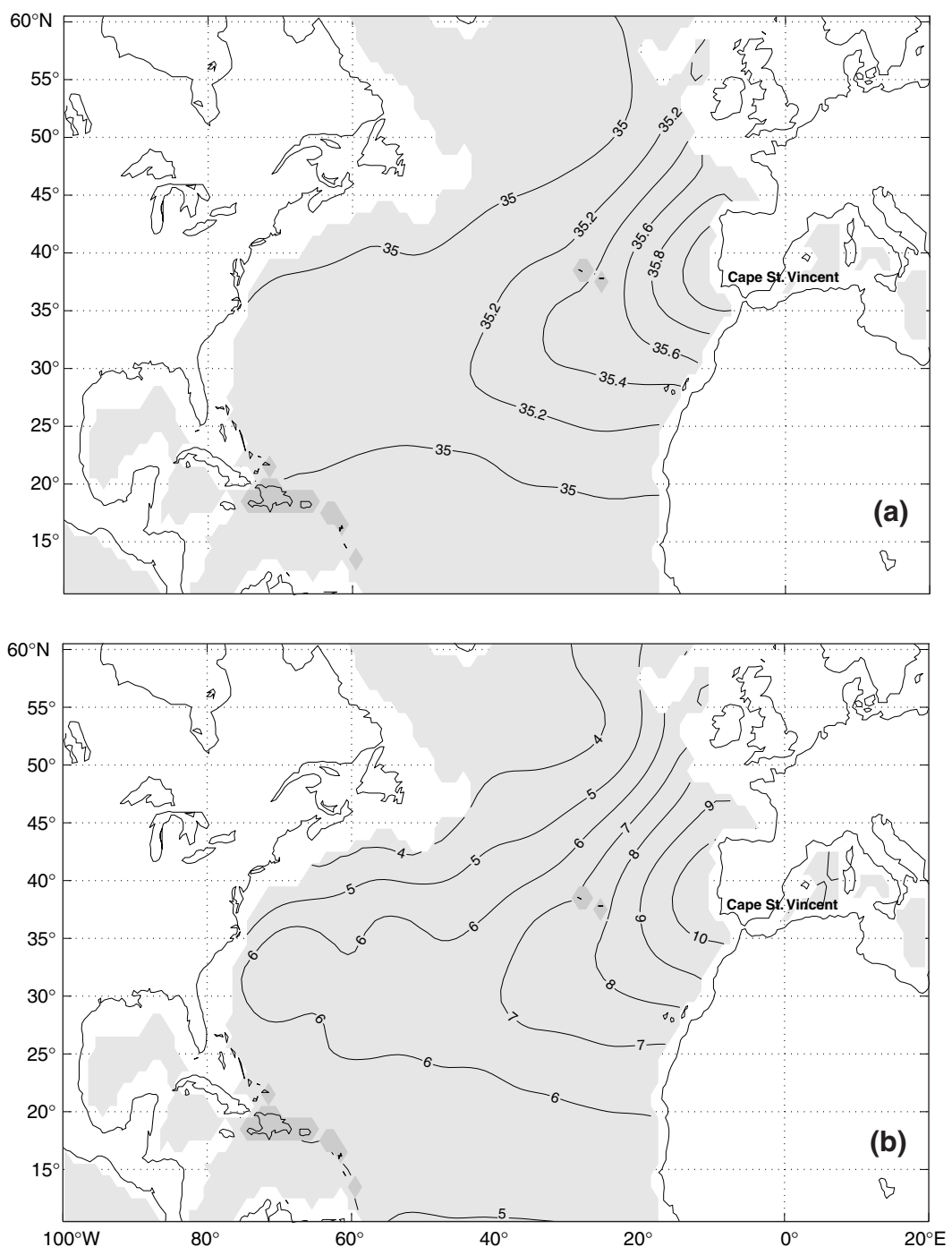


Fig. 5.7.1 Salinity (a) and temperature (b) contours at 1100 m depth in the North Atlantic from Levitus (1982) climatology. The contour interval for salinity is 0.2‰ and for temperature is 1°C.

The Mediterranean Sea, the *Mare Nostrum* of the Romans, is a semi-enclosed sea with a broad history intimately related to the development of western civilization, but only recently have oceanographers recognized that the waters of the Mediterranean provide them with a model of the world ocean itself (Lacombe, 1990). Geographically it

has a zonal extent of about 4000 km and a mean meridional width of 1000 km, with a mean depth of 1500 m and a maximum depth of up to 5000 m in the Ionian Sea. It is divided by the Strait of Sicily into Western and Eastern basins (Fig. 5.7.2). Mainly an evaporative basin, it acts to transform relatively fresh North Atlantic surface water (salinity of

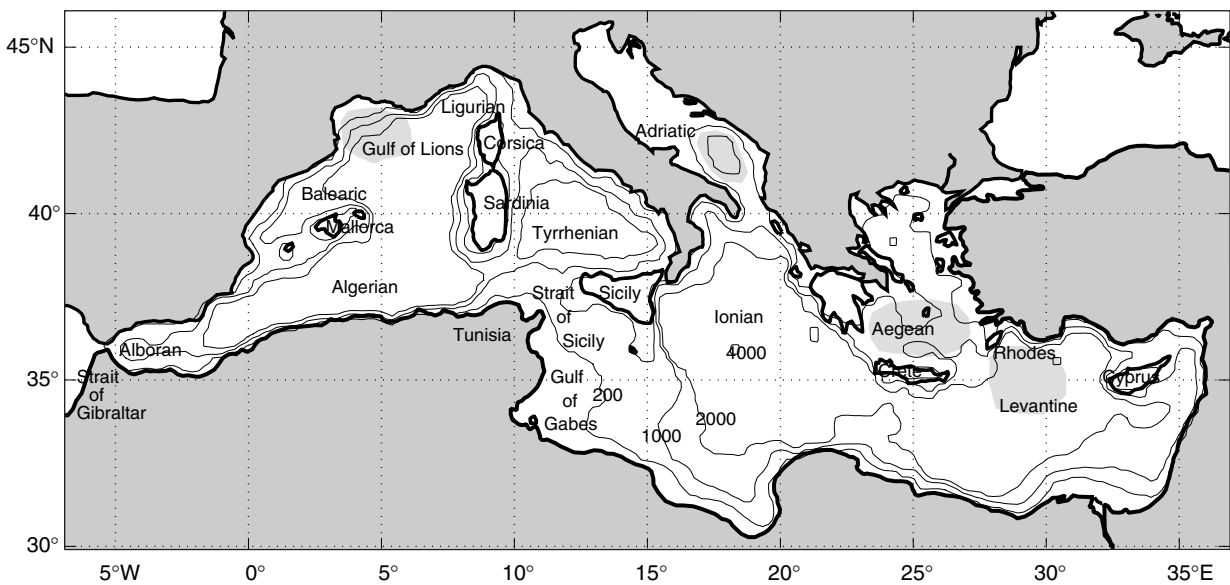


Fig. 5.7.2 Map of the Mediterranean Sea indicating names of places mentioned in the text. The shaded areas in the Gulf of Lions, Adriatic, Aegean and Levantine correspond to known regions of water mass formation. The 200, 1000, 2000 and 4000 m depth contours are also shown.

36.1%) into a dense Mediterranean Water, which has a salinity of 38.4‰, a temperature of 13°C and a density of 1029.7 kg m^{-3} , as it outflows at depth through the Strait of Gibraltar. The Mediterranean Sea is often regarded as a ‘laboratory basin’ for oceanographic circulation studies, especially of the thermohaline circulation, which is particularly active despite the relatively small size of the sea. It is one of the few places in the world where deep convection and water mass formation take place. In the present climate, deep convection occurs only in the Atlantic Ocean; the Labrador, Greenland and Mediterranean Seas; and occasionally also in the Weddell Sea. Convection in these regions feeds the thermohaline circulation, the global meridional-overturning circulation of the ocean responsible for roughly half of the poleward heat transport demanded of the atmosphere–ocean system (Marshall and Schott, 1999; see also Bryden and Imawaki, Chapter 6.1). It is conjectured that the resulting Mediterranean outflow plays an important though indirect role in the North Atlantic circulation (Reid, 1979) and, consequently, in the thermohaline conveyor belt at global scales and on time scales of global climate change (Wu and Haines, 1996). According to Reid (1979) the Mediterranean outflow helps maintain the high salinity of the Norwegian Sea. Without this source of high-salinity water the Norwegian–Greenland

Sea might not provide the denser waters that fill the Arctic Basin and thus contribute a major component of the North Atlantic Deep Water. It is the relatively saline North Atlantic Deep Water, transported by the deep western boundary current, that penetrates into the low-salinity waters of the Weddell Sea, where it is cooled further and enriched with brine to provide the Antarctic Bottom Water – the densest water found in the oceans of the world. To the extent that these suggested linkages are correct, the exchange between the Atlantic Ocean and the Mediterranean Sea is of significant importance.

5.7.2 Formation of Mediterranean Water

There are several places within the Mediterranean where preconditioning (i.e. a cyclonic circulation with convex curvature of isopycnals that bring dense, and usually weakly stratified, waters close to the surface) and air–sea fluxes combine to induce convective processes (for details on the convection mechanisms, see Marshall and Schott, 1999). These are the Gulf of Lions in the Western Mediterranean, the region south of Rhodes, the Levantine Basin, the southern part of the Adriatic Sea, and in recent years the south region of the Aegean Sea (Roether *et al.*, 1996) in the Eastern Mediterranean (Fig. 5.7.2). Of these sites, the Gulf of Lions region

is where convective processes reaching depths of more than 2000 m have been extensively documented since the Mediterranean Ocean Convective (MEDOC) experiment (MEDOC Group, 1970). The water mass distribution in the Western Mediterranean comprises three layers. In the upper layer, and originating mostly from the inflow through the Strait of Gibraltar, is the Modified Atlantic Water (MAW). Between 150 to 500 m depth, a warm and salty layer is found, referred to as Levantine Intermediate Water (LIW), which is formed by shallow convection in the Eastern Mediterranean Basin and then slowly spreads into the Western Mediterranean through the Strait of Sicily. Beneath the LIW layer, the basin is filled with near-homogeneous Western Mediterranean Deep Water (WMDW). It is this WMDW that is formed by deep convection processes in the Gulf of Lions and which contributes importantly to the characteristic of the Mediterranean outflow (Stommel *et al.*, 1973; Kinder and Parrilla, 1987). Based on a newly composed hydrographic climatology, Krahmann (1997) estimates a WMDW production rate in the northwestern Mediterranean of $1.8 \pm 0.6 \times 10^{13} \text{ m}^3 \text{ yr}^{-1}$, corresponding to $0.6 \pm 0.2 \text{ Sv}$. The average yearly WMDW production is made up of $1.3 \times 10^{13} \text{ m}^3$ of LIW and $0.5 \times 10^{13} \text{ m}^3$ of MAW. Thus, the formation rate of LIW and slight variations of its characteristics have implications on the WMDW formation rate and its variability. Actually, it is becoming clear from recent observations that deep water formation is not a process that recurs every year with certainty and regularity. The intensity of convection shows great variability from one year to the next and from one decade to another. For example, in the Gulf of Lions, 1969, the year of the first MEDOC experiment (MEDOC Group, 1970), was a year of strong convection, but convection in 1971 was not as strong (Gascard, 1978). Vigorous deep convection to 2200 m returned in 1987 causing a very homogeneous water body of potential temperature 12.79°C and salinity 38.45‰ (Leaman and Schott, 1991). Convection reached only to 1700 m in 1991 and did not mix the water column as thoroughly (Schott *et al.*, 1996). Fluctuations in the composition and possibly also the volume of the Mediterranean outflow are the result of the variability in WMDW formation, coupled to the LIW formation variability (Nittis and Lascaratos, 1998). Recent findings that in the last decade an

influx of Aegean Sea water has replaced 20% of the deep waters of the Eastern Mediterranean, which were previously only formed in the Adriatic Sea (Roether *et al.*, 1996), also affect such fluctuations.

Apart from these observed interannual variations in deep and intermediate water formation, there is a well-documented increase in the salinity of the deep waters of the Western Mediterranean over the past 40 years (Lacombe *et al.*, 1985; Leaman and Schott, 1991). Observations also suggest that in the past 10 years there has been a jump in the salinity of the newly formed deep waters in the Eastern basin (Roether *et al.*, 1996). It has been argued that this salinity increase has resulted from the diversion of the Nile and Russian rivers for irrigation so that the effective net evaporation over the Mediterranean basin has increased. Application of hydraulic control models then project that the overall Mediterranean salinity will increase by about 0.13‰ over the next 100 years or so (Rohling and Bryden, 1992). However, it remains unclear what the implications of such an increase in salinity would be on the overall circulation of the Mediterranean and North Atlantic.

5.7.3 Outflow of Mediterranean Water at the Strait of Gibraltar

The Strait of Gibraltar is the Mediterranean's only communication with the World Ocean; it is about 60 km long, 15 km wide at its narrowest section (Tarifa narrows) and only 280 m deep at its main sill (Fig. 5.7.3). There are three main components to the flow (Lacombe and Richez, 1982; Candela, 1991): a tidal, mainly barotropic flow, with magnitudes of up to 2.5 m s^{-1} (Candela *et al.*, 1990); a barotropic subinertial component driven by atmospheric pressure fluctuations within the Mediterranean and with magnitudes close to 0.4 m s^{-1} (Candela *et al.*, 1989); and a baroclinic subinertial component driven by the internal pressure gradient due to the density difference between the Mediterranean and the Atlantic Waters, with magnitudes of about 0.5 m s^{-1} , and likely to be hydraulically controlled (Armi and Farmer, 1988). Therefore, the Strait is dynamically very energetic with tidal, subinertial and long-term currents all being of significant amplitude. This situation makes studying the exchange flows particularly difficult, requiring long and careful measurements

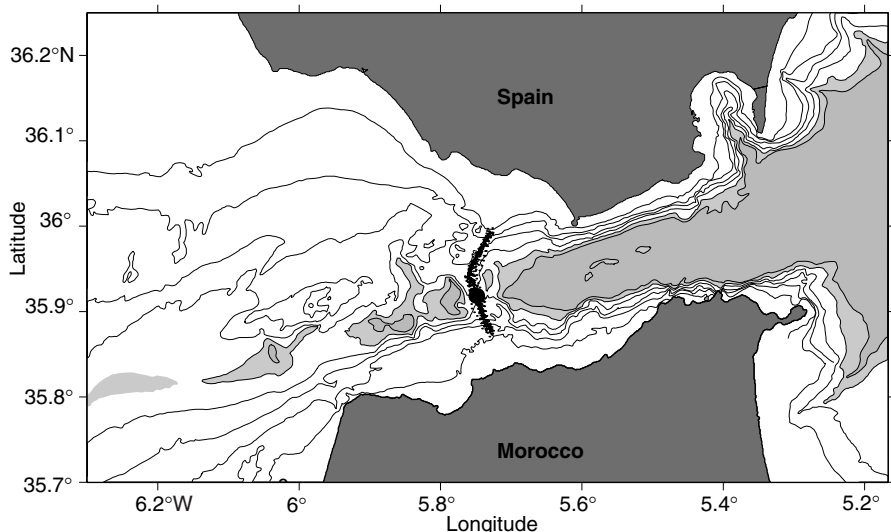


Fig. 5.7.3 Map of the Strait of Gibraltar showing the location of the sill mooring indicated in the text (large dot). The 50, 100, 200, 300, 400 and 500 m depth contours are also shown. Depths larger than 400 m are shaded. The small dots distributed along Gibraltar's main sill indicate the positions where current profiles were obtained from a ship-mounted ADCP during a tidal cycle.

not only of currents but also of water characteristics and in particular of the fluctuations of the interface that separates the inflowing Atlantic from the outflowing Mediterranean Waters (Bryden *et al.*, 1994).

The Strait of Gibraltar has been the subject of several field measuring programmes in recent years (Bryden and Kinder, 1991). The longest continuous record, 2 years (October 1994–October 1996) of continuous measurements of the current profile and water properties at a mid-sill location on Gibraltar's main sill (Fig. 5.7.3), comes from a 2.5-year measurement programme that concluded in October 1996. These observations were obtained with an upward-looking, bottom-mounted, broadband 150 kHz Acoustic Doppler Current Profiler (ADCP), capable of measuring the entire 280 m water column at this mid-sill location, with a vertical resolution of 10 m. In addition, during two cruises on board the RV *Poseidon* in April 1996 and in October 1997, consecutive crossings of the strait were performed over the sill section measuring the current profile using a ship-mounted ADCP through a complete semidiurnal tidal cycle (Figure 5.7.3 shows the location of the current profiles measured by the ship over the sill). The April 1996 cruise coincided with a period of neap tides (small amplitude), while those of October 1997 were performed during spring tides (large amplitude), providing an idea of the across-strait

current structure during both tidal extremes. From these sections it is clear that the currents at the sill present large cross-strait variability; however, the mid-sill moored ADCP measurements capture the main time variability of the currents and both sets of observations are used here to estimate a time series of the exchange through the Strait. In calculating the exchange through the Strait, it is important to obtain estimates of the quality, as well as the quantity, of the water being exchanged. In order to distinguish Atlantic from Mediterranean waters it is essential to have simultaneous measurements of the density structure of the water column along with those of the currents. In addition, it is mandatory to take into account the contribution to the mean exchange from the high correlation between the barotropic (tidal and subinertial) currents and the depth of the interface separating Atlantic and Mediterranean Water types at the sill (Bryden *et al.*, 1994). For this reason, simultaneously with the bottom-mounted ADCP measurements, an additional mooring was installed that contained several (3 to 5) instruments in the water column, depending on the deployment period, which made it possible to construct time series of the depth of the interface between the Atlantic and Mediterranean Water cores. Based on previous work (Bryden *et al.*, 1994), as well as these observations, it was decided to use the 37 salinity as the characteristic value delimiting the boundary between

the two layers. Estimates of Atlantic and Mediterranean Water exchanges were calculated using hourly time series of current velocities at 10 m depth intervals from the surface to the bottom, hourly time series of the depth of the interface, and a realistic cross-section bottom relief together with the cross-strait current structure based on the aforementioned ship surveys done during spring and neap tidal cycles. These, after being low-pass filtered to retain periods longer than 3 months, are shown in Figure 5.7.4.

An important result from these calculations is that both the Atlantic and Mediterranean Water transports show a small, but appreciable, seasonal cycle. Of the two, the outward Mediterranean lower-layer flow is a more reliable estimate, showing an annual transport range of 0.28 Sv with

minimum outflow around early summer (July 1995) and a maximum in late winter (February 1995 and 1996). The seasonal cycle on the inflow is not as well represented in these observations, although maximum inflow tends to occur during the summer of 1995 with a second maximum at the beginning of 1996. Minimum inflows occur around late winter (February 1995 and 1996) coinciding with the maximal outflows. Bormans *et al.* (1986) suggested a seasonal cycle in the inflow of about 6%, with maximum transport in the spring. They attributed the increase to changes in interface depth and argued that winter water mass formation processes raise the interface level within the Mediterranean, while draining of the Levantine Intermediate Water reservoir occurs during the rest of the year, effectively lowering the interface. The

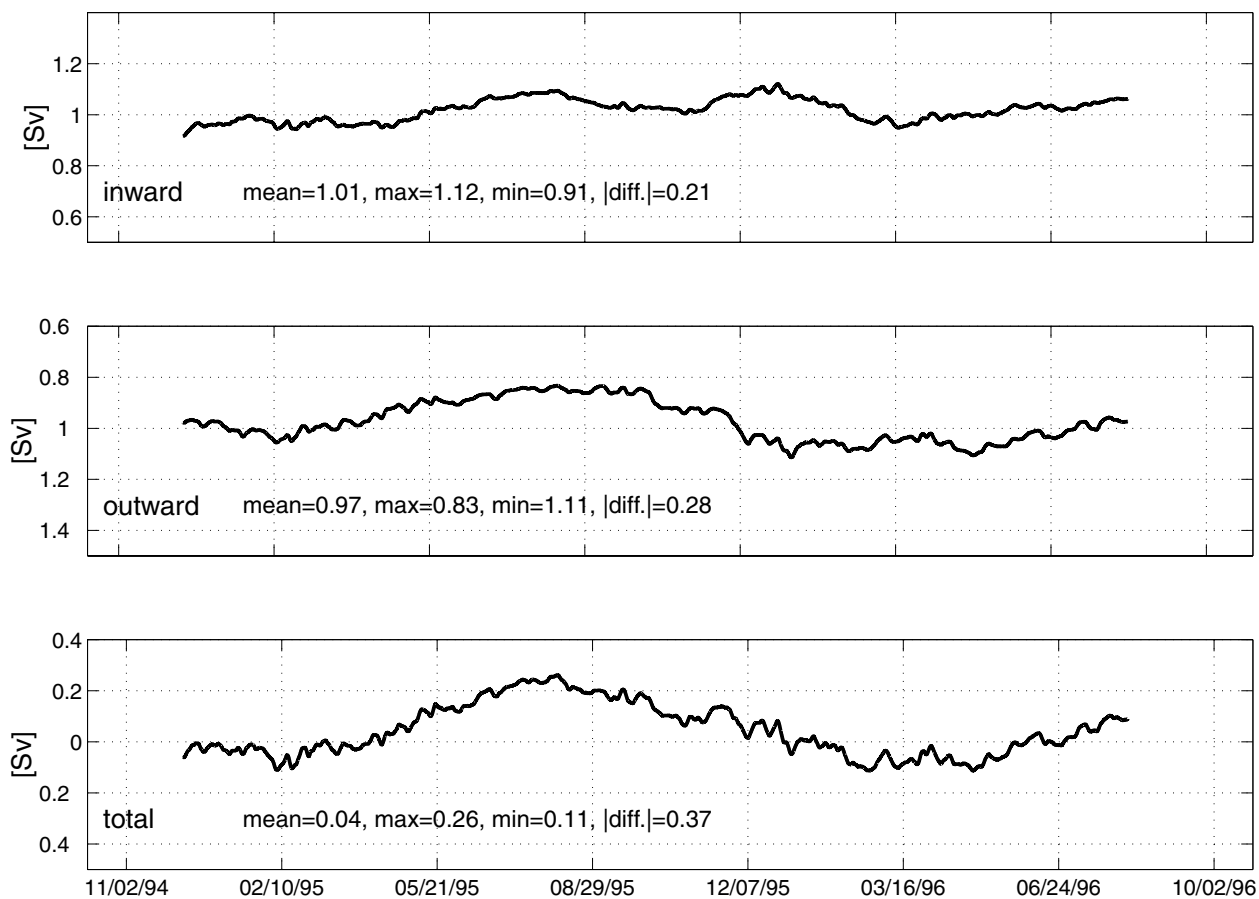


Fig. 5.7.4 Low-passed (periods larger than three months) transport estimates in the Strait of Gibraltar. The transport calculations are done from hourly time series of currents measured at the mid-point of Gibraltar's main sill with a vertical resolution of 10 m, time series of the depth of the 37‰ isoline separating Atlantic and Mediterranean Waters and information of the cross-strait current structure based on shipboard current observations across the sill during two complete semidiurnal tidal cycles at springs and neaps. The inflow (upper), outflow (middle) and total (bottom) transports are indicated in Sverdrups ($1 \text{ Sv} = 10^6 \text{ m}^3 \text{ s}^{-1}$). The mean, maximum, minimum and range of each plot are also indicated. The time axis of the lower plot is common to all three panels.

observations shown in Fig. 5.7.4 do not seem to support this argument. Originally the calculated barotropic or total transport showed a mean value of 0.086 Sv, which is about twice of the expected value based on estimates of net evaporation over the Mediterranean Basin (Garrett *et al.*, 1993b). This pointed to uncertainties in the estimates of the upper-layer inflow, where the cross-section is wider and transport estimates based on only mid-strait current measurements were considered unreliable. Therefore currents in the upper 100 m were reduced by 9% in order to have a mean total transport value of 0.04 Sv over the 2 years of observations, in accordance with historical net evaporation estimates. Apart from this mean correction the seasonal cycle present in the total flow has the correct phase to be the principal contribution to the observed seasonal sea-level rise within the Sea, although to explain fully the observed sea-level change one has to take into account also the effects due to evaporation and seasonal changes in heat content. Evaporation and heat loss from the Mediterranean also have seasonal cycles, with maximum loss of both heat and moisture during winter; heat is actually gained from the atmosphere by the Mediterranean during April–August (Bunker, 1976b). The effect of seasonal air–sea forcing over the Mediterranean on the instantaneous transport through the strait, however, may be quite small, as the residence time involved in the transformation of Atlantic Water to Mediterranean Water is on the order of decades (Lacombe *et al.*, 1981). It is more likely that seasonal fluctuations of transport result from dynamic effects more local to the strait, or from mechanisms of draining and filling of the LIW and/or WMDW reservoirs, as suggested by Bormans *et al.* (1986). At periodicities of days to months there is a clear increase of variability of the exchange in both layers during the late fall and winter periods (Astraldi *et al.*, 1999).

At interannual time scales, the formation of Mediterranean Water masses may occur under different conditions in different years, changing the characteristic temperatures and salinities of the outflow (Lacombe *et al.*, 1985). As a result, different volumes of outflow in different years might transport the same flux properties. This variability in the characteristics of the outflow is generally thought to be a small effect, but investigators have noted a wide range in the maximum of salinity

observed west of the sill: Schott (1928) found a maximum of 37.25‰ over several years of observations, Boyum (1963) a maximum of 38.2‰, and Kinder and Parrilla (1987) a maximum of 38.44‰. Based on hydrographic sections in the Gulf of Cadiz, Ochoa and Bray (1991) estimated an equivalent transport of ‘pure’ Mediterranean Water of 0.7 Sv, assuming salinities of 38.4‰ and 35.6‰ for Mediterranean and Atlantic Waters. They also estimated a freshwater flux equivalent to 0.53 m yr^{-1} of evaporation excess over the Mediterranean and a heat flux higher in the autumn of 1986 than in the spring (6.0 W m^{-2} versus 2.2 W m^{-2}), due to warmer surface temperatures in the autumn. Salt fluxes from our observations, computed by the same method as Bryden *et al.* (1994), show a mean value of $1.3 \text{ Sv} \text{‰}$ with a large standard deviation of $0.4 \text{ Sv} \text{‰}$ in the 2 years, which implies a mean net evaporation over the Mediterranean Sea of 0.45 m yr^{-1} , when mass and salt conservation equations for the whole Mediterranean Basin are taken into account. This net evaporation is similar to previous estimates (Bryden *et al.*, 1994), but shows appreciable interannual differences of 0.15 m yr^{-1} . Temperature fluxes, computed as in Macdonald *et al.* (1994), give a mean inward flux of $3 \text{ Sv} \text{ }^{\circ}\text{C}$, with a considerable interannual difference of $1 \text{ Sv} \text{ }^{\circ}\text{C}$. This mean temperature flux through Gibraltar implies a mean heat loss through the Mediterranean Sea surface of about 3 W m^{-2} , considering that the estimated 0.04 Sv of net inward flow leaves the surface of the Mediterranean at 25°C . This heat loss is a factor of two smaller than the 6 W m^{-2} obtained by Macdonald *et al.* (1994) based on direct current and temperature measurements done in the strait between October 1985 and October 1986. However, in contrast, climatological estimates of the basin mean heat flux based on sea surface measurements have typically shown a heat gain by the Sea of $20\text{--}30 \text{ W m}^{-2}$ (Garrett *et al.*, 1993b; Josey *et al.*, 1997). Further research is required to resolve this discrepancy. Although both observed salt and heat flux interannual differences seem to be small with respect to their effect on the North Atlantic water mass structure, it is still not possible to conclude that they are negligible.

From a climatic point of view it is important to know the mean values of the inflow and outflow as accurately as possible as well as any interannual variabilities. Recent numerical model studies

(Gerdes *et al.*, 1999) suggest that a correct representation of the Mediterranean salt tongue in the North Atlantic requires correct inclusion of the outflow mass volume rather than the frequently used procedure of only specifying a salinity source at the location of the Strait of Gibraltar. The transport estimates shown here, which are close to 1 Sv each way, are significantly higher, about 30%, than those calculated from earlier data (Bryden *et al.*, 1994). This increase principally comes from the mean currents at the mid-sill loca-

tion being 30% larger in the 1994–96 period from those measured in the October 1985–October 1986 period (Fig. 5.7.5). This significant change in magnitude between two measuring periods separated by nearly a decade is surprising and points to the importance of monitoring the exchange flows at Gibraltar as an indication of long-term climatic changes occurring in the Mediterranean Sea. Another important aspect of these new measurements is that they show relatively large interannual differences of the outflow, increasing from 0.98 Sv

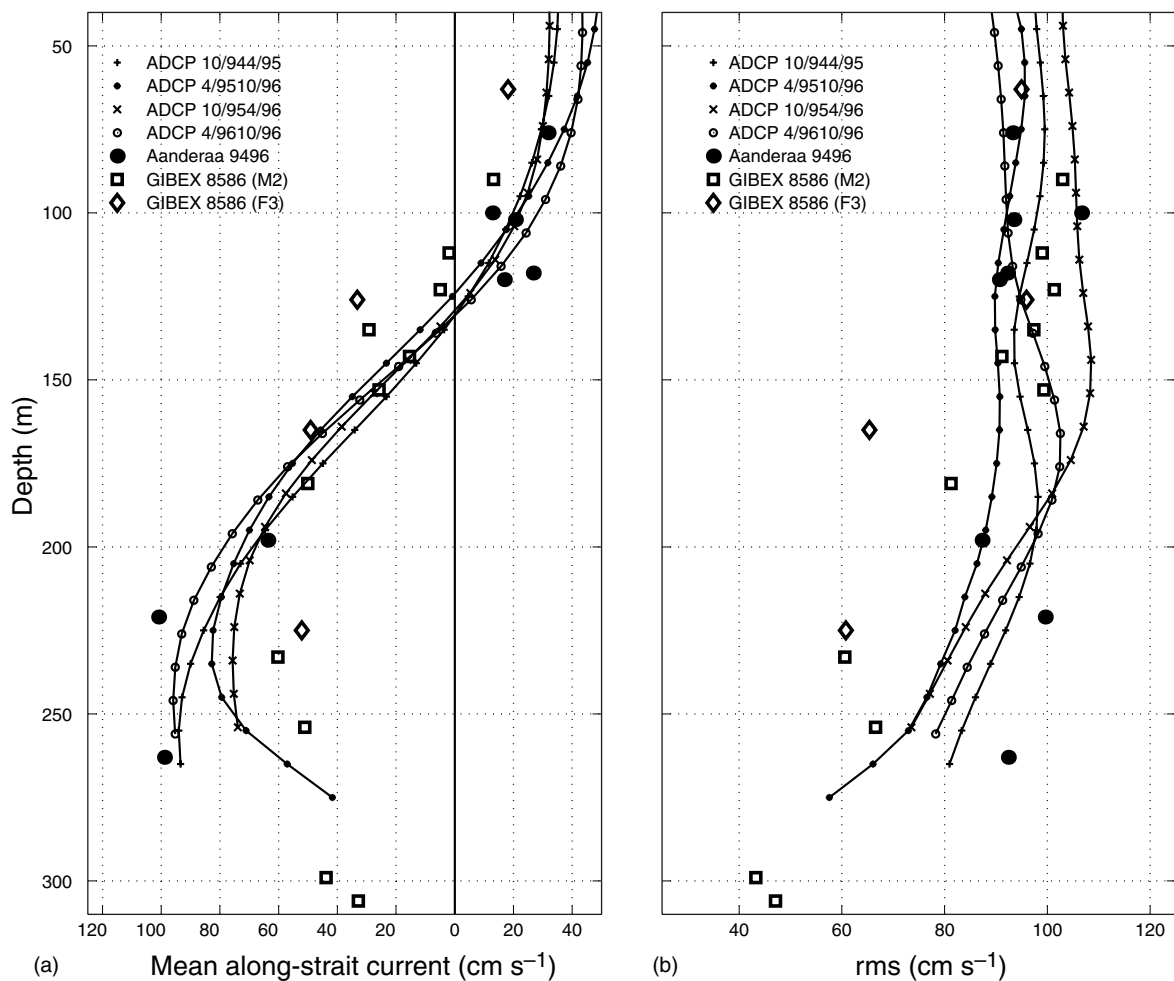


Fig. 5.7.5 Mean (a) and rms values (b) of the along-strait current measured at the sill in the Strait of Gibraltar. The continuous lines correspond to observations obtained with a bottom-mounted ADCP at the location indicated in Figure 5.7.3. The ADCP profiled the whole water column, with a 10 m depth resolution, at four 6-month-long deployment intervals between October 1994 and October 1996. The specific time interval for each deployment is indicated in the plots. Concurrent with the sill ADCP there were currents measured with Aanderaa current meters on a nearby mooring. These are indicated by large dots at the specific depth of each instrument. Each dot corresponds to a 6-month-long measuring period within the October 1994 to October 1996 observation interval. Also indicated are currents measured with Aanderaa current meters at a nearby sill location (squares and diamonds), but during the Gibraltar Experiment (GIBEX) between October 1985 and October 1986. Details on the specific location of the M2 and F3 moorings, as well as the length of the measuring periods for each instrument during GIBEX, can be found in Candela *et al.* (1990).

in February 1995 to 1.07 Sv in March 1996. This increase of close to 0.1 Sv from 1995 to 1996 is significant and could very well have implications on the effects of the outflow in the water structure of the North Atlantic. Close monitoring of the Gibraltar Exchange will certainly render valuable information for climate studies of the Mediterranean Sea and the Global Circulation.

5.7.4 The effect of Mediterranean Water outflow on the circulation of the North Atlantic and the World Oceans

The Mediterranean Water exits the Strait of Gibraltar as a single, dense plume that flows down the northern continental slope of the Gulf of Cadiz as a gravity-driven boundary current over complicated topography. As the outflow spreads northwestward along the southern Spanish and Portuguese coasts, it slowly loses its high salinity as it mixes with fresh North Atlantic Central Water (Baringer and Price, 1997a; Bower *et al.*, 1997). By the time the flow reaches the vicinity of Cape St Vincent it is neutrally buoyant (Ochoa and Bray, 1991; Zenk and Armi, 1990). From this point, part of the outflow is trapped along the continental slope flowing northward, while another part flows westward into the ocean interior (Reid, 1994; Iorga and Lozier, 1999a). It is known that a large portion of this westward branch is implicated in the formation of sub-mesoscale coherent vortices, Meddies, that contain a core of warm and salty Mediterranean Water (Käse and Zenk, 1996; Bower *et al.*, 1997). Meddies are typically 20–100 km in diameter and 200–1000 m thick, centred about 1000 m depth. Richardson *et al.* (1989) estimated that 8–12 Meddies form each year based on estimates of the number of coexisting Meddies and their average lifetime (2–3 years), and that they may transport about 25% of the salinity anomaly flux that comes through the Strait of Gibraltar. Arhan *et al.* (1994) suggested that Meddies may be responsible for more than 50% of the zonal salinity flux at the level of the Mediterranean Water in the North Atlantic, based on simultaneous observations of three Meddies along a hydrographic section at 15°W, and previous work showing that some Meddies drift westward at a speed five times the background flow. Recently, Bower *et al.* (1997) have estimated a Meddy formation rate of 15–20 Meddies per year

based on observations of RAFOS (reverse of SOund Fixing And Ranging) floats seeded in the Gibraltar outflow in the Gulf of Cadiz. This Meddy production rate supports the idea that a large portion of the observed zonal salinity anomaly flux, about 50%, is directly related to Meddies. With regard to the observational basis for the pathways of the Mediterranean outflow, we do not yet know how much of the outflow proceeds north along the Iberian continental slope and how much flows or circulates slowly westward from the Strait. We cannot yet estimate with certainty the outflow advected as Meddies versus how much is advected in concentrated boundary currents, just as we are still unclear on the mixing mechanisms that erode the high-salinity core of the outflow (Bryden and Webb, 1998). Quantifying and understanding these details are at the heart of being able to answer with certainty the role played by the Mediterranean outflow on the North Atlantic circulation.

The outflow of the Mediterranean is only about 1 Sv. This is a relatively small transport compared with those found in the North Atlantic, but its salinity of 38.4‰ and temperature of 13°C are extremely high compared with any other waters in that depth range. The effect of these large contrasts in water mass properties is two-fold: first, they help identify both a northward flow along the eastern boundary to the Greenland–Scotland sill and a westward flow across the Atlantic that turns southward along the western boundary, reaching the Antarctic Circumpolar Current and the Weddell Sea. Second, even at those distant places where this water shallows or outcrops, such as near Iceland and in the Weddell Sea, it retains salinities high enough to form, when cooled enough, the densest waters of the northern North Atlantic and the Weddell Sea (Reid, 1994). Also, the Mediterranean outflow is the source of the mid-depth changes of heat and salt to the waters entering the North Atlantic. As the Mediterranean outflow pours down from the Strait of Gibraltar it joins the subsurface waters flowing northward along the eastern boundary. These northward flows include waters from the South Atlantic, and before they interact with the outflow they are relatively low in temperature and salinity. After the encounter, these flows carry the outflow water northward to about 40°N and then divide, a portion continuing northward along the boundary

towards Iceland and the rest turning with the westward limbs of the large cyclonic and anticyclonic gyres. The northward part carries warm and saline water that mixes with the Norwegian–Greenland Sea Waters in the passages east and west of Iceland. The westward part crosses the Atlantic, and as it approaches the western boundary near 25–35°N it turns both northward, forming the deepest part of the Gulf Stream above about 3000 m, and southward, joining the southward flow along the deep western boundary and the eastward limb of the cyclonic gyre. As a result of these gyral flows, the added heat and salt from the Mediterranean outflow are spread both northward by the cyclonic gyre and southward along the western boundary into the South Atlantic Ocean, where its contribution makes the southward flow warmer and more saline than the incoming circumpolar waters to the east (Reid, 1994). However, recent analysis based on a new North Atlantic climatology (Iorga and Lozier, 1999a,b) does not support the presence of a westward current of Mediterranean Water that crosses the North Atlantic. Instead, Iorga and Lozier's inverse model exhibits a westward current at $\sim 35^{\circ}\text{N}$, which derives its waters from the poleward, eastern boundary current off Africa rather than from the Mediterranean outflow. This would imply that the main mechanism for the westward propagation of the Mediterranean outflow is 'diffusion' by meddies rather than a well-defined current. With respect to the northward flow as an eastern boundary current, their work does give evidence for the presence of the northward branch of Mediterranean Water penetrating past 55°N on its way to the Nordic Seas. However, recent work by McCartney and Mauritzen (2001) based on regional water mass distributions and geostrophic shear rejects Reid's deep source hypothesis in favour of a shallow source hypothesis. Rather than a flow of deep Mediterranean Overflow Water along the eastern boundary rising from depth to feed the Nordic Seas, the inflow is supplied directly by transformed North Atlantic Current waters from the same depth range as the inflow. This shallow source hypothesis is also supported by the recent high-resolution ocean circulation modelling work of New *et al.* (2000a), which proposes shallow sources composed of water masses of western origin carried by branches of the North Atlantic Current and the more saline Eastern

North Atlantic Water transported northwards from the Bay of Biscay region in a 'Shelf Edge Current' around the continental margin. Clearly more work is needed to identify if any of the proposed sources of saline waters to the Nordic Seas is exclusive of the others, or more likely the main contributor during certain periods. In any event what is well recognized is that the warm and saline deep water flowing out of the North Atlantic extends throughout the Antarctic, Indian and Pacific Oceans, identified as a salinity maximum that lies above the bottom over most of the southern hemisphere and projects back into the Atlantic Ocean through the Drake Passage. The salinity decreases along the path of flow but it remains high enough where the saline layer shallows in the Weddell Sea to contribute to the formation of the densest abyssal water of the world's open ocean (Reid, 1994).

A possible line of research to investigate the implication of the Mediterranean outflow on the North Atlantic circulation is to use numerical simulations, though they must be validated through a systematic comparison of their output with actual observations. Recent modelling efforts have been quite successful at reproducing the observed structure and have helped us to understand the dynamics governing the behaviour of the Mediterranean salt tongue in the North Atlantic (Spall, 1999; Stephens and Marshall, 1999). However, it seems essential that the models should not only simulate the mean observed features, but they should also reproduce the observed transient behaviour of the system. For climate change studies the models should exhibit interannual and longer-term variations of the same nature and magnitude as are observed. Models useful for predicting climate changes resulting from an increase in salinity of the Mediterranean outflow should capture or parameterize accurately critical small-scale processes, such as the pathways of the descending outflow plume after it exits the Strait of Gibraltar and its mixing. This poses a particular challenge for numerical algorithms because the strong current is of such small scale and involves mixing processes that occur on even smaller scales. Hence, it is of outmost importance to establish some degree of confidence in the models' ability to represent the real outflow characteristics by a thorough validation based on comparing the model simulations with real data. Before model error estimates are

available, model simulations and predictions must be taken with care. After proper validation, the models can be used as a means of obtaining predictions of the response of the outflow to external forcings. Such experiments may be used also to study feedback processes and to identify the principal elements involved. However, one has to be very careful not to stretch the available evidence and venture into unsupported speculations on what might happen if, for example, the present trends of salinity increase of the deep waters in the Mediterranean persist; and in what ways this might affect the deep water formation processes in the North Atlantic, and consequently the thermohaline circulation of the world's oceans.

All evidence points towards a very important contribution of the Mediterranean outflow to the thermohaline circulation of the World Ocean and therefore on climate. Nonetheless, the evidence remains sketchy and incomplete. Much further research is required to enable us to understand the mean state and the variability of the Mediterranean outflow and to model its characteristics properly in large-scale climate models, before a certain assessment can be made. Both components are important because their proper understanding

would provide models with a good chance of correctly predicting future changes in the outflow and their consequences for the ocean's circulation and climate.

Acknowledgements

The reported transport measurements in the Strait of Gibraltar between October 1994 and October 1996 were done in collaboration with Richard Limeburner from the Woods Hole Oceanographic Institution in Woods Hole, Massachusetts, USA, and with Juan Rico Palma from the Instituto Hidrográfico de la Marina in Cadiz, Spain. These measurements were supported by the US Office of Naval Research contract N00014-94-1-0347 and by grant OCE-93-13645 from the US National Science Foundation. The Instituto Hidrográfico de la Marina in Cadiz, Spain, provided invaluable logistic support during the field work and the use of the hydrographic ships B.H. *Tofíño* and B.H. *Malaspina*. Uwe Send from the Institut für Meereskunde Regionale Ozeanographie, Kiel, Germany, is greatly acknowledged for providing shipboard ADCP observations collected by the RV *Poseidon* in April 1996 and October 1997.

This Page Intentionally Left Blank

5.8

Transformation and Age of Water Masses

P. Schlosser, J. L. Bullister, R. Fine, W. J. Jenkins, R. Key, J. Lupton,
W. Roether and W. M. Smethie, Jr

5.8.1 Background

During the past decades, natural and anthropogenic trace substances such as tritium (^3H), radiocarbon (^{14}C), or Chlorofluorocarbons (CFCs) have been used in studies of the dynamics of natural systems, and as an analogue for the penetration of anthropogenic CO_2 into the ocean. Early applications of tracers to studies of the ocean were directed at determination of circulation patterns and mean residence times of specific water masses, as well as estimates of mixing coefficients (e.g. Begemann and Libby, 1957; Broecker *et al.*, 1960; Munk, 1966; Münnich and Roether, 1967; Craig, 1969; Rooth and Östlund, 1972; Gammon *et al.*, 1982). These exploratory studies suggested that tracers add significantly to our understanding of the oceanic circulation. In order to exploit this potential fully, the first global tracer study, the GEochemical Ocean SECTIONS Study (GEOSECS; Craig and Turekian, 1980; see Broecker and Peng, 1982, for summary of GEOSECS tritium and ^{14}C results), was launched as part of the International Decade of Ocean Exploration (IDOE). GEOSECS explored a large set of ocean tracers for studies of physical, chemical and biological processes in the ocean. Its success, manifested in a host of new results, led to the design of the Transient Tracers in the Ocean (TTO) programme. In contrast to GEOSECS, TTO was restricted to the Atlantic Ocean (NAS, North Atlantic Study; TAS, Tropical Atlantic Study; SAVE, South Atlantic Ventilation Experiment). It was a more focused programme than GEOSECS (smaller number of tracers), designed to resolve

oceanographic features and processes at a much higher resolution than achieved during GEOSECS. It demonstrated that a very close coordination of tracer programmes with physical oceanography studies is required for full utilization of the tracer data.

During the final stages of TTO, plans for the World Ocean Experiment (WOCE) were developed. As part of its World Hydrographic Programme (WHP), especially during the One-Time Survey, a set of tracers was measured on a global scale with unprecedented spatial resolution (both lateral and vertical). The original implementation plan (WCRP, 1988a) included a larger number of tracers (CFCs, $^3\text{H}/^3\text{He}$, ^{14}C , ^{39}Ar , stable isotopes of water, helium isotopes, ^{228}Ra , ^{90}Sr , ^{137}Cs , ^{85}Kr) than could actually be measured systematically (CFCs, $^3\text{H}/^3\text{He}$, ^{14}C , $\text{H}_2^{18}\text{O}/\text{H}_2^{16}\text{O}$, helium isotopes). Although both carbon tetrachloride (CCl_4) and CFC-113 have distinctly different atmospheric release histories from CFC-11 and CFC-12, and offer the potential to provide additional valuable information on time-dependent processes (including deep water formation) in the ocean, measurements of these compounds were made on only a small subset of the WHP One-Time Survey cruises. This was due in part to difficulties in analysing these compounds (especially CFC-113) in seawater samples, and to concerns about the non-conservative behaviour of CCl_4 in seawater (Wallace *et al.*, 1994). Nevertheless, the resulting multitracer data set, which presently is under evaluation, exceeds those obtained from pre-WOCE tracer studies by a

wide margin. The good coverage of most regions of the world ocean, together with the possibility of integrating the tracer data into a rich oceanographic data set of unprecedented proportions for many types of observations (e.g. hydrographic measurements, Eulerian and Lagrangian current measurements, satellite observations, etc.) and models, offers the possibility for tracer studies of many oceanographic problems at a new level of detail.

In this contribution, we briefly describe the existing WOCE data set and demonstrate the type of results that can be expected from its interpretation on the basis of selected examples. These examples include: (1) the ventilation of the upper waters in the Pacific Ocean (see Price, Chapter 5.3); (2) the penetration of near-surface signals into the deep ocean via the deep western boundary current in the Atlantic (see Hogg, Chapter 4.5); (3) the renewal of Antarctic Intermediate Water (see Rintoul *et al.*, Chapter 4.6; Hanawa and Talley, Chapter 5.4); (4) the deep water formation around Antarctica; (5) the spreading of intermediate water in the Pacific Ocean; (6) the bottom water circulation in the Pacific Ocean; (7) the addition of glacial meltwater around Antarctica; and (8) the circulation of the Indian Ocean and the exchange with the Pacific Ocean (see Gordon, Chapter 4.7). The preliminary results presented here demonstrate the potential of the WOCE tracer data set for obtaining insights into the oceanic circulation that were not possible on the basis of pre-WOCE data sets.

5.8.2 Tracer methodology and techniques

In this section we briefly discuss the underlying principles of tracer applications in oceanographic studies. Detailed accounts can be found, for example, in Broecker and Peng (1982), Roether and Rhein (1989) or Schlosser and Smethie (1995).

There are several ways in which tracers can be used in oceanographic (and other environmental) studies:

1 *As analogues to dyes.* The time-dependent delivery of ^3H (Dreisigacker and Roether, 1978; Doney *et al.*, 1992), CFCs (Warner and Weiss, 1985; Bu and Warner, 1995; Bullister and Wisegarver, 1998; Walker *et al.*, 2000), and bomb ^{14}C (Druffel and Linick, 1978; Druffel,

1980) to the ocean is relatively well known. It occurs mostly from the atmosphere over large spatial (frequently global) scales. The resulting signal allows us to follow, and estimate time scales for, the penetration of these tracers from their entry point into the interior of the ocean. This is close to performing a gigantic dye experiment. Also, the inventory of these tracers in subsurface water masses is directly dependent on the rate of formation of the water masses during the time interval of the tracer input (roughly the last 40 years). This has been demonstrated with CFC-11 inventories (Orsi *et al.*, 1999; Rhein *et al.*, 2000; Smethie and Fine, 2001).

- 2 *As radioactive 'clocks'.* Radioactive tracers such as ^{14}C or ^3H decay at a known rate. If we can determine the concentrations of the tracer at the entry point into a specific water body (e.g. a deep ocean basin), and compare it with the mean concentration within this reservoir, then we can derive a mean residence time of the water from the concentration difference due to radioactive decay in the reservoir (e.g. ^{14}C). Alternatively, in some cases we can measure both the radioactive mother and daughter products (e.g. ^3H and ^3He) and can calculate an apparent age or an isolation time of specific water masses.
- 3 *As markers of water masses with special sources.* Some tracers have distinct sources in certain areas or at certain depths in the ocean. Examples are stable isotopes of water ($\text{H}_2^{18}\text{O}/\text{H}_2^{16}\text{O}$, $^{2\text{H}}\text{H}^{16}\text{O}/\text{H}_2^{16}\text{O}$), or mantle helium with a $^3\text{He}/^4\text{He}$ ratio that is significantly higher (about one order of magnitude) than that of atmospheric 'background' helium in the ocean. The former is typically added in high latitudes where fractionation of stable isotopes due to preferential removal of the light isotope during precipitation leads to precipitation and runoff that is significantly lighter in $\delta^{18}\text{O}$ (of the order of -10 to -20‰) compared with the bulk of the ocean water ($\delta^{18}\text{O} \approx 0\text{‰}$) (e.g. Craig and Gordon, 1965). The latter is injected along the spreading centres of the Mid-Ocean Ridges or at Hot Spots. The injection depths range from roughly 1000 m to roughly 2500 m depth, but there can be injections into waters as shallow as 130 m depth (see below). The $\delta^3\text{He}$ values of helium plumes close to their injection

points are several tens of per cent higher than background $\delta^3\text{He}$ values in the deep ocean. Finally, ^4He is injected into the ocean through the addition of glacial meltwater (Schlosser, 1986; Schlosser *et al.*, 1990; Weppernig *et al.*, 1996).

- 4 As tests for numerical models of ocean circulation and mixing. Tracer distributions are controlled by their input to the ocean and by advective and mixing processes. Thus, tracer distributions in ocean circulation models are sensitive to these parameters in the model.

The magnitude of the WOCE programme contributed to technological advances in tracer oceanography. These advances reached from the establishment of new laboratories (e.g. the Accelerator Mass Spectrometry Facility at the Woods Hole Oceanographic Institution) to refinements of existing technologies. Such refinements include, for example, the preparation at sea of helium isotope samples for mass spectrometric measurement (Jenkins *et al.*, 1991) or the advancement of CFC measurement techniques (e.g. Bulsiewicz *et al.*, 1998).

The establishment of the US National Oceanographic Sciences Accelerator Mass Spectrometry facility (NOSAMS) at the Woods Hole Oceanographic Institution (e.g. Jones *et al.*, 1994; McNichol *et al.*, 1994; Schneider *et al.*, 1994; von Reden *et al.*, 1994) probably had the most significant impact on the WOCE tracer programme. During GEOSECS, ^{14}C measurements required the extraction of the total inorganic carbon from approximately 250 litres of seawater. The collection of such large amounts of water was only possible through the use of Gerard-Ewing samplers, which require extra casts at each ^{14}C station. Given the large number of ^{14}C samples planned for the WOCE survey, this method would have required too much ship time and the ^{14}C programme would have had to be reduced significantly, with serious implications for the value of the resulting data set. Therefore, during the US Pacific WOCE field work (Key, 1996), both large-volume and small-volume AMS samples were collected along many of the WOCE sections. Both the proven β -counting Large-Volume (LV) technique, which had a precision of $\pm 2\text{--}4\%$, and the AMS technique, with a precision of $\approx \pm 4\%$ (Elder *et al.*, 1998), were utilized.

5.8.3 Exemplary results

5.8.3.1 Thermocline ventilation in the Pacific Ocean using tritium/ ^3He data

The subsurface transport of subducted surface waters from the subtropics to the tropics has been implicated in the long-term modulation of El Niño events in the Pacific (e.g. Gu and Philander, 1997; Guilderson and Schrag, 1997). Fine *et al.* (1987) identified a tongue of tritium penetrating the tropics, tracing the cell in the North Pacific, and thereby placing an upper bound on the time scales associated with the transit of these waters. The WOCE Pacific expedition provided us with an opportunity to delineate this circulation more completely, and refine our knowledge of its character.

A 1991 tritium section along 135°W (P17C, Fig. 5.8.1a, see Plate 5.8.1a, p. 428) traces the equatorward movement from the subtropical North Pacific of the tritium tongue, which extends more than 3000 km meridionally. As it extends southward, it follows isopycnals ($26.0 < \sigma_0 < 26.5 \text{ kg m}^{-3}$), rising from a depth of approximately 250 m at 30°N to about 75 m at 10°N , then deepening about 100 m at the equator. The tritium tongue is underlain by a ^3He maximum (Fig. 5.8.1b, see Plate 5.8.1b, p. 428) at a depth of about 450 m in the subtropics. This deeper, tritiogenic ^3He maximum is characteristic of the subtropical thermocline, and is a widespread feature in other regions of the world ocean such as the North Atlantic (e.g. Jenkins, 1998) or the Nordic seas (Schlosser *et al.*, 1995). As the tongues extend into the tropics, the tritium and ^3He maxima become largely depth-coincident, supporting a net meridional advective origin for their existence.

The shallow distribution of excess ^3He , especially in the North Pacific, is dominated by *in-situ* decay of tritium (Jenkins, 1996). This conclusion is supported by the fact that the shallow ^3He maximum is almost everywhere underlain by a deeper ^3He minimum (Fig. 5.8.1b, see Plate 5.8.1b, p. 428). In addition, the tritiogenic ^3He flux is large compared with the mantle-derived flux (Jenkins, 1996), and there is little hydrographic evidence of large-scale vertical exchange of water across these horizons (e.g. see Wijffels *et al.*, 1996a).

Figure 5.8.2 represents the same meridional section, with the exception that ^3He is plotted versus potential density anomaly instead of depth. A strong front in both Tritium and ^3He exists at the

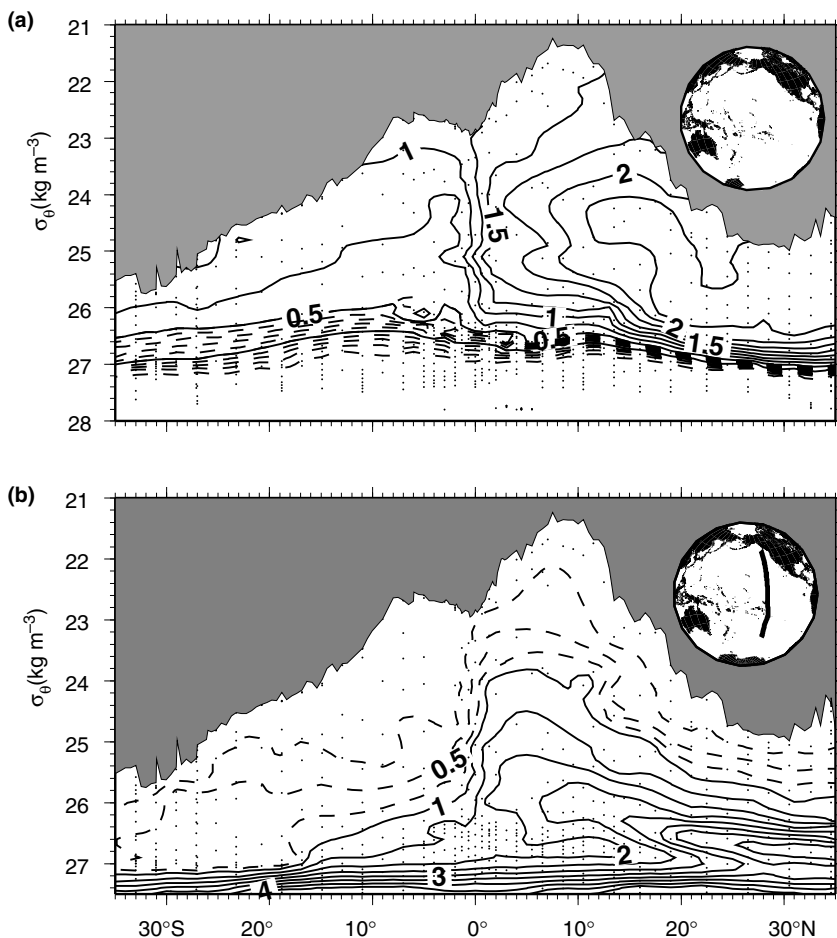


Fig. 5.8.2 Same as Figure 5.8.1 (see Plate 5.8.1, p. 428), except that tritium (a) and ${}^3\text{He}$ (b) are plotted versus the potential density anomaly instead of depth.

equator for $24 < \sigma_0 < 26.5 \text{ kg m}^{-3}$. This feature is a consequence of the strongly asymmetric global fallout pattern for tritium (Weiss and Roether, 1980; Doney *et al.*, 1992). Above $\sigma_0 = 24 \text{ kg m}^{-3}$, tritium isopleths appear to splay, presumably in response to divergent flow at the equator. The ${}^3\text{He}$ maximum appears to migrate upward across isopycnals as it extends toward the equator. Particularly between the 10°N and the equator, the excess ${}^3\text{He}$ isopleths appear to burst upward toward the surface. The latter is a signature of extensive diapycnal exchange in the region.

Between 15°N and the equator, the tritium tongue appears to be vertically bifurcated, with one core at $\sigma_0 \approx 25.5 \text{ kg m}^{-3}$, and a lighter core at about 24.5 kg m^{-3} . Examination of a zonal section at 10°N (Fig. 5.8.3) reveals that the lighter tongue is more centrally distributed (between 170°E and 130°W), while the heavier tongue extends from

the western boundary. McPhaden and Fine (1988) argued that this mid-longitude penetration (as evidenced by Fine *et al.*'s earlier observations) was a result of dynamical constraints. Huang (2000b), using the FSU (Florida State University) wind data climatology, has computed Sverdrup transport from the subtropics, and shown that a mid-longitude maximum in transport exists. The 'light' lens of tritium is consistent with this pathway, while the 'denser' tongue appears to be associated with southward transport along the western boundary.

As pointed out by Fine *et al.* (1987), the presence of bomb tritium in this overturning cell places a crude lower bound of about a decade to its circulation. In order to place a tighter constraint on the time scale, we combine the tritium and ${}^3\text{He}$ data to compute a tritium/ ${}^3\text{He}$ age distribution (Fig. 5.8.4, see Plate 5.8.4, p. 428). The mean meridional equatorward age gradient on $\sigma_0 = 26 \text{ kg m}^{-3}$

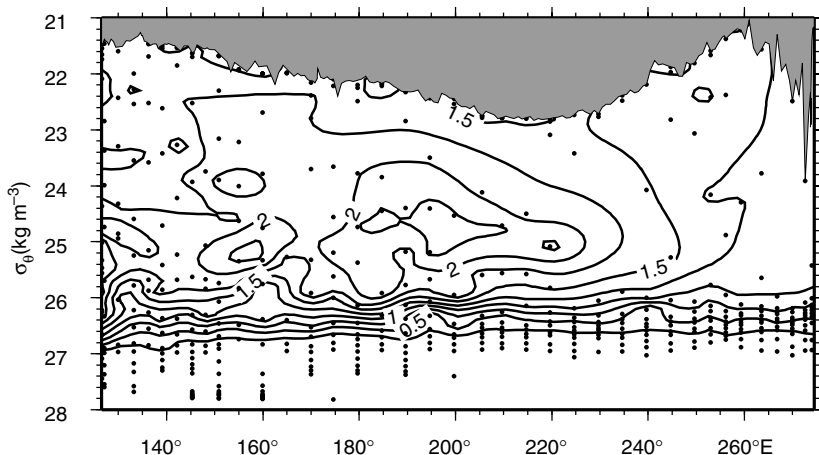


Fig. 5.8.3 Zonal section of the tritium distribution at 10°N (WHP section P4).

is approximately 0.05 yr km⁻¹ for both 30°S to 10°S and 30°N to 10°N. This gradient corresponds to a mean meridional velocity of about 7×10^{-3} m s⁻¹. In general, the $^3\text{H}/^3\text{He}$ age for the density range $26.0 < \sigma_0 < 26.5$ starts at about 5–10 years in the subtropics (a reflection of the ventilation time scale of these waters within the subtropics) and increases to 15–20 years in the tropics. If interpreted in a straightforward manner, the advective time scale for the tongue would appear to be close to 10 years, but considerable caution must be exercised in the presence of mixing (e.g. see Jenkins, 1998). Further, more quantitative interpretation would require a more complete modelling of the tracer distributions and evolution.

The existence of these thermocline tritium maxima within the subtropical gyre can be explained by a combination of subduction (e.g. Jenkins, 1987; Price, Chapter 5.3), simple mixing processes (Robbins *et al.*, 2000), and the time history of the surface water tritium transient (see Jenkins, 1998). In particular, the lighter tritium core in the North Pacific correlates with the density of Subtropical Underwater (STUW). O'Connor *et al.* (2000) use mostly WOCE Pacific data to make the first estimates of subduction rates for North and South Pacific STUW. Applying the inverse tracer age gradient corrected for vortex stretching after Jenkins (1987, 1998), the CFCs give subduction rates of 5 and 7 Sv (1 Sv = 10^6 m³ s⁻¹) for STUW in the North and South Pacific, respectively. Comparison with subduction rates calculated from WOCE drifters for the same period show good agreement given the uncertainties intrinsic to both methods. The results suggest that the subduction

rate for STUW is higher in the South Pacific because of differences in buoyancy forcing and deeper mixed layers in the South.

5.8.3.2 Tracing the deep thermohaline circulation in the Atlantic Ocean using CFCs

A fairly extensive set of CFC measurements was obtained in the Atlantic Ocean prior to the WOCE programme. In the North Atlantic these measurements were obtained from a variety of field programmes carried out between the early 1980s and the early 1990s and in the South Atlantic primarily from the South Atlantic Ventilation Experiment (SAVE) expedition in 1988 and 1989. These observations reveal information on the flow paths and spreading rates of two of the major deep ocean water masses, North Atlantic Deep Water (NADW) and Antarctic Bottom Water (AABW), in the Atlantic Ocean. As will be shown below, the WOCE data add greatly to the pre-WOCE data sets with respect to pathways and spreading rates by allowing us to follow the tracer-bearing waters deeper into the interior of the Atlantic Ocean, as well as providing information on temporal variability (see also Hogg, Chapter 4.5; Lazier *et al.*, Chapter 5.5; Saunders, Chapter 5.6; Candela, Chapter 5.7).

The earliest CFC measurements from the TTO/NAS and TTO/TAS expeditions in 1981 and 1983 showed a CFC maximum in upper NADW that was intensified along the western boundary and extended eastward from the western boundary along the equator (Weiss *et al.*, 1985; Hogg, Chapter 4.5). Other measurements revealed two distinct deep CFC maxima throughout the subtropical

North Atlantic: the upper NADW maximum at about 1500 m depth and a deeper maximum in lower NADW at about 3500 m depth. These features were strongest in the Deep Western Boundary Current (DWBC) (Fine and Molinari, 1988; Smethie, 1993). Pickart (1992) showed that the upper maxima occurred at a density too low to be categorized as classical Labrador Sea Water and referred to this water mass as upper Labrador Sea Water. Using measurements collected in the early 1990s, Pickart *et al.* (1996) presented evidence that the source of this water was winter convection on the northern side of the North Atlantic Current in the southern Labrador Sea. WOCE measurements in the subtropical North Atlantic in the early 1990s (Rhein *et al.*, 1995) revealed the same two maxima but at much lower concentrations. Both the upper NADW maximum and lower NADW maximum were observed to extend eastward along the equator and to cross the equator along the western boundary into the South Atlantic. The upper maximum was observed as far as 10°S and the deep maximum as far as 5°S.

In the western subtropical North Atlantic, relatively high CFC concentrations observed in the interior basin revealed recirculation of the DWBC water in the deep Gulf Stream recirculation gyre (Hogg *et al.*, 1986; Pickart and Smethie, 1993), the Abaco gyre (Johns *et al.*, 1997a) and the Guyana gyre (Molinari *et al.*, 1992). Water mass ages in the DWBC derived from CFC-11/CFC-12 ratios indicated a spreading rate of 1–2 cm s^{−1} (Weiss *et al.*, 1985; Smethie, 1993; Smethie *et al.*, 2000). These rates are considerably lower than those calculated from current meter measurements in the DWBC. This difference demonstrates the importance of deep recirculation gyres in ventilating the interior and slowing the overall equatorial spreading rate of NADW from its northern source regions. Streamtube models of CFC concentrations in the DWBC that include exchange with the interior (Pickart *et al.*, 1989; Rhein, 1994) yield current speeds of 5–10 cm s^{−1}. These values are in agreement with results from long-term current meter measurements in the DWBC. A detailed description of the evolution of the CFC signal in the North Atlantic is presented by Smethie *et al.* (2000).

In addition to providing information on spreading pathways and time scales, CFC inventories provide quantitative information on rates of water mass formation. The total amount of CFCs in a

particular water mass is a direct reflection of how rapidly that water mass formed from near-surface water and the formation rate can be calculated from the CFC inventory of the water mass. Calculations based on pre-WOCE CFC-11 data reveal a total NADW formation rate about 17 Sv, which includes the first estimate of 2.2 Sv for upper Labrador Sea Water (Smethie and Fine, 2001).

CFC concentrations in bottom water in the South Atlantic in the late 1980s were much lower than in the North Atlantic. The CFC distribution in the Argentine Basin showed the entry of AABW through gaps in the Falkland Ridge. They also indicated a split of this flow with one branch flowing westward to the western boundary and the other flowing to the northeast and then into the interior (Warner *et al.*, 1990; Coles *et al.*, 1996). The CFC signal had just begun to enter the Brazil Basin with AABW, and by 1992 was barely detectable at 5°S (Rhein *et al.*, 1995). In NADW the upper CFC maximum was barely detectable at 19°S in the DWBC and the lower NADW CFC maximum extended only to 10°S. The CFC concentration was undetectable in the Angola Basin at this time.

The WOCE programme was carried out at different times in the North and South Atlantic oceans. The North Atlantic programme was performed between 1996 and 1998 with 1997 being the major field year. The South Atlantic programme, including the tropical Atlantic, was carried out primarily between 1993 and 1996, with a portion of the field work being done as part of the Deep Basin Experiment and as part of the German WOCE programme between 1990 and 1996.

The zonal CFC distribution in the Argentine Basin was measured in 1993 (WOCE line A11; about 45 to 30°S; 60°W to 20°E) and was similar to that measured during the SAVE programme, but concentrations were higher. Highest concentrations in AABW were found overlying the western flank of the Mid-Atlantic Ridge. These data, together with other evidence, revealed that the primary inflow of AABW through gaps in the Falkland Escarpment flowed to the northeast and then back to the west in a deep anticyclonic gyre (Smythe-Wright and Boswell, 1998), confirming the SAVE observations. A meridional section through the western South Atlantic (WOCE line A17; about 10°N to 51°S; 60 to 30°W) parallel to the South American coastline (Fig. 5.8.5, see Plate 5.8.5, p. 428)

was occupied in 1994 (Messias and Memery, 1998). Comparison of these data with the SAVE data show a sharp increase in the CFC concentration in AABW in the Brazil Basin, which was just above background during SAVE. CFCs were detected in AABW all the way to the equator just south of the Mid-Ocean Ridge (Rhein *et al.*, 1998b). The prominent upper NADW and lower NADW CFC maxima observed in the North Atlantic, but barely detectable during SAVE, were observed at 24°S, 20°S and 10°S, indicating eastward zonal flow of NADW away from the DWBC. Several cruises were completed in the equatorial Atlantic as part of the WOCE Deep Basin Experiment and repeat hydrography programmes between 1991 and 1996. The CFC concentrations in the deep water increased as expected during this time, but the increase was not as smooth as would be expected from the source functions, indicating variability in mixing and transports (Rhein *et al.*, 1998a; Andrié *et al.*, 1999). These cruises confirmed that both the upper and lower CFC maxima split near the equator with one branch extending in the DWBC across the equator and the other spreading along the equator (Andrié *et al.*, 1998; Messias *et al.*, 1999). There is some recirculation of the lower CFC maximum in the Guyana Basin. The WOCE observations suggest that this recirculation does not extend to the Mid-Atlantic Ridge and has a strength of $\approx 3 \pm 1.5$ Sv (Plähn and Rhein, 1998).

From a comparison of the equatorial CFC distribution measured in 1993 with that measured during TTO in 1983 (Fig. 5.8.6), Andrié *et al.*

(1998) determined the spreading rate in the upper maximum to be 1.4 cm s^{-1} eastward along the equator. This estimate is in good agreement with tracer-based estimates for the DWBC in the North Atlantic. Measurements made in the Romanche and Chain fracture zones revealed the lower NADW-CFC maximum extending eastward into both fracture zones, clearly demonstrating the flow of lower NADW into the eastern basin. These CFC data also showed that there was a vertically varying recirculation of upper NADW from the DWBC to the interior and then back to the northwest along the Mid-Atlantic Ridge north of the equator, but that lower NADW did not recirculate (Andrié *et al.*, 1999).

The one-time North Atlantic WOCE survey provides excellent tracer coverage for the subpolar region, but only moderate coverage for the subtropical Atlantic. However, the two meridional lines along 52°W (Fig. 5.8.7, see Plate 5.8.7, p. 428) and 66°W (A20 and A22, respectively) provide coverage in the interior of the western subtropical basin where past tracer observations were limited. The CFC distributions along these sections show that the upper NADW and lower NADW-CFC maxima extend over 1000 km into the interior from the DWBC (Smethie, 1999), providing the strongest tracer evidence yet of the important role deep recirculation gyres play in the large-scale thermohaline circulation. These data also show the spreading of classical Labrador Sea Water that formed during the high NAO (North Atlantic Oscillation) index period of the late 1980s and early 1990s into the

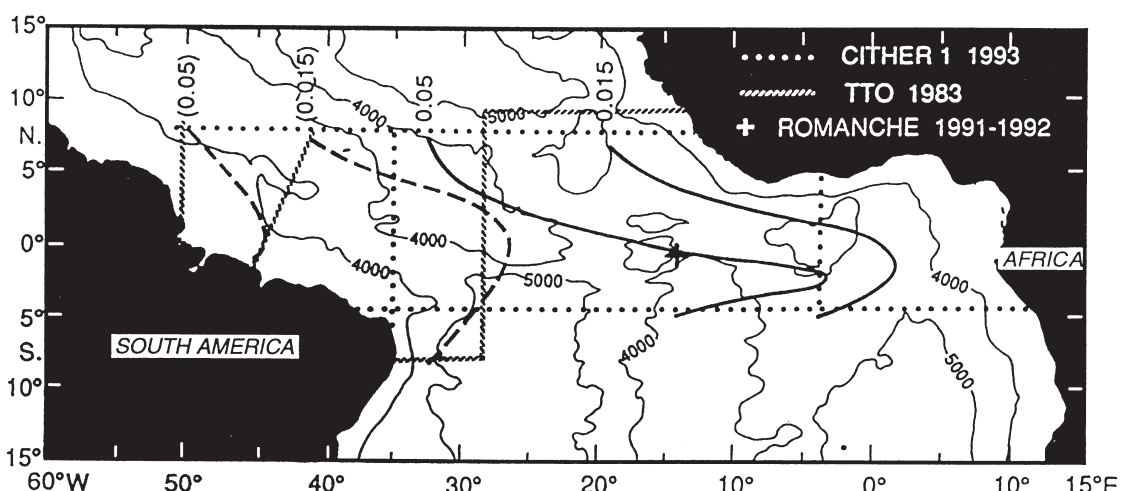


Fig. 5.8.6 Lateral distribution of the CFC-11 0.015 and 0.05 pmol kg^{-1} isolines in upper NADW in the equatorial Atlantic Ocean in 1983 and 1993. The 1983 isolines are dashed and the 1993 lines are solid. From Andrié *et al.* (1998).

subtropical Atlantic. Earlier data (Molinari *et al.*, 1998) and CFC measurements from WOCE repeat hydrography cruises in the mid-1990s clearly show extensive spreading of this newly formed Labrador Sea Water. Its transit time to the Irminger Sea, the Newfoundland Basin, and the northeastern Atlantic was determined to be 6 months, 1 year, and 5 years, respectively (Sy *et al.*, 1997). On the basis of the CFC-11 inventory calculated from the data obtained during the North Atlantic One-Time Survey, the formation rate of classical Labrador Sea Water during the high NAO index period was estimated to be 8–11 Sv (Rhein *et al.*, 2001). The CFC coverage obtained during the WOCE One-Time Survey will allow us to determine the circulation pathways of the various components of NADW in greater detail than has been possible with data collected in the past. Additionally, it will provide the data needed to determine the CFC inventories (and hence formation rates) for the various NADW components more accurately than has been possible with earlier data.

In addition to the results described above, the WOCE repeat hydrography programme allowed us to establish a tracer time series along a section across the Labrador Sea (AR7W; about 53 to 60°N; 48 to 56°W). This time series (Fig. 5.8.8, see Plate 5.8.8, p. 428) will be used to put the results of the One-Time Survey into the context of the variability observed in the North Atlantic Ocean, specifically that in the Labrador Sea. It also will contribute to a better understanding of the processes that determine the setting of the initial tracer boundary conditions in areas where major water masses are formed. Such time series provide substantial insight into the initial boundary conditions for the individual tracers (e.g. saturation levels of CFCs), as well as those for derived quantities (e.g. the tritium/ ^3He age). Knowledge of the temporal evolution of these boundary conditions is important for proper use of tracers in qualitative, as well as quantitative studies (e.g. integration into ocean circulation models).

5.8.3.3 Antarctic Intermediate Water renewal in the Atlantic Ocean

Antarctic Intermediate Water (AAIW) is apparent as a salinity minimum over much of the Atlantic (e.g. Emery and Meincke, 1986; Clarke *et al.*, Chapter 1.2). It represents one of the principal contributors to the upper, northward branch of

the global thermohaline circulation (THC) (e.g. Rintoul, 1991), and is, thus, important for the freshwater and salinity balance on a global scale. The AAIW core depth is generally 800–1000 m, but slopes toward shallower depths in the south where it is formed by surface forcing at latitudes close to the Antarctic Circumpolar Current. Details of AAIW formation are still under investigation (e.g. Gordon *et al.*, 1992; Hanawa and Talley, Chapter 5.4).

AAIW is renewed on a decadal time scale. Therefore, its tracer signatures provide integrated information on pathways of AAIW, as well as its renewal rates. Warner and Weiss (1992), using CFC data collected during TTO/TAS, AJAX and SAVE, found high and rather uniform CFC concentrations in the AAIW core layer south of about 20°S, and far lower concentrations further north with a concentration increase toward the western boundary. They identified the high-CFC pool with the subtropical anticyclonic gyre, and noted that part of the gyre waters moved on northward as a western boundary current. This is in contrast, for example, to the circulation in the Indian Ocean, where the most recently ventilated water enters and circulates in a compact anticyclonic gyre in the southwestern corner of the Indian Ocean (Fine, 1993).

The expansion of the tracer data base during WOCE has prompted a more comprehensive tracer study of AAIW (Rose, 1999). In this study, the entire layer of AAIW was dealt with. The contributions of water admixed from the adjoining water masses above and below it (South Atlantic Central Water, SACW, and upper Circumpolar Deep Water, uCDW) were separated by means of a multiparameter water mass analysis (Tomczak and Large, 1989), utilizing the complete hydrographic data set. Figure 5.8.9 shows the resulting fractions of pure AAIW versus depth and versus density (σ_0) along the WOCE WHP sections A8 (11°S), A9 (19°S) and A10 (30°S). A vertical integration of this fraction in space yielded an effective vertical extension (layer thickness) of pure AAIW (Fig. 5.8.10). By areal integration of the latter, the total volume of AAIW was obtained as $14.1 \times 10^6 \text{ km}^3$. The CFC data span about a decade. They were converted into a quasynchronous data set using temporal trends derived from the available observations repeated at (essentially) the same location. CFCs increase strongly above the AAIW layer

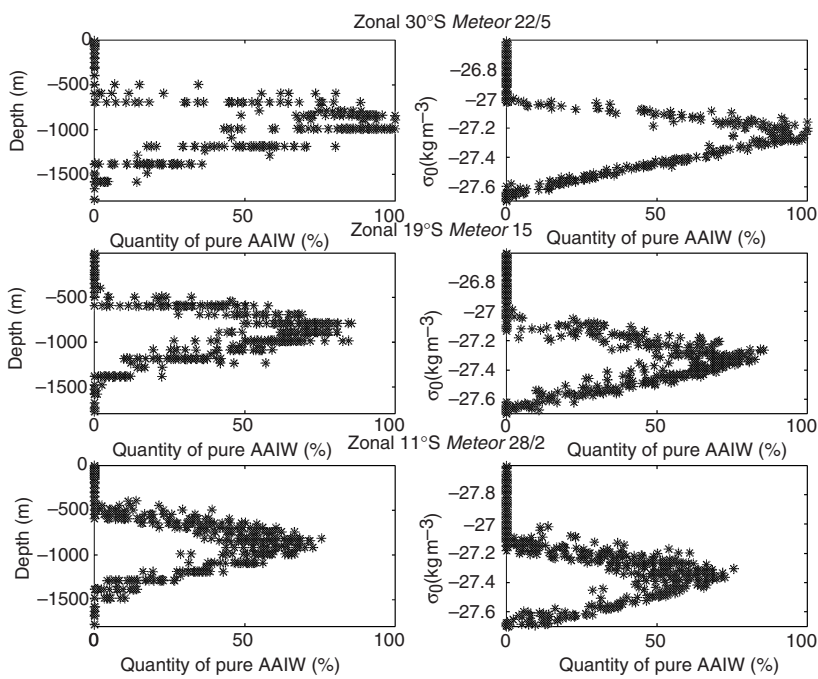


Fig. 5.8.9 Fractional contribution of pure AAIW (%) as a function of density (σ_0) along WHP sections A8 (about 11°S, upper panel), A9 (19°S, centre) and A10 (30°S, bottom panel), obtained by multiparameter water mass analysis.

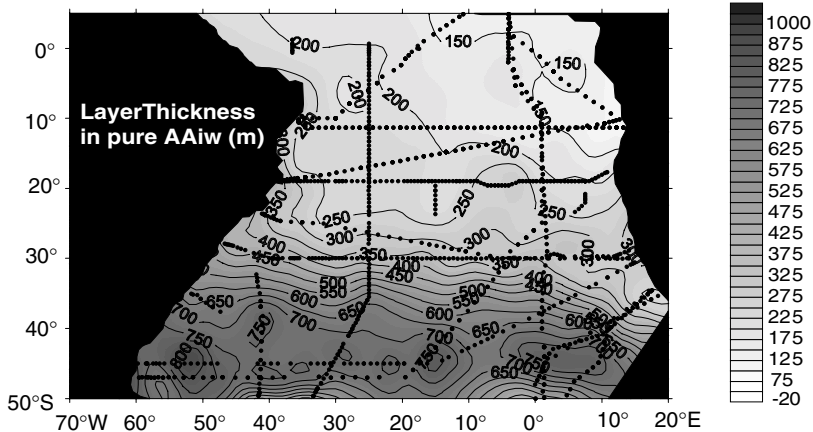


Fig. 5.8.10 Horizontal map of vertical extension of pure AAIW, obtained by integrating the fractional contributions (Fig. 5.8.9) vertically. The points indicate the CFC stations and illustrate the sections employed for the study.

towards higher concentrations in the SACW, while the underlying uCDW is virtually CFC-free. The resulting net CFC addition from the SACW by vertical mixing was corrected for by means of an advection-mixing model, which accounts for one-dimensional, isopycnal south-to-north advection and mixing, as well as for diapycnal mixing, with prescribed concentrations at the respective outcrops. The model parameters were chosen to reproduce CFCs and salinity along WHP sections A8 to A10 (Fig. 5.8.11).

Figure 5.8.12 shows the resulting CFC-11 distribution (Fig. 5.8.12a) and CFC-11 concentration ages (Fig. 5.8.12b) in the core layer of pure AAIW. The apparent ages in Fig. 5.8.12b increase from a few years south of 50°S up to more than 40 years in the centre of the northern cyclonic gyre (Angola Dome). In keeping with Warner and Weiss (1992), a strong north-south gradient centred at about 20°S is evident, which extends into a bifurcation at the western boundary. The northward arm of the bifurcation feeds a pronounced northward tongue

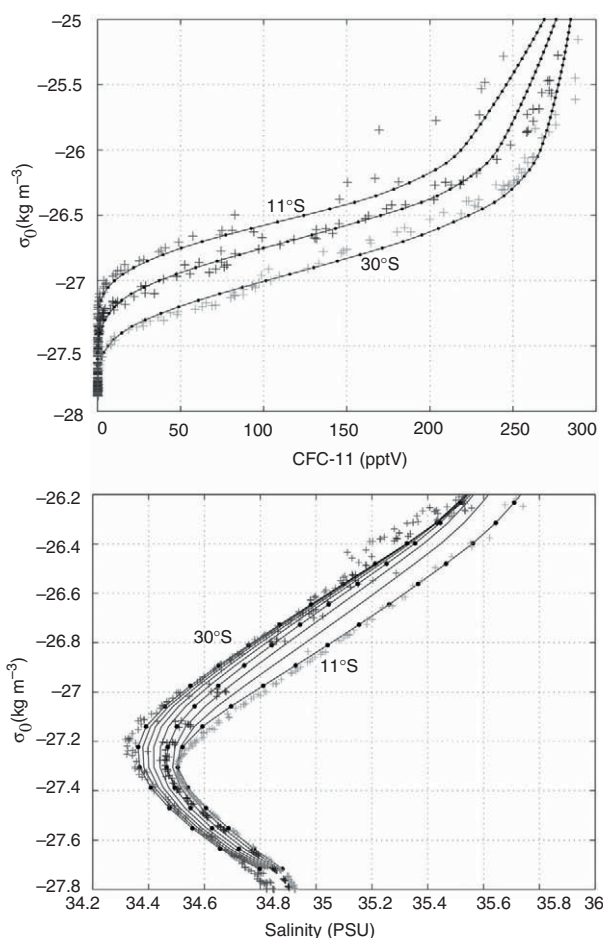


Fig. 5.8.11 Model profiles of CFC-11 partial pressure (ppt; upper panel), 1992 (quasi-synoptic data, see text), and salinity (lower panel), in comparison with observations along A8–A10.

of AAIW concentrated along this boundary, with an indication of an eastward extension near the equator. The bifurcation provides evidence against the hypothesis of a continuous northward western boundary current south of 20°S, supporting recent results from float observations (Boebel *et al.*, 1997). The fact that the CFC (or CFC age) isolines south of 20°S are virtually zonal indicates that the supply region of AAIW must also be of a rather zonal nature. Still, the degree of zonality is surprising, considering that the flow regime is anticyclonic. This feature, which is as yet unexplained, is also found in the SACW (Roether and Putzka, 1996) and should allow us to examine the specific roles of recirculation, mixing and ventilation in the gyre. A surprising finding is that the vertical extension of pure AAIW (Fig. 5.8.10) shows a structure somewhat similar to that of Figure 5.8.12, although Figure 5.8.10 is entirely independent of any tracer

data. If this correspondence is real, it means that AAIW thins vertically as it ages.

The AAIW formation rate was estimated by means of a CFC balance using a simple box model (Fig. 5.8.13). The centre box conceptually represents the volume of pure AAIW, coast to coast between 48 and 18°S, and the southern box represents a supply region. Advectional loss occurs through the western boundary region north of 18°S. The time-dependent CFC concentration in the source box was chosen to match observations, and the concentrations in the waters leaving the centre box in the northwest were fixed by prescribing a delay amounting to the corresponding age difference according to Figure 5.8.12b. Additionally a diffusive CFC input across the southern boundary of the centre box was accounted for. The tracer balance yielded a rate of advective AAIW renewal of $6.8 \pm 1.4 \text{ Sv}$ (for both CFC-11 and CFC-12). Without the correction for mixing, the value would be about 10% higher. The major error contributions are (i) the uncertainty of the total CFC content of the centre box, largely due to the mentioned correction for the SACW contribution, and (ii) the CFC time curve in the source box (for details, see Rose, 1999). The deduced rate should be considered an average over the period of CFC invasion. It compares rather well with earlier results (e.g. Rintoul, 1991). In those studies AAIW is usually defined as the water between selected isopycnals, and error estimates are missing. The study of Rose (1999) shows that tracer data provide useful information on the structure of subsurface water masses, and can be used to obtain robust formation rates, quite independently of other methods. The specific approach applied may well be similarly applicable for the study of other intermediate water masses in the ocean.

5.8.3.4 Mid-depth circulation in the Pacific inferred from ^3He data

Submarine hydrothermal fluids that are injected into the oceans from deep sea spreading ridges and from certain active seamounts contain high concentrations of mantle helium. The $^3\text{He}/^4\text{He}$ ratio of this helium is 8–30 times enriched relative to atmospheric helium ($^3\text{He}/^4\text{He} = 1.4 \times 10^{-6}$ in air, $^3\text{He}/^4\text{He} = 1–4 \times 10^{-5}$ in submarine hydrothermal fluids). Typical hydrothermal fluids have ^3He concentrations ranging from 0.2×10^{-9} to $2.5 \times 10^{-9} \text{ cm}^3 \text{ STP g}^{-1}$ (STP, Standard Temperature

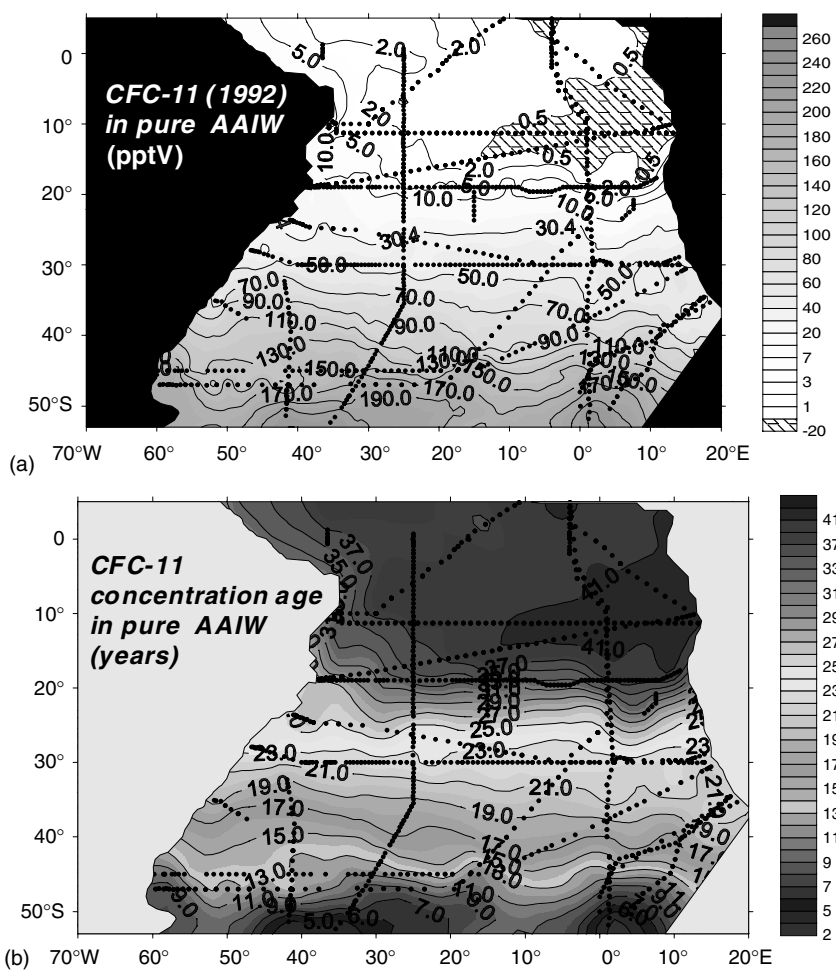


Fig. 5.8.12 Horizontal map of CFC-11 partial pressure (ppt; upper panel), and of the corresponding CFC-11 concentration age (years; lower panel) in the core layer of pure AAIW (i.e. a contribution by CFC admixture from the SACW is corrected for).

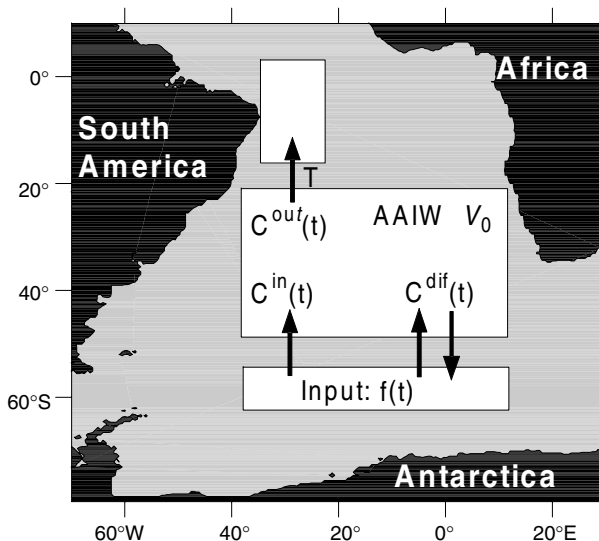


Fig. 5.8.13 Box model of AAIW to estimate renewal, see text. The centre box represents vertically integrated pure AAIW (Fig. 5.8.10), coast to coast, 18–48°S.

and Pressure), several orders of magnitude higher than the background ${}^3\text{He}$ in seawater ($\approx 6 \times 10^{-14} \text{ cm}^3 \text{ STP g}^{-1}$) (Butterfield *et al.*, 1990). The injection of these ${}^3\text{He}$ -rich fluids into the deep ocean produces hydrothermal plumes that can easily be detected against the oceanic background of dissolved atmospheric helium using precise ${}^3\text{He}/{}^4\text{He}$ measurements (e.g. Lupton, 1998). The largest fraction of this mantle helium is injected at the crest of the Mid-Ocean Ridges at depths of 2000–2500 m. The ${}^3\text{He}/{}^4\text{He}$ ratio of the ‘pure’ injected fluid is $\approx 1 \times 10^{-5}$, or about 8 times the atmospheric value. Because helium is a stable, conservative tracer that is lost from the ocean only by gas exchange with the atmosphere, the deep and intermediate waters of all major deep ocean basins have accumulated excess ${}^3\text{He}$ of mantle origin. To a large degree, the amount of this excess hydrothermal helium is controlled by the relative

strength of the hydrothermal input, which is in turn roughly proportional to the spreading rate of the ridges. The final distribution is determined by advection and mixing of the injected hydrothermal fluids. In the Pacific Ocean, where the ridges are spreading the fastest, the deep water masses have the highest ${}^3\text{He}$ excesses derived from hydrothermal activity. In fact, the deep Pacific is everywhere enriched in ${}^3\text{He}$ by about 20% compared with background values. In the Atlantic Ocean the mantle helium excess is typically only 1–2%, due to the much slower spreading rate of the Mid-Atlantic Ridge, while the Indian Ocean has intermediate mantle ${}^3\text{He}$ excesses of $\approx 10\%$ above background.

It has long been recognized that the distribution of mantle ${}^3\text{He}$ has great potential for delineating the patterns of circulation and mixing of deep and intermediate water masses. This potential is probably greatest in the Pacific Ocean because of the stronger deep ${}^3\text{He}$ signal in this ocean. However, most of the mantle helium sources in the Pacific are distributed along the East Pacific Rise (EPR)

system in the eastern Pacific and along the Juan de Fuca Ridge (JdFR) system in the northeast Pacific. Because the GEOSECS station tracks were mainly located in the central part of the Pacific basin (see Fig. 5.8.14), the GEOSECS helium work produced only a rough picture of the mantle helium distribution in the deep Pacific. The potential of ${}^3\text{He}$ for mapping the deep circulation could not be realized on the basis of the pre-WOCE data set.

The completion of helium sections as part of the WOCE Hydrographic Programme, as well as from other expeditions such as Helios and NOAA's Climate and Global Change (CGC) Program, have resulted in a much more comprehensive map of the deep helium field (Lupton, 1998), which has now been mapped in considerable detail in the Pacific (Fig. 5.8.14). This work has identified several areas in the Pacific where the hydrothermal activity is of sufficient strength to produce intense ${}^3\text{He}$ -rich plumes which clearly indicate the regional circulation. Among these are two large jets which extend westward into the Pacific basin from the crest of the EPR at $\approx 10^\circ\text{N}$ and $\approx 15^\circ\text{S}$

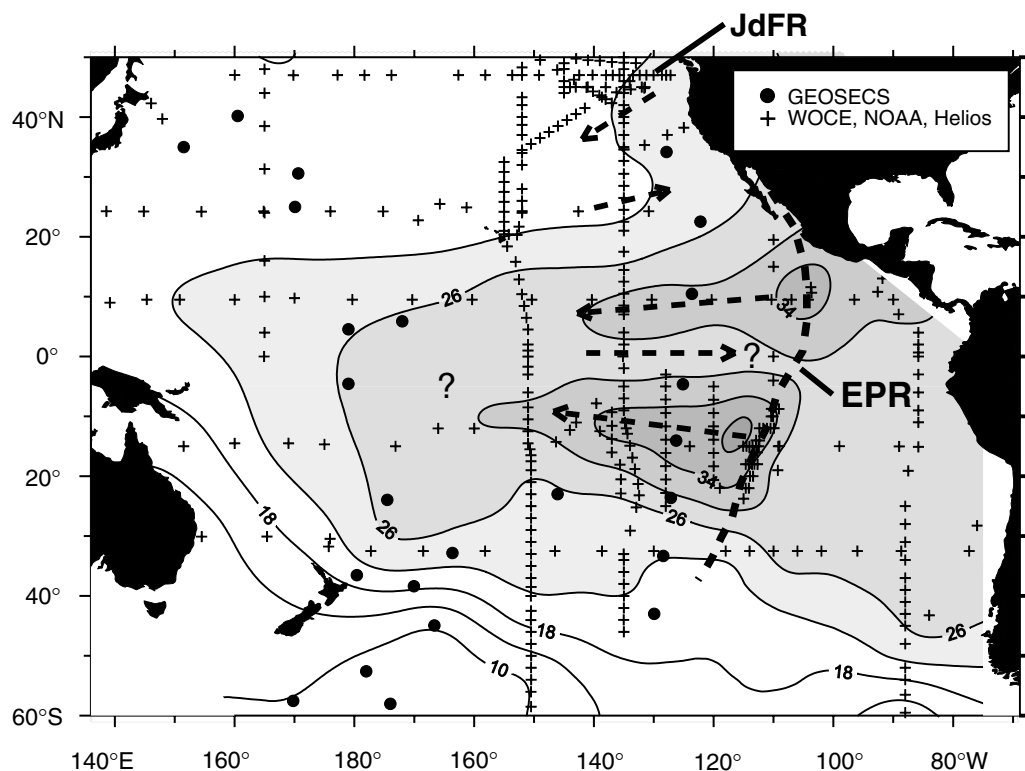


Fig. 5.8.14 Map of $\delta{}^3\text{He}$ (%) contoured on a surface at 2500 m depth in the Pacific. Contour interval is 4%. The major helium sources lie along the East Pacific Rise (EPR) and Juan de Fuca Ridge (JdFR) systems. The dashed arrows indicate areas where the helium plumes define regional circulation patterns. Data along WOCE sections P4 and P6 from Jenkins (unpublished data). All other data from Lupton (1998).

with a pronounced minimum between these plumes centred on the equator. This ${}^3\text{He}$ minimum is consistent with the interpretation of Talley and Johnson (1994), who postulate the existence of a deep eastward flow on the equator based on the WOCE hydrographic data. In the North Pacific, the helium distribution shows a weaker plume extending from the Juan de Fuca Ridge southwestward toward Hawaii, and an eastward transport indicated by the ${}^3\text{He}$ minimum in the eastern Pacific at $\approx 20^\circ\text{N}$. Many of these features are also evident in the WOCE P17 section along 135°W , which crosses many of the major helium plumes in the Pacific (Fig. 5.8.15, see Plate 5.8.15, p. 428). The striking symmetry of the two EPR plumes north and south of the equator is evident in the P17 helium section, as is the ${}^3\text{He}$ minimum on the equator. The maximum in ${}^3\text{He}$ at $\approx 45^\circ\text{N}$ latitude in the P17 section corresponds to the core of the plume from the Juan de Fuca Ridge in the northeast Pacific. Finally, as will be discussed below, the upward slope in the $\delta{}^3\text{He}$ contours at $\approx 20^\circ\text{N}$ and $\approx 1200\text{ m}$ depth in the P17 section has been attributed to helium injection from the Loihi Seamount (Lupton, 1996).

Although the majority of the mantle helium injection occurs along active portions of the Mid-Ocean Ridge system, helium plumes emanating from hydrothermally active seamounts have also

been detected. Because seamount hydrothermal sources are typically much shallower than Mid-Ocean Ridges, the helium injected at active seamounts has potential for tracing regional circulation patterns at intermediate to shallow depths. The marine environment of the Macdonald Seamount in the South Pacific has been observed in active eruptive state (Cheminée *et al.*, 1991), with injections of ${}^3\text{He}$ into the overlying water column at a depth of $\approx 130\text{ m}$ (Craig *et al.*, 1988). Very recently, ${}^3\text{He}$ plumes have been detected at depths between 150 and 1500 m emanating from several active seamounts in the Kermadec Arc northeast of New Zealand (de Ronde *et al.*, 1999). Loihi Seamount, on the southeastern flank of the island of Hawaii, has active hydrothermal vents on its summit and produces a ${}^3\text{He}$ plume centred at $\approx 1100\text{ m}$ depth, which has been tracked for considerable distances from the Hawaiian Islands. Using WOCE data, Lupton (1996) presented evidence that the Loihi helium is transported eastward as a continuous plume all the way to the coast of Mexico (see Fig. 5.8.16). The Loihi plume is of particular interest not only because it indicates a circulation pattern at shallow to intermediate depths, but also because the helium injected at Loihi has a distinct isotopic signature associated with the hot spot character of the seamount. Thus, the ${}^3\text{He}/{}^4\text{He}$ ratio of the helium injected at Loihi

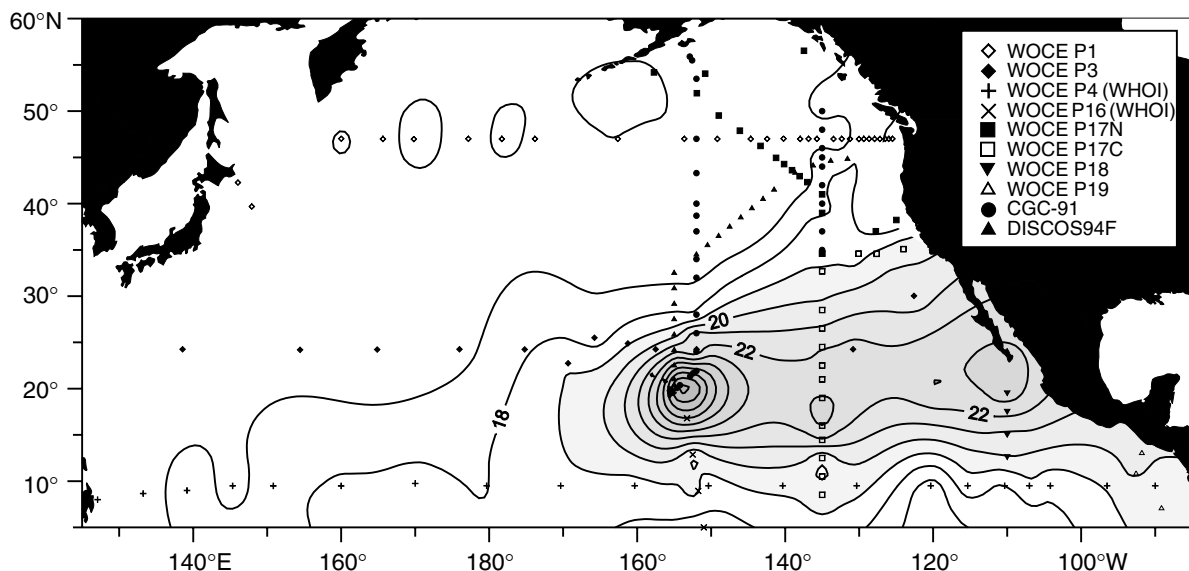


Fig. 5.8.16 Map of $\delta{}^3\text{He}$ (%) contoured on a surface at 1100 m depth in the north Pacific. Contour interval is 1% in $\delta{}^3\text{He}$. All measurements from Lupton (1996, 1998) except for WOCE sections P4 and P16C, which are from Jenkins (unpublished data).

(${}^3\text{He}/{}^4\text{He}$: $3\text{--}4 \times 10^{-5}$) is a factor of ≈ 3 higher than that of the helium injected at Mid-Ocean Ridges (Lupton, 1996). This raises the possibility that helium from seamounts such as Loihi could be distinguished from Mid-Ocean Ridge helium plumes using high-precision helium isotopic measurements.

It is of interest to compare the pathways of specific water masses that can be inferred from the helium pattern with other descriptions of the intermediate and deep circulation. The helium distribution requires a circulation pattern which differs from the classical model for the deep Pacific circulation (Stommel and Arons, 1960b), but is consistent (Lupton, 1998) with the circulation patterns predicted by Reid (1997) on the basis of a steric height analysis of hydrographic data. In particular, all of the major pathways predicted by the helium plumes agree with Reid's steric height analysis. This comparison would not have been possible before the WOCE Pacific sections were completed, since neither the steric height maps nor the helium distribution had sufficient resolution for this comparison.

5.8.3.5 Deep and bottom water circulation in the Pacific derived from ${}^{14}\text{C}$ data

After initial studies of the deep water renewal times using ${}^{14}\text{C}$, the first attempt to determine the global distribution of radiocarbon in the ocean was made during the GEOSECS expedition (1971–78). Much of the utility of the GEOSECS $\Delta^{14}\text{C}$ data set has been drawn from its assessment of the ocean's uptake of bomb ${}^{14}\text{C}$ (Broecker *et al.*, 1985c, 1995), as well as from refinement of the deep water renewal times. Defining the limits of the bomb ${}^{14}\text{C}$ 'dye patch' offers a direct way of visualizing the ventilation of the thermocline over a decadal time scale. Quantifying the total inventory of bomb ${}^{14}\text{C}$ in the ocean has been used to set limits on the rate at which ${}^{14}\text{CO}_2$ invades the ocean across the air-sea boundary. During the 1980s, TTO and SAVE increased the Atlantic Ocean radiocarbon data set significantly and provided the first opportunity to study how the bomb-produced inventory and distribution had changed during the years since GEOSECS. No large-scale radiocarbon programmes were carried out in the Pacific during the 1980s and only the relatively limited INDIGO expeditions provided ${}^{14}\text{C}$ data for the Indian Ocean.

Although the WOCE $\Delta^{14}\text{C}$ data is still sparse compared with the standard hydrographic survey, it represents an unprecedented global data set for studies of the deep circulation and the penetration of the bomb signal into the deep ocean.

It is generally accepted that Pacific bottom waters are ventilated by the northward flow of Circumpolar (Common) Deep Water. The primary pathway is as a deep western boundary current passing along the Tonga–Kermadec trench (e.g. Whitworth *et al.*, 1999). As it moves northward, part of the bottom water is lost due to slow upwelling. Significant questions exist about the depth to which this upwelling occurs and about the primary return pathway of the modified bottom water to the south. ${}^{14}\text{C}$ is an ideal tracer to study the long-term mean of this flow pattern. Additionally, the ${}^{14}\text{C}$ distribution can be used to estimate mean net transports and residence times.

Based on the GEOSECS radiocarbon data, Stuiver *et al.* (1983) estimated a net transport of circumpolar water to the North Pacific of $25 \times 10^6 \text{ m}^3 \text{s}^{-1}$. This transport implied a deep water mean residence time of 510 years and an upwelling rate of 5 m yr^{-1} . The calculations were based on the difference in $\Delta^{14}\text{C}$ between circumpolar source waters ($\Delta^{14}\text{C} \approx -160\text{\textperthousand}$) and the lowest values found at the presumed mid-depth return flow in the North Pacific ($\Delta^{14}\text{C} \approx -256\text{\textperthousand}$). Given this relatively simple approach, the WOCE Pacific measurements confirm the GEOSECS results ($\Delta^{14}\text{C}$ range ≈ -160 to $-260\text{\textperthousand}$). These transport and upwelling estimates were in reasonable agreement with similar estimates based on geostrophic calculations (e.g. Warren, 1973).

However, due to the lack of spatial resolution, the GEOSECS data set is of limited value for studies of the overall flow pattern. The WOCE data set represents a major step forward with respect to this problem. The spatial resolution of the WOCE data is high enough that a reasonably detailed picture of the mean large-scale bottom water flow can now be inferred. Figure 5.8.17 (see Plate 5.8.17, p. 428) shows an objectively contoured distribution of the near-bottom $\Delta^{14}\text{C}$ values for the entire Pacific. Both GEOSECS and WOCE data were used in constructing the map. The deepest data points from stations where the bottom depth was at least 3500 m and where the deepest data point was within 250 m of the bottom were used. The northward flow of Circumpolar Deep Water

along the South Pacific island arch–trench system near the dateline is strongly implied by the relatively high $\Delta^{14}\text{C}$ values. Across the equator most of the water appears to turn westward and then flows clockwise around the basin. Details of the near-bottom $\Delta^{14}\text{C}$ distribution in the North Pacific are difficult or impossible to determine from this map due to the colour scale, the large south-to-north $\Delta^{14}\text{C}$ gradient, and the limited data resolution. However, the implied flow pattern can be traced to at least the Aleutian Island Arch in manually drawn maps combined with meridional vertical sections. Eastward flow over the Aleutian Trench is consistent with detailed current studies in this region (Warren and Owens, 1988). If the bottom flow is continuous around the edge of the basin from the far western edge to the northern edge, the circulation pattern is different from that described by Wijffels *et al.* (1998), who used data from the WOCE P10 section at 149°E. They concluded that the deep and bottom water flow was clockwise and against the western boundary until it reached approximately 20°N. At that point they describe the flow as turning directly eastward and ascribe the deep chemical front found at 20°N to the juxtaposition of this current and one representing southward flow along the westward boundary up to 20°N, where it turns eastward. Based on the near-bottom $\Delta^{14}\text{C}$ distribution, some fraction of the bottom water crossing the equator splits from the main flow and continues to flow toward the northeast where it passes south of the Hawaiian Island chain.

Figure 5.8.17 (see Plate 5.8.17, p. 428) indicates that the oldest bottom waters are found in the northeastern Pacific ($\Delta^{14}\text{C} \approx -220\text{\textperthousand}$), but not immediately adjacent to the North American continent. The separation of the oldest waters from both the Aleutians to the north and North America to the east can be clearly seen in meridional sections through the region (P16 and P17; ≈ 170 and 135°W, respectively). The displacement of the oldest water away from the boundary conflicts with what was implied by the GEOSECS section in the eastern Pacific, which did not extend north of $\approx 35^\circ\text{N}$. It is also inconsistent with the results from all numerical ocean models that include simulations of ^{14}C (e.g. Toggweiler *et al.*, 1991). These model simulations suggest that the oldest waters should be found adjacent to the continental rise.

Old bottom water ($\Delta^{14}\text{C} \approx -210\text{\textperthousand}$) extends southward to at least 20°S in the eastern basin. South of this point, the meridional $\Delta^{14}\text{C}$ gradient is quite strong, indicating significant mixing with waters of southern origin. Northward transport of Circumpolar Deep Water in the southeastern South Pacific is topographically blocked initially by the Chile Rise at about 40°S and subsequently by the Sala Y T Gomez Ridge at about 25°S.

Key *et al.* (1996) used an advection–diffusion model and the WOCE data available at the time to calculate a net bottom water transport across the equator of $\approx 20 \times 10^6 \text{ m}^3 \text{ s}^{-1}$ and a resulting upwelling rate of 9 m yr^{-1} . These values agree with Warren (1973), but are somewhat higher than more recent estimates (Whitworth *et al.*, 1999). They are inconsistent with inversion results using most of the WOCE zonal sections and some meridional sections (Ganachaud and Wunsch, 1998; A. Ganachaud, personal communication, 1999). The results from this inversion of hydrographic lines predict a total northward transport of Circumpolar Deep Water of $(8 \pm 2) \times 10^6 \text{ m}^3 \text{ s}^{-1}$. Further analysis will be required to resolve this discrepancy.

Between the northward-flowing Circumpolar Deep Water and the thermocline waters, Pacific Deep Water is observed. North Pacific Deep Water is the oldest and most isolated water mass in the World Ocean. There is significant information in the ^{14}C data on the return flow of northward flowing bottom waters. Strong evidence for this return flow is obtained by examining data from WOCE cruise P6 (zonal section at $\approx 32^\circ\text{S}$). Figure 5.8.18 shows the P6 $\Delta^{14}\text{C}$ results for depths greater than 1000 m. It contains three prominent features: (1) The waters with the highest $\Delta^{14}\text{C}$ values included in the figure are observed at 1000 m depth near the base of the thermocline. (2) Two low- $\Delta^{14}\text{C}$ areas around longitudes 155°W and 75°W and centred around ≈ 2600 m depth with $\Delta^{14}\text{C} \approx -210\text{\textperthousand}$. (3) A relatively high-concentration region centred at $\approx 175^\circ\text{W}$ and 5000 m depth with $\Delta^{14}\text{C}$ values of $\approx -170\text{\textperthousand}$.

The relatively high $\Delta^{14}\text{C}$ values of $-150\text{\textperthousand}$ at the base of the thermocline are not surprising. They appear as a ‘feature’ simply because they are significantly higher than values normally found in deep and bottom waters. The relatively high values found between 180°W and 150°W are in the core of the northward-flowing Circumpolar Deep

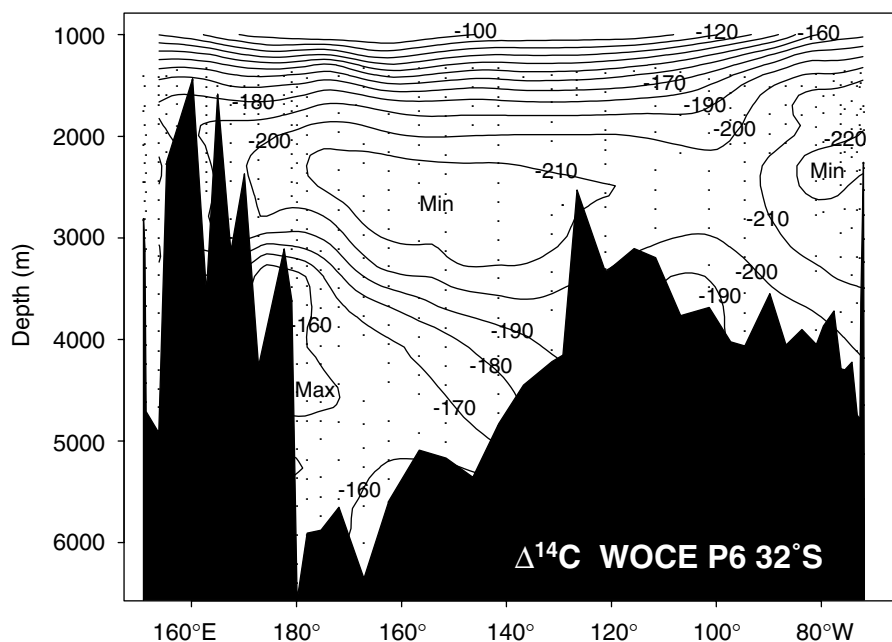


Fig. 5.8.18 $\Delta^{14}\text{C}$ for deep and bottom waters of WOCE section P6 at 32°S.

Water. The flow hugs the flank of the Tonga-Kermadec Ridge at this latitude as a deep western boundary current. Recently, Whitworth *et al.* (1999) described the flow and transport in this region based on a 2-year current meter array (WOCE PCM9) deployment. They found that the boundary current was 550 km wide and had a maximum mean velocity of 9.6 cm s^{-1} . They estimated a mean net northward transport from 2000 m to the bottom of $(16.0 \pm 11.9) \times 10^6 \text{ m}^3 \text{ s}^{-1}$. Of this, approximately $(15.8 \pm 9.2) \times 10^6 \text{ m}^3 \text{ s}^{-1}$ was northward-flowing Circumpolar Deep Water and $(0.2 \pm 5.1) \times 10^6 \text{ m}^3 \text{ s}^{-1}$ was northward-flowing Pacific Deep Water.

One possible interpretation of the $\Delta^{14}\text{C}$ distribution in Figure 5.8.18 is that the two minima centred around 2200 m are the core of southward-flowing Pacific Deep Water. To produce $\Delta^{14}\text{C}$ values this low, this water most likely originated in the North Pacific. Regardless, these minima extend upward in the water column to depths significantly shallower than 2000 m. We are not yet able to determine the transport or velocity with this data. It is, however, noteworthy that the flow is apparently divided into two branches rather than being more or less uniformly distributed across the basin. This implication could not have been derived with the GEOSECS data, nor were all these regions sampled with the WOCE current meter array (Whitworth *et al.*, 1999). Even without rigorous

analysis this section strongly implies significant mid-depth return flow. After having observed this feature in the $\Delta^{14}\text{C}$ distribution, further investigation showed that similar information is contained in the silicate distribution, but the feature is subtle and was not noticed independently.

5.8.3.6 Deep water formation in the Southern Ocean

Mainly during the 1980s, a few studies using CFCs were performed in the Southern Ocean prior to the WOCE field phase. They demonstrated that CFCs should be a valuable tool for studies of the deep water formation processes and rates, as well as the circulation pathways (see Rintoul *et al.*, Chapter 4.6). Strong tracer signals were observed in the deep and bottom water of the Weddell Sea (Bullister, 1989; Schlosser *et al.*, 1991b), and in the Ross Sea (Trumbore *et al.*, 1991; Keir *et al.*, 1992). These signals were used, together with other tracer data, to derive deep water formation rates for the Weddell Sea (e.g. Mensch *et al.*, 1996). However, the database was very patchy and no circumpolar assessment could be performed.

A number of WHP One-Time Survey sections crossed the Atlantic, Indian and Pacific sectors of the Southern Ocean. These studies complement earlier hydrographic studies performed in this region, and provide a much more detailed view of distributions of CFCs in this region. Normalized,

depth-averaged CFC-11 concentrations in the dense (neutral density $>28.27\text{ kg m}^{-3}$) layer of AABW around Antarctica, based on CFC data collected along a number of WHP sections, with additional data from pre-WOCE sections, especially for the Atlantic sector, are shown in Figure 4.6.13 (Rintoul *et al.*, Chapter 4.6). Now that the One-Time Survey has been completed, significantly better coverage is available. However, the more limited CFC coverage presented in Figure 4.6.13 clearly highlights the major regions where new AABW is being formed, the major pathways of transport away from the source regions, and the importance of topography in limiting the areal extent of these dense waters around Antarctica. Of particular interest are the very high ($>2\text{ pmol kg}^{-1}$) concentrations of CFC-11 found in the southern Weddell Sea (Weddell Sea Bottom Water), in the Ross Sea (Ross Sea Bottom Water), and along Adélie Land in Antarctica (south of Tasmania; Adélie Land Bottom Water). The intensity of the CFC-11 signal extending from the southern Weddell Sea northward toward the tip of the Antarctic Peninsula, and then branching northward (toward the Argentine Basin) and eastward, confirm that this region is a major source of new AABW. The presence of strong CFC signals in RSBW and in bottom waters off Adélie Land demonstrate that vigorous formation of bottom waters also occurs in these regions. The high CFC signal found in the Australian–Antarctic Basin can be observed extending eastward towards the Princess Elizabeth Trough ($\approx 80^\circ\text{E}$) and northward along the Kerguelan Plateau. These combined CFC observations confirm the presence of multiple regions of bottom water formation around the Antarctic continent. The distributions also outline the major pathways for the flow of these waters away from the source regions.

The observed CFC concentrations in this region, when utilized in models of deep water formation, can also help to provide quantitative information on the rates of bottom water formation and outflow from this region. Haine *et al.* (1998) used CFC and carbon tetrachloride (CCl_4) data collected in 1993 and 1994 (not shown in Figure 4.6.13) to map the flow path of AABW from the Weddell Sea to the Crozet–Kerguelen Gap. They applied a streamtube advection–mixing model to estimate a transit time of 23 ± 5 years which corresponds to an apparent current speed

of $1.2 \pm 0.3\text{ cm s}^{-1}$. They also estimated that the water was diluted by a factor of 8 to 15 since it departed the near-surface region of the Weddell continental shelves, and combining this with current meter measurements, estimated a volume flux of 0.8 to 1.6 Sv from the Weddell Sea shelves.

As discussed above, CFC inventories provide quantitative information on formation rates of subsurface water masses. Orsi *et al.* (1999) determined the total CFC inventories for the Atlantic sector and the combined Indian–Pacific sectors shown in Figure 4.6.13. The dissolved CFC content in newly formed AABW as a function of time was modelled using the CFC atmospheric input histories (Walker *et al.*, 2000), observations of the CFC content of newly formed AABW, and the assumption that the CFC saturation level of newly formed AABW (relative to the overlying atmosphere) remained constant over time. Observations indicate that the dissolved CFC content of newly forming AABW is not in equilibrium with the overlying atmosphere. Measurements of dissolved CFCs in dense waters formed on the shelves in the southern Weddell Sea in the region around the Filchner Ice Shelf are substantially undersaturated with respect to the overlying atmosphere (Schlosser *et al.*, 1991b; Mensch *et al.*, 1996). Measurements of CFCs in these dense waters sinking along the slope in this region show that they undergo further mixing with low-CFC Weddell Deep Water as they descend to form new WSBW. Orsi *et al.* (1999) examined CFC saturations in newly formed AABW, based on observations near several source regions around Antarctica (Weddell Sea, Ross Sea and Adelie region). They found roughly similar CFC saturation ratios of 35% (relative to the atmosphere at the time of sampling) for newly formed Weddell, Ross and Adélie Bottom Waters descending across the 2500 db isobath. Using this CFC saturation, Orsi *et al.* (1999) derived average production rates for new AABW of 4.9 Sv for the Atlantic sector, and 3.2 Sv for the Indian and Pacific sectors (8.1 Sv total). These production rate estimates are for newly formed AABW, of density >28.27 , which has reached a depth of $>2500\text{ m}$ along the slope around Antarctica. Such water represents the product of extensive, rapid mixing of high-CFC shelf waters ($\approx 70\%$ saturated relative to the overlying atmosphere) with very low-CFC Circumpolar Deep

Water (typical saturation levels <3%) along the pathway. This mixing roughly doubles the initial volume of the strongly ventilated shelf component, and reduces the CFC saturation level to $\approx 35\%$.

5.8.3.7 Addition of glacial meltwater around Antarctica traced by ${}^4\text{He}$

Helium isotopes and stable isotopes of water (mainly $\delta^{18}\text{O}$) have been developed as a tool to study the addition of fresh water from melting of the glacial ice sheets around Antarctica (e.g. Weiss *et al.*, 1979; Jacobs *et al.*, 1985; Schlosser, 1986; Schlosser *et al.*, 1990; Weppernig *et al.*, 1996). Most of the stable isotope data, including all published noble gas results, are from studies performed in the Weddell Sea. They allowed us to examine the pathways of Ice Shelf Water, a fresh shelf water type that is produced around Antarctica through interaction of near-surface water with glacial ice shelves (e.g. Lusquinos, 1963; Jacobs *et al.*, 1970, 1979; Foldvik *et al.*, 1985a–c), from its source onto the continental slope (e.g. Schlosser *et al.*, 1990). Additionally, these tracers are among the very few tools that can be used to quantify the relative contributions of ISW and other shelf water to Antarctic Bottom Water (AABW; e.g. Weppernig *et al.*, 1996).

The WOCE One-Time Survey allowed us to collect the first helium isotope data set in areas

outside the Weddell Sea with the goal to determine the contribution of glacial meltwater to the freshwater budget on the shelves of the Southern Ocean. Preliminary results from WOCE WHP line S4 (Pacific) clearly show the presence of glacial meltwater in the upper water layers on the continental shelves (marked by high ${}^4\text{He}$ concentrations in Figure 5.8.19). There seems to be some transport of this water into the deep water of the Ross Sea (Fig. 5.8.19). A 1994 cruise of the US ice-breaker *Palmer* extended the WOCE data from line S4P toward the continental shelf. A section along the continental slope constructed from the Palmer stations (Fig. 5.8.20) clearly shows the penetration of water with high ${}^4\text{He}$ concentrations off the shelf between about 130° and 160°W . It should be noted that most of the glacial meltwater seems to be concentrated in the upper $\approx 500\text{ m}$ of the water column. The ${}^4\text{He}$ excess corresponds to a glacial meltwater fraction of about 0.5%. Further east, the section reaches too deep into the central Amundsen–Bellingshausen seas, and the ${}^4\text{He}$ signal is diluted.

The ${}^4\text{He}$ results from WOCE and other cruises carried out in the same time frame as the WOCE One-Time Survey can be used to calculate the fraction of glacial meltwater contained in the surface waters of the Pacific sector of the Southern Ocean. Maps of the glacial meltwater fractions can then be used to study the spreading of this freshwater component and its impact on the density structure

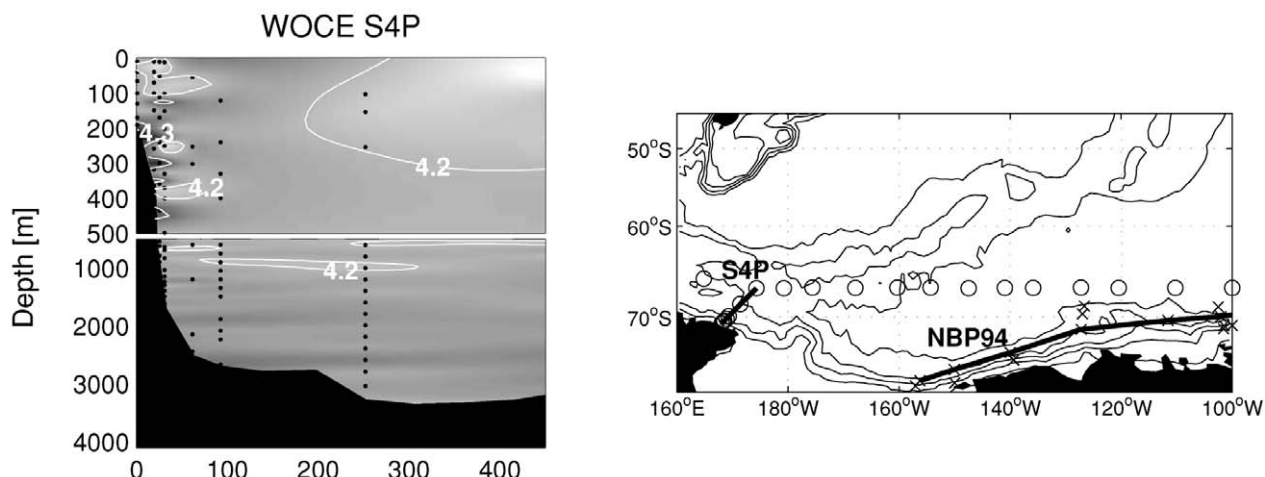


Fig. 5.8.19 ${}^4\text{He}$ concentrations along WOCE WHP section S4 (Pacific). The high ${}^4\text{He}$ concentrations are indicative of glacial meltwater added to the water column.

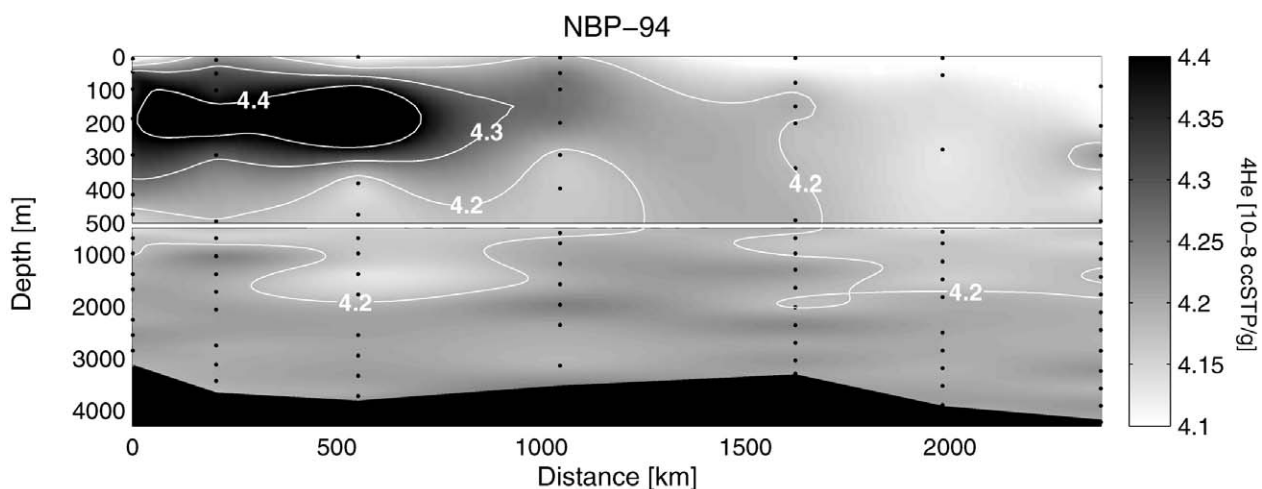


Fig. 5.8.20 Same as Figure 5.8.19, except for a section along the bottom of the continental slope in the Pacific sector of the Southern Ocean.

of the water masses close to the Antarctic continent (Hohmann *et al.*, 2001). The ${}^4\text{He}$ results are consistent with those obtained using neon measurements, which were performed during WOCE in addition to the helium isotope measurements.

5.8.3.8 Interocean exchange between the Pacific and Indian Oceans

The throughflow of water from the Pacific to the Indian Ocean via the Indonesian Archipelago (Wyrtki, 1961a) plays an important role in the global thermohaline circulation and transport of heat and fresh water (e.g. Gordon, 1986; Gordon, Chapter 4.7). It is the only interocean exchange that occurs in the tropics. Upper ocean tritium data from the GEOSECS programme provided direct evidence for the throughflow of water from the Pacific into the Indian Ocean (Fine, 1985). Data from the WOCE Arlindo programme 1993–98 (e.g. Gordon and Fine, 1996) has provided considerable detail about the pathways and sources of the water involved in the interocean exchange.

The WOCE Arlindo data established that the throughflow source is in the North Pacific (Gordon and Fine, 1996). The Mindanao Current of the North Pacific Ocean is the source of thermocline through intermediate waters entering the northwestern Indonesian Seas. These North Pacific waters carry high-salinity subtropical waters and low-salinity intermediate waters, which are well

ventilated with substantial concentrations of CFCs, into the Indian Ocean. In addition, at lower thermocline depths South Pacific water enters the eastern Indonesian Seas and contributes to the throughflow. There is a decidedly seasonal signal in the throughflow that is amplified in response to the El Niño-Southern Oscillation (ENSO) phase. Data show that the ratio of North to South Pacific water changes in the following way: During an El Niño phase, similar to northwest monsoon conditions, there is a diminished throughflow and North Pacific contribution, while during a La Niña phase, similar to the southeast monsoon conditions, the throughflow and the North Pacific contribution are stronger.

The CFCs can be used to identify waters within the Indonesian Seas that are involved in decadal climate processes. Using the CFC partial pressures (Fig. 5.8.21) the most recently ventilated waters from the Mindanao Current are observed in the Makassar Strait above 300 dbar, while further downstream they are redistributed and mixed with water of South Pacific origin. The throughflow waters mix significantly within the Indonesian Seas such that there is an isohaline structure in the Banda Sea. An inverse model analysis shows that the isohaline structure can be accounted for by isopycnal mixing of different source waters, vertical exchanges, and possible interannually variable backflushing (Waworuntu *et al.*, 2000). The model solutions suggest that there are strong baroclinic flows during the northwest monsoon, and more barotropic flows during the southwest monsoon.

The WOCE programme is providing extensive data for analysing the fate of this throughflow water within the Indian Ocean.

5.8.4 Outlook

The WOCE tracer survey provided the most extensive, global, high-quality data sets for a variety of transient and 'steady-state' tracers. The integration of tracer data collection into a major oceanographic programme that observed the ocean circulation with many variables in a coherent fashion has never been achieved before. This offers the possibility to extract a wealth of new results on the physical climate system and biogeochemical processes.

Preliminary examination of the data reveals many features that will shed new light on global and regional elements of the ocean circulation. Some of the early results discussed above, although mostly qualitative and semiquantitative in nature, are indicative of the rich set of results that we expect to obtain from the WOCE multi-tracer data set. Present efforts are directed at a synthesis of the individual data sets on a global scale. Future work will include combining the tracer data with other measurements performed during WOCE to address a variety of global and regional oceanographic problems along the lines of those presented in this contribution. Additionally, there will be targeted efforts to integrate the tracer data into the set of variables used to advance the performance of global circulation models (see Willebrand and Haidvogel, Chapter 7.2). Many of these efforts will go on in parallel, i.e. results from WOCE tracer studies will be produced on a continuous basis even if the nature of the studies will vary.

The use of tracer inventories provides an independent means of estimating water mass formation rates. In contrast to current meter arrays or hydrographic sections across strong boundary flows, tracer inventories represent the integrated effects of water mass formation from all sources on decadal time scales, and the results are less susceptible to shorter-term fluctuations on the mean water mass formation rate. The development and refinement of techniques for estimating water mass formation rates using tracer inventories are still in the early stages. Significant improvements are anticipated as more data become available, and

techniques are being refined for estimating inventories from these data. Significant improvements are also possible by advancing our understanding of the boundary conditions for input and export of tracers in the water masses. Detailed comparisons of observational data sets with model simulations should also provide insight of mutual benefit.

In terms of deriving oceanographic information that complements that from other methods, we are only at the beginning of exploiting the deep helium tracer field. Thus far most of the analysis has been descriptive in nature rather than quantitative. However, the helium field has now been mapped in sufficient detail to allow direct comparison with models that include tracer transport equations, as well as helium sources and sinks (e.g. Farley *et al.*, 1995). Future work should refine these modelling efforts and expand them to include inverse modelling studies, either on a regional or basin scale. The combination of the helium isotope data with hydrographic and other tracer data from the WOCE survey and augmenting studies will provide valuable insights into ocean circulation and mixing.

The extensive tracer data set collected as part of WOCE offers the opportunity to study in greater detail than was previously possible the formation rates of dense waters around Antarctica. This should help to improve our understanding of the subsequent mixing processes that occur as these deep and bottom waters move away from Antarctica. It also represents a key element in studies of the long-term variability of deep and bottom water in the Southern Ocean (Broecker *et al.*, 1999).

Tracers have been used extensively in the past to constrain rates of biogeochemical processes. Recently transient tracers have been used directly in the calculation of the ocean uptake of anthropogenic CO₂ (Gruber *et al.*, 1996; Wallace, Chapter 6.3). In addition, a number of three-dimensional global models are being developed and used to simulate key ocean circulation processes, and to provide predictive capabilities for possible future changes related to climate variability (Böning and Semtner, Chapter 2.2; Willebrand and Haidvogel, Chapter 7.2). The ability of these models to simulate realistically water mass formation rates, and estimate the uptake of important atmospheric trace gases (such as CO₂) in the Southern Ocean, must

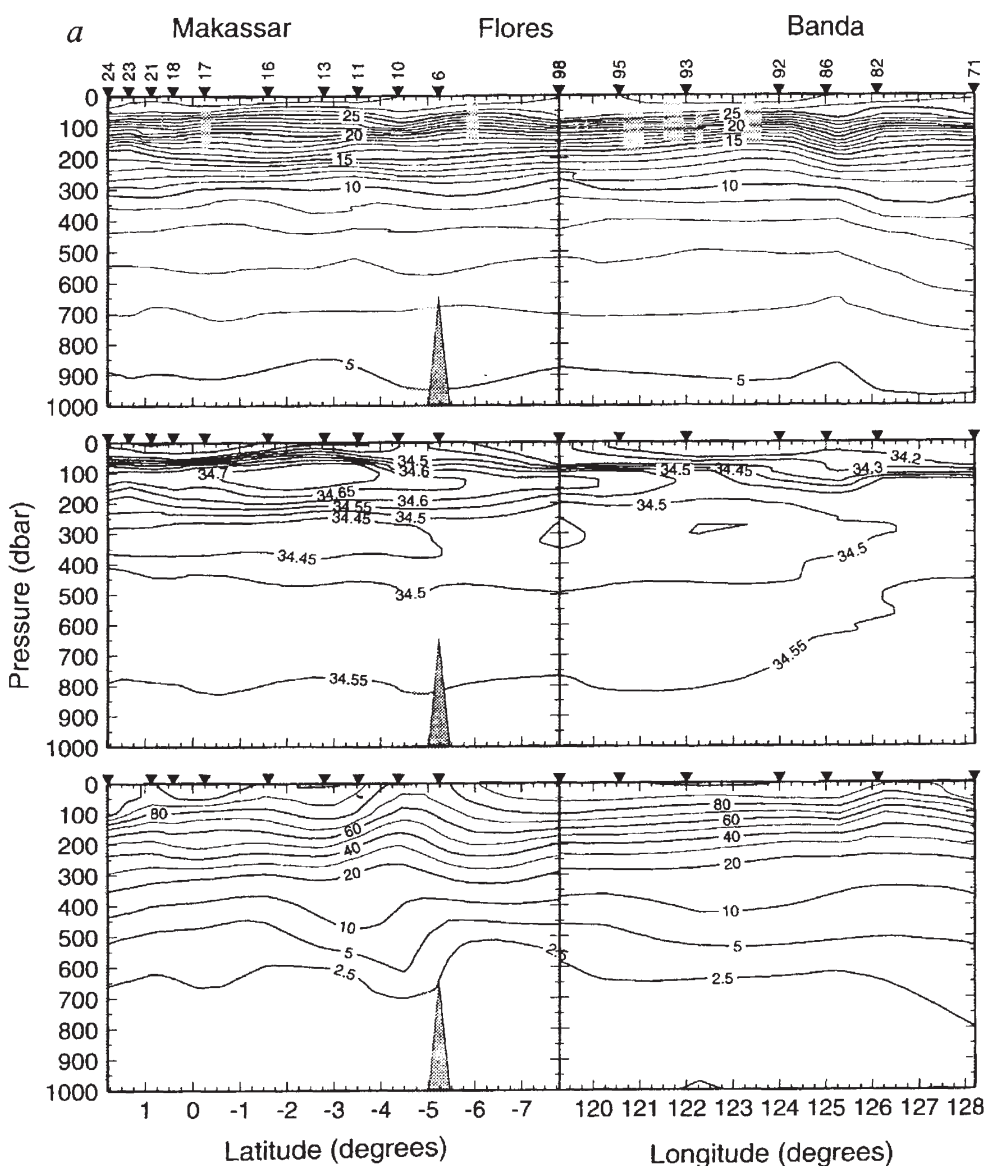


Fig. 5.8.21 Sections of (top to bottom) potential temperature, salinity and percentage saturation (relative to the present atmosphere) of CFC-11 during the 1993 southeast monsoon. Filled triangles at the top of the panel represent the station positions. Sections are along the Makassar Strait, Flores Sea into the southern Banda Sea. From Gordon and Fine (1996), their Fig. 2a.

be tested if we want to obtain confidence in their predictive capabilities. Comparisons of model and observed tracer inventories derived from the WOCE programme will provide an important test of these models.

Acknowledgements

The collection of the WOCE tracer data reported in this contribution was primarily supported by numerous grants by the National Science Founda-

tion (RF: OCE92-07237, OCE94-13222, OCE95-29847, OCE98-11535; WJ: OCE-9207162, OCE-9313928, OCE-9633276; JL: OCE91-05884, OCE-92-96237, OCE92-96169, OCE97-30431, OCE98-20132; RK: OCE-9986310, OCE-9617972; PS: OCE 91-11404; WMS: OCE 95-37864; OCE 98-11034) and the National Oceanographic and Atmospheric Administration (JB: OGP and OACES; RF: NA37RJ0200; JL: VENTS Program; PS: NA16RC0512, NA46GP0112, NA86GP0375, CORC). Support was also provided by the BMBF,

Bonn-Bad Godesberg, Germany, under grants 03F0121A and 03F0157A. Interpretation of the tracer data requires access to the hydrographic and nutrient data that were provided by several groups including ODF, BIO and IfM Kiel. The South

Atlantic AAIW study was the subject of the doctoral dissertation of Henning Rose at the University of Bremen. Gerhard Bönisch provided the Labrador Sea tritium/ ^3He time series. L-DEO contribution 6033.

SECTION

6

LARGE-SCALE OCEAN TRANSPORTS

Chapter 6.1

OCEAN HEAT TRANSPORT

Harry L. Bryden and Shiro Imawaki

455

Chapter 6.2

OCEAN TRANSPORT OF FRESH WATER

Susan E. Wijffels

475

Chapter 6.3

STORAGE AND TRANSPORT OF EXCESS CO₂ IN THE OCEANS:

THE JGOFS/WOCE GLOBAL CO₂ SURVEY

Douglas W. R. Wallace

489

This Page Intentionally Left Blank

6.1

Ocean Heat Transport

Harry L. Bryden and Shiro Imaaki

6.1.1 The global heat balance

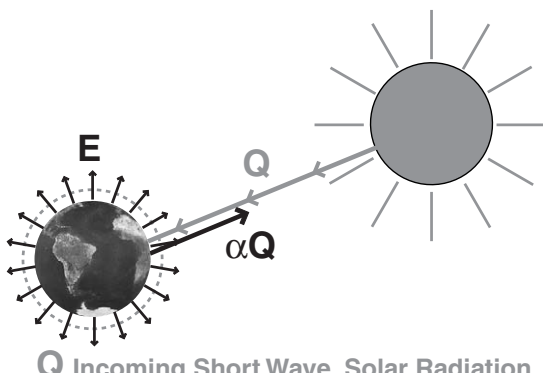
The earth is heated by solar short-wave radiation, which falls predominantly in tropical regions, and is cooled by outgoing long-wave (black-body) radiation, which is reasonably uniform over the globe (Fig. 6.1.1). Satellite measurements at the top of the atmosphere show that the net incoming short-wave radiation from the sun exceeds the outgoing long-wave radiation back to space for latitudes equatorward of about 35° , so that tropical and subtropical regions gain heat from space. Poleward of 35° , outgoing radiation exceeds incoming radiation, so subpolar and polar regions lose heat to space (Fig. 6.1.2). To maintain the heat balance for the earth, the atmosphere and oceans must transport energy poleward and the maximum combined atmosphere plus ocean energy transport at 35° latitude is about 5.5 PW (1 PW = 10^{15} W). Whether the atmosphere or the ocean is dominant in transporting heat poleward is a question of long-standing interest (Bryden, 1993). One recent separation of the total atmosphere plus ocean energy transport as a function of latitude into three components (ocean heat transport, dry static atmospheric energy transport, and latent heat transport associated with the meridional freshwater transport, which is a combined atmosphere–ocean process) indicates that the oceans and atmosphere may contribute about equally in maintaining the global heat balance (Fig. 6.1.3). The freshwater transport is considered by Wijffels (Chapter 6.2).

To assess the role of the oceans in maintaining this global heat balance, three methods have been

used in recent years:

- 1 the *traditional method*, in which bulk formula estimates of air–sea heat exchange based on surface observations are integrated over a given surface area to infer the regional ocean heat transport divergence required to balance the air–sea heat flux;
- 2 the *residual method*, in which the atmospheric energy transport is subtracted from the radiation budget requirements to derive the ocean heat transport; and
- 3 the *direct method*, in which the product of ocean velocity and temperature measured over the boundaries of a closed volume are integrated to determine the ocean heat transport divergence for the volume.

The advantage of the traditional method is that it can be applied over arbitrary areas of the ocean, while its disadvantage has been an inability to identify biases in the surface observations or flux parameterizations that make large-area estimates suspect. The primary advantage of the residual method is the availability of satellite radiation measurements of the total ocean plus atmosphere energy transport requirement, while the disadvantage has been that any uncertainty in either the radiation measurements or the atmospheric transport feeds directly into ocean heat transport estimates. The advantage of the direct method is that it deals with ocean circulation and the mechanisms of ocean heat transport, while its disadvantage has been that direct estimates could only be made at a few locations where high-quality observations were available.



Q Incoming, Short Wave, Solar Radiation
 αQ Reflected Solar Radiation (α is Albedo)
E outgoing, Long Wave, Black Body Radiation

Fig. 6.1.1 Schematic of the earth's radiation balance. Q is incoming, short-wave, solar radiation; αQ , reflected solar radiation (α is albedo); E , outgoing, long-wave, black body radiation.

One of the goals of the World Ocean Circulation Experiment (WOCE) was to remedy the principal disadvantage of the direct method; i.e. a consistent goal in designing the WOCE observational programme was to make the necessary measurements so that ocean heat transport could be directly determined as a function of latitude in each ocean basin (WCRP, 1986). These transports could then be used as a constraint on air-sea heat fluxes and as a rigorous test of ocean and coupled atmosphere-ocean general circulation models (Böning and Semtner, Chapter 2.2; Wood and Bryan, Chapter 2.3). With the completion of the WOCE observational phase and the beginning of the WOCE analysis and synthesis phase, it is an appropriate time to review progress in the methods for determining ocean heat transport and to reassess the direct estimation of ocean heat transports from the WOCE observations.

6.1.2 Bulk formula estimates of ocean heat transport

Over the past decade, several new attempts have been made to improve the estimates of air-sea heat exchange using bulk formula parameterizations. da Silva *et al.* (1994) have applied carefully chosen parameterizations to the Comprehensive Ocean Atmosphere Data Set (COADS) of ship-of-opportunity surface marine observations from 1945 to 1989. Large *et al.* (1997) have applied similar

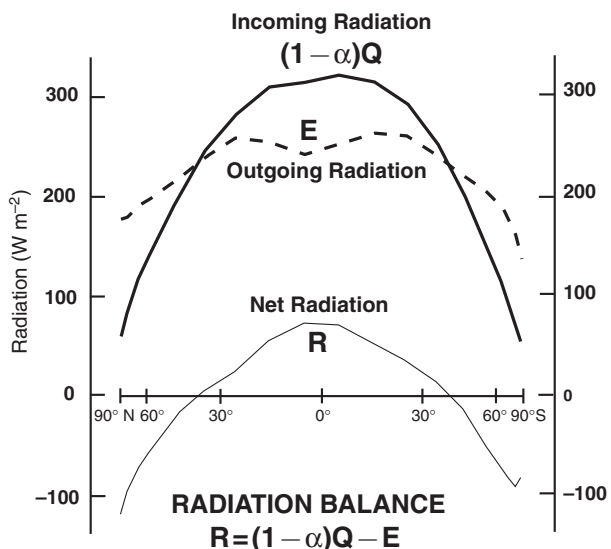


Fig. 6.1.2 Latitudinal profiles of net incoming short-wave radiation, outgoing long-wave radiation, and the net radiative heating of the earth. Values are from tables in Stephens *et al.* (1981) and a uniform bias in net incoming radiation of 9 W m^{-2} has been subtracted to ensure radiation balance over the earth. Note the latitudinal scale is stretched so that it is proportional to the surface area of the earth.

parameterizations to National Center for Environmental Prediction (NCEP) re-analyses of surface conditions and combined conventional radiation formulae with estimates of cloud fraction from the International Satellite Cloud Climatology Program (ISCCP) data set for the period 1985 to 1988. Josey *et al.* (1999) have enhanced the COADS-based calculations for the period 1980 to 1993 by adjusting for systematic biases in individual ship observations and by using an improved algorithm to convert visual wind observations to wind speed (Fig. 6.1.4, see Plate 6.1.4, p. 492). Recent efforts have attempted to identify and correct uncertainties in the ship observations and to develop methods for quantifying them (Gleckler and Weare, 1997; Kent *et al.*, 1999). In each of the global climatologies, however, there is a substantial overall heat gain by the ocean with a globally averaged heating of 30 W m^{-2} or more: 31 W m^{-2} for the COADS analysis, 43 W m^{-2} for the NCEP analysis, and 30 W m^{-2} for the enhanced COADS analysis, which is commonly called the Southampton Oceanography Centre (SOC) climatology.

To ensure a consistent set of air-sea fluxes, da Silva *et al.* (1994) developed inverse models to adjust bulk formula parameterization coefficients

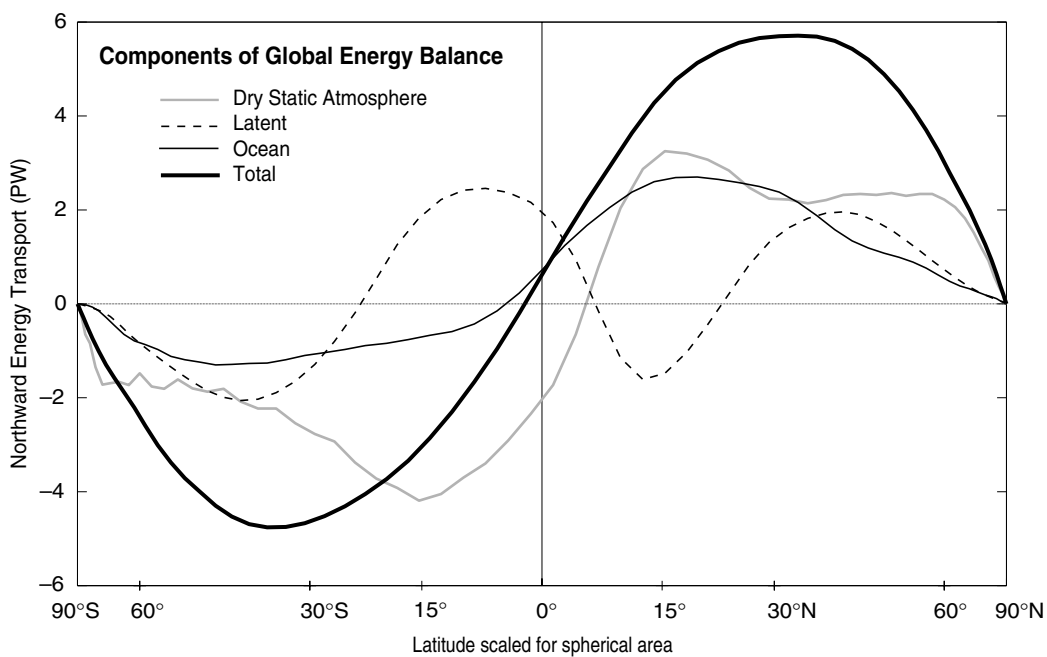


Fig. 6.1.3 Components of atmosphere and ocean energy transports required to balance the net radiative heating based on figures kindly provided by Keith (1995). The total energy transport is that required to balance the net radiative heating/cooling of the earth following Figure 6.1.2. The standard atmospheric energy transport is here divided into the dry static atmospheric energy transport and the latent heat transport, because the latent heat transport is fundamentally a joint atmosphere–ocean process as the atmospheric water vapour transport is balanced by an opposing oceanic freshwater transport. The ocean heat transport is determined by integrating over the oceans the spatial distribution of atmosphere–surface heat exchange calculated by subtracting the atmospheric energy transport divergence from the radiative heating at the top of the atmosphere.

so that the globally averaged air–sea exchange is effectively zero and the globally averaged net evaporation equals the runoff from the continents. Additional calculations also constrained the meridional ocean heat transport to have fixed values at the equator and at 24°N in the Atlantic, to agree with direct estimates of ocean heat transport. The effect of these adjustments is to reduce the incoming radiation and to increase the evaporative heat loss by the oceans. Large *et al.* (1997) similarly reduced the amount of incoming radiation by 12.5% and decreased the humidity by 7%, thereby increasing the evaporation, to achieve global heat balance. Josey *et al.* (1999) argued that such uniform adjustments are not appropriate. Comparison of the SOC climatological values with buoy measurements of air–sea fluxes at three sites suggested that adjustments vary by region, with good agreement between climatology and measurements in the eastern subtropical North Atlantic, but with offsets of 17 and 23 W m⁻² in the Arabian Sea and tropical Pacific, respectively. In the latter case, the difference is primarily due to smaller short-wave

radiative heating of the ocean as seen in the buoy measurements. Moreover, applying da Silva *et al.*'s (1994) uniform adjustments actually increased the differences between the SOC climatology and the buoy measurements at all three sites. Josey *et al.* (1999) concluded that adjustments to the climatological fluxes must be done locally, by different adjustments in different regions, and that more comparisons between buoy measurements and climatological fluxes are needed to form a basis for regional adjustments. Beyond the uncertainties in bulk formula parameters and possible biases in marine surface observations, the inadequate coverage of the vast Southern Ocean, particularly in wintertime, in the climatological databases may lead to serious underestimates of ocean heat loss. The unadjusted climatologies do not exhibit the expected area of large net heat loss by the oceans south of 45°S; rather they show ocean heat gain to 60°S and then relatively small heat losses south of 60°S.

Overall, estimates of air–sea heat exchange made by applying bulk formula parameterizations either

to marine observations or to atmospheric analyses of surface conditions appear to have uncertainties of 30 W m^{-2} . The causes of such uncertainty are unclear but recent work suggests that the amount of heat loss over strong western boundary currents may be significantly underestimated in the flux climatologies (Josey *et al.*, 1999). Despite substantial improvements in the observational databases and in the flux parameterizations over the past two decades, the conclusion remains the same as that delivered by the Cage Group (Bretherton *et al.*, 1982): heat fluxes computed by bulk formula are uncertain by $25\text{--}30\text{ W m}^{-2}$. While such uncertainty may be tolerable for seasonal or local climate analyses, an uncertainty of 30 W m^{-2} in air-sea heat exchange means that an integration of fluxes over an area $4000\text{ km by } 4000\text{ km}$ will result in an uncertainty in ocean heat transport divergence of 0.5 PW ; and larger areas will have proportionately larger uncertainties.

6.1.3 Residual method estimates of ocean heat transport

Until recently, the residual method of subtracting atmospheric energy transport from the radiation requirement at the top of the atmosphere was applied exclusively to zonal averages (e.g. Carissimo *et al.*, 1985). While the errors in incoming and outgoing radiation are about 5 W m^{-2} , and because the globally averaged incoming and outgoing radiation balance within 10 W m^{-2} , a major uncertainty in the residual method is considered to be in the atmospheric energy transport estimates. In several respects, the atmospheric energy transport derived from analysis of the observational rawinsonde network by Oort and collaborators (Carissimo *et al.*, 1985) seems too small. First, subtracting such atmospheric transport from the radiation requirement yielded ocean heat transports that seem unreasonably large (Talley, 1984; Bryden *et al.*, 1991). Second, comparisons with Geophysical Fluid Dynamics Laboratory (GFDL) model synthesis of the enhanced First GARP (Global Atmospheric Research Programme) Global Experiment (FGGE) observational data set and with a year-long European Centre for Medium Range Weather Forecasts (ECMWF) model synthesis for 1986 showed that the rawinsonde analysis yielded maximum poleward atmospheric transports about 1 PW smaller than the

model syntheses (Masuda, 1988; Michaud and Derome, 1991). Thus, ocean heat transports derived from the residual method have been uncertain by at least 1 PW due to the uncertainty in atmospheric energy transport.

Trenberth and Solomon (1994) made a major advance with the residual method by applying it pointwise, subtracting atmospheric flux divergence from the net radiation at the top of the atmosphere, to derive the spatial distribution of surface heat flux. While Trenberth and Solomon used Earth Radiation Budget Experiment (ERBE) radiation data and ECMWF analyses from a single year (1988), Keith (1995) applied similar techniques using nearly four years of ERBE data (1985–88), three years of ECMWF analyses (1989–92) and one year of National Meteorological Center (NMC) analyses (1991–92). The patterns of derived surface heat flux over the open ocean are visually similar to maps of air-sea heat exchange derived from bulk formulae (Fig. 6.1.5). But there are also clear problems in the patterns of residual surface heat flux. Most notably, the annual average surface heat flux over land is not zero; instead, it exhibits fluctuations of up to $\pm 100\text{ W m}^{-2}$, with a suggested error of 30 W m^{-2} (Trenberth and Solomon, 1994). Such an error in the residual method would be of the same magnitude as that in bulk formula estimates of air-sea exchange. Both Trenberth and Solomon and Keith argue that the large errors in surface heat flux over land may be due to problems in representing orographic effects in the atmospheric models that lead to dipoles of strong positive and negative fluxes near topography, and that the surface heat flux over the relatively smooth oceans may be more accurately represented. While possibly true over the open ocean, there are indications that land effects invade the ocean along some boundaries, particularly off South America.

Trenberth and Solomon (1994) suggested that residual method ocean heat transport estimates could be made by masking the land and integrating the surface heat flux just over ocean areas. Their integration of surface heat flux over the entire ocean yielded a net heating of the oceans by 0.7 PW , suggesting a globally averaged bias toward heating the ocean of only 2 W m^{-2} , which is substantially smaller than the global bias in bulk formula estimates of air-sea exchange and substantially smaller than the radiation uncertainties of 5 and 10 W m^{-2} referred to above. Both Trenberth

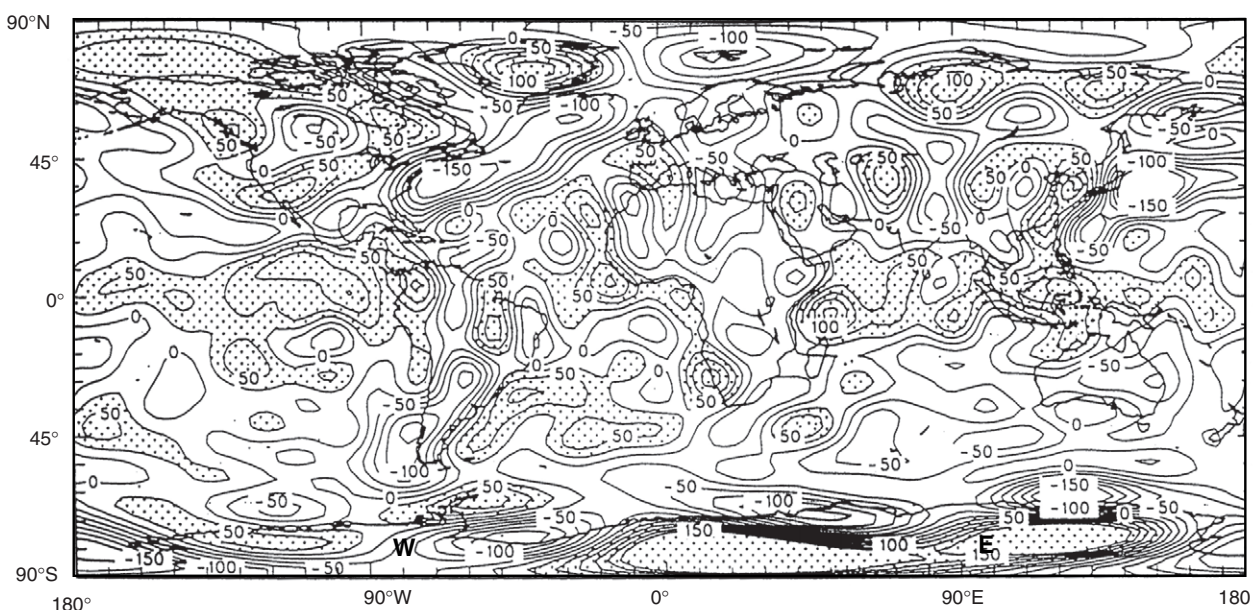


Fig. 6.1.5 Spatial distribution of the annual mean atmosphere–surface heat flux in W m^{-2} (Keith, 1995). The surface heat flux is determined by subtracting the atmospheric energy transport divergence from the net radiative heating at the top of the atmosphere. Over land, the surface heat flux should be close to zero on an annual average basis; large heating or cooling over land is likely due to problems in the atmospheric divergence. Reprinted from Tellus, 47A, D.A. Keith, Meridional energy transport: Uncertainty in zonal means, 30–44, 1995, with permission from Munksgaard International publishers.

and Solomon (1994) and Keith (1995) estimate ocean heat transport as a function of latitude by integrating the residual surface heat flux only over the oceans; each makes corrections to remove the net heating of the ocean; and each suggests that the error in residual ocean heat transport is about 0.7 PW. Within such errors, they find the residual ocean heat transports to be in agreement with available direct estimates of ocean heat transport.

Keith (1995) also investigated the discrepancy between model-derived atmospheric energy transports and the rawinsonde-derived transports. Both the NMC and ECMWF transports were 30% larger than rawinsonde transports, with the largest discrepancy appearing in the dry static energy transport. Keith could identify no reason for the substantially smaller rawinsonde transport and suggested caution in relying on model analyses while there is still a discrepancy of 1 PW with observationally based atmospheric energy transport estimates.

The residual method for estimating ocean heat transport has improved dramatically over the past decade. The patterns and magnitudes of residual surface heat fluxes are similar to those of air–sea heat exchanges calculated from bulk formulae. Furthermore, the initial residual surface heat flux

calculations by Trenberth and Solomon (1994) and by Keith (1995) suggest that their overall uncertainty over the open ocean may be considerably smaller than the persistent uncertainty in bulk formula calculations. While errors in the residual surface heat fluxes are presently quoted to be 30 W m^{-2} , there appears to be further scope for improving the residual fluxes, not only in advancing the atmospheric model physics, but also in applying additional constraints to the atmospheric flux divergences so that, for example, there is no annual average surface heat gain or loss over land.

6.1.4 Direct estimates of ocean heat transport

Directly estimating ocean heat transport juxtaposes a trivial calculation with the most subtle issues in ocean circulation. Given a mass-conserving circulation scheme, be it from a numerical simulation, a conceptual model or an observationally based analysis, the multiplication of velocity by potential temperature and subsequent integration over the boundaries of an enclosed area of the ocean to determine ocean heat transport convergence into the region is a straightforward task. The validity of

such ocean heat transport estimates, however, is entirely dependent on the validity of the circulation scheme. Is there enough cold deep water flowing equatorward and enough warm surface water flowing poleward? Are the boundary currents and gyre-scale circulations represented reasonably? Are the wind-driven Ekman transports accurate? Are the eddy fluxes realistically included? All such questions (and more) must be answered affirmatively before the estimated ocean heat transport can be considered a reliable measure of the ocean's role in maintaining the global heat balance. Ultimately, estimating ocean heat transport is a matter of quantifying the ocean circulation. Ocean heat transport can be a useful summary of the circulation; but heat transport values without a firm understanding of the circulation are vacuous.

Direct estimates of ocean heat transport are usually made using zonal coast-to-coast hydrographic sections. Prior to WOCE, successful heat transport estimates had been made primarily where the magnitude of the western boundary current transport was known: at 24°N in the Atlantic (Hall and Bryden, 1982), where the Gulf Stream transport through Florida Straits is 30 Sv ($1 \text{ Sv} = 10^6 \text{ m}^3 \text{ s}^{-1}$) (Niiler and Richardson, 1973; Larsen, 1992); and at 24°N in the Pacific (Bryden *et al.*, 1991), where the Kuroshio transport over the Okinawa Trough is 27 Sv (Bingham and Talley, 1991). The reason is that, in combination with the requirement for total mass conservation for the section, the boundary current transport puts a strong constraint on the interior circulation of the ocean determined by geostrophic calculations across the breadth of the interior ocean. It is well known that geostrophic velocity estimates depend on a reference level velocity or, alternatively, the choice of a zero velocity surface. Without constraints imposed by the western boundary current transports, very small changes in reference velocity can create enormous changes in the interior circulation. For example, across the 6000-km wide 24°N Atlantic section, a modification in reference velocity of 0.1 cm s^{-1} changes the interior ocean transport by 28 Sv. Thus, a small change in the reference level velocity (or zero velocity surface) can dramatically alter the strength of the basin-scale circulation and resultant heat transport estimates. Knowledge of the boundary current transports constrains the interior circulation and effectively determines the overall reference level velocity.

During WOCE, a large number of zonal hydrographic sections were carried out: across six latitudes in the Pacific, ten in the Atlantic and four in the Indian Ocean (Fig. 3.1.4a, see Plate 3.1.4a, p. 172). Current meter arrays at five of these latitudes (24°N and 30°S in the Atlantic, 20–32°S in the Indian, and 30°N and 30–32°S in the Pacific) were deployed to measure the strength of the deep and/or shallow boundary currents so that estimates of meridional ocean heat transport could be made more accurately. Analysis of the circulation and meridional heat transport across these five critical latitudes has not yet been completed so, in a sense, we await the best direct estimates of circulation and heat transport that will be made from WOCE. Nevertheless, notable progress has recently been made on the Atlantic circulation and heat transport, using WOCE sections as well as hydrographic sections from the 1980s, and a global inverse analysis of high-quality pre-WOCE sections has derived a consistent pattern of circulation and heat transport. While there has been progress in the Pacific and Indian Ocean analyses, much remains to be done. We will review these results here before discussing the challenges in developing circulation and heat transport estimates for all of the WOCE sections.

6.1.4.1 Atlantic Ocean heat transport

Atlantic transoceanic sections across 55°N, 24°N, 30°S and 45°S early in WOCE have already been analysed for meridional ocean heat transport (Saunders and King, 1995b; Bacon, 1997; Lavín *et al.*, 1998; Holfort and Siedler, 2001). In addition, three transoceanic sections across 14°N, 11°N and 11°S during the 1980s have been recently analysed for heat transport (Friedrichs and Hall, 1993; Klein *et al.*, 1995; Speer *et al.*, 1996). Each of these studies includes a consideration of the flow through Bering Strait, whose effect is small for Atlantic heat transport; and each considers the uncertainty in the resulting estimate of ocean heat transport. There is general agreement that the uncertainty in careful estimates of ocean heat transport is about 0.3 PW.

Each individual study of Atlantic heat transport shows the vertical distribution of the zonally averaged meridional circulation, which is responsible for nearly all of the heat transport. For each section, except 55°N, which is too far north for Antarctic water masses to penetrate, the deep

circulation exhibits northward-flowing Antarctic Bottom Water (AABW), southward-flowing North Atlantic Deep Water (NADW) and northward-flowing Antarctic Intermediate Water (AAIW). While the exact definition of water mass characteristics varies across these studies, there is a remarkable consistency in the deep circulation transports (Table 6.1.1): northward-flowing AAIW enters the South Atlantic with a small transport of about 4 Sv, which decreases to the north; southward-flowing NADW has a transport of about 20 Sv, except at 11°N where Friedrichs and Hall's analysis suggests strong recirculation gyres in the NADW with only a small net southward transport; and northward-flowing AABW enters the South Atlantic with a transport of 6–7 Sv and decreases to the north. The sum of these three components can be taken to be an estimate of the net southward flow of deep water, the deep limb of the global conveyor belt; except for some loss of AAIW up into the upper thermocline circulation, this overall deep water flow might be expected to be constant over a range of latitudes. Indeed, except for the Friedrichs and Hall analysis, the net southward flow of intermediate and deep waters varies only between 11 and 18 Sv from 45°S to 24°N.

The reason for the discrepancy with Friedrichs and Hall's (1993) values is that their analysis concentrated on the March 1989 circulation when the section was occupied while all others concentrated on the annual average circulation. Because the March 1989 trade winds were weak, there is weak northward Ekman transport and the analysed southward transport is then weaker than the annual averaged value. In effect, Friedrichs and

Hall imposed a weak northward flow over the breadth of the 11°N section to compensate for the weak wind-driven transport and their northward deep water flow in the eastern basin of 8 Sv is indicative of such compensation. When Friedrichs and Hall adjusted their analysis to reflect annual average conditions, the overall southward transport of deep water increased to 12 Sv within the range of all other analyses. Thus, there is agreement among all these studies that the annual average southward deep water transport through the Atlantic is 11–18 Sv.

With such agreement in the overall meridional circulation of intermediate and deep waters, we can have confidence in the associated heat transport estimates made for the Atlantic. The ocean heat transport is northward throughout the Atlantic; within estimated errors of 0.3 PW the heat transport increases from 0.5 PW at 45°S to a maximum of 1.2–1.3 PW between 14°N and 24°N and then decreases to 0.3 PW by 55°N (Fig. 6.1.6). While Friedrichs and Hall's reported heat transport of 0.3 PW for March 1989 is quite small due to the small net southward transport of deep water, their estimate for the annual averaged heat transport across 11°N of 1.1 PW fits in well with the pattern of heat transport derived from the other analyses of annual averaged heat transport because it has a similar size of net southward deep water transport.

The problems encountered in the Friedrichs and Hall (1993) analysis demonstrate the importance of determining annual average ocean heat transports rather than instantaneous transports. Instantaneous transports can vary enormously depending

Table 6.1.1 Overturning circulation in the Atlantic Ocean

| | 24°N | | | 14°N | 11°N | 11°S | 45°S |
|------------------------|----------------------------|--------------|--------------|----------------------------------|----------------------------------|----------------------------------|---------------------------------|
| | 1957 | 1981 | 1992 | | | | |
| AAIW | 2.5 | 1.7 | 0.7 | 0.7 | 2.1 | 4.7 | 4.1 |
| NADW | –22.6 | –21.1 | –20.8 | –16.2 | –7.3 | –26.3 | –21.7 |
| AABW | 2.3 | 3.2 | 2.6 | 0.3 | 2.1 | 3.3 | 6.6 |
| Sum | –17.8 | –16.2 | –17.5 | –15.2 | –3.1 | –18.3 | –11.0 |
| Reference | Lavín <i>et al.</i> (1998) | | | Klein <i>et al.</i> (1995) | Friedrichs and Hall (1993) | Speer <i>et al.</i> (1996) | Saunders and King (1995b) |
| Heat transport (PW) | 1.27 | 1.20 | 1.33 | 1.22 | 0.3 or 1.1 | 0.60 | 0.53 |

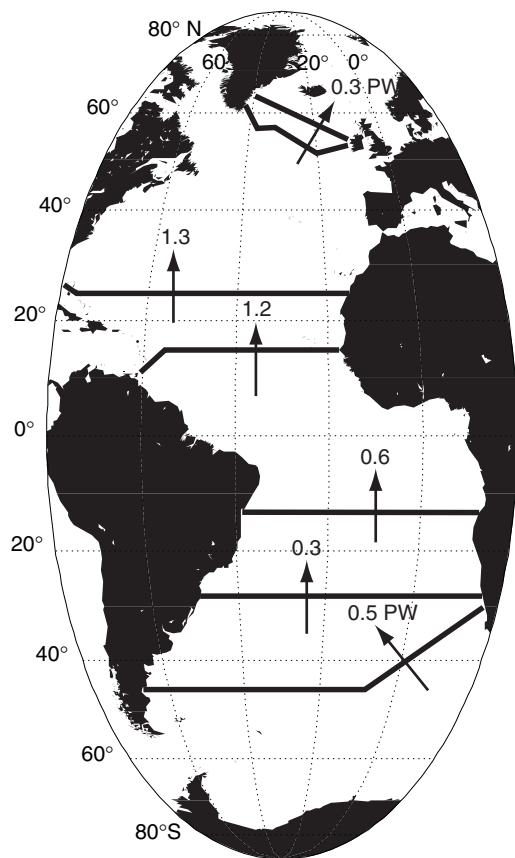


Fig. 6.1.6 Northward ocean heat transport in PW (1 PW = 1×10^{15} W) through the Atlantic derived from careful analyses of transoceanic sections: 45°S from Saunders and King (1995b), 30°S from Holfort and Siedler (2001), 11°S from Speer *et al.* (1996), 14.5°N from Klein *et al.* (1995), 24°N from Lavín *et al.* (1998), and 55°N from Bacon (1997).

on the size of the Ekman transport and/or boundary currents. For example, consider that the seasonal Ekman transport varies by 10 Sv over a section of width 5000 km and depth 4000 m. Compensation for the Ekman transport can generally be done in a depth-independent manner because changes in baroclinic structure require much longer time scales for adjustment. With three-quarters of the section area in deep water (below 1000 m depth), most of the compensation for seasonal changes is in the deep water flow; in this example the deep water flow would vary by 7.5 Sv. For a temperature difference between the Ekman transport and the barotropic temperature of 20°C, the seasonal change in heat transport would be 0.8 PW. Is this interesting or important? We would argue that such seasonal heat transport

variation is not particularly interesting because the barotropic compensating velocity would be only 0.05 cm s^{-1} and over 6 months the water would move only 10 km before sloshing back in the other direction. The key assumption, of course, is that the baroclinic structure remains constant on seasonal time scales and there are few, if any, observations with which we can test such an assumption. Theory and numerical simulations, however, tend to confirm this assumption (Böning and Herrmann, 1994, for the Atlantic; Wacongne and Pacanowski, 1996, and Lee and Marotzke, 1998, for the Indian Ocean) and observationally based analyses of the 24°N Atlantic section have not yet revealed significant seasonal fluctuations in the mid-ocean baroclinic structure (Fillenbaum *et al.*, 1997; Baringer and Molinari, 1999).

Koltermann *et al.* (1999) also estimated heat transports across 24°N, 36°N and 48°N in their study of decadal changes in the North Atlantic thermohaline circulation from the 1950s to the 1980s to the 1990s. Their circulation and heat transport across 24°N are reasonably time invariant and similar to those of Lavín *et al.* (1998), but their estimates at 36°N and 48°N exhibit large decadal variability, both in heat transport and in meridional overturning circulation. Their analysis procedure fixed the Gulf Stream transport at 24°N to be 32 Sv, as measured in Florida Straits, and at 36°N and 48°N to equal the Sverdrup transport based on Hellerman and Rosenstein (1983) winds – about 17 Sv and 5 Sv, respectively. Because such transports are far less than observed Gulf Stream transports across 36°N and 48°N and because the treatment of western boundary current transports is so critical for direct estimates of ocean heat transport, we question the heat transports at 36°N and 48°N estimated by Koltermann *et al.*

6.1.4.2 Pacific Ocean heat transport

In the Pacific Ocean, Wijffels *et al.* (1996a) have analysed a 1989 trans-Pacific hydrographic section across 10°N; Tsimplis *et al.* (1998) examined two WOCE sections across 17°S and 32°S; Wijffels *et al.* (2000) examined the WOCE section across 32°S; and Koshlyakov and Sazhina (1995) analysed a WOCE section at 67°S across the Ross Sea. Ongoing work to quantify the heat transport in the North Pacific will be discussed in Section 6.1.6.

At 10°N Wijffels *et al.* (1996a) found the upper level circulation and deep water circulation to be

separate and unrelated: for the zonally averaged circulation, the northward-flowing bottom water is balanced by southward-flowing, slightly warmer deep water; and the northward, wind-driven Ekman transport is balanced by upper thermocline flow southward at an average temperature about 9°C less than the Ekman flow. The northward heat transport of 0.73 PW is due principally to this shallow Ekman-upper thermocline cell and is sensitive to the size of the Ekman transport. Because of the 16 000 km width of the 10°N section, small changes in wind stress lead to large changes in Ekman transport and the overall meridional heat transport is sensitive (proportional) to the size of the Ekman transport. Wijffels *et al.* estimated that a 6 Sv change in Ekman transport, comparable to the differences among existing climatologies, would cause a 0.4 PW change in meridional heat transport.

In the South Pacific, the circulation and heat transport is complicated by the net northward mass transport associated with the Indonesian Throughflow from the Pacific Ocean to the Indian Ocean, which is of poorly determined size. Tsimplis *et al.*'s (1998) inverse model for the combined 17°S and 32°S trans-Pacific sections could not identify the size of the Throughflow. Their meridional circulation again implied separate deep water and upper level circulation cells, with a similar deep circulation of northward-flowing bottom water balanced by southward-flowing deep water and a similar upper level circulation with the poleward, wind-driven Ekman transport compensated by equatorward flow of slightly colder upper thermocline waters. In an attempt to determine ocean heat transport independent of the size of the Throughflow, they separated the heat transport into contributions from the horizontal gyre and from the vertical meridional overturning, each with mass conservation imposed, leaving the undetermined net Throughflow transport to occur at the section-averaged temperature. The resulting meridional heat fluxes due to the horizontal gyre and vertical meridional overturning are small, only -0.17 PW and -0.04 PW (southward) at 17°S and 32°S, respectively. These heat transports appear to be sensitive not only to the size of the Ekman transport, but also to the strength of the East Australian Current and to the distribution of the reference level velocities through the different sub-basins of the South Pacific.

In the Tsimplis *et al.* (1998) analysis procedure, the mass transport associated with the Indonesian Throughflow, whatever its magnitude, flows northward across the 32°S and 17°S sections at the section-averaged temperatures of about 4°C. Because the Throughflow from the Pacific Ocean to the Indian Ocean through the Indonesian archipelago is generally assumed to have a temperature much greater than 4°C, the Throughflow leads to a heat transport divergence such that the Pacific Ocean must gain heat from the atmosphere. The magnitude of the heat transport divergence in the Pacific is equal to the product of the Throughflow transport times the difference in temperature between the Throughflow (generally about 20°C) and the section-averaged temperature across the southern boundary of the Pacific at 32°S. For a typical value for the Throughflow of 10 Sv, the heat transport divergence over the Pacific of 0.7 PW associated with the Throughflow is much larger than the meridional heat fluxes due to the horizontal or vertical-meridional circulations across 32°S.

Wijffels *et al.* (2000) revisited the WOCE 32°S section using an inverse analysis including added constraints on the circulation provided by silica conservation and by both moored current meter measurements in the deep western boundary current near the Tonga-Kermadec Ridge and neutrally buoyant float trajectories deployed across the section at a depth of about 900 m. These direct velocity measurements significantly reduced the uncertainty in the derived flows from the inverse solution and provided details of the horizontal structure of the circulation, particularly in the deep waters, which appeared to match the direction of the flow implied by tracer distributions. The heat transport estimates are still dominated by the assumed size of the Throughflow, with a southward heat transport of 0.2 PW for no Throughflow but with a heat transport divergence for the Pacific north of 32°S of 0.75 PW for a 10 Sv Throughflow. Thus, while the Wijffels *et al.* circulation across 32°S is better resolved by the addition of direct velocity measurements, their heat transport across 32°S is similar to that derived by Tsimplis *et al.* and both estimates are very sensitive to the size of the Indonesian Throughflow.

For the small ocean area of the South Pacific/Southern Ocean south of 67°S, Koshlyakov and Sazhina (1995) found a southward heat transport

of 0.03 PW due to 8 Sv of waters above 2000 m flowing toward Antarctica, compensated by 8 Sv flowing northward below 2000 m depth. The uncertainty in the size of the horizontal heat transport, however, makes this heat transport estimate unreliable because any small difference in temperature between the 131 Sv branch of the Antarctic Circumpolar Current entering the area and subsequently leaving the area would swamp the overturning heat flux of 0.03 PW.

6.1.4.3 Indian Ocean

As for the Pacific, the unknown size of the Indonesian Throughflow complicates quantitative estimates of heat transport divergence in the Indian Ocean. Because the Throughflow entering the Indian Ocean is warm (about 20°C) relative to its temperature as it exits the Indian Ocean across the southern boundary at 32°S, the overall effect of the Throughflow is to lead to an ocean heat transport convergence over the Indian Ocean. Most of the analyses of Indian Ocean circulation and heat transport assume a certain size and temperature for the entering Throughflow, and these assumed values for the Throughflow have a strong effect on the resulting estimate of heat transport divergence for the Indian Ocean.

Macdonald's (1993) inverse calculations of the circulation across 32°S were not able to determine the size of the Throughflow. Her results indicated that not only the heat transport but also the size of the meridional overturning circulation varied substantially with the size of the Throughflow. With zero Throughflow, Macdonald's estimate of the southward heat transport across 30°S was 1.2 PW. While she did not quantify the changes in heat transport divergence over the Indian Ocean, increasing the Throughflow resulted in a decreased meridional circulation, with the amount of deep water flowing equatorward dropping from 21 Sv for a 0 Sv Throughflow to 5 Sv for a 20 Sv Throughflow.

Toole and Warren (1993) analysed the circulation and heat transport from a 1987 trans-Indian hydrographic section across 32°S. They emphasized the role of deep western boundary currents carrying deep water northward and estimated a large meridional overturning in the Indian Ocean whereby 27 Sv of deep and bottom water flowed across 32°S and returned much warmer and shallower in the southward flow of the Agulhas Current.

Their estimate of the overall heat gain by the Indian Ocean north of 32°S was 0.98 PW. In a re-analysis of the same measurements, Robbins and Toole (1997) showed that Toole and Warren's overturning circulation was incompatible with silica conservation in the Indian Ocean. Imposing a silica conservation constraint within $\pm 100 \text{ kmol s}^{-1}$ reduced the meridional overturning to about 12 Sv, as now most of the northward-flowing deep western boundary current transport recirculates southward across 32°S over the interior ocean. With silica conservation, the heat gain by the Indian Ocean north of 32°S is reduced to 0.42 PW. Each of these analyses was done with a Throughflow of 7 Sv, similar to recent estimates for its transport (Wijffels *et al.*, 1996b), and with an Agulhas Current transport of 85 Sv, appreciably larger than recent measurements of the Agulhas Current that feature a newly identified Undercurrent (Beal and Bryden, 1997).

Ganachaud *et al.* (2000) have very recently used the 1987 32°S section along with WOCE sections across 20°S, 8°S and across the Indonesian Throughflow at 110°E in an inverse analysis of Indian Ocean circulation that utilizes biogeochemical flux constraints in addition to mass, heat and salt constraints. They initially set reference levels in the Agulhas Current at 32°S to agree with recent measurements (Beal and Bryden, 1999), set the Throughflow to be 7 Sv and imposed a silica flux constraint of $\pm 700 \text{ kmol s}^{-1}$. The resulting circulation exhibited a Throughflow transport of 15 Sv, a meridional overturning with 11 Sv of deep water flowing into the Indian Ocean across 32°S below 2000 m depth, and a small net heat gain of only 0.1 PW for the Indian Ocean north of 32°S.

Since there are large uncertainties in the size of the Throughflow transport as well as in what physical processes over the subtropical and tropical Indian Ocean can convert large amounts of cold deep water into warm upper layer waters, the circulation of the Indian Ocean and its meridional heat transport, particularly across its southern boundary at 32°S, are ongoing research topics. Revised estimates are likely when the WOCE measurements are thoroughly analysed.

6.1.4.4 Global synthesis

Macdonald (1998) and Macdonald and Wunsch (1996) have made an impressive global inverse analysis of selected high-quality hydrographic

sections covering all ocean basins taken prior to the WOCE observational period. In a sense, it is one summary of the global ocean circulation and of ocean heat transport prior to WOCE. Here we display their pattern for the deep circulation colder than 3.5°C (Fig. 6.1.7, see Plate 6.1.7, p. 492) and list their estimates of meridional heat (or temperature) transports for zonal transoceanic sections (Table 6.1.2). As with any such global view, it is possible to criticise each region about the details of the circulation; indeed, Macdonald discusses the shortcomings of the inverse circulation in comparison to many regional analyses. The advantage of such a single global synthesis, however, is that the circulation and related ocean heat transport across each section are consistent with those for all other sections within the constraints imposed in the inverse model. The pattern of heat transport divergence

from the global inverse solution (Fig. 6.1.8) demonstrates this consistency.

The worry with inverse solutions is that they deviate as little as possible from the initial circulation, with its necessary choice of reference velocity, so that if a poor initial circulation is chosen, the final circulation may exhibit problems. With the global inverse solution, it is unclear how far an error in one region will propagate through the global solution. For example, Macdonald used the Friedrichs and Hall (1993) circulation at 11°N in the Atlantic as an initial solution and the final inverse solution exhibits substantial deep water flows in the eastern basin, which we suggested above were related to inappropriate initial conditions. The alternating upwelling out of and downwelling into the deep waters north and south of the 11°N section (Fig. 6.1.7, see Plate 6.1.7, p. 492)

Table 6.1.2 Ocean heat transport estimates (PW)

| Individual section analysis | Macdonald (1998) | Gordon et al. (1998b) | |
|--|------------------|-----------------------|---------------|
| | | Years 81–120 | Years 361–400 |
| Atlantic | | | |
| 55°N | 0.28 | | |
| 48°N | | 0.65 | 0.54 |
| 24°N | 1.27 | 1.07 | 1.14 |
| 14°N | 1.22 | | |
| 11°N | | 1.39 | 1.12 |
| 11°S | 0.60 | 0.89 | |
| 23°S | | 0.33 | 0.67 |
| 30°S | 0.29 | | 0.60 |
| 45°S | 0.53 | | 0.64 |
| Pacific | | | |
| 47°N | −0.09 | −0.08 | 0.17 |
| 24°N | 0.76 | 0.45 | 0.50 |
| 10°N | 0.70 | 0.44 | 0.67 |
| Pacific + Indian | | | |
| 32°S | | −1.34 | −1.19 |
| 32°S | | | −1.14 |
| Ocean heat transport estimates (positive northward in petawatts, PW) from analyses of individual hydrographic sections or a regional inverse model, from a global synthesis of pre-WOCE hydrographic sections (Macdonald, 1998), and from a coupled ocean–atmosphere numerical model without flux adjustment (Gordon et al., 1998). For the Atlantic the individual section analysis of heat transport at 55°N is by Bacon (1997), at 24°N by Lavin et al. (1998), at 14°N by Klein et al. (1995), at 11°S by Speer et al. (1996), at 30°S by Hoffort and Siedler (2001) and at 45°S by Saunders and King (1995b). For the Pacific, the 47°N heat transport estimate at 47°N is by Roemmich and McCallister (1989), at 24°N by Bryden et al. (1991) and at 10°N by Wijffels et al. (1996a). Because of the Indonesian Throughflow, heat transport estimates in the South Pacific and Indian Ocean make sense only when combined. The decrease in Atlantic heat transport in the coupled model from years 81–120 to years 361–400 is due to a decrease in the meridional overturning. | | | |

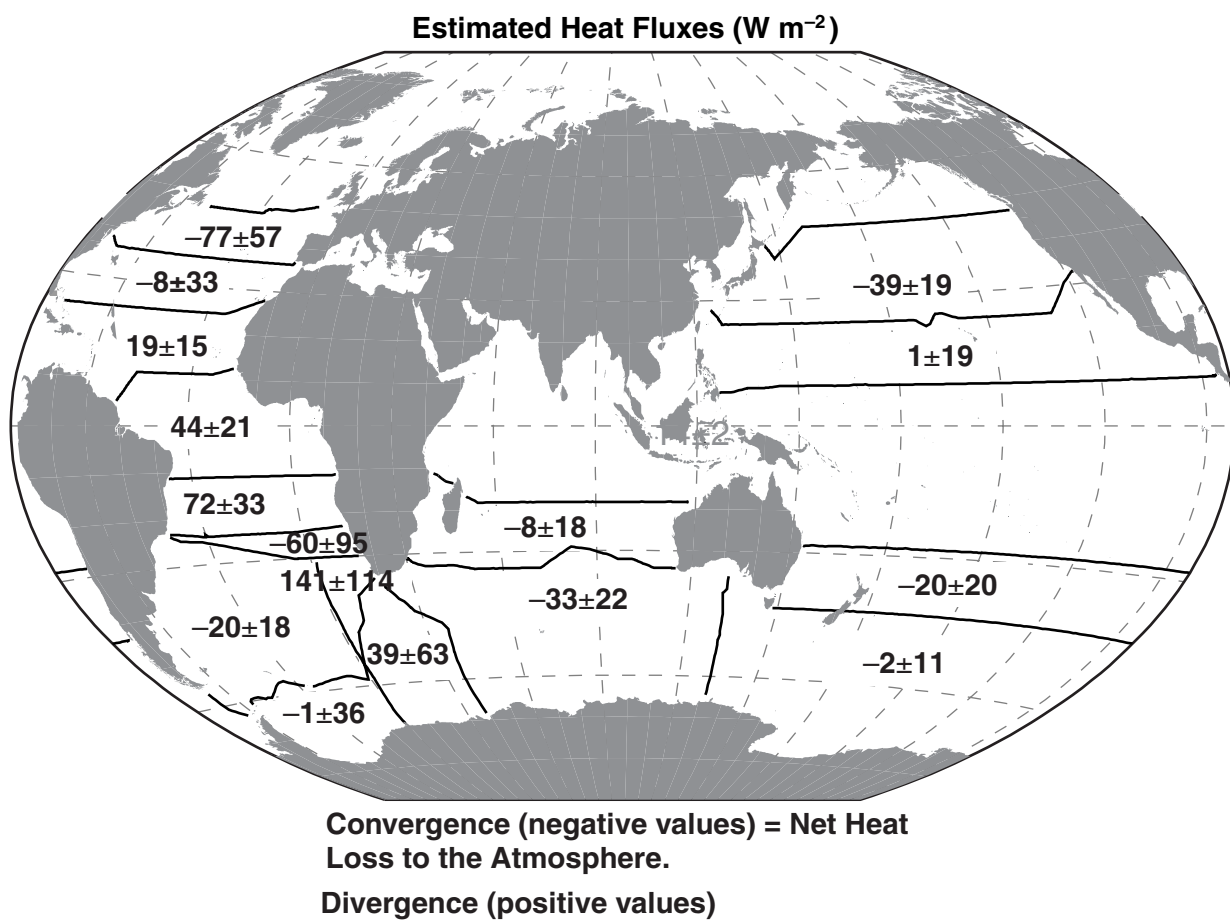


Fig. 6.1.8 Heat transport divergence derived by global inverse analysis of high-quality pre-WOCE hydrographic sections by Macdonald (1998). Reprinted from *Progress in Oceanography*, 41, A.M. Macdonald, The global ocean circulation: a hydrographic estimate and regional analysis, 281–382, 1998, with permission from Elsevier Science.

may indicate that problems in one section are locally confined. There are vertical exchanges of decreasing magnitude away from 11°N in the Atlantic, however, so it may be that a problem at one location affects the final circulation far away from the initial location. Another substantial problem with Macdonald's global circulation is the large conversion of cold deep waters into warm upper layer waters in the Indian Ocean, which is now considered to be incompatible with silica conservation. Despite these problems, Macdonald's global circulation solution presents a consistent set of ocean heat transport estimates that are reasonably close (and within the errors estimated by Macdonald) to careful estimates of ocean heat transport throughout the Atlantic Ocean based on analyses of individual sections.

6.1.5 Discussion

Direct estimates of ocean heat transport are valuable for establishing a baseline for the air-sea flux

climatologies, in assessing the residual estimates of ocean heat transport, and in evaluating ocean and coupled atmosphere-ocean general circulation models. Furthermore, the mechanisms of ocean heat transport must be understood if we are to evaluate how ocean circulation and heat transport will be modified under changing climate conditions.

6.1.5.1 Comparison of direct and indirect estimates of ocean heat transport

Both da Silva *et al.* (1994) and Josey *et al.* (1999) have compared the ocean heat transports implied by their air-sea flux climatologies with direct estimates. da Silva *et al.* actually constrained their flux climatology so that its implied heat transports at 24°N and at the equator in the Atlantic matched direct estimates of ocean heat transport across these latitudes. Josey *et al.* compared their net air-sea heat exchange with the divergence of meridional ocean heat transport over regions of the

Atlantic where they considered the direct estimates to be reliable. While their air-sea heat exchanges generally exhibited more heat gain by the ocean than the divergence estimates, they argued that the differences were within expected uncertainties in the divergences, except for western boundary current regions where there may be strong heat losses from the ocean that are not reflected in the climatological fluxes.

For residual estimates of ocean heat transport, both Trenberth and Solomon (1994) and Keith (1995) demonstrate that their residual estimates of ocean heat transport, after they mask the continents, are in reasonable agreement with direct estimates. It is important to point out, however, that the sum of atmospheric energy transport and such residual estimates of ocean heat transport are still about 1 PW less than required by the radiation balance at the top of the atmosphere due to atmosphere-land exchanges. Whether such a deficit is ultimately a problem with the atmospheric or oceanic circulations remains the essential question about the residual method.

6.1.5.2 Model ocean heat transports

Heat fluxes in ocean general circulation models are commonly tested against direct estimates of ocean heat transport (Bryan, 1982). In the Atlantic, a model heat transport across 24°N that is small compared with the direct estimate is usually a symptom of a meridional overturning in the model that is of insufficient size or too shallow (Böning *et al.*, 1996). In the Pacific, small model heat transport across 24°N is a symptom of a problem in simulating the Kuroshio (Wilkin *et al.*, 1995). Comparing model heat transports with well-determined direct estimates of ocean heat transports has become a basic first test for the validity of ocean and coupled atmosphere-ocean general circulation models.

As models improve, the question arises as to whether a model that has correctly simulated ocean heat transport at a few latitudes can then be relied upon to determine ocean heat transport at other locations. It is a difficult question to answer. On short time scales, an ocean model is nearly a global or basin-scale inversion of the climatological data used to initialize the model. Because ocean climatologies are horizontally sparse in the underlying data coverage, fine features such as deep western boundary currents may not be present in the clima-

tology and experience suggests that inversion of a data set without a significant circulation feature can lead to biases in the results (Marotzke and Wunsch, 1993). At this stage, model circulation and heat transport must be critically compared with the observed circulation and heat transport.

Over intermediate time scales of decades, ocean models are slowly adjusting the initial circulation to the air-sea fluxes forcing the model. The extent to which the model heat transport divergences balance the air-sea fluxes becomes an important indicator of model equilibrium. Any imbalance means that the model circulation is drifting toward a state different from the initial or observed circulation. At this intermediate stage, three forms of ocean heat transport need to be considered: the heat transport associated with the model circulation; the heat transport associated with the model air-sea exchanges; and the heat transport associated with the drift in model heat content. The drift is a measure of the consistency between the model circulation and the model air-sea forcing and can be used as one measure of the uncertainty in model heat transport. An example of such considerations is Saunders *et al.*'s (1999) analysis of the Pacific Ocean heat fluxes in the global ocean model OCCAM, where the effective surface fluxes are determined by relaxation to observed surface temperature and salinity. In OCCAM, the model heat transport divergences over the Pacific are in broad agreement with the Large *et al.* (1997) climatological estimates of air-sea flux and the globally averaged model drift in heat content is about 10 W m^{-2} . Such agreement may be taken to imply the quality of both the model circulation and of the air-sea forcing or flux climatology. Nevertheless, careful comparison with observed circulation and heat transports are still required. For OCCAM, the model heat transports are found to be smaller than the direct estimates of ocean heat transport across 10°N and 24°N in the Pacific, and the reason may be smaller-than-normal wind stresses in the tropics due to the model's use of winds during an El Niño year. Thus, even when a model is near equilibrium, model heat transports should be compared with the observed ocean circulation and heat transport to verify that the air-sea forcing is realistic.

Coupled ocean-atmosphere models have usually required flux adjustment to keep the ocean (or atmosphere) from drifting quickly away from its

observed state (Wood and Bryan, Chapter 2.3). Under flux adjustment, an amount of heat (or fresh water) is taken away from the ocean but not put into the atmosphere. The size of such flux adjustment can be used to represent the model error in ocean heat transport; in early coupled model runs it was quite large (Manabe *et al.*, 1992). Recently, however, coupled models have been run both by the National Center for Atmospheric Research and by the Hadley Centre for hundreds of years without flux adjustment (Boville and Gent, 1998; Gordon *et al.*, 1998b) and the model ocean and atmosphere have not drifted too far from their initial states. Boville and Gent showed that the reason that such a coupled model can run without substantial drift is that the ocean heat transport in the ocean component and the ocean heat transport required by the atmospheric component are very similar in magnitude and latitudinal structure. Ocean heat transports from the Hadley Centre coupled model are in general agreement with Macdonald's (1998) global synthesis estimates (Table 6.1.2) and such a coupled model may ultimately have the ability to help refine our estimates of ocean heat transport. Again, however, we suggest careful comparison between the air-sea heat exchanges in the model and global flux climatologies, comparison between model ocean heat transports and direct estimates of ocean heat transport, and assessment of the (regional) drifts in model heat content to evaluate critically such a coupled model.

6.1.5.3 Mechanisms of ocean heat transport

For oceanographers, it is traditional to discuss ocean circulation in terms of the transport of various water masses, as we did above for the deep Atlantic circulation in terms of AABW, NADW and AAIW. In fact, the precise definitions of these water masses change from section to section and the spatial variations in water mass characteristics and transports provide information on the amounts of mixing and advection in the interior ocean. Applying a consistent definition of the density boundaries between water masses for Atlantic sections at 45°S, 11°S, 11°N, 14°N and 24°N, Speer *et al.* (1996) were surprised by the substantial exchange and mixing across the water mass boundaries required for a consistent circulation of AAIW, NADW and AABW from 45°S to 24°N in the Atlantic. Thus, argued from the perspective of

water mass analysis, the advection and mixing of each water mass must be sorted before the circulation can be considered finalized.

For ocean heat transport, however, the net meridional advection of water masses is generally the most important factor because small changes in water mass characteristics due to mixing contribute little to heat transport on basin scales. Analysis of the circulation and heat transport can then be focused on the net flow in a set of layers separated by isopycnals (e.g. Robbins and Toole, 1997). Such analyses naturally emphasize the vertical-meridional overturning aspects of the basin-scale circulation because eddies or gyre-scale circulation within any single density layer can contribute little to heat transport, as the temperature along each density surface exhibits only small variations (which are compensated by salinity). Thus, analysis in density coordinates effectively sees only the meridional overturning defined in density classes.

Yet ocean circulation is commonly discussed in terms of wind-driven gyre circulation and thermo-haline-driven vertical-meridional overturning. As discussed above, the Atlantic circulation and heat transport are dominated by the meridional overturning. The North Pacific provides a contrast in that its subtropical gyre exhibits a circulation in which warm water flows northward in the Kuroshio along the western boundary, loses heat to the atmosphere and returns southward in the central and eastern Pacific at colder temperature (Bryden *et al.*, 1991). One naturally describes such a process of northward heat transport as being due to the wind-driven horizontal circulation. In a density analysis, however, the warm, less dense water is transformed into colder, denser water, so this same process also becomes an overturning in density.

To preserve the distinction between the mechanisms of horizontal circulation and vertical-meridional overturning, we prefer to break up the calculation of ocean heat transport into horizontal and vertical components, as follows. For a zonal transoceanic section, separate meridional velocity, v , and potential temperature, Θ , into three components:

- section-averaged values $\langle v \rangle$ and $\langle \Theta \rangle'$
- zonally averaged baroclinic values $\langle v \rangle(z)$ and $\langle \Theta \rangle(z)$

- deviations from zonal averages $v'(x, z)$ and $\Theta'(x, z)$

where $v = \langle v \rangle + \langle v \rangle(z) + v'(x, z)$ and $\Theta = \langle \Theta \rangle + \langle \Theta \rangle(z) + \Theta'(x, z)$

The geostrophic heat transport can then be broken up into three corresponding components:

1 barotropic component,

$$\rho C_p \langle v \rangle \langle \Theta \rangle \int L(z) dz$$

due to the net transport across the section at the section-averaged temperature, where $L(z)$ is the width of the section at each depth and $\int L(z) dz$ is the area of the section and C_p is specific heat capacity at constant pressure.

2 baroclinic heat transport,

$$\int \rho C_p \langle v \rangle(z) \langle \Theta \rangle(z) L(z) dz$$

due to the zonally averaged vertical-meridional circulation; and

3 horizontal heat transport,

$$\int dz \int dx \rho C_p v' \Theta'$$

due to the large-scale gyre circulation and the smaller-scale eddies.

For some sections, such as those across 24°N in the Atlantic and Pacific where there are strong, confined western boundary currents, it can be convenient to separate mid-ocean and western boundary contributions to each of the barotropic, baroclinic and horizontal components (Bryden, 1993); but here we emphasize the breakdown for the entire transoceanic section. The horizontal heat transport can be further divided into temporally varying eddy and time-averaged steady circulation components if time series data are available. Even for the single section the horizontal heat transport can be separated into eddy and gyre components by defining the contributions by various spatial scales to the horizontal heat transport, $v' \Theta'$, contribution. These components are essentially the same as those recommended by Bryan (1982). We repeat them here because it is different from the breakdown into baroclinic and barotropic components used by Hall and Bryden (1982). Although the Hall and Bryden breakdown remains equally valid for calculating ocean heat transport, we no longer find that breakdown as useful for understanding the mechanisms of ocean heat transport.

The wind-driven Ekman component can be included either as a separate barotropic component associated with the surface temperature or as a part of the baroclinic heat transport where the surface currents are the sum of geostrophic and wind-driven contributions. Because the Ekman transport is associated with the wind-driven circulation, whereas the baroclinic heat transport tends to be associated with the thermohaline circulation, one may prefer to consider the Ekman transport as a separate barotropic component. The problem then is to identify the temperature (and other properties) to associate with the Ekman transport: is it the surface temperature or some weighted average of temperature over the upper 50 m? During WOCE, underway Acoustic Doppler Current Profiler (ADCP) current measurements were routinely made on almost every hydrographic section. The resulting upper ocean current profiles can be used to isolate the wind-driven, ageostrophic velocity profile through the Ekman layer (e.g. Chereskin *et al.*, 1997) and consequently to define the relevant temperature to associate with the Ekman transport.

Besides separating the horizontal gyre and vertical overturning contributions, an added advantage of this breakdown is that both the baroclinic heat transport and the horizontal heat transport conserve mass by definition, and hence contribute directly to the total ocean heat transport. Only the barotropic component includes a net mass transport; therefore in closing the mass budget only this barotropic component need be considered, along with other mass transports into or out of an enclosed region, to finalize the estimate of ocean heat transport convergence for the region. For the Indian or Pacific Ocean, this means that even without knowing the size of the Indonesian Throughflow we can estimate the contributions from the horizontal and meridional overturning circulations. The effects of the Throughflow on the Pacific and Indian Ocean heat balances can then be estimated from a consideration of the barotropic component and how it is compensated over the basin.

We recommend that ocean heat transport be separated into these baroclinic, horizontal and barotropic components when analysing WOCE sections or numerical models for their heat transports. It is often helpful also to consider the circulation in density coordinates. The key is to

understand ocean circulation. It is not sufficient just to calculate the heat transport. The mechanisms of ocean heat transport must be understood and the above separation represents a quantitative method to present the mechanisms of ocean heat transport for comparisons between ocean basins and between observed and simulated basin-scale ocean circulations.

6.1.6 Challenges

Using the WOCE data sets to best advantage for the determination of the circulation and heat transport in each ocean basin is clearly the principal challenge over the next few years. While the Atlantic circulation and heat transport will undoubtedly be refined from continued analysis, the Pacific and Indian Ocean circulations represent the principal challenge for developing our understanding of the global ocean circulation and ocean heat transport. We know that about 15 Sv of cold deep waters exit the South Atlantic into the Southern Ocean; somewhere in the Indian, Pacific or Southern Ocean these waters must rise and warm before they return to flow northward through the Atlantic. There are two common conjectures for the required upwelling and warming of deep waters: the Warm Water Pathway argues that deep waters upwell in the tropical and equatorial Pacific and Indian oceans and are then carried back into the Atlantic by the Agulhas Current around southern Africa (Gordon, 1986); the Cold Water Pathway argues that deep waters upwell around the Antarctic and then warm as they flow eastward in the Antarctic Circumpolar Current, through Drake Passage, and then northward into the Atlantic (Rintoul, 1991). Clearly the upwelling of deep waters and their warming need not occur simultaneously.

The Warm Water Pathway attributes a crucial role to warming of the cold waters in the Pacific and Indian tropical regions and hence implies a sizeable heat gain by the ocean from the atmosphere and a sizeable southward ocean heat transport across the combined southern boundary of the Pacific–Indian Ocean at about 32°S. Determining the circulation and associated meridional heat transport across 32°S in the Pacific and Indian oceans would critically test the Warm Water Pathway conjecture. As shown above, there is little evidence for a deep upwelling in the equatorial

Pacific as the deep and shallow water circulations appear to be separate and self-contained and the present estimate of 12 Sv upwelling in the equatorial Indian Ocean remains controversial because the large mixing processes that must accompany such upwelling have not been measured and are not understood.

The Cold Water Pathway attributes a crucial role for the warming of upwelled waters to the Southern Ocean and attributes a small role for the Indian and Pacific equatorial regions. While it is hard to believe that the Antarctic circumpolar region of the Southern Ocean could gain much heat from the atmosphere (Trenberth and Solomon, 1994), da Silva *et al.*'s (1994) adjusted air–sea flux climatology does include sizeable ocean heat gain over latitudes south of 45°S. Validation of the Cold Water Pathway with such polar and subpolar heat gain may require a concerted programme of buoy measurements of air–sea fluxes in the inhospitable Southern Ocean region. Indirectly, however, determining the circulation and heat transport across 32°S in Pacific and Indian Oceans could help to validate the Cold Water Pathway if their deep and shallow circulations were found to be separate and self-contained so there were effectively no poleward heat transports out of the Pacific and Indian Oceans.

Thus, the principal challenge is to quantify the circulation and heat transports of the Pacific and Indian Oceans, particularly across their southern boundaries. The WOCE measurements included sections across southern boundaries of the Pacific and Indian Oceans, time series measurements of deep western boundary current at 32°S in the Pacific and at 20°S in the Indian, and time series measurements of western boundary at 30°S in the East Australian Current and at 31°S in the Agulhas Current. Along each section, upper ocean currents were monitored by the shipboard underway ADCP and nutrients and biogeochemical tracers were measured throughout the water column. In addition, there are long time-series of sea surface height from the TOPEX/POSEIDON altimetric satellite, subsurface float measurements at about 1000 m depth, and surface drifter measurements. Classical analysis of open-ocean hydrographic measurements has concentrated on identifying a zero velocity surface for geostrophic velocity and transport estimates based on the distribution of temperature, salinity, oxygen and nutrients. During

WOCE, there is additional information on reference level velocity from the sea surface height, underway ADCP, drifter and float trajectories, as well as multiple geochemical tracer distributions. Most importantly, for the southern boundaries of the Indian and Pacific, there are measurements of the western boundary currents that have proven vital in the past for constraining mid-ocean geostrophic calculations and ultimately the estimates of ocean heat transport.

While the Indian and Pacific boundary current measurements have not been completely analysed, much progress has been made on the analysis of heat transport across 30°N in the Pacific using a combination of time series measurements of the western boundary current and a transoceanic section. Thus, we conclude this chapter on ocean heat transport with a summary of this recent analysis to show the potential for combining different measurements made during WOCE to determine the basin-scale circulation and heat transport.

The most comprehensive set of western boundary current measurements during WOCE were made by Japanese scientists who deployed 33 current meters on nine moorings across the Kuroshio south of Japan from October 1993 to November 1995 (Imawaki *et al.*, 1997, 2000a). Hydrographic surveys along the line of moorings were repeatedly made during this 2-year intensive observation period by the Affiliated Surveys of the Kuroshio off Cape Ashizuri (ASUKA) Group. The velocity field of the Kuroshio is determined by geostrophic calculation using the repeated hydrographic survey data referenced to velocities observed at mid and abyssal depths. The mass and temperature transports for the Kuroshio between the Japanese coast and 30°N are then estimated from these absolute

geostrophic velocities and hydrographic data. The most complete surveys comprise four sets of full-depth hydrographic data across the full extent of the Kuroshio during the first year of the intensive survey period, when almost complete data was recovered from the moored current meters. The transport results for these four surveys are shown in Table 6.1.3 (H. Uchida, personal communication).

The ASUKA line was purposely located along a TOPEX/POSEIDON satellite track so that long-term monitoring of the Kuroshio could be attempted for the first time. An experimental procedure was developed to estimate a time series of 10-day mass and temperature transports of the Kuroshio from TOPEX/POSEIDON altimetry data with the aid of correlations found between the measured transports and the differences in sea surface height across the Kuroshio (Ichikawa *et al.*, 1999; Imawaki *et al.*, 2000a). The estimated 3-year mean mass transport and temperature transport are $63 \times 10^9 \text{ kg s}^{-1}$ and 3.50 PW, respectively, which are very close to the averages shown in Table 6.1.3. The annual mean Kuroshio transport is found to be fairly large compared with the Sverdrup transport estimated from the climatological mean wind stress field at this latitude; but the observed seasonal cycle in Kuroshio transport is much smaller than predicted by linear Sverdrup theory using observed winds (Imawaki *et al.*, 2000b).

To estimate the meridional heat transport across 30°N where the Kuroshio was being monitored, a trans-Pacific hydrographic survey was carried out along 30°N by three Japanese vessels (Research Vessels *Shoyo*, *Bosei-maru* and *Kaiyo-maru*) between October 1993 and January 1994 (Fukasawa *et al.*, 2000). For estimating heat transport, the

Table 6.1.3 Kuroshio transports

| Month | Mass transport (10^9 kg s^{-1}) | Temperature transport (PW) | Mean potential temperature (°C) |
|----------|---|----------------------------|---------------------------------|
| Jan 1994 | 52.12 | 2.44 | 11.7 |
| May 1994 | 62.12 | 3.83 | 15.5 |
| Jul 1994 | 76.43 | 4.19 | 13.7 |
| Sep 1994 | 52.08 | 3.56 | 17.1 |
| Mean | 60.75 | 3.51 | 14.4 |

Temperature transport is based on the Celsius scale. Mean potential temperature is estimated by dividing the temperature transport by the mass transport and using C_p as a constant of $3.99 \times 10^3 \text{ J kg}^{-1} \text{ °C}^{-1}$.

flow of the interior ocean is divided into baroclinic and barotropic components: the baroclinic field is obtained by geostrophic calculation using the trans-Pacific hydrographic data with a reference level of 2500 dbar. The barotropic mass transport is calculated so that the interior mass transport balances the Kuroshio transport at the western boundary. The interior temperature transport is estimated from these baroclinic and barotropic mass transports and the hydrographic data (Table 6.1.4).

The initial estimate of heat transport across 30°N is based on the January 1994 survey, which is chosen among the four Kuroshio surveys in 1994 because the westernmost part of the trans-Pacific section across 30°N was measured during 11–14 January 1994 by *Kaiyo-maru*. At that time, a very strong cyclonic mesoscale eddy was located right at the join between the western end of the mid-ocean section and the southern end of the Kuroshio section (see Imawaki and Uchida, 1995). Therefore a northward flow associated with this eddy was observed in the 30°N section and a southwestward flow opposing the Kuroshio was observed in the Kuroshio section. As a result, the

net transport of the Kuroshio at this time is smaller than the mean value. For this reason, the Kuroshio data obtained simultaneously with the trans-Pacific hydrographic data is used initially to determine the heat transport in order to minimize the effect of this eddy. Climatological mean data are used for estimating mass and temperature transports of the surface Ekman flow (Hellerman and Rosenstein, 1983; Levitus and Boyer, 1994b). In this initial analysis, the mass and heat transports through the Bering Straits are ignored, because the annual mean mass transport is fairly small, i.e. only $0.8 \times 10^9 \text{ kg s}^{-1}$ (Coachman and Aagaard, 1988). The net ocean heat transport across 30°N is then estimated to be 0.62 PW.

The joining of time series western boundary current measurements to a one-time transoceanic section is a subtle issue still to be resolved. Should only an instantaneous estimate of heat transport be made for the particular time period when the transoceanic section is made? Or can we join the structure of the time-averaged western boundary current onto a matching point in the transoceanic section? As stated earlier, we prefer to emphasize

Table 6.1.4 Meridional heat transport across 30°N in the North Pacific

| Component | Mass transport (10^9 kg s^{-1}) | Temperature transport (PW) | Mean potential temperature (°C) |
|------------------|---|----------------------------|---------------------------------|
| Kuroshio | 52.12 | 2.44 | 11.7 |
| Tsushima current | 2.2 | 0.14 | 16.0 |
| Ekman transport | 0.38 | 0.03 | 19.1 |
| Interior | –54.70 | –1.99 | 8.9 |
| Baroclinic | –25.46 | –1.61 | 15.8 |
| Barotropic | –29.24 | –0.38 | 3.2 |
| Net | 0.0 | 0.62 | |

The Kuroshio south of Japan was measured along the ASUKA line during 19–22 January 1994 by RV *Shojo*. The moored current meter measurements during this period were used to choose the reference velocities for the geostrophic transport calculations. These estimates are the net transports between the Japanese coast and 30°N, and not necessarily exclusively for the northeastward-flowing Kuroshio.

The flow of the interior ocean is divided into baroclinic and barotropic components. The baroclinic field was measured along 30°N during October 1993 and January 1994 by RV *Shojo*, *Bosei-maru* and *Kaiyo-maru*. The westernmost part of the section, connected to the ASUKA line, was measured during 11–14 January 1994 by *Kaiyo-maru*. The barotropic mass transport is calculated so that the net mass transport across the 30°N latitude circle is zero. The barotropic temperature transport is estimated from this mass transport and the hydrographic data.

For the Tsushima Current (Isobe, 1994) and Ekman transport (Hellerman and Rosenstein, 1983), climatological annual mean values are adopted.

Temperature transport is based on the Celsius scale. Mean potential temperature is estimated by dividing the temperature transport by the mass transport and using C_p as a constant of $3.99 \times 10^3 \text{ J kg}^{-1} \text{ °C}^{-1}$.

the annual average heat transport across each transoceanic section for comparison among all such heat transport estimates to quantify the ocean's role in maintaining the global heat balance. Thus, we are actively investigating how best to join time series western boundary current measurements with a one-time transoceanic section.

6.1.7 Summary

A fundamental issue in the global climate system is the relative amounts of heat carried by the oceans and the atmosphere to balance the global heat budget in which radiative heating from the sun occurs predominantly in tropical regions while radiative cooling to space occurs more uniformly over the globe. Progress in estimating ocean heat flux by three methods was reviewed with emphasis on the direct method using transoceanic hydrographic sections completed during the WOCE field programme.

The residual method subtracts atmospheric energy transport from the radiation budget requirement for total ocean plus atmosphere energy transport to determine ocean heat transport as a residual. Previously this method was applied to zonal averages. New studies have derived spatial patterns of atmosphere–surface heat flux by subtracting atmospheric energy transport divergence from the net radiation at the top of the atmosphere. Such patterns exhibit substantial and unrealistic annually averaged heat fluxes over the land but the patterns of heat flux over the oceans appear realistic. Masking the land to consider only these air–sea heat fluxes yields ocean heat transports in broad agreement with existing direct estimates of ocean heat transport. Dipole patterns of heat gain and heat loss over land topography, however, suggest that refinements in atmospheric energy transport are still needed.

The bulk formula method for determining air–sea heat exchange from marine observations has been used to produce several new global air–sea flux climatologies. Depressingly, each exhibits an overall global imbalance such that on average the ocean gains heat at a rate of $30\text{--}50\text{ W m}^{-2}$. There is evidence that spatially uniform corrections are not appropriate. Refinement of the air–sea fluxes will require accurate area-averaged estimates of ocean heat transport divergence over a variety of oceanic regions and additional buoy measurements

of air–sea heat exchange in inhospitable subpolar and polar regions.

Making direct estimates of ocean heat transport from transoceanic sections in each ocean basin was a primary objective in designing the WOCE field programme. While many zonal hydrographic sections were taken during WOCE, there are relatively few published estimates of heat transport from WOCE sections to date. Most of the recent estimates are for the Atlantic Ocean, for which there is general agreement that there is northward ocean heat transport at all latitudes. There is also general understanding that this northward heat transport is associated with the thermohaline circulation in which North Atlantic Deep Water is formed in the polar and subpolar North Atlantic and subsequently flows southward throughout the Atlantic. For the Pacific and Indian Oceans, analyses of pre-WOCE transoceanic sections have concentrated on estimating the heat transports across the southern boundary at approximately 30°S . There is general confusion in that there appears to be only a small poleward heat transport across 30°S out of the Pacific Ocean and the estimates of poleward heat transport across 30°S in the Indian Ocean range from 0.1 to 1.3 PW. Uncertainty in the size of the Indonesian Throughflow clouds the determination of ocean heat transports across 30°S in the Indian and Pacific Oceans.

A variety of new measurements were made during WOCE with the aim of providing accurate reference velocities for geostrophic calculations. Such new measurements include satellite altimeter measurements of sea surface height (Fu, Chapter 3.3), direct current measurements by underway and lowered ADCPs (King *et al.*, Chapter 3.1) and by surface drifters (Niiler, Chapter 4.1) and subsurface floats (Davis and Zenk, Chapter 3.2), and a variety of geochemical tracer measurements (Schlosser *et al.*, Chapter 5.8). Because experience suggests that measurements of western boundary currents provide the strongest constraints to estimates of ocean heat transport, careful analysis of WOCE observations of shallow and deep boundary currents in the Pacific, Indian and Atlantic Oceans, along with velocities from subsurface floats, likely holds the key to direct determinations of ocean heat transport in each ocean basin and the subsequent understanding of the role of the oceans in maintaining the global heat balance.

6.1.8 Outlook for direct estimates of ocean heat transport

Analysis of WOCE measurements for ocean circulation and heat transport has taken two primary paths to date: careful analysis of individual sections and large-scale inverse analyses using many sections. Analysis of individual sections has been hampered by some data sets not yet being available for general analysis, either because they have not been finally processed or because they have not been made publicly available. The successful synthesis of the Pacific 32°S section, where for the first time subsurface float trajectories could be included in the analysis, suggests that ocean circulation and heat transport across each of the WOCE sections will have a much firmer basis when all measurements made along the section during WOCE (including hydrographic, tracer, ADCP and LADCP (Lowered ADCP), subsurface and surface float, altimetric, and moored current meter measurements) can be considered in the analysis. Large-scale inverse analyses have generally combined many WOCE sections and made

reasonable, but not carefully determined, choices for the initial reference level, with the idea that the inverse solution would iron out the conflicting parts of the initial circulation. As a result, the inverse solutions can be criticised as unrealistic in some way by scientists who have worked on one piece of the problem. An additional issue is a lack of understanding of how far a poor choice of initial reference level will spread inaccuracies in the final inverse solution. Can the inverse solution with enough data and constraints fix any initial problems? Or will an inverse solution always spread any initial problems throughout the final solution? Ultimately the goal should be to combine the results from carefully analysed individual sections into a large-scale inverse model, which would start from an initial circulation with minimal problems and whose solution would ensure that the overall circulation is consistent for all the considered sections. Only at that point would the ocean circulation necessary for determining the ocean heat transport be well defined.

6.2

Ocean Transport of Fresh Water

Susan E. Wijffels

6.2.1 The importance of freshwater transport

The majority of water cycling through the atmosphere derives from the ocean, causing either distillation or freshening of ocean surface waters. The steady-state portion of the salinity distribution in the ocean reflects a balance between the exchange of fresh water at the surface and compensating mixing and advective ocean processes. Hence, in the long-term, the transport and circulation of fresh water (and salinity) by the ocean mirrors the transport of latent heat by the atmosphere, which comprises as much as 1.5 PW of the total of 4 PW of poleward atmospheric energy transport (Rosen, 1999). Oceanic freshwater transport is therefore a fundamental parameter in the planetary energy budget (see Grassl, Chapter 1.1 and Clarke *et al.*, Chapter 1.2).

As both atmospheric, ocean and coupled climate models improve, the need for accurate estimates of the components of the planetary energy budget becomes increasingly acute. Without good estimates of the partition of energy transport between the ocean and the atmosphere, and between diabatic and adiabatic processes, diagnosing errors in the models or assessing the effects of new physical parameterizations is made more difficult. For ocean-only models in particular, the lack of accurate estimates of surface freshwater forcing has fuelled the use of unphysical model boundary conditions, the effect of which will be discussed below.

Freshwater forcing imposes a vertical velocity at the ocean's surface, resulting in a Sverdrup-like dynamical response that can be significant

(Huang and Schmitt, 1993). In addition, the ocean thermohaline circulation, as modelled in coarse-resolution climate models, is also sensitive to the strength of freshwater forcing, especially at high latitudes (Weaver *et al.*, 1993; Rahmstorf, 1996). The stability of the thermohaline circulation, in particular, is sensitive to both the freshwater forcing and the strength of ocean vertical mixing (Zhang *et al.*, 1999b).

Historically, as has been the case for ocean heat transport (see Bryden and Imawaki, Chapter 6.1), most estimates of oceanic freshwater transport derive indirectly from measurements of atmospheric vapour transport (for a recent example, see Trenberth and Guillemot, 1998) or from surface observations (ship and island) of rainfall rates and the variables required to estimate evaporation (e.g. da Silva *et al.*, 1994). Since the 1980s, estimates based on *in-situ* ocean data started to appear. These *direct* estimates of oceanic fresh-water transport provide both an independent check of the atmospherically based numbers as well as insight into the oceans' response to the surface forcing.

6.2.2 Indirect estimates of oceanic freshwater transport

In recent years, many new estimates of both atmospheric and surface fluxes of fresh water have appeared, based on the development of data-assimilating atmospheric general circulation models and the availability of new satellite data sets that measure variables used to deduce evaporation, the radiometric signature of precipitation or

the net moisture content of the atmospheric column (Xie and Arkin, 1997).

Estimates based on data-assimilating atmospheric modelling systems are difficult to assess for several reasons. First, the model output often doesn't obey total mass conservation (Trenberth and Guillemot, 1998). Second, the lack of atmospheric profile data over the oceans is a severe limitation for these estimates: the assimilation of scant island station data into these systems produces 'bull's eyes' in the flux fields indicative of biases between the models and observations over the oceans (Trenberth and Guillemot, 1998). As the vapour exchange with the oceans dominates the air-sea fluxes, these flux biases are problematic for global budgets.

Surface flux estimates of evaporation rely on empirical relations based on either radiometric parameters measured from satellites or marine meteorological measurements such as wind speed, relative humidity and sea surface temperature measured from ships and islands. Though constantly improving, these formulae are required to apply under a large range of conditions and can also suffer small biases which, when accumulated over large areas, can dominate basin totals. Ship-based measurements can also suffer biases.

Precipitation is particularly challenging to estimate over the ocean, due to its sporadic nature in both time and space. Here, satellite estimates may be the only means of progress, but these also rely on empirical algorithms that require 'tuning'. Lack of suitable open ocean time series for calibrating the satellite estimates is a limitation, as island stations likely suffer biases due to local small-scale orographic effects.

It is not the intention here to catalogue or assess the presently available flux estimates exhaustively, but rather to highlight the need for suitable independent estimates of large areal averages that can be used to assess the new data sets being produced, and in particular identify the small but crucial biases that impact dramatically on ocean circulation models.

To demonstrate the difficulties, a set of recent flux estimates has been assembled (Table 6.2.1). Each member of the ensemble is assumed to be as valid as the next. As a group, these estimates and their variance can therefore be used as a gross quantitative measure of the present state of knowledge about the mean annual exchange of water

between the ocean and the atmosphere. Based on the products in Table 6.2.1, ensembles of flux estimates have been formed: an eight-member ensemble of precipitation (P) estimates, a six-member ensemble of evaporation (E) estimates, and a 13-member ensemble of E-P (net freshwater flux) estimates. After mapping to a common geographic grid, the pointwise means and standard deviation of the ensembles were formed.

The ensemble mean E-P (Fig. 6.2.1a) shows the major source regions of atmospheric vapour: the subtropical oceans under the atmospheric high-pressure centres. The major atmospheric water sinks are the tropical convergence zones and the subpolar oceans. Interestingly, while the northern hemisphere western boundary currents undergo strong cooling (Bryden and Iimaki, Chapter 6.1), they are subject to only weak freshwater forcing. Over both the Kuroshio and Gulf Stream there occurs almost total cancellation between enhanced evaporation (Fig. 6.2.2a) and enhanced precipitation (Fig. 6.2.3a), both of which are likely associated with atmospheric storm tracks.

Variability within the ensemble of net flux estimates (Fig. 6.2.1b) reveals a global background uncertainty of about 250 mm yr^{-1} , which when integrated over the Pacific down to 30°S adds up to $1 \times 10^9 \text{ kg s}^{-1}$ of freshwater transport, which is as large as the natural flux itself (Wijffels *et al.*, 1992). The largest uncertainty occurs over the tropics and the mid-latitude storm tracks, as well as a region in the Southeast Pacific off Chile, which is an important water mass formation region (McCartney, 1977).

Variability among evaporation products is much less (Fig. 6.2.2b), suggesting the bulk of the uncertainty in the total water flux derives from estimates of precipitation, which is confirmed by Figure 6.2.3b. Not surprisingly, the difficulty of measuring precipitation over the open ocean dominates errors in the net water flux to the ocean.

6.2.3 Impacts of uncertainties on model development

The large uncertainties in estimates of freshwater fluxes over the oceans has retarded efforts to model the climate system. In the realm of atmospheric modelling, the lack of a reliable benchmark against which to compare models is a difficulty, with differences among models often smaller than

Table 6.2.1 Surface flux estimates used in this study. Surface latent heating rates were converted to an equivalent evaporative water flux (E) using the latent heat of vaporization at the appropriate seasonal sea surface temperature taken from Levitus and Boyer (1994a). Baumgartner and Reichel (1975) only provide zonal flux integrals and thus is not used in Figures 6.2.1–6.2.3. In three data sets runoff R is also available.

| Source | Type | Parameters | Temporal coverage |
|---|---|------------|-------------------|
| Surface observations (SOC) | Josey <i>et al.</i> (1996) | E, P | Climatology |
| Surface observations (COADS) | da Silva <i>et al.</i> (1994) | E, P | Climatology |
| Surface observations | Baumgartner and Reichel, (1975) [not gridded] | E–P, R | Climatology |
| Surface observations | Esbensen and Kushnir (1981) | E | Climatology |
| Surface observations | Oberhuber (1988) | E, P | Climatology |
| Blended satellite and surface observations | Legates and Wilmott (1990) | P | 1979–96 |
| Surface observations | Jaeger (1983) | P | Climatology |
| Blended satellite and surface observations and model output | Xie and Arkin (1997) | P | 1979–98 |
| Blended satellite and surface observations (Limb90/MSU) | Tod Mitchell, personal communication (1999) | P | 1979–92 |
| Satellite observations | Jourdan <i>et al.</i> (1997) | E–P | Climatology |
| Atmospheric re-analysis (ECMWF) | Keith (1995) | E–P, R | 1989 |
| Atmospheric re-analysis (ECMWF) | Barnier <i>et al.</i> (1995) | E | 1986–88 |
| Atmospheric re-analysis (NCEP) | Trenberth and Guillemot (1998) | E–P | 1979–95 |
| Atmospheric re-analysis (NCEP) | Kalnay <i>et al.</i> (1996) | E, P, R | Climatology |

those among observational estimates. For instance, Gaffen *et al.* (1997) concluded that the majority of atmospheric models participating in the Atmospheric Model Intercomparison Project (AMIP) overestimate the poleward transport of moisture compared with estimates based on direct observations. However, such direct observations are based on mostly non-existent observations over the oceans (which cover the majority of the planet's surface area) and have unknown accuracy (Oort and Piexoto, 1983).

Ocean modelling efforts, however, suffer an even greater disadvantage. Ocean models require surface freshwater forcing. When forced with 'observed' freshwater fluxes the models can drift off to unrealistic states (McWilliams, 1996), and it has been difficult to distinguish the cause: inaccurate model physics versus errors in the forcing field. To avoid this problem (and because freshwater forcing of surface buoyancy has been considered of secondary dynamical importance in comparison to thermal forcing), the practice of

relaxing to an observed salinity field at the surface (Haney condition for salinity) has become the convention. While a Haney condition for heat is plausible given both sensible and radiational cooling of warm temperature anomalies by the atmosphere, such a flux formulation for salinity has not been physically justified.

In the realm of coupled climate modelling, the component ocean and atmospheric models are often first 'spun-up' separately before coupling. In order to maintain a stable 'realistic' climate, flux adjustments are introduced into the coupled system, which are essentially the difference between the flux out of the atmosphere model spun-up over the observed sea surface temperature field, and the flux into the ocean model run under relaxation forcing (Gordon and O'Farrell, 1997). This common expedient propagates freshwater flux errors from the unrealistic ocean spin-up under surface relaxation into the coupled system. Typical freshwater flux adjustments have magnitudes as large as the natural fluxes themselves, and the resulting

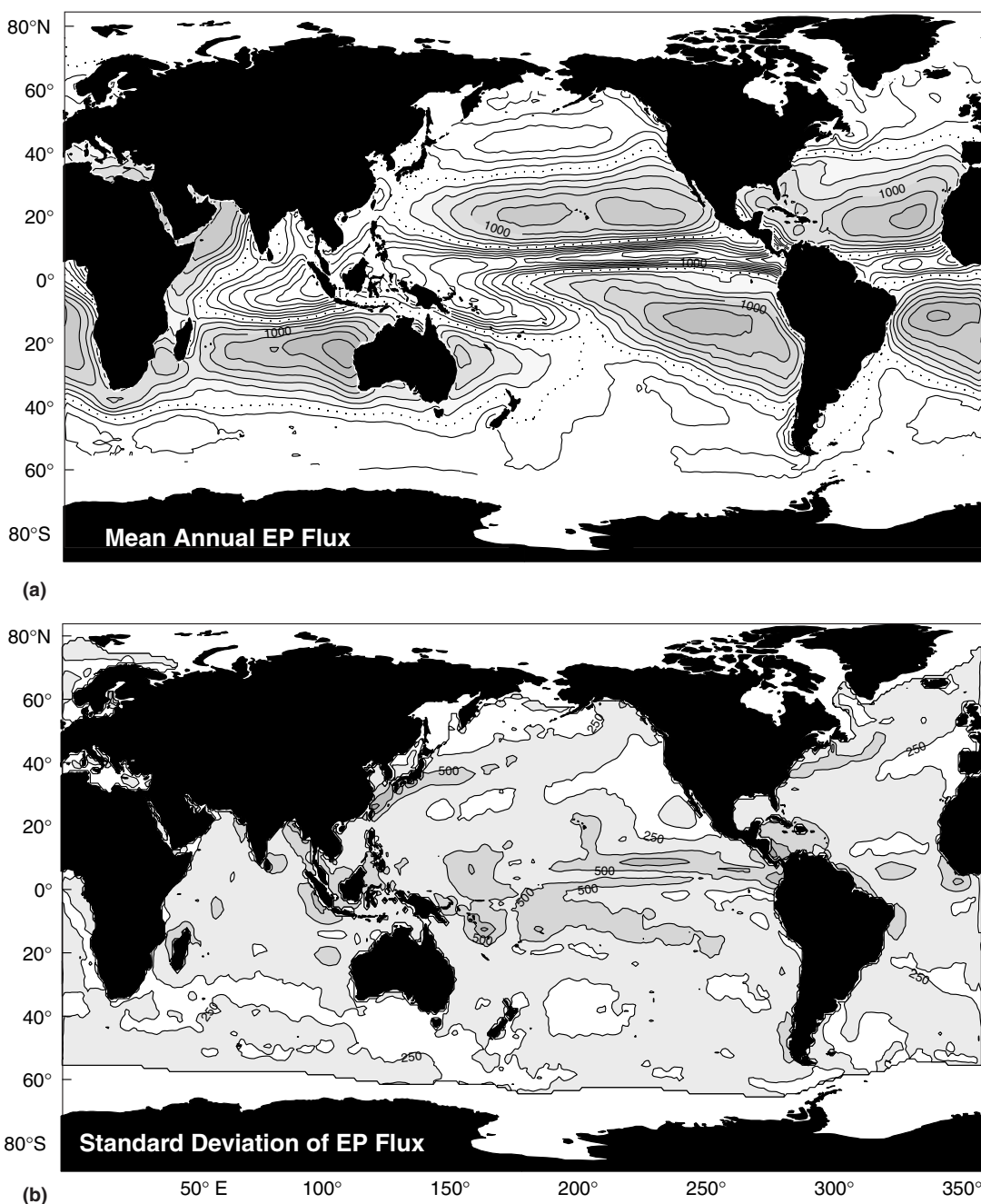


Fig. 6.2.1 Average (a) and standard deviation (b) of an ensemble of 13 estimates of E-P over the oceans based on the products in Table 6.2.1. The contour interval is 250 mm yr^{-1} , with the zero contour dotted.

total water flux to the ocean has spatial patterns that are highly unrealistic. McWilliams (1996) points out that with such unrealistic forcing, it is no surprise that the model's salinity field is also unrealistic. The result is that the use of salinity, the next best observationally known ocean quantity after temperature, has been greatly limited as a means of identifying and correcting physical errors in ocean models.

6.2.4 Direct ocean estimates of freshwater transport

Direct estimates of oceanic freshwater transport are an independent means of measuring the freshwater exchange between the ocean and atmosphere, and so have the potential to address some of the problems outlined above. In order to be of use, however, the strengths and limitations of these estimates need to be clearly examined.

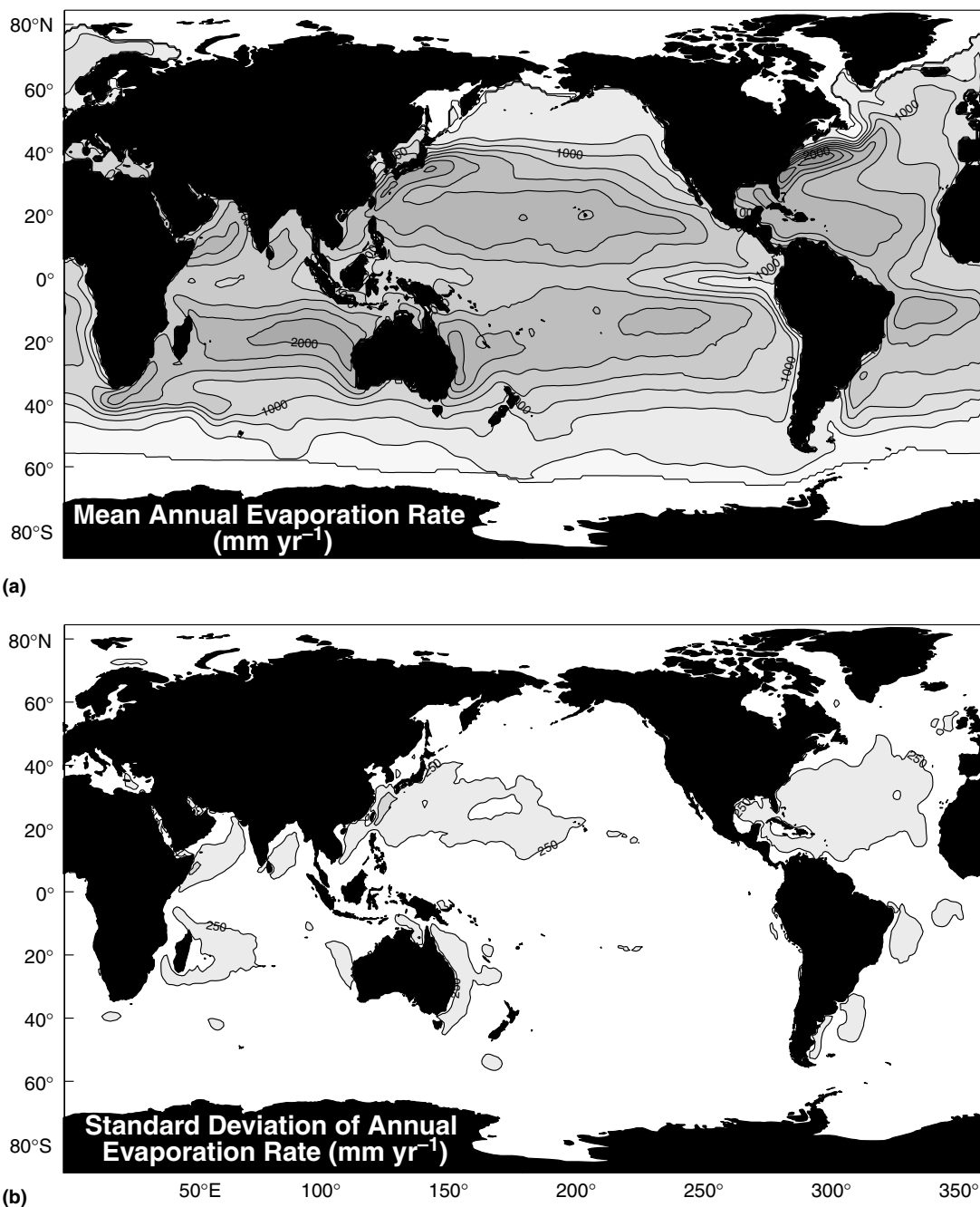


Fig. 6.2.2 Average (a) and standard deviation (b) of an ensemble of six estimates of evaporation over the oceans based on the products in Table 6.2.1. Units are mm yr^{-1} and the contour interval is 250 mm yr^{-1} .

Direct estimates of oceanic freshwater fluxes are determined in the same way as those of heat (Bryden and Imawaki, Chapter 6.1), using long hydrographic lines that enclose volumes of ocean, for which budget equations can be written. The technique relies on the assumptions that we can measure the steady-state portion of the velocity and the salinity field, and that geostrophic dynamics apply everywhere, except for an Ekman balance in

the mixed layer. Freshwater fluxes achieved by the temporal rectification of the salt and velocity fields at either the seasonal or eddy time scales are ignored in these estimates, although, as seen below, these fluxes have been found to be small over most of the ocean.

For a volume of ocean enclosed by a hydrographic line, salt conservation applies in the steady state as the flux of salt through the atmosphere is

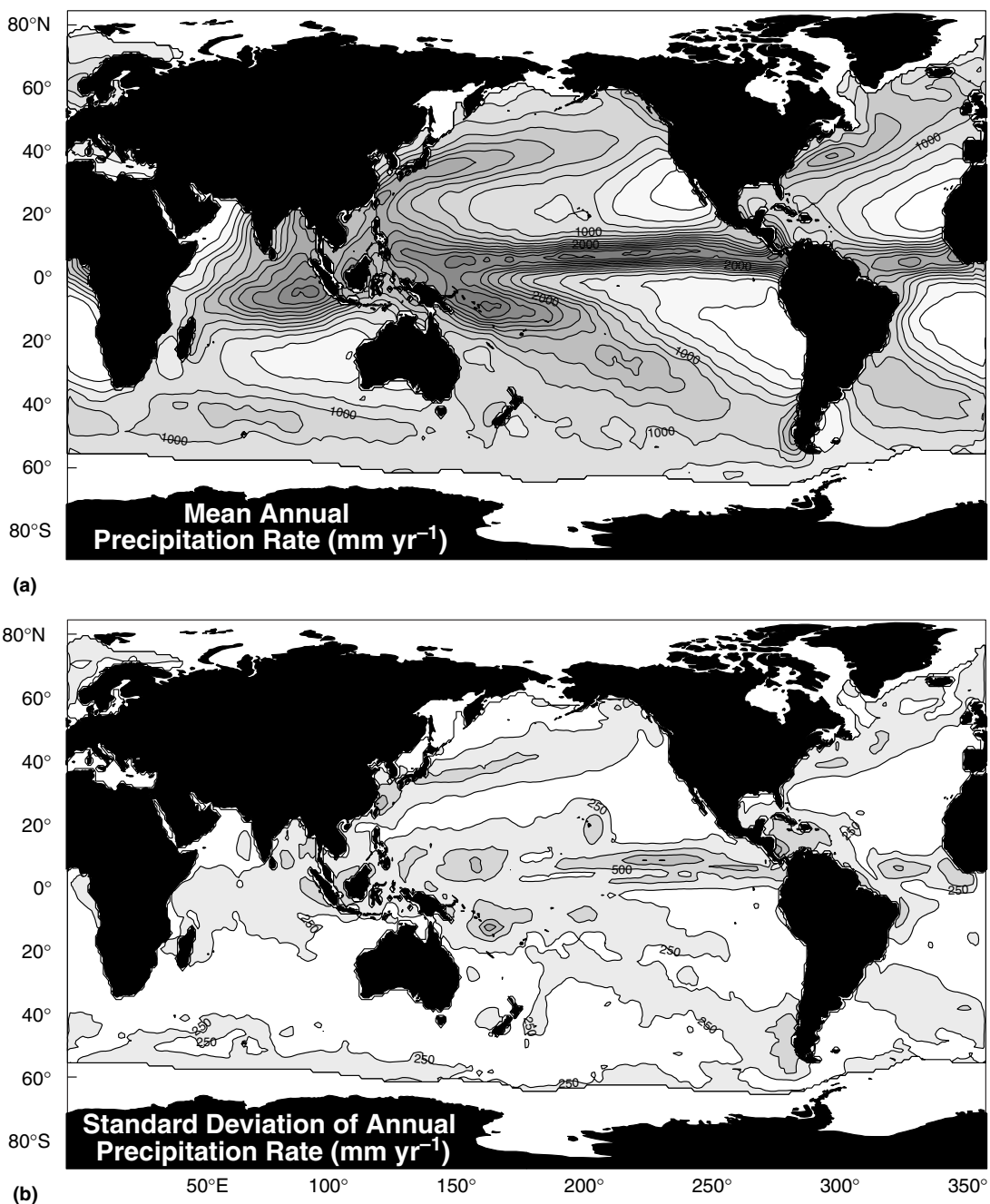


Fig. 6.2.3 Average (a) and standard deviation (b) of an ensemble of eight estimates of precipitation over the oceans based on the products in Table 6.2.1. Units are mm yr^{-1} and the contour interval is 250 mm yr^{-1} .

negligible:

$$\iint \rho S v \, dx \, dz = T_i^S \quad (6.2.1)$$

where (ρ is the *in-situ* density, S the salinity, v the cross-track velocity and x the along-track direction. T_i^S represents the total salt transport associated with the interbasin exchange (e.g. Bering Strait or the Indonesian Throughflow).

Mass conservation is written as:

$$\iint \rho v \, dx \, dz + [P - E + R] = T_i^M \quad (6.2.2)$$

where E , P and R are the net fluxes respectively into the surface of the ocean volume of evaporation, precipitation and runoff, and T_i^M is the interbasin mass transport. In the haline ocean, the pure

water part of the above total mass transport is just:

$$\iint \rho(1-S)v \, dx \, dz + [P-E+R] = T_i^M - T_i^S \quad (6.2.3)$$

Hence, the LHS of (6.2.3) is, strictly speaking, the oceanic freshwater transport. Generally, estimates of the mass flux across a section have uncertainties much larger than $P-E+R$, suggesting that (6.2.3) alone is not useful for calculating the surface forcing. We thus define a section areal average salinity and its deviation:

$$\bar{S} = \frac{\iint S \, dx \, dz}{\iint dx \, dz}; \quad S' = S - \bar{S} \quad (6.2.4)$$

For simplicity, we also assume that the interbasin flux of salt occurs at a known salinity, S_i , so that the salt flux is just $T_i^S = S_i^* T_i^M$. Combining (6.2.1), (6.2.2) and (6.2.4), the surface freshwater flux can now be written as a simple product of the salinity deviation and the velocity field:

$$[P-E+R] = - \frac{T_i^M S'_i - \iint \rho S' v \, dx \, dz}{\bar{S}} \quad (6.2.5)$$

Here the first term on the right can be termed the ‘leakage’ term and the second term is due to correlations of salinity and velocity across the section, which effect a freshwater transport.

The above equation only applies to perfect measurements of the long-term mean salinity and velocity field, and neglects fluxes of fresh water (salt) due to horizontal mixing and temporal correlations of salt and velocity. Ignoring the latter for the moment, the velocity and salinity measured by a hydrographic section (and the associated circulation analysis) has an error such that the true long-term mean is given by the sum of the measured velocity v_o and its error v_e :

$$v_{\text{true}} = v_o + v_e \quad (6.2.6)$$

The same is true for the salinity measurement. Note that for most studies using hydrographic sections, a circulation error of $\iint v_e \, dx \, dz \approx 2 \text{ Sv}$ is usually assumed, which is much larger than $P-E+R$. However, this circulation error has an associated highly correlated error in the salt balance equation ($\iint v_e \bar{S} \, dx \, dz$), which largely cancels

when the two are combined as in (6.2.5). Ignoring small changes in ρ (which in practice can be carried with either v or S), and replacing v and S' in (6.2.5) with the observed quantities, the error in the freshwater flux due to measurement errors can be written as:

$$\text{error}_{[P-E+R]}$$

$$= \frac{\iint \rho [S'_o v_e + S'_e v_o + S'_e v_e] \, dx \, dz}{\bar{S}} \quad (6.2.7)$$

$$\approx \frac{1 \text{ psu} * 5 \text{ Sv} + 0.1 \text{ psu} * 30 \text{ Sv} + 0.1 \text{ psu} * 5 \text{ Sv}}{35 \text{ psu}} \quad (6.2.8)$$

$$\approx |0.15 \text{ Sv}| + |0.09 \text{ Sv}| + |0.01 \text{ Sv}| \approx 0.17 \text{ Sv}$$

Each of the terms in equation (6.2.7) can be grossly estimated using scale arguments to get an upper bound on the freshwater errors (6.2.8). The first error term is the spatial correlation of the net error in the circulation field (conservatively $\sim 5 \text{ Sv}$) and the real salinity variation ($\sim 1 \text{ psu}$); the second term is due to correlations between errors in measuring salinity ($\sim 0.1 \text{ psu}$) and the true velocity field; and the last term is the correlation of errors in the velocity and salinity field.

While the synoptic salinity field is well resolved by modern hydrographic sections, it is the long-term mean field that is needed for equation (6.2.5). Temporal changes in salinity can be addressed in only a few regions where time series exist. Generally, comparison of historical and modern sections has revealed only small changes in the large-scale salinity field. Bindoff and Church (1992) estimate that the freshening of the Antarctic mode and intermediate waters they observe in the southern hemisphere subtropics between 1960s and 1990s only requires a change of about 40 mm yr^{-1} in freshwater flux at the latitudes where these waters are formed. Compared with the uncertainty of around 250 mm yr^{-1} in present-day mean flux estimates (Fig. 6.2.1) these changes are small. Dobroliubov (1997) found differences of 0.14 Sv or less between freshwater transports based on Atlantic sections made in the early 1980s and 1990s. Larger differences were found with sections made in the 1950s and 1960s, though these are suspected of deriving from poor data resolution and might not be real. In the tropics, interannual changes in flux distribution

and sea surface salinity are as large as the seasonal cycle and, due to the faster advection time scales in the tropical ocean, are more likely to penetrate below the mixed layer and alter the subsurface salinity field. Thus tropical sections might be more likely to suffer interannual biases than those at higher latitudes.

The possibility that temporal fluctuations in the velocity and salinity field rectify to produce a mean flux must also be examined, as this flux has been

ignored in equation (6.2.5). In most of the ocean the dominant velocity variability is at mesoscale eddy time and space scales (Stammer, 1997b) and in the seasonal cycle. Using estimates of lateral mixing rates based on eddy length scales, energy levels from satellite altimeter data and mean climatological salt gradients, Stammer (1998) estimates that the eddy freshwater fluxes are small ($< 0.05 \text{ Sv}$) except along western boundary currents extensions ($\sim 40^\circ$ of latitude).

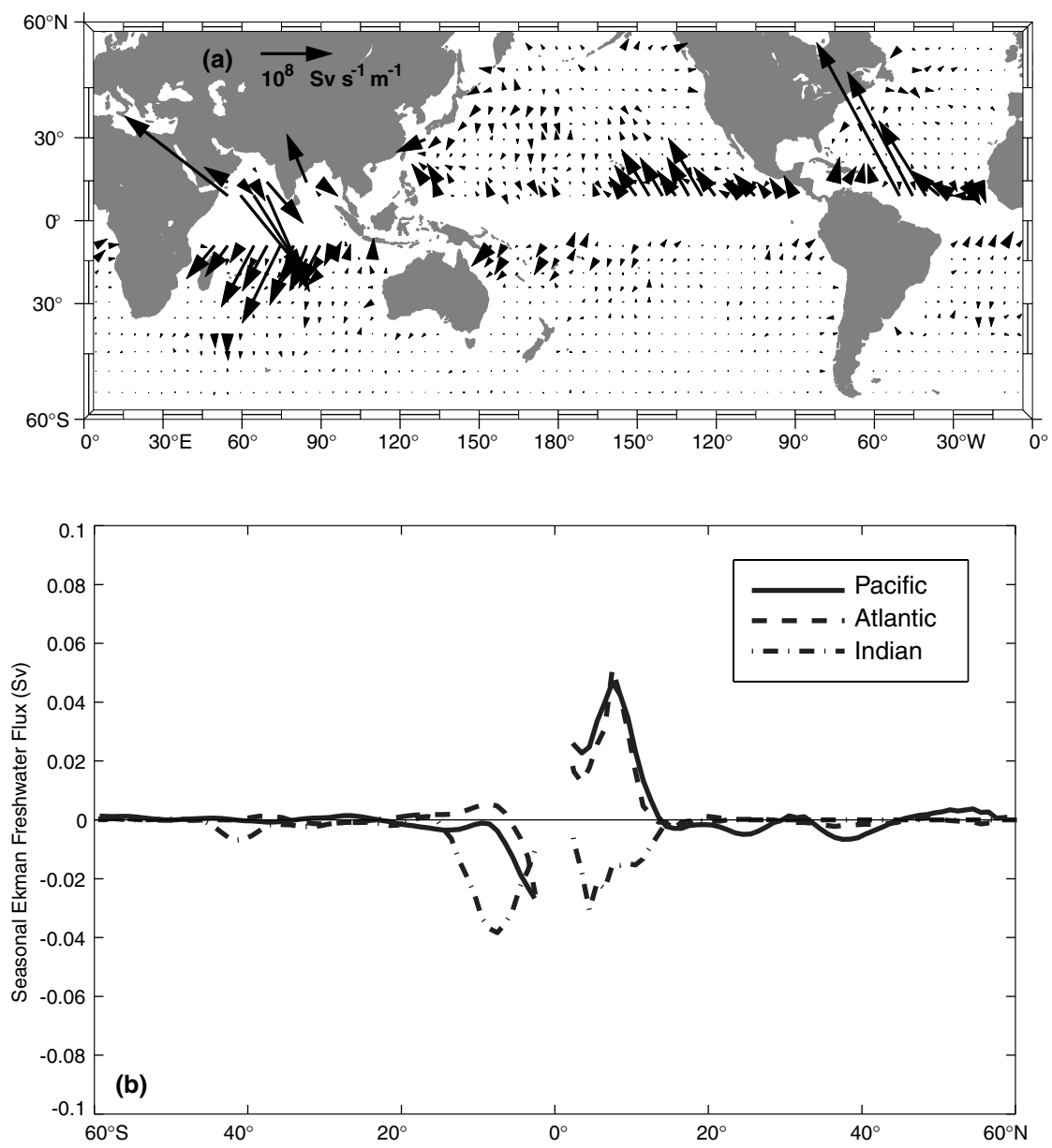


Fig. 6.2.4 Seasonal rectification flux of the Ekman mass flux and sea surface salinity: (a) shown as a vector flux; (b) integrated across the ocean basins (Sv).

A second source of temporal rectification between S and v is in the seasonal cycle in the Ekman layer. Seasonal changes in wind strength can coincide with changes in freshwater forcing and salinity. To examine how large these fluxes might be, the rectification flux was calculated for each ocean basin using the Hellerman and Rosenstein (1983) wind-stress climatology and the Levitus and Boyer (1994b) sea surface salinity (Fig. 6.2.4). Outside the tropics the freshwater flux is less than 0.02 Sv, which is negligible. These estimates, along with those from Stammer (1998), agree with those from high-resolution modelling studies, which find the temporal rectification terms (over all time scales) give fluxes of <0.1 Sv outside of the tropics (McCann *et al.*, 1994).

In total then, the expected uncertainty in the direct flux estimates might be as large as 0.17 Sv outside of the tropics (6.2.8), but may reach 0.3 Sv in the tropics. Independently, Dobroliubov (1997) finds similar uncertainties. To go beyond the simple scaling argument in equation (6.2.7) requires simultaneous time series of both velocity and salinity overbasin scales, measurements that are not yet available.

6.2.5 Comparison of direct and indirect flux estimates

In comparing direct ocean flux estimates with estimates of the surface flux, runoff from the continents must be taken into account (Fig. 6.2.5). Despite attempts to catalogue the runoff of major rivers (Hils, personal communication, 1999) there appear to be few global estimates of runoff. Here we utilize Baumgartner and Reichel's (1975) compilation, which, globally, roughly agrees with the runoff estimated from the net E-P over land based on Keith's (1995) analysis of ECMWF output and the NCEP (Kalnay *et al.*, 1996) long-term runoff (Fig. 6.2.5). Note that in Keith's (1995) estimates there are areas of negative flux (where the accumulation decreases) expressing the non-conserving nature of the re-analysis moisture field. Given the limited availability of global runoff data sets, assessing the errors in the runoff fluxes is difficult and will remain an added uncertainty in these comparisons. Here, the Baumgartner and Reichel (1975) runoff is added to the surface fluxes integrated over the ocean basins to predict the ocean transport of fresh water.

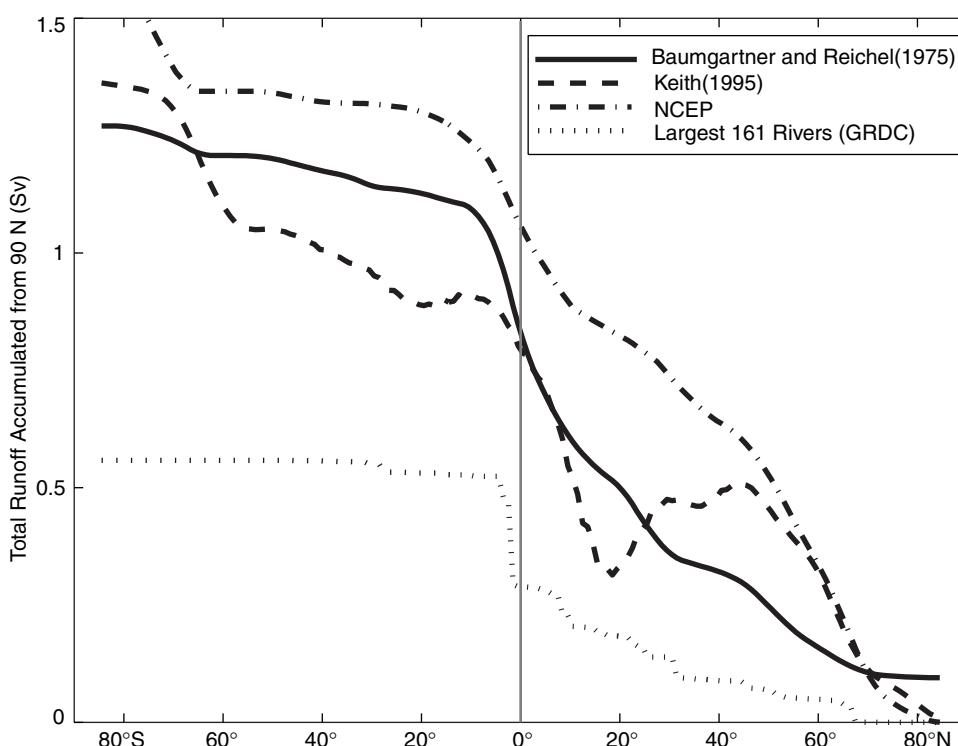


Fig. 6.2.5 Total runoff into the oceans cumulated from north to south (Sv) from four sources: Baumgartner and Reichel (1975), Keith (1995), Kalnay *et al.* (1996) and the largest 161 rivers as catalogued at the Global Runoff Data Center (Hils, personal communication, 1997).

All three ocean basins exchange large amounts of water through linking passages: the Southern Ocean, the Indonesian Archipelago and the Bering Strait. As these interbasin fluxes are much larger than the exchange through the atmosphere, we choose instead to present only the divergent part of the oceanic freshwater flux (in contrast to Wijffels *et al.*, 1992). This is equivalent to removing an unknown constant equal to the Pacific–Indian Throughflow for the Indian and South Pacific Oceans, and the Bering Strait flow in the North Pacific and Atlantic. Hence in the plots to follow, the direct transport estimates shown will be the divergence relative to the entrances of the Bering and Throughflow straits (South of Mindanao, Philippines).

While the size and salinity of the Bering Strait flow is relatively well known (Coachman and Aagaard, 1988), that of the Pacific–Indian Throughflow is not. Hence, investigators have had to make assumptions about both its size and salinity in order to generate an estimate of the basin divergence – that is to calculate the ‘leakage’ term in equation (6.2.4). Direct estimates for the long-term average Throughflow range between 5 and 10 Sv (Meyers, 1996; Molcard *et al.*, 1996; Gordon *et al.*, 1999a), though synoptically, higher variability (0–20 Sv) is observed (Fieux *et al.*, 1994; Bray *et al.*, 1997). For a 5–10 Sv transport range the resulting freshwater estimates between the Throughflow entrance channels and 30°S WOCE section in the Pacific is only about 0.2 Sv (Wijffels *et al.*, 2000), consonant with our estimates of the general uncertainty. Clearly, however, increased knowledge of the freshwater flux associated with the Throughflow is needed.

The majority of direct flux estimates derive from single-section or regional analyses of long hydrographic lines, many of which were accomplished during WOCE (Table 6.2.2). To date few truly global syntheses have been completed, with the exception of MacDonald (1995). The latter study, however, specified freshwater fluxes using Baumgartner and Reichel (1975) and so is not included here. The flux divergences produced from the Southern Ocean analysis of Sloyan and Rintoul (2000b) are included in basin integral plots (Figs 6.2.6–6.2.8, see Plates 6.2.6–6.2.8, p. 492) by assuming zero freshwater flux from the Antarctic continent.

Figures 6.2.6–6.2.8 (see Plates 6.2.6–6.2.8, p. 492) present the divergent part of the freshwater transport for each ocean basin found from

accumulating the surface and runoff fluxes southwards from basin reference points. In the Indian Ocean transports are relative to a zero flux condition at the Throughflow channels (Pacific side); for the Pacific, zero flux is applied at Bering Strait and the Throughflow channels (Pacific side); while the Atlantic curve is relative to a zero flux at Bering Strait, and thus includes the freshwater fluxes into the Arctic Oceans.

In the Indian Ocean, only two latitudes are currently constrained by direct flux estimates: 32 and 18°S (Fig. 6.2.6, see Plate 6.2.6, p. 492). Over the evaporative zone between latitudes 15 and 40°S, the indirect flux estimates are fairly consistent (similar slopes) and are also in reasonable agreement with the direct estimates. It is in the regions of high precipitation north of 10°S and south of 40°S that the curves diverge, confirming again the large scatter among available estimates of precipitation over the ocean. Note in particular the 0.5 Sv variability in the net freshwater divergence north of 18°S.

The Atlantic Ocean is best covered by direct flux estimates (Fig. 6.2.7, see Plate 6.2.7, p. 492), which are remarkably consistent, except for the estimates of Dobroliubov (1997) at 24°N. Nearly all of the major transport maxima are delineated by the direct estimates. Again, the indirect estimates diverge most strongly over regions of high precipitation. When integrated over the Atlantic between Bering Strait and 40°S, the indirect transport divergences range between 1.0 and –0.1 Sv, while the direct estimates indicate very little net fresh-water divergence over the basin.

Problems with biases in the indirect transport estimates are even more pronounced in the Pacific Ocean due to its huge size (Fig. 6.2.8, see Plate 6.2.8, p. 492). Not surprisingly the indirect estimates vary wildly over the South Pacific where little *in-situ* atmospheric data is available. Here again, despite the variations in assumptions made to close the ocean mass balance, Throughflow sizes and different data sets, the direct estimates are quite consistent, and show much less scatter than the indirect estimates. It is remarkable that despite 25 years between sections, the estimates of Wunsch *et al.* (1983) and Wijffels *et al.* (2000) are very similar.

Though a more consistent and larger set of direct ocean transports estimates can be anticipated from the WOCE synthesis, the ensemble available to date can already be used to reassess ideas about the interocean exchange of fresh water. Using

Table 6.2.2 Direct estimates of oceanic freshwater convergence north of a given latitude. Units are in $\text{kg}^9 \text{s}^{-1}$. Negative numbers indicates the ocean to the north receives a net excess of precipitation and runoff over evaporation. Atlantic convergences are shown relative to the Bering Strait and so include the Arctic Ocean. Pacific convergences are relative to Bering Strait and the Indonesian Throughflow passages south of the Philippines

| Latitude | Pacific | Indian | Atlantic | Total | Source |
|----------|---------|--------------------|----------|-------|--|
| 58°N | | | −0.13 | | Dobroliubov (1997) [1980s data] |
| | | | −0.20 | | Dobroliubov (1997) [1990s data] |
| 55°N | | | −0.17 | | Bacon (1997) |
| 47°N | −0.27 | | | | Roemmich and McCallister (1989) |
| 45°N | | | −0.26 | | Dobroliubov (1997) [1980s data] |
| | | | −0.25 | −0.52 | Dobroliubov (1997) [1990s data] |
| 35°N | −0.56 | | −0.49 | | Roemmich and McCallister (1989) |
| | | | −0.37 | −0.93 | Dobroliubov (1997) [1980s data] |
| 24°N | −0.29 | | | | Dobroliubov (1997) [1990s data] |
| | −0.21 | | −0.03 | −0.23 | Roemmich and McCallister (1989) |
| | | | −0.44 | | Bryden <i>et al.</i> (1991) |
| | | | −0.53 | | Hall and Bryden (1982) |
| 11°N | | | 0.12 | | Dobroliubov (1997) [1980s data] |
| 10°N | 0.03 | | | 0.15 | Dobroliubov (1997) [1990s data] |
| 11°S | | | −0.23 | | Friedrichs and Hall (1993) |
| | | | −0.15 | | Wijffels <i>et al.</i> (1996a) |
| 12°S | | | −0.33 | | Holfort and Siedler (1997) |
| 17°S | −0.30 | | | | Holfort and Siedler (1997) |
| 18°S | | −0.14* | | | Sloyan and Rintoul (2000b) |
| 19°S | | −0.03 ^T | | | Sloyan and Rintoul (2000)/Robbins and Toole (1997) |
| | | | −0.10 | −0.43 | Holfort and Siedler (1997) |
| 23°S | | | 0.12 | | Holfort and Siedler (1997) |
| 28°S | −0.06 | | | | Wunsch <i>et al.</i> (1983) |
| 27°S | | | 0.16 | | Holfort and Siedler (1997) |
| 30°S | | | 0.24 | | Holfort and Siedler (1997) |
| 32°S | 0.09 | | | | Tsimplis <i>et al.</i> (1998) |
| | 0.06 | | | | Wijffels <i>et al.</i> (2000) |
| | 0.33* | 0.20* | | | Sloyan and Rintoul (2000b) |
| | | 0.31 | | 0.61 | Robbins and Toole (1997) |
| 40°S | | | 0.01* | | Sloyan and Rintoul (2000b) |
| | | | 0.02 | | Saunders and King (1995b) |
| 43°S | −0.08 | | | | Wunsch <i>et al.</i> (1983) |

Note: *Indicates a convergence for the ocean volume south of the designated latitude and not the ocean volume to the north, as for the other estimates; ^Tan estimate derived from the sum of the 32°S flux number and the divergences between 32°S and 18°S. Numbers in the column marked 'total' are a sum of the italicized estimates in the various basins for that latitude band.

the Baumgartner and Reichel (1975) climatology, Wijffels *et al.* (1992) deduced that the Pacific received an excess of roughly 0.5 Sv of fresh water, which was then redistributed by the interocean circulation to the evaporative basins of the Atlantic and Indian Oceans via exchange through the Indonesian Throughflow, Bering Strait and

Southern Ocean. However, the new direct ocean estimates indicate a different scenario.

Figure 6.2.8 (see Plate 6.2.8, p. 492) shows that between Bering Strait and 30°S the freshwater divergence over the Pacific is small, indicating a net balance of evaporation and precipitation over that basin. Direct estimates for the Atlantic/Arctic also

suggest a net divergence of fresh water much smaller than previously thought: Holfort and Siedler's (1997) estimates of a 0.24 Sv convergence between Bering Strait and 30°S is roughly half that predicted by Baumgartner and Reichel (1975), while the estimates at 40°S indicate almost no net divergence over the Atlantic/Arctic. The Indian Ocean direct estimates, however, are consonant with a large net evaporation, as predicted previously (Fig. 6.2.6, see Plate 6.2.6, p. 492).

Hence, if the Pacific Ocean is not the source of the excess oceanic fresh water required to supply the Indian deficit, only one possibility remains: excess precipitation and ice melt over the Southern Ocean. Indeed Sloyan and Rintoul estimate that 0.54 Sv of excess fresh water is removed by the Southern Ocean circulation south of 30–40°S, highlighting the importance of the Southern Ocean in the global oceanic freshwater balance. Based on the independent estimates in Table 6.2.2, the excess evaporation occurring north of Sloyan and Rintoul's lines add up to 0.39 Sv. The freshwater global balance is thus $0.54 - 0.39 = 0.15 \pm 0.29$ Sv: indistinguishable from zero.

6.2.6 Mechanisms of oceanic freshwater transport

Stommel and Csanady (1980) pointed out that ocean heat and freshwater transport is related to the rates of conversion of water from one part of temperature–salinity (T/S) space to another. They went further and attempted to model this process assuming salinity was a simple function of temperature. Recent analyses of freshwater fluxes across ocean sections and in general circulation models (Rahmstorf, 1996) reveal that this assumption is incorrect, though the underlying idea remains a powerful one, as it links forcing fluxes to water mass volume and exchange in T/S space. Speer and Tziperman (1992) recast this approach in terms of density classes and express the competition between density class conversion by surface fluxes and that by interior diapycnal mixing, an idea employed in Sloyan and Rintoul's (2000b) analysis. The challenge in analysing ocean sections will be in distinguishing the water mass conversion occurring at the surface and that due to internal mixing. Use of freshwater fluxes will be a key element in this work.

Definition of a tracer transport mechanism across an ocean section is somewhat *ad hoc*. Hall

and Bryden (1982) chose to form zonal averages (and deviations) of velocity and properties on pressure surfaces and termed the resulting products the 'overturning' component of tracer transport, while the residual, associated with the correlation of velocity and tracer at a pressure level, was termed the 'horizontal' or gyre component. A similar decomposition can be carried out within density layers (e.g. Wijffels *et al.*, 1996a; Robbins and Toole, 1997), and as density is largely determined by temperature, more closely relates back to Stommel and Csanady's (1980) suggestion. Freshwater divergence is also achieved by the interbasin flows, the 'leakage' term in equation (6.2.4). Unfortunately, few detailed decompositions of the oceanic freshwater flux across hydrographic lines are available, but those that are reveal interesting mechanisms.

Wijffels *et al.* (1996a) find that at 10°N in the Pacific, the small net freshwater divergence over the Pacific relative to Bering Strait is achieved by a balance between three major flux mechanisms: net export of very fresh water through Bering Strait; northward freshwater transport by the shallow meridional circulation where the northward Ekman flux is fresh and the compensating southward thermocline flow more saline; and a southward freshwater flux by the subthermocline horizontal circulation where salty South Pacific waters flow north in the eastern Pacific and fresh North Pacific Intermediate water flows south in the western Pacific. The deep and bottom water circulations in the low-latitude Pacific achieve little net freshwater transport.

In the Indian Ocean, Robbins and Toole (1997) diagnose a large net evaporation north of the section at 32°S of 0.31 ± 0.09 Sv. They find three mechanisms acting to import fresh water to supply this net evaporation: a leakage term associated with the inflow of fresh Indonesian Archipelago waters that are distilled and leave across 32°S as salty thermocline waters; upwelling of deep and intermediate waters and their export as salty thermocline waters; and horizontal inflow of fresh Antarctic Intermediate Water in the east that leaves saltier in the west. Wijffels *et al.* (2000) have similarly found the import of fresh water by the recirculation and modification of Antarctic intermediate waters to be an important transport mechanism at 32°S in the Pacific. It is likely that the production and northward export of fresh

mode and intermediate waters from the Southern Ocean to the southern subtropical gyres may be the single most important mechanism for balancing the large net flux (0.61 Sv; see Table 6.2.2) received by the oceans south of 30°S from the atmosphere and through ice flows.

The ability of ocean general circulation models to reproduce the estimated freshwater fluxes and their mechanisms will be a stringent test of model realism. In ocean-only models, surface flux forcing will determine the net equilibrium transports (unless the problematic relaxation boundary conditions are used), but internal model physics will determine how this flux is achieved.

6.2.7 Global budgets

Direct oceanic freshwater transport estimates are presently available in all basins at six latitudes (Table 6.2.2), allowing the global meridional freshwater transport to be examined. Since few of the major rivers flow meridionally, the zonally integrated meridional ocean transport of fresh water

is largely equal and opposite to transport in the atmosphere (Wijffels *et al.*, 1992). These estimates can be compared with direct estimates of atmospheric moisture transport or those produced by atmospheric general circulation models (Fig. 6.2.9). Gaffen *et al.* (1997) examined the moisture budget in atmospheric models in the AMIP and concluded that most models overestimate the poleward flux of moisture, based on a comparison with Oort and Piexoto's (1983) observations. The available direct ocean measurements are still too sparse for any conclusions to be drawn on this issue, though generally the direct estimates agree more with the AMIP ensemble and less with Oort and Piexoto's estimates, except at higher latitudes (30°S and 50°N) where the opposite is true. It is worth noting that Oort and Piexoto's estimates are reliant on scarce *in-situ* atmospheric data over the large tropical and southern hemisphere oceans, and so are likely less reliable there. To constrain the total meridional moisture transport in the atmosphere more usefully, a larger number of direct ocean transport estimates are required as well as a better

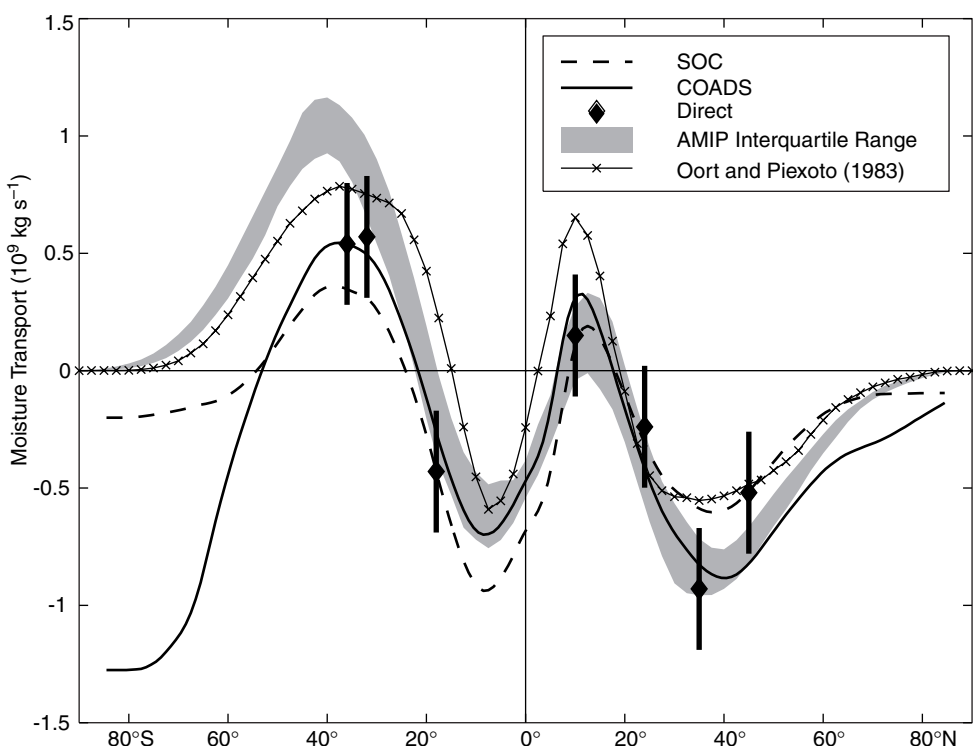


Fig. 6.2.9 Total ocean meridional freshwater transport (10^9 kg s^{-1}): estimates based on ocean data are shown using the sources in Table 6.2.2; indirect estimates are based on indicated sources plus the Baumgartner and Riechel (1975) continental runoff. Shaded is the interquartile range for the atmospheric models participating in AMIP as reported by Gaffen *et al.* (1997). Oort and Piexoto's (1983) direct atmospheric estimate is marked as x-x.

estimate of their errors – those shown in Fig. 6.2.9 are based on the scale arguments discussed earlier and so are rather conservative.

6.2.8 Summary

Direct estimates of oceanic freshwater transport can be determined to useful accuracy from the analysis of ocean sections. Most significant is that, in contrast to values based on integrating surface fluxes, the error in the direct ocean estimates are largely independent of the size of the area of ocean enclosed. While they can only shed light on the long-term mean flux at locations where sections have been made, they provide estimates of large areal integrals that are not reliably gained from any other source. It is the combination of these estimates with those that do resolve both the true spatial and temporal variability (e.g. satellite data sets) that holds much potential.

Until surface flux products or atmospheric models improve, the direct estimates are likely to remain the most accurate of large areal averages of the water flux between the ocean and the atmosphere. When synthesized globally, direct oceanic freshwater transports can be used to assess the performance of atmospheric and coupled models. Estimates available to date show more agreement with atmospheric model output than with direct estimates of atmospheric moisture fluxes.

Presently, direct oceanic freshwater fluxes are not as well reported or analysed as are the companion heat fluxes. While most estimates are fairly consonant with each other and error estimates made here based on simple scaling arguments, others are quite anomalous (such as Dobroliubov, 1997). Tracking down the source of these differences requires a detailed breakdown of the mechanisms making up these fluxes.

In respect of freshwater flux estimates, the full potential of the WOCE data set is yet to be realized. We can anticipate global, better-documented and more accurate freshwater transport estimates to be produced. In addition there may be great potential in the idea of ‘tuning’ surface flux products using direct ocean estimates to remove flux biases (e.g. Isemer *et al.*, 1989; da Silva *et al.*, 1994). This may lead to flux products that are accurate enough to force ocean climate models directly with confidence

and thus remove the need to use the unphysical surface relaxation boundary condition. This in turn will open the door for the much more meaningful use of salinity as a model diagnostic.

The limited number of direct oceanic freshwater transport estimates presently available points to the need to reassess our view of basin-wide balances and interbasin exchanges. Already, the idea that the Atlantic Ocean is highly evaporative and must import large amounts of oceanic fresh water must be revised: the new estimates suggest near-zero gain down to 40°S (Saunders and King, 1995b). We can also deduce a larger freshwater exchange than previously estimated between the Southern Ocean and the basins to the north via the injection of Antarctic Intermediate Waters into the southern hemisphere subtropical gyres. It is noteworthy that this horizontal $v' S'$ flux effected by the subtropical gyres is not accounted for in simple box models of the global thermohaline circulation (e.g. Broecker *et al.*, 1990). Such models must fold this upper ocean transport into the deep water component of the global thermohaline circulation, confusing the role of freshwater transport as a control on the circulation (Rahmstorf, 1996). More careful and detailed studies of how the ocean transports fresh water are required to pick apart the relative role of the shallow wind-driven gyres relative to that of the deep circulation in balancing the surface forcing. The data collected during WOCE will make such analyses possible.

Acknowledgements

Thanks is given to the following: Dr Hils from the Global Runoff Data Center for providing the Center’s runoff data; Sergie Dobroliubov for providing his results; Steve Covey for access to the AMIP numbers; Todd Mitchell for advice and access to some of the new climatologies; Siobhan O’Farrel and Tony Hirst for use of the CSIRO coupled model output; Stefan Rahmstorf for bringing some of the new modelling work to my attention; Jim Mansbridge for help with data processing; and the International WOCE Office for sponsoring my attendance at the WOCE Conference in Halifax. This article was supported by the Australian Climate Change Research Project funded by Environment Australia.

6.3

Storage and Transport of Excess CO₂ in the Oceans: The JGOFS/WOCE Global CO₂ Survey

Douglas W. R. Wallace

6.3.1 Introduction

During the WOCE Hydrographic Programme One-Time Survey, and as a major component of International JGOFS (Joint Global Ocean Flux Study), a Global Survey of CO₂ in the Oceans was conducted in order to measure the global distribution of inorganic carbon in the oceans (Sabine *et al.*, 1997). The rationale for this large effort was to improve characterization of the ocean's past, present and future role in removing Excess (or Anthropogenic) CO₂ from the atmosphere. Prior to the Global Survey, this could only be assessed on the global scale using models, whereas an overall aim of the CO₂ Survey was to enable this to be addressed from observations. The data would also be used to assess and advance the state-of-the-art in ocean carbon cycle modelling.

6.3.2 Background

6.3.2.1 Excess CO₂: budgets, uncertainties, definitions

Budget and uncertainties

During the 1980s, the ocean's inventory of carbon increased at a rate of $\sim 2 \text{ PgCyr}^{-1}$ (1 PgC is 10^{15} g of carbon; Siegenthaler and Sarmiento, 1993; Schimel *et al.*, 1996), thereby absorbing 36% of the 5.5 PgC of fossil-fuel derived carbon released annually to the atmosphere. In comparison, the

atmospheric inventory increased at a rate of 3.3 PgCyr^{-1} . This implies that net uptake or release of carbon by the only other accessible carbon reservoir, the terrestrial biosphere, must have been close to zero globally. Given that there are known to be net CO₂ releases associated with deforestation, there must therefore be additional, poorly characterized, carbon sinks on land.

Of the major terms in the carbon budget, the atmospheric increase is accurately determined from measurements (uncertainty of 0.2 PgCyr^{-1}). This is a consequence of the limited variability of the atmospheric CO₂ concentration and the existence of a high-quality, global measurement network (Conway *et al.*, 1994). The fossil-fuel term is the next most accurately known term with an uncertainty of the order of 0.5 PgCyr^{-1} . The oceanic uptake term is potentially the next most tractable in terms of measurements, however present-day estimates are primarily based on models. Current estimates of the uncertainty of the ocean uptake term, based largely on the level of agreement between models, are 0.8 PgCyr^{-1} (Schimel *et al.*, 1996). Increasing insight concerning global-scale uptake is now being provided by time-series measurements of O₂/N₂ in the atmosphere, but at present this approach has similar levels of uncertainty (Keeling *et al.*, 1993, 1996; Bender *et al.*, 1996; Langenfelds *et al.*, 1999; Battle *et al.*, 2000). Whereas the increase of carbon inventories in the ocean is not as

geographically uniform as that in the atmosphere, it is a great deal less heterogeneous than the distribution of carbon, and carbon inventory changes, in the terrestrial biosphere. Furthermore, most of the carbon in the oceans is present as inorganic carbon, comprising three main chemical species (dissolved CO_2 , HCO_3^- and CO_3^{2-}). This can be contrasted with the single predominant carbon species found in the atmosphere (CO_2) and the vast multitude of carbon species, both inorganic and particularly organic, which are significant for carbon storage on land. Consequently estimates of carbon storage on land are extremely difficult or impossible to constrain by direct measurement on a global scale.

Excess CO_2

The budget summarized above is a budget for 'Excess CO_2 '. This refers to carbon inventory changes within an environmental reservoir relative to the inventory that existed during the 'preindustrial' era. Analysis of high-resolution ice cores (Indermuhle *et al.*, 1999; Smith *et al.*, 1999a) reveals that atmospheric levels of CO_2 have varied by no more than about 20 μatm ($1\ \mu\text{atm} = 0.101325\text{Pa}$) through most of the Holocene. Around the year 1750 atmospheric levels started to rise from a late-Holocene level of about 280 μatm : initially due to Excess CO_2 releases associated with land-use changes and later due to fossil-fuel combustion. It is generally assumed that prior to 1750 the global carbon cycle was in a steady state that has now been significantly perturbed as a direct result of human activity. Hence the preindustrial era against which Excess CO_2 levels are assessed ended around 1750.

We refer to the rate of carbon inventory (or concentration) change within an environmental reservoir since 1750 as 'storage of Excess CO_2 '. In order to be significant for storage, an environmental reservoir must have a large capacity to absorb or release carbon and must be able to exchange carbon on time scales relevant to the time scale of the anthropogenic perturbation (i.e. years to centuries). For example, the enormous oceanic carbon reservoir exchanges with the atmosphere over time scales ranging from 1 year up to the ventilation time of the deep ocean (several hundred years). Hence the oceans are a potentially very significant reservoir for storing Excess CO_2 , as are the atmosphere and the terrestrial biosphere (including carbon contained in soils).

In estimating oceanic levels of Excess CO_2 , it is almost invariably assumed that the major factor driving changes in the ocean's carbon inventory since 1750 has been air-sea exchange and the increased partial pressure of CO_2 in the atmosphere ($p\text{CO}_2$). Possible interannual variability in CO_2 uptake driven by other, presumably natural, causes is currently debated (amplitude $< 2\text{ PgC yr}^{-1}$: Francey *et al.*, 1995; Keeling *et al.*, 1995; Lee *et al.*, 1998; Battle *et al.*, 2000). However, it is generally assumed that on decadal and longer time scales there is much less natural variability.

Uptake versus storage

An important distinction should be made between the rate of uptake and the rate of storage of Excess CO_2 . Uptake refers to the flux or net transfer of carbon from one major environmental reservoir to another. Storage refers to changes of inventory within the reservoir. On the global scale these quantities must be equivalent, of course, but this is not necessarily the case on local or regional scales. For most of the land surface, the rate of uptake and rate of storage of Excess CO_2 will be near identical at (almost) all spatial geographical scales. This is because lateral carbon transport within the terrestrial biosphere is severely restricted (trees don't move much).

This is certainly not the case for carbon in the atmosphere and the ocean. For the atmospheric reservoir, the uptake of Excess CO_2 (emissions) is spatially non-uniform, being concentrated in industrial regions, yet the inventory change (storage) is almost globally uniform as a result of rapid atmospheric transport and mixing. For the ocean, uptake of Excess CO_2 refers to a change in the air to sea (and, possibly, riverine) flux of carbon relative to the preindustrial flux. Once again, on the global scale these must balance carbon inventory changes (i.e. storage), but on the local and regional scale uptake of Excess CO_2 across the air-sea interface may be significantly decoupled, geographically, from storage due to transport effects (Sarmiento *et al.*, 1992; Caldeira and Duffy, 2000).

Net versus Excess fluxes

The discussion of uptake raises a related issue that frequently confuses. Both the uptake (flux) and storage of Excess CO_2 refer to changes evaluated with respect to preindustrial conditions. In the case of the terrestrial biosphere this distinction

may not, once again, be too critical because the lack of lateral transport implies that preindustrial net fluxes should have been close to zero on some long-term average everywhere. (However, Sarmiento and Sundquist (1992) point out that fluxes associated with weathering, and carbon transported via rivers and groundwater, should be considered.) Hence it should now be possible to equate long-term measurements of the net CO₂ flux into or out of the terrestrial biosphere with the flux of Excess CO₂.

This is certainly not the case in the ocean where spatial variation in surface heating, biological productivity and respiration are convoluted by lateral and vertical circulation to produce natural spatial variability of annually averaged net air-sea CO₂ fluxes. The net CO₂ fluxes associated with these natural processes occurred throughout the preindustrial era, and should not be confused with the uptake of Excess CO₂, which refers only to the change of the air-sea flux since 1750. Although we can estimate the net air-sea flux of CO₂ from measurements of the air-sea $p\text{CO}_2$ difference (e.g. Takahashi *et al.*, 1997) there is no easy way to separate the natural component of this flux from its anthropogenic or Excess component. The net flux across the air-sea interface is therefore a (spatially and temporally variable) mixture of both natural and Excess (or anthropogenic) components.

6.3.2.2 What controls Excess CO₂ uptake?

The elevation of atmospheric $p\text{CO}_2$ over preindustrial levels means that natural areas of CO₂ outgassing from the ocean now release less CO₂ to the atmosphere than during preindustrial times. On the other hand, natural areas of CO₂ uptake have become correspondingly larger sinks for CO₂, as have regions that were naturally regions of zero net transfer. An interesting combination of the complex chemistry of CO₂ in seawater and ocean circulation does allow for the counterintuitive case where, locally, the air-to-sea transfer of CO₂ can theoretically be lower than that of the preindustrial ocean (see Section 6.3.5.3).

Given about 1 year, surface ocean waters will re-equilibrate with the ‘new’ atmospheric $p\text{CO}_2$ and the further uptake of Excess CO₂ will become negligible. This implies that the major regions for Excess CO₂ uptake from the atmosphere are regions where ‘old’, poorly ventilated ocean waters regain close contact with the atmosphere (and where, in

addition, gas exchange is efficient in transferring CO₂ across the air-sea interface). These regions may, or may not, be coincident with regions of deep water formation: the Excess CO₂ uptake from the atmosphere will take place close to where these poorly ventilated waters are returned to the sea surface, and not necessarily where the newly ventilated surface waters are transported back into the deep ocean again. On the other hand, the storage of Excess CO₂ within the ocean water column will be largest in regions where recently ventilated waters accumulate or converge.

6.3.2.3 Why does Excess CO₂ uptake matter?

CO₂ that is stored in the ocean does not affect the earth’s radiation balance, so oceanic uptake of Excess CO₂ mitigates the potential for global warming. In order to predict the magnitude of future climate change resulting from greenhouse gas emissions, a requirement is the prediction of future atmospheric CO₂ levels for given emissions scenarios. There is also an immediate sociopolitical requirement for better understanding of the global carbon cycle as a consequence of the endorsement of the Kyoto Protocol in 1997. Attempts to limit the future growth of atmospheric CO₂ concentration, however modest, will involve major, and potentially costly, changes in energy and technology policy. The inclusion of certain terrestrial carbon sinks in carbon emission budgeting increases the need to better define global carbon sinks and sources. Furthermore, future assessment of the effectiveness of measures taken to reduce emissions will ultimately be judged by their long-term effect on atmospheric CO₂ levels, which in turn requires an understanding of long-term storage changes in the other key carbon reservoirs (oceans and the terrestrial biosphere).

There are therefore at least three key scientific questions of relevance to global carbon cycle science arising from current policy-related issues:

- 1 How large are present-day oceanic and terrestrial carbon sources and sinks, where do they operate, and what processes are responsible?
- 2 How will terrestrial and, particularly, oceanic carbon sources and sinks behave in the future under higher CO₂ and a possibly altered climate and ocean circulation?
- 3 How will we monitor and assess the effectiveness of emissions controls and sequestration activities

on global atmospheric CO₂ levels (including checking our forecasts of sink behaviour)?

The answers to most of these questions, including those dealing specifically with the behaviour of the terrestrial biosphere, will rely to a great extent on a combination of carbon cycle models that are coupled and checked against global data sets covering the behaviour of the oceanic and atmospheric carbon reservoirs. The complexity and variability of carbon storage and uptake on land means that the long-standing approach of separately determining storage and fluxes in the ocean and atmosphere and evaluating regional and global behaviour of the terrestrial biosphere by difference will likely be required well into the future. In this regard, it is notable that the JGOFS/WOCE Global CO₂ Survey was the first global-scale, coordinated attempt to constrain Excess CO₂ storage in the oceans, by measurement.

6.3.2.4 Modelling of Excess CO₂ uptake

Global inventory

As mentioned above most estimates of Excess CO₂ storage in the oceans are based on models of ocean uptake (e.g. Sarmiento *et al.*, 1992; Siegenthaler and Joos, 1992; Stocker *et al.*, 1994; Caldeira and Duffy, 2000). These studies have converged on similar global storage estimates (about 2 PgCyr⁻¹) although independent lines of evidence sometimes implied significantly different values (e.g. Tans *et al.*, 1990 estimated 0.5 PgCyr⁻¹). While the models have generally been calibrated or validated through comparison with transient tracer uptake (e.g. bomb ¹⁴C and more recently the CFCs), there must always be room for doubt concerning systematic error in indirect estimates based on models. The tracers used for calibration are clearly imperfect analogues for Excess CO₂ penetration, particularly in their limited ability to assess the ventilation of water masses of intermediate 'age' (Wallace, 1995; Broecker, 2001). The possibility that a degree of unconscious tuning or selection of models in favour of the expected ocean carbon uptake magnitude may have occurred cannot be completely ruled out. It is therefore encouraging that an independent approach to estimating oceanic Excess CO₂ uptake, using measured time series of O₂/N₂ in the atmosphere (Keeling *et al.*, 1993, 1996; Bender *et al.*, 1996; Langenfelds *et al.*, 1999; Battle *et al.*, 2000), supports the consensus model based estimate of about 2 PgC yr⁻¹.

Regional storage and uptake

On the issue of where Excess CO₂ is taken up and stored in the oceans (as opposed to simply how much) there is much less consensus among models. The powerful atmospheric O₂/N₂ time series approach can less readily address this question due to the homogenizing tendency of atmospheric mixing and transport and the large seasonal exchanges of oxygen between the atmosphere and ocean. Very significant differences in modelled regional storage and uptake between ocean models exist. A perhaps extreme example is to compare carbon storage calculated with the two-dimensional zonally averaged model of Stocker *et al.* (1994) with distributions predicted by the three-dimensional Ocean Biogeochemistry General Circulation Model (GCM) of Sarmiento *et al.* (1995). Figure 6.3.1 illustrates the difference in Excess CO₂ storage as a function of latitude in the North Atlantic Ocean for these two models. The overall inventory for the North Atlantic north of 24°N is nearly identical for both models, but the latitudinal distributions of the inventory differ very greatly. Figure 6.3.1 also shows, for comparison, the distribution of Excess CO₂ inventories in the Atlantic Ocean calculated from (pre-WOCE) ocean CO₂ data using a so-called 'preformed-CO₂' method of calculating Excess CO₂ concentrations and inventories (Gruber *et al.*, 1996; see Section 6.3.4.1). The direct estimates are clearly much more consistent with the distributions predicted by the three-dimensional GCM than those predicted by the two-dimensional, zonally averaged model. This comparison shows clearly that models can indeed converge on consistent large-scale estimates for carbon storage while differing drastically on the details of how and where Excess CO₂ is stored. It also shows that observation-based estimates might prove very useful in identifying deficiencies of models.

A similar point can be made by comparing the model-based predictions of Excess CO₂ storage in the Southern Ocean shown by Sabine *et al.* (1999) and Caldeira and Duffy (2000): the details of modelling deep ventilation in this region lead to extremely large differences in predicted storage between different models. This was noted earlier by England (1995), who showed the high sensitivity of Southern Ocean CFC storage to the parameterization of mixing in models. A major, ongoing programme of ocean carbon model intercomparisons is currently exploring these differences (Orr *et al.*, 2001).

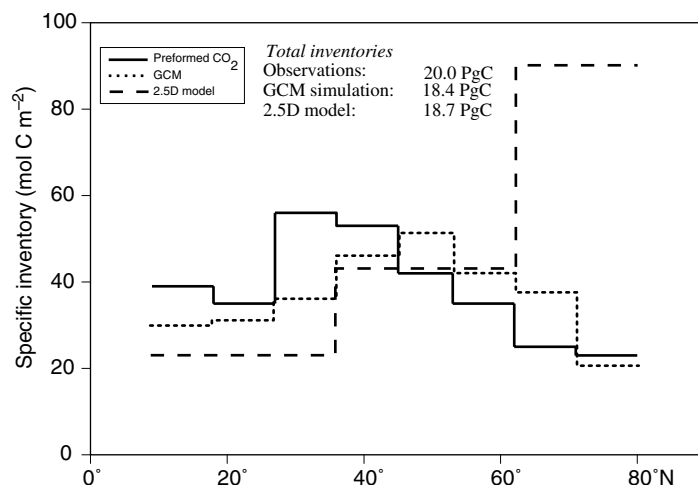


Fig. 6.3.1 Comparison of two model results (Stocker *et al.*, 1994; Sarmiento *et al.*, 1995) predicting the distribution of Excess CO₂ storage as a function of latitude in the North Atlantic as well as an observation-based estimate derived using a preformed CO₂ method. Figure redrawn from information and estimates presented by Gruber *et al.* (1996). The specific inventory refers to the total inventory contained within the ocean within the respective latitude band divided by the total area of the ocean surface in that latitude band. The total inventories refer to the year 1982 for the latitude range 10°N to 80°N, at which time inorganic carbon data were collected during the Transient Tracers in the Oceans programme (TTO).

The carbon cycle GCMs can also be used to assess the regional distribution of the uptake of Excess CO₂ from the atmosphere. This uptake is referred to by modellers as the ‘Perturbation Flux’, which is the perturbation of the natural air-sea CO₂ flux associated with higher concentrations of atmospheric CO₂. The issue of where Excess CO₂ is taken up across the air-sea interface may be of critical importance for our ability to predict future CO₂ uptake by the oceans under a climate-altered ocean circulation (Caldeira and Duffy, 2000). As noted earlier (Section 6.3.2.1), the uptake of Excess CO₂ cannot be determined from air-sea flux estimates and hence model predictions of the geographical distribution of this flux cannot readily be evaluated. Model predictions of the total (natural plus Excess) flux can, of course, be compared against the observation-based estimates. Within this chapter I argue that use of CO₂ survey data to estimate budgets for the transport and storage of Excess CO₂ offers a way to separate these components on regional scales (Section 6.3.4.3).

Global inverse modelling of atmospheric CO₂

The carbon storage term for the terrestrial biosphere is notoriously difficult to assess directly and has been assessed perhaps most reliably through consideration of the global mass balance for the

other reservoirs (atmosphere and ocean), leaving the terrestrial biosphere storage term to be calculated by difference. Most recently atmospheric O₂/N₂ time series have proven particularly useful for this. Information concerning the specific location and mechanisms of carbon storage in the terrestrial biosphere has proven particularly difficult to obtain. Over the past decade attention has focused on inferring net fluxes of carbon into and out of the terrestrial biosphere based on inverse modelling of atmospheric CO₂ data. This approach utilizes spatially resolved data on fossil fuel CO₂ release and atmospheric concentrations as constraints within atmospheric transport models. The task is to find a distribution of carbon sources and sinks that, when combined with known fossil fuel sources, reproduces the observed spatial distributions of CO₂ (or its stable isotopes) in the atmosphere.

Most examples of this approach have focussed on modelling meridional CO₂ gradients in the atmosphere (e.g. studies by Keeling and Heimann, 1986; Keeling *et al.*, 1989; Tans *et al.*, 1990; Ciais *et al.*, 1995; etc.). The natural preindustrial transport of carbon between the hemispheres is, however, a key factor for the interpretation of present-day meridional gradients. This is illustrated schematically in Figure 6.3.2. Early studies

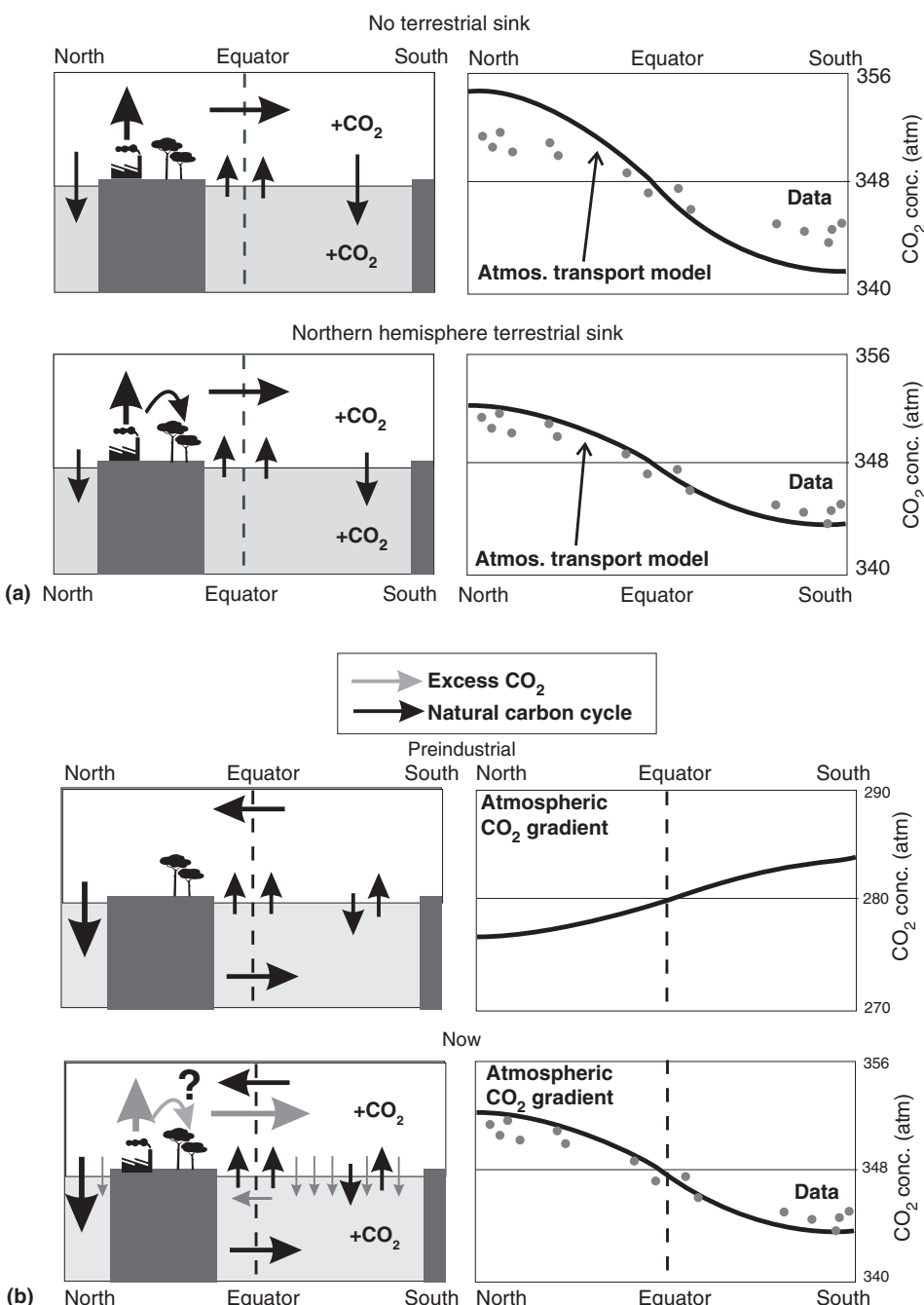


Fig. 6.3.2 Schematic representation of source–sink behaviour and the role of atmospheric and ocean transport driving interhemispheric $p\text{CO}_2$ gradients, based loosely on the analysis by Tans *et al.* (1990).

(a) In the upper right panel the solid line is the predicted present-day interhemispheric gradient based on fossil fuel emissions and an atmospheric transport model. Annual average concentrations in microatmospheres (μatm) from atmospheric $p\text{CO}_2$ monitoring stations are shown schematically as the data points (these are not actual data or model results). The lower panel shows the model-predicted distribution after an extra northern hemisphere terrestrial sink is invoked in order to bring the model predictions closer to the observations. ‘ $+\text{CO}_2$ ’ refers to the net storage of Excess CO_2 in both the atmosphere and ocean.

(b) The potential effect of oceanic interhemispheric transport, as suggested initially by Keeling *et al.* (1989) and also by Broecker and Peng (1992). In the upper right panel, a preindustrial gradient between the hemispheres is shown with opposite sense to the contemporary gradient. One possibility is that such a gradient was maintained by net southward transport of carbon by the ocean. The lower panels emphasize the degree to which such oceanic transport and the preindustrial gradient might complicate the interpretation of present-day atmospheric distributions and the inference of a northern hemisphere terrestrial sink for Excess CO_2 . The perturbation of the natural carbon exchanges are depicted by arrows with lighter shading.

by Keeling and Heimann (1986) and Keeling *et al.* (1989) inferred that during the preindustrial period, atmospheric CO₂ was approximately 1 μatm lower in the northern hemisphere than in the southern hemisphere. This natural gradient is now reversed due to fossil fuel emission, with the northern hemisphere $p\text{CO}_2$ now being approximately 3 μatm higher. Assuming that net terrestrial biosphere carbon storage was in steady state for the preindustrial era, the natural gradient must have been supported by either (1) an interhemispheric southwards oceanic transport of order 1 PgCyr⁻¹ (Keeling *et al.*, 1989); (2) effects of seasonal co-variation of atmospheric CO₂ concentration and atmospheric circulation patterns that are not resolved by atmospheric transport models (the seasonal rectifier of Keeling *et al.*, 1989; see also Denning *et al.*, 1995), or (3) a combination of both. Resolution of this issue is central to the interpretation of present-day meridional atmospheric $p\text{CO}_2$ gradients (Fig. 6.3.2). Modelling of such gradients has led to the inference that there is a large, northern hemisphere, terrestrial carbon sink (e.g. Tans *et al.*, 1990). However such inference is clearly sensitive to the assumed or modelled magnitude of the oceanic carbon transport (Broecker and Peng, 1992) and/or the seasonal rectifier effect (Law *et al.*, 1996).

The geographical distribution of contemporary air-sea CO₂ flux estimates has also sometimes been used as a constraint in order to resolve better terrestrial sink distributions (e.g. Tans *et al.*, 1990). Indeed, the regional terrestrial sink distribution inferred by atmospheric inverse modelling can be extremely sensitive to the distribution and magnitude of the air-sea carbon flux (Fan *et al.*, 1998). Problems of data scarcity, variability and accuracy involved with estimating air-sea CO₂ fluxes (Takahashi *et al.*, 1997) currently limits the power of this approach. Improved surface observation strategies and gas-exchange parameterizations can significantly strengthen this constraint in the future. However, alternative approaches to estimating regional air-sea exchanges should also be considered, in a manner analogous to what has been done previously using the heat and freshwater transport divergence in the ocean (cf MacDonald and Wunsch, 1996; Bryden and Imawaki, Chapter 6.1; Wijffels, Chapter 6.2). Notably, the possibility of defining meridional oceanic transports of carbon, and assessing carbon

transport divergence and convergence on regional scales should be explored. However, it must be remembered that (in contrast to heat and fresh water) it cannot be assumed that regional carbon storage is negligible over decadal time scales. Rather, storage of Excess CO₂ is highly significant for the contemporary ocean.

In Section 6.3.4.3, we discuss methods whereby the anthropogenic or Excess component of the contemporary carbon transport can be separated from the total transport. This permits estimation of the preindustrial or natural oceanic carbon transport, which should prove of value for assessing the magnitude of the seasonal rectifier effect within atmospheric transport models, and for better resolving the contemporary distribution of terrestrial sinks.

6.3.3 The JGOFS/WOCE Global CO₂ Survey

6.3.3.1 The JGOFS-WOCE collaboration

During the late 1980s planning was underway for two major international oceanographic research programmes related to global change: WOCE (part of the World Climate Research Programme, see Thompson *et al.*, Chapter 1.3) and JGOFS (part of the International Geosphere-Biosphere Programme). A key component of WOCE (e.g. Woods, 1985a) was the WOCE Hydrographic Programme (WHP), which provides an unprecedented 'snapshot' of the distribution of water masses and chemical tracers throughout the World Ocean during the 1990s. Included with this snapshot was the measurement of boundary currents and hydrographic properties at high density along zonal heat-flux lines where transports of heat and fresh water could be estimated. In addition to temperature and salinity, traditional hydrographic properties such as dissolved oxygen and inorganic nutrients were measured in order to define water mass characteristics. Transient tracers, including the CFCs and ^{3}H - ^{3}He , give a picture of the formation and spreading of water masses away from the sea surface, and their distribution act as constraints on ocean circulation and climate modelling. As part of WOCE, a concerted effort was made to define accuracy standards and quality assurance procedures to ensure that the WHP data set would be of the highest quality possible (King *et al.*, Chapter 3.1).

The JGOFS programme was planned as a decade-long study of the biogeochemistry of the ocean, with a major focus on carbon fluxes and supported three major classes of activities:

- Time-series sites where long-term records of biogeochemical parameters could be collected. The first such site was established off Bermuda. A second site was established off Hawaii. A European-supported site was subsequently established off the Canary Islands.
- Regional process studies of seasonal to annual duration where specific processes could be examined. The first such process study was the North Atlantic Bloom Experiment, which focused on the Spring Bloom in the northeastern Atlantic. Subsequent major process studies were conducted in the equatorial Pacific, the Arabian Sea and the Southern Ocean.
- A Global Survey. This was to provide global-scale data concerning carbon fluxes and transports. The scientific goals of the Global CO₂ Survey required similar data coverage and many of the same supporting measurements and information as were planned for the WHP. Based on negotiations between the two programmes, a formal agreement was reached prior to the start of the field work, which resulted in the establishment of a JGOFS CO₂ measurement program on the WHP cruises.

6.3.3.2 Goals of the Global CO₂ Survey

The Global CO₂ Survey had three primary goals:

- 1 to quantify the uptake of Excess CO₂ by the oceans;
- 2 to provide a global description of carbon dioxide in the oceans to aid the development of models of the ocean's role in the global carbon cycle; and
- 3 to characterize the transport of inorganic carbon within the ocean and between the ocean and the atmosphere in order to reveal carbon sources and sinks for the atmosphere.

These goals would be attained through making measurements sufficient to calculate the full speciation of inorganic carbon on discrete samples collected during WOCE cruises, as well as through measurement of *p*CO₂ on surface water and air on a semicontinuous basis along the WOCE transects. The former required measurement on discrete

water samples from hydrographic casts of at least two carbonate system parameters. The latter required measurements on a continuous pumped seawater stream together with supporting thermosalinograph data. Attainment of the overall goals of the CO₂ Survey would rely heavily on the WOCE data-stream: particularly the WOCE hydrographic, dissolved oxygen, nutrient and tracer measurements as well as the boundary current transport data required for calculating carbon transports.

Figure 6.3.3 presents a map of the WOCE lines on which CO₂-related profiles were collected. Analysis time and personnel restrictions meant that, normally, sampling of CO₂ parameters did not take place at all hydrographic stations along these cruise tracks but rather at between 25 and 50% of the stations occupied.

6.3.3.3 Implementation

Scientific leadership and guidance

No single body was responsible for the implementation and organisation of the CO₂ Survey. General scientific oversight was provided by the International JGOFS Science Steering Committee and, specifically, by the Intergovernmental Oceanographic Commission/JGOFS Ocean CO₂ Panel. The WOCE Hydrographic Programme Planning Committee took an active role in assisting with logistic planning as well as with devising a data management plan. Much of the scientific impetus for the Survey arose within the USA, particularly with the US Department of Energy (DOE) supported Global CO₂ Survey Science Team. This group of investigators, who were involved with the task of planning and making their own at-sea measurements, received long-term support to plan and guide their programme. The group worked as a team, under the initial guidance of J. Downing (then of the Pacific Northwest Laboratory). The Department of Energy's Office of Health and Environmental Research at that time had the foresight to allow the Science Team to reach out both nationally and internationally in order to establish standard methods and data quality control (see Section 6.3.3.4). Funding was also provided for carbon measurements to be made on non-US WOCE cruises that would otherwise have been unsupported. Significant support to the US-DOE CO₂ Survey Science Team was provided by a group of US investigators organized within the National

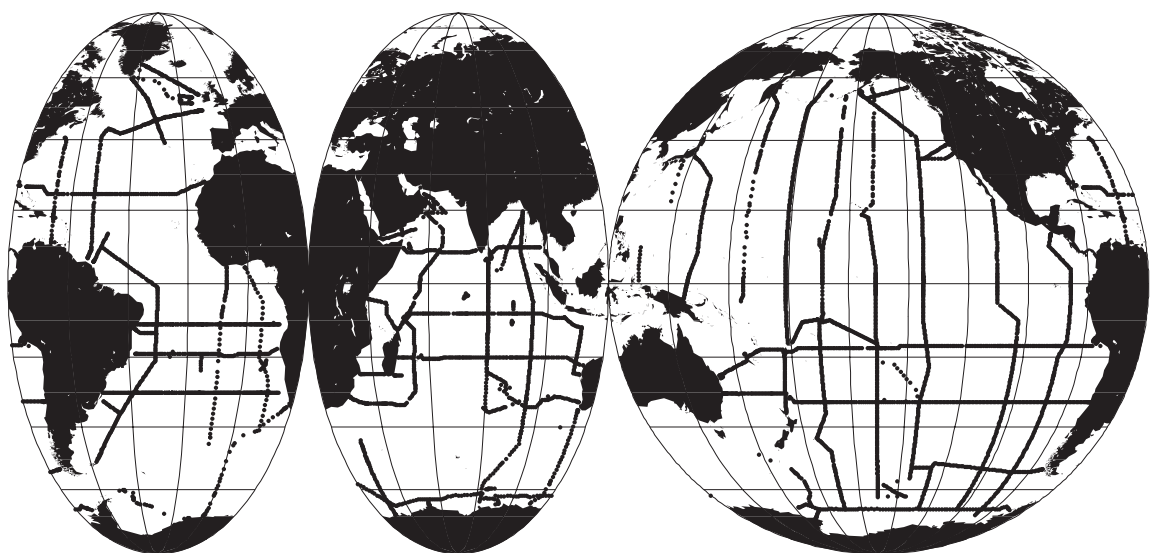


Fig. 6.3.3 Map showing WOCE cruise tracks on which measurements of inorganic carbon were made on discrete water samples as part of the JGOFS/WOCE Global Survey of CO₂ in the Oceans. The map shows lines that the author knows were sampled for ocean carbon by the international community: additional WOCE lines, not shown here, may also have been sampled. The map does not show sections occupied outside of WOCE (e.g. JGOFS, non-WOCE lines occupied under the NOAA-OACES programme, etc.)

Oceanographic and Atmospheric Administration's (NOAA) Ocean–Atmosphere Carbon Exchange Study (OACES) programme, as well as by the US and International JGOFS Scientific Steering Committees. The NOAA-OACES programme, in particular, played a major role in collecting extensive data sets for a wide range of ocean carbon-related parameters along a large number of sections, including several WOCE sections.

The measurement problem

There are four measurable quantities that can be used to define the speciation and concentration of inorganic carbon in seawater (Park, 1969; DOE, 1994). These are the total dissolved inorganic carbon or TCO₂, the pH, the partial pressure of dissolved CO₂ ($p\text{CO}_2$) and the total alkalinity of seawater. Measurement of any two of these four allows the concentration of the dissolved CO₂, bicarbonate ion (HCO₃[−]) and carbonate ion (CO₃^{2−}) species to be separately estimated. Of these, only the first three are changing directly as a result of the uptake of Excess CO₂ by the oceans. First and foremost, the $p\text{CO}_2$ is increasing as a result of the tendency of the surface ocean to maintain equilibrium with the increasing $p\text{CO}_2$ of the atmosphere. This implies (for constant alkalinity): increasing TCO₂ and decreasing pH. Table

6.3.1 summarizes the expected annual changes of the four measurable quantities for surface seawater which maintains equilibrium with the current rate of increase of atmospheric $p\text{CO}_2$. Also shown are the typical ranges of these parameters in the ocean, together with the currently best-attainable measurement accuracy for each parameter. The expected annual increase in surface water concentrations provides an obvious target for the accuracy required of CO₂ Survey data in order that there be potential to document the interannual to decadal build up of CO₂ within the ocean. During the initial planning stages for the CO₂ Survey such a target seemed impossible to reach, and it is a measure of the success of the technical work conducted for the Survey that such a target now appears to be approachable.

Pre-WOCE data coverage and quality

Prior to the Global CO₂ Survey, the data coverage for CO₂ parameters was patchy and limited in scope and quality. The pre-WOCE data consisted largely of the measurements of TCO₂, $p\text{CO}_2$ and alkalinity made during the Geochemical Ocean Sections (GEOSECS) expeditions between 1972 and 1978, as well as similar measurements made during the Transient Tracers in the Ocean (TTO) North and Tropical Atlantic Surveys in 1981–83.

Table 6.3.1 Oceanic ranges and state-of-the-art analytical capabilities for the four measurable parameters that can be used to define inorganic carbon specification in seawater

| Parameter | Oceanic minimum | Oceanic maximum | Best precision ^a | Best accuracy ^a | Annual increase ^b | Signal-to-noise ^c |
|--|-------------------|-------------------|-----------------------------|----------------------------|------------------------------|------------------------------|
| TCO ₂ ($\mu\text{mol kg}^{-1}$) | 1900 ^d | 2350 ^d | 0.5 | 1.0 | 0.85 | 0.8 |
| pH @ 20°C | 7.45 | 8.25 | 0.0005 | 0.003 | -0.002 | 0.7 |
| Total alkalinity ($\mu\text{mol kg}^{-1}$) | 2250 ^d | 2450 ^d | 2 | 3 | 0 | - |
| pCO ₂ @ 20°C (μatm) | 200 | 2000 | 2 | 3 | 1.8 | 0.6 |

^a Author's estimates.
^b For temperature of 10°C, salinity of 35 and total alkalinity of 2300 $\mu\text{mol kg}^{-1}$.
^c Defined as (annual increase)/(best accuracy).
^d Normalized to a salinity of 35.

The South Atlantic Ventilation Experiment (SAVE: 1988–89) included a significant CO₂-related data set. Additional data sets in the SW Indian Ocean had been collected by Alain Poisson and co-workers (see references in Sabine *et al.*, 1999) and a widespread series of measurements in many regions had been made by Arthur Chen and co-workers (e.g. see review by Chen, 1993).

These pre-WOCE data were collected by many groups of investigators using several different techniques at a time when no common standards or reference materials were available. Analytical differences between measurement groups and within the same measurement group between cruises were significant. For example in a pre-JGOFS international intercomparison, interlaboratory differences were found to be as large as 29 $\mu\text{mol kg}^{-1}$ for total alkalinity and 21–29 $\mu\text{mol kg}^{-1}$ for TCO₂ (Poisson *et al.*, 1990). The latter is equivalent to the expected increase in surface water Excess CO₂ concentration over a >20-year time period! For these reasons, the compilation and comparison of different early data sets has been plagued by a need to estimate adjustments and offsets to the various data sets in order to assemble an internally consistent data set. Such adjustments were frequently made on the basis of comparisons of measurements made in deep waters at nearby locations on different cruises (Section 6.3.3.4; see also Gruber *et al.*, 1996). One result of this is that are several versions of the same historical ocean carbon data sets in existence today, each of which have had different corrections applied.

Data archiving, reporting and availability

Data from the US component of the CO₂ Survey (including data collected by the DOE and NOAA

programmes) and certain international efforts were processed and reported independently of the WHP data under the terms of an agreement worked out with the WOCE Hydrographic Programme Planning Committee. Data were quality-assured, assembled and disseminated through the Carbon Dioxide Information and Analysis Center (CDIAC) at the Oak Ridge National Laboratory. Data are available as Numeric Data Packages (which include detailed data documentation) directly from CDIAC (<http://www.cdiac.esd.ornl.gov>). At the international level, CO₂ data have frequently been reported via the WOCE data stream (see Lindstrom and Legler, Chapter 3.5) although the normal WOCE quality assessment procedures have not usually been followed because CO₂ data are not official WOCE measurement parameters. Some countries (e.g. Germany) have reported CO₂ data collected during WOCE cruises through their national JGOFS data reporting systems. The status of some international (non-US) data sets remains unclear and the International JGOFS programme is currently assessing their status (B. Balino, personal communication).

6.3.3.4 Data quality control and assurance

Choice, development and standardization of methods

At the outset of the CO₂ Survey only the gas-stripping and coulometric titration method for TCO₂ determination (Johnson *et al.*, 1985, 1987) had the demonstrated accuracy required to meet Survey goals. This technique was chosen as a contractually required procedure for measurement groups involved with the US-DOE supported CO₂ Survey cruise legs. Internationally, most but not all CO₂ Survey cruises have included measurement of TCO₂ by coulometry. In order to promote data

quality, the US DOE CO₂ Survey Science Team developed and distributed standardized instrumentation for TCO₂ analysis (Johnson and Wallace, 1992). Several training sessions were organized, as well as an international workshop on coulometric TCO₂ analysis.

CO₂ Survey Measurement groups were expected to include at least one other independent measure of the carbonate system on their cruise legs: no restriction was imposed on the choice of this second parameter. Some groups measured total alkalinity, and others chose to make measurements of *p*CO₂ or pH on discrete water samples.

Over the course of the CO₂ Survey significant methodological advances were made concerning the measurement of TCO₂ (e.g. Johnson *et al.*, 1993), total alkalinity (e.g. Millero *et al.*, 1993; Mintrop *et al.*, 2000), continuous-flow (e.g. Körtzinger *et al.*, 2000) and discrete-sample (Wanninkhof and Thoning, 1993; Neill *et al.*, 1997) *p*CO₂ measurement, and pH (e.g. McElligott *et al.*, 1998). Most importantly, standardized methods for sampling, analysis and data workup were documented in a *Handbook of Methods* (DOE, 1994). This publication greatly assisted the rapid dissemination of accurate measurement techniques, worldwide, during the Survey.

Certified Reference Materials

A critical advance of the Global Survey, once again implemented by the US DOE CO₂ Survey Science Team, and particularly by A. Dickson of Scripps Institution of Oceanography, was the development and distribution of Certified Reference Materials (CRMs) for TCO₂ and, later, for total alkalinity (Dickson and Anderson, 2001). The use of reference materials had long been advocated (SCOR, 1985; Poisson *et al.*, 1990). However, it required the prospect of long-term support by the DOE programme, as well as community acceptance of the reference materials, to bring such long-standing recommendations to reality.

The CRMs are samples of surface seawater that were initially collected in the Pacific Ocean and then UV-sterilized, poisoned, equilibrated with the atmospheric *p*CO₂ and then sealed within carefully-stoppered 500 ml glass bottles. A random subset of the bottles from each batch are analysed by Certified methods for TCO₂ (with a long-term reproducibility of the order of 1 $\mu\text{mol kg}^{-1}$ by vacuum extraction/manometry in the laboratory of

C. D. Keeling) and total alkalinity (by potentiometric titration in A. Dickson's laboratory with a long-term reproducibility of the order of 0.8 $\mu\text{mol kg}^{-1}$), as well as for salinity and nutrient content. Tabulated values of Certified concentrations for the 44 separate batches of CRMs produced since January 1990 are listed at http://www.mpl.ucsd.edu/people/adickson/CO2_QC/index.html. (See also Dickson and Anderson, 2001.) The CRMs have been extensively tested and proven to be stable with respect to their Certified concentrations for periods of at least 2 years after bottling.

The CRM bottles are then shipped to the various laboratories making inorganic carbon measurements in seawater. Within these laboratories, regular analyses of CRMs are interspersed with normal sample analysis. Between 1990 and 1998, the Dickson laboratory produced and distributed about 20 000 CRM bottles. The majority (65%) were used within the USA, and the remainder were distributed to 18 other countries. At least 50% of these were used to support CO₂ Survey field measurements (Dickson and Anderson, 2001). On board WOCE cruises, CO₂ Survey investigators analysed CRMs at least daily in order to check the performance of their seagoing analytical systems and to provide quality assurance of the results obtained (see Section 6.3.3.4).

Shore-based analyses: a link to the past?

At the outset of the Survey the US DOE CO₂ Survey Science Team established an additional data assessment mechanism, as a means to relate the WOCE-era data (made with the benefit of CRMs) to pre-WOCE ocean carbon data sets (collected when CRMs were not available). The laboratory of C. D. Keeling at Scripps Institution of Oceanography was supported to make replicate analyses of TCO₂ on a limited number of samples collected from each cruise on which a US-DOE supported CO₂ measurement team had participated. These samples were collected, sealed, and shipped back to California (DOE, 1994). The samples were subsequently analysed using a gas extraction/manometry technique identical to that used to assign the Certified TCO₂ value for the CRMs. The concept behind the shore-based analyses was two-fold:

- 1 *Quality assessment.* The shore-based programme potentially allowed 'closure of the circle' with

respect to ship-board analytical quality. Certified Reference Materials (whose TCO₂ concentration had been determined and Certified in the Keeling laboratory by manometry) were analysed at sea, during all cruises by coulometric titration. Replicates of a number of seawater samples that had been analysed at sea were also shipped back to the Keeling laboratory and analysed by manometry. In a perfect analytical world, any offsets revealed between the coulometric determination of the CRM concentration and its Certified (manometry-determined) value would show up as an identical offset between the at-sea coulometric and shore-based manometric measurements on the replicate seawater samples.

2 *Links to historical ocean carbon data.* Near-identical sampling and analysis procedures had been used by the Keeling laboratory on a subset of samples collected during the GEOSECS, SAVE and TTO programmes. The Keeling

shore-based measurements have suffered to a lesser extent from the inevitable offsets associated with changes in measurement procedures associated with the seagoing measurements. Hence the collection of samples for shore-based manometry provided an opportunity to link the at-sea coulometric analyses made during WOCE, with pre-WOCE at-sea measurements made prior to the introduction of CRMs. Two potential disadvantages with the shore-based manometric analyses should be mentioned: (a) the procedure is time-consuming which means that only a limited number of samples could be analysed; (b) there is a risk of post-sampling concentration changes over the period (sometimes months) between sample collection and analysis.

Figure 6.3.4 presents the results of the shore-based (manometric) versus ship-based (coulometric) analyses of replicate samples collected throughout

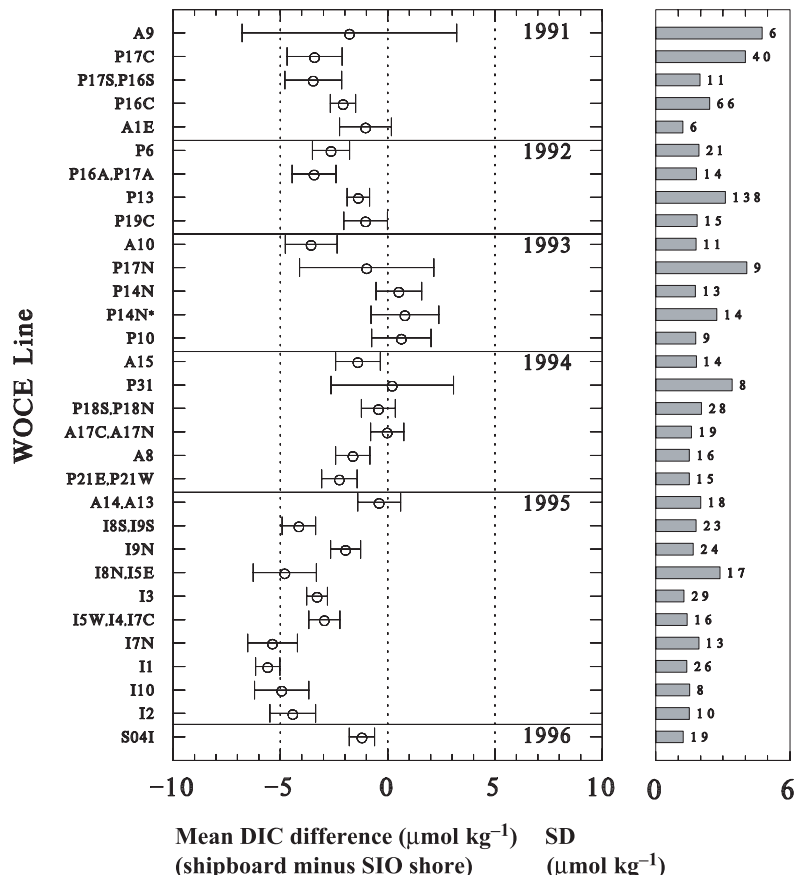


Fig. 6.3.4 Shore-based (manometric, SIO) versus ship-based (coulometric) TCO₂ analyses on replicate samples collected at sea. For each WOCE leg, the mean and 95% confidence interval of the offset between the shore-based manometric analysis and the shipboard coulometric analysis is shown. The right-hand panel shows the standard deviation (SD) of an individual shipboard minus share-based difference determination and the number of such differences.

the CO₂ Survey. The results indicated a systematically higher difference between the shore-based and shipboard replicate analyses than the difference between the Certified Value for a CRM and its shipboard determination by coulometry. The difference averages of the order 2.2 $\mu\text{mol kg}^{-1}$, with the shore-based (manometric) analyses giving the higher results. The reason for this difference, and its inter-cruise variability, is hard to explain. It might, for example, result partly from slow abiotic hydrolysis during sample transport and storage of a dissolved or particulate organic carbon fraction not present in the CRMs.

It was therefore not possible to 'close the circle' perfectly with respect to data accuracy. A small, unexplained, but reasonably systematic deviation remains between the shipboard and shore-based measurements. The source of this deviation needs further investigation. At present it appears reasonable, however, to assume that the factors leading to such a deviation may well have applied to pre-WOCE shore-based versus shipboard analyses as well.

Sabine *et al.* (1999) tested this assumption by comparing the shipboard data collected during the Indian Ocean WOCE cruises with deep-water data collected in 1977–78 during GEOSECS. A deep-water ($>2000\text{ m}$) offset of $+22.5 \pm 3 \mu\text{mol kg}^{-1}$ of GEOSECS-WOCE (GEOSECS data higher) was observed after correcting for hydrography variability using multivariate analysis. Keeling manometric analyses made on stored GEOSECS samples from the Indian Ocean were $16.5 \pm 5 \mu\text{mol kg}^{-1}$ lower than the GEOSECS shipboard values (Weiss *et al.*, 1983). For the WOCE data from the Indian Ocean, the Keeling analyses averaged $4 \mu\text{mol kg}^{-1}$ higher than the shipboard analyses (P. Guenther, personal communication, Fig. 6.3.4). The overall expected difference between the two shipboard data sets is therefore $+20.5 \mu\text{mol kg}^{-1}$, which is almost exactly what was observed.

This single example points out that it might indeed be possible to use the WOCE CRM-calibrated shipboard data set as a reference, with the shore-based manometric analyses acting as a transfer standard between the WOCE shipboard data and earlier shipboard data sets. This will be of particular value for regions where it cannot be readily assumed that deep-water values are temporally constant (e.g. for the Atlantic Ocean). Whether the apparent consistency demonstrated in

the Indian Ocean will hold for other ocean basins remains to be seen.

At-sea data quality evaluation

In general the shipboard data collected during the CO₂ Survey was of very high quality, especially for the primary parameter, TCO₂. The most complete assessment of data quality to date has been for the 14-month duration, nine-leg US WOCE Indian Ocean expedition, with assessments covering TCO₂ (Johnson *et al.*, 1998b), total alkalinity (Millero *et al.*, 1998) and surface *p*CO₂ (Sabine and Key, 1997) having been published. Figures 6.3.5a and b show summary plots of the analyses of Certified Reference Materials during this expedition. In the case of TCO₂, the shipboard data were independently calibrated and only checked against the Certified (manometric) value. The mean difference between the Certified and coulometric values averaged only $-0.96 \mu\text{mol kg}^{-1}$ ($n=983$) with the standard deviation of the difference being $<1 \mu\text{mol kg}^{-1}$. For total alkalinity the approach in the Indian Ocean was slightly different, in that individual data sets were adjusted, on a cruise-by-cruise basis in order that the mean result of the CRM analyses matched that of the Certified value. In this case, the overall mean difference between measured and Certified values must average zero for each cruise. Nevertheless, the relatively low standard deviation and lack of clear trends in the data within each cruise leg show once again that data quality was tightly controlled. The standard deviation of the CRM analyses for alkalinity did vary significantly between the cruise legs because of issues related to equipment maintenance and operation. This difference in performance between the primary parameter (TCO₂) and the second parameter (in this case total alkalinity) reflects the significant effort that went into perfecting TCO₂ measurement prior to the Survey (Section 6.3.3.4). For the Indian Ocean comparisons it should be noted that identical equipment and procedures were used throughout, albeit by various measurement groups.

The overall consistency of data sets was also assessed empirically through the comparison of deep profile data at cross-over locations where two separate WOCE cruise legs occupied stations in close ($>100\text{ km}$) geographical proximity to each other (Johnson *et al.*, 1998b; Millero *et al.*, 1998). For TCO₂ the absolute leg-to-leg differences

assessed in this way were always $< 3 \mu\text{mol kg}^{-1}$ with a mean absolute difference (leg to leg) of $1.8 \mu\text{mol kg}^{-1}$. For total alkalinity, the mean absolute difference at the cross-overs was $2.4 \mu\text{mol kg}^{-1}$ (Millero *et al.*, 1998; Sabine *et al.*, 1999).

This level of agreement is within that expected from the estimated accuracy and precision of the individual cruise data sets and no additional corrections to the data are warranted.

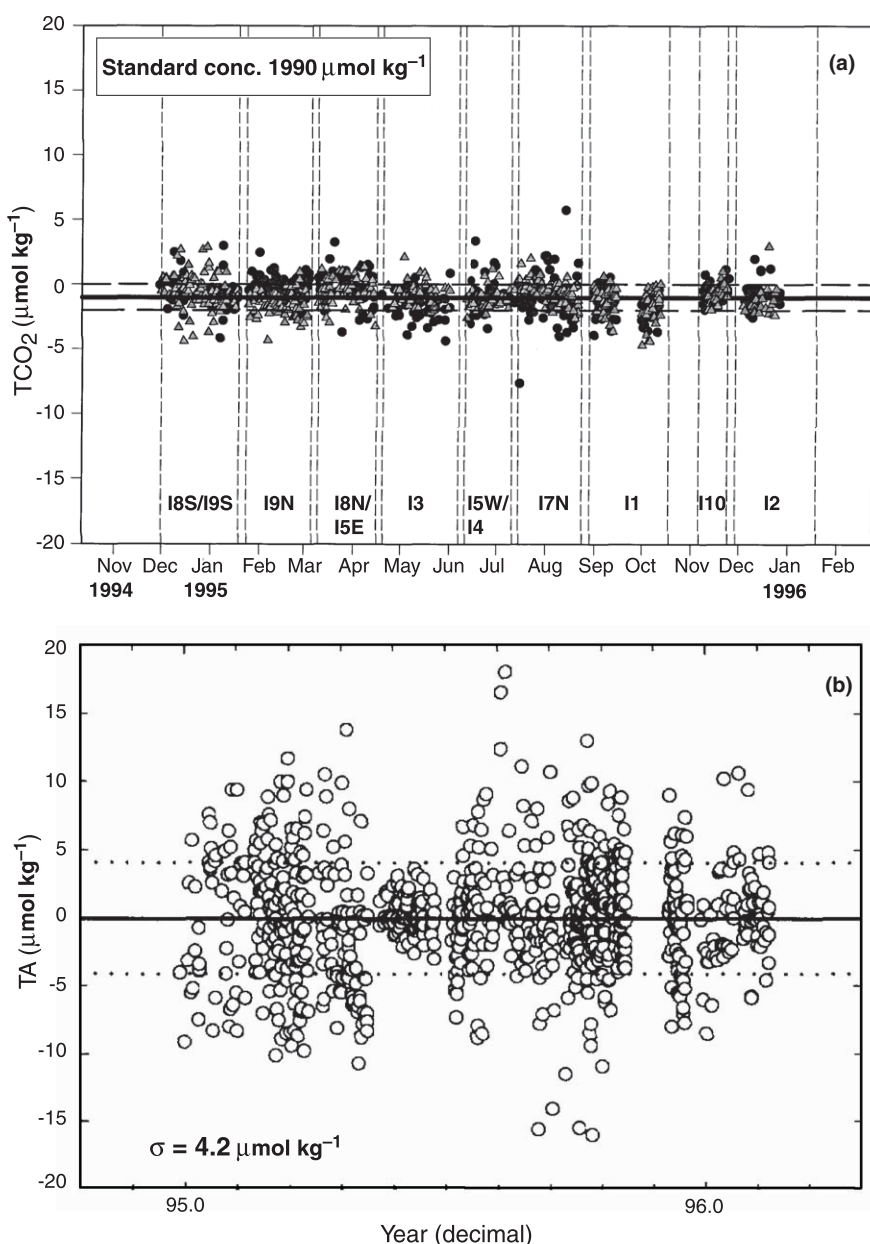


Fig. 6.3.5 Results of all analyses of Certified Reference Materials during the Indian Ocean CO₂ Survey (from Johnson *et al.*, 1998b; Millero *et al.*, 1998). Results are plotted as deviations of the shipboard measured values from the Certified values for the reference material (shipboard – Certified).

(a) TCO₂. The shipboard measurements were independently calibrated. Different symbols are used to refer to analyses made using two separate shipboard coulometer systems. Gaps between the various legs of the Indian Ocean expedition are marked with vertical lines. The solid and dashed lines refer to the mean value and $\pm 0.05\%$ of this mean value, respectively.

(b) Total alkalinity (TA). The shipboard measurements were adjusted so that the mean offset from the Certified value averaged zero for each cruise leg.

Lamb *et al.* (2001) are completing a detailed cross-over analysis of data collected on different cruises of the Pacific Ocean WOCE Survey. In this case, measurements were made by groups from four countries on 22 WOCE cruises (and several non-WOCE cruises) using various equipment and procedures. Preliminary findings of this study are once again that overall agreement between the cruises is excellent, although it appears that adjustments to the shipboard data from a few Pacific cruises will be recommended.

6.3.4 Synthesis of Global CO₂ Survey data: Review

This section is intended to convey only a flavour of the type of synthesis that will be forthcoming over the next several years from the Global CO₂ Survey. To do this I review the existing literature that has emerged from the Survey, discussing only papers that deal with results collected on WOCE cruises. It is important to note that many complementary syntheses are emerging from related programmes, including the JGOFS and NOAA-OACES programmes.

6.3.4.1 Concentration distribution of Excess CO₂

Preformed-CO₂ methods for Excess CO₂ separation

The oceanic inventory of Excess CO₂ can, in principle, be calculated directly using so-called

'preformed-CO₂' methods to separate the Excess or anthropogenic component from the large and variable natural background of oceanic dissolved inorganic carbon. Here I apply the term 'preformed-CO₂ method' to methods that utilize some form of back-calculation from observed concentrations to so-called 'preformed' concentrations. Conceptually, 'preformed' concentrations refer to concentrations at water mass surface outcrops at the time of water mass formation (usually late winter), in the case of CO₂ these have increased with time.

The underlying principle (Brewer, 1978; Chen and Millero, 1979), is to correct measured TCO₂ concentrations for changes incurred since a water mass lost its ability to exchange gases directly with the atmosphere (see flowchart in Fig. 6.3.6). Inorganic carbon builds up naturally in subsurface waters due to oxidation of organic matter and dissolution of metal carbonates. These effects can be diagnosed using the apparent oxygen utilization and alkalinity deviations from the so-called 'preformed alkalinity', respectively. If the preformed TCO₂ for the same water mass as it existed in the preindustrial era can be estimated, then the difference between the two calculated preformed values (present–preindustrial) is the Excess CO₂ content of the water mass. These basic steps are summarized in Figure 6.3.6. Obvious problems arise in practice in applying accurately the required corrections and, particularly, in estimating the preindustrial preformed TCO₂ values (Broecker *et al.*,

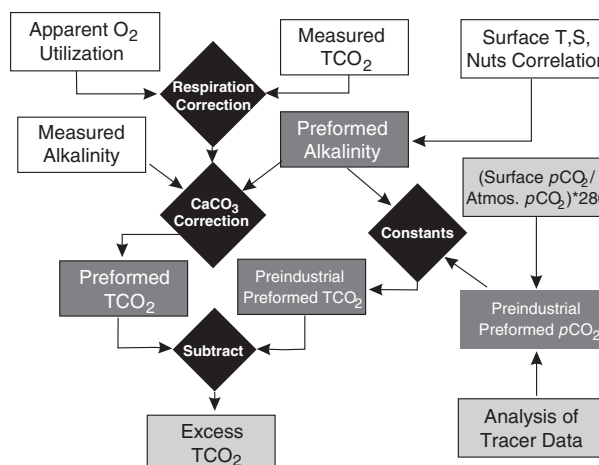


Fig. 6.3.6 Flow-chart illustrating the basic sequence of steps required to make an estimate of the Excess CO₂ content of a water sample using the preformed techniques discussed in the text. Various authors have taken different approaches to implementing each of the steps shown here, however all methods make use of these basic steps either explicitly or implicitly. Note that 'Constants' refers to the equilibrium constants describing the solubility and speciation of CO₂ in seawater and '280' refers to the preindustrial atmospheric pCO₂. Nuts, nutrients.

1985b). Gruber *et al.* (1996) clarified and partially addressed some of the problematic issues inherent in the earlier studies by introducing a quasiconservative carbon-based tracer ΔC^* defined as:

$$\begin{aligned} \Delta C^* &= C^{\text{meas}} + r_{\text{C}:O_2} (O_2^{\text{eq}} - O_2^{\text{meas}}) \\ &\quad - 0.5 (Alk^{\text{meas}} - Alk^0 - r_{\text{NO}_3:O_2} (O_2^{\text{eq}} - O_2^{\text{meas}})) \\ &\quad - C_{(p\text{CO}_2=280, Alk^0, S)}^{\text{eq}} \end{aligned} \quad (6.3.1)$$

The last term represents the TCO_2 concentration in equilibrium with the preindustrial atmosphere ($p\text{CO}_2 = 280 \mu\text{atm}$) for the sample's potential temperature (θ), salinity (S), and preformed alkalinity (Alk^0). $(O_2^{\text{eq}} - O_2^{\text{meas}})$ is the apparent oxygen utilization, the superscript 'meas' refers to concentrations measured in water samples, and $r_{\text{C}:O_2}$ and $r_{\text{NO}_3:O_2}$ are stoichiometric ratios (both negative) relating inorganic carbon and nitrate changes to dissolved oxygen changes, respectively. The sum of the first three terms simply defines a sample's preformed TCO_2 concentration. This is similar in concept to other preformed quantities such as preformed nutrients and mixes conservatively within the ocean interior. The last term in equation (6.3.1) generally does not mix conservatively: Gruber *et al.* (1996) maintained conservative mixing properties of ΔC^* by artificially linearizing the thermodynamic equations used to calculate C^{eq} as a function of θ , S and Alk^0 .

Because ΔC^* is referenced against equilibrium with the preindustrial atmosphere, uptake of Excess CO_2 causes ΔC^* values to increase. However ΔC^* also include a contribution (of either sign) from non-equilibrium conditions in surface waters:

$$C_{\text{excess}} = \Delta C^* - \Delta C_{\text{diseq}}^* \quad (6.3.2)$$

The last term in equation (6.3.2) is the 'air-sea disequilibrium' defined (conceptually) as the difference between the actual TCO_2 concentration of the mixed layer at the time of water mass formation and the TCO_2 concentration in equilibrium with the atmosphere at that time. It is assumed that the air-sea disequilibrium has not changed significantly since 1750. Observations show that the disequilibrium varies regionally: for example due to effects of rapid sea surface temperature (solubility) changes and the finite rate of air-sea gas exchange. The air-sea disequilibrium for a

multicomponent water mass therefore represents the weighted average of individual air-sea disequilibria for various mixture components. In order to estimate Excess CO_2 , the air-sea disequilibria must be estimated.

Two estimation approaches have been proposed: one for deep ocean density surfaces with regions 'far away from the outcrop... where one can safely assume that there is no anthropogenic CO_2 ', and the other for shallower and well-ventilated layers where 'anthropogenic CO_2 has already affected the entire density surface' (Gruber *et al.*, 1996). The air-sea disequilibria for a deep isopycnal can be estimated directly based on ΔC^* measured in regions known to be free of Excess CO_2 (equation (6.3.2)). For density surfaces where anthropogenic tracers and hence Excess CO_2 are present throughout, transient tracer data are used to estimate the atmospheric $p\text{CO}_2$ with which the water mass had contact during its formation. First, tracers such as CFC-11 or the ^3H - ^3He age are used to assign a 'ventilation year' (t) or age to a water parcel. Knowledge of the time-history of atmospheric $p\text{CO}_2$ allows the equilibrium ΔC^* for seawater for that ventilation year to be calculated ($\Delta C^{\text{eq}}_{p\text{CO}_2(t), \text{Alk}^0, \theta, S}$). The air-sea disequilibrium is then the difference between the measured ΔC^* and this calculated equilibrium value. Usually this is calculated as a mean difference for an isopycnal over a range of water mass ages.

A problem can arise in applying this technique to near-surface waters within which seasonal processes cause assumptions of the preformed CO_2 techniques to break down. For example, oxygen produced seasonally by photosynthesis in the surface layer can be lost to the atmosphere with little or no corresponding stoichiometric gain of CO_2 from the atmosphere (due to the slower equilibration rate for CO_2). Most measurement programmes, including the WOCE sections, have been conducted in summer, whereas preformed values and air-sea disequilibria derived from the analysis of deep-water distributions conceptually refer to conditions during late winter. Gruber (1998) dealt with this problem by assigning Excess CO_2 concentrations calculated from depths of 100–200 m to the mixed layer. Sabine *et al.* (1999) assumed that surface waters contained at-equilibrium levels of Excess CO_2 (i.e. the difference of ΔC^{eq} calculated for contemporary and preindustrial atmospheric $p\text{CO}_2$).

Gruber *et al.* (1996) performed a detailed and careful error analysis and determined that the

uncertainty in Excess CO₂ concentrations based on their method is of the order of 10 $\mu\text{mol kg}^{-1}$ (i.e. about 20% of the current surface ocean Excess CO₂ concentration). For the calculation of inventories, as suggested by the discussion below, an important and difficult-to-assess issue is whether these errors are randomly or systematically distributed.

Atlantic Ocean

Gruber (1998) presented estimates of Excess CO₂ concentrations in the Atlantic Ocean based mainly on pre-WOCE data (TTO and SAVE), but also including data from two WOCE cruises in the South Atlantic (*Meteor* 15/3 cruise along A9 (19°S) and the *Meteor* 11/5 cruise along A12 (~ 58°S) and A21 (Drake Passage)). Qualitatively, the distributions closely match those of other transient tracers, such as the CFCs, with large accumulations and deep penetration found within the thermocline waters of the subtropical gyres of both hemispheres. This accumulation in the mid-latitude water column reflects convergence of Excess CO₂ driven by the convergence of surface waters. Relatively shallow penetration and low inventories were found in the tropical and equatorial zone (20°S to 20°N), whereas very deep penetration was observed in high northern latitudes associated with deep-water formation. Relatively low deep-water concentrations and low inventories were detected in high southern latitudes (>50°S) apparently because of the relatively short time available for newly formed deep waters in this region to pick up Excess CO₂ from the atmosphere, in part because ice cover restricts gas exchange (Poisson and Chen, 1987). Dilution by rapid mixing with old waters also makes the Excess signal hard to detect in this region, and Caldeira and Duffy (2000) suggest that any absorbed Excess CO₂ is rapidly transported out of the region along isopycnals.

According to Gruber (1998) Excess CO₂ at levels > 5 $\mu\text{mol kg}^{-1}$ were found all the way to the bottom throughout much of the North Atlantic north of 40–50°N in 1982. South of this, zonally averaged Excess CO₂ levels dropped to levels approaching zero below about 2000 m, although a weak Excess CO₂ signal (< 5 $\mu\text{mol kg}^{-1}$) associated with Antarctic Bottom Water was detected spreading from the south below about 4000 m.

In contrast to the surface distribution of CFCs, Excess CO₂ levels are highest in warm tropical waters (approx. 40–50 $\mu\text{mol kg}^{-1}$ in 1989) and

are lower (30–40 $\mu\text{mol kg}^{-1}$) in colder, high-latitude waters. This is a consequence of the strong temperature dependence of the buffer capacity of seawater with respect to CO₂ addition (Revelle factor), which more than compensates for the fact that both CO₂ and the CFCs are both more soluble in colder water. For a given $p\text{CO}_2$ increase, warm waters are able to absorb significantly more Excess CO₂ from the atmosphere than cold waters.

Holfort *et al.* (1998) analysed data from three WOCE sections in the South Atlantic between 10 and 30°S (A8, A9, A10) as well as several pre-WOCE sections from the same region. Their primary aim was to examine carbon transports (Section 6.3.4.3). However, in order that the transport of Excess CO₂ could be estimated, it was necessary to estimate the Excess CO₂ distribution across all of the sections. The Excess CO₂ calculation method used was not described in their paper, and is described schematically in Figure 6.3.7. A significant difference with the method used by Gruber (1998) was that it was nowhere assumed that deep water was uncontaminated with Excess CO₂ in order to calculate air-sea disequilibria. Rather a factor analogous to Gruber's air-sea disequilibrium term was extrapolated from regions where transient tracers were detectable into regions of the water column where transient tracers (including CCl₄) were undetectable.

Figure 6.3.8 shows a comparison between the zonal-average profiles resulting from Holfort *et al.*'s (1998) estimates and Gruber's (1998) estimates for the South Atlantic between 10 and 30°S. Overall the profiles are very similar: noticeable in all the profiles are relatively high and uniform concentrations in the Antarctic Intermediate Water (AAIW) between 500 and 1000 m, with Excess CO₂ levels in this water mass being higher towards the south, closer to the AAIW formation region (cf. Brewer, 1978). The main difference between the two analyses is the presence in the Holfort *et al.* (1998) profiles of a background, non-zero level of Excess CO₂ (3–5 $\mu\text{mol kg}^{-1}$) throughout the deep-water column. In contrast, Gruber's (1998) values drop to zero between 2000 and 4000 m. Whereas this 3–5 $\mu\text{mol kg}^{-1}$ background level is well within the acknowledged uncertainty of both separation techniques, it represents a systematic difference that can contribute significantly to total water column inventories. This possibility

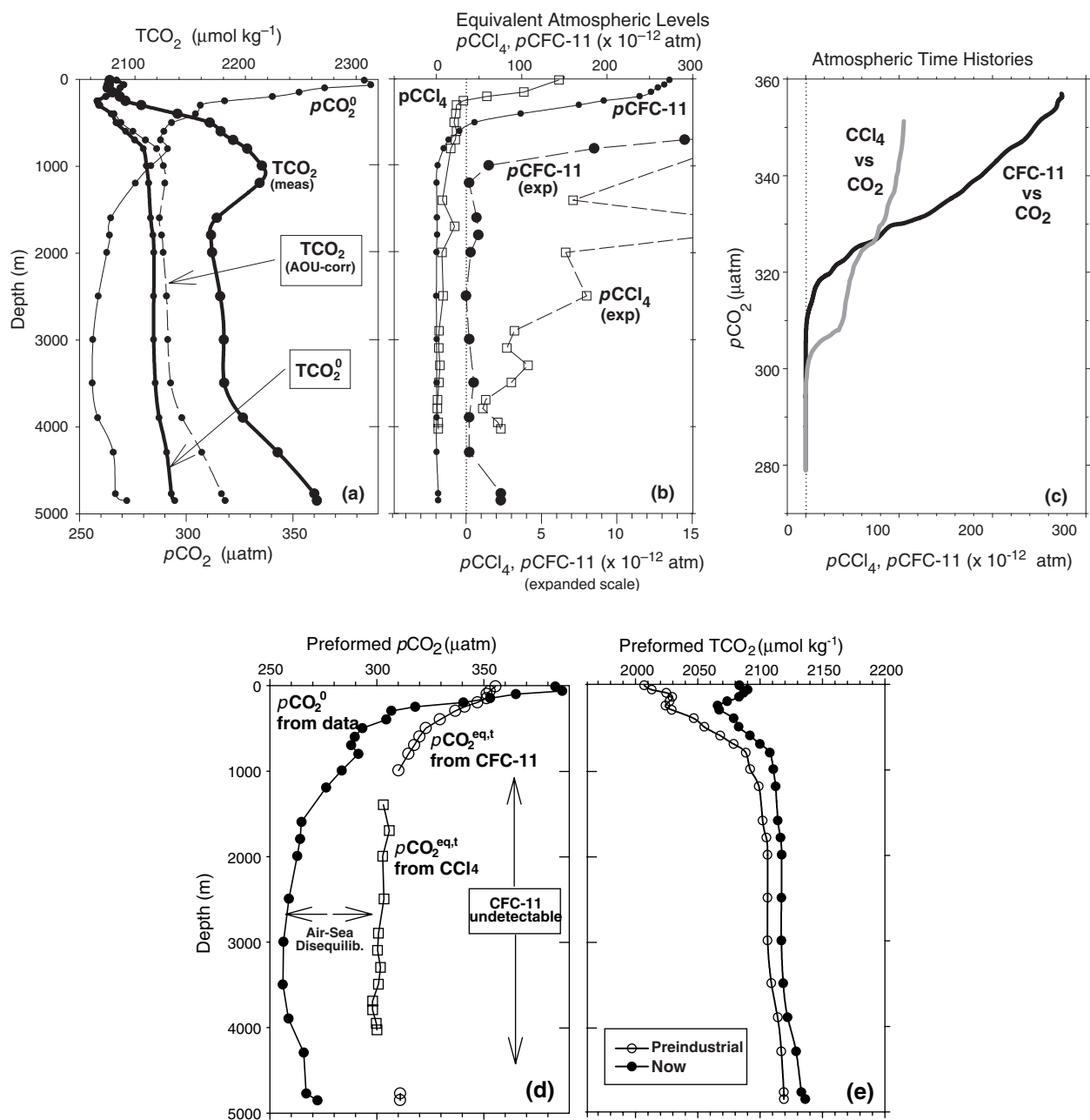


Fig. 6.3.7 Example of the application of the preformed-CO₂ method used by Holfort *et al.* (1998) to calculate Excess TCO₂ concentrations. Example profiles from the western basin of the South Atlantic at 19°S are used to illustrate the method. The procedure used was as follows:

- 1 Preformed values for TCO₂ (TCO₂⁰) and pCO₂ (pCO₂⁰) were calculated as a function of depth (panel a), based on the measured TCO₂ data and alkalinity data (not shown), after correcting these measured values for the effects of oxygen utilization and carbonate dissolution. Panel (a) shows that the oxygen-based correction dominates the correction of the TCO₂ data.
- 2 'Equivalent atmospheric concentrations' for CFC-11 and CCl₄ samples (i.e. the partial pressures, pCFC-11 and pCCl₄) were calculated as a function of depth based on measured concentrations and the gas solubility at the potential temperature and salinity of the samples (panel b). For clarity, the profiles are also shown on an expanded scale to emphasize deep-water distributions. Detection limits for these compounds are of the order of 0.1 to 0.5 × 10⁻¹² atm.
- 3 The temporal relationship between pCO₂ and pCFC-11 (and pCCl₄) in the atmosphere (and hence also in surface water at equilibrium with the atmosphere) was reconstructed based on the atmospheric time histories of these gases (panel c; see also Körtzinger *et al.*, 1999a, for the Excess CO₂ versus pCFC-11 time history). CFC-11 became

was noted by Gruber (1998), who estimated the uncertainties of his calculated inventories at 20% for exactly this reason. For example, Gruber's (1998) inventory of Excess CO₂ between 20 and 30°S is about 37 molC m⁻². A 2000-m thick layer with Excess CO₂ content of 4 µmol kg⁻¹ would contribute an additional 8 molC m⁻², or 21%, to this inventory. This difference lies at the edge of Gruber's (1998) suggested uncertainty level, thereby supporting his recommendation that 'more refined techniques are necessary in order to obtain improved estimates of this error'.

This difference between the two techniques may be related to the fact that CFC-11 is undetectable throughout most of this depth range at these latitudes (e.g. Wallace *et al.*, 1994; Roether and Putzka, 1996). This may have led Gruber (1998) to assume that this depth range was also uncontaminated with Excess CO₂. On the other hand, both

Wallace *et al.* (1994) and Roether and Putzka (1996) measured detectable levels of anthropogenic CCl₄ within this depth range over wide regions where CFC-11 was completely undetectable. Anthropogenic CCl₄ has been present in the ocean since the 1920s, at which time surface seawater already contained about 14 µmol kg⁻¹ of Excess CO₂. Excess CO₂, having been introduced since about 1750, will have penetrated even further into the deep ocean than CCl₄ and considerably further than the CFCs (introduced in 1950s) and tritium (introduced in 1960s). In the approach used by Holfort *et al.* (1998), these deep CCl₄ data were used to estimate air-sea disequilibria for deep waters (Fig. 6.3.7) and this implied non-zero Excess CO₂ levels between 2000 and 4000 m. The detection of CCl₄ throughout most of the low-to-mid-latitude South Atlantic (including the North Atlantic Deep Water and parts of the eastern basin)

detectable in the environment around 1950 whereas CCl₄ started increasing significantly around 1910–20. The time histories are shown up until 1992.

- 4 Surface water $p\text{CFC-11}$ (and $p\text{CCl}_4$) were assumed to have remained close to equilibrium with the atmosphere, whereas surface water $p\text{CO}_2$ was expected to have deviated, proportionally, much further from equilibrium (due to the longer air-sea equilibration time for CO₂). Where CFC-11 was detectable, an effective equilibrium value of the preformed $p\text{CO}_2$ for the year of water mass formation (t), $p\text{CO}_2^{\text{eq},t}$, was estimated from the water sample's $p\text{CFC-11}$ and the reconstructed temporal equilibrium relationship between the gases (panel c). Where CFC-11 was undetectable but CCl₄ was detectable, the $p\text{CCl}_4$ was used for this purpose. A typical profile of $p\text{CO}_2^{\text{eq},t}$ is presented (panel d).
- 5 This approach does not deal explicitly with the effect of subsurface mixing of waters with different ages. It also does not account for non-conservative behaviour of the preformed $p\text{CO}_2$ ($p\text{CO}_2^0$) during mixing. With respect to the former issue, the equilibrium relationship between $p\text{CFC-11}$ and $p\text{CO}_2^{\text{eq},t}$ has been quasilinear over much of the time-history of the tracer input (panel c). Hence for subsurface, along-isopycnal mixing between waters with ages corresponding to this linear portion of the relationship, a reasonable estimate of the 'effective' value $p\text{CO}_2^{\text{eq},t}$ should still result. With respect to the latter issue, a refinement of this approach based on the use of preformed TCO₂ concentrations and linearization of the equilibrium constants linking $p\text{CO}_2$ and TCO₂ (cf. Gruber *et al.*, 1996) could be developed and implemented.
- 6 The difference at each depth between the measurement-derived $p\text{CO}_2^0$ and the tracer-derived estimate of $p\text{CO}_2^{\text{eq},t}$ (panel d) is analogous to the air-sea disequilibrium of Gruber *et al.* (1996; see also equation (6.3.2)). In our South Atlantic sections this difference was frequently positive near the surface due to seasonal effects discussed in the text. At depth, the inferred air-sea disequilibrium reached about 45 µatm, indicative of CO₂ undersaturation in newly formed deep waters. These values are comparable to Gruber's (1998) estimates (cf. his Fig. 7). In practice, for all depths where either CFC-11 or CCl₄ was detectable, we expressed the air-sea disequilibria as a ratio: $p\text{CO}_2^0/p\text{CO}_2^{\text{eq},t}$. Values for this ratio based on our South Atlantic data varied from close to 1 just below the surface layer to a minimum of about 0.85 (denoting undersaturation) at depth. Where all transient tracers including CCl₄ were undetectable, this ratio was assumed to remain constant at its lowest value.
- 7 These air-sea $p\text{CO}_2$ disequilibrium ratios were applied to the preindustrial equilibrium $p\text{CO}_2$ level of 280 µatm in order to calculate the preindustrial, preformed $p\text{CO}_2$ as a function of depth: $p\text{CO}_2^{0,t=\text{preind}}$. (Here we assumed that the air-sea disequilibrium has remained constant throughout the industrial era.) These estimates of $p\text{CO}_2^{0,t=\text{preind}}$ were used together with the potential temperature, salinity and the preformed alkalinity to calculate profiles of the preindustrial preformed TCO₂ or $\text{TCO}_2^{0,t=\text{preind}}$ (panel e).
- 8 Finally, the differences between the observation-based TCO₂⁰ values (panels a and e) and the estimated preindustrial values ($\text{TCO}_2^{0,t=\text{preind}}$) was assumed equal to the Excess TCO₂ concentration (see also Fig. 6.3.6).

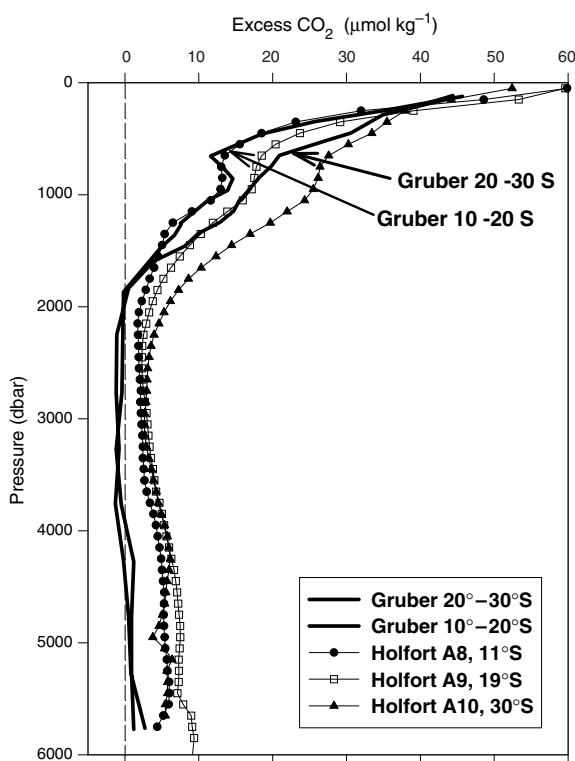


Fig. 6.3.8 Comparison of zonally averaged Excess CO₂ concentration profiles for various latitudes as estimated by Holfort *et al.* (1998) with those estimated for latitude bands by Gruber (1998) for the South Atlantic between 30°S and 10°S. The WOCE data are from three *Meteor* cruises occupied during the early to mid-1990s. The Gruber analyses are based primarily on analysis of data collected during the South Atlantic Ventilation Experiment (SAVE) during 1987–89 but include some WOCE data.

suggests that no portion of the Atlantic Ocean can necessarily be assumed to be free of Excess CO₂. It is therefore possible that Gruber (1998) may have slightly underestimated deep water Excess CO₂ levels in this region and other portions of the deep Atlantic (see also the analysis by Wanninkhof *et al.*, 1999).

Körtzinger *et al.* (1998) calculated the distribution of Excess CO₂ from measurements made along the WOCE A2 section (zonal section between 43 and 49°N) occupied during *Meteor* 30/2 in 1994. A classical preformed-CO₂ back-calculation technique was used, very similar to one of the original methods (Chen and Millero, 1979), but including the nitrate correction of Brewer (1978). The air-sea disequilibrium was assumed constant with depth and was evaluated, in effect, by assuming that deep water of the eastern basin

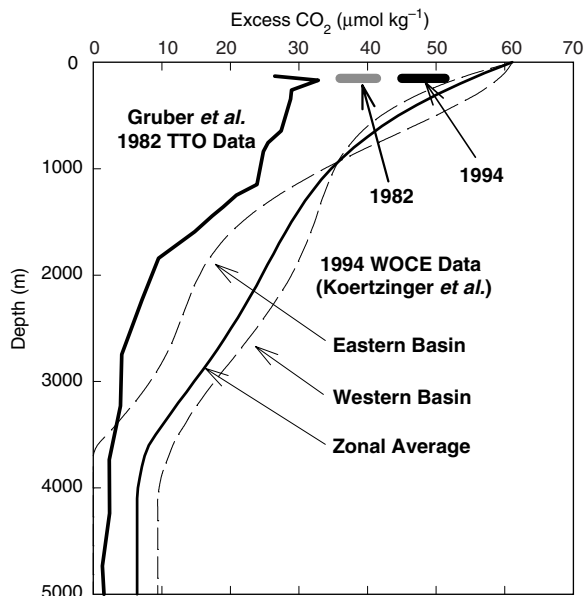


Fig. 6.3.9 Comparison of Körtzinger *et al.* (1998) Excess TCO₂ profiles with analyses presented by Gruber *et al.* (1996) for the North Atlantic in the latitude range 40–50°N. The Gruber *et al.* estimates are zonal average profiles based on TTO data collected during 1982. The Koertzinger *et al.* estimates are based on data collected along WOCE A2 in 1994 and are shown as separate average polynomial fits to estimates from the Eastern and Western basins (Koertzinger *et al.*, 1998) as well as an areally weighted average of these two profiles representing the zonal average. Also shown are the theoretically calculated concentrations of Excess CO₂ for 1982 and 1994 based on assumed equilibrium of surface waters with the atmospheric pCO₂. Ranges of equilibrium values appropriate for surface temperatures of 10–20°C are presented and have been calculated with the equilibrium constants of Mehrbach *et al.* (1973) as refit by Dickson and Millero (1987).

below 3500 m contained zero Excess CO₂. (Note, however, that Gruber *et al.*'s (1996) analysis of data from a wider region also implied low or negligible Excess CO₂ in the deepest waters of this region.) The Excess CO₂ content was estimated and presented for the eastern and western basins along A2 (see Fig. 6.3.9). Also shown is the zonal average (40–50°N) calculated by Gruber (1998) using the TTO data collected in 1982. The large difference between the studies is a result of the increase of Excess CO₂ between 1982 and 1994 (the time of the A2 section). However, differences between the back-calculation procedures may also contribute (see Wanninkhof *et al.*, 1999). For comparison, the expected change in surface water

levels for this time period has been plotted assuming surface waters in this region have maintained equilibrium with respect to the increasing atmospheric $p\text{CO}_2$. Both Excess CO₂ estimates deviate significantly from the theoretical values in the upper layers: this may reflect problems with calculating Excess CO₂ levels in the upper ocean using summertime data (see Section 6.3.4.1). Uncertainties in the upper 200 m of the water column can therefore be significant.

To date no comprehensive analysis of the Atlantic Ocean CO₂ data collected during WOCE has been conducted, although this is being planned (e.g. Mintrop and Wallace, 1999). However, based on Gruber's (1998) analysis, the North Atlantic Ocean contained a total of about $22 \pm 5 \text{ PgC}$ of Excess CO₂ in 1982 and the South Atlantic contained about $18 \pm 4 \text{ PgC}$ Excess CO₂ in 1989. The stated uncertainty is larger than the estimated effect of purely random errors due to the possible effect of systematic error when calculating inventories (see Gruber (1998) and the discussion above). The global inventories of oceanic Excess CO₂ (all oceans) predicted by the Princeton Ocean Biogeochemistry Model were 106 PgC (1982) and 120 PgC (1989). Simple scaling of the basin-scale estimates by this modelled temporal increase of the global inventory implies a total Atlantic Ocean inventory of about 43 PgC for the year 1989.

Indian Ocean

Sabine *et al.* (1999) performed a comprehensive analysis of the basin-wide inventory of Excess CO₂ based on data collected during the US WOCE Survey of the Indian Ocean (December 1994 through January 1996). Data from nine US WOCE legs were used together with data from I6S collected during the French CIVA1 cruise and some pre-WOCE data from the Southwestern Indian Ocean. Two separate methods were used to examine Excess CO₂: a time-series comparison with data collected two decades earlier during GEOSECS (see Section 6.3.4.2) and a slightly modified version of Gruber's ΔC^* technique.

Figure 6.3.10a reproduces the Excess CO₂ distribution along 92°E. A very clear maximum in inventories is found at about 40°S, coincident with the Subtropical Convergence marking the transition from high-salinity subtropical gyre waters to low-salinity Antarctic waters. Clearly this is where Excess CO₂ is being carried into the deep ocean

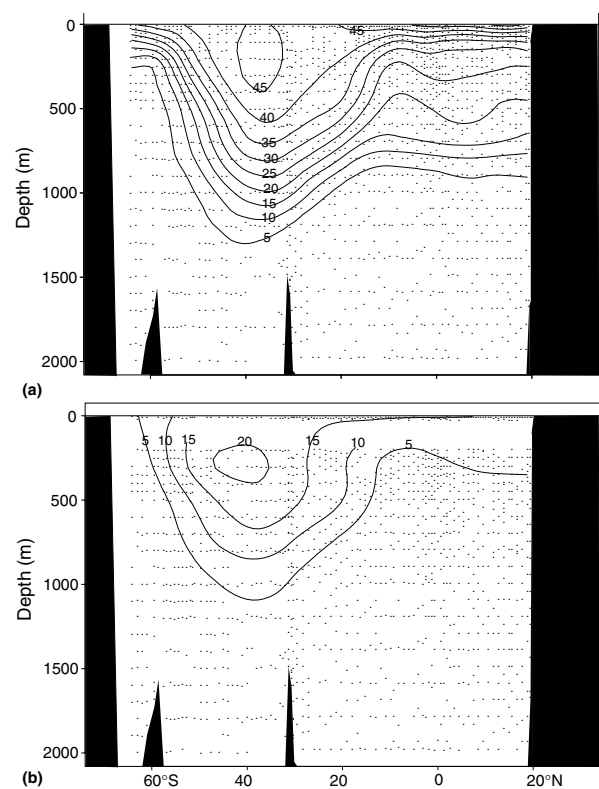


Fig. 6.3.10 Excess CO₂ and its temporal increase in the Indian Ocean. Figures reproduced from those presented by Sabine *et al.* (1999).

- (a) Total concentration of Excess CO₂ along 92°E in the Indian Ocean based on data collected during the US WOCE Indian Ocean expedition.
- (b) Temporal increase of Excess CO₂ between 1977 and 1978 and 1995 along the same section estimated using a multivariate time-series approach. Data are from GEOSECS (1977–78) and the US-WOCE Indian Ocean expedition (1995).

following uptake by surface waters elsewhere (see Section 6.3.2.1 above). South of 40°S, and similar to the findings of Gruber (1998) for the Atlantic, very little Excess CO₂ is found in the water column. This finding was in dramatic contradiction with results from the three-dimensional Ocean Biogeochemistry General Circulation Model of Sarmiento *et al.* (1995), which predicted 2.5 times higher inventories in this region. The difference has been attributed to inappropriate model physics in this region (cf. England, 1995). Further north in the Indian Ocean the model and data-based estimates agreed reasonably well.

Goyet *et al.* (1999) introduced a fundamentally different approach to the estimation of Excess CO₂ for the analysis of data from the WOCE I1 line

(9°N) using a multiparameter mixing analysis (based on an approach described by Tomczak and Large, 1989). First of all, end-member concentrations for regional water types contributing to the water sampled along the section were specified. Next, local biogeochemical changes to TCO₂ concentrations were estimated stoichiometrically using deviations of measured oxygen and alkalinity from values predicted using the (conservative) mixing model and the end-member concentrations. These 'biogeochemically corrected' TCO₂ concentrations along the section were assumed to be created by the mixing of the end-members' TCO₂ concentrations, each of which was assumed to be composed of a natural and an Excess CO₂ component. The actual Excess CO₂ component in water sampled along the section would be expected to be lower than the level predicted by instantaneous mixing of the Excess CO₂ components of the end-members. (This is because the end-members' Excess CO₂ concentrations are increasing with time.) The contribution of an end-member's Excess CO₂ component to the biogeochemically corrected TCO₂ concentration along the section was therefore assigned a functional dependence that allowed it to decrease with depth, allowing the effects of depth-dependent ventilation times (water-mass ages) on the Excess CO₂ levels to be accounted for. Finally, the end-members' Excess CO₂ concentrations as well as the coefficients of the depth-dependent functions were solved iteratively with the mixing model in order to minimize the residuals relative to the biogeochemically corrected measured values.

This approach represents perhaps the most radical departure from the long-standing methods introduced by Brewer (1978) and Chen and Millero (1979). It relaxes several assumptions inherent in earlier techniques: notably no explicit assumptions are required concerning the preformed (surface) preindustrial concentrations, the required stoichiometric corrections are small, and mixing of multiple different water sources can be treated explicitly. On the other hand, some of the procedures, assumptions and statistical weighting involved in the approach as currently described are difficult to assess. The Excess CO₂ distribution calculated for I1 section data using this technique showed significant differences with the estimates derived using the ΔC* approach on the same data set (Coatanoan *et al.*, 2001). Differences were particularly notable in the upper thermocline

(200–600 m) where the ΔC* approach gave Excess CO₂ levels about 12 μmol kg⁻¹ higher than the mixing model calculations. The mixing model approach gave slightly higher values in deep waters (>800 m). Overall the ΔC* approach gave water column inventories that averaged 20% higher than those estimated using the mixing model approach.

There is as yet no basin-scale estimate for the entire Indian Ocean based on the mixing model approach. Using the ΔC* approach, Sabine *et al.* (1999) estimated a total inventory for the Indian Ocean (between 20°E and 120°E) of 20.3 ± 3 PgC for the year 1995.

Pacific Ocean

In contrast to the comprehensive syntheses of pre-WOCE Atlantic data and WOCE Indian Ocean data discussed above, the synthesis of Pacific Data is not as far advanced. In part this is because the measurements were collected over several years (1990–96) by several different groups, as opposed to the concentrated approach employed in the Indian Ocean during the US WOCE effort.

Brewer *et al.* (1997) used data collected along P17N in the Northeastern Pacific (135°W to 160°W) to illustrate a historical and conceptual review of preformed-CO₂ calculation techniques. In their review the emphasis was on the calculation of the preformed *p*CO₂ as a function of depth. In particular the high sensitivity of Excess CO₂ calculations to the assumed stoichiometric value of the C:O₂ respiratory coefficient was emphasized.

To date the only other analysis of Excess CO₂ calculations resulting from WOCE cruises was reported by Feely *et al.* (1999) based on data collected along 150°W. (A time series comparison by Ono *et al.* (1998) is discussed in Section 6.3.4.2.) Feely *et al.* (1999) used the ΔC* method to calculate Excess CO₂ concentrations from 60°S to about 55°N. They found the largest area-specific inventories in the subtropics and the sub-Antarctic zone north of 55°S. In the South Pacific the deepest penetration and largest inventories were at 48°S. Inventories at the equator were almost a factor of two smaller. Inventories north of 48°N were also small. A comparison was made with two ocean carbon cycle models. As with the Indian Ocean and the Atlantic comparison, the measurement-based inventories were similar to the modelled inventories along most of the section, with the exception of both high-latitude regions (>55°S

and >40°N), where the models gave much higher inventories than the ΔC* calculations.

There is to date no basin-wide estimate of Pacific inventories based on the recent WOCE data, although this is presently being prepared (R. Feely, personal communication). A rough estimate of the Pacific contribution based on an earlier version of a preformed-CO₂ estimation technique and various historical data sets gave a total of about 31.3 PgC for 1980 (Chen, 1993). When scaled similarly to the Atlantic estimates given above this suggests an inventory of about 37 PgC in 1989. (Note that this estimate is presented only to allow a rough comparison with the other basin inventories and is subject to revision based on the WOCE data, using improved analysis techniques.)

Summary

The differences and uncertainties associated with the various Excess CO₂ separation techniques (e.g. those highlighted by the discussion of the Indian Ocean I1 section distributions) emphasize the model and assumption sensitivity of Excess CO₂ separation. The factors underlying Excess CO₂ estimation differences, and, particularly, which calculation approach gives a better indication of the 'true' values, remain unclear (Coatanoan *et al.*, 2001). The identification and resolution of such differences is important, however, if the goal of using such distributions to guide model improvement is to be attained. As Orr *et al.* (2000) has pointed out: 'we validate model predictions to understand where they may be wrong and how to improve them; we should do the same for data-based estimates such as those for anthropogenic CO₂...'. There may be significant utility in attempting to evaluate the various Excess CO₂ calculation techniques using model-generated data as input. The current generation of three-dimensional ocean carbon GCMs could be used to generate known target fields of Excess and natural carbon. Effects of spatial and temporal variability, gas exchange and complex mixing could be simulated in the creation of these fields. Finally, sets of 'model data' similar to the data collected during the CO₂ Survey could be generated and the various Excess CO₂ techniques applied in order to reconstruct the known or target fields. In this way, the relative ability of various approaches could be evaluated. An analysis of this type is currently underway for the Indian Ocean (C. Sabine, personal communication).

6.3.4.2 Time series comparison methods

Background

The preformed methods described above seek to estimate the total oceanic inventory of Excess CO₂: i.e. all the extra carbon added since about 1750. Several fundamental problems with most such approaches exist that can introduce significant uncertainty into the estimation of Excess CO₂. Wallace (1995) showed that evaluation of the Excess CO₂ increase through the direct comparison of TCO₂ data collected over decadal or longer intervals is now possible. Specifically changes in TCO₂ that are not associated with analytical error or natural variability in other physical or biogeochemical factors (e.g. temperature, salinity, AOU, alkalinity) can be attributed to the build-up of Excess TCO₂. In any such comparison, variability of these parameters is encountered and has to be corrected for before the Excess CO₂ change can be identified. Two separate such approaches have to date been applied to WOCE data sets.

A multivariate approach

Wallace (1995) introduced an empirical, multivariate technique to remove the influence of natural variability on TCO₂ concentration differences. In order to compare two data sets collected at different times, the following steps were proposed:

- a multivariate predictor equation is established based on regional TCO₂ data collected at one point in time (T1), through regression with 'oceanographically related' predictor variables such as potential temperature, AOU, salinity, total alkalinity, nutrient concentrations, etc. On basin scales these regressions explain most of the observed subsurface TCO₂ variance other than that arising from analytical error.
- This predictor equation is applied to independent variables as they were measured at a different point in time (T2, e.g. 10 years earlier or later) and a TCO₂ distribution is predicted.
- The predicted TCO₂ distribution, calculated from the T1 predictor equation and the T2 independent variables, is compared with the T2 observed TCO₂ concentrations and the residuals calculated.
- The multivariate predictor equation is assumed to account for natural TCO₂ variability (e.g. that associated with changes in temperature, dissolved oxygen, salinity, etc.). The residuals

(or, more accurately, temporal differences in the spatial pattern of residuals) are therefore interpreted as reflecting additional ‘non-natural’ TCO₂ variability, primarily that resulting from a temporal increase in the Excess CO₂ concentration of seawater.

- In the case of comparisons with historical data sets, systematic calibration errors of the earlier data are to be expected. Such offsets appear as systematic non-zero values for residuals in deep waters where the increase of Excess CO₂ over time should usually be small. Such deep-water residuals from GEOSECS-WOCE data comparisons, in depth ranges where transient tracers such as the CFCs and CCl₄ are absent, were interpreted as a TCO₂ calibration errors with the GEOSECS data (Wallace, 1995; Sabine *et al.*, 1999). The GEOSECS data were accordingly corrected throughout the water column for this deep-water offset.

This approach allows all available data to be compared and relaxes certain assumptions of the preformed techniques: notably no particular value for the stoichiometric relationship between oxygen utilization and TCO₂ increase is assumed – rather a value is estimated empirically from the data (as a partial regression coefficient). Wallace (1995) examined this residual variability in the western basin of the South Atlantic subtropical gyre based on data collected in 1973–74 during GEOSECS, during 1988–89 during SAVE, and along WOCE A8 (11°S), A9 (19°S) and A10 (30°S) during 1991–93. The vertical profiles of the TCO₂ residuals resulting from this comparison closely matched what might be expected for a profile of Excess CO₂ increase over 20 years based on the distribution of CFC-11. Sabine *et al.* (1999) subsequently applied this approach to the Indian Ocean survey TCO₂ data in comparison with GEOSECS. The distribution of the temporal build-up of Excess CO₂ calculated in this empirical way closely matched the distribution estimated using the inventory approach (see Fig. 6.3.10b).

A data selection and correction approach

Ono *et al.* (1998) compared North Pacific TCO₂ data collected during 1994 along a WOCE section (P2 at 30°N) with GEOSECS data collected from seven stations during 1973. The comparison was made with respect to fixed density layers,

hence only water with similar temperatures was compared. For each GEOSECS station at a selected density level, a subset of the P2 data was selected for comparison. This subset of (interpolated) values at the various density levels were chosen from a subset of the P2 stations based on similarity in:

- *Geographical position.* Only P2 stations within $\pm 20^\circ$ of longitude of a GEOSECS station were selected for comparison.
- *Salinity.* Comparisons were restricted to values at which the interpolated P2 salinity on a particular density surface was within a specified tolerance range of the GEOSECS station’s (interpolated) salinity.

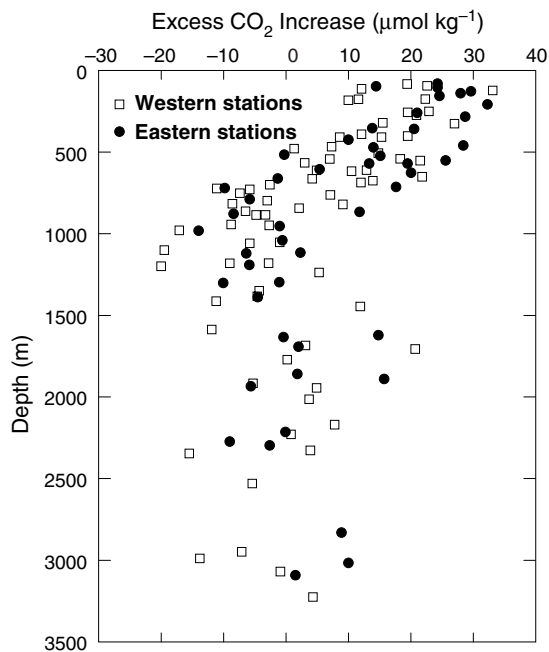


Fig. 6.3.11 Temporal increase of Excess CO₂ in the North Pacific at 30°N as estimated by Ono *et al.* (1998; their Fig. 6) using a data-selection and correction approach. The recent measurements were made along WOCE line P2 in 1994. The GEOSECS data were collected in 1973. Different symbols refer to accumulation in the western part of the section (to the west of 175°W: open squares) and accumulation in the eastern portion (between 150°W and 175°W: filled circles). The GEOSECS stations used for these two groupings were Stations 223, 225, 226, 214 (Western) and 213, 212, 204 (Eastern). Note that the analytical precision of the CO₂ system data during WOCE was significantly better than was achieved during GEOSECS, so that time-series comparisons with GEOSECS data are noisier than comparisons between WOCE and future data sets are likely to be.

- *AOU*. Of the samples left available for comparison after these geographically and salinity-based selections, only the 2–4 interpolated values with the closest agreement of AOU between GEOSECS and P2 were finally compared.

Even after this restrictive data-selection procedure, significant differences in salinity and AOU remained between the GEOSECS and P2 values for any given isopycnal. These were corrected for by comparing salinity-normalized values of TCO₂ and by correcting the TCO₂ values to a common value of AOU using a stoichiometric coefficient $\Delta\text{CO}_2:\Delta\text{O}_2$ of -0.768 . Uncertainties associated with this stoichiometric coefficient are minimized because the AOU difference between the two cruises was always $<17\text{ }\mu\text{mol kg}^{-1}$ as a result of the data selection.

Systematic TCO₂ differences of the order $13\pm8\text{ }\mu\text{mol kg}^{-1}$ remained between GEOSECS and P2 values in waters deeper than $\sigma_0=27.5$. It was assumed that Excess CO₂ had not penetrated this deep and that these offsets represented analytical errors in the GEOSECS data that were corrected for on a station-by-station basis. Results from the comparison are illustrated as profiles in Fig. 6.3.11. A clear temporal increase is seen down to depths of the order of 750 m, with the near-surface increase averaging about $22\text{ }\mu\text{mol kg}^{-1}$ over the 20-year interval between the two cruises. This near-surface rate of increase is similar to the expected increase ($17\text{--}19\text{ }\mu\text{mol kg}^{-1}$) if surface waters had maintained a constant relative equilibrium with the increasing atmospheric *p*CO₂.

Peng *et al.* (1998) reported a similar analysis for the Indian Ocean WOCE Section I8NR along 80°E (sampled in 1995) based on comparison with GEOSECS data collected in 1978. An assumed invariance of deep water (>2000 m) properties was also used to correct the GEOSECS TCO₂ data by a constant offset and values were then compared on isopycnals within the main thermocline (300–1000 m). No data-selection procedure was used, and the comparison was based primarily on station position (latitude). Only small GEOSECS-WOCE differences were observed in TCO₂-related properties such as AOU and alkalinity on the chosen isopycnals, and the TCO₂ differences between the cruises were adjusted for these differences using stoichiometric corrections. WOCE-era TCO₂ concentrations were found to be significantly higher than

the corrected GEOSECS values on all isopycnal surfaces examined down to $\sigma_0=27.2$. The temporal increase was considerably greater between 20°S and 10°S ($6\text{--}25\text{ }\mu\text{mol kg}^{-1}$) than in the equatorial zone (almost undetectable at $1\text{--}5\text{ }\mu\text{mol kg}^{-1}$).

Summary

These studies have shown that decadal time-scale increases in TCO₂ due to Excess CO₂ uptake are indeed detectable above the natural TCO₂ variability using direct measurements. Because of their reduced dependence on assumptions and models such measurement-based comparisons will ultimately become a powerful and reliable test of models' ability to assess Excess CO₂ storage. At present the need to correct historical data sets for analytical inaccuracies of the pre-WOCE data sets limits the use of such techniques to locations where deep-water Excess CO₂ build-up can safely be assumed to be negligible. If the improved data accuracy and precision attained during the CO₂ Survey can be maintained, future comparisons with the WOCE-era CO₂ Survey data set will be much more robust and can be applied more generally, as they will no longer require analytical offsets to be estimated and applied based on comparisons with deep-water values.

6.3.4.3 Within-ocean transport of inorganic carbon

Background

The meridional transport of carbon carried by the ocean circulation is of significance for global carbon cycle research for two main reasons:

- 1 The 'natural' preindustrial transport of carbon between the hemispheres is a key constraint for the modelling and interpretation of atmospheric *p*CO₂ meridional gradients (Section 6.3.2.4).
- 2 The within-ocean transport divergence of Excess CO₂ can be compared with regional estimates of Excess CO₂ storage to infer regional distributions of the air-sea uptake of Excess CO₂. As previously discussed (Section 6.3.2.1), Excess CO₂ uptake cannot be directly measured but is modelled using carbon cycle GCMs. Inferences concerning sensitivity of future uptake to climate change may be sensitive to how this uptake is modelled (Caldeira and Duffy, 2000). It will therefore be useful to have a means to validate models' depiction of this process.

To-date observation-based studies of ocean carbon transport have been conducted exclusively in the Atlantic Ocean although analysis of Pacific Ocean transports is now commencing (P. Robbins, personal communication).

Atlantic carbon transport: methods

Brewer *et al.* (1989) were the first to estimate carbon transports in a manner similar to the analysis of heat and freshwater transports by Bryden and Hall (1980) and Roemmich and Wunsch (1985). Their analysis was based on a limited data set collected in the Florida Straits and along 25°N. Martel and Wunsch (1993a) subsequently calculated carbon transports using a circulation-model-based inversion of North Atlantic data. Analyses of interhemispheric transports published by Broecker and Peng (1992) and Keeling and Peng (1995), although frequently cited in the carbon modelling literature, were simple ‘box-overturning’ calculations intended primarily to illustrate the rough magnitude of interhemispheric carbon transports. These earlier estimates are discussed in detail by Holfort *et al.* (1998). Here we focus on WOCE-era studies and also contribute a general picture of the carbon transport in the Atlantic Ocean. Stoll *et al.* (1996) and Holfort *et al.* (1998) have published meridional transport calculations using zonal WOCE sections from the northern North Atlantic (AR7E at 58°N) and the mid-latitude South Atlantic (A8, A9 and A10, 10–30°S), respectively. A study by Rosón *et al.* (2001) based on data collected along A5 (24.5°N) using the mass transport estimates of Lavín *et al.* (1998) is also discussed.

All of these WOCE-era studies used zonal sections of TCO₂ to calculate meridional carbon transports. The net transport across the bounding hydrographic sections was calculated with an approach similar to that used to estimate the North–South transport of heat and fresh water. That is:

$$T_C = \int_W^E \int_{-H}^0 \nu \cdot \rho_{S,T,P} \cdot C \, dx \, dz \quad (6.3.3)$$

where (T_C) is the transport of dissolved inorganic carbon, (ρ_{S,T,P}) is the *in-situ* density, C is the concentration of dissolved inorganic carbon, and (ν) is the velocity orthogonal to the east–west section, from the western (W) to the eastern (E) ocean boundary over the entire water column (i.e. to the

bottom depth, −H). For all sections the ocean was assumed to be in geostrophic balance. An additional wind-driven velocity (Ekman transport) near the surface (<50 m) was calculated from annual mean wind-stress data. The geostrophic velocity was calculated from the observed density field using initial estimates of a geographically variable level-of-no-motion. The approaches used to estimate the along-section distribution of the barotropic velocity component varied between the studies. In all cases the velocity field was adjusted to be consistent with long-term average measurements or estimates of western boundary mass transports.

The treatment of net mass flux across the sections is critical and has been the cause of some confusion in the literature (Holfort *et al.*, 1998). In contrast to the convention used for heat transport estimation, the carbon transport estimates for the three WOCE-era studies include the carbon carried by any net mass transport across each section. A net mass transport is required to balance: (1) net mass transport through Bering Strait (Coachman and Aagaard, 1988); and (2) removal and addition of fresh water within the Arctic and Atlantic basins. The carbon transport carried by this net mass transport can be very significant (up to 2000 kmol s^{−1} or 0.75 PgCyr^{−1} at 10–30°S, according to Holfort *et al.*, 1998). However several early literature estimates of meridional carbon transport did not include this component (e.g. Brewer *et al.*, 1989; Broecker and Peng, 1992; Martel and Wunsch, 1993a; Keeling and Peng, 1995). Such studies assumed zero net meridional mass transport in order to estimate the carbon uptake within the North Atlantic basin (i.e. ‘downstream’ of Bering Strait). Such an approach is valid for estimating carbon transport divergence from data collected along a single zonal section provided that the effects of net freshwater addition and removal within the Atlantic basin, which alter the TCO₂ concentration and therefore affect the carbon transport, are properly accounted for. Broecker and Peng (1992) and Keeling and Peng (1995) corrected for freshwater input by normalizing water-column carbon concentrations to a constant mean salinity. However, Robbins (2001) has shown that such an approach may fail to conserve salt within the North Atlantic. Furthermore, normalization to a constant salinity implicitly assumes that freshwater inputs carry no inorganic carbon.

River runoff, on the other hand, is important for the Atlantic freshwater balance and carries significant concentrations of TCO₂. It is possible that riverine inputs of carbon to the North Atlantic are not correctly accounted for with the salinity normalization used by Broecker and Peng (1992) and Keeling and Peng (1995).

Consideration of the net mass transport, including the freshwater transport divergence, is critical for comparing transports at different sections (including transport through Bering Strait) and for assessing the effects of runoff on the carbon budget. An early review of Atlantic carbon transports (Fig. 9 in Sarmiento *et al.*, 1995, see also Section 6.3.4.3) erroneously compared some observation-based transport estimates, which were based on a zero net transport assumption, with the net carbon transport through Bering Strait. As a result the net divergence of the carbon transport between Bering Strait and 18°S was underestimated by as much as 0.75 PgCyr⁻¹ (Holfort *et al.*, 1998).

In the three WOCE-era studies discussed here the carbon transports across each section and through Bering Strait can be directly compared. Most of these studies utilized sections covering the entire Atlantic from east to west. (The AR7E section of Stoll *et al.* (1996) was unable to sample the East Greenland Current due to ice-cover and did not cover transport routes via the Labrador Sea and English Channel.) All of these studies benefited from relatively high-resolution carbon data along the sections.

Present-day carbon transports are composed of a natural (or preindustrial) component and a component representing the transport of Excess CO₂. Both long-term storage (of Excess CO₂) and net air-sea exchange can balance the contemporary divergence of carbon transport. Riverine inputs and transport divergence of dissolved organic carbon (DOC) can also play a role in balancing regional budgets (Rintoul and Wunsch, 1991; Sarmiento *et al.*, 1995; Stoll *et al.*, 1996; Holfort *et al.*, 1998). The CO₂ Survey was planned at a time when a major controversy concerning the measurement of DOC in seawater had broken out. Consequently, few DOC measurements were made along WOCE sections (except, significantly, as part of the NOAA-OACES programme) and the DOC transport divergence can usually not be calculated. The contribution of this divergence to regional carbon budgets, while significant, is likely

to be relatively small compared with carbon divergences driven by air-sea exchanges and river inputs (cf. Holfort *et al.*, 1998; Sarmiento *et al.*, 1995). Recent sections collected in the North Atlantic have included DOC measurements so that its contribution will be estimable in future studies (D. Hansell, personal communication).

The Excess CO₂ transport can be estimated directly by using the preformed CO₂ techniques to calculate the Excess CO₂ (C_{excess}) distribution along a section and substituting C_{excess} for C in equation (6.3.3). Subtraction of this Excess CO₂ transport from the total contemporary transport gives an estimate of the preindustrial or natural transport (assuming ocean circulation is unchanged since 1750). For the preindustrial era it can be assumed that storage of inorganic carbon was negligible. This makes it possible to estimate the regional magnitude of air-sea and riverine carbon inputs for the preindustrial era. When compared with present-day estimates of riverine inputs and net air-sea flux based on contemporary surface $p\text{CO}_2$ data, the anthropogenic perturbation of the net air-sea flux can then be assessed on a regional basis.

Needless to say, there are many uncertainties in these approaches, some of which are difficult to quantify. Holfort *et al.* (1998) identified, not surprisingly, the Ekman transport (where this is significant) and the specification of the barotropic velocity distribution as significant sources of uncertainty. Uncertainty in specification of the deep, subthermocline circulation may have a larger effect on the uncertainty of the carbon transport than on heat transport, especially in the Atlantic Ocean. This is because significant lateral and vertical gradients in dissolved carbon concentrations are found at all depths, whereas deep ocean temperatures are relatively uniform spatially below the thermocline. Better constraints for the specification of the barotropic velocity distribution through inverse modelling must therefore be developed.

Dissolved inorganic carbon concentrations do vary seasonally in the oceans' upper layers due to the formation and degradation of organic material and the air-sea exchange of CO₂. Measurements or estimates of the variability of dissolved and particulate as well as inorganic forms of carbon in winter and summer along a section are required to address this, but such data are rarely available. The possibility of correlation of seasonal concentration

variability with seasonal variability in the mass transport must be considered in future studies. To date most carbon transport estimates are based on annual mean mass transports (e.g. annual mean Ekman transports) multiplied by inorganic carbon distributions that were measured exclusively in summertime.

Atlantic carbon transport: WOCE-era results

Holfort *et al.* (1998) constructed preindustrial, contemporary and Excess carbon budgets for the South Atlantic subtropical gyre (10–30°S) based mainly on analysis of WOCE and SAVe data. They estimated a contemporary transport of carbon southwards across 20°S of $\sim 2150 \text{ kmol s}^{-1}$ (0.81 PgCyr^{-1} ; $1 \text{ PgCyr}^{-1} = 2640 \text{ kmol s}^{-1}$). Based on sensitivity studies and the analysis of several sections, the uncertainty of this estimate was placed at about 200 kmol s^{-1} . A notable finding was that the net transport of Excess CO₂ across 20°S in the Atlantic was of the order of 430 kmol s^{-1} (0.16 PgCyr^{-1}) northwards (with an uncertainty of about 100 kmol s^{-1}). Hence the preindustrial southwards carbon transport was estimated to have been 2580 kmol s^{-1} or 0.98 PgCyr^{-1} . The net northwards transport of Excess CO₂ results from the labelling of the northward-flowing upper limb of the Atlantic's meridional overturning circulation with Excess CO₂, whereas deeper, older southward-flowing waters at this latitude still contain little Excess CO₂ (see Fig. 6.3.8). This net northward transport across 20°S is of a significant magnitude (order 50%) relative to the total estimated rate of storage of Excess CO₂ within the Atlantic north of this latitude (Holfort *et al.*, 1998).

Most recently, Rosón *et al.* (2000) have analysed carbon transports across the WOCE A5 section at 24.5°N based on the mass transports calculated by Lavín *et al.* (1998). Using their estimates, together with the other literature estimates, we are able to construct a first-order picture of the distribution of carbon transport within the contemporary Atlantic (Fig. 6.3.12). The contemporary transport is directed towards the south throughout the Atlantic with a pronounced maximum found at the 24.5°N section. This picture shows that large regional divergences in meridional carbon transport can be identified using the CO₂ Survey data. The observed carbon transport distribution is suggestive of net carbon input to the ocean within the northern North Atlantic basin

including its marginal seas (e.g. as a result of net uptake across the air-sea interface and riverine inputs) and net carbon loss (e.g. via outgassing) within the tropical Atlantic. This picture agrees qualitatively with the distribution of the net annual air-sea flux of CO₂ estimated from surface water *p*CO₂ measurements (Takahashi *et al.*, 1997). The latter indicated a transition region at approximately 20°N between regions of net CO₂ uptake in the northern North Atlantic ($> 20^\circ\text{N}$) and a CO₂ outgassing region in the equatorial and tropical Atlantic.

It should be remembered, however, that the contemporary divergence of the carbon transport can be balanced both by net carbon addition and removal (e.g. river inputs of carbon, air-sea fluxes) but also by storage of excess CO₂ within the water column. (The latitudinal distribution of the carbon storage term can be assessed from the distribution of the specific inventories of Excess CO₂ shown in

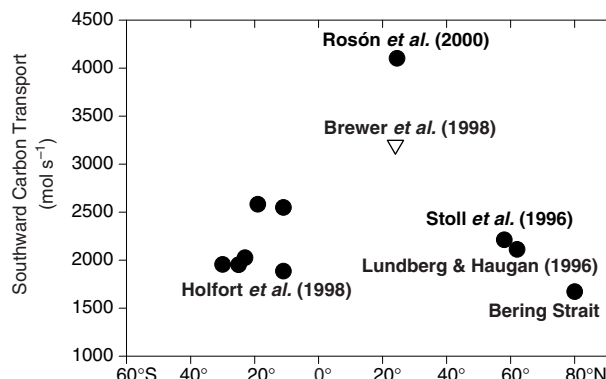


Fig. 6.3.12 Carbon transport as a function of latitude in the North Atlantic based on WOCE-era studies presented by Stoll *et al.* (1996), Holfort *et al.* (1998) and Rosón *et al.* (2000). Some prior literature estimates are also used (Lundberg and Haugan, 1996 and Brewer *et al.*, 1989). The latter estimate has been adjusted to include the carbon transport component associated with net mass transport across the section driven by the Bering Strait throughflow and the Atlantic's net freshwater balance. A significant discrepancy is seen between the transport estimates across 24.5°N of Rosón *et al.* (2000) and those of Brewer *et al.* (1989). Rosón *et al.* (2000) investigate this difference and suggest that it results from: (1) the relatively sparse transport matrix in deep water used by Brewer *et al.* (1989); and (2) possibly too high TCO₂ concentration estimates for Brewer *et al.*'s (1989) northward flowing Florida Current waters (the latter data were collected prior to the introduction of CRMs).

Fig. 6.3.1.) We are currently in the process of estimating the Excess CO₂ transport across the sections shown in Fig. 6.3.12 in order that the transport distribution in the preindustrial ocean can be estimated.

Comparisons with earlier budgets and models

Sarmiento *et al.* (1995) presented an early overview of the carbon transport and transport divergence in the North Atlantic for both contem-

porary and preindustrial times. Two budgets were presented: one based purely on results from the Princeton Ocean Biogeochemistry Model (Fig. 6.3.13a) and another (Fig. 6.3.13b) based primarily on literature estimates of carbon transports and air-sea fluxes estimated from surface *p*CO₂ data (Takahashi *et al.*, 1995). In Fig. 6.3.13c we present an updated budget based on direct transport estimates made from the WOCE section data (Holfort *et al.*, 1998), and storage

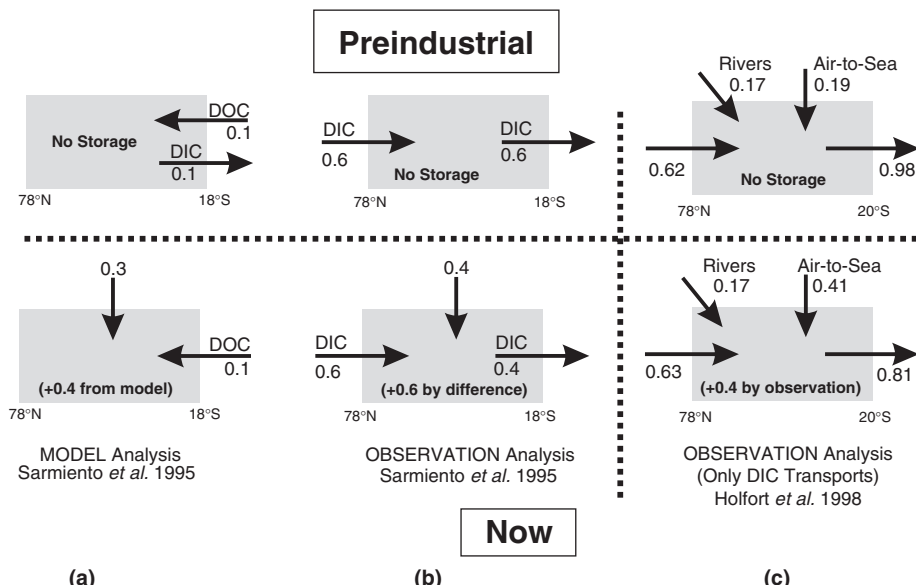


Fig. 6.3.13 Comparison of present-day and preindustrial carbon budgets (in PgCyr⁻¹) for the North and Equatorial Atlantic as summarized by Sarmiento *et al.* (1995) and this study based on the transport calculations of Holfort *et al.* (1998). DIC stands for dissolved inorganic carbon and is identical to TCO₂. DOC stands for dissolved organic carbon.

- The Sarmiento *et al.* (1995) model analysis is based on carbon transport, air-sea flux (natural and Excess components) and Excess CO₂ storage as simulated by the Princeton Ocean Biogeochemistry Model. Note that the model implies that almost all present-day CO₂ uptake in the region represents uptake of Excess CO₂ and that the net preindustrial air-sea flux for this latitude range was negligible.
- Analysis of transports and fluxes based on 'observations' as reported by Sarmiento *et al.* (1995). The total air-sea flux estimate for the present-day is based on Takahashi *et al.*'s (1995) estimates, however the Excess CO₂ component of this flux (0.38 PgCyr⁻¹) was taken from the Princeton Ocean Biogeochemical Model. The DIC inflow is the estimated inflow through Bering Strait, the DIC outflow is an average taken from literature and conference abstracts (but likely these estimates were based on an assumption of zero net flow, see text). The present-day accumulation rate was calculated by difference. The preindustrial budget was calculated by setting the storage term to zero and correcting the total air-sea flux for the model-derived Excess CO₂ component.
- An estimate based on the transport estimates through the South Atlantic (reported by Holfort *et al.*, 1998) and the Excess CO₂ inventories (reported by Gruber, 1998). Note the larger outflow due to the inclusion of net mass transport across 20°S. River inputs were estimated (roughly) by estimating an average freshwater alkalinity end-member concentration from surface water salinity-alkalinity regressions and calculating the TCO₂ concentration that would be in equilibrium with that alkalinity. River discharges were taken from Perry *et al.* (1996). I assumed that organic carbon transported via rivers is buried, or respiration and outgassing, close to shore. The storage term was estimated based on the Excess CO₂ inventories of Gruber (1998) and assuming that the mean penetration depth for Excess CO₂ is in steady state (see Holfort *et al.*, 1998 for discussion). Note that the resulting estimate of air-sea CO₂ flux, which was calculated by difference, is consistent with the completely independent estimate by Takahashi *et al.* (1995).

estimates calculated from observation-based Excess CO₂ inventories (Gruber, 1998; see Fig. 6.3.1).

Two points should be made with respect to Sarmiento *et al.*'s (1995) 'observational' budget (Fig. 6.3.13b). First their contemporary export at 18°S was underestimated due to these numbers having been calculated with an assumption of zero net mass transport across the section (Section 6.3.4.3). This means that their preindustrial transport estimate at 18°S is also significantly too low. Second, the observation-based estimates do not appear to allow for a contribution of carbon derived from riverine input within the North Atlantic. The model-based estimate (Fig. 6.3.13a) is surprising in that it implies that the Atlantic Ocean north of 18°S was neither a source nor a sink of CO₂ for the atmosphere during the preindustrial era. In other words, the model implies that the present-day net CO₂ uptake by this region is made up exclusively of the uptake of Excess CO₂. This is a counterintuitive result given that this region as a whole is a region of significant net heat loss, which would tend to drive a natural net uptake of CO₂ from the atmosphere (cf. Watson *et al.*, 1995). In this regard, it may be relevant that Murnane *et al.* (1999) show that the net northward heat transport in the Atlantic in the Princeton Ocean Biogeochemical Model is a factor of two to three times lower than heat transports estimated based on observations and transport calculations (e.g. MacDonald and Wunsch, 1996). It is by no means clear whether such a model can adequately address the net uptake and meridional transport of carbon in the Atlantic if the heat transport is poorly represented.

The North Atlantic budget in Figure 6.3.13c, on the other hand, based on within-ocean data only, implies a very different picture. Note first that for the contemporary Atlantic, the budget-derived estimate of the net air-sea CO₂ flux based on transport divergence and storage estimates, together with an estimate for riverine carbon input, very closely matches a completely independent estimate based on sea-surface *p*CO₂ data (Takahashi *et al.*, 1995). Of course both estimates have very large uncertainties, which implies the agreement could be fortuitous. Second, note that in the preindustrial era this region was a significant net sink for CO₂, in contrast with the model-based budget (Fig. 6.3.13a). Finally, note that the implied Excess CO₂ uptake estimated from the regional budget is

considerably smaller than the Excess CO₂ uptake estimated by the GCM. Indeed, in the regional budget (Fig. 6.3.13c), air-sea exchange supplies only about 50% of the Excess CO₂ storage, whereas in the model, Excess CO₂ uptake across the air-sea interface supplies >75% of the storage. This difference points to a fundamental difference in the importance attached to the advective supply of Excess CO₂ in the GCM as compared to the observation-based transport estimates. Because both Excess CO₂ and heat are carried into the North Atlantic with the upper limb of the meridional overturning circulation, this difference may be related to the underestimation of the meridional heat transport in the GCM.

The regional budget based on transport calculations suggests that the net air-sea flux of CO₂ within the North Atlantic has not increased over time by as much as one might expect based on the observed storage of Excess CO₂ within the Basin (e.g. the analysis by Gruber, 1998). The reason for this is presumably that a large portion of the upper layer waters that are presently entering the North Atlantic have already had sufficient time to approach equilibrium with the contemporary (increased) atmospheric *p*CO₂ prior to their transit across the equator. Hence the potential for these waters to absorb further additional Excess CO₂ during their transit through the North Atlantic is limited. Given that there is likely to be additional Excess CO₂ uptake across the air-sea interface between 20°S and the Equator, the transport estimates imply that most of the Excess CO₂ currently stored within the North Atlantic water column (e.g. see Fig. 6.3.1) will have actually crossed the air-sea interface in the southern hemisphere ocean prior to being carried northwards by the ocean circulation. Present carbon cycle models do not appear to replicate this situation and this requires further investigation.

A counterintuitive consequence of excess CO₂ transport

This implied role for the transport of 'pre-equilibrated' surface waters into the North Atlantic raises the previously unrecognized (and counterintuitive) possibility that certain ocean regions might release Excess CO₂ back to the atmosphere (i.e. Excess CO₂ uptake can be locally negative). In other words, the local net air-to-sea flux of CO₂ can actually be smaller now than it was in 1750, despite the fact that atmospheric *p*CO₂ has

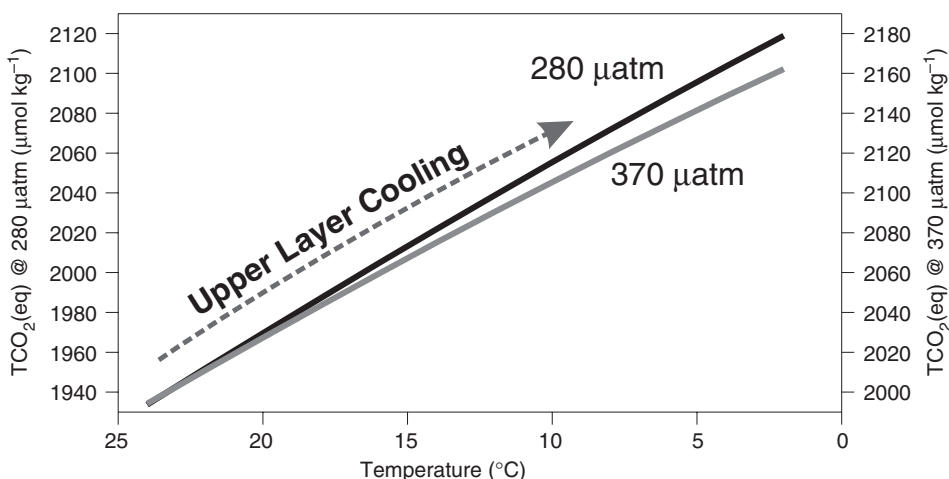


Fig. 6.3.14 The variation of the equilibrium TCO₂ concentration in seawater (salinity = 35, total alkalinity = 2300 µmol kg⁻¹) as a function of temperature. The TCO₂ concentration is shown for equilibrium with the preindustrial atmosphere (280 µatm) and for equilibrium with the contemporary atmosphere (370 µatm). Note that two separate concentration axes are used for these two different $p\text{CO}_2$ values. Both concentration axes cover the same total range but their origins are shifted relative to each other. The temperature range covers the range of temperatures encountered during the cooling of surface North Atlantic waters prior to formation of North Atlantic Deep Water.

continually increased. Such a situation can occur even in the absence of any changes in ocean circulation, ocean biology, heat flux, etc.

This possibility arises because the thermodynamic capacity of seawater to absorb further CO₂ decreases as more and more CO₂ is absorbed. This behaviour is not shared by other anthropogenic gases such as the CFCs. For non-reactive gases (e.g. the CFCs), the amount (mass) of gas that can be absorbed by the surface ocean in response to a given perturbation of its atmospheric partial pressure is given by Henry's Law. The relative air-sea partitioning is therefore constant, irrespective of the equilibrium partial pressure of the gas in the air-ocean system. This is not the case for CO₂, the uptake of which is dependent on the buffer capacity of seawater. This buffer capacity is dependent on the concentration of dissolved carbonate ion, which tends to decrease as more and more CO₂ is added to seawater. Hence the uptake capacity for CO₂ is reduced at higher $p\text{CO}_2$.

Consider a highly idealized model of the Atlantic conveyor in which the upper limb of the meridional overturning circulation (MOC) has had sufficient time to reach equilibrium with respect to contemporary atmospheric $p\text{CO}_2$, prior to crossing the equator. Within the North Atlantic these upper waters cool strongly so that CO₂ solubility

increases, tending to drive CO₂ uptake from the atmosphere into the ocean. At some point the upper waters become dense enough to sink out of the surface layer and return southwards with the lower limb of the MOC. We assume that an identical circulation and cooling occurred in both the preindustrial and contemporary ocean and that, in both cases, the upper limb of the MOC had sufficient time to pre-equilibrate with the contemporary atmospheric $p\text{CO}_2$ levels prior to entering the North Atlantic. For the contemporary ocean, with surface waters originating at elevated $p\text{CO}_2$ levels (e.g. 370 µatm), the CO₂ solubility within the North Atlantic will increase as the surface water is cooled, as it did in preindustrial times. Figure 6.3.14 shows how much an initially 'at-equilibrium' concentration of TCO₂ must increase in order to maintain equilibrium with the atmosphere during this cooling (for a fixed alkalinity). This increase is shown for two scenarios: a preindustrial scenario where atmospheric $p\text{CO}_2$ is 280 µatm and the present-day situation ($p\text{CO}_2 = 370 \mu\text{atm}$). The mass of CO₂ that must be transferred across the air-sea interface in order to maintain equilibrium between surface water and the atmosphere is now $\sim 15-20 \mu\text{mol kg}^{-1}$ less than it was for the preindustrial situation. This is a result of the decreased buffer capacity of seawater at higher

$p\text{CO}_2$ levels. Hence the contemporary local net transfer of CO_2 across the air-sea interface can in principle be smaller than that which took place in 1750, despite the fact that atmospheric $p\text{CO}_2$ levels are now much higher. It is quite possible that certain regions of the North Atlantic may indeed be behaving in this way. This behaviour is, essentially, unique to CO_2 : it does not apply for example to non-reactive gases such as the CFCs.

In reality within the North Atlantic, CO_2 does not completely equilibrate between the atmosphere and surface ocean during this cooling. Nevertheless, the buffer capacity change acts to decrease the driving force for gas exchange (i.e. the air-sea $\Delta p\text{CO}_2$) and hence tends to decrease the net flux from the atmosphere to the ocean.

6.3.5 Conclusions and outlook

The JGOFS/WOCE CO_2 Survey made use of the sampling opportunities provided by the WOCE Hydrographic Programme to collect an ocean carbon data set of unprecedented extent and quality. As such the Survey represented an excellent example of cooperation at the interface between two large global change research programmes. With respect to implementation, an early focus on measurement techniques development and standardization, quality control, and a team-oriented approach to project coordination paid off with a significant improvement in data quality compared with prior efforts.

The data resulting from this large field effort are now being used in the early stages of synthesis. Initial efforts are focusing on the distribution of the Excess CO_2 inventory for comparison with GCM-based predictions. A global picture of the ocean's Excess CO_2 inventory will likely be produced within the next 3 years. Present results are revealing important areas of agreement and disagreement with models, the causes of which need to be investigated in detail. The possibility of detecting the temporal increase of Excess CO_2 in the oceans has been demonstrated, implying that future measurement campaigns can now be designed to estimate, independently of models, the regional and global Excess CO_2 uptake. Further development, refinement and testing of methods to reliably extract the Excess CO_2 signal from ocean data are required. However, the critical point is that the Survey has provided an accurately

determined baseline against which future inventory increases can be reliably gauged.

Efforts are also underway to make use of ocean carbon data collected along WOCE heat-flux lines to investigate meridional carbon transport. A major driving force for this type of analysis is to estimate the preindustrial ocean transport, in order to clarify which natural factors may have led to a preindustrial interhemispheric gradient of atmospheric CO_2 . To date most studies of ocean carbon transport have focused on the Atlantic Ocean, however such research is also underway in the Pacific (P. Robbins, personal communication). In the Atlantic it appears that there may be significant disagreements between GCM-based transports and observed transports that need to be further investigated. Advection plays a potentially very important role for the storage of Excess CO_2 in the North Atlantic and it is therefore critical that carbon cycle models accurately parameterize advection (and heat transport), together with mixing and deep-water formation, in order to assess accurately the sensitivity of Excess CO_2 uptake to future change.

Last but not least, one of the major goals of the Survey was to provide a global description of the distribution of carbon in the oceans in order to aid the further development of models. To this end, various new methods of interpolating the still-sparse carbon-related data set in space and time are being developed. For example, Goyet *et al.* (1997, 2000) have applied interpolation and mapping tools to existing global climatologies of correlated hydrographic properties (e.g. the Levitus climatology) in order to make an initial global climatology for CO_2 -related parameters. It is expected that efforts along these lines will continue: a goal is to provide global-scale data products from the CO_2 Survey that will be of considerable use to carbon-cycle investigations of the future.

Acknowledgements

The Global CO_2 Survey was unarguably the brain-child of Peter Brewer. His scientific inspiration and imagination, as well as his hard work in the long, convoluted corridors of the US Department of Energy's headquarters, are the main reasons that the Survey took place. Support as well as imaginative programme management by John Downing and Mike Riches made the Survey a reality. I

acknowledge all the members of the US DOE CO₂ Survey Science Team, the NOAA-OACES investigators and the international CO₂ Survey investigators for their cooperation and hard work throughout the Survey. I particularly want to thank my colleague Ken Johnson for his enormous selfless effort: his contribution was central to the Survey's success. Thanks also to Rick Wilke, Craig Neill and Ernie Lewis for their superb field and laboratory work and Jürgen Holfort for his collaboration, and patient education of a chemical oceanographer concerning ocean transport. Special thanks go to Peter Guenther, Dave Keeling,

Andrew Dickson, Gabriel Rosón, Niki Gruber and Chris Sabine for providing me with materials that helped me write this chapter.

The Survey was supported actively by both the JGOFS and WOCE scientific communities. This support was of particular value during a mid-term funding crisis within the US. Finally, a major thank you is in order to the WOCE Chief Scientists, PIs, students and technicians who provided laboratory space, logistical support, and vast amounts of hard-won supporting data to the CO₂ chemists involved with the Survey.

This Page Intentionally Left Blank

SECTION

7

INSIGHTS FOR THE FUTURE

Chapter 7.1

TOWARDS A WOCE SYNTHESIS

Lynne D. Talley, Detlef Stammer and Ichiro Fukumori

525

Chapter 7.2

NUMERICAL OCEAN CIRCULATION MODELLING: PRESENT STATUS AND FUTURE DIRECTIONS

J. Willebrand and D. B. Haidvogel

547

Chapter 7.3

THE WORLD DURING WOCE

*Bob Dickson, Jim Hurrell, Nathan Bindoff, Annie Wong, Brian Arbic,
Breck Owens, Shiro Imaaki and Igor Yashayaev*

557

Chapter 7.4

OCEAN AND CLIMATE PREDICTION – THE WOCE LEGACY

Neville Smith

585

This Page Intentionally Left Blank

7.1

Towards a WOCE Synthesis

Lynne D. Talley, Detlef Stammer and Ichiro Fukumori

7.1.1 Exploiting the WOCE data set

The primary goal of WOCE is to obtain an understanding of the large-scale circulation of the world ocean, its time variability, and its impact on climate. This knowledge is necessary in its own right and will also help to improve coupled models for climate diagnosis and prediction. A global WOCE survey of the circulation has been completed. Analysis of these data sets is now proceeding, as are improvements in ocean general circulation models and developments in constraining models by the observations. The thrust of these efforts, current progress and future plans are described briefly in this chapter. The WOCE bibliography, maintained by the WOCE International Project Office, already numbers more than 1200 refereed articles at the end of 2000, many of which contribute significantly to understanding regional oceanography.

Description and understanding of the oceans at basin and global scales is being addressed during the WOCE Analysis, Interpretation, Modelling and Synthesis (AIMS) phase, as discussed extensively in various chapters of this book. Central issues include the ventilation and the renewal rates of water masses, the determination of oceanic transport of heat, fresh water and tracers, their divergences, and a description of ocean variability during the WOCE period. These activities build on the existence of and widespread access to the comprehensive and pre-assembled WOCE data set, as well as continued development of ocean general circulation models with ever-more sophisticated algorithms and enhanced resolution, and development of data assimilation methods. A number of

regional process experiments were undertaken as part of WOCE to address specific scientific questions such as the detailed mechanisms of ventilation through subduction and convection, thermocline and abyssal mixing rates, and abyssal upwelling quantification and processes.

From global WOCE (including altimetry) and pre-WOCE data sets (e.g. existing long oceanographic time series) and through improved modelling capabilities, it is evident that the ocean has vigorous variability on all time and space scales. Increasing emphasis is being put therefore on the changing ocean state and its relation to changing atmospheric forcing conditions at time scales of intraseasonal to decadal. In order to proceed towards understanding this variability, a requirement of the WOCE synthesis phase is to provide the best possible description of the time-evolving ocean state during the WOCE period. WOCE syntheses therefore merge information from various WOCE data sets to enhance our understanding of the ocean circulation in a way that is more complete than can be done from one data set or model alone. Three associated and overlapping activities are central to synthesis activities: (1) analysis, which includes the assembly and synthesis of data with ocean models, which can be as simple as geostrophy; (2) model testing and improvements, which include comparison of model results with the WOCE data set and the estimate of formal model error descriptions as input for, e.g. ocean state estimation; and (3) ocean state estimation (assimilation), by which ocean circulation models are combined with WOCE and other data sets.

The two goals of this chapter are to review the current status of data-based analyses including production of climatologies and atlases (Section 7.1.2), and to give an in-depth description (Section 7.1.4) of current progress in WOCE state estimation (data assimilation) related to regional and global estimates of the ocean state. Progress with ocean general circulation models is reviewed briefly in Section 7.1.3, as modelling is a major component of synthesis; Böning and Semtner (Chapter 2.2) and Willebrand & Haidvogel (Chapter 7.2) provide more complete reviews. We give a tentative prediction of where WOCE synthesis activities will lead and especially what progress can be expected from ocean state estimation over the next few years (Section 7.1.5).

7.1.2 Data-based analyses

Most observation-oriented research is being carried out initially using observations in combination with simple analytical or inverse models. The process of data assembly and availability status are described by Lindstrom and Legler (Chapter 3.5), as well as in the WOCE AIMS plan (WOCE International Project Office, 1997). Many of the data collection and assembly efforts will continue past the end of the WOCE AIMS phase and will provide a significant heritage for future organized programmes such as CLIVAR (Climate Variability and Predictability) or GOOS (Global Ocean Observing System). Links to the WOCE data sets and a large amount of information about WOCE, as well as the WOCE bibliography, can be found at <http://oceanic.cms.udel.edu/woce>. The 'online' data sources listed through the rest of this text can be accessed at time of writing through this central address.

Primary global WOCE data sources are hydrographic and velocity observations from research ships including Conductivity-Temperature-Depth (CTD) data, chemistry and Acoustic Doppler Current Profiler (ADCP) measurements, expendable bathythermographs (XBTs) and XCTDs deployed from merchant ships, subsurface floats, surface drifters, and current meter arrays in restricted locations. With respect to ocean variability unprecedented information is being obtained from the precise TOPEX/POSEIDON altimeter data set (Fu, Chapter 3.3). The global data sets are being combined to answer questions about large-scale processes and to provide a basic description of the

ocean during the 1990s. A number of focused regional process studies combined various observational techniques to tackle specific problems.

Where are we now with analysis of WOCE data sets? How healthy is the synthesis phase given the natural tendency for investigators to move on to the next large programme? A more general question relates to the overall 'success' of the WOCE observational programme – how appropriate and well designed were the observational programmes? Is there anything that we as a community would do differently if the planning were to begin again, at the same stage of technical development and computer power as was available in the mid-1980s? The subsections here address the large-scale circulation, process experiments and variability studies. Most of these topics are dealt with in much greater detail in other chapters of this book. Inverse model results are emphasized here because they are not included separately elsewhere in the book.

7.1.2.1 Large-scale circulation and water mass descriptions

Circulation and direct transport estimates relevant to the long-time average ocean circulation are derived from WOCE hydrographic observations and average velocity fields from surface drifters and subsurface floats. Results from many of the WOCE hydrographic sections have been published, including water mass descriptions, transports and regional studies. Some of these results are summarized in Section 4 of this book. This work will continue over the next several years, and forms one basis for the ongoing basin-oriented and global work. Tracer analysis is approached initially on a more basin-wide scale than hydrography because the value tracers add to traditional hydrographic analysis is an inventory of water mass ages and ventilation paths, which are larger-scale questions than are easily answered with individual sections. Current progress in using tracers is described by Schlosser *et al.* (Chapter 5.8). These are areas of continuing major activity for WOCE investigators and are well represented in the large WOCE bibliography.

Work on synthesizing the WOCE circulation observations into basin-wide descriptions has also begun. These take the form of property mapping and merging of all available information to produce the best estimate of circulation at all vertical levels, including both geostrophic calculations

using hydrographic data and direct velocity observations.

Lagrangian measurements

Surface drifters have revealed large-scale convergences and divergences as well as the average 'Ekman' layer flow. Using surface drifters drogued at 15 m, Ralph and Niiler (1999) produced the first large-scale map of the ageostrophic component of near-surface flow and a complete Ekman spiral, providing a basis in observations over a very large region for one of the fundamental tenets of large-scale oceanography, that of Ekman-like response to the winds. They were able to show that the ageostrophic component is proportional to wind speed rather than wind stress, and inversely proportional to the square root of the Coriolis parameter. Their result has been confirmed with a much larger data set and the results are shown in Figure 4.1.9 (Niiler, Chapter 4.1).

Subsurface floats were deployed on a global scale for the first time during WOCE and are a major element of WOCE circulation mapping. Floats have already revealed or validated major circulation patterns in many regions (Davis and Zenk, Chapter 3.2). Results from this new and growing global data set are being produced at an increasing rate. The following are a few examples. In the tropical Pacific, Davis (1998b) has shown vigorous zonal circulation with a significant seasonal component throughout the tropical region in strong contrast with the gyre circulations of the mid-latitude South Pacific. He found general agreement with the mid-latitude circulation patterns produced by Reid (1997) based on geostrophy and careful selection of reference velocities based on tracers.

In the northern North Atlantic, where subsurface float density exceeds that in any other region, Lavender *et al.* (2000c) have shown that the cyclonic boundary circulation of the Labrador Sea is accompanied by a weak but permanent anticyclonic circulation offshore of the boundary circulation (Fig. 3.2.8, see Plate 3.2.8, p. 172), with potential major ramifications for the location of mid-depth convection producing Labrador Sea Water. The stability of the North Atlantic Current and its meanders along the western boundary and of its eastward turn as it separates have been demonstrated with subsurface floats (Rossby, 1996). In the South Atlantic, Davis *et al.* (1996) used floats to examine

the validity of general circulation model results and showed the importance of eddies in the confluence of the Brazil and Falkland Currents. Boebel *et al.* (1997) used floats and other direct velocity data sets to show the westward flow of intermediate waters towards the western boundary and bifurcation of the flow at the coast (Fig. 3.2.7), confirming that the source of intermediate waters to the tropics comes from within the subtropical gyre rather than from the western boundary.

Geostrophic circulation analyses

Full assimilation of hydrographic and velocity data with models is rapidly developing (see Section 7.1.4 below). However, methods employing hydrographic observations short of full assimilation are and have been used fruitfully, including geostrophic velocity reference level choices based on geostrophic shear and water mass properties (as in McCartney, 1992; Reid, 1994), box inverse models (as in Wunsch, 1978), beta-spiral methods applied over a large area (as in Olbers *et al.*, 1985), and grid-based adjoint inverses (as in Schlitzer, 1995). These methods can also incorporate direct velocity measurements as constraints or as initial velocity choices.

The first global box inverse models have been produced recently, using zonal, pre-WOCE, hydrographic sections (Macdonald and Wunsch, 1996; Macdonald, 1998) and with WOCE data including nutrients (Ganachaud and Wunsch, 2001). Global mass transports from these two efforts are shown in Figures 7.1.1 and 7.1.2 (see Plates 7.1.1 and 7.1.2, p. 588). The deep water formation rate for the North Atlantic in both works is comparable to earlier estimates. Macdonald tested the sensitivity of the global inverse to variations in Pacific-Indian transport through the Indonesian archipelago, showing that the region of influence of the throughflow is limited to the Indian and South Pacific Ocean, without a significant effect on the global over-turning cell magnitude. Ganachaud and Wunsch's new result of a bottom water formation rate of 22 Sv (1 Sverdrup = $10^6 \text{ m}^3 \text{ s}^{-1}$) for the Southern Ocean is made possible by the new circumpolar hydrographic observations, and indicates that the higher range suggested by Schmitz (1995) is likely valid.

On basin scales, analyses including WOCE data are well underway. Perusal of the abstracts from any of the WOCE basin workshops indicates the

large amount of synthesis work, including a number of box inverse models. Reid (personal communication) has nearly completed an Indian Ocean circulation analysis similar to his previous Pacific and Atlantic works (e.g. Reid, 1994), and incorporating all WOCE Hydrographic Programme (WHP) data along with historical data. Ganachaud *et al.* (2000) focus on the Indian Ocean portion of their global inverse, showing a somewhat higher Indonesian Throughflow and lower inflowing deep water than in previous estimates, thus somewhat reducing the strength of the overturning circulation compared with previous results. They also use the inverse model results to calculate surface heat and fresh water fluxes, providing a useful constraint on climatologies. Sloyan (1997) used hydrographic sections, including several WHP sections, in a box inverse of the Southern Ocean, including air-sea and dianeutral fluxes to constrain the water mass transformations. She diagnosed the formation rate of SubAntarctic Mode Water (SAMW) north of the Antarctic Circumpolar Current (ACC), and showed that the sources of SAMW are thermocline water north of and surface water south of the ACC. The southward meridional heat transport across 30°S was dominated by the Indian Ocean.

A consortium in the US and Australia (Robbins, Wijffels, Toole, Johnson and Talley) is currently making a box inversion of the Pacific WHP data using initial reference velocity fields based on examination of all of the sections, and incorporating constraints from direct velocity measurements. Initial results for heat transports and convergences are encouraging. Robust results can be obtained despite the use of intersecting, non-synoptic sections, showing that zonal heat redistribution is larger than meridional in the South Pacific. Heat flux convergences for the many boxes formed by the intersecting sections have been compared with many different air-sea flux climatologies, showing that model-data-based climatologies are better than data-only climatologies in the data-poor southern South Pacific, and providing bias estimates for the net heat fluxes computed from the various climatologies.

For the South Atlantic, Holfort and Siedler's (2001) inversion of WOCE sections provides results for mass, heat, fresh water and nutrient transports and the conclusion that the warm water that feeds the North Atlantic Deep Water overturning is both

upper ocean and Antarctic Intermediate Water, with a higher fraction of the upper ocean waters. B. A. King (personal communication) is using a box inverse to study the southwestern Atlantic circulation; results thus far suggest that excess intermediate water enters at Drake Passage and excess surface water leaves the box, supporting Rintoul's (1991) result of net upwelling in the southwestern Atlantic.

Cunningham (2000) used a Bernoulli inverse to construct streamlines for the North Atlantic, with emphasis on the North Atlantic Current and subpolar region. He found a northward influx of 14 Sv into the eastern subpolar region and that the Irminger Basin circulation is equally fed from the North Atlantic Current west of the Reykjanes Ridge and westward flow south of Iceland. Constraints on the outflow from the Mediterranean are being produced using an inverse model in a box around the outflow, with initial results showing almost all flow exiting to the north and west despite the prevalence of Meddies to the southwest (D. Slater and H. L. Bryden, personal communication).

Work on global inversions will continue with the complete WOCE data set, providing improved estimates of air-sea fluxes, diapycnal velocities, and complete circulation schemes. These inversions are of increasing complexity, which in its limit is equivalent to state estimation. For instance, a group at the Alfred-Wegener-Institut in Germany is using a number of complementary inversion and data assimilation techniques to study the mean and time-varying circulation of the Atlantic. Continuing section and basin-oriented work will contribute to further improvement of the global-scale work. Results may also eventually be used to test basic hypotheses about ocean dynamics.

Basin-scale property mapping as an aid to circulation analyses is included in some of the above-mentioned works, particularly that of Reid. The basin atlases, described below, will include property maps. The potential vorticity field is important for planetary wave propagation (e.g. de Szoeke and Chelton, 1999) and also provides information like that of other tracers for circulation. O'Dwyer and Williams (1997) mapped the global potential vorticity field using historical data, showing the zonality of potential vorticity at mid-depth and large regions of potential vorticity that deviate from zonal at abyssal depths, including near

homogeneity in the deep North Pacific. WOCE hydrographic data allows local features to be more closely defined, as in the Indian Ocean potential vorticity fields mapped using WHP and historical data (McCarthy and Talley, 1999). The Indian Ocean potential vorticity field is zonal at all depths in the tropics; at mid-latitudes the zonality fills most of the mid-depth layer while at greater depths contours of potential vorticity follow the bathymetry; homogenization does not occur at any depth or in any region.

Transport calculations

For heat and freshwater transport calculations, the continuing battle to improve surface fluxes has not yet been won, although significant progress in producing higher-quality flux data sets has occurred in WOCE (Josey *et al.*, 1999; WGASF, 2000). The remaining large error bars on surface fluxes mean that direct transport estimates based on *in-situ* measurements remain the best. Heat and freshwater transport estimates from WHP sections and from surface fluxes are summarized in Section 6. These section-based works are preliminary, as almost all are based on single section analyses without an attempt at a unified circulation picture for at least an entire basin. Basin-wide and global transport estimates based on consistent analyses of the complete data set will likely improve the current estimates, and will also make direct ocean transport estimates available for many additional sections.

7.1.2.2 Process studies

Dedicated local observational studies clarify issues important for ocean circulation and hence ocean- and climate-related modelling. WOCE process studies have been carried out with multiple observational tools, many with integrated modelling studies. Completed are the subduction experiment in the eastern North Atlantic (Price, Chapter 5.3), a mixing experiment in the same region (Toole and McDougall Chapter 5.2), and an experiment on abyssal circulation, upwelling and mixing in the geographically restricted Brazil Basin (Hogg, Chapter 4.5). Other regions that have been studied intensively with respect to a specific process are the Labrador Sea for convection (Lazier *et al.*, Chapter 5.5), the Weddell Sea (Rintoul *et al.*, Chapter 4.6), and flow through the Indonesian passages (Gordon, Chapter 4.7). Many of these

latter experiments were carried out with both WOCE and non-WOCE resources; all contribute importantly to understanding ocean circulation processes and hence the goals of WOCE.

A regional study of North Atlantic Deep Water (NADW) formation in the subpolar North Atlantic is in the synthesis phase. Field work was started late in WOCE (in 1996) and is continuing, now as part of CLIVAR and national research programmes. Components of this work include transformation of upper ocean waters in the subpolar gyre, inflow and outflow over the Greenland–Scotland ridge, flow into and out of the Labrador Sea, and ongoing study of Labrador Sea Water formation. Learning how the thick surface layer changes properties, especially temperature and salinity, is central to the overall NADW problem. It is apparent from the new observations that this subpolar layer does not change properties in the continuous and large-scale fashion suggested by McCartney and Talley (1982) using a coarser and non-synoptic data set; rather the North Atlantic Current (subarctic front) and underlying circulation following the topography provide a complex circulation for the surface layer, with preferred regions of convection near topographic features (Talley, 1999b).

Exchange between the Nordic Seas and the North Atlantic is a central practical problem for basin- and global-scale ocean models, which do not resolve straits sufficiently to model the physics correctly there. This problem is described by Saunders (Chapter 5.6). One thrust of the ongoing NADW work is to describe as completely as possible the overflow and to model it theoretically and with high-resolution numerical models. Recent results presented at the WOCE North Atlantic workshop show in particular the presence and strength of eddies in the Denmark Strait, which might influence interpretation of moored results within the strait (Krauss and Käse, 1998; Käse, 2000; Käse and Oschlies, 2001).

7.1.2.3 Variability studies

WOCE goals include observing, where possible, the ocean's variability at time scales relevant for climate. There are many open questions, ranging from simply characterizing the variability and its spatial structure, to understanding its source and relationship to forcing. Thus in addition to the long-term average circulation and water properties, studies

include the adjustment of the ocean to changing forcing through planetary wave propagation and the eddy field, the seasonal adjustment of the circulation, and interannual (several years) and decadal phenomena using both historical and WOCE data. Relevant WOCE data sets include especially the XBT, altimetric and Lagrangian data sets, as well as extensions of hydrographic time series and current meter statistics.

A question that has been posed since the start of WOCE is to determine the representativeness of the WOCE data set. One way to phrase this is to ask how useful the large-scale fields determined in WOCE are for understanding the long-term 'mean' circulation. One obvious measure is where the WOCE period fits relative to various known interannual and decadal climate phenomena and then to determine the size of the WOCE 'mean' signal compared with the extrema of these climate phenomena. The latter requires detailed examination in every region, although one rule of thumb is that outside the tropics, temperature variations due to climate variations are on the order of 1°C in the upper ocean. These regional studies are being carried out, most notably in the North Atlantic and some regions of the southern hemisphere, as attention has shifted from describing the mean fields to unravelling the climate variability signal. WOCE provides an extremely good sampling for one period for all of these studies.

Some of the interannual and decadal climate phenomena that affect ocean properties and that have received major attention are El Niño, the Atlantic tropical dipole, the North Atlantic Oscillation, the Pacific North American mode (decadal Pacific oscillation), the Arctic Oscillation, southern hemisphere annular modes and the Antarctic Circumpolar Wave. Indian Ocean tropical and subtropical dipoles have also been described recently (Saji *et al.*, 1999; Behera and Yamagata, 2001). Knowledge of these phenomena is expanding rapidly, including their interconnections. It is likely that other patterns will also be described and that understanding and hence quantification of already-known climate phenomena will be greatly advanced in the near future. This is particularly true for the southern hemisphere, which has not yet received the full scrutiny given to the tropics and the northern hemisphere. These interannual and decadal indices are shown in Figure 7.1.3. Dickson (Chapter 7.3) provide a complete discussion of the

WOCE period in the context of several of these well-described climate cycles.

The baroclinic and barotropic planetary wave fields at seasonal and shorter time scales are evident in any basin-scale general circulation model (e.g. Semtner and Chervin, 1992; Böning *et al.*, 1996) and are observed with satellite altimetry (e.g. Stammer and Wunsch, 1999). The latter found that seasonal variations in surface slope are maximum in the tropics and northeastern Atlantic and north-eastern Pacific, and are correlated with changes in wind only in the latter two regions, contradicting earlier ideas that most of the energy outside the western boundary currents is due to local wind effects. There is much geographic variation in surface height and eddy energy, both in amplitude (e.g. historical studies by Wyrtki, 1975, and more modern equivalents) and in wave propagation as demonstrated with altimetry (Chelton and Schlax, 1996). The latter showed that phase speeds depend on more than Coriolis parameter variation, and hence must be a function of the ocean's stratification, circulation and possibly topography (Killworth *et al.*, 1997; de Szoeke and Chelton, 1999).

Gyre-scale seasonal variations in the thermocline have been shown from the WOCE high-resolution XBT programme in the Pacific. Although the phasing of the wind field with these variations has been studied, the dynamical relationship between them has not yet been unequivocally established and remains an open question. Morris *et al.* (1996) reported an annual cycle in the subtropical gyre in the western South Pacific, with isotherm slopes steepest and the geostrophic circulation most intense in late spring, 2–3 months after the maximum Ekman pumping. McCarthy *et al.* (2000) showed a puzzling phase relation between subsurface isotherm depth, Sverdrup transport and sea surface height on interannual time scales across both the South and North Pacific subtropical gyres, with surface height increasing as expected with increased Sverdrup transport, but the subsurface isotherms shoaling at the same time.

Variations in meridional heat transport at mid-latitudes are also being studied using high-resolution XBT transects. Roemmich *et al.* (2001) used a large number of transects at 24°N in the Pacific to obtain 0.76 PW of northward heat transport, with a robust error estimate of 0.12 PW; they are the first to estimate the interannual variations, at 0.3 PW, a substantial fraction of the mean.

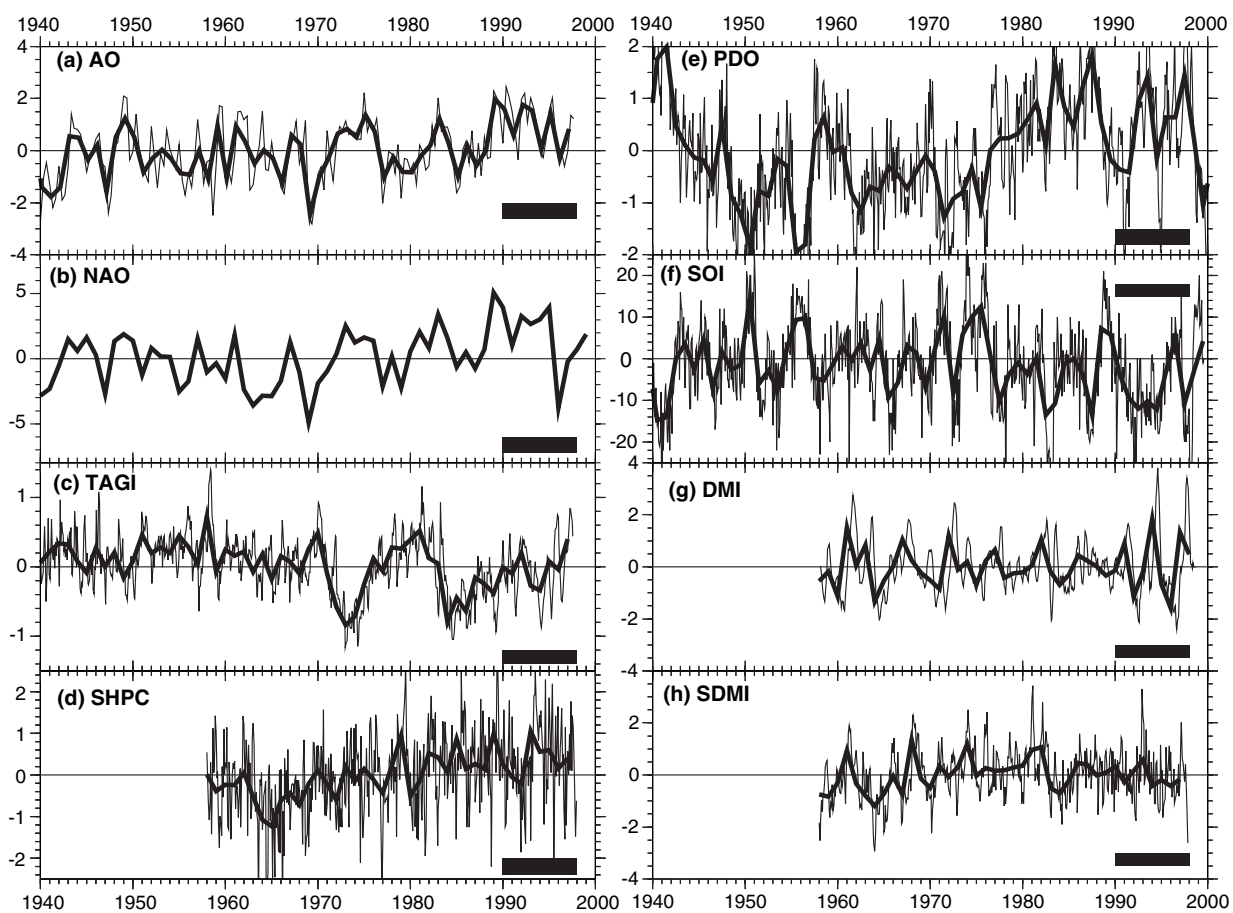


Fig. 7.1.3 Various climate indices since 1940 and the WOCE observational period (horizontal bar).

(a) Arctic Oscillation index (AO) (Thompson and Wallace, 1998); (b) North Atlantic Oscillation (NAO) (http://www.cgd.ucar.edu/cas/climind/nao_winter.html; Hurrell, 1995a); (c) Tropical Atlantic Gradient Index (TAGI) (Chang *et al.*, 1997); (d) Southern Hemisphere principal component (SHPC) (Thompson *et al.*, 2000); (e) Pacific Decadal Oscillation (PDO) (<http://tao.atmos.washington.edu/pdo>; Mantua *et al.*, 1997); (f) Southern Oscillation Index (SOI): Sea Level Pressure (SLP) at Tahiti minus SLP at Darwin, from http://tao.atmos.washington.edu/data_sets, based on Ropelewski and Jones (1987); (g) Indian Ocean dipole (DMI) (Saji *et al.*, 1999); (h) subtropical Indian Ocean dipole (SDMI) (Behera and Yamagata, 2000). Heavy line, annual average; light line, monthly values (for b–h) and January–March values (AO only). See Dickson *et al.* (Chapter 7.3) for more analysis of the climate states during WOCE.

At seasonal to interannual time scales, variation in the upper ocean structure of the tropical Pacific was a central focus for the Tropical Ocean Global Atmosphere (TOGA) programme. In other tropical and mid-latitude regions, WOCE data sets as well as time series of hydrographic, XBT and surface data dating back several decades have been used profitably to learn about these time scales. In the North Pacific, the oceanic signature of the decadal time scale has been clarified using the XBT data set collected since the 1970s and continued in the 1990s as part of WOCE (Deser *et al.*, 1996 and Schneider *et al.*, 1999b, showing the subsurface propagation of temperature anomalies around the subtropical gyre; Tourre *et al.*, 1999,

describing the decadal cycle of temperature anomalies throughout the mid-latitudes).

The magnitude of the Indonesian Throughflow is important qualitatively for the global thermohaline circulation and quantitatively for global heat budgets. Several major field projects are placing bounds on the transport, which has a large interannual range but which appears to average around 9 Sv through Makassar Strait with a range of 2.5 Sv based on current meter measurements (Gordon and Susanto, 1999; Gordon *et al.*, 1999a). Transports were minimum during an El Niño and maximum during a La Niña during the limited observational period. The Throughflow is estimated at 10–15 Sv for all passages based on pressure gauge pairs

(Chong *et al.*, 2000). Variations in the geostrophic transport through the Indonesian Throughflow based on XBTs show a mean of 5 Sv and a large seasonal and interannual component, with the transport reaching as high as 12 Sv (Meyers *et al.*, 1995), the latter in agreement with current meter measurements in Makassar Strait (Gordon *et al.*, 1999a; see also Gordon, Chapter 4.7).

Monitoring the transport of the Kuroshio south of Japan has been carried out with *in-situ* current and hydrographic observations (WOCE PCM5 array) and TOPEX/POSEIDON altimetry data (Imawaki *et al.*, 1997, 2000a, Fig. 7.3.11). The 7-year long record (1992–99) shows a mean transport of 57 Sv with large variability. Of this, 42 Sv flows on through, excluding recirculations, and has only a small seasonal signal compared with the transport of the western boundary current inferred with the theory for a wind-driven, flat-bottom ocean. Thus most of the variability of the 57 Sv is due to variations in the recirculation.

Variations in production rates and properties of various components of the NADW cell in the North Atlantic have been studied using WOCE and historical data. Some studies have employed current meter arrays in strategic locations such as the Denmark Strait Overflow and most include repeat hydrography. These studies are continuing as part of CLIVAR, and should be a part of any climate-monitoring system.

Interannual to decadal variation in water properties have been studied in most oceans where there are repeat hydrographic data, including considering the WOCE survey as a 1990s ‘data point’, for comparison with previous decades (Dickson *et al.*, Chapter 7.3).

Because the mid-latitude North Atlantic is the seat of a major decadal climate phenomenon, the North Atlantic Oscillation (NAO), considerable effort has been given to characterizing upper ocean anomalies of temperature and salinity in the North Atlantic, their relation to circulation, and relation to the NAO. Hansen and Bezdek (1996) and Sutton and Allen (1997) demonstrated the propagation of surface temperature anomalies originating near the western boundary eastward with the North Atlantic Current.

Labrador Sea Water (LSW) is a major component of the NADW that departs southward from the North Atlantic into the southern hemisphere. Ongoing hydrographic work along a section in the

Labrador Sea during WOCE has continued the time series started as Ocean Weather Station Bravo, but with coast-to-coast coverage including the boundary currents. Major shifts in LSW properties (temperature, salinity and thickness) were apparent from earlier data, but the shifts towards fresher and colder LSW in the 1990s were especially large (Lazier, 1995). The response of LSW production and properties to the NAO both within the Labrador Sea and downstream several years later in the subtropical gyre has been clearly demonstrated (Curry *et al.*, 1998), with LSW thinning and warming when the NAO index decreases, and vice versa. Sy *et al.* (1997) showed that the entire subpolar North Atlantic at mid-depth responded within 5 years to changes in convection properties in the Labrador Sea. Koltermann *et al.* (1999) compare mass, heat and freshwater transports in the North Atlantic for the 1950s, 1980s and 1990s, concluding that there was highest northward transport of warm water and southward transport of deep water in the 1980s, coinciding with a decrease in production and transport of Labrador Sea Water.

Time series at point locations were continued during WOCE at several locations, including at Bermuda and at Ocean Weather Stations Mike (Norwegian Sea) and Papa (northeast Pacific). A new time series was established at Hawaii. Ongoing hydrographic work in the western North Pacific continues long-time-series hydrographic sections there. Repeat sections have also been established in the Southern Ocean at key locations crossing the Antarctic Circumpolar Current. Many of the results obtained from incorporation of the WOCE time series, and from considering the WOCE one-time survey as a decadal data point, are described by Dickson *et al.* (Chapter 7.3).

7.1.2.4 Climatologies and atlases

The WOCE observational programmes produce both basic data sets and averaged fields (climatologies). The latter will be substantial improvements to currently available climatologies and will serve as a basic description of the mean ocean state, helping to improve and initialize circulation models. Averaged fields include means over different time periods and regions, and various sets of statistics. These statistics are necessary for the state estimation efforts described below, which will use basic data for the most part rather than climatological

data. Ultimately we hope that the best climatologies will become available from model–data combinations using the WOCE and historical data sets. Most of the WOCE data sets and expected climatologies are described here: hydrographic, upper ocean thermal, velocity and surface fluxes.

Hydrographic data

Hydrographic climatologies are being produced by a number of different groups; the principal efforts are described here. The most widely used climatologies are from the National Oceanographic and Atmosphere Administration (NOAA) (Levitus, 1982; Levitus *et al.*, 1994b), utilizing the global pre-WOCE hydrographic data set with quality control; the 1994 version includes monthly and annual climatologies of temperature and salinity on a 1° latitude by 1° longitude grid at 33 standard depths. It is now understood that averaging along isopycnals/isoneutral surfaces is superior to averaging at standard depths, as the latter results in spurious climatological features in the neighbourhood of the strong isopycnal slopes that occur at major fronts (e.g. Lozier *et al.*, 1995). New climatologies employing evolving methods and the ever-enlarging hydrographic data set will continue to be produced at NOAA.

Climatologies of the South Atlantic (without WOCE data) and South Pacific (with WOCE and historical data) have been produced by the WOCE Hydrographic Programme Special Analysis Center (WHP SAC) in Hamburg (Gouretski and Jancke, 1995, 1996), with a preliminary version for the world ocean. The input data were subjected to major quality control, and many data were adjusted using regional average temperature–salinity relations. Along-isopycnal mapping was used, using objective analysis, prior to interpolation to standard depths for the output climatology. The mapped fields are provided on a 1° grid at up to 43 standard depths in the vertical. The quality-controlled and adjusted data and the averaged fields are available online.

The Lozier *et al.* (1995) climatology for the North Atlantic is the basis for the first interactive (electronic) climatology/atlas, which is being developed further as Hydrobase by R. G. Curry (personal communication, 1999). The goal in this work is to provide the most flexible access to the data sets, allowing the investigator to construct whatever average is most useful, along with error estimates.

This then allows comparison of fields from different time periods more easily than does a single climatology (e.g. Curry *et al.*, 1998). Rigorous quality control of the input data sets is performed; this is the step that requires the most time prior to making the atlas available. The quality-controlled data sets are available through the atlas. Averaging is along isopycnals, although output can be at standard depths as well as on isopycnals. Bin averaging is used in the horizontal, but is being migrated to optimal interpolation. The interactive atlas is available for the Atlantic Ocean, and is continually updated with newly collected data sets. A North Pacific version has been produced (Macdonald *et al.*, 2001). The remainder of the world ocean is under construction and will be available in late 2000 (R. G. Curry, personal communication, 1999).

WOCE has produced the most comprehensive hydrographic data set ever collected, both in terms of global coverage and in types of observations. To present both a quick, accessible view of the data sets in cross-section and isopycnal maps of properties, atlases of hydrographic data are being constructed for each ocean basin (Pacific, Atlantic, Indian and Southern), in both printed and interactive electronic formats. Atlases are being produced by different groups for each ocean basin working in close collaboration to produce uniform products. The WOCE one-time survey station sampling strategy was optimized to resolve features along sections with a minimum of spatial aliasing, including the all-important density field for geostrophic calculations. The survey was intentionally not optimized for horizontal (along-isopycnal) coverage, given the existence of historical data that provide reasonable coverage of most regions for the basic properties (temperature, salinity, oxygen and nutrients). Therefore the isopycnal maps will incorporate high-quality historical data as well as WOCE data. The electronic atlases for the WOCE hydrographic data set will include the information in the printed atlases, links to the original data sets, and interactive plotting capability.

Upper ocean thermal fields

Upper ocean thermal fields are constructed primarily from XBT observations collected by merchant ships. This data set is much larger than the research ship hydrographic data set. A new source of upper ocean thermal data is profiles from profiling subsurface floats, which collect temperature data

when they cycle to the surface. WOCE's contribution to upper ocean thermal data sets has been three-fold: collection of XBT data; development of the profiling float; and provision of the framework for quality control and archiving of the datasets. In these efforts, only the high-resolution XBT programme (closely spaced profiles along selected seasonally repeated merchant ship transects) was entirely a WOCE programme; all other XBT work has been joint with other climate programmes, such as Tropical Ocean Global Atmosphere (TOGA), which recognize the importance of regular thermal sampling in the upper ocean for climate studies. Float work and especially technical development was also supported by other programmes in addition to WOCE, although the primary impetus and much of the funding came from WOCE.

The thermal data are used as inputs to developing coupled prediction models. The Global Temperature–Salinity Pilot Project (GTSPP), run by the National Oceanographic Data Center (NODC) in the US, is the central resource for this programme at this time. After collection of XBT data at NODC, data are quality-controlled by three data assembly centres: the US's Scripps Institution of Oceanography (SIO) (Pacific Ocean), Australia's Commonwealth Scientific and Industrial Research Organization (Indian Ocean), and the US's NOAA Atlantic Oceanographic and Meteorological Laboratory (Atlantic Ocean). Data are available online from the NODC. Profiling float data, for which collection began around 1995, are still in an experimental stage, particularly with regard to archiving; at this time only the temperature profiles are sent to NODC.

Climatologies, including monthly averages of temperature, heat storage and mixed-layer depth fields and anomalies, have been produced by the Joint Environmental Data Analysis Center (JEDAC) at SIO (White, 1995) and are easily accessible online at SIO and through the World Meteorological Organisation/Intergovernmental Oceanographic Commission site at Lamont-Doherty Earth Observatory. Analyses for the Indian Ocean are available online from CSIRO in Australia. The fields are used for basic research and comparison with models (e.g. Auad *et al.*, 1998).

Velocity data sets

Velocities are measured directly in three ways in WOCE: current meters at fixed sites, Lagrangian

drifters and floats, and acoustic Doppler current profiling. Current meter records, including means and statistics, constitute a type of climatology, albeit based only on the time period of each current meter record. Pre-WOCE (pre-1989) current meter statistics were compiled by Dickson (1990), with an update from the WOCE period compiled by Dickson, Medler and Wooltorton; both are available online through the WOCE Current Meter Data Assembly Centre (CMDAC). The CMDAC also maintains statistics for WOCE current meters.

WOCE provided a major expansion of subsurface float coverage compared with the limited deployments prior to WOCE and critical breakthroughs in float technology with the aim of global coverage. Many of the subsurface floats at mid-depth deployed in WOCE are still functioning and data are still being recorded. The next few years will see continuation and expansion of the WOCE profiling float coverage (the Argo programme), largely for the temperature (and salinity) profiling capabilities of the floats, as part of international climate programmes. Velocity (displacement) means and statistics will be available for much of the world at the end of the deployment period; results for the tropical Pacific (Davis, 1998b), southwestern Atlantic (Davis *et al.*, 1996) and Labrador Sea (Lavender *et al.*, 2000a) are already published, as described in the previous subsection. Maps will likely be included in the hydrographic atlases along with isopycnal property maps. These groups also construct dynamic topography maps from the averaged float displacements, for better comparison and integration with hydrographic data sets.

TOGA and WOCE, as well as many other funding agencies in many countries, have provided the most comprehensive surface drifter coverage yet available. These observations include water temperature as well as velocity, and many drifters also measure meteorological parameters. Surface drifter data and products are available online at this time through the surface drifter data assembly centre.

Surface fluxes

Surface flux products, including winds and components of heat and water fluxes, are computed and compiled by a number of different organizations, described by Lindstrom and Legler, Chapter 3.5, Bryden and Imawaki, Chapter 6.1, and Wijffels,

Chapter 6.2. Climatologies are available from these many different sources. The surface flux Special Analysis Center has its own data products for the North Atlantic, tropical Pacific and tropical Indian Oceans, including monthly means and anomalies for many years as well as overall means. Other primary sources are the NCEP and ECMWF re-analysis projects, climatologies produced by the Southampton Oceanography Centre (Josey *et al.*, 1999), and a large number of products accessible through the online LDEO Data System.

Discriminating between these many different products, which are relatively easy to access through the WOCE Special Analysis Center website, has been a large challenge for WOCE. A major and much-desired recent activity of the air-sea flux community has been the comparison of the many available flux products and parameterizations. An international working group designated by SCOR (Scientific Committee on Ocean Research) and the WCRP has recently completed this comparison. This Working Group on Air-Sea Fluxes (WGASF) considered the requirements for surface flux data sets, determined what data sets are currently available, and analysed their strengths and weaknesses. It is not possible to summarize their results briefly here; the reader is referred to their report (WGASF, 2000).

7.1.3 Model evaluation and development

WOCE synthesis involves the development and testing of models for a range of purposes including: (1) revealing and studying the physics of processes relevant to the general circulation; (2) simulation of the ocean circulation with good representation of eddy statistics important for defining the semi-permanent features of the circulation; (3) good simulation of the ocean circulation at resolutions that are useful for coupled climate modelling; and (4) use in ocean state estimation as a way of providing the most consistent representation of the observed fields. The first three topics are covered well in other chapters in this book.

Models used for ocean state estimation must be evaluated with respect to their realism in simulating observed processes. The models must be reasonably consistent with ocean data prior to using them for state estimation. Such comparisons are a usual step in using the models to understand and simulate processes that have not been observed as

a result of undersampling. By incorporating data in the models through state estimation, another stage of model evaluation is reached, ultimately leading also to model improvements where needed (e.g. see Fu and Smith, 1996; Stammer *et al.*, 1996). The two examples discussed here that indicate that models, at least in some of their state variables, show an intriguing agreement with what has actually been observed in the ocean.

A comparison of sea surface height time series simulated by the POCM 4C model (R. Tokmakian, personal communication; see Chapter 2.2) with data from five tide gauge stations on the west coast of the Americas is given in Fig. 2.2.3 of Böning and Semtner (Chapter 2.2). The model noticeably simulates most of the observed climate events, at least qualitatively – the correlation coefficients vary between 0.57 and 0.88. A similarly encouraging result can be found from a comparison of velocity fields from the MIT model (Marshall *et al.*, 1997a,b) with TOGA-TAO velocity data at 0°N, 140°W (Fig. 7.1.4; T. Lee, personal communication, 1999). The comparison indicates reasonable skill in simulating the time mean and variability of the upper equatorial Pacific circulation, an important prerequisite for using the model to study seasonal to interannual variability. The mean flow field shows some biases, however, in the core of the undercurrent.

Uncertainties in prescribed mixing coefficients and surface forcing fields are believed to cause these observed model-data differences. Model development efforts aim at reducing such differences in order to provide a best possible model for process-oriented studies and data assimilation. See Böning and Semtner (Chapter 2.2) and Willebrand and Haidvogel (Chapter 7.2) for detailed discussions of ongoing and anticipated model improvement activities.

It should be noted that ocean state estimation often includes estimation of surface flux fields that bring the model into consistency with ocean observations. Resulting estimates need to be consistent with meteorological centre-provided fields and their uncertainties. Inconsistencies in turn will shed light on errors in the atmospheric and ocean models.

7.1.4 Ocean state estimation

While data-based studies make use primarily of simple models, such as geostrophy and mass

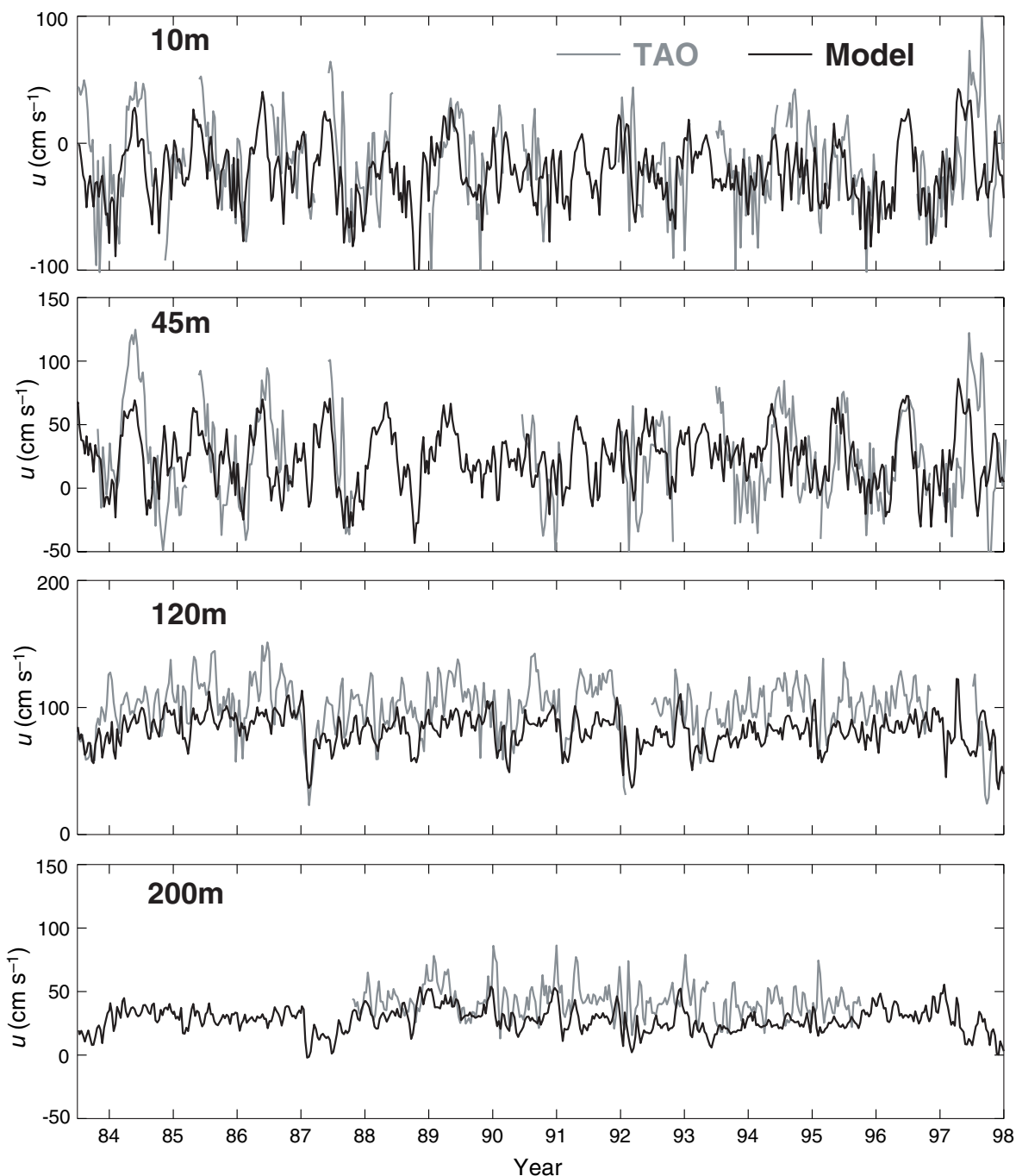


Fig. 7.1.4 Comparison of zonal velocity at four depths in the MIT model (Marshall *et al.*, 1997a,b) with current meter measurements obtained from a TOGA-TAO mooring at 0°N , 140°W . The comparison indicates reasonable skill in simulating the time mean and variability of the upper equatorial Pacific circulation, an important prerequisite for using the model to study seasonal to interannual variability. Figure courtesy of T. Lee, personal communication (1999).

conservation, numerical ocean circulation models provide a comprehensive means of analysing observations based on a more general physical principle. Moreover, a truly optimal analysis of the ocean will be achieved by utilizing all available measurements, including altimetry, hydrography, float and

drifter velocities, XBT temperature profiles, and ultimately tracer and nutrient data. Ocean state estimation, often referred to as data assimilation, involves combining these diverse observations with ocean models. We expect that such an approach will lead to estimates of the time-evolving ocean

state and its uncertainties, as well as insight into missing model physics and uncertain model parameters, such as mixing. Considerable experience is needed in assessing the realism of ocean models and in evaluating the adequacy and design of climate-observing systems. Both areas benefit greatly from data analyses and ocean state estimation during the WOCE synthesis phase, as will be described below.

Although the field of ocean state estimation is still in its early stage of development, the substantial progress achieved over the last years has given rise to great expectations of what can be attained in the near future. Several attempts are now underway to estimate the time-evolving ocean state for up to a decade from basin to global scales. Examples include synthesis activities in the Indian, Pacific and Atlantic Oceans, with many accompanied by efforts on the global scale.

7.1.4.1 The estimation problem

Thorough treatments of ocean state estimation can be found in the text books by Bennett (1992) and Wunsch (1996) and recent applications are summarized in Malanotte-Rizzoli (1996). Marotzke and Willebrand (1996) discuss details of a variety of ocean inverse models. Procedurally, ocean state estimation interpolates and extrapolates data information in space, time, and among different variables exploiting the model equations. In the process, the information is combined with other data, which further improves the description of the oceanic state. In essence, state estimation is a dynamic extrapolation as well as a synthesis and averaging process.

Figures 7.1.5 and 7.1.6 (see Plates 7.1.5 and 7.1.6, p. 588) illustrate the extrapolation and averaging effects of data assimilation. Figure 7.1.5 (see Plate) shows sea-level anomalies as a function of longitude and time in the tropical Pacific Ocean (Fukumori, 1995). The figure illustrates how assimilation (b) corrects the model (c) to be consistent with TOPEX/POSEIDON observations (a), including the magnitude of seasonal changes and the westward-propagating waves. At the same time, the assimilation eliminates noise from the data and interpolates over data dropouts (grey area in the left panel). Figure 7.1.6 (see Plate 7.1.6, p. 588) illustrates how assimilation extrapolates data information (sea level) into improvements of different properties of the ocean, such as subsurface

temperature (a) and subsurface zonal velocity (b). Sea-level information (TOPEX/POSEIDON) corrects the model (red) into an estimate (blue) that is in closer agreement with independent *in situ* measurements (black), consistent with formal error estimates (bars) (Fukumori *et al.*, 1999).

As opposed to numerical simulations, ocean state estimation is mathematically an inverse problem. That is, instead of computing properties of the ocean (e.g. model equivalent of data) given the state (numerical simulation), assimilation estimates the state based on observations. The difference between state estimation and simpler inversions described in Section 7.1.2.1 is in the underlying model dynamics. Instead of simple balances and conservation statements applied over large regions or with a steady-state assumption, data assimilation employs the full, time-dependent, non-linear physics embodied in numerical ocean circulation models at every model gridpoint. As such, the unknowns (\mathbf{x}) are independent variables of the model, such as temperature, salinity and velocity, over the entire model domain, and various model parameters, as well as uncertainties in external forcing and boundary conditions.

From a practical standpoint, the distinguishing property of data assimilation in relation to other inverse problems is its enormous dimensionality. Typical ocean models contain on the order of several million independent variables at any particular instant. The size of the problem precludes any direct method of solution and, as a result, devising methods of assimilation has been one of the central issues in ocean state estimation.

Many of the so-called ‘advanced’ assimilation methods originate in estimation and control theories (e.g. Bryson and Ho, 1975), which in turn are based on ‘classic’ inverse methods. These include the adjoint, representer, Kalman filter and related smoothers, and Green’s function methods. These techniques are characterized by their explicit assumptions under which the inverse problem is solved consistently. The assumptions include, for example, the data and model weights used in the inversion and specific statistical criteria in choosing particular ‘optimal’ solutions, such as least-squares, minimum error variance and maximum likelihood. As with ‘classic’ inverse methods, these assimilation schemes are equivalent to each other and result in the same solution so long as the assumptions are the same. Using specific weights

allows for explicitly accounting for uncertainties in models and data, as well as evaluation of *a posteriori* errors. However, because of significant algorithmic and computational requirements in implementing these optimal methods, many studies have explored alternate simpler approaches.

In practice, most inversions, and hence assimilation, amount to solving a least-squares problem. A solution is sought that minimizes a sum of differences between the knowns and unknowns, which, in state estimation, is typically written as a sum over time (t) of model–data misfits and deviations from model equations:

$$\mathcal{J} = \sum_t (y(t) - Hx(t))^T R(t)^{-1} (y(t) - Hx(t)) + \sum_t (x(t+1) - F[x(t)])^T Q(t)^{-1} (x(t+1) - F[x(t)]) \quad (7.1.1)$$

Matrices R and Q are weights that, statistically, correspond to error covariances of data ($y(t) \approx Hx(t)$) and model evolution ($x(t+1) \approx F[x(t)]$) constraints, respectively. Such an objective (cost) function mathematically defines the state estimation problem.

Recent innovations in estimation theory, combined with improvements in computational capabilities, have enabled applications of optimal estimation methods feasible for many data-assimilation problems. Various approximations have been put forth to reduce the computational requirements of statistically optimal methods such as the adjoint method (e.g. Courtier *et al.*, 1994) and Kalman filtering and smoothing (e.g. Fukumori and Malanotte-Rizzoli, 1995). Adjoint model compilers have been advanced (e.g. Giering and Kaminski, 1998) reducing programming efforts in model adjoint code generation. Examples of global data assimilation using general circulation models and employing these advances can be found, for example, in Stammer *et al.* (1997) and Fukumori *et al.* (1999). Results from an extension of the former study are further described in the following section.

The simpler approaches include optimal interpolation, ‘3Dvar’, ‘direct insertion’, ‘feature models’, and ‘nudging’. Many of these techniques originated in practical atmospheric weather forecasting, sequentially modifying model fields with observations. The methods are characterized by various *ad hoc* assumptions to effect the simplification, but their relationship to the underlying mathematical problem of equation (7.1.1) is at

times obscured. Many of the simpler approaches do not account for model and data uncertainties. Observations that lie formally in the future are generally not used in the estimate.

An important related question is how to use ocean data containing mesoscale eddy signals in the assimilation context. Many existing examples, including the one discussed below, are coarse-resolution approaches and do not permit eddies to develop in the models. In such situations eddies are considered part of data error (more precisely, model representation error) and the respective information is filtered out in the cost function. On the one hand, such removal of information can be achieved through prior data smoothing. On the other hand, prior smoothing might not be practical in general circumstances in which measurements are sparse. A proper choice of prior error covariance matrices R and Q can account for uncertainties as a function of geographic location and spatial scales, down-weighting signals associated with eddies. In comparison, there is no prior smoothing or down-weighting necessary for assimilating eddy signal containing data into eddy-resolving models so long as the two are consistent with each other. Further discussion of the importance of prior error prescription is given in Section 7.1.4.3.

7.1.4.2 Work in progress

Most of the present focus in ongoing ocean state estimation is on the time-evolving large-scale circulation using primarily altimetric observations (see Fukumori, 2000, for a review). Precise and accurate TOPEX/POSEIDON (T/P) sea surface height observations are now available on a routine basis over most of the globe from September 1992 through the present. At present information from WOCE *in-situ* data, such as XBTs, floats and the WOCE hydrography, are mostly being used as independent information to test the altimetric assimilation.

Here we mention only a few examples that seem relevant for WOCE synthesis and that can illustrate the full potential of ocean state estimation for the synthesis problem. One example is the global ocean state estimation as it results from an ongoing effort at the Massachusetts Institute of Technology, NASA’s Jet Propulsion Laboratory and Scripps Institution of Oceanography. The state estimation system is based on a general circulation model and

a dual assimilation approach utilizing the model's adjoint and an approximate Kalman filter and smoother. The forward component is the general circulation model described in Marshall *et al.* (1997a,b). The adjoint component is obtained from the forward model by using the Tangent-linear and Adjoint Compiler of Giering and Kaminski, (1998). This compiler has proven to be extremely flexible since it allows one to easily regenerate the adjoint code whenever a change in the forward code is necessary (Marotzke *et al.*, 1999). The approximate filter is an extension of the reduced-state filter described by Fukumori and Malanotte-Rizzoli (1995).

Ongoing computations include a 6-year estimate of the time-evolving ocean circulation (1992 through 1997) with up to 1° spatial resolution, a complete mixed-layer model (Large *et al.*, 1994) and an eddy parameterization (Gent and McWilliams, 1990). Data include the absolute and time-varying T/P data from October 1992 through December 1997, SSH anomalies from the ERS-1 and ERS-2 satellites, monthly mean SST data (Reynolds and Smith, 1994), time-varying NCEP re-analysis fluxes of momentum, heat and fresh water, and NSCAT estimates of wind stress errors. Monthly means of the model state are required to remain within assigned bounds of the monthly mean Levitus *et al.* (1994b) climatology. To bring the model into consistency with the observations, the initial potential temperature (θ) and salinity (S) fields are modified, as well as the surface forcing fields. Changes in those fields (often referred to as 'control' terms) are determined as a best-fit in a least-squares sense of the model state to the observations and their uncertainties over the full data period. In the current configuration, there are 10^8 – 10^9 elements in the control vector.

A schematic of this experiment is shown in Figure 7.1.7 listing the data used to constrain the model, the control variables (initial conditions and time-varying surface forcing) that bring the model into agreement with the data, and the WOCE data set that at this point is being used for testing the results. Once convergence is obtained, the next step is to include more and more of those data into the optimization procedure, starting with XBT and P-ALACE (Profiling-Autonomous Lagrangian Circulation Explorer) profiles of temperature and salinity, and continuing all the way to Lagrangian velocity measurements. Because this optimization

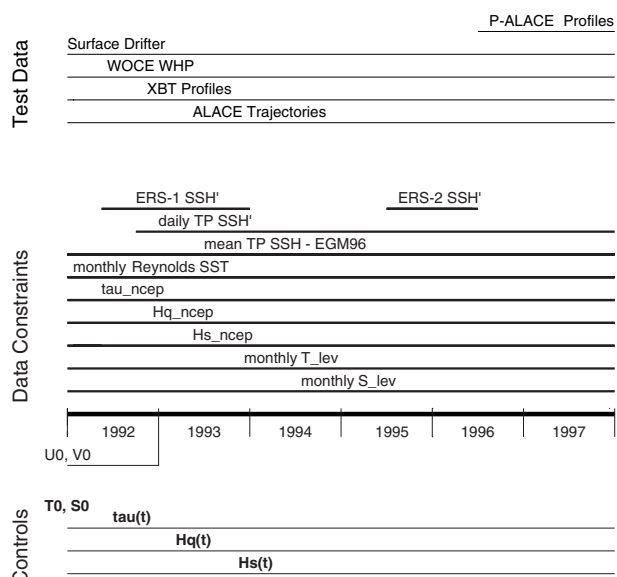


Fig. 7.1.7 Schematic of the ongoing MIT/SIO optimization. The middle part of the figure shows the data constraints and their distribution in time. The lower part shows the 'control' parameters, which are the initial T and S fields, and the time-varying surface forcing (wind stress, heat and freshwater fluxes). Those parameters are adjusted to bring the model into consistency with the data. The top part shows the WOCE data set, which at this point is being used for testing purposes of the results. From Stammer *et al.* (2000b).

is not fully converged yet, we will show here only a few preliminary results from the ongoing work. More details are given in Stammer *et al.* (1997, 2000b).

In Figure 7.1.8 (see Plate 7.1.8, p. 588) we display the time-mean of the estimated (time-varying) changes of the National Center for Environmental Prediction (NCEP) fields of the zonal windstress τ_x and surface heat flux H_q that are required to minimize model-data differences over the 6-year long assimilation period. The figure is taken from 43 iterations and is still subject to changes, as for all following figures. Changes in mean net heat flux are $\pm 20 \text{ W m}^{-2}$ over the bulk of the ocean, but can be as high as 80 W m^{-2} near boundary currents. Overall those changes are fully consistent with current understanding of uncertainties in the meteorological fields and agree especially in the tropical East Pacific with known deficiencies of stratus cover in the atmospheric model. Changes in wind stress show a strengthening of the easterlies over the tropical Pacific where the NCEP reanalysis is known to be too weak. It should be

noted that the small-scale features in the wind stress changes arise to some extent from the lack of a full wind stress error covariance function in the current optimization. The displayed changes and similar changes in meridional wind stress and fresh water flux will be used to understand and improve uncertainties in meteorological forcing fields after a fully optimized solution has been obtained.

Estimated mean fields of sea surface height and the near-surface flow field and the flow and temperature fields at 610 and 2450 m depth are shown in Figures 7.1.9 (see Plate 7.1.9, p. 588). All major ocean current structures are well represented and the largest deficiency – the lack of small-scale structures – can be primarily attributed to the still coarse resolution of the optimization. (The figure actually stems from iterations being performed on a 2° spatial resolution.)

The model–data misfit of absolute sea surface height is displayed in Figure 7.1.10 (see Plate 7.1.10, p. 588). Differences are as large as 40 cm, especially in the Southern Ocean. There is a close correlation of the residuals with independent information about the error of the EGM96 geoid model over many parts of the global ocean. The associated difference between the first-guess mean flow field at 575 m depth and that obtained from the constrained model is shown in the lower panel of the figure. In many events, changes in the large-scale current structure are apparent with maximum amplitudes about 1.2 cm s^{-1} , or a full 30% of the mean.

An important climate-related issue is the question of the amount of heat the ocean carries and how variable it is in time. To illustrate what can be expected from the estimated fields for a WOCE synthesis, Figure 7.1.11 shows the simulated convergence of zonally integrated heat transports as they result in the North Atlantic between 36° and 30°N (a) and between 25° and 10°N (b). There is a significant amount of high-frequency variation present in the regional heat flux convergence superimposed on seasonal and interannual variability. This needs to be analysed in terms of its relation to (local and remote) air–sea interactions, heat storage and, ultimately, its climate implications.

7.1.4.3 Prescribing *a priori* errors

The weights R and Q in equation (7.1.1) define the mathematical problem of ocean state estimation. Suitable specification of these weights is essential to obtaining sensible solutions, and is a

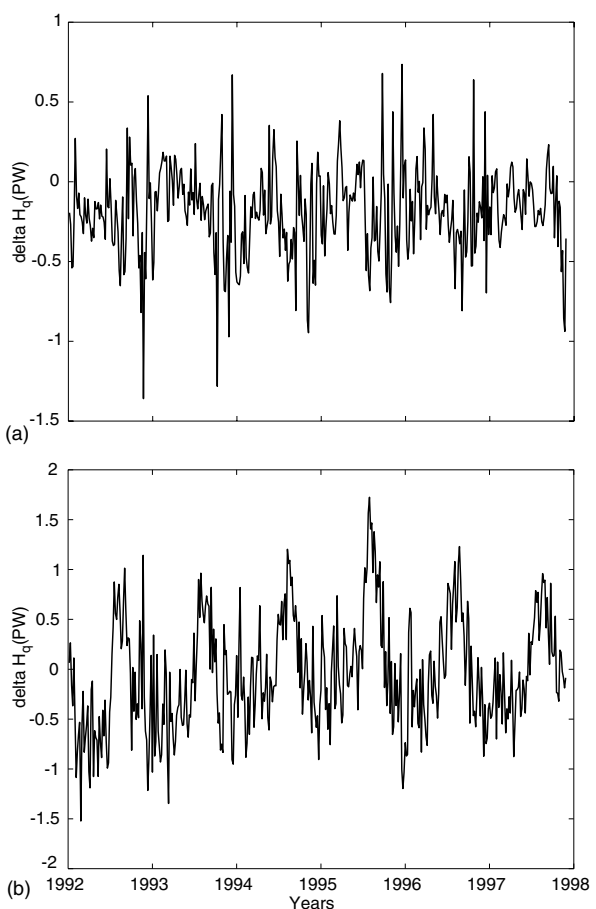


Fig. 7.1.11 The convergence of zonally integrated heat transports in the North Atlantic in the constrained MIT model. Panel (a) shows the convergence between 36° and 30°N; panel (b) shows the same field, but between 25° and 10°N. There is a significant amount of high-frequency variation superimposed on seasonal and interannual variability. This needs to be analysed in terms of its relation to (local and remote) air–sea interactions, heat storage and, ultimately, its climate implications.

fundamental issue in ocean state estimation. In fact, while further advances in computational capabilities will directly solve many of the technical issues of estimation, the improvements will not resolve the weight identification. Using different weights amounts to solving different problems, which thereby leads to different solutions. Poor specification of the weights will result in inaccuracies or even outright ‘failures’ of the estimation.

Statistical considerations suggest a suitable choice of the weights being *a priori* error covariances of the respective terms in equation (7.1.1). Specifically, weights R and Q should be regarded as errors in data and model constraints rather than merely data and model errors. In particular,

so-called representation error (e.g. Lorenc, 1986), which corresponds to real processes that are measured but are not represented or resolvable by the models, should be considered part of the uncertainties of the data constraint (R) instead of those of the model constraint (Q). Consequently, data constraint error R , like model constraint error Q , is model dependent.

Representation errors are processes beyond the model phase space. Such errors are not resolvable by models and thus inconsistent with them. Such errors include, for instance, eddies for non-eddy-resolving models, and tides and diabatic processes for quasi-geostrophic models. Forcing models to fit representation errors necessarily increases the model constraint error, Q . Consequently, such corrections can result in so-called ‘overfitting’ of models to data that lead to model degradation rather than improvement by the assimilation, in particular, for aspects of the model that are not directly measured. Therefore, representation errors should generally be considered part of data constraint error, i.e. part of the model error that cannot be corrected by data assimilation. It should be noted, however, that possible effects of representation error on processes within the modelled phase space can be corrected, because such effects, as opposed to their sources, are within the model space. For example, eddy effects on large-scale circulation as simulated by a non-eddy-permitting model can be corrected, even when the eddies themselves cannot be resolved by assimilation.

A better understanding of what models and observing systems do and do not represent is arguably one of the most urgent and important issues in estimation. While some components of representation errors are distinguishable (e.g. eddies for non-eddy-resolving models), many are not as easily identifiable because it is not necessarily clear what the model phase space really is. Even when distinguishable, a quantitative description of representation errors is often lacking. Data representation is also an issue. Many *in-situ* measurements are sparse and information on what the observations accurately resolve is often unavailable. For instance, some island tide gauge stations may not reflect conditions of the open ocean nearby. Variabilities associated with geographically or temporally offset hydrographic stations or mooring measurements are not accurately known but can provide information of the measurement’s representativeness.

Advancing model and data representations can only be achieved by improving model physics, forcing, boundary conditions, etc., or making more comprehensive observations that contribute more information. Therein lie the relative merits of modelling, observations and assimilation. Assimilation is not a panacea that can correct all model errors and compensate all deficiencies of observations. Data assimilation does not add information independent from observations or model physics, but merely allows compensation of one by the other within their common phase space essentially through averaging the two. Although assimilation provides a new dimension to ocean state estimation, results are ultimately limited to what models and observations resolve and especially our understanding of their nature.

A major difficulty in assessing model and data uncertainties has been a lack of global oceanic data sets of sufficient quality and duration. The advent of TOPEX/POSEIDON altimetry and the other systematic large-scale ocean observing systems, including those of WOCE, have made significant contributions to this end. Fu *et al.* (1993) devised a simple means of evaluating model and data errors by comparing observations and model simulations. Menemenlis and Chechelnitsky (2000) and Tokmakian and Challenor (1999) extended the approach by utilizing time-lagged model–data differences and multiple data sets, respectively. Adaptive Kalman filter methods have also been explored to estimate simultaneously from observations prior errors in addition to the oceanic state (Blanchet *et al.*, 1997).

However, error estimates resulting from these empirical methods are limited due to duration and extent of the data sets, and the methods only provide partial guidance for error specification. The validity of these and other error specifications must be carefully assessed in terms of their consistencies (e.g. Fukumori *et al.*, 1999). In the absence of a wide user community, such as exists for meteorological analyses, accurate ocean state estimation will require a concerted effort within the general oceanographic community, i.e. modellers, observationalists and assimilators alike, to quantify and assess the various assumptions that form the basis of data assimilation. Namely, what do available observations and numerical models represent, how accurately do they do so, and how do we improve upon them?

7.1.4.4 Observing system design and sensitivity studies

In order to achieve maximum return from long-term climate observations, a well-designed observing system is required. Ocean models and data assimilation systems are beginning now to support the design of such an observing system and to test its usefulness to measure climate-relevant quantities in a quantitative and yet cost-efficient way.

A posteriori errors with and without particular data sets provide one measure of the impact of certain observing systems. For instance, by comparing separate ocean estimations using different data sets, Carton *et al.* (1996b) found TOPEX/POSEIDON altimeter data to have a larger impact in resolving intraseasonal variability of the tropical Pacific Ocean than data from a mooring array or a network of XBTs.

Forward simulations also allow the testing of sensitivity of model solutions to varying forcings, initial conditions, and/or model parameters, by deducing effects of particular aspects of the circulation on other elements of the model. In comparison, the model's adjoint can be utilized to examine the reverse sensitivity, namely the dependence (rather than effect) of properties on other elements of the model. An example of such use of the adjoint is shown in Figure 7.1.12 (see Plate 7.1.12, p. 588; from Marotzke *et al.*, 1999). The figure shows the sensitivity of the MIT model's annual mean heat transport across 29°N in the North Atlantic with respect to changes in initial temperature and salinity fields near the surface and at depth, respectively. The figure clearly identifies the influence of hydrography along the boundaries on the estimated heat flux and identifies measurements along the western and eastern boundaries as the most important measurement for improving heat transport estimates at this latitude. Likewise one can study the impact of local and remote forcing fields on heat transports, or, for example, on the strength of the meridional overturning circulation or any other scientifically important quantity. Such information will lead to a better understanding of physical adjustment processes in the ocean and allow us to define key measurements required to understand the response of the ocean to atmospheric changes and to accurately measure climate fluctuations in the atmosphere–ocean system.

7.1.5 Summary and outlook

WOCE is contributing enormously to our ability to describe and understand the ocean, and to creating the technical capability needed through development and large-scale use of new observing methods, ocean models and state estimation. These tools and understanding are being carried forward as a basis for study of climate variations. Our treatment of the WOCE synthesis above was separated into a review of the more purely data-based analyses and a progress report on ocean state estimation, combining data with models and including new results. Our conclusions are also separated into these two areas.

7.1.5.1 Observation-based synthesis

WOCE was originally conceived of and designed to produce a description of the large-scale ocean circulation and its transports of heat, mass and fresh water, to understand the climatic state of the ocean and to understand the relevant processes that set that state. The practical design was for global *in-situ* coverage at the space and time scales relevant for climate, with temporal as well as complete geographic coverage, and with complementary global satellite observations. It was recognized at the outset that description of a 'mean' state is a moving target in the sense that any specific period of observations will produce a somewhat different answer, with the differences being complex and regional, depending on the state of the many different, largely uncoupled, climate modes. Several major categories of WOCE observations help to define the climate context, particularly the upper ocean thermal and satellite observations. However it is also clear, and remains clear after WOCE, that a 'mean' state is a relevant concept. The WOCE data sets and modelling are providing a major step in learning about these largest-scale processes, which one can think of as also including the statistics of the shorter time-scale variability that depends on the existence of this mean state. Inter-annual to decadal climate variations provide in most cases only about a 10% change to the mean state, with the exception of the strong ENSO conditions that affected the upper ocean in the tropical Pacific during WOCE.

The comprehensiveness of the WOCE data set both in types of measurements and geographical coverage are truly exceptional. Never before has a global view been possible, from ongoing satellite

coverage of the surface to ongoing large-scale coverage of the upper ocean, to the global description of properties, tracers and circulation at depth. Because of the massive scale of WOCE, it has generally been much more difficult to isolate specific urgent questions, leading to concerns about its being an unfocused experiment, unlike for instance the tropical Pacific experiments with a unified goal – to describe and predict El Niño. The WOCE data sets are being used to describe a plethora of questions of the same scope as El Niño; some of these problems that are first being addressed with WOCE are blossoming into larger ongoing projects. We have made an attempt in this chapter, and the attempt is made in more depth throughout this book, to cover the many different thrusts taken with WOCE data. The results are clearly accretionary. Taken as whole, even at this time, and clearly further along in the analysis, WOCE will provide many significant advances for large-scale oceanography.

A major strength of WOCE has been the collection of many different types of complementary data and development of models and investigator expertise for every basin. WOCE ‘synthesis’ means approaching individual ocean descriptions or processes using as many of the data types and modelling tools as are available and useful to the specific problem. The existence of concurrent upper ocean and satellite time series along with all of the background information at the largest scale for the WOCE hydrographic programme, as well as basin-scale and global models, has allowed a description of the time-varying response of the ocean that was not possible before. The coexistence of a complete mid-depth mean circulation from floats, along with hydrographic and process-oriented measurements and model analysis of the same regions, has meant that new and potentially important circulation features have been exposed. The coexistence of full tracer data sets, temperature/salinity and direct velocity measurements at depth is allowing significant advances in describing the mean circulation and ventilation time scales. Well-designed local current arrays with hydrographic and basin-scale float measurements have enabled major circulation elements to be quantified. One of the major advances of WOCE, quantification of the diapycnal diffusion rate (Ledwell *et al.*, 1993) and its geographic variations (e.g. Ledwell *et al.*, 2000), has been considerably

strengthened by the existence of concurrent larger-scale data sets in addition to those observations specifically designed for measuring diffusivity.

Was it useful to have undertaken the whole exercise of observing the global ocean? Models are becoming global, climate-relevant processes are global, and the existence of global data sets to test hypotheses and provide context for regional process descriptions is critical. The latter has not perhaps received proper credit. Every analysis of every regional process (using WOCE data) requires a larger-scale context (provided also by the larger WOCE data sets). Many basin-scale analyses are underway, all drawing to some extent on the context/boundary conditions provided by the larger data sets. The importance, persistence, and basic physics of various ocean processes are much more clearly revealed if they can be found and studied in more than one setting, meaning more than one basin. The particular scientific questions that will be answered by the global data sets *per se* are of the same ilk as those for each region – describing the global thermohaline circulation, global heat and property transports, global variability. All require global coverage. But how important was synopticity, even in the loose WOCE sense of coverage over about 10 years? It was important for two reasons – the most efficient way to obtain enough information to make the global estimates and the regional descriptions with global context was to do it as quickly as possible, using the same technology throughout with the same sampling philosophy. Some data sets, such as transient tracers used for ventilation studies, require a reasonable amount of synopticity.

What would have been better done differently, if anything? Better coordination could have reduced the amount of time required to cover regions. Satellite programmes that were an integral part of the description did not begin until after WOCE had started, resulting in unfortunately incomplete coverage overlap. Throughout the design and execution of WOCE there was pressure to have modellers and observers coordinate their efforts more seamlessly. However, at a practical level, this can only be accomplished if investigators have an immediate common goal that requires the integration of different approaches that each provide enough valid information to allow synergy. That this did not happen was perhaps a consequence of the state of ocean modelling, in particular

computational capabilities, at the beginning of WOCE. Remarkable advances in regional and global-scale modelling during WOCE are closing the gaps between observers and modellers. Analysis of many WOCE data sets now takes place with reference to modelling, and most importantly, the maturation of models and the collection of global data sets is allowing ocean state estimation to develop rapidly.

Should global observations continue to be taken? The answer is a resounding yes, but clearly in a different way than during WOCE. The technologies that were developed and put into widespread use during WOCE should be included, so that the next set of large-scale questions may be addressed. The community has chosen to continue working with problems that are more clearly the variability of the ocean and atmosphere, given the large data set that now exists to describe the 'mean' state. The appropriate technologies have been selected, mostly involving autonomous measurements from satellites, floats, drifters and large moored arrays with telemetry. Processes important to climate that were not explored fully in WOCE, particularly in more remote regions such as the southern hemisphere, should be pursued. Should there be a future WOCE-type hydrography survey? A complete *repetition* of WOCE hydrography in the near future is unlikely and unnecessary given the long time scales that these measurements address. However, monitoring of global carbon inventories and studying the physical and biological processes that affect them through use of transient and other tracers are best accomplished from large-scale research ship coverage at present and likely will remain so for at least a decade, thus requiring at least partial coverage through the intervening years until a new global survey is undertaken.

7.1.5.2 State estimation

Ocean data assimilation has long been a focus of theoreticians and modellers. The tremendous efforts of the community have brought us well along the way to success. There are now several ongoing WOCE-related assimilation efforts in the US, Europe and Japan. Maturation of this ongoing international work will result in fully successful WOCE syntheses. Ongoing efforts in section and box inversion and in ocean state estimation are still largely preliminary. Model resolution, spatial extent, and employed physics must further be

expanded and the entire WOCE data set must eventually be incorporated. The results so far illustrate the potential for model–data combination. Among many possible applications, one expects the production of much better estimates of the magnitudes and mechanisms of property flux divergences, and the study of oceanic biogeochemical cycles that are dependent upon the circulation.

What progress is there in ocean state estimation? At the beginning of WOCE there was little confidence in the prospect of bringing models and data together in a full ocean state estimation. It has now been shown that such a synthesis is technically feasible. Moreover, the field is rapidly migrating towards operational applications of ocean state estimation, allowing us to estimate changes in the ocean circulation on seasonal to longer climate-relevant time scales, similar to re-analysis projects in the atmospheric community.

What are the gaps in knowledge needed for state estimation? The attempt to accurately prescribe *a priori* model and data errors is as much a state estimation problem as it is a fundamental issue in data analysis and numerical modelling. Such complete statistics are likely not possible for every data type, and estimating them requires close collaboration between observers and modellers. For climate applications, our knowledge about details of the connection of the changing atmospheric forcing with changes happening in the deep ocean over hundreds of years is only rudimentary. However, if we are to estimate the deep ocean state in the presence of large climate fluctuations, such as ENSO events, model drift has to be separated from actual changes in the deep ocean due to climate changes over, say, the last 500 years. There are also many technical issues to be addressed, ranging from questions about efficiencies of methodologies, to the representation of the ocean's topography and its impact on connection between basins, e.g. in the eastern North Atlantic where the deep water is supplied through a narrow fracture zone. The representation of mixing in general is a complex question and there is hope that ocean state estimation will be able to contribute substantially to estimates of the three-dimensional and possibly time-varying mixing tensors.

What are the strategies for the future for state estimation? A number of groups around the world are developing the capability to assimilate oceanographic data. These efforts include those aimed at

estimating the state of the general circulation as part of WOCE as well as those focusing on operational applications such as mesoscale forecasting and predictions of seasonal-to-interannual climate variability. Several of the major efforts focus on operational assimilation and/or mesoscale forecasting. Various remote sensing and *in-situ* upper ocean data sets are used, such as satellite altimetry, sea surface temperature, upper ocean temperature profiles from XBTs and profiling floats, and some velocity information. Many of these data sets were collected as part of WOCE and are continuing as part of a global ocean observation system and/or CLIVAR. Recent development and expansion in assimilation activities along these lines is remarkable, and is continuing with substantial individual and agency investments of time and funding. For instance, the Global Ocean Data Assimilation Experiment (GODAE) is an international initiative centred on data assimilation and aims to conduct regular, near-real-time global data assimilation to demonstrate the practical utility of ocean observations.

Only a few ocean state estimation efforts include one of the basic WOCE data sets, hydrography, and are focused on estimating a general circulation rather than on prediction. An example of one such effort in the US, in which the coauthors (DS and IF) are engaged, is a consortium funded by NSF, NASA and ONR – ‘Estimation of the Circulation and Climate of the Ocean’ (ECCO), which is building on the already existing MIT/SIO ocean state estimation efforts and parallel ones at JPL. The central technical goal of ECCO is a complete global-scale ocean state estimation over the 15-year period 1985–2000 at the highest possible resolution (given available computer resources) along with a complete error description. But to develop the technical understanding required to incorporate all available data types, develop associated error

covariances, and to continue to improve models in support of the global estimate, ECCO is beginning with coarser-resolution global and basin-wide models and developing near-real-time capabilities in support of the climate community needs.

What is required for the future for successful state estimation? The importance of accurately prescribing *a priori* model and data errors has been discussed above in detail. Other issues include suitable access to data and computational resources. Ready availability of observations is an obvious requirement for the estimation process. Appropriate data reduction and quality control must be applied to the observations. In light of the extent of the WOCE observational data set, such processing, including data assemblage amenable for model integration, is a non-trivial task.

A major limitation for ongoing state estimation efforts in some countries is the available computational resources. In spite of advances made in practical estimation, data assimilation is computationally intensive. Even moderate-sized general circulation models strain extant supercomputers when used in rigorous state estimation. The paradigm of shared resources at supercomputing facilities has so far failed to meet the requirements of ocean state estimation in the US. An alternate means of providing the necessary computational resources is urgently needed.

Acknowledgements

Grant support from the National Science Foundation OCE-9712209 (LT), OCE-9730071 (DS) and from NASA NAG5-7857 (DS) is acknowledged as well as support from the Jet Propulsion Laboratory, California Institute of Technology, under contract with the National Aeronautics and Space Administration (IF).

This Page Intentionally Left Blank

7.2

Numerical Ocean Circulation Modelling: Present Status and Future Directions

J. Willebrand and D. B. Haidvogel

7.2.1 Remarks on the history of ocean modelling

When the WOCE programme commenced in the early 1980s, development of ocean models was heading in two different and almost mutually exclusive directions. On the one hand, models based on the Quasi-Geostrophic (QG) approximation with a small number of adiabatic layers and an idealized geometrical configuration were used to study dynamical aspects of ocean circulation on the basin scale, focusing on explicitly resolved instability processes and mesoscale eddies but excluding diabatic processes such as the thermohaline circulation (e.g. Holland, 1978). On the other hand, models based on the full thermodynamic Primitive Equation (PE) system were used to simulate the global-scale circulation in a realistic geometry, and to study the ocean's role in global climate (e.g. Bryan and Lewis, 1979). The coarse resolution of PE models prevented them from properly resolving western boundary currents and other dynamically important, sub-basin-scale processes. There was reason to expect that both lines of development would eventually converge, and a 'marriage' of both model types was actually predicted (WCRP, 1983). That prediction was subsequently realized with the completion of the WOCE Community Modelling Experiment (Bryan and Holland, 1989).

Over the last decade or so the status of ocean modelling has changed dramatically. Increased computer power has permitted gains in model resolution and integration times, the WOCE

programme has provided better observations for validation, and observational and theoretical studies have led to a better understanding and parameterization of unresolved processes. These improvements have been accompanied by a substantial increase in the size of the modelling community. Again, however, two lines of modelling exist that are fairly distinct, although both are based on the fully thermodynamic PE formulation. Models of high resolution (around 10 km) now exist that resolve energetic boundary currents and associated instability processes on basin to global scales, and which describe many aspects of the ocean circulation with a considerable degree of realism. While these models still have deficiencies (see Böning and Semtner, Chapter 2.2), they begin to give a dynamically consistent description of the ocean circulation down to spatial scales of order of the first baroclinic deformation radius. Due to the immense computing requirements, they are however restricted to relatively short integration times and/or to single ocean basins, and are thus not immediately suitable for use in climate studies.

In contrast, ocean climate models have changed only moderately. They differ from their ancestors in having somewhat better resolution (typically 100–400 km, cf. Wood and Bryan, Chapter 2.3) and moderately improved parameterizations of sub-grid-scale mixing and the effects of mesoscale eddies. The applications of these models have however greatly expanded. They are used in very long integrations for climate purposes, are often

run as part of global coupled ocean–atmosphere models, and are also coupled to biogeochemical transport models, e.g. for carbon cycle and biological production studies. By and large, ocean climate models simulate the right magnitudes for the large-scale transports of heat, carbon and other substances. However, they lack a proper representation of boundary currents and other important small- and meso-scale processes, including water mass transformation processes, which are crucial for the thermohaline circulation, and are therefore less well suited for direct comparison with ocean observations.

When looking into the future, one is tempted to draw an analogy to the situation at the beginning of WOCE, and to predict that both lines of modelling will ultimately converge. That process may take a considerable time. As we will emphasize below, the reason for this is fundamentally one of economics; despite rapid and sustained increases in computer power and availability, bridging the gap between short-term, eddy-resolving simulations and global coupled climate modelling of long duration is not achievable in the near future on the basis of current trends in computer performance alone.

The purpose of this chapter is to discuss some of the issues that the modelling community is likely to face in the next decade and beyond. While we will not cover aspects of data assimilation into ocean models (cf. Talley *et al.*, Chapter 7.1), our discussion should apply to the prognostic component of assimilation models. We begin with a discussion of the space–time scales covered by current models, and the prospects for improvement via increased computing power. Next, we review several areas wherein additional gains in model performance might be sought, including the governing equations, sub-grid-scale parameterizations, and vertical coordinates and spatial discretization. A considerable limitation on the fidelity of current ocean models is the uncertainties in forcing by, and coupling to, the atmosphere.

Lastly, as a cautionary remark, we note that in the past important developments have often occurred that were *not* anticipated at all. A striking example is the hysteresis behaviour of the thermohaline circulation, and the associated question of instability and multiple stable equilibrium states (e.g. Rahmstorf, 1995). The possibility of such a behaviour, which attracts so much interest today, was not noticed in the early planning stage of WOCE.

7.2.2 Space–time scales of ocean processes and models

The temporal and spatial scales of oceanic motions extend over many decades. A frequency–wave-number diagram is a convenient way to summarize scales of processes, even though it constitutes a linear view of a non-linear system and hence is necessarily limited in its interpretation. Figure 7.2.1 indicates the temporal and spatial scales of several relevant ocean processes. Also shown are the dispersion curves for gravity and planetary waves, in each case barotropic, and the first four baroclinic modes representative of mid-ocean mid-latitude conditions. Due to limitations in the speed and storage of computers, ocean models are restricted to certain ranges of scales; these are shown for several models typical of the present state-of-the-art (rectangles in Fig. 7.2.1).

For global climate studies, the main interest frequently is on the ocean's behaviour on spatial scales from a thousand kilometres to global, and on temporal scales from a few months to many centuries (and several thousands of years for certain palaeoclimate problems). These scales are at the heart of the thermohaline and wind-driven ocean circulation, and are explicitly resolved by current ocean climate models (labelled T in Fig. 7.2.1).

Motions on these large scales are however influenced by various smaller-scale processes. Boundary currents with a scale of 50 km at mid-latitudes constitute an integral part of the circulation. Mesoscale eddies interact with the circulation in various ways, in particular through baroclinic/barotropic instability processes, and have similar spatial scales and temporal scales of months. Obviously, ocean climate models are far from resolving these processes, which therefore have to be parameterized (see below), and even global eddy-permitting models (labelled E in Fig. 7.2.1) are presently only marginally able to account for the dynamics at the scale of the deformation radius.

At even smaller scales of a few kilometres, flows through narrow straits and deep overflows across sills can be crucial for the large-scale water mass distribution. Convection processes that are fundamental for the thermohaline circulation have scales of less than a kilometre. Ocean convection models (labelled C in Fig. 7.2.1) are appropriate to describe the latter process. Finally, turbulence and mixing (labelled L in Fig. 7.2.1) occurring at scales

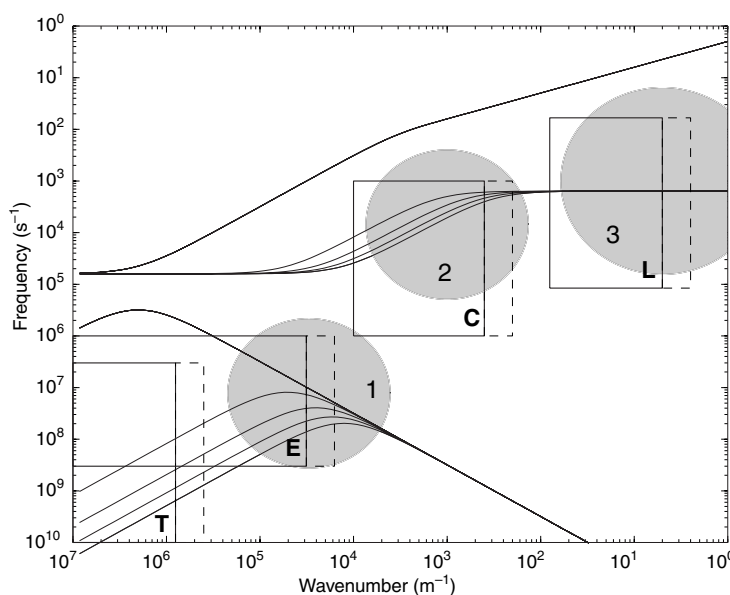


Fig. 7.2.1 Space–time scales covered by ocean models. Rectangles indicate the temporal and spatial (horizontal) scale range explicitly resolved by current ocean models: T, ocean climate models; E, global eddy-resolving models; C, ocean convection models; L, large eddy simulation of ocean mixed layer. The dashed lines indicate the expected gain in resolution within 6 years, based on an assumed doubling of CPU speed every 18 months. The thin lines are dispersion curves for linear gravity waves (upper set) and planetary waves (lower set). Each set displays the barotropic and the first four baroclinic modes, for typical mid-latitude conditions. The shaded circles give an indication of some relevant processes that are not resolved in most ocean models: 1, eddies/fronts/western boundary currents; 2, organized deep-ocean convection; 3, three-dimensional turbulence.

of metres and below dominate the surface boundary layer, and ultimately determine the overall strength of the thermohaline circulation at long time scales.

The area covered by the rectangles – which can be taken as an indication of the computational effort necessary to run the corresponding model – will increase with future advances in computer performance. In the past, computer speeds have doubled roughly every 18 months. Future increases in computing power, unless invested in increased model complexity, can be used for longer integration times or increasing the resolution. If one makes the latter choice, with the present rate of increase the model grid-size in all three dimensions could be halved every 6 years (together with halving the time step, which is usually necessary for stability reasons). Figure 7.2.1 also indicates the amount by which the spatial scale of models can be expected to expand within that time. It is obvious that closing the gap between ocean climate models and the scales of the Rossby radius, not to mention the smaller scales, can only be a very distant goal.

7.2.3 Modelling issues

Numerical circulation models ‘work’ by integrating certain equations of motion over discrete intervals in space and time (the ‘grid spacing’ and ‘time step’, respectively). Three issues therefore arise: the choice of equations that should properly represent the dynamics on the resolved scales of motion, the selection of parameterized forms to incorporate the effects of processes that are not explicitly resolved (sub-grid-scale parameterizations), and the selection of a discrete space/time grid together with the appropriate numerical algorithms. See e.g. McWilliams (1998) for a more extensive discussion.

7.2.3.1 Governing equations

With few exceptions, oceanic circulation models today are based on the hydrostatic primitive equations. These follow from the complete equations of fluid motion with several standard approximations (Haidvogel and Beckmann, 1999). First, mass conservation is approximated by the incompressibility condition (i.e. volume conservation). Note that this approximation does *not* remove all effects of the

finite compressibility of seawater from the primitive equations, although it removes sound waves from the system. Second, the related Boussinesq approximation ignores the small density variations in the ocean except for those associated with the coefficient of gravity. Both approximations together have a relative error of approximately 2%, which at present is much smaller than the errors arising from uncertainties in forcing and parameterizations or from the numerical discretization. In the future, however, one can envision a situation where such an error may no longer be negligible, in particular when very accurate sea surface height observations become available. In such a case, the anelastic approximation constitutes an alternative; this also eliminates sound waves, but has a smaller relative error of only 0.2%. See Mellor and Ezer (1995) and Dukowicz (1997) for recent explorations of non-Boussinesq effects in large-scale ocean models.

Third, the shallow water approximation – which consists of the hydrostatic approximation with the additional neglect of the horizontal component of the Coriolis vector (traditional approximation) – is valid when the vertical scale of motion H is much smaller than the lateral scale L ; its accuracy is approximately of order H/L . For ocean climate models and most eddy-resolving models, the shallow-water approximation is well justified, and the more complete equations of motion are unnecessary. For models with a very high resolution of order 10 km where this error may no longer be tolerable, Marshall *et al.* (1997b) have introduced the quasihydrostatic approximation, which keeps the full Coriolis vector and has an accuracy of $(H/L)^2$. For some process studies (e.g. of convection, three-dimensional turbulence, etc.), the shallow-water approximation is no longer valid, and non-hydrostatic models have to be considered.

Specialized alternative forms of the governing equations have also been proposed for purposes of superior computational performance, for more robust behaviour when applied using ‘open’ boundary conditions, and/or for more complete removal of high-frequency variability. Examples include the balance equations (McWilliams *et al.*, 1990; Allen, 1991), various filtered systems (Browning *et al.*, 1990), and equations based on Lattice Boltzmann methods (Salmon, 1999). None of these alternate forms has received systematic large-scale

application, and more study is warranted in this area.

Many of the models mentioned above use a rigid-lid condition to approximate the surface mass balance. This approximation essentially filters out barotropic gravity waves and long barotropic Rossby waves, and in addition introduces some subtleties in the freshwater budget (see, e.g., Huang, 1993). The overall error of the rigid-lid-approximation for the barotropic circulation is approximately given by the ratio of surface mass flux ($P-E$, in m s^{-1}) to the vertical Ekman pumping velocity, and has a magnitude of 1–3% or smaller. Much larger errors can however occur in marginal seas when the surface salinity varies between oceanic and freshwater values. The problems can be avoided by the use of the correct free-surface boundary condition, although this necessitates specialized time-stepping treatment to remain computationally competitive with rigid formulations.

7.2.3.2 Sub-grid-scale parameterizations

Perhaps the most pressing concern, particularly for global climate modelling on non-eddy-resolving grids, is the improvement of parameterizations for ‘sub-grid-scale’ processes. For coupled climate models with typical grid spacing of several hundred kilometres, these processes encompass all of the energetic mesoscale variability, as well as many sub-basin-scale thermodynamic processes such as dense overflows, deep convection and diapycnal mixing processes in boundary layers and in the ocean interior. At present, a wide variety of closure approaches is used. While traditionally many of them are largely *ad hoc* in form and motivation, dynamically motivated parameterizations are increasingly becoming available. Recent reviews of sub-grid-scale closures can be found in Haidvogel and Beckmann (1999) and Chassignet and Verron (1998).

Sub-grid-scale transports are traditionally represented by Fickian diffusion and friction, following the classical ideas of Prandtl and Kolmogorov. While the lateral coefficients and mixing lengths are often chosen to be constant or to depend on grid spacing, one may increasingly expect formulations that reflect their dependence on energy and length scale of the sub-grid-scale motions, and/or the rate of strain such as in the early work by Smagorinsky (1963). In ocean models that do not

resolve mesoscale eddies, the lateral sub-grid-scale transport mainly results from the eddies. Following the work of Gent and McWilliams (1990), there are presently intense efforts to develop parameterization schemes based on eddy dynamics and the physics of baroclinic instability. Typically, these transport parameterizations are diffusive for layer thickness (Gent *et al.*, 1995) or potential vorticity (e.g. Killworth, 1997), in addition to an isopycnal diffusion of tracers. These parameterizations should be globally dissipative in order to simulate the instability process; locally, however, this is not necessarily so, and there exist parameterizations (e.g. through topographic stress) that describe the generation of mean flow by a pre-existing eddy field (cf. Eby and Holloway, 1994). The parameterization of eddy-induced momentum transports is much less advanced. While globally it is perhaps less critical, due to the overriding geostrophy constraint, in regions of strong currents there are strong dynamical eddy-mean flow interactions that are not represented in most models.

Vertical (diapycnal) mixing in the ocean is associated with energy conversions, and parameterizations are often based on energy arguments. In their most simple form, these suggest formulating mixing coefficients in terms of stability frequency and/or Richardson number. Double-diffusive mixing has been included in models only to a limited extent, and can be important at least for the regional water mass distribution (Zhang *et al.*, 1998b; Merryfield *et al.*, 1999). It is now documented that diapycnal mixing is distributed rather inhomogeneously, and is concentrated over regions of rough topography (Polzin *et al.*, 1997), a fact that so far has not been properly accounted for in models. Tides are among the likely causes for that inhomogeneity (Munk and Wunsch, 1998), and the parameterization of mixing might be facilitated in a model that includes both the circulation and the tides.

The surface mixed layer has received special attention because of its important role in air-sea exchange. The ocean modeller can now choose from various Bulk models of the Kraus-Turner type, models with specified exchange as Price-Weller-Pinkel (Price *et al.*, 1986), Pacanowski and Philander (1981), or KPP (K-profile parameterization; Large *et al.*, 1994), TKE (turbulent kinetic energy) schemes (Gaspar *et al.*, 1990), and various levels of second-order closure schemes (Mellor and

Yamada, 1982). A systematic intercomparison of the properties, behaviour and accuracy of these parameterizations in the context of circulation models is lacking, and it is not entirely clear how one would go about doing so for air-sea coupling on the decadal time scales of interest to climate modelling.

The diapycnal mixing across isopycnals in the ocean is very weak. In a model based on isopycnal layers, diapycnal mixing can be easily controlled. For other classes of numerical models, in particular for geopotential and terrain-following coordinate models, weak diapycnal mixing may be difficult to achieve, and may depend on the rotation of the mixing tensors away from the native lateral coordinate directions. Horizontal and along-sigma mixing has long been the default for these classes of models; however, algorithms for stable and conservative isopycnal rotation of diffusion tensors are now available (Griffies *et al.*, 1998).

Parameterizations are not only needed to represent unresolved physical processes, but also to compensate for deficiencies of the numerical algorithm. Monotonicity and positive definiteness are important characteristics of a tracer distribution, but not necessarily a property of numerical algorithms. The choice of diffusive closure is therefore closely allied with the form of the discrete horizontal advection operator (e.g. Shchepetkin and McWilliams, 1998). Also, dissipative parameterizations are necessary to check numerical instabilities. These requirements may best be satisfied by biharmonic or higher-order operators, with viscous coefficients chosen adaptively, e.g. such that grid-Reynolds and/or grid-Peclet numbers are $O(1)$. For the credibility and acceptance of model results it seems important to state explicitly whether a parameterization is primarily physically based or numerically required.

A strong test of a sub-grid-scale closure would involve a high-resolution simulation (using the 'complete' equations of motion) that resolves the processes under consideration, followed by a demonstration that a coarse-resolution experiment with the new parameterization gives quantitatively identical net (i.e. large-scale and/or time-mean) results; however, this sort of systematic testing is not often performed. The role of such simulation studies, including the application of large-eddy simulations (e.g. Wang *et al.*, 1998), will become increasingly important in the future.

7.2.3.3 Vertical coordinate systems

The choice of the vertical discretization is of particular importance for ocean circulation models. Currently, a variety of forms are used. Among these are models featuring alternative treatments of topography and the vertical coordinate. Examples include vertical coordinate systems based upon geopotential levels, isopycnal layers, and topography-following ('sigma') surfaces. While the first of these approaches is still the most prevalent, all three have by now been applied successfully to large-scale circulation modelling (Willebrand *et al.*, 2001). Nevertheless, all three approaches have inherent limitations, including poor convergence upon vertical grid refinement over topography, spurious pressure gradient errors, poor representation of vertical structure in shallow or weakly stratified regions, and/or excessive diapycnal diffusion.

For models expressed in geopotential coordinates, the form of the topography changes with vertical resolution and placement of the grid boxes, especially in regions with very gentle and very steep topographic slopes. Some flexibility exists in choosing the levels, although a grid spacing that varies according to a smooth analytic function has some formal advantages (Treguier *et al.*, 1996). However, it is usually not possible to find a single discretization that is simultaneously accurate for both topography and stratification. Convergence of the numerical solution under refinement of the vertical grid is also very slow for stepwise approximations to the underlying bathymetry (Haidvogel and Beckmann, 1999). Spatial approximations that remove the staircase representation – e.g. the sigma coordinate method (see below) or the use of 'shaved cells' (Adcroft *et al.*, 1997) – seem to avoid this problem.

A geopotential coordinate model initialized with a uniform barotropic (vertically unsheared) flow field over a sloping bottom will, in the presence of finite horizontal viscosity, undergo an artificial energy transfer from the barotropic to the baroclinic mode on the deep side of each topographic step. This spurious generation of vertical shear is proportional to the prescribed eddy coefficient and the relative change in fluid depth over one grid size.

Though free of the foregoing types of errors, a problem of terrain-following coordinate systems is the possibility of significant systematic errors in the horizontal pressure gradients (Haney, 1991;

Beckmann and Haidvogel, 1993; Mellor *et al.*, 1994). These errors arise due to the splitting of the pressure gradient term into an 'along-coordinate surface' component and a 'hydrostatic correction'. Unfortunately, both terms are large, and cancellation of the hydrostatic resting pressure is not exact, due to numerical truncation errors in the two terms. The resulting pressure gradient errors depend on the steepness of the topography, both the horizontal and vertical resolution, and the strength of the stratification. In addition, topographic smoothing is often necessary to ensure stable and accurate simulations using realistic bathymetry. Interestingly, the relative change in fluid depth over a single grid step is also found to be related to the robustness of the results from terrain-following models (Beckmann and Haidvogel, 1993).

Models using isopycnic coordinates have their own unique limitations. Chief among these are the need to handle vanishing layer thicknesses and/or isopycnals intersecting topography, the difficulty in representing intrinsically non-isopycnic processes that occur (e.g.) at the ocean surface, and pressure gradient errors (similar to those that arise with terrain-following models) when compressibility effects are considered. The first of these can in principle be handled with specialized advection schemes, though this treatment is formally of low order and hence of reduced accuracy. The latter errors can be substantially reduced (though not fully eliminated) by various corrective methods (e.g. Eden and Willebrand, 1999; Sun *et al.*, 1999).

In the future, important gains are likely to be made by further innovations in the area of vertical coordinates. In particular, it is in principle feasible to design new coordinate systems that merge the best properties of the three coordinate treatments currently in use. Such improved coordinates would likely be nearly geopotential at the ocean surface in order to provide uniform resolution of the oceanic mixed layer, would be quasi-isopycnal in the bulk of the oceanic interior in order to limit spurious diapycnal mixing, and would more closely follow bottom topography in regions of strong slopes in order to more accurately incorporate the constraints of underlying bathymetric features. Several groups are currently exploring approaches to such hybrid vertical coordinates, and their experience with these new systems is eagerly awaited.

7.2.4 Atmospheric forcing and coupling

Dynamically, the ocean is forced at the surface through the fluxes of momentum, heat and fresh water. Errors in these fluxes, which are only known to limited accuracy (cf. Liu and Katsaros, Chapter 3.4), constitute a primary source of model error, and future improvements in accuracy are most urgent. Furthermore, the fluxes depend on the state not only of the atmosphere, but also of the ocean. This dependence represents the fundamental rationale for the two-way coupling of both systems, and introduces a conceptual problem for the flux formulation when an ocean model is operated in stand-alone mode.

7.2.4.1 Local coupling

The flux of momentum is the principal driving force for the ocean circulation. Except for a weak dependence of the drag coefficient on near-surface atmospheric stability, and hence effectively on sea surface temperature, the wind stress depends only on atmospheric parameters. Hence the momentum flux coupling is essentially one-sided, and the wind stress can be specified for ocean-only models. For several aspects of the large-scale circulation, e.g. for upper ocean transports, the dependence of circulation variables on wind stress is approximately linear. In low latitudes, the accuracy of the wind stress is a limiting factor for the accuracy of model simulations. In high latitudes, the direct wind effect on the circulation is somewhat weaker, but changes in surface density, through wind-induced mixing or through advection of sea-ice, can significantly influence the thermohaline circulation, as discussed by Mauritzen and Hakkinen (1997).

The flux of heat constitutes the main driving force for the thermohaline component of the circulation, and is likewise important for the atmospheric circulation. The net flux of heat depends both on atmospheric parameters as well as on Sea Surface Temperature (SST), and hence constitutes a true coupling of both systems. The heat content within the ocean is conserved, and obviously even a small but systematic error in the basin-average surface heat flux will in time have a big effect on the overall heat budget. Moreover, errors in heat flux can significantly distort the oceanic temperature distribution and hence its circulation patterns. This has been demonstrated in an Atlantic model driven with fixed mean heat fluxes derived from

the COADS (Comprehensive Ocean–Atmosphere Data Set) data, where the oceanic response became completely unrealistic after a few decades of integration (Schiller, 1995).

The net freshwater flux constitutes an important forcing for the thermohaline circulation. Its dependence on ocean–atmosphere parameters corresponds to that of heat flux. Note that since the freshwater flux does not depend on surface salinity, the (frequently employed) replacement by a restoring condition for surface salinity has therefore no physical justification. As discussed by Wijffels (Chapter 6.2), the accuracy of observed estimates is far from satisfactory. As the overall salt content of the ocean is conserved on usual oceanic time scales, systematic errors in the freshwater budget add up and lead to a drift in the salinity distribution.

7.2.4.2 Large-scale coupling

The difference in time scales between atmospheric and oceanic motions leads to a fundamental difference when either system is considered in stand-alone mode, with the other system prescribed. The atmospheric time scale is short compared with that of the ocean, and hence it is sensible to run an atmosphere-only model to study atmospheric response to SST changes, by using the bulk formulae with prescribed SST. For ocean-only models, the corresponding procedure would be to prescribe the atmospheric parameters in these expressions. Such a procedure would, however, ignore the rapid atmospheric reaction to SST changes, and lead to rather unrealistic fluxes. This may be acceptable as long as only the sensitivity of the ocean model is considered, but is clearly unacceptable for climate variability studies.

In principle, air–sea coupling on climate time scales can only be properly simulated through coupled ocean–atmosphere models (Wood and Bryan, Chapter 2.3). Because these are extremely demanding in terms of computational resources, at least for investigations of qualitative aspects of ocean climate variability, there is some value in intermediate approaches that attempt to formulate explicitly the atmospheric reaction, or more precisely the reaction of the various fluxes, to SST changes. The situation is perhaps most obvious for the flux of heat. The bulk formula that expresses the net heat flux in terms of SST and atmospheric parameters is often used in a linearized form,

where the SST is restored to a prescribed temperature T^* with a coupling strength λ , both of which depend on atmospheric parameters. The coupling strength mainly reflects the temperature dependence of latent heat flux, and would take typical local values around $50 \text{ W m}^{-2} \text{ K}^{-1}$. A consequence of such a value is that the model's sea surface temperature cannot be very different from the specified temperature T^* . As was noted by Bretherton (1982), the coupling with the atmosphere must become weaker with increasing spatial scales. At small scales, the atmospheric response to SST anomalies can effectively be removed by horizontal transports, and hence a large flux can persist. At the global scale, the only process that can remove heat from the atmosphere is long-wave radiation, which corresponds to a much weaker coupling of $2\text{--}3 \text{ W m}^{-2} \text{ K}^{-1}$.

As the strength of this ocean–atmosphere coupling is crucial for the stability of the thermo-haline circulation, this issue is important for ocean climate studies. The most simple and frequent recourse is to use an intermediate value of λ that is representative of the scale of interest. Alternatively, the scale dependence of the coupling can explicitly be included, based on approximations of the atmospheric heat budget (Rahmstorf and Willebrand, 1995). Similar approximations can be made for the atmospheric water transport (Rahmstorf *et al.*, 1996). Energy balance models (e.g. Lohmann *et al.*, 1995) constitute a further step in this hierarchy, permitting a somewhat more accurate description of the thermodynamic processes and of the mean horizontal transports in the atmosphere.

Formulations such as those mentioned above describe a dynamically somewhat passive atmosphere that reacts only by transporting anomalies in the heat and freshwater budgets. While locally the atmospheric momentum budget is indeed independent of SST, atmospheric circulation patterns on larger scales may well be influenced by SST. This is particularly the case for coupled oscillation modes of the ocean–atmosphere system. Recently, some attempts have been made to formulate the dynamical atmospheric response to changes in SST and also to the thermocline depth, in order to simulate El Niño (Eckert and Latif, 1997) or decadal variability modes in the North Pacific (Münnich *et al.*, 1998). The extent to which such formulations can be used to investigate climate variability has not yet been established.

7.2.4.3 Other coupled components

Coupled modelling of (e.g.) global biogeochemical cycles further enhances the central importance of spatial representation for two reasons. First, the natural scales of variability for biogeochemical interactions are often much finer than those characterizing the physical system itself; this necessitates finer resolution of these coupled fields for comparable levels of accuracy. Second, the regional distributions of biogeochemical interactions are highly heterogeneous and often highly localized spatially – e.g. on the narrow continental shelves of the world's oceans.

In recent years, the increasing need for multidisciplinary research tools has led to the adaptation of ocean circulation models for use in coupled physical–biogeochemical studies and in other multi-component configurations. Several mutually related areas of coupled modelling are currently being actively developed within the scientific community, including coupled modelling systems for the global climate system (atmosphere, sea ice, ocean, land); and the coupling of physical with biological, chemical and/or geological models to study certain aspects of environmental cycles and dynamics – e.g. the carbon cycle, plankton dynamics, and sediment transport. While certain classes of problems (e.g. coupled climate modelling) have a short history and vigorous model development and comparison continues, other classes of problems are relatively unexplored. Trenberth (1992) and Hofmann and Lascara (1998) offer recent overviews.

These coupled model studies will place more demands on the physical completeness, numerical integrity, and sub-grid-scale parameterizations of ocean models. Generalized coupling strategies, sophisticated parameterization schemes, and further attention to parallel computer performance are all necessary ingredients for future progress in these interdisciplinary areas. Finally, given the relative dearth of observational data (in particular, for the bio-geochemical variables), advanced forms of model/data fusion (data assimilation; see Malanotte-Rizzoli, 1996) are essential for the regional-to-global-scale simulation systems envisioned for the future.

7.2.5 Organization of model development

Numerical ocean models are highly specialized tools that have the form of a computer program

with typically 100 000 or so lines of code. Compared with other specialized tools, e.g. instruments for measuring physical or chemical variables in the ocean, two differences are noteworthy.

First, modelling groups often develop their own tool, rather than taking an existing one from the shelf. As described above, model development requires that choices be made on governing equations, model resolution, parameterizations, numerical representation, and other things, and that these choices be implemented efficiently. Traditionally, model development takes place in relatively small groups, mostly at universities or government research laboratories. Extensive testing and validation of a model is, in principle, necessary before it can be applied to the problem one wants to solve, and the development of a new model from scratch needs many person-years. One therefore can argue that the principal limitation for model development arises from the limited manpower in the field, and that having an overly large model diversity may not be the most efficient use of human resources. A more efficient way is the construction of 'community models' that can be used by many different groups. These models ideally have a flexible modular structure so that each user can develop modules, e.g. for parameterizations, specific numerical algorithms such as advection schemes or solvers for elliptic equations, and others. Modules developed by different groups are freely exchanged and stand in competition with each other, so that the model's evolution is governed by the usual scientific selection process rather than by the decisions of one individual or group. The Modular Ocean Model (MOM) developed at the Geophysical Fluid Dynamics Laboratory (GFDL) Princeton can be taken as a paradigm; it probably constitutes the best known example, which has been serving a large community very successfully. However, a single model cannot accommodate all possible choices without becoming unwieldy. In particular, it is difficult to combine different vertical coordinate representations into a single model code, although that might be an attractive option for scientific reasons. Likewise, certain aspects of the numerical algorithms (e.g. alternative spatial discretizations, parallelization schemes, etc.) do not always lend themselves easily to straightforward combination.

Second, different models, unlike oceanographic instruments, normally have not been systematically

calibrated against each other. This implies that the results of one modelling group cannot exactly be reproduced by another group that has a somewhat different model. Strictly speaking, the lack of reproducibility characterizes a result as non-scientific, and in any case contributes to a lack of credibility of ocean models. Some other areas of climate research have found it useful to organize quantitative intercomparisons of different models, often through the World Climate Research Programme (WCRP) or other international programmes; probably most well known is the Atmospheric Model Intercomparison Project (AMIP). For the ocean, a few limited intercomparison studies for models of the North Atlantic have been performed, such as DAMEE (Haidvogel and Beckmann, 1999) and DYNAMO (Willebrand *et al.*, 2001), which have demonstrated a large sensitivity of model results to the numerical representation of certain small-scale processes for the large-scale circulation.

A systematic intercomparison programme for ocean models would need to address several difficulties. The time scale for ocean thermohaline equilibrium is of order 1000 years, whereas observations and climatological averages extend roughly over the last 50 years. The concept of a (statistical) equilibrium, which has been useful for several intercomparison projects, is hence not applicable with regard to any model–data comparison, and one has to address the transient oceanic response to a well-defined atmospheric forcing. Obviously, the choice of appropriate initial conditions is important in such exercises. The oceanic circulation depends to a much larger extent than the atmospheric state on surface fluxes, which are notoriously poorly known; hence, specific care must be taken to prevent small differences in surface forcing from dominating the differences between models.

In contrast to atmospheric models, most ocean models cannot explicitly resolve motions at the deformation scale. Hence they do not simulate important processes, such as intense boundary currents, and only integral properties can sensibly be compared with ocean observations or with more realistic high-resolution models. It is at present not clear to what extent the response behaviour of the models used in climate simulations is influenced by their coarse resolution. A specific issue should therefore be an assessment of the response of these models under changing forcing versus that of

state-of-the-art high-resolution models. Global data sets, such as hydrographic atlases, are usually very smooth, and do not show important features of the ocean circulation at the deformation scale. Satellite altimetry (cf. Fu, Chapter 3.3) has been very useful for determining synoptic and seasonal variability, but less so for longer-term means. One may expect that with the AIMS-phase of WOCE this situation will greatly improve, and that analysed data sets of higher quality will become available for model validation.

It is obvious that a model intercomparison does not automatically lead to model improvement. Nevertheless, we believe that tightly organized intercomparison studies should be one important element of an internationally coordinated numerical experimentation programme. As differences between different models run under identical conditions are usually of the same order as differences within one model when run under slightly different conditions, any model intercomparison should always be accompanied by carefully planned sensitivity experiments. Perhaps the principal result of such studies will be a better and more quantitative appreciation of the shortcomings of different model concepts. The open information on model performance associated with an intercomparison project will be very useful not only for model development/improvement, but also for potential users of models in other communities, and should ultimately lead to an overall gain in model credibility.

7.2.6 Concluding remarks

Speaking about the future – particularly in a rapidly evolving field such as ocean circulation modelling – is of course a highly uncertain undertaking. Several conclusions and paths to future progress nonetheless appear reasonably certain.

At their current horizontal (and possibly vertical) resolution, and in view of the current state-of-the-art in sub-grid-scale parameterizations, it appears that *current coupled climate models are seriously misrepresenting many important oceanic processes*. These misrepresentations arise from various sources, though many are attributable to the unique complexities of the oceanic geometry and topography. As a consequence, important dynamical, thermodynamical and biogeochemical

processes, such as narrow western boundary currents, localized overflows, abyssal choke points and coastal ecosystems, are partially or wholly unresolved in today's climate models. While the impact of this deficiency on climate simulations has yet to be established, it follows that systematic efforts to document model deficiencies and to identify the leading-order processes responsible for these deficiencies need to be given a high priority. Necessary components of these efforts include a coordinated numerical experimentation programme, continued community model development and involvement, and the utilization of a more complete observational picture of the ocean circulation as it becomes available through WOCE-AIMS and other future programmes.

Furthermore, prognostic models need improvement to incorporate more correctly those processes that are at present poorly represented. Taking it as a matter of faith that the currently employed equations of motion are 'good enough' in their continuous form to reproduce all important processes, two paths to progress are indicated. On the one hand, as computer resources increase, continued enhancements in spatial representation are needed, in particular through better resolution but also through use of higher-order methods, improved (possibly adaptive) vertical coordinates, and nested and/or unstructured spatial grids. On the other hand, one has to accept that for the near future models of coarse resolution are needed for the study of climate variability on longer time scales. Therefore, continuing improvement of parameterizations of those processes that require sub-grid-scale treatment is also necessary. In particular, this includes such processes as narrow flows along boundaries, through straits and over sills, transports by mesoscale eddies, topographic interactions, small-scale diapycnal mixing, and others.

Last, and perhaps most importantly, we must pay serious attention to improvements in how atmosphere–ocean forcing and coupling are implemented. Of all the likely sources of uncertainty in the ocean component of climate models, errors arising from inaccurately known air–sea fluxes are probably still dominant. Intensive, continuing international efforts are required to provide sustained improvements in atmosphere–ocean flux observations, and further understanding of poorly understood component processes.

7.3

The World during WOCE

Bob Dickson, Jim Hurrell, Nathan Bindoff, Annie Wong, Brian Arbic, Breck Owens, Shiro Imawaki and Igor Yashayaev

7.3.1 Assessing the representativeness of the WOCE data set

From the start, it has been clear that the primary WOCE goal of compiling a coherent global ocean description would also require us to ask whether the new WOCE dataset is in any sense ‘representative’ of the long-term behaviour of the ocean. This secondary goal forms the subject of this chapter. Equally clearly, we can expect to provide only a partial answer, for two main reasons.

First, to assess how the WOCE period varied from some pre-existing state, we need pre-existing data, and *that* requirement simply can’t be built in to the experiment design. The very fact that the WOCE data set is of unprecedented scope, accuracy and quality means that comparable data will not exist in many ocean areas and depths.

Second, even where such comparisons prove possible, their value and validity will depend on whether our past and present sampling was adequate to resolve the amplitudes and time scales of ocean variability. Our longest time series may well be adequate for this task, but these are few and sparse. It will be much less obvious whether and to what extent the relatively infrequent repeat hydrography of the WOCE Hydrographic Programme (for example) was able to resolve the important variability of the upper, intermediate and deep ocean.

To illustrate the point, our comparison of section pairs from the mid- and South Atlantic (Section 7.3.4) will show that the variability signal was large in the top 1000 m but was inconsistent from section to section, suggesting that high-frequency

variability (the estimated ‘eddy error’) was masking any smaller-amplitude but more extensive decadal changes. Below 2000 m, on the other hand, though the temperature change seemed consistent between sections (cooling), the magnitude of the temperature change was small (order 0.03°C), and small systematic errors in the salinity data (hence density) from earlier years argued against decomposing this change into components along isopycnals and those due to isopycnal displacement. The signals between 1000 and 2000 db were however of consistent sign (warming) from 32°S to 36°N, had good signal-to-eddy noise ratios, and the decompositions of the signals didn’t change qualitatively when the possible systematic salt errors were corrected.

For these sorts of reasons, we can expect the WOCE snapshot to be blurred in the near-surface layers and for the intermediate layers to carry the most reliable and accessible signal of decade-to-decade variability in the sparse section data available to us; these intermediate layers will form one focus of this chapter. Bindoff and McDougall (1994) have shown that the most thorough diagnosis of water mass changes results from an examination of changes on isobaric and neutral surfaces; both are employed here. A second focus will concern the long-term variability of the convectively formed mode waters of the North Atlantic; here, we can expect the signals to be large, vertically homogeneous and relatively well described over many decades. We place our third emphasis on the changes in transport of the Gulf Stream,

Kuroshio and their eastward ‘extensions’. Their importance to the general circulation is obvious, but our assessment of their behaviour during WOCE will necessarily be based more on indirect than direct evidence.

In assessing the representativeness of the main WOCE field phase (1990–97), we deliberately include the Nordic Seas and Arctic Ocean, even though these sea areas lay outside the WOCE survey grid. Our justification is that polar amplification and feedback are recurrent features of numerical climate modelling, whose improvement is the ultimate aim of WOCE; moreover it is now demonstrable that Arctic change may feed south to affect lower latitudes.

If we provide less-than-adequate coverage of other important parameters or issues (notably the sea surface temperature, expendable bathythermograph, sea level and remotely sensed data sets, the higher frequencies of ocean–atmosphere variability, observation–model comparisons, etc.), this will be understood to reflect the biases and inadequacies of the authorship rather than of WOCE. Some of the inadequacies of this chapter will be met elsewhere in this volume.

7.3.2 The state of the atmosphere during WOCE

7.3.2.1 Introduction

The atmospheric circulation during the WOCE period of the 1990s was anomalous in several respects. Over the Northern Hemisphere (NH), the dominant patterns of atmospheric variability have tended to remain in one phase such that Sea-Level Pressure (SLP) has been lower than average over the middle and high latitudes of the North Pacific and North Atlantic oceans, as well as over much of the Arctic, while it has been higher than average over the subtropical oceans, especially the Atlantic (Fig. 7.3.1a). Moreover, in the past 30 years, trends in these leading patterns of variability appear to be unprecedented in the observational record. Over the Southern Hemisphere (SH), similarly remarkable changes have been documented in the leading pattern of variability such that SLP during the 1990s has been anomalously low over the high latitudes and anomalously high over the subtropics (Fig. 7.3.1b). These changes in atmospheric circulation have led to stronger than average westerlies over the middle latitudes of both hemispheres.

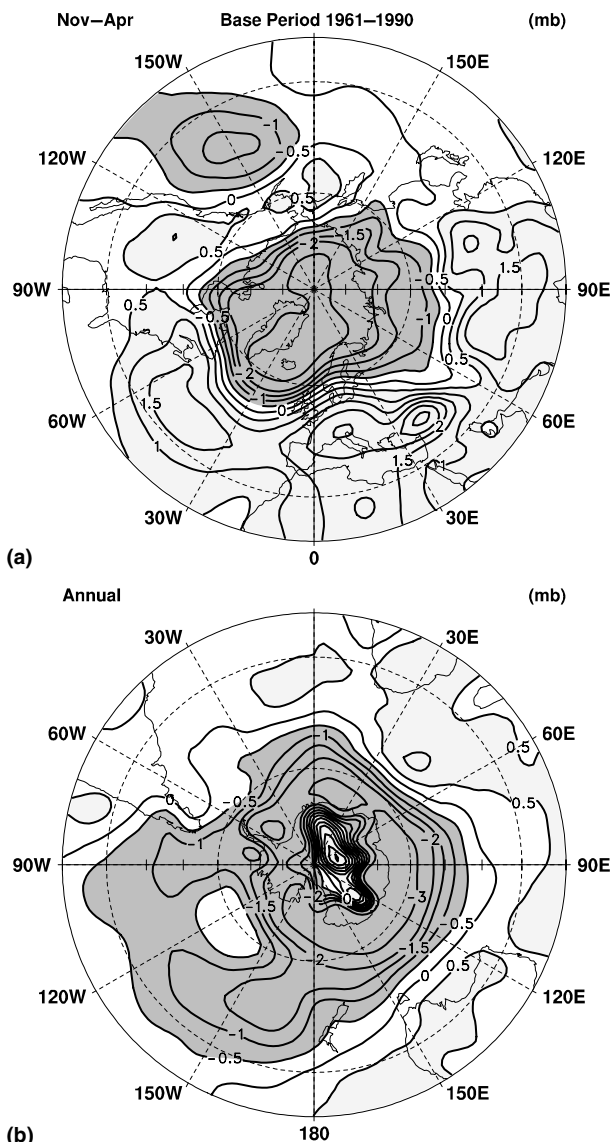


Fig. 7.3.1 Local anomalies in sea level pressure during 1990–97 expressed as departures in mb from the 1961–90 base period. Cold season (November through April) averages are shown over (a) the northern hemisphere poleward of 20°N while annual averages are shown over (b) the southern hemisphere poleward of 20°S. The contour increment is 0.5 mb and values greater than (less than) 0.5 (–0.5) mb are given by light (dark) shading. Values over the elevated terrain of Antarctica are not reliable.

Over the tropics, the Southern Oscillation (SO) has persisted in a strong negative phase during most of the WOCE period, reflecting higher than average (lower than average) surface pressure over much of the western (central and eastern) equatorial Pacific with weakened tropical easterlies.

The SLP patterns shown in Figure 7.3.1 are deviations from the 1961–90 mean field obtained from the atmospheric re-analysis of the National Centers for Environmental Prediction (NCEP; Kalnay *et al.*, 1996). An advantage of the NCEP products is their global coverage; however, considerable uncertainties exist as well, as the re-analysed SLP field is only as good as the input database, and observations are scarce over vast portions of the tropics and the SH in particular. Moreover, problems encoding the observations and other documented technical problems (see the NCEP re-analysis problem list at <http://www.cdc.noaa.gov/cdc/reanalysis/problems.shtml>) cast doubt on the reliability of the results. A.B. Mullan (1999, personal communication), for instance, has shown that the NCEP SLP fields do not agree well with station records throughout parts of New Zealand and Australia, including Darwin. If such problems exist in relatively data-rich regions, one must suspect the fields in data-sparse regions, such as over the tropical and southern oceans. For this reason, we have chosen not to present the anomalous SLP field over the tropics in Figure 7.3.1. Over the NH, the pattern and magnitude of anomalies in Figure 7.3.1a are very close to those obtained from other historical SLP data sets (e.g. the updated data of Trenberth and Paolino (1980) used by Hurrell and van Loon (1997) and Thompson *et al.* (2000), among others), so we have confidence in the NCEP analysis. Over the SH, less confidence can be placed in the magnitude of the NCEP anomalies, but the pattern of change is consistent with the results of studies using station and gridded SLP records from other sources (e.g. Hurrell and van Loon, 1994) as well as with changes and trends in other measures of the atmospheric circulation (Thompson *et al.*, 2000). Values of SLP over the elevated terrain of Antarctica are certainly not reliable, however, because of problems in reducing data to sea level.

The anomalies in the atmospheric circulation during the WOCE period are strongly related to variations in modes of natural variability. Over the NH, these variations have been most pronounced during the cold season, while those over the SH have shown less seasonality. Therefore, the spatial patterns of the most pronounced anomalies in SLP during the WOCE period are summarized by the cold season (November–April) map over the NH (Fig. 7.3.1a) and the annual mean map over the SH (Fig. 7.3.1b). In addition, to gain insight into

the temporal behaviour of the leading modes of atmospheric variability and to place the WOCE period into a longer-term perspective, time series of several leading atmospheric circulation indices are shown in the following sections.

7.3.2.2 The North Atlantic

The dominant pattern of atmospheric circulation variability over the North Atlantic is known as the North Atlantic Oscillation (NAO), and its winter-time index is shown in Figure 7.3.2a (updated from Hurrell, 1995a). The NAO, which is linked to changes in the surface westerlies across the Atlantic onto Europe, refers to a meridional oscillation in atmospheric mass with centres of action near Iceland and over the subtropical Atlantic from the Azores across the Iberian Peninsula. Positive values of the NAO index indicate stronger than average westerlies over the middle latitudes with low-pressure anomalies in the Icelandic region and high-pressure anomalies across the subtropical Atlantic. This phase of the oscillation is also associated with cold winters over the northwest Atlantic and warm winters over Europe, as well as wet conditions from Iceland through Scandinavia and winter dry conditions over southern Europe (Hurrell, 1995a).

A sharp reversal is evident in the index over the past 30 years and, since 1980, the NAO has tended to remain in a highly positive phase with associated negative SLP anomalies over the subpolar North Atlantic and most of the Arctic and positive SLP anomalies over the subtropical Atlantic (Fig. 7.3.1a). The most pronounced anomalies have occurred since the winter of 1988–89 (Hurrell, 1995a; Walsh *et al.*, 1996; Thompson and Wallace, 1998; Watanabe and Nitta, 1999) when the index registered its most positive values in the instrumental record (>170 years). While the signature of the NAO is strongest during winter, it is the dominant mode of atmospheric behaviour throughout the year (Barnston and Livezey, 1987; Rogers, 1990).

Thompson and Wallace (1998, 2000) and Thompson *et al.* (2000) have recently drawn attention to the fact that the NAO may be the regional manifestation of a hemispheric mode of variability characterized by exchanges of atmospheric mass between the polar cap and the middle latitudes, as shown by the leading pattern of variability in the hemispheric pressure field. They name this mode

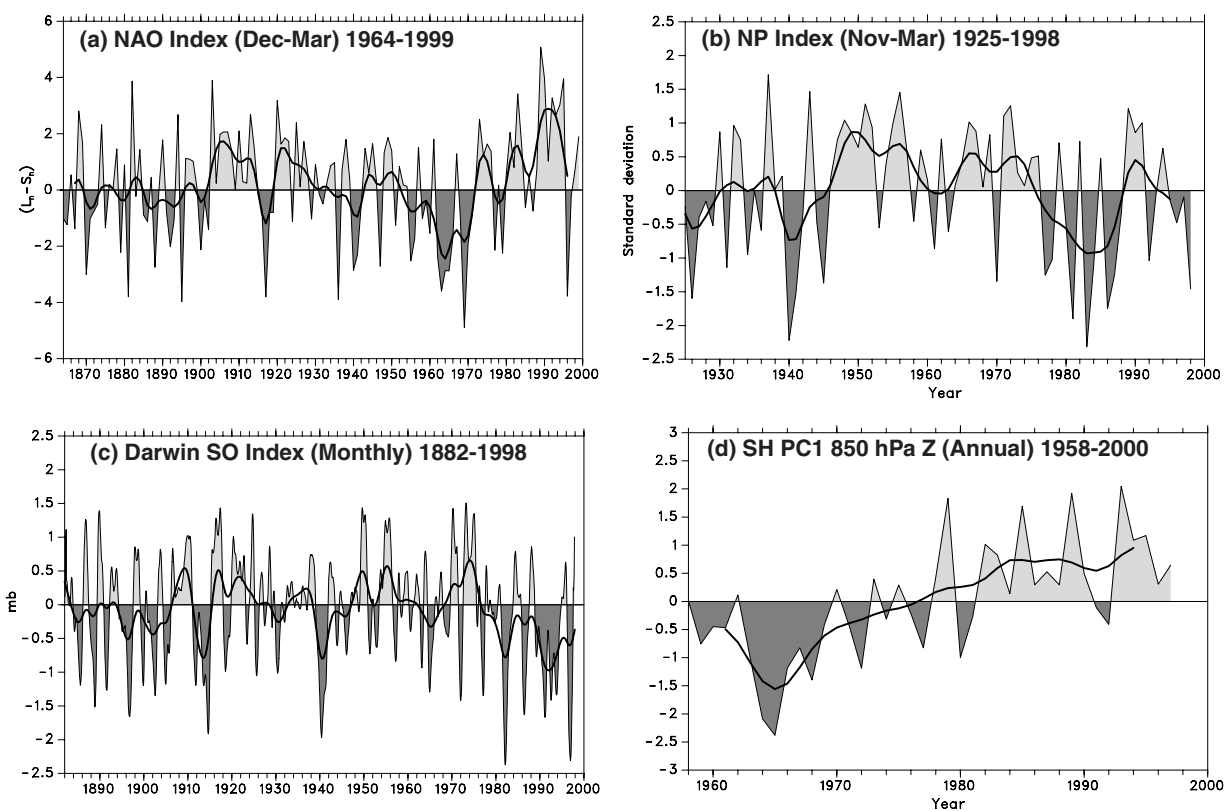


Fig. 7.3.2 Time series of (a) the winter (December through March) index of the North Atlantic Oscillation (NAO), 1864–1999, based on the difference of normalized sea-level pressures (SLP) between Lisbon, Portugal and Stykkisholmur, Iceland. The SLP anomalies at each station were normalized by division of each seasonal pressure by the long-term (1864–1983) standard deviation. (b) The winter (November through March) time series of the North Pacific index (NP), 1925–98; i.e. the area-weighted sea-level pressure over the region 30°N–65°N, 160°E–140°W. The values are normalized by the standard deviation (2.3 mb) after removing the 1925–89 mean. (c) Monthly values of the Darwin Southern Oscillation (SO) index, 1882–1998, based on the Darwin SLP record. Anomalies are not normalized and are relative to the 1882–1981 mean. Darwin anomalies are multiplied by -1 , so as to be consistent with the standard Tahiti–Darwin index. (d) Time series (from D.Thompson) of the (annual) leading principal component of 850 mb height over 90°S–20°S from the NCEP re-analyses, 1958–97. The time series has been normalized. The heavy solid lines in (a), (b) and (d) represent the indices smoothed with a low-pass filter to remove fluctuations with periods less than 4 years, while in (c) the monthly anomalies are smoothed with an 11-term filter and with a low-pass spline filter that removes periods less than 10 years. See text for further details.

the Arctic Oscillation (AO), and its wintertime index and pattern are very similar to that of the NAO shown in Figure 7.3.2a. Both circulation indices, therefore, account for much of the observed pressure falls over the Arctic in recent years (Walsh *et al.*, 1996); the strengthening of the subpolar westerlies from the surface of the North Atlantic to the lower stratosphere (Thompson *et al.*, 2000); most of the surface warming over Europe and Asia, as well as the cooling over the northwest Atlantic, over the past 30 years (Hurrell, 1996; Thompson *et al.*, 2000); pronounced regional anomalies in precipitation (Hurrell, 1995a; Hurrell and van Loon, 1997; Dai *et al.*,

1997; Thompson *et al.*, 2000); changes in storm activity and a recent northward shift of the Atlantic storm track (Hurrell, 1995b); and changes in within season atmospheric variability such as blocking (Nakamura, 1996b).

In order to place the recent extreme values of the NAO into a longer-term perspective, Jones *et al.* (1997) extended the wintertime record back to the early 1820s using station data from Iceland and Gibraltar and found that the amplitude of the oscillation over the past 10 years is unprecedented. Hurrell and van Loon (1997) showed that quasi-decadal (6–10 year) variability has become more pronounced over the latter half of this century,

while quasibiennial variability dominated in the early record. Cook *et al.* (1998) used tree ring data from Europe and the eastern USA to reconstruct the NAO index back to 1701 and found similar concentrations of spectral power, but they also identified a multidecadal oscillation with a period near 70 years. Osborn *et al.* (1999), however, question the reliability of the Cook *et al.* (1998) reconstruction based on the small percentage of variance it captures in the 1824–73 portion of the Jones *et al.* (1997) index, although problems with the early instrumental data cannot be ruled out. Most recently, Stockton and Glueck (1999) used tree ring data from Morocco and Finland, in addition to Greenland ice core data, to reconstruct a NAO index 555 years in length. They find that while there could have been several periods of consistently high or low index values such as those evident in Figure 7.3.2a, the reconstructed values during such periods are not as great in magnitude as the most recent values, such as during the 1960s and since the 1980s, in the instrumental records. The fact that the highest observed values of the index (post 1989) occur after the Stockton–Glueck chronology ends suggests that these recent high values may indeed be unprecedented.

7.3.2.3 The North Pacific

Over the North Pacific, a simple and robust index to measure climate variability is the area-weighted mean SLP averaged over most of the extratropical North Pacific ocean (Fig. 7.3.2b, updated from Trenberth and Hurrell, 1994). This North Pacific (NP) index reflects changes in the intensity of the Aleutian low pressure centre, and it is closely related to a well-known pattern of natural atmospheric circulation variability termed the Pacific–North American (PNA) pattern (Wallace and Gutzler, 1981). A feature of the time series is a striking regime shift after about 1976, which has been particularly evident during the winter half of the year (November to March). The regime shift is characterized by a deeper than normal Aleutian low-pressure system, accompanied by stronger than normal westerly winds across the central North Pacific and enhanced southerly flow along the west coast of North America (e.g. Trenberth and Hurrell, 1994). Consequently, over much of the past two decades, there have been increases in surface air temperatures and Sea Surface Temperatures (SSTs) over much of western North America and the eastern

North Pacific but decreases in SSTs over the central North Pacific. While positive values of the NP index were recorded for three consecutive winters beginning in 1988–89, as well as during the winter season of 1993–94, the index has remained negative in recent years, including the WOCE period, continuing the tendency apparent since the mid-1970s. Moreover, while the largest pressure falls over the North Pacific were evident during winter from the mid-1970s through the 1980s, the largest SLP anomalies during the 1990s have occurred during spring. From March through May, SLP anomalies in excess of -3 hPa reflect an eastward shifted and intensified Aleutian low (not shown), and it is this springtime anomaly that contributes the most to the cold season differences in Figure 7.3.1a.

Numerous recent studies have suggested that the mid-1970s change in the atmospheric circulation is but a single realization of lower-frequency interdecadal variations over the North Pacific. Most of these studies have been based on analyses of historical SST records, which show subtly different patterns of variability for interannual versus decadal and longer time scales (Kawamura, 1994; Deser and Blackmon, 1995; Zhang *et al.*, 1997; Enfield and Mestas-Nuñez, 1999). The interannual variability over the Pacific is dominated by the El Niño–Southern Oscillation (ENSO) phenomenon, with the strongest SST signals of one sign along the equator over the central and eastern Pacific and a boomerang-shaped pattern of weaker SST signals of opposite sign over the middle latitudes of both hemispheres. The higher-latitude changes in the Pacific arise from teleconnections that form an atmospheric bridge to force the anomalous surface fluxes that drive the SST anomalies (e.g. Lau and Nath, 1996; Trenberth *et al.*, 1998). The lower-frequency SST variability, on the other hand, is less equatorially confined in the central and eastern Pacific, and it is relatively more prominent over the extratropical North Pacific. The corresponding SLP signature is also stronger over the North Pacific, and its wintertime counterpart in the middle troposphere more closely resembles the PNA pattern (see also Zhang *et al.*, 1996).

Interdecadal fluctuations in the dominant pattern of North Pacific SLP variability, which is well represented by the NP index in Figure 7.3.2b, have closely paralleled those in the leading North Pacific SST pattern, as represented by the index of the so-called Pacific Decadal Oscillation (PDO) of

Mantua *et al.* (1997). The relationship is such that cooler than average SSTs occur during periods of lower than average SLP over the central North Pacific and vice versa. The PDO index (not shown) hints even more strongly that the mid-1970s regime has continued through the 1990s. In addition, there is evidence of shifts in the polarity of the PDO in the mid-1920s and the mid-1940s. Minobe (1997) examined a number of different climate indices around the Pacific, including more than 300 years of tree ring data from North America, and concluded that the interdecadal variability has a dominant time scale of 50–70 years, roughly consistent with the implied periods in the short record of Figure 7.3.2b. Recent evidence suggests that the phase of the PDO may also play a key role in modulating ENSO teleconnections across North America on interdecadal time scales (Gershunov and Barnett, 1998), though direct effects on the Atlantic Ocean have proved elusive.

7.3.2.4 The tropical Pacific

The decadal changes over the North Pacific have been linked to variations in the tropics (Nitta and Yamada, 1989; Trenberth, 1990; Trenberth and Hurrell, 1994; Zhang *et al.*, 1997), and several modelling studies have confirmed that North Pacific atmospheric variability is controlled in part by anomalous tropical Pacific SST forcing (e.g. Kitoh, 1991; Chen *et al.*, 1992; Graham *et al.*, 1994; Kumar *et al.*, 1994; Lau and Nath, 1994; Miller *et al.*, 1994). Fluctuations in tropical Pacific SSTs are related to the occurrence of El Niño. The atmospheric phenomenon tied to El Niño is termed the Southern Oscillation (SO), which is a global-scale 'see-saw' or standing wave in atmospheric mass (thus evident in SLP), involving exchanges of air between the eastern and western hemispheres centred in tropical and subtropical latitudes. The oscillation is characterized by the inverse variations in SLP at Darwin (12.4°S, 130.9°E) in northern Australia and Tahiti (17.5°S, 149.6°W) in the south Pacific: the annual mean pressures at these two stations are anticorrelated at ~ -0.8 . A simple index of the SO is, therefore, often defined by the normalized Tahiti minus Darwin SLP anomalies, or simply by the normalized negative Darwin record (Fig. 7.3.2c; updated from Trenberth and Hoar, 1996). During an El Niño event, the SLP tends to be higher than usual at Darwin and lower than usual at Tahiti. Negative

values of the SO index, therefore, are typically associated with warmer than average SSTs in the central and eastern tropical Pacific and weaker than average easterly trade winds.

Although the SO has a period of 2–7 years, the strength of the oscillation has varied over the past 100 years: strong variations from 1880 to the 1920s and after about 1950 and, except for the strong event during 1939–42, weaker variations from the mid-1920s to 1950 (Fig. 7.3.2c). Like the recent behaviour of the NAO, a remarkable feature of the SO index, however, is the amplitude of decadal and longer-term variability in recent years, which is lacking from earlier periods. In particular, a pronounced change toward more negative values is evident since the mid-1970s, including prolonged warm conditions from 1990–95, the beginning of the WOCE period. One interpretation of this change is given by Trenberth and Hoar (1996, 1997). They have statistically analysed the SO index shown in Figure 7.3.2c to assess the likelihood that its behaviour in the past 20 years or so is part of a natural decadal time scale variation. Their conclusion was that both the recent trend for more warm ENSO events since 1976 and the prolonged warm conditions since 1990 are unexpected given the previous record, with a probability of occurrence about once in 2000 years.

7.3.2.5 The southern hemisphere

The leading pattern of variability over the SH exists year round and is characterized by equivalent barotropic fluctuations in the zonal mean circulation between middle and high latitudes with a node near 45°S (e.g. Rogers and van Loon, 1982; Szeregi and Karoly, 1987; Yoden *et al.*, 1987; Kidson, 1988; Karoly, 1990; Hartmann and Lo, 1998; Thompson and Wallace, 2000). An annual index of this mode, based on 850 hPa geopotential height data from the NCEP re-analyses, is shown in Figure 7.3.2d (D.W.J. Thompson, 1999, personal communication). The mode explains 27% of month-to-month variations in lower tropospheric heights poleward of 20°S over the SH (Thompson *et al.*, 2000), and its time series shows a secular trend over the past few decades toward the high-index polarity, consistent with the lower than average SLPs during the 1990s at high latitudes (Fig. 7.3.1b) and stronger westerlies in middle latitudes.

These findings support earlier studies of recent decadal changes in the atmospheric circulation

over the SH by van Loon *et al.* (1993) and Hurrell and van Loon (1994); see also Chen and Yen (1997) and Meehl *et al.* (1998). All of these studies show evidence for a change in the atmospheric circulation beginning in the mid to late 1970s, with SLP in the circumpolar trough generally lower in the 1980s than in the 1970s. Hurrell and van Loon (1994) showed that the most pronounced changes have occurred during the second half of the year, so that the tropospheric polar vortex remained strong into November. This was associated with a delayed breakdown in the stratospheric polar vortex and the ozone deficit in the Antarctic spring.

7.3.2.6 Summary of atmospheric changes

The above results indicate that the state of the atmosphere during the WOCE period was characterized by pronounced deviations from the long-term mean conditions over both hemispheres. Over the North Atlantic, the NAO remained in a highly positive phase, with an amplitude unprecedented in the \sim 170-year observational record. The result has been stronger than average westerlies over the middle latitudes during the 1990s, associated with low-pressure anomalies extending from the Icelandic region across the Arctic and high-pressure anomalies over the subtropical Atlantic. The atmospheric circulation over the North Pacific has been characterized by a deeper than normal Aleutian low-pressure system since the mid-1970s, accompanied by stronger than normal westerly winds across the central North Pacific and enhanced southerly flow along the west coast of North America. The changes over the North Pacific have been linked to anomalously warm conditions over the tropical Pacific, including prolonged warm conditions during much of the 1990s that appear to be unprecedented in the observational record. As a result, the tropical Pacific easterlies have remained anomalously weak during much of the WOCE period. Over the SH, changes are more difficult to quantify because of the paucity of data. Nevertheless, the leading mode of atmospheric variability is characterized by zonally symmetric out-of-phase fluctuations in atmospheric mass between high and subtropical latitudes, and the time series of this mode shows a strong trend toward lower than average SLPs during the 1990s at high latitudes with stronger westerlies in middle latitudes.

7.3.3 The analysis of decadal change in intermediate water masses of the World Ocean

The oceans play a central role in defining the earth's climate, transporting heat and fresh water around the globe as part of the thermohaline circulation (e.g. Broecker, 1997). Models of climate change predict that the thermohaline circulation will weaken and that the surface waters will freshen poleward of mid-latitudes, and become saltier in the extratropical regions. In addition, the predicted warming of surface waters is latitude-dependent, with the Southern Ocean initially tending to warm less than the equivalent latitudes in the northern hemisphere.

Ocean ventilation will cause these changes in surface temperature and salinity to effect change in the ocean interior. However, changes in the temperature and salinity structure of the deep ocean below 500 m are largely unknown and their study is strongly hampered by the sparsity of the historical data. This is particularly true of the more poorly sampled Indian, Pacific and Southern Oceans, yet it is precisely these observations that are critical to the verification and validation of the results from coupled ocean-atmosphere models.

Two later sections, 7.3.4 and 7.3.9, report decadal changes in temperature and salinity at intermediate depths in two large areas of the world ocean – changes in the Atlantic and changes in the Pacific and Indian Oceans. In both cases changes along isobars are divided into components that represent different physical mechanisms of climate change. The Atlantic calculation focuses on the depth range 1000–2000 dbar and employs a simpler interpretation because of the uncertain role of mixing, as discussed below. The Pacific-Indian calculation focuses on waters above 1500 m depth where mixing is weaker compared with advection and allows an interpretation in terms of changes in surface forcing.

7.3.3.1 A kinematic subduction model for interpretation of water mass changes

The subduction of surface water into the interior of the ocean has been a subject of considerable research. The similarity of the θ -S curve of the winter mixed layers with the θ -S curves obtained from vertical profiles led Iselin (1939) to propose that the main thermocline was formed from surface waters

that had sunk into the ocean interior and moved towards the equator. Stommel (1979) examined the connection between the ocean mixed layer and the geostrophic flow below, and showed that the convergent Ekman layer pumped water down into the deep geostrophic flow along isopycnal surfaces. This analysis was extended by Woods (1985b), who showed that, in addition to Ekman pumping, subduction occurs where the maximum depth of the winter mixed layer decreases in thickness in the direction of motion (see also Price, Chapter 5.3; Nurser and Marshall, 1991; Pedlosky and Robbins, 1991).

All of this research on ventilated thermoclines has assumed a steady circulation in the deep and surface ocean. Here we consider the effect of the warming or freshening of surface waters on the thermocline temperature and salinity structure.

Pure warming

Suppose the water in the mixed layer has been warmed through increased heat flux from the atmosphere (Fig. 7.3.3a) and there is no change in the pattern of precipitation–evaporation or winds.

In the subduction region this warmed surface water will sink into the ocean interior between the upper and lower material surfaces and is transported equatorward toward the hydrographic cast. At this cast, at some later time, the average temperature between these two surfaces will have increased. However, because the salinity of the subducted water is unchanged in this scenario the salt content between the two material surfaces is also unchanged. This warming of the water between the material surfaces means that the density will have decreased slightly, and as a consequence the depth of isopycnals will have increased slightly.

On the θ –S diagram (Fig. 7.3.3b) the warming at the surface without a change in salinity results in a warming on pressure surfaces at the hydrographic cast. Along the isopycnal, ρ_1 , the warming on pressure surfaces ($\theta'|_z > 0$) has resulted in both a cooling and a freshening on density surfaces (respectively $\theta'|_n, S'|_n < 0$). Thus the subduction of warmed surface water into the thermocline where the θ –S relation has a positive slope leads to a cooling and freshening on isopycnals. This counterintuitive result was first described by Church *et al.* (1991).

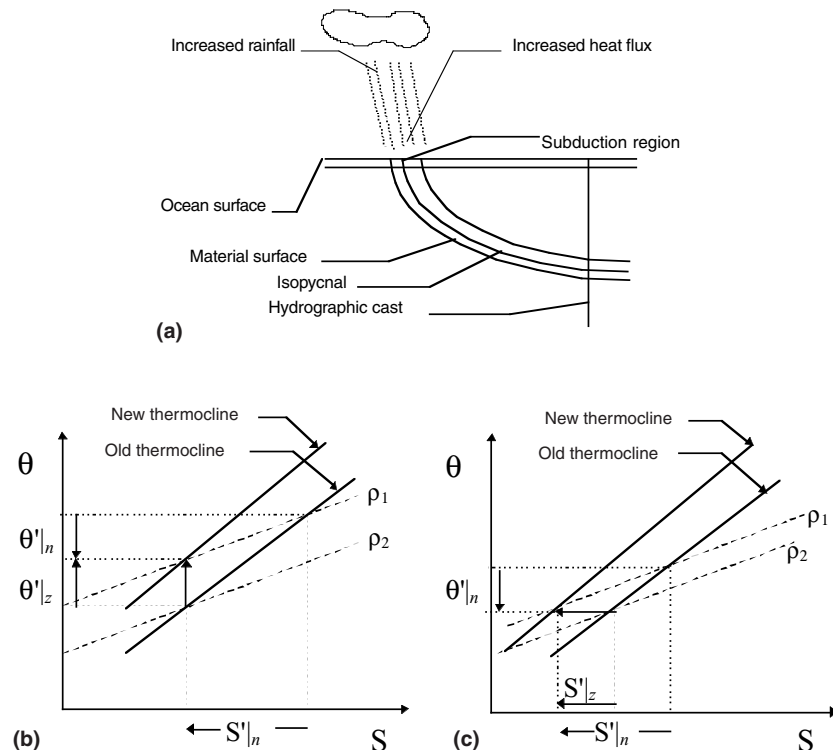


Fig. 7.3.3 (a) The subduction scenario for pure warming and pure freshening, where changes in the surface waters are subducted into the ocean and transported between the material surfaces towards the hydrographic cast. (b) θ –S changes caused by pure warming of surface waters. (c) θ –S changes caused by pure freshening of surface waters. The temperature and salinity changes on pressure surfaces are $\theta'|_z, S'|_z$, and on isopycnals are $\theta'|_n, S'|_n$ (Bindoff and McDougall, 2000).

The essential characteristics of this ‘pure warming’ process are that at a given depth (1) the salinity of the water column is unchanged and (2) the potential temperature has increased.

Pure freshening

Instead of warming the surface waters, suppose now that the water in the mixed layer has been freshened by increased precipitation–evaporation and there is no change in the heat flux from the atmosphere (Fig. 7.3.3a) or in the winds. Following the same scenario as in the ‘pure warming’ process, after subduction and transport to the hydrographic cast between the two material surfaces, the potential temperature is unchanged, the salinity has decreased, and density surfaces are now slightly deeper (Fig. 7.3.3c). Along the isopycnal, ρ_1 , the freshening on pressure surfaces ($S'|_z < 0$) has resulted in both a cooling and a freshening on density surfaces (respectively $\theta'|_n, S'|_n < 0$).

Thus changes on density and pressure surfaces must be treated carefully if they are to be interpreted in terms of changes in surface water masses. The distinguishing feature between the warming and freshening processes is how they affect temperature and salinity on both pressure and density surfaces. It is possible to separate formally the relative roles of pure warming and freshening (Bindoff and McDougall, 1994). This is important because models of climate change for increased greenhouse gases show increased precipitation at high latitudes as well as increased surface temperatures (Gordon and O’Farrell, 1997), both of which contribute significantly to the modelled buoyancy changes. Such changes may equally well occur as a result of natural climate variability.

Pure heave

Pure heave occurs where water masses are unchanged ($\theta'|_n, S'|_n = 0$) but isopycnals have been displaced vertically. Although this process has no signature on the θ – S diagram, it can lead to large temperature and salinity changes on pressure surfaces. Experience has shown that temperature and salinity differences on pressure surfaces in deep waters between repeated hydrographic sections taken 6 months apart are characterized by the pure heave process (Bindoff and McDougall, 1994) and probably resulted from variations in the seasonal winds.

Thus, the principal advantage of using temperature and salinity changes on density surfaces lies in

their ability to discriminate between changes due to pure heave (resulting mainly from short-term fluctuations due to dynamical processes such as propagating Rossby waves or seasonal variations in gyre circulation) and those due to surface forcing. A secondary advantage is that on density surfaces the prior noise in the thermocline is much smaller and changes of temperature and salinity on density surfaces tend to have larger signal-to-noise ratios.

The analysis that follows for the South Atlantic is essentially similar to that for the Pacific (Section 7.3.9). However, for the Atlantic Ocean basins: (1) there are multiple sources for the intermediate water; and (2) isopycnal mixing along the tenuous paths from the sources is likely to be important. As a result, the complete analysis, decomposing the observed changes into freshening and warming, is not warranted, and the decompositions of the observed changes on isobaric surfaces were instead limited to changes along neutral surfaces and those due to heave.

7.3.4 Climatic warming of Atlantic Intermediate Waters

In this section, the interdecadal temperature variability of the Atlantic Ocean is investigated by comparing hydrographic sections worked in the 1920s, 1950s, 1980s and 1990s. Previous studies (Roemmich and Wunsch, 1984; Parrilla *et al.*, 1994; Bryden *et al.*, 1996; Joyce and Robbins, 1996; Arhan *et al.*, 1998; Levitus, 1989; Joyce *et al.*, 1999) have concentrated on changes in the North Atlantic since the 1950s. Here, we re-analyse these changes and extend the analysis to the South Atlantic and back to the 1920s.

For this study we extracted data from the following sources: three South Atlantic sections from the *Meteor* expedition of 1925–27 (Defant, 1936), plus a total of seven North Atlantic and four South Atlantic sections from the International Geophysical Year (IGY, 1956–60), (Fuglister, 1960; Worthington and Wright, 1970), five North Atlantic sections from 1981–85 (Roemmich and Wunsch, 1984; McCartney, 1992; Knapp, 1988; Hendry, 1989), one from 1992 (Parrilla *et al.*, 1994), and one from 1993 (Arhan *et al.*, 1998). These were supplemented by two 1983 sections (McCartney and Woodgate-Jones, 1991; Warren and Speer, 1991) and one 1994 section (Holfort *et al.*, 2000) from the South Atlantic. All section data

were mapped onto standard grids, regularly spaced in the vertical and horizontal, before differencing. Pressure is the vertical coordinate used in the grid.

Figure 7.3.4 (see Plate 7.3.4, p. 588) summarizes the calculated changes, averaged over the 1000–2000 dbar depth interval, except at 48°N where the maximum cooling signal was between 500 and 1500 dbar. The changes are partitioned into three components: (a) the isobaric θ change, (b) the isopycnal θ change, and (c) changes in θ due to isopycnal displacements. The components of the 1950s-minus-1920s changes are calculated on the assumption that the titrated *Meteor* salinities, although containing large random errors, do not contain significant systematic errors (Mantyla, 1994).

The measurement errors of *Meteor* and IGY temperatures (Fuglister, 1960), as well as those of the more recent Conductivity-Temperature-Depth (CTD) temperatures, are much smaller than the changes reported here. Errors caused by sparser sampling of the *Meteor* and IGY sections, and by the non-coincidence of cruise tracks from different decades, were investigated and found to be small. For all of our sections, the largest source of error in the changes between 1000 and 2000 dbar is that due to mesoscale eddies. Following previous work (Parrilla *et al.*, 1994), we estimate eddy errors by taking the standard deviation of the section-averaged signals and dividing by the square root of the number of eddy diameters (taken to be 100 km) across the section. The eddy errors of the vertically averaged isobaric changes are shown in Figure 7.3.4a (see Plate 7.3.4a, p. 588).

Except at 48°N, the section changes show an isobaric warming, of $0.5^{\circ}\text{C century}^{-1}$, between 1000 and 2000 dbar. This warming rate is consistent with the trend seen at the Bermuda time series station (Roemmich and Wunsch, 1984; Joyce and Robbins, 1996). Our map, with its comprehensive geographical coverage, is a good complement to the Bermuda time series, which samples only one point in the ocean, but has excellent temporal coverage. Together, they argue convincingly that there have been widespread changes in temperature at intermediate depths over the entire Atlantic Ocean since at least the 1920s. In the North Atlantic between the 1950s and 1980s, the warmings are mostly due to downward displacements of isopycnal (neutral) surfaces, while isopycnal change dominates all but the most recent of the South Atlantic signals.

Though depressions of isopycnal surfaces in the North Atlantic may arise from a range of causes, such coherent and large-scale changes as we see here suggest that the cause may involve variations in the formation rate of intermediate water masses at source. Correlations between time series of the source-thickness of Labrador Sea Water (LSW) – the major water mass in the North Atlantic between 1000 and 2000 dbar – and the temperature anomalies at Bermuda have led to the proposal (Curry *et al.*, 1998) that the thickness of the LSW layer is a major controlling factor in intermediate-depth temperature anomalies of the subtropical North Atlantic. We suggest that, additionally, there may have been changes in the thickness of the layers above or below the LSW intermediate-layer. If the intermediate-layer temperature changes were due only to thickening and thinning of the LSW, one might expect to see isopycnal displacements of opposite sign at the top and bottom of the LSW layer – roughly at 1000 and 2000 dbar, respectively. However, the 1980s-minus-1950s differences on all of our North Atlantic sections from 8 to 36°N show a consistent downward displacement of isopycnals of ~ 30 –100 dbar (not shown) throughout the entire extent of the 1000–2000-dbar layer. This is consistent with either a deepening thermocline or a shallowing of the abyssal layer (Bacon, 1998). Our calculations indicate that the thermocline motions concurrent with the wind-driven sea-level changes calculated by Sturges *et al.* (1998) are not consistent with the isopycnal displacements we observe. Thus, our analysis does not support the idea that these changes are simply due the effect of wind forcing on thermocline depth. Another possibility is that the thermocline has deepened due to changes in the amount of fluid being pumped downwards from its surface outcrops (Huang and Pedlosky, 1999), but we do not yet have a quantitative measure of this effect.

In contrast to the North Atlantic warmings, those in the South Atlantic are generally dominated by isopycnal change, the 1990s-minus-1980s signal at 11°S being an exception. This isopycnal warming extends north into the southern North Atlantic. There are several sources for waters between 1000 and 2000 dbar: deep convection in the Labrador Sea, overflows from the Mediterranean Sea, and Antarctic Intermediate Water (AAIW). Although the core of the AAIW layer is shallower, salinity data (Bainbridge, 1981) suggest that AAIW

comprises a large fraction of the 1000–2000-dbar layer in the South Atlantic and a lesser fraction of this layer in the southern North Atlantic. For this reason, the large warmings (and compensating increases in salinity) along isopycnals in the South Atlantic, and the lesser warmings along isopycnals in the southern North Atlantic, are suggestive of changes in AAIW, especially since the warmings in the southern North Atlantic are more pronounced in the western part (Fig. 7.3.4b, see Plate 7.3.4b, p. 588), where the presence of AAIW is strongest. Likewise, the coolings along isopycnals in the northern North Atlantic are suggestive of changes in LSW (Fig. 7.3.4b, see Plate 7.3.4b, p. 588).

Our study has broadened the geographical extent of the warmings at intermediate depths reported by previous authors (Roemmich and Wunsch, 1984; Parrilla *et al.*, 1994; Bryden *et al.*, 1996; Joyce and Robbins, 1996; Arhan *et al.*, 1998; Levitus, 1989; Joyce *et al.*, 1999) by showing that these warmings extend into the South Atlantic. We find that the isopycnal-displacement mechanism, which is of widespread significance in the North Atlantic (Levitus, 1989), is not the only one of importance. Changes on isopycnals also form a large and widespread component of the changes observed on isobars. However, unlike the displacement mechanism, changes along isopycnals respond very slowly to changes in forcing, so that by serving as integrators over long time scales, they might be the more sensitive indicator of long-term climate change (suggestion of anonymous reviewer). In this light, the isopycnal warmings we observe, extending back into the 1920s, may well indicate that recent changes in the climate of the ocean are a response to climatic forcing over longer periods than we have previously realized.

7.3.5 Spin-up of the North Atlantic gyre circulation

From the subtropics northwards over the northern North Atlantic and Nordic Seas, the status of the marine environment during WOCE is overwhelmingly determined by the extreme long-term behaviour of the NAO.

As described earlier (Section 7.3.2.2), the WOCE field phase occurred at a most unusual interval in the climatic history of the North Atlantic, at the end of a period in which the principal atmospheric forcing mode in that sector had amplified over

three or four decades to its most extreme positive state (generally) in a 176-year instrumental record and possibly much longer. In the present context, the importance of this extreme climatic shift lies in the wide range of variables attributed to the changing NAO, which have the potential to cause change in the marine environment. These include variations in wind speed, latent and sensible heat flux (Cayan, 1992a,b,c), evaporation/precipitation (Cayan and Reverdin, 1994; Hurrell, 1995a), the distribution, prevalence and intensity of Atlantic storms (Rogers, 1990, 1994, 1997; Hurrell, 1995b; WASA Group, 1997; Alexandersson *et al.*, 1998), hence effects on the wave climate (Bacon and Carter, 1993; Kushnir *et al.*, 1997; WASA Group, 1997; Carter, 1999; Cotton and Challenor, 1999), sea surface temperature (Cayan, 1992c; Hansen and Bezdek, 1996), the strength of the Labrador Current (Myers *et al.*, 1989), the characteristics and distribution of water masses (Lazier, 1995; McCartney *et al.*, 1996, 1997; Houghton, 1996; Joyce and Robbins, 1996; Molinari *et al.*, 1997, Sy *et al.*, 1997; Joyce *et al.*, 1999; Curry *et al.*, 1998; Curry and McCartney, 2001), the extent of the marginal ice zone (Fang and Wallace, 1994; Mysak *et al.*, 1996; Deser *et al.*, 2000), Davis Strait ice volume (Deser and Blackmon, 1993), the iceberg flux past Newfoundland (Drinkwater, in Rhines, 1994), and the intensity of deep convection at the main Atlantic sites (Greenland Sea, Labrador Sea and Sargasso; Dickson *et al.*, 1996; Talley, 1996b; Dickson, 1997; Joyce *et al.*, 2000).

Certain of these responses seem more critical than others. In particular we highlight here the radical interannual and interdecadal changes in the production of the convectively formed mode waters of the west Atlantic (Labrador Sea Water and the Eighteen-Degree Water), which Dickson *et al.* (1996) suggest to be part of a coordinated pan-Atlantic pattern of convective activity, driven by the changing NAO. Specifically they suggest that convective activity at all three main sites evolved over decades to a long-term extreme state – in phase but of differing sign – during the NAO minimum of the 1960s, at which time the ventilation of the Greenland Sea and Sargasso was at a maximum and that of the Labrador Sea was tightly capped. Since then until the mid-1990s, all three centres have evolved rather more rapidly towards their opposite extreme states, in which convection in the Greenland Sea and Sargasso is suppressed

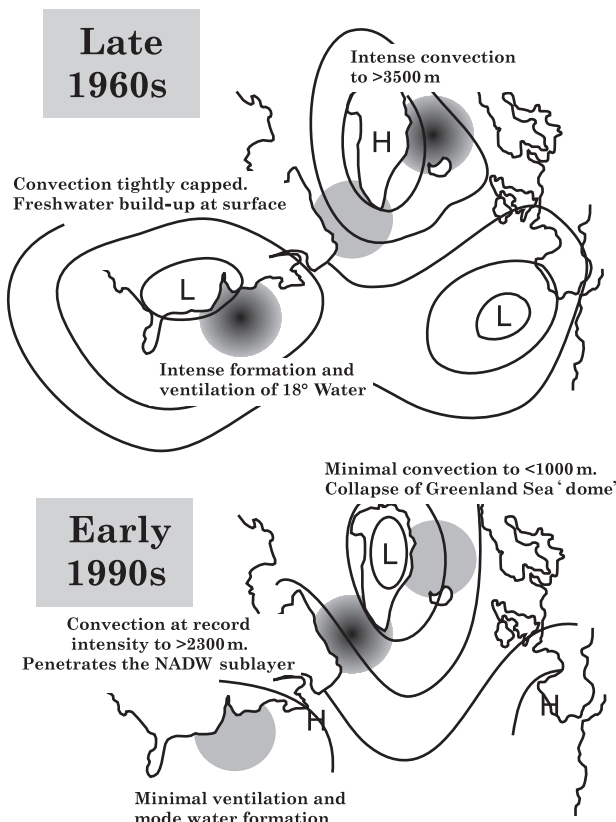


Fig. 7.3.5 Schematic description of changes in the distribution of winter convective activity in the North Atlantic during contrasting extreme states of the NAO (low index 1960s, high index 1990s). A representative mean pressure anomaly field is indicated for each case. From Dickson (1997). Reprinted with permission from *Nature* 386, copyright 1997, Macmillan Magazines Limited.

but vertical exchange in the Labrador Sea is reaching deeper than previously observed (Fig. 7.3.5).

The mechanism is thought to involve the sort of change in the distribution of Atlantic winter storm activity that has long been associated with opposite extreme states of the NAO (Rogers, 1990). From the late 1950s to 1970, under the more-southerly of its two main cells, a regime of cold winter air temperatures and extreme snowcover greatly enhanced the land-sea temperature gradient at the US eastern seaboard, spinning-up more storms than normal offshore (Dickson and Namias, 1976; Hayden, 1981) and causing them to develop more rapidly to occlusion in a narrow band following the main coastal baroclinic gradient. The local effect was to focus the centre of maximum storm activity off the US eastern seaboard where the cold, stormy conditions caused maximum formation and ventilation of the Eighteen-Degree Water

pycnostad, and some increase in its density (Jenkins, 1982; Talley and Raymer, 1982; Talley, 1996b). The remote effect was to reduce storminess over the Labrador Sea to a post-war minimum in the 1960s, so that Labrador Sea convection became increasingly suppressed and fresh water built up at the surface (Lazier, 1980, 1988, 1995). LSW production resumed abruptly in winter 1971–72 with a rapid removal of the surface freshwater accumulation by vertical spreading as the cold winter regime ended at the US east coast and intense, chill northwesterlies and storminess returned to the Labrador Sea. Since then the tendency has been towards intensifying and deepening ventilation of the Labrador Sea, with a progressive cooling and freshening of LSW into the WOCE period of the 1990s, and ultimately, during the deepest-reaching convection since 1992, an increase in LSW density as convection began to excavate the cold but saline sublayer of North Atlantic Deep Water (Dickson et al., 1996). It is this cold, fresh, and dense new vintage of LSW that Sy et al. (1997) use, together with its chlorofluorocarbon (CFC) signature, to derive modern estimates of LSW spreading rates within the Labrador–Irminger Basin that are an order of magnitude greater than published values, and transocean spreading rates at LSW depths that are three or four times faster than previous estimates (e.g. Read and Gould, 1992).

Changes in the formation and renewal of these vertically homogeneous mode waters are important in their own right in carrying the signal of climatic change to intermediate and greater depths and from there, by horizontal spreading, throughout the ocean basin. And the changes in the characteristics of LSW have certainly been remarkable. In the early 1990s, thus including much of the WOCE field phase, LSW was fresher, colder and denser than at any other time in the history of deep measurements in the Labrador Sea (Fig. 7.3.6 a–c, see Plate 7.3.6a–c, p. 588). From 1966 to 1992, the overall freshening of the water column of the Labrador Sea was equivalent to mixing in *an extra 6 m of fresh water* at the sea surface (7 m if we extend the period to 1994), and its cooling has been equivalent to a *loss of 8 W m⁻² continuously for 26 years* (Lazier, 1995). Beneath the convective layer, the freshening by ≈ 0.01 per decade over the past three to four decades (apparently still continuing) reflects the recent large-scale freshening of the upper Nordic Seas (Section 7.3.6,

below), passed on by the dense northern overflows through Denmark Strait and the Faroe Bank Channel (see Saunders, Chapter 5.6). As the net result of these changes, the steric height in the central Labrador Sea in the mid-1990s was typically 6–9 cm lower than in the late 1960s.

As already described, these changes have a value in tracing out the rates and pathways by which LSW-spreads across the basin. However, the major importance of these changes is likely to lie in their influence on the Atlantic gyre circulation itself. As Curry and McCartney (2001) point out, the main North Atlantic Current is driven by the gradient of potential energy anomaly (PE') across the mutual boundary between the subtropical and subpolar gyres. Since PE' reflects the vertical density structure and heat content of the upper ocean to well below the wind-driven layer, it follows that coordinated changes of opposite sign in the production and characteristics of the mode waters in each gyre will have the potential to drive deep-seated changes in the PE' gradient, and hence in the strength of the Atlantic gyre circulation. If these changes in the density and heat content of mode waters are attributable to the NAO, then the amplification of the NAO to extreme values over the past three or four decades is likely to have been followed by a corresponding multidecadal spin-up of the Atlantic gyre circulation.

From the observed PE' differences between the centres of the two gyres, Curry and McCartney calculate that the long-term increase in the NAO index to the mid-1990s was accompanied by a 30% increase in the 0–2000 dbar eastgoing baroclinic mass transport along the gyre–gyre boundary, from 50 Sv ($1\text{ Sv} = 10^6 \text{ m}^3 \text{ s}^{-1}$) in 1970 to 65 Sv in the mid-1990s (Fig. 7.3.7, see Plate 7.3.7, p. 588). Both subpolar and subtropical gyres contributed equally to the changes in their transport index. Thus in response to the NAO, the North Atlantic gyre circulation during WOCE is likely to have been at its strongest for more than a century.

Needless to say, as Curry and McCartney point out, reality is more complex than this simple partnership between the circulation indices of ocean and atmosphere.

1 Though local wind and buoyancy forcing *was* the principal influence on potential energy anomaly in the subpolar gyre, the passage of Great Salinity Anomalies (Dickson *et al.*, 1988;

Belkin *et al.*, 1998) had a temporary damping effect on transport as they passed through the Labrador Basin in 1968–72 and 1980–84 (see also Curry *et al.*, 1998).

- 2 Though wind and buoyancy forcing did contribute to PE' changes in the subtropical gyre, the PE' history of that basin seems mainly to reflect thermocline ‘heave’ as a lagged low-frequency baroclinic adjustment to changing wind stresses further east.
- 3 Since advection moves the heat content anomalies around after their formation, the PE' pattern becomes a subtle quadripole rather than a dipole, with opposite dynamic height departures in the western and eastern parts of either gyre.

Nonetheless, this neat and convincing synthesis of the observational record by Curry and McCartney does appear to justify the view that decadal change in the ocean may be the result of a coupled system, not merely the response of a passive ocean to a decadally evolving atmosphere; and they certainly emphasize the unusual nature of the Atlantic circulation and its mode waters during WOCE.

7.3.6 Altered patterns of exchange in Nordic Seas

The changes observed in the hydrographic character of the Greenland, Norwegian and Icelandic Seas at all levels during WOCE were among the starker observed anywhere. In part these variations reflect decadal changes in the intensity and depth of vertical exchange in the convection centre of the Greenland Sea – part of the coordinated pan-Atlantic pattern of convective change described earlier (Fig. 7.3.5). But the altered properties of the deep and bottom waters in the Greenland Sea suggest a more complex origin.

As Swift *et al.* (1983) point out, the deep water of the Greenland Sea (GSDW) is the coldest and freshest deep-water component in the Arctic Ocean/Nordic Seas system, while that of the Arctic Ocean (AODW) is the warmest and most saline. Other local deep waters are a mixture of the two. Since the deep waters filling the Greenland Sea Basin are very much more homogeneous in space than their observed variation in time, the implication seems clear – that cooling of waters in the deep Greenland Sea can only be carried out from above, by convection, while warming can only be effected from outside the basin, by lateral exchange

through Fram Strait (Meincke *et al.*, 1992; Rudels, 1995).

For this reason, the well-known cooling:warming cycle of deep water (>2000 m) in the Greenland Sea since the late 1950s (Clarke *et al.*, 1990; successively updated by Meincke *et al.*, 1992; Meincke and Rudels, 1995; Visbeck and Rhein, 2000; D. Quadfasel, personal communication) has conventionally been interpreted as evidence of a changing balance between vertical and horizontal exchange processes.

Thus the cooling of the deepwater to the early 1970s (Fig. 7.3.8c, showing $\theta > 2500$ m; from Visbeck and Rhein, 2000) is interpreted as the result of intensifying convection, culminating (though

the record is gappy) in the winter of 1971 when Malmberg (1983) reports convection reaching to 3500 m. Since then, the evidence is of a progressive reduction in the intensity and penetration of winter convection, with no convective renewal of waters deeper than 1600 m during the 1980s (GSP Group, 1990; Meincke *et al.*, 1992), or deeper than 1000 m in the most recent years (Meincke and Rudels, 1995). Schlosser *et al.* (1991a) use tracers to estimate a (model-dependent) $80 \pm 10\%$ reduction in deep water formation from the ≈ 0.47 Sv of the 1960s and 1970s to the 0.1 Sv of the 1980s.

Over the period (post 1982) in which both the temperature and salinity of the deep water are known with adequate precision, Figure 7.3.8c,d

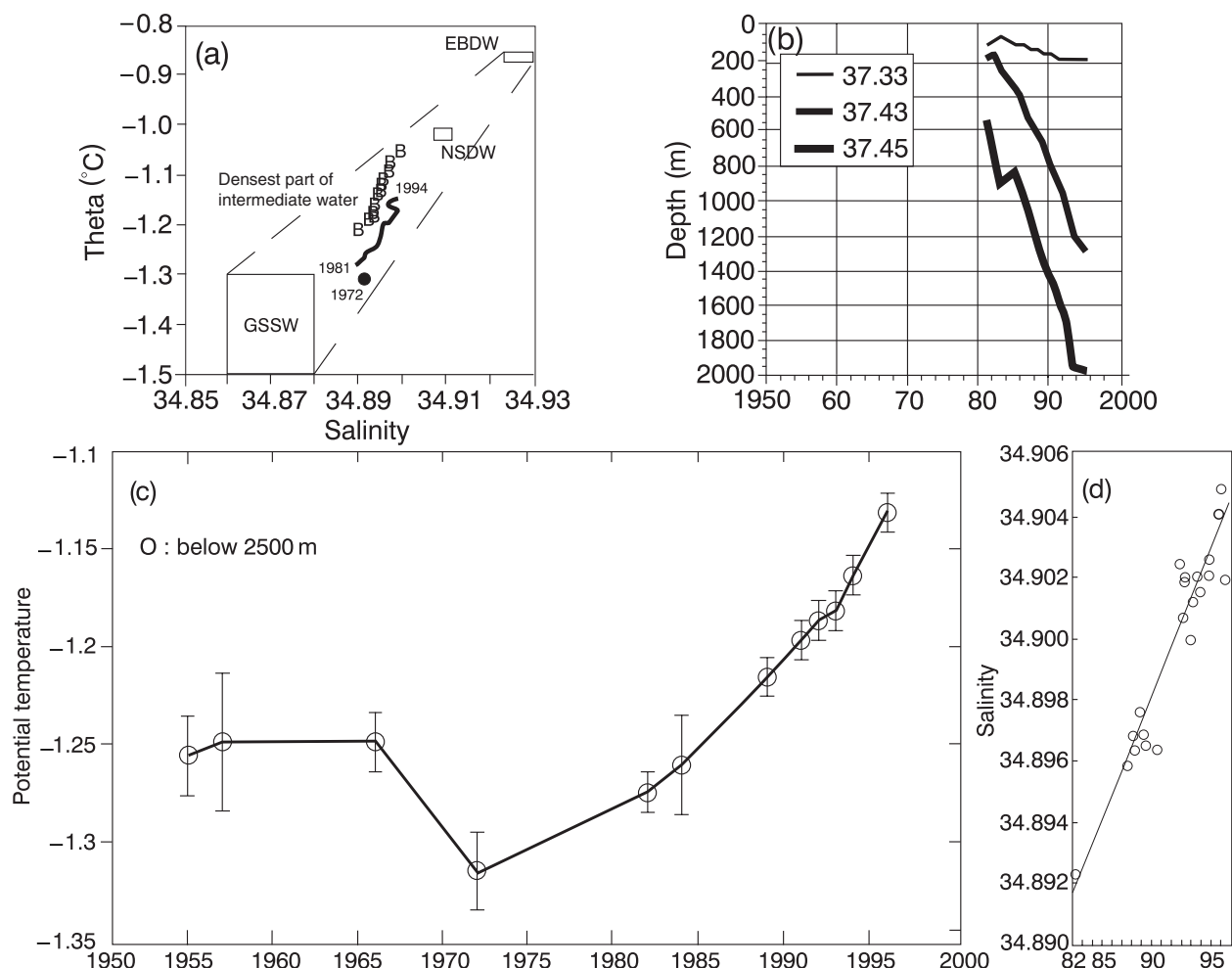


Fig. 7.3.8 Evidence of convective shutdown in the Greenland Sea from the early 1970s. (a) The shift in GSDW characteristics away from those of GSSW and towards those of EBDW (Bönisch *et al.*, 1997); (b) the deepening of isopycnal surfaces as the Greenland Sea 'Dome' collapses (Bönisch *et al.*, 1997); (c) the increase in potential temperatures at $z > 2500$ m (Visbeck and Rhein, 2000); and (d) the increase in salinity at $z = 2000$ – 3000 m (D. Quadfasel, personal communication) as vertical exchange with the surface gives way to horizontal exchange with the deep Arctic Ocean through Fram Strait, and/or other means of deep water renewal.

confirms that this weakening convection was accompanied by a progressive, almost linear increase in the temperature and salinity of the deepest layers to unprecedented values by the mid-1990s, at which time deepwater properties lay quite outside the defined range for GSDW (compare Figure 7.3.8 c,d with the GSDW properties as defined by Swift *et al.*, 1983; i.e. temperatures between -1.26 and -1.29°C and salinities between 34.889 and 34.892). Verduin and Quadfasel (1999) confirm that this warming and salinification was not confined to the deep layers but typified much of the water column of the Greenland Sea deeper than 1000 m.

There would be little debate that a part of this change is due to dwindling convection. However, three supplementary mechanisms have been advanced. First, there is the evidence, already mentioned, that reduced vertical exchange has been replaced by increased deep horizontal exchange through Fram Strait. Perhaps the best evidence for this is the shift in GSDW characteristics away from those of Greenland Sea Surface Water (GSSW) and towards those of Eurasian Basin Deep Water (Fig. 7.3.8a) reported by Boenisch *et al.* (1997). This seems confirmed in the subtle but steady decline in the oxygen content of GSDW as deep temperatures have risen (Swift *et al.*, 2001), since this, too, is the expected net result of a weakening convective link with the surface and an increasing exchange with the less-oxygenated deep waters of the Arctic Ocean (Aagaard *et al.*, 1991).

A second mechanism is thought to be the collapse of the ‘domed’ density structure in the Greenland Sea as a reduced wind stress curl (Jónsson, 1991) supported a less intense cyclonic basin circulation there (Rudels and Quadfasel, 1991; Meincke *et al.*, 1992). The evidence lies in the steady deepening of intermediate and deep isopycnals in the Greenland Sea since the early 1980s, reported by Boenisch *et al.* (1997; Fig. 7.3.8b). Meincke and Rudels (1995) and Meincke *et al.* (1999) combine the two mechanisms by suggesting that the collapse of the dome might have caused a compensating influx of Canadian Basin Deep Water (CBDW) and Eurasian Basin Deep Water (EBDW) into the centre of the Basin at intermediate depths.

While accepting that cold conditions in the deep Greenland sea were the result of deep convection, Visbeck and Rhein (2000) point out that the subsequent deep warming has been accompanied by a slow but significant increase of CFC concentrations

in the bottom layers that cannot be explained by deep exchanges of ‘old’ water through Fram Strait. They propose an alternative bottom water ventilation pathway to explain continued deep water renewal in the absence of deep convection. By this mechanism, ventilated intermediate water spreads laterally to the basin margins where enhanced diapycnal mixing over the rough topography of Mohn’s Ridge is responsible for transferring some portion of its tracer signal and warmth to the deeper layers.

Whether, following these scenarios, strong vertical exchange in the Greenland Sea gave way to enhanced lateral exchange with the Arctic Ocean, or merely with its own boundaries, there seems to be clear evidence of interbasin exchange with deep waters of the Norwegian Sea. NSDW is composed partly of GSDW (Swift and Koltermann, 1988) and, until the early 1990s, had exhibited a low-amplitude and lagged version of the temperature changes shown by GSDW itself (Østerhus and Gammelsrod, 1999). There was also an apparent lag with decreasing depth in the Norwegian Sea, so that the recent abrupt warming appeared first at 2000 m in 1987, where the greatest change in the GSDW had been recorded, but not until 1990 at 1200 m. In the early 1990s, as GSDW production dwindled to near extinction, there are some indications that NSDW ceased to warm further at depth and that the connecting flow through the Jan Mayen Channel may have temporarily reversed (Østerhus and Gammelsrod, 1999 and personal communication; see also Bourke *et al.*, 1993).

Though their wider influence is certainly regulated by the gaps and passageways that form their connections to neighbouring seas, the Nordic Seas are potentially important as a source of change for both the climatically sensitive Arctic Ocean and for the northern overflows that form the headwaters of the meridional overturning circulation (MOC). It is worth recording, then, that over much of the water column, the hydrographic character of these seas during WOCE was beyond the range of our past experience; in one way or another, these extreme anomalies appear to have arisen through a changing balance, sense or pattern of ‘exchange’.

7.3.7 System-wide changes in the Arctic Ocean

For some time now, we have known or supposed that variability in the Arctic has some special role

to play in the processes of global change. Polar amplification and feedback are recurrent themes in numerical climate modelling (Manabe and Stouffer, 1993). However, we have hitherto lacked many of the ocean time series needed to demonstrate the basic features of long-term hydrographic change within the Arctic Ocean.

This situation improved dramatically during the 1990s. First, there was a major increase in the ship-based ocean-observing effort, contributed both by surface ships (*Polarstern* and *Oden* in 1987 and 1991, the first US/Canadian Trans-Arctic Section in the summer of 1994 aboard *Polar Sea* and *Louis St Laurent*, and three further *Polarstern* cruises in 1993, 1995 and 1996 were highlights), and by the almost-annual submarine surveys of the US SCICEX Program (1993–99). Second, the release of a vast military archive of ocean data supplied the improved ocean ‘climatology’ (Environmental Working Group, 1997) against which the new data sets might be compared for evidence of change. And third, whether we use the newly described Arctic Oscillation (AO; Thompson and Wallace, 1998) or the North Atlantic Oscillation (NAO; Dickson *et al.*, 2000) as the more appropriate index of Arctic climate, it seems clear that winter climatic forcing over the Arctic and its subjacent seas was at a century-long extreme state during the 1990s (Walsh *et al.*, 1996). This meant that when data and climatology were compared, the changes identified were spectacular and of a large-enough amplitude to be traceable through a gappy observing system and stand out against a still-shaky climatology. Three main changes in particular have characterized the WOCE period of the 1990s.

The first was a more intense and more widespread influence of Atlantic water than previously observed, with a warming and spreading of the Atlantic-derived sublayer across the Eurasian Basin (Quadfasel *et al.*, 1991; Carmack *et al.*, 1995, 1997; Aagaard *et al.*, 1996; Swift *et al.*, 1997; Morison *et al.*, 1998a,b, 2001; see also Kolatschek *et al.*, 1996; McLaughlan *et al.*, 1996). As the winter NAO index increased from its lowest values on record (generally) in the 1960s to its highest recorded values during the early 1990s (see Fig. 7.3.2a), the increasingly anomalous southerly airflow that accompanies such a change over Nordic seas is held responsible for a progressive warming and perhaps a strengthening of the two streams of

Atlantic water that enter the Arctic Ocean, across the Barents Sea shelf and along the Arctic Slope west of Spitsbergen. By the late 1980s–early 1990s, when the NAO reached its interannual and interdecadal maximum, the superposition of a short-term warming event on the long-term warming trend meant that both Atlantic-inflow streams were running between 1 and 2°C warmer than normal (Grotfendt *et al.*, 1998; Dickson *et al.*, 2000). Adlandsvik’s barotropic transport model (Adlandsvik, 1989; Adlandsvik and Loeng, 1991; Loeng *et al.*, 1997) suggests that the transport through the Barents Sea pathway may have increased by around a quarter at this time, and we have possible proxy evidence from sea-level records to suggest that the West Spitsbergen Current was similarly boosted. From an annual standard section across the West Spitsbergen Current at 76°20'N, the warming of the inflow through Fram Strait is seen to be accompanied by a progressive freshening and decrease in density in the upper 500 m since the 1960s, and the indications are that freshening also affected the Barents Sea branch of the Atlantic Current (Dickson *et al.*, 2000). Since the increasing NAO is associated both with a major increase in precipitation along the length of the Norwegian Atlantic Current ($\Delta P \approx +15$ cm per winter in positive NAO years compared with negative NAO years), and with decreased winter production of sea ice (Deser *et al.*, 2000), a broad-scale freshening throughout the Atlantic water domain is not unexpected. Entering the Eurasian Basin, Morison’s comparison of SCICEX data with ‘climatology’ (Fig. 7.3.9, from Morison *et al.*, 2001; see Plate 7.3.9, p. 588) showed that the Atlantic sublayer had shoaled and warmed by up to 2°C and extended in distribution by about 20% (Morison *et al.*, 1998b), so that the mutual front between waters of Pacific and Atlantic origin had shifted from the Lomonosov to the Alpha-Mendeleev Ridge.

Accompanying this change at shallower depths, Steele and Boyd (1998) reveal that the cold halocline layer, which acts to insulate the sea ice from the warm Atlantic layer below, had dwindled away in the Eurasian Basin, with profound effects on the surface energy and mass balance of sea ice in that region. Hydrography, tracers and modelling all suggest that this change stemmed from the eastward diversion of Russian river input in response to the altered atmospheric circulation (see Maslowski’s

model output, in Dickson, 1999), and Arctic-wide, the whole pattern of atmospheric pressure and ice drift appears to have shifted counterclockwise in a similar sense. A record extent of open water was recorded in the eastern Arctic in the early 1990s (Serreze *et al.*, 1995; Maslanik *et al.*, 1996; McPhee *et al.*, 1998).

The third new feature to emerge during the 1990s was the evidence to link this long-term variability of the Arctic Ocean with seas further south. A combination of current measurements, upward-looking sonar and satellite imagery show that the amplifying NAO was accompanied by an increased annual efflux of ice through the western Fram Strait to a record volume-flux of $4687 \text{ km}^3 \text{ yr}^{-1}$ in 1994–95 (Vinje *et al.*, 1998; see also Kwok and Rothrock, 1999) and the southward recirculation of extreme warmth from the eastern Fram Strait (see above) was also observed to affect the Denmark Strait Overflow, some 2500 km further south (Dickson *et al.*, 1999).

Thus although not a part of the WOCE Field Experiment, a sufficient observing effort was in place across the Arctic during the 1990s to capture an unprecedented, extreme and system-wide suite of changes. If our longest proxies for the dominant forcing prove valid, these would have included effects of the most positive winter NAO index for over 500 years (Stockton and Glueck, 1999; see Section 7.3.2.2). Of direct importance to the aims of WOCE, these changes document a potential for global as well as regional effects on climate, acting locally through the effect of a changing ocean stratification and ice cover on surface heat flux, and remotely through the variable export of fresh waters and heat to the headwaters of the global thermohaline circulation. The latter seems particularly apt in view of the global importance that coupled models currently assign to relatively minor changes in freshwater distribution at high latitudes (Rahmstorf and Ganopolski, 1999).

7.3.8 Interdecadal variability of Kuroshio transport

Passing into the Pacific sector, we find that the climatic variability over the North and Equatorial Pacific over the past few decades has hardly been less extreme than that of the North Atlantic. In mid-latitudes, the NP index, reflecting the area-weighted mean SLP averaged over most of the

extratropical North Pacific Ocean (Trenberth and Hurrell, 1994) underwent a striking change amounting to a regime shift after about 1976. For most of the years since then, including the WOCE period, the index has been negative, reflecting an eastward-shifted and intensified Aleutian low (Section 7.3.2.3). At lower latitudes (Section 7.3.2.4), the Southern Oscillation has recently exhibited an unusual amplitude of decadal and longer-term variability (much like the recent behaviour of the NAO), with a pronounced change toward more negative values since the mid-1970s, and prolonged warm conditions into the start of the WOCE period in 1990–95.

The large scale of these climatic events suggest the possibility of a response in the circulation of the North Pacific. Though there is increasing evidence to link decade-scale fluctuations of ocean and atmosphere in this sector (e.g. Mantua *et al.*, 1997; Nakamura *et al.*, 1997), this has tended to concern the ocean surface rather than the interior. South of Japan, however, Qiu and Joyce (1992) have used the twice yearly hydrographic surveys along 137°E conducted by the Japan Meteorological Agency (JMA) from 1967 to 1988 to compute the long-term variations in the geostrophic transport of the Kuroshio, defined as the total eastward flow north of 30°N referenced to a depth of 1.25 km. Apart from resolving the fact that there is no apparent difference in Kuroshio transport between its straight-path and meander-path years (the WOCE period was essentially ‘straight-path’), these authors describe a decadal increase of 10.8 Sv in their Kuroshio transport between 1970 and 1980 and between 1982 and 1988. Miller *et al.* (1998) use a general circulation model to suggest that decadal transport variations of the Kuroshio current system over the same period were a response to large-scale wind forcing.

For the latitudes of the Kuroshio Extension (32–37°N) east of Japan, Deser *et al.* (1999) appear to confirm this increased transport in two ways. First the Sverdrup transport, inferred from the wind stress curl field, shows a decadal increase of 11.5 Sv between the 1970s and 1980s. Second, combining the change in ocean temperature across the Kuroshio Extension between the 1970s and 1980s with climatological salinity profiles from Levitus and Boyer (1994b), they find that the depth-averaged geostrophic transport referenced to 1 km increased by 11.6 Sv between 32°N and

37°N. (They note a 4- to 5-year delay between the decadal scale variation in thermocline depth near the western boundary and the basin-wide pattern of wind stress curl.) In the present context, the question is whether this apparent increase in Kuroshio transport from the 1970s to the 1980s was maintained into the period of WOCE. Two main time series are available to help answer it.

In Figure 7.3.10a,b we use the hydrographic section data collected by JMA along 137°E to extend the available time series of geostrophic transport estimates south of Japan to 1997. The reference level is 1200 dbar. These figures provide separate estimates of transport both for the eastward flow of the Kuroshio itself and for the net throughflow of the Kuroshio current system. The geostrophic transport estimate labelled 'Kuroshio' (Fig. 7.3.10a) is integrated from the Japanese coast

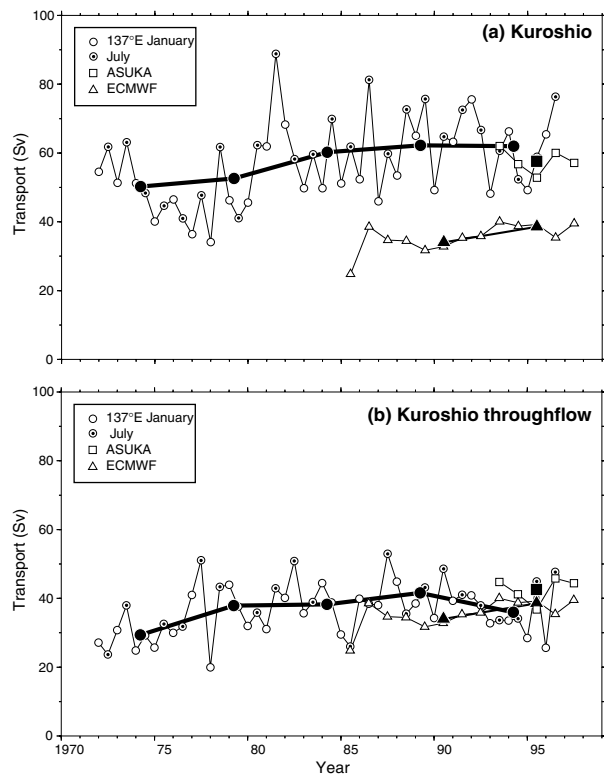


Fig. 7.3.10 Time series of transport of (a) the Kuroshio and (b) the Kuroshio throughflow south of Japan. Three kinds of estimates are shown in each panel: geostrophic transports referred to 1200 dbar across 137°E, transports estimated from direct/remote measurements across ASUKA line, and the Sverdrup transports calculated from the ECMWF windfield. Five-year means are shown as well as annual or biannual estimates. See Figure 7.3.11 for locations, and text for details.

south to the latitude at which the eastward-flowing current reverses. The transport labelled 'Kuroshio throughflow' (Fig. 7.3.10b) is the integral of the entire Kuroshio current system, including westward recirculations, from the Japanese coast to a fixed point at 26°N, 137°E, close to the point of intersection with the diagonal ASUKA line (see Fig. 7.3.11 for locations).

Each figure includes three time series: (1) geostrophic estimates from repeat hydrography along 137°E in January and July, (2) direct/remote measurements of transport based on ASUKA observations and TOPEX/POSEIDON satellite data, and (3) Sverdrup transports calculated from the European Centre for Medium Range Weather Forecasts (ECMWF) wind field. The 'ASUKA' time series is obtained by combining TOPEX/POSEIDON altimeter data with intensive direct current measurements and repeat hydrography along the ASUKA line (Imawaki *et al.*, 1997, 2001; ASUKA stands for Affiliated Surveys of the Kuroshio off Cape Ashizuri). That labelled 'ECMWF' was obtained by integrating the wind stress curl at 30°N over the entire North Pacific (analysis of ECMWF data, kindly provided by Dr Kunio Kutsuwada, Tokai University). They are shown both as 5-year means and as individual section estimates for 137°E, and as annual means for ASUKA

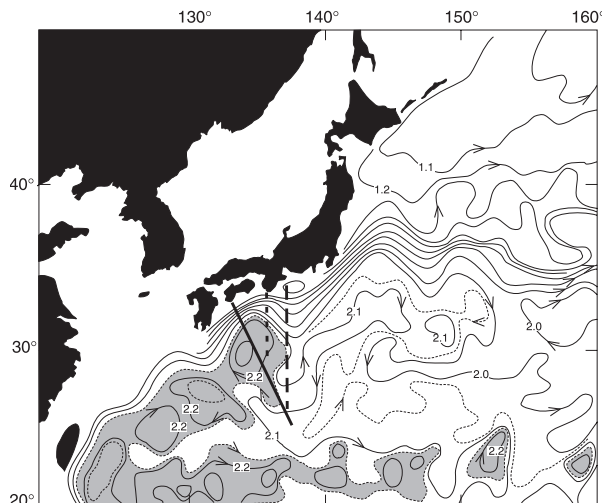


Fig. 7.3.11 Map showing locations of three sections crossing the Kuroshio south of Japan: the ASUKA line (solid line), the 135°15'E meridional line (dotted), and the 137°E meridional line (dashed). The distribution of the climatological mean geopotential anomaly at the sea surface relative to 1000 dbar is also shown, adapted from Hasunuma and Yoshida (1978).

and ECMWF. As illustrated, the long-term fluctuations (5-year mean) of Kuroshio transport and Kuroshio throughflow at 137°E show both similarities and differences: low values in the early 1970s are common to both series, but the slight upward trend thereafter in ‘Kuroshio’ transport appears to be maintained through the 1980s into the 1990s, while that of ‘Kuroshio throughflow’ begins to decline. The Sverdrup transport, inferred from the wind stress curl field, agrees better with the transport of the Kuroshio throughflow than with that of the eastward-flowing Kuroshio because the latter includes the transport of the eastward flow associated with the local anticyclonic eddy located on the offshore side of the Kuroshio (see Fig. 7.3.11).

It is apparent from the 137°E series that the January and July values are quite different, so that the slight overall trend may not be well resolved by this biannual series. However, we can supplement these results with an even longer time series at twice the resolution. Since 1956, the Kobe Marine Observatory of JMA has worked hydrographic sections across the Kuroshio at 135°15'E on board the Research Vessel (RV) *Shumpu-Maru*. The observations were carried out four times per year, initially by Nansen bottle, then STD, then CTD. From this data set, geostrophic velocities were calculated relative to the 1000 dbar level and a time series of Kuroshio transport estimates was then derived by integrating these over the 90-mile width covering the strongest part of the Kuroshio’s eastward flow (Nakamura and Hinata, 1999). If westward flow was encountered in this 90-mile band, the integration was truncated accordingly.

The result is a time series of Kuroshio eastward transport covering more than 40 years from 1956

to 1997 (Fig. 7.3.12; from Nakamura and Hinata, 1999). While the individual estimates are somewhat noisy, a very clear signal of interdecadal variability is nevertheless apparent, with relatively small transports in the 1950s, large in the 1960s, small in the 1970s and large in the 1980s, thus some evidence of a fluctuation of ~20-year period, with a somewhat different phase in the 1990s. The overall pattern of change agrees very well with the interdecadal fluctuation in the transport of the Kuroshio Extension inferred by Deser *et al.* (1999) and is therefore accepted here as the longest and best-resolved expression of the behaviour of the Kuroshio available to us. The match with Deser’s series suggests that the fluctuation may also be a manifestation of the same oceanic response of the North Pacific subtropical gyre to the interdecadal fluctuation in atmospheric forcing, with the same 4- to 5-year delay expected in the ocean’s response. Table 7.3.1 expresses the relative strength of the Kuroshio on this transect during the WOCE field phase relative to earlier years. The transport in the 1990s is almost as large as in the 1980s.

Little is known about how the Kuroshio is affected by El Niño events, which dominate the interannual variability of the tropical Pacific (see Section 7.3.2.4). Some hint of the relationship between the Kuroshio Extension and El Niño events has been shown. Yamagata *et al.* (1985) and Jacobs *et al.* (1994) suggest that planetary-scale oceanic waves generated by the 1982–83 El Niño event may have crossed the North Pacific to cause a northward re-routing of the Kuroshio Extension a decade later. These intermittent but protracted events may result in the blurring of the WOCE ‘snapshot’. To determine the climatological mean state of the oceans, long-term continuous monitoring is required.

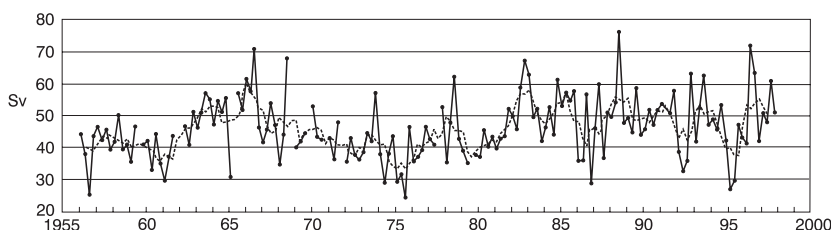


Fig. 7.3.12 Time series of the Kuroshio transport from 1956 to 1997 south of Japan (135°15'E; see Fig. 7.3.11 for location). Geostrophic velocities relative to 1000 dbar are integrated over the 90 miles that span the strongest part of the Kuroshio. Estimates are made four times per year. The dotted line is the running average over five estimates. Adapted from Nakamura and Hinata (1999).

Table 7.3.1 Five-year means of Kuroshio eastward transport at 135°15'E

| Period | Mean transport (Sv) | Seasons/years of missing data |
|---------|------------------------|---------------------------------------|
| 1956–59 | 41.5 | Summer/1959 |
| 1960–64 | 45.5 | Autumn/1961, Winter/1962 |
| 1965–69 | 49.0 | Spring/1965, Autumn/1968, Autumn/1969 |
| 1970–74 | 41.5 | Autumn/1970, Autumn/1971 |
| 1975–79 | 40.4 | Summer/1977, Summer/1979 |
| 1980–84 | 48.6 | |
| 1985–89 | 49.7 | |
| 1990–94 | 48.9 | |
| 1995–97 | 47.8 | |

Before averaging, values for the seasons with missing data were estimated from the values of preceding and succeeding seasons by linear interpolation.

Table 7.3.2 The three main water masses, Sub-Antarctic Mode Water (SAMW), North Pacific Intermediate Water (NPIW) and Antarctic Intermediate Water (AAIW), the sections on which they occur, and their density range. The depth range, temperature range and salinity end points are the zonal average depth, temperature, and salinity defined by the density range of these water masses

| Water mass | Section | Neutral density | Depth range (dbar) | Temperature range (°C) | Salinity end points |
|------------|---------|-----------------|--------------------|------------------------|---------------------|
| SAMW | 32°S | 26.8–27.1 | 447–782 | 11.52–8.10 | 35.06–34.65 |
| | 43°S | 26.8–27.1 | 203–667 | 11.33–7.59 | 35.01–34.53 |
| NPIW | 24°N | 26.4–27.2 | 430–740 | 9.94–4.99 | 34.19–34.21 |
| AAIW | 10°N | 27.1–27.6 | 524–1111 | 7.66–4.10 | 34.58–34.57 |
| | 17°S | 27.1–27.6 | 566–1102 | 7.21–3.82 | 34.49–34.52 |
| | 32°S | 27.1–27.6 | 780–1330 | 8.10–3.62 | 34.65–34.52 |
| | 43°S | 27.1–27.6 | 670–1300 | 7.59–3.64 | 34.53–34.48 |

1 dbar \sim 1 m

7.3.9 Evidence of water mass changes in the Pacific and Indian Oceans

Here we focus on large-scale changes observed in three distinct intermediate water masses of the Pacific and Indian Oceans: Sub-Antarctic Mode Water (SAMW), Antarctic Intermediate Water (AAIW) and North Pacific Intermediate Water (NPIW), all of which are key components of the thermohaline circulation in these regions. Typically, we compare observations from the 1960s and 1970s with WOCE hydrographic data from the late 1980s and early 1990s and are therefore describing the observed differences over a period of 20 years or so (Bindoff and Church, 1992; Johnson and Orsi, 1997; Bindoff and McDougall, 2000; Wong *et al.*, 1999). We have based our studies on hydrographic data because they provide concurrent measurements of the two main oceanic variables: temperature and salinity. As a result we

were able to determine the relative roles of these two variables in decadal oceanic changes. These observations are restricted temporally and spatially to the availability of historical hydrographic data. However, even with limited coverage, comparisons of hydrographic data have shown remarkable water mass changes that are coherent on basin-wide scales.

7.3.9.1 Warming of SAMW

Along the 43°S parallel between Australia and New Zealand, a repeat of the 1967 SCORPIO section by RV *Franklin* in 1989–90 showed a strong cooling and freshening signal on density surfaces, with a downward displacement of isopycnals (Bindoff and Church, 1992). The cooling and freshening was strongest in SAMW (26.8 to 27.1 $\gamma_n \text{ kg m}^{-3}$, see Table 7.3.2), and coincided with a significant warming on pressure surfaces. Using

the method of Bindoff and McDougall (1994), these changes in SAMW were most simply explained by the ‘pure warming’ process, consistent with the warming of surface waters south of Australia and their subsequent subduction; the ‘pure freshening’ process (freshening of the source waters) was less important.

Johnson and Orsi (1997) later showed that these changes, first noted in the Tasman Sea, have a broad geographical distribution. Comparing repeat occupations of a meridional section along 170°W between 60°S and the Equator in 1968–69 and 1990, and a short zonal section along 35°S from the dateline to 169°W in 1969 and 1991, they found a robust cooling (and freshening) on isopycnals, with peak differences exceeding -1.0°C (-0.25 psu) around the SAMW layer at the base of the subtropical thermocline, and extending into the AAIW layer below. More generally they showed that while this pattern of change on density surfaces in SAMW was strongest in the region south of Australia, it extended over almost the whole South Pacific, with the exception of the southeastern region from 100°W to South America (Fig. 7.3.13, see Plate 7.3.13, p. 588).

The apparently contradictory result of warming (and increased salinity) on density surfaces in this

southeastern region also coincides with the change from a positive to negative slope in the θ –S relation. If Figure 7.3.3b were to have a negative slope (see also Bindoff and McDougall, 1994), it would show that warming of surface waters leads to warming (and increased salinity) on density surfaces in these circumstances, so that this change remains consistent with the pattern of cooling and freshening on density surfaces found further to the west. The simplest interpretation of the changes on this density horizon in SAMW for the whole South Pacific is that the surface waters feeding this water mass have been warmed during this ~ 20 -year period.

7.3.9.2 Freshening of NPIW and AAIW

The two intermediate waters, NPIW and AAIW, which originate respectively in the sub-polar North Pacific (Warner *et al.*, 1996) and in the Southern Ocean, have similar roles in ventilating the intermediate depths of the Pacific Ocean. NPIW is of much smaller volume and is confined to the North Pacific, while AAIW can be found in the Atlantic, Indian and Pacific Oceans. Both of these water masses are characterized by a salinity minimum.

To identify any change in their properties, six WOCE hydrographic sections covering parts of the Pacific and Indian oceans were compared with

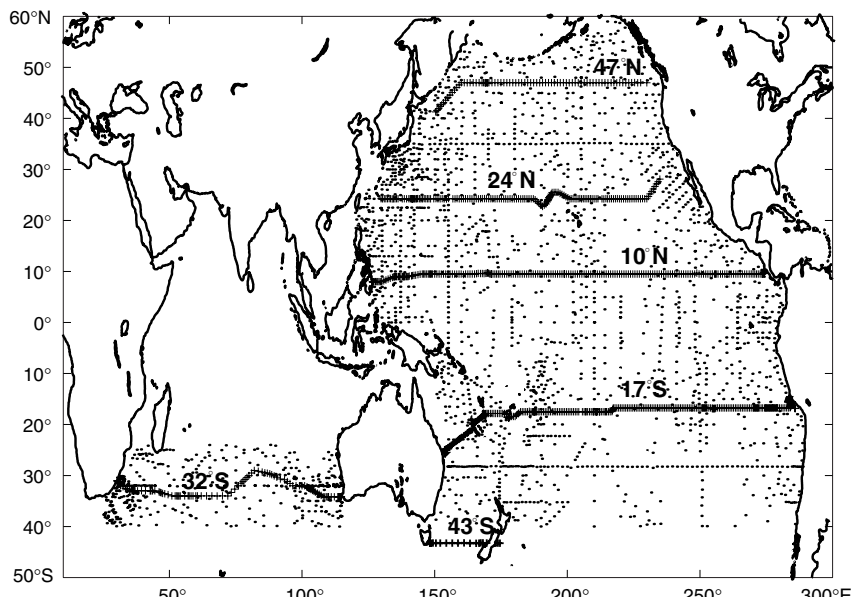


Fig. 7.3.14 Locations of the historical data (shown by dots) and modern data (shown by crosses) used in the comparison of Figures 7.3.15 and 7.3.16 (Wong *et al.*, 1997). The historical data are mainly high-quality Nansen bottle data from IGY programmes during the early 1960s and were obtained from Professor J. Reid (Reid and Mantyla, 1995). The WOCE sections are obtained from the WOCE WHPO (WOCE Hydrographic Program Office, 1998). Reprinted with permission from Nature 400, copyright 1999, Macmillan Magazines Limited.

available historical data from the 1960s (Fig. 7.3.14). Running zonally along 47°N , 24°N , 10°N , 17°S , 32°S and 43°S , these sections cover the subpolar, subtropical and equatorial regions of the North Pacific, the subtropical gyres of the South Pacific and Indian Ocean, and the southern Tasman Sea. These transoceanic sections thus cover major and distinct oceanographic features of the global ocean.

The results of the section comparisons show a remarkably coherent pattern of change (Fig. 7.3.15). In the North Pacific Ocean, NPIW (26.4 to $27.2 \gamma_n \text{kg m}^{-3}$, see Table 7.3.2) has undergone statistically significant cooling (and freshening) on density surfaces at 24°N , and NPIW isopycnal depths are now significantly deeper (Fig. 7.3.15b). An intermediate salinity minimum is not present at 47°N , but waters in the 26.4 to $27.2 \gamma_n \text{kg m}^{-3}$ layer also show significant cooling (and freshening) on density surfaces. AAIW (27.1 to $27.6 \gamma_n \text{kg m}^{-3}$,

see Table 7.3.2) is now colder and fresher on density surfaces on all of the sections where it occurs, and with the exception of the 43°S section, the cooling (and freshening) on isopycnals is statistically significant at the 90% confidence level (Fig. 7.3.15c-f). At 32°S , the SAMW layer (26.8 to $27.1 \gamma_n \text{kg m}^{-3}$) has also experienced cooling (and freshening) on density surfaces, which has been attributed to warming of surface waters (Bindoff and McDougall, 2000).

Three of the sections (10°N , 32°S and 43°S) show that the zonally averaged depth of isopycnals is now deeper in AAIW and that the thickness of AAIW in these sections has decreased. This decreased thickness of intermediate waters implies that the potential vorticity has also decreased, with further implications for the strength of the gyre circulation (Wong, 1999).

While it was concluded for SAMW that the observed cooling and freshening on density surfaces

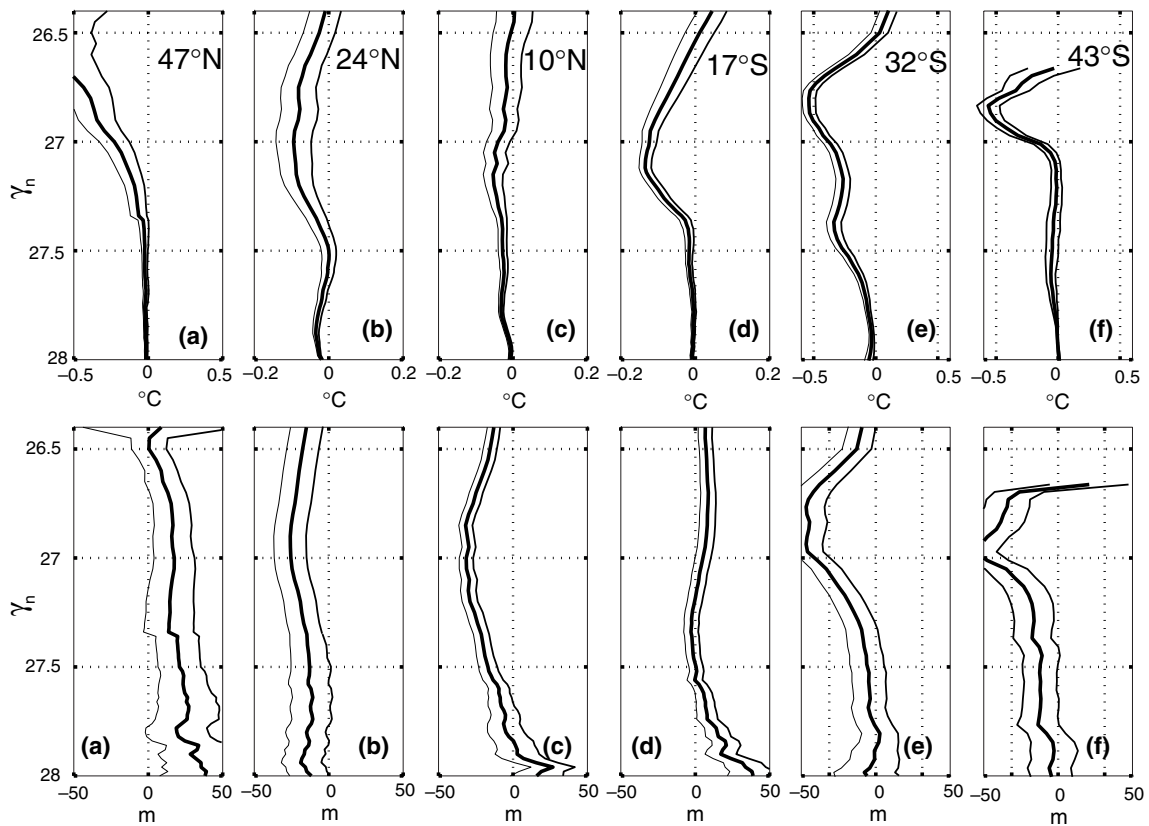


Fig. 7.3.15 Zonally averaged differences of temperature on density surfaces (top panels) and height of density surfaces (bottom panels) along each of the six WOCE sections at respectively 47°N , 24°N , 10°N , 17°S , 32°S and 43°S (a, b, c, d, e and f). The thin lines are 90% confidence intervals calculated from an estimate of the number of degrees of freedom, the error in differencing the two sections and our estimate of the prior noise in the data caused by mesoscale eddies and seasonal variations but not interannual variability. Positive depth changes mean that density surfaces are shallower in the 1980s and 1990s.

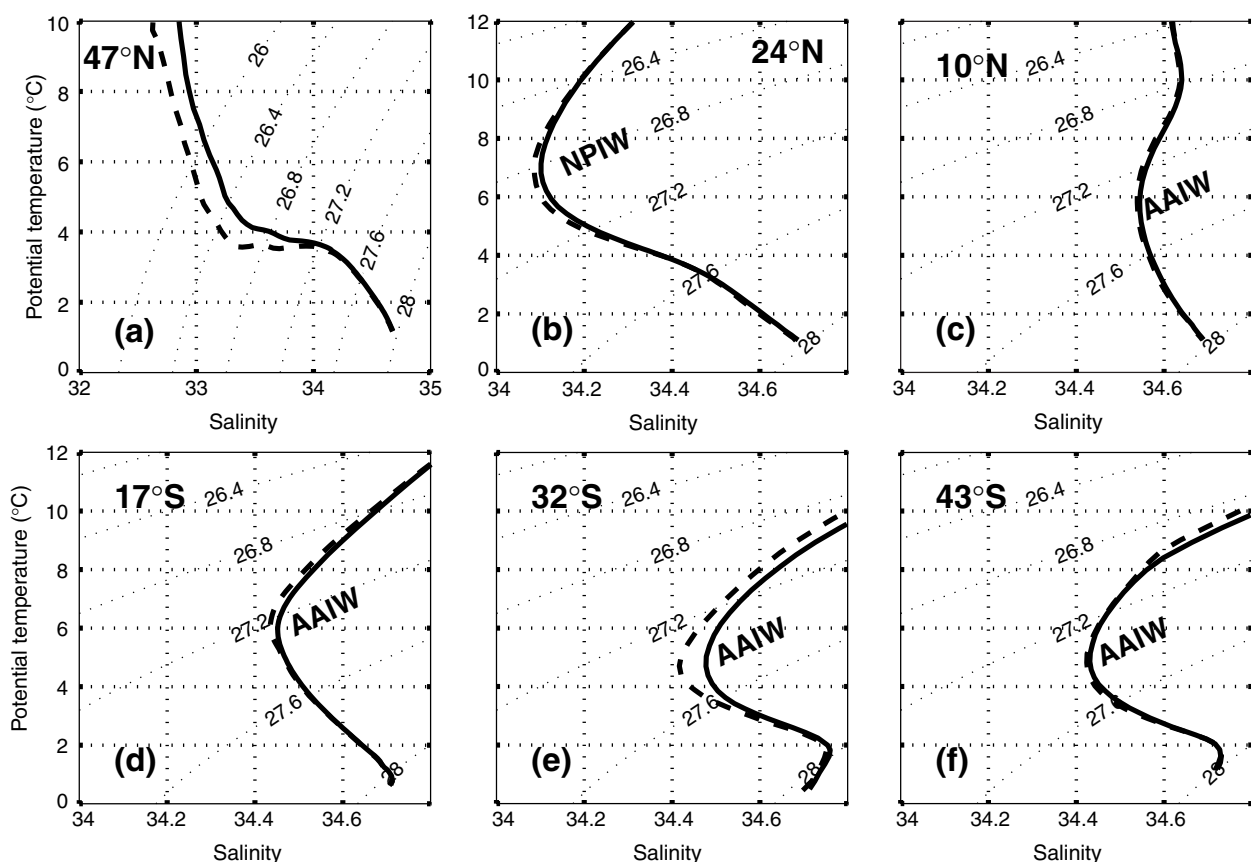


Fig. 7.3.16 The change in the zonally averaged θ -S properties along each of the six WOCE sections at, respectively, 47°N, 24°N, 10°N, 17°S, 32°S and 43°S. (From Wong *et al.*, 1999). Reprinted with permission from Nature 400, copyright 1999, Macmillan Magazines Limited.

is most simply explained by the subduction of warmed surface waters, the interpretation of the cooling (and freshening) of AAIW and NPIW on density surfaces is quite different. Both AAIW and NPIW are characterized by a distinct salinity minimum in θ -S properties (Fig. 7.3.16), and in five of the comparisons, the zonally averaged θ -S properties have freshened at the salinity minimum. There, the process of pure warming cannot formally be distinguished from the heave process (Bindoff and McDougall, 2000) and as a consequence this process does not have a distinct signature in the θ -S plots. However, using the simple arguments described earlier, it can be seen that the only way to displace the salinity minimum to fresher values (i.e. cooler and fresher on density surfaces) is by the subduction of fresher surface water. Hence the cooling and freshening on density surfaces observed in AAIW and NPIW is largely a response to fresher surface waters (Bindoff and McDougall, 1994, 2000; Wong, 1999). This implication is supported by observations of surface salinity trends

from four ocean stations off the Pacific coast of Canada (including Ocean Station Papa; Freeland and Whitney, 1997; Freeland *et al.*, 1997).

The magnitude of the freshening of intermediate waters on each section is roughly consistent with the large-scale ocean circulation. The primary source of AAIW is thought to be in the southeastern Pacific (McCartney, 1977; England, 1992) from where AAIW spreads around the South Pacific subtropical gyre and into the North Pacific equatorial region. Another branch follows the fast Antarctic Circumpolar Current (ACC) through Drake Passage to the Atlantic and Indian Oceans and the Tasman Sea. The 17°S section shows a larger salinity change than that shown by AAIW at 10°N (Fig. 7.3.16, or Fig. 7.3.15c,d), qualitatively consistent with the theory that the 10°N section lies further downstream from the supposed source. The 32°S section in the Indian Ocean is relatively close to the source and shows the largest salinity change of 0.06. AAIW on the 43°S section is a mixture of water that has been transported around

the South Pacific subtropical gyre and water from the Southern Ocean and its weak signal is therefore to be expected.

7.3.9.3 Discussion

The apparently large scales of the warming of SAMW in the South Pacific and Indian oceans, and the freshening of NPIW and AAIW across the North and South Pacific and the Indian oceans, suggest that these changes are not random, but rather a systematic modification of the shallow thermocline circulation. The warming of SAMW is largely consistent with the observed warming of surface waters over the last thirty years of up to 0.5°C (Bottomley *et al.*, 1990) in its source regions.

The evidence for freshening of the surface ocean at high latitudes does not exist in the observational database, but models of climate change due to increasing greenhouse gases (Manabe and Stouffer, 1994; Gordon and O'Farrell, 1997) all predict increased precipitation–evaporation poleward of 50°. The pattern of change suggested by these models is broadly consistent with the observed changes in SAMW, AAIW and NPIW properties.

An increase in rainfall at high latitudes would suggest a need for increased evaporation at lower latitudes so that the overall salt content of the oceans is conserved. There is some evidence that the observed high-latitude freshening is partially balanced (up to 60%) by increased salinity of shallower central waters on the 24°N, 10°N and 17°S sections (Wong, 1999; Wong *et al.*, 1999, 2001).

These observations suggest that it may be possible to verify the results from coupled ocean–atmosphere models and in consequence to begin to test quantitatively detection and attribution methods for evidence of climate change in the oceans.

7.3.10 Summary and Conclusions

In answering the question 'How was the World during WOCE?' two conclusions were perhaps inevitable: that we would be unable to form an opinion for some sea areas and depths that don't have much of a past observational record; and that for those areas that do, we would discover that something had changed. As Wunsch (1992) points out:

The ocean is a turbulent fluid in intimate contact with another turbulent fluid, the atmosphere.

Although I am unaware of any formal theorems on the subject, experience with turbulent systems suggests that it is very unlikely that any components of such a complex nonlinear system can actually remain fully steady; the frequency/wavenumber spectrum of the ocean circulation is almost surely everywhere filled.

However, while change *per se* would be unsurprising, it is still worth trying to determine the sense and amplitude of the major changes that were passing through the ocean–atmosphere system in the 1990s, while the WOCE data set was being collected, in order to have some assessment, however limited, of its 'representativeness'. Within the scope accessible to us (see Section 7.3.1), the following seem to be the main currents of change.

- 1 The interdecadal temperature variability of the Atlantic Ocean at intermediate depths shows elements of coherent long-term change over a broad band of latitudes from 32°S to 36°N. Comparing hydrographic sections worked in the 1920s, 1950s, 1980s and 1990s, it was found that the largest statistically significant changes were generally found between 1000 and 2000 dbar. Over this pressure range, temperatures have increased by $\sim 0.5^\circ\text{C century}^{-1}$ on surfaces of constant pressure (isobars). (A cooling of $\sim 3^\circ\text{C century}^{-1}$, which occurred between the 1950s and 1980s at 48°N, is the exception.) In the North Atlantic between the 1950s and 1980s, the warmings are mostly due to downward displacements of isopycnal (neutral) surfaces, while changes *on* isopycnal surfaces dominate all but the most recent of the South Atlantic signals.
- 2 The WOCE field phase (1990–97) occurred at a most unusual interval in the climatic history of the North Atlantic, at the end of a period in which the principal recurrent mode of atmospheric forcing in this sector – the winter NAO – had amplified over three or four decades to its most extreme positive state (generally) in a 176-year instrumental record, and possibly much longer. A varied and extreme response is evident in sea areas dominated by the NAO – the North Atlantic, Nordic Seas and Arctic Ocean.
- 3 Since convective sites are important in carrying the signal of climate change to intermediate and greater depths (and from there, by horizontal spreading, throughout the ocean basin), the

response in the production of the convectively formed mode waters (Greenland Sea Deep Water, Labrador Sea Water and Eighteen Degree Water) appears to have been particularly important. Driven by wind and buoyancy forcing associated with the changing NAO, convective activity at all three sites evolved over decades to a long-term extreme state – in phase but of differing sign – during the NAO minimum of the 1960s, at which time the ventilation of the Greenland Sea and Sargasso was at a maximum and that of the Labrador Sea was tightly capped. Since then all three centres evolved rather more rapidly towards their opposite extreme states by the 1990s, during which convection in the Greenland Sea and Sargasso was suppressed but vertical exchange in the Labrador Sea reached deeper than previously observed.

- 4 In the West Atlantic, these coordinated changes of opposite sign in the production and characteristics of the mode waters had important repercussions on the strength of the Atlantic gyre circulation. The strength of the main North Atlantic Current is determined by the gradient of potential energy anomaly (PE') across the mutual boundary between the Atlantic subtropical and subpolar gyres, which in turn reflects the density and heat content of the mode waters in each gyre. From the observed PE' differences between the centres of the two gyres, Curry and McCartney (2001) calculate that the long-term increase in the NAO index to the mid-1990s was accompanied by a 30% increase in the 0–2000 dbar east-going baroclinic mass transport along the gyre–gyre boundary, from 50 Sv in 1970 to 65 Sv in the mid-1990s. Both subpolar and subtropical gyres contributed equally to this change. If this link with the NAO proves valid, then the North Atlantic gyre circulation during WOCE is likely to have been at its strongest for more than a century.
- 5 The Nordic Seas are important as a source of change for both the climatically sensitive Arctic Ocean and for the northern overflows that form the headwaters of the meridional overturning circulation (MOC). Over the period (post 1982) for which both the temperature and salinity of the deep waters are known with adequate precision, we have observed a progressive, almost linear, increase in the temperature and salinity of the deep Greenland Sea to unprecedented values

by the mid-1990s, by which time GSDW properties lay quite outside their defined range. This change is attributed to an altered balance between vertical and horizontal exchange processes, with a progressive shutdown in deep winter convection in the Greenland Sea (part of the same coordinated pan-Atlantic pattern of convective change as described earlier) and a corresponding increase in the horizontal exchange of warm saline deep waters through Fram Strait. Alternative (perhaps additional) explanations include the collapse of the ‘domed’ density structure in the Greenland Sea and the enhanced importance of diapycnal mixing over the rough topography of Mohn’s Ridge as a mechanism for deep water renewal.

- 6 Variability in the Arctic has long been thought to play some special role in the processes of global change. Three main changes in particular have characterized the WOCE Period of the 1990s. The first was a more intense and more widespread influence of Atlantic water than previously observed, with a warming (by up to 2°C) and spreading (by ~20%) of the Atlantic-derived sublayer across the Eurasian Basin (Morison *et al.*, 1998a,b, 2001); as the winter NAO index amplified, the increasingly anomalous southerly airflow that accompanies such a change over Nordic seas is held responsible for a progressive warming and perhaps a strengthening of the two streams of Atlantic water that enter the Arctic Ocean. Second, the cold halocline layer, which acts to insulate the sea ice from the warm Atlantic layer below, was shown to have weakened in the Eurasian Basin (Steele and Boyd, 1998), with profound effects on the surface energy and mass balance of sea ice in that region; hydrography, tracers and modelling all suggest an eastward diversion of Russian river input in response to the altered atmospheric circulation. Third, we have new observational evidence that the amplifying NAO was accompanied by an increased annual efflux of ice through the western Fram Strait (Vinje *et al.*, 1998; Kwok and Rothrock, 1999); relatively minor changes in freshwater distribution are assigned a high importance in current climate models.
- 7 During the past few decades, the climatic variability over the North and Equatorial Pacific has hardly been less extreme than that of the North Atlantic. In mid-latitudes, the NP index

of Trenberth and Hurrell, reflecting the area-weighted mean SLP averaged over most of the extratropical North Pacific Ocean, underwent a striking change amounting to a regime shift after about 1976. For most of the years since then, including the WOCE period, the index has been negative, reflecting an eastward-shifted and intensified Aleutian low. At lower latitudes, the Southern Oscillation has recently exhibited an unusual amplitude of decadal and longer-term variability (much like the recent behaviour of the NAO), with a pronounced change toward more negative values since the mid-1970s, and prolonged warm conditions into the start of the WOCE period in 1990–95.

- 8** To investigate the possibility of a response in the Kuroshio and its extension, (analogous to the changes in the North Atlantic Current described earlier), the longest time series available to us is a 40-year series (1956–97) of geostrophic transport estimates by the Kobe Marine Observatory, covering the strongest part of the Kuroshio's eastward flow at 135°15'E, south of Japan. A clear signal of interdecadal variability is apparent, with relatively small transports in the 1950s, large in the 1960s, small in the 1970s and large in the 1980s, thus some evidence of a fluctuation of ~20-year period. The overall pattern of change agrees very well with the shorter geostrophic transport series by Qiu and Joyce (1992) at 137°E, and the interdecadal fluctuation in the transport of the Kuroshio Extension inferred by Deser *et al.* (1999). Thus the fluctuation may also be a manifestation of the same oceanic response of the North Pacific subtropical gyre to the interdecadal fluctuation in wind forcing. The transport of the Kuroshio in the 1990s is almost as large as in the 1980s.
- 9** A comparison of hydrographic data from the 1960s and 1970s with WOCE hydrographic data from the late 1980s and early 1990s reveals coherent changes in three distinct intermediate water masses of the Pacific and Indian Oceans: Sub-Antarctic Mode Water (SAMW), Antarctic Intermediate Water (AAIW) and North Pacific Intermediate Water (NPIW). All are key components of the thermohaline circulation in these regions. Over this ~20-year period the evidence is of an extensive isopycnal cooling and freshening of the SAMW layer over much of the South Pacific, consistent with the warming of surface

waters south of Australia and their subsequent subduction; the 'pure freshening' process is of lesser importance. In the case of NPIW and AAIW, the results of section comparisons from 47°N to 43°S show a remarkably coherent pattern of change, with significant cooling (and freshening) on density surfaces on all of the sections where they occur. The magnitude of the freshening of intermediate waters on each section is roughly consistent with the large-scale ocean circulation. While the cooling and freshening of SAMW on density surfaces was most simply explained by the subduction of warmed surface waters, the interpretation of the cooling (and freshening) of AAIW and NPIW on density surfaces is by the subduction of fresher surface water. The warming of SAMW is largely consistent with the observed warming of surface waters over the last 30 years of up to 0.5°C in its source regions. The observational database is not adequate to comment on the supposed freshening of the surface ocean at high latitudes, but such a change seems consistent with modelled scenarios of climate change due to increasing greenhouse gases. The apparently large scales of the warming of SAMW in the South Pacific and the freshening of intermediate water in both Pacific and Indian Oceans suggest that these changes are not random, but rather a systematic modification of the shallow thermohaline circulation.

- 10** The state of the southern hemisphere atmosphere during WOCE is more difficult to quantify because of the paucity of data. Nevertheless, the leading mode of atmospheric variability is characterized by zonally symmetric out-of-phase fluctuations in atmospheric mass between high and subtropical latitudes, and the time series of this mode shows a strong trend toward lower than average SLPs during the 1990s at high latitudes with stronger westerlies in middle latitudes.

Acknowledgements

Brian Arbic/Brech Owens thank M. Arhan for providing the data at 7.5°N; G. Siedler and J. Holfort for the 1994 11°S data; J. Dunworth, G. Heimerdinger and T. McKee for providing the rest of the data from archived sources; P. Robbins

for contributing invaluable data analysis routines; A. Fischer, G. Brown and the WHOI graphics department for producing Figure 7.3.4; T. Joyce, P. Robbins, R. Millard, B. Warren, N. Fofonoff, C. Frankignoul, J. Pedlosky, and seminar attendees at the AGU Ocean Sciences Meeting, WHOI, URI, MIT, Lamont and GFDL for useful discussions; and R. Pickart, G. Eshel, R. Schmitt, H. Bryden and T. Haine for improvements to the text. BA was supported by a fellowship from the US Office of Naval Research while this research was undertaken. Shiro Imawaki gratefully acknowledges the assistance of Dr Hiroshi Uchida of Japan Science

and Technology Corporation (JST) in the computation and graphics of Kuroshio transport. Igor Yashayaev gratefully acknowledges the help of Allyn Clarke and John Lazier in compiling the historic and WOCE hydrographic data used in the studies of interannual to decadal variability in the Labrador Sea (Fig. 7.3.6). Ruth Curry and Mike McCartney, WHOI, Martin Visbeck of LDEO and Monika Rhein of Institut für Ostseeforschung, Warnemunde, and Jamie Morison, Applied Physics Laboratory, University of Washington kindly permitted the use of key figures still in press (our Figs 7.3.7, 7.3.8c and 7.3.9).

This Page Intentionally Left Blank

7.4

Ocean and Climate Prediction – the WOCE Legacy

Neville Smith

7.4.1 The long-term context

This chapter focuses on the future and examines the likely legacy from the World Ocean Circulation Experiment (WOCE) for ocean and climate prediction. WOCE will be recorded as a period of greater than usual effort, but we should not forget the larger context within which the Experiment was conducted. We are working from a rich and broad history and it is useful to devote just a little space to recognizing this development.

The laying of undersea cables to connect the American and European continents during the middle of the nineteenth century provided one of the initial motivations for examining the deep ocean. At about that time, investigation of the ocean for purely scientific purposes also became more common. The British *Challenger* expedition from 1872 to 1876 and German exploration on the *Gazelle* from 1874 to 1876 were two of the early successful deep sea expeditions, taking systematic measurements of ocean currents, temperature, chemistry and biology, as well as sampling bottom sediments. Another important factor that motivated scientific interest and observation was commerce. Valuable trading routes had been created on the open seas and travel time was a critical element of commercial success. Knowledge of marine and ocean conditions was vital. M. F. Maury, superintendent of the Depot of Charts and Instruments at Washington, DC, in the middle part of the nineteenth century, realized that scientific study and systematic observations of the sea

could improve safety and decrease voyage times. Maury began to collect and collate information on surface currents and weather conditions leading to the publication of *The Physical Geography of the Sea* (Maury, 1859), which was one of the first practical applications of ocean science and observations. This international system of voluntary observation remains in place today, nearly 150 years later, and was an important method for WOCE.

These scientific endeavours marked the start of what Neumann and Pierson (1966) termed the first era of oceanographic research. The three-dimensional structure of the ocean was being observed for the first time. Thermometers were available to measure temperature with depth, and Knudsen (1900, 1901) introduced chlorine titration for more accurate determination of salinity and empirical tables for determining density from temperature and salinity. The first scientific expeditions into high latitudes took place at this time, one of the more adventurous being Fridtjof Nansen's drift with the *Fram* through the Arctic Seas from 1893 to 1896 (Greve, 1994).

The second era was born out of the realization that the ocean was not stationary, leading to exploration and study of ocean currents. Expeditions of the early twentieth century made more accurate physical and chemical measurements and the station spacing was closer, driven in part by theoretical revelations on ocean dynamics (Rossby, 1936, 1937). While this era probably marked the

first awareness of spatial and temporal sampling problems, many years would pass before the ramifications of aliasing and poor spatial resolution were appreciated, and it was not until WOCE that a systematic attempt was made to resolve such uncertainties.

World War II marked the start of a third era, which was characterized by significant technological advances, such as the bathythermograph for continuously recording temperature as a function of depth, and by highly organized, intensive oceanographic surveys that sought quasisynoptic sampling of large regions. This era also marked the introduction of non-ship instrumentation such as drifting and moored buoys. One of the more imaginative innovations of this period was the neutrally buoyant float (Swallow, 1955). The principles of this technology provide the basis for modern autonomous float instrumentation. Like the previous era, significant advances in theory, not the least being the first theoretical explanations of the gyres and intense western boundary currents (for example, Stommel, 1948), also marked this period.

The modern era has introduced a variety of autonomous *in-situ* measurement methods, such as profiling floats (Davis and Zenk, Chapter 3.2) and moorings (Hogg, Chapter 4.5), remote sensing from satellites (Fu, Chapter 3.3; Liu and Katsaros, Chapter 3.4), and advanced numerical ocean models, made possible by high-performance computers (Böning and Semtner, Chapter 2.2; Willebrand and Haidvogel, Chapter 7.2). The growth in computing power has been phenomenal over the last 50 years, as has our ability to sense remotely the state of the ocean and climate. The previous chapters provide many of the technical and scientific details behind the contribution from WOCE to these advances.

These simple reflections are important when we try to examine the legacy of WOCE for current and future research programmes and, in particular, for the efforts to establish a sustained global ocean observing system. Good research would have taken place irrespective of WOCE and we would likely have seen enhanced contributions to the ocean observing system simply as a first-order response to growing societal demand. However, as will be shown in this chapter, WOCE has made distinctive contributions to scientific and technical development in ways that would not have happened

through chance, and it is these aspects I would like to draw out here. The views are eclectic in that I will develop the focus around observations and concentrate largely on those aspects of the WOCE observational programme that offer greatest promise in a follow-on, sustained effort within the framework of the Global Ocean Observing System (GOOS), and those aspects which seem destined to enhance our ability to predict ocean and climate variability. I leave discussion of the many other contributions of WOCE to earlier chapters in this volume.

A convenient starting point is the second goal of WOCE (WCRP, 1988a):

To determine the representativeness of the specific WOCE data sets for the long-term behaviour of the ocean, and to find methods for determining long-term changes in the ocean circulation.

Within this goal there were several subobjectives including:

- 1 To determine the representativeness of specific WOCE data sets.
- 2 To identify those oceanographic parameters, indices and fields that are essential for continuing measurements in a climate observing system on decadal time scales.
- 3 To develop cost-effective techniques suitable for deploying in a climate observing system.

It seems natural, perhaps even obligatory, that research programmes such as WOCE include as part of their objectives a 'legacy goal' that aims to ensure that the practical benefits of the finite-lifetime research programme are passed forward to future generations. For observations, the selection of elements that are sustained beyond the observing period of the research programme must be founded on robust scientific understanding and proven usefulness (Nowlin, 1999). There are of course many observational methods that have proven extremely effective for WOCE, but which may not be strong candidates for sustained implementation, either because the methods were highly technical and specialized or because they have limited practical application at this time.

The issues of *representativeness* and *long-term climate* are perhaps the clearest links through to new research programmes and, in particular, to the

Climate Variability and Predictability Programme (CLIVAR, of the World Climate Research Programme; WCRP 1995a, 1998). Indeed, knowledge of representativeness is tantamount to understanding ocean climate variability, and determining the significance of change is equivalent to determining predictability. One important distinction, however, is that for WOCE oceanic variability is interesting not only for its direct role in the coupled climate system, but also for its semi-independent role in the ocean circulation as manifested through mesoscale eddies and vertical mixing, among other things.

The term ‘sustained’ is now often used to describe elements implemented for GOOS and for research (Smith, 1998; Nowlin *et al.*, 2000; Fig. 7.4.1). While there remain clear distinctions between the practical objectives of GOOS and the scientific goals of research programmes like CLIVAR, a very strong synergy is emerging in the development of the observing system (Smith and Koblinsky, 1999). A research programme like CLIVAR needs elements maintained for the long-term and with broad, global objectives, as well as short-term, hypothesis (process)-driven elements that are often implemented regionally. The common thread is the broad base, for GOOS in terms of multiple applications and long-term, regular usage, and for CLIVAR (and research in general) in terms of support for multiple scientific objectives and multidisciplinary research.

This chapter begins by discussing briefly some of the more important linkages for WOCE, in particular to the CLIVAR research programme and the development of the climate module of GOOS (Section 7.4.2). The focus is on shorter time scales (seasonal-to-interannual) and climate prediction, but some implications on the longer decadal-to-centennial time scales, including climate change, are also discussed. Section 7.4.3 introduces those elements of the WOCE observational programme that are relevant to these issues. For the most part, these observations are examined in detail in other chapters of this volume. Section 7.4.4 looks at both the scientific and practical aspects of seasonal-to-interannual prediction and the contributions WOCE has made, and continues to make, to these developments. This discussion touches on issues of theoretical and practical predictability, the need for ocean data, and the development of models. Section 7.4.5 focuses on ocean estimation and the contribution from WOCE to enhanced capabilities for ocean data assimilation and ocean and climate prediction on longer time scales. The Global Ocean Data Assimilation Experiment (GODAE) is attempting to exploit this legacy. Section 7.4.6 discusses climate issues on longer time scales, an area where WOCE is contributing a distinctive and important legacy. Section 7.4.7 examines some recent developments in GOOS and, in particular, the ‘institutionalization’ of Goal 2 of WOCE. The chapter concludes with an overview of what

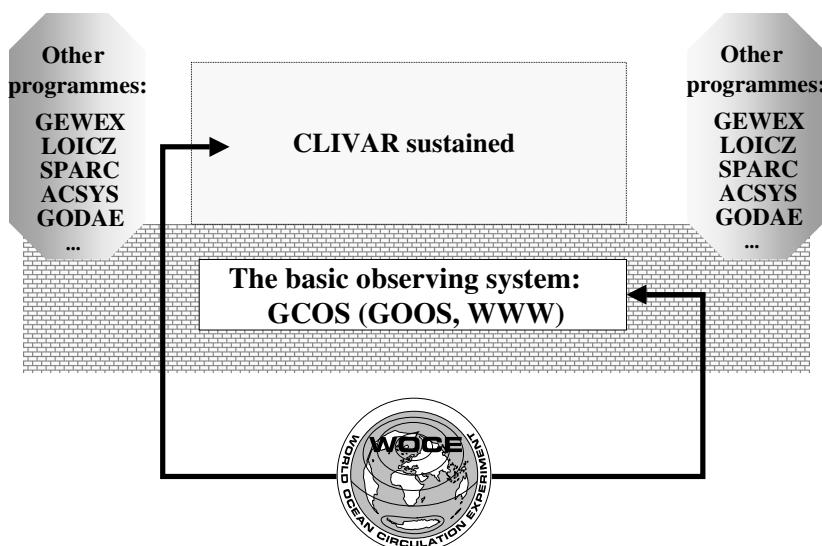


Fig. 7.4.1 WOCE observations are laying the foundations for both the basic, operational observing system of GOOS and the sustained observing system of CLIVAR.

WOCE has meant for the development of a global ocean observing system, operational oceanography and for the development of enhanced capabilities for ocean and climate prediction.

7.4.2 Building from WOCE

The nature of ocean and climate problems and their intrinsic large (global) scales has meant that international cooperation and collaboration has become an essential aspect of the science. The International Geophysical Year (in 1958), the International Decade of Ocean Exploration, and the First Global Experiment of the Global Atmospheric Research Programme provide examples where the community worked together to tackle problems that were beyond the capacity of individuals or small groups. The Tropical Oceans-Global Atmosphere Experiment (TOGA, 1985) is a modern example of 'programme science' whereby the combined efforts of many researchers and research groups were able to advance our knowledge of climate variability, particularly El Niño, and develop methods and systems of practical importance. TOGA is widely judged as having been a successful experiment (WCRP, 1995a). By the end of 1994, experimental and operational El Niño forecast systems existed (Anderson *et al.*, 2001) and moves were underway to sustain the important elements of the TOGA observing system and, in particular, the TOGA (now Tropical) Atmosphere–Ocean array (TAO) (McPhaden, 1995; McPhaden *et al.*, 1998). The latter has in fact taken rather longer than expected, not because of doubts in the scientific value, but because there was little experience in transitioning experimental ocean observing systems to long-term sustained (operational) support and little in the way of established operational funding and infrastructure mechanisms.

The WOCE observation programme began mid-way through TOGA and immediately the community recognized the synergy between the observational strategies of WOCE and TOGA. This recognition manifested as joint management and implementation of several elements including the expendable bathythermograph (XBT) network, sea-level sites and the surface drifter velocity programme. Through this same period, efforts were initiated to develop a plan for a more permanent observing system in support of climate. The planning of the Ocean Observing System Development

Panel (1995) grew mainly from within the WOCE community but accepted the broader mandate to develop a general conceptual plan for climate observations within the framework of GOOS and the Global Climate Observing System, including climate aspects of the carbon cycle.

With the publication of the Ocean Observing System Development Panel (1995) Report, the focus shifted toward the realities of implementation. Within GOOS, the so-called Climate Module (or, equivalently, the ocean component of the Global Climate Observing System) was the vehicle within which plans for implementation of an ocean observing system for climate were developed (see, for example, the Intergovernmental Oceanographic Commission/World Meteorological Organization, 1999). In a scientific volume such as this, many would query the usefulness of introducing such programmatic aspects, yet, as will become evident in later sections, it is these very developments that are critical for the proper exploitation of the legacy of WOCE. The business community speaks of short- and long-term returns on investment. Such a concept applies equally here. WOCE itself, though a major undertaking, must be treated as a finite, relatively short-period investment of resources and effort. The research outcomes from WOCE, such as the advances in scientific knowledge and technical capability detailed in this volume, constitute the short-term return. It is through the development of appropriate institutions and sustained infrastructure that we can assure commensurate long-term returns.

CLIVAR was in the first instance a reaction to the success of TOGA and the need to build upon this scientific momentum. It was also an attempt to develop a more general, global basis for climate research and climate prediction and to provide a coherent, general framework for the post-WOCE period and the approach to research of the physical climate system. As noted in Section 7.4.1, the outcomes from Goal 2 of WOCE provide a significant underpinning for the climate research of CLIVAR. For the purposes of this discussion CLIVAR can be viewed as a research programme with interests in time scales ranging from the intraseasonal through to decadal and centennial, including climate change. The El Niño–Southern Oscillation phenomenon (ENSO) is arguably the climate mode that is of dominant interest to CLIVAR, though others might argue that climate change, in the long term, is of

equal or greater importance. CLIVAR is in essence a research programme for coupled modes of the physical climate system, and the oceans are a key element.

The question then arises as to the relevance of the wide spectrum of ocean circulation and variability to these coupled modes. For ENSO at least, it is accepted that the tropical oceans play an important role, though it is clearly the low-frequency, large-scale signals that are of greatest interest. For decadal and longer time scale variations, it is reasoned that the sequestering and subsequent release of heat (and moisture/salinity), involving the global ocean, is a key process (Bryden and Imawaki, Chapter 6.1; Wijffels, Chapter 6.2). In general, as the time scales of interest grow longer, we expect the ocean to play a more critical role. However, one must develop these ideas more deeply if the true legacy of WOCE is to be understood. In Section 7.4.5 I will argue that we not only need to build upon the knowledge (and observing systems) that impact directly on the scales of interest, but also to exploit the improved understanding of the oceanic variability itself in order to estimate properly these large-scale, low-frequency signals. We might state this most simply by renovating and restating WOCE Goal 2:

In order to find methods for determining long-term changes in climate, we must first determine how well the ocean circulation can be determined on the basis of irregular, unevenly spaced observations that do not resolve many of the energetic modes of ocean variability.

It is conceivable that many oceanic modes of variability do not directly impact useful predictability of the climate system, just as we accept (for the time being at least) that the details of day-to-day weather changes do not affect ENSO forecasts to first order. Yet, just as we are finding the regular analyses from Numerical Weather Prediction are useful for climate analysis and prediction, we may also find that analysing and understanding ocean ‘weather’ is important for determining ocean climate. It is this aspect that is being pursued within the Global Ocean Data Assimilation Experiment (see, for example, Smith, 2000, and Section 7.4.5).

7.4.3 WOCE observations

Other chapters have discussed in detail the various efforts mounted in WOCE to observe the ocean,

using both direct and remote techniques, and discussed the way these observations have been applied to improving our knowledge of the ocean circulation. My purpose here is to discuss briefly some elements and their importance for the subject of this chapter, elements that were designed and implemented for the purposes of WOCE, but which through good practice and judgement have proven useful for many other purposes.

7.4.3.1 General strategy

The word ‘World’ in WOCE immediately shifts the focus to the global domain. The WOCE objectives also make clear that the full depth of the ocean must also be considered. At the risk of oversimplifying the aims and implementation of the WOCE observational programme, the strategy can be reduced to a few tasks:

- Observe the fluxes of momentum, heat and moisture through the surface to determine the forcing of the ocean circulation;
- Observe the full-depth, global physical and dynamical properties and relevant chemical properties, including tracers, in order to make a first estimate of the total circulation, including the oceanic fluxes of heat and fresh water (historical observations could in places aid this task);
- Gather selected other observations and conduct process studies in order to understand likely errors in these estimates. These included:
 - high-density cross-sections to quantify the impact of the mesoscale field on fluxes;
 - dedicated boundary measurements to understand the influence of narrow currents at the land-ocean interface and in narrow constrictions of the bathymetry;
 - full-depth and selected depth fixed-point measurements to quantify high-frequency effects;
 - various broad-scale strategies that sampled the seasonally varying upper ocean;
 - repeated deep sections in order to provide some estimate of the first-order variability about the long-term mean;
 - selected process experiments; and
 - dedicated measurements in regions known to have distinctive modes of variability (e.g. at high latitudes).

At the heart was the aim to provide an estimate of the mean state (a ‘snapshot’) of the ocean

circulation. In addition there are the tasks associated with Goal 2 that have been discussed in Section 7.4.1.

7.4.3.2 Remote sensing

Remote sensing was an important component of the strategy, particularly for surface wind vectors and surface topography. As it transpired, the approach for accurate altimetric measurements for surface topography proved to be extremely effective and clearly stands out as one of the key successes of WOCE. However, as we have witnessed recently, altimetric measurements have utility over and above that for determining global ocean circulation. The 1997–98 El Niño was among the largest ever recorded and certainly was the best observed. Altimetric measurements from TOPEX/POSEIDON greatly assisted in the monitoring and description of the event (McPhaden, 1999) and have been shown useful for predictions (Ji *et al.*, 2000).

While the utility of altimetric data for studying seasonal-to-interannual variability was anticipated, it is only in recent times that this use has been demonstrated for real-time monitoring and prediction (e.g. Le Traon and Dibarboore, 1999). The altimeter data have also been extremely effective for placing interannual variability in the context of global variability. Nerem *et al.* (1999) show that the 1997–98 event had a first-order effect on global mean sea level as estimated from TOPEX/POSEIDON data. This result also suggests that interannual effects will almost certainly affect the representativeness of the WOCE data.

The strategy for surface wind vector measurements relied heavily on the ability of Numerical Weather Prediction Centers to provide accurate surface fields and on the availability of high-quality remotely sensed winds (WCRP, 1989b). The failure of NSCAT and the less-than-expected improvement in numerical weather prediction model estimates limited the quality of WOCE products (Taylor *et al.*, 2001). The data from TAO remain critical for good estimates of the tropical Pacific wind fields (McPhaden *et al.*, 1998) and the lack of such data in other tropical regions remains a key issue (e.g. in the Atlantic; Servain *et al.*, 1998). The key message has two aspects. First, we retain a heavy reliance on high-quality direct surface wind measurements for climate prediction and, second, for the required

spatial resolution, sampling density and accuracy, we cannot rely on numerical weather prediction model estimates alone and must continue the quest for further remote measurements.

7.4.3.3 Direct measurements

WOCE recognized the need for high-quality direct measurements to complement the data collected remotely and as a ‘ground reference’ for fields derived from numerical weather prediction. Some improvements were made to the Volunteer Observing Ship (VOS) programme, though as yet there have been few examples of effective action (Taylor *et al.*, 2000). The surface drifter programme was perhaps the most successful WOCE ‘increment’ to the surface marine network (Niiler, Chapter 4.1), providing badly needed extra surface pressure measurements in remote regions in addition to the direct samples of the surface circulation that were required by WOCE.

In terms of climate prediction, the most obvious synergies between WOCE and other observational efforts occurred in XBT measurements from the Ship-of-Opportunity Programme (SOOP) and sea-level measurements. A single programme was developed to address jointly the needs of WOCE and TOGA, combining broad-scale and frequently repeated sampling, which are most apt for tropical sampling, with high-density basin sections at low frequency (TWXXPC, 1993). As with the VOS, the most serious deficiency of this strategy was the inability to deliver truly global coverage. This is less of an issue with ENSO prediction since the focus is regional, but the lack of temporal sampling becomes an issue. Perhaps the most important attribute was that SOOP did at least provide some global context for interannual variability and a baseline for extending interest beyond the tropical Pacific.

Smith *et al.* (1999b) reviews the application of XBT data, particularly within the WOCE programme. The high-density XBT lines provided a unique capability within WOCE to measure the upper ocean transports of heat, mass and fresh water on interannual time scales, overcoming the sampling and representativeness issues for at least some regions of the oceans. Roemmich and Gilson (2000) have analysed data from the Pacific lines P37/10/44 together with TOPEX/POSEIDON altimetric data to determine the scale-dependent correlation of subsurface temperature and dynamic

height. They showed that eddy variability was the dominant mechanism for interannual change in equatorward transport (over the period 1991–99), a potentially important mechanism for coupled model prediction on interannual time scales. Such results, together with other studies on sampling and representativeness (Smith *et al.*, 1999b), are able to guide future measurement strategies and provide direction on the minimal requirements for *in-situ* data. There are also many examples of XBT data being used to monitor boundary currents. Meyers (1996) has monitored the upper portion of the Indonesian Throughflow using data from an XBT line established in 1984, initially as part of the TOGA network, but more recently as a WOCE contribution. This line (designated as IX1) is the basis for constructing the longest continuous estimate of the variability of upper part of the Indonesian Throughflow.

The utility of sea-level measurements for monitoring tropical ocean variability has been known for some time (e.g. Wyrtki, 1979), though by the end of TOGA the consensus was that sea-level measurements were not the highest priority for ENSO prediction (OOSDP, 1993; International Toga Project Office, 1994). The tropical island data were a shared interest with WOCE and arrangements were made for fast delivery of data, including key data sets beyond the tropics, to aid in the calibration of altimetric data. More recently a study and review were conducted to determine the appropriate network for all applications, including climate change (OOSDP, 1997). The study concluded that the global tide gauge network had multiple benefits, including for initialization of climate models.

One of the observational methods that are now revolutionizing the way we do oceanography has its origins firmly in WOCE. Floats were originally developed as a way of taking Lagrangian measurements of ocean currents at depth. In order to solve the problem of providing regular fixes on the position of the float, a depth-cycling version was developed that would regularly rise from the pre-assigned depth to the surface where satellites could be used for fixing and communication. It was quickly realized that this also provided a convenient platform for gathering information on temperature profiles. The design was adapted to include temperature sensors and the profiling float was born. Through a recent initiative called Argo

(Argo Science Team, 1998), a global programme of regularly profiling floats is being developed with the promise of around 80 000–100 000 profiles of temperature and salinity over the upper 2000 m being returned annually, from around 3000 floats.

As noted above, there was an understandable emphasis on deep measurements in WOCE since it was believed that the mean circulation was fundamentally determined by the slow, deep circulation of heat and fresh water. Given the limited resources and limited lifetime, it was not feasible to resolve fully the upper ocean variability; this places some limitation on the utility of WOCE observations for studying seasonal-to-interannual predictability, at least on the shorter time scales (see Section 7.4.5 and Talley *et al.*, Chapter 7.1).

There are, however, several aspects of the deep measurement programme of WOCE that are of direct relevance to ocean and climate prediction. For example, the Japan Meteorological Agency lines at 137°E provide a unique view of interannual variability as a function of depth in the western and equatorial Pacific (e.g. Qiu and Joyce, 1992) and, together with other North Pacific data sets, provide a context for developing theories on predictability on interannual-to-decadal time scales. Johnson *et al.* (2000) used data collected during regular cruises to service the tropical mooring array to provide a fuller context for upper-ocean variability in the equatorial Pacific during 1996–98. Dickson *et al.* (Chapter 7.3) provide several other examples of enhanced knowledge of variability resulting from deep ocean measurements taken through WOCE.

Ocean and climate prediction can be thought of as a challenge in two parts. First, through observation and modelling, one must try to identify and delineate ocean modes (signals) and processes that are important for the future evolution of (coupled) climate modes. Then, again through the skilful application of models, one attempts to follow the pathways and progress of these modes into the future, all the while accepting the fact that natural and artificial error growth will erode skill along the paths and with time (see also the discussion in Section 7.4.6). As the lead times are pushed further into the future we expect errors associated with intermediate and deep water circulation to play an increasingly important role. In this respect, tracer measurements taken during WOCE have a unique

and important role. The transient tracers (e.g. Chlorofluorocarbons (CFCs) and tritium/helium-3) provide one of the few methods for following rates of water mass formation and identifying newly ventilated water masses (e.g. Doney *et al.*, 1998a; Smethie *et al.*, 2000; Schlosser *et al.*, Chapter 5.8). Tracers also provide a method for following the pathways of newly ventilated waters and for determining rates and time scales for water mass spreading. Warner *et al.* (1996) provide just one example among many of how measurements and inventories of CFCs and other tracers can be used to follow the three-dimensional circulation, knowledge that is critical for understanding prediction and quantifying predictability, particularly on interannual, decadal and longer time scales. England and Hirst (1997) provide one illustration of how such information can be effective in validating and understanding the sensitivity of climate models.

Ultimately, *all* ocean data are important for improving our capacity to undertake ocean and climate prediction. Prediction and predictability depend fundamentally on knowledge of processes and WOCE has made a singular contribution to enhancing understanding, particularly at longer time scales. Moreover, the methods developed by WOCE, from profiling floats through to tracer measurements, provide the technical knowledge that will be needed as we extend our horizons beyond ENSO prediction to global prediction, at longer time scales, and with a higher premium on detail. The comprehensiveness of the WOCE data set is also a unique asset that will be of value as the present generation of climate models evolve into more complex representations of the environment.

7.4.3.4 The future

For endeavours such as GOOS and GODAE, WOCE observations and observational techniques provide a substantial foundation. Altimetry and profiling floats (Argo) are arguably the outstanding contributions. However, significant developments are also emerging from other techniques used by WOCE. Both the VOS and SOOP are likely to undergo major renovation (Smith *et al.*, 1999b; Taylor *et al.*, 2001) and we are seeing enhanced efforts in fixed-point and surface reference data collection (Send *et al.*, 2001). The sea-level network has changed emphases in recognition of a new capability (for example, the role of preci-

sion altimetry in monitoring global change) and because of improved ability to use sea-level data for ocean and climate data assimilation (Intergovernmental Oceanographic Commission, 1997; Ocean Observations Panel for Climate, 1997).

7.4.4 WOCE and climate prediction

One of the fundamental questions posed by TOGA concerned predictability. Were observed interannual variations in climate, of which ENSO is the most prominent, predictable? If so, could it be exploited for practical purpose, and what were the limits of this predictability? Based on research before and during TOGA, it was determined that not only was ENSO predictable, but it could be exploited in a practical way. Cane and Zebiak (1987) provided the first practical demonstration and many simple and complex coupled models have followed (Barnston *et al.*, 1999).

But TOGA also left a number of questions unanswered. For example:

- What role do the oceans outside the tropical Pacific, and deeper than 500 m, play in prediction and predictability?
- What are the reasons for temporal variations in skill?
- What are the key data sets for prediction?

The plan here is to explore the role WOCE may play in answering these questions.

7.4.4.1 ENSO prediction

There are now many models developed for predicting ENSO and, in theory, other seasonal-to-interannual climate variations. It is accepted that these models have skill (see, for example, Wang *et al.*, 2001). Trenberth (1998b) discussed the performance of various models during the 1997–98 El Niño event and concluded that the models had performed well in general. Barnston *et al.* (1999) performed an evaluation based on published forecasts and, though agreeing that models displayed skill, noted that the translation and interpretation of model predictions to the public lacked precision and objectivity.

The determination of predictability is normally done with data analyses or model simulations. In the case of ENSO, studies dating back to Bjerknes (1966, 1969) have shown that signals in the

tropical Pacific are predictable. Experience is showing, however, that our levels of skill may be limited by the imperfect assimilation of information from beyond the tropical Pacific and by lack of representation of longer-period signals (Balmaseda *et al.*, 1995; see also Liu and Philander, Chapter 4.4). Kleeman *et al.* (1996) and Latif *et al.* (1997), among others, have examined the anomalous conditions through the early 1990s and considered mechanisms for the modulation of ENSO, including extratropical effects.

WOCE data and analyses are likely to play a key role in resolving these issues since they provide the first systematic coverage of the mid-latitude oceans. Studies (e.g. Anderson *et al.*, 2001) are suggesting that the influence of the other tropical oceans may be an important factor. WOCE data will provide the foundations for such research. WOCE data may also provide a foundation for identifying other predictable climate signals. CLIVAR is setting out ambitiously to determine predictable modes beyond ENSO and WOCE data sets provide an initial platform for such studies. In general, one might expect the key information for longer lead-times (e.g. greater than 6 months) to be located outside the equatorial waveguide and beyond the focus of the ENSO observing system. It is the WOCE observations that are providing some opportunity to test such ideas.

There is also an inexorable trend toward global models for ENSO prediction, in part because of the issues raised above and in part because representation of the impacts of ENSO requires a global view. It has to be conceded at present that coupled models for ENSO have relatively little skill beyond the tropical region (see, for example, Wang *et al.*, 2001). The WOCE data beyond the Pacific (e.g. in the Indian Ocean) provide a platform to test and validate such global models. This trend toward global domains is being accompanied by a trend toward more general skill evaluation, typically global rather than just for the ENSO region (e.g. Stockdale *et al.*, 1998). Again, the existence of WOCE (and other) global data sets provides the opportunity to validate properly outside the region of the ENSO observing system.

7.4.4.2 Impacting next-generation global climate prediction models

The impact of WOCE on climate prediction does, of course, extend beyond the availability of data

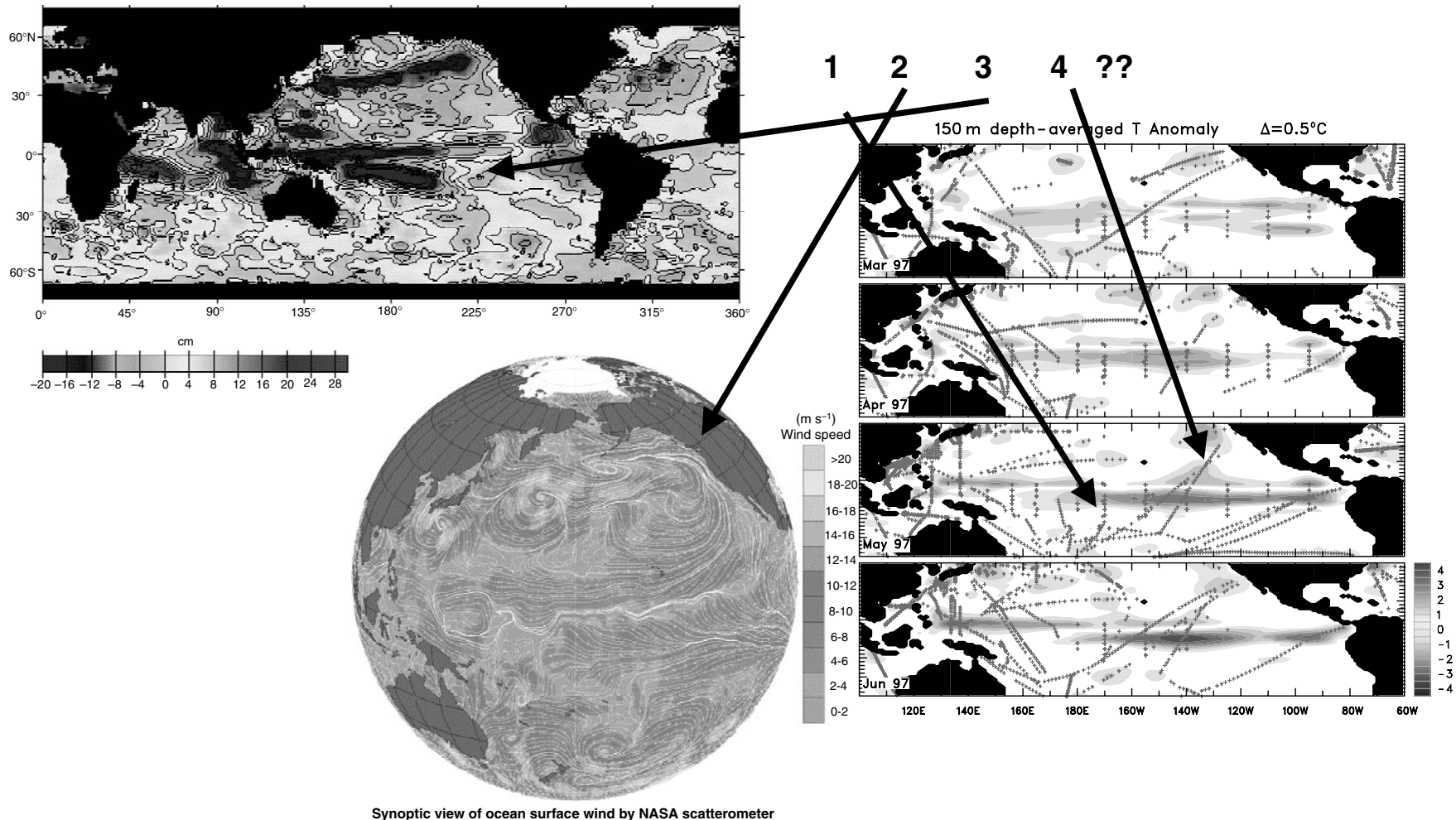
provided by WOCE. The inexorable move toward global coupled models and, implicitly, global ocean models, means that the climate prediction community will benefit from ocean modelling and data assimilation research that has been, and continues to be, undertaken within WOCE. For example, Fukumori *et al.* (1999) discusses useful measures of consistency in ocean state estimation, including formal error estimates, the model–data residuals, and comparisons with independent data, in an assimilation of TOPEX/POSEIDON data into a global ocean circulation model. Such results have direct applications in present climate prediction systems.

It should also be noted that as we move to operational implementation of climate prediction models, agencies are seeking systems that are more general. That is, the ocean component of the climate model may also be used to provide ocean analyses on a range of time scales. This expansion is being aided by the experience and research results gained through WOCE. For example, the model discussed by Wang *et al.* (2001) also serves to provide global ocean analyses and will be the basis for climate change studies. Such synergy has two-way benefits, allowing the research on global issues, such as that of WOCE, to be entrained into operational systems.

7.4.4.3 Data sets for initialization?

Several earlier chapters (for example, Talley *et al.*, Chapter 7.1) have demonstrated the great progress that has been made in the area of data assimilation. While current climate prediction models rely for the most part on relatively simple data assimilation systems (e.g. Stockdale *et al.*, 1998), the trend is towards more complex schemes in order to exploit better new data sets (e.g. altimetry, Behringer *et al.*, 1998) and to account for other effects (e.g. salinity, Vossepoel *et al.*, 1999). In some cases (e.g. Kleeman *et al.*, 1995; Rienecker *et al.*, 1999) more sophisticated techniques are being used, both to understand better the impact of the data and to provide a more sophisticated merging of observed and modelled information.

The adoption of more sophisticated assimilation techniques is also greatly improving the ability of climate prediction models to blend different data sets (e.g. subsurface temperature and sea level), to take account of known errors in the data and to take better advantage of output statistics. An



Synoptic view of ocean surface wind by NASA scatterometer

Fig. 7.4.2 A variety of data are available for initialization of ENSO prediction models including altimetry (top left), satellite winds (bottom middle) and SOOP XBTs and moorings for both $T(z)$ and winds (right). What is the correct ranking? 1, 2, 3 and 4 as shown? Will this change as models improve? Is there redundancy or are we still limited by observations?

aspect that is common to TOGA and WOCE is the overriding importance of having access to high-quality winds. TOGA addressed this issue by supporting an array of moorings in the tropical Pacific (TAO; McPhaden, 1995) that would provide accurate estimates of the surface wind forcing in the equatorial Pacific. As noted previously, the WOCE strategy sought global estimates. In order to use the wind data effectively, better quantification of the errors must be obtained. In the more sophisticated applications, this information on errors allows a more consistent blending of the assimilated surface information (including the wind forcing) with subsurface and other data.

An outstanding question concerns the relative importance of various data sets for climate prediction (Fig. 7.4.2). At this time, the greatest value for ENSO prediction is attached to the tropical mooring array, but further research is required to quantify better the relative impact of each data set. For example, the results of Roemmich and Gilson (2000) demonstrate the synergy of XBT measurements and altimetry. In the tropical region, can altimetric measurements reduce some of the subsurface sampling requirements for climate prediction? Will the next generation surface wind scatterometer data, and improved models, also lessen the need for *in-situ* data? Conversely, we might argue that the combination of Argo, mooring data and XBTs provides for much of the requirements and that remote sensing should be regarded as partly redundant. These are all difficult issues and will require substantial further research.

7.4.4.4 Beyond seasonal-to-interannual prediction

I will not dwell to any great extent on climate prediction and variability problems beyond seasonal-to-interannual prediction (see WCRP, 1998, for a discussion), either on shorter time scales or at longer time scales. However, it is useful to consider the approach that is being adopted for intraseasonal-to-seasonal problems. While the focus is on process studies and, to a large extent, surface and non-oceanographic observations, the legacy from TOGA and WOCE is being promoted as a needed background for these studies. In other words, by preserving the effective components of these observing systems (such as the SOOP in the Indian Ocean), CLIVAR is able to develop

research strategies without the need to ‘reinvent’ the basic observing system. Using Fig. 7.4.1 to picture this schematically, we can envisage a range of process studies being placed ‘on top’ of the combined basic and CLIVAR observing systems; the process studies can be planned and implemented safe in the knowledge that basic requirements are being met. The WOCE data and their continuation provide a baseline for future studies of variability and prediction, at both shorter and longer time scales (Section 7.4.5).

7.4.5 The mean state and long-term change

Interest in climate change issues intensified through the 1980s and the prospect of climate change influenced the design and establishment of WOCE. The development and publication of the First Assessment Report of the Intergovernmental Panel on Climate Change (IPCC, 1990) coincided with the initial implementation phase of WOCE. It was inevitable that WOCE was influenced by the First Assessment and that subsequent Assessments were shaped to some extent by WOCE results.

The principal focus of this chapter is prediction of climate and the related observations needed for initialization, and it is useful to extend this examination to longer time scales and to predictions on decadal-to-centennial time scales. In theory, the principal role of data assimilation is to constrain (correct) the model evolution so that it more accurately mimics variations of the real world. In practice, however, the unconstrained mean state of seasonal prediction models is usually far from reality, so the most immediate impact of the data is often correcting the mean state of the ocean (Anderson *et al.*, 2001).

We might anticipate that knowledge of the mean state would also be important for prediction and estimation of long-period variations. Indeed, recent research has highlighted the importance of the initialization procedure for climate change integrations (Bryan, 1998; Stouffer and Dixon, 1998). Bryan (1998) found the NCAR climate model adjusted on two time scales after initialization: a ‘fast’ mode, where the upper ocean, atmosphere and sea ice sought equilibrium, and a slow ‘drift’ mode that appeared to involve the slow adjustment of the deep ocean. Gordon *et al.* (2000) successfully initialized the Hadley Centre coupled

model with a representation of the observed ocean mean state. This method has the obvious advantage of greatly simplifying the spin-up problem. A second advantage is that it allows the coupled model perturbations to grow upon a background (mean) state that resembles reality, thus enhancing our ability to represent correctly the growth and pathways of slow climate variations. Clearly the WOCE data set and the knowledge developed in ocean state estimation provides a powerful baseline for future studies.

The assessment of past and current rates of sea-level rise has been accorded special attention in climate change assessments (Warrick and Oerlemans, 1990; Warrick *et al.*, 1996). The need for high-quality global sea-level measurements gelled nicely with the emphasis within WOCE on a high-quality and timely global sea-level measurement network. It is clear from a recent review (Ocean Observations Panel for Climate, 1997) that WOCE research and results have profoundly influenced the strategy for monitoring and assessing the rate of sea-level rise.

Knowledge of the influence of ocean processes and in particular of thermal expansion on sea level has grown through WOCE observations and WOCE research. Bryden *et al.* (1996), Bindoff and McDougall (2000) and Levitus *et al.* (2000) are just three of the many studies that have exploited hydrographic and time series data to identify significant changes in oceanic properties over long periods, some of which are consistent with ocean thermal expansion driven by increasing temperatures.

The extent to which these observations collectively can determine the mean state of the ocean remains an open question (see also the discussion in Section 7.4.1 and Talley *et al.*, Chapter 7.1). Wunsch (1977) was the first to provide a general framework for the determination of the general circulation of the oceans. He adapted methods developed in control theory to provide an estimate of the ocean circulation, consistent with observations and knowledge of dynamics and physics, under the assumption that the circulation was invariant with time. Such methods have been applied many times in WOCE (see, for example, Rintoul *et al.*, Chapter 4.6; Bryden *et al.*, Chapter 6.1). The planning for WOCE addressed the problem of temporal variability by requiring the surveys in each basin to be 'synoptic' (that is, the survey times should be short compared with the

periods of the dominant variability), and by planning for selected measurements that would resolve well the key modes of temporal variability. Time series data do show considerable variability over long time scales and the mean over the WOCE period can often differ considerably from the long-term mean (see Fig. 1 of Levitus *et al.*, 2000, for example). There is also considerable spatial variability, suggesting that we should be cautious about overinterpreting the representativeness of the WOCE data for the mean state (Dickson *et al.*, Chapter 7.3). Indeed, the strategy for the WOCE synthesis phase (WOCE International Project Office, 1997) stresses the need for interpreting the WOCE snapshot within the context of observed (and unobserved) variability.

The concept of a mean state has now been largely replaced by images of an ocean with rich temporal and spatial variability. Theory, models and data suggest that the climate system has natural modes of variability on long time scales so that it is more appropriate to think of an ever-changing and adjusting ocean and climate system rather than one with a single mean state. WOCE will provide the most comprehensive estimate to date of the ocean state, an estimate that will also take full account of uncertainties. Talley *et al.* (Chapter 7.1) and Dickson *et al.* (Chapter 7.3) address many of the issues for the WOCE synthesis related to longer-term variability, issues that ultimately dictate the utility and representativeness of the 1990s for past and future times. A key theme that is emerging in the approach is that the assumption of temporal invariance must be relaxed to accommodate seasonal and longer-period variations in ocean state estimation (WOCE International Project Office, 1997). Such an approach extracts greater value from the data (the temporal variations become part of the signal rather than treated as noise) and provides an improved framework for evaluating the representativeness of the WOCE snapshot.

The impact of the WOCE data is clear, even dominant, in present collections of global ocean data. In a perverse way, it has to some extent weakened the confidence held in historical analyses. It has become clear that older data lacked the accuracy and precision required to delineate subtle climate variations and that, if the variability of the oceans in the past resembled the variability of the oceans today (a relatively safe assumption),

then we must attribute far greater errors to the estimates than we might hitherto have done. For example, Roemmich and Cornuelle (1993) and Gilson *et al.* (1998) were able to exploit the dense XBT/XCTD sampling along the P14C track to determine the representativeness of upper ocean transport estimates from historical and contemporary hydrographic sections and to improve understanding of the relationship between steric height and sea-level changes. Such results enhance the value of data sets and provide improved estimates of error. To the extent that WOCE has been able to define sampling standards for measuring climate variations (see, for example, Bryden *et al.*, 1996; Dickson *et al.*, Chapter 7.3), a powerful and enduring legacy of WOCE will be that it provides a baseline against which both future and past changes can be measured.

7.4.6 Ocean variability and prediction: GODAE

7.4.6.1 The changing nature of oceanography
 One of the fundamental tenets of climate prediction and associated research is that the mechanisms involve interaction between two or more of the physical earth systems components – the air, oceans, land or ice. For seasonal time scales and longer, the ocean is one of the important components: it provides the long-term memory, storing and sequestering heat and water and releasing it later, often at a different, remote location. Questions of predictability must be answered through development of a thorough understanding of the coupled modes of the climate system, with the implication that modes that are ‘internal’ are of secondary importance. In reality, there are probably few modes that are truly internal. Atmospheric weather, for example in the form of tropical storms, is known to interact with the underlying ocean and provide both negative and positive feedbacks. Ocean eddies, though a product of oceanic instability, evolve depending upon both the surface forcing and the background state of the ocean.

WOCE treated the ocean as an independent entity and did not mount observational or modelling projects focused on other components of the climate system. To a large extent other WCRP programmes picked these up, though without any certainty that the specific interests of WOCE would be included. Of course, the objectives of WOCE were

developed with a full recognition that the primary rationale for undertaking WOCE was because of the global ocean’s role in climate, particularly with respect to climate change. For the atmosphere, we are accustomed to treating weather prediction as the primary rationale and treating its role within the climate system as subsidiary. This is reasonable since the dominant short-term benefit is through weather prediction and associated applications. Oceanography, it may be argued, has now reached a similar point and we should develop our strategies around the multiple use of ocean observations and the intrinsic benefits of observing and predicting the ocean for its own sake. This does not mean we downplay the importance of climate, but that we develop a much broader basis. We lift the study of ocean variability and prediction to a higher level, and place increased emphasis on the practical benefits of routine and regular monitoring and prediction of the ocean. The investment on behalf of climate prediction is enhanced through such a conceptual approach.

7.4.6.2 A problem in ocean estimation

We can reduce the problem to one of ocean state estimation: How well can we estimate the state of the ocean at any point in time given an irregularly distributed suite of observations, with uneven global coverage and variations in quality and type? If we can develop the answer to this question, then we can quantify the accuracy and information content provided to climate prediction and other applications with a dependency on ocean information.

Within the context of WOCE, these issues have been discussed in earlier chapters of this volume. In order to illustrate some of the nuances of ocean estimation and, in particular, the relevance of WOCE results, Figure 7.4.3 shows schematically four different perspectives.

The situation in Figure 7.4.3a, a model assimilation and forecast sequence, is perhaps the most familiar. The model is launched from a previously determined state (the last analysis, $t=t_0-\Delta t$) and integrated forward, assimilating synoptic observations to produce an estimate of the state at $t=t_0$, the initial condition (an analysis). From the current time the model state is projected forward to produce a prediction, in effect based on the extrapolation in time of the information inserted prior to $t=t_0$. The data are in general not located on a trajectory surface (line) of the model, so some

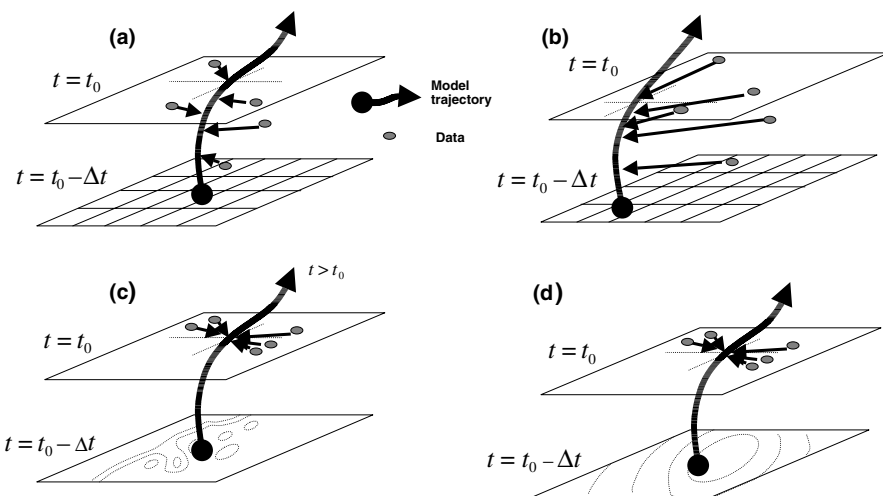


Fig. 7.4.3 A schematic of four different situations in ocean estimation. The critical issues are:

- 1 the density of the observations relative to the grid on which the estimate is being derived (a) and (b);
- 2 the proximity and location of the information relative to the location where the estimate is required (b);
- 3 the density of the observations relative to the dominant (unresolved) scales of variability (c) and (d); and
- 4 the ability of the model to project information in space and time (all).

extrapolation and interpretation must take place (the process of data assimilation) in order to provide the appropriate constraint (guidance) for the model evolution. The accuracy of the initial condition is governed by the density of information relative the most energetic space and time scales, and by the errors introduced by the model and assimilation.

The case shown in Figure 7.4.3b is similar but now the data are not surrounding the model trajectory, but are remote and not evenly distributed in space relative to where the information is required. We are trying to integrate the model forward in a region of scant (or no) data and the real work must be done in bringing the known remote information to bear on the solution. If the information is downstream, either due to currents or waves propagating away from the trajectory location, or is truly remote (several times the dominant spatial scale), the model integration will be effectively unconstrained.

The process of estimating the ocean state on the model trajectory involves issues that are similar to those of predictability theory. Figure 7.4.3c shows a case where the model trajectory must be ‘predicted’ by extrapolating observations through a chaotic field. It follows that in general the ‘prediction’ of the model trajectory will have large uncertainty. Figure 7.4.3d differs only in that the observation separation and distance from the model trajectory are within the decorrelation

scales of the field; now, the data can be brought to bear on the model trajectory with some certainty.

In all cases there is also the issue of the capacity of the model and assimilation method to, first, ingest information without undue distortion or introduction of bias, and second, to carry (retain) ingested information as the model is integrated forward.

WOCE has impacted all aspects of this problem. Through data gathering and analysis within process studies, we now have a better knowledge of the unresolved variability (the ‘noise’), as well as of the climate signal, and can thus better quantify the errors in data assimilation. We also have a better appreciation of what truly represents a ‘gap’ in the sense that we cannot infer the state at that location with any useful skill from contemporary information. Through modelling, WOCE has been able to quantify better the ability of models to ingest and carry information and to identify processes and parameterizations that are critical for this to be done effectively.

7.4.6.3 A Global Ocean Data Assimilation Experiment

The vision and rationale for GODAE

The concept of a Global Ocean Data Assimilation Experiment (GODAE) was born out of the theoretical ideas above and as a result of the recognition that oceanography needed to move to a

different phase. GODAE (2001) describes this vision thus:

A global system of observations, communications, modelling and assimilation, that will deliver regular, comprehensive information on the state of the oceans, in a way that will promote and engender wide utility and availability of this resource for maximum benefit to the community.

To a large extent, GODAE is made possible because of the scientific and technical advances provided by WOCE. Even before WOCE, many people had thought oceanography should be moving toward a more operational footing, just as in meteorology. This did not happen for several reasons, including:

- the lack of needed global observations;
- the lack of suitable global ocean models, particularly with a capability to resolve the mesoscale;
- lack of ocean data assimilation know-how;
- lack of computational power to integrate global models;
- lack of the necessary communications to enable real-time exchange of data and products;
- the immaturity of the user community; and
- lack of investment.

By the late part of the 1990s, it became clear that many of these obstacles were no longer insurmountable and that, indeed, there was a real prospect in the near future to have available most of the needed elements (Smith and Lefebvre, 1997). In short, it was apparent that global ocean data assimilation/estimation on a routine basis was feasible.

GODAE is the response to a demand for an efficient, integrated system for global ocean products, provided regularly, and in real-time. The underlying rationale for GODAE as an international experiment is that the vision above will not be realized serendipitously, or through individuals or individual nations. The needed capacity will arrive only with a concerted effort to ensure, first, proper integration of the components, and second, the commitment to proving value and viability. The specific objectives of GODAE are to (GODAE, 2001):

- 1 Apply state-of-the art ocean models and assimilation methods for short-range open-ocean forecasts, for boundary conditions to extend

predictability of coastal and regional subsystems, and for initial conditions of climate forecast models.

- 2 Provide global ocean analyses for developing improved understanding of the oceans, improved assessments of the predictability of ocean systems, and as a basis for improving the design and effectiveness of the global ocean observing system.

The objectives are purposefully broad and have the desirable balance between practical goals (forecasts, information for subsystems) and strategic objectives (science, evolution of the observing system).

What will GODAE deliver?

The anticipated outcomes of GODAE include:

- improved coastal, open ocean and climate forecasts;
- a more responsive, efficient and sustainable system for data assembly and distribution;
- an improved foundation for oceanic research and enhanced partnerships between the operational and research communities; and
- an enhanced, but cost-effective and sustainable ocean observing system.

On the basis of analysis of expected remote sensing and other observing capabilities, and on expected improvements in modelling and data assimilation, the period 2003–05 was designated as the focus for an operational trial. On this time scale it also seems feasible to attract the needed material and intellectual investment.

The GODAE components

The essential building blocks of GODAE are observational networks, models and estimation tools. In the GODAE context, these elements are inextricably linked, with obvious interdependencies. Remotely sensed data provide the only real avenue to global data coverage (see Section 7.4.3). Recent initiatives to develop a sustained global ocean observing system offer the potential to satisfy GODAE data needs. GODAE attaches high priority to global coverage and the complementarity between *in-situ* and remote sensing data. Argo is a GODAE Pilot Project (Argo Science Team, 1998) and is a central element of the concept. The Argo schedule follows that of GODAE and

constitutes a major step toward the global observing system.

It is obvious that GODAE owes a great deal to WOCE. Argo, for example, grew out of the innovative technical advances of the WOCE observational programme. GODAE is, however, not a research programme and in no way should be considered a follow-on research programme. A comparison of the goals of GODAE with those of WOCE makes evident the very distinct aims. GODAE aims to deliver practical applications of the advances made possible by WOCE observations and modelling and, in that way, build a lasting manifestation of the WOCE legacy.

GODAE outputs

The generation of globally consistent fields of upper ocean temperature, salinity and velocity from the synthesis of incomplete information provided by the multivariate *in-situ* and remote data streams through models and assimilation is an identifying characteristic of GODAE. GODAE outputs will include coherent, organized data sets, synoptic ocean analyses, short-range ocean forecasts, high-quality scientific re-analyses, and statistical attributes and errors of products.

GODAE is in the process of defining and executing a range of Pilot Projects, work programmes and implementation tasks, including Argo, remote sensing assessments and data delivery. Box 7.4.1 shows the phases of GODAE. The long-term legacy of GODAE will be a set of observing and data assimilation systems that will contribute to the core of the Global Ocean Observing System.

Box 7.4.1 GODAE phases

| |
|---|
| GODAE will evolve through phased development from the present to 2007. |
| 1998–99: Concept development |
| • Define scope and develop needed international cooperation and participation. |
| 2000–02: Development/preoperational phase |
| • The development and testing of GODAE components. |
| 2003–05: Operational phase |
| • GODAE will be realized and the real-time trials of candidate systems takes place. |
| 2006–07: Postoperational consolidation phase |
| • Final phase of synthesis, assessment and consolidation. |

7.4.7 Institutionalizing the benefits of WOCE

Thus far I have discussed in general terms how the knowledge gleaned through WOCE is being exploited for the benefit of research and operational applications. However, that alone is not sufficient if we are to ensure that the methods, practices and standards developed by WOCE are carried through for the benefit of following generations. Within meteorology, the various mechanisms of the World Weather Watch (WWW) are available to ensure that standards are maintained through the observational networks and that information is circulated in a timely manner for the benefit of the entire operational community.

Over the years, some of this functionality has been developed for oceanography, either through partnerships with meteorology or through the creation of bodies whose sole purpose was to be the guardian for a certain data stream. However, as TOGA came to a close and various activities within oceanography begin to mature, it was realized that a more permanent and general mechanism was needed. A Joint Technical Commission for Oceanography and Marine Meteorology (JCOMM) was proposed (jointly sponsored by the Intergovernmental Oceanographic Commission and the World Meteorological Organization) and agreed, in order to provide the long-term technical support for implementation and maintenance of the observing system. Figure 7.4.4 shows the structure of JCOMM in relation to the major organizations.

This is a major step forward for the oceanographic community, a step that was made possible by the advances in TOGA and WOCE. The JCOMM is the working and functioning part of GOOS. It ensures that systems get implemented according to agreed standards, in much the same way as WOCE worked according to its implementation plan (WCRP, 1988a). JCOMM will ensure that the observing systems perform efficiently and effectively, again according to agreed metrics, and that the nations collectively invest the needed resources to sustain the observing network.

It is envisaged that the surface drifter programme, the Voluntary Observing Ship Programme, the Ship-of-Opportunity Programme, the global sea-level observing system, the ENSO observing system, the Global Temperature–Salinity Profile

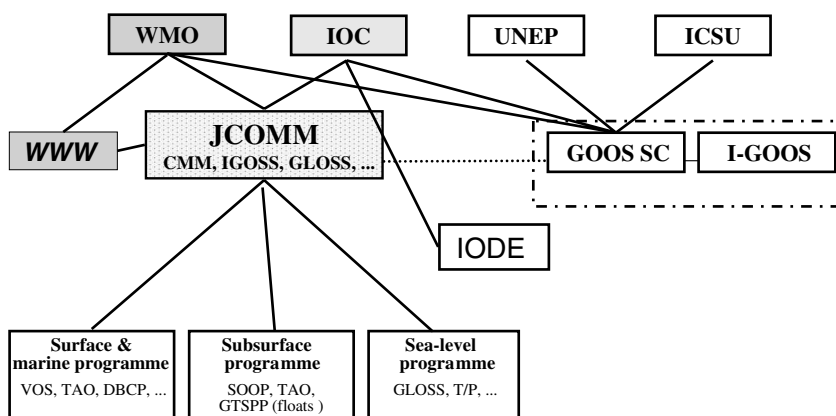


Fig. 7.4.4 Schematic of the organizational structure of the new JCOMM.

Project, among other elements, will all now fall within the jurisdiction of JCOMM. In other words, the JCOMM will be a practical manifestation of the experimental observing systems and data management practices of TOGA and WOCE.

7.4.8 Conclusions

This chapter has examined the legacy of WOCE and its impact on climate prediction and the development of global, operational oceanography. I have argued that the benefits of WOCE are flowing, and will continue to flow, through to these efforts in many different ways. At the heart of this legacy is the improvement in knowledge and scientific skills that has come about from WOCE. This flow-on effect may not have been formally embedded in the goals of WOCE but was, in hindsight, inevitable because of the interconnectivity of oceanic and climate processes. One cannot study ENSO without some knowledge of the global (world) ocean circulation and, in turn, one cannot begin to understand the representativeness of global ocean data sets without factoring in the influence of seasonal-to-interannual variability associated with ENSO.

The observational phase of WOCE, 1990–97, is leaving behind a powerful and tangible legacy for oceanography and climate prediction in the form of contributions to a global ocean (and climate) observing system and a baseline estimate of the ocean state for the 1990s against which future samples can be measured. The WOCE data provide the foundations upon which research into variability and predictability can build; this same knowledge is vital for ocean models (e.g., the

development of parameterizations) and assimilation (specification of the statistical models).

Predictability can and will be ‘mined’ from the WOCE global data set. At this time, two of the most likely candidates are associated with ENSO, namely the influence of the tropical oceans beyond the Pacific (e.g. the Indian Ocean) and the modulating impact of mid-latitude and deeper waters on the ENSO cycle. The CLIVAR research programme is actively seeking further predictable signals, aided by the information and knowledge built up through WOCE.

While I did not dwell in detail on data assembly and processing (see Lindstrom and Legler, Chapter 3.5), the experience from WOCE has been essential for the planning of both research and operational systems. The creation of the JCOMM was made possible in part because of the development of rigorous and sustainable data management practices within WOCE.

I have emphasized the central importance of WOCE to the development of future operational observing systems and, in particular, to the development of GODAE. Put bluntly, WOCE and TOGA scientific and technological developments *do provide* the basis for future global ocean observing systems. GODAE has been enabled by both observational and modelling/assimilation advances. The remaining synthesis and interpretation phase of WOCE will be extremely important to GODAE because of the synergy between WOCE and GODAE modelling and data assimilation.

We can look forward with optimism to a future that will see operational satellites and global ocean *in-situ* networks operating routinely in the service

of a range of ocean applications. Research should prosper both through the added motivation and stimulus provided by a vibrant applications sector, but also through the knowledge that it will no

longer have to bear the sole burden of implementing and maintaining the observing networks and infrastructure that are needed for the study of the world ocean circulation.

References

The numbers in square brackets at the end of reference indicate the chapters in which it is cited.

- Aagaard, K. and E.C. Carmack, 1989: The role of sea ice and other fresh water in the Arctic circulation. *J. Geophys. Res.* **94**, 14485–14498. [1.2, 4.7]
- Aagaard, K. and E.C. Carmack, 1994: The Arctic Ocean and climate: A perspective. In: *The Polar Oceans and their Role in Shaping the Global Environment*, O.M. Johannessen, R.D. Muench and J.E. Overland (eds), American Geophysical Union, Washington, DC, pp. 5–20. [4.7]
- Aagaard, K. and S.-A. Malmberg, 1978: *Low Frequency Characteristics of the Denmark Strait Overflow*. International Council for the Exploration of the Sea, Copenhagen. ICES CM 1978/C: 47. [5.6]
- Aagaard, K., E. Fahrbach, J. Meincke and J.H. Swift., 1991: Saline outflow from the Arctic Ocean: Its contribution to the deep waters of the Greenland, Norwegian and Iceland seas. *J. Geophys. Res.* **96**, 20433–20441. [7.3]
- Aagaard, K., L.A. Barrie, E.C. Carmack *et al.*, 1996: US, Canadian researchers explore Arctic Ocean. *Eos Trans. Amer. Geophys. Union* **77**, 209, 213. [7.3]
- Adamec, D., 1998: Modulation of the seasonal signal of the Kuroshio Extension during 1994 from satellite data. *J. Geophys. Res.* **103**, 10209–10222. [3.3]
- Adcroft, A., C. Hill and J. Marshall, 1997: Representation of topography by shaved cells in a height coordinate ocean model. *Mon. Wea. Rev.* **125**, 2293–2315. [7.2s]
- Adlandsvik, B., 1989: *Wind-driven Variations in the Atlantic Inflow to the Barents Sea*. International Council for the Exploration of the Sea, Copenhagen. ICES CM 1989/C: 18, 13 pp. [7.3]
- Adlandsvik, B. and H. Loeng, 1991: A study of the climate system in the Barents Sea. *Polar Res.* **10**, 45–49. [7.3]
- Alderson, S.G. and S.A. Cunningham, 1999: Velocity errors in acoustic Doppler current profiler measurements due to platform attitude variations and their effect on volume transport estimates. *J. Atmos. Oceanic Technol.* **16**, 96–106. [3.1]
- Alexandersson, H., T. Schmitt, K. Iden and H. Tuomenvirta, 1998: Long-term variations of the storm climate over NW Europe. *Glob. Ocean Atmos. System* **6**, 97–120. [7.3]
- Allan, R., J. Lindesay and C. Reason, 1995: Multidecadal variability in the climate system over the Indian Ocean region during the Austral summer. *J. Climate* **8**, 1853–1873. [4.7]
- Allen, J.S., 1991: Balance equations based on momentum equations with global invariants of potential entropy and energy. *J. Phys. Oceanogr.* **21**, 265–276. [7.2]
- Alley, R.B., D.A. Meese, C.A. Shuman, *et al.*, 1993: Abrupt increase in Greenland snow accumulation at the end of the Younger Dryas event. *Nature*, **362**, 527–529. [1.2]
- Alverson, K. and F. Oldfield, 2000: *Abrupt Climate Change*. CLIVAR Exchanges, International CLIVAR Project Office (unpublished document), 5(1), pp. 7–10. [1.2]
- Anderson, D.L.T. and D.J. Carrington, 1993: Modeling interannual variability in the Indian Ocean using momentum fluxes from the operational weather analyses of the United Kingdom Meteorological Office and European Centre for Medium Range Weather Forecasts. *J. Geophys. Res.* **98**, 12483–12499. [4.3]
- Anderson, D.L.T. and R.A. Corry, 1985a: Ocean response to low frequency wind forcing with application to seasonal variation in the Florida Straits – Gulf Stream. *Prog. Oceanogr.* **14**, 7–40. [2.2]
- Anderson, D.L.T. and R.A. Corry, 1985b: Seasonal transport variation in the Florida Straits: A model study. *J. Phys. Oceanogr.* **15**, 773–786. [2.2]
- Anderson, D.L.T. and A.E. Gill, 1975: Spin up of a stratified ocean, with application to upwelling. *Deep-Sea Res.* **22**, 583–596. [4.2, 4.6]

- Anderson, D.L.T.** and P.D. Killworth, 1977: Spin-up of a stratified ocean, with topography. *Deep-Sea Res.* **24**, 709–732. [2.2]
- Anderson, D.L.T.**, T.N. Stockdale, M.K. Davey *et al.*, 2000: Ocean data needs for ENSO and seasonal forecast systems. In: *Observing the Ocean in the 21st Century*, N.R. Smith and C.J. Koblinsky (eds), Bureau of Meteorology, Melbourne, Australia, Chapter 34. [7.4]
- Ando, K.** and M.J. McPhaden, 1997: Variability of the surface layer hydrography in the tropical Pacific ocean. *J. Geophys. Res.* **102**, 23063–23078. [4.3]
- Andrié, C.**, J.-F. Ternon, M.-J. Messias, L. Memery and B. Bourlès, 1998: Chlorofluoromethane distributions in the deep equatorial Atlantic during January–March 1993. *Deep-Sea Res. I*, **45**, 903–930. [4.5, 5.8]
- Andrié, C.**, J.-F. Ternon, B. Bourlès, Y. Gouriou and C. Oudot, 1999: Tracer distributions and deep circulation in the western tropical Atlantic during CITHER1 and ETAMBOT cruises, 1993–1996. *J. Geophys. Res.* **104**, 21195–21215. [4.3, 4.5, 5.8]
- Anonymous**, 1998: Mapping the Net's Terra Incognita. *Science* **282**, 375 pp. [2.1]
- Antonov, J.I.**, S. Levitus, and T.P. Boyer, 2000: Steric sea level rise during the 1957–1994 period. *Eos Trans. Amer. Geophys. Union*, (in press). [1.2]
- Aoyama, M.**, T. Joyce, T. Kawano and Y. Takatsuki, 2000: Offsets of IAPSO standard seawater for P103 through P129. *Deep-Sea Res.* (submitted). [3.1]
- Argo Science Team**, 1998: *On the Design and Implementation of Argo: An Initial Plan for a Global Array of Profiling Floats*. International CLIVAR Project Office Report Number 21, GODAE Report No. 5, GODAE International Project Office, Melbourne Australia, 32 pp. [7.4]
- Arhan, M.**, H. Mercier and J. Lutjeharms, 1999: The disparate evolution of three Agulhas rings in the South Atlantic Ocean. *J. Geophys. Res.* **104**, 20987–21005. [4.7]
- Arhan, M.**, A.C. de Verdière and H. Mercier, 1989: Direct observations of the mean circulation at 48°N in the Atlantic Ocean. *J. Phys. Oceanogr.* **19**, 161–181. [4.2]
- Arhan, M.**, A.C. de Verdière and L. Memery, 1994: The eastern boundary of the Subtropical North Atlantic. *J. Phys. Oceanogr.* **24**, 1295–1316. [5.7]
- Arhan, M.**, H. Mercier, B. Bourles and Y. Gouriou, 1998: Hydrographic sections across the Atlantic at 7°30'N and 4°30'S. *Deep-Sea Res.* **45**, 829–872. [1.2, 4.3, 7.3]
- Arkin, P.A.** and P.E. Ardanuy, 1989: Estimating climatic-scale precipitation from space: a review. *J. Climate* **2**, 1229–1238. [3.4]
- Armi, L.**, 1978: Some evidence for boundary mixing in the deep ocean. *J. Geophys. Res.* **83**, 1971–1979. [4.5, 4.6, 5.2]
- Armi, L.**, 1979: Reply to comments by C. Garrett. *J. Geophys. Res.* **84**, 5097–5098. [5.2]
- Armi, L.** and H. Stommel, 1983: Four views of the North Atlantic Subtropical Gyre. *J. Phys. Oceanogr.* **13**, 828–857. [1.3]
- Armi, L.** and D.M. Farmer, 1988: The flow of Mediterranean Water through the Strait of Gibraltar. *Prog. Oceanogr.* **21**, 1–195. [5.7]
- Armi, L.**, D. Hebert, N. Oakey *et al.*, 1989: Two years in the life of a Mediterranean salt lens. *J. Phys. Oceanogr.* **19**, 354–370. [5.2]
- Arnault, S.**, B. Bourles, Y. Gouriou and R. Chuchla, 1999: Intercomparison of the upper layer circulation of the western equatorial Atlantic Ocean: In situ and satellite data. *J. Geophys. Res.* **104**, 21171–21194. [4.3]
- Astraldi, M.**, S. Balopoulos, J. Candela *et al.*, 1999: Mediterranean Straits: Water exchange rates, dynamics and kinematics. *Prog. Oceanogr.* **44**, 65–108. [5.7]
- Atlas, R.S.**, R.N. Hoffman, S.C. Bloom, J.C. Jusem and J. Ardizzone, 1996: A multiyear global surface wind velocity data set using SSM/I wind observations. *Bull. Amer. Meteor. Soc.* **77**, 869–882. [3.4]
- Atlas, R.S.**, S.C. Bloom, R.N. Hoffman *et al.*, 1999: Geophysical validation of NSCAT winds using atmospheric data and analysis. *J. Geophys. Res.* **104**, 11405–11424. [3.4]
- Attema, E.P.W.**, 1991: The Active Microwave Instrument on board the ERS-1 satellite. *Proc. IEEE* **79**, 791–799. [3.4]
- Auad, G.**, A.J. Miller and W.B. White, 1998: Heat storage simulation and associated heat budgets in the Pacific Ocean: Part 2. Interdecadal timescale. *J. Geophys. Res.* **103**, 27621–27635. [7.1]
- Bacon, S.**, 1994: Skill in an inversion solution: CONVEX-91 hydrographic results compared with ADCP measurements. *J. Atmos. Oceanic Technol.* **11**, 1569–1591. [3.1]
- Bacon, S.**, 1997: Circulation and fluxes in the North Atlantic between Greenland and Ireland. *J. Phys. Oceanogr.* **27**, 1420–1435. [6.1, 6.2]
- Bacon, S.**, 1998: Decadal variability in the outflow from the Nordic Seas to the deep Atlantic Ocean. *Nature* **394**, 871–874. [5.6, 7.3]
- Bacon, S.** and D.J.T. Carter, 1993: A connection between mean wave height and atmospheric pressure gradient in the North Atlantic. *Int. J. Climatol.* **13**(4), 423–436. [7.3]

- Bacon, S., H.M. Snaith and M.J. Yelland, 2000: An evaluation of some recent batches of IAPSO standard seawater. *J. Atmos. Oceanic Technol.* 17, 854–861. [3.1]
- Bainbridge, A.E., 1981: *Geosecs Atlantic Expedition, Vol. 2: Sections and Profiles*. National Science Foundation, Washington, DC. [7.3]
- Baines, P.G. and W. Cai, 2000: Analysis of an interactive instability mechanism for the Antarctic Circumpolar Wave. *J. Climate* 13, 1831–1844. [4.6]
- Baker, Jr, D.J., 1982: A note on Sverdrup balance in the Southern Ocean. *J. Mar. Res.* 40(suppl.), 21–26. [4.6]
- Baker, M.A. and C.H. Gibson, 1987: Sampling turbulence in the stratified ocean: Statistical consequences of strong intermittency. *J. Phys. Oceanogr.* 17, 1817–1836. [5.2]
- Balmaseda, M.A., M.K. Davey and D.L.T. Anderson, 1995: Decadal and seasonal dependence of ENSO prediction skill. *J. Climate* 8, 2705–2715. [7.4]
- Banks, H.T., 2000: Ocean heat transport in the South Atlantic in a coupled climate model. *J. Geophys. Res.* 105, 1071–1091. [2.3]
- Banks, H.T., R.A. Wood, J.M. Gregory, T.C. Johns and G.S. Jones, 2000: Are observed decadal changes in intermediate water masses a signature of anthropogenic climate change? *Geophys. Res. Lett.* 27, 2961–2964. [1.2, 2.3]
- Baringer, M.O. and R. Molinari, 1999: Atlantic Ocean baroclinic heat flux at 24 to 26°N. *Geophys. Res. Lett.* 26, 353–356. [6.1]
- Baringer, M.O. and J.F. Price, 1990: A simple model of the descending Mediterranean outflow plume. In: *The Physical Oceanography of Sea Straits*, L.J. Pratt (ed.), Kluwer Acad. Publ., Dordrecht, pp. 537–544. [5.6]
- Baringer, M.O. and J.F. Price, 1997a: Mixing and spreading of the Mediterranean outflow. *J. Phys. Oceanogr.* 27, 1654–1677. [5.7]
- Baringer, M.O. and J.F. Price, 1997b: Momentum and energy balance of the Mediterranean outflow. *J. Phys. Oceanogr.* 27, 1678–1692. [5.6]
- Barnett, T.P., K. Hasselmann, M. Chelliah *et al.*, 1999: Detection and attribution of recent climate change: a status report. *Bull. Amer. Meteor. Soc.* 80, 2631–2659. [2.3]
- Barnier, B., 1998: Forcing the ocean. In: *Ocean Modeling and Parameterization*, E. P. Chassignet and J. Verron (eds), NATO Science Series, Series C: Math. Phys. Sci., Kluwer Acad. Publ., Dordrecht, Vol. 516, 451 pp. [2.2]
- Barnier, B., L. Siefridt and P. Marchesiello, 1995: Thermal forcing for a global ocean circulation model using a three-year climatology of ECMWF analyses. *J. Mar. Res.* 6, 363–380. [5.1, 6.2]
- Barnston, A.G. and R.E. Livezey, 1987: Classification, seasonality and persistence of low-frequency atmospheric circulation patterns. *Mon. Wea. Rev.* 115, 1083–1126. [7.3]
- Barnston, A.G., Y. He and M.H. Glantz, 1999: Predictive skill of statistical and dynamical climate models in SST forecasts during the 1997–98 El Niño episode and the 1998 La Niña onset. *Bull. Amer. Meteor. Soc.* 80, 217–244. [2.3, 7.4]
- Bartello, P. and G. Holloway, 1991: Passive scalar transport in β -plane turbulence. *J. Fluid Mech.* 223, 521–536. [5.2]
- Barth, N., D. Chelton, P. Niiler and M. Schlax, 2001: Comparison of velocity variance in the Pacific Ocean using altimeter and drifter data. *J. Geophys. Res.* (submitted). [4.1]
- Barthelet, P., L. Terray and S. Valcke, 1998: Transient CO₂ experiment using the ARPEGE/OPAICE non-flux-corrected coupled model. *Geophys. Res. Lett.* 25, 2277–2280. [2.3]
- Barton, E.D. and A.E. Hill, 1989: Abyssal flow through the Amirante Trench (western Indian Ocean). *Deep-Sea Res.* 36, 1121–1126. [4.3]
- Basu, S., S.D. Meyers and J.J. O'Brien, 2000: Annual and interannual sea-level variations in the Indian Ocean from TOPEX/POSEIDON observations and ocean model simulations. *J. Geophys. Res.* 105, 975–994. [3.3]
- Battisti, D.S., 1988: Dynamics and thermodynamics of a warming event in a coupled tropical atmosphere-ocean model. *J. Atmos. Sci.* 45, 2889–2919. [3.3]
- Battle, M., M. Bender, P.P. Tans *et al.*, 2000: Global carbon sinks and their variability, inferred from atmospheric O₂ and Δ¹³C. *Science* 287, 2467–2470. [6.3]
- Baturin, N.G. and P.P. Niiler, 1997: Effects of instability waves in the mixed layer of the equatorial Pacific. *J. Geophys. Res.* 102, 27771–27794. [4.1]
- Baumgartner, A. and E. Reichel, 1975: *The World Water Balance: Mean Annual Global, Continental and Maritime Precipitation*. Elsevier, Amsterdam, 179 pp. [4.7, 6.2]
- Beal, L.M. and H.L. Bryden, 1997: Observations of an Agulhas Undercurrent. *Deep-Sea Res.* I, 44, 1715–1724. [3.1, 4.2, 4.5, 6.1]
- Beal, L.M. and H.L. Bryden, 1999: The velocity and vorticity structure of the Agulhas Current at 32°S. *J. Geophys. Res.* 104, 5151–5176. [1.2, 3.1, 4.7, 6.1]
- Beal, L.M., A. Ffield and A. Gordon, 2000: Spreading of Red Sea overflow waters in the Indian Ocean. *J. Geophys. Res.* 105, 8549–8564. [4.7]
- Beckmann, A., 1998: The representation of bottom boundary layer processes in numerical ocean circulation models. In: *Ocean Modeling and Parameterization*, E.P. Chassignet and J. Verron

- (eds), Kluwer Acad. Publ., Dordrecht, pp. 135–154. [5.2]
- Beckmann, A.** and R. Döscher, 1997: A method for improved representation of dense water spreading over topography in geopotential-coordinate models. *J. Phys. Oceanogr.* 27, 581–591. [2.2, 2.3, 5.6]
- Beckmann, A.** and D. B. Haidvogel, 1993: Numerical simulation of flow around a tall isolated seamount. Part I: Problem formulation and model accuracy. *J. Phys. Oceanogr.* 23, 1736–1753. [7.2]
- Beckmann, A.**, C.W. Böning, B. Brügge and D. Stammer, 1994a: On the generation and role of eddy variability in the central North Atlantic ocean. *J. Geophys. Res.* 99, 20381–20391. [2.2, 3.3]
- Beckmann, A.**, C.W. Böning, C. Köberle and J. Willebrand, 1994b: Effects of increased horizontal resolution in a simulation of the North Atlantic ocean. *J. Phys. Oceanogr.* 24, 326–344. [2.2]
- Beckmann, A.**, H.H. Hellmer and R. Timmermann, 1999: A numerical model of the Weddell Sea: Large scale circulation and water mass distribution. *J. Geophys. Res.* 104, 23375–23391. [4.6]
- Begemann, F.** and W.F. Libby, 1957: Continental water balance, ground water inventory and storage times, surface ocean mixing rates and worldwide water circulation patterns from cosmic-ray and bomb tritium. *Geochim. Cosmochim. Acta* 12, 277–296. [5.8]
- Behera, S.K.** and T. Yamagata, 2001: Subtropical SST dipole events in the southern Indian Ocean, *Geophys. Res. Lett.* (submitted). [7.1]
- Behringer, D.W.**, M. Ji and A. Leetmaa, 1998: An improved coupled model for ENSO prediction and implications for ocean initialization. Part I: the ocean data assimilation system. *Mon. Wea. Rev.* 126, 1013–1021. [3.2, 7.4]
- Belkin, I.M.** and A.L. Gordon, 1996: Southern Ocean fronts from the Greenwich meridian to Tasmania. *J. Geophys. Res.* 101, 3675–3696. [3.3, 4.6]
- Belkin, I.M.**, S. Levitus, J. Antonov and S-A. Malmberg, 1998: 'Great Salinity Anomalies' in the North Atlantic. *Prog. Oceanogr.* 41(1), 1–68. [7.3]
- Bender, M.**, T. Ellis, P. Tans, R. Francey and D. Lowe, 1996: Variability in the O₂/N₂ ratio of southern hemisphere air, 1991–1994 – Implications for the carbon cycle. *Glob. Biogeochem. Cycles* 10, 9–21. [6.3]
- Bennett, A.F.**, 1992: *Inverse Methods in Physical Oceanography*. Cambridge Monographs on Mechanics and Applied Mathematics, Cambridge University Press, 346 pp. [7.1]
- Bentamy, A.**, N. Grima and Y. Quilfen, 1998: Validation of the gridded weekly and monthly wind fields calculated from ERS-1 scatterometer wind observations. *Glob. Atmos. Ocean System* 6, 373–396. [3.4]
- Bentamy, A.**, P. Queffeulou, Y. Quilfen and K.B. Katsaros, 1999: Ocean surface wind fields estimated from satellite active and passive microwave instruments. *IEEE Trans., Geosci. Remote Sens.* 37(5), 2469–2486. [3.4]
- Bentamy, A.**, K.B. Katsaros, W. Drennan and E. Forde, 2000: Daily surface wind fields produced by merged satellite data. *Proc., Symposium on Gas Transfer at Water Surfaces* (submitted). [3.4]
- Beranger, K.**, K. Viau, B. Barnier, E. Garnier, J.-M. Moline and L. Siefridt, 1999: *An Atlas of Climatic Estimates of Air–Sea Fluxes*. LEGI, IMG, Grenoble, France. [5.1]
- Berliand, M.E.** and T.G. Berliand, 1952: Measurement of the effective radiation of the earth with varying cloud amounts. *Izv. Acad. Sci. USSR Ser. Geophys. English Transl.*, No. 1. [5.1]
- Bertacchi Uvo, C.B.**, C.A Repelli, S.E. Zebiak and Y. Kushnir, 1998: The relationships between tropical Pacific and Atlantic SST and northeast Brazil monthly precipitation. *J. Climate* 11, 551–562. [1.2]
- Bi, K.**, 1995: *Variability of the surface layer circulation in the western equatorial Pacific*. Ph.D. Dissertation, University of California at San Diego, CA, 165 pp. [4.1]
- Bianchi, G.G.** and I.N. McCave, 1999: Holocene periodicity in North Atlantic climate and deep-ocean flow south of Iceland. *Nature* 397, 515–517. [5.6]
- Bindoff, N.L.** and J.A. Church, 1992: Warming of the water column in the southwest Pacific Ocean. *Nature* 357, 6373, 59–62. [4.6, 6.2, 7.3]
- Bindoff, N.L.** and T.J. McDougall, 1994: Diagnosing climate change and ocean ventilation using hydrographic data. *J. Phys. Oceanogr.* 24, 1137–1152. [4.6, 7.3]
- Bindoff, N.L.** and T.J. McDougall, 2000: Decadal changes along an Indian Ocean section at 32°S and their interpretation. *J. Phys. Oceanogr.* 30, 1207–1222. [1.2, 4.6, 7.3, 7.4]
- Bingham, F.M.**, 1992: The formation and spreading of subtropical mode water in the North Pacific. *J. Geophys. Res.* 97, 11177–11189. [5.4]
- Bingham, F.M.** and R. Lukas, 1995: The distribution of intermediate water in the western equatorial Pacific during January–February 1986. *Deep-Sea Res.* 42, 1545–1573. [4.3, 4.4]
- Bingham, F.M.** and L.D. Talley, 1991: Estimates of Kuroshio transport using an inverse technique. *Deep-Sea Res.* 38(suppl.) 521–543. [3.1, 6.1]
- Bingham, F.M.**, T. Suga and K. Hanawa, 1992: Comparison of upper thermal conditions in the western

- North Pacific between two pentads: 938–42 and 1978–82. *J. Oceanogr.* **48**, 405–425. [5.4]
- Birkett, C., R. Murtugudde and T. Allan, 1999: Indian Ocean climate event brings floods to East Africa's lakes and the Sudd Marsh. *Geophys. Res. Lett.* **26**, 1031–1034. [1.2]
- Bishop, J. K. B. and W. B. Rossow, 1991: Spatial and temporal variability of global surface solar irradiance. *J. Geophys. Res.* **96**, 16839–16858. [3.4]
- Bishop, J. K., W. B. Rossow and E. G. Dutton, 1997: Surface solar irradiance from the international Satellite Cloud Climatology project 1983–1991. *J. Geophys. Res.* **102**, 6883–6910. [5.1]
- Bjerknes, J., 1966: A possible response of the atmospheric Hadley circulation to equatorial anomalies of ocean temperature. *Tellus* **18**, 820–829. [7.4]
- Bjerknes, J., 1969: Atmospheric teleconnections from the equatorial Pacific. *Mon. Wea. Rev.* **97**, 163–172. [7.4]
- Blanchet, I., C. Frankignoul and M. A. Cane, 1997: A comparison of adaptive Kalman filters for a tropical Pacific Ocean model. *Mon. Wea. Rev.* **125**, 40–58. [7.1]
- Blanke, B. and P. Delecluse, 1993: Variability of the tropical Atlantic Ocean simulated by a general circulation model with two different mixed-layer physics. *J. Phys. Oceanogr.* **23**, 1363–1388. [2.3]
- Blanke, B. and S. Raynaud, 1997: Kinematics of the Pacific Equatorial Undercurrent: An Eulerian and Lagrangian approach from GCM results. *J. Phys. Oceanogr.* **27**, 1038–1053. [4.4]
- Bleck, R., C. Rooth, D. Hu and L. T. Smith, 1992: Salinity-driven thermocline transients in a wind- and thermohaline-forced isopycnic coordinate model of the North Atlantic. *J. Phys. Oceanogr.* **22**, 1486–1505. [2.2]
- Bleck, R., 1998: Ocean modeling in isopycnic coordinates. In: *Ocean Modeling and Parameterization*, E. P. Chassignet and J. Verron (eds), NATO Science Series, Series C: Math. Phys. Sci., Kluwer Acad. Publ., Dordrecht, Vol. 516, 451 pp. [2.2]
- Blumenthal, M. B., 1987: *Interpretation of equatorial current meter data as internal waves*. Ph.D. Dissertation, WHOI, Woods Hole, MA, 371 pp. [5.2]
- Boddem, J. and R. Schlitzer, 1995: Intercean exchange and meridional mass and heat fluxes in the South Atlantic. *J. Geophys. Res.* **100**, 15821–15834. [4.7]
- Boebel, O., C. Schmid and W. Zenk, 1997: Flow and recirculation of Antarctic Intermediate Water across the Rio Grande Rise. *J. Geophys. Res.* **102**, 209677–20986. [5.8, 7.1]
- Boebel, O., C. Duncombe Rae, S. Garzoli *et al.*, 1998: Float experiment studies interocean exchanges at the tip of Africa. *Eos Trans. Amer. Geophys. Union* **79**, 7–8. [3.2]
- Boebel, O., R. E. Davis, R. Peterson *et al.*, 1999: The intermediate depth circulation of the western South Atlantic. *Geophys. Res. Lett.* **26**, 3329–3332. [3.2]
- Bönnisch, G., J. Blindheim, J. L. Bullister, P. Schlosser and D. W. R. Wallace, 1997: Long-term trends of temperature, salinity, density and transient tracers in the central Greenland Sea. *J. Geophys. Res.* **102**, 18553–18571. [7.3]
- Boer, G. J., G. Flato, M. C. Reader and D. Ramsden, 1999: A transient climate change simulation with greenhouse gas and aerosol forcing: experimental design and comparison with the instrumental record for the 20th century. *Climate Dyn.* **16**, 427–450. [2.3]
- Boicourt, W. C., W. J. Wiseman Jr., A. Valle-Levinson and L. P. Atkinson, 1998: Continental shelf of the Southeastern United States and the Gulf of Mexico: In the shadow of the western boundary current. In: *The Sea*, Vol. 11, A. R. Robinson and K. K. Brink (eds), John Wiley, NY, pp. 135–182. [1.2]
- Bond, G., W. Showers, M. Cheseby *et al.*, 1997: A pervasive millennial scale cycle in North Atlantic Holocene and glacial climates. *Science* **278**, 1257–1266. [1.2]
- Bonekamp, H., A. Sterl and G. J. Komen, 1999: Interannual variability in the Southern Ocean from an ocean model forced by European Center for Medium-Range Weather Forecasts reanalysis fluxes. *J. Geophys. Res.* **104**, 13317–13331. [4.6]
- Böning, C. W., 1988: Characteristics of particle dispersion in the North Atlantic: an alternative interpretation of SOFAR float results. *Deep-Sea Res.* **35**, 1379–1385. [3.2]
- Böning, C. W. and F. O. Bryan, 1996: Large-scale transport processes in high-resolution circulation models. In: *The Warmwatersphere of the North Atlantic Ocean*. W. Krauss (ed.), Gebr. Bornträger, Stuttgart, pp. 91–128. [2.2]
- Böning, C. W. and P. Herrmann, 1994: Annual cycle of poleward heat transport in the ocean: Results from high-resolution modeling of the North and Equatorial Atlantic. *J. Phys. Oceanogr.* **24**, 91–107. [2.2, 4.3, 6.1]
- Böning, C. W. and F. A. Schott, 1993: Deep currents and the eastward salinity tongue in the equatorial Atlantic: results from an eddy-resolving, primitive equation model. *J. Geophys. Res.* **98**, 6991–6999. [4.3]
- Böning, C. W., R. Dösscher and R. G. Budich, 1991: Seasonal transport variation in the western subtropical North Atlantic: Experiments with an eddy-resolving model. *J. Phys. Oceanogr.* **21**, 1271–1289. [2.1, 2.2]

- Böning, C.W., W.R. Holland, F.O. Bryan, G. Danabasoglu and J.C. McWilliams, 1995: An overlooked problem in model simulations of the thermohaline circulation and heat transport in the Atlantic Ocean. *J. Climate* 8, 515–523. [2.3]
- Böning, C.W., F.O. Bryan, W.R. Holland and R. Döscher, 1996: Deep-water formation and meridional overturning in a high-resolution model of the North Atlantic. *J. Phys. Oceanogr.* 26, 1142–1164. [2.2, 6.1, 7.1]
- Böning, C.W., C. Dieterich, B. Barnier and Y. Jia, 2000: Seasonal cycle of meridional heat transport in the subtropical North Atlantic: Intercomparison of the DYNAMO models and observations near 25° N. *Prog. Oceanogr.* (in press). [2.2]
- Borenäs, K.M. and P.A. Lundberg, 1988: On the Deep-water flow through the Faroe Bank Channel. *J. Geophys. Res.* 93, 1281–1292. [5.6]
- Bormans, M., C. Garrett and K. Thompson, 1986: Seasonal variability of the surface inflow through the Strait of Gibraltar. *Oceanol. Acta* 9, 403–414. [5.7]
- Born, G.H., J.A. Dunne and D.B. Lame, 1979: SEASAT mission overview. *Science* 204, 1405–1406. [2.1]
- Born, G.H., B.D. Tapley, J.C. Ries and R.H. Stewart, 1986: Accurate measurement of mean sea level changes by altimetric satellites. *J. Geophys. Res.* 91, 11775–11782. [3.3]
- Bottomley, M., C.K. Folland, J. Hsiung, R.E. Newell and D.E. Parker, 1990: *Global Ocean Surface Temperature Atlas GOSTA Series*. Meteorological Office, Bracknell, UK, 333 pp. [7.3]
- Boulanger, J.-P. and L.-L. Fu, 1996: Evidence of boundary reflection of Kelvin wave and first-mode Rossby waves from TOPEX/POSEIDON sea level data. *J. Geophys. Res.* 101, 16361–16371. [3.3]
- Boulanger, J.-P. and C. Menkes, 1999: Long equatorial wave reflection in the Pacific Ocean from TOPEX/POSEIDON data during the 1992–1998 period. *Climate Dyn.* 15, 205–225. [3.3]
- Bourassa, M.A., L.M.H. Freilich, D.M. Legler, W.T. Liu and J.J. O'Brien, 1997: Wind observations from new satellite and research vessels agree. *Eos Trans. Amer. Geophys. Union* 78, 597 and 602. [3.4]
- Bourke, R.H., R.A. Paquette, R.F. Blythe and M.D. Stone, 1993: On the deep and bottom waters of the Greenland Sea from summer 1989 and 1990 data. *J. Geophys. Res.* 98, 4629–4638. [7.3]
- Bourlès, B., R.L. Molinari, E. Johns, W.D. Wilson and K.D. Leaman, 1999a: A synoptic study of the upper layer circulation in the western tropical North Atlantic. *J. Geophys. Res.* 104, 1361–1376. [4.3]
- Bourlès, B., Y. Gouriou and R. Chuchla, 1999b: On the circulation in the upper layer of the western equatorial Atlantic. *J. Geophys. Res.* 104, 21151–21170. [4.3]
- Bourras, D. and L. Eymard, 1988: Direct retrieval of the surface latent heat flux from satellite data: comparison to Liu *et al.* (1984) method on data of the SEMAPHORE Experiment. *9th Conf. on Satellite Meteorol. and Oceanogr.*, 1, 278–282. [3.4]
- Boville, B.A. and P.R. Gent, 1998: The NCAR Climate System Model, version one. *J. Climate* 11, 1115–1130. [2.3, 6.1]
- Bowden, K., 1954: The direct measurement of subsurface currents in the ocean. *Deep-Sea Res.* 2, 33–47. [3.2]
- Bowditch, N.V., 1966: *American Practical Navigator*. US Navy Hydrographic Office Pub. No. 9, US Naval Oceanographic Office. [4.1]
- Bower, A.S. and T. Rossby, 1989: Evidence of cross-frontal exchange processes in the Gulf Stream based on isopycnal RAFOS float data. *J. Phys. Oceanogr.* 19, 1177–1190. [3.2]
- Bower, A.S., L. Armi and I. Ambar, 1997: Lagrangian observations of Meddy formation during a Mediterranean undercurrent seeding experiment. *J. Phys. Oceanogr.* 27, 2545–2575. [3.2, 5.7]
- Bower, A.S., P.L. Richardson, H.D. Hunt *et al.*, 2000: Warm-water pathways in the subpolar North Atlantic: An overview of the ACCE RAFOS float programme. *International WOCE Newsletter*, No. 38, 14–16, WOCE International Project Office (unpublished document). [3.2]
- Bower, A.S. and H.D. Hunt, 2000a: Lagrangian observations of the deep western boundary current in the North Atlantic Ocean. Part 1: Large-scale pathways and spreading rates. *J. Phys. Oceanogr.* 30, 764–783. [3.2]
- Bower, A.S. and H.D. Hunt, 2000b: Lagrangian observations of the deep western boundary current in the North Atlantic Ocean. Part 2: the Gulf Stream–deep western boundary current crossover. *J. Phys. Oceanogr.* 30, 784–804. [3.2]
- Boyd, P.W., A. Watson, C.S. Law *et al.*, 2000: Phytoplankton bloom upon mesoscale iron fertilisation of polar Southern Ocean waters. *Nature* (in press). [1.2]
- Boyer, D.L., Chen, R.-R. and L. Tao, 1993: Physical model of bathymetric effects on the Antarctic Circumpolar Current. *J. Geophys. Res.* 98, 2587–2608. [4.6]
- Boyle, E.A., 1990: Quaternary deepwater paleoceanography. *Science* 249, 863–870. [2.1]
- Boyum, G., 1963: Hydrology and currents in the area west of Gibraltar. *Results from the*

- 'Helland-Hansen' Expedition, May 1965, NATO No. 7, Geophysical Institute, Bergen. [5.7]
- Bradley, E.F. and R.A. Weller (eds), 1995a: *Joint Workshop of the TOGA COARE Flux and Atmospheric Working Groups*, 11–13 July, 1995, Boulder, CO, USA. TOGA COARE International Project Office, UCAR, Boulder, Co, USA, 35 pp. [3.1]
- Bradley, E.F. and R.A. Weller (eds), 1995b: *Third Workshop of the TOGA COARE Air-Sea Interaction (Flux) Working Group*, 2–4 August, 1995, University of Hawaii, Honolulu, HI. TOGA COARE International Project Office, UCAR, Boulder, CO, 34 pp. [3.1]
- Bradley, E.F. and R.A. Weller (eds), 1997: *Fourth Workshop of the TOGA COARE Air-Sea Interaction (Flux) Working Group*, 9–11 October, 1996, WHOI, MA., USA. TOGA COARE Inter-national Project Office, UCAR, Boulder, CO, 61 pp. [3.1]
- Bradley, E.F., P.A. Coppin and J.S. Godfrey, 1991: Measurement of sensible and latent heat flux in the western equatorial Pacific Ocean. *J. Geophys. Res.* **96**, 3375–3389. [3.4]
- Bray, N. A., S. Hautala, J. Chong and J. Pariwono, 1996: Large-scale sea level, thermocline and wind variations in the Indonesian throughflow region. *J. Geophys. Res.* **101**, 12239–12254. [4.7]
- Bray, N.A., S.E. Wijffels, J.C. Chong *et al.*, 1997: Characteristics of the Indo-Pacific throughflow in the eastern Indian Ocean. *Geophys. Res. Lett.* **24**, 2569–2572. [4.7, 6.2]
- Bretherton, F.P., 1982: Ocean climate modeling. *Prog. Oceanogr.* **11**, 93–129. [7.2]
- Bretherton, F.P., D.M. Burridge, J. Crease, F.W. Dobson, E.B. Kraus and T.H. Vonder Haar, 1982: *The Cage Experiment: A Feasibility Study*. WCP 22, WMO Geneva, 95 pp. [6.1]
- Brewer, P.G., 1978: Direct measurement of the oceanic CO₂ increase. *Geophys. Res. Lett.* **5**, 997–1000. [6.3]
- Brewer, P.G., C. Goyet and D. Dyrssen, 1989: Carbon dioxide transport by ocean currents at 25°N latitude in the Atlantic Ocean. *Science* **246**, 477–479. [6.3]
- Brewer, P.G., C. Goyet and G. Friedrich, 1997: Direct observation of the oceanic CO₂ increase revisited. *Proc. Natl. Acad. Sci.* **94**, 8308–8313. [6.3]
- Brink, K.H., 1998: Deep-sea forcing and exchange processes. In: *The Sea*, Vol. 10, K.H. Brink and A.R. Robinson (eds), John Wiley, NY, pp. 151–167. [1.2]
- Brink, K.H. and A.R. Robinson (eds), 1998: *The Sea*, Vol. 10, John Wiley, NY, 604 pp. [1.2]
- Brink, K.H., Chapman, D.C. and G.R. Halliwell, 1987: A stochastic model for wind-driven currents over the continental shelf. *J. Geophys. Res.* **92**, 1783–1797. [1.2]
- Broccoli, A.J., N-C. Lau and M.J. Nath, 1998: The cold ocean–warm land pattern: model simulation and relevance to climate change detection. *J. Climate* **11**, 2743–2763. [2.3]
- Broecker, W.S., 1991: The great ocean conveyor. *Oceanogr.* **4**, 79–89. [1.2, 2.1, 4.7]
- Broecker, W.S., 1997: Thermohaline circulation, the Achilles heel of our climate system: will man-made CO₂ upset the current balance? *Science* **278**, 1582–1588. [2.3, 7.3]
- Broecker, W.S., 2001: Carbon futures. In: *Geosphere–Biosphere Interactions and Climate*, Bengtsson, L. and C.U. Hammer (eds.), Cambridge University Press, Cambridge (In Press) [6.3]
- Broecker, W.S. and T.-H. Peng, 1982: *Tracers in the Sea*. Eldigio Press, Palisades, NY, 692 pp. [5.8]
- Broecker, W.S. and T.-H. Peng, 1992: Interhemispheric transport of carbon dioxide by ocean circulation. *Nature* **356**, 587–589. [6.3]
- Broecker, W.S., R. Gerard, M. Ewing and B.C. Heezen, 1960: Natural Radiocarbon in the Atlantic Ocean. *J. Geophys. Res.* **65**, 2903–2931. [5.8]
- Broecker, W.S., D.M. Peteet and D. Rind, 1985a: Does the ocean–atmosphere system have more than one stable mode of operation? *Nature* **315**, 21–26. [5.6]
- Broecker, W.S., T. Takahashi and T.-H. Peng, 1985b: Reconstruction of past atmospheric CO₂ contents from the chemistry of the contemporary ocean. *US Dep. Energy Report DOE/OR-857*, 79 pp. [6.3]
- Broecker, W.S., T.-H. Peng, G. Ostlund and M. Stuiver, 1985c: The distribution of bomb radiocarbon in the ocean. *J. Geophys. Res.* **90**, 6953–6970. [5.8]
- Broecker, W.S., T.-H. Peng, J. Jouzel and G. Russell, 1990: The magnitude of global fresh-water transports of importance to ocean circulation. *Climate Dyn.* **4**, 73–79. [6.2]
- Broecker, W.S., S. Sutherland, W. Smethie, T.-H. Peng and G. Ostlund, 1995: Oceanic radiocarbon: Separation of the natural and bomb components. *Glob. Biogeochem. Cycles* **9**, 263–288. [5.8]
- Broecker, W.S., S.L. Peacock, S. Walker *et al.*, 1997: How much deep water is formed in the Southern Ocean? *J. Geophys. Res.* **103**, 15833–15843. [4.6]
- Broecker, W.S., S. Sutherland and T.-H. Peng, 1999: A possible 20th-century slowdown of Southern Ocean Deep Water formation. *Science* **286**, 1132–1135. [5.8]
- Brooks, C.E.P., 1923: Variations in the levels of the central African lakes Victoria and Albert. *Geophys. Mem. London* **2**, 337–344. [2.1]

- Browning, G. L., W. R. Holland, H.-O. Kreiss and S. J. Worley, 1990: An accurate hyperbolic system for approximately hydrostatic and incompressible oceanographic flows. *Dyn. Atmos. Oceans* **14**, 303–332. [7.2]
- Bruce, J. G., D. R. Johnson and J. C. Kindle, 1994: Evidence for eddy formation in the eastern Arabian Sea during the northeast monsoon. *J. Geophys. Res.* **99**, 7651–7664. [3.3]
- Bryan, F., 1986: High latitude salinity effects and inter-hemispheric thermohaline circulations. *Nature* **323**, 301–304. [5.6]
- Bryan, F., 1987: Parameter sensitivity of primitive equation ocean general circulation models. *J. Phys. Oceanogr.* **17**, 970–985. [2.2, 2.3, 4.3, 5.2]
- Bryan, F., 1998: Climate drift in a multicentury integration of the NCAR Climate System Model. *J. Climate* **11**, 1455–1471. [2.3, 7.4]
- Bryan, F. O. and W. R. Holland, 1989: A high resolution simulation of the wind- and thermohaline-driven circulation in the North Atlantic Ocean. In: *Parameterization of Small-Scale Processes*, Proc. Hawaiian Winter Workshop, P. Müller and D. Henderson (eds), Hawaii Inst. Geophys. Spec. Publ., pp. 99–115. [2.2, 7.2]
- Bryan, K., 1969: A numerical method for the study of the circulation of the world ocean. *J. Comp. Phys.* **4**, 347–376. [2.2, 2.3, 5.2]
- Bryan, K., 1982: Seasonal variation in meridional overturning and poleward heat transport in the Atlantic and Pacific Oceans: A model study. *J. Mar. Res.* **40**, 39–53. [2.2, 6.1]
- Bryan, K., 1984: Accelerating the convergence to equilibrium of ocean climate models. *J. Phys. Oceanogr.* **14**, 666–673. [2.3]
- Bryan, K. and M. D. Cox, 1968: A nonlinear model of an ocean driven by wind and differential heating. Parts I and II. *J. Atmos. Sci.* **25**, 945–967, 968–978. [2.2]
- Bryan, K. and M. D. Cox, 1972: The circulation of the World Ocean: A numerical study. Part I, A homogenous model. *J. Phys. Oceanogr.* **2**, 319–335. [4.6]
- Bryan, K. and L. J. Lewis, 1979: A water mass model of the world ocean. *J. Geophys. Res.* **84**, 2503–2517. [2.2, 7.2]
- Bryan, K. and M. J. Spelman, 1985: The ocean's response to a CO₂-induced warming. *J. Geophys. Res.* **90**, 11679–11688. [2.2]
- Bryan, K., F. G. Komro, S. Manabe and M. J. Spelman, 1982: Transient climate response to increasing atmospheric carbon dioxide. *Science* **215**, 56–58. [2.2]
- Bryan, K., J. K. Dukowicz and R. D. Smith, 1999: On the mixing coefficient in the parameterization of bolus velocity. *J. Phys. Oceanogr.* **29**, 2442–2456. [2.2]
- Bryden, H. L., 1979: Poleward heat flux and conversion of available potential energy in Drake Passage. *J. Mar. Res.* **37**, 1–22. [4.6]
- Bryden, H. L., 1993: Ocean heat transport across 24° latitude. In: *Interactions Between Global Climate Subsystems: The Legacy of Hann*, G. A. McBean and M. Hantel (eds), Geophys. Monographs, Vol. 75, pp. 65–75. [6.1]
- Bryden, H. L. and E. C. Brady, 1985: Diagnostic model of the three-dimensional circulation in the upper Equatorial Pacific Ocean. *J. Phys. Oceanogr.* **15**, 1255–1273. [4.3]
- Bryden, H. L. and E. C. Brady, 1989: Eddy momentum and heat fluxes and their effects on the circulation of the Equatorial Pacific Ocean. *J. Mar. Res.* **47**, 55–79. [4.3]
- Bryden, H. L. and M. M. Hall, 1980: Heat transport by currents across 25°N latitude in the Atlantic Ocean. *Science* **207**, 884–886. [3.1, 6.3]
- Bryden, H. L. and R. A. Heath, 1985: Energetic eddies at the northern edge of the Antarctic Circumpolar Current in the Southwest Pacific. *Prog. Oceanogr.* **14**, 65–87. [4.6]
- Bryden, H. L. and T. H. Kinder, 1991: Steady two-layer exchange through the Strait of Gibraltar. *Deep-Sea Res.* **38**(suppl.), S445–S463. [5.7]
- Bryden, H. L. and D. J. Webb, 1998: A perspective on the need to build a dam across the Strait of Gibraltar. *EGS News Letter* **69**, December 1998, 1–3 (unpublished document). [5.7]
- Bryden, H. L., D. Roemmich and J. Church, 1991: Ocean heat transport across 24°N in the Pacific. *Deep-Sea Res.* **38**, 297–324. [1.2, 4.5, 6.1, 6.2]
- Bryden, H. L., J. Candela and T. H. Kinder, 1994: Exchange through the Strait of Gibraltar. *Prog. Oceanogr.* **33**, 201–248. [5.7]
- Bryden, H. L., M. J. Griffiths, A. M. Lavin, R. C. Maillard, G. Parilla and W. M. Smethie, 1996: Decadal changes in water mass characteristics at 24°N in the Subtropical North Atlantic Ocean. *J. Climate* **9**, 3162–3086. [7.3, 7.4]
- Bryson, A. E., Jr. and Y.-C. Ho, 1975: *Applied Optimal Control*. Hemisphere, NY (revised), 481 pp. [7.1]
- Bu, X. and M. Warner, 1995: Solubility of chlorofluorocarbon 113 in water and seawater. *Deep-Sea Res.* **42**, 1151–1161. [5.8]
- Bullister, J. L., 1989: Chlorofluorocarbons as time dependent tracers in the Ocean. *Ocean. Mag.* **2**, 12–17. [5.8]
- Bullister, J. L. and D. P. Wisegarver, 1998: The solubility of carbon tetrachloride in water and seawater. *Deep-Sea Res.* **45**, 1285–1302. [5.8]

- Bulsiewicz, K., H. Rose, O. Klatt, A. Putzka and W. Roether, 1998: A capillary-column chromatographic system for efficient chlorofluorocarbon measurement in ocean waters. *J. Geophys. Res.* **100**, 15959–15970. [5.8]
- Bunker, A.F., 1976a: Computations of surface energy flux and annual air-sea interaction cycles of the North Atlantic Ocean. *Mon. Wea. Rev.* **104**, 1122–1140. [3.4, 5.1]
- Bunker, A.F., 1976b: Wintertime interactions of the atmosphere with the Mediterranean Sea. *J. Phys. Oceanogr.* **2**, 225–238. [5.7]
- Busalacchi, A.J., R.M. Atlas and E.C. Hackert, 1993: Comparison of special sensor microwave imager vector wind stress with model-derived and subjective products for the tropical Pacific. *J. Geophys. Res.* **98**, 6961–6977. [3.4]
- Butt, J. and E. Lindstrom, 1994: Currents off the east coast of New Ireland, Papua New Guinea, and their relevance to the regional undercurrents in the Western Equatorial Pacific Ocean. *J. Geophys. Res.* **99**, 12503–12514. [4.3, 4.4]
- Butterfield, D.A., G.J. Massoth, R.E. McDuff, J.E. Lupton and M.C. Lilley, 1990: The chemistry of phase separated hydrothermal fluids from ASHES Vent Field, Juan de Fuca Ridge. *J. Geophys. Res.* **95**, 12895–12921. [5.8]
- Byrne, D., A.L. Gordon and W. Haxby, 1995: Agulhas Eddies: A synoptic view using Geosat ERM data. *J. Phys. Oceanogr.* **25**, 902–917. [4.7]
- Cai, W. and P. Baines, 1996: Interactions between thermohaline- and wind-driven circulations and their relevance to the dynamics of the Antarctic Circumpolar Current, in a coarse-resolution global ocean general circulation model. *J. Geophys. Res.* **101**, 14073–14093. [4.6]
- Cai, W.J. and R.J. Greatbatch, 1995: Compensation for the NADW outflow in a global ocean circulation model. *J. Phys. Oceanogr.* **25**, 226–241. [4.7]
- Cai, W., P.G. Baines and H.B. Gordon, 1999: Southern mid- to high-latitude variability, a zonal wavenumber-3 pattern, and the Antarctic Circumpolar Wave in the CSIRO coupled model. *J. Climate* **12**, 3087–3104. [2.3, 4.6]
- Cairns, J.L. and G.O. Williams, 1976: Internal wave observations from a midwater float, 2. *J. Geophys. Res.* **81**, 1943–1950. [5.2]
- Caldeira, K. and P.B. Duffy, 2000: The role of the Southern Ocean in uptake and storage of anthropogenic carbon dioxide. *Science* **287**, 620–622. [6.3]
- Caldwell, D.R., 1976: Fine-scale temperature structure in the bottom mixed layer on the Oregon shelf. *Deep-Sea Res.* **23**, 1025–1036. [5.2]
- Caldwell, D.R. and J.M. Moum, 1995: Turbulence and mixing in the ocean. In: *Rev. Geophys. (suppl.) US National Report to IUGG 1991–1994*, 1285–1394. [5.2]
- Callahan, J.E., 1972: The structure and circulation of deep water in the Antarctic. *Deep-Sea Res.* **19**, 563–575. [4.6]
- Candela, J., 1991: The Gibraltar Strait and its role in the dynamics of the Mediterranean Sea. *Dyn. Atmos. Oceans* **15**, 267–300. [5.7]
- Candela, J., C.D. Winant and H.L. Bryden, 1989: Meteorologically forced subinertial flows through the Strait of Gibraltar. *J. Geophys. Res.* **94**, 12667–12674. [5.7]
- Candela, J., C.D. Winant and A. Ruiz, 1990: Tides in the Strait of Gibraltar. *J. Geophys. Res.* **95**, 7313–7335. [5.7]
- Cane, M.A., 1980: On the dynamics of equatorial currents, with application to the Indian Ocean. *Deep-Sea Res.* **27**, 525–544. [4.3]
- Cane, M.A. and S.E. Zebiak, 1987: A theory for El Niño and the Southern Oscillation. *Science* **228**, 1085–1087. [7.4]
- Cane, M.A., A.C. Clement, A. Kaplan *et al.*, 1997: Twentieth century sea surface temperature trends. *Science* **275**, 957–960. [4.4]
- Carissimo, B.C., A.H. Oort and T.H. Vonder Haar, 1985: Estimating the meridional energy transports in the atmosphere and ocean. *J. Phys. Oceanogr.* **15**, 82–91. [6.1]
- Carmack, E.C. and T.D. Foster, 1975: Circulation and distribution of oceanographic properties near the Filchner Ice Shelf. *Deep-Sea Res.* **22**, 77–90. [4.6]
- Carmack, E.C. and P.D. Killworth, 1978: Formation and interleaving of abyssal water masses off Wilkes Land, Antarctica. *Deep-Sea Res.* **25**, 357–369. [4.6]
- Carmack, E.C., R.W. Macdonald, R.G. Perkin, F.A. McLaughlin and R. Pearson, 1995: Evidence for warming of Atlantic water in the southern Canadian Basin of the Arctic Ocean: Results from the Larsen-93 Expedition. *Geophys. Res. Lett.* **22**, 1061–1064. [7.3]
- Carmack, E.C., K. Aagaard, J.H. Swift *et al.*, 1997: Changes in temperature and tracer distributions within the Arctic Ocean: Results from the 1994 Arctic Ocean Section. *Deep-Sea Res.* **44**, 1487–1502. [7.3]
- Carnes, M.R., J.L. Mitchell and P.W. de Witt, 1990: Synthetic temperature profiles derived from Geosat altimetry: Comparison with air-dropped expendable bathythermograph profiles. *J. Geophys. Res.* **95**, 17979–17992. [3.3]
- Carter, D.J.T., 1999: Variability and trends in the wave climate of the North Atlantic: a review.

- In: *Proc. 9th ISOPE Conf.*, 30 May–4 June 1999, Brest France, Vol. III, pp. 12–18. [7.3]
- Carton, J.A., X. Cao, B.S. Giese and A.M. da Silva, 1996a:** Decadal and interannual SST variability in the tropical Atlantic. *J. Phys. Oceanogr.* **26**, 1165–1175. [4.3]
- Carton, J.A., B.S. Giese, X. Cao and L. Miller, 1996b:** Impact of altimeter, thermistor, and expendable bathythermograph data on retrospective analyses of the tropical Pacific Ocean. *J. Geophys. Res.* **101**, 14147–14159. [7.1]
- Cassou, C., P. Noyret, E. Sevault *et al.*, 1998:** Distributed ocean–atmosphere modeling and sensitivity to the coupling flux precision: the CATHODE project. *Mon. Wea. Rev.* **126**, 1035–1053. [2.3]
- Cavanié, A. and P. Lecomte, 1987:** *Study of a Method to De-alias Winds from ERS-1 Data*. ESA Final Report, Contract No. 6874/87/GP-1. [3.4]
- Cayan, D.R., 1992a:** Latent and sensible heat flux anomalies over the Northern Oceans: The connection to monthly atmospheric circulation. *J. Climate* **5**, 354–369. [7.3]
- Cayan, D.R., 1992b:** Variability of latent and sensible heat fluxes estimated using bulk formulae. *Atmos. Ocean* **30**(1), 1–42. [7.3]
- Cayan, D.R., 1992c:** Latent and sensible heat flux anomalies over the Northern Oceans: Driving the sea surface temperature. *J. Phys. Oceanogr.* **22**, 859–881. [7.3]
- Cayan, D.R. and G. Reverdin, 1994:** Monthly precipitation and evaporation variability estimated over the North Atlantic and North Pacific. In: *Atlantic Climate Change Program: Proceedings of the Principal Investigators' Meeting*, Princeton, NJ, 9–11 May 1994. pp. 28–32. [7.3]
- Cazenave A., K. Dominh, M.C. Gennero and B. Ferret, 1998:** Global mean sea level changes observed by TOPEX/POSEIDON and ERS-1. *Phys. Chem. Earth* **23**, 1069–1075. [1.2]
- Chambers, D.P., B.D. Tapley and R.H. Stewart, 1997:** Long-period ocean heat storage rates and basin-scale heat fluxes from TOPEX. *J. Geophys. Res.* **102**, 10525–10533. [3.3]
- Chambers, D.P., B.D. Tapley and R.H. Stewart, 1999:** Anomalous warming in the Indian Ocean coincident with El Niño. *J. Geophys. Res.* **104**, 3035–3047. [3.3]
- Chang, P., L. Ji and H. Li, 1997:** A decadal climate variation in the tropical Atlantic Ocean from thermodynamic air–sea interactions. *Nature* **385**, 516–518. [1.2, 4.3, 7.1]
- Chang, P. and S.G.H. Philander, 1989:** Oceanic adjustment in baroclinic currents. *Deep-Sea Res.* **36**, 17–37. [4.4]
- Chao, Y. and L.-L. Fu, 1995:** A comparison between the TOPEX/POSEIDON data and a global ocean general circulation model during 1992–1993. *J. Geophys. Res.* **100**, 24965–24976. [2.2, 3.3]
- Chao, Y., A. Gangopadhyay, F.O. Bryan and W.R. Holland, 1996:** Modeling the Gulf Stream system: How far from reality? *Geophys. Res. Lett.* **23**, 3155–3158. [2.2]
- Charlson, R.J., J.E. Lovelock, M.O. Andreae and S.G. Warren, 1987:** Oceanic phytoplankton, atmospheric sulphur, cloud albedo and climate. *Nature* **326**, 655–661. [1.2, 2.3]
- Charney, J. and J. DeVore, 1979:** Multiple flow equilibria in the atmosphere and blocking. *J. Atmos. Sci.* **36**, 1205–1216. [4.6]
- Charnock, H., 1955:** Wind stress on a water surface. *Quart. J. Roy. Meteor. Soc.* **81**, 639–640. [3.4]
- Charnock, H., 1997:** John Crossley Swallow, 11 October 1923–3 December 1994. Elected F.R.S. 1968. *Biogr. Mem. Fell. R. Soc. London* **43**, 503–519. [3.2]
- Chassignet, E.P. and J. Verron (eds), 1998:** *Ocean Modeling and Parameterization*. NATO Science Series, Series C: Math. Phys. Sci., Kluwer Acad. Publ., Dordrecht, Vol. 516, 451 pp. [2.2, 7.2]
- Chassignet, E.P., L.T. Smith, R. Bleck and F.O. Bryan, 1996:** A model intercomparison: Numerical simulations of the North and Equatorial Atlantic oceanic circulation in depth and isopycnic coordinates. *J. Phys. Oceanogr.* **26**, 1849–1867. [2.2]
- Chelton, D.B. and M.G. Schlax, 1996:** Global observations of oceanic Rossby waves. *Science* **272**, 234–238. [3.3, 7.1]
- Chelton, D.B., M.G. Schlax, D.L. Witter and J.G. Richman, 1990:** Geosat altimeter observations of the surface circulation of the southern ocean. *J. Geophys. Res.* **95**, 17877–17903. [3.3, 4.6]
- Chelton, D.B. and A.M. Mestas-Nunez, 1997:** The large-scale, wind-driven response of the North Pacific. *International WOCE Newsletter*, No. 25, 3–6, WOCE International Project Office (unpublished document). [2.2]
- Chelton, D.B., J. Ries, B. Haines, L.-L. Fu and P.S. Callahan, 2000:** Satellite altimetry. In: *Satellite Altimetry and Earth Sciences*, L.-L. Fu and A. Cazenave (eds), Academic Press, London pp 1–131. [3.3]
- Cheminée, J.-L., P. Stoffers, G. McMurtry, H. Richnow, D. Puteanus and P. Sedwick, 1991:** Gas-rich submarine exhalations during the 1989 eruption of Macdonald Seamount. *Earth Planet. Sci. Lett.* **107**, 318–327. [5.8]
- Chen, C.-T., 1993:** The oceanic anthropogenic CO₂ sink. *Chemosphere* **27**, 1041–1064. [6.3]

- Chen, C.-T. and F.J. Millero, 1979: Gradual increase of oceanic CO₂. *Nature* 277, 205–206. [6.3]
- Chen, D., W.T. Liu, S.E. Zebiak, M.A. Cane, Y. Kushnir and D. Witter, 1999: Sensitivity of the tropical Pacific Ocean simulation to the temporal and spatial resolution of wind forcing. *J. Geophys. Res.* 104, 11261–11272. [3.4]
- Chen, T.-C., H. van Loon, K.-D. Wu and M.-C. Yen, 1992: Changes in the atmospheric circulation over the North Pacific–North America area since 1950. *J. Meteor. Soc. Japan* 70, 1137–1146. [7.3]
- Chen, T.-C. and M.-C. Yen, 1997: Interdecadal variation of the Southern Hemisphere circulation. *J. Climate* 10, 805–812. [7.3]
- Cheney, R.E., J.G. March and B.D. Beckley, 1983: Global mesoscale variability from collinear tracks of Seasat Altimeter data. *J. Geophys. Res.* 88, 4343–4354. [3.3]
- Cheney, R.E., L. Miller, R. Agreen, N. Doyle and J. Lillibridge, 1994: TOPEX/POSEIDON: The 2-cm solution. *J. Geophys. Res.* 99, 24555–24564. [3.3]
- Chereskin, T., 1995: Direct evidence for an Ekman balance in the California Current. *J. Geophys. Res.* 100, 18261–18269. [4.1]
- Chereskin, T.K. and A.J. Harding, 1993: Modeling the performance of an acoustic Doppler current profiler. *J. Atmos. Oceanic Technol.* 10, 41–63. [3.1]
- Chereskin, T.K. and D. Roemmich, 1991: A comparison of measured and wind-derived Ekman transport at 11°N in the Atlantic Ocean. *J. Phys. Oceanogr.* 21, 869–878. [3.1, 4.1]
- Chereskin, T.K., W.D. Wilson, H.L. Bryden, A. Ffield and J. Morrison, 1997: Observations of the Ekman balance at 8°30'N in the Arabian Sea during the 1995 southwest monsoon. *Geophys. Res. Lett.* 24, 2541–2544. [3.1, 6.1]
- Chong, J.C., J. Sprintall, S. Hautala, W.L. Morawitz, N.A. Bray and W. Pandoe, 2000: Shallow throughflow variability in the outflow straits of Indonesia. *Geophys. Res. Lett.* 27, 125–128. [7.1]
- Chou, S.H., R.M. Atlas and J. Ardizzone, 1995: Estimates of surface humidity and latent heat fluxes over oceans from SSM/I data. *Mon. Wea. Rev.* 123, 2405–2435. [3.4]
- Christoph, M., T.P. Barnett and E. Roeckner, 1998: The Antarctic Circumpolar Wave in a coupled ocean–atmosphere GCM. *J. Climate* 11, 1659–1672. [2.3, 4.6]
- Chu, P.C., S. Lu and W.T. Liu, 1999: Uncertainty of South China Sea prediction using NSCAT and National Centers for Environmental Prediction winds during tropical storm Ernie, 1996. *J. Geophys. Res.* 104, 11273–11289. [3.4]
- Church, J.A., J.S. Godfrey, D.R. Jackett and T.J. McDougall, 1991: A model of sea level rise caused by ocean thermal expansion. *J. Climate* 4, 438–456. [7.3]
- Church, J.A., J.M. Gregory, P. Huybrechts, M. Kuhn, K. Lambeck, M.T. Nhuan, D. Qin, P.L. Woodworth, 2001: Changes in Sea Level. In: Climate Change 2001: The Scientific Basis. Contribution of Working Group I to the *Third Assessment Report of the Intergovernmental Panel on Climate Change* [Houghton, J.T., Y. Ding, D.J. Griggs, M. Noguer, P. van der Linden, X. Dai and K. Maskell (eds.)]. Cambridge University Press, (in press) [1.1, 1.2].
- Ciais, P., P.P. Tans and M. Trolier, 1995: A large northern-hemisphere terrestrial CO₂ sink indicated by the ¹³C/¹²C ratio of atmospheric CO₂. *Science* 269, 1098–1102. [6.3]
- Cione, J.J., S. Raman and L.J. Pietrafesa, 1993: The effect of Gulf Stream-induced baroclinicity on U.S. East Coast winter cyclones. *Mon. Wea. Rev.* 121, 2, 421–430. [1.2]
- Clarke, A.J. and X. Liu, 1993: Observations and dynamics of semiannual and annual sea levels near the eastern equatorial Indian Ocean boundary. *J. Phys. Oceanogr.* 23, 386–399. [4.3]
- Clarke, A.J. and X. Liu, 1994: Interannual sea level in the Northern and Eastern Indian Ocean. *J. Phys. Oceanogr.* 24, 1224–1235. [4.3]
- Clarke, R.A., 1984: Transport through the Cape Farewell–Flemish Cap section. *Rapp. P-v. Reun. Cons. Int. Explor. Mer* 185, 120–130. [2.3, 4.5, 5.6]
- Clarke, R.A. and J.-C. Gascard, 1983: The formation of Labrador Sea Water: Part I: large-scale processes. *J. Phys. Oceanogr.* 13, 1764–1778. [5.4, 5.5]
- Clarke, R.A., J.H. Swift, J.A. Reid and K.P. Koltermann, 1990: The formation of Greenland Sea Deep Water: Double diffusion or deep convection? *Deep-Sea Res.* 37, 1385–1424. [7.3]
- Clarke, R.A., R.M. Hendry and I. Yashayaev, 1998: A western Boundary Current meter array in the North Atlantic near 42°N. *WOCE International Newsletter*, No. 33, 33–34, WOCE International Project Office (unpublished document). [1.2]
- Clement, A. and A.L. Gordon, 1995: Velocity structure of the Benguela Current. *J. Geophys. Res.* 100, 22591–22601. [4.7]
- Coachman, L.K. and K. Aagaard, 1988: Transports through Bering Strait: Annual and interannual variability. *J. Geophys. Res.* 93, 15535–15539. [6.1, 6.2, 6.3]
- Coale, K.H., K.S. Johnson, S.E. Fitzwater *et al.*, 1996: A massive phytoplankton bloom induced by

- ecosystem-scale iron fertilization experiment in the equatorial Pacific Ocean. *Nature* **383**, 495–501. [1.2]
- Coatanoan, C., C. Goyet, N. Gruber, C.L. Sabine and M. Warner, 2001: Comparison of two approaches to quantify anthropogenic CO₂ in the ocean: results from the northern Indian Ocean. *Glob. Biogeochem. Cycles* (in press). [6.3]
- Coles, V.J., M.S. McCartney, D.B. Olson and W.M. Smethie, 1996: Changes in Antarctic Bottom Water properties in the Western South Atlantic in the late 1980s. *J. Geophys. Res.* **101**, 8957–8970. [4.5, 4.6, 5.8]
- Colin, C. and B. Bourles, 1994: Western boundary currents and transports off French Guiana as inferred from Pegasus observations. *Oceanol. Acta* **17**, 143–157. [4.3]
- Colin, C., B. Bourles, R. Chuchla and F. Dangu, 1994: Western boundary current variability off French Guiana as observed from moored current measurements. *Oceanol. Acta* **17**, 343–354. [4.3]
- Collins, C.A. and R.H. Heinmiller, 1989: The POLYMODE program. In: *Ocean Development and International Law*, NY, Vol. 20, No. 4, pp. 391–408. [1.3]
- Collins, M., 2000: The El-Niño Southern Oscillation in the second Hadley Centre coupled model and its response to greenhouse warming. *J. Climate* **13**, 1299–1312. [2.3]
- Conkright, M.E., S. Levitus, T. O'Brien, T.P. Boyer, J.I. Antonov and C. Stephens, 1998: *World Ocean Atlas 1998, CD-ROM Data Set Documentation*. NODC Internal Report 15, Silver Spring, MD, 16 pp. [4.7]
- Conway, T.J., P.P. Tans, L.S. Waterman *et al.*, 1994: Evidence for interannual variability of the carbon cycle from the National Oceanic and Atmospheric Administration/Climate Monitoring and Diagnostics Laboratory global air sampling network. *J. Geophys. Res.* **99**, 22831–22855. [6.3]
- Cook, E.R., R.D' Arrigo and K.R. Briffa, 1998: The North Atlantic oscillation and its expression in circum-Atlantic tree-ring chronologies from North America and Europe. *Holocene* **8**, 9–17. [7.3]
- Cotton, P.D. and P.G. Challenor, 1999: North Atlantic wave climate variability and the North Atlantic Oscillation Index. In: *Proc. 9th ISOPE Conf.*, 30 May–4 June 1999, Brest, France. [7.3]
- Coughlan, M.J. 1999: Response of the United Nations System to the 1997/8 El Niño event. *World Meteorological Organisation, WMO Bulletin*, **48**, 3, 263–267. [1.2]
- Courtier, P., J.-N. Thépaut and A. Hollingsworth, 1994: A strategy for operational implementation of 4D-Var, using an incremental approach. *Quart. J. Roy. Meteor. Soc.* **120**, 1367–1387. [7.1]
- Coward, A.C., 1996: Current Status of the OCCAM Global Ocean Model. *Sigma* (UK WOCE Newsletter; unpublished document) **20**, 4–6. [4.6]
- Cox, M.D., 1975: A baroclinic model of the world ocean: Preliminary results. In: *Numerical Models of the Ocean Circulation*, National Academy of Sciences, Washington, DC, pp. 107–118. [4.6]
- Cox, M.D., 1985: An eddy resolving numerical model of the ventilated thermocline. *J. Phys. Oceanogr.* **15**, 1312–1324. [2.1, 2.2]
- Cox, M.D., 1989: An idealized model of the World Ocean. Part I: The global scale water masses. *J. Phys. Oceanogr.* **19**, 1730–1752. [2.2]
- Cox, M. and K. Bryan, 1984: A numerical model of the ventilated thermocline. *J. Phys. Oceanogr.* **14**, 674–687. [5.1]
- Cox, P.M., R.A. Betts, C.D. Jones, S.A. Spall, and I.J. Totterdell, 2000: Acceleration of global warming due to carbon-cycle feedbacks in a coupled climate model. *Nature*, **408**, 184–187. [2.3]
- Craig, H., 1969: Abyssal carbon and radiocarbon in the Pacific. *J. Geophys. Res.* **74**, 5491–5506. [5.8]
- Craig, H. and L.I. Gordon, 1965: Deuterium and oxygen 18 variations in the ocean and the marine atmosphere. In: *Stable Isotopes in Oceanographic Studies and Paleotemperatures*, E. Tongiorgi (ed.), Spoleto Conf. Proc., Cons. Naz. Ric., V. Lischi Figli, pp. 9–130. [5.8]
- Craig, H. and K.K. Turekian, 1980: The GEOSECS program 1976–1979. *Earth Planet. Sci. Lett.* **49**, 263–265. [5.8]
- Craig, H., V. Craig, R. Comer, J. Costello and K. Farley, 1988: The 1987 eruption of Tamarii (aka Macdonald) Seamount: a shipboard view from the summit. *Eos Trans. Amer. Geophys. Union* **69**, 1478. [5.8]
- Crease, J., 1962: Velocity measurements in the deep water of the western North Atlantic, summary. *J. Geophys. Res.* **67**, 3173–3176. [3.2, 4.5]
- Crease, J., 1965: The flow of Norwegian Sea Water through the Faroe Bank Channel. *Deep-Sea Res.* **12**, 143–150. [5.6]
- Cresswell, G., A. Frische, J. Peterson and D. Quadfasel, 1993: Circulation in the Timor Sea. *J. Geophys. Res.* **98**, 14379–14390. [4.6, 4.7]
- Cresswell, S., E. Ruprecht and C. Simmer, 1991: Latent heat flux over the North Atlantic Ocean: A case study. *J. Appl. Meteor.* **30**, 1627–1635. [3.4]
- Cronin, M.F. and M.J. McPhaden, 1997: The upper ocean heat balance in the western equatorial Pacific warm pool during September–December 1992. *J. Geophys. Res.* **102**, 8533–8553. [4.3]

- Cronin, M. and D.R. Watts, 1996: Eddy-mean flow interaction in the Gulf Stream at 68°W. Part I: Eddy energetics. *J. Phys. Oceanogr.* **26**, 2107–2131. [2.2]
- Crossley, J.F., J. Polcher, P.M. Cox, N. Gedney and S. Planton, 2000: Uncertainties linked to land surface processes in climate change simulations. *Climate Dyn.* (In press). [2.3]
- Cubasch, U., G. Meehl, G. Boer *et al.*, 2001: In: Climate Change 2001: The Scientific Basis. Contribution of Working Group I to the *Third Assessment Report of the Intergovernmental Panel on Climate Change* [Houghton, J.T., Y. Ding, D.J. Griggs, M. Noguer, P. van der Linden, X. Dai and K. Maskell (eds.)]. Cambridge University Press, (in press). [1.2]
- Culkin, F. and P.S. Ridout, 1998: Stability of IAPSO standard seawater. *J. Atmos. Oceanic Technol.* **15**, 1072–1075. [3.1]
- Cummins, P.F., 2000: Remarks on potential vorticity mixing over topography and momentum conservation. *Deep-Sea Res.* **47**, 737–743. [5.2]
- Cummins, P.F., G. Holloway and A.E. Gargett, 1990: Sensitivity of the GFDL ocean general circulation model to a parameterization of vertical diffusion. *J. Phys. Oceanogr.* **20**, 817–830. [2.2]
- Cunningham, S.A., 2000: Circulation and volume flux of the North Atlantic using synoptic hydrographic data in a Bernoulli inverse. *J. Mar. Res.* **58**, 1–35. [7.1]
- Cunningham, S.A. and T.W.N. Haine, 1995a: Labrador Sea Water in the Eastern North Atlantic. Part I: A synoptic circulation inferred from a minimum in potential vorticity. *J. Phys. Oceanogr.* **25**, 649–665. [5.5]
- Cunningham, S.A. and T.W.N. Haine, 1995b: Labrador Sea Water in the Eastern North Atlantic. Part II: Mixing dynamics and the advective-diffusive balance. *J. Phys. Oceanogr.* **25**, 666–678. [5.5]
- Cunningham, S.A., M.J. Griffiths, B.A. King and M. Brandon, 1997: Comparison of bottom-tracking and profiling LADCP data in a section across the ACC at Drake Passage. *International WOCE Newsletter*, No. 26, 39–40, WOCE International Project Office (unpublished document). [3.1]
- Cuny, J., P.B. Rhines, P.P. Niiler and S. Bacon, 2000: Labrador Sea boundary currents and the fate of the Irminger Sea Water. *J. Phys. Oceanogr.* (submitted). [5.5]
- Curry, J.A. and P.J. Webster, 1999: Thermodynamics of atmospheres and oceans. *Int. Geophys. Series*, **65**, 471 pp. [1.2]
- Curry, R. and M.S. McCartney, 2001: Ocean gyre circulation changes associated with the North Atlantic Oscillation. *J. Phys. Oceanogr.* (in press). [7.3]
- Curry, R.G., M.S. McCartney and T.M. Joyce, 1998: Oceanic transport of subpolar climate signals to mid-depth subtropical waters. *Nature* **391**, 575–577. [5.5, 7.1, 7.3]
- Cushman-Roisin, B., 1987: Subduction. In: *Dynamics of the Oceanic Surface Mixed Layer*, P. Muller and D. Henderson (eds), Hawaii Inst. Geophys. Spec. Publ., pp. 181–196. [5.3]
- Cutler, A.N. and J.C. Swallow, 1984: *Surface Currents of the Indian Ocean (to 25°S, 100°E)*. Inst. Oceanogr. Sci., Wormley, UK, Report No. 187, 42 pp. [4.3]
- da Silva, A.M., C. Young and S. Levitus, 1994: Atlas of surface marine data 1994 Volume 1: Algorithms and procedures. *NOAA Atlas NESDIS 6*, 83 pp. [2.3, 5.1, 6.1, 6.2]
- da Silveira, I.C.A., L.B. De Miranda and W.S. Brown, 1994: On the origins of the north Brazil Current. *J. Geophys. Res.* **99**, 22501–22512. [4.3]
- Dai, A., I.Y. Fung and A.D. Del Genio, 1997: Surface observed global land precipitation variations during 1900–88. *J. Climate* **10**, 2943–2962. [7.3]
- Danabasoglu, G., J.C. McWilliams and P.R. Gent, 1994: The role of mesoscale tracer transports in the global ocean circulation. *Science* **264**, 1123–1126. [2.2, 2.3]
- Dansgaard, W., S.J. Johnsen, H.B. Clausen *et al.*, 1993: Evidence for general instability of past climate from a 250 kyr ice-core record. *Nature* **364**, 218–220. [1.2]
- Davis, E.S., C.E. Dunn, R.H. Stanton and J.B. Thomas, 1999: The GRACE mission: Meeting the technical challenges. In: *Proc. 50th International Astronautical Congress*, 4–8 October 1999, Amsterdam, The Netherlands, Paper IAF-99-B. 2.05 [3.3]
- Davis, R.E., 1991: Observing the general circulation with floats. *Deep-Sea Res.* **38**(suppl. 1), 531–571. [3.2]
- Davis, R.E., 1994: Diapycnal mixing in the ocean: Equations for large-scale budgets. *J. Phys. Oceanogr.* **24**, 777–800. [5.1, 5.2]
- Davis, R.E., 1998a: Autonomous floats in WOCE. *International WOCE Newsletter*, No. 30, 3–6, WOCE International Project Office (unpublished document). [5.5]
- Davis, R.E., 1998b: Preliminary results from directly measuring mid-depth circulation in the tropical and South Pacific. *J. Geophys. Res.* **103**, 24619–24639. [2.1, 3.2, 4.2, 4.3, 7.1]
- Davis, R.E., R. DeSzeke and P. Niiler, 1981: Variability in the upper ocean during MILE, Part II: Modeling the mixed layer response. *Deep-Sea Res.* **28A**, 1453–1475. [4.1]

- Davis, R. E., D. C. Webb, L. A. Regier and J. Dufour, 1992: The Autonomous Lagrangian Circulation Explorer (ALACE). *J. Atmos. Oceanic Technol.* 9, 264–285. [3.2]
- Davis, R. E., P. D. Killworth and J. R. Blundell, 1996: Comparison of autonomous Lagrangian Circulation Explorer and fine resolution Antarctic model results in the South Atlantic. *J. Geophys. Res.* 101, 855–884. [7.1]
- Davis, R. E., J. T. Sherman and J. Dufour, 2000: Profiling ALACEs and other advances in autonomous subsurface floats. *J. Atmos. Oceanic Technol.* (In press). [3.2]
- DBCP, 1999: Global drifting buoy observations: A DBCP implementation strategy. *DBCP Technical Document No. 15. IOC/WMO.* 37 pp. [4.1]
- de Jode, G., 1593: *Speculum Orbis Terrarum.* Edition of Cornelis de Jode, Antwerp. (Available from General Microfilm Co., Cambridge, MA, USA.) [2.1]
- de las Heras, M. M. and R. Schlitzer, 1999: On the importance of intermediate water flows for the global ocean overturning. *J. Geophys. Res.* 104, 15515–15536. [4.7]
- de Miranda A. P., B. Barnier and W. K. Dewar, 1999: Mode waters and subduction rates in a high resolution South Atlantic simulation. *J. Mar. Res.* 57, 213–244. [2.2]
- de Ronde, C. E. J., E. T. Baker, G. J. Massoth *et al.*, 1999: Discovery of active submarine venting along the southern Kermadec arc, offshore New Zealand: Initial results from the NZAPLUME cruise. *Eos Trans. Amer. Geophys. Union* 80, No. 46, F1159. [5.8]
- de Ruijter, W., A. Biastoch, S. Drijfhout *et al.*, 1999: Indian-Atlantic interocean exchange: dynamics, estimation and impact. *J. Geophys. Res.* 104, 20885–20910. [4.7]
- de Szoeke, R. A., 1987: On the wind driven circulation of the South Pacific Ocean. *J. Phys. Oceanogr.* 17, 613–630. [4.2]
- de Szoeke, R. A. and D. B. Chelton, 1999: The modification of long planetary waves by homogeneous potential vorticity layers. *J. Phys. Oceanogr.* 29, 500–511. [7.1]
- de Szoeke, R. A. and M. D. Levine, 1981: The advective flux of heat by mean geostrophic motions in the Southern Ocean. *Deep-Sea Res.* 28, 1057–1085. [4.6]
- Deacon, G. E. R., 1937: The hydrology of the southern ocean. *Discovery Reports* 15, 1–124. [4.6]
- Deardorff, J. W., G. E. Willis and D. K. Lilly, 1969: Laboratory investigation of non-steady penetrative convection. *J. Fluid Mech.* 35, 7–31. [5.5]
- DeCosmo, J., K. B. Katsaros, S. D. Smith *et al.*, 1996: Air-sea exchange of water vapor and sensible heat: The Humidity Exchange over the Sea (HEXOS) results. *J. Geophys. Res.* 101, 12001–12006. [3.4]
- Defant, A., 1936: *The Troposphere: Scientific Results of the German Atlantic Expedition of the Research Vessel 'Meteor' 1925–1927.* Verlag von Walter de Gruyter and Co., Berlin and Leipzig. [7.3]
- Defant, A., 1941: Quantitative Untersuchungen zur Statik und Dynamik des Atlantischen Ozeans. Die absolute Topographie des physikalischen Meeresniveaus und der Drückflächen sowie die Wasserbewegungen im Raum des Atlantischen Ozeans. In: *Wissenschaftliche Ergebnisse der Deutschen Atlantischen Expedition auf dem Forschungs- und Vermessungsschiff 'Meteor' 1925–27*, Vol. 6, Part 2, 1, pp. 191–260. [2.1, 3.2, 4.2]
- Defant, A., 1961: *Physical Oceanography*, Vol. 1. Pergamon Press, New York, 729 pp. [4.2]
- Delcroix, T. and C. Henin, 1988: Observations of the Equatorial Intermediate Current in the western Pacific Ocean (165°E). *J. Phys. Oceanogr.* 18, 363–366. [4.3]
- Delcroix, T., J. Picaut and G. Eldin, 1991: Equatorial Kelvin and Rossby Waves Evidenced in the Pacific Ocean through Geosat sea-level and surface-current anomalies. *J. Geophys. Res.* 96, 3249–3262. [3.3]
- Delecluse, P., 1994: Modelling the ocean circulation. In: *Long-Term Climatic Variations: Data and Modelling*, J.-C. Duplessy and M.-T. Spyridakis (eds), Springer-Verlag, Berlin, 567 pp. [4.3]
- Delecluse, P., M. K. Davey, Y. Kitamura, S. G. H. Philander, M. Suarez and L. Bengtsson, 1998: Coupled general circulation modelling of the tropical Pacific. *J. Geophys. Res.* 103, 14357–14373. [2.3]
- Delworth, T. L., 1996: North Atlantic interannual variability in a coupled ocean-atmosphere model. *J. Climate*, 9, 2356–2375. [2.3]
- Delworth, T. L. and R. J. Greatbatch, 1999: Multi-decadal thermohaline circulation variability driven by atmospheric surface flux forcing. *J. Climate* 13, 1481–1495. [2.3]
- Dengg, J., A. Beckmann and R. Gerdes, 1996: The Gulf Stream separation problem. In: *The Warmwatersphere of the North Atlantic Ocean* W. Krauss (ed.) Gebr. Bornträger, Stuttgart, pp. 253–290. [2.2]
- Dengler, M. A. S. and D. R. Quadfasel, 2001: Equatorial deep jets and abyssal mixing in the Indian Ocean. *J. Phys. Oceanogr.* (submitted). [4.3]
- Denker, H. and R. H. Rapp, 1990: Geodetic and oceanographic results from the analysis of one

- year of Geosat data. *J. Geophys. Res.* **95**, 13151–13168. [3.3]
- Denning, A.S., I.Y. Fung and D. Randall, 1995:** Latitudinal gradient of atmospheric CO₂ due to seasonal exchange with land biota. *Nature* **376**, 240–243. [6.3]
- Deser, C. and M.L. Blackmon, 1993:** Surface climate variations over the North Atlantic Ocean during winter: 1900–1989. *J. Climate* **6**, 1743–1753. [7.3]
- Deser, C. and M.L. Blackmon, 1995:** On the relationship between tropical and North Pacific sea surface temperature variations. *J. Climate* **8**, 1677–1680. [7.3]
- Deser, C., M.A. Alexander and M.S. Timlin, 1996:** Upper ocean thermal variations in the North Pacific during 1970–1991. *J. Climate* **9**, 1840–1855. [4.4, 5.3, 7.1]
- Deser, C., M.A. Alexander and M.S. Timlin, 1999:** Evidence for a wind-driven intensification of the Kuroshio Current Extension from the 1970s to the 1980s. *J. Climate* **12**, 1697–1706. [7.3]
- Deser, C., J.E. Walsh and M.S. Timlin, 2000:** Arctic Sea Ice variability in the context of recent winter-time atmospheric circulation trends. *J. Climate* **13**, 617–633. [7.3]
- Dewar, W.K., 1998:** Topographic and barotropic transport controlled by bottom friction. *J. Mar. Res.* **56**, 295–328. [4.2]
- Dickson, A.G., G.C. Anderson and J. Afghan, 2001:** Sea water based reference materials for CO₂ analysis: 1. Preparation, distribution and use (in preparation). [6.3]
- Dickson, A.G. and F.J. Millero, 1987:** A comparison of the equilibrium constants for the dissociation of carbonic acid in seawater media. *Deep-Sea Res.* **34**, 1733–1743. [6.3]
- Dickson, R.R., 1990:** Flow statistics from long-term current-meter moorings: The global data-set in January 1989. *WOCE International Project Office*, WOCE Report No. 46/90, 33 pp. (unpublished manuscript). [7.1]
- Dickson, R.R., 1997:** From the Labrador Sea to global change. *Nature* **386**, 649–650. [7.3]
- Dickson, R.R., 1999:** All change in the Arctic. *Nature* **397**, 389–391. [7.3]
- Dickson, R.R. and J. Brown, 1994:** The production of North Atlantic Deep Water: Sources, rates and pathways. *J. Geophys. Res.* **99**, 12319–12341. [2.3, 4.5, 5.6]
- Dickson, R.R. and J. Namias, 1976:** North American influences on the circulation and climate of the North Atlantic sector. *Mon. Wea. Rev.* **104**, 1256–1265. [7.3]
- Dickson, R.R., W.J. Gould, P.A. Gurbat and P.D. Killworth, 1982:** A seasonal signal in ocean currents to abyssal depths. *Nature* **295**, 193–198. [2.2]
- Dickson, R.R., J. Meincke, S.-A. Malmberg and A.J. Lee, 1988:** The ‘Great Salinity Anomaly’ in the northern North Atlantic 1968–1982. *Prog. Oceanogr.* **20**, 103–151. [7.3]
- Dickson, R.R., E.M. Gmitrowicz and A.J. Watson, 1990:** Deep water renewal in the northern North Atlantic. *Nature* **344**, 848–850. [4.5]
- Dickson, R.R., J. Lazier, J. Meincke, P. Rhines and J. Swift, 1996:** Long-term coordinated changes in the convective activity of the North Atlantic. *Prog. Oceanogr.* **38**, 241–295. [2.3, 5.4, 7.3]
- Dickson, R.R., J. Meincke, I. Vassie, J. Jungclaus and S. Østerhus, 1999:** Possible predictability in overflow from the Denmark Strait. *Nature* **397**, 243–246. [5.6, 7.3]
- Dickson, R.R., T.J. Osborn, J.W. Hurrell *et al.*, 2000:** The Arctic Ocean response to the North Atlantic Oscillation. *J. Climate* **13**, 2671–2696. [7.3]
- Didden, N. and F. Schott, 1993:** Eddies in the North Brazil Current retroflection region observed by GEOSAT altimetry. *J. Geophys. Res.* **98**, 20121–20131. [4.3]
- Dijkstra, H.A. and J.D. Neelin, 1999:** Imperfections of the thermohaline circulation: multiple equilibria and flux correction. *J. Climate* **12**, 1382–1392. [2.3]
- Dixon, K.W., J.L. Bullister, R.H. Gammon and R.J. Stouffer, 1996:** Examining a coupled climate model using CFC-11 as an ocean tracer. *Geophys. Res. Lett.* **23**, 1957–1960. [2.3]
- Dobroliubov, S.A., 1997:** Freshwater transport in the North Atlantic Ocean: Intercomparison of balance and direct estimates. Abstract OA8: *Intercomparison and Validation of the Ocean-Atmosphere Flux Field*. EGS 22nd General Assembly, Vienna, Issue 15(suppl. 2), p. C405. [6.2]
- Dobson F.W., F.P. Bretherton, D.M. Burridge, J. Crease and E.B. Krauss, 1982:** Report of the JSC/CCCO ‘CAGE’ experiment: A feasibility study. *World Climate Programme Report*, WCP-22, 95 pp. [1.3]
- DOE, 1994:** *Handbook of Methods for the Analysis of the Various Parameters of the Carbon Dioxide System in Sea Water*; version 2, A.G. Dickson and C. Goyet (eds), ORNL/CDIAC-74, Oak Ridge National Laboratory, TN, USA. [6.3]
- Dööscher, R. and R. Redler, 1997:** The relative importance of northern overflow and subpolar deep convection for the North Atlantic thermohaline circulation. *J. Phys. Oceanogr.* **27**, 1894–1902. [2.3]
- Domingues, C.M., S. Wijffels, M. Tomczak and J.A. Church, 1999:** Volume transports and structure of

- the Leeuwin Current at 22°S – WOCE ICM6. *International WOCE Newsletter*, No. 37, 36–40, WOCE International Project Office (unpublished document). [1.2]
- Donelan, M.A., W.M. Drennan and K.B. Katsaros, 1997:** The air-sea momentum flux conditions of wind sea and swell. *J. Phys. Oceanogr.* 27, 2087–2099. [3.4]
- Doney, S.C. and J.L. Bullister, 1992:** A chlorofluorocarbon section in the eastern North Atlantic. *Deep-Sea Res.* 39, 1857–1883. [2.3]
- Doney, S.C., D.M. Glover and W.J. Jenkins, 1992:** A model function of the global bomb-tritium distribution in precipitation, 1960–1986. *J. Geophys. Res.* 97, 5481–5492. [5.8]
- Doney, S.C., J.L. Bullister and R. Wanninkhof, 1998a:** Climatic variability in ocean ventilation rates diagnosed using chlorofluorocarbons. *Geophys. Res. Lett.* 25, 1399–1402. [7.4]
- Doney, S.C., W.G. Large and F.O. Bryan, 1998b:** Surface ocean fluxes and water-mass transformation rates in the coupled NCAR Climate System Model. *J. Climate* 11, 1420–1441. [2.3, 5.1]
- Donguy, J.R. and G. Meyers, 1995:** Observations of geostrophic transport in the western tropical Indian Ocean. *Deep-Sea Res.* 42, 1007–1028. [4.3]
- Donohue, K.A., E. Firing and L. Beal, 2000a:** Comparison of three velocity sections of the Agulhas Current and Agulhas Undercurrent. *J. Geophys. Res.* (in press). [3.1]
- Donohue, K.A., E. Firing and S. Chen, 2000b:** Absolute geostrophic velocity within the Subantarctic Front in the Pacific Ocean. *J. Geophys. Res.* (submitted). [4.6]
- Döös, K., 1995:** Intercean exchange of water masses. *J. Geophys. Res.* 100, 13499–13514. [4.7]
- Döös K. and A. Coward, 1997:** The Southern Ocean as the Major Upwelling Zone of North Atlantic Deep Water. *International WOCE Newsletter*, No. 27, 3–4, WOCE International Project Office. (unpublished document). [2.2, 4.2, 4.6]
- Döös, K. and D.J. Webb, 1994:** The Deacon Cell and the other meridional cells of the Southern Ocean. *J. Phys. Oceanogr.* 24, 429–442. [4.2, 4.6]
- Dööscher, R., C.W. Böning and P. Herrmann, 1994:** Response of circulation and heat transport in the North Atlantic to changes in thermohaline forcing in northern latitudes: A model study. *J. Phys. Oceanogr.* 24, 2306–2320. [2.2]
- Douglas, B., 1991:** Global sea level rise. *J. Geophys. Res.* 96, 6981–6992. [3.3]
- Douglas, B.C., 1992:** Global sea level acceleration. *J. Geophys. Res.* 97, 12699–12706. [1.2]
- Dreisigacker, E. and W. Roether, 1978:** Tritium and Sr-90 in North Atlantic surface water. *Earth Planet. Sci. Lett.* 38, 301–312. [5.8]
- Druffel, E.M., 1980:** Radiocarbon in annual coral rings of Belize and Florida. *Radiocarbon* 22, 363–371. [5.8]
- Druffel, E.M. and T.W. Linick, 1978:** Radiocarbon in annual coral rings of Florida. *Geophys. Res. Lett.* 5, 913–915. [5.8]
- du Penhoat, Y., T. Delcroix and J. Picaut, 1992:** Interpretation of Kelvin/Rossby waves in the equatorial Pacific from model–Geosat data intercomparison during the 1986–1987 El Niño. *Oceanol. Acta* 15(5), 545–554. [3.3]
- Duda, T.F. and D.C. Jacobs, 1995:** Comparison of shear measurements and mixing predictions with a direct observation of diapycnal mixing in the Atlantic thermocline. *J. Geophys. Res.* 100, 13481–13498. [5.2]
- Duffy, P.B., J. Bell, C. Covey, L. Sloan and CMIP investigators, 2000:** Effect of flux adjustments on temperature variability in climate models. *Geophys. Res. Lett.* 27, 764–766. [2.3]
- Düing, W., 1980:** GATE-2 Equatorial A-Scale Oceanography. *Deep-Sea Res.* 26 (suppl. 2), 365 pp. [1.3]
- Düing, W. and F. Schott, 1978:** Measurements in the source region of the Somali Current during the monsoon reversal. *J. Phys. Oceanogr.* 8, 278–289. [4.3]
- Dukowicz, J.K. and R.D. Smith, 1994:** Implicit free-surface method for the Bryan–Cox–Semtner ocean model. *J. Geophys. Res.* 99, 7991–8014. [2.2]
- Dukowicz, J., 1997:** Steric sea level in the Los Alamos POP Code – Non-Boussinesq effects. In: *Numerical Methods in Atmospheric and Oceanic Modeling*, the Andrew J. Robert Memorial Volume, C. Lin, R. Leprise and H. Ritchie (eds.), Ottawa, Canadian Meteorological and Oceanographic Society, pp. 533–546. [7.2]
- Duncombe Rae, C.M., S.L. Garzoli and A.L. Gordon, 1996:** The eddy field of the South-East Atlantic Ocean: A statistical census from the BEST Project. *J. Geophys. Res.* 101, 11949–11964. [4.7]
- Durrieu De Madron, X. and G. Weatherly, 1994:** Circulation, transport and bottom boundary layers of the deep currents in the Brazil Basin. *J. Mar. Res.* 52, 583–638. [4.5, 5.2]
- Dutkiewicz, S., L. Rothstein and T. Rossby, 1999:** Pathways of cross-frontal exchange in the North Atlantic Current. *J. Geophys. Res.* (submitted). [3.2]
- DYNAMO Group, 1997:** DYNAMO, *Dynamics of North Atlantic Models: Simulation and Assimilation with High Resolution Models*. Inst. für Meereskunde and Christian-Albrechts Universität, Kiel, Germany, No. 294, 334 pp. [2.2, 2.3, 5.2, 5.3, 5.6]
- Ebbesmeyer, C.C. and E.J. Lindstrom, 1986:** Structure and origin of 18° water observed during

- POLYMODE Local Dynamics Experiment. *J. Phys. Oceanogr.* **16**, 443–453. [5.4]
- Ebuchi, N., 1999: Statistical distribution of wind speeds and directions globally observed by NSCAT. *J. Geophys. Res.* **104**, 11393–11403. [3.4]
- Eby, M. and G. Holloway, 1994: Sensitivity of a large-scale ocean model to a parameterization of topographic stress. *J. Phys. Oceanogr.* **24**, 2577–2588. [7.2]
- Eckert, C. and M. Latif, 1997: Predictability limits of ENSO: The role of stochastic forcing. *J. Climate* **10**, 1488–1504. [7.2]
- Eden, C. and J. Willebrand, 1999: Neutral density revisited. *Deep-Sea Res.* **46**, 33–54. [7.2]
- Egbert, G.D., 1997: Tidal data inversion: interpolation and inference. *Prog. Oceanogr.* **40**, 53–80. [3.1, 4.2]
- Egbert, G.D. and R.D. Ray, 2000: Significant dissipation of tidal energy in the deep ocean inferred from satellite altimeter data. *Nature* **405**, 775–778. [4.2, 5.2]
- Ekman V.W., 1905: On the influence of the earth's rotation on ocean currents. *Arkiv. For Matematik, Astronomi och Fysik*, **2**, 11, 52 pp. [1.2, 4.1]
- Elder, K.L., A. McNichol and A.R. Gagnon, 1998: Reproducibility of seawater, inorganic and organic carbon C-14 results at NOSAMS. *Radio-carbon* **40**, 223–230. [5.8]
- Ellis, H., 1751: A letter to the rev. Dr. Hales, F.R.S. from Captain Henry Ellis, F.R.S. dated Jan. 7, 1751, at Cape Monte Africa, Ship Earl of Halifax. *Phil. Trans. Roy. Soc. Lond.* **47**, 211–214. [4.4]
- Emery, W.J. and J. Meincke, 1986: Global water masses: Summary and review. *Oceanol. Acta*, **9**, 383–391. [5.8]
- Enfield, D.B. and D.A. Mayer, 1997: Tropical Atlantic sea surface temperature variability and its relation to El Niño-Southern Oscillation. *J. Geophys. Res.* **102**, 929–945. [1.2]
- Enfield, D.B. and A.M. Mestas-Nuñez, 1999: Multiscale variabilities in global sea surface temperatures and their relationships with tropospheric climate patterns. *J. Climate* **12**, 2719–2733. [7.3]
- England, M.H., 1992: On the formation of Antarctic Intermediate Bottom Water in ocean general circulation models. *J. Phys. Oceanogr.* **22**, 918–926. [7.3]
- England, M.H., 1995: Using chlorofluorocarbons to assess ocean climate models. *Geophys. Res. Lett.* **22**, 3051–3054. [6.3]
- England, M.H., 1999: WOCE chemical tracer measurements aid the assessment of ocean climate models. *International WOCE Newsletter*, No. 35, 6–11, WOCE International Project Office (unpublished document). [2.3]
- England, M.H. and A.C. Hirst, 1997: Chlorofluorocarbon uptake in a world ocean model. Part 2: Sensitivity to surface thermohaline forcing and subsurface mixing parameterizations. *J. Geophys. Res.* **102**, 15709–15731. [2.2, 7.4]
- England, M.H. and E. Maier-Reimer, 2001: Using chemical tracers in ocean models. *Rev. Geophys.* (in press). [2.3]
- England, M.H., J. Godfrey, A. Hirst and M. Tomczak, 1993: The mechanism for Antarctic Intermediate Water renewal in a World Ocean model. *J. Phys. Oceanogr.* **23**, 1553–1560. [4.6]
- England, M.H., V. Garçon and J.-F. Minster, 1994: Chlorofluorocarbon uptake in a world ocean model. Part I: Sensitivity to the surface gas forcing. *J. Geophys. Res.* **99**, 25215–25223. [2.3]
- England, M.H. and S. Rahmstorf, 1999: Sensitivity of ventilation rates and radiocarbon uptake to subgrid-scale mixing in ocean models. *J. Phys. Oceanogr.* **29**, 2802–2827. [2.2]
- Environmental Working Group, 1997: *Joint US-Russian Atlas of the Arctic Ocean, Oceanography Atlas for the Winter Period*. CD-ROM, NODC. [7.3]
- Eriksen, C.C., 1980: Evidence for a continuous spectrum of equatorial waves in the Indian Ocean. *J. Geophys. Res.* **85**, 3285–3303. [5.2]
- Eriksen, C.C., 1981: Deep currents and their interpretation as equatorial waves in the western Pacific Ocean. *J. Phys. Oceanogr.* **11**, 48–70. [4.3, 5.2]
- Eriksen, C.C., 1982: Observations of internal wave reflection off sloping bottoms. *J. Geophys. Res.* **87**, 525–538. [5.2]
- Eriksen, C.C., 1985: Implications of ocean bottom reflection for internal wave spectra and mixing. *J. Phys. Oceanogr.* **15**, 1145–1156. [5.2]
- Eriksen, C.C., 1998: Internal wave reflection and mixing at Fieberling Guyot. *J. Geophys. Res.* **103**, 2977–2994. [5.2]
- Esbensen, S.K. and Y. Kushnir, 1981: The heat budget of the Global Ocean: An atlas based on estimates from marine surface observations. *Climatic Res. Institution, Oregon State Univ., Corvallis*, Rep. **29**, 27 pp. [5.1, 6.2]
- Esbensen, S.K., D.B. Chelton, D. Vickers and J. Sun, 1993: An analysis of errors in Special Sensor Microwave Imager evaporation estimates over the global oceans. *J. Geophys. Res.* **98**, 7081–7101. [3.4]
- European Space Agency, 1978: *Space Oceanography, Navigation and Geodynamics*. ESA Report SP-137, Schloss-Elmau, January 1978. [1.3]
- Evenson, A.J. and G. Veronis, 1975: Continuous representation of wind stress and wind stress curl over the world ocean. *J. Mar. Res.* **33**, 131–144. [4.2]

- Eymard, L., C. Klapiz and R. Bernard, 1989: Comparison between Nimbus-7 SMMR and ECMWF model analyses: The problem of the surface latent heat flux. *J. Atmos. Oceanic Technol.* 6, 866–881. [3.4]
- Ezer, T. and G.L. Mellor, 1997: Simulations of the Atlantic Ocean with a free surface sigma coordinate ocean model. *J. Geophys. Res.* 102, 15647–15657. [2.2]
- Fahrbach, E., M. Knoche and G. Rohardt, 1991: An estimate of water mass transformations in the southern Weddell Sea. *Mar. Chem.* 35, 25–44. [4.6]
- Fahrbach, E., G. Rohardt, M. Schröder and V. Strass, 1994a: Transport and structure of the Weddell Gyre. *Ann. Geophys.* 12, 840–855. [4.6]
- Fahrbach, E., R.G. Peterson, G. Rohardt, P. Schlosser and R. Bayer, 1994b: Suppression of bottom water formation in the southeastern Weddell Sea. *Deep-Sea Res. I*, 41, 389–411. [4.6]
- Fahrbach, E., M. Schröder and A. Klepikov, 1998: Circulation and water masses in the Weddell Sea. In: *Physics of Ice-Covered Seas*, Lecture notes from a summer school in Savonlinna, Finland, 6–17 June, 1994, Helsinki University Press. [4.6]
- Fairall, C.W., E.F. Bradley, D.P. Rogers, J.B. Edson and G.S. Young, 1996: Bulk parameterization of air-sea fluxes for Tropical Ocean–Global Atmosphere/Coupled Ocean–Atmosphere Response Experiment (TOGA/COARE). *J. Geophys. Res.* 101, 3747–3764. [3.4]
- Fan, S., M. Gloor, J. Mahlman *et al.*, 1998: A large terrestrial carbon sink in North America implied by atmospheric and oceanic carbon dioxide data and models. *Science* 282, 442–446. [6.3]
- Fang, Z. and J.M. Wallace, 1994: Arctic sea-ice variability on a time-scale of weeks and its relation to atmospheric forcing. *J. Climate* 7, 1897–1914. [7.3]
- Fanning, A.F. and A.J. Weaver, 1996: An atmospheric energy-moisture balance model: climatology, interpentadal climate change and coupling to an ocean general circulation model. *J. Geophys. Res.* 101, 15111–15128. [2.3]
- Fanning, A.F. and A.J. Weaver, 1997a: A horizontal resolution and parameter sensitivity study of heat transport in an idealized coupled climate model. *J. Climate* 10, 2469–2478. [2.2]
- Fanning, A.F. and A.J. Weaver, 1997b: On the role of flux adjustments in an idealised coupled climate model. *Climate Dyn.* 3, 691–701. [2.3]
- Farley, K.A., E. Maier-Reimer, P. Schlosser and W.S. Broecker, 1995: Constraints on mantle ^3He fluxes and deep-sea circulation from an oceanic general circulation model. *J. Geophys. Res.* 100, 3829–3839. [5.8]
- Feely, R.A., C.L. Sabine, R.M. Key and T.H. Peng, 1999: CO₂ synthesis results: estimating the anthropogenic carbon dioxide sink in the Pacific Ocean. *US JGOFS News*, 9, 1–5 (unpublished document). [6.3]
- Feller, W., 1957: *An Introduction to Probability Theory and Its Applications*, 2nd edn. Wiley, New York, 461 pp. [2.1]
- Feng, M., M.A. Merrifield, R. Pinkel *et al.*, 1998a: Semidiurnal tides observed in the western equatorial Pacific during the Tropical Ocean–Global Atmosphere/Coupled Ocean–Atmosphere Response Experiment. *J. Geophys. Res.* 103, 10253–10272. [3.1]
- Feng, M., P. Hacker and R. Lukas, 1998b: Upper ocean heat and salt balances in response to a westerly wind burst in the western equatorial Pacific during TOGA COARE. *J. Geophys. Res.* 103, 10289–10311. [4.3]
- Ferron, B., H. Mercier, K. Speer, A. Gargett and K. Polzin, 1998: Mixing in the Romanche Fracture Zone. *J. Phys. Oceanogr.* 28, 1929–1945. [4.5, 5.2]
- Ferry, N., G. Reverdin and A. Oschlies, 2000: Seasonal sea-surface height variability in the North Atlantic Ocean. *J. Geophys. Res.* 105, 6307–6326. [3.3]
- Ffield, A. and A.L. Gordon, 1992: Vertical mixing in the Indonesian thermocline. *J. Phys. Oceanogr.* 22, 184–195. [4.4, 4.7]
- Ffield, A. and A.L. Gordon, 1996: Tidal mixing signatures in the Indonesian Seas. *J. Phys. Oceanogr.* 26, 1924–1937. [4.3, 4.7]
- Ffield, A., K. Vranes, A.L. Gordon, R.D. Susanto and S.L. Garzoli, 2000: Temperature variability within Makassar Strait. *Geophys. Res. Lett.* 27, 237–240. [4.7]
- Fieux, M. and H. Stommel, 1975: Preliminary look at feasibility of using marine reports of sea surface temperature for documenting climatic change in the western North Atlantic. *J. Mar. Res.* 33(suppl.), 83–95. [5.4]
- Fieux, M. and J.C. Swallow, 1988: Flow of deep water into the Somali Basin. *Deep-Sea Res.* 35, 303–309. [4.3]
- Fieux, M., F. Schott and J.C. Swallow, 1986: Deep boundary currents in the western Indian Ocean revisited. *Deep-Sea Res.* 33, 415–426. [4.3]
- Fieux, M., C. Andrié, P. Delecluse, *et al.*, 1994: Measurements within the Pacific–Indian oceans throughflow region. *Deep-Sea Res.* 41, 1091–1130. [4.3, 4.7]
- Fieux, M., R. Molcard and A.G. Ilahude, 1996: Geostrophic transport of the Pacific–Indian Oceans throughflow. *J. Geophys. Res.* 101, 12421–12432. [4.7, 6.2]

- Fillenbaum, E.R., T.N. Lee, W.E. William and R.J. Zantopp, 1997: Meridional heat transport variability at 26.5°N in the North Atlantic. *J. Phys. Oceanogr.* 27, 153–174. [2.2, 6.1]
- Fine, R.A., 1985: Direct evidence using tritium data for the throughflow from the Pacific to the Indian Ocean. *Nature* 315, 478–480. [4.4, 4.7, 5.8]
- Fine, R.A., 1993: Circulation of Antarctic Intermediate Water in the South Indian Ocean. *Deep-Sea Res.* 40, 2021–2042. [4.6, 4.7, 5.8]
- Fine, R.A. and R.L. Molinari, 1988: A continuous deep western boundary current between Abaco (26.5°N) and Barbados (13°N). *Deep-Sea Res.* 35, 1441–1450. [5.8]
- Fine, R.A., J.L. Reid and H.G. Östlund, 1981: Circulation of tritium in the Pacific Ocean. *J. Phys. Oceanogr.* 11, 3–14. [4.4]
- Fine, R.A., W.H. Peterson and H.G. Östlund, 1987: The penetration of tritium into the tropical Pacific. *J. Phys. Oceanogr.* 17, 553–564. [4.3, 4.4, 5.8]
- Fine, R.A., R. Lukas, F.M. Bingham, M.J. Warner and R.H. Gammon, 1994: The western equatorial Pacific: a water mass crossroads. *J. Geophys. Res.* 99, 25063–25080. [4.4]
- Firing, E., 1987: Deep zonal currents in the central equatorial Pacific. *J. Mar. Res.* 45, 791–812. [4.3, 5.2]
- Firing, E., 1988: Shallow equatorial jets. *J. Geophys. Res.* 93, 9213–9222. [5.2]
- Firing, E., 1989: Mean zonal currents below 1500 m near the equator, 159°W. *J. Geophys. Res.* 94, 2023–2028. [4.3]
- Firing, E. and R.L. Gordon, 1990: Deep ocean acoustic Doppler current profiling. *Proceedings of the IEEE Fourth Working Conference on Current Measurement*, 3–5 April 1990, Maryland, G.F. Appell and T.B. Curtin (eds), pp. 192–201. [3.1]
- Firing, E., S.E. Wijffels and P. Hacker, 1998: Equatorial subthermocline currents across the Pacific. *J. Geophys. Res.* 103, 21413–21423. [3.1, 4.3]
- Fischer, J. and F.A. Schott, 1997: Seasonal transport variability of the deep western boundary current in the equatorial Atlantic. *J. Geophys. Res.* 102, 27751–27769. [2.2, 3.2, 4.3, 4.5]
- Fischer, J. and F.A. Schott, 2000: Labrador Sea Water tracked by profiling floats from the boundary current into the North Atlantic. *J. Phys. Oceanogr.* (submitted). [3.2]
- Fischer, J. and M. Visbeck, 1993: Deep velocity profiling with self-contained ADCPs. *J. Atmos. Oceanic Technol.* 10, 764–773. [3.1]
- Fiúza, A.F.G., M. Hamann, I. Ambar, G. Diaz Del Rio, N. Gonzalez and J.M. Cabanas, 1998: Water masses and their circulation off western Iberia during May 1993. *Deep-Sea Res.* 45, 1127–1160. [1.2]
- Flament, P., S. Kennan, R. Knox, P. Niiler and R. Bernstein, 1996: The three-dimensional structure of an upper ocean vortex in the tropical Pacific Ocean. *Nature* 383, 610–613. [4.3]
- Fleischmann, U. and M. Rhein, 2000: The contribution of Iceland-Scotland overflow water to the formation of North East Atlantic deep water in the Iceland Basin and the West-European Basin. *International WOCE Newsletter*, No. 38, 20–26, WOCE International Project Office (unpublished document). [5.6]
- Fleming, K., P. Johnstom, D. Swartz, Y. Yokoyama, K. Lambeck and J. Chappell, 1998: Refining the eustatic sea-level curve since the Last Glacial Maximum using far- and intermediate-field sites. *Earth and Planetary Science Letters* 163, 327–42. [1.2]
- Florenchie, P. and J. Verron, 1998: South Atlantic Ocean experiment: simulation experiments with a quasi-geostrophic model and assimilation of TOPEX/POSEIDON and ERS-1 altimeter data. *J. Geophys. Res.* 103, 24737–24758. [4.7]
- Fofonoff, N.P., 1962: Dynamics of ocean currents. In: *The Sea*, Vol. 1: *Physical Oceanography*, M.N. Hill (ed.), Wiley, NY, pp. 3–30. [4.2]
- Fofonoff, N.P. and R.C. Millard, Jr., 1983: Algorithms for computation of fundamental properties of seawater. *UNESCO Technical Papers in Marine Science*, UNESCO, Paris; No. 44, 53 pp. [1.2]
- Foldvik, A., T. Gammelsrød and T. Tørresen, 1985a: Circulation and water masses on the southern Weddell Sea shelf. In: *Oceanology of the Antarctic Continental Shelf*, vol. 43 of Antarctic Research Series, S.S. Jacobs (ed.), American Geophysical Union, Washington, DC, pp. 5–20. [4.6, 5.8]
- Foldvik, A., T. Gammelsrød and T. Tørresen, 1985b: Physical oceanography studies in the Weddell Sea during the Norwegian Antarctic Research Expedition 1978/79. *Polar Res.* 3, 195–207. [5.8]
- Foldvik, A., T. Gammelsrød and T. Tørresen, 1985c: Hydrographic observations from the Weddell Sea during the Norwegian Antarctic Research Expedition 1976/77. *Polar Res.* 3, 177–193. [5.8]
- Follows, M.J. and J.C. Marshall, 1994: Eddy driven exchange at ocean fronts. *Ocean Modelling*, 102, 5–9. (unpublished document). [5.3]
- Foster, T.D., 1995: Abyssal water mass formation off the eastern Wilkes Land coast of Antarctica. *Deep-Sea Res.* 42, 501–522. [4.6]
- Foster, T.D. and E.C. Carmack, 1976: Frontal zone mixing and Antarctic Bottom Water formation in the southern Weddell Sea. *Deep-Sea Res.* 23, 301–317. [4.2, 4.6]

- FRAM Group**, 1991: An eddy-resolving model of the Southern Ocean. *Eos Trans. Amer. Geophys. Union* **72**, 169–175. [2.2, 3.3, 4.6]
- Francey, R.J.**, P.P. Tans and C.E. Allison, 1995: Changes in oceanic and terrestrial carbon uptake since 1982. *Nature* **373**, 326–330. [6.3]
- Frankignoul, C.**, F. Bonjean and G. Reverdin, 1996: Interannual variability of surface currents in the tropical Pacific during 1987–1993. *J. Geophys. Res.* **101**, 3629–3647. [4.1]
- Fratantoni, D.M.** and P.L. Richardson, 1999: SOFAR float observations of an intermediate-depth eastern boundary current and mesoscale variability in the eastern tropical Atlantic Ocean. *J. Phys. Oceanogr.* **29**, 1265–1278. [1.2, 4.3]
- Fratantoni, D.M.**, W.E. Johns and T.L. Townsend, 1995: Rings of the North Brazil current: their structure and behavior inferred from observations and a numerical simulation. *J. Geophys. Res.* **100**, 10633–10654. [4.3]
- Freeland, H.**, 2001: Observations of the abyssal water through the Samoa Passage. *J. Phys. Oceanogr.* (In press). [4.5]
- Freeland, H.** and F. Whitney, 1997: Evidence of secular change in the northeast Pacific Ocean. *International WOCE Newsletter*, No. 26, 34–36, WOCE International Project Office (unpublished document). [7.3]
- Freeland, H.**, P.B. Rhines and H.T. Rossby, 1975: Statistical observations of the trajectories of neutrally buoyant floats in the North Atlantic. *J. Mar. Res.* **33**, 383–404. [3.2]
- Freeland, H.**, K. Denman, C. Wong, F. Whitney and R. Jacques, 1997: Evidence of change in the winter mixed layer in the Northeast Pacific Ocean. *Deep-Sea Res.* **44**, 2117–2129. [7.3]
- Freilich, M.H.** and S. Dunbar, 1993: A preliminary C-band scatterometer model function for the ERS 1 AMI instrument. *Proc. First ERS-1 Symposium*, Eur. Space Agency Spec. Publ., ESA SP-359, pp. 79–84. [3.4]
- Freilich, M.H.** and S. Dunbar, 1999: The accuracy of the NSCAT 1 vector winds: Comparisons with National Data Buoy Center buoys. *J. Geophys. Res.* **104**, 11231–11246. [3.4]
- Friedrichs, M.A.M.** and M.M. Hall, 1993: Deep circulation in the Tropical North Atlantic. *J. Mar. Res.* **51**, 697–736. [6.1, 6.2]
- Frouin, R.**, C. Gautier and J. Morcrette, 1988: Downward longwave irradiance at the ocean surface from satellite data: Methodology and in-situ validation. *J. Geophys. Res.* **93**, 597–619. [3.4]
- Fu, L.-L.**, 1983: Recent progress in the application of satellite altimetry to observing the mesoscale variability and general circulation of the oceans. *Rev. Geophys. Space Phys.* **21**, 1657–1666. [3.3]
- Fu, L.-L.** and D.B. Chelton, 2000: Large-scale ocean circulation and variability. In: *Satellite Altimetry and Earth Sciences*, L.-L. Fu and A. Cazenave (eds), Academic Press, London, pp. 133–169. [3.3]
- Fu, L.-L.** and R.E. Cheney, 1995: Applications of satellite altimetry to ocean circulation studies: 1987–1994. *Rev. Geophys.* **32**(suppl.), 213–223. [3.3]
- Fu, L.-L.** and R.A. Davidson, 1995: A note on the barotropic response of sea level to time-dependent wind forcing. *J. Geophys. Res.* **100**, 24955–24963. [3.3]
- Fu, L.-L.** and G. Pihos, 1994: Determining the response of sea level to atmospheric pressure forcing using TOPEX/POSEIDON data. *J. Geophys. Res.* **99**, 24633–24642. [3.3]
- Fu, L.-L.** and R.D. Smith, 1996: Global ocean circulation from satellite altimetry and high-resolution computer simulation. *Bull. Amer. Meteor. Soc.* **77**, 2625–2636. [2.2, 3.3, 7.1]
- Fu, L.-L.**, I. Fukumori and R.N. Miller, 1993: Fitting dynamic models to the Geosat sea level observations in the Tropical Pacific Ocean. Part II: A linear, wind-driven model. *J. Phys. Oceanogr.* **23**, 2162–2181. [7.1]
- Fu, L.-L.**, E.J. Christensen, C.A. Yamarone *et al.*, 1994: TOPEX/POSEIDON Mission Overview. *J. Geophys. Res.* **99**, 24369–24381. [3.3]
- Fu, L.-L.**, B. Cheng and B. Qiu, 2000: 25-Day Period Large-Scale Oscillations in the Argentine Basin Revealed by the TOPEX/POSEIDON Altimeter. *J. Phys. Oceanogr.* (in press). [3.3]
- Fuglister, F.C.**, 1960: *Atlantic Ocean Atlas*. Woods Hole Oceanographic Institution, MA. [3.1, 7.3]
- Fukasawa, M.**, H. Yoritaka, I. Yasuda and H. Uchida, 2000: Estimated heat flux across WHP P2 using PCM-5 time series as constraint. (in preparation). [6.1]
- Fukumori, I.**, 1995: Assimilation of TOPEX sea level measurements with a reduced-gravity shallow water model of the tropical Pacific Ocean. *J. Geophys. Res.* **100**, 25027–25039. [7.1]
- Fukumori, I.**, 2000: Data assimilation by models. In: *Satellite Altimetry and Earth Sciences*, L.-L. Fu and A. Cazenave (eds), Academic Press, London, pp. 237–265. [3.3, 7.1]
- Fukumori, I.** and P. Malanotte-Rizzoli, 1995: An approximate Kalman filter for ocean data assimilation: An example with an idealized Gulf Stream model. *J. Geophys. Res.* **100**, 6777–6793. [7.1]
- Fukumori, I.**, R. Raghunath and L.-L. Fu, 1998: The nature of global large-scale sea level variability in relation to atmospheric forcing: A modeling

- study. *J. Geophys. Res.* **103**, 5493–5512. [2.2, 3.3]
- Fukumori, I., R. Raghunath, L.-L. Fu and Y. Chao, 1999: Assimilation of TOPEX/POSEIDON altimeter data into a global ocean circulation model: How good are the results? *J. Geophys. Res.* **104**, 25647–25666. [3.3, 7.1, 7.4]
- Fung, I. Y., D. E. Harrison and A. A. Lacis, 1984: On the variability of the net longwave radiation at the ocean surface. *Rev. Geophys.* **22**, 177–193. [5.1]
- Fyfe, J. C., G. Boer and G. Flato, 1999: The Arctic and Antarctic Oscillations and their projected changes under global warming. *Geophys. Res. Lett.* **26**, 1601–1604. [2.3]
- Gaffen, D. J., R. D. Rosen, D. A. Salstein and J. S. Boyle, 1997: Evaluation of tropospheric water vapour simulations from the atmospheric Model Intercomparison Project. *J. Climate* **10**, 1648–1661. [6.2]
- Gammon, R. H., J. Cline and D. Wisegarver, 1982: Chlorofluoromethanes in the Northeast Pacific Ocean: Measured vertical distributions and application as transient tracers of upper ocean mixing. *J. Geophys. Res.* **87**, 9441–9454. [5.8]
- Ganachaud, A., 1999: *Large-scale oceanic circulation and fluxes of freshwater, heat, nutrients and oxygen*. Ph.D. Dissertation, MIT-WHOI Joint Program, Woods, MA, 266 pp. [4.7, 5.2]
- Ganachaud, A. and C. Wunsch, 1998: Large scale oceanic nutrient and oxygen fluxes. *International WOCE Newsletter*, No. 32, 12–13. WOCE International Project Office (unpublished document). [5.8]
- Ganachaud, A. and C. Wunsch, 2001: The oceanic meridional overturning circulation, mixing, bottom water formation and the transport of heat energy. *Nature* (submitted). [7.1]
- Ganachaud, A., C. Wunsch, M.-C. Kim and B. Tapley, 1997: Combination of TOPEX/POSEIDON data with a hydrographic inversion for determination of the oceanic general circulation and its relation to geoid accuracy. *Geophys. J. Int.* **128**, 708–722. [3.3]
- Ganachaud, A., C. Wunsch, J. Marotzke and J. Toole, 2000: The meridional overturning and large-scale circulation of the Indian Ocean. *J. Geophys. Res.* **105** (C11), 26117–26134. [6.1, 7.1]
- Ganopolski, A., S. Rahmstorf, V. Petoukhov and M. Claussen, 1998: Simulation of modern and glacial climates with a coupled global model of intermediate complexity. *Nature* **391**, 351–356. [1.2]
- Gargett, A. E., 1988: Reynolds number effects on turbulence in the presence of stable stratification. In: *Small-Scale Turbulence and Mixing in the Ocean*, J. C. J. Nihoul and B. M. Jamart (eds), Elsevier, NY, pp. 517–528. [5.2]
- Gargett, A. E., 1989: Ocean turbulence. *Ann. Rev. Fluid Mech.* **21**, 419–452. [5.2]
- Garrett, C., 1979: Comment on ‘Some evidence for boundary mixing in the deep ocean’ by Laurence Armi. *J. Geophys. Res.* **84**, 5095–5096. [5.2]
- Garrett, C., 1991: Marginal mixing theories. *Atmos. Ocean* **29**, 313–339. [5.2]
- Garrett, C. and D. Gilbert, 1988: Estimates of vertical mixing by internal waves reflected off a sloping bottom. In: *Small-Scale Turbulence and Mixing in the Ocean*. Proceedings of the 19th International Liege Colloquium on Ocean Hydrodynamics, J. C. Nihoul and B. M. Jamart (eds), Elsevier, NY, pp. 405–424. [5.2]
- Garrett, C. and W. H. Munk, 1972a: Space time scales of internal waves. *Geophys. Fluid Dyn.* **2**, 225–264. [5.2]
- Garrett, C. and W. H. Munk, 1972b: Oceanic mixing by breaking internal waves. *Deep-Sea Res.* **19**, 823–832. [5.2]
- Garrett, C. and W. H. Munk, 1975: Space time scales of internal waves: A progress report. *J. Geophys. Res.* **80**, 291–297. [5.2]
- Garrett, C. and W. H. Munk, 1979: Internal waves in the ocean. *Ann. Rev. Fluid Mech.* **11**, 339–369. [4.2]
- Garrett, C. and A. Tandon, 1997: The effects on water mass formation of surface mixed layer time-dependence and entrainment fluxes. *Deep-Sea Res.* **44**, 1991–2006. [5.1, 5.2]
- Garrett, C., P. MacCready and P. B. Rhines, 1993a: Boundary Mixing and Arrested Ekman Layers: Rotating, Stratified Flow Near a Sloping Boundary. *Ann. Rev. Fluid Mech.* **25**, 291–323. [5.2]
- Garrett, C., R. Outbridge and K. Thompson, 1993b: Interannual variability in Mediterranean heat and buoyancy fluxes. *J. Climate* **6**, 900–910. [5.7]
- Garrett, C., K. Speer and E. Tragou, 1995: The relationship between water mass transformation and the surface buoyancy flux, with application to Phillips’ Red Sea model. *J. Phys. Oceanogr.* **25**, 1696–1705. [5.1, 5.3]
- Garrett, J. F., 1980: The availability of the FGGE drifting buoy system data set. *Deep-Sea Res.* **27**, 1083–1086. [4.1]
- Garternicht, U. and F. Schott, 1997: Heat fluxes of the Indian Ocean from a global eddy-resolving model. *J. Geophys. Res.* **102**, 21147–21159. [4.3]
- Garzoli, S. L., A. L. Gordon, V. Kamenkovich, D. Pillsbury and C. Duncombe-Rae, 1996: Variability and sources of the southeastern Atlantic circulation. *J. Mar. Res.* **54**, 1039–1071. [1.2, 4.7]

- Garzoli, S. L., G. J. Goni, A. J. Mariano and D. B. Olson, 1997: Monitoring the upper south-eastern Atlantic transports using altimeter data. *J. Mar. Res.* 55, 453–481. [3.3]
- Garzoli, S., P. Richardson, C. Duncombe Rae, D. Fratantoni, G. Goñi and A. Roubicek, 1999: Three Agulhas rings observed during the Benguela Current Experiment. *J. Geophys. Res.* 104, 20971–20985. [4.7]
- Gascard, J.-C., 1978: Mediterranean deep water formation, baroclinic eddies and ocean eddies. *Oceanol. Acta* 1, 313–315. [5.7]
- Gaspar, P. and R. M. Ponte, 1997: Relation between sea level and barometric pressure determined from altimeter data and model simulations. *J. Geophys. Res.* 102, 961–971. [3.3]
- Gaspar, P., Y. Gregoris and J.-M. Lefevre, 1990: A simple eddy kinetic energy model for simulations of the oceanic vertical mixing: tests at station Papa and Long-Term Upper Ocean Study site. *J. Geophys. Res.* 95, 16179–16193. [7.2]
- Gautier, C., G. Diak and S. Masse, 1980: A simple physical model to estimate incident solar radiation at the surface from GOES satellite data. *J. Appl. Meteor.* 19, 1821–1844. [3.4]
- Gent, P.R. and J.C. McWilliams, 1990: Isopycnal mixing in ocean circulation models. *J. Phys. Oceanogr.* 20, 150–155. [2.2, 2.3, 3.2, 4.6, 5.2, 7.1, 7.2]
- Gent, P.R., J. Willebrand, T.J. McDougall and J.C. McWilliams, 1995: Parameterizing eddy-induced transport in ocean circulation models. *J. Phys. Oceanogr.* 25, 463–474. [2.2, 5.2, 7.2]
- Gent, P.R., F.O. Bryan, G. Danabasoglu *et al.*, 1998: The NCAR Climate System Model global ocean component. *J. Climate* 11, 1278–1306. [2.3]
- Gent, P.R., W.G. Large and F.O. Bryan, 2000: What sets the mean transport through Drake Passage? *J. Geophys. Res.* (in press). [2.3, 4.6, 4.3]
- Gerdes, R. and C. Köberle, 1995: On the influence of DSOW in a numerical model of the North Atlantic general circulation. *J. Phys. Oceanogr.* 25, 2624–2642. [2.2]
- Gerdes, R., C. Köberle, A. Beckmann, P. Herrmann and J. Willebrand, 1999: Mechanisms for spreading of Mediterranean water in coarse-resolution numerical models. *J. Phys. Oceanogr.* 29, 1682–1700. [5.7]
- Gershunov, A. and T.P. Barnett, 1998: Interdecadal modulation of ENSO teleconnections. *Bull. Amer. Meteor. Soc.* 79, 2715–2725. [7.3]
- Gibson, C. H., 1982: Alternative interpretations for microstructure patches in the thermocline. *J. Phys. Oceanogr.* 12, 374–383. [5.2]
- Giering, R. and T. Kaminski, 1998: Recipes for adjoint code construction. *Association for Computing Machinery Transactions on Mathematical Software* 24, 437–474. [7.1]
- Gilbert, D., 1993: A search for evidence of critical internal wave reflection on the continental rise and slope off Nova Scotia. *Atmos. Ocean* 32, 99–122. [5.2]
- Gilbert, D. and C. Garrett, 1989: Implications for ocean mixing of internal wave scattering off irregular topography. *J. Phys. Oceanogr.* 19, 1716–1729. [5.2]
- Gill, A.E., 1968: A linear model of the Antarctic Circumpolar Current. *J. Fluid Mech.* 32, 465–488. [4.6]
- Gill, A.E., 1982: *Atmosphere–Ocean Dynamics*. Academic Press, NY, 662 pp. [1.2, 3.3, 4.2, 4.6]
- Gill, A.E. and P.P. Niiler, 1973: The theory of the seasonal variability in the ocean. *Deep-Sea Res.* 20, 141–177. [2.2, 3.3]
- Gille, S. T., 1994: Mean sea-surface height of the Antarctic Circumpolar Current from GEOSAT data: Method and application. *J. Geophys. Res.* 99, 18255–18273. [3.3 4.6]
- Gille, S. T., 1997: The Southern Ocean momentum balance: evidence for topographic effects from numerical model output and altimeter data. *J. Phys. Oceanogr.* 27, 2219–2232. [4.6]
- Gille, S. T. and K.A. Kelly, 1996: Scales of spatial and temporal variability in the Southern Ocean. *J. Geophys. Res.* 101, 8759–8773. [3.3]
- Gilson, J., D. Roemmich, B. Cornuelle and L.-L. Fu, 1998: Relationship of TOPEX/POSEIDON altimetric height to steric height and circulation in the North Pacific. *J. Geophys. Res.* 103, 27947–27965. [3.3, 7.4]
- Gleckler, P.J. and B.C. Weare, 1997: Uncertainties in global ocean surface heat flux climatologies derived from ship observations. *J. Climate* 10, 2764–2781. [6.1]
- Gnanadesikan, A., 1999: A simple predictive model for the structure of the oceanic pycnocline. *Science* 283, 2077–2079. [5.2]
- Gnanadesikan, A. and R.W. Hallberg, 2000: On the relationship of the Circumpolar Current to Southern Hemisphere winds in coarse-resolution ocean models. *J. Phys. Oceanogr.* 30, 2013–2034. [4.6]
- GODAE (Global Ocean Data Assimilation Experiment), 2001: *GODAE Strategic Plan*, GODAE International Project Office (to appear). [7.4]
- Godfrey, J.S., 1989: A Sverdrup model of the depth-integrated flow for the world ocean allowing for island circulations. *Geophys. Astrophys. Fluid Dyn.* 45, 89–112. [1.2, 4.2, 4.6, 4.7]

- Godfrey, J.S., 1996: The effect of the Indonesian throughflow on ocean circulation and heat exchange with the atmosphere: A review. *J. Geophys. Res.* 101, 12217–12238. [4.7]
- Godfrey, J.S. and T.J. Golding, 1981: The Sverdrup relation in the Indian Ocean and the effects of Pacific–Indian Ocean throughflow on Indian Ocean circulation and on the East Australian Current. *J. Phys. Oceanogr.* 10, 11771–11779. [4.7]
- Godfrey, J.S. and E.J. Lindstrom, 1989: On the heat budget of the Equatorial West Pacific surface mixed layer. *J. Geophys. Res.* 94, 8007–8017. [4.3]
- Godfrey, J.S., A. Hirst and J. Wilkin, 1993: Why does the Indonesian throughflow appear to originate from the Northern Hemisphere? *J. Phys. Oceanogr.* 23, 1087–1098. [4.3, 4.4]
- Godfrey, J.S., R.A. Houze, Jr., R.H. Johnson *et al.*, 1998: Coupled Ocean–Atmosphere Response Experiment (COARE): An interim report. *J. Geophys. Res.* 103, 14395–14450. [1.2, 4.3]
- Gonella, J., G. Reverdin and M. Fieux, 1983: Dynamical oceanography – hypothesis in favour of the genesis of the equatorial jet in the Indian Ocean by attenuation of the Somalian eddy after the end of the southwest monsoon. *Compte rendu de l'Academie des Sciences Paris* 29, Ser. II, 899–902. [4.3]
- Goodman, J. and J. Marshall, 1999: A model of decadal middle-latitude atmosphere–ocean coupled modes. *J. Climate* 12, 621–641. [4.6]
- Goodman, P.J., 1998: The role of North Atlantic Deep Water Formation in an OGCM's ventilation and thermohaline circulation. *J. Phys. Oceanogr.* 28, 1759–1785. [4.7]
- Gordon, A.L., 1982: Weddell Deep Water variability. *J. Mar. Res.* 40, 199–217. [1.2, 4.6]
- Gordon, A.L., 1985: Indian–Atlantic transfer of Thermocline Water at Agulhas Retroflection. *Science* 227(4690), 1030–1033. [4.7]
- Gordon, A.L., 1986: Inter-ocean exchange of thermocline water. *J. Geophys. Res.* 91, 5037–5046. [4.3, 4.4, 4.7, 5.8, 6.1]
- Gordon, A.L., 1995: When is ‘Appearance’ Reality? Indonesian Throughflow is in fact primarily derived from North Pacific Water Masses. *J. Phys. Oceanogr.* 25, 1560–1567. [4.7]
- Gordon, A.L., 1996a: Comment on the South Atlantic's role in global circulation. In: *The South Atlantic: Present and Past Circulation*, G. Wefer, W.H. Berger, G. Siedler and D.J. Webb (eds), Springer-Verlag, Berlin, pp. 121–124. [4.7]
- Gordon, A.L., 1996b: Communication between oceans. *Nature* 382, 399–400. [4.7]
- Gordon, A.L., 1998: Western Weddell Sea thermohaline stratification. In: *Ocean, Ice and Atmosphere: Interactions at Antarctic Continental Margin*, Vol. 75 of Antarctic Research Series, S.S. Jacobs and R. Weiss (eds), American Geophysical Union, Washington, DC, pp. 215–240. [4.6]
- Gordon, A.L. and R.A. Fine, 1996: Pathways of water between the Pacific and Indian oceans in the Indonesian seas. *Nature* 379, 146–149. [4.7, 5.8]
- Gordon, A.L. and B. Huber, 1990: Southern Ocean winter mixed layer. *J. Geophys. Res.* 95, 11655–11672. [4.7]
- Gordon, A.L. and J. McClean, 1999: Thermohaline stratification of the Indonesian Seas – model and observations, *J. Phys. Oceanogr.* 29, 198–216. [4.7]
- Gordon, A.L. and E.J. Molinelli, 1982: *Southern Ocean Atlas. Thermohaline and Chemical Distributions and the Atlas Data Set*. Columbia University Press, NY, 11 pp. and 233 Plates. [2.1, 4.6]
- Gordon, A.L. and W.B. Owens, 1987: Polar oceans. *Rev. Geophys.* 25, 227–233. [3.3]
- Gordon, A.L. and A.R. Piola, 1983: Atlantic Ocean upper layer salinity budget. *J. Phys. Oceanogr.* 13, 1293–1300. [4.7]
- Gordon, A.L. and R.D. Susanto, 1999: Makassar Strait Transport: Initial estimate based on Arlindo Results. *Mar. Tech. Soc.* 32, 34–45. [4.7, 7.1]
- Gordon, A.L., E. Molinelli and T. Baker, 1978: Large scale relative dynamic topography of the Southern Ocean. *J. Geophys. Res.* 83, 3023–3032. [4.6, 4.7]
- Gordon, A.L., J.R.E. Lutjeharms and M.L. Gründlingh, 1987: Stratification and circulation at the Agulhas Retroflection. *Deep-Sea Res.* 34, 565–599. [4.7, 5.4]
- Gordon, A.L., R.F. Weiss, W.M. Smethie, Jr. and M.J. Warner, 1992: Thermocline and intermediate water communication between the South Atlantic and Indian Oceans. *J. Geophys. Res.* 97, 7223–7240. [4.7, 5.8]
- Gordon, A.L., B. Huber, H. Hellmer and A. Ffield, 1993: Deep and bottom water of the Weddell Sea's western rim. *Science* 262, 95–97. [4.6]
- Gordon, A.L., S. Ma, D.B. Olson *et al.*, 1997: Advection and Diffusion of Indonesian Throughflow within the Indian Ocean South Equatorial Current. *Geophys. Res. Lett.* 24, 2573–2576. [4.7]
- Gordon, A.L., R.D. Susanto, A. Ffield and D. Pillsbury, 1998a: Makassar Strait Transport: Preliminary Arlindo results from MAK-1 and MAK-2. *International WOCE Newsletter*,

- No. 33, 30–32, WOCE International Project Office (unpublished document). [4.7]
- Gordon, C., C. Cooper, C. A. Senior *et al.*, 1998b:** The simulation of SST, sea ice extents and ocean heat transports in a version of the Hadley Centre coupled model without flux adjustments. *Hadley Centre Technical Note No. 1*, Meteorological Office, Bracknell, 50 pp. [6.1]
- Gordon, A.L., R.D. Susanto and A. Ffield, 1999a:** Throughflow within Makassar Strait. *Geophys. Res. Lett.* **26**, 3325–3328. [4.3, 4.7, 6.2, 7.1]
- Gordon, A.L., B. Barnier, K. Speer and L. Stramma, 1999b:** World Ocean Circulation Experiment: South Atlantic results. *J. Geophys. Res.* **104**, 20859–20861. [4.7]
- Gordon, C., C. Cooper, C. A. Senior *et al.* 2000:** The simulation of SST, sea ice extents and ocean heat transports in a version of the Hadley Centre coupled model without flux adjustments. *Climate Dyn.* **16**, 147–168. [2.3, 7.4]
- Gordon, H.B. and S.P. O'Farrell, 1997:** Transient climate change in the CSIRO coupled model with dynamic sea ice. *Mon. Wea. Rev.* **125**, 875–907. [2.3, 6.2, 7.3]
- Gould, W.J., J. Loynes and J. Backhaus, 1985:** *Seasonality in slope current transports N.W. of Shetland*. Int. Council for the Exploration of the Sea, Copenhagen. ICES CM 1985/C:7. [5.6]
- Gouretski, V.V. and K. Jancke, 1995:** *A consistent pre-WOCE hydrographic data set for the South Atlantic: station data and gridded fields*. WOCE International Project Office, WOCE Report No. 127/95, 31 pp+figures. SAC Technical Report No. 1 (unpublished manuscript). [7.1]
- Gouretski, V.V. and K. Jancke, 1996:** *A new hydrographic data set for the South Pacific: synthesis of WOCE and historical data*. WHP Special Analysis Centre, WOCE International Project Office. Technical Report No. 2 (WOCE Report No. 127/95) (unpublished manuscript) 53 pp+figures. [7.1]
- Gouretski, V.V. and K. Jancke, 1998:** Deep water property comparison for the Atlantic WOCE cruises. *International WOCE Newsletter*, No. 32, 7–11, WOCE International Project Office (unpublished document). [3.1]
- Gouriou, Y. and J. Toole, 1993:** Mean circulation of the upper layers of the western equatorial Pacific Ocean. *J. Geophys. Res.* **98**, 22495–22520. [4.3]
- Gouriou, Y., B. Bourlès, H. Mercier and R. Chuchla, 1999:** Deep jets in the equatorial Atlantic Ocean. *J. Geophys. Res.* **104**, 21217–21226. [4.3, 4.5]
- Goyet, C., R. Healy, S.J. McCue and D.M. Glover, 1997:** Interpolation of TCO_2 data on a $1^\circ \times 1^\circ$ grid throughout the water column below 500 m depth in the Atlantic Ocean. *Deep-Sea Res.* **44**, 1945–1955. [6.3]
- Goyet, C., C. Coatanoan, G. Eischeid *et al.*, 1999:** Spatial variation of total CO_2 and total alkalinity in the northern Indian Ocean: a novel approach for the quantification of anthropogenic CO_2 in seawater. *J. Mar. Res.* **57**, 135–163. [6.3]
- Goyet, C., R.J. Healy and J.P. Ryan, 2000:** *Global distribution of total inorganic carbon and total alkalinity below the deepest winter mixed layer depths*. ORNL/CDIAC-127, NDP-076. Carbon Dioxide Information Analysis Center, Oak Ridge National Laboratory, US Department of Energy, Oak Ridge, TN, 35 pp. [6.3]
- Graf, J., C. Sasaki, C. Winn *et al.*, 1998:** NASA Scatterometer Experiment. *Asta Astronautica* **43**, 397–407. [3.4]
- Graham, N.E., T.P. Barnett, R. Wilde, M. Ponater and S. Schubert, 1994:** On the roles of tropical and midlatitude SSTs in forcing interannual to interdecadal variability in the winter Northern Hemisphere circulation. *J. Climate* **7**, 1416–1441. [7.3]
- Greatbatch, R.J. and A. Goulding, 1989:** Seasonal variations in a linear barotropic model of the North Atlantic driven by the Hellerman and Rosenstein wind stress field. *J. Phys. Oceanogr.* **19**, 572–595. [2.2]
- Green, J.S.A., 1970:** Transfer properties of the large-scale eddies and the general circulation of the atmosphere. *Quart. J. Roy. Meteor. Soc.* **96**, 157–185. [4.6]
- Greenslade, D.J.M., D.B. Chelton and M.G. Schlax, 1997:** The midlatitude resolution capability of sea level fields constructed from single and multiple satellite altimeter datasets. *J. Atmos. Oceanic Technol.* **14**, 849–870. [3.3]
- Gregg, M.C., 1987:** Diapycnal mixing in the thermocline: A review. *J. Geophys. Res.* **92**, 5249–5286. [5.2]
- Gregg, M.C., 1989:** Scaling turbulent dissipation in the thermocline. *J. Geophys. Res.* **94**, 9686–9698. [4.2, 5.2]
- Gregg, M.C., 1998:** Estimation and geography of diapycnal mixing in the stratified ocean. Physical processes in lakes and oceans. *Coastal and Estuarine Studies* **54**, 305–338. [5.2]
- Gregg, M.C. and E. Kunze, 1991:** Shear and strain in Santa Monica basin. *J. Geophys. Res.* **96**, 16709–16719. [5.2]
- Gregg, M. and T. Sanford, 1980:** Signatures of mixing from the Bermuda Slope, the Sargasso Sea and the Gulf Stream. *J. Phys. Oceanogr.* **10**, 105–127. [5.2]

- Gregg, M.C., H. Peters, J.C. Wesson, N.S. Oakey and T.J. Shay, 1985: Intensive measurements of turbulence and shear in the equatorial undercurrent. *Nature* 318, 140–144. [5.2]
- Gregg, M.C., D.P. Winkel, T.B. Sanford and H. Peters, 1995: Turbulence produced by internal waves in the oceanic thermocline at mid- and low-latitudes. *Dyn. Atmos. Oceans* 24, 1–14. [4.3, 5.2]
- Gregory J.M., J.A. Church, G.J. Boer *et al.*, 2001: Comparison of results from several AOGCMs for global and regional sea-level change 1900–2100. *Climate Dyn.* (accepted). [1.2]
- Gregory, J.M. and J.F.B. Mitchell, 1997: The climate response to CO₂ of the Hadley Centre coupled AOGCM with and without flux adjustment. *Geophys. Res. Lett.* 24, 1943–1946. [2.3]
- Greve, M., 1994: *Fridtjof Nansen*. Translated by M.E. Davies, H. Aschehoug & Co (W. Nygaard), Oslo, Norway, 56 pp. [7.4]
- Griffies, S.M., A. Gnanadesikan, R.C. Pacanowski, V.D. Larichev, J.K. Dukowicz and R.D. Smith, 1998: Isoneutral diffusion in a z-coordinate ocean model. *J. Phys. Oceanogr.* 28, 805–830. [7.2]
- Griffiths, G., 1994: Using 3DF GPS heading for improving underway ADCP data. *J. Atmos. Oceanic Technol.* 11, 1135–1143. [3.1]
- Grima, N., A. Bentamy, K. Katsaros and Y. Quilfen, 1999: Sensitivity of an oceanic general circulation model forced by satellite wind stress fields. *J. Geophys. Res.* 104, 7967–7989. [3.4]
- Grotendt K., K. Logemann, D. Quadfasel and S. Ronksi, 1998: Is the Arctic Ocean warming? *J. Geophys. Res.* 103, 27679–27687. [7.3]
- Gruber, N., 1998: Anthropogenic CO₂ in the Atlantic Ocean. *Glob. Biogeochem. Cycles* 12, 165–191. [6.3]
- Gruber, N., J.L. Sarmiento and T.F. Stocker, 1996: An improved method for detecting anthropogenic CO₂ in the oceans. *Glob. Biogeochem. Cycles* 10, 809–837. [5.8, 6.3]
- GSP Group, 1990: The Greenland Sea Project – a venture toward improved understanding of the ocean's role in climate. *Eos Trans. Amer. Geophys. Union* 71, 750–751, 754–755. [7.3]
- Gu, D. and S.G.H. Philander, 1997: Interdecadal climate fluctuations that depend on exchanges between the tropics and extratropics. *Science* 275, 805–807. [4.3, 4.4, 5.3, 5.8]
- Guilderson, T. and D. Schrag, 1997: Abrupt shift in subsurface temperatures in the tropical Pacific associated with changes in El Niño. *Science* 281, 240–243. [5.8]
- Guilyardi, E. and G. Madec, 1997: Performance of the OPA/ARPEGE T21 global ocean–atmosphere coupled model. *Climate Dyn.* 13, 149–165. [2.3]
- Gupta, S.K., W. Darnell and A.C. Wilber, 1992: A parameterization for longwave surface radiation from satellite data: Recent improvements. *J. Appl. Meteor.* 31, 1361–1367. [3.4]
- Hacker, P., E. Firing, W.D. Wilson and R. Molinari, 1996: Direct observations of the current structure east of the Bahamas. *Geophys. Res. Lett.* 23, 1127–1130. [3.1]
- Hacker, P., E. Firing, J. Hummon, A.L. Gordon and J.C. Kindle, 1998: Bay of Bengal currents during the northeast monsoon. *Geophys. Res. Lett.* 25, 2769–2772. [4.3]
- Hagemann, S. and L. Dümenil, 1998: A parametrization of the lateral waterflow for the global scale. *Climate Dyn.* 14, 17–31. [2.3]
- Haidvogel, D.B. and A. Beckmann, 1999: *Numerical Ocean Circulation Modeling*. Imperial College Press, London, 320 pp. [7.2]
- Haidvogel, D.B., J.L. Wilkin and R.E. Young, 1991: A semi-spectral primitive equation ocean circulation model using vertical sigma and orthogonal curvilinear horizontal coordinates. *J. Comp. Phys.* 94, 151–185. [2.2]
- Haine, T.W.H., A.J. Watson, M.I. Liddicoat and R.R. Dickson, 1998: The flow of Antarctic Bottom Water to the southwest Indian Ocean estimated using CFCs. *J. Geophys. Res.* 103, 27637–27653. [5.8]
- Hall, M.M. and H.L. Bryden, 1982: Direct estimates and mechanisms of ocean heat transport. *Deep-Sea Res.* 29, 339–359. [1.2, 2.2, 2.3, 6.1, 6.2]
- Hall, M.M., M. McCartney and J.A. Whitehead, 1997: Antarctic Bottom Water flux in the equatorial western Atlantic. *J. Phys. Oceanogr.* 27, 1903–1926. [4.3, 4.5]
- Hallberg, R.W. and P.B. Rhines, 1996: Buoyancy driven circulations in an ocean basin with isopycnals intersecting the sloping boundary. *J. Phys. Oceanogr.* 26, 913–940. [5.5]
- Hallock, Z.R. and W.J. Teague, 1996: Evidence for a North Pacific deep western boundary current. *J. Geophys. Res.* 101, 6617–6624. [4.5]
- Han, W., J.P. McCreary, Jr., D.L.T. Anderson and A.J. Mariano, 1999: Dynamics of the Eastern Surface Jets in the Equatorial Indian Ocean. *J. Phys. Oceanogr.* 29, 2191–2209. [4.3]
- Hanawa, K., 1987: Interannual variations in the wintertime outcrop area of Subtropical Mode Water in the North Pacific. *Atmos. Ocean* 25, 358–374. [5.4]
- Hanawa, K. and I. Hoshino, 1988: Temperature structure and mixed layer in the Kuroshio region over the Izu Ridge. *J. Mar. Res.* 46, 683–700. [5.4]
- Hanawa, K. and T. Suga, 1995: A review on the subtropical mode water of the North Pacific (NPSTMW). In: *Biochemical Processes and Ocean*

- Flux in the Western Pacific*, H. Sakai and Y. Nozaki (eds), Terra Sci. Pub., Tokyo, pp. 613–627. [5.4]
- Hanawa, K.** and H. Yoritaka, 2000: The North Pacific subtropical mode water observed in the long XBT cross sections along the 32.5°N line. *J. Geophys. Res.* (in press). [5.4]
- Hanawa, K.**, N. Iwasaka, T. Watanabe, T. Suga and Y. Toba, 1988a: *The XBT observations. The subtropical mode water in 1987 winter*. Preliminary Report of the Hakuho Maru Cruise KH87-1, Ocean Research Institute, University of Tokyo, pp. 46–54. [5.4]
- Hanawa, K.**, T. Watanabe, N. Iwasaka, T. Suga and Y. Toba, 1988b: Surface thermal condition in the western North Pacific during the ENSO events. *J. Meteor. Soc. Japan* 66, 445–456. [5.4]
- Haney, R. L.**, 1991: On the pressure gradient force over steep topography in sigma coordinate ocean models. *J. Phys. Oceanogr.* 21, 610–619. [7.2]
- Hansen, B.** and S. Østerhus, 2000: North Atlantic–Nordic Seas exchanges. *Prog. Oceanogr.* 45, 109–208. [5.6]
- Hansen, D. V.** and H. F. Bezdek, 1996: On the nature of decadal anomalies in the North Atlantic Sea surface temperature. *J. Geophys. Res.* 101, 8749–8758. [7.1, 7.3]
- Hansen, D. V.** and C. A. Paul, 1984: Genesis and effects of long waves in the equatorial Pacific. *J. Geophys. Res.* 89, 10431–10440. [4.3]
- Hansen, D. V.** and P. M. Poulain, 1996: Quality control and interpolation of WOCE/TOGA drifter data. *J. Atmos. Oceanic Technol.* 13, 900–909. [4.1]
- Harper S.**, 2000: Thermocline ventilation and pathways of tropical–subtropical water mass exchange. *Tellus* 52A, 330–345. [4.4]
- Hartmann, D. L.** and F. Lo, 1998: Wave-driven zonal flow vacillation in the Southern Hemisphere. *J. Atmos. Sci.* 55, 1303–1315. [7.3]
- Harvey, J.**, 1982: θS relationships and water masses in the eastern North Atlantic. *Deep-Sea Res.* 29, 1021–1033. [5.4]
- Harvey, J. G.** and A. Theodorou, 1986: The circulation of Norwegian Sea overflow water in the eastern North Atlantic. *Oceanol. Acta* 9(4), 393–402. [5.6]
- Hasselmann, K.**, 1976: Stochastic climate models: Part 1. Theory. *Tellus* 28A, 473–485. [2.1]
- Hasselmann, K.**, L. Bengtsson, U. Cubasch *et al.*, 1995: Detection of anthropogenic climate change using a fingerprint method. In: *Proceedings of Symposium on Modern Dynamical Meteorology*, P. Ditlevsen (ed.), ECMWF Press, Reading, UK. [2.3]
- Hastenrath, S.** and L. Greischar, 1989: *Climatic Atlas of the Indian Ocean*, Part III: *Upper-Ocean Structure*. University of Wisconsin Press, Madison, WI, 247 charts. [4.3]
- Hastenrath, S.** and L. Greischar, 1991: The monsoonal regimes of the tropical Indian Ocean. Observed surface flow fields and their geostrophic and wind-driven components. *J. Geophys. Res.* 96, 12619–12633. [4.3]
- Hasumi, H.** and N. Sugino, 1999a: Effects of locally enhanced vertical diffusivity over rough bathymetry on the world ocean circulation. *J. Geophys. Res.* 104, 23367–23374. [2.2, 2.3, 4.2]
- Hasumi, H.** and N. Sugino, 1999b: Atlantic deep circulation controlled by heating in the Southern Ocean. *Geophys. Res. Lett.* 26, 1873–1876. [4.2]
- Hasunuma, K.** and K. Yoshida, 1978: Splitting of the subtropical gyre in the western North Pacific. *J. Oceanogr. Soc. Japan* 34, 160–172. [7.3]
- Haug, G.**, D. Sigman, R. Tiedemann, T. Pedersen and M. Sarnthein, 1999: Onset of permanent stratification in the subarctic Pacific Ocean. *Nature* 401, 779–782. [4.7]
- Hautala, S. L.** and S. C. Riser, 1993: A nonconservative β -spiral determination of the deep circulation in the eastern South Pacific. *J. Phys. Oceanogr.* 23, 1975–2000. [4.3]
- Hautala, S. L.** and D. H. Roemmich, 1998: Subtropical mode water in the Northeast Pacific Basin. *J. Geophys. Res.* 103, 13055–13066. [5.4]
- Hautala, S. L.**, D. H. Roemmich and W. J. Schmitz, Jr., 1994: Is the North Pacific in Sverdrup balance along 24°N? *J. Geophys. Res.* 99, 16041–16052. [2.1]
- Hautala, S.**, J. Reid and N. Bray, 1996: The distribution and mixing of Pacific water masses in the Indonesian Seas. *J. Geophys. Res.* 101, 12375–12389. [4.7]
- Hayden, B. P.**, 1981: Secular variation in the Atlantic coast extratropical cyclones. *Mon. Wea. Rev.* 109, 159–167. [7.3]
- Haywood, J. M.**, R. J. Stouffer, R. T. Wetherald, S. Manabe and V. Ramaswamy, 1997: Transient response of a coupled model to estimated changes in greenhouse gas and sulfate concentrations. *Geophys. Res. Lett.* 24, 1335–1338. [2.3]
- Hazeleger, W.** and S. S. Drijfhout, 1998: Mode water variability of the subtropical gyre: Response to anomalous forcing. *J. Phys. Oceanogr.* 28, 266–288. [5.3, 5.4]
- Hazeleger, W.** and S. S. Drijfhout, 1999: Stochastically forced mode water variability. *J. Phys. Oceanogr.* 29, 1772–1786. [5.4]
- Hazeleger, W.** and S. S. Drijfhout, 2000: Eddy subduction in a model of the subtropical gyre. *J. Phys. Oceanogr.* 30, 677–695. [5.3]

- Hegerl, G.C., K. Hasselmann, U. Cubasch *et al.*, 1997: Multi-fingerprint detection and attribution analysis of greenhouse gas, greenhouse gas-plus-aerosol and solar forced climate change. *Climate Dyn.* 13, 613–634. [2.3]
- Helffrich, K., 1994: Thermals with background rotation and stratification. *J. Fluid Mech.* 259, 265–280. [5.5]
- Hellerman, S. and M. Rosenstein, 1983: Normal monthly wind stress over the World Ocean with error estimates. *J. Phys. Oceanogr.* 13, 1093–1104. [1.2, 2.2, 4.2, 4.3, 4.7, 6.1, 6.2]
- Hellmer, H.H., S.S. Jacobs and A. Jenkins, 1998: Oceanic erosion of a floating Antarctic glacier in the Amundsen Sea. In: *Ocean, Ice and Atmosphere: Interactions at Antarctic Continental Margin*, Vol. 75 of Antarctic Research Series, S.S. Jacobs and R. Weiss (eds), American Geophysical Union, Washington, DC, pp. 83–100. [4.6]
- Hendry, R.M., 1989: *Canadian Technical Report of Hydrography and Ocean Sciences* 118, 112 pp. [7.3]
- Heney, F.S., 1991: Scaling of internal wave model predictions for the dynamics of oceanic internal waves. In: *'Aha Huliko' – Hawaiian Winter Workshop Proceedings*, P. Muller and D. Henderson (eds), Honolulu, HI, pp. 233–236. [5.2]
- Heney, F.S. and N. Pomphrey, 1983: Eikonal description of internal wave interactions: A non-diffusive picture of 'induced diffusion.' *Dyn. Atmos. Oceans* 7, 189–219. [5.2]
- Heney, F.S., J. Wright and S.M. Flatte, 1986: Energy and action flow through the internal wave field: an eikonal approach. *J. Geophys. Res.* 91, 8487–8495. [5.2]
- Hewitt, C.D. and J.F.B. Mitchell, 1998: A fully coupled GCM simulation of the climate of the mid-Holocene. *Geophys. Res. Lett.* 25, 361–364. [2.3]
- Heywood, K.J., M.D. Sparrow, J. Brown and R.R. Dickson, 1999: Frontal structure and Antarctic bottom water flow through the Princess Elizabeth Trough, Antarctica. *Deep-Sea Res.* 46, 1181–1200. [3.1]
- Hickey, B.M., 1998: Coastal oceanography of western North America from the tip of Baja California to Vancouver Island. In: *The Sea*, A.R. Robinson and K.H. Brink (eds), John Wiley, NY, Vol. II, pp. 345–393. [1.2]
- Hirst, A.C., 1998: The Southern Ocean response to global warming in the CSIRO coupled ocean-atmosphere model. *Environ. Modeling and Software (Special Issue on Global Change)* 14, 227–241. [1.1, 1.2]
- Hirst, A.C. and J.S. Godfrey, 1993: The Role of Indonesian Throughflow in a Global Ocean GCM. *J. Phys. Oceanogr.* 23, 1057–1086. [4.7]
- Hirst, A.C. and T.J. McDougall, 1996: Deep water properties and surface buoyancy flux as simulated by a z -coordinate model including eddy-induced advection. *J. Phys. Oceanogr.* 26, 1320–1343. [5.2]
- Hirst, A.C. and T.J. McDougall, 1998: Meridional overturning and dianeutral transport in a z -coordinate ocean model including eddy-induced advection. *J. Phys. Oceanogr.* 28, 1205–1223. [4.6, 5.2]
- Hirst, A.C., H.B. Gordon and S.P. O'Farrell, 1996: Global warming in a coupled climate model including oceanic eddy-induced advection. *Geophys. Res. Lett.* 23, 3361–3364. [5.2]
- Hofmann E.E. and C.M. Lascara, 1998: Overview of interdisciplinary modeling for marine ecosystems. In: *The Sea*, K.H. Brink and A.R. Robinson (eds), John Wiley, NY, Vol. 10, pp. 507–540. [7.2]
- Hogg, N.G., 1973: On the stratified Taylor column. *J. Fluid Mech.* 58, 517–537. [4.2]
- Hogg, N.G., 1988: Stochastic wave radiation by the Gulf Stream. *J. Phys. Oceanogr.* 18, 1687–1701. [3.3]
- Hogg, N.G. and W.B. Owens, 1999: Direct measurement of the deep circulation within the Brazil Basin. *Deep-Sea Res. II* 46, 335–353. [2.1, 3.2, 4.5]
- Hogg, N.G. and W. Zenk, 1997: Long-period changes in the bottom water flowing through Vema Channel. *J. Geophys. Res.* 102, 15639–15646. [1.2, 4.5, 4.6]
- Hogg, N.G., P. Biscaye, W. Gardner and W.J. Schmitz Jr., 1982: On the transport and modification of Antarctic Bottom Water in the Vema Channel. *J. Mar. Res.* 40(suppl.), 231–263. [4.5, 5.2]
- Hogg, N.G., R.S. Pickart, R.M. Hendry and W.M. Smethie Jr., 1986: The northern recirculation gyre of the Gulf Stream. *Deep-Sea Res.* 33, 1139–1165. [5.8]
- Hogg, N.G., W.B. Owens, G. Siedler and W. Zenk, 1996: Circulation in the Deep Brazil Basin. In: *The South Atlantic: Present and Past Circulation*, G. Wefer, W.H. Berger, G. Siedler and D.J. Webb (eds), Springer-Verlag, Berlin, pp. 249–260. [3.2]
- Hogg, N.G., G. Siedler and W. Zenk, 1999: Circulation and variability at the southern boundary of the Brazil Basin. *J. Phys. Oceanogr.* 29, 145–157. [4.5]
- Hohmann, R., P. Schlosser, A. Ludin and R. Weppernig, 2001: Excess helium and neon in

- the Southeast Pacific: tracers for glacial meltwater. *J. Geophys. Res.* (submitted). [5.8]
- Holfort, J.** and G. Siedler, 1997: The heat and mass transport in the South Atlantic. *International WOCE Newsletter*, No. 28, 3–5, WOCE International Project Office (unpublished document). [6.2]
- Holfort, J.** and G. Siedler, 2001: The meridional oceanic transports of heat and nutrients in the South Atlantic. *J. Phys. Oceanogr.* 31, 5–29. [4.7, 6.1, 7.1]
- Holfort, J.**, K. M. Johnson, B. Schneider, G. Siedler and D. W. R. Wallace, 1998: Meridional transport of dissolved inorganic carbon in the South Atlantic Ocean. *Glob. Biogeochem. Cycles* 12, 479–499. [6.3]
- Holfort, J.**, M. Vanicek and G. Siedler, 2000: What causes long-term temporal changes in the South Atlantic? *Geophys. Res. Lett.* 27(B), 1187–1190. [7.3]
- Holland, M. M.**, J. A. Curry and J. L. Schramm, 1997: Modelling the thermodynamics of a sea ice thickness distribution. 2. Sea ice/ocean interactions. *J. Geophys. Res.* 102, 23093–23107. [1.2]
- Holland, W. R.**, 1978: The role of mesoscale eddies in the general circulation of the ocean – numerical experiments using a wind-driven quasigeostrophic model. *J. Phys. Oceanogr.* 8, 363–392. [2.1, 7.2]
- Holland, W. R.** and L. B. Lin, 1975: On the generation of mesoscale eddies and their contribution to the oceanic general circulation. Parts I and II. *J. Phys. Oceanogr.* 5, 642–669. [2.2]
- Holliday, N. P.** and P. C. Reid, 2001: Is there a connection between high transport of water through the Rockall Trough and ecological changes in the North Sea? *ICES J. Mar. Sci.* (In press). [1.2]
- Holloway, G.**, 1992: Representing topographic stress for large-scale ocean models. *J. Phys. Oceanogr.* 22, 1033–1046. [4.2]
- Holloway, G.**, 1997: Eddy transport of thickness and momentum in layer and level models. *J. Phys. Oceanogr.* 27, 1153–1157. [5.2]
- Houghton, R. W.**, 1996: Subsurface quasi-decadal fluctuations in the North Atlantic. *J. Climate* 9, 1363–1373. [7.3]
- Howden, S. D.**, E. Gottlieb, C. Koblinsky, T. Rossby and L. Wang, 2000: Gulf Stream observations from TOPEX/POSEIDON and in comparison with in-situ measurements near 71°W. *J. Geophys. Res.* (in press). [3.3]
- Hsiung, J.**, R. E. Newell and T. Houghtby, 1989: The annual cycle of oceanic heat storage and ocean meridional heat transport. *Quart. J. Roy. Meteor. Soc.* 115, 1–28. [2.2, 4.3]
- Hsu, S. A.** and B. W. Blanchard, 1989: The relationship between total precipitable water and surface-level humidity over the sea surface: A further evaluation. *J. Geophys. Res.* 94, 14539–14545. [3.4]
- Huang, B.**, 1996: *Subtropical-tropical thermocline water exchanges in the Pacific Ocean*. M. S. Thesis, University of Wisconsin-Madison, 207pp. [4.4]
- Huang, B.** and Z. Liu, 1999: Pacific tropical–subtropical thermocline water exchanges in the NCEP ocean model. *J. Geophys. Res.* 104, 11065–11076. [4.4]
- Huang, R. X.**, 1990: On the three-dimensional structure of the wind-driven circulation in the North Atlantic. *Dyn. Atmos. Oceans* 15, 117–159. [5.3]
- Huang, R. X.**, 1991: The three-dimensional structure of wind-driven gyres: Ventilation and subduction. *US National Report to International Union of Geodesy and Geophysics 1987–1990, Supplement to Reviews of Geophys.* 590–609. [5.3]
- Huang, R. X.**, 1993: Real freshwater flux as a natural boundary condition for the salinity balance and thermohaline circulation forced by evaporation and precipitation. *J. Phys. Oceanogr.* 23, 2428–2446. [2.3, 7.2]
- Huang, R. X.**, 1999: Mixing and energetics of the oceanic thermohaline circulation. *J. Phys. Oceanogr.* 29, 727–746. [5.2]
- Huang, R. X.**, 2000a: An analytic solution of the ideal-fluid thermocline. *J. Phys. Oceanogr.* (submitted). [5.3]
- Huang, R. X.**, 2000b: Interior communication and the structure of the thermocline in Subtropical and Tropical Oceans. *J. Phys. Oceanogr.* (submitted). [5.8]
- Huang, R. X.** and R. L. Chou, 1994: Parameter sensitivity study of the saline circulation. *Climate Dyn.* 9, 391–409. [5.2]
- Huang, R. X.** and J. Pedlosky, 1999: Climate variability inferred from a layered model of the ventilated thermocline. *J. Phys. Oceanogr.* 29, 779–790. [4.4, 5.3, 7.3]
- Huang, R. X.** and B. Qiu, 1994: Three-dimensional structure of the wind-driven circulation in the subtropical North Pacific. *J. Phys. Oceanogr.* 24, 1608–1622. [5.3]
- Huang, R. X.** and S. Russell, 1995: Ventilation of the subtropical North Pacific. *J. Phys. Oceanogr.* 24, 2589–2605. [5.3]
- Huang, R. X.** and R. W. Schmitt, 1993: The Goldsborough-Stommel circulation of the world oceans. *J. Phys. Oceanogr.* 23, 1277–1284. [6.2]
- Hudson, J. G.**, Y. H. Xie and S. S. Yum, 1998: Vertical distributions of cloud condensation nuclei spectra over the summertime Southern Ocean. *J. Geophys. Res.* 103, 16609–16624. [1.2]

- Hughes, C. W. and E. Ash, 2000: Eddy forcing of the mean flow in the Southern Ocean. *J. Geophys. Res.* (In press). [4.6]
- Hughes, C. W., M. S. Jones and S. Carnochan, 1998: Use of transient features to identify eastward currents in the Southern Ocean. *J. Geophys. Res.* 103, 2929–2944. [4.2, 4.6]
- Hughes, C. W., M. Meredith and K. Heywood, 1999: Wind driven transport fluctuations through Drake Passage: a southern mode. *J. Phys. Oceanogr.* 29, 1971–1992. [4.6]
- Huppert, H. E., 1975: Some remarks on the initiation of inertial Taylor columns. *J. Fluid Mech.* 67, 397–412. [4.2]
- Huppert, H. E. and K. Bryan, 1976: Topographically generated eddies. *Deep-Sea Res.* 23, 655–679. [4.2]
- Hurrell, J. W., 1995a: Decadal trends in the North Atlantic Oscillation: Regional temperatures and precipitation. *Science* 269, 676–679. [7.1, 7.3]
- Hurrell, J. W., 1995b: An evaluation of the transient eddy forced vorticity balance during northern winter. *J. Atmos. Sci.* 52, 2286–2301. [7.3]
- Hurrell, J. W., 1996: Influence of variations in extra-tropical wintertime teleconnections on Northern Hemisphere temperature. *Geophys. Res. Lett.* 23, 665–668. [7.3]
- Hurrell, J. W. and H. van Loon, 1994: A modulation of the atmospheric annual cycle in the Southern Hemisphere. *Tellus* 46A, 325–338. [7.3]
- Hurrell, J. W. and H. van Loon, 1997: Decadal variations in climate associated with the North Atlantic oscillation. *Climate Dyn.* 36, 301–326. [7.3]
- Huyer, A., R. L. Smith, P. J. Stabeno, J. A. Church and N. J. White, 1988: Current off southeastern Australia: Results from the Australian Coastal Experiment. *Aust. J. Mar. Freshwater Res.* 39, 245–288. [1.2]
- Hwang, C., 1996: A study of the Kuroshio's seasonal variabilities using an altimetric-gravimetric geoid and TOPEX/POSEIDON altimeter data. *J. Geophys. Res.* 101, 6313–6335. [3.3]
- Ichikawa, H., S. Imawaki, H. Uchida, S. Umatani and M. Fukasawa, 1999: Mean values of volume and temperature transports of the Kuroshio south of Japan in 1993–1995. Proceedings of the Fourth International Scientific Symposium: *Role of Ocean Sciences for Sustainable Development* (IOC/WESTPAC), 2–7 February 1998, Okinawa, Ocean Research Institute, University of Tokyo, pp. 22–31. [6.1]
- Ilahude, A. G. and A. L. Gordon, 1996: Thermocline stratification within the Indonesian Seas. *J. Geophys. Res.* 101, 12401–12409. [4.7]
- Imawaki, S. and H. Uchida, 1995: Detecting sea level profiles across the Kuroshio by a satellite altimeter. *Annals of the Disaster Prevention Res. Institute, Kyoto University*, No. 38B-2, pp. 655–662 (in Japanese with English abstract). [6.1]
- Imawaki, S., H. Uchida, H. Ichikawa, M. Fukasawa, S. Umatani and ASUKA Group, 1997: Time series of the Kuroshio transport derived from field observations and altimetry data. *International WOCE Newsletter*, No. 25, 15–18, WOCE International Project Office (unpublished document). [1.2, 2.2, 3.3, 6.1, 7.1, 7.3]
- Imawaki, S., H. Uchida, H. Ichikawa, M. Fukasawa, S. Umatani and ASUKA Group, 2001: Satellite altimeter monitoring the Kuroshio transport south of Japan. *Geophys. Res. Lett.* (submitted). [6.1, 7.1, 7.3]
- Indermuehle, A., T. F. Stocker, F. Joss, et al., 1999: Holocene carbon-cycle dynamics based on CO₂ trapped in ice at Taylor Dome, Antarctica. *Nature* 398, 121–126. [6.3]
- Intergovernmental Oceanographic Commission, 1984: Ocean Observing System Development Panel. *IOC Technical Series* No. 27, 31 pp. [1.3]
- Intergovernmental Oceanographic Commission, 1997: *GLOSS Implementation Plan*. IOC/GLOSS-V10, Intergovernmental Oceanographic Commission, UNESCO, Paris, 91 pp. and annexes. [7.4]
- Intergovernmental Oceanographic Commission/World Meteorological Organization, 1999: *Global Physical Observations for GOOS/GCOS: An Action Plan for Existing Bodies and Mechanisms*. GOOS Report No. 66; GCOS Report No. 51. 50 pp. and annexes. [7.4]
- International TOGA Project Office, 1994: *TOGA Scientific Steering Group, Report of the 13th Session*. International TOGA Project Office, Geneva, No. 11, 13 pp. + 3 Appendices. [7.4]
- Inui, T. and Z. Liu, 2001: A possible explanation for the decadal variability pattern of cold temperature anomalies. *J. Phys. Oceanogr.* (submitted). [5.3]
- Inui, T., K. Takeuchi and K. Hanawa, 1999: A numerical investigation of the subduction process in response to an abrupt intensification in the west-erlies. *J. Phys. Oceanogr.* 29, 1993–2015. [5.3]
- Iorga, M. C. and M. S. Lozier, 1999a: Signatures of the Mediterranean outflow from a North Atlantic climatology 1. Salinity and density fields. *J. Geophys. Res.* 104, 25985–26009. [5.7]
- Iorga, M. C. and M. S. Lozier, 1999b: Signatures of the Mediterranean outflow from a North Atlantic climatology 2. Diagnostic velocity fields. *J. Geophys. Res.* 104, 26011–26029. [5.7]
- IPCC, 1990: *Climate Change. The IPCC Scientific Assessment*, J. T. Houghton, G. J. Jenkins and J. J. Ephraums (eds), Cambridge University Press, 365 pp. [7.4]

- IPCC, 1995: *Climate Change 1995 – The Science of Climate Change*, J.T. Houghton *et al.*, (eds), Cambridge University Press, 572 pp. [2.3]
- IPCC, 2001: Climate Change 2001: The Scientific Basis. Contribution of Working Group I to the *Third Assessment Report of the Intergovernmental Panel on Climate Change* [Houghton, J.T., Y. Ding, D.J. Griggs, M. Noguer, P. van der Linden, X. Dai and K. Maskell (eds.)]. Cambridge University Press, in press. [1.2, 2.3.]
- Iselin, C.O.D., 1939: The influence of vertical and lateral turbulence on the characteristics of the waters at mid-depths. *Trans. Amer. Geophys. Union* 20, 414–417. [5.3, 5.4, 7.3]
- Isemer, H.J. and L. Hasse, 1987: *The Bunker Climate Atlas of the North Atlantic Ocean*, Vol. 2: *Air–Sea Interactions*. Springer-Verlag, Berlin, 218 pp. [5.1]
- Isemer, H.-J., J. Willebrand and L. Hasse, 1989: Fine adjustment of large scale air–sea energy flux parameterisations by direct estimates of ocean heat transport. *J. Climate* 2, 1173–1184. [6.2]
- Ishida, A., Y. Kashino, H. Mitsudera and T. Kadokura, 1998: Mean circulation and variability in the global high-resolution GCM – the Equatorial Currents System in the Pacific Ocean. *Proc. of the Inter-national Symposium Triangle '98*, 29 Sept.–2 Oct., 1998, Kyoto, Japan, pp. 178–189. [4.3]
- Ishii, M., S. Hasegawa, I. Sugimoto, I. Ishikawa, I. Yoshikawa and M. Kimoto, 1998: An El Niño prediction experiment with a JMA ocean–atmosphere coupled model, Kookai. *Proceedings of the WMO International Workshop on Dynamical Extended Range Forecasting, Toulouse 1997*. World Meteorological Organisation, WMO/TD No. 881, pp. 105–108. [2.3]
- Isobe, A., 1994: Tsushima Warm Current in the Tsushima/Korea Straits. *Kaiyo Monthly* 26, 802–809 (in Japanese). [6.1]
- Ivchenko, V., A. Krupitsky, V. Kamenkovich and N. Wells, 1999: Modeling the Antarctic Circumpolar Current: a comparison of FRAM and equivalent barotropic model results. *J. Mar. Res.* 57, 29–45. [4.6]
- Jacobs, G.A. and J.L. Mitchell, 1996: Ocean circulation variations associated with the Antarctic Circumpolar Wave. *Geophys. Res. Lett.* 23, 2947–2950. [2.3, 3.3]
- Jacobs, G.A., G.H. Born, M.E. Parke and P.C. Allen, 1992: The global structure of the annual and semiannual sea-surface height variability from Geosat altimeter data. *J. Geophys. Res.* 97, 17813–17828. [3.3]
- Jacobs, G.A., W.J. Emery and G.H. Born, 1993: Rossby waves in the Pacific Ocean extracted from Geosat altimeter data. *J. Phys. Oceanogr.* 23, 1155–1175. [3.3]
- Jacobs, G.A., H.E. Hurlburt, J.C. Kindle *et al.*, 1994: Decade-scale trans-Pacific propagation and warming effects of an El Niño anomaly. *Nature* 370, 360–363. [3.3, 7.3]
- Jacobs, G.A., W.J. Teague, J.L. Mitchell and H.E. Hurlburt, 1996: An examination of the North Pacific Ocean in the spectral domain using Geosat altimeter data and a numerical ocean model. *J. Geophys. Res.* 101, 1025–1044. [3.3]
- Jacobs, S.S., 1991: On the nature and significance of the Antarctic Slope Front. *Mar. Chem.*, 35, 9–24. [4.5]
- Jacobs, S.S. and D.T. Georgi, 1977: Observations on the southwest Indian/Antarctic Ocean. In: *A Voyage of Discovery: George Deacon 70th Anniversary Volume*, M. Angel (ed.), Pergamon Press, Oxford, pp. 43–84. [4.6]
- Jacobs, S.S., A.F. Amos and P.M. Bruchhausen, 1970: Ross Sea oceanography and Antarctic Bottom Water formation. *Deep-Sea Res.* 17, 935–962. [5.8]
- Jacobs, S.S., A.L. Gordon and A.F. Amos, 1979: Effects of glacial ice melting on Antarctic Surface Water. *Nature* 277, 469–471. [5.8]
- Jacobs, S.S., R.G. Fairbanks and Y. Horibe, 1985: Origin and evolution of water masses near the Antarctic Continental Margin: evidence from $H_2^{18}O/H_2^{16}O$ ratios in seawater. In: *Oceanology of the Antarctic Continental Shelf*, Antarctic Research Series 43, American Geophysical Union, Washington, DC, pp. 59–85. [5.8]
- Jaeger, L., 1983: Monthly and areal patterns of mean global precipitation. In: *Variations in the Global Water Budget*, A. Street-Perrot *et al.* (eds), D. Reidel Publ. Co., pp. 129–140. [6.2]
- Jeffreys, H., 1925: On fluid motions produced by differences of temperature and humidity. *Quart. J. Roy. Meteor. Soc.* 51, 347–356. [5.2]
- Jenkins, W.J., 1982: On the climate of a subtropical gyre: decade timescale variations in water mass renewal in the Sargasso Sea. *J. Mar. Res.* 40 (suppl.), 265–290. [5.4, 7.3]
- Jenkins, W.J., 1987: 3H and 3He in the beta triangle: Observations of gyre ventilation and oxygen utilization rates. *J. Phys. Oceanogr.* 17, 763–783. [5.3, 5.8]
- Jenkins, W.J., 1996: Tritium and 3He in the WOCE Pacific Program. *International WOCE Newsletter*, No. 23, 6–8, WOCE International Project Office (unpublished document). [5.8]

- Jenkins, W.J., 1998: Studying subtropical thermocline ventilation and circulation using tritium and ^3He . *J. Geophys. Res.* 103, 15817–15831. [5.3, 5.8]
- Jenkins, W.J. and P.B. Rhines, 1980: Tritium in the deep North Atlantic Ocean. *Nature* 286, 877–880. [5.5]
- Jenkins, W.J., D.E. Lott., M.W. Davis., S.P. Birdwhistell and M.O. Matthewson, 1991: Measuring helium isotopes and tritium in seawater samples. In: *WOCE Hydrographic Operations and Methods*, *WOCE Operations Manual*, Vol. 3, Section 3.1, Part 3.1.3, WHP Office Report WHPO 91-1, WOCE Report No. 68/91 (unpublished document), 21 pp. [5.8]
- Ji, M., A. Leetmaa and J. Derbe, 1995: An ocean analysis system for seasonal to interannual climate studies. *Mon. Wea. Rev.* 123, 460–481. [4.4]
- Ji, M., R.W. Reynolds and D.W. Behringer, 2000: Use of TOPEX/POSEIDON sea level data for ocean analyses and ENSO prediction: some preliminary results. *J. Climate* 13, 216–231. [3.3, 7.4]
- Jia, Y., 2000: Formation of an Azores Current due to Mediterranean overflow in a modelling study of the North Atlantic. *J. Phys. Oceanogr.* 103, 2342–2358. [4.2, 5.3]
- Johannessen, O.M., E.V. Shalina and M.W. Miles, 1999: Satellite evidence for an Arctic sea ice cover in transformation. *Science*, 289, 1937–1939. [1.1]
- Johns, E., R.A. Fine and R. Molinari, 1997a: Deep flow along the western boundary south of the Blake Bahama Outer Ridge. *J. Phys. Oceanogr.* 27, 2187–2208. [5.5, 5.8]
- Johns, T.C., R.E. Carnell, J.F. Crossley *et al.*, 1997b: The second Hadley Centre coupled atmosphere-ocean GCM: model description, spinup and validation. *Climate Dyn.* 13, 103–134. [2.3]
- Johns, W.E., T.N. Lee, F.A. Schott, R.J. Zantopp and R.H. Evans, 1990: The North Brazil Current retroflection: seasonal structure and eddy variability. *J. Geophys. Res.*, 95, 22103–22120. [4.3]
- Johns, W.E., D.M. Fratantoni and R.J. Zantopp, 1993: Deep western boundary current variability off northwestern Brazil. *Deep-Sea Res. I* 40, 293–310. [4.5]
- Johns, W.E., T.N. Lee, R.C. Beardsley, J. Candela, R. Limeburner and B. Castro, 1998: Annual cycle and variability of the North Brazil Current. *J. Phys. Oceanogr.* 28, 103–128. [4.3]
- Johnson, G.C., 1993: A deep inertial jet on a sloping bottom near the equator. *Deep-Sea Res.* 40, 1781–1792. [4.3]
- Johnson, G.C., 1998: Deep water properties, velocities, and dynamics over Ocean trenches. *J. Mar. Res.* 56, 329–347. [4.5]
- Johnson, G.C. and H.L. Bryden, 1989: On the size of the Antarctic Circumpolar Current. *Deep-Sea Res.* 36, 39–53. [4.6]
- Johnson, G.C. and M.J. McPhaden, 1999: Interior pycnocline flow from the subtropical to the equatorial Pacific Ocean. *J. Phys. Oceanogr.* 19, 3073–3089. [4.3, 4.4]
- Johnson, G.C. and D.W. Moore, 1997: The Pacific subsurface countercurrents and an inertial model. *J. Phys. Oceanogr.* 27, 2448–2459. [4.3, 4.4]
- Johnson, G.C. and A.H. Orsi, 1997: Southwest Pacific Ocean water mass changes between 1968/9 and 1990/1. *J. Climate* 10, 306–316. [4.6, 7.3]
- Johnson, G.C. and T.B. Sanford, 1992: Secondary circulation in the Faroe Bank Channel outflow. *J. Phys. Oceanogr.* 22(8), 927–933. [5.6]
- Johnson, G.C. and L.D. Talley, 1997: Deep tracer and dynamical plumes in the tropical Pacific Ocean. *J. Geophys. Res.* 102, 24953–24964. [4.3]
- Johnson, G.C. and J.M. Toole, 1993: Flow of deep and bottom waters in the Pacific at 10°N. *Deep-Sea Res. I* 40, 371–394. [4.3, 4.5]
- Johnson, G.C., B.A. Warren and D.B. Olson, 1991a: Flow of bottom water in the Somali Basin. *Deep-Sea Res.* 38, 637–652. [4.3]
- Johnson, G.C., B.A. Warren and D.B. Olson, 1991b: A deep boundary current in the Arabian Basin. *Deep-Sea Res.* 38, 653–661. [4.3]
- Johnson, G.C., D.L. Rudnick and B.A. Taft, 1994a: Bottom water variability in the Samoa Passage. *J. Mar. Res.* 52, 177–196. [4.5]
- Johnson, G.C., T.B. Sanford and M.O. Baringer, 1994b: Stress on the Mediterranean Outflow plume: Part I. Velocity and water property measurements. *J. Phys. Oceanogr.* 24(10), 2072–2083. [5.6]
- Johnson, G.C., D.L. Musgrave, B.A. Warren, A. Ffield and D.B. Olson, 1998: Flow of bottom and deep water in the Amirante Passage and Mascarene Basin. *J. Geophys. Res.* 103, 30973–30984. [4.3, 4.5]
- Johnson, G.C., M.J. McPhaden, G.D. Rowe and K.E. McTaggart, 2000: Upper equatorial Pacific Ocean current and salinity variability during the 1996–1998 El Niño–La Niña cycle. *J. Geophys. Res.* 105, 1037–1053. [7.4]
- Johnson, J.A. and R.B. Hill, 1975: A three-dimensional model of the southern ocean with bottom topography. *Deep-Sea Res.* 22, 745–751. [4.6]
- Johnson, K.M. and D.W.R. Wallace, 1992: *The Single-Operator Multiparameter Metabolic*

- Analyzer for Total Carbon Dioxide with Coulometric Detection.* DOE Research Summary. No. 19, Carbon Dioxide Information Analysis Center, Oak Ridge National Laboratory, Oak Ridge, TN, 4 pp. [6.3]
- Johnson, K. M., A. E. King and J. M. Sieburth, 1985: Coulometric TCO₂ analysis for marine studies: An Introduction. *Mar. Chem.*, **16**, 61–82. [6.3]
- Johnson, K. M., J. M. Sieburth, J. M. Williams and L. Brandstrom, 1987: Coulometric total carbon dioxide analysis for marine studies: automation and calibration. *Mar. Chem.* **21**, 117–133. [6.3]
- Johnson, K. M., K. D. Wills, D. B. Butler, W. K. Johnson and C. S. Wong, 1993: Coulometric total carbon dioxide analysis for marine studies: maximizing the performance of an automated gas-extraction system and coulometric detector. *Mar. Chem.* **44**, 167–188. [6.3]
- Johnson, K. M., A. Dickson, G. Eischeid *et. al.*, 1998b: Coulometric total carbon dioxide analysis for marine studies: assessment of the quality of total inorganic carbon measurements made during the US Indian Ocean CO₂ Survey 1994–1996. *Mar. Chem.* **63**, 21–37. [6.3]
- Johnson, R. E., 1973: Antarctic Intermediate Water in the South Pacific Ocean. In: *Oceanography of the South Pacific Ocean 1972*, R. Frazer (compiler) New Zealand National Commission for UNESCO, pp. 55–69. [4.4]
- Johnson, T. J., R. H. Stewart, C. K. Shum and B. D. Tapley, 1992: Distribution of Reynolds stress carried by mesoscale variability in the Antarctic Circumpolar Current. *Geophys. Res. Lett.* **19**, 1201–1204. [3.3]
- Jones, A., D. L. Roberts and M.-J. Woodage, 1999a: *The Indirect Effects of Anthropogenic Sulphate Aerosol Simulated Using a Climate Model with an Interactive Sulphur Cycle.* Hadley Centre Technical Note No. 14, Meteorological Office, Bracknell, UK. [2.3]
- Jones, C., P. Peterson and C. Gautier, 1999b: A new method for deriving ocean surface specific humidity and air temperature: An artificial neural network approach. *J. Appl. Meteor.* **38**, 1229–1246. [3.4]
- Jones, E. P., L. G. Anderson and J. H. Swift, 1998: Distribution of Atlantic and Pacific waters in the upper Arctic Ocean: Implications for circulation. *Geophys. Res. Lett.* **25**, 769–772. [4.7]
- Jones, G. A., A. R. Gagnon, R. J. Schneider, K. F. von Reden and A. P. McNichol, 1994: High-precision AMS radiocarbon measurements of central Arctic Ocean seawaters. *Nuclear Instr. and Methods*, **B92**, 426–430. [5.8]
- Jones, H. and J. Marshall, 1993: Convection with rotation in a neutral ocean: a study of open-ocean convection. *J. Phys. Oceanogr.* **23**, 1009–1039. [5.5]
- Jones, H. and J. Marshall, 1997: Restratification after deep convection. *J. Phys. Oceanogr.* **27**, 2276–2287. [5.5]
- Jones, P. D., T. Jonsson and D. Wheeler, 1997: Extension of the North Atlantic Oscillation using early instrumental pressure observations from Gibraltar and south-west Iceland. *Int. J. Climatol.* **17**, 1433–1450. [7.3]
- Jones, W. L., F. J. Wentz and L. C. Schroeder, 1978: Algorithm for inferring wind stress from SEASAT-A. *Spacecraft and Rockets*, **15**, 368–374. [3.4]
- Jónsson, S., 1991: Seasonal and interannual variability of wind stress curl over the Nordic Seas. *J. Geophys. Res.* **96**, 2649–2659. [7.3]
- Josey, S. A., E. C. Kent, D. Oakley and P. K. Taylor, 1996: A new global air-sea heat and momentum flux climatology. *International WOCE Newsletter*, No. 24, 3–5, WOCE International Project Office (unpublished document). [6.2]
- Josey, S. A., R. Pascal and P. Taylor, 1997: Air-sea interaction studies in the Mediterranean Sea. In: Abstracts Volume of the International Conference, *Progress in Oceanography of the Mediterranean Sea*, Rome, 17–19 November, 1997, 253 pp. [5.7]
- Josey, S. A., E. C. Kent and P. K. Taylor, 1998: *The Southampton Oceanography Centre (SOC) Ocean–Atmosphere Heat, Momentum and Freshwater Flux Atlas.* Southampton Oceanography Centre, Report 6, 30 pp + Figs. [5.1]
- Josey, S. A., E. C. Kent and P. K. Taylor, 1999: New insights into the ocean heat budget closure problem from analysis of the SOC air-sea flux climatology. *J. Climate* **12**, 2856–2880. [1.2, 5.1, 6.1, 7.1]
- Josey, S. A., E. C. Kent and P. K. Taylor, 2000: On the wind stress forcing of the ocean in the SOC and Hellerman and Rosenstein climatologies. *J. Phys. Oceanogr.* (submitted). [1.2]
- Jourdan, D. and C. Gautier, 1994: Comparison between global latent heat flux computed from multi-sensor (SSM/I and AVHRR) and from in-situ data. *J. Atmos. Oceanic Technol.* **12**, 46–72. [3.4]
- Jourdan, D., P. Peterson and C. Gautier, 1997: Oceanic freshwater budget and transport as derived from satellite radiometric data. *J. Phys. Oceanogr.* **27**, 457–467. [6.2]
- Joyce, T. M., 1977: A note on the lateral mixing of water masses. *J. Phys. Oceanogr.* **7**, 626–629. [5.2]
- Joyce, T. M., 1988: Wind-driven cross-equatorial flow in the Pacific Ocean. *J. Phys. Oceanogr.* **18**, 19–24. [4.3]

- Joyce, T.M., 1989: On in situ calibration of shipboard ADCPs. *J. Atmos. Oceanic Technol.* **6**, 169–172. [3.1]
- Joyce, T.M. and W.J. Jenkins, 1993: Spatial variability of subducting water in the North Atlantic: A pilot study. *J. Geophys. Res.* **98**, 10111–10124. [5.3]
- Joyce, T.M. and P. Robbins, 1996: The long-term hydrographic record at Bermuda. *J. Climate* **9**, 3121–3131. [1.2, 5.4, 7.3]
- Joyce, T.M., C. Wunsch and S.D. Pierce, 1986: Synoptic Gulf Stream velocity profiles through simultaneous inversion of hydrographic and acoustic Doppler data. *J. Geophys. Res.* **91**, 7573–7585. [3.1]
- Joyce, T.M., K.A. Kelly, D.M. Schubert and M.J. Caruso, 1990: Shipboard and altimetric studies of rapid Gulf Stream variability between Cape Cod and Bermuda. *Deep-Sea Res.* **37**, 897–910. [3.3]
- Joyce, T.M., J.R. Luyten, A. Kubryakov, F.B. Bahr *et al.*, 1998: Meso- to large-scale structure of subducting water in the subtropical gyre of the eastern North Atlantic ocean. *J. Phys. Oceanogr.* **28**, 40–61. [5.3, 5.4]
- Joyce, T.M., R.S. Pickart and R.C. Millard, 1999: Long-term hydrographic changes at 52° and 66°W in the North Atlantic subtropical gyre and Caribbean. *Deep-Sea Res.* **46**, 245–278. [1.2, 7.3]
- Joyce, T.M., C. Deser and M.A. Spall, 2000: On the relation between decadal variability of Subtropical Mode Water and the North Atlantic Oscillation. *J. Climate* **13**, 2550–2569. [7.3]
- Jungclaus, J.H. and J.O. Backhaus, 1994: Application of a transient reduced gravity plume model to the Denmark Strait overflow. *J. Geophys. Res.* **99**, 12375–12396. [5.6]
- Kaempf, J. and J.O. Backhaus, 1998: Shallow, brine-driven free convection in polar oceans: Nonhydrostatic numerical process studies. *J. Geophys. Res.* **103**, 5577–5593. [1.2]
- Kalnay, E., M. Kanamitsu, R. Kistler, *et al.*, 1996: The NCEP/NCAR 40-year reanalysis project. *Bull. Amer. Meteor. Soc.* **77**, 437–471. [5.1, 6.2, 7.3]
- Kamenkovich, V.M., 1962: On the theory of the Antarctic Circumpolar Current. *Tr. Inst. Okeanol. Im. P.P. Shirshov Acad. Nauk SSSR* **56**, 241–293. [4.6]
- Kamenkovich, V.M., Y.P. Leonov, D.A. Nechaev, D.A. Byrne and A.L. Gordon, 1996: On the Influence of Bottom Topography on the Agulhas Eddy. *J. Phys. Oceanogr.* **26**, 892–912. [4.7]
- Kaneko, I., Y. Takatsuki, H. Kamiya and S. Kawae, 1998: Water property and current distributions along the WHP-P9 section (137°–142°E) in the western North Pacific. *J. Geophys. Res.* **103**, 12959–12984. [4.3]
- Kantha, L.H. and C.C. Tierney, 1997: Global baroclinic Tides. *Prog. Oceanogr.* **40**, 163–178. [4.2]
- Karoly, D.J., 1990: The role of transient eddies in low-frequency zonal variations of the Southern Hemisphere circulation. *Tellus* **42A**, 41–50. [7.3]
- Karoly, D.J., P.C. McIntosh, P. Berrisford, T.J. McDougall and A.C. Hirst, 1997: Similarities of the Deacon Cell in the Southern Ocean and Ferrel cells in the atmosphere. *Quart. J. Roy. Meteor. Soc.* **123**, 519–526, Part B. [4.6]
- Käse, R.H., 2000: Topographic effects on eddies and mixing in the Denmark Strait overflow plume. In: F. Schott, C. Böning, H. Bryden *et al.*, *Report of the WOCE North Atlantic Workshop*. WOCE International Project Office, WOCE Report No. 169/2000, pp. 61–62. (unpublished manuscript). [7.1]
- Käse, R.H. and A. Oschlies, 2000: Flow through Denmark Strait. *J. Geophys. Res.* (in press). [7.1]
- Käse, R.H. and W. Zenk, 1996: Structure of the Mediterranean Water and meddy characteristics in the northeastern Atlantic. In: *The Warmwatersphere of the North Atlantic Ocean*, W. Krauss (ed.), Gebr. Borntraeger, Berlin, Stuttgart, Chapter 12, pp. 365–395. [3.2, 5.7]
- Käse, R.H., W. Zenk, T.B. Sanford and W. Hiller, 1985: Currents, fronts and eddy fluxes in the Canary Basin. *Prog. Oceanogr.* **14**, 231–257. [5.4]
- Katsaros, K.B., 1990: Parameterization schemes and models for estimating the surface radiation budget. In: *Surface Waves and Fluxes*, G.L. Geernaert and W.J. Plant (eds), Dordrecht, Kluwer Acad. Publ., Vol. II, pp. 339–368. [3.4]
- Katsaros, K.B., E. Forde, P. Chang and W.T. Liu, 2000: QuikSCAT facilitates early identification of tropical depressions in 1999 hurricane season. *Geophys. Res. Lett.* (submitted). [3.4]
- Kattenberg, A., F. Giorgi, H. Grassl *et al.*, 1996: Climate models – projections of future climate. In: *Climate Change 1995, The Science of Climate Change*, J.T. Houghton *et al.* (eds), Cambridge University Press, pp. 285–357. [1.1]
- Kawabe, M. and K. Taira, 1998: Water masses and properties at 165°E in the western Pacific. *J. Geophys. Res.* **103**, 12941–12958. [4.3]
- Kawamura, R., 1994: A rotated EOF analysis of global sea surface temperature variability with interannual and interdecadal scales. *J. Phys. Oceanogr.* **24**, 707–715. [7.3]
- Kawase, M., 1987: Establishment of deep ocean circulation driven by deepwater production. *J. Phys. Oceanogr.* **17**, 2294–2317. [2.2]

- Kawase, M. and J. L. Sarmiento, 1985: Nutrients in the Atlantic thermocline. *J. Geophys. Res.* **90**, 8960–8979. [4.4]
- Kawase, M. and J. L. Sarmiento, 1986: Circulation and nutrients in middepth Atlantic waters. *J. Geophys. Res.* **91**, 9749–9770. [4.4]
- Keeling, C. D. and Heimann, M., 1986: Meridional eddy diffusion model of the transport of atmospheric carbon dioxide. 2. Mean annual carbon cycle. *J. Geophys. Res.* **91**, 7782–7796. [6.3]
- Keeling, C. D., R. B. Bacastow, A. L. Carter *et al.*, 1989: A three dimensional model of atmospheric CO₂ transport based on observed winds: 1. Analysis of observational data. In: *Aspects of Climate Variability in the Pacific and the Western Americas*, D. H. Peterson (ed.), American Geophysical Union, Washington, DC, pp. 165–236. [6.3]
- Keeling, C. D., T. P. Whorf, M. Wahlen and J. Vanderplicht, 1995: Interannual extremes in the rate of rise of atmospheric carbon dioxide since 1980. *Nature* **375**, 666–670. [6.3]
- Keeling, R. F. and T. H. Peng, 1995: Transport of heat, CO₂ and O₂ by the Atlantic's thermohaline circulation. *Phil. Trans. Roy. Soc. Lond. B* **348**, 133–142. [6.3]
- Keeling, R. F., R. P. Najjar and M. L. Bender, 1993: What atmospheric oxygen measurements can tell us about the global carbon cycle. *Glob. Biogeochem. Cycles* **7**, 37–67. [6.3]
- Keeling, R. F., S. C. Piper and M. Heimann, 1996: Global and hemispheric CO₂ sinks deduced from changes in atmospheric O₂ concentration. *Nature* **381**, 218–221. [6.3]
- Keffer, T., 1985: The ventilation of the World's oceans: Maps of the potential vorticity field. *J. Phys. Oceanogr.* **15**, 509–523. [4.2]
- Keigwin, L. D., W. B. Curry, S. J. Lehmann and S. Johnsen, 1994: The role of the deep ocean in North Atlantic climate change between 70 and 130 kyr ago. *Nature* **371**, 323–325. [1.1]
- Keir, R. S., R. L. Michel and R. F. Weiss, 1992: Ocean mixing versus exchange in Antarctic Shelf Waters near 150°E. *Deep-Sea Res.* **39**, 97–119. [5.8]
- Keith, D. W., 1995: Meridional energy transport: uncertainty in zonal means. *Tellus* **47A**, 30–44. [6.1, 6.2]
- Kelley, D. E., 1984: Effective diffusivities within oceanic thermohaline staircases. *J. Geophys. Res.* **89**, 10484–10488. [5.2]
- Kelley, D. E., 1990: Fluxes through diffusive staircases: A new formulation. *J. Geophys. Res.* **95**, 3365–3371. [5.2]
- Kelly, K. A., 1991: The meandering Gulf Stream as seen by the GEOSAT Altimeter: surface transport, position, and velocity variance from 73° to 46°W. *J. Geophys. Res.* **96**, 16721–16738. [3.3]
- Kelly, K. A. and S. T. Gille, 1990: Gulf stream surface transport and statistics at 69° W from the GEOSAT altimeter. *J. Geophys. Res.* **95**, 3149–3161. [3.3]
- Kelly, K. A. and B. Qiu, 1995a: Heat flux estimates for the western North Atlantic. Part I: assimilation of satellite data into a mixed layer model. *J. Phys. Oceanogr.* **25**, 2344–2360. [3.3]
- Kelly, K. A. and B. Qiu, 1995b: Heat flux estimates for the western North Atlantic. Part II: the upper ocean heat balance. *J. Phys. Oceanogr.* **25**, 2361–2373. [3.3]
- Kelly, K. A., T. M. Joyce, D. M. Schubert and M. J. Caruso, 1991: The Mean Sea Surface and Geoid along the Geosat Subtrack from Bermuda to Cape Cod. *J. Geophys. Res.* **96**, 12699–12709. [3.3]
- Kelly, K. A., M. J. Caruso and J. A. Austin, 1993: Wind-forced variations in sea-surface height in the Northeast Pacific Ocean. *J. Phys. Oceanogr.* **23**, 2392–2411. [3.3]
- Kelly, K. A., S. Singh and R. X. Huang, 1999: Seasonal variations of sea-surface height in the Gulf Stream region. *J. Phys. Oceanogr.* **29**, 313–327. [3.3]
- Kennan, S. C., P. P. Niiler and A. Sybrandy, 1998: Advances in drifting buoy technology. *International WOCE Newsletter*, No. 30, 7–10, WOCE International Project Office (unpublished document). [4.1]
- Kent, E. C. and P. K. Taylor, 1995: A comparison of sensible and latent heat flux estimations for the North Atlantic Ocean. *J. Phys. Oceanogr.* **25**, 1530–1549. [5.1]
- Kent, E. C., P. G. Challenor and P. K. Taylor, 1999: A statistical determination of the random observational errors present in voluntary observing ships' meteorological reports. *J. Atmos. Oceanic Technol.* **16**, 920–929. [6.1]
- Kessler, W. S. and J. P. McCreary, 1993: The annual wind-driven Rossby wave in the subthermocline Equatorial Pacific. *J. Phys. Oceanogr.* **23**, 1192–1207. [4.3]
- Key, R. M., 1996: WOCE Pacific Ocean radiocarbon program. *Radiocarbon* **38**, 415–423. [3.1, 5.8]
- Key, R. M., C. Rooth, G. Östlund and M. Stuiver, 1996: Ventilation of the Deep Pacific Ocean, AGU/ASLO 1996 Ocean Sciences Meeting, San Diego, CA, EOS **76**, No. 3, p. OS40. [5.8]
- Kidson, J. W., 1988: Indices of the Southern Hemisphere zonal wind. *J. Climate* **1**, 183–194. [7.3]
- Kiehl J. T. and K. E. Trenberth, 1997: Earth's Annual Global Mean Energy Budget. *Bull. Amer. Meteor. Soc.* **78**, 197–208. [1.2]

- Killworth, P.D., 1995: Hydraulic control and maximal flow in rotating, stratified hydraulics. *Deep-Sea Res.* **42**, 859–871. [5.6]
- Killworth, P.D., 1997: On the parameterization of eddy transfer. Part I: Theory. *J. Mar. Res.* **55**, 1171–1197. [5.2, 7.2]
- Killworth, P.D. and N.R. Edwards, 1999: A turbulent bottom boundary layer code for use in numerical ocean models. *J. Phys. Oceanogr.* **29**, 1221–1238. [2.2, 2.3]
- Killworth, P.D. and M.M. Nanneh, 1994: Isopycnal momentum budget of the Antarctic Circumpolar Current in the Fine Resolution Antarctic Model. *J. Phys. Oceanogr.* **24**, 1201–1223. [4.6]
- Killworth, P.D., D. Stainforth, D.J. Webb and S.M. Paterson, 1991: The development of a free surface Bryan-Cox-Semtner ocean model. *J. Phys. Oceanogr.* **21**, 1333–1348. [2.3]
- Killworth, P.D., D.B. Chelton and R.A. De Szoeke, 1997: The speed of observed and theoretical long extra-tropical planetary waves. *J. Phys. Oceanogr.* **27**, 1946–1966. [3.3, 7.1]
- Killworth, P.D., D.A. Smeed and A.J.G. Nurser, 2000: The effects on ocean models of relaxation towards observations at the surface. *J. Phys. Oceanogr.* **30**, 160–174. [5.1]
- Kinder, T.H. and G. Parrilla, 1987: Yes, some of the Mediterranean outflow does come from great depth. *J. Geophys. Res.* **92**, 2901–2906. [5.7]
- Kindle, J.C. and J.D. Thompson, 1989: The 26- and 50-day oscillations in the western Indian Ocean: model results. *J. Geophys. Res.* **94**, 4721–4736. [3.3]
- Kindle, J.C., H.E. Hurlburt and E.J. Metzger, 1989: On the seasonal and interannual variability of the Pacific–Indian Ocean throughflow. *Western Pacific International Meeting and Workshop on TOGA-COARE*, J. Picaut, R. Lukas and T. Delcroix (eds), Noumea, New Caledonia, pp. 355–366. [4.7]
- King, B.A. and S.G. Alderson, 1994: SR1 repeat hydrography/ADCP, Drake Passage, November 1993. *International WOCE Newsletter*, No. 15, 13–15, WOCE International Project Office (unpublished document). [3.1]
- King, B.A. and E.B. Cooper, 1993: Comparison of ships heading determined from an array of GPS antennas with heading from conventional gyrocompass measurements. *Deep-Sea Res.* **40**, 2207–2216. [3.1]
- King, B.A., S.G. Alderson and D. Cromwell, 1996: Enhancement of shipboard ADCP data with DGPS position and GPS heading measurements. *Deep-Sea Res.* **43**, 937–947. [3.1]
- Kitamura, Y. and N. Sugino, 1987: Effect of vertical viscosity and diffusivity on tropical ocean circulation: subsurface eastward flow. *J. Oceanogr. Soc. Japan* **43**, 1–20. [4.3]
- Kitani, K., 1973: An oceanographic study of the Okhotsk Sea – particularly in regard to cold waters. *Bull. Far Seas Fish. Res. Lab.* **9**, 45–77. [5.4]
- Kitoh, A., 1991: Interannual variations in an atmospheric GCM forced by the 1970–1989 SST Part II: low frequency variability of the wintertime Northern Hemisphere extratropics. *J. Meteor. Soc. Japan* **69**, 271–291. [7.3]
- Kleeman, R., A.M. Moore and N.R. Smith, 1995: Assimilation of sub-surface thermal data into an intermediate tropical coupled ocean–atmosphere model. *Mon. Wea. Rev.* **123**, 3103–3113. [7.4]
- Kleeman, R., R. Colman, N.R. Smith and S.B. Power, 1996: A recent change in the mean state of the Pacific Ocean: Observational evidence and atmospheric and oceanic responses. *J. Geophys. Res.* **101**, 20483–20500. [7.4]
- Kleeman, R., J.P. McCreary and B.A. Klinger, 1999: A mechanism for generating ENSO decadal variability. *Geophys. Res. Lett.* **26**, 1743–1746. [5.3]
- Klein, B., R.L. Molinari, T.J. Müller and G. Siedler, 1995: A transatlantic section at 14.5°N: Meridional volume and heat fluxes. *J. Mar. Res.* **53**, 929–957. [6.1]
- Klein, B. and N. Hogg, 1996: On the variability of 18 Degree Water formation as observed from moored instruments at 55°W. *Deep-Sea Res.* **43**, 1777–1806. [5.4]
- Klinck, J.M., 1993: Effects of wind, density, and bathymetry on a one-layer Southern Ocean model. *J. Geophys. Res.* **97**, 20179–20189. [4.6]
- Knapp, G.P., 1988: *Hydrographic Data from R. V. Endeavor Cruise 129*. Woods Hole Oceanographic Institution, Technical Report, WHOI-88-41, 111 pp. [7.3]
- Knox, R.A., 1976: On a long series of measurements of Indian Ocean equatorial currents near Addu Atoll. *Deep-Sea Res.* **23**, 211–221. [4.3]
- Knudsen, M., 1900: Ein hydrographische Lehrsatz. *Analien der Hydrographie und Marinen Meteorologie* **28**, 316–320. [7.4]
- Knudsen, M. (ed.), 1901: *Hydrographical Tables*. G.E.C. Gad, Copenhagen, 63 pp. [7.4]
- Knutson, T.R. and S. Manabe, 1998: Model assessment of decadal variability and trends in the tropical Pacific Ocean. *J. Climate* **11**, 2273–2296. [2.3]
- Knutson, T.R., S. Manabe and D. Gu, 1997: Simulated ENSO in a global coupled ocean–atmosphere model: Multidecadal amplitude modulation and CO₂ sensitivity. *J. Climate* **10**, 42–63. [2.3]

- Koblinsky, C.J., P.P. Niiler and W.J. Schmitz, Jr., 1989: Observations of wind-forced deep ocean currents in the North Pacific. *J. Geophys. Res.* **94**, 10773–10790. [3.3]
- Körtzinger, A., L. Mintrop and J.C. Duinker, 1998: On the penetration of anthropogenic CO₂ into the North Atlantic Ocean. *J. Geophys. Res.* **103**, 18681–18689. [6.3]
- Körtzinger, A., M. Rhein and L. Mintrop, 1999a: Anthropogenic CO₂ and CFCs in the North Atlantic Ocean – a comparison of man-made tracers. *Geophys. Res. Lett.* **26**, 2065–2068. [6.3]
- Körtzinger, A., Mintrop, L., Wallace, D.W.R., Johnson, K.M., Neill, C., Tilbrook, B., Towler, P., Inoue, H., Ishii, M., Shaffer, G., Torres, R.F., Ohtaki, E., Yamashita, E., Poisson, A., Brunet, C., Schauer, B., Goyet, C., and G. Eischeid, 2000: The International At-sea Intercomparison of CO₂ systems during the R/V Meteor cruise 36/1 in the North Atlantic Ocean. *Mar. Chem.*, **72**, 171–192. [6.3]
- Kolatschek, J., H. Eicken, V. Yu. Alexandrov and M. Kreyscher, 1996: The sea-ice cover of the Arctic Ocean and the Eurasian marginal seas: A brief overview of present day patterns and variability. In: *Berichte zur Polarforschung*, R. Stein, G. I. Ivanov, M. A. Levitan and K. Fahl (eds), Alfred-Wegener Institut für Polar und Meeresforschung, Bremerhaven, Germany, Vol. 212, 2–18 pp. [7.3]
- Koltermann, K. P., A. V. Sokov, V. P. Tereschenkov, S. A. Dobroliubov, K. Lorbacher and A. Sy, 1999: Decadal changes in the thermohaline circulation of the North Atlantic. *Deep-Sea Res.* **46**, 109–138. [6.1, 7.1]
- Konda, M., N. Imasato and A. Shibata, 1996: A new method to determine near-sea surface air temperature by using satellite data. *J. Geophys. Res.* **101**, 14349–14360. [3.4]
- Koshlyakov, M.N. and T.G. Sazhina, 1995: Meridional volume and heat transport by large-scale geostrophic currents in the Pacific sector of the Antarctic. *Oceanology* (English Translation), **35**, 767–777. [6.1]
- Kosro, P.M., 1985: *Shipboard acoustic current profiling during the Coastal Ocean Dynamics Experiment*. Ph.D. Thesis, University of California, San Diego, 119 pp. [3.1]
- Krahmann, G., 1997: *Saisonale und zwischen-jährliche Variabilität westlichen Mittelmeer-Analyse historischer Daten*. Dissertation, University of Kiel, Kiel, Germany, 168 pp. [5.7]
- Krasnopol'sky, V.M., W.H. Gemmill and L.C. Breaker, 1999: A multi-parameter empirical ocean algorithm for SSM/I retrievals. *Canadian J. Remote Sens.* **25**(5), 486–503. [3.4]
- Kraus, E.B. and J.A. Businger, 1994: *Atmosphere–Ocean Interaction*. Oxford University Press, Oxford, 362 pp. [3.4]
- Krauss, W., 1996: A note on overflow eddies. *Deep-Sea Res.* **43**, 1661–1667. [5.6]
- Krauss, W. and C. Böning, 1987: Lagrangian properties of eddy fields in the northern North Atlantic as deduced from satellite-tracked buoys. *J. Mar. Res.* **45**, 259–291. [3.3]
- Krauss, W. and R.H. Käse, 1998: Eddy formation in the Denmark Strait Overflow. *J. Geophys. Res.* **103**, 15525–15538. [2.2, 5.6, 7.1]
- Krupitsky, A. and M. Cane, 1994: On topographic pressure drag in a zonal channel. *J. Mar. Res.* **52**, 1–23. [4.6]
- Krupitsky, A., V. Kamenkovich, N. Naik and M. Cane, 1996: A linear equivalent barotropic model of the Antarctic Circumpolar Current with realistic coastline and bottom topography. *J. Phys. Oceanogr.* **26**, 1803–1824. [4.6]
- Kubota, M. and A. Shikauchi, 1995: Air temperature at ocean surface derived from surface-level humidity. *J. Oceanogr.* **51**, 619–634. [3.4]
- Kuhn, T.S., 1962: *The Structure of Scientific Revolutions*. University of Chicago Press, Chicago, 172 pp. [2.1]
- Kumar, A., A. Leetmaa and M. Ji, 1994: Simulations of atmospheric variability induced by sea surface temperature anomalies and implications for global warming. *Science* **266**, 632–634. [7.3]
- Kummerow, C., W. Barnes, T. Kozu, J. Shiue and J. Simpson, 1998: The tropical rainfall measuring mission (TRMM) sensor package. *J. Atmos. Oceanic Technol.* **15**, 809–817. [3.4]
- Kunze, E., 1985: Near-inertial wave propagation in geostrophic shear. *J. Phys. Oceanogr.* **15**, 544–565. [5.2]
- Kunze, E., 1990: The evolution of salt fingers in inertial wave shear. *J. Mar. Res.* **48**, 471–504. [5.2]
- Kunze, E. and E. Boss, 1998: A model for vortex-trapped internal waves. *J. Phys. Oceanogr.* **28**, 2104–2115. [5.2]
- Kunze, E. and T.B. Sanford, 1996: Abyssal mixing: Where it is not. *J. Phys. Oceanogr.* **26**, 2286–2295. [5.2]
- Kunze, E. and J.M. Toole, 1997: Tidally-driven vorticity, diurnal shear, and turbulence atop Fieberling Seamount. *J. Phys. Oceanogr.* **27**, 2663–2693. [5.2]
- Kunze, E., A.J. Williams III and M.G. Briscoe, 1990: Observations of shear and vertical stability from a neutrally buoyant float. *J. Geophys. Res.* **95**, 18127–18142. [4.3, 5.2]
- Kunze, E., R.W. Schmitt and J.M. Toole, 1995: The energy balance in a warm-core ring's near-inertial critical layer. *J. Phys. Oceanogr.* **25**, 942–957. [5.2]

- Kuragano, T.** and M. Kamachi, 2000: Global statistical space-time scales of oceanic variability estimated from the TOPEX/POSEIDON altimeter data. *J. Geophys. Res.* 105, 955–974. [3.3]
- Kushnir, Y.**, V.J. Cardone, J.G. Greenwood and M. Cane, 1997: On the recent increase in North Atlantic wave heights. *J. Climate* 10, 2107–2113. [7.3]
- Kwok, R.** and D.A. Rothrock, 1999: Variability of Fram Strait Ice Flux and the North Atlantic Oscillation. *J. Geophys. Res. Oceans* 104, 5177–5189. [7.3]
- LaBrecque, J.L.**, S.T. Lowe, L.E. Young, E. Caro, L.J. Romans and S.C. Wu, 1998: The first Spaceborne Observations of GPS Signals Reflected from the Ocean Surface. *Eos Trans. Amer. Geophys. Union* 79(45), F199. [3.3]
- Lacombe, H.**, 1990: Water, salt, heat, and wind in the Med. *Oceanus* 33, 26–36. [5.7]
- Lacombe, H.** and C. Richez, 1982: The regime of the Strait of Gibraltar. In: *Hydrodynamics of Semi-Enclosed Seas*, J.C.J. Nihoul (ed.), Elsevier, Amsterdam, pp. 13–73. [5.7]
- Lacombe, H.**, J.C. Gascard, J. Gonella and J.P. Bethoux, 1981: Response of the Mediterranean to the water and energy fluxes across its surface, on seasonal and interannual scales. *Oceanol. Acta* 4, 247–255. [5.7]
- Lacombe, H.**, P. Tchernia and L. Gamberoni, 1985: Variable bottom water in the Western Mediterranean basin. *Prog. Oceanogr.* 14, 319–338. [5.7]
- Lagerloef, G.S.E.**, G.T. Mitchum, R.B. Lukas and P.P. Niiler, 1999: Tropical Pacific near-surface currents estimated from altimeter, wind, and drifter data. *J. Geophys. Res.* 104, 23313–23326. [3.3]
- Lamb, M.F.**, C.L. Sabine, R.A. Feely *et al.*, 2001: Internal consistency and synthesis of Pacific Ocean CO₂ Survey data. *Deep-Sea Res.* (submitted). [6.3]
- Langenfelds, R.L.**, R.J. Francey and L.P. Steele, 1999: Partitioning of the global fossil CO₂ sink using a 19-year trend in atmospheric O₂. *Geophys. Res. Lett.* 26, 1897–1900. [6.3]
- Large, W.G.**, 1998: Modeling and parameterizing the ocean planetary boundary layer. In: *Ocean Modeling and Parameterization*, E.P. Chassignet and J. Verron (eds), Kluwer Acad. Publ., Dordrecht, pp. 81–120. [5.2]
- Large, W.G.** and G.B. Crawford, 1995: Observations and simulations of upper ocean response to wind events during the Ocean Storms Experiment. *J. Phys. Oceanogr.* 25, 2831–2852. [3.4]
- Large, W.G.** and P.R. Gent, 1999: Validation of vertical mixing in an equatorial ocean model using large eddy simulations and observations. *J. Phys. Oceanogr.* 29, 449–464. [3.4]
- Large, W.G.** and S. Pond, 1982: Sensible and latent heat flux measurements over the ocean. *J. Phys. Oceanogr.* 12, 464–482. [3.4]
- Large, W.G.**, J.C. McWilliams and S.C. Doney, 1994: Oceanic vertical mixing: a review and a model with a nonlocal boundary layer parameterization. *Rev. Geophys.*, 32, 363–403. [2.3, 7.1, 7.2]
- Large, W.G.**, G. Danabasoglu, S.C. Doney and J.C. McWilliams, 1997: Sensitivity to surface forcing and boundary layer mixing in a global ocean model: Annual mean climatology. *J. Phys. Oceanogr.* 27, 2418–2447. [5.1, 6.1]
- Larsen, J.C.**, 1992: Transport and heat flux of the Florida Current at 27°N derived from cross-stream voltages and profiling data: theory and observations. *Phil. Trans. Roy. Soc., Lond. A* 338, 169–236. [1.2, 6.1]
- Larson, N.G.** and M.C. Gregg, 1983: Turbulent dissipation and shear in thermohaline intrusions. *Nature*, 306, 26–32. [5.2]
- Latif, M.** and T.P. Barnett, 1996: Decadal climate variability over the North Pacific and North America: dynamics and predictability. *J. Climate* 9, 2407–2423. [2.3]
- Latif, M.**, R. Kleeman and C. Eckert, 1997: Greenhouse warming, decadal variability or El Niño? An attempt to understand the anomalous 1990s. *J. Climate* 10, 2221–2239. [7.4]
- Lau, K.M.** and H. Weng, 1999: Interannual, decadal–interdecadal, and global warming signals in sea surface temperature during 1955–97. *J. Climate* 12, 1257–1267. [2.3]
- Lau, N.-C.** and M.J. Nath, 1994: A modeling study of the relative roles of tropical and extratropical SST anomalies in the variability of the global atmosphere–ocean system. *J. Climate* 7, 1184–1207. [7.3]
- Lau, N.-C.** and M.J. Nath, 1996: The role of the ‘atmospheric bridge’ in linking tropical Pacific ENSO events to extratropical SST anomalies. *J. Climate* 9, 2036–2057. [7.3]
- Lavender, K.L.**, R.E. Davis and W.B. Owens, 2000a: Mid-depth recirculation observed in the interior Labrador and Irminger Seas by direct velocity measurements. *Nature* 407, 66–69. [3.2, 5.5, 7.1]
- Lavender, K.L.**, R.E. Davis and W.B. Owens, 2000b: Observations of open-ocean deep convection in the Labrador Sea from subsurface floats. *J. Phys. Oceanogr.* (submitted). [3.2]
- Lavender, K.L.**, R.E. Davis and W.B. Owens, 2000c: Direct velocity measurements in the Labrador and Irminger Seas describe pathways of Labrador Sea Water. *Nature* (submitted). [5.5, 7.1]
- Lavín, A.**, H.L. Bryden and G. Parrilla, 1998: Meridional transport and heat flux variations in

- the subtropical North Atlantic. *Glob. Atmos. Ocean System* 6, 269–293. [2.2, 6.1, 6.3]
- Law, R. M., P. J. Rayner, A. S. Denning et al.**, 1996: Variations in modeled atmospheric transport of carbon dioxide and the consequences for CO₂ inversions. *Glob. Biogeochem. Cycles* 10, 783–796. [6.3]
- Lazier, J. R. N.**, 1980: Oceanographic conditions at Ocean Weather Ship *Bravo*, 1964–1974. *Atmos. Ocean* 18, 227–238. [5.5, 7.3]
- Lazier, J. R. N.**, 1988: Temperature and salinity changes in the deep Labrador Sea, 1962–1986. *Deep-Sea Res.* 35, 1247–1253. [7.3]
- Lazier, J. R. N.**, 1995: The salinity decrease in the Labrador Sea over the past thirty years. In: *Natural Climate Variability on Decade-to-Century Time Scales*, D. G. Martinson *et al.* (eds), National Academy Press, Washington, DC, pp. 295–304. [7.1, 7.3]
- Le Provost, C.**, 2000: Ocean Tides, pp. 267–303. In: *Satellite Altimetry and Earth Sciences*, L.-L. Fu and A. Cazenave (eds), Academic Press. [3.3]
- Le Provost, C., A. F. Bennett and D. E. Cartwright**, 1995: Ocean tides for and from TOPEX/POSEIDON. *Science* 267, 639–642. [3.3]
- Le Traon, P. Y. and G. Dibarboire**, 1999: Mesoscale mapping capabilities of multiple-satellite altimeter missions. *J. Atmos. Oceanic Technol.* 16, 1208–1223. [3.3, 7.4]
- Le Traon, P. Y. and P. De Mey**, 1994: The eddy field associated with the Azores Front east of the Mid-Atlantic Ridge as observed by the GEOSAT altimeter. *J. Geophys. Res.* 99, 9907–9923. [3.3]
- Le Traon, P. Y. and J.-F. Minster**, 1993: Sea-level variability and Semiannual Rossby Waves in the South Atlantic Subtropical Gyre. *J. Geophys. Res.* 98, 12315–12326. [3.3]
- Le Traon, P. Y. and R. Morrow**, 2000: Ocean currents and eddies. In: *Satellite Altimetry and Earth Sciences*, L.-L. Fu and A. Cazenave (eds), Academic Press, London (in press). [3.3]
- Le Traon, P. Y. and F. Ogor**, 1998: ERS-1/2 orbit error improvement using TOPEX/POSEIDON: the 2 cm challenge. *J. Geophys. Res.* 103, 8045–8057. [3.3]
- Le Traon, P. Y., M. C. Rouquet and C. Boissier**, 1990: Spatial scales of mesoscale variability in the North Atlantic as deduced from GEOSAT data. *J. Geophys. Res.* 95, 20267–20285. [3.3]
- Le Traon, P. Y., F. Nadal and N. Ducet**, 1998: An improved mapping method of multi-satellite altimeter data. *J. Atmos. Oceanic Technol.* 15, 522–534. [3.3]
- Leaman, K. D. and F. A. Schott**, 1991: Hydrographic structure of the convection regime in the Gulf of Lions: Winter 1987. *J. Phys. Oceanogr.* 21, 575–598. [5.7]
- Ledwell, J., A. Watson and C. Law**, 1993: Evidence for slow mixing across the pycnocline from an open-ocean tracer-release experiment. *Nature* 364, 701–703. [4.6, 5.2, 7.1]
- Ledwell, J. R., A. J. Watson and C. B. Law**, 1998: Mixing of a tracer in the pycnocline. *J. Geophys. Res.* 103, 21499–21529. [4.2, 5.2]
- Ledwell, J., E. Montgomery, K. Polzin, L. St Laurent, R. Schmitt and J. Toole**, 2000: Evidence for enhanced mixing over rough topography in the abyssal ocean. *Nature* 403, 179–182. [4.5, 4.6, 5.2, 7.1]
- Lee, K., R. Wanninkhof, T. Takahashi, S. C. Doney and R. Feely**, 1998: Low interannual variability in recent oceanic uptake of atmospheric carbon dioxide. *Nature* 396, 155–159. [6.3]
- Lee, N. T., J. A. Yoder and L. P. Atkinson**, 1991: Gulf Stream frontal eddy influence on productivity of the southeast U.S. continental shelf. *J. Geophys. Res.* 96, 22191–22205. [1.2]
- Lee, T. and J. Marotzke**, 1998: Seasonal cycles of meridional overturning and heat transport of the Indian Ocean. *J. Phys. Oceanogr.* 28, 923–943. [4.3, 6.1]
- Lee, T. N., W. E. Johns, F. Schott and R. J. Zantopp**, 1990: Western boundary current structure and variability east of Abaco, Bahamas at 26°N. *J. Phys. Oceanogr.* 20, 446–466. [2.2]
- Lee, T. N., W. E. Johns, R. J. Zantopp and E. R. Fillenbaum**, 1996: Moored observations of Western Boundary Current variability and thermocline circulation at 26.5°N in the subtropical North Atlantic. *J. Phys. Oceanogr.* 26, 962–983. [2.2, 4.5]
- Leetmaa, A. and H. Stommel**, 1980: Equatorial current observations in the western Indian Ocean. *J. Phys. Oceanogr.* 10, 258–269. [4.3]
- Leetmaa, A., D. R. Quadfasel and D. Wilson**, 1982: Development of the flow field during the onset of the Somali Current, 1979. *J. Phys. Oceanogr.* 12, 1325–1342. [4.3]
- Legates, D. R. and C. J. Willmott**, 1990: Mean seasonal and spatial variability in gauge corrected global precipitation. *Int. J. Climatol.* 10, 111–127. [6.2]
- Legeckis, R. and G. Reverdin**, 1987: Long waves in the Equatorial Atlantic Ocean during 1983. *J. Geophys. Res.* 92, 2835–2842. [4.3]
- LeGrand, P. and J. Minster**, 1999: Impact of the GOCE gravity mission on ocean circulation estimates. *Geophys. Res. Lett.* 26, 1881–1884. [3.3]
- LeGrand, P., H. Mercier and T. Reynaud**, 1998: Combining T/P altimetric data with hydrographic

- data to estimate the mean dynamic topography of the North Atlantic and improve the geoid. *Ann. Geophys.* **16**, 638–650. [3.3]
- Lemke, P., W.D. Hibler, G. Flato, M. Harder and M. Kreysher, 1997: On the improvement of sea-ice models for climate simulations: The sea-ice model intercomparison project. *Ann. Glaciol.* **25**, 183–187. [1.1]
- Lemoine, F. et al., 1998: *The Development of the Joint NASA GSFC and the National Imagery and Mapping Agency (NIMA) Geopotential Model EGM96*. NASA/TP-1998-206861. NASA Goddard Space Flight Center, Greenbelt, MD. [3.3]
- Lentz, S.J. and J.H. Trowbridge, 1991: The bottom boundary layer over the northern California shelf. *J. Phys. Oceanogr.* **21**, 1186–1201. [5.2]
- Lenz, E., 1845: Bermerkungen bei die Temperatur des Weltmeeres in verschiedenen Tiefen. *Bull. de la Classe Physico-Mathematique de l'Academie Impériale des Sciences de Saint-Petersbourg* **5**, 67–74. [4.4]
- Leuliette, E.W. and J.M. Wahr, 1999: Coupled pattern analysis of sea-surface temperature and TOPEX/POSEIDON sea-surface height. *J. Phys. Oceanogr.* **29**, 599–611. [3.3]
- Levis, S., J.A. Foley and D. Pollard, 1999: Potential high-latitude vegetation feedbacks on CO₂-induced climate change. *Geophys. Res. Lett.* **26**, 747–750. [2.3]
- Levitus, S., 1982: Climatological Atlas of the World Ocean. *NOAA Professional Paper* **13**, 173 pp. [1.2, 2.2, 4.4, 5.7, 6.2, 7.1]
- Levitus, S., 1989: Interannual variability of temperature and salinity at intermediate depths of the North Atlantic Ocean, 1970–1974 versus 1955–1959. *J. Geophys. Res.* **94**, 6091–6131. [7.3]
- Levitus, S. and T.P. Boyer, 1994a: *Quality Control and Processing of Historical Oceanographic Temperature, Salinity, and Oxygen Data*. NOAA Technical Report 81, NESDIS X. [6.2]
- Levitus, S. and T.P. Boyer, 1994b: *World Ocean Atlas 1994*. Vol. 4, *Temperature*. NOAA Atlas NESDIS 4; US Govt Printing Office, 117 pp. [2.3, 3.3, 4.1, 5.3, 6.1, 7.1, 7.3]
- Levitus, S., R. Burgett and T. P. Boyer, 1994: *World Ocean Atlas 1994*, Vol. 3: *Salinity* NOAA Atlas NESDIS 3, Rep. US Govt Printing Office, Washington, DC, 99 pp. [5.1, 7.1]
- Levitus, S., J.I. Antonov, T.P. Boyer and C. Stephens, 2000: Warming of the World Ocean. *Science* **287**, 2225–2229. [1.2, 5.1, 7.4]
- Lewis, M.R., M.E. Carr, G.C. Feldman, W. Esaias and C. McLain, 1990: Satellite estimates of the influence of penetrating solar radiation on the heat budget of the equatorial Pacific. *Nature* **347**, 543–545. [4.3]
- Li, X., Y. Chao, J.C. McWilliams and L.-L. Fu, 2000: A comparison of two vertical mixing schemes in a Pacific Ocean General Circulation Model. *J. Climate* (in press). [3.3]
- Li, Z. and H.G. Leighton, 1993: Global climatologies of the solar radiation budgets at the surface and in the atmosphere from five years of ERBE data. *J. Geophys. Res.* **98**, 4919–4930. [3.4]
- Lien, R.C., D.A. Caldwell, M.C. Gregg and J.N. Moum, 1995: Turbulence variability at the equator in the central Pacific at the beginning of the 1991–93 El Niño. *J. Geophys. Res.* **100**, 6881–6898. [5.2]
- Lilly, J.M. and P.B. Rhines, 2000: Coherent eddies in the Labrador Sea observed from a mooring. *J. Phys. Oceanogr.* (in press). [5.5]
- Lilly, J., P. Rhines, M. Visbeck et al., 1999: Observing deep convection in the Labrador Sea during winter 1994–1995. *J. Phys. Oceanogr.* **29**, 2065–2098. [5.5]
- Lindstrom, E., R. Lukas, R. Fine et al., 1987: The western Equatorial Pacific Ocean Circulation Study. *Nature* **330**, 533–537. [4.4]
- Lindstrom, E., J. Butt, R. Lukas and S. Godfrey, 1990: The flow through Vityaz Strait and St. George's Channel, Papua New Guinea. In: *The Physical Oceanography of Sea Straits*, Kluwer Acad. Publ., Dordrecht, pp. 171–189. [4.3]
- Liu, W.T., 1986: Statistical relation between monthly precipitable water and surface-level humidity over global oceans. *Mon. Wea. Rev.* **114**, 1591–1602. [3.4]
- Liu, W.T., 1990: Remote sensing of surface turbulence flux. In: *Surface Waves and Fluxes*, G. L. Geernaert and W. J. Plant (eds), Kluwer Acad. Publ., Dordrecht, Vol. II, pp. 293–309. [3.4]
- Liu, W.T. and C. Gautier, 1990: Thermal forcing on the tropical Pacific from satellite data. *J. Geophys. Res.* **95**, 13209–13217. [3.4]
- Liu, W.T. and W.G. Large, 1981: Determination of surface stress by Seasat-SASS: A case study with JASIN Data. *J. Phys. Oceanogr.* **11**, 1603–1611. [3.4]
- Liu, W.T. and P.P. Niiler, 1984: Determination of monthly mean humidity in the atmospheric surface layer over oceans from satellite data. *J. Phys. Oceanogr.* **14**, 1451–1457. [3.4]
- Liu, W.T. and P.P. Niiler, 1990: The sensitivity of latent heat flux to the air humidity approximations used in ocean circulation models. *J. Geophys. Res.* **95**, 9745–9753. [3.4]

- Liu, W. T. and W. Tang, 1996: *Equivalent Neutral Wind*. Jet Propulsion Laboratory, Pasadena, CA, JPL Pub. 96-17, 16 pp. [3.4]
- Liu, W. T., K. B. Katsaros and J. A. Businger, 1979: Bulk parameterization of air-sea exchanges in heat and water vapor including the molecular constraints at the interface. *J. Atmos. Sci.* 36, 1722–1735. [3.4]
- Liu, W. T., W. Tang and P. P. Niiler, 1991: Humidity profiles over ocean. *J. Climate* 4, 1023–1034. [3.4]
- Liu, W. T., W. Tang and F. J. Wentz, 1992: Precipitable water and surface humidity over global oceans from SSM/I and ECMWF. *J. Geophys. Res.* 97, 2251–2264. [3.4]
- Liu, W. T., A. Zheng and J. Bishop, 1994: Evaporation and solar irradiance as regulators of the seasonal and interannual variabilities of sea surface temperature. *J. Geophys. Res.* 99, 12623–12637. [3.4]
- Liu, W. T., W. Tang and L. L. Fu, 1995: Recent warming event in the Pacific may be an El Niño. *Eos Trans. Amer. Geophys. Union* 76(43), 429–437. [3.4]
- Liu, W. T., W. Tang and R. Atlas, 1996: Responses of the tropical Pacific to wind forcing as observed by spaceborne sensors and simulated by an ocean general circulation model. *J. Geophys. Res.* 101, 16345–16359. [3.4]
- Liu, W. T., W. Tang and P. S. Polito, 1998: NASA scatterometer provides global ocean-surface wind fields with more structures than numerical weather prediction. *Geophys. Res. Lett.* 25, 761–764. [3.4]
- Liu, W. T., L. Li and W. Tang, 1999: Sensitivity of space-based microwave radiometer observations to ocean surface evaporation. *Proc. IGARSS '99, IEEE*. [3.4]
- Liu, W. T., H. Hu and S. H. Yueh, 2000: Interplay between wind and rain observed in Hurricane Floyd. *Eos Trans. Amer. Geophys. Union* 81(23), 253, 257. [3.4]
- Liu, Z., 1993: Thermocline forced by varying wind. II: annual and decadal Ekman pumping. *J. Phys. Oceanogr.* 23, 2523–2541. [4.4]
- Liu, Z., 1994: A simple model of the mass exchange between the subtropical and tropical ocean. *J. Phys. Oceanogr.* 24, 1153–1165. [4.3, 4.4]
- Liu, Z., 1998: The role of ocean in the response of tropical climatology to global warming: the west/east sea surface temperature contrast. *J. Climate* 11, 864–875. [4.4]
- Liu, Z., 1999a: Planetary wave modes in thermocline circulation: Non-Doppler-shift mode, advective mode and Green mode. *Quart. J. Roy. Meteor. Soc.* 125, 1315–1339. [4.4]
- Liu, Z., 1999b: Forced planetary wave response in a thermocline gyre. *J. Phys. Oceanogr.* 29, 1036–1055. [4.4]
- Liu, Z. and B. Huang, 1998: Why is there a tritium maximum in the central equatorial Pacific thermocline? *J. Phys. Oceanogr.* 28, 1527–1533. [4.4]
- Liu, Z. and S. G. H. Philander, 1995: How different wind patterns affect the tropical-subtropical thermocline circulation in the upper ocean. *J. Phys. Oceanogr.* 25, 449–462. [4.4]
- Liu, Z. and S. Shin, 1999: On thermocline ventilation of active and passive tracers. *Geophys. Res. Lett.* 26, 357–360. [4.4, 5.3]
- Liu, Z. and R. Zhang, 1999: Propagation mechanisms of interdecadal upper ocean variability in the North Pacific. *Geophys. Res. Lett.* 26, 739–742. [5.3]
- Liu, Z., S. G. H. Philander and R. Pacanowski, 1994: A GCM study of tropical-subtropical upper ocean mass exchange. *J. Phys. Oceanogr.* 24, 2606–2623. [4.3, 4.4]
- Liu, Z., L. Wu and E. Bayler, 1999b: Rossby wave–coastal Kelvin wave interaction. I: Low frequency adjustment in a closed basin. *J. Phys. Oceanogr.* 29, 2383–2404. [4.4]
- Loeng, H., V. Ozhigin and B. Adlandsvik, 1997: Water fluxes through the Barents Sea. *ICES. J. Mar. Sci.* 54, 310–317. [7.3]
- Lohmann, G., R. Gerdes and D. Chen, 1995: Sensitivity of the thermohaline circulation in a coupled oceanic GCM – atmospheric EBM experiments. *Climate Dyn.* 12, 403–416. [7.2]
- Lorenc, A. C., 1986: Analysis methods for numerical weather prediction. *Quart. J. Roy. Meteor. Soc.* 112, 1177–1194. [7.1]
- Loschnigg, J. and P. J. Webster, 2000: A coupled ocean–atmosphere system of SST modulation for the Indian Ocean. *J. Climate* 13, 3342–3360. [4.3]
- Lozier, M. S., W. B. Owens and R. G. Curry, 1995: The climatology of the North Atlantic. *Prog. Oceanogr.* 36, 1–44. [5.7, 7.1]
- Lu, P. and J. P. McCreary, 1995: Influence of the ITCZ on the flow of the thermocline water from the subtropical to the equatorial Pacific Ocean. *J. Phys. Oceanogr.* 25, 3076–3088. [4.3, 4.4]
- Lu, P., J. P. McCreary, Jr. and B. A. Klinger, 1998: Meridional circulation cells and sources of the Pacific Equatorial Undercurrent. *J. Phys. Oceanogr.* 28, 62–84. [4.3, 4.4]
- Lueck, R. and T. Mudge, 1997: Topographically-induced mixing around a shallow seamount. *Science* 276, 1831–1833. [5.2]
- Lukas, R., 1986: The termination of the Equatorial Undercurrent in the Eastern Pacific. *Prog. Oceanogr.* 16, 63–90. [4.3]

- Lukas, R., 1987: Horizontal Reynolds stresses in the central equatorial Pacific. *J. Geophys. Res.* 92, 9453–9463. [4.3]
- Lukas, R., 1988: On the role of western Pacific air-sea interaction in the El Niño-Southern Oscillation phenomenon. *Proc. US TOGA Western Pacific Air-Sea Interaction Workshop, Honolulu, HI, US TOGA Report, US TOGA8*, pp. 43–69. [4.3]
- Lukas, R. and E. Firing, 1984: The geostrophic balance of the Pacific Equatorial Undercurrent. *Deep-Sea Res.* 31, 61–66. [4.3]
- Lukas, R. and E. Firing, 1985: The annual Rossby wave in the central Equatorial Pacific Ocean. *J. Phys. Oceanogr.* 15, 55–67. [4.3]
- Lukas, R. and E.J. Lindstrom, 1991: The mixed layer of the western equatorial Pacific Ocean. *J. Geophys. Res.* 96(suppl.), 3343–3357. [4.3]
- Lukas, R., E. Firing, P. Hacker *et al.*, 1991: Observations of the Mindanao Current during the Western Equatorial Pacific Ocean Circulation Study. *J. Geophys. Res.* 96, 7089–7104. [4.4]
- Lukas, R., T. Yamagata and J.P. McCreary, 1996: Pacific low-latitude western boundary currents and the Indonesian throughflow. *J. Geophys. Res.* 101, 12209–12216. [4.7]
- Lundberg, L. and P. M. Haugan, 1996: A Nordic Seas–Arctic Ocean carbon budget from volume flows and inorganic carbon data. *Glob. Biogeochem. Cycles* 10, 493–510. [6.3]
- Lupton, J.E., 1996: A far-field helium plume from Loihi Seamount. *Science* 272, 976–979. [5.8]
- Lupton, J.E., 1998: Hydrothermal helium plumes in the Pacific Ocean. *J. Geophys. Res.* 103, 15853–15868. [4.2, 5.8]
- Lusquinos, A.L., 1963: Extreme temperatures in the Weddell Sea. *Arbok Univ. Bergen, Mat. Naturv. Ser.* 23, 3–19. [5.8]
- Luther, D.S. and E.S. Johnson, 1990: Eddy energetics in the upper equatorial Pacific during the Hawaii-to-Tahiti Shuttle experiment. *J. Phys. Oceanogr.* 20, 913–944. [4.3]
- Luther, D.S. and the SAFDE PIs, 1997: The Sub-Antarctic Flux and Dynamics Experiment (SAFDE). *International WOCE Newsletter*, No. 29, 32–35, WOCE International Project Office. (unpublished document). [4.6]
- Luther, D.S., D.R. Watts, A.D. Chave, J.G. Richman and S.R. Rintoul, 1998: *The Sub-Antarctic Flux and Dynamics Experiment (SAFDE): Overview with Some Descriptive Results*. WOCE Conference on Ocean Circulation and Climate, Halifax, Canada, 24–29 May 1998 (unpublished document) p. 67. [4.6]
- Luther, M.E. and J.J. O'Brien, 1985: A model of the seasonal circulation of the Arabian Sea forced by observed winds. *Prog. Oceanogr.* 14, 353–385. [4.3]
- Luther, M.E. and J.J. O'Brien, 1989: Modelling the variability in the Somali Current. Mesoscale/synoptic coherent structures. In: *Geophysical Turbulence*, J.C.J. Nihoul and B.M. Jamart (eds), Elsevier Science Publishers B.V., Amsterdam, pp. 373–386. [4.3]
- Luther, M.E., J.J. O'Brien and A.H. Meng, 1985: Morphology of the Somali Current system during the Southwest Monsoon. In: *Coupled Ocean-Atmosphere Models*, J. C. J. Nihoul (ed.), Elsevier, Amsterdam, pp. 405–437. [4.3]
- Lutjeharms, J.R.E., 1996: The exchange of water between the South Indian and South Atlantic Oceans. In: *The South Atlantic: Present and Past Circulation*, G. Wefer, W.H. Berger, G. Siedler and D.J. Webb (eds), Springer-Verlag, Berlin, pp. 125–162. [4.7]
- Lutjeharms, J. and J. Cooper, 1996: Inter-ocean leakage through Agulhas current filaments. *Deep-Sea Res.* 43, 213–238. [4.7]
- Lutjeharms, J. and D. Webb, 1995: Modelling the Agulhas Current system with FRAM (Fine Resolution Antarctic Model). *Deep-Sea Res.* 42, 523–551. [4.7]
- Lux, M., H. Mercier and M. Arhan, 2001: Interhemispheric exchanges of mass and heat in the equatorial Atlantic in January–March 1993. *Deep-Sea Res.* (in press). [4.3]
- Luyten, J.R. and D.H. Roemmich, 1982: Equatorial currents at semiannual period in the Indian Ocean. *J. Phys. Oceanogr.* 12, 406–413. [3.3, 4.3]
- Luyten, J.R. and J. Swallow, 1976: Equatorial undercurrents. *Deep-Sea Res.* 23, 999–1001. [4.3, 5.2]
- Luyten, J.R., J. Pedlosky and H. Stommel, 1983: The ventilated thermocline. *J. Phys. Oceanogr.* 13, 292–309. [4.2, 4.3, 4.4, 5.3, 5.4]
- Lysne, J., P. Chang and B. Giese, 1997: Impact of the extratropical Pacific on equatorial variability. *Geophys. Res. Lett.* 24, 2589–2592. [4.4]
- Maamaatuaiahutapu, K., V. Garcon, C. Provost and H. Mercier, 1998: Transports of the Brazil and Malvinas Currents at their confluence. *J. Mar. Res.* 56, 417–438. [1.2]
- MacDonald, A.M., 1993: Property fluxes at 30°S and their implications for the Pacific–Indian throughflow and the global heat budget. *J. Geophys. Res.* 98, 6851–6868. [4.7, 6.1]
- MacDonald, A.M., 1995: *Oceanic fluxes of mass, heat and freshwater: A global estimate and perspective*. Ph.D. Thesis, MIT-WHOI, 312 pp. [6.2]
- MacDonald, A.M., 1998: The global ocean circulation: a hydrographic estimate and regional

- analysis. *Prog. Oceanogr.* **41**, 281–382. [4.6, 5.2, 6.1, 7.1]
- MacDonald, A. M.** and C. Wunsch, 1996: An estimate of global ocean circulation and heat fluxes. *Nature* **382**, 436–439. [2.2, 3.3, 4.2, 4.3, 4.7, 6.1, 6.3, 7.1]
- MacDonald, A. M.**, J. Candela and H. L. Bryden, 1994: An estimate of net heat transport through the Strait of Gibraltar. In: *Seasonal and Interannual variability of the Western Mediterranean Sea*, P. E. La Violette (ed.), Coastal and Estuarine Studies, American Geophysical Union, Washington, DC, Vol. 46, pp. 13–32. [5.7]
- MacDonald, A. M.**, T. Suga and R. G. Curry, 2001: An isopycnally averaged North Pacific climatology. *J. Geophys. Res.* (submitted). [7.1]
- Madden, R. A.** and P. R. Julian, 1994: Observations of the 40–50 day tropical oscillation: a review, *Mon Weather Rev.*, **122**, 814–827.
- Madec, G.** and P. Delecluse, 1997: The OPA/ARPEGE and OPA/LMD global ocean atmosphere coupled model. *International WOCE Newsletter*, No. 26, 12–15, WOCE International Project Office (unpublished document). [2.3]
- Madec, G.**, P. Delecluse, M. Imbard and C. Levy, 1998: *OPA8.1 ocean general circulation model reference manual*. Note no. 11, Institut Pierre et Simon Laplace, Université Pierre-et-Marie Curie, Place Jussieu, Paris, France, 91 pp. [2.3]
- Maes, C.**, 1998: Estimating the influence of salinity on sea level anomaly in the ocean. *Geophys. Res. Lett.* **25**, 3551–3554. [3.3, 4.7]
- Maier-Reimer, E.**, U. Mikolajewicz and K. Hasselmann, 1993: Mean circulation of the Hamburg LSG OGCM and its sensitivity to the thermohaline surface forcing. *J. Phys. Oceanogr.* **23**, 731–757. [2.3]
- Maier-Reimer, E.**, U. Mikolajewicz and A. Winguth, 1996: Future ocean uptake of CO₂: interaction between ocean circulation and biology. *Climate Dyn.* **2**, 711–721. [2.3]
- Malanotte-Rizzoli, P.**, 1996: *Modern Approaches to Data Assimilation in Ocean Modeling*. Elsevier, Amsterdam, The Netherlands, Vol. 61, 455 pp. [7.1, 7.2]
- Malkus, J. S.** 1962: *Interchange of properties between sea and air: Large scale interaction*. The Sea, M. N. Hill, Ed., Vol. 1, Wiley (Interscience), New York, 88–294. [3.4]
- Malmberg, Sv.-A.**, 1983: Hydrographic investigations in the Iceland and Greenland Seas in late winter 1971 – ‘Deep Water Project.’ *Jökull* **33**, 133–140. [7.3]
- Maltrud, M. E.**, R. D. Smith, A. J. Semtner and R. C. Malone, 1998: Global eddy-resolving ocean simulations driven by 1985–1995 atmospheric winds. *J. Geophys. Res.* **103**, 30825–30853. [2.2, 4.6]
- Manabe, S.** and R. J. Stouffer, 1979: A CO₂-climate sensitivity study with a mathematical model of the global climate. *Nature* **282**, 491–493. [2.2]
- Manabe, S.** and R. J. Stouffer, 1980: Sensitivity of a climate model to an increase of CO₂ concentration in the atmosphere. *J. Geophys. Res.* **85**, 5529–5554. [2.2]
- Manabe, S.** and R. J. Stouffer, 1988: Two stable equilibria of a coupled ocean–atmosphere model. *J. Climate* **1**, 841–866. [1.2, 2.3, 5.6]
- Manabe, S.** and R. J. Stouffer, 1993: Century-scale effects of increased atmospheric CO₂ on the ocean–atmosphere system. *Nature* **364**, 215–218. [1.1, 2.3, 7.3]
- Manabe, S.** and R. J. Stouffer, 1994: Multiple century response of a coupled ocean–atmosphere model to an increase of atmospheric carbon dioxide. *J. Climate* **7**, 5–23. [2.1, 7.3]
- Manabe, S.** and R. J. Stouffer, 1997: Coupled ocean–atmosphere model response to freshwater input: Comparison to Younger Dryas event. *Paleoceanography* **12**, 321–336. [1.2, 2.3]
- Manabe, S.** and R. T. Wetherald, 1975: The effect of doubling CO₂ concentration on the climate of a general circulation model. *J. Atmos. Sci.* **32**, 3–15. [2.2]
- Manabe, S.**, K. Bryan and M. J. Spelman, 1979: A global ocean–atmosphere model with seasonal variation for future studies of climate sensitivity. *Dyn. Atmos. Oceans* **3**, 393–426. [2.3]
- Manabe, S.**, R. J. Stouffer, M. J. Spelman and K. Bryan, 1991: Transient responses of a coupled ocean–atmosphere model to gradual changes of atmospheric CO₂. Part I: Annual mean response. *J. Climate* **4**, 785–818. [2.3]
- Manabe, S.**, M. J. Spelman and R. J. Stouffer, 1992: Transient response of a coupled ocean–atmosphere model to gradual changes of atmospheric CO₂. Part II: Seasonal response. *J. Climate* **5**, 105–126. [6.1]
- Mann, C. R.**, 1969: Temperature and salinity characteristics of the Denmark Strait overflow. *Deep-Sea Res.* (suppl. 16), 125–137. [5.6]
- Mantisi, F.**, C. Beauverger, A. Poisson and N. Metzl, 1991: Chlorofluoromethanes in the western Indian sector of the Southern Ocean and their relations with geochemical tracers. *Mar. Chem. Amsterdam* **35**(1–4), 151–167. [4.6]
- Mantua, N. J.**, S. R. Hare, Y. Zhang, J. M. Wallace and R. C. Francis, 1997: A Pacific interdecadal climate oscillation with impacts on salmon

- production. *Bull. Amer. Meteor. Soc.* 78, 1069–1079. [7.1, 7.3]
- Mantyla, A.W.**, 1980: Electrical conductivity comparisons of standard seawater batches P29 to P84. *Deep-Sea Res.* 27, 837–846. [3.1]
- Mantyla, A.W.**, 1994: The treatment of inconsistencies in Atlantic deep water salinity data. *Deep-Sea Res.* 41, 1387–1405. [7.3]
- Mantyla, A.W.** and J. L. Reid, 1995: On the origins of deep and bottom waters of the Indian Ocean. *J. Geophys. Res.* 100, 2417–2439. [4.6]
- Markham, C.G** and D. R. McLain, 1977: Sea surface temperature related to rain in Ceara, north-eastern Brazil. *Nature* 265, 320–323. [1.2]
- Marotzke, J.**, 1997: Boundary mixing and the dynamics of three-dimensional thermohaline circulations. *J. Phys. Oceanogr.* 27, 1713–1728. [2.3, 4.2]
- Marotzke, J.** and P. H. Stone, 1995: Atmospheric transports, the thermohaline circulation and flux adjustments in a simple coupled model. *J. Phys. Oceanogr.* 25, 1350–1364. [2.3]
- Marotzke, J.** and J. Willebrand, 1991: Multiple equilibria of the global thermohaline circulation. *J. Phys. Oceanogr.* 21, 1372–1385. [2.1]
- Marotzke, J.** and C. Wunsch, 1993: Finding the steady state of a general circulation model through data assimilation: Application to the North Atlantic Ocean. *J. Geophys. Res.* 98, 20149–20167. [6.1]
- Marotzke, J.** and J. Willebrand, 1996: The North Atlantic mean circulation: combining data and dynamics. In: *The Warmwatersphere of the North Atlantic Ocean*, W. Krauss, ed. 55–90. [7.1]
- Marotzke, J.**, R. Giering, Q. K. Zhang, D. Stammer, C. N. Hill and T. Lee, 1999: Construction of the adjoint MIT ocean general circulation model and application to Atlantic heat transport sensitivity. *J. Geophys. Res.* 104, 29529–29548. [7.1]
- Marsh, J.G.**, C. J. Koblinsky, F. Lerch *et al.*, 1990: Dynamic sea surface topography, gravity, and improved orbit accuracies from the direct evaluation of Seasat altimeter data. *J. Geophys. Res.* 95, 13129–13150. [3.3]
- Marsh, R.**, 2000: Recent variability of the North Atlantic thermohaline circulation inferred from surface heat and freshwater fluxes. *J. Climate* 13, 3239–3260. [5.1]
- Marsh, R.** and A. L. New, 1996: Modeling 18° water variability. *J. Phys. Oceanogr.* 26, 1059–1080. [5.4]
- Marsh, R.**, M. J. Roberts, R. A. Woods and A. L. New, 1996: An intercomparison of a Bryan-Cox-type ocean model and an isopycnic ocean model. Part II: The subtropical gyre and meridional heat transport. *J. Phys. Oceanogr.* 26, 1528–1551. [2.2]
- Marsh, R.**, A. J. G. Nurser, A. P. Megann and A. L. New, 2000: Water mass transformation in the Southern Ocean of a global isopycnic coordinate GCM. *J. Phys. Oceanogr.* 30, 1013–1045. [4.7]
- Marshall, D.**, 1995a: Influence of topography on the large-scale ocean circulation. *J. Phys. Oceanogr.* 25, 1622–1635. [4.6]
- Marshall, D.**, 1995b: Topographic steering of the Antarctic Circumpolar Current. *J. Phys. Oceanogr.* 25, 1636–1650. [4.6]
- Marshall, D.**, 1997: Subduction of water masses in an eddying ocean. *J. Mar. Res.* 55, 201–222. [5.3]
- Marshall, D.** and J. Marshall, 1995: On the thermodynamics of subduction. *J. Phys. Oceanogr.* 25, 138–151. [5.3]
- Marshall, J.C.** and A. J. G. Nurser, 1992: Fluid dynamics of oceanic thermocline ventilation. *J. Phys. Oceanogr.* 22, 583–595. [5.3]
- Marshall, J.** and F. Schott, 1999: Open-ocean convection: observations, theory and models. *Rev. Geophys.* 37, 1–64. [1.2, 5.5, 5.7]
- Marshall, J.** and G. Shutts, 1981: A note on rotational and divergent eddy fluxes. *J. Phys. Oceanogr.* 11, 1677–1680. [4.6]
- Marshall, J.C.**, A. J. G. Nurser and R. G. Williams, 1993a: Inferring the subduction rate and period over the North Atlantic. *J. Phys. Oceanogr.* 23, 1315–1329. [5.3, 5.4]
- Marshall, J.**, D. Olbers, H. Ross and D. Wolf-Gladrow, 1993b: Potential vorticity constraints on the dynamics and hydrography in the Southern Ocean. *J. Phys. Oceanogr.* 23, 465–487. [4.6]
- Marshall, J.**, A. Adcroft, C. Hill, L. Perelman and C. Heisey, 1997a: A finite-volume, incompressible Navier-Stokes model for studies of the ocean on parallel computers. *J. Geophys. Res.* 102, 5753–5766. [7.1]
- Marshall, J.**, C. Hill, L. Perelman and A. Adcroft, 1997b: Hydrostatic, quasi-hydrostatic and non-hydrostatic ocean modeling. *J. Geophys. Res.* 102, 5733–5752. [7.1, 7.2]
- Marshall, J.**, D. Jamous and J. Nilsson, 1999: Reconciling thermodynamic and dynamic methods of computation of water-mass transformation rates. *Deep-Sea Res.* 46, 545–572. [5.1, 5.2, 5.3]
- Martel, F.** and C. Wunsch, 1993a: The North Atlantic circulation in the early 1980s – an estimate from inversion of a finite difference model. *J. Phys. Oceanogr.* 23, 898–924. [3.3, 6.3]
- Martel, F.** and C. Wunsch, 1993b: Combined inversion of hydrography, current meter data and altimetric elevations for the North Atlantic

- circulation. *Manuscripta Geodaetica* **18**, 219–226. [3.3]
- Martin**, T. and P. Wadhams, 1999: Sea-ice flux in the East Greenland Current. *Deep-Sea Res.* **46**, 1063–1082. [1.2]
- Maslanik**, J.A., M.C. Serreze and R.G. Barry, 1996: Recent decreases in Arctic summer ice cover and linkages to atmospheric circulation anomalies. *Geophys. Res. Lett.* **23**, 1677–1680. [7.3]
- Masuda**, K., 1988: Meridional heat transport by the atmosphere and the ocean: Analysis of FGGE data. *Tellus* **40A**, 285–302. [6.1]
- Masumoto**, Y. and G. Meyers, 1998: Forced Rossby waves in the southern tropical Indian Ocean. *J. Geophys. Res.* **103**, 27589–27602. [3.3]
- Masumoto**, Y. and T. Yamagata, 1993: Simulated seasonal circulation in the Indonesian seas. *J. Geophys. Res.* **98**, 12501–12509. [4.7]
- Masuzawa**, J., 1969: Subtropical Mode Water. *Deep-Sea Res.* **16**, 463–472. [5.4]
- Masuzawa**, J., 1972: Water characteristics of the North Pacific central region. In: *Kuroshio – Its Physical Aspects*, H. Stommel and K. Yoshida (eds), University of Tokyo Press, Tokyo, pp. 95–127. [5.4]
- Mata M.**, M. Tomczak, S. Wijffels and J.A. Church, 2000: East Australian Current Volume Transport at 30°S: Estimates from the WOCE hydrographic section PR11/P6 and the PCM3 current meter array. *J. Geophys. Res.* (accepted). [1.2]
- Matear**, R.J. and Hirst, A.C., 1999: Climate change feedback on the future oceanic CO₂ uptake. *Tellus* **51B**, 722–733. [1.1, 1.2]
- Mauritzen**, C., 1996a: Production of dense overflow waters feeding the North Atlantic across the Greenland–Scotland Ridge. Part 1: Evidence for a revised circulation scheme. *Deep-Sea Res.* **43**, 769–806. [5.5, 5.6]
- Mauritzen**, C., 1996b: Production of dense overflow waters feeding the North Atlantic across the Greenland–Scotland Ridge. Part 2: An inverse model. *Deep-Sea Res.* **43**, 807–835. [5.6]
- Mauritzen**, C. and S. Hakkinnen, 1997: Influence of sea ice on the thermohaline circulation in the Arctic–North Atlantic Ocean. *Geophys. Res. Lett.* **24**, 3257–3260. [7.2]
- Maury**, M.F., 1859: *The Physical Geography of the Sea*. Harper and Bros, NY. [7.4]
- Maxworthy**, T. and S. Narimousa, 1994: Unsteady, turbulent convection into a homogeneous, rotating fluid with oceanographic applications. *J. Phys. Oceanogr.* **24**, 865–887. [5.5]
- Mayer**, D.A. and R.H. Weisberg, 1993: A description of COADS surface meteorological fields and the implied Sverdrup transports for the Atlantic Ocean from 30°S to 60°N. *J. Phys. Oceanogr.* **23**, 2201–2221. [4.3]
- McCann**, M.P., A.J. Semtner, Jr. and R.M. Chervin, 1994: Transports and budgets of volume, heat, and salt from a global eddy-resolving ocean model. *Climate Dyn.* **10**, 59–80. [6.2]
- McCarthy**, M.C. and L.D. Talley, 1999: Three-dimensional isoneutral potential vorticity structure in the Indian Ocean. *J. Geophys. Res.* **104**, 13251–13267. [5.4, 7.1]
- McCarthy**, M.C., L.D. Talley and M.O. Baringer, 1997: Deep upwelling and diffusivity in the southern Central Indian Basin. *Geophys. Res. Lett.* **24**, 2801–2804. [4.5]
- McCarthy**, M.C., L.D. Talley and D.L. Roemmich, 2000: Seasonal to interannual variability from XBT and TOPEX/POSEIDON data in the South Pacific subtropical gyre. *J. Geophys. Res.* (in press). [7.1]
- McCartney**, M.S., 1977: Subantarctic Mode Water. In: *A voyage of Discovery, George Deacon 70th Anniversary Volume*. M. Angel (ed.), Pergamon Press, Oxford, pp. 103–119. [4.6, 5.4, 6.2, 7.3]
- McCartney**, M.S., 1982: The subtropical circulation of Mode Waters. *J. Mar. Res.* **40**(suppl.), 427–464. [4.4, 4.6, 5.3, 5.4]
- McCartney**, M.S., 1992: Recirculating components to the deep boundary current of the northern North Atlantic. *Prog. Oceanogr.* **29**, 283–383. [7.1, 7.3]
- McCartney**, M.S. and C. Mauritzen, 2000: On the origin of the warm inflow to the Nordic Seas. *Prog. Oceanogr.* (submitted). [5.7]
- McCartney**, M.S. and L.D. Talley, 1982: The subpolar mode water of the North Atlantic Ocean. *J. Phys. Oceanogr.* **12**, 1169–1188. [5.4, 7.1]
- McCartney**, M.S. and M. Woodgate-Jones, 1991: A deep-reaching anticyclonic eddy in the subtropical gyre of the eastern South Atlantic. *Deep-Sea Res.* **38**(suppl.), S411–S443. [7.3]
- McCartney**, M.S., R.G. Curry and H.F. Bezdek, 1996: North Atlantic's Transformation Pipeline chills and redistributes Subtropical Water. *Oceanus* **39** (2), 19–23. [7.3]
- McCartney**, M.S., R.G. Curry and H.F. Bezdek, 1997: The interdecadal warming and cooling of Labrador Sea Water. *ACCP Notes* **IV**(1), 1–11. [7.3]
- McClean**, J.L., A.J. Semtner and V. Zlotnicki, 1997: Comparisons of mesoscale variability in the Semtner-Chervin 1/4° model, the Los Alamos Parallel Ocean Program 1/6° model, and TOPEX/POSEIDON data. *J. Geophys. Res.* **102**, 25203–25226. [2.2, 3.3]

- McComas, C.H. and F.P. Bretherton, 1977: Resonant interaction of oceanic internal waves. *J. Geophys. Res.* 82, 1397–1412. [5.2]
- McComas, C.H. and P. Muller, 1981: The dynamic balance of internal waves. *J. Phys. Oceanogr.* 11, 970–986. [5.2]
- McCreary, J., 1984: Equatorial beams. *J. Mar. Res.* 42, 395–430. [4.3]
- McCreary, J. and P. Kundu, 1988: A numerical investigation of the Somali Current during the southwest Monsoon. *J. Mar. Res.* 46, 25–58. [4.4]
- McCreary, J. and P. Lu, 1994: On the interaction between the subtropical and the equatorial oceans: the subtropical cell. *J. Phys. Oceanogr.* 24, 466–497. [4.3, 4.4]
- McCreary, J.P., Jr. and Z. Yu, 1992: Equatorial dynamics in a 2-1/2 layer model. *Prog. Oceanogr.* 29, 61–132. [4.3]
- McDonagh, E. and K. Heywood, 1999: The origin of an anomalous ring in the southeast Atlantic. *J. Phys. Oceanogr.* 29, 2050–2064. [4.7]
- McDougall, T.J., 1984: The relative roles of diapycnal and isopycnal mixing on subsurface water mass conversion. *J. Phys. Oceanogr.* 14, 1577–1589. [5.1]
- McDougall, T.J., 1985a: Double-diffusive interleaving. Part I: Linear stability analysis. *J. Phys. Oceanogr.* 15, 1532–1541. [5.2]
- McDougall, T.J., 1985b: Double-diffusive interleaving. Part II: Finite-amplitude, steady-state interleaving. *J. Phys. Oceanogr.* 15, 1542–1556. [5.2]
- McDougall, T.J., 1987: Thermobaricity, cabbeling and water mass conversion. *J. Geophys. Res.* 92, 5448–5464. [5.1]
- McDougall, T.J., 1988: Some implications of ocean mixing for ocean modelling. In: *Small-Scale Turbulence and Mixing in the Ocean*, J.C.J. Nihoul and B.M. Jamart (eds), Elsevier Science Publ., Amsterdam, pp. 21–36. [5.2]
- McDougall, T.J., 1998: Three-dimensional residual-mean theory. In: *Ocean Modeling and Parameterization*, E.P. Chassignet and J. Verron (eds), Kluwer Acad. Publ., Dordrecht, pp. 269–302. [5.2]
- McDougall, T.J. and P.C. McIntosh, 1996: The temporal-residual-mean velocity. Part I: Derivation and the scalar conservation equations. *J. Phys. Oceanogr.* 26, 2653–2665. [5.2]
- McDougall, T.J. and P.C. McIntosh, 2000: The temporal-residual-mean velocity. Part II: Isopycnal interpretation and the tracer and momentum equations. *J. Phys. Oceanogr.* (in press). [5.2]
- McDowell, S.E. and H.T. Rossby, 1978: Mediterranean water: an intense mesoscale eddy off the Bahamas. *Science* 202, 1085–1087. [3.2]
- McElligott, S., R.H. Byrne, K. Lee, R. Wanninkhof, F.J. Millero and R.A. Feely, 1998: Discrete water column measurements of CO₂ fugacity and pHT in seawater: A comparison of direct measurements and thermodynamic calculations. *Mar. Chem.* 60, 63–73. [6.3]
- McIntosh, P.C. and T.J. McDougall, 1996: Isopycnal Averaging and the Residual Mean Circulation. *J. Phys. Oceanogr.* 26, 1655–1660. [4.6]
- McIntosh, P.C. and S.R. Rintoul, 1997: Do box inverse models work? *J. Phys. Oceanogr.* 27, 291–308. [3.1]
- McLaughlin, F.A., E.C. Carmack, R.W. Macdonald and J.K.B. Bishop, 1996: Physical and geochemical properties across the Atlantic/Pacific water mass front in the southern Canadian Basin. *J. Geophys. Res.* 101, 1183–1197. [7.3]
- McNichol, A.P., G.A. Jones, D.L. Hutton, A.R. Gagnon and R.M. Key, 1994: The rapid preparation of seawater SC₂ for radiocarbon analysis at the National Ocean Sciences AMS Facility. *Radiocarbon* 36, 237–246. [5.8]
- McPhaden, M.J., 1982a: Variability in the Central Equatorial Indian Ocean. Part I: Ocean Dynamics. *J. Mar. Res.* 40, 157–176. [4.3]
- McPhaden, M.J., 1982b: Variability in the Central Equatorial Indian Ocean, Part II: Oceanic Heat and Turbulent Energy Balances. *J. Mar. Res.* 40, 403–419. [4.3]
- McPhaden, M.J., 1984: On the dynamics of the equatorial subsurface countercurrents. *J. Phys. Oceanogr.* 14, 1216–1225. [4.3, 4.4]
- McPhaden, M.J., 1985: Fine-structure variability observed from CTD measurements from the central equatorial Pacific. *J. Geophys. Res.* 90, 11726–11740. [4.3]
- McPhaden, M.J., 1993: Trade wind fetch related variations in Equatorial Undercurrent depth, speed, and transport. *J. Geophys. Res.* 98, 2555–2559. [4.3]
- McPhaden, M.J., 1995: The tropical atmosphere-ocean array is completed. *Bull. Amer. Meteor. Soc.* 76, 739–741. [7.4]
- McPhaden, M.J., 1999: Genesis and evolution of the 1997–98 El Niño. *Science* 283, 950–954. [7.4]
- McPhaden, M.J. and R.A. Fine, 1988: A dynamical interpretation of the tritium maximum in the Central Equatorial Pacific. *J. Phys. Oceanogr.* 18, 1454–1457. [4.3, 4.4, 5.8]
- McPhaden, M.J. and S.P. Hayes, 1991: On the variability of winds, sea surface temperature and surface layer heat content in the western equatorial Pacific. *J. Geophys. Res.* 96, suppl., 3331–3342. [4.3]
- McPhaden, M.J., A.J. Busalacchi, R. Cheney *et al.*, 1998: The Tropical Ocean–Global Atmosphere

- observing system: A decade of progress. *Special issue: The TOGA decade: Reviewing the progress of El Niño research and prediction. J. Geophys. Res.* 103, 14169–14240. [1.2, 4.3, 7.4]
- McPhee, M.G., T.P. Stanton, J.H. Morison and D.G. Martinson, 1998: Freshening of the Upper Ocean in the Central Arctic: Is perennial sea ice disappearing? *Geophys. Res. Lett.* 25, 1729–1732. [7.3]
- McWilliams, J.C., 1996: Modelling the oceanic general circulation. *Ann. Rev. Fluid Mech.* 28, 215–248. [2.2, 6.2]
- McWilliams, J.C., 1998: Oceanic general circulation models. In: *Ocean Modeling and Parameterization*: E.P. Chassignet and J. Verron (eds), Kluwer Acad. Publ., Dordrecht, pp. 1–44. [2.2, 7.2]
- McWilliams, J.C. and J.E. Masterson, 1982: *Plan for the Development and Utilization of Ocean Surface Drifting Buoys (Drifters)*. UCAR Special Publication, September 1982, Boulder, CO, 37 pp. [4.1]
- McWilliams, J.C., G. Danabasoglu and P.R. Gent, 1996, Tracer budgets in the warm water sphere. *Tellus* 48, 179–192. [5.1]
- McWilliams, J.C., W.R. Holland and J.H.S. Chow, 1978: A description of numerical Antarctic Circumpolar Currents. *Dyn. Atmos. Oceans* 2, 213–291. [4.6]
- McWilliams, J.C., N.J. Norton, P.R. Gent and D.B. Haidvogel, 1990: A linear balance model of wind-driven, mid-latitude ocean circulation. *J. Phys. Oceanogr.* 20, 1349–1378. [7.2]
- McWilliams, J.C., G. Danabasoglu and P.R. Gent, 1996: Tracer budgets in the Warmwatersphere. *Tellus* 48, 179–192. [5.1]
- MEDOC Group, 1970: Observations of formation of deep-water in the Mediterranean Sea, 1969. *Nature* 227, 1037–1040. [5.7]
- Meehl, G.A., J.W. Hurrell and H. van Loon, 1998: A modulation of the mechanism of the semiannual oscillation in the Southern Hemisphere. *Tellus* 50A, 442–450. [7.3]
- Mehrbach, C., C.H. Culberson, J.E. Hawley and R.M. Pytkowicz, 1973: Measurement of the apparent dissociation constants of carbonic acid in seawater at atmospheric pressure. *Limnol. Oceanogr.* 18, 897–907. [6.3]
- Mehta V.M. and T. Delworth 1995: Decadal variability of the Tropical Atlantic Ocean surface temperature in shipboard measurements and in a global ocean-atmosphere model. *J. Climate* 8, 172–190. [1.2]
- Meincke, J. and B. Rudels, 1995: Greenland Sea Deep Water: A balance between convection and advection. *Nordic Seas Symposium*, Hamburg, March 1995. *Extended Abstr. Vol.*, University of Hamburg, pp. 143–148. [7.3]
- Meincke, J., S. Jonsson and J.H. Swift, 1992: Variability of convective conditions in the Greenland Sea. *ICES Mar. Sci. Symp.* 195, 32–39. [7.3]
- Meincke, J., B. Rudels and H.J. Friedrich, 1999: The Arctic Ocean–Nordic Seas Thermohaline System. *ICES J. Mar. Sci.* 54, 283–299. [7.3]
- Mellor, G.L. and T. Ezer, 1995: Sea level variations induced by heating and cooling: An evaluation of the Boussinesq approximation in ocean models. *J. Geophys. Res.* 100, 20565–20577. [7.2]
- Mellor, G.L. and T. Yamada, 1982: Development of a turbulence closure model for geophysical fluid problems. *Geophys. and Space Phys.* 20, 851–875. [7.2]
- Mellor, G.L., T. Ezer and L.-Y. Oey, 1994: The pressure gradient conundrum of sigma coordinate ocean models. *J. Atmos. Oceanic Technol.* 11, 1126–1134. [7.2]
- Menemenlis, D. and M. Chechelnitsky, 2000: Error estimates for an ocean general circulation model from altimeter and acoustic tomography data. *Mon. Wea. Rev.* 128, 763–778. [7.1]
- Mensch, M., R. Bayer, J.L. Bullister, P. Schlosser and R. Weiss, 1996: The distribution of tritium and CFCs in the Weddell Sea during the mid 1980s. *Prog. Oceanogr.* 38, 377–415. [5.8]
- Mensch, M., W.M. Smethie, Jr., P. Schlosser, R. Weppernig and R. Bayer, 1998: Transient tracer observations from the western Weddell Sea during the drift and recovery of Ice Station Weddell. In: *Ocean, Ice and Atmosphere: Interactions at Antarctic Continental Margin*, Vol. 75 of Antarctic Research Series, S.S. Jacobs and R. Weiss (eds), American Geophysical Union, Washington, DC, pp. 241–256. [4.6]
- Mercier, H. and K.G. Speer, 1998: Transport of bottom water in the Romanche Fracture Zone and the Chain Fracture Zone. *J. Phys. Oceanogr.* 28, 779–790. [4.5]
- Meredith, M.P., J.M. Vassie, K.J. Heywood and R. Spencer, 1996: On the temporal variability of the transport through Drake Passage. *J. Geophys. Res.* 101, 22485–22494. [4.6]
- Merryfield, W.J., G. Holloway and A.E. Gargett, 1998: Differential vertical transport of heat and salt by weak stratified turbulence. *Geophys. Res. Lett.* 25, 2773–2776. [5.2]
- Merryfield, W.J., G. Holloway and A.E. Gargett, 1999: A global ocean model with double-diffusive mixing. *J. Phys. Oceanogr.* 29, 1124–1142. [7.2]
- Messias, M.-J. and L. Mémery, 1998: South Atlantic chlorofluoromethane distributions along the WHP lines A17, A13, and A14. *International WOCE*

- Newsletter*, No. 31, 21–27, WOCE International Project Office (unpublished document). [5.8]
- Messias, M.-J., C. Andrié, L. Meméry and H. Mercier, 1999:** Tracing the North Atlantic Deep Water through the Romanche and Chain fracture zones with chlorofluoromethanes. *Deep-Sea Res.* **46**, 1247–1278. [5.8]
- Meyers, G., 1979:** On the annual Rossby wave in the tropical North Pacific Ocean. *J. Phys. Oceanogr.* **9**, 663–674. [3.3]
- Meyers, G., 1996:** Variation of Indonesian throughflow and the El Niño-Southern Oscillation. *J. Geophys. Res.* **101**, 12255–12263. [4.3, 4.7, 6.2, 7.4]
- Meyers, G., R.J. Bailey and A.P. Worby, 1995:** Geostrophic transport of Indonesian throughflow. *Deep-Sea Res.* **42**, 1163–1174. [4.3, 4.6, 4.7, 7.1]
- Michaud, R. and J. Derome, 1991:** On the mean meridional transport of energy in the atmosphere and oceans as derived from six years of ECMWF analyses. *Tellus* **43A**, 1–14. [6.1]
- Miller, A.J., D.R. Cayan, T.P. Barnett, N.E. Graham and J.M. Oberhuber, 1994:** Interdecadal variability of the Pacific Ocean: Model response to observed heat flux and wind stress anomalies. *Climate Dyn.* **9**, 287–302. [5.3, 7.3]
- Miller, A.J., D.R. Cayan and W.B. White, 1998:** A westward intensified decadal change in the North Pacific Thermocline and gyre-scale circulation. *J. Climate* **11**, 3112–3127. [4.4, 7.3]
- Miller, D.K. and K.B. Katsaros, 1991:** Satellite-derived surface latent heat fluxes in a rapidly intensifying marine cyclone. *Mon. Wea. Rev.* **120**, 1093–1107. [3.4]
- Millero, F.J., J.-Z. Zhang, K. Lee and D.M. Campbell, 1993:** Titration alkalinity of seawater. *Mar. Chem.* **44**, 661–667. [6.3]
- Millero, F.J., A. Dickson, G. Eischeid *et al.*, 1998:** Total alkalinity measurements in the Indian Ocean during the WOCE World Hydrographic Program CO₂ Survey cruises 1994–1996. *Mar. Chem.* **63**, 9–20. [6.3]
- Milliff, R.F. and J. Morzel, 2001:** The global distribution of the time-average wind-stress curl from NSCAT. *J. Atmos. Sci.* **58**, 109–131. [3.4]
- Milliff, R.F., W.G. Large, J. Morzel, G. Danabasoglu and T.M. Chin, 1999:** Ocean general circulation model sensitivity to forcing from scatterometer winds. *J. Geophys. Res.* **104**, 11337–11358. [3.4, 5.1]
- Mills, E.L., 1983:** Problems of deep-sea biology. An historical perspective. In: *The Sea*, Vol. 8, G.T. Rowe (ed.), John Wiley, NY, pp. 1–79. [2.1]
- Minobe, S., 1997:** A 50–70 year climatic oscillation over the North Pacific and North America. *Geophys. Res. Lett.* **24**, 683–686. [7.3]
- Minster, J.-F., A. Cazenave, Y.V. Serafini, F. Mercier, M.C. Gennero and P. Rogel, 1999:** Annual cycle in mean sea level from TOPEX/POSEIDON and ERS-1: Inference on the global hydrological cycle. *Glob. Planetary Change* **20**, 57–66. [3.3]
- Mintrop, L. and D.W.R. Wallace, 1999:** *CO₂ in the Northern North Atlantic*. Report of a Workshop at the Hanse Institute for Advanced Study, 9–11 June 1999, Delmenhorst, Germany. Institut für Meereskunde, Kiel, Informal Report, 25 pp. [6.3]
- Mintrop, L., F.F. Perez, M. Gonzalez-Davila, J. Santana-Casiano and A. Koertzinger, 2000:** Alkalinity determination by potentiometry: Intercalibration using three different methods. *Ciencias Marinas* **26**, 23–37. [6.3]
- Mitchell, J.F.B., T.C. Johns, J.M. Gregory and S.F.B. Tett, 1995:** Climate response to increasing levels of greenhouse gases and sulphate aerosols. *Nature* **376**, 501–504. [2.3]
- Mitchell, J.L., J.M. Dastugue, W.J. Teague and Z.R. Hallock, 1990:** The estimation of geoid profiles in the northwest Atlantic from simultaneous satellite altimetry and airborne expendable bathythermograph sections. *J. Geophys. Res.* **95**, 17965–17977. [3.3]
- Mitchum, G.T., 1997:** A tide gauge network for altimeter calibration. In: *IGS/PSMSL Sea Level Workshop*, R. Neilan, P. Woodworth and P. Van Scy (eds), Jet Propulsion Laboratory, Pasadena, CA. [3.3]
- Mitchum, G.T., 1998:** Monitoring the stability of satellite altimeters with tide gauges. *J. Atmos. Oceanic Technol.* **15**, 721–730. [3.3]
- Mitsuzawa, K. and G. Holloway, 1998:** Characteristics of deep currents along trenches in the northwest Pacific. *J. Geophys. Res.* **103**, 13085–13092. [4.2]
- Miyama, T., T. Awaji, K. Akitomo and N. Imasato, 1995:** Study of seasonal transport variations in the Indonesian Seas. *J. Geophys. Res.* **100**, 20517–20541. [4.7]
- MODE Group, The, 1978:** The Mid-Ocean Dynamics Experiment. *Deep-Sea Res.* **25**, 859–910. [1.3, 2.1, 3.2]
- Molcard, R., M. Fieux, J. Swallow, A. Ilahude and J. Banjarnahor, 1994:** Low frequency variability of currents in Indonesian channels. *Deep-Sea Res.* **41**, 1643–1661. [4.7]
- Molcard, R., M. Fieux and A.G. Ilahude, 1996:** The Indo-Pacific throughflow in the Timor Passage. *J. Geophys. Res.* **101**, 12411–12420. [4.7, 6.2]

- Molcard, R., M. Fieux and F. Syamsudin, 2001:** The throughflow within Ombai Strait. *Deep-Sea Res.* (in press). [4.7]
- Molinari, R.L. and E. Johns, 1994:** Upper layer temperature structure of the western Tropical Atlantic. *J. Geophys. Res.* **99**, 18225–18233. [4.3]
- Molinari, R.L., J. Swallow and J.F. Festa, 1986:** Evolution of the near-surface thermal structure in the Western Indian Ocean during FGGE, 1979. *J. Mar. Res.* **44**, 739–762. [4.3]
- Molinari, R.L., D. Olson and G. Reverdin, 1990a:** Surface current distributions in the tropical Indian Ocean derived from the compilations of surface buoy trajectories. *J. Geophys. Res.* **95**, 7217–7238. [4.3]
- Molinari, R.L., E. Johns and J.F. Festa, 1990b:** The annual cycle of meridional heat flux in the Atlantic Ocean at 26.5°N. *J. Phys. Oceanogr.* **20**, 476–482. [2.2]
- Molinari, R.L., R.A. Fine and E. Johns, 1992:** The Deep Western Boundary Current in the tropical North Atlantic. *Deep-Sea Res.* **39**, 1967–1984. [5.8]
- Molinari, R.L., D. Mayer, J. Festa and H. Bezdek, 1997:** Multi-year variability in the near-surface temperature structure of the midlatitude western North Atlantic Ocean. *J. Geophys. Res.* **102**, 3267–3278. [7.3]
- Molinari, R.L., R.A. Fine, W.D. Wilson, R.G. Curry, J. Abell, and M.S. McCartney, 1998:** The arrival of recently formed Labrador Sea Water in the Deep Western Boundary Current at 26.5°N. *Geophys. Res. Lett.* **25**, 2249–2252. [5.8]
- Molinelli, E.J., 1981:** The Antarctic influence on Antarctic intermediate water. *J. Mar. Res.* **39**, 267–293. [4.6]
- Montgomery, R.B., 1938:** Circulation in the upper layers of the southern North Atlantic deduced with the use of isentropic analysis. *Papers in Physical Oceanography and Meteorology* **6**, 1–55. [5.3, 5.4]
- Montgomery, R.B. and E.D. Stroup, 1962:** Equatorial waters and currents at 150°W in July–August 1952. *Johns Hopkins Oceanographic Studies* **1**, 68 pp. [4.4]
- Moore, J.K., M.R. Abbott and J.G. Richman, 1999:** Location and dynamics of the Antarctic Polar Front from satellite sea-surface temperature data. *J. Geophys. Res.* **104**, 3059–3073. [3.3]
- Morawitz, W.M., P.J. Sutton, P.F. Worcester, B.D. Cornuelle, J.F. Lynch and R. Pawlowicz, 1996:** Three-dimensional observations of a deep convective chimney in the Greenland sea during winter 1988/89. *J. Phys. Oceanogr.* **26**, 2316–2348. [4.2]
- Morey, S., J. Shriver and J. O'Brien, 1999:** The effects of Halmahera on the Indonesian throughflow. *J. Geophys. Res.* **104**, 23281–23296. [4.7]
- Morison, J., M. Steele and R. Anderson, 1998a:** Hydrography of the upper Arctic Ocean measured from the Nuclear Submarine, USS PARGO. *Deep-Sea Res.* **45**, 15–38. [7.3]
- Morison, J., K. Aagaard and M. Steele, 1998b:** *Report on the Study of the Arctic Change Workshop*, 10–12 November 1997. University of Washington, ARCSS Report No. 8, 63 pp. [7.3]
- Morison, J., K. Aagaard and M. Steele, 2001:** Recent changes in the Arctic: a review. *Arctic*. (in press). [7.3]
- Morozov, E.G., 1995:** Semidiurnal internal wave field. *Deep-Sea Res.* **42**, 135–148. [4.2]
- Morris, M.Y., 1996:** Mean and low frequency fluctuations in the circulation of the western/central Pacific Ocean. Ph.D. thesis, University of California, San Diego. 211 pp. [4.3]
- Morris, M., D. Roemmich and B. Cornuelle, 1996:** Observations of variability in the South Pacific subtropical gyre. *J. Phys. Oceanogr.* **26**, 2359–2380. [7.1]
- Morris, M., N. Hogg and W.B. Owens, 1997:** Diapycnal mixing estimated from advective budgets in the deep Brazil Basin. *International WOCE Newsletter*, No. 28, 23–25, WOCE International Project Office (unpublished document). [4.5, 5.2]
- Morrow, R.A., J.A. Church, R. Coleman, D.B. Chelton and N. White, 1992:** Eddy momentum flux and its contribution to the Southern Ocean momentum balance. *Nature* **357**, 482–484. [3.3]
- Morrow, R.A., R. Coleman, J.A. Church and D.B. Chelton, 1994:** Surface eddy momentum flux and velocity variance in the Southern Ocean from GEOSAT altimetry. *J. Phys. Oceanogr.* **24**, 2050–2071. [3.3, 4.6]
- Motoi, T., A. Kitoh and H. Koide, 1998:** Antarctic Circumpolar Wave in a coupled ocean–atmosphere model. *Ann. Glaciol.* **27**, 483–487. [2.3]
- Moum, J.N., T.K. Chereskin, M.M. Park and L.A. Ringer, 1987:** Monitoring geostrophic currents at the equator. *Deep-Sea Res.* **34**, 1149–1161. [3.1]
- Moum, J.N., D.A. Caldwell and C.A. Paulson, 1989:** Mixing in the equatorial surface layer and thermocline. *J. Geophys. Res.* **94**, 2005–2021. [5.2]
- Muench, J.E. and E. Kunze, 1999:** Internal wave interactions with equatorial deep jets. Part I: Momentum-flux divergences. *J. Phys. Oceanogr.* **29**, 1453–1467. [4.3, 5.2]
- Muench, J.E., E. Kunze and E. Firing, 1994:** The potential vorticity structure of equatorial deep jets. *J. Phys. Oceanogr.* **24**, 418–428. [5.2]
- Muench, R.D., H.J.S. Fernando and G.R. Stegen, 1990:** Temperature and salinity staircases in the

- northwestern Weddell Sea. *J. Phys. Oceanogr.* **20**, 295–306. [5.2]
- Müller, P., 1995: Ertel's potential vorticity theorem in physical oceanography. *Rev. Geophys.* **33**, 67–97. [4.2]
- Müller, P., G. Holloway, F. Henyey and N. Pomphrey, 1986: Non-linear interactions among internal gravity waves. *Rev. Geophys.* **24**, 493–536. [5.2]
- Müller, T. J. and G. Siedler, 1992: Multi-year current time series in the eastern North Atlantic Ocean. *J. Mar. Res.* **50**, 63–98. [4.5]
- Munk, W.H., 1950: On the wind driven ocean circulation. *J. Meteor.* **7**, 79–93. [4.2]
- Munk, W.H., 1966: Abyssal recipes. *Deep-Sea Res.* **13**, 707–730. [4.2, 4.5, 5.2, 5.8]
- Munk, W.H., 1981: Internal waves and small-scale processes. In: *Evolution of Physical Oceanography*, B. Warren and C. Wunsch (eds), MIT Press, Cambridge, MA, pp. 264–291. [5.2]
- Munk, W.H. and G.F. Carrier, 1950: The wind driven circulation in ocean basins of various shapes. *Tellus* **2**, 158–167. [4.2]
- Munk, W.H. and E. Palmén, 1951: Note on dynamics of the Antarctic Circumpolar Current. *Tellus* **3**, 53–55. [3.3, 4.6]
- Munk, W. and C. Wunsch, 1998: Abyssal recipes II: energetics of tidal and wind mixing. *Deep-Sea Res.* **45**, 1977–2010. [4.2, 5.2, 7.2]
- Münnich, K.O. and W. Roether, 1967: Transfer of bomb-¹⁴C and tritium from the atmosphere to the oceans: Internal mixing of the ocean on the basis of tritium and ¹⁴C profiles. *Radioactive Dating and Low-level Counting*, International Atomic Energy Agency, Vienna, pp. 93–104. [5.8]
- Münnich, M., M. Latif, S. Venzke and E. Maier-Reimer, 1998: Decadal oscillations in a simple coupled model. *J. Climate* **11**, 3309–3319. [7.2]
- Murnane, R.J., J.L. Sarmiento and C. Le Quéré, 1999: Spatial distribution of air-sea CO₂ fluxes and the interhemispheric transport of carbon by the oceans. *Glob. Biogeochem. Cycles* **13**, 287–305. [6.3]
- Murphy, J.M. and J.F.B. Mitchell, 1995: Transient response of the Hadley Centre coupled ocean-atmosphere model to increasing carbon dioxide. Part I. Control climate and flux adjustment. *J. Climate* **8**, 36–80. [2.3]
- Murray, S.P. and D. Arief, 1988: Throughflow into the Indian Ocean through the Lombok Strait. January 1985–January 1986. *Nature* **333**, 444–447. [4.7]
- Murray, S.P., D. Arief, J.C. Kindle and H.E. Hurlburt, 1989: Characteristics of circulation in an Indonesian Archipelago Strait from hydrography, current measurements and modeling results. NATO Advanced Research Workshop on The Physical Oceanography of Sea Straits, Les Arcs, Kluwer Acad. Publ., Dordrecht [4.7]
- Murtugudde, R., A. J. Busalacchi and J. Beauchamp, 1998: Seasonal-to-interannual effects of the Indonesian throughflow on the tropical Indo-Pacific basin. *J. Geophys. Res.* **103**, 21425–21441. [4.7]
- Myers, P.G. and A.J. Weaver, 1997: On the circulation of the North Pacific Ocean: climatology, seasonal cycle and interpentadal variability. *Prog. Oceanogr.* **38**, 1–49. [4.3]
- Myers, R.A., J. Helbig and D. Holland, 1989: *Seasonal and Interannual Variability of the Labrador Current and West Greenland Current*. International Council for the Exploration of the Sea, Copenhagen. ICES CM 1989/C: **16**, 18 pp. [7.3]
- Mysak, L.A., R.G. Ingram, J. Wang and A. van der Baaren, 1996: The anomalous sea-ice extent in Hudson Bay, Baffin Bay and the Labrador Sea during three simultaneous NAO and ENSO episodes. *Atmos. Ocean* **34**(2), 313–343. [7.3]
- Nakamura, H., 1996a: A pycnostad on the bottom of the ventilated portion in the central subtropical North Pacific: Its distribution and formation. *J. Oceanogr.* **52**, 171–188. [5.4]
- Nakamura, H., 1996b: Year-to-year and interdecadal variability in the activity of intraseasonal fluctuations in the Northern Hemisphere wintertime circulation. *Theor. Appl. Climatol.* **55**, 19–32. [7.3]
- Nakamura, T. and T. Hinata, 1999: Seasonal and interannual variations of the Kuroshio south of Japan. *Weather Service Bull.* **66** (special issue), S33–S41 (in Japanese). [7.3]
- Nakamura, H., G. Lin and T. Yamagata, 1997: Decadal climate variability in the North Pacific during recent decades. *Bull. Amer. Meteor. Soc.* **78**, 2215–2225. [7.3]
- National Academy of Sciences, 1983: *Proceedings of a Workshop on Global Observations and Understanding of the General Circulation of the Oceans*. National Academy Press, Washington, DC, 418 pp. [1.3]
- National Research Council, 1982: *Data Management and Computation*, Vol. 1: *Issues and Recommendations*. Committee on Data Management and Computation (CODMAC), Space Science Board, National Research Council, National Academy Press, 167 pp. [1.3]
- National Research Council, 1997: *Satellite Gravity and the Geosphere*, J. Dickey (ed.), National Academy Press, Washington, DC, 112 pp. [3.3]
- Neelin, J.D. and H.A. Dijkstra, 1995: Ocean-atmosphere interaction and the tropical climatology. Part I: The dangers of flux correction. *J. Climate* **8**, 1343–1359. [2.3]

- Neelin, J.D., D.S. Battisti, A.C. Hirst *et al.*, 1998: ENSO theory. *J. Geophys. Res.* 103, 14261–14290. [2.3]
- Neill, C., K.M. Johnson, E. Lewis and D.W.R. Wallace, 1997: Accurate headspace analysis of fCO₂ in discrete water samples using batch equilibration. *Limnol. Oceanogr.* 42, 1774–1783. [6.3]
- Nerem, R.S., 1995: Measuring global mean sea-level variations from TOPEX/POSEIDON altimeter data. *J. Geophys. Res.* 100, 25135–25152. [3.3]
- Nerem, R.S., 1999: Measuring very low frequency sea level variations using satellite altimeter data. *Global and Planetary Change* 20, 157–171. [1.2]
- Nerem, R.S. and G.T. Mitchum, 2000: Sea level changes, pp. 329–349. In: *Satellite Altimetry and Earth Sciences*, L.-L. Fu and A. Cazenave (eds), Academic Press, London. [3.3]
- Nerem, R.S., B.D. Tapley and C.-K. Shum, 1990: Determination of the ocean circulation using Geosat altimetry. *J. Geophys. Res.* 95, 3163–3180. [3.3]
- Nerem, R.S., E. Schrama, C. Koblinsky and B. Beckley, 1994: A preliminary evaluation of ocean topography from the TOPEX/POSEIDON mission. *J. Geophys. Res.* 99, 24565–24583. [3.3]
- Nerem, R.S., B.J. Haines, J. Hendricks, J.-F. Minster, G.T. Mitchum and W.B. White, 1997: Improved determination of global mean sea-level variations using TOPEX/POSEIDON altimeter data. *Geophys. Res. Lett.* 24, 1331–1334. [3.3]
- Nerem, R.S., D.P. Chambers, E.W. Leuliette, G.T. Mitchum and B.S. Giese, 1999: Variations in global mean sea level associated with the 1997–98 ENSO event. *Geophys. Res. Lett.* 26, 3005–3008. [1.2, 3.3, 7.4]
- Neshyba, S.J., C.N.K. Mooers, R.L. Smith and R.T. Barber (eds), 1989: Poleward flows along eastern ocean boundaries. In: *Coastal and Estuarine Studies*, Vol. 34, Springer-Verlag, NY, 374 pp. [1.2]
- Neumann, G. and W.J. Pierson, 1966: *Principles of Physical Oceanography*. Prentice Hall, Englewood Cliffs, NJ, 545 pp. [7.4]
- New, A.L., R. Bleck, Y. Jia, R. Marsh, M. Huddleston and S. Barnard, 1995: An isopycnic model study of the North Atlantic. Part I: Model experiment. *J. Phys. Oceanogr.* 25, 2667–2699. [5.3, 5.4]
- New, A.L., S. Barnard, P. Herrmann and J.-M. Molines, 2000a: On the origin and pathway of the saline inflow to the Nordic Seas: Insight from models. *Prog. Oceanogr.* (in press). [5.7]
- New, A.L., Y. Jia, M. Coulibaly and J. Dengg, 2000b: On the role of the Azores current in the ventilation of the North Atlantic Ocean. *Prog. Oceanogr.* (in press). [5.3]
- Niebauer, H., 1998: Variability in Bering Sea ice cover as affected by a regime shift in the North Pacific in the period 1947–1996. *J. Geophys. Res.* 103, 27717–27737. [4.7]
- Niiler, P.P., 1995: Heat and momentum convergence of the tropical Pacific as measured by Lagrangian drifters. *Proc. of the International Scientific Conference of the Tropical Ocean Global Atmosphere (TOGA) Programme*, WMO/TD #717, 437 pp. [4.1]
- Niiler, P. and N. Barth, 2001: The annual mean surface circulation in the eastern Pacific. *Proceedings of the 25th Anniversary Commemoration, CICECE*, Ensenada, Mexico, September 1998. (in press). [4.1]
- Niiler, P.P. and E.B. Kraus, 1977: One-dimensional models of the upper ocean. In: *Modeling and Prediction of the Upper Layers of the Ocean*, E.B. Kraus (ed.), Pergamon Press, pp. 143–172. [4.1]
- Niiler, P.P. and J.D. Paduan, 1995: Wind-driven motions in the northeast Pacific as measured by Lagrangian drifters. *J. Phys. Oceanogr.* 25, 2819–2830. [2.1]
- Niiler, P.P. and W.S. Richardson, 1973: Seasonal variability of the Florida Current. *J. Mar. Res.* 31, 144–167. [6.1]
- Niiler, P.P., R.E. Davis and H.J. White, 1987: Water-following characteristics of a mixed layer drifter. *Deep-Sea Res.* 34, 1867–1881. [4.1]
- Niiler, P.P., A. Sybrandy, K. Bi, P. Poulain and D. Bitterman, 1995: Measurements of the water-following capability of Holey-sock and TRISTAR drifters. *Deep-Sea Res.* 42, 1951–1964. [4.1]
- Nitta, T. and S. Yamada, 1989: Recent warming of tropical sea surface temperature and its relationship to the Northern Hemisphere circulation. *J. Meteor. Soc. Japan* 67, 375–383. [5.4, 7.3]
- Nittis, K. and A. Lascaratos, 1998: Interannual variability of LIW formation: A high resolution numerical study. *Rapp. Comm. int. Mer Médit. CIESM* 35, 178–179. [5.7]
- NOAA (1997–1998) NOAA Climate Diagnostics Bulletin(s), Figures A 1.1. NCEP, Silver Springs, MD, 79 pp. [4.1]
- Nof, D., 1996: What controls the origin of the Indonesian throughflow? *J. Geophys. Res.* 101, 12301–12314. [4.7]
- Nøst, O.A. and S. Østerhus, 1998: Impact of grounded icebergs on the hydrographic conditions near the Filchner Ice Shelf. In: *Ocean, Ice and Atmosphere: Interactions at Antarctic Continental Margin*, Vol. 75 of Antarctic Research Series, S.S. Jacobs and R. Weiss (eds), American Geophysical Union, Washington, DC, pp. 267–284. [4.6]
- Nowlin, W.D., 1999: A strategy for long-term ocean observations. *Bull. Amer. Meteor. Soc.* 80, 621–627. [3.3, 7.4]

- Nowlin, Jr., W.D. and M. Clifford, 1982: The kinematic and thermohaline zonation of the Antarctic Circumpolar Current at Drake Passage. *J. Mar. Res.* 40(suppl.), 481–507. [4.6]
- Nowlin, Jr., W.D. and J.M. Klinck, 1986: The physics of the Antarctic Circumpolar Current. *Rev. Geophys. Space Phys.* 24, 469–491. [4.6, 4.7]
- Nowlin, Jr., W.D., S.J. Worley and T. Whitworth, III, 1985: Methods for making point estimates of eddy heat flux as applied to the Antarctic circumpolar current. *J. Geophys. Res.* 90, 3305–3324. [4.6]
- Nowlin, W.D. Jr., M. Briscoe, N. Smith *et al.*, 2000: Evolution of a sustained ocean observing system. *Bull. Amer. Meteor. Soc.* (submitted) [7.4]
- Nurser, A.J.G. and J.C. Marshall, 1991: On the relationship between subduction rates and diabatic forcing of the mixed layer. *J. Phys. Oceanogr.* 21, 1793–1802. [7.3]
- Nurser, A.J.G., R. Marsh and R.G. Williams, 1999: Diagnosing water mass formation from air-sea fluxes and surface mixing. *J. Phys. Oceanogr.* 29, 1468–1487. [5.1, 5.2]
- O'Connor, B.M., R.A. Fine, K.A. Maillet and D.B. Olson, 2000: Formation rates of Subtropical Underwater in the Pacific Ocean. *Deep-Sea Res.* (submitted). [5.8]
- O'Dwyer, J. and R.G. Williams, 1997: The climatological distribution of potential vorticity over the abyssal Ocean. *J. Phys. Oceanogr.* 27, 2488–2506. [7.1]
- Oakey, N.S. and J.A. Elliott, 1980: The variability of temperature gradient microstructure observed in the Denmark Strait. *J. Geophys. Res.* 85, 1933–1944. [5.2]
- Obata, A., R. Furue, S. Aoki and N. Sugino, 1996: Modeling layered structure in deep Pacific circulation. *J. Geophys. Res.* 101, 3663–3674. [4.2]
- Oberhuber, J.M., 1988: An atlas based on the COADS data set: the budgets of heat, buoyancy and turbulent kinetic energy at the surface of the global ocean. Max-Planck Institut für Meteorologie, Hamburg, Report No. 15, 19 pp. [5.1, 6.2]
- Oberhuber, J.M., 1993: Simulation of the Atlantic circulation with a coupled sea ice-mixed layer-isopycnal general circulation model, Parts I and II. *J. Phys. Oceanogr.* 23, 808–829, 830–845. [2.2, 2.3]
- Ochoa, J. and N.A. Bray, 1991: Water mass exchange in the Gulf of Cadiz. *Deep-Sea Res.* 38 (suppl.) S465–S503. [5.7]
- Ohlmann, J.C., P.P. Niiler, C.A. Fox and R.R. Leben, 2001: Eddy energy and shelf interactions in the Gulf of Mexico. *J. Geophys. Res.* (in press). [4.1]
- Olbers, D.J., 1998: Comment on 'On the obscurantist physics of "form drag" in theorizing about the Circumpolar Current'. *J. Phys. Oceanogr.* 28, 1647–1654. [4.6]
- Olbers, D.J. and C. Völker, 1996: Steady states and variability in oceanic zonal flows. In: *Decadal Climate Variability Dynamics and Predictability*, D. Anderson and J. Willebrand (eds), Springer-Verlag, Berlin, pp. 407–443. [4.6]
- Olbers, D.J. and M. Wenzel, 1989: Determining diffusivities from hydrographic data by inverse methods with applications to the circumpolar current. In: *Modelling the Ocean General Circulation and Geochemical Tracer Transport*, Vol. 284 of NATO ASI Series C, J. Willebrand and D.L.T. Anderson (eds), Kluwer Acad. Publ., Dordrecht, pp. 95–122. [4.6, 5.2]
- Olbers, D.J. and C. Wübbel, 1991: The role of wind and buoyancy forcing of the Antarctic Circumpolar Current. In: *Strategies for Future Climate Research*, M. Latif (ed.), Max-Planck Institut für Meteorologie, pp. 161–191. [4.6]
- Olbers, D.J., M. Wenzel and J. Willebrand, 1985: The inference of North Atlantic circulation patterns from climatological hydrographic data. *Rev. Geophys.* 23, 313–356. [5.2, 7.1]
- Olbers, D.J., V. Gouretski, G. Seiss and J. Schröter, 1992: *Hydrographic Atlas of the Southern Ocean*. Alfred Wegener Institute for Polar and Marine Research, Bremerhaven, 17 pp. + 82 plates. [4.2, 4.6]
- Ollitrault, M., 1999: MARVOR floats reveal intermediate circulation in the western equatorial and tropical South Atlantic (30°S to 5°N). *International WOCE Newsletter*, No. 34, 7–10, WOCE International Project Office (unpublished document). [3.2]
- Ollitrault, M., G. Loaëc and C. Dumortier, 1994: MARVOR: a multicycle RAFOS float. *Sea Tech.* 35, 39–44. [3.2]
- Ollitrault, M., 1999: MARVOR floats reveal intermediate circulation in the western equatorial and tropical South Atlantic (30°S to 5°N). *International WOCE Newsletter*, No. 34, 7–10, WOCE International Project Office (unpublished document). [3.2]
- Olson, D.B., R.A. Fine and A.L. Gordon, 1992: Convective modifications of water masses in the Agulhas. *Deep-Sea Res.* 39(suppl.), S163–S181. [5.4]
- Ono, T., S. Watanabe, K. Okuda and M. Fukasawa, 1998: Distribution of total carbonate and related properties in the North Pacific along 30°N. *J. Geophys. Res.* 103, 30873–30883. [6.3]

- OOPC (Ocean Observations Panel for Climate), 1997: *Report of the International Sea Level Workshop*. NOAA (and as GCOS Report No. 43, GOOS Report No. 55 and ICPO Report No. 16), 133 pp. [7.4]
- OOPC (Ocean Observing System Development Panel), 1993: *Interim Design for the Ocean Component of the Global Climate Observing System*. Texas A&M University, College Station, TX, 105 pp. [7.4]
- OOPC (Ocean Observing System Development Panel), 1995: *Scientific Design for the Common Module of the Global Ocean Observing System and the Global Climate Observing System: an Ocean Observing System for Climate*. Texas A&M University, College Station, TX, 265 pp. [7.4]
- Oort, A.H. and J.P. Peixóto, 1983: Global angular momentum and energy balance requirements from observations. *Adv. Geophys.* 25, 355–490. [6.2]
- Orr, J., E. Maier-Reimer, U. Mikolajewicz *et al.*, 2001: Estimates of anthropogenic carbon uptake from four 3-D global ocean models. *Glob. Biogeochem. Cycles* (accepted). [6.3]
- Orsi, A.H., T.W. Whitworth III and W.D. Nowlin Jr., 1995: On the meridional extent and fronts of the Antarctic Circumpolar Current. *Deep-Sea Res.* 42, 641–673. [4.6, 4.7]
- Orsi, A.H., G.C. Johnson and J.L. Bullister, 1999: Circulation, mixing and production of Antarctic Bottom Water. *Prog. Oceanogr.* 43, 55–109. [4.6, 5.8]
- Osborn, T.J., K.R. Briffa, S.F.B. Tett, P.D. Jones and R.M. Trigo, 1999: Evaluation of the North Atlantic oscillation as simulated by a coupled climate model. *Climate Dyn.* 15, 685–702. [7.3]
- Osborn, T.R., 1980: Estimates of the local rate of diffusion from dissipation measurements. *J. Phys. Oceanogr.* 10, 83–89. [4.2, 5.2]
- Osborn, T.R., 1988: Signatures of doubly diffusive convection and turbulence in an intrusive regime. *J. Phys. Oceanogr.* 18, 146–155. [5.2]
- Osborn, T.R. and C.S. Cox, 1972: Oceanic fine structure. *Geophys. Fluid Dyn.* 3, 321–345. [5.2]
- Østerhus, S. and T. Gammelsrod, 1999: The abyss of the Nordic Seas is warming. *J. Climate* 12, 3297–3304. [7.3]
- Østerhus, S., Hansen, B., Kristiansen, R. and P. Lundberg, 1999: The overflow through the Faroe Bank Channel. *International WOCE Newsletter*, No. 35, 35–37, WOCE International Project Office (unpublished document). [5.6]
- Östlund, H.G. and C.G.H. Rooth, 1990: The North Atlantic tritium and radiocarbon transients 1972–1983. *J. Geophys. Res.* 95, 20147–20165. [2.1]
- Owens, W.B. and B.A. Warren, 2000: Deep circulation in the northwest corner of the Pacific Ocean. *Deep-Sea Res.* II (In press). [4.5]
- Pacanowski, R.C., 1995: MOM2 Documentation, User's Guide and Reference Manual. Technical Report 3, GFDL Ocean Group Technical Report. NOAA/Geophysical Fluid Dynamics Laboratory, Princeton, NJ. [5.2]
- Pacanowski, R.C. and S.G.H. Philander, 1981: Parameterization of vertical mixing in numerical models of tropical oceans. *J. Phys. Oceanogr.* 11, 1443–1451. [4.3, 7.2]
- Padman, L. and T.M. Dillon, 1987: Vertical fluxes through the Beaufort Sea thermohaline staircase. *J. Geophys. Res.* 92, 10799–10806. [5.2]
- Paduan, J.D. and P.P. Niiler, 1993: Structure of velocity and temperature in the northeast Pacific as measured with Lagrangian drifters in fall 1987. *J. Phys. Oceanogr.* 23, 585–600. [4.1]
- Paillet, J. and M. Arhan, 1996: Shallow pycnocline and mode water subduction in the eastern North Atlantic. *J. Phys. Oceanogr.* 26, 96–114. [5.3]
- Park, K., 1969: Oceanic CO₂ system: an evaluation of ten methods of investigation. *Limnol. Oceanogr.* 14, 179–186. [6.3]
- Park, Y.-H. and L. Gambéroni, 1995: Large-scale circulation and its variability in the south Indian Ocean from TOPEX/POSEIDON altimetry. *J. Geophys. Res.* 100, 24911–24929. [3.3]
- Park, Y.-H., L. Gambéroni and E. Charriaud, 1993: Frontal structure, water masses, and circulation in the Crozet Basin. *J. Geophys. Res.* 98, 12361–12385. [4.6]
- Parke, M.E., R.L. Stewart, D.L. Farless and D.E. Cartwright, 1987: On the choice of orbits for an altimetric satellite to study ocean circulation and tides. *J. Geophys. Res.* 92, 11693–11707. [3.3]
- Parrilla, G., A. Lavin, H. Bryden, M. Garcia and R. Millard, 1994: Rising temperatures in the subtropical North Atlantic Ocean over the past 35 years. *Nature* 369, 48–51. [1.2, 7.3]
- Pazan, S.E. and P.P. Niiler, 2000: Recovery of near surface velocity from undrogued drifters. *J. Ocean Atmos. Technol.* (in press). [4.1]
- Pedlosky, J., 1987a: An inertial theory of the equatorial undercurrent. *J. Phys. Oceanogr.* 17, 1978–1985. [4.3, 4.4]
- Pedlosky, J., 1987b: *Geophysical Fluid Dynamics*, 2nd edn. Springer-Verlag, NY, 710 pp. [3.3, 4.1, 4.2]
- Pedlosky, J., 1988: Entrainment and termination of the equatorial undercurrent. *J. Phys. Oceanogr.* 18, 880–886. [4.4]

- Pedlosky, J., 1991: The link between western boundary current and equatorial undercurrent. *J. Phys. Oceanogr.* **21**, 1553–1558. [4.3]
- Pedlosky, J., 1996: *Ocean Circulation Theory*. Springer-Verlag, Berlin, 453 pp. [1.2, 2.1, 4.2, 5.3]
- Pedlosky, J. and P. Robbins, 1991: The role of finite mixed-layer thickness in the structure of the ventilated thermocline. *J. Phys. Oceanogr.* **21**, 1019–1031. [7.3]
- Pedlosky, J. and R. Xin Huang, 1999: Climatic forcing of the ventilated thermocline. (submitted). [7.3]
- Peixóto, J. and A. Oort, 1992: *Physics of Climate*. American Institute of Physics, NY, 520 pp. [4.7]
- Peltier W.R., 1998: Postglacial variations in the level of the sea: implications for climate dynamics and solid-earth physics. *Rev. Geophys.* **36**, 603–689. [1.2]
- Peng, T-H., R. Wanninkhof, J. L. Bullister, R. A. Feely and T. Takahashi, 1998: Quantification of decadal anthropogenic CO₂ uptake in the ocean based on dissolved inorganic carbon measurements. *Nature* **396**, 560–563. [6.3]
- Perigaud, C., 1990: Sea-level oscillations observed with Geosat along two shear fronts of the Pacific North Equatorial Counter Current. *J. Geophys. Res.* **95**, 7239–7248. [3.3]
- Perigaud, C. and P. Delecluse, 1992: Annual sea-level variations in the Southern Tropical Indian Ocean from Geosat and shallow water simulations. *J. Geophys. Res.* **97**, 20169–20178. [3.3]
- Perry, G., P. B. Duffy and N. L. Miller, 1996: An extended data set of river discharges for validation of general circulation models. *J. Geophys. Res.* **101**, 21339–21349. [6.3]
- Peters, H., M. C. Gregg and J. M. Toole, 1988: On the parameterization of equatorial turbulence. *J. Geophys. Res.* **93**, 1199–1218. [4.3]
- Peters, H., M. C. Gregg and T. B. Sanford, 1995: On the parameterization of equatorial turbulence: Effect of fine-scale variations below the range of the diurnal cycle. *J. Geophys. Res.* **100**, 18333–18348. [4.3]
- Peterson, R. G. and L. Stramma, 1991: Upper-level circulation in the South Atlantic Ocean. *Prog. Oceanogr.* **26**, 1–73. [4.3]
- Peterson, R. G. and W. B. White, 1998: Slow oceanic teleconnections linking the Antarctic Circumpolar Wave with the tropical El Niño Southern Oscillation. *J. Geophys. Res.* **103**, 24573–24583. [3.3, 4.6, 4.7]
- Petoukhov, V., A. Ganopolski, V. Brovkin *et al.*, 2000: CLIMBER-2: a climate system model of intermediate complexity. Part I. Model description and performance for present climate. *Climate Dyn.* **16**, 1–17. [2.3]
- Philander, S. G. H., 1986: Unusual conditions in the Tropical Atlantic Ocean in 1984. *Nature* **322**, (6076), 236–238. [4.3]
- Philander, S. G. H., 1990: *El Niño, La Niña and the Southern Oscillation*. Academic Press, San Diego, CA, 293 pp. [1.2, 2.3, 4.3]
- Philander, S. G. H. and R. C. Pacanowski, 1980: The generation of equatorial currents. *J. Geophys. Res.* **85**, 1123–1136. [4.3]
- Philander, S. G. H. and R. C. Pacanowski, 1986: A model of the seasonal cycle in the tropical Atlantic Ocean. *J. Geophys. Res.* **91**, 14192–14206. [4.3]
- Phillips, H. E. and S. R. Rintoul, 2000: Eddy variability and energetics from direct current measurements in the Antarctic Circumpolar Current south of Australia. *J. Phys. Oceanogr.* **30**, 3050–3076. [4.6]
- Phillips, O. M., 1977: *The Dynamics of the Upper Ocean*, 2nd edn. Cambridge University Press, NY, 336 pp. [5.2]
- Picaut, J. and R. Tournier, 1991: Monitoring the 1979–1985 Equatorial Pacific transports with expendable bathythermograph data. *J. Geophys. Res.* **96**, 3263–3277. [4.3]
- Picaut, J., M. Ioulalen, T. Delcroix, M. J. McPhaden and C. Menkes, 1996: Mechanism of the zonal displacements of the Pacific warm pool: Implications for ENSO. *Science* **274**, 1486–1489. [4.3]
- Picaut, J., F. Masia and Y. duPenhoat, 1997: An advective–reflective conceptual model for the oscillatory nature of the ENSO. *Science* **277**, 663–666. [3.3]
- Pickart, R. S., 1988: Entrainment and homogenization of a passive tracer in a numerical model gyre. *J. Geophys. Res.* **93**, 6761–6773. [5.5]
- Pickart, R. S., 1992: Water mass components of the North Atlantic Deep Western Boundary Current, *Deep-Sea Res.* **39**, 1553–1572. [5.8]
- Pickart, R. S. and W. M. Smethie, Jr., 1993: How does the Deep Western Boundary Current cross the Gulf Stream? *J. Phys. Oceanogr.* **23**, 2602–2616. [5.8]
- Pickart, R. S. and W. M. Smethie, 1998: Temporal evolution of the Deep Western Boundary Current where it enters the sub-tropical domain. *Deep-Sea Res. I* **45**, 1053–1083. [4.5]
- Pickart, R. S., N. G. Hogg and W. M. Smethie, Jr., 1989: Determining the strength of the deep western boundary current using the chlorofluoromethane ratio. *J. Phys. Oceanogr.* **19**, 940–951. [5.8]
- Pickart, R. S., W. M. Smethie, Jr., J. R. N. Lazier, E. P. Jones and W. J. Jenkins, 1996: Eddies of newly formed upper Labrador Sea Water. *J. Geophys. Res.* **101**, 20711–20726. [5.8]

- Pickart, R.S., M.A. Spall and J.R.N. Lazier, 1997: Mid-depth ventilation in the western boundary current system of the sub-polar gyre. *Deep-Sea Res.* **44**, 1025–1054. [5.4]
- Pickart, R.S., D.J. Torres and R.A. Clarke, 2000a: Hydrography of the Labrador Sea during active convection. *J. Phys. Oceanogr.* (submitted). [5.5]
- Pickart, R.S., K. Lavender, G.W.K. Moore, F. Straneo, J.R.N. Lazier and M.A. Spall, 2000b: Is Labrador Sea Water formed in the Irminger Basin? *Deep-Sea Res.* (submitted). [5.5]
- Pierce A.F. and B.F. Phillips, 1988: ENSO events, the Leeuwin Current and larval recruitment of the western rock lobster. *J. Cons. Int. Explor. Mer*, **45**(1), 13–21. [1.2]
- Pierce, S.D., J.A. Barth and R.L. Smith, 1999: Improving acoustic Doppler current profiler accuracy with wide-area differential GPS and adaptive smoothing of ship velocity. *J. Atmos. Oceanic Technol.* **16**, 591–596. [3.1]
- Pierce, S.D., R.L. Smith, P.M. Kosro, J.A. Barth and C.D. Wilson, 2000: Continuity of the poleward undercurrent along the eastern boundary of the mid-latitude north Pacific. *Deep-Sea Res.* **47**, 811–829. [1.2]
- Pinkel, R. and S. Anderson, 1997a: Shear, strain, and Richardson number variations in the thermocline. Part I: Statistical description. *J. Phys. Oceanogr.* **27**, 264–281. [5.2]
- Pinkel, R. and S. Anderson, 1997b: Shear, strain, and Richardson number variations in the thermocline. Part II: Modeling mixing. *J. Phys. Oceanogr.* **27**, 282–290. [5.2]
- Pinkel, R. and J.A. Smith, 1992: Repeat-sequence coding for improved precision of Doppler sonars and sodars. *J. Atmos. Oceanic Technol.* **9**, 149–163. [3.1]
- Pinkel, R., M. Merrifield, J. Picaut, S. Rutledge, D. Siegel and L. Washburn, 1997: Solitary waves in the Western Equatorial Pacific Ocean. *Geophys. Res. Lett.* **24**, 1603–1606. [4.3]
- Pinker, R.T. and I. Laszlo, 1992: Modeling surface solar irradiance of satellite applications on a global scale. *J. Appl. Meteor.* **31**, 194–211. [3.4]
- Piola, A. and D.T. Georgi, 1982: Circumpolar properties of Antarctic Intermediate Water and Subantarctic Mode Water. *Deep-Sea Res.* **29**, 687–711. [4.6, 5.4]
- Piola, A. and A.L. Gordon, 1984: Pacific and Indian Ocean upper layer salinity budget. *J. Phys. Oceanogr.* **14**, 747–753. [4.7]
- Piola, A. and A.L. Gordon, 1986: On oceanic heat and freshwater fluxes at 30°S. *J. Phys. Oceanogr.* **16**, 2184–2190. [4.7]
- Piola, A. and A.L. Gordon, 1989: Intermediate water in the southwestern South Atlantic. *Deep-Sea Res.* **36**, 1–16. [4.6]
- Pittock, A.B., 1978: A critical look at long-term sun-weather relations. *Rev. Geophys. Space Phys.* **16**, 400–420. [2.1]
- Plähn O. and M. Rhein, 1998: Measured and modeled CFC distribution of lower NADW in the Guiana Basin. *J. Geophys. Res.* **103**, 2831–2848. [5.8]
- Poisson, A. and C.T. Chen, 1987: Why is there little anthropogenic CO₂ in the Antarctic Bottom Water? *Deep-Sea Res.* **34**, 1255–1275. [6.3]
- Poisson, A., F. Culkin and P. Ridout, 1990: *Inter-comparison of total alkalinity and total inorganic carbon determinations in seawater*. UNESCO Technical Papers in Marine Science, UNESCO, Paris, No. 59, 18 pp. [6.3]
- Polito, P.S. and P. Cornillon, 1997: Long baroclinic Rossby waves detected by TOPEX/POSEIDON. *J. Geophys. Res.* **102**, 3215–3235. [3.3]
- Pollard, R.T. and J. Read, 1989: A method of calibrating shipmounted acoustic doppler profilers and the limitations of gyro compasses. *J. Atmos. Oceanic Technol.* **6**, 859–865. [3.1]
- Pollard, R.T., M.J. Griffiths, S.A. Cunningham, J.F. Read, F.F. Perez and A.F. Rios, 1996: Vivaldi 1991 – A study of the formation, circulation and ventilation of Eastern North Atlantic Central Water. *Prog. Oceanogr.* **37**, 167–192. [5.4]
- Polovina, J.J., G.T. Mitchum and G.T. Evans, 1995: Decadal and basin-scale variation in the mixed layer depth and the impact on biological production in the Central and North Pacific, 1960–88. *Deep-Sea Res I* **42**, 1701–1716. [1.2]
- Polzin, K., 1996: Statistics of the Richardson number: mixing models and fine structure. *J. Phys. Oceanogr.* **26**, 1409–1425. [4.3]
- Polzin, K., 1999: A rough recipe for the energy balance of quasi-steady internal lee waves. In: 'Aha Huliko'o Proceedings Hawaiian Winter Workshop. Dynamics of Oceanic Internal Gravity Waves', P. Muller and D. Henderson (eds), Honolulu, HI, pp. 117–129. [5.2]
- Polzin, K., 2000: Abyssal mixing: Inertial sub-range solution for the energy balance of the finescale internal wave field. *J. Mar. Res.* (submitted). [5.2]
- Polzin, K.L. and E. Firing, 1997b: Estimates of diapycnal mixing using LADCP and CTD data from I8S. *International WOCE Newsletter*, No. 29, 39–42, WOCE International Project Office. (unpublished document). [3.1, 5.2]
- Polzin, K.L., J.M. Toole and R.W. Schmitt, 1995: Finescale parameterizations of turbulent dissipation. *J. Phys. Oceanogr.* **25**, 306–328. [5.2]

- Polzin, K.L., K.G. Speer, J.M. Toole and R.W. Schmitt, 1996: Intense mixing of Antarctic Bottom Water in the equatorial Atlantic Ocean. *Nature* 380, 54–57. [5.2]
- Polzin, K.L., J.M. Toole, J.R. Ledwell and R.W. Schmitt, 1997: Spatial variability of turbulent mixing in the Abyssal Ocean. *Science* 276, 93–96. [4.2, 4.6, 5.2, 7.2]
- Polzin, K.L., E. Kunze, J. Hummon and E. Firing, 2000a: The finescale response of lowered ADCP velocity profiles. *J. Atmos. Oceanic Technol.* (submitted). [3.1]
- Polzin, K.L., E. Kunze, J. M. Toole and R. W. Schmitt, 2000b: The partition of small-scale energy into internal waves and geostrophic motions. *J. Phys. Oceanogr.* (submitted). [5.2]
- Ponte, R.M., 1994: Understanding the relation between wind- and pressure-driven sea-level variability. *J. Geophys. Res.* 99, 8033–8039. [3.3]
- Ponte, R.M. and P. Gaspar, 1999: Regional analysis of the inverted barometer effect over the global ocean using TOPEX/POSEIDON data and model results. *J. Geophys. Res.* 104, 15587–15602. [3.3]
- Ponte, R.M. and J. Luyten, 1989: Analysis and interpretation of deep equatorial currents in the equatorial Pacific. *J. Phys. Oceanogr.* 19, 1025–1038. [4.3]
- Ponte, R.M. and J. Luyten, 1990: Deep velocity measurements in the western equatorial Indian Ocean. *J. Phys. Oceanogr.* 20, 44–52. [4.3]
- Ponte, R.M., J.R. Luyten and P.L. Richardson, 1990: Equatorial deep jets in the Atlantic Ocean. *Deep-Sea Res.* 37, 711–713. [4.5, 5.2]
- Potemra, J., 1999: Seasonal variations of upper ocean transport from the Pacific to the Indian Ocean via Indonesian Straits. *J. Phys. Oceanogr.* 29, 2930–2944. [4.7]
- Potemra, J.T., R. Lukas and G.T. Mitchum, 1997: Large-scale estimation of transport from the Pacific to the Indian Ocean. *J. Geophys. Res.* 102, 27795–27812. [3.3, 4.7]
- Poulain, P.-M., 1993: Estimates of horizontal divergence and vertical velocity in the Equatorial Pacific. *J. Phys. Oceanogr.* 23, 601–607. [4.1]
- Poulain, P.-M. and P.P. Niiler, 1989: Statistical analysis of the surface circulation in the California current system using satellite-tracked drifters. *J. Phys. Oceanogr.* 19, 1588–1601. [4.1]
- Poulain, P.-M., J.D. Illeman and P.P. Niiler, 1987: *Drifter observations in the California Current System 1985–1986*. Scripps Institution of Oceanography, University of California, San Diego. Data Report, SIO Ref. 87-27, 72 pp. [4.1]
- Poulain, P.-M., A. Warn-Varnas and P.P. Niiler, 1996: Near-surface circulation of the Nordic sea as measured by Lagrangian drifters. *J. Geophys. Res.* 101, 18237–18258. [4.1]
- Pratt, L.J. and P.A. Lundberg, 1991: Hydraulics of rotating strait and sill flow. *Ann. Rev. Fluid Mech.* 23, 81–106. [5.6]
- Prentice, I.C., G. Farquhar, M. Fasham *et al.*, 2001: The carbon cycle and atmospheric CO₂. In: The IPCC Working Group 1, Third Assessment Report, Cambridge University Press, Chapter 3 [1.2]
- Price, J.F. and M.O. Baringer, 1994: Outflow and deep water production by marginal seas. *Prog. Oceanogr.* 33, 161–200. [2.2, 5.2]
- Price, J.F. and J. Yang, 1998: Marginal sea overflows for climate simulations. In: *Ocean Modeling and Parameterization*, E.P. Chassignet and J. Verron (eds), Kluwer Acad. Publ., Dordrecht, pp. 155–170. [5.2]
- Price, J.F., R.A. Weller and R. Pinkel, 1986: Diurnal cycling: Observations and models of the upper ocean response to diurnal heating, cooling, and wind mixing. *J. Geophys. Res.* 91, 8411–8427. [7.2]
- Price, J.F., R.A. Weller and R.R. Schudlich, 1987: Wind-driven ocean currents and Ekman transport. *Science* 238, 1534–1538. [4.1]
- Price, J.F., M.O. Baringer, R.G. Lueck *et al.*, 1993: Mediterranean outflow mixing and dynamics. *Science* 259, 1277–1282. [5.2]
- Provost, C., C. Escoffier, K. Maamaatauaiahutapu, A. Kartavtseff and V. Garçon, 1999: Subtropical mode waters in the South Atlantic Ocean. *J. Geophys. Res.* 104, 21033–21049. [5.4]
- Qiu, B., 1992: Recirculation and seasonal change of the Kuroshio from altimetry observations. *J. Geophys. Res.* 97, 17801–17813. [3.3]
- Qiu, B., 1994: Determining the mean Gulf Stream and its recirculations through combining hydrographic and altimetric data. *J. Geophys. Res.* 99, 951–962. [3.3]
- Qiu, B., 1995: Variability and energetics of the Kuroshio Extension and its recirculation gyre from the first two-year TOPEX data. *J. Phys. Oceanogr.* 25, 1827–1842. [3.3]
- Qiu, B., 1999: Seasonal eddy field modulation of the North Pacific subtropical Countercurrent: TOPEX/POSEIDON observations and theory. *J. Phys. Oceanogr.* 29, 2471–2486. [3.3]
- Qiu, B. and F.-F. Jin, 1997: Antarctic circumpolar wave: an indication of ocean–atmosphere coupling in the extratropics. *Geophys. Res. Lett.* 24, 2585–2588. [4.6]
- Qiu, B. and T.M. Joyce, 1992: Interannual variability in the mid- and low-latitude western North

- Pacific. *J. Phys. Oceanogr.* **22**, 1062–1079. [7.3, 7.4]
- Qiu, B. and K.A. Kelly, 1993: Upper-ocean heat balance in the Kuroshio Extension region. *J. Phys. Oceanogr.* **23**, 2027–2041. [3.3]
- Qiu, B., K.A. Kelly and T.M. Joyce, 1991: Mean flow and variability in the Kuroshio Extension from GEOSAT altimetry data. *J. Geophys. Res.* **96**, 18491–18507. [3.3]
- Qiu, B., W. Miao and P. Müller, 1997: Propagation and decay of forced and free baroclinic Rossby waves in off-equatorial oceans. *J. Phys. Oceanogr.* **27**, 2405–2417. [3.3]
- Quadfasel, D. and F. Schott, 1982: Water mass distribution at intermediate layers off the Somali coast during the onset of the southwest monsoon, 1979. *J. Phys. Oceanogr.* **12**, 1358–1372. [4.3]
- Quadfasel, D. and F. Schott, 1983: Southward subsurface flow below the Somali Current. *J. Geophys. Res.* **88**, 5973–5979. [4.3]
- Quadfasel, D., A. Sy, D. Wells and A. Tunik, 1991: Warming in the Arctic. *Nature* **350**, 385. [7.3]
- Quadfasel, D., A. Frische and G. Cresswell, 1996: The circulation in the source area of the South Equatorial Current in the eastern Indian Ocean. *J. Geophys. Res.* **101**, 12483–12488. [4.7]
- Quadfasel, D., J. Fischer, F. Schott and L. Stramma, 1997: Deep water exchange through the Owen Fracture Zone in the Arabian Sea. *Geophys. Res. Lett.* **24**, 2805–2808. [4.3]
- Quay, P.D., M. Stuiver and W.S. Broecker, 1983: Upwelling rates for the equatorial Pacific Ocean derived from the ^{14}C distribution. *J. Mar. Res.* **41**, 769–792. [4.4]
- Quilfen, Y., B. Chapron, T. Elfouhaily, K.B. Katsaros and J. Tournadre, 1998: Observations of tropical cyclones by high-resolution scatterometry. *J. Geophys. Res.* **103**, 7767–7786. [3.4]
- Rahmstorf, S., 1995: Bifurcations of the Atlantic thermohaline circulation in response to changes in the hydrological cycle. *Nature* **378**, 145–149. [4.7, 7.2]
- Rahmstorf, S., 1996: On the freshwater forcing and transport of the North Atlantic thermohaline circulation. *Climate Dyn.* **12**, 799–811. [2.3, 4.7, 6.2]
- Rahmstorf, S., 2001: Abrupt climate change. In: *Encyclopedia of Ocean Sciences*, J. Steele, S. Thorpe and K. Turekian (eds), Academic Press, London. [1.2]
- Rahmstorf, S. and A. Ganopolski, 1999: Long-term global warming scenarios computed with an efficient coupled climate model. *Climatic Change*, **43**, 353–367. [1.1, 1.2, 2.3, 7.3]
- Rahmstorf, S. and J. Willebrand, 1995: The role of temperature feedback in stabilising the thermohaline circulation. *J. Phys. Oceanogr.* **25**, 787–805. [1.1, 2.3, 7.2]
- Rahmstorf, S., J. Marotzke and J. Willebrand, 1996: Stability of the thermohaline circulation. In: *The Warmwatersphere of the North Atlantic Ocean*, W. Krauss (ed.), Gebr. Bornträger, Stuttgart, pp. 129–157. [2.3, 7.2]
- Ralph, E.A. and P.P. Niiler, 1999: Wind-driven currents in the tropical Pacific. *J. Phys. Oceanogr.* **29**, 2121–2129. [4.1, 7.1]
- Ralph, E., K. Bi, P. Niiler and Y. duPenhoat, 1997: A Lagrangian description of the western equatorial Pacific response to the wind burst of December 1992: Heat advection of the Warm Pool. *J. Climate* **10**, 1706–1721. [4.1]
- Raney, R.K., 1998: The delay/Doppler radar altimeter. *IEEE Trans. Geoscience Remote Sens.* **36**, 1578–1588. [3.3]
- Rao, R.R. and R. Sivakumar, 2000: On the possible mechanisms of the evolution of a mini-Warm Pool during the pre-summer monsoon season and the genesis of Onset Vortex in the southeastern Arabian Sea. *Quart. J. Roy. Meteor. Soc.* (in press). [4.3]
- Rao, R.R., R.L. Molinari and J.F. Festa, 1989: Evolution of the climatological near-surface thermal structure of the tropical Indian Ocean I: Description of the monthly mixed layer depth, sea surface temperature, surface current and surface meteorological fields. *J. Geophys. Res.* **94**, 10801–10815. [4.3]
- Rapp, R.H. and Y.M. Wang, 1994: Dynamic topography estimates using GEOSAT data and a gravimetric geoid in the Gulf Stream region. *Geophys. J. Int.* **117**, 511–528. [3.3]
- Rapp, R.H., C. Zhang and Y. Yi, 1996: Analysis of dynamic ocean topography using TOPEX data and orthonormal functions. *J. Geophys. Res.* **101**, 22583–22598. [3.3]
- Ratier, A. (ed.), 1988: Observing the ocean by altimetry. *CNES Magazine*, No. 3, October 1998. Centre National d'Études Spatiales, Toulouse (http://www.cnes.fr/WEB_UK/espace_pro/cnesmag/index.html), pp. 11–29. [1.3]
- Rayner, N.A., E.B. Horton, D.E. Parker, C.K. Folland and R.B. Hackett, 1996: *Version 2.2 of the Global Sea Ice and Sea Surface Temperature Dataset, 1903–1994*. CRTN 74, Hadley Centre, Meteorological Office, Bracknell, UK. [2.3]
- Read, J.F. and W.J. Gould, 1992: Cooling and freshening of the subpolar North Atlantic Ocean since the 1960s. *Nature* **360**, 55–57. [1.2, 7.3]
- Read, J.F. and R.T. Pollard, 1993: Structure and transport of the Antarctic Circumpolar Current and Agulhas Return Current at 40°E. *J. Geophys. Res.* **98**, 12281–12295. [4.6, 4.7]
- Read, J.F. and R.T. Pollard, 1997: Deep inflow into the Mozambique Basin. *International WOCE*

- Newsletter*, No. 29, 7–10, WOCE International Project Office (unpublished document). [4.5]
- Redler, R. and C.W. Böning, 1997: Effect of the overflow on the circulation in the subpolar North Atlantic; a regional model study. *J. Geophys. Res.* 102, 18529–18552. [2.2, 2.3]
- Redler, R. and J. Dengg, 1999: Spreading of CFCs in numerical models of differing resolution. *International WOCE Newsletter*, No. 35, 12–14, WOCE International Project Office. (unpublished document). [2.2]
- Reid, J.L., 1965: Intermediate waters of the Pacific Ocean. *John Hopkins Oceanographic Studies*, 2, 85 pp. [4.4, 5.4]
- Reid, J.L., 1978: On the mid-depth circulation and salinity field in the North Atlantic Ocean. *J. Geophys. Res.* 83, 5063–5067. [5.7]
- Reid, J.L., 1979: On the contribution of the Mediterranean Sea outflow to the Norwegian–Greenland Sea. *Deep-Sea Res.* 26, 1199–1223. [5.7]
- Reid, J.L., 1981: On the mid-depth circulation of the world ocean. In: *Evolution of Physical Oceanography*, B.A. Warren and C. Wunsch (eds), MIT Press, Cambridge, MA, 70–111. [4.2]
- Reid, J.L., 1982: On the use of dissolved oxygen concentration as an indicator of winter convection. *Naval Res. Rev.* 34, 28–39. [5.4]
- Reid, J.L., 1986: On the total geostrophic circulation of the South Pacific Ocean: Flow patterns, tracers and transports. *Prog. Oceanogr.* 16, 1–61. [4.2, 4.4]
- Reid, J.L., 1989: On the total geostrophic circulation of the South Atlantic Ocean: Flow patterns, tracers and transports. *Prog. Oceanogr.* 23, 149–244. [4.2, 4.5]
- Reid, J.L., 1994: On the total geostrophic circulation of the North Atlantic Ocean: Flow patterns, tracers, and transports. *Prog. Oceanogr.* 33, 1–92. [4.2, 5.7, 7.1]
- Reid, J.L., 1997: On the total geostrophic circulation of the Pacific Ocean: flow patterns, tracers and transports. *Prog. Oceanogr.* 39, 263–352. [3.2, 4.2, 4.7, 5.8, 7.1]
- Reid, J. and A. Mantyla, 1995: World dataset, ftp site minerva.ucsd.edu, San Diego. [7.3]
- Reid, Jr., J.L. and R.J. Lynn, 1971: On the influence of the Norwegian–Greenland and Weddell seas upon the bottom waters of the Indian and Pacific Oceans. *Deep-Sea Res.* 18, 1063–1088. [4.6]
- Reid, Jr., J.L., and W.D. Nowlin, Jr., 1971: Transport of water through Drake Passage. *Deep-Sea Res.* 18, 51–64. [4.6]
- Reid, Jr., J.L., W.D. Nowlin, Jr. and W.C. Patzert, 1977: On the characteristics and circulation of the southwestern Atlantic Ocean. *J. Phys. Oceanogr.* 7, 62–91. [4.6]
- Reid, P.C., B. Planque and M. Edwards, 1998: Is observed variability in the long-term results of the Continuous Plankton Recorder survey a response to climate change? *Fisheries Oceanography* 7, 282–288. [1.2]
- Reppin, J., F.A. Schott and J. Fischer, 1999: Equatorial currents and transports in the upper central Indian Ocean: Annual cycle and inter-annual variability. *J. Geophys. Res.* 104, 15495–15514. [4.3]
- Reverdin, G., 1987: The upper equatorial Indian ocean: The climatological seasonal cycle. *J. Phys. Oceanogr.* 17, 903–927. [4.3]
- Reverdin, G., P. Rual, Y. du Penhoat and Y. Gouriou, 1991: Vertical structure of the seasonal cycle in the central equatorial Atlantic Ocean: XBT sections from 1980 to 1988. *J. Phys. Oceanogr.* 21, 277–291. [4.3]
- Reverdin, G., C. Frankignoul, E. Kestenare and M.J. McPhaden, 1994: Seasonal variability in the surface currents of the Equatorial Pacific. *J. Geophys. Res.* 99, 20323–20344. [4.1, 4.3]
- Reynolds, R.R. and T.M. Smith, 1994: Improved global sea surface temperature analyses using optimum interpolation. *J. Climate* 7, 929–948. [3.4, 4.1, 5.1, 7.1]
- Rhein, M., 1994: The Deep Western Boundary Current: Tracers and velocities, *Deep-Sea Res.* 41, 263–281. [5.8]
- Rhein, M., L. Stramma and U. Send, 1995: The Atlantic Deep Western Boundary Current: Water masses and transports near the equator. *J. Geophys. Res.* 100, 2441–2457. [4.3, 4.5, 5.8]
- Rhein, M., L. Stramma and G. Krahmann, 1998a: The spreading of Antarctic bottom water in the tropical Atlantic. *Deep-Sea Res.* 45, 507–527. [4.6, 5.8]
- Rhein, M., O. Plähn, R. Bayer, L. Stramma and M. Arnold, 1998b: Temporal evolution of the tracer signal in the Deep Western Boundary Current, tropical Atlantic. *J. Geophys. Res.* 103, 15869–15883. [5.8]
- Rhein, M., J. Fischer, W.M. Smethie *et al.*, 2001: Labrador Sea Water: Pathways, CFC-inventory and formation rates. *J. Phys. Oceanogr.* (In press) 663. [5.8]
- Rhines, P.B., 1994: Climate change in the Labrador Sea, its convection and circulation. In: *Atlantic Climate Change Program*, Proceedings of the Principal Investigators' Meeting, Princeton, NJ, 9–11 May 1994, pp. 85–96. [7.3]
- Rhines, P.B., 1998: Circulation, convection and mixing in rotating, stratified basins with sloping topography. In: *Physical Processes in Lakes and Oceans*, J. Imberger (ed.), American Geophysical

- Union, Washington, DC, Coastal and Estuarine Series, Vol. 54, pp. 435–451. [5.5]
- Rhines, P.B.**, 1993: Oceanic general circulation: wave and advection dynamics. In: *Modelling Oceanic Interactions*, J. Willebrand and D. Anderson (eds), NATO ASO series, Springer, Berlin, pp. 67–149. [5.1]
- Rhines, P.B.** and W.R. Young, 1982a: A theory of the wind driven circulation. *J. Mar. Res.* **40**, 559–596. [4.2]
- Rhines, P.B.** and W.R. Young, 1982b: Homogenization of potential vorticity in planetary gyres. *J. Fluid Mech.* **122**, 347–367. [4.2]
- Ribbe, J.**, 1997: What drives mid latitude convection and the formation of Subantarctic mode water. *International WOCE Newsletter*, Nos 29, 20 and 25–26, WOCE International Project Office (unpublished document). [5.4]
- Ribbe, J.** and M. Tomczak, 1997a: Effect of the missing Indonesian throughflow in the fine resolution Antarctic Model, *J. Phys. Oceanogr.* **27**, 445–455. [4.7]
- Ribbe, J.** and M. Tomczak, 1997b: On convection, subduction and the formation of Subantarctic Mode Water in the Fine Resolution Antarctic Model-FRAM. *J. Mar. Sys.* **13**, 137–154. [5.4]
- Richards, K.J.**, 1998: Interleaving at the equator: its parameterization and effect on the large scale. In: *Ocean Modelling and Parameterization*, E. Chassignet and J. Verron (eds), NATO Science Series, Series C: Math. Phys. Sci., Kluwer Acad. Publ., Dordrecht, pp. 235–252. [4.3]
- Richards, K.J.** and R. Pollard, 1991: The structure of the upper ocean in the western equatorial Pacific. *Nature* **350**, 48–50. [4.3]
- Richardson, P.L.**, 1989: Worldwide ship drift distributions identify missing data. *J. Geophys. Res.* **96**, 6169–6176. [4.1]
- Richardson, P.L.**, 1997: Drifting in the wind: leeway error in shipdrift data. *Deep-Sea Res. I* **44**, 1877–1903. [4.1]
- Richardson, P.L.** and D.M. Fratantoni, 1999: Float trajectories in the deep western boundary current and deep equatorial jets in the tropical Atlantic. *Deep-Sea Res. II* **46**, 305–334. [4.3, 4.5]
- Richardson, P.L.** and G. Reverdin, 1987: Seasonal cycle of velocity in the Atlantic North Equatorial Countercurrent as measured by surface drifters, current meters and ship data. *J. Geophys. Res.* **92**, 3691–3708. [3.3]
- Richardson, P.L.** and W.J. Schmitz, Jr., 1993: Deep cross-equatorial flow in the Atlantic measured with SOFAR floats. *J. Geophys. Res.* **98**, 8371–8387. [4.3]
- Richardson, P.L.**, D. Walsh, L. Armi, M. Schroeder and J.F. Price, 1989: Tracking three Meddies with SOFAR floats. *J. Phys. Oceanogr.* **19**, 371–383. [5.7]
- Richardson, P.L.**, A.S. Bower and W. Zenk, 2000: A census of Meddies tracked by floats. *Prog. Oceanogr.* **45**, 209–250. [3.2]
- Rienecker, M.M.**, A. Borovikov, C. Keppenne and D. Adamec, 1999: Impact of multivariate assimilation on estimates of the state of the tropical Pacific Ocean. In: *Proceedings of 3rd WMO Symposium on Data Assimilation in Meteorology and Oceanography*, Quebec. [7.4]
- Rintoul, S.R.**, 1991: South Atlantic interbasin exchange. *J. Geophys. Res.* **96**, 2675–2692. [4.6, 4.7, 5.8, 6.1, 7.1]
- Rintoul, S.R.**, 1998: On the origin and influence of Adélie Land Bottom Water. In: *Ocean, Ice and Atmosphere: Interactions at Antarctic Continental Margin*, Vol. 75 of Antarctic Research Series, S.S. Jacobs and R. Weiss (eds), American Geophysical Union, Washington, DC, pp. 151–171. [4.6]
- Rintoul, S.R.** and J.L. Bullister, 1999: A late winter hydrographic section from Tasmania to Antarctica. *Deep-Sea Res.* **46**, 1417–1454. [4.6, 4.7]
- Rintoul, S.R.** and S. Sokolov, 2000: Baroclinic transport variability of the Antarctic Circumpolar Current south of Australia (WOCE repeat section SR3). *J. Geophys. Res.* (in press). [4.6]
- Rintoul, S.R.** and C. Wunsch, 1991: Mass, heat, oxygen and nutrient fluxes and budgets in the North Atlantic Ocean. *Deep-Sea Res.* **38**(suppl.), S355–S377. [6.3]
- Rintoul, S.R.**, S. Sokolov and J.A. Church, 2001: A six year record of austral summer baroclinic transport variability of the Antarctic Circumpolar Current at 140°E, derived from XBT and altimeter measurements. *J. Geophys. Res.* (submitted). [4.6]
- Riser, S.C.** and T. Rossby, 1983: Quasi-Lagrangian structure and variability of the subtropical western North Atlantic circulation. *J. Mar. Res.* **41**, 127–162. [3.2]
- Rix, N.** and J. Willebrand, 1996: Parameterization of mesoscale eddies as inferred from a high-resolution model. *J. Phys. Oceanogr.* **26**, 2281–2285. [2.2]
- Roach, A.T.**, K. Aagaard, C.H. Pease *et al.*, 1995: Direct measurements of transport and water properties through the Bering Strait. *J. Geophys. Res.* **100**, 18443–18458. [4.7]
- Robbins, P.E.**, 2001: Oceanic carbon transport carried by freshwater divergence: are salinity normalizations useful? *J. Geophys. Res.* (submitted). [6.3]

- Robbins, P. E. and W. J. Jenkins, 1998: Observations of temporal changes of tritium-³He age in the eastern North Atlantic thermocline: Evidence for changes in ventilation? *J. Mar. Res.* 56, 1125–1161. [5.3]
- Robbins, P. E. and J. M. Toole, 1997: The dissolved silica budget as a constraint on the meridional overturning circulation of the Indian Ocean. *Deep-Sea Res.* 44, 879–906. [4.3, 4.7, 5.2, 6.1, 6.2]
- Robbins, P. E., J. F. Price, W. B. Owens and W. J. Jenkins, 2000: On the importance of lateral diffusion for the ventilation of the lower thermocline in the subtropical North Atlantic. *J. Phys. Oceanogr.* 30, 67–89. [4.2, 5.3, 5.8]
- Roberts, M. J. and R. A. Wood, 1997: Topographic sensitivity studies with a Bryan–Cox-type ocean model. *J. Phys. Oceanogr.* 27, 823–836. [2.2, 2.3, 5.6]
- Roberts, M. J., R. Marsh, A. L. New and R. A. Wood, 1996: An intercomparison of a Bryan–Cox-type ocean model and an isopycnic ocean model. Part I: The subpolar gyre and high-latitude processes. *J. Phys. Oceanogr.* 26, 1495–1527. [2.2, 2.3]
- Robertson, A. W., 1996: Interdecadal variability over the North Pacific in a multi-century climate simulation. *Climate Dyn.* 12, 227–241. [2.3]
- Robinson, A. R. (ed.), 1983: *Eddies in Marine Science*. Springer-Verlag, Heidelberg, 609 pp. [1.3]
- Robinson, A. R. and H. Stommel, 1959: The oceanic thermocline and the associated thermohaline circulation. *Tellus* 11, 295–308. [4.4]
- Robinson, A. R. and P. Welander, 1963: Thermal circulation on a rotating sphere: with application to the oceanic thermocline. *J. Mar. Res.* 21, 25–38. [4.4]
- Robinson, A. R., D. E. Harrison, Y. Mintz and A. J. Semtner, 1977: Eddies and the general circulation of an idealized oceanic gyre: A wind and thermally driven primitive equation numerical experiment. *J. Phys. Oceanogr.* 7, 182–207. [2.2]
- Robitaille, D. Y. and A. J. Weaver, 1995: Validation of subgrid-scale mixing schemes using CFCs in a global ocean model. *Geophys. Res. Lett.* 22, 2917–2920. [2.3]
- Roden, G. I., 1970: Aspects of the mid-Pacific transition zone. *J. Geophys. Res.* 75, 1097–1109. [5.4]
- Roden, G. I., 1998: Upper ocean thermocline, oxygen, nutrient, and flow structure near the date line in the summer of 1993. *J. Geophys. Res.* 103, 12919–12939. [4.3]
- Rodriguez, E., B. Pollard and J. Martin, 2000: Wide swathe ocean altimetry using radar interferometry. *IEEE Trans., Geosci. Remote Sens.* (in press). [3.3]
- Rodwell, M. J., D. P. Rowell and C. K. Folland, 1999: Oceanic forcing of the wintertime North Atlantic Oscillation and European climate. *Nature* 398, 320–323. [1.2, 2.3]
- Roeckner, E., J. M. Oberhuber, A. Bacher, M. Christoph and I. Kirchner, 1996: ENSO variability and atmospheric response in a global coupled atmosphere–ocean GCM. *Climate Dyn.* 12, 737–754. [2.3]
- Roemmich, D., 1983: The balance of geostrophic and Ekman transports in the equatorial Atlantic Ocean. *J. Phys. Oceanogr.* 13, 1534–1539. [4.3]
- Roemmich, D., 1987: Estimates of net transport, upwelling, and heat flux in the tropical oceans from inverse methods and related geostrophic methods. In: *Further Progress in Equatorial Oceanography*, E. Katz and J. Witte (eds), Nova University Press, pp. 165–176. [4.4]
- Roemmich, D. and B. Cornuelle, 1992: The Subtropical Mode Water of the South Pacific Ocean. *J. Phys. Oceanogr.* 22, 1178–1187. [5.4]
- Roemmich, D. and B. Cornuelle, 1993: How representative are individual hydrographic sections of the long-term behaviour of the oceans? In: *Workshop on the Use of Sub-Surface Thermal Data for Climate Studies*, Brest, France, 13–16 September 1993, Int. TOGA Project Office, Report No. 9/WOCE Report No. 110/93, 64 pp. [7.4]
- Roemmich, D. and J. Gilson, 2000: Eddy transport of heat and thermocline waters in the North Pacific: A key to interannual/decadal climate variability? *J. Phys. Oceanogr.* (in press). [7.4]
- Roemmich, D. and T. McCallister, 1989: Large scale circulation of the North Pacific Ocean. *Prog. Oceanogr.* 22, 171–204. [4.5, 5.2, 6.1, 6.2]
- Roemmich, D. and C. Wunsch, 1984: Apparent changes in the climatic state of the deep North Atlantic Ocean. *Nature* 307, 447–450. [7.3]
- Roemmich, D. and C. Wunsch, 1985: Two transatlantic sections: meridional circulation and heat flux in the subtropical North Atlantic Ocean. *Deep-Sea Res.* 32, 619–664. [2.2, 6.3]
- Roemmich, D., S. Hautala and D. Rudnick, 1996: Northward abyssal transport through the Samoan Passage and adjacent regions. *J. Geophys. Res.* 101, 14039–14055. [4.5, 5.2]
- Roemmich, D., J. Gilson, B. Cornuelle and R. Weller, 2000: The mean and time-varying meridional transport of heat at the tropical/subtropical boundary of the North Pacific Ocean. *J. Geophys. Res.* (submitted). [7.1]
- Roether, W. and A. Putzka, 1996: Transient-tracer information on ventilation and transport of South Atlantic Waters. In: *The South Atlantic: Present and Past Circulation*, G. Wefer, W. H. Berger, G. Siedler and D. J. Webb (eds), Springer-Verlag, Berlin, pp. 45–62. [5.8, 6.3]

- Roether, W. and M. Rhein, 1989: Chemical tracers in the Ocean. In: *Landolt-Börnstein*, New Series, Group V, Vol. 3b, J. Sündermann (ed.), Springer-Verlag, Chapter 4.3, pp. 59–122. [5.8]
- Roether, W., B. Manca, B. Klein *et al.*, 1996: Recent Changes in the Eastern Mediterranean Deep Waters. *Science* 271, 333–335. [5.7]
- Rogers, J.C., 1990: Patterns of low-frequency monthly sealevel pressure variability (1899–1986) and associated wave cyclone frequencies. *J. Climate* 3, 1364–1379. [7.3]
- Rogers, J.C., 1994: Atlantic storm track variability and the North Atlantic Oscillation. In: *Atlantic Climate Change Program: Proceedings of the Principal Investigators' Meeting*, Princeton, NJ, 9–11 May 1994, pp. 20–24. [7.3]
- Rogers, J.C., 1997: North Atlantic storm track variability and its association to the North Atlantic Oscillation and climate variability of Northern Europe. *J. Climate* 10, 1635–1647. [7.3]
- Rogers, J.C. and H. van Loon, 1982: Spatial variability of sea level pressure and 500 mb height anomalies over the Southern Hemisphere. *Mon. Wea. Rev.* 110, 1375–1392. [7.3]
- Rohling, E.J. and H.L. Bryden, 1992: Man-induced salinity and temperature increases in the western Mediterranean deep water. *J. Geophys. Res.* 97, 11191–11198. [5.7]
- Rooth, C.G. and H.G. Östlund, 1972: Penetration of tritium into the Atlantic thermocline. *Deep-Sea Res.* 19, 481–492. [5.8]
- Ropelewski, C.F. and P.D. Jones, 1987: An extension of the Tahiti–Darwin Southern Oscillation Index. *Mon. Wea. Rev.* 115, 2161–2165. [7.1]
- Rosati, A. and K. Miyakoda, 1988: A general circulation model for upper ocean simulation. *J. Phys. Oceanogr.* 18, 1601–1626. [5.1]
- Rose, H., 1999: *Untersuchung der Zirkulation und der Erneuerung des Antarktischen Zwischenwassers im Südatlantic aus FCKW-Daten*, Doctoral Dissertation, University of Bremen, Sept. 1999, 148 pp. [5.8]
- Rosen, R.D., 1999: The global energy cycle. In: *Global Energy and Water Cycles*, K. A. Browning and R. J. Gurney (eds), Cambridge University Press, 292 pp. [6.2]
- Rosón, G., A.F. Rios, A. Lavin, F.F. Perez and H.L. Bryden, 2001: Carbon distribution, fluxes and budgets in the subtropical North Atlantic Ocean (24.5°N). *J. Geophys. Res.* (submitted). [6.3]
- Ross, C.K., 1976: *Overflow 73 – Transport of Overflow Water Through Denmark Strait*. International Council for the Exploration of the Sea, Copenhagen. ICES CM 1976/C: 15. [5.6]
- Rossby, C.G., 1936: Dynamics of steady ocean currents in the light of experimental fluid mechanics. *Papers in Physical Oceanography and Meteorology*, 5, 1–43. [7.4]
- Rossby, C.G., 1937: On the mutual adjustment of pressure and velocity distributions in certain simple current systems. *J. Mar. Res.* 1, 15–28. [7.4]
- Rossby, H.T., S.C. Riser and A.J. Mariano, 1983: The western North Atlantic – a Lagrangian viewpoint. In: *Eddies in Marine Science*, A.R. Robinson (ed.), Springer-Verlag, Berlin, pp. 66–91. [3.2]
- Rossby, H.T., E.R. Levine and D.N. Connors, 1985: The isopycnal Swallow float – a simple device for tracking water parcels in the ocean. *Prog. Oceanogr.* 14, 511–525. [3.2]
- Rossby, T., 1996: The North Atlantic Current and surrounding waters: at the crossroads. *Rev. Geophys.* 34, 463–481. [3.2, 7.1]
- Rossby, T. and E. Gottlieb, 1998: The Oleander Project: Monitoring the variability of the Gulf Stream and adjacent waters between New Jersey and Bermuda. *Bull. Amer. Meteor. Soc.* 79, 5–18. [1.2, 3.1]
- Rossby, T. and D. Webb, 1970: Observing abyssal motion by tracking Swallow floats in the SOFAR channel. *Deep-Sea Res.* 17, 359–365. [3.2]
- Rossby, T., D. Dorson and J. Fontaine, 1986: The RAFOS system. *J. Atmos. Oceanic Technol.* 3, 672–679. [3.2]
- Rossby, T., M.D. Prater, H.-M. Zhang *et al.* 2000: Warm-water pathways in the subpolar North Atlantic: Some case studies. *International WOCE Newsletter*, No. 38, 17–19, WOCE International Project Office (unpublished document). [3.2]
- Rossow, W.B. and R.A. Schiffer, 1991: ISCCP cloud data products. *Bull. Amer. Meteor. Soc.* 72, 2–20. [3.4, 5.1]
- Rothstein, L.M., M.J. McPhaden and P.A. Proehl, 1988a: Wind forced wave-mean flow interactions in the equatorial waveguide. Part I: the Kelvin wave. *J. Phys. Oceanogr.* 18, 1435–1447. [4.3]
- Rothstein, L.M., R.H. Zhang, A.J. Busalacchi and D. Chen, 1988b: A numerical simulation of the mean water pathways in the subtropical and tropical Pacific Ocean. *J. Phys. Oceanogr.* 28, 322–342. [4.4]
- Roulet, G. and G. Madec, 2000: Salt conservation, free surface and varying levels: a new formulation for ocean GCMs. *J. Geophys. Res.* 105, 23927–23942. [2.3]
- Rowe, G.D., E. Firing and G.C. Johnson, 2000: Pacific equatorial subsurface countercurrent velocity, transport, and potential vorticity. *J. Phys. Oceanogr.* 30, 1172–1187. [3.1, 4.3]

- Ruddick, B. and D. Hebert, 1988: The mixing of meddy Sharon. In: *Small-Scale Turbulence and Mixing in the Ocean*, J.C.J. Nihoul and B.M. Jamart (eds), Elsevier Science Publs., pp. 249–261. [5.2]
- Ruddick, B., D. Walsh and N. Oakey, 1997: Variations in apparent mixing efficiency in the North Atlantic Central Water. *J. Phys. Oceanogr.* 27, 2589–2605. [5.2]
- Rudels, B., 1995: The thermohaline circulation of the Arctic Ocean and the Greenland Sea. *Phil. Trans. Roy. Soc. Lond. A* 352, 287–299. [7.3]
- Rudels, B. and D. Quadfasel, 1991: Convection and deep water formation in the Arctic Ocean–Greenland Sea system. *J. Mar. Sys.* 2(3/4), 435–450. [1.2, 7.3]
- Rudels, B., D. Quadfasel, H. Friedrich and M.-N. Houssais, 1989: Greenland Sea convection in the winter of 1987–1988. *J. Geophys. Res.* 94, 3223–3227. [1.2]
- Rudels, B., E. Jones, L. Anderson and G. Kattner, 1994: On the intermediate depth waters of the Arctic Ocean. In: *The Polar Oceans and their Role in Shaping the Global Environment*, O.M. Johannessen, R.D. Muench and J.E. Overland (eds), American Geophysical Union, Washington, DC, pp. 5–20. [4.7]
- Rudels, B., L. Anderson and E. Jones, 1996: Formation and evolution of the surface mixed layer and halocline of the Arctic Ocean. *J. Geophys. Res.* 101, 8807–8821. [4.7]
- Rudnick, D.L., 1997: Direct velocity measurements in the Samoan Passage. *J. Geophys. Res.*, 102, 3293–3302. [4.5]
- Rudnick, D.L. and R. Ferrari, 1999: Compensation of horizontal temperature and salinity gradients in the ocean mixed layer. *Science* 283, 526–529. [5.2, 5.5]
- Rumford, B., Count of, 1800: Essay VII, The propagation of heat in fluids. In: *Essays, Political, Economical, and Philosophical, A New Edition*, T. Cadell, Jr. and W. Davies (eds), London, pp. 197–386. [4.4]
- Rüth, C., R. Well and W. Roether, 2000: Primordial ^{3}He in South Atlantic deep waters from sources on the Mid-Atlantic Ridge. *Deep-Sea Res.* 47, 1059–1075. [4.5]
- Sabine, C.L. and R.M. Key, 1997: *Surface Water and Atmospheric Underway Carbon Data Obtained During the World Ocean Circulation Experiment Indian Ocean Survey Cruises (R/V Knorr, December 1994–January 1996)*. Carbon Dioxide Information Analysis Center, Oak Ridge National Laboratory, US Department of Energy, Oak Ridge, TN, USA, ORNL/CDIAC-103, NDP-064, 38 pp. [6.3]
- Sabine, C.L., D.W.R. Wallace and F.J. Millero, 1997: Survey of CO_2 in the oceans reveal clues about global carbon cycle. *Eos Trans. Amer. Geophys. Union.* 78, 54–55. [6.3]
- Sabine, C.L., R.M. Key, K.M. Johnson *et al.*, 1999: Anthropogenic CO_2 inventory of the Indian Ocean. *Glob. Biogeochem. Cycles*, 13, 179–198. [6.3]
- Saji, N. H., B. N. Goswami, P. N. Vinayachandran and T. Yamagata, 1999: A dipole mode in the tropical Indian Ocean. *Nature* 401, 360–363. [1.2, 4.3, 7.1]
- Salmon, R., 1999: The lattice Boltzmann method as a basis for ocean circulation modeling. *J. Mar. Res.* 57, 503–535. [7.2]
- Salmon, R. and R. Hollerbach, 1991: Similarity solutions of the thermocline equations. *J. Mar. Res.* 49, 249–280. [2.2]
- Samelson, R.M., 1998: Large-scale circulation with locally enhanced vertical mixing. *J. Phys. Oceanogr.* 28, 712–726. [4.2]
- Sandström, J.W., 1916: *Meteorologische Studien im schwedischen Hochgebirge*. Goteborgs K. Ventenskaps-och Vitterhetssamhalles Handl, Series 4, 22(2), 48 pp. [5.2]
- Sandström, J.W. and B. Helland-Hansen, 1903: *Über die Berechnung von Meereströmungen*. Reports on Norwegian Fishery and Marine Investigations, Bergen, Vol. 2(4), 43 pp. [3.2]
- Saravanan, R., 1998: Atmospheric low-frequency variability and its relationship to midlatitude SST variability: studies using the NCAR Climate System Model. *J. Climate* 11, 1386–1404. [2.3]
- Saravanan, R., G. Danabasoglu, S.C. Doney and J.C. McWilliams, 2000: Decadal variability and predictability in the midlatitude ocean–atmosphere system. *J. Climate* 13, 1073–1097. [2.3]
- Sarmiento, J.L., 1983: A tritium box model of the North Atlantic thermocline. *J. Phys. Oceanogr.* 13, 1269–1274. [5.3, 5.4]
- Sarmiento, J.L., 1986: On The North and Tropical Atlantic heat balance. *J. Geophys. Res.* 91, 641–657. [2.2]
- Sarmiento, J.L. and E.T. Sundquist, 1992: Revised budget for the oceanic uptake of anthropogenic carbon-dioxide. *Nature* 356, 589–593. [6.3]
- Sarmiento, J.L., C.G.H. Rooth and W. Roether, 1982: The North Atlantic tritium distribution in 1972. *J. Geophys. Res.* 87, 8047–8056. [4.4, 5.4]
- Sarmiento, J.L., J.C. Orr and U. Siegenthaler, 1992: A perturbation simulation of CO_2 uptake in an ocean general circulation model. *J. Geophys. Res.* 97, 3621–3636. [6.3]
- Sarmiento, J.L., R. Murnane and C. le Quéré, 1995: Air–sea CO_2 transfer and the carbon budget of the

- North Atlantic, *Phil. Trans. Roy. Soc. Lond. B* 348, 211–219. [6.3]
- Sarmiento, J. L., T. M. C. Hughes, R. J. Stouffer and S. Manabe, 1998: Stimulated response of the ocean carbon cycle to anthropogenic climate warming. *Nature* 393, 245–249. [1.1, 1.2]
- Sato, O. T., P. S. Polito and W. T. Liu, 2000: Importance of salinity measurements in the heat storage estimation from TOPEX/POSEIDON. *Geophys. Res. Lett.* 27, 549–551. [3.3]
- Saunders, P. M., 1987: Flow through Discovery Gap. *J. Phys. Oceanogr.* 17, 631–643. [4.5, 5.2, 5.6]
- Saunders, P. M., 1990: Cold outflow from the Faroe Bank Channel. *J. Phys. Oceanogr.* 20, 29–43. [5.6]
- Saunders, P. M., 1994: The flux of overflow water through the Charlie-Gibbs Fracture Zone. *J. Geophys. Res.* 99, 12343–12355. [4.5, 5.6]
- Saunders, P. M., 1996: The flux of dense cold water overflow southeast of Iceland. *J. Phys. Oceanogr.* 26, 85–95. [4.5, 5.6]
- Saunders, P. M. and W. J. Gould, 1988: CTD data from RRS *Challenger* cruise 15/87 around the Faroe Islands. Inst. Oceanogr. Sci., Deacon Lab., Report No. 256, 79 pp. [5.6]
- Saunders, P. M. and B. A. King, 1995a: Bottom currents derived from a shipborne ADCP on WOCE cruise A11 in the South Atlantic. *J. Phys. Oceanogr.* 25, 329–347. [3.1]
- Saunders, P. M. and B. A. King, 1995b: Oceanic fluxes on the WOCE A11 section. *J. Phys. Oceanogr.* 25, 1942–1958. [2.3, 3.1, 4.2, 4.6, 4.7, 6.1, 6.2]
- Saunders, P. M., A. C. Coward and B. A. de Cuevas, 1999: Circulation of the Pacific Ocean seen in a global ocean model: Ocean Circulation and Climate Advanced Modelling project (OCCAM). *J. Geophys. Res.* 104, 18281–18299. [2.2, 4.1, 6.1]
- Sausen, R., K. Barthel and K. Hasselmann, 1988: Coupled ocean–atmosphere models with flux correction. *Climate Dyn.* 2, 145–163. [2.3]
- Schiller, A., 1995: The mean circulation north of 30°S determined with the adjoint method applied to an ocean general circulation model. *J. Mar. Res.* 53, 453–497. [7.2]
- Schiller, A., J. S. Godfrey, P. C. McIntosh, G. Meyers and S. E. Wijffels, 1998: Seasonal near-surface dynamics and thermodynamics of the Indian Ocean and Indonesian Throughflow in a global ocean general circulation model. *J. Phys. Oceanogr.* 28, 2288–2312. [4.7]
- Schimel, D., D. Alves, I. Enting *et al.*, 1996: CO₂ and the carbon cycle. In: *Climate Change 1995: The Science of Climate Change: Contribution of WG I to the Second Assessment Report of the IPCC*, J. T. Houghton *et al.* (eds), Cambridge University Press, Cambridge, pp. 65–86. [6.3]
- Schlesinger, M. E., W. L. Gates and Y. J. Han, 1985: The role of the ocean in CO₂-induced climate warming: Preliminary results from the OSU coupled atmosphere–ocean GCM. In: *Coupled Ocean–Atmosphere Models*, J. C. J. Nihoul (ed.), Elsevier, pp. 447–478. [2.2]
- Schlitzer, R., 1995: An adjoint model for the determination of the mean oceanic circulation, air–sea fluxes and mixing coefficients. *Berichte zur Polarforschung* 156, 103 pp. [7.1]
- Schlitzer, R., 1996: Mass and heat transports in the South Atlantic derived from historical hydrographic data. In: *The South Atlantic: Present and Past Circulation*, G. Wefer, W. H. Berger, G. Siedler and D. J. Webb (eds), Springer-Verlag, Berlin, pp. 305–323. [4.7]
- Schlosser, P., 1986: Helium: a new tracer in Antarctic oceanography. *Nature* 321, 233–235. [5.8]
- Schlosser, P. and W. M. Smethie, Jr., 1995: Transient tracers as a tool to study variability of ocean circulation. In: *Natural Climate Variability on Decade-to-Century Time Scales*, D. G. Martinson *et al.* (eds), National Research Council, National Academy Press, Washington, DC, pp. 274–288. [5.8]
- Schlosser, P., R. Bayer, A. Foldvik, T. Gammelsrød, G. Rohardt and K. O. Münnich, 1990: ¹⁸O and helium as tracers of Ice Shelf Water and water/ice interaction in the Weddell Sea. *J. Geophys. Res.* 95, 3253–3263. [5.8]
- Schlosser, P., G. Bönisch, M. Rhein and R. Bayer, 1991a: Reduction of deepwater formation in the Greenland Sea during the 1980s: Evidence from tracer data. *Science* 251, 1054–1056. [7.3]
- Schlosser, P., J. L. Bullister and R. Bayer, 1991b: Studies of deep water formation and circulation in the Weddell Sea using natural and anthropogenic tracers. *Mar. Chem.* 35, 97–122. [5.8]
- Schlosser, P., G. Bönisch, B. Kromer *et al.*, 1995: Mid 1980s distribution of tritium, ³He, ¹⁴C and ³⁹Ar in the Greenland/Norwegian seas and the Nansen Basin of the Arctic Ocean. *Prog. Oceanogr.* 35, 1–28. [5.8]
- Schmid, C., G. Siedler and W. Zenk, 2000: Dynamics of intermediate water circulation in the subtropical South Atlantic. *J. Phys. Oceanogr.* 30, 3191–3211. [5.3]
- Schmitt, R. W., 1981: Form of the temperature–salinity relationship in the Central Water: evidence for double-diffusive mixing. *J. Phys. Oceanogr.* 11, 1015–1026. [5.2]
- Schmitt, R. W., 1988: Mixing in a thermohaline staircase. In: *Small-Scale Turbulence and Mixing*

- in the Ocean*, J.C.J. Nihoul and B.M. Jamart (eds), Elsevier, NY, pp. 435–452. [5.2]
- Schmitt, R.W.**, 1994: Double diffusion in oceanography. *Ann. Rev. Fluid Mech.* **26**, 255–286. [5.2]
- Schmitt, R.W.**, 1998: Double-diffusive convection: Its role in ocean mixing and parameterization schemes for large-scale modeling. In: *Ocean Modeling and Parameterization*, E. Chassignet and J. Verron (eds), Kluwer Acad. Publ., Dordrecht, pp. 215–234. [5.2]
- Schmitt, R.W.**, 1999: Spice and the demon. *Science* **283**, 498–499. [5.2]
- Schmitt, R.W.**, P.S. Bogden and C.E. Dorman, 1989: Evaporation minus precipitation and density fluxes for the North Atlantic. *J. Phys. Oceanogr.* **19**, 1208–1221. [5.1]
- Schmittner, A.** and T.F. Stocker, 1999: The stability of the thermohaline circulation in global warming experiments. *J. Climate* **12**, 1117–1133. [2.3]
- Schmitz, W.J.**, 1988: Exploration of the eddy field of the mid-latitude North Pacific. *J. Phys. Oceanogr.* **18**, 459–468. [3.2]
- Schmitz, W.J.**, 1995: On the interbasin-scale thermo-haline circulation. *Rev. Geophys.*, **33**, 151–173. [4.2, 4.6, 4.7, 5.4, 7.1]
- Schmitz, W.J.**, 1996a: *On the World Ocean Circulation*. Vol. I: *Some Global Features/North Atlantic Circulation*. Woods Hole Oceanographic Institution, Technical Report, WHOI-96-03, 141 pp. [1.2, 4.2, 4.6, 4.7]
- Schmitz, W.J.**, 1996b: *On the World Ocean Circulation*, Vol. II: *The Pacific and Indian Oceans/A Global Update*. Woods Hole Oceanographic Institution, Technical Report, WHOI-96-08, 237 pp. [1.2, 4.2, 4.6, 4.7]
- Schmitz, W.J.** and P.L. Richardson, 1991: On the sources of the Florida Current. *Deep-Sea Res.* **38** (suppl.), S389–S409. [4.3]
- Schmitz, W.J.** and M.S. McCartney, 1993: On the North Atlantic circulation. *Rev. Geophys.* **31**, 29–49. [2.1, 4.2, 4.4, 4.5]
- Schneider, N.**, 1998: The Indonesian throughflow and the global climate system. *J. Climate* **11**, 676–689. [4.7]
- Schneider, N.**, S. Venzke, A.J. Miller *et al.*, 1999a: Pacific thermocline bridge revisited. *Geophys. Res. Lett.* **26**, 1329–1332. [5.3]
- Schneider, N.**, A.J. Miller, M.A. Alexander and C. Deser, 1999b: Subduction of decadal North Pacific temperature anomalies: observations and dynamics. *J. Phys. Oceanogr.* **29**, 1056–1070. [4.3, 4.4, 5.3, 5.4, 7.1]
- Schneider, R.J.**, G.A. Jones, A.P. McNichol *et al.*, 1994: Methods for data screening, flagging, and error analysis at the National Ocean Sciences AMS Facility. *Nuclear Instr. and Methods*. **B92**, 172–175. [5.8]
- Schopf, P.S.**, D.L.T. Anderson and R. Smith, 1981: Beta-dispersion of low frequency Rossby waves. *Dyn. Atmos. Oceans* **5**, 187–214. [4.4]
- Schopf, P.S.** and M.J. Suarez, 1988: Vacillations in a coupled ocean-atmosphere model. *J. Atmos. Sci.* **45**, 549–566. [3.3]
- Schott, F.**, 1983: Monsoon response of the Somali Current and associated upwelling. *Prog. Oceanogr.* **12**, 357–381. [4.3]
- Schott, F.**, 1986: Seasonal variation of cross-equatorial flow in the Somali Current. *J. Geophys. Res.* **91**, 10581–10584. [4.3]
- Schott, F.** and C.W. Böning, 1991: Evaluation of the WOCE model in the western equatorial Atlantic: Upper-layer circulation. *J. Geophys. Res.* **96**, 6993–7004. [4.3]
- Schott, F.** and K.D. Leaman, 1991: Observations with moored Acoustic Doppler Current Profilers in the convection regime in the Golfe du Lion. *J. Phys. Oceanogr.* **21**, 558–574. [5.5]
- Schott, F.** and H. Stommel, 1978: Beta spirals and absolute velocities in different oceans. *Deep-Sea Res.* **25**, 961–1010. [4.4]
- Schott, F.A.**, T.N. Lee and R. Zantopp, 1988: Variability of structure and transport of the Florida Current in the period range of days to seasonal. *J. Phys. Oceanogr.* **18**, 1209–1230. [2.1]
- Schott, F.**, J.C. Swallow and M. Fieux, 1989: Deep currents underneath the equatorial Somali Current. *Deep-Sea Res.* **36**, 1191–1199. [4.3]
- Schott, F.**, J.C. Swallow and M. Fieux, 1990: The Somali Current at the equator: Annual cycle of currents and transports in the upper 1000 m and connection to neighbouring latitudes. *Deep-Sea Res.* **37**, 1825–1848. [4.3]
- Schott, F.**, J. Fischer, J. Reppin and U. Send, 1993a: On the mean and seasonal currents and transports at the western boundary of the equatorial Atlantic. *J. Geophys. Res.* **98**, 14353–14368. [4.3, 4.5]
- Schott, F.**, M. Visbeck and J. Fischer, 1993b: Observations of vertical currents and convection in the central Greenland Sea during the winter of 1988–1989. *J. Geophys. Res.* **98**, 14401–14421. [1.2, 5.5]
- Schott, F.**, J. Reppin, J. Fischer and D. Quadfasel, 1994: Currents and transports of the Monsoon Current south of Sri Lanka. *J. Geophys. Res.* **99**, 25127–25141.
- Schott, F.A.**, L. Stramma and J. Fischer, 1995: The warm water inflow into the western tropical Atlantic boundary regime, spring 1994. *J. Geophys. Res.* **100**, 24745–24760. [4.3]

- Schott, F., M. Visbeck, U. Send, J. Fischer, L. Stramma and Y. Desaubies, 1996: Observations of deep convection in the Gulf of Lions, northern Mediterranean, during the winter of 1991/92. *J. Phys. Oceanogr.* **26**, 505–524. [4.2, 5.5, 5.7]
- Schott, F., J. Fischer, U. Garternicht and D. Quadfasel, 1997: Summer monsoon response of the northern Somali Current, 1995. *Geophys. Res. Lett.* **24**, 2565–2568. [3.1, 4.3]
- Schott, F.A., J. Fischer and L. Stramma, 1998: Transports and pathways of the upper-layer circulation in the western tropical Atlantic. *J. Phys. Oceanogr.* **28**, 1904–1928. [4.3, 4.7]
- Schott, F., Stramma, L. and J. Fischer, 1999: Interaction of the North Atlantic Current with the deep Charlie–Gibbs Fracture Zone throughflow. *Geophys. Res. Lett.* **26**, 369–372. [5.6]
- Schott, G., 1928: Die Wasserbewegungen im Gebiete der Gibraltarstrasse. *Journal du Conseil International pour l'Exploration de la mer.* **III**, No. 2, Copenhagen, September. [5.7]
- Schröder, M. and E. Fahrbach, 1999: On the structure and the transport of the eastern Weddell Gyre. *Deep-Sea Res.* **46**, 501–527. [4.6]
- Schroeder, E.H., H. Stommel, D.W. Menzel and W.H. Sutcliffe, Jr, 1959: Climate stability of eighteen degree water at Bermuda. *J. Geophys. Res.* **64**, 363–366. [5.4]
- Schudlich, R.R. and J.F. Price, 1992: Diurnal cycles of turbulent dissipation, current and temperature in a model of the equatorial upper ocean. *J. Phys. Oceanogr.* **97**, 5409–5422. [5.2]
- Schulz, J., P. Schlüssel and H. Grassl, 1993: Water vapor in the atmospheric boundary layer over oceans from SSM/I measurements. *Int. J. Remote Sens.* **14**, 2773–2789. [3.4]
- Schulz, J., J. Meywerk, S. Ewald, and P. Schlüssel, 1997: Evaluation of satellite-derived latent heat fluxes. *J. Climate*, **10**, 2782–2795. [3.4]
- SCOR, 1985: *Oceanic CO₂ measurements*. Report of the Third Meeting of the Working Group 75, Les Houches, France, October 1985. [6.3]
- Seckmeyer, G., B. Mayer, G. Bernhard *et al.*, 1995: Geographical differences in the UV measured by intercompared spectroradiometers. *Geophys. Res. Lett.* **22**, 1889–1892. [1.1]
- Seidov, D. and B. Haupt, 1999: Last glacial and meltwater interbasin water exchanges and sedimentation in the world ocean. *J. Phys. Oceanogr.* **14**, 760–769. [4.7]
- Sekine, Y. and K. Kutsuwada, 1994: Seasonal variation in volume transport of the Kuroshio south of Japan. *J. Phys. Oceanogr.* **24**, 261–272. [2.2]
- Semtner, A.J. and R.M. Chervin, 1988: A simulation of the global ocean circulation with resolved eddies. *J. Geophys. Res.* **93**, 15502–15522, 15767–15775. [2.2]
- Semtner, A.J. and R.M. Chervin, 1992: Ocean general circulation from a global eddy-resolving model. *J. Geophys. Res.* **97**, 5493–5550. [2.1, 2.2, 3.3, 4.3, 4.7, 7.1]
- Semtner, A.J. and Y. Mintz, 1977: Numerical simulations of the Gulf Stream and mid-ocean eddies. *J. Phys. Oceanogr.* **7**, 208–230. [2.2]
- Send, U., 1994: Accuracy of current profile measurements: effect of tropical and midlatitude internal waves. *J. Geophys. Res.* **99**, 16229–16236. [3.1]
- Send, U. and J. Marshall, 1995: Integral effects of deep convection. *J. Phys. Oceanogr.* **25**, 855–872. [5.5]
- Send, U., F. Schott, F. Gaillard and Y. Desaubies, 1995: Observation of a deep convection regime with acoustic tomography. *J. Geophys. Res.* **100**, 6927–6941. [5.5]
- Send, U., R. Weller, S. Cunningham *et al.*, 2001: Oceanographic time series observatories. In: *Observing the Ocean in the 21st Century*, N.R. Smith and C.J. Koblinsky (eds), Bureau of Meteorology, Melbourne, Australia, Chapter 24. [7.4]
- Serreze, M.C., J.A. Maslanik, J.R. Key, R.F. Kokaly and D.A. Robinson, 1995: Diagnosis of the record minimum in Arctic sea-ice area during 1990 and associated snow cover extremes. *Geophys. Res. Lett.* **22**, 2183–2186. [7.3]
- Servain, J., 1991: Simple climatic indices for the tropical Atlantic Ocean and some applications. *J. Geophys. Res.* **96**, 15137–15146. [4.3]
- Servain, J., A.J. Busalacchi, M.J. McPhaden *et al.*, 1998: A Pilot Research Moored Array in the Tropical Atlantic (PIRATA). *Bull. Amer. Meteor. Soc.* **79**, 2019–2031. [4.3, 7.4]
- Shchepetkin, A.F. and J.C. McWilliams, 1998: Quasi-monotonic advection schemes based on explicit locally adaptive dissipation. *Mon. Wea. Rev.* **126**, 1541–1580. [7.2]
- Sherman, J.T. and R.E. Davis, 1995: Observations of temperature microstructure in NATRE. *J. Phys. Oceanogr.* **25**, 1913–1929. [5.2]
- Shetye, S.R., S.S.C. Shenoi, A.D. Gouveia, G.S. Michael, D. Sundar and G. Nampoothiri, 1991: Wind-driven coastal upwelling along the western boundary of the Bay of Bengal during the Southwest Monsoon. *Contin. Shelf Res.* **11**, 1397–1408. [4.3]
- Shin, S. and Z. Liu, 2000: On the response of equatorial thermocline to extratropical buoyancy forcing. *J. Phys. Oceanogr.* **30**, 2883–2905. [4.4]
- Shindell, D.T., R.L. Miller, G. Schmidt and L. Pandolfo, 1999: Simulation of recent northern winter climate trends by greenhouse-gas forcing. *Nature* **399**, 452–455. [2.3]

- Shriver, J.F. and H.E. Hurlburt, 1997: The contribution of the global thermohaline circulation to the Pacific to Indian Ocean throughflow via Indonesia. *J. Geophys. Res.* 102, 5491–5511. [4.4, 4.7]
- Shum, C.K., R.A. Werner, D.T. Sandwell, B.H. Zhang, R.S. Nerem and B.D. Tapley, 1990: Variations of global mesoscale eddy energy observed from GEOSAT. *J. Geophys. Res.* 95, 17865–17876. [3.3]
- Shuto, K., 1996: Interannual variations of water temperature and salinity along the 137°E meridian. *J. Oceanogr.* 52, 575–595. [5.4]
- Siedler, G. and J.D. Woods (eds), 1980: GATE-1 oceanography and surface layer meteorology in the B/C scale. *Deep-Sea Res.* 26(suppl. 1), 294 pp. [1.3]
- Siedler, G., A. Kuhl and W. Zenk, 1987: The Madeira mode water. *J. Phys. Oceanogr.* 17, 1561–1570. [5.3, 5.4]
- Siedler, G., N. Zangenberg, R. Onken and A. Morlière, 1992: Seasonal changes in the tropical Atlantic circulation: observation and simulation of the Guinea Dome. *J. Geophys. Res.* 97, 703–715. [4.3]
- Siefridt, L., 1994: *Validation des données de vent ERS-1 et des flux de surface du CEPMMT dans le contexte de la modélisation des circulations océaniques à l'échelle d'un bassin*. Ph.D. Thesis, Université Joseph Fourier, Grenoble, France. [3.3]
- Siegenthaler, U. and F. Joos, 1992: Use of a simple model for studying oceanic tracer distributions and the global carbon cycle. *Tellus* 44B, 186–207. [6.3]
- Siegenthaler, U. and J.L. Sarmiento, 1993: Atmospheric carbon dioxide and the ocean. *Nature* 365, 119–125. [6.3]
- Sjoberg, B. and A. Stigebrandt, 1992: Computations of the geographical distribution of the energy flux to mixing processes via internal tides and the associated vertical circulation in the ocean. *Deep-Sea Res.* 39, 269–291. [4.2]
- Slinn, D.N., 1999: Internal wave reflection. In: 'Aha Huliko'o Proceedings Hawaiian Winter Workshop. Dynamics of Oceanic Internal Gravity Waves, II. University of Hawaii at Manou, HI, January 1999, P. Muller and D. Henderson (eds), pp. 141–147. [5.2]
- Slinn, D.N. and J.J. Riley, 1999: Internal wave reflection from sloping boundaries. *J. Fluid Mech.* (submitted). [5.2]
- Slocum, J., 1900: *Sailing alone around the world*. Century Company, New York and Sampson Low, London. Republished by Dover Publications, New York 1956, 294pp [3.2]
- Sloyan, B., 1997: *The circulation of the southern ocean and the adjacent ocean basins determined by inverse methods*. Ph.D. Thesis, Institute of Antarctic and Southern Ocean Studies, University of Tasmania, 479 pp. [7.1]
- Sloyan, B.M. and S.R. Rintoul, 2000: Estimates of area-averaged diapycnal fluxes from basin-scale budgets. *J. Phys. Oceanogr.* 30, 2320–2341. [4.6, 4.7]
- Sloyan, B.M. and S.R. Rintoul, 2001a: The Southern Ocean limb of the global deep overturning circulation. *J. Phys. Oceanogr.* (submitted). [4.6, 6.2]
- Sloyan, B.M. and S.R. Rintoul, 2001b: Circulation, renewal and modification of Antarctic mode and intermediate water. *J. Phys. Oceanogr.* (In press). [4.6]
- Smagorinsky, J., 1963: General circulation experiments with the primitive equations. I: The basic experiment. *Mon. Wea. Rev.* 91, 99–164. [7.2]
- Smethie, W.M., Jr., 1993: Tracing the thermohaline circulation in the western North Atlantic using chlorofluorocarbons. *Prog. Oceanogr.* 31, 51–99. [5.8]
- Smethie, W.M., Jr., 1999: Meridional distribution of CFCs in the Western Subtropical Atlantic Ocean. *International WOCE Newsletter*, No. 37, 15–17, WOCE International Project Office (unpublished document). [5.8]
- Smethie, W.M., Jr. and R.A. Fine, 2001: Rates of North Atlantic Deep Water formation calculated from chlorofluorocarbon inventories. *Deep-Sea Res.* (in press). [5.8]
- Smethie, W.M., R.A. Fine, A. Putzka and E.P. Jones, 2000: Tracing the flow of North Atlantic deep water using chlorofluorocarbons. *J. Geophys. Res.* 105, 14297–14324. [5.8, 7.4]
- Smith, H.J., H. Fischer, M. Wahnen, D. Mastroianni and B. Deck, 1999a: Dual modes of the carbon cycle since the last Glacial Maximum. *Nature* 400, 248–250. [6.3]
- Smith, L.T., D.B. Boudra and R. Bleck, 1990: A wind-driven isopycnic coordinate model of the north and equatorial Atlantic Ocean – 2. The Atlantic basin experiments. *J. Geophys. Res.* 95, 13105–13128. [2.2]
- Smith, N.R., 1998: Sustained observing systems for the atmosphere and ocean. In: *Proceedings of the CLIVAR Conference*, 1–3 December 1998, Paris (unpublished manuscript). [7.4]
- Smith, N.R., 2000: The Global Ocean Data Assimilation Experiment. *Adv. Space Res.* 25, 1089–1098. [7.4]
- Smith, N.R. and C. Koblinsky, 1999: The First International Conference on the Ocean Observing System for Climate. In: *Proceedings of OceanObs '99*, Saint Raphael, France, October 1999. [7.4]
- Smith, N. and M. Lefebvre, 1997: The Global Ocean Data Assimilation Experiment (GODAE).

- In: *Monitoring the Oceans in the 2000s: An Integrated Approach*, International Symposium, Biarritz, 15–17 October. [7.4]
- Smith, N. R.**, D.E. Harrison, R. Bailey *et al.*, 1999b: The role of XBT sampling in the ocean thermal network. In: *Proceedings of OceanObs '99*, Saint Raphael, France, October 1999. [7.4]
- Smith, P. C.**, 1975: A streamtube model for bottom boundary currents in the ocean. *Deep-Sea Res.* **22**, 853–873. [5.6]
- Smith, R. D.**, J.K. Dukowicz and R.C. Malone, 1992a: Parallel ocean general circulation modeling. *Physica D*, **60**, 38–61. [3.3]
- Smith, R. D.**, M.E. Maltrud, F.O. Bryan and M.W. Hecht, 2000: Numerical simulation of the North Atlantic Ocean at 1/10°. *J. Phys. Oceanogr.* **30**, 1532–1561. [2.1, 2.2, 3.3]
- Smith, S. D.** and F.W. Dobson, 1984: The Heat Budget at Ocean Weather Station Bravo. *Atmos. Ocean*, **22**, 1–22. [5.5]
- Smith, S. D.**, R.J. Anderson, W.A. Oost *et al.*, 1992b: Sea surface wind stress and drag coefficients: The HEXOS results. *Bound.-Layer Meteor.* **60** (1–2), 109–142. [3.4]
- Smith, S. R.**, C. Harvey and D.M. Legler, 1996: *Handbook of Quality Control Procedures and Methods for Surface Meteorology Data*. WOCE Data Assembly Centre for Surface Meteorology, Florida State University, WOCE International Project Office, WOCE Report No. 141/96, 49 pp. (COAPS Technical Report 96-1) (unpublished manuscript). [3.1]
- Smith, W.H.F.** and D.T. Sandwell, 1994: Bathymetric prediction from dense altimetry and sparse shipboard bathymetry. *J. Geophys. Res.* **99**, 21803–21824. [5.2]
- Smythe-Wright, D.** and S. Boswell, 1998: Abyssal circulation in the Argentine Basin. *J. Geophys. Res.* **103**, 15845–15851. [5.8]
- Spall, M. A.**, 1995: Frontogenesis, subduction and cross-front exchange at upper-ocean fronts. *J. Geophys. Res.* **100**, 2543–2557. [5.3]
- Spall, M. A.**, 1999: A simple model of the large scale circulation of the Mediterranean Water and Labrador Sea Water. *Deep-Sea Res. II* **46**, 181–204. [5.7]
- Spall, M. A.** and R.S. Pickart, 2000: Where does dense water sink? A subpolar gyre example. *J. Phys. Oceanogr.* (in press). [5.5]
- Spall, M. A.** and J.F. Price, 1998: Mesoscale variability in Denmark Strait: The PV outflow hypothesis. *J. Phys. Oceanogr.* **28**, 1598–1623. [5.6]
- Spall, M. A.**, R.A. Weller and P. Furey, 2000: Modelling the three-dimensional upper ocean heat budget and subduction rate during the Subduction Experiment. *J. Phys. Oceanogr.* **105**, 26151–26166. [5.3]
- Sparrow, M. D.**, K.J. Heywood, J. Brown and D.P. Stevens, 1996: Current structure of the south Indian Ocean. *J. Geophys. Res.* **101**, 6377–6392. [4.6]
- Speer, K. G.**, 1993: Conversion among North-Atlantic surface-water types. *Tellus Series a-Dynamic Meteorology and Oceanography* **45A**, 72–79. [5.1]
- Speer, K. G.**, 1997: A note on average cross-isopycnal mixing in the North Atlantic Ocean. *Deep-Sea Res.* **44**, 1981–1990. [5.2]
- Speer, K. G.** and E. Tziperman, 1992: Rates of water mass formation in the North Atlantic Ocean. *J. Phys. Oceanogr.* **22**, 93–104. [2.3, 4.6, 5.1, 5.3, 6.2]
- Speer, K. G.** and W. Zenk, 1993: The flow of Antarctic Bottom Water into the Brazil Basin. *J. Phys. Oceanogr.* **23**, 2667–2682. [4.5]
- Speer, K. G.**, H.J. Isemer and A. Biastach, 1995a: Water mass formation from revised COADS data. *J. Phys. Oceanogr.* **25**, 2444–2457. [5.1, 5.3]
- Speer, K. G.**, G. Siedler and L. Talley, 1995c: The Namib Col Current. *Deep-Sea Res. I* **42**, 1933–1950. [4.5]
- Speer, K. G.**, J. Holfort, T. Reynaud and G. Siedler, 1996: South Atlantic heat transport at 11°S. In: *The South Atlantic: Present and Past Circulation*, G. Wefer, W.H. Berger, G. Siedler and D.J. Webb (eds), Springer-Verlag, Berlin, 646 pp. [4.3, 6.1]
- Speer, K. G.**, S.R. Rintoul and B. Sloyan, 1997: Subantarctic mode water formation by air-sea fluxes. International WOCE Newsletter, No. 29, 29–31, WOCE International Project Office (unpublished document). [5.1, 5.4]
- Speer, K. G.**, J. Gould and J. LaCasce, 1999: Year-long float trajectories in the Labrador Sea Water of the eastern North Atlantic Ocean. *Deep-Sea Res.* **46**, 165–179. [3.2]
- Speer, K. G.**, S.R. Rintoul and B.M. Sloyan, 2000: The diabatic Deacon cell. *J. Phys. Oceanogr.* (in press). [4.6]
- Speich, S.**, B. Blanke and G. Madec, 2000: Warm and cold water routes of an OGCM thermohaline conveyor belt. *Geophys. Res. Lett.* (in press). [4.7]
- Spencer, N.E.** and P.L. Woodworth, 1993: Data holdings of the Permanent Service for Mean Sea Level (November 1993). Bidston, Birkenhead, 81 pp. [1.2]
- Spencer, R.W.**, 1993: Global oceanic precipitation from the MSU during 1979–1992 and comparisons to other climatologies. *J. Climate* **6**, 1301–1326. [3.4, 5.1]

- Sprintall, J., J. Chong, F. Syamsudin *et al.*, 1999: Dynamics of the South Java Current in the Indo-Australian Basin. *Geophys. Res. Lett.* **26**, 2493–2496. [4.3]
- Sprintall, J., A. Gordon, R. Murtugudde and R.D. Susanto, 2000: A semi-annual equatorial western Indian Ocean forced Kelvin wave observed in the Indonesian Seas in May 1997. *J. Geophys. Res.* **105**, 17217–17230. [4.7]
- St Laurent, L.C., 1999: *Diapycnal advection by double diffusion and turbulence in the ocean*. Ph.D. Thesis, MIT-WHOI Joint Program in Physical Oceanography, 139 pp. [4.5, 5.2]
- St Laurent, L. and R.W. Schmitt, 1999: The contribution of salt fingers to vertical mixing in the North Atlantic Tracer Release Experiment. *J. Phys. Oceanogr.* **29**, 1404–1424. [5.2]
- St Laurent, L.C., J.M. Toole, R.W. Schmitt and K.L. Polzin, 2000: Buoyancy forcing by turbulence above rough topography in the abyssal Brazil Basin. *J. Phys. Oceanogr.* (submitted). [5.2]
- Stahr, F.R. and T.B. Sanford, 1999: Transport and bottom boundary layer observations of the North Atlantic Deep Western Boundary Current at the Blake Outer Ridge. *Deep-Sea Res.* **46**, 205–243. [5.2, 5.6]
- Stammer, D., 1997a: Steric and wind-induced changes in TOPEX/POSEIDON large-scale sea surface topography observations. *J. Geophys. Res.* **102**, 20987–21009. [2.2, 3.3]
- Stammer, D., 1997b: Global characteristics of ocean variability estimated from regional TOPEX/POSEIDON altimeter measurements. *J. Phys. Oceanogr.* **27**, 1743–1769. [3.3, 6.2]
- Stammer, D., 1998: On eddy characteristics, eddy transports, and mean flow properties. *J. Phys. Oceanogr.* **28**, 727–739. [3.3, 6.2]
- Stammer, D. and C. Dieterich, 1999: Space-borne measurements of the time-dependent geostrophic ocean flow field. *J. Atmos. Oceanic Technol.* **16**, 1198–1207. [3.3]
- Stammer, D. and C. Wunsch, 1999: Temporal changes in eddy energy of the oceans. *Deep-Sea Res. II* **46**, 77–108. [3.3, 7.1]
- Stammer, D., R. Tokmakian, A. Semtner and C. Wunsch, 1996: How well does a 1/4° global circulation model simulate large-scale oceanic observations. *J. Geophys. Res.* **101**, 25779–25811. [2.1, 2.2, 3.3, 7.1]
- Stammer, D., C. Wunsch, R. Giering *et al.*, 1997: *The Global Ocean Circulation Estimated from TOPEX/POSEIDON Altimetry and the MIT General Circulation Model*. MIT Press, Cambridge, MA, Report No. 49, 40 pp. [3.3, 7.1]
- Stammer, D., C.W. Böning and C. Dieterich, 2000a: The role of variable wind forcing in generating eddy energy in the North Atlantic. *Prog. Oceanogr.* (in press). [2.2]
- Stammer, D., C. Wunsch, R. Giering *et al.*, 2000b: The global ocean circulation and transports during 1992–1997, estimated from ocean observations and a general circulation model. (in preparation). [7.1]
- Stammer, D., C. Wunsch and R.M. Ponte, 2000c: De-aliasing of global high frequency barotropic motions in altimeter observations. *Geophys. Res. Lett.* **27**, 1175–1178. [3.3]
- Steele, M. and T. Boyd, 1998: Retreat of the cold halocline layer in the Arctic Ocean. *J. Geophys. Res.* **103**, 10419–10435. [7.3]
- Stephens, G.L., G.C. Campbell and T.H. Vonder Haar, 1981: Earth radiation budgets. *J. Geophys. Res.* **86**, 9739–9760. [6.1]
- Stephens, J.C. and D.P. Marshall, 1999: Dynamics of the Mediterranean Salinity Tongue. *J. Phys. Oceanogr.* **29**, 1425–1441. [5.7]
- Stephens M., Z. Liu and H. Yang, 2000: On the evolution of subduction planetary waves with application to Pacific decadal thermocline variability. *J. Phys. Oceanogr.* (in press). [4.4]
- Stern, M.E., 1967: Lateral mixing of water masses. *Deep-Sea Res.* **14**, 747–753. [5.2]
- Stevens, D.P. and V.O. Ivchenko, 1997: The zonal momentum balance in an eddy-resolving general-circulation model of the Southern Ocean. *Quart. J. Roy. Meteor. Soc.* **123**, 929–951. [4.2, 4.6]
- Stockdale, T.N., D.L.T. Anderson, J.O.S. Alves and M.A. Balmaseda, 1998: Global seasonal rainfall forecasts using a coupled ocean–atmosphere model. *Nature* **392**, 370–373. [2.3, 7.4]
- Stocker, T.F. and A. Schmittner, 1997: Influence of CO₂ emission rates on the stability of the thermo-haline circulation. *Nature* **388**, 862–865. [2.3]
- Stocker, T.F., W.S. Broecker and D.G. Wright, 1994: Carbon uptake experiments with a zonally-averaged ocean circulation model. *Tellus* **46B**, 103–122. [6.3]
- Stockton, C.W. and M.F. Glueck, 1999: Long-term variability of the North Atlantic Oscillation (NAO). *Ann. Mtg, Amer. Meteor. Soc.*, 4 pp. [7.3]
- Stoffelen, A. and D. Anderson, 1997: Scatterometer data interpretation: Estimation and validation of the transfer function CMOD4. *J. Geophys. Res.* **102**, 5767–5780. [3.4]
- Stoll, M.H.C., H.M. van Aken, H.J.W. deBaar and C.J. deBoer, 1996: Meridional carbon dioxide transport in the northern North Atlantic. *Mar. Chem.* **55**, 205–216. [6.3]

- Stommel, H., 1948: The westward intensification of wind-driven ocean currents. *Trans. Amer. Geophys. Union* **29**, 202–206. [2.1, 4.2, 7.4]
- Stommel, H., 1955: Direct measurements of sub-surface currents. *Deep-Sea Res.* **2**, 284–285. [3.2]
- Stommel, H., 1957: A survey of ocean current theory. *Deep-Sea Res.* **4**, 149–184. [4.6]
- Stommel, H., 1958: The abyssal circulation. Letter to the editors. *Deep-Sea Res.* **5**, 80–82. [4.2, 4.5]
- Stommel, H., 1961: Thermohaline Convection with Two Stable Regimes of Flow. *Tellus* **13**, 224–230. [5.6]
- Stommel, H., 1965: *The Gulf Stream*, 2nd edn. University of California Press, Berkeley, 248 pp. [4.2]
- Stommel, H., 1979: Determination of water-mass properties of water pumped down from the Ekman layer to the geostrophic flow below. *Proc. Nat. Acad. Sci. US.* **76**, 3051–3055. [5.3, 5.4, 7.3]
- Stommel, H., 1982: Is the South Pacific helium-3 plume dynamically active? *Earth Planet. Sci. Lett.* **61**, 63–67. [4.3]
- Stommel, H., 1989: The Slocum Mission. *Oceanogr.* **3**, 22–25. [3.2]
- Stommel, H. and A. B. Arons, 1960a: On the abyssal circulation of the world ocean. I. Stationary planetary flow patterns on a sphere. *Deep-Sea Res.* **6**, 140–154. [1.2, 4.2, 4.3, 4.4, 4.6, 5.2]
- Stommel, H. and A. B. Arons, 1960b: On the abyssal circulation of the world ocean. II. An idealized model of the circulation pattern and amplitude in oceanic basins. *Deep-Sea Res.* **6**, 217–233. [1.2, 4.2, 4.3, 4.4, 5.2, 5.8]
- Stommel, H. M. and G. T. Csanady, 1980: A relation between the TS curve and global heat and atmospheric water transports. *J. Geophys. Res.* **85**, 495–501. [6.2]
- Stommel, H. and F. Schott, 1977: The beta spiral and the determination of the absolute velocity field from hydrographic station data. *Deep-Sea Res.* **24**, 325–329. [3.2]
- Stommel, H., H. L. Bryden and P. Mangelsdorf, 1973: Does some of the Mediterranean outflow come from great depth? *Pure and Applied Geophysics* **105**, 879–889. [5.7]
- Stone, P., 1972: A simplified radiative-dynamical model for the static stability of the rotating atmosphere. *J. Atmos. Sci.* **29**, 405–418. [3.3, 4.6]
- Stouffer, R. J. and K. W. Dixon, 1998: Initialization of coupled models for use in climate studies: A review. In: *Research Activities in Atmospheric and Oceanic Modelling* Report No. 27, World Meteorological Organisation, WMO/TD-No.865, I.I–I.8. [2.3, 7.4]
- Stramma, L. and J.R.E. Lutjeharms, 1997: The flow field of the subtropical gyre of the South Indian Ocean. *J. Geophys. Res.* **102**, 5513–5530. [5.4]
- Stramma, L. and F. Schott, 1996: Western equatorial circulation and interhemispheric exchange. In: *The Warmwatersphere of the North Atlantic Ocean*, W. Krauss (ed), Gebr. Bornträger, Stuttgart, pp. 195–227. [4.3, 4.7]
- Stramma, L. and F. Schott, 1999: The mean flow field of the tropical Atlantic Ocean. *Deep-Sea Res.* **46**, 279–303. [4.3]
- Stramma, L., J. Fischer and J. Reppin, 1995: The North Brazil Undercurrent. *Deep-Sea Res.* **42**, 773–795. [4.3]
- Straub, D.N., 1993: On the transport and angular momentum balance of channel models of the Antarctic Circumpolar Current. *J. Phys. Oceanogr.* **23**, 776–782. [4.6]
- Strub, P. T., T.K. Chereskin, P.P. Niiler, C. James and M.D. Levine, 1997: Altimeter-derived variability of surface velocities in the California Current system; 1. Evaluation of Topex altimeter velocity resolution. *J. Geophys. Res.* **102**, 12727–12748. [1.2, 3.3, 4.1]
- Stuiver, M., P.D. Quay and H.G. Ostlund, 1983: Abyssal water carbon-14 distribution and the age of the world oceans. *Science* **219**, 849–851. [5.8]
- Sturges, W., B.G. Hong and A.J. Clarke, 1998: Decadal wind forcing of the North Atlantic subtropical gyre. *J. Phys. Oceanogr.* **28**, 659–668. [7.3]
- Stutzer, S. and W. Krauss, 1998: Mean circulation and transport in the South Atlantic: combining model and drifter data. *J. Geophys. Res.* **103**, 30985–31002. [4.7]
- Suga, T. and K. Hanawa, 1990: The mixed-layer climatology in the northwestern part of the North Pacific subtropical gyre and the formation area of Subtropical Mode Water. *J. Mar. Res.* **48**, 543–566. [5.4]
- Suga, T. and K. Hanawa, 1995a: Subtropical Mode Water south of Honshu, Japan in the spring of 1988 and 1989. *J. Oceanogr.* **51**, 1–19. [5.4]
- Suga, T. and K. Hanawa, 1995b: The Subtropical Mode Water circulation in the North Pacific. *J. Phys. Oceanogr.* **25**, 958–970. [5.4]
- Suga, T. and K. Hanawa, 1995c: Interannual variations of North Pacific Subtropical Mode Water in the 137°E section. *J. Phys. Oceanogr.* **25**, 1012–1017. [5.4]
- Suga, T., K. Hanawa and Y. Toba, 1989: The Subtropical Mode Water in the 137°E section. *J. Phys. Oceanogr.* **19**, 1605–1618. [5.4]
- Suga, T., Y. Takei and K. Hanawa, 1997: Thermostad distribution in the North Pacific

- subtropical gyre: The Subtropical Mode Water and the Central Mode Water. *J. Phys. Oceanogr.* 27, 140–152. [5.4]
- Suginohara, N.** and S. Aoki, 1991: Buoyancy-driven circulation as horizontal convection on a β -plane. *J. Mar. Res.* 49, 295–320. [4.3]
- Sun, S.**, R. Bleck, C.G. Rooth, J. Dukowicz, E.P. Chassignet and P. Killworth, 1999: Note on the inclusion of thermobaricity in numerical ocean models framed in isopycnic coordinates. *J. Phys. Oceanogr.* 29, 2719–2729. [7.2]
- Sundermeyer, M.A.** and J.F. Price, 1998: Lateral mixing and the North Atlantic Tracer Release Experiment: Observations and numerical simulations of Lagrangian particles and a passive tracer. *J. Geophys. Res.* 103, 21481–21497. [3.2, 5.2, 5.5]
- Susanto, R.D.**, A. Gordon, J. Sprintall, and B. Herunadi, 2000: Intraseasonal variability and tides in Makassar Strait. *Geophys. Res. Lett.* 27, 1499–1502. [4.7]
- Sutton, R.T.** and M.R. Allen, 1997: Decadal predictability of North Atlantic sea surface temperature and climate. *Nature* 388, 563–567. [1.2, 7.1, 7.3]
- Sverdrup, H.U.**, 1933: On vertical circulation in the ocean due to the action of the wind with application to conditions within the Antarctic circumpolar current. *Discovery Reports VII*, 139–170. [4.6]
- Sverdrup, H.U.**, 1947: Wind-driven currents in a baroclinic ocean; with application to the equatorial currents of the eastern Pacific. *Proc. Natl. Acad. Sci. USA* 33, 318–326. [2.1, 4.2]
- Sverdrup, H.U.**, M.W. Johnson and R.H. Fleming, 1942: *The Oceans: their Physics, Chemistry and General Biology*. Prentice-Hall, Englewood Cliffs, NJ, 1087 pp. [2.1, 3.1, 4.1, 4.6]
- Swallow, J.C.**, 1955: A neutral-buoyancy float for measuring deep currents. *Deep-Sea Res.* 3, 74–81. [3.2, 7.4]
- Swallow, J.C.**, 1971: The Aries current measurements in the western North Atlantic. *Phil. Trans. Roy. Soc. Lond. A* 270, 451–460. [4.5]
- Swallow, J.C.** and J.G. Bruce, 1966: Current measurements off the Somali coast during the southwest monsoon of 1964. *Deep-Sea Res.* 13, 861–888. [4.3]
- Swallow, J.C.** and B.V. Hamon, 1960: Some measurements of deep currents in the Eastern North Atlantic. *Deep-Sea Res.* 6, 155–168. [3.2]
- Swallow, J.C.** and L.V. Worthington, 1957: Measurements of deep currents in the western North Atlantic. *Nature*, 179, 1183–1184. [4.5]
- Swallow, J.C.** and L.V. Worthington, 1961: An observation of a deep countercurrent in the western North Atlantic. *Deep-Sea Res.* 8, 1–19. [4.5]
- Swallow, J.C.**, B.C. McCartney and N.W. Millard, 1974: The Minimode float tracking system. *Deep-Sea Res.* 21, 573–595. [3.2]
- Swallow, J.C.**, R.L. Molinari, J.G. Bruce, O.B. Brown and R.H. Evans, 1983: Development of near-surface flow pattern and water-mass distributions in the Somali Basin in response to the southwest monsoon of 1979. *J. Phys. Oceanogr.* 13, 1398–1415. [4.3]
- Swallow, J.C.**, F. Schott and M. Fieux, 1991: Structure and transport of the East African Coastal Current. *J. Geophys. Res.* 96, 22245–22257. [4.3]
- Swenson, M.S.** and D.V. Hansen, 1999: Tropical Pacific Ocean mixed layer budget: the Pacific cold tongue. *J. Phys. Oceanogr.* 29, 83–91. [4.3]
- Swift, J.H.**, 1984: The circulation of Denmark Strait and Iceland–Scotland overflow waters in the North Atlantic. *Deep-Sea Res.* 31, 1339–1355. [5.6]
- Swift, J.H.** and K. Aagaard, 1981: Seasonal transitions and water mass formation in the Iceland and Greenland seas. *Deep-Sea Res.* 28, 1107–1129. [5.6]
- Swift, J.H.** and K.P. Koltermann, 1988: The origin of Norwegian Sea Deep Water. *J. Geophys. Res.* 93, 3563–3569. [7.3]
- Swift, J.H.**, T. Takahashi and H.D. Livingston, 1983: The contribution of the Greenland and Barents Seas to the deep water of the Arctic Ocean. *J. Geophys. Res.* 88, 5981–5986. [7.3]
- Swift, J.H.**, E.P. Jones, K. Aagaard *et al.*, 1997: Waters of the Makarov and Canada Basins. *Deep-Sea Res.* 44, 1503–1529. [4.7, 7.3]
- Swift, J.H.**, K. Aagaard and E.C. Carmack, 2001: The center of the Greenland Sea. *J. Geophys. Res.* (in press). [7.3]
- Sy, A.**, M. Rhein, J.R.N. Lazier *et al.*, 1997: Surprisingly rapid spreading of newly formed intermediate waters across the North Atlantic Ocean. *Nature* 386, 675–679. [5.5, 5.8, 7.3]
- Sybrandy, A.L.** and P.P. Niiler, 1991: *WOCE/TOGA Lagrangian Drifter Construction Manual*, SIO Ref. Series 91/6. WOCE International Project Office, WOCE Report No. 63/91, 58 pp. (unpublished manuscript). [4.1]
- Szeredi, I.** and D.J. Karoly, 1987: Horizontal structure of monthly fluctuations of the Southern Hemisphere troposphere from station data. *Aust. Meteor. Mag.* 35, 119–129. [7.3]
- Taft, B.A.**, 1963: Distribution of salinity and dissolved oxygen on surfaces of uniform potential specific volume in the South Atlantic, South Pacific and Indian Oceans. *J. Mar. Res.* 21, 129–146. [4.4]
- Tai, C.K.**, 1990: Estimating the surface transport of meandering oceanic jet streams from satellite altimetry: surface transport estimates for the Gulf

- Stream and Kuroshio Extension. *J. Phys. Oceanogr.* **20**, 860–879. [3.3]
- Tai, C. K. and W. B. White, 1990: Eddy variability in the Kuroshio Extension as revealed by GEOSAT altimetry: Energy propagation away from the jet, Reynolds stress and seasonal cycle. *J. Phys. Oceanogr.* **20**, 1761–1777. [3.3]
- Tai, C. K. and C. Wunsch, 1983: Absolute measurement by satellite altimetry of the dynamic topography of the Pacific Ocean. *Nature* **301**(5899), 408–410. [3.3]
- Takahashi, T., T. T. Takahashi and S. C. Sutherland, 1995: An assessment of the role of the North Atlantic as a CO₂ sink. *Phil. Trans. Roy. Soc. Lond. B*, **348**, 143–152. [6.3]
- Takahashi, T., R. A. Feely, R. Weiss *et al.*, 1997: Global air-sea flux of CO₂: An estimate based on measurements of sea-air pCO₂ difference. In: *NAS Colloquium Volume on Carbon Dioxide and Climate Change*, C.D. Keeling (ed), *Proc. Natl. Acad. Sci. USA* **94**, 8292–8299. [6.3]
- Talley, L. D., 1984: Meridional heat transport in the Pacific Ocean. *J. Phys. Oceanogr.* **14**, 231–241. [6.1]
- Talley, L. D., 1985: Ventilation of the subtropical North Pacific: The shallow salinity minimum. *J. Phys. Oceanogr.* **15**, 633–649. [4.2, 5.3]
- Talley, L. D., 1988: Potential vorticity distribution in the North Pacific. *J. Phys. Oceanogr.* **18**, 89–106. [5.4]
- Talley, L. D., 1991: An Okhotsk Sea water anomaly: Implications for sub-thermocline ventilation in the North Pacific. *Deep-Sea Res.* **38** (suppl.), S171–S190. [5.4]
- Talley, L. D., 1993: Distribution and formation of North Pacific Intermediate Water. *J. Phys. Oceanogr.* **23**, 517–537. [5.4]
- Talley, L. D., 1996a: Antarctic Intermediate Water in the South Atlantic. In: *The South Atlantic: Present and Past Circulation*, G. Wefer, W. H. Berger, G. Siedler and D. J. Webb (eds), Springer-Verlag., pp. 219–238. [4.6, 5.4]
- Talley, L. D., 1996b: North Atlantic circulation and variability, reviewed for the CNLS Conference, Los Alamos, May 1995. *Physica D* **98**, 625–646. [5.4, 7.3]
- Talley, L. D., 1997: North Pacific intermediate water transports in the mixed water region. *J. Phys. Oceanogr.* **27**, 1795–1803. [5.4]
- Talley, L. D., 1999a: Some aspects of ocean heat transport by the shallow, intermediate and deep overturning circulations. In: *Mechanisms of Global Climate Change at Millennial Time Scales*, Clark, Webb and Keigwin (eds), American Geophysical Union, Washington, DC. *Geophys. Mono. Ser.* **112**, 1–22. [5.4]
- Talley, L. D., 1999b: Mode waters in the subpolar North Atlantic in historical data and during the WOCE period. *International WOCE Newsletter*, No. 37, 3–6, WOCE International Project Office (unpublished document). [5.4, 7.1]
- Talley, L. D., 1999c: Simple coupled midlatitude climate models. *J. Phys. Oceanogr.* **29**, 2016–2037. [4.6]
- Talley, L. D. and M. O. Baringer, 1997: Preliminary results from WOCE hydrographic sections at 80°E and 32°S in the central Indian Ocean. *Geophys. Res. Lett.* **24**, 2789–2792. [4.3]
- Talley, L. D. and G. C. Johnson, 1994: Deep, zonal subequatorial currents. *Science* **263**, 1125–1128. [4.2, 4.3, 4.5, 5.8]
- Talley, L. D. and T. M. Joyce, 1992: The double silica maximum in the North Pacific. *J. Geophys. Res.* **97**, 5465–5480. [4.2]
- Talley, L. D. and M. S. McCartney, 1982: Distribution and circulation of Labrador Sea water. *J. Phys. Oceanogr.* **12**, 1189–1205. [5.4, 5.5]
- Talley, L. D. and M. E. Raymer, 1982: Eighteen Degree Water variability. *J. Mar. Res.* **40**(suppl.), 725–775. [5.4, 7.3]
- Tandon, A. and C. Garrett, 1996: On a recent parameterization of mesoscale eddies. *J. Phys. Oceanogr.* **26**, 406–411. [5.2]
- Tandon, A. and C. Garrett, 1997: Water mass formation from thermodynamics: a framework for examining compatibility with dynamics. *International WOCE Newsletter*, No. 28, 34–36. WOCE International Project Office (unpublished document). [5.1]
- Tandon, A. and K. Zahariev, 2000: Quantifying the role of mixed layer entrainment for water mass conversion in the North Atlantic. *J. Phys. Oceanogr.* (in press). [5.1]
- Taneda, T., T. Suga and K. Hanawa, 2000: Subtropical mode water variation in the northwestern part of the north Pacific subtropical gyre. *J. Geophys. Res.* **105**, 19591–19598. [5.4]
- Tang, G. L., 1991: A two-dimensional thermodynamical model for sea ice advance and retreat in the Newfoundland marginal ice zone. *J. Geophys. Res.* **96**, 4723–4737. [1.2]
- Tanimoto, Y., N. Iwasaka, K. Hanawa and Y. Toba, 1993: Characteristic variations of sea surface temperature with multiple time scales on the North Pacific. *J. Climate* **6**, 1153–1160. [5.4]
- Tans, P. P., I. Y. Fung and T. Takahashi, 1990: Observational constraints on the global atmospheric CO₂ budget. *Science* **247**, 1431–1438. [6.3]

- Tapley, B. and M.C. Kim, 2000: Applications to geodesy, pp. 371–406. In: *Satellite Altimetry and Earth Sciences*, L.-L. Fu and A. Cazenave (eds), Academic Press. [3.3]
- Tapley, B.D., R.S. Nerem, C.K. Shum, J.C. Ries and D.N. Yuan, 1988: Determination of the general ocean circulation from a joint gravity field solution. *Geophys. Res. Lett.* 15, 1109–1112. [3.3]
- Tapley, B.D., M.M. Watkins, J.C. Ries *et al.*, 1996: The Joint Gravity Model 3. *J. Geophys. Res.* 101, 28029–28049. [3.3]
- Taylor, G.I., 1917: Motion of solids in fluids when the motion is not irrotational. *Proc. Roy. Soc. A* 93, 99–113. [4.2]
- Taylor, G.I., 1953: Dispersion of soluble matter in solvent flowing slowly through a tube. *Proc. Roy. Soc. London A* 219, 186–203. [5.2]
- Taylor, P.K. and R.A. Weller, 1991: Meteorological measurements from WOCE research ships. *WOCE Operations Manual*, Vol. 3: *The Observational Programme*. Part 3.1.3: WHP Operations and Methods, Section 3: Underway Measurements. WOCE International Project Office. (Unpublished manuscript). US WOCE WHP Office Report WHPO 91-1, WOCE Report 68/91, various paginations. [3.1]
- Taylor, P.K., E.F. Bradley, C.W. Fairall *et al.*, 2001: Surface fluxes and surface reference sites. In: *Observing the Ocean in the 21st Century*, N.R. Smith and C.J. Koblinsky (eds), Bureau of Meteorology, Melbourne, Australia, Chapter 34. [7.4]
- Tett, S.F.B., 1995: Simulation of El-Nino/Southern Oscillation like variability in a global AOGCM and its response to CO₂ increase. *J. Climate* 8, 1473–1502. [2.3]
- Tett, S.F.B., P.A. Stott, M.R. Allen, W.J. Ingram and J.F.B. Mitchell, 1999: Causes of twentieth century temperature changes near the Earth's surface. *Nature* 399, 569–572. [2.3]
- Thadathil, P., A. Shikauchi, Y. Sugimori and M. Kubota, 1993: A statistical method to get surface level air-temperature from satellite observations of precipitable water. *J. Oceanogr.* 49, 551–558. [3.4]
- The Lab Sea Group, 1998: The Labrador Sea Deep Convection Experiment. *Bull. Amer. Meteor. Soc.* 79, 2033–2058. [5.5]
- Thierry, V., 2000: Observation et modélisation de la variabilité saisonnière dans l'océan Atlantique équatorial profond, *Doctoral Dissertation*, Université de Bretagne Occidentale, 203pp. [4.3]
- Thiria, S., C. Mejia, F. Badran and M. Crepon, 1993: A neural network approach for modeling nonlinear transfer functions: Application for wind retrieval from spaceborne scatterometer data. *J. Geophys. Res.* 98, 22827–22841. [3.4]
- Thompson, D.W.J. and J.M. Wallace, 1998: The Arctic Oscillation signature in the wintertime geopotential height and temperature fields. *Geophys. Res. Lett.* 25, 1297–1300. [7.1, 7.3]
- Thompson, D.W.J. and J.M. Wallace, 2000: Annular modes in the extratropical circulation Part I: month-to-month variability. *J. Climate* 13, 1000–1016. [7.3]
- Thompson, D.W.J., J.M. Wallace and G.C. Hegerl, 2000: Annular modes in the extratropical circulation. Part II: Trends, *J. Climate* 13, 1018–1036. [7.1, 7.3]
- Thompson, R.O.R.Y. and R.J. Edwards, 1981: Mixing and water-mass formation in the Australian Subantarctic. *J. Phys. Oceanogr.* 11, 1399–1406. [5.4]
- Thomson, C. Wyville, 1877: *A Preliminary Account of the General Results of the Voyage of the HMS Challenger*. MacMillan, London, 424 pp. [4.1]
- Thorpe, S.A., 1978: The near-surface ocean mixing layer in stable heating conditions. *J. Geophys. Res.* 83, 2875–2885. [5.2]
- Thorpe, S.A., 1979: Breaking internal waves in sheer flows. In: *Twelfth Symposium on Naval Hydrodynamics*, National Academy of Science, Washington, DC, pp. 623–628. [5.2]
- Tierney, C., J. Wahr, F. Bryan and V. Zlotnicki, 2000: Short-period oceanic circulation: implications for satellite altimetry. *Geophys. Res. Lett.* 27, 1255–1258. [3.3]
- Timmermann, A., J. Oberhuber, A. Bacher, M. Esch, M. Latif and E. Roeckner, 1999a: Increased El Niño frequency in a climate model forced by future greenhouse warming. *Nature* 398, 694–669. [1.2]
- Timmermann, A., M. Latif, A. Grotzner and R. Voss, 1999b: Modes of climate variability as simulated by the coupled atmosphere–ocean model ECHAM3/LSG, part I: ENSO-like climate variability and its low-frequency modulation. *Climate Dyn.* 15, 605–618. [2.3]
- TOGA (Tropical Oceans–Global Atmosphere Experiment), 1985: *TOGA Implementation Plan*. International TOGA Project Office, Boulder, CO. [7.4]
- Toggweiler, J.R. and B. Samuels, 1993: New radiocarbon constraints on the upwelling of abyssal water to the ocean's surface. In: *The Global Carbon Cycle*, M. Heimann (ed.), NATO ASI Series, Springer-Verlag, Berlin and Heidelberg, Vol. 15, pp. 333–363. [4.6]
- Toggweiler, J.R. and B. Samuels, 1998: On the ocean's large scale circulation in the limit of no

- vertical mixing. *J. Phys. Oceanogr.* **28**, 1832–1852. [4.2, 4.6, 5.2]
- Toggweiler, J.R.**, K. Dixon and K. Bryan, 1989: Simulations of radiocarbon in a coarse-resolution world ocean model, 1. Steady state prebomb distributions. *J. Geophys. Res.* **94**, 8217–8242. [2.2]
- Toggweiler, J.R.**, K. Dixon and W.S. Broecker, 1991: The Peru upwelling and the ventilation of the South Pacific thermocline. *J. Geophys. Res.* **96**, 20467–20497. [4.4, 5.8]
- Tokmakian, R.**, 1996: Comparison of time series from two global models with tide-gauge data. *Geophys. Res. Lett.* **23**, 3759–3762. [2.2]
- Tokmakian, R.**, 1998: A high-resolution ocean model with variable forcing of wind, heat, and freshwater: Initial evaluation. *International WOCE Newsletter*, No. 32, 26–28, WOCE International Project Office (unpublished document). [2.2]
- Tokmakian, R.** and P.G. Challenor, 1999: On the joint estimation of model and satellite sea surface height anomaly errors. *Ocean Modelling* **1**, 39–52. [7.1]
- Tomczak, M.** and J. Godfrey, 1994: *Regional Oceanography: An Introduction*. Pergamon Press, London, 422 pp. [4.7]
- Tomczak, M.** and D.G.B. Large, 1989: Optimum multiparameter analysis of mixing in the thermocline of the Eastern Indian Ocean. *J. Geophys. Res.* **94**, 16141–16149. [5.8, 6.3]
- Toole, J.M.**, 1981: Sea ice, winter convection, and the temperature minimum layer in the Southern Ocean. *J. Geophys. Res.* **86**, 8037–8047. [4.6]
- Toole, J.M.** and D.T. Georgi, 1981: On the dynamics and effects of double-diffusively driven intrusions. *Prog. Oceanogr.* **10**, 121–145. [5.2]
- Toole, J.M.** and M.E. Raymer, 1985: Heat and fresh water budgets of the Indian Ocean – revisited. *Deep-Sea Res.* **32**, 917–928. [4.3, 4.7]
- Toole, J.M.** and B.A. Warren, 1993: A hydrographic section across the subtropical South Indian Ocean. *Deep-Sea Res.* **40**, 1973–2019. [3.1, 4.3, 4.6, 4.7, 5.4, 6.1]
- Toole, J.M.**, H. Peters and M.C. Gregg, 1987: Upper ocean shear and density variability at the equator during TROPIC HEAT. *J. Phys. Oceanogr.* **17**, 1397–1406. [4.3]
- Toole, J.M.**, K.L. Polzin and R.W. Schmitt, 1994: Estimates of diapycnal mixing in the abyssal ocean. *Science* **264**, 1120–1123. [4.6, 5.2]
- Toole, J.M.**, R.W. Schmitt, K.L. Polzin and E. Kunze, 1997: Near-boundary mixing above the flanks of a midlatitude seamount. *J. Geophys. Res.* **102**, 947–959. [5.2]
- Tourre, Y.M.**, Y. Kushnir and W.B. White, 1999: Evolution of interdecadal variability in sea level pressure, sea surface temperature, and upper ocean temperature over the Pacific Ocean. *J. Phys. Oceanogr.* **29**, 1528–1541. [7.1]
- Treguier, A.M.**, 1998: Evaluating eddy mixing coefficients from eddy resolving ocean models: A case study. *J. Mar. Res.* **57**, 89–108. [5.2]
- Treguier, A.M.** and J.C. McWilliams, 1990: Topographic influences on wind-driven, stratified flow in a β -plane channel: An idealized model for the Antarctic circumpolar current. *J. Phys. Oceanogr.* **20**, 321–343. [3.3, 4.6]
- Treguier, A.M.**, J.K. Dukowicz and K. Bryan, 1996: Properties of nonuniform grids used in ocean general circulation model. *J. Geophys. Res.* **101**, 20877–20881. [7.2]
- Treguier, A.M.**, I.M. Held and V.D. Larichev, 1997: On the parameterization of quasi-geostrophic eddies in primitive equation models. *J. Phys. Oceanogr.* **27**, 567–580. [2.2, 2.3]
- Trenberth, K.E.**, 1990: Recent observed interdecadal climate changes in the Northern Hemisphere. *Bull. Amer. Meteor. Soc.* **71**, 988–993. [5.4, 7.3]
- Trenberth, K.E.** (ed.), 1992: *Climate System Modeling*. Cambridge University Press, 788 pp. [2.3, 7.2]
- Trenberth, K.E.**, 1998a: The heat budget of the atmosphere and ocean. *Proceedings of the First International Conference on Reanalysis*. World Meteorological Organisation, WMO/TD No. 876, WCRP 104, 17–20. [2.2]
- Trenberth, K.E.**, 1998b: Development and forecasts of the 1997/98 El Niño: CLIVAR Scientific issues, *CLIVAR Exchanges*, International CLIVAR Project Office (unpublished document) **3**, 2/3, 4–14. [7.4]
- Trenberth, K.E.** and M.J. Coughlan, 1998: The 1997–98 El Niño event. *CLIVAR Exchanges*, International CLIVAR Project Office (unpublished document) **3**(1), 11–12. [1.2]
- Trenberth, K.E.** and C.J. Guillemot, 1998: Evaluation of the atmospheric moisture and hydrological cycle in the NCEP/NCAR reanalyses. *Climate Dyn.* **14**, 213–231. [6.2]
- Trenberth, K.E.** and T. Hoar, 1996: The 1990–95 El Niño–Southern Oscillation event: Longest on record. *Geophys. Res. Lett.* **23**, 57–60. [1.2, 7.3]
- Trenberth, K.E.** and T. Hoar, 1997: El Niño and climate change. *Geophys. Res. Lett.* **24**, 3057–3060. [7.3]
- Trenberth, K.E.** and J.W. Hurrell, 1994: Decadal atmospheric–ocean variations in the Pacific. *Climate Dyn.* **9**, 303–319. [7.3]
- Trenberth, K.E.** and D.A. Paolino, 1980: The Northern Hemisphere sea-level pressure data

- set: Trends, errors and discontinuities. *Mon. Wea. Rev.* 108, 855–872. [7.3]
- Trenberth, K.E. and A. Solomon, 1994: The global heat balance: heat transports in the atmosphere and ocean. *Climate Dyn.* 10, 107–134. [6.1]
- Trenberth, K.E., W.G. Large and J.G. Olson, 1990: The mean annual cycle in global ocean wind stress. *J. Phys. Oceanogr.* 20, 1742–1760. [1.2]
- Trenberth, K.E., G.W. Branstator, D. Karoly, A. Kumar, N.-C. Lau and C. Ropelewski, 1998: Progress during TOGA in understanding and modeling global teleconnections associated with tropical sea surface temperatures. *J. Geophys. Res.* 103, 14291–14324. [7.3]
- Trumbore, S.E., S.S. Jacobs and W.M. Smethie, Jr., 1991: Chlorofluorocarbon evidence for rapid ventilation of the Ross Sea. *Deep-Sea Res.* 38, 845–870. [5.8]
- Tsimplis, M.N., S. Bacon and H.L. Bryden, 1998: The circulation of the subtropical South Pacific derived from hydrographic data. *J. Geophys. Res.* 103, 21443–21468. [6.1, 6.2]
- Tsuchiya, M., 1968: Upper waters of the intertropical Pacific Ocean. *Johns Hopkins Oceanographic Studies* 4, 1–50. [4.4]
- Tsuchiya, M., 1972: A subsurface north equatorial countercurrent in the eastern Pacific Ocean. *J. Geophys. Res.* 77, 5981–5986. [4.3]
- Tsuchiya, M., 1975: Subsurface countercurrents in the eastern equatorial Pacific Ocean. *J. Mar. Res.* 33, 145–175. [4.3]
- Tsuchiya, M., 1981: The origin of the Pacific equatorial 13°C water. *J. Phys. Oceanogr.* 11, 794–812. [4.3, 4.4]
- Tsuchiya, M., 1991: Flow path of the Antarctic Intermediate water in the western equatorial South Pacific Ocean. *Deep-Sea Res.* 38(suppl.), S273–S279. [4.3, 4.4]
- Tsuchiya, M. and L.D. Talley, 1996: Water-property distributions along an eastern Pacific hydrographic section at 135°W. *J. Mar. Res.* 54, 541–564. [5.4]
- Tsuchiya, M. and L.D. Talley, 1998: A Pacific hydrographic section at 88°W: Water-property distribution. *J. Geophys. Res.* 103, 12899–12918. [4.3, 5.4]
- Tsuchiya, M., R. Lukas, R.A. Fine, E. Firing and E. Lindstrom, 1989: Source waters of the Pacific Equatorial Undercurrent. *Prog. Oceanogr.* 23, 101–147. [4.3, 4.4]
- Tsuchiya, M., L.D. Talley and M.S. McCartney, 1994: Water mass distributions in the western Atlantic: A section from South Georgia Island (54°S) northward across the equator. *J. Mar. Res.* 52, 55–81. [5.4]
- Tsujino, H. and N. Sugino, 1999: Thermohaline circulation enhanced by wind forcing. *J. Phys. Oceanogr.* 29, 1506–1516. [4.2]
- Tsujino, H., H. Hasumi and N. Sugino, 2000: Deep Pacific circulation controlled by depth-dependent vertical diffusivity. *Phys. Oceanogr.* (submitted). [2.2]
- TWXXPPC (TOGA/WOCE XBT/XCTD Programme Planning Committee), 1993: *Workshop on the Use of Sub-Surface Thermal Data for Climate Studies*, Brest, France, 13–16 September 1993. International TOGA Project Office Report No. 9/WOCE Report No. 110/93 (unpublished manuscript), 64 pp. [7.4]
- Tziperman, E., 1986: On the role of interior mixing and air-sea fluxes in determining the stratification and circulation of the oceans. *J. Phys. Oceanogr.* 7, 680–693. [5.1]
- Tziperman, E. and K.G. Speer, 1994: A study of water mass transformation in the Mediterranean Sea: Analysis of climatological data and a simple 3-box model. *Dyn. Atmos. Oceans* 21, 53–82. [5.1]
- Uchida, H., S. Imawaki and J-H. Hu, 1998: Comparison of Kuroshio surface velocities derived from satellite altimeter and drifting buoy data. *J. Phys. Oceanogr.* 54, 115–122. [4.1]
- Uhlhorn, E.W., K.B. Katsaros and M.D. Powell, 2000: Assimilation of scatterometer-derived winds into real-time tropical cyclone surface wind analyses. *Preprints, 10th Conference on Sat. Meteor. and Oceanogr.* Long Beach, CA, American Meteorological Society, 214–215. [3.4]
- Van Aken, H.M., J. Punjanan and S. Saimima, 1988: Physical aspects of the flushing of the East Indonesian basins. *Neth. J. Sea Res.* 22, 315–339. [4.7]
- Van Ballegooyen, R., M. Gründlingh and J. Lutjeharms, 1994: Eddy fluxes of heat and salt from the southwest Indian Ocean into the southeast Atlantic Ocean: A case study. *J. Geophys. Res.* 99, 14053–14070. [4.7]
- Van Loon, H., J.W. Kidson and A.B. Mullan, 1993: Decadal variation of the annual cycle in the Australian dataset. *J. Climate* 6, 1227–1231. [7.3]
- Van Woert, M.L. and J.M. Price, 1993: Geosat and advanced very high resolution radiometer observations of oceanic and planetary waves adjacent to the Hawaiian Islands. *J. Geophys. Res.* 98, 14619–14650. [3.3]
- Vanicek, M., 1998: *Wassermassen und tracerausbreitung im tiefen Südatlantik*. Ph.D. Thesis, Christian-Albrechts-Universität, Kiel, 153 pp. [4.5]

- Vanmarcke, E.**, 1983: *Random Fields: Analysis and Synthesis*. MIT Press, Cambridge, MA, 382 pp. [2.1]
- Verduin, J.** and D. Quadfasel, 2000: Long-term temperature and salinity trends in the central Greenland Sea. In: *European Sub-Polar Ocean Programme, Scientific Report*, E. Jansen (ed.), [7.3]
- Veronis, G.**, 1975: The role of models in tracer studies. In: *Numerical Models of Ocean Circulation*, R.O. Reid (ed.), National Academy of Science, Washington, DC, pp. 133–146. [5.2]
- Veronis, G.**, 1981: Dynamics of large-scale ocean circulation. In: *Evolution of Physical Oceanography*, B.A. Warren and C. Wunsch (eds), MIT Press, Cambridge, MA, pp. 140–183. [4.2]
- Verschell, M.**, J. Kindle and J. O'Brien, 1995: Effects of Indo-Pacific throughflow on the upper tropical Pacific and Indian Oceans. *J. Geophys. Res.* 100, 18409–18420. [4.7]
- Verschell, M.A.**, M.A. Bourassa, D.E. Weissman and J.J. O'Brien, 1999: Ocean model validation of the NASA scatterometer winds. *J. Geophys. Res.* 104, 11359–11373. [3.4]
- Vialard, J.** and P. Delecluse, 1998a: An OGCM study for the TOGA decade. Part I: Role of salinity in the physics of the Western Pacific Fresh Pool. *J. Phys. Oceanogr.* 28, 1071–1106. [4.3]
- Vialard, J.** and P. Delecluse, 1998b: An OGCM study for the TOGA decade. Part I: Barrier-layer formation and variability. *J. Phys. Oceanogr.* 28, 1071–1106. [4.3]
- Vinje, T.**, N. Nordlund and A. Kvambakk, 1998: Monitoring ice thickness in Fram Strait. *J. Geophys. Res.* 103, 10437–10450. [1.2, 7.3]
- Visbeck, M.** and M. Rhein, 2000: Is bottom boundary layer mixing slowly ventilating Greenland Sea Deep Water? *J. Phys. Oceanogr.* 30, 215–224. [7.3]
- Visbeck, M.** and F. Schott, 1992: Analysis of seasonal current variations in the western Equatorial Indian Ocean: Direct measurements and GFDL model comparison. *J. Phys. Oceanogr.* 22, 1112–1128. [4.3]
- Visbeck, M.**, J. Marshall, T. Haine and M. Spall, 1997: Specification of eddy transfer coefficients in coarse-resolution ocean circulation models. *J. Phys. Oceanogr.* 27, 381–402. [2.2, 2.3, 4.6]
- Visser, P.N.A.M.**, K.F. Wakker and B.A.C. Ambrosius, 1993: Dynamic Sea Surface Topography from GEOSAT Altimetry. *Mar. Geod.* 16(3), 215–239. [3.3]
- Viudez, A.**, 2000: Volume and mass transport across isosurfaces of a balanced fluid property. *J. Phys. Oceanogr.* 30, 1478–1485. [5.1]
- Vivier, F.**, K.A. Kelly and L. Thompson, 1999: Contributions of wind forcing, waves, and surface heating to sea-surface height observations in the Pacific Ocean. *J. Geophys. Res.* 104, 20767–20788. [3.3]
- Völker, C.**, 1999: Momentum balance in zonal flows and resonance of baroclinic Rossby waves. *J. Phys. Oceanogr.* 29, 1666–1681. [4.6]
- von Reden, K.F.**, R.J. Schneider, G.J. Cohen and G.A. Jones, 1994: Performance characteristics of the 3MV Tandetron AMS system at the National Ocean Sciences AMS Facility. *Nuclear Instr. and Methods* B92, 7–11. [5.8]
- Voss, R.**, R. Sausen and U. Cubasch, 1998: Periodically synchronously coupled integrations with the atmosphere–ocean general circulation model ECHAM3/LSG. *Climate Dyn.* 14, 249–266. [2.3]
- Vossepoel, F.C.**, R.W. Reynolds and L. Miller, 1999: Use of sea level observations to estimate salinity variability in the tropical Pacific. *J. Atmos. Oceanic Technol.* 16, 1401–1415. [7.4]
- Wacongne, S.**, 1990: On the difference in strength between Atlantic and Pacific undercurrents. *J. Phys. Oceanogr.* 20, 792–799. [4.3]
- Wacongne, S.** and R. Pacanowski, 1996: Seasonal heat transport in a primitive equation model of the Indian Ocean. *J. Phys. Oceanogr.* 26, 2666–2699. [4.3, 6.1]
- Wadley, M.R.** and G.R. Bigg, 1996: Abyssal channel flow in ocean general circulation models with application to the Vema Channel. *J. Phys. Oceanogr.* 26, 38–48. [2.3]
- Wagner, C.A.** and R.E. Cheney, 1992: Global sea level change from satellite altimetry. *J. Geophys. Res.* 97, 15607–15616. [3.3]
- Wagner, D.**, E. Ruprecht and C. Simmer, 1990: A combination of microwave observations from satellite and an EOF analysis to retrieve vertical humidity profiles over the ocean. *J. Appl. Meteor.* 29, 1142–1157. [3.4]
- Wahr, J.**, M. Molenaar and F. Bryan, 1998: Time variability of the Earth's gravity field: hydrological and oceanic effects and their possible detection using GRACE. *J. Geophys. Res.* 103, 30205–30229. [3.3]
- Wajsowicz, R.C.**, 1996: Flow of a western boundary current through multiple straits: An electrical circuit analogy for the Indonesian throughflow and archipelago. *J. Geophys. Res.* 101, 12295–12300. [4.7]
- Wajsowicz, R.C.**, 1999: Variations in gyre closure at the water mass crossroads of the western equatorial Pacific Ocean. *J. Phys. Oceanogr.* 29, 3001–3024. [4.7]

- Walsh, G., 1982: On the relation between sea-surface heat flow and thermal circulation in the ocean. *Tellus* 34, 187–195. [4.6, 5.1]
- Walker, S.J., R.F. Weiss and P.K. Salameh, 2000: Reconstructed histories of the annual mean atmospheric mole fractions for the halocarbons CFC-11, CFC-12, CFC-113, and carbon tetrachloride. *J. Geophys. Res.* 105, 14285–14296. [5.8]
- Wallace, D.W.R., 1995: *Monitoring Global Ocean Carbon Inventories*. Ocean Observing System Development Panel Background, Texas A&M University, College Station, TX, 54 pp. [6.3]
- Wallace, D.W.R. and J.R.N. Lazier, 1988: Anthropogenic chlorofluoromethanes in newly formed Labrador Sea Water. *Nature*, 332, 61–63. [5.5]
- Wallace, D.W.R., P. Beining and A. Putzka, 1994: Carbon tetrachloride and chlorofluorocarbons in the South Atlantic Ocean, 19°S. *J. Geophys. Res.* 99, 7803–7819. [5.8, 6.3]
- Wallace, J.M. and D.S. Gutzler, 1981: Teleconnections in the geopotential height field during the Northern Hemisphere winter. *Mon. Wea. Rev.* 109, 784–812. [7.3]
- Walsh, J.E., W.L. Chapman and T.L. Shy, 1996: Recent decrease of sea level pressure in the central Arctic. *J. Climate* 9, 480–486. [7.3]
- Wang, D., 1995: On thermally forced equatorial deep circulation in a GCM. *J. Phys. Oceanogr.* 25, 2155–2165. [4.3]
- Wang, D. and P. Muller, 1999: Internal wave generation in the equatorial undercurrent. In: 'Aha Huliko'o Proceedings Hawaiian Winter Workshop, Dynamics of Oceanic Internal Gravity Waves', P. Muller and D. Henderson (eds), Honolulu, HI, pp. 181–187. [5.2]
- Wang, D., J.C. McWilliams and W.G. Large, 1998: Large-eddy simulation of the diurnal cycle of deep equatorial turbulence. *J. Phys. Oceanogr.* 28, 129–148. [5.2, 7.2]
- Wang, G. and E.A.B. Eltahir, 2000: Biosphere-atmosphere interactions over West Africa. 1. Development and validation of a coupled dynamic model. *Quart. J. Roy. Meteor. Soc.* 126, 1239–1280. [2.3]
- Wang, G., R. Kleeman, N. Smith and F. Tseytlin, 2001: Seasonal predictions with a coupled global ocean-atmosphere model system at the BMRC, *J. Climate* (submitted). [7.4]
- Wang, L. and R.X. Huang, 1995: A linear homogeneous model of wind-driven circulation in a β -plane channel. *J. Phys. Oceanogr.* 25, 587–603. [4.6]
- Wang, L. and C. Koblinsky, 1996: Annual variability of the subtropical recirculations in the North Atlantic and North Pacific: a TOPEX/POSEIDON study. *J. Phys. Oceanogr.* 26, 2462–2479. [3.3]
- Wang, L. and C. Koblinsky, 1997: Can the TOPEX/POSEIDON altimetry data be used to estimate air-sea heat flux in the North Atlantic? *Geophys. Res. Lett.* 24, 139–142. [3.3]
- Wang, L. and C. Koblinsky, 1999: Large change of the mesoscale variability in the Kuroshio Extension region during the first 5 years of the TOPEX/POSEIDON Mission. *Geophys. Res. Lett.* 26, 2243–2246. [3.3]
- Wang, W. and M.J. McPhaden, 1999: The surface layer heat balance in the equatorial Pacific Ocean, Part I: Mean seasonal cycle. *J. Phys. Oceanogr.* 29, 1812–1831. [4.3]
- Wang, X., P.H. Stone and J. Marotzke, 1999: Global thermohaline circulation. Part I: Sensitivity to atmospheric moisture transport. *J. Climate* 12, 71–82. [2.3]
- Wanninkhof, R. and K. Thoning, 1993: Measurement of fugacity of CO_2 in surface water using continuous and discrete sampling methods. *Mar. Chem.* 44, 189–204. [6.3]
- Wanninkhof, R., S.C. Doney, T.-H. Peng, J.L. Bullister, K. Lee and R.A. Feely, 1999: Comparison of methods to determine the anthropogenic CO_2 invasion into the Atlantic Ocean. *Tellus* 51B, 511–530. [6.3]
- Warner, M.J. and R.F. Weiss, 1985: Solubilities of chlorofluorocarbons 11 and 12 in water and seawater. *Deep-Sea Res.* 32, 1485–1497. [5.8]
- Warner, M.J. and R.F. Weiss, 1992: Chlorofluoromethanes in South Atlantic Antarctic Intermediate Water. *Deep-Sea Res.* 39, 2053–2075. [2.3, 5.8]
- Warner, M.J., R.F. Weiss and W.M. Smethie, Jr., 1990: Chlorofluorocarbon distributions in the Deep Argentine Basin. *Eos Trans. Amer. Geophys. Union* 71, 168. [5.8]
- Warner, M.J., J.L. Bullister, D.P. Wisegarver, R.H. Gammon and R.F. Weiss, 1996: Basin-wide distributions of chlorofluorocarbons CFC-11 and CFC-12 in the North Pacific: 1985–1989. *J. Geophys. Res.* 101, 20525–20542. [7.3, 7.4]
- Warren, B.A., 1972: Insensitivity of subtropical mode water characteristics to meteorological fluctuations. *Deep-Sea Res.* 19, 1–20. [5.4]
- Warren, B.A., 1973: Transpacific hydrographic sections at Lats. 43°S and 28°S: the SCORPIO Expedition-II. Deep water. *Deep-Sea Res.* 20, 9–38. [5.8]
- Warren, B.A., 1981: Deep circulation of the world ocean. In: *Evolution of Physical Oceanography*, B.A. Warren and C. Wunsch (eds), MIT Press, Cambridge, MA, pp. 6–41. [4.2, 4.4, 5.7]
- Warren, B.A., 1983: Why is no deep water formed in the North Pacific? *J. Marine Res.* 41, 327–347. [4.7]

- Warren, B.A., 1994: Driving the meridional overturning in the Indian Ocean. *Deep-Sea Res.* 41, 1349–1360. [4.3]
- Warren, B.A., 1999: Approximating the energy transport across oceanic sections. *J. Geophys. Res.* 104, 7915–7919. [4.7]
- Warren, B.A. and G.C. Johnson, 1992: Deep currents in the Arabian Sea in 1987. *Mar. Geology* 104, 279–288. [4.3]
- Warren, B.A. and W.B. Owens, 1988: Deep currents in the central Subarctic Pacific Ocean. *J. Phys. Oceanogr.* 18, 529–551. [4.5, 5.8]
- Warren, B.A. and K.G. Speer, 1991: Deep circulation in the eastern South Atlantic Ocean. *Deep-Sea Res.* 38(suppl.), S281–S322. [4.5, 7.3]
- Warren, B., H. Stommel and J.C. Swallow, 1966: Water masses and patterns of flow in the Somali Basin during the Southwest monsoon of 1964. *Deep-Sea Res.* 13, 825–860. [4.3]
- Warrick, R.A. and J. Oerlemans, 1990: Sea level rise. In: *Climate Change*, J.T. Houghton, G.J. Jenkins and J.J. Ephraums (eds), The IPCC Scientific Assessment, pp. 260–281. [7.4]
- Warrick, R.A., C. Le Provost, M.F. Meier, J. Oerlemans and P.L. Woodworth, 1996: Changes in sea level. In: *Climate Change 1995, The Science of Climate Change*, J.T. Houghton et al. (eds), Cambridge University Press, pp. 359–405. [7.4]
- WASA Group, 1997: *Changing Waves and Storms in the Northeast Atlantic?* GKSS Forschungszentrum Geesthacht GmbH, Rept 97/E/46, Geesthacht Germany, 23 pp. [7.3]
- Washington, W.M. and J. Meehl, 1984: Seasonal cycle experiments on the climate sensitivity due to a doubling of CO₂ with an atmospheric general circulation model coupled to a simple mixed layer ocean model. *J. Geophys. Res.* 89, 9475–9503. [2.2]
- Washington, W.M. and G.A. Meehl, 1989: Climate sensitivity due to increased CO₂: Experiments with a coupled atmosphere and ocean general circulation model. *Climate Dyn.* 4, 1–38. [2.2]
- Washington, W.M. et al., 2000: Parallel climate model (PCM): control and transient simulations. *Climate Dyn.* 16, 755–774
- Watanabe, M. and T. Nitta, 2000: Decadal changes in the atmospheric circulation and associated surface climate variations in the Northern Hemisphere winter. *J. Climate* 12, 495–510. [7.3]
- Watanabe, T., 1990: *Study on formation processes of SST anomalies in the western North Pacific: Role of East Asian Winter Monsoon.* D.Sc. Thesis, Tohoku University (in Japanese), 121 pp. [5.4]
- Watson, A.J. and J.R. Ledwell, 2000: Oceanographic tracer release experiments using sulphur hexafluoride. *J. Geophys. Res.* 105 (C6), 14325–14337. [1.2, 5.2]
- Watson, A.J., P.D. Nightingale and D.J. Cooper, 1995: Modelling atmosphere–ocean CO₂ transfer. *Phil. Trans. Roy. Soc. Lond. B* 348, 125–132. [6.3]
- Watson, A.J., M.J. Messias, E. Fogelquist, et al. 1999: Mixing and convection in the Greenland Sea from a tracer-release experiment. *Nature*, 401, 902–904. [1.2]
- Waworuntu, J.M., R.A. Fine, D.B. Olson and A.G. Gordon, 2000: Recipe for the Banda Sea Water. *J. Mar. Res.* 58, 457–569. [5.8]
- WCRP (World Climate Research Programme), 1981: *Report of the Meeting on Coordination of Plans for Future Satellite Systems and Ocean Experiments to be Organised within WCRP.* World Climate Programme Report, WCP-8, 52 pp. and appendices. [1.3]
- WCRP (World Climate Research Programme), 1983: *Large-scale oceanographic experiments in the World Climate Research Programme.* Papers presented at the JSC/CCCO Study Conference in Tokyo, 10–21 May 1983. WCRP-No. 1, 544 pp. [1.3, 7.2]
- WCRP (World Climate Research Programme), 1986: *Scientific Plan for the World Ocean Circulation Experiment.* World Climate Research Programme, WMO/TD-No. 122, 83 pp. [1.3, 3.1, 6.1]
- WCRP (World Climate Research Programme), 1987: *WOCE Core Project 3 Meeting on the Gyre Dynamics Experiment*, London, UK, 2–5 September 1986. World Meteorological Organisation, WMO/TD-No. 192, 36 pp. [4.5]
- WCRP (World Climate Research Programme), 1988a: *World Ocean Circulation Experiment Implementation Plan*, Vol. I: *Detailed Requirements.* World Meteorological Organisation, WMO/TD-No. 242, WCRP-11, various paginations. [1.3, 3.1, 4.1, 5.8, 7.4]
- WCRP (World Climate Research Programme), 1988b: *World Ocean Circulation Experiment Implementation Plan*, Vol. II: *Scientific Background.* World Meteorological Organisation, WMO/TD-No. 243, WCRP-No. 12. July 1998, various paginations. [1.3, 3.1]
- WCRP (World Climate Research Programme), 1988c: *WOCE Surface Velocity Programme Planning Committee Report of First Meeting: SVP-1 and TOGA Pan-Pacific Surface Current Study.* World Climate Research Programme, WMO/TD-No. 323. WCRP-26, 33 pp. [4.1]
- WCRP (World Climate Research Programme), 1989a: *Report of the International WOCE Scientific Conference*, UNESCO, Paris, 28 November–2

- December 1988. World Climate Research Programme, WMO/TD-No. 295, various paginations. [1.3]
- WCRP (World Climate Research Programme), 1989b: WOCE surface flux determinations – a strategy for in situ measurements. *Report of the Working Group on In Situ Measurements for Fluxes*, P.K. Taylor (ed.), La Jolla, CA, March, 1989. World Climate Research Programme, WMO/TD-No. 304, 161 pp. [7.4]
- WCRP (World Climate Research Programme), 1995a: *The CLIVAR Science Plan*. Prepared by the CLIVAR Scientific Steering Group, August 1995. World Climate Research Programme, WMO/TD-No. 690, 157 pp. [7.4]
- WCRP (World Climate Research Programme), 1995b: Comparison of TOGA tropical Pacific Ocean model simulations with the WOCE/TOGA surface velocity programme drifter data set. *Report Assembled by the Global Drifter Center and edited by WMO*, June 1995. WCRP-No. 4 1995, 156 pp. [4.1]
- WCRP (World Climate Research Programme), 1998: *CLIVAR Initial Implementation Plan*. World Climate Research Programme, WMO/TD-No. 869, No. 103, ICPO No. 14 June 1998, 314 pp. and Appendices. [1.2, 1.3, 7.4]
- Weatherly, G.L., Y. Y. Kim and E. A. Kontar, 2000: Eulerian measurements of the North Atlantic Deep Water deep western boundary current at 18°S. *J. Phys. Oceanogr.* 30, 971–986. [1.2, 1.3, 4.5]
- Weatherly, J.W., B.P. Brieglieb, W.G. Large and J.A. Maslanik, 1998: Sea ice and polar climate in the NCAR CSM. *J. Climate* 11, 1472–1486. [2.3]
- Weaver, A.J. and E. Sarachik, 1990: On the importance of vertical resolution in certain ocean circulation models. *J. Phys. Oceanogr.* 20, 600–609. [4.3]
- Weaver, A.J., J. Marotzke, P. Cummins and E.S. Sarachik, 1993: Stability and variability of the thermohaline circulation. *J. Phys. Oceanogr.* 23, 39–60. [2.1, 6.2]
- Webb, D.J., 1993: A simple model of the effect of the Kerguelen Plateau on the strength of the Antarctic Circumpolar Current. *Geophys. Astrophys. Fluid Dyn.* 70, 57–84. [4.2, 4.6]
- Webb, D.J., P.D. Killworth, A.C. Coward and S.R. Thompson, 1991: *The FRAM Atlas of the Southern Ocean*. Natural Environment Research Council, Swindon, UK, 67 pp. [4.2, 4.6]
- Webb, D.J., A.C. Coward, B.A. de Cuevas and C.S. Gwilliam, 1997: A multiprocessor ocean general circulation model using message passing. *J. Atmos. Oceanic Technol.* 14, 175–183. [2.2, 5.6]
- Webster *et al.*, 2000: <http://paos.colorado.edu/~webster/jasminereport>. [4.3]
- Webster, P., V. Magaña, T. Palmer *et al.*, 1998: Monsoon: processes, predictability, and the prospects for prediction. *J. Geophys. Res.* 103, 14451–14510. [4.7]
- Webster, P.J., A.M. Moore, J.P. Loschnigg and R.R. Leben, 1999: Coupled ocean–atmosphere dynamics in the Indian Ocean during 1997–98. *Nature* 401, 356–360. [1.2, 4.3]
- Wefer, G., W.H. Berger, G. Siedler and D.J. Webb, (eds), 1996: *The South Atlantic: Present and Past Circulation*. Springer-Verlag, Berlin, 644 pp. [4.7]
- Weijer, W.W., 2000: *Impact of interocean exchange on the Atlantic overturning circulation*. Ph.D. Dissertation, Utrecht University, 196 pp. [4.7]
- Weijer, W.W., W. de Ruijter, H. Dijkstra and P. van Leeuwen, 1999: Impact of interbasin exchange on the Atlantic overturning circulation. *J. Phys. Oceanogr.* 29, 2266–2284. [4.7]
- Weijer, W., W.P.M. de Ruijter and H.A. Dijkstra, 2001a: Stability of the Atlantic overturning circulation: competition between Bering Strait fresh water flux and Agulhas heat and salt sources. *J. Phys. Oceanogr.* (In press). [4.7]
- Weijer, W., W.P.M. de Ruijter, A. Sterl and S.S. Drijfhout, 2001b: Response of the Atlantic overturning circulation to South Atlantic sources of buoyancy. *J. Phys. Oceanogr.* (In press). [4.7]
- Weisberg, R.H., 1984: Instability waves observed on the equator in the Atlantic Ocean during 1983. *Geophys. Res. Lett.* 11, 857753–857756. [4.3]
- Weisberg, R.H., J.H. Hickman, T.Y. Tang and T.J. Weingartner, 1987: Velocity and temperature observations during the seasonal response of the equatorial experiment at 0°, 28°W. *J. Geophys. Res.* 92, 5061–5075. [4.3]
- Weiss, R.F., H.G. Oestlund and H. Craig, 1979: Geochemical studies in the Weddell Sea. *Deep-Sea Res.* 26, 1093–1120. [5.8]
- Weiss, R.F., W.S. Broecker, H. Craig and D. Spencer, 1983: *GEOSECS Indian Ocean Expedition*, Vol. 5, *Hydrographic Data 1977–1978*. National Science Foundation, US Govt Printing Office, Washington, DC, 48 pp. [6.3]
- Weiss, R.F., J.L. Bullister, R.H. Gammon and M.J. Warner, 1985: Atmospheric chlorofluoromethanes in the deep equatorial Atlantic. *Nature*, 314, 608–610. [4.3, 4.4, 4.5, 5.8]
- Weiss, W. and W. Roether, 1980: The rates of tritium input to the world oceans. *Earth Planet. Sci. Lett.* 49, 434–446. [5.8]
- Weisse, R., U. Mikolawejcz, A. Sterl and S.S. Drijfhout, 1999: Stochastically forced variability in the Antarctic Circumpolar Current. *J. Geophys. Res.* 104, 11049–11064. [4.6]

- Weissman, D.E. and H.C. Gruber, 1999: Satellite scatterometer studies of ocean surface stress and drag coefficients using a direct model. *J. Geophys. Res.* 104, 11329–11335. [3.4]
- Welander, P., 1959: On the vertically integrated mass transport in the oceans. In: *The Atmosphere and the Sea in Motion*, B. Bolin (ed.), Rockefeller Institute Press, NY, pp. 95–101. [4.2]
- Welander, P., 1971: The thermocline problem. *Phil. Trans. Roy. Soc. Lond. A*, 270, 415–421. [5.2]
- Weller, R.A. and S.P. Anderson, 1996: Surface meteorology and air-sea fluxes in the western equatorial Pacific warm pool during the TOGA Coupled Ocean-Atmosphere Response Experiment. *J. Climate* 9, 1959–1990. [4.3]
- Wells, N.C. and B.A. de Cuevas, 1995: Vorticity dynamics of the Southern Ocean from a General Circulation Model. *J. Phys. Oceanogr.* 25, 2569–2582. [4.6]
- Wentz, F.J., 1996: A well-calibrated ocean algorithm for special sensor microwave/imager (SSM/I). *J. Geophys. Res.* 102, 8703–8718. [3.4]
- Wentz, F.J. and D.K. Smith, 1999: A model function for the ocean-normalized radar cross-section at 14 GHz derived from NSCAT observations. *J. Geophys. Res.* 104, 11449–11514. [3.4]
- Weppernig, R., P. Schlosser, S. Khatiwala and R.G. Fairbanks, 1996: Isotope data from Ice Station Weddell: Implications for deep water formation in the Weddell Sea. *J. Geophys. Res.* 101, 25723–25739. [4.6, 5.8]
- Wesson, J. and M. Gregg, 1994: Mixing at Camarinal Sill in the Strait of Gibraltar. *J. Geophys. Res.* 99, 9847–9878. [5.2]
- WGASF Group, The 2000: Intercomparison and validation of Ocean-Atmosphere energy flux fields. *Final Report of the Joint WCRP/SCOR Working Group on Air-Sea Fluxes (SCOR Working Group 110)* P.K. Taylor (ed.), WCRP, Geneva, in press (may be obtained at: <http://www.soc.soton.ac.uk/JRD/MET/WGASF>) 306 pp. [1.2, 3.1, 5.1, 7.1]
- Whitburn, A.-M., (ed.), 1994: The Atlantic Climate Change Program, *Proceedings of the Principal Investigators Meeting*. 9–11 May 1994. NOAA/GFDL, Princeton, NJ, University Corporation for Atmospheric Science/NOAA, 179 pp. [1.3]
- White, M.A. and K.J. Heywood, 1995: Seasonal and interannual changes in the North Atlantic subpolar gyre from GEOSAT and TOPEX/POSEIDON altimetry. *J. Geophys. Res.* 101, 24931–24942. [2.2]
- White, W.B., 1995: Design of a global observing system for gyre-scale upper ocean temperature variability. *Prog. Oceanogr.* 36, 169–217. [5.3, 7.1]
- White, W.B., 2000: Influence of the Antarctic Circumpolar Wave on Australia precipitation from 1958–1996. *J. Climate* 13, 2125–2141. [4.6]
- White, W.B. and N.J. Cherry, 1998: Influence of the Antarctic Circumpolar Wave upon New Zealand temperature and precipitation during Autumn–Winter. *J. Climate* 12, 960–976. [4.6]
- White, W. and R. Peterson, 1996: An Antarctic circumpolar wave in surface pressure, wind, temperature and sea ice extent. *Nature* 380, 699–702. [2.3, 4.6, 4.7]
- White, W.B. and C.-K. Tai, 1995: Inferring interannual changes in global upper ocean heat storage from TOPEX altimetry. *J. Geophys. Res.* 100, 24943–24954. [3.3]
- White, W.B. and T. Walker, 1985: The influence of the Hawaiian Archipelago upon the wind-driven subtropical gyre in the Western North Pacific. *J. Geophys. Res.* 90, 7061–7074. [4.1]
- White, W.B., C.-K. Tai and J. DiMento, 1990a: Annual Rossby wave characteristics in the California Current region from the Geosat exact repeat mission. *J. Phys. Oceanogr.* 20, 1297–1311. [3.3]
- White, W.B., N. Graham and C.-K. Tai, 1990b: Reflection of Annual Rossby Waves at the maritime western boundary of the tropical Pacific. *J. Geophys. Res.* 95, 3101–3116. [3.3]
- White, W.B., S.-C. Chen and R. Peterson, 1998a: The Antarctic Circumpolar Wave: A beta-effect in ocean–atmosphere coupling over the Southern Ocean. *J. Phys. Oceanogr.* 28, 2345–2361. [4.6]
- White, W., Y. Chao and C.-K. Tai, 1998b: Coupling of biennial oceanic Rossby waves with the overlying atmosphere in the Pacific basin. *J. Phys. Oceanogr.* 28, 1236–1251. [3.3]
- Whitehead, J.A., 1998: Topographic control of oceanic flows in deep passages and straits. *Rev. Geophys.* 36(3), 423–440. [5.6]
- Whitehead, J.A. and L.V. Worthington, 1982: The flux and mixing rates of Antarctic Bottom Water within the North Atlantic. *J. Geophys. Res.* 87, 7903–7924. [4.5, 5.2]
- Whitworth, III, T., 1983: Monitoring the net transport of the Antarctic Circumpolar Current at Drake Passage. *J. Phys. Oceanogr.* 13, 2045–2057. [4.6]
- Whitworth, III, T. and R.G. Peterson, 1985: The volume transport of the Antarctic Circumpolar Current from three-year bottom pressure measurements. *J. Phys. Oceanogr.* 15, 810–816. [4.6]
- Whitworth, III, T., W.D. Nowlin, Jr. and S.J. Worley, 1982: The net transport of the Antarctic Circumpolar Current through Drake Passage. *J. Phys. Oceanogr.* 12, 960–971. [4.6]

- Whitworth, III, T., W.D. Nowlin Jr., R.D. Pillsbury, M.I. Moore and R.F. Weiss, 1991: Observations of the Antarctic Circumpolar Current and the Deep Boundary Current in the Southwest Atlantic Ocean. *J. Geophys. Res.* **96**, 15105–15118. [4.5]
- Whitworth, III, T., W.D. Nowlin, Jr., A.H. Orsi, R.A. Locarnini and S.G. Smith, 1994: Weddell Sea Shelf Water in the Bransfield Strait and Weddell–Scotia Confluence. *Deep-Sea Res.* **41**, 629–641. [4.6]
- Whitworth, III, T., A.H. Orsi, S.-J. Kim, W.D. Nowlin Jr. and R.A. Locarnini, 1998: Water masses and mixing near the Antarctic Slope Front. In: *Ocean, Ice and Atmosphere: Interactions at Antarctic Continental Margin*, Vol. 75 of Antarctic Research Series, S.S. Jacobs and R. Weiss (eds), American Geophysical Union, Washington, DC, pp. 1–27. [4.6]
- Whitworth, III, T., B. Warren, W. Nowlin, Jr., S. Rutz, R. Pillsbury and M. Moore, 1999: On the deep western-boundary current in the Southwest Pacific Basin. *Prog. Oceanogr.* **43**, 1–54. [4.5, 4.6, 5.8]
- WHPO (WOCE Hydrographic Programme Office), 1994a: *WOCE Operations Manual, WHP Operations and Methods*, WHPO 91-1. WOCE International Project Office, WOCE Report No. 68/91, November 1994, rev. 1. (unpublished manuscript). [3.1]
- WHPO (WOCE Hydrographic Programme Office), 1994b: *WOCE Operations Manual, Requirements for WHP Data Reporting*, WHPO 90-1. WOCE International Project Office, WOCE Report No. 67/91, May 1994, rev. 2, 142 pp. (unpublished manuscript). [3.1]
- WHPO (WOCE Hydrographic Programme Office), 1998: *WOCE Hydrographic Program Data*, <http://whpo.ucsd.edu>, Scripps Institution Oceanography, San Diego, CA. [7.3]
- Wijffels, S.E., 1993: *Exchanges between hemispheres and gyres: a direct approach to the mean circulation of the equatorial Pacific*. Ph.D. Thesis, Publ. WHOI-93-42, MIT-WHOI Joint Program, 294 pp. [4.3, 4.4, 5.2]
- Wijffels, S., R. Schmitt, H. Bryden and A. Stigebrandt, 1992: On the transport of freshwater by the oceans. *J. Phys. Oceanogr.* **22**, 155–162. [4.7, 5.1, 6.2]
- Wijffels, S.E., E. Firing and H. Bryden, 1994: Direct observations of the Ekman balance at 10°N in the Pacific. *J. Phys. Oceanogr.* **24**, 1666–1679. [3.1, 4.1]
- Wijffels, S.E., E. Firing and J. Toole, 1995: The mean structure and variability of the Mindanao Current at 8°N. *J. Geophys. Res.* **100**, 18421–18435. [4.3]
- Wijffels, S.E., J.M. Toole, H.L. Bryden, R.A. Fine, W.J. Jenkins and J.L. Bullister, 1996a: The water masses and circulation at 10°N in the Pacific. *Deep-Sea Res.* **43**, 501–544. [5.2, 5.8, 6.1, 6.2]
- Wijffels, S.E., N.A. Bray, S. Hautala, G. Meyers and W.M.L. Morawitz, 1996b: The WOCE Indonesian Throughflow repeat hydrography sections: I10 and IR6. *International WOCE Newsletter*, No. 24, 25–28, WOCE International Project Office (unpublished document). [6.1]
- Wijffels, S.E., M.E. Hall, T. Joyce, D.J. Torres, P. Hacker and E. Firing, 1998: Multiple deep gyres of the western North Pacific: A WOCE section along 149°E. *J. Geophys. Res.* **103**, 12985–13010. [3.1, 4.2, 4.3, 5.8]
- Wijffels, S.E., J.M. Toole and R.E. Davis, 2000: Revisiting the South Pacific subtropical circulation: A synthesis of WOCE observations along 32°S. *J. Geophys. Res.* **105** (submitted). [3.2, 6.1, 6.2]
- Wilheit, T.T., A.T.C. Chang and L.S. Chiu, 1991: Retrieval of monthly rainfall indices from microwave radiometric measurements using probability distribution functions. *J. Atmos. Oceanic Technol.* **8**, 118–136. [3.4]
- Wilkin, J. and R.A. Morrow, 1994: Eddy kinetic energy and momentum flux in the Southern Ocean: Comparison of a global eddy-resolving model with altimeter, drifter and current-meter data. *J. Geophys. Res.* **99**, 7903–7916. [3.3]
- Wilkin, J.L., J.V. Mansbridge and J.S. Godfrey, 1995: Pacific Ocean heat transport at 24°N in a high-resolution global model. *J. Phys. Oceanogr.* **25**, 2204–2214. [6.1]
- Willebrand, J., S.G.H. Philander and R.C. Pacanowski, 1980: The oceanic response to large-scale atmospheric disturbances. *J. Phys. Oceanogr.* **10**, 411–429. [2.2, 3.3]
- Willebrand, J., B. Barnier, C.W. Böning *et al.*, 2001: Circulation characteristics in three eddy-permitting models of the North Atlantic. *Prog. Oceanogr.* (in press). [2.2, 5.6, 7.2]
- Williams, R.G., 1989: The influence of air-sea interaction on the ventilated thermocline. *J. Phys. Oceanogr.* **19**, 1255–1267. [5.3, 5.4]
- Williams, R.G., 1991: The role of the mixed layer in setting the potential vorticity of the main thermocline. *J. Phys. Oceanogr.* **21**, 1803–1814. [5.3]
- Williams, R.G., M.A. Spall and J.C. Marshall, 1995: Does Stommel's mixed layer demon work? *J. Phys. Oceanogr.* **25**, 3089–3102. [5.3]
- Wilson, C.D. and E. Firing, 1992: Sunrise swimmers bias Doppler current profiles. *Deep-Sea Res.* **39**, 885–892. [3.1]

- Wilson, S., 2000: Launching the Argo armada: taking the ocean's pulse with 3000 free-ranging floats. *Oceanus* 42, 17–19. [3.3, 3.4]
- Wilson, W.D., W.E. Johns and R.L. Molinari, 1994: Upper layer circulation in the western tropical North Atlantic during August 1989. *J. Geophys. Res.* 99, 22513–22523. [4.3]
- Wilson, W.D. and W.E. Johns, 1997: Velocity structure and transport in the Windward Island passages. *Deep-Sea Res.* 44, 487–520. [4.3]
- Winkel, D., M. Gregg and T. Sanford, 1992: Simultaneous observations of shear and turbulence in the Florida Current. In: *AMS 10ths Symposium on Turbulence and Diffusion*, 29 September–2 October, 1992, Portland OR, pp. (J5)101–(J5)104. [5.2]
- Winton, M., 1997: The damping effect of bottom topography on internal decadal-scale oscillations of the thermohaline circulation. *J. Phys. Oceanogr.* 27, 203–208. [5.5]
- Winton, M., R. Hallberg and A. Gnanadesikan, 1998: Simulation of density-driven frictional downslope flow in z -coordinate ocean models. *J. Phys. Oceanogr.* 28, 2163–2174. [2.3]
- Witter, D.L. and A.L. Gordon, 1999: Interannual variability of the South Atlantic Circulation from four years of TOPEX/POSEIDON altimeter observations. *J. Geophys. Res.* 104, 20927–20948. [3.3, 4.7]
- WOCE International Project Office, 1995: *The Status, Achievements and Prospects for WOCE (1995): the Background to the World Ocean Circulation Experiment; Its Present Status and Achievements; A Strategy for the Future*. WOCE International Project Office, WOCE Report No. 130/95, 30 pp. (unpublished manuscript). [1.3]
- WOCE International Project Office, 1997: *WOCE Analysis, Interpretation, Modelling and Synthesis (AIMS): Strategy Document*. WOCE International Project Office, WOCE Report No. 153/97, 51 pp. (unpublished manuscript). [1.3, 7.1, 7.4]
- WOCE International Project Office, 1999: *Report of the WOCE/CLIVAR Workshop on Ocean Modelling for Climate Studies*, Boulder, CO, August 1998. WOCE International Project Office, WOCE Report No. 165/99, ICPO No. 28, 56 pp. (unpublished manuscript). [2.2, 2.3]
- Wolff, J.-O., E. Maier-Reimer and D.J. Olbers, 1991: Wind-driven flow over topography in a zonal β -plane channel: A quasi-geostrophic model of the Antarctic Circumpolar Current. *J. Phys. Oceanogr.* 21, 236–264. [4.6]
- Wolff, J.-O., E. Maier-Reimer and S. Legutke, 1997: *The Hamburg Ocean Primitive Equation Model*, HOPE. DKRZ Technical Report No. 13, 100 pp. [2.3]
- Wong, A.P.S., 1999: Water mass changes in the North and South Pacific Oceans between the 1960s and 1985–94. PhD Thesis, University of Tasmania, 230pp. [1.2, 7.3]
- Wong, A.P.S., N.L. Bindoff and J.A. Church, 1999: Large-scale freshening of intermediate waters in the Pacific and Indian oceans. *Nature* 400, 440–443. [1.2, 2.3, 4.6, 7.3]
- Wong, A.P.S., N.L. Bindoff and J.A. Church, 2001: Freshwater and heat changes in the North and South Pacific Oceans between the 1960s and 1985–1994. *J. Climate* (submitted). [1.2, 7.3]
- Wong, T., B.R. Barkstrom, G.G. Gibson and S. Weckmann, 1998: Observations of the radiative impacts of ENSO events using data from ERBE and CERES. *Eos Trans. Amer. Geophys. Union* 79(45), 147. [3.3]
- Wood, R.A., 1988: Unstable waves on oceanic fronts: large-amplitude behavior and mean flow generation. *J. Phys. Oceanogr.* 18, 775–787. [3.3]
- Wood, R.A., A.B. Keen, J.F.B. Mitchell and J.M. Gregory, 1999: Changing spatial structure of the thermohaline circulation in response to atmospheric CO_2 forcing in a climate model. *Nature* 399, 572–575. [2.3]
- Woodbury, K., M. Luther and J.J. O'Brien, 1989: The wind-driven seasonal circulation in the southern tropical Indian Ocean. *J. Geophys. Res.* 94, 17985–18002. [3.3]
- Woods, J.D., 1968: Wave-induced shear instability in the summer thermocline. *J. Fluid Mech.* 32, 791–800. [4.2]
- Woods, J.D., 1985a: The World Ocean Circulation Experiment. *Nature* 314, 501–511. [1.3, 6.3]
- Woods, J.D., 1985b: The physics of thermocline ventilation. In: *Coupled Atmosphere–Ocean Models*, J.C.J. Nihoul (ed.), Elsevier, 767 pp. [5.3, 5.4, 7.3]
- Woodworth, P.L., 1990: A search for accelerations in records of European mean sea level. *Int. J. Climatol.* 10, 129–143. [1.2]
- Woodworth, P.L., 1999: High waters at Liverpool since 1768: the UK's longest sea level record. *Geophys. Res. Lett.* 26, 1589–1592. [1.2]
- Worby, A.P., R.A. Massom, I. Allison, V.I. Lytle and P. Heil, 1998: East Antarctic sea ice: A review of its structure, properties and drift. In: *Antarctic Sea Ice Properties, Processes and Variability*, M. Jeffries (ed.), American Geophysical Union, Antarctic Research Series., Vol. 74, pp. 41–67. [1.2]
- Worthington, L.V., 1959: The 18° Water in the Sargasso Sea. *Deep-Sea Res.* 5, 297–305. [5.4]

- Worthington, L.V., 1976: On the North Atlantic Circulation. *Johns Hopkins Oceanographic Studies* 6, 110 pp. [4.2, 5.1, 5.4, 5.7]
- Worthington, L.V., 1981: The water masses of the world ocean: Some results of a fine-scale census. In: *Evolution of Physical Oceanography*, B.A. Warren and C. Wunsch (eds), MIT Press, Cambridge, MA, pp. 42–69. [1.2, 4.2, 4.6, 5.1]
- Worthington, L.V. and G.H. Volkmann, 1965: The volume transport of the Norwegian Sea overflow water in the North Atlantic. *Deep-Sea Res.* 12, 667–676. [5.6]
- Worthington, L.V. and W.R. Wright, 1970: *North Atlantic Ocean Atlas*. Woods Hole Oceanographic Institution, MA. [7.3]
- Wright, D.G., 1981: Baroclinic instability in Drake Passage. *J. Phys. Oceanogr.* 11, 231–246. [4.6]
- Wright, P., 1988: *An Atlas Based on the COADS Data Set: Fields of Mean Wind, Cloudiness, and Humidity at the Surface of the Global Ocean*. Max Planck Institut für Meteorologie, Hamburg, Report 14, 7 pp. + figures. [5.1]
- Wu, P. and K. Haines, 1996: Modeling the dispersal of Levantine Intermediate Water and its role in the Mediterranean deep water formation. *J. Geophys. Res.* 101, 6591–6607. [5.7]
- Wunsch, C., 1970: On oceanic boundary mixing. *Deep-Sea Res.* 17, 293–301. [4.6]
- Wunsch, C., 1977: Determining the general circulation of the ocean: A preliminary discussion. *Science* 196, 871–875. [3.2, 7.4]
- Wunsch, C., 1978: The North Atlantic general circulation west of 50°W determined by inverse methods. *Rev. Geophys.* 16, 583–620. [7.1]
- Wunsch, C., 1981: An interim relative sea surface for the North Atlantic Ocean. *Mar. Geod.* 5, 103–119. [3.3]
- Wunsch, C.I., 1983: A World Ocean Circulation Experiment. In: *Proceedings of a Workshop on Global Observations and Understanding of the General Circulation of the Oceans*, National Academy Press, Washington, DC, 418 pp. [1.3]
- Wunsch, C., 1992: Decade-to-century changes in the ocean circulation. *Oceanogr.* 5(2), 99–106. [2.1, 7.3]
- Wunsch, C., 1996: *The Ocean Circulation Inverse Problem*. Cambridge University Press, 437 pp. [2.1, 3.3, 4.2, 5.2, 7.1]
- Wunsch, C., 1997: The vertical partition of oceanic horizontal kinetic energy. *J. Phys. Oceanogr.* 27, 1770–1794. [3.3]
- Wunsch, C., 1999a: The interpretation of short climate records, with comments on the North Atlantic and Southern Oscillations. *Bull. Amer. Meteor. Soc.* 80, 245–255. [2.1]
- Wunsch, C., 1999b: Where do ocean eddy heat fluxes matter? *J. Geophys. Res.* 104, 13235–13249. [2.3, 3.3]
- Wunsch, C. and E.M. Gaposchkin, 1980: On using satellite altimetry to determine the general circulation of the oceans with application to geoid improvement. *Rev. Geophys. Space Phys.* 18, 725–745. [3.3]
- Wunsch, C. and D. Roemmich, 1985: Is the North Atlantic in Sverdrup balance? *J. Phys. Oceanogr.* 15, 1876–1880. [2.1]
- Wunsch, C. and D. Stammer, 1995: The global frequency-wavenumber spectrum of oceanic variability estimated from TOPEX/POSEIDON altimetric measurements. *J. Geophys. Res.* 100, 24895–24910. [4.6]
- Wunsch, C. and D. Stammer, 1997: Atmospheric loading and the oceanic ‘inverted barometer’ effect. *Rev. Geophys.* 35, 79–107. [3.3]
- Wunsch, C. and D. Stammer, 1998: Satellite altimetry, the marine geoid and the oceanic general circulation. *Ann. Rev. Earth Planet. Sci.* 26, 219–254. [2.1, 3.3]
- Wunsch, C., D.-X. Hu, and B. Grant, 1982: Mass, heat, salt and nutrient fluxes in the South Pacific Ocean. *J. Phys. Oceanogr.*, 87, 5647–5662. [5.2]
- Wunsch, C., D.-X. Hu and B. Grant, 1983: Mass, heat, salt and nutrient fluxes in the South Pacific Ocean. *J. Phys. Oceanogr.* 13, 725–753. [5.2, 6.2]
- Wüst, G., 1935: *The Stratosphere of the Atlantic Ocean. Scientific Results of the German Atlantic Expedition of the Research Vessel ‘Meteor’ 1925–27* (English translation, W.J. Emery (ed.), Amerind, New Delhi, 1978), Vol. 6, pp. 109–288. [2.1, 4.2, 4.5, 5.3, 5.4]
- Wüst, G. and A. Defant, 1936: *Atlas zur Schichtung und Zirkulation des Atlantischen Ozeans. Schnitte und Karten von Temperatur, Salzgehalt und Dichte*. In: *Wissenschaftliche Ergebnisse der Deutschen Atlantischen Expedition auf dem Forschungs- und Vermessungsschiff ‘Meteor’ 1925–1927*. 103 plates. [5.7]
- Wyrtki, K., 1961a: Physical Oceanography of Southeast Asian waters. *NAGA Report* 2, 195 pp. [4.3, 4.7, 5.8]
- Wyrtki, K., 1961b: The thermohaline circulation in relation to the general circulation in the oceans. *Deep-Sea Res.* 8, 39–64. [5.2]
- Wyrtki, K., 1973a: Physical oceanography of the Indian Ocean. In: *Ecological Studies. Analysis and Synthesis*, B. Zeitzschel (ed.), Springer-Verlag, Berlin, Vol. 3, pp. 18–36. [5.4]
- Wyrtki, K., 1973b: An equatorial jet in the Indian Ocean. *Science* 181, 262–264. [4.3]

- Wyrtki, K., 1975: Fluctuations of dynamic topography in the Pacific Ocean. *J. Phys. Oceanogr.* 5, 450–459. [4.1, 4.4, 7.1]
- Wyrtki, K., 1979: Sea level variations: monitoring the breath of the Pacific. *Eos*, 60, 25–27. [7.4]
- Wyrtki, K. and B. Kilonsky, 1984: Mean water and current structure during the Hawaii-to-Tahiti shuttle experiment. *J. Phys. Oceanogr.* 14, 242–254. [4.3, 4.4]
- Wyrtki, K., L. Magaard and J. Hager, 1976: Eddy energy in the oceans. *J. Geophys. Res.* 81, 2641–1646. [4.1]
- Wyrtki, K., E. Firing, D. Halpern *et al.*, 1981: The Hawaii-to-Tahiti shuttle experiment. *Science* 211, 22–28. [4.3]
- Xie, P. and P.A. Arkin, 1996: Analyses of global monthly precipitation using gauge observations, satellite estimates, and numerical model predictions. *J. Climate* 9, 840–858. [5.1]
- Xie, P.P. and P.A. Arkin, 1997: Global precipitation: A 17-year monthly analysis based on gauge observations, satellite estimates, and numerical model outputs. *Amer. Meteor. Soc.* 78, 2539–2558. [6.2]
- Yamagata, T., Y. Shibao and S. Umatani, 1985: Interannual variability of the Kuroshio Extension and its relation to the Southern Oscillation/El Niño. *J. Oceanogr. Soc. Japan* 41, 274–281. [7.3]
- Yaremchuk, M.N., N.L. Bindoff, J. Schröter, D. Nechaev and S.R. Rintoul, 2000: On the zonal and meridional circulation and ocean transports between Tasmania and Antarctica. *J. Geophys. Res.* (in press). [4.6]
- Yasuda, I., 1997: The origin of the North Pacific Intermediate Water. *J. Geophys. Res.* 102, 893–909. [5.4]
- Yasuda, T. and K. Hanawa, 1997: Decadal changes in the mode waters in the midlatitude North Pacific. *J. Phys. Oceanogr.* 27, 858–870. [5.4]
- Yasuda, T. and K. Hanawa, 1999: Composite analysis of North Pacific subtropical mode water properties with respect to the strength of the wintertime East Asian monsoon. *J. Oceanogr.* 55, 531–541. [5.4]
- Yoden, S., M. Shiotani and I. Hirota, 1987: Multiple planetary flow regimes in the Southern Hemisphere. *J. Meteor. Soc. Japan* 65, 571–586. [7.3]
- You, Y., 1999: Dianutral mixing, transformation and transport of Antarctic Intermediate Water in the South Atlantic Ocean. *Deep-Sea Res.* 46, 393–435. [4.7]
- Young, W.R., 1981: *The vertical structure of the wind-driven circulation*. MIT-WHOI Joint Program, Ph.D. Thesis No. 81-89, 215 pp. [4.6]
- Young, W.R., P.B. Rhines and C.J.R. Garrett, 1982: Shear-flow dispersion, internal waves and horizontal mixing in the ocean. *J. Phys. Oceanogr.* 12, 515–527. [5.2]
- Yuan, X. and D. Martinson, 2000: Antarctic sea ice extent variability and its global connectivity. *J. Climate* 13, 1697–1717. [4.7]
- Yueh, S.H., R. West, F. Li, W.-Y. Tsai and R. Lay, 2000: Dual-polarized Ku-band backscatter signatures of hurricane ocean winds. *IEEE Trans., Geosci. Remote Sens.* 38, 73–88. [3.4]
- Yukimoto, S., M. Endoh, Y. Kitamura *et al.*, 1996: Interannual and interdecadal variabilities in the Pacific in a MRI coupled GCM. *Climate Dyn.* 12, 667–683. [2.3]
- Yukimoto, S., 1999: The decadal variability of the Pacific with the MRI coupled models. In: *Beyond El Niño: Decadal and Interdecadal Climate Variability*, A. Navarra (ed.), Springer-Verlag, Berlin. [2.3]
- Zahariev, K. and C. Garrett, 1997: An apparent surface buoyancy flux associated with the nonlinearity of the equation of state. *J. Phys. Oceanogr.* 27, 362–368. [5.1]
- Zang, X. and C. Wunsch, 1999: The observed dispersion relationship for North Pacific Rossby wave motions. *J. Phys. Oceanogr.* 29, 2183–2190. [3.3]
- Zangenberg, N. and G. Siedler, 1998: Path of the North Atlantic Deep Water in the Brazil Basin. *J. Geophys. Res.* 103, 5419–5428. [3.2, 4.5]
- Zaucker, F. and W. Broecker, 1992: The influence of atmospheric moisture transport on the fresh water balance of the Atlantic drainage basin. *J. Geophys. Res.* 97, 2765–2773. [4.7]
- Zaucker, F., T.F. Stocker and W.S. Broecker, 1994: Atmospheric freshwater fluxes and their effect on the global thermohaline circulation. *J. Geophys. Res.* 99, 12433–12457. [4.7]
- Zebiak, S.E., 1993: Air-sea interaction in the Equatorial Atlantic region. *J. Climate* 6, 1567–1586. [4.3]
- Zebiak, S.E. and M.A. Cane, 1987: A model El Niño-Southern Oscillation. *Mon. Wea. Rev.* 115 (10), 2262–2278. [4.3]
- Zenk, W., 2000: Labrador Sea Water in the Iceland Basin: An overview of the present Kiel RAFOS float programme. *International WOCE Newsletter*, No. 39, 3–6, WOCE International Project Office (unpublished document). [3.2]
- Zenk, W. and L. Armi, 1990: The complex spreading pattern of Mediterranean Water off the Portuguese continental slope. *Deep-Sea Res.* 37, 1805–1823. [5.7]

- Zenk, W., G. Siedler, B. Lenz and N.G. Hogg, 1999a: Antarctic Bottom Water flow through the Hunter Channel. *J. Phys. Oceanogr.* **29**, 2785–2801. [4.5, 4.6]
- Zenk, W., G. Siedler, J. Holfort and O. Boebel, 1999b: Float observations showing the equatorial crossing of Antarctic Intermediate Water in the western Pacific. *International WOCE Newsletter*, No. 34, 10–14, WOCE International Project Office (unpublished document). [3.2]
- Zenk, W., A. Pinck, S. Becker and P. Tillier, 2000: The float park: A new tool for a cost-effective collection of Lagrangian time series with dual release RAFOS floats. *J. Atmos. Oceanic Technol.* **(17**, 1439–1443). [3.2]
- Zhang, H.-M. and N.G. Hogg, 1992: Circulation and water mass balance in the Brazil Basin. *J. Mar. Res.* **50**, 385–420. [4.5]
- Zhang, H.-M. and L.D. Talley, 1998: Heat and buoyancy budgets and mixing rates in the upper thermocline of the Indian and global oceans. *J. Phys. Oceanogr.* **28**, 1961–1978. [5.2]
- Zhang, H.-M., M.D. Prater and T. Rossby, 1999a: Isopycnal Lagrangian statistics from the North Atlantic Current RAFOS float observations. *J. Geophys. Res.* (submitted). [3.2]
- Zhang, J., R.W. Schmitt and R.X. Huang, 1998b: Sensitivity of the GFDL Modular Ocean Model to the parameterization of double-diffusive processes. *J. Phys. Oceanogr.* **28**, 589–605. [7.2]
- Zhang, R.-H. and S. Levitus, 1997: Structure and cycle of decadal variability of upper-ocean temperatures in the North Pacific. *J. Climate*, **10**, 710–727. [1.2]
- Zhang, J., R.W. Schmitt and R.X. Huang, 1999b: The relative influence of diapycnal mixing and hydrologic forcing on the stability of the thermohaline circulation. *J. Phys. Oceanogr.* **29**, 1096–1108. [5.2, 6.2]
- Zhang, R.H., L.M. Rothstein and A.J. Busalacchi, 1998a: Origin of upper ocean warming and El Niño change on decadal scales in the tropical Pacific Ocean. *Nature* **391**, 879–883. [4.3, 4.4]
- Zhang, Y., J.M. Wallace and N. Iwasaka, 1996: Is climate variability over the North Pacific a linear response to ENSO? *J. Climate* **9**, 1468–1478. [7.3]
- Zhang, Y., J.M. Wallace and D.S. Battisti, 1997: ENSO-like interdecadal variability: 1900–1993. *J. Climate* **10**, 1004–1020. [2.3, 3.3, 7.3]
- Zlotnicki, V., 1991: Sea level differences across the Gulf Stream and Kuroshio Extension. *J. Phys. Oceanogr.* **21**, 599–609. [3.3]
- Zlotnicki, V., L.-L. Fu and W. Patzert, 1989: Seasonal variability in a global sea level observed with GEOSAT altimetry. *J. Geophys. Res.* **94**, 17959–17969. [3.3]
- Zlotnicki, V., G. Siedler and B. Klein, 1993: Can the weak surface currents of the Cape Verde frontal zone be measured with altimetry. *J. Geophys. Res.* **98**, 2485–2493. [3.3]

Acronyms, abbreviations and terms

| | |
|--------|--|
| AABW | Antarctic Bottom Water |
| AAIW | Antarctic Intermediate Water |
| ACC | Antarctic Circumpolar Current |
| ACCE | Atlantic Climate Change Experiment |
| ACCP | Atlantic Climate Change Program (US) |
| ACSYS | Arctic Climate System Study |
| ACW | Antarctic Circumpolar Wave |
| ADCP | Acoustic Doppler Current Profiler |
| ADEOS | ADvanced Earth Observing Satellite (Japanese NASDA satellite) |
| AIMS | Analysis, Interpretation, Modelling and Synthesis (Phase of WOCE) |
| AIRS | Atmospheric InfraRed Sounder |
| AJAX | 1980s survey of Southern Oceans |
| ALACE | Autonomous LAgrangian Circulation Explorer |
| AMI | Advanced Microwave Instrument |
| AMIP | Atmospheric Model Intercomparison Project |
| AMS | Accelerator Mass Spectrometry |
| AMSR | Advanced Microwave Scanning Radiometer |
| AMSU | Advanced Microwave Sounding Units |
| AO | Arctic Oscillation |
| AODW | Arctic Ocean Deep Water |
| AOML | Atlantic Oceanographic & Meterological Laboratory (NOAA, USA) |
| Argo | Operational profiling float programme (CLIVAR-GODAE) |
| ARGOS | Satellite location and data transmission system |
| ASUKA | Affiliated Surveys of the Kuroshio off Cape Ashizuri (Japan) |
| AVHRR | Advanced Very High Resolution Radiometer (on ERS satellites) |
| AXBT | Air-dropped expendable bathythermograph |
| BODC | British Oceanographic Data Centre |
| BSH | Bundesamt für Seeschiffahrt und Hydrographie (Germany) |
| BW | Bottom Water |
| C/A | Coarse Acquisition (Degradation of GPS Signals) |
| CBDW | Canadian Basin Deep Water |
| CCCO | Committee on Climate Changes and the Ocean |
| CDIAC | Carbon Dioxide Information Analysis Center (US Department of Energy) |
| CDW | Circumpolar Deep Water |
| CEFAS | Centre for Environment Fisheries & Aquaculture Science (UK) |
| CERES | Clouds and Earth's Radiant Energy System |
| CFC | Chlorofluorocarbon |
| CGFZ | Charlie-Gibbs Fracture Zone |
| CLIVAR | Climate Variability and Predictability project (a part of WCRP) |
| CMAP | CPC Merged Analysis of Precipitation |
| CMDAC | Current Meter Data Assembly Center (WOCE) |
| CME | Community Modelling Experiment/Effort (USA) |
| CMIP | Coupled Model Intercomparison Project |
| COADS | Comprehensive Ocean-Atmosphere Data Set |
| COAPS | Center for Ocean-Atmosphere Prediction Studies (USA) |
| COARE | Coupled Ocean-Atmosphere Response Experiment |
| COG | Committee on Oceanography and GARP |
| CP | Core Project (WOCE) |

| | |
|--------------|--|
| CPC | Climate Prediction Center (USA) |
| CRC | Climate Research Committee (USA) |
| CRC | Co-operative Research Centre (Australia) |
| CRM | Certified Reference Manual |
| CSIRO | Commonwealth Scientific and Industrial Research Organisation (Australia) |
| CSM | Climate System Model |
| CTD | Conductivity-Temperature-Depth (profiler) |
| CUEA | Coastal Upwelling Experiment-A |
| DAC | Data Assembly Centre (WOCE) |
| DBCP | Data Buoy Cooperation Panel |
| DBE | Deep Basin Experiment (WOCE) |
| DGPS | Differential Global Positioning System |
| DIU | Data Information Unit |
| DKRZ | Deutsches Klimarechenzentrum (German Climate Computing Centre) |
| DMS | Dimethylsulphide |
| DMSP | Defense Meteorological Space Program |
| DOE | Department of Energy (US) |
| DORIS | Doppler Orbitography and Radiopositioning Integrated by Satellite |
| DPC | Data Products Committee |
| DQE | Data Quality Expert |
| DSOW | Denmark Strait Overflow Water |
| DWBC | Deep Western Boundary Current |
| DYNAMO | Dynamics of North Atlantic Models (EU Project) |
| EACC | East African Coast Current |
| EAZO | Energetically Active Zones of the Ocean |
| EBDW | Eurasian Basin Deep Water |
| ECCO | Estimation of the Circulation and Climate of the Ocean |
| ECMWF | European Centre for Medium Range Weather Forecasts |
| EEZ | Exclusive Economic Zone |
| EIC | Equatorial Intermediate Current |
| ENSO | El Niño-Southern Oscillation |
| ENVISAT | ESA Satellite |
| EOLE | 1971 Satellite measuring winds, temperatures and pressures from balloons |
| EPR | East Pacific Rise |
| ERBE | Earth Radiation Budget Experiment |
| ERS-1, ERS-2 | European Remote Sensing Satellites |
| ESA | European Space Agency |
| EU | European Union |
| EUC | Equatorial Undercurrent |
| FGGE | First GARP Global Experiment |
| FRAM | Fine Resolution Antarctic Model (UK) |
| FSU | Florida State University (USA) |
| GARP | Global Atmospheric Research Programme |
| GATE | GARP Atlantic Tropical Experiment |
| GCM | General Circulation Model |
| GCOM | Global Change Observation Mission |
| GCOS | Global Climate Observing System |
| GDP | Global Drifter Programme |
| GEOSAT | US Navy Altimeter Satellite |
| GEOSECS | GEochemical Ocean SECtions Study |
| GERB | Global Earth Radiation Budget |

| | |
|-----------|--|
| GEWEX | Global Energy and Water Cycle Experiment |
| GFDL | Geophysical Fluid Dynamics Laboratory (USA) |
| GLOBEC | Global Ocean Ecosystems Dynamics (SCOR-IOC) |
| GLONASS | Global Navigation Satellite System |
| GM | Gent-McWilliams eddy parameterization |
| GM | Garrett and Munk internal wave spectrum |
| GOALS | Global Ocean Atmosphere Land System (CLIVAR component) |
| GOCE | Gravity Field and Steady-State Ocean Circulation Explorer (proposed satellite) |
| GODAE | Global Ocean Data Assimilation Experiment (GOOS) |
| GOOS | Global Ocean Observing System |
| GPCP | Global Precipitation Climatology Project |
| GPS | Global Positioning System |
| GRACE | Gravity Recovery and Climate Experiment (proposed to NASA) |
| GSDW | Greenland Sea Deep Water |
| GSSW | Greenland Sea Surface Water |
| GTS | Global Telecommunication System |
| GTSPP | Global Temperature-Salinity Pilot Project |
| HEM | Horizontal Electric Field Meter |
| HOPE | Hamburg Ocean Primitive Equation Model |
| IAPSO | International Association of Physical Sciences of the Ocean |
| IB | Inverted Barometer |
| ICSU | International Council for Science (Formerly: International Council of Scientific Unions) |
| IDOE | International Decade of Ocean Exploration |
| IES | Inverted Echo Sounder |
| IFREMER | Institut Français de Recherche pour l'Exploitation de la Mer |
| IGBP | International Geosphere-Biosphere Programme (ICSU) |
| IGOS | Integrated Global Observing Strategy |
| IGOSS | Integrated Global Observing Services System |
| IGY | International Geophysical Year |
| IMET | Improved Meteorological Measurements system (USA) |
| IOC | Intergovernmental Oceanographic Commission |
| IODE | International Oceanographic Data and Information Exchange (IOC) |
| IOSDL | Institute of Oceanographic Sciences Deacon Laboratory (UK) |
| IOSTMW | Indian Ocean SubTropical mode water |
| IPCC | Intergovernmental Panel on Climate Change |
| IPO | International Planning/Project Office |
| ISCCP | International Satellite Cloud Climatology Project |
| ISO | IntraSeasonal Oscillation |
| ISOS | International Southern Ocean Studies |
| ISW | Ice Shelf Water |
| ITCZ | InterTropical Convergence Zone |
| IT or ITF | Indonesian Throughflow |
| IW | Intermediate Water, Irminger Water |
| IWP | Intergovernmental WOCE Panel |
| JASON | NASA/CNES altimeter satellite (planned launch 2001) |
| JCOMM | Joint IOC-WMO Technical Commission for Oceanography and Marine Meteorology |
| JdFR | Juan de Fuca Ridge |
| JDIMP | Joint Data and Information Management Panel |
| JEBAR | Joint Effect of Baroclinicity and Relief |
| JEDAC | Joint Environmental Data Analysis Center |
| JGM | Joint Gravity Model |

| | |
|--------|---|
| JGOFS | Joint Global Ocean Flux Study (IGBP) |
| JMA | Japan Meteorological Agency |
| JOC | Joint Organising Committee |
| JODC | Japan Oceanographic Data Centre |
| JPL | Jet Propulsion Laboratory (USA) |
| JSC | Joint Scientific Committee |
| KAPEX | Cape of Good Hope Experiment |
| LADCP | Lowered Acoustic Doppler Current Profiler |
| LCDW | Lower Circumpolar Deep Water |
| LCPW | Lower Central Pacific Water |
| LDEO | Lamont–Doherty Earth Observatory (USA) |
| LEIC | Lower Equatorial Intermediate Current |
| LGM | Last Glacial Maximum |
| LH | Latent heat |
| LIW | Levantine Intermediate Water |
| LMD | Laboratoire de Météorologie Dynamique (France) |
| LODYC | Laboratoire d’Océanographie Dynamique et de Climatologie (France) |
| LSG | Large Scale Geostrophic |
| LSW | Labrador Sea Water |
| MARVOR | French hybrid float of RAFOS and ALACE technology |
| MAW | Modified Atlantic Water |
| MEDOC | Mediterranean Ocean Convection (Experiment) |
| MEDS | Marine Environment Data System (Canada) |
| METOP | Meteorology Operational Platform |
| MISR | Multiangle Imaging Spectroradiometer |
| MMW | Madeira Mode Water |
| MOC | Meridional Overturning Circulation |
| MODE | Mid-Ocean Dynamics Experiment |
| MODIS | Moderate-Resolution Imaging Spectroradiometer |
| MOI | Monsoon Index |
| MOM | Modular Ocean Model |
| MPI | Max-Planck-Institut für Meteorologie (Germany) |
| MSU | Microwave Sounding Unit |
| NABE | North Atlantic Bloom Experiment |
| NAC | North Atlantic Current |
| NADW | North Atlantic Deep Water |
| NAO | North Atlantic Oscillation |
| NAS | North Atlantic Study |
| NASA | National Aeronautics and Space Administration (USA) |
| NASDA | National Space Development Agency (Japan) |
| NASTMW | North Atlantic SubTropical Mode Water |
| NATRE | North Atlantic Tracer Release Experiment |
| NBC | North Brazil Current |
| NBUC | North Brazil Undercurrent |
| NCAR | National Center for Atmospheric Research, Boulder, USA |
| NCEP | National Center for Environmental Prediction (NOAA) |
| NDBC | National Data Buoy Center (USA) |
| NE(C)C | North Equatorial (Counter) Current |
| NEADW | North East Atlantic Deep Water |
| NEG | Numerical Experimentation Group |
| NEUC | Northern Equatorial Undercurrent |

| | |
|------------|---|
| NGCC | New Guinea Coastal Current |
| NGDC | National Geophysical Data Center (USA) |
| NH | Northern Hemisphere |
| NICC | North Intermediate Counter Current |
| NMC | National Meteorological Center |
| NOAA | National Oceanographic and Atmospheric Administration (USA) |
| NODC | National Oceanographic Data Center (USA) |
| NOSAMS | National Oceanographic Sciences Accelerator Mass Spectrometry (USA) |
| NPCMW | North Pacific Central Mode Water |
| NPIW | North Pacific Intermediate Water |
| NPSTMW | North Pacific SubTropical Mode Water |
| NSCAT | Scatterometer Sensor on ADEOS satellite |
| NSCC | Northern Subsurface Counter Current |
| NSDW | Norwegian Sea Deep Water |
| NSF | National Science Foundation (USA) |
| NWP | Numerical Weather Prediction |
| OASIS | Ocean, Atmosphere, Sea, Ice, Soil (Software for coupling components of climate models) |
| OCCAM | Ocean Circulation and Climate Advanced Modelling project (UK) |
| ODAS | Ocean Data Acquisition System (moored buoy) |
| OGCM | Ocean General Circulation Model |
| OOPC | Ocean Observations Panel for Climate |
| OOSDP | Ocean Observing System Development Panel (replaced by OOPC) |
| OPA | Ocean model of Laboratoire d'Océanologie Dynamique et de Climatologie, Paris |
| OPA/ARPEGE | OPA coupled to the atmospheric model of Meteo France/European Centre for Medium Range Weather Forecasts |
| OPYC | Ocean isopycnic model |
| P | Precipitation |
| P-ALACE | Profiling-Autonomous Lagrangian Circulation Explorer |
| PDO | Pacific Decadal Oscillation |
| PE | Primitive Equation or Potential Energy |
| PEQUOD | Pacific Equatorial Dynamics programme |
| PF | Polar Front |
| PI | Principal Investigator |
| PIES | Pressure and Inverted Echo Sounder |
| PIRATA | Pilot Research Moored Array in the Tropical Atlantic |
| PNA | Pacific-North American (Mode of climate variability) |
| POCM | Parallel Ocean Circulation Model (US) |
| POLYGON | USSR mesoscale experiment |
| POLYMODE | 1970s US-USSR mesoscale experiment |
| POM | Princeton Ocean Model |
| POMS | Pilot Ocean Monitoring Study |
| POP | Parallel Ocean Program |
| PR | Precipitation Radar |
| PSMSL | Permanent Service for Mean Sea Level (UK) |
| PV | Potential Vorticity |
| PW | Petawatts |
| QBO | Quasi-Biennial Oscillation |
| QC | Quality Control |
| QG | Quasi-Geostrophic |
| RAFOS | Type of float. RAFOS is reverse of SOFAR |

| | |
|---------|---|
| RSBW | Ross Sea Bottom Water |
| RV | Research Vessel |
| SA | Selective Availability for GPS |
| SAC | Special Analysis Centre |
| SACW | South Atlantic Central Water |
| SADCP | Shipboard Acoustic Doppler Current Profiler |
| SAESTMW | South Atlantic Eastern SubTropical Mode Water |
| SAF | Subantarctic Front |
| SAFDE | Subantarctic Flux and Dynamics Experiment |
| SAMW | Subantarctic Mode Water |
| SASTMW | South Atlantic SubTropical Mode Water |
| SAVE | South Atlantic Ventilation Experiment |
| SC(S) | Somali Current (system) |
| SCC | Surface Counter Current |
| SCICEX | Submarine Arctic Sciences Cruise Exercise |
| SCOR | Scientific Committee on Oceanic Research (ICSU) |
| SEC | South Equatorial Current |
| SEIC | South Equatorial Intermediate Current |
| SEISAMW | Southeast Indian Subantarctic Mode Water |
| SEUC | Southern Equatorial Undercurrent |
| SEVIRI | Spinning Enhanced Visible and Infrared Imager |
| SH | Southern Hemisphere |
| SICC | South Intermediate CounterCurrent |
| SIO | Scripps Institution of Oceanography (USA) |
| SLP | Sea Level Pressure |
| SMMR | Scanning Multichannel Microwave Radiometer |
| SMWG | Synthesis and Modelling WG (WOCE) |
| SO(I) | Southern Oscillation (Index) |
| SOC | Southampton Oceanography Centre |
| SOFAR | Sound Fixing and Ranging |
| SOOP | Ship-of-Opportunity Programme |
| SPESTMW | South Pacific Eastern SubTropical Mode Water |
| SPMW | Subpolar Mode Water |
| SPSTMW | South Pacific SubTropical Mode Water |
| SSCC | Southern Subsurface CounterCurrent |
| SSD | Sea Surface Density |
| SSG | Scientific Steering Group |
| SSH | Sea Surface Height |
| SSM/I | Special Sensor Microwave Imager |
| SSS | Sea Surface Salinity |
| SST | Sea Surface Temperature |
| SSW | Standard Sea Water |
| STMW | SubTropical Mode Water |
| STP | Standard Temperature and Pressure |
| STR | Software Test Report |
| STUW | SubTropical UnderWater |
| Sv | Sverdrup (unit of current transport = $10^6 \text{ m}^3 \text{ s}^{-1}$) |
| SVP | Surface Velocity Programme (of TOGA and WOCE) (replaced by GDP) drifter |
| SVP-B | SVP 'barometer' drifter |
| SYNOP | Synoptic Ocean Prediction (US National Science Foundation/Office of Naval Research Program) |

| | |
|------------|--|
| TAGI | Tropical Atlantic Gradient Index |
| T/P | TOPEX/POSEIDON altimeter satellite |
| TAO | Tropical Atmosphere Ocean array |
| TAS | Tropical Atlantic Study |
| THC | Thermohaline circulation |
| TIROS | Television Infrared Observation Satellite |
| TMI | The Microwave Imager |
| TOGA | Tropical Ocean and Global Atmosphere (WCRP) |
| TRM | Temporal-Residual-Mean |
| TRMM | Tropical Rainfall Measuring Mission |
| T-S or T/S | Temperature/Salinity |
| TT0 | Transient Tracers in the Ocean (Experiment) |
| TWXXPPC | TOGA-WOCE XBT/XCTD Planning Committee |
| UCDW | Upper Circumpolar Deep Water |
| UDEL | University of Delaware (USA) |
| UH | University of Hawaii (USA) |
| UNESCO | United Nations Educational, Scientific and Cultural Organization |
| UOP | Upper Ocean Panel (CLIVAR) |
| VOS | Volunteer Observing Ship (WMO) |
| WCRP | World Climate Research Programme |
| WDC | World Data Center (USA) |
| WGASF | Working Group on Air-Sea Fluxes |
| WHOI | Woods Hole Oceanographic Institution (USA) |
| WHP | WOCE Hydrographic Programme |
| WHPO | WOCE Hydrographic Programme Office |
| WJ | Wyrtki Jet |
| WMDW | Western Mediterranean Deep Water |
| WMO | World Meteorological Organization (UN) |
| WOCE | World Ocean Circulation Experiment (project of WCRP) |
| WSBW | Weddell Sea Bottom Water |
| WSDW | Weddell Sea Deep Water |
| WWW | World Wide Web (Internet) |
| XBT | Expendable Bathythermograph |
| XCP | Expendable Current Profiler |
| XCTD | Expendable CTD profiler |

Index

Page numbers in **bold** refer to main discussions; those in *italic* refer to illustrations and tables.

- AABW (Antarctic Bottom Water) 227, 243, 260, **265**, 294–296, 301, 305, 334, 460–461
CFC tracer studies 435, **436**–437, 447–448
circulation 22
coupled ocean–atmosphere models 88, 89, 90
DBE (Deep Basin Experiment) 267, 268
formation 21, 265, 305
global overturning circulation 298
heat transport 468
NADW formation 262
see also CDW (Circumpolar Deep Water)
AAIW (Antarctic Intermediate Water) 18, 227, 228, 230, 232, 253, 266, 267, **292**–294, 294, 305, 312, 314, 376, 382, 383–384, 461, 528, 566–567
circulation 22
excess CO₂ levels 505
heat transport 468
large-scale freshening 576, 576, 577–580, 582
renewal in Atlantic Ocean, CFC tracer studies 438–440, 439, 440, 441
WOCE float programme data 133
Absolute velocity 123
estimation 144
WOCE float programme 127–129
Abyssal circulation 211–213, 259, 260, 297
diapycnal mixing 339–340
see also Deep circulation
Abyssal regions
mixing 352–354, 355
abyssal currents 353
tracer studies 209
Brazil Basin experiment 352
time scale for penetration 51
ACC (Antarctic Circumpolar Current) 6, 17, 18, 22, 73, 119, 207, 209, 210, 211, 253, **271**–302, 272, 376, 464, 470
Antarctic Slope Front 271
dynamics 280–291, 301
meridional circulation 282–285, 283, 284, 285, 339
Sverdrup balance 280–282, 301
see also Choke-points
eddies
energy 201
heat flux 279–280
mean flow interactions 168
transport modelling 82
interocean exchange 271, 301, 303–304, 305, 313, 314
Mediterranean Water 427
mixed layer fluxes 321
modelling 273
momentum fluxes 280
observations 274–280, 275, 276
Polar Front 271, 274
SAF (Subantarctic Front) 271, 274, 382, 383
SSD (sea surface density) gradients 326
SSS (sea surface salinity) gradients 324
SST (sea surface temperature) gradients 322
tracer studies 432
transport 274–279, 278
altimetric estimation 167
baroclinic mechanisms 288–290, 289
barotropic formstress mechanism 287–288
eddy flux 82, 285–287
NADW (North Atlantic Deep Water) 305
subtropical/subpolar exchanges 271
theoretical predictions 285–291
topographic steering 290–291, 292
water mass formation/conversion 291–296
WOCE float programme 128, 131
WOCE planning 38
ACCE (Atlantic Circulation and Climate Change Experiment) 131
Accelerator Mass Spectrometer *see* AMS
ACCP (Atlantic Climate Change Program) 38
Acoustic Doppler Current Profilers *see* ADCPs
ACSYS (Arctic Climate System Study) 7
ACW (Antarctic Circumpolar Wave) 92, 160, **279**, 313, 530
ADCPs (Acoustic Doppler Current Profilers) 111–112, 121, 470, 471, 473, 526, 534
ACC observations 277
accuracy 111, 113, 118
data management 40, 181
deep convection studies 392
depth-averaged water velocity 111–112
geostrophic profile reference velocities 119
Global Positioning System (GPS) 111, 112–113
heading uncertainty 113–114
Indonesian Throughflow observations 309
interior circulation studies 208
lowered ADCP profiling *see* LADCPs
Mediterranean Water outflow observations 423
northern overflow observations 407
principle of operation 111
shipboard observations
applications 117–120
evolution of systems 112–115
tropical Indian Ocean zonal flows 236, 239
WOCE
Data system 188
Hydrographic Programme (WHP) 100, 112
planning 37
Adélie Land Bottom Water 295, 296, 447
ADEOS-2 179–180
Advanced Microwave Instrument *see* AMI
Advanced Microwave Sounding Radiometer *see* AMSR
Advanced Microwave Sounding Units *see* AMSU
Aerosol 15, 80
Affiliated Surveys of the Kuroshio off Cape Ashizuri *see* ASUKA
Age of water masses 431–452, 526
see also Tracer studies
Agulhas Current 19, 20, 118, 118, 208, 266, 293, 306, 310, 376, 464, 470
autonomous float programme 131
eddies 311–312
interannual variability 170
heat/freshwater fluxes 311–313
interocean exchange 305, 310–313
leakage 310, 311, 313
transport 22, 310–311
Air temperature, shipboard data collection 120
Air-dropped Expendable Bathy Thermograph *see* AXBT
Air-sea fluxes *see* Atmosphere–ocean interactions
AIRS (Atmospheric Infrared Sounder) 179, 180

- ALACE (Autonomous LAgrangian Circulation Explorer) *see* Floats
 WOCE float programme 126, 126, 127, 130, 131, 132, 136, 138
 Altimetry 5, 12, 51, 56, 141–172, 470, 473, 530, 590
 ACC (Antarctic Circumpolar Current) 280
 accuracy 141, 142–143
 tide gauge data comparison 142, 142, 161
 current transport estimates 165–167
 eddies
 diffusion coefficients 169, 169
 energy variation 169–170, 170, 201
 mean flow interaction 167–168
 spatial/temporal scales 168–169
 geostrophic velocity variability 163–165, 164
 Global Drifter Programme 201
 sampling biases 198
 global sea surface height variability 162–163, 163
 heat storage estimates 149, 150–151
 measurement geometry 141–142, 142
 ocean state estimation 538, 539, 542
 ocean topography estimates 144–147, 146
 sea-ice thickness 7
 sea-level variability 8, 28, 142–143, 148–162
 annual variation 158–159, 530
 atmospheric pressure forcing 148–149
 extratropical Rossby waves 153–155, 154
 global mean-sea-level change 160–162, 161
 interannual variability 159–160
 steric effect 149–151
 subsurface variability relation 155, 157–158
 tropical Rossby/Kelvin waves 155, 156
 wind-forced 151–153
 tide signals removal 143
 WOCE Data system 188, 526
 WOCE planning 35, 37
 AMI (Advanced Microwave Instrument) 175, 176, 177
 AMIP (Atmospheric Model Intercomparison Project) 477, 487, 555
 Amirante Passage 244, 266
 AMS (Accelerator Mass Spectrometer) radiocarbon measurements 103
 WOCE tracer programme 433
 AMSR (Advanced Microwave Sounding Radiometer) 180
 AMSU (Advanced Microwave Sounding Unit) 180
 Analytical theory for oceanic circulation 47, 49
- Antarctic
 ozone hole 6
 sea-ice thickness 7
 Antarctic Bottom Water *see* AABW
 Antarctic Circumpolar Current *see* ACC
 Antarctic Circumpolar Wave *see* ACW
 Antarctic Intermediate Water *see* AAIW
 Anthropogenic (Excess) CO₂ 489, 490, 495, 503, 504, 507, 511, 515, 519
 carbon budget 490, 491
 climate change 7–8, 26, 79
 concentration distribution 503–511
 Atlantic Ocean 505–509, 506, 508
 Indian Ocean 509–510, 509
 Pacific Ocean 510–511
 preformed-CO₂ methods 503–505, 503
 coupled ocean–atmosphere models 93
 sea-level rise 8
 time series comparison methods 511–513, 512
 data selection/correction approach 512–513
 multivariate approach 511–512
 within-ocean transport 513
 Antilles Current 264
 AO (Arctic Oscillation) 23, 25, 530, 531, 560, 572
 coupled ocean–atmosphere models 92
 AODW (Arctic Ocean Deep Water) 569
 APEX *see* Floats
 Arabian Sea 322
 Arctic Climate System Study *see* ACSYS
 Arctic Ocean
 deep convection 7
 freshwater budget 306
 surface layer salinity 23
 transfer to North Atlantic from North Pacific 23
 multiyear sea ice 6–7
 system-wide changes during WOCE years 571–573
 Arctic Ocean Deep Water *see* AODW
 Arctic Oscillation *see* AO
 Argentine Basin, CFC tracer studies 436
 Argo programme 57, 137, 138, 158, 171, 173, 534, 591, 599, 600
see also Floats, subsurface
 ARGOS satellite location system 32, 194, 196
Aries expedition 31, 32, 270
 Arlindo programme 308, 309, 449–450
 ASUKA (Affiliated Surveys of the Kuroshio off Cape Ashizuri) 471, 574, 575
 Atlantic Circulation and Climate Change Experiment *see* ACCE
 Atlantic Climate Change Program *see* ACCP
 Atlantic dipole 25, 530
 Atlantic Ocean
 box inverse models 528
 carbon transport 514–518, 516, 517
 deep circulation
 convection 6
- thermohaline circulation tracer studies 435–438, 437
 DWBCs (Deep Western Boundary Currents) 260, 262–265
 eddy energy distribution 201
 Ekman velocity estimation 119–120
 equatorial circulation 226–233, 245
 below 1000m 230–232, 231
 meridional heat/freshwater transports 232–233
 upper 1000m 227–229, 228
 upper ocean near South America 229–230
 excess CO₂ concentration distribution 505–509, 506, 508
 freshwater flux
 estimates 484, 485, 486
 ice sheet input 6
 heat flux
 direct estimates 460–462, 461, 462
 intermediate waters interdecadal temperature variability 565–567
 meridional temperature gradient variability 25
 meridional overturning circulation 312
 northern overflows 401–417
 surface water mass transformation rates 332, 332, 333, 334
 thermal equator 5
 tropical–extratropical exchanges 256
 velocity data sets 534
 WHP
 one-time sampling 110
 repeat hydrography 106
see also North Atlantic Ocean; South Atlantic Ocean
 Atlases of WOCE data 108, 532–535
 Atmosphere
 atmospheric models 80
 carbon dioxide (CO₂) measurements 489
 circulation during WOCE 558, 558–563, 582
 North Atlantic 559–561, 560
 North Pacific 561–562
 southern hemisphere 562–563, 582
 tropical Pacific 562
 coupled ocean–atmosphere models 80–81
 sub-grid-scale processes 80
 Atmosphere–ocean interactions 3, 5–6, 54
 bulk formula estimates 456–458
 bulk parameterization 173–174
 CO₂ transfer 7, 8, 11, 16, 60–61, 80
 data sets 534–535
 heat flux 5–6, 14–15, 455, 459
 latent 15, 177–178
 momentum transfer 13–14
 net long-wave radiation 178–179
 ocean circulation 17
 particle exchanges 15–16
 satellite data 173–180
 sea ice cover effects 7, 16–17

- sea-level variability 148
 sensible heat 178–179
 short-wave radiation 178
 SST decadal variation 366
 surface flux 12–17
 time-scale 4
 water exchange/surface salinity 15
 water mass transformation 317
 wind stress, scatterometers 174,
 175–177, 176
 WOCE Data System 188
 Atmospheric Infrared Sounder *see* AIRS
 Atmospheric Model Intercomparison
 Project *see* AMIP
 Atmospheric pressure measurements,
 drifters 195, 197, 204
 Autonomous Lagrangian Circulation
 Explorer floats *see* ALACE floats
 AXBT (Air-dropped Expendable Bathymeter)
 Thermograph) 157
 Azores Current 71, 210
- Baffin Island Current 390
 Barometric pressure data 120
 Bathymetry 22, 40, 188
 Benguela Current 21
 altimetric transport estimation 166
 interocean exchange transport
 310–311, 313
 Bering Strait 401, 460
 carbon transport 514, 515
 interocean exchange 305, 306–307,
 313, 314
 freshwater flux 484, 485, 486
 Beta 151, 153, 154, 237, 286, 287
 plane 289
 spiral 123, 251
 topographic 290–291
 Biogeochemical cycles 83
 Bottle samples *see* Sample
 measurements
 Bottom frictional processes 259
 Bottom pressure gauges 49
 Bottom water masses
 formation 259
 Pacific Ocean circulation tracer studies
 444–446, 446
 Boundary conditions 83, 340
 Boundary currents 18–21, 20
 Global Drifter Programme data
 197–198
 heat flux 5
 WHP data collection 105
 wind-driven modelling studies 67, 68
 Boundary layer 80, 82
 bottom 90, 350
 surface 80, 81
 Boundary mixing 340
 Boussinesq approximation 318, 550
 Bowen-ratio 178
 Box inverse models 527, 528
 Brazil Basin
 AABW (Antarctic Bottom Water) 265
 moored current meter arrays 265
 tracer experiments 352, 353
 Brazil Basin Experiment 49, 52, 133, 211,
 529
 see also DBE (Deep Basin Experiment)
 Brazil Current 19, 303, 376, 527
 SST (sea surface temperature) 322
 Bulk formula estimates 326–328,
 456–458, 473
- Cabbeling 320
 CAGE 34
 California Current 19, 21, 164, 165, 377
 Canadian Basin Deep Water *see* CBDW
 Canary Current 19, 201, 377
 Cape Farewell 411, 415, 416
 Cape of Good Hope Experiment
 see KAPEX
 Carbon budget 489–495
 predominant carbon species 490
 Carbon cycle 16
 carbon (^{14}C) tracer studies 432
 Pacific Ocean deep/bottom water
 circulation 444–446, 446
 WHP one-time survey standards 103
 meridional carbon transport 513
 ocean CO_2 storage 491
 ocean models 8
 see also Anthropogenic (Excess) CO_2 ;
 Coulometric TCO₂ measurement;
 CRMs
 Carbon dioxide (CO₂) 101, 105
 atmosphere–ocean exchanges 16
 limiting factors 16
 modelling 60–61
 seasonal 11–12
 atmospheric measurements 489
 coupled ocean–atmosphere models 80
 excess 489, 490
 concentration distribution 503–511
 net flux 490–491
 preformed-CO₂ methods 503–505,
 503, 506
 see also Anthropogenic (Excess)
 CO₂
 interhemispheric gradients 493–495,
 494
 JGOFS/WOCE global survey 489,
 495–520
 certified reference materials 499
 data collection/distribution 498
 data quality assurance 498–503
 goals 496
 implementation 496–498
 measurable parameters 497, 498
 measurement methods 497, 498, 499
 planning 495–496
 sampling lines 496, 497
 shore-based analyses 499–501, 500
 synthesis of data 503–520
 ocean uptake 16, 489, 490, 491–492
 modelling 492–495
 pre-WOCE global data 497
 sinks 489, 490, 491, 492, 493, 495
 ocean function 7, 8, 11, 16
 storage 490, 491
 global estimates 492
 regional estimates 492–493, 493
 Carbon Dioxide Information and
 Analysis Center *see* CDIAC
 Carbon tetrachloride tracer studies
 see CCl₄ tracer studies
 Carbon transport 24, 51, 52
 Atlantic Ocean 514–518, 516, 517
 methods 514–515
 atmosphere–ocean net flux 518–520,
 519
 riverine inputs 515, 518
 within-ocean 513–520
 see also Anthropogenic (Excess) CO_2 ;
 Carbon cycle; CDIAC
 CBDW (Canadian Basin Deep Water)
 571
 CCCO (Committee on Climate Changes
 and the Oceans) 3
 WOCE planning 33–36, 39
 CCl₄ (carbon tetrachloride) tracer studies
 431
 Atlantic Ocean 507
 CDIAC (Carbon Dioxide Information
 and Analysis Center) 498
 see also Carbon cycle
 CDW (Circumpolar Deep Water) 260,
 261, 262, 265, 294, 295, 296,
 339, 438
 circulation 22
 tracer studies 444, 445, 446
 Central Water *see* SACW (South Atlantic
 Central Water)
 Certified reference materials *see* CRMs
 CFC (chlorofluorocarbon) tracer studies
 431, 592
 AABW (Antarctic Bottom Water) 297
 formation rate 296
 AAIW (Antarctic Intermediate Water)
 293
 renewal in Atlantic Ocean 438–440,
 439, 440, 441
 Adélie Land Bottom Water 296
 Atlantic Ocean
 deep thermohaline circulation
 435–438
 equatorial 227, 230
 coupled ocean–atmosphere models 90,
 93
 Indonesian Seas interocean exchange
 450, 451
 Southern Ocean deep water formation
 446–448
 thermohaline circulation modelling
 75
 WHP one-time survey 105
 CFC-11 431, 432, 436, 439, 447
 CFC-12 431, 436
 CFC-113 431
 Challenger expedition 378, 585
 drifters/drifting buoys 193, 194
 Charlie–Gibbs Fracture Zone 402,
 403–404, 408, 409, 410

- Chlorofluorocarbon tracer studies
see CFC tracer studies
 Choke-points
 ACC (Antarctic Circumpolar Current)
 observations 277
 monitoring 54
 repeat hydrography 106
 Circulation 17–23, 47
 boundary currents 18–21, 20
 buoyancy-driven flows 23
 high-resolution models 51
 historical framework 47, 48–49, 51,
 56, 58
 mapping, WOCE data-based analyses
 526–529
 regional studies 48
 wind-driven 17–21
 WOCE goals 37
 Circumpolar Deep Water *see* CDW
 Climate change 3, 595
 anthropogenic (global warming) 7–8,
 26, 79
 climate drift 87
 predictive models 3, 50
 regional impacts 29–30
 sudden 26–27, 27
 see also Sea-level change
 Climate models 79
 climate prediction 81, 593, 595
 flux adjustment 86
 heat budget 455–456
 heat transport 84–85
 water budget 88
 Climate sensitivity, global 93
 Climate system 4–5
 ocean impact 27–30
 Climate variability 3
 interannual/decadal phenomena 530,
 531
 long-term ocean–atmosphere
 interactions 6
 prediction 591, 592–595, 601
 coupled ocean–atmosphere models
 79, 86, 93–95
 data assimilation techniques 593,
 594, 595
 limits of modelling approach 50
 long-term observations 4, 5, 50, 56
 mean state of ocean 595–596
 time scales 595
 TOGA data 3–4
 WOCE data 8
 Climate Variability and Predictability
 study of WCRP *see* CLIVAR
 Climatology 166–167
 changes 87
 hydrographic data 533
 online access 534
 surface 84
 WOCE observational programmes
 532–535
 CLIVAR (Climate Variability and
 Predictability study of WCRP) 5,
 6, 8, 9, 25, 35, 43, 79, 173, 190,
 379, 526, 529, 532, 545, 587,
 587, 588–589, 593, 595
 repeat hydrography 106
 Clouds
 condensation nuclei 15
 coupled ocean–atmosphere models 80,
 83, 93
 satellite short-wave radiation flux data
 178
 solar radiation absorption/reflection
 14, 80
 surface heat flux estimation 327
 water/ice measurement sensors 5
 CMDAC (Current Meter Data Assembly
 Centre) 534
 CMIP (Coupled Model Intercomparison
 Project) 95
 CO₂ *see* Carbon dioxide
 COARE (Coupled Ocean–Atmosphere
 Response Experiment) 219–220
 Coastal Upwelling Experiment
 see CUEA
 Cold water pathway/cold route *see*
 Meridional overturning circulation
 Committee on Climate Changes and the
 Oceans *see* CCCO
 Condensation nuclei 15
 Conductivity–Temperature–Depth mea-
 surements *see* CTD measurements
 Continental climate 6, 11
 Convection
 diurnal mixed layer 17
 see also Deep convection
 Coriolis force 205, 209, 247, 392
 wind-driven Ekman current 201, 202,
 203
 Coulometric TCO₂ measurement
 498–499
 shore-based analyses comparisons
 500–501, 500
 see also Carbon cycle
 Coupled Model Intercomparison Project
 see CMIP
 Coupled ocean–atmosphere models 24,
 79–96, 553–554
 acronyms 96
 climate sensitivity 93
 component coupling 82
 components 79–83
 atmosphere 80–81
 land surfaces 81
 ocean 81–82
 sea ice 82
 decadal variability 92
 flux adjustment 84–86, 85
 forcing 83
 freshwater budget 82–83, 86
 freshwater transport 88, 88, 477
 future climate simulations 93–95
 heat budget 84–85
 heat transport 87–88, 467–468
 initialization
 categories 86–87
 techniques 87
 interannual variability 91–92
 intermediate complexity models 80
 past climate simulations 92–93
 sea surface temperature 87
 thermohaline overturning circulation
 88–90, 89, 93–94, 94
 time-scales 79
 upper ocean thermal field data 534
 water mass formation/ventilation
 processes 90–91
 Coupled Ocean–Atmosphere Response
 Experiment *see* COARE
 CRMs (certified reference materials) 499,
 501, 502
 see also Carbon cycle
 Cryosphere 7
 CTD (Conductivity–Temperature–Depth)
 measurements 49, 526
 altimeter sea level data relation 157
 combined with ADCP data 119
 data formats 109
 data quality assurance 108, 109
 deep convection studies 394, 398
 early studies 31, 32
 WHP (WOCE Hydrographic
 Programme) 100, 102–111
 one-time survey 103, 103, 105
 standards 103, 103, 107
 WOCE Data System 187
 CUEA (Coastal Upwelling Experiment)
 48
 Current Meter Data Assembly Centre
 see CMDAC
 Current meters
 data management 40, 51
 ocean variability studies 530
 see also Moored current meter arrays
 Currents
 altimetry 162–170
 baroclinic 276, 277, 278
 barotropic 165, 276–277
 float programme measurements *see*
 Floats, subsurface
 transport/variability estimates
 165–167
 turbulent mixing 349–351
 vertical shear
 geostrophic calculations 99, 100
 quantitative data 99
 reference velocity calculation 100
 DACs (Data Assembly Centres) 41, 107,
 108, 183, 185
 ADCPs 188
 Current Meter 188
 data format 109
 float data 130, 188
 hydrographic data 187
in-situ sea-level data 188
 meteorological data 121
 planning 40
 surface drifter data 187
 Surface Meteorology 188
 total data sets submitted 40
 upper ocean thermal data 188
 Dansgaard/Oeschger events 26
 Data Assembly Centres *see* DACs

- Data assimilation *see* Ocean state estimation
 Data collection/distribution 526
 conversion errors 108–109
 Global Drifter Programme 194
 drifter design features 195, 196
 JGOFS/WOCE global CO₂ survey 498
 WHP measurements 108
 WOCE float programme 130
 WOCE planning 39–41
see also WOCE Data System
 Data formats 109
 Data Information Unit *see* DIU
 Data online sources 526, 534, 535
 Data Products Committee *see* DPC
 Data quality assurance 40–41
 CTD measurements 108, 109
 JGOFS/WOCE global CO₂ survey 498–503
 certified reference materials 499
 shore-based analyses 499–501, 500
 shipboard observations 107–108
 meteorology 121
 upper ocean thermal field data 534
 Data Quality Experts *see* DQEs
 Data sharing policy 39–41, 185
 DBE (Deep Basin Experiment) 128, 130, 211, 260, 265, 266–269, 268
 Lagrangian measurements 267–268
 moored arrays 267
 time scales 268, 270
 tracer studies 267, 352, 353
see also Brazil Basin Experiment
 Deacon Cell 283
 Decadal time scale changes 530, 531
 coupled ocean–atmosphere models 92
 deep water masses 25–26
 intermediate water masses 25–26
 Atlantic Ocean heat flux 565–567
 Kuroshio Current transport 573–575, 574, 575, 576, 582
 mode waters 385–386
 repeat hydrographic data 532, 557
 salinity 25–26
 temperature 25–26, 366
 thermocline transient response 365, 365–370, 366, 367, 368, 369
 Deep Basin Experiment *see* DBE
 Deep circulation 259–270
 Atlantic Ocean 262–265
 Indian Ocean 265–266
 mixing rates 266, 266
 moored current meter arrays 259, 260, 261, 261
 Pacific Ocean 261–262
 WOCE objectives 259–260
 Deep convection 21, 205, 215, 387–400, 401, 529
 density flux 387, 389, 390, 391–392
 Gulf of Lions 421–422
 heat fluxes 387, 389, 389
 mode waters formation 581
 North Atlantic Ocean 304
 North Pacific Ocean 304
 plumes 391–393, 392, 398
 restratification process 396–398, 397, 398
 salinity variability 390, 393–396, 394, 395
 temperature variability 393–396, 393, 394, 395
 ventilation 390, 391
 Deep jets
 Atlantic Ocean 264
 deep reversing jets 233, 245
 equatorial 222, 244–245
 turbulent mixing 349
 tropical Pacific Ocean 224–225
 Deep seasonal mixed layer 17
 Deep water formation *see* Convection; Overturning; Ventilation
 Deep water masses
 circulation 21–22
 bathymetry 22
 global overturning 297–298
 North Atlantic Ocean 24
 Pacific Ocean tracer studies 444–446, 446
see also Mixing
 decadal time scale changes 25–26
 diapycnal (vertical) mixing 211–212, 339
 formation 21, 259
 coupled ocean–atmosphere models 90–91
 equatorial Indian Ocean 243
 Southern Ocean tracer studies 446–448
 thermohaline circulation models 75
 TRM (Temporal–Residual–Mean) approach 344–345
 Deep Western Boundary Currents
see DWBCs
 Deep-sea reversing thermometers 107
 Defense Meteorological Space Program *see* DMSP
 Denmark Strait 89, 529
 NADW formation 262
 near-bottom mixing 351
 northern overflows 401, 402, 403, 405–406, 411, 569, 573
 transport interannual variability 532
 transport means 410–411
 Denmark Strait Overflow Water *see* DSOW
 Density budgets, diapycnal volume fluxes 319, 319–320
 Density flux 338
 deep convection 387, 389, 390, 391–392
 restratification process 396–397
 surface water mass 331
 transformation estimation 332
 Depth-averaged water velocity, ADCP data 111–112
 Deterministic weather forecasting 4
 DGPS (Differential Global Positioning System) 113
 Diapycnal circulation 5, 318
 Diapycnal (vertical) mixing 338
 abyssal circulation 339–340
 global-scale thermohaline circulation 338–339
 numerical models 551
 ocean interior 346–349, 346, 351, 354–355
 Diapycnal volume fluxes
 density budgets 319–320
 seasonal thermocline 321
 water mass formation 318–319, 319
 Differential Global Positioning System *see* DGPS
 Diffusion *see* Mixing
 Diffusive flux 337, 338
 mesoscale/microscale lateral dispersion 345–346
 microstructure-based estimates 346–347
 near-bottom mixing 350–351
 surface water mass transformation 320
 thermohaline intrusions 346
 Dimethylsulphide *see* DMS
 Discovery Gap 266, 412
 DIU (Data Information Unit) 41, 42, 183, 186
 DMS (dimethylsulphide) condensation nuclei 15
 DMSP (Defense Meteorological Space Program) satellites 174, 177
 Documentation, WHP cruise summaries 108
 DORIS 35
 Double-diffusive mixing 337, 338
 numerical models 551
 ocean interior 348, 355
 thermohaline intrusions 346
 DPC (Data Products Committee) 183–185
 DQEs (Data Quality Experts) 107, 108
 Drag coefficient 13
 Drake Passage 41, 54, 106, 119, 376, 383, 470, 528
 ACC (Antarctic Circumpolar Current) transport 276, 277, 278, 279, 280, 303, 305
 deep water masses circulation 22, 271
 eddy fluxes 272, 273
 Drifter Data Centre 194
 Drifters/drifting buoys 5, 32, 49, 51, 57, 58, 193, 206, 470, 471, 473, 588, 590
Challenger expedition 193, 194
 data management 40, 194
 WOCE Data System 187
 design 193–194, 195, 195–196, 196
 drogues 32
 sensor data transmission 196
 detached drogues 196, 197
 early research programmes 32
 interior circulation studies 208
 operational life 194, 196–197
 tropical Pacific Ocean 222
 velocity data sets 534
 water-following capabilities assessment 193
 wind-slip correction 196, 197
 WOCE measurements 526, 527

- Drifters (*cont.*)
 WOCE planning 37
see also Global Drifter Programme
- DSOW (Denmark Strait Overflow Water) 63, 64, 390
- North Atlantic thermohaline circulation models 73, 74
- DWBCs (Deep Western Boundary Currents) 259, 260–266, 261
- Atlantic Ocean 260, 262–265, 263
- CFC tracer studies 436–437
- Indian Ocean 265–266
- Pacific Ocean 260, 261–262, 262
- wind-driven models 68, 70
- WOCE float programme 136
- DYNAMO project 62, 67, 68, 75, 414, 415, 555
- Earth Radiation Budget Experiment *see* ERBE
- East African Coast Current 233
- East Australian Current 19, 20, 29, 131, 376, 463, 470
- East Greenland Current 23, 306, 402
- East North Atlantic Water 379
- East Pacific Rise *see* EPR
- Eastern boundary currents/return flows 19, 21, 24
- EBDW (Eurasian Basin Deep Water) 571
- ECCO (Estimation of the Circulation and Climate of the Ocean) 545
- Eddies 24
- Agulhas Current interocean exchange 311
- altimetry 162, 167–169
- diffusion coefficients 169, 169
- mean flow interaction 167–168
- mesoscale energy variation 169–170, 170
- spatial/temporal scales 168–169
- temporal meridional mean 338, 340–345, 354
- annual cycle of energy 158–159
- cross-equatorial transport 311–312
- early studies 31, 32
- energy transfer 200–201
- flux parameterization 70–73, 82
- generation 70, 167–168
- Global Drifter Programme energy distribution data 195, 200–201, 200
- heat fluxes *see* Eddy fluxes
- high-resolution models 70–73
- kinetic energy 82, 163–164, 165, 170
- mean flow interaction 167–168, 341
- mesoscale/microscale lateral dispersion 345–346
- North Brazil retroflection 227
- potential energy 82
- Reynolds stress 167, 168
- subduction effects 363–364
- subtropical eastern Atlantic 167–168
- wind forcing 151–153
- Eddy fluxes
- ACC (Antarctic Circumpolar Current) 272–273, 279–280, 301
- Agulhas Current interocean exchanges 311–312
- mixed layer 321
- residual mean flow theory 341
- Southern Ocean 271, 303
- tropical Pacific Ocean 220–221
- Eddy-resolving models 38, 61, 62, 72–73, 75, 80, 363–364, 551
- EGM96 147
- EIC (Equatorial Intermediate Currents) 245
- equatorial Atlantic Ocean 227, 228
- Pacific Ocean 225
- Eighteen Degree Water *see* NASTMW (North Atlantic Subtropical Mode Water)
- Ekman layer
- depth scaling 203, 203
- Global Drifter Programme data 201–202
- Ekman transport 14, 24, 151, 194
- ACC (Antarctic Circumpolar Current) 282, 283, 284, 285
- Ekman layer depth scaling 203, 203
- freshwater flux estimates 482, 483
- Global Drifter Programme data 195, 199, 201–203, 202, 203
- heat transport
- direct estimates 462, 463
- meridional in Atlantic Ocean 232
- Indian Ocean
- equatorial 244
- tropical 233, 237–238, 239
- Indonesian Seas 309
- overturning circulation 298, 300
- Pacific Ocean
- tropical 199, 216, 218–219
- tropical–subtropical water exchanges 249, 252
- shipboard ADCP data 119–120
- subduction 360, 361, 361, 362, 369–370, 373, 374
- WOCE data-based analyses 527
- Eltanin Survey 49, 50
- ENSO (El Niño–Southern Oscillation) 6, 18, 24–25, 54, 215, 335, 530, 542–543, 588, 589
- altimetric data 159–160, 171
- coupled ocean–atmosphere models 79, 84, 86, 91, 92
- Indonesian Throughflow transport rates 308–310, 450, 531
- interocean transport changes 306, 313
- Kuroshio Extension 575
- mid-latitude propagation of effects 155
- ocean heat storage 162
- Pacific Ocean
- solar radiation absorption 14
- surface circulation from drifter data 199
- tropical SSTs 562
- prediction 588, 591, 592–593, 594, 595, 601
- regional impacts 30
- remote sensing 590
- heat flux 178, 179
- temporal variability 221–222
- TOGA study 3, 4
- wind stress effects 13–14
- Entrainment flux 320, 321
- ENVISAT 171
- EOLE satellite system 32
- EPR (East Pacific Rise) 224, 442, 443
- Equatorial Deep Jets 222
- Indian Ocean 244–245
- Equatorial Intermediate Currents *see* EIC
- Equatorial Subsurface Countercurrents 253, 254
- Equatorial UnderCurrent *see* EUC
- ERBE (Earth Radiation Budget Experiment) 178, 458
- ERS-1/2 5, 41, 105, 142, 162, 175, 177, 188, 539
- Estimation of the Circulation and Climate of the Ocean *see* ECCO
- EUC (Equatorial UnderCurrent) 216, 217, 218, 219, 225, 245, 255
- Atlantic Ocean 227, 228
- dynamics 221
- Indian Ocean 236, 240
- Pacific Ocean 220, 222, 255
- Intermediate Waters dynamics 254
- tropical–subtropical water exchanges 249, 250, 251
- EUC/SEC (Equatorial Undercurrent–South Equatorial Current) system turbulent mixing 349
- Eurasian Basin Deep Water *see* EBDW
- EUROFLOAT 131
- Evaporation 15, 173, 179
- coupled ocean–atmosphere models 82, 83
- direct estimates 480–481
- indirect estimates 476, 479
- Mediterranean Sea
- interannual variability 425
- salinity 422
- seasonal cycle 425
- satellite data 177
- shipboard meteorological data 120
- surface fluxes estimation 327, 328, 330
- Evaporation/precipitation difference
- ACC (Antarctic Circumpolar Current) changes across Southern Atlantic 304
- atmosphere–ocean interactions 173, 179
- direct ocean estimates 480–481
- indirect estimates 476, 478
- North Atlantic Ocean 304
- North Pacific Ocean 304
- Exchange pathway 247
- Exchange window 251
- Expendable Bathythermographs *see* XBTs
- Expendable instruments 57

- Falklands/Malvinas current 19, 527
 Faroe Bank Channel 89
 northern overflows *see*
 Iceland–Scotland overflow
 FGGE (First GARP Global Experiment)
 32, 33, 458
 drifters 195, 197
 Fieberling Guyot 351, 351
 Findlater jet 242
 Fine Resolution Antarctic Model (FRAM)
 see Numerical models
 First GARP Global Experiment *see* FGGE
 Floats, subsurface 123–139, 470, 471,
 473, 591
 absolute mean velocity measurements
 127–129
 AJAX 438
 ALACE (Autonomous LAgrangian
 Circulation Explorer) 37, 41, 206
 APEX 127
 autonomous floats 126–127, 126
 basin-wide studies 131–135, 132
 data management 40, 130
 WOCE Data System 188
 deep convection studies 392–393
 design development 124–126
 historical background 123–127
 instrumentation 130–131
 interior circulation studies 208
 Labrador Sea 391
 MARVOR 126, 127, 130, 131, 133
 P-ALACE (Profiling Autonomous
 Lagrangian Circulation Explorer)
 32, 127
 data assimilation 539
 deep convection studies 394
 Labrador Sea 391
 North Atlantic programme 134, 135
 restratification process 397
 RAFOS
 Deep Basin Experiment 267
 WOCE float programme 125–126,
 127, 130, 131, 132, 133, 134,
 135, 136, 137, 138
 regional studies 135–137
 sampling bias 129
 SOFAR 32, 125, 125, 127
 SOLO 127
 underwater gliders 127
 upper ocean thermal field data sets
 533, 534
 velocity data sets 534
 WOCE float programme 126, 127,
 129–132, 136, 138, 526, 527
 see also Argo programme
 Florida Current 67, 227
 Florida Straits 54
 Flux adjustment 84–86, 87
 Flux correction *see* Flux adjustment
 Flux studies
 mean mass flux estimations 48
 model time scales 63–64
 surface flux data sets 534–535
 WHP (WOCE Hydrographic
 Programme) 100, 101, 104
 FOCAL/SEQUAL experiment 226
- Fram* 585
 Fram Strait 23, 402, 570, 571, 573, 581
 Freshwater budget
 Arctic Sea 306
 coupled ocean–atmosphere models
 82–83, 84, 86
 global 487, 487–488
 sea-level variability 149–150
 see also Salinity
 Freshwater flux/transport 17, 17, 23–24,
 51, 52, 475–488, 589
 Agulhas Retroflection 311–313
 Bering Strait 306–307
 coupled ocean–atmosphere models 88,
 88
 deep convection 390
 diffusive mixing 338
 direct ocean estimates 478–483, 485
 indirect estimate comparisons
 483–486
 equatorial Atlantic Ocean 232–233
 glacial meltwater
 addition around Antarctica 448,
 448–449, 449
 ice sheet input 6, 23
 global observation system 100, 101
 Indian Ocean 304
 indirect estimates 475–476, 477, 478,
 479, 480
 model development 476–478
 Indonesian Throughflow 307
 interocean exchange 484–485
 mechanisms 486–487
 North Atlantic Ocean 304
 North Pacific Ocean 304
 numerical models 553
 Southern Ocean 303, 304
 subduction, kinematic model 565
 surface flux data sets 534–535
 surface water masses 330–331, 331
 bulk formulae 326–328
 transformation 332
 tropics 215, 245
 WHP data collection 104, 105
 WOCE data-based analyses 529
 WOCE goals 37
 Friction 259, 289
- GARP (Global Atmospheric Research
 Programme) 32, 33, 458
 GATE 33
 Gazelle expedition 585
 GCMs (General Circulation Models) 6,
 12, 79, 216
 altimetry 143–148, 159
 applications 79
 baroclinic mechanisms 288
 carbon transport 518
 CO₂ uptake 492, 493
 diapycnal transports 343–344
 eddy-resolving 162
 equilibrium versus non-equilibrium
 solutions 62–64
 freshwater transport 475–476, 486, 487
- geophysical fluid dynamics 47
 heat transport 467
 Southern Ocean circulation 300
 subsurface countercurrents 226
 thermal expansion simulations 28
 Wyrtki Jets 236
 see also Models; Numerical models
 GCOM (Global Change Observation
 Mission) 180
 GCOS (Global Climate Observing
 System) 9, 43, 190, 588
 General Circulation Models *see* GCMs
 Geochemical Ocean Sections Study
 see GEOSECS
 GEOS-3 142
 GEOSAT 142, 144, 151, 153, 155, 157,
 158, 162, 163, 165, 167, 169, 274
 GEOSECS (GEOchemical Ocean SECTIONS
 Study) 101, 268, 431, 433, 442,
 444, 449
 CO₂ data 497, 501, 512, 513
 Geostrophic adjustments 163–165
 Geostrophic currents 194, 209
 tropical Pacific Ocean 217, 218–219,
 218
 Global Drifter Programme data 199
 WOCE data-based analyses 527–529
 Geostrophic shear
 conversion into absolute velocity 123
 shipboard ADCP data 119–120
 Geostrophic velocity variability,
 altimetric data 163–165, 164
 GERB (Global Earth Radiation Budget)
 sensor 180
 GEWEX (Global Energy and Water Cycle
 Experiment) 6
 Gibbs Fracture Zone *see* Charlie–Gibbs
 Fracture Zone
 Global Atmospheric Research Programme
 see GARP
 Global Change Observation Mission
 see GCOM
 Global Climate Observing System
 see GCOS
 Global conveyer belt 6, 21, 47, 52, 53
 Global Drifter Programme 5, 194, 204
 data density distribution 197, 197
 data set 194–195
 eddy energy distribution 200, 200–201
 altimeter data comparisons 201
 instrumental methodology 195–198
 sampling biases 198
 wind-driven Ekman currents 14,
 201–203, 202, 203
 see also Drifters/drifting buoys
 Global Earth Radiation Budget sensor
 see GERB sensor
 Global energy budget 11, 12, 23
 Global Energy and Water Cycle
 Experiment *see* GEWEX (Global
 Energy and Water Cycle
 Experiment)
 Global mean velocity/velocity variance
 143–144, 198–201
 standard error ellipse computations
 199

- Global observation systems 5, 8–9, 49, 50, 52–55, 590
 early programmes 32, 33
 ongoing maintenance 58
 WHP (WOCE Hydrographic Programme) 100–101
 WOCE planning 37
- Global Ocean Data Assimilation Experiment *see* GODAE
- Global Ocean Ecosystem Dynamics *see* GLOBEC
- Global Ocean Observing System *see* GOOS
- Global Positioning System *see* GPS
- Global Precipitation Climatology Project *see* GPCP
- Global Temperature–Salinity Pilot Project *see* GTSP
- Global warming *see* Climate change, anthropogenic
- GLOBEC (Global Ocean Ecosystem Dynamics) 43
- GLONASS 113
- GOCE (Gravity Field and Steady-State Ocean Circulation Explorer) 143, 147, 171
- GODAE (Global Ocean Data Assimilation Experiment) 5, 8, 9, 190, 545, 587, 589, 592, 597–600, 601
 components 599–600
 outputs 600
 phases 600
 rationale 598–599
- GOOS (Global Ocean Observing System) 9, 35, 40, 43, 190, 526, 586, 587, 588, 592
 Climate Module 588
- GPCP (Global Precipitation Climatology Project) 179
- GPS (Global Positioning System) 111, 112–113, 138, 171
 Differential GPS 113
 heading uncertainty reduction 113–114
 interior circulation studies 208
 lowered ADCP systems 116
 position accuracy 113
 SA (Selective Availability)/SPS (Standard Positioning Service) 113
 WOCE planning 37
- GRACE (Gravity Recovery and Climate Experiment) 143, 147, 171
- Gravity Field and Steady-State Ocean Circulation Explorer *see* GOCE
- Gravity Recovery and Climate Experiment *see* GRACE
- Great Australian Bight 305
- Great salinity anomaly 399
- Great Whirl 240, 242
- Greenhouse gas concentrations 7, 12, 26, 79
 coupled ocean–atmosphere models 93, 94, 94
- Greenland Currents 389, 390
- Greenland, palaeoclimate records 26–27, 26
- Greenland Sea 6, 567
 changes during WOCE 569
 cooling warming cycle 570–571, 570
 deep convection 21, 387, 399
 thermohaline fluxes 306
- Greenland Sea Deep Water *see* GSDW
- Greenland Sea Surface Water *see* GSSW
- Greenland–Iceland–Scotland ridge *see* Iceland–Scotland Ridge
- GSDW (Greenland Sea Deep Water) 569, 571, 581
- GSSW (Greenland Sea Surface Water) 571
- GTSP (Global Temperature–Salinity Pilot Project) 534
- Guinea Dome 230
- Gulf of Lions 17
 deep convection 387, 392, 421–422
 restratification 397
- Gulf Stream 19, 56, 126, 137, 197
 altimetry 151, 163, 163, 165, 167
 branching 71
 diffusivity values 350
 eddy fluxes 71, 151
 extension 163
 heat flux 151, 460, 462
 inshore edge instabilities 29
 lateral induction 360–361
 Mediterranean Water 427
 separation 71
 SSD (sea surface density) gradients 326
 SSS (sea surface salinity) gradients 325
 SST (sea surface temperature) gradients 322
 subduction models 363–364
 subsurface temperature field 157
 surface height variability 157, 163, 163
 system 162–163
 transport 165, 167, 557
 wind-driven models 71, 72
- Gulf Stream Extension, mode waters formation 376, 378
- Guyana Basin 437
- Gyres
 circulation 24, 206
 wind-driven 14, 18, 19, 67
 density field 18
 heat transport 5
 recirculation 19
 subpolar 18, 90
 subtropical 18, 19, 24, 92, 132, 151, 376
- HadCM2 85, 85, 86
- HadCM3 82, 85, 85, 87, 88, 89, 93, 94, 95
- Hawaiian Islands 199
- Heat budget
 equatorial Indian Ocean surface 239
 equatorial Pacific 219–220
 global 11, 12, 455–456, 456, 457
 assessment methods 455, 473
 satellite data 149, 150–151, 162, 177–179
- tropical Indian Ocean 233
- Heat flux/transport 5, 7, 13, 14–15, 17, 23–24, 25, 51, 52, 53, 84–85, 92, 104–105, 120, 173–174, 177–180, 279–280, 307, 310, 312–313, 453–474, 488, 528, 539, 540, 542, 553–554, 564–565, 567, 573, 589
- ACC (Antarctic Circumpolar Current) 279–280
- Agulhas Retroflection 311–313
- assessment methods 455–456
- atmosphere–ocean interactions 173
- bulk formula estimates 326–328, 456–458, 473
- coupled ocean–atmosphere models 82, 84–85, 87–88
 climate sensitivity 93
- deep convection layers 387, 389, 389
- diffusive mixing 338
- direct estimates 459–466, 473, 474
 Atlantic Ocean 460–462, 461, 462
 global analysis 464–466, 465, 466
 Indian Ocean 464
 indirect estimates comparison 466–467
 Pacific Ocean 462–464
- by eddies *see* Eddy fluxes
- equatorial Atlantic Ocean 232–233
- evaporation 15
- global 11, 12, 464–466, 465, 466
 cold water pathway 470
 observation systems 100, 101
 warm water pathway 470
- heat storage 17
- hydrographic sections 104–105
- interannual variability 530
- latent heat 15, 177–178
- loss 17
- mechanisms 468–470
- mesoscale eddies 341
- modelling 467–468
- net heat flux 15
- net long-wave radiation 178–179
- numerical models 553
 large-scale coupling 553–554
- radiation 14
 short-wave 178
- residual method 458–459, 459, 467, 473
- sea ice effects 16, 23
- sea-level variability 149–151
- sensible heat 15, 178–179
- shipboard meteorological data collection 120
- Southern Ocean 303, 304
- storage 149, 151, 162
- subduction, kinematic model 564–565
- surface water mass 328–330, 330
 bulk formulae 326–328
 data sets 534–535
 transformation 332
- thermocline response to decadal variability 366
- thermohaline circulation modelling 75–76, 76

- tropical Indian Ocean 233
 tropics 215, 245
 WHP data collection 104–105
 WOCE data-based analyses 529
 WOCE goals 37
 Heinrich events 26–27
 Helios 442
 Helium (^3He) tracer studies 432
 glacial meltwater addition around Antarctica 448, 448–449, 449
 mantle helium 440, 442, 443
 Pacific Ocean
 deep helium field mapping 442–443, 442
 mid-depth circulation 440–444, 442
 thermocline ventilation 433–435, 434
 seamount hydrothermal sources 443
 HEMs (seafloor electrometers) 277, 278
 HOPE model 81
 Horizontal pressure field 205
 Horizontal pressure gradient 209
 Humidity, shipboard meteorological data collection 120
 Hunter Channel 267
 Hurricanes 175
 Hydrographic climatologies 533
 Hydrographic measurements 99–102
 data management 40
 see also WHP (WOCE Hydrographic Programme)
 Hydrographic sections 41, 49, 50, 99–102, 215, 526
 AAIW (Antarctic Intermediate Water) 293
 ACC (Antarctic Circumpolar Current) 274, 275, 276–277, 276, 278
 Benguela Current transport 311
 freshwater flux direct estimates 479
 heat flux/transport 470
 Atlantic Ocean 460
 direct estimates 460, 462, 463, 464–466
 global analysis 464–466
 Indian Ocean 464
 ocean model comparisons 87–88
 Pacific Ocean 219, 462, 463
 Kuroshio Current transport time series 574, 574, 575, 575
 large-scale intermediate water mass changes in Pacific/Indian Oceans 577–578, 577, 578, 579
 models evaluation 64
 SAMW (Subantarctic Mode Water) 293
 tropical Indian Ocean 237, 242
 WOCE planning 37
- Ice ages 26, 27
 Ice sheets
 Antarctica ^3He tracer studies 448, 448–449, 449
 freshwater input 6
- palaeorecords 26
 volume-associated sea-level change 27
 Ice Shelf Water 295
 tracer studies *see* ISW tracer studies
 Ice–ocean interactions 7
 see also Sea ice
 Icebergs 82, 83
 calving 82
 Iceland Basin 402, 403
 WOCE float programme 137
 Iceland Sea
 changes during WOCE 569
 thermohaline fluxes 306
 Iceland–Scotland overflow 22, 94, 94, 137, 401, 402, 403, 403, 411, 569
 transport means/variability 407–410, 408, 409
 Iceland–Scotland Ridge 401, 402, 529
 NADW formation 262
 ICSU (International Council for Science) 3, 32, 39
 IESs (Inverted Echo Sounders) 277, 278
 IFREMER 188
 IGBP (International Geosphere–Biosphere Programme) 189
 IGOS (Integrated Global Observing Strategy) 5
 IGY (International Geophysical Year) 25, 32, 39, 100, 260, 566, 588
 float observations 125
 IMET (Improved Meteorological Measurements) 120, 121
 Improved Meteorological Measurements *see* IMET
 Incompressibility 318
 Indian Ocean
 AABW (Antarctic Bottom Water) entry 260–261
 ACC (Antarctic Circumpolar Current) freshwater transport 304
 box inverse models 528
 deep circulation quantification 265–266
 deep cross-equatorial flows 243–245
 DWBCs (Deep Western Boundary Currents) 261
 Ekman velocity estimation 119–120
 equatorial deep jets 244–245
 excess CO₂ concentration distribution 509, 509–510
 float programme 131, 132
 freshwater flux 304, 330, 335, 484, 485, 486
 heat flux/transport 470, 471
 direct estimates 464
 hydrographic sections 100
 intermediate waters long-term changes 26
 interocean exchange 304, 305, 310, 311
 tracer studies 449–450
 meridional overturning circulation 339
 near-equatorial circulation 233–245, 234, 246
 cross-equatorial currents 237–239, 238
 equatorial flow relation to higher-latitude flow 242–243
 equatorial zonal flows 233, 235, 236–237
 surface heat budget 239
 western boundary current flows 239–242
 potential vorticity field 529
 SSS (sea surface salinity) 324
 SST (sea surface temperature) variation 25, 322, 322, 323, 323
 subtropical mode waters 382
 thermal expansion rates 28
 tropical–extratropical exchanges 255–256
 tropical/subtropical dipoles 236, 246, 530, 531
 water mass large-scale changes 576, 576–580, 578, 579
 WHP one-time survey 102, 105, 110
 Indian Ocean Dipole 236, 246, 530, 531
 INDIGO expeditions 444
 Indonesian Seas 54
 interocean exchange 305, 307–310, 313
 freshwater flux 484
 tracer studies 449–450, 451
 Indonesian Throughflow 18, 22, 209, 216, 219, 220, 222, 243, 246, 252, 255, 305, 527, 528, 529
 altimetric transport estimation 166
 freshwater flux 484, 485
 heat transport estimates 463, 464
 interocean transport 307–308
 ENSO-associated changes 308–309
 interannual variability 531–532
 thermohaline fluxes 309–310
 transport profile 309
In-situ unmanned instruments 58
 Insolation *see* Radiation
 Instability 29
 baroclinic 288–290
 barotropic 287–288
 Integrated Global Observing Strategy *see* IGOS
 Interannual variability 4, 6, 530, 531
 Aguilhas Current eddies 170
 coupled ocean–atmosphere models 91–92
 Denmark Strait northern overflows 532
 equatorial Atlantic Ocean 226
 heat flux/transport 530
 Indonesian Throughflow transport 531–532
 Kuroshio Current transport 532
 LSW (Labrador Sea Water) 532, 568
 measurement methods 532
 Mediterranean outflow 425, 427
 Mediterranean Water 425
 mode waters 384–385
 NADW (North Atlantic Deep Water) 532
 Pacific Ocean 531
 repeat hydrographic data 532, 557
 sea-level 159–160
 tropical Indian Ocean 243
 Southern Ocean 92
 surface water mass transformation 335
 Interglacial periods 26, 27

- Intergovernmental Oceanographic Commission *see* IOC
- Interior circulation 205–214
- classical hydrology 206–207, 207
 - Deep Basin Experiment 266–269, 268
 - potential vorticity 209–210
 - response to change in forcing 205–206
 - Sverdrup's relation 209
 - theoretical aspects 209–210
 - topographic effects 210
 - tracer measurements 209
 - WOCE studies 208–209
- Interior ocean
- diapycnal mixing 346, 346–349
 - internal wave field 338
 - mixing/stirring 337–355
- Interleaving 346
- Intermediate water masses 563
- decadal time scale changes 25–26
 - temperature variability in Atlantic 565–567
 - formation 21
 - coupled ocean–atmosphere models 90–91
- Indian Ocean large-scale changes 576, 576–580
- Pacific Ocean 252–253, 253, 254, 255
- dynamics 254, 255
 - large-scale changes 576, 576–580
 - tropical–subpolar exchange 252–254
- Internal tides 211, 212
- Internal wave field 206, 211
- interior ocean 338
 - mixing 347–348, 349, 350
- Internal wave shear
- abyssal mixing 352
 - Brazil Basin 352
 - tracers dispersion 345
- International collaboration 32, 33, 34, 43, 101, 101–102, 588
- data management 181
 - float programme 129, 131, 134
- International Council for Science *see* ICSU
- International Geophysical Year *see* IGY
- International Geosphere–Biosphere Programme *see* IGBP
- International Satellite Cloud Climatology Project *see* ISCCP
- International Southern Ocean Studies *see* ISOS
- Interocean exchange 303–314
- ACC (Antarctic Circumpolar Current) 271, 301, 303–304, 305, 313, 314
 - Agulhas Retroflection 305, 310–313
 - Bering Strait 305, 306–307, 313, 314
 - ENSO-related changes 306, 308–310, 313
 - freshwater flux 484–485
 - global thermohaline circulation 304–305
 - Indian Ocean 304
 - Indonesian Seas 305, 307–310, 313
 - interocean links 305
 - northern oceans 304
 - south of Australia 305–306
- subduction process 368
- tracer studies 432, 449–450, 451
- see also* Indonesian Throughflow
- Intertropical Convergence Zones 252
- SSS (sea surface salinity) 324
- Inverted Echo Sounders *see* IESs
- IOC (Intergovernmental Oceanographic Commission) 3, 33, 39, 194
- WMO Joint Commission for Oceanography and Marine Meteorology (JCOMM) 9
- Irminger Basin 402, 412, 528
- WOCE float programme 134, 137
- Irminger Sea 389, 390, 391
- Irminger Water *see* IW
- Iron-enrichment experiments 16
- ISCCP (International Satellite Cloud Climatology Project) 178
- Island Rule 209
- ISOS (International Southern Ocean Studies) 48, 274, 275, 276, 277, 278
- Isthmus of Panama 304
- ISW (Ice Shelf Water) tracer studies 448–449
- IW (Irminger Water) 390
- Izu-Ogasawara Ridge 132
- Jason-1 171
- JCOMM (Joint Technical Commission for Oceanography) 600–601, 601
- WMO Joint Commission for Oceanography and Marine Meteorology 9
- JEBAR (Joint Effect of Baroclinicity and Relief) 223
- JGM (Joint Gravity Models) 144
- JGM-3 144–145, 145, 147
- JGOFS (Joint Global Ocean Flux Study) 8, 16, 39, 101, 102
- CO₂ global survey 489–520
 - Handbook of Methods* 499
 - planning 496
- Joint Effect of Baroclinicity and Relief *see* JEBAR
- Joint Global Ocean Flux Study *see* JGOFS
- Joint Gravity Models *see* JGM
- Joint Technical Commission for Oceanography *see* JCOMM
- Juan de Fuca Ridge 442, 443
- CAPEX (Cape of Good Hope Experiment) 136
- Kelvin waves 205
- tropical Indian Ocean 236
 - interannual sea level variation 243
 - tropics 155, 156
- Kelvin–Helmholz instability 216, 246, 351, 411
- Kermadec Arc 443
- Kinetic energy 81, 82, 163–164, 165, 170
- Kuroshio Current 19, 20, 67–68, 69, 197, 198, 376
- direct heat transport estimates 460
 - direct velocity observations 128
 - eddy transport modelling 82
 - SSD (sea surface density) gradients 326
 - SSS (sea surface salinity) gradients 324–325
 - SST (sea surface temperature) gradients 322
- transport 558
- altimetric estimation 165, 166, 167
 - interannual variability 532
 - interdecadal variability 573–575, 574, 575, 576, 582
 - surveys 471, 471–472
- Kuroshio Extension
- eddy energy variation 170
 - eddy–mean flow interactions 167–168
 - heat balance from altimetric data 151
 - mode waters formation 380
- Kyoto protocol 491
- La Niña 159, 160
- Indonesian Throughflow transport rates 308–309, 310, 531
- Laboratory models 391
- Labrador Current 23, 390
- WOCE float programme 134
- Labrador Sea 6, 17, 102, 387, 567, 568, 569
- circulation mapping from floats 527
 - deep convection 21, 387, 389, 389, 391, 398, 399, 529
 - convective layer 387, 387
- NADW formation 262, 264
- Profiling ALACE data 134–135, 135
- restratification 397, 398, 398
 - thermohaline fluxes 306
 - velocity data sets 534
- WOCE float programme 134
- Labrador Sea Water *see* LSW
- LADCPs (Lowered Acoustic Doppler Current Profilers) 100, 112, 115–117, 121
- ACC (Antarctic Circumpolar Current) 277
- ambiguity errors 116–117
 - applications of observations 117–120
 - bottom-reflected sound interference 115, 116
 - data accuracy 117, 118
 - magnetic compass errors 116
 - relative velocity profile accuracy 115, 116
- Lagrangian measurements
- DBE (Deep Basin Experiment) 267–268
 - float programme 123–139
 - ocean variability studies 530
 - WOCE data set 527
- Land surfaces, coupled ocean–atmosphere models 81

- Latent heat flux 15, 173
 parameterization 173–174
 satellite data 177–178
- Lateral induction 360–361, 374
- Law of the Sea 39
- LCDW (Lower Circumpolar Deep Water) 294
 global overturning circulation 298, 299
- LCPW (Lower Central Pacific Water) 223
- Leewin Current 19, 21, 30
- LEIC (Lower Equatorial Intermediate Current) 222
- LIW (Levantine Intermediate Water) 422, 425
- Loihi Seamount 443, 444
- Lombok Strait 307
- Long-term observations 25–26
 climate variability prediction 4, 5, 50
 methods 56–58
 ocean behaviour prediction 56
 stochastic variability 54–55, 55, 56, 57
- Long-wave radiation, satellite data 178–179
- Lower Central Pacific Water *see* LCPW
- Lower Circumpolar Deep Water *see* LCDW
- Lower Equatorial Intermediate Current *see* LEIC
- Lowered Acoustic Doppler Current Profilers *see* LADCPs
- LSW (Labrador Sea Water) 376, 379–380, 386, 390, 391, 407, 527, 566, 567, 568
- CFC tracer studies 436, 437–438
 formation 529, 580
 interannual variability 532, 568
 WOCE float programme 134, 137
- Macdonald Seamount 443
- Madden–Julian Oscillations 215, 221–222, 242
- Madeira Mode Water *see* MMW
- Makassar Strait 307, 309, 310, 450, 531, 532
- Marginal seas 419
- Maritime climate 6, 11
- MARVOR *see* Floats
- Mass transport 463, 471, 472, 480
- MAW (Modified Atlantic Water) 422
- Mean mass flux estimations 48
- Mean seasonal cycle 221–222
- Meanders 19
 in the Eastern Atlantic 167
 in the Gulf Stream 378
- Measurement methods 590–592
- Measurement standards 103
 data quality assurance 107–108
 definition/development 106–111
 expert protocols development 107
 metadata requirements 106
- Meddies 125, 427, 428, 528
 float studies 136
 generation 427
- salt transport 427
 speed 427
- Mediterranean Ocean Convection experiment *see* MEDOC experiment
- Mediterranean outflow 22, 210, 414, 419, 420, 421, 422–427, 423
 box inverse models 528
 effect on North Atlantic circulation 427–429
 global thermohaline circulation contribution 429
 interannual variability 425, 427
 meddies 427, 428
 near-bottom mixing 351
 North Atlantic salt tongue modelling 426
- Strait of Gibraltar 422–427, 423, 424
 seasonal cycle 424–425
 transport estimates 426–427, 426
- Mediterranean Sea 420, 421
 deep convection 21, 387, 399
 freshwater budget modelling 83
 high-salinity outflow waters 29
 SSS (sea surface salinity) 323
 thermohaline circulation 421
- Mediterranean Water 419–429
 formation 421–422
 interannual variation 425
 salinity 421, 422, 425
- MEDOC (Mediterranean Ocean Convection) experiment 422
- Meltwater runoff 6, 7
- Meridional overturning circulation 6, 88, 460–461, 464, 468–469
- ACC (Antarctic Circumpolar Current) dynamics 282–285, 283, 284, 285, 339
- Atlantic Ocean 304, 312
 cold water pathway/cold route 305, 470
- ocean models 75, 81, 86
- Southern Ocean 272, 273, 298, 303–304, 339
- warm water pathway/warm route 305, 470–471
- Meridional transport 206
 equatorial Atlantic Ocean 232–233
 Indian Ocean 237
- Mesoscale eddies 49, 206, 267, 270, 337–338
 altimetry 169–170, 170
 bottom-generated internal waves 352
 mixing 340, 341
 ocean models 82
 parameterization 340
 TRM approach 340–345
- Mesoscale ocean variability
 altimetry 162
 high-resolution models 61, 69–73
- Meteor expedition 41, 100, 206, 260, 357, 505, 566
- Meteorological data
 Global Drifter Programme 195
 shipboard collection 120–121
 wind-driven circulation models 65
- Meteorology Operational Platform
see METOP
- Methane 80
- METOP (Meteorology Operational Platform) 180
- Microwave sounding unit *see* MSU
- Microwave/Imager 174, 177, 179
- Mid-Atlantic Ridge 211, 267, 269, 437
- Mid-Ocean Dynamics Experiment *see* MODE
- Milankovitch cycles 6, 14, 26
- Mindanao Current 217, 250, 252, 253, 254, 450
- MISR (Multiangle Imaging Spectroradiometer) 180
- Mixed layer 373–374
 deep convection 387, 389, 389
 depth 17, 83
 diurnal mixed layer 17
 mixing processes 320–321, 321
 winter thickness, mode waters formation 376
- Mixing 339–340, 529
 abyssal oceans 339–340, 352–354
 convection 387, 388
 plumes 391–393, 392, 398
- diapycnal 81, 211–212, 339–340
 horizontal 81–82
 layer thickness 82
 mesoscale eddies 340, 341
 mesoscale/microscale lateral dispersion 345–346
- near-bottom 350–351
 northern overflows 411–412, 412
- numerical models 551
- ocean currents 349–351
- Pacific Ocean tracer studies 435
 parameterization 81
 thermohaline circulation energy budget 338–339
- thermohaline intrusions 346
- vertical advective–diffusive balance 340
see also Convection; Diffusive flux
- MMW (Madeira Mode Water) 376, 379
 seasonal variation 384
- MODE (Mid-Ocean Dynamics Experiment) 32, 38, 48, 49, 61, 125
- Mode waters 17, 373–386
 characteristics 374–376, 375
 stability 384
- core layers 375–376
 definition 374
 geographical distribution 376–384, 378
 identification 374–375, 375
 intermediate waters association 376
- North Atlantic Ocean 377–380
- North Pacific Ocean 380–381
- Southern Ocean 382–384
- subtropical Indian Ocean 382
- subtropical South Atlantic Ocean 381–382
- subtropical South Pacific Ocean 382
- temporal variability 384–386
 abrupt shifts 385–386
 decadal 385–386
 interannual 384–385

- Mode waters (*cont.*)
 temporal variability (*cont.*)
 seasonal 384
 WOCE observational phase 579–580, 581
- Models 59–60
 box inverse 527, 528
 climate prediction 79, 86, 93–95, 593, 595
 coupled *see* Coupled ocean–atmosphere models
 eddy-permitting 38, 61, 62, 72–73, 75, 80, 363–364, 551
 equilibrium versus non-equilibrium solutions 62–64
 General Circulation *see* GCMs
 grid size 62, 63, 70, 549
 historical development 60–62
 oceanic feedbacks incorporation 60–61
 integration time 63–64, 73, 77
 mesoscale ocean variability 61, 69–73
 northern overflows 412–416
 numerical *see* Numerical models
 ocean heat transport 467–468
 ocean state estimation 535–537
 sea level variability 65
 space–time scales 548–549, 549, 554
 streamtube 358, 359, 413, 414, 447
 sub-grid-scale parameterizations 550–551
 subduction 361–365, 362, 363, 364
 sudden climate change 27
 surface boundary conditions 317
 thermal expansion estimations 28
 thermohaline circulation 22–23, 73–76, 77
 wind-driven circulation 64–69, 77
 WOCE activities 59, 77, 95, 189, 525, 535
 z-coordinate 81, 90, 344
- Moderate-Resolution Imaging
 Spectroradiometer *see* MODIS
- Modified Atlantic Water *see* MAW
- MODIS (Moderate-Resolution Imaging Spectroradiometer) 180
- Molecular diffusion 338, 339
- Momentum transfer 589
 ACC (Antarctic Circumpolar Current) 280, 283–285
 atmosphere–ocean interactions 173
 coupled ocean–atmosphere models 82, 84
 interior ocean circulation 209
 numerical models 553
 parameterization 173–174
 sea ice effects 16
- Monsoons variability 6
 NPSTMW (North Pacific Sub Tropical Mode Water) 384–385
- Moored current meter arrays 49
 ACC (Antarctic Circumpolar Current) observations 277
- DBE (Deep Basin Experiment) 267
 deep circulation quantification 259, 260, 261, 261
- Atlantic Ocean 263, 264, 265
 Indian Ocean 265–266
 Pacific Ocean 261, 262
 deep convection studies 392
 DWBCs quantification 259, 260, 261, 471
 early studies 31, 32
 interior circulation studies 208–209
 Mediterranean Water outflow 423
 northern overflow studies 404–405, 404, 405, 407, 410, 411, 413
 transport interannual variability measurements 532
 velocity data sets 534
 WOCE Data System 188
- Mozambique Channel 306
- MSU (microwave sounding unit) 327
- Multiangle Imaging Spectroradiometer *see* MISR
- MultiMet 120
- Multiple equilibria 86
- NADW (North Atlantic Deep Water) 207, 227, 232, 262–264, 263, 265, 294, 461
 Atlantic Ocean northern overflows 410
 CFC tracer studies 435–438, 437
 circulation 22
 coupled ocean–atmosphere models 89
 DBE (Deep Basin Experiment) 267, 268, 269
 formation 304, 305, 310, 313, 314, 528, 529
 global overturning circulation 296–297, 298, 301
 heat transport 468
 interannual variability 532
 interocean exchange 305, 312, 313, 314
 lower (lNADW) 227, 230, 231
 Mediterranean water contribution 419
 middle (mNADW) 227
 mixing 212, 213
 thermohaline circulation models 73, 74, 75, 75
 transport by ACC (Antarctic Circumpolar Current) 305
 upper (uNADW) 227, 230, 231
- Namib Col Current 268
- NAO (North Atlantic Oscillation) 6, 7, 25, 335, 531, 559–561, 560, 572, 573, 580, 581
 anomalous amplitude during WOCE 559–560, 563, 567, 568, 580
 coupled ocean–atmosphere models 79, 87, 92
 Eighteen Degree Water variations 385–386
 long-term reconstructed values 560–561
- LSW (Labrador Sea Water)
 interannual variability 532
 spreading 391
 tracer studies 437–438
- North Atlantic gyre circulation response 569, 581
- NAS (North Atlantic Study) 431, 435
- NASTMW (North Atlantic Subtropical Mode Water; Eighteen Degree Water) 373, 374, 377–379, 567, 568, 581
 decadal variation 385
 interannual variation 385
 seasonal variation 384
- National Geophysical Data Center *see* NGDC
- National Oceanographic Sciences Accelerator Mass Spectrometry *see* NOSAMS
- NATRE (North Atlantic Tracer Release Experiment) 345, 346, 347, 348
- NBC (North Brazil Current) 227, 229, 230, 304
- NBUC (North Brazil UnderCurrent) 228, 229
- NEADW (North East Atlantic Deep Water) 390
- Near-bottom mixing 350–351
- Near-surface circulation 12
- NEC (North Equatorial Current) 250
 annual variation 159
- NECC (North Equatorial Countercurrent) 216, 219, 227, 245, 254
 annual variation 159
 tropical Indian Ocean 243
 tropical–subtropical water exchanges 249, 250, 252
- Neptune Effect 344
- Neutrally buoyant floats *see* Floats, subsurface
- New Guinea Coastal Current 217
- New Guinea Coastal Undercurrent 135, 225, 250, 252, 253
- New Ireland Coastal Undercurrent 250, 252
- NGDC (National Geophysical Data Center) 188
- NICC (North Intermediate CounterCurrent) 222, 223
- NIMBUS 177
- Nitrate 110
- Nordic Sea overflows *see* Northern overflows
- North Atlantic Current 527, 529, 569, 581
 eddy transport modelling 82
 Mediterranean Water 427
 WOCE float programme 134, 136
- North Atlantic Deep Water *see* NADW
- North Atlantic Ocean
 boundary currents 19, 20, 21
 CFC distribution 90
 circulation mapping from floats 527
 CO₂ storage estimates 492
 deep western boundary current 206–207
 diapycnal volume fluxes 318–319
 gyre circulation spin-up 567–569, 568, 581

- heat transport 24
 hydrographic data sets 533
 low salinity water transfer from North Pacific 23
 meridional overturning 304
 mode waters 377–380
 multiyear timescale atmospheric variability 25
 ocean basin models development 61, 62
 Rossby waves 153
 surface water mass transformation rates 332, 332, 333, 334
 thermal expansion rates 28
 thermohaline circulation 27, 73–75, 74, 75, 86, 88
 WHP one-time survey 102
 wind-driven circulation models 67, 68, 68
 winter subpolar mixed layer fluxes 321
 WOCE float programme 134–135, 135, 136, 137
 North Atlantic Oscillation *see* NAO
 North Atlantic Study *see* NAS
 North Atlantic Subtropical Mode Water *see* NASTMW
 North Atlantic Tracer Release Experiment *see* NATRE
 North Brazil Current *see* NBC
 North Brazil UnderCurrent *see* NBUC
 North East Atlantic Deep Water *see* NEADW
 North Equatorial Countercurrent *see* NECC
 North Equatorial Current *see* NEC
 North Indian Water 240
 North Intermediate CounterCurrent *see* NICC
 North Pacific Central Mode Water *see* NPCMW
 North Pacific Deep Water, tracer studies 445, 446
 North Pacific Eastern Subtropical Mode Water *see* NPESTMW
 North Pacific Equatorial Countercurrent 198
 North Pacific Intermediate Water *see* NPIW
 North Pacific Ocean atmospheric circulation during WOCE 561–562, 563
 decadal SST variation, thermocline response 365–367, 365, 366, 367, 368, 369, 369
 heat transport 24
 low salinity water transfer to North Atlantic 23
 mode waters 380–381
 multiyear timescale atmospheric variability 25
 tracer measurements 209
 wind-driven circulation models 67–68
 wind-forced sea-level variability 152, 152
 WOCE float programme 132
- North Pacific Subtropical Mode Water *see* NPSTMW
 Northern overflows 401–417, 568–569
 analytical models 412–414
 Denmark Strait 401, 402, 403, 405–406, 410–411, 532, 569, 573
 Iceland–Scotland overflow 402, 407–410, 408, 409
 mixing processes 411–412, 412
 moored array measurements 404–405, 404, 405, 407, 410, 411, 413
 numerical models 414–416
 paths 402–404, 404
 sources 401–402, 403
 transport means/variability 404–411, 405
 data re-analyses 405–406, 406
 statistics 407, 407
 variability 416
 WOCE studies 416–417
- Northern seas changes during WOCE 569–571, 581
 exchanges 529
- Northern Subsurface CounterCurrent *see* NSCC
 Norwegian Current 571
 Norwegian Sea 198 changes during WOCE 569 thermohaline fluxes 306
- Norwegian Sea Deep Water *see* NSDW
 NOSAMS (National Oceanographic Sciences Accelerator Mass Spectrometry) 433
 NPCMW (North Pacific Central Mode Water) 380, 386
 NPESTMW (North Pacific Eastern Subtropical Mode Water) 380–381 seasonal variation 384
- NPIW (North Pacific Intermediate Water) 18, 253, 381 large-scale freshening 576, 576, 577–580, 582
- NPSTMW (North Pacific Subtropical Mode Water) 373, 375, 380 decadal variation 386 monsoon-related interannual variation 384–385 seasonal variation 384
- NSCC (Northern Subsurface CounterCurrent) 222, 225 Pacific 245
- NSDW (Norwegian Sea Deep Water) 571
- Numerical models 547–556 adjustment to equilibrium 93 advection-diffusion models 247, 340 atmospheric forcing 553 box models 60 Bryan–Cox/MOM model 81 CLIMBER 94 Community Modelling Effort 61 coupled climate 79 coupled physical-biogeochemical studies 554
- DAMEE 555 diagnostic 79, 86 eddy-resolving 72–73, 363–364
- FRAM (Fine Resolution Antarctic Model) 210, 283, 288, 300 general circulation model 79, 80 *see also* GCMs governing equations 549–550 high-resolution 48, 49 history 60–62 horizontal resolution 63 integration period 63, 64 inverse 147–148 isopycnic 90 MIT model 535, 536 MOM (Modular Ocean Model) 555 NCAR CSM 90, 91 non-linearity 82, 84, 206, 211, 548 OCCAM (Ocean Circulation and Climate Advanced Modelling Project) 210, 467 ocean–atmosphere coupling 553–554 OPA model 81 OPYC model 81 organization of development 554–556 POCM (Parallel Ocean Climate Model) 65, 535 Princeton Ocean Biogeography Model 517, 517, 518 prognostic 79, 86 quasi-geostrophic 282–283 sigma coordinate 80 space–time scales 548–549, 549, 554 spinup 87 streamtube models sub-grid-scale parameterizations 550–551 vertical coordinate systems 552
- Nutrient measurements WHP data accuracy 110–111 standards 107
- WHP one-time survey 105
- Observation systems 4–5, 8–9, 48, 56 atmospheric 5 sea-levels 8 ship-based scalar measurements 47, 48 time series data 49 *see also* Global observation systems Ocean colour 195 Ocean, coupled ocean–atmosphere models 81–82 Ocean energy cascade 337 Ocean Observing System Development Panel *see* OOSDP Ocean state estimation (data assimilation) 535, 535–542, 544–545, 597–598, 598 climate prediction 593, 595 error estimates 540–541 observation system design 542 ongoing work 538–540, 539 representation errors 541 techniques 537–538
- Ocean tides 142, 143

- Oden* 572
 One-time WHP survey 102–103
 achievements 105, 121
 CFC tracer studies 437, 438
 CO₂ 101, 105, 495, 496
 data accuracy
 nutrient measurements 110–111
 oxygen measurements 110–111
 quality assurance 108
 salinity measurements 109–110
 exclusion of high latitudes 105
 hydrographic data sets 533
 measurement standards 103, 103, 104
 parameters measured 105
 sampling grid 102, 103, 105
 cross-overs as data consistency check 109, 110
 tracer studies 431, 448, 449
 Southern Ocean 446–447
 OOSDP (Ocean Observing System Development Panel) 35, 588
 Operational atmospheric analysis 14, 15
 Overflow
 bottom boundary layer 350
 entrainment 22, 23
 water 89–90
 see also Northern overflows;
 Sill overflows
 Overturning 21–22, 34, 81, 283
 Oxygen measurements
 seasonal distribution in tropical Indian Ocean 240, 241
 WHP
 data accuracy 110–111
 one-time survey 105
 standards 107
 Oyashio Current 68, 69
 Ozone
 Antarctic ozone hole 6
 atmospheric profile observations 5
- P-ALACE (Profiling Autonomous LAgrangian Circulation Explorer)
see Floats
- Pacific Decadal Oscillation *see* PDO
 Pacific North Equatorial Current 200
 Pacific Ocean
 atmospheric circulation during WOCE 561–562, 563
 box inverse models 528
 circulation mapping from floats 527
 deep helium field mapping 442–443, 442, 443
 DWBCs (Deep Western Boundary Currents) 260, 261–262, 262
 eastern boundary currents 21
 eddy energy distribution 201
 Ekman velocity estimation 119–120
 equatorial mean subthermocline zonal currents 222–226, 223
 Equatorial Intermediate Currents 225
 reversing jets 224–225
- Rossby wave beams 226
 subsurface countercurrents (Tsuchiya jets) 225–226
 excess CO₂ concentration distribution 510–511
 flows within equatorial thermocline 216–222, 217
 budget studies 219–220
 eddy diffusion 220–221
 Equatorial UnderCurrent dynamics 221
 temporal variability 221–222
 thermohaline phenomena 220
 upper ocean flow pathways 217–219, 218
 freshwater flux 330, 331, 335, 484, 485, 486
 ACC (Antarctic Circumpolar Current) 304
 halocline 304
 heat flux/transport 470, 471–472, 472
 direct estimates 462–464
 hydrographic sections 100
 interior circulation 209
 Intermediate Waters
 long-term changes 26
 tropical–subpolar exchange 252–254, 255
 interocean exchange 304, 305, 313
 tracer studies 449–450, 451
 see also Indonesian Seas; Indonesian Throughflow
 meridional overturning circulation 339
 Rossby waves 154–155
 seasonal/interannual variability studies 531
 solar radiation absorption 14
 SST (sea surface temperature) variation 322, 322, 323, 323
 STUW (Subtropical Underwater) subduction rates 435
 surface circulation
 Global Drifter Programme data 199
 tropical 194
 surface water mass transformation rates 332, 332, 333, 334
 surface/subsurface temperature monitoring 25
 thermal expansion rates 28
 tracer studies 433–435, 434, 435
 deep/bottom water circulation 444–446, 446
 mid-depth circulation 440–444, 442
 thermocline ventilation 433–435, 434, 435
 water mass transformation 432
 tropical–subpolar water exchanges 252–254, 255
 tropical–subtropical water exchanges 248, 248–252, 249
 interior pathway 251, 252
 particle subduction dynamics 251–252, 251
 tropical/subtropical recirculating cells 251
 western boundary pathway 251, 252
- velocity data sets 534
 water mass large-scale changes 576, 576–580, 577, 578, 579
 WHP one-time survey 102–103, 105, 109–110
 see also North Pacific Ocean; South Pacific Ocean
 Pacific–North American pattern *see* PNA pattern
 Palaeoclimate records 26
 coupled ocean–atmosphere model simulations 92–93
 Parameter estimation 173–174
 Parameterization 81, 83, 173–174, 550–551
 bottom boundary layer 344
 diapycnal mixing 340, 341, 343–344, 551
 eddy fluxes 285–286, 340, 341–342
 isopycnal mixing 551
 Partial pressure of dissolved CO₂
 see *p*CO₂
 Particle exchanges 15–16
*p*CO₂ (partial pressure of dissolved CO₂) 497, 499
 data quality 501
 PDO (Pacific Decadal Oscillation) 25, 530, 531, 561–562
 Permanent Service for Mean Sea Level *see* PMSL
 Peru Current 19, 377
 pH measurements 497, 499
 Phosphate, WHP data accuracy 110, 111
 Phytoplankton 16
 Pilot Ocean Monitoring Study *see* POMS
 PIlot Research Array in the Tropical Atlantic *see* PIRATA
 PIRATA (PIlot Research Array in the Tropical Atlantic) 227
 Planetary waves
 baroclinic 153
 barotropic 152–153
 see also Rossby waves
 Platinum resistance thermometers 107
 Plumes 391–393, 392, 398
 deep helium field mapping 443, 444
 northern outflow models 413, 414
 PNA (Pacific–North American) pattern 561
 POLYGON 61
 POLYGON-70 32
 POLYMODE 32, 38, 48, 61, 125
 Polynyas
 deep convection processes 21
 Weddell Sea 295
 POMS (Pilot Ocean Monitoring Study) 34, 35
 Potential vorticity field 528–529
 interior circulation 209–210
 Precipitation 17
 atmosphere–ocean interactions 15, 173
 condensation nuclei 15
 coupled ocean–atmosphere models 82, 83
 direct ocean estimates 480–481
 ice–ocean interactions 7

- indirect estimates 476, 480
 MSU (microwave sounding unit) data 327
 satellite data 179
 shipboard meteorological data collection 120
 SSS (sea surface salinity) 324
 surface fluxes estimation 327, 330
 Predictability 4–6, 17, 30, 55–56
 Profiling Autonomous LAgrangian Circulation Explorer *see* Floats, subsurface
 PSMSL (Permanent Service for Mean Sea Level) 27
- QBO (QuasiBiennial Oscillation) 6
 Quasi-geostrophic equations 61
 QuikSCAT 175, 176, 179–180
- Radiation
 budget 178
 heat transfer 14–15
 long wave 14, 178, 455
 satellite data 178–179
 sea ice reflection 16
 short wave 23, 86, 178, 455
 solar 14, 15, 16–17, 23, 83
 surface absorption 17
 Radiocarbon measurements *see* Carbon cycle
 RAFOS *see* Floats
 Random walk phenomena 54–55
 Rapid ocean-related changes 6–7, 51
 Recirculation
 east of the Bahamas 264
 Gulf Stream region 19, 151, 167, 205
 Kuroshio region 167–168
 Red Sea
 deep water exit flows 22
 SSS (sea surface salinity) 323
 Red Sea Water 243, 266, 312, 313
 Regional WOCE float programmes 135–137
 Relaxation 84
 Remote sensing 590
 GODAE (Global Ocean Data Assimilation Experiment) data 599
see also Satellite technology
 Repeat hydrography, WHP 102, 105–106
 achievements of programme 106, 121
 data quality assurance 108
 interannual/decadal variability studies 532, 557
 magnitude of survey 102, 103
 Representativeness 530, 557–558, 586–587
 Restratiification 396–398, 397, 398
 Reykjanes Ridge 404, 407
 Reynold numbers 164, 167, 168, 282
 Rigid lid approximation 83
- River runoff 17, 23, 29
 Atlantic Ocean carbon transport 515, 518
 coupled ocean–atmosphere models 82, 83
 freshwater flux direct estimates 483, 483
 Romanche Fracture Zone 266, 353
 Ross Sea 401, 446, 448
 Ross Sea Bottom Water *see* RSBW
 Rossby radius 59, 60, 80, 168, 169, 286
 Rossby waves 148, 149, 151, 153–155, 159, 167, 205, 256, 281
 extratropical 153–155, 154
 Pacific Ocean equatorial beams 226
 tropical 155
 Indian Ocean 236
 Roughness
 abyssal mixing 353
 momentum transfer 16
 space-based wind field measurements 56, 174, 175
 RSBW (Ross Sea Bottom Water) 447
- SA (Selective Availability) 113
 SACs (Special Analysis Centres) 40, 183
 Air-Sea Fluxes 188
 hydrographic data 187
 online access 535
 surface flux data sets 535
 SACW (South Atlantic Central Water) 438, 440
 SAF (Subantarctic Front) 271, 274, 382, 383
 SAFDE (Subantarctic Flux and Dynamics Experiment) 278
 Salinity 6, 7
 ACC (Antarctic Circumpolar Current) changes across Southern Atlantic 304
 Arctic Ocean surface layer 23
 atmosphere–ocean interactions 13
 measurements 123
 calibration issues 107, 109
 data accuracy 109–110
 Global Drifter Programme 195
 WHP one-time survey 105, 109–110
 WHP standards 107
 Mediterranean Water 421, 422
 interannual variability 425
 Pacific Intermediate Waters 252–253, 253, 254
 sea ice effects 16
 seasonal distribution in tropical Indian Ocean 240–241, 240
 surface ocean
 evaporation/precipitation difference 15
 latitude effects 15
 mixed layer stabilization 17
 variability
 decadal time scale 25–26
- deep convection-related 393–396, 394, 395
see also Freshwater flux/transport
 Salinometer analysis 107
 Salt crystal condensation nuclei 15
 Salt fingers 348
 Salt flux divergence 83
 Salt lenses *see* Meddies
 Samoan Passage 260, 261, 262, 266
 Sample measurements
 data quality assurance 108
 WHP (WOCE Hydrographic Programme) 100, 102–111
 data formats 109
 SAMW (Subantarctic Mode Water) 95, 253, 292–294, 294, 334, 373, 374, 377, 381, 382–383
 formation 528
 global overturning circulation 298
 large-scale warming 576–577, 576, 580, 582
 Sargasso Sea 567
 internal waves 352
 SST (sea surface temperature) 385
 Satellite technology 5, 8, 43, 56, 58
 air-sea fluxes 173–180
 altimetry *see* Altimetry
 data management 181
 WOCE Data system 188
 early applications 32, 35
 float programmes 138
 Global Positioning System *see* GPS
 heat flux 15, 327
 radiation data 327
 SST (sea surface temperature) 321
 surface drifter tracking 193, 194
 wind stress fields 14
 WOCE
 implementation 41
 strategies development 50
 SAVE (South Atlantic Ventilation Experiment) 101, 110, 431, 435, 437, 438, 444, 498, 512
 Scaling 337–338
 Scatterometers 174, 175–177, 176, 179–180
 WOCE Data system 188
 SCOR (Scientific Committee for Oceanic Research) 3
 WOCE planning 33, 34
 Sea ice
 air-sea exchange processes 16–17, 23
 coupled ocean–atmosphere models 82
 formation 16
 leads 15, 16
 melting 17, 330
 models 82
 polynyas 15
 snow cover 16
 thickness 27
 measurement systems 7
 multiyear sea ice 6–7
see also Ice sheets
 Sea surface density *see* SSD
 Sea surface height *see* SSH
 Sea surface salinity *see* SSS

- Sea surface temperature *see* SST
 Sea-level change 7, 8, 27–29
 climate change assessment 596
 contributing factors 28–29
 global mean-sea-level 160–162, 161
 over last 200 years 27–28
 thermal expansion 28
 SEASAT 142, 144, 162, 175
 Seasonal variations 4, 6, 17, 530
 carbon dioxide exchange 11–12
 Mediterranean outflow 424–425
 Mediterranean Sea evaporation 425
 mode waters 384
 Pacific Ocean 531
 sea surface height 158–159
 temperature cycles 11, 17
 subduction response 365–366, 365, 366
 thermocline 530
 mixing processes 320–321, 321
 tropical Indian Ocean
 oxygen distribution 240, 241
 salinity 240–241, 240
 SeaWinds 175, 176
 SEC (South Equatorial Current) 216, 219, 245
 equatorial Atlantic Ocean 227
 Global Drifter Programme data 200
 Pacific Ocean 222
 WOCE float programme 131–132, 135
 SECTIONS 33, 34
 SEIC (Southern Equatorial Intermediate Current) 222
 SEISAMW (Southeastern Indian Subantarctic Mode Water) 382, 383
 Selective Availability *see* SA
 Sensible heat flux 15, 173, 328
 parameterization 173–174
 satellite data 178–179
 SEQUAL 226
 SEVIRI (Spinning Enhanced Visible and Infrared Imager) 180
 Shadow zones 359, 366
 Shelf circulations 23, 29
 offshore forcing 29
 Shelf productivity 29–30
 Shetland–Faroe–Iceland–Greenland ridge system *see* Iceland–Scotland overflow
 Ship-drift measurements 99, 193, 198
 Global Drifter Programme data
 comparisons 200, 201
 tropical Indian Ocean zonal flows 236
 Ship-of-Opportunity Programme *see* SOOP
 Shipboard observations
 air-sea heat flux 15
 coulometric TCO₂ measurements 498–499
 CRMs (certified reference materials) 499
 shore-based analyses comparisons 499–501, 500
 cruise documentation summaries 108
 meteorology 120–121
 methods 100, 111–120
 wind stress fields 14
 WOCE planning 37, 38
 WOCE systems 58, 99–122, 526
 Short-wave radiation, satellite data 178
 SICC (South Intermediate CounterCurrent) 222
 Silicate, WHP data accuracy 110
 Sill overflows
 coupled ocean–atmosphere models 89, 94
 Nordic Seas *see* Northern overflows
 thermohaline circulation models 73, 74, 74
 Skylab 142
 Snow cover 16
 Snow melt 17
 SO (Southern Oscillation) 562, 573, 582
 SOFAR (Sound Fixing and Ranging) *see* Floats
 SOI (Southern Oscillation Index) 236, 531
 Solar cycles 6
 SOLO *see* Floats
 Somali Current 19, 233, 240, 241, 242, 243, 244, 246
 Somali Current System 239–242, 241, 245
 SOOP (Ship-of-Opportunity Programme) 590, 592
 South Atlantic Central Water *see* SACW
 South Atlantic Ocean
 boundary currents 19
 deep western boundary 206–207
 box inverse models 528
 hydrographic data sets 533
 subtropical mode waters 381–382
 thermal expansion rates 28
 WHP one-time survey 102
 wind-forced sea-level variability 151–152
 WOCE float programme 132–134, 132, 136
 South Atlantic Ventilation Experiment *see* SAVE
 South Equatorial Current *see* SEC
 South Equatorial Undercurrent 227
 South Intermediate CounterCurrent *see* SICC
 South Pacific Ocean
 hydrographic data sets 533
 subtropical mode waters 382
 WOCE float programme 131–132, 132, 135
 South Pacific Subtropical Mode Water *see* SPSTMW
 Southeastern Indian Subantarctic Mode Water *see* SEISAMW
 Southern Equatorial Intermediate Current *see* SEIC
 Southern Gyre 236, 242
 Southern Ocean
 atmospheric pressure measurements 195
 box inverse models 528
 circulation models 300
 CO₂ storage estimates 492
 deep convection 7
 deep water formation, tracer studies 446–448
 eddy fluxes 301
 flow dynamics 271–274, 300–301
 freshwater flux 330, 485
 global overturning circulation 296–300, 299
 interannual variability 92
 internal wave shears 352–353
 meridional overturning 303–304, 339
 mode waters 382–384
 ocean basin models development 61
 repeat hydrography 106
 shipboard meteorological data
 collection 121
 surface water mass transformation rates 332, 332, 333, 334
 wind stress 13
 wind-driven circulation models 71
 winter heat losses 17
 WOCE objectives 300, 301, 302
 WOCE planning 38
 Southern Oscillation *see* SO
 Southern Oscillation Index *see* SOI
 Southern Subsurface CounterCurrent *see* SSCC
 Special Analysis Centres *see* SACs
 Special Sensor Microwave/Imager *see* SSM/I
 Spinning Enhanced Visible and Infrared Imager *see* SEVIRI
 SPMW (Subpolar Mode Water) 373, 377, 379, 380
 SPOT 35
 SPS (Standard Positioning Service) 113
 SPSTMW (South Pacific Subtropical Mode Water) 382
 interannual variation 385
 seasonal variation 384
 SSCC (Southern Subsurface CounterCurrent) 222, 225, 245
 SSD (sea surface density), surface water mass 325, 325–326, 326
 transformation estimation 332
 SSH (sea surface height) 142, 471, 473
 altimetry 142–143, 148–163, 163
 annual cycle 158–159
 atmospheric forcing 65, 66, 70, 71, 71, 72, 148–149, 535
 data assimilation 539, 540, 540
 data management 40
 interannual variability 159–160
 tropical Indian Ocean 243
 Kelvin waves 155, 156
 Rossby waves 151, 153
 extratropical 153–155, 154
 tropical 155
 steric effect 149–151
 subsurface variability relation 155, 157–158
 tide gauge data 65, 66
 SSM/I (Special Sensor Microwave/Imager) 174, 177, 179

- SSS (sea surface salinity)
 data management 40
 WOCE Data system 188
surface water mass 323–325, 324
- SST (sea surface temperature) 21
 coupled ocean–atmosphere models 87, 92
 Global Drifter Programme data 194, 195
interocean exchange of anomalies 305
North Pacific Ocean 561, 562
numerical modelling 553, 554
seasonal variations, subduction
 response 365–366, 365, 366
shipboard measurements 120
solar radiation absorption/reflection 14
surface water mass 321–323, 322, 323, 327
- SVP drifter design 195, 204
tropical
 anomalies 25
 atmospheric convection 215
 Indian Ocean 239, 242, 245
 ocean circulation 215, 216, 245
 Pacific Ocean 222
upper ocean thermal field data sets 533–534
 WOCE Data system 188
- Stability 93–94
- Standard Positioning Service *see* SPS
- Steric height, interior circulation studies 206–207, 207
- Stirring 337
 mesoscale eddies 337–338
- STMW (Subtropical Mode Water) 373, 376
 Indian Ocean 382
 South Atlantic Ocean 381
 South Pacific Ocean 382
- Stochastic theory of climate 54
- Strait of Gibraltar 419, 422
 Atlantic–Mediterranean Water exchange
 measurements 423–424, 423, 424
 seasonal cycle 424–425
- Mediterranean Water outflow 422–427
- Strait of Sicily 420
- Streamtube models
 AABW (Antarctic Bottom Water)
 formation 447
 northern outflows 413, 414
 thermocline mass flux 358, 359
- STUW (Subtropical Underwater) 377, 435
- Subantarctic Flux and Dynamics Experiment *see* SAFDE
- Subantarctic Front *see* SAF
- Subantarctic Intermediate Water 357
 see also AAIW
- Subantarctic Mode Water *see* SAMW
- Subduction 18, 256, 357–371, 529
 continuous models 361–362, 362
 eastward bias 360, 366
Ekman pumping 360, 361, 361, 362, 369–370, 373, 374
kinematic model 563–565, 564
- freshening processes 565
pure heave 565
warmed surface water 564–565
- lateral induction 360–361, 374
- mode waters 376, 383, 384
- numerical models 362–365, 363, 364
- Pacific Ocean STUW tracer studies 435
- rate 360
- surface layer dynamics 360–361
- surface water mass transformation 319, 320
- Sverdrup transport 358, 360
- T/S (temperature/salinity) relationship 357, 358
- tracer studies 364–365
- ventilated thermocline model 359, 359
- Subduction layers 247
 temperature anomalies 256
- Subpolar Mode Water *see* SPMW
- Subsurface fields, sea-level variability
 relation 155, 157–158
- Subtropical cell 251
- Subtropical Countercurrent 170
- Subtropical Mode Water *see* STMW
- Subtropical Underwater *see* STUW
- Surface boundary layer 81
- Surface circulation 14
 eddy energy distribution 200–201, 200
 global mean velocity/velocity variance 198–201
- instrumental methodology 195, 195–198, 196
- ship drift measurements 99
- TOGA observing system 4
- wind-driven 17–21
- see also* Upper ocean structure/currents
- Surface flux 84
 data sets 534–535
 errors 84
- Surface meteorology, data management 40, 188
- Surface mixed layer 17
 numerical models 551
- Surface Velocity Programme drifters
 see Global Drifter Programme
- Surface water mass 317–336
 diapycnal circulation 318
 diapycnal volume fluxes 318–319
 density budgets 319–320, 319
- formation 332–335
- seasonal thermocline/mixed layer mixing 320–321, 321
- SSD (sea surface density) 325–326, 325, 326
- SSS (sea surface salinity) 323–325, 324
- SST (sea surface temperature) 321–323, 322, 323
- surface fluxes
 bulk formulae 326–328
 density 331
 freshwater 326–327, 330–331, 331
 heat 326–330, 330
- transformation 332–335
 interannual variability 335
 ocean basin rates 332–334, 332, 333
- theoretical aspects 318–321
- Sverdrup transport 18, 152, 206, 209, 211, 358, 360
- ACC (Antarctic Circumpolar Current)
 dynamics 273, 280–282, 301
- model simulations 68, 69
- topographic effects 210
- tropical Indian Ocean 237, 243
- SVP (Surface Velocity Programme)
 drifters *see* Global Drifter Programme
- Swallow floats 31, 124–125, 124, 137, 260
- SYNOP (Synoptic Ocean Prediction) study 71
- TAGI (Tropical Atlantic Gradient Index) 531
- Tahiti–Darwin pressure *see* SOI (Southern Oscillation Index)
- TAO (Tropical Atmosphere Ocean)
 mooring array 25, 215, 588, 590
 tropical Pacific Ocean 222
- TAS (Tropical Atlantic Study) 431, 435
- Tasman Sea 305, 306
- TCO₂ (total dissolved inorganic carbon)
 equilibrium concentration variation with temperature 519, 519
- measurement 497
 certified reference materials 499
 coulometry 498–499
 data quality 501
- meridional carbon transport calculation 514, 515
- preformed-CO₂ methods 503–504, 506
- time series comparison methods 511–513
- Temperature 123
 atmosphere–ocean interactions 13
 data accuracy 109
 decadal time scale changes 25–26
 deep convection-related variability 393–396, 393, 394, 395
- deep ocean 21
- global observation systems 100, 101
- surface *see* SST (sea surface temperature)
- thermal equator 5
- upper ocean thermal field data sets 533–534
- WHP measurement standards 107
- WHP one-time survey 105
- Temporal–Residual–Mean circulation *see* TRM circulation
- Thermal expansion 7, 8, 150, 161–162, 596
 sea-level change 28
- Thermal wind equation 143–144
- Thermocline 247, 254–255, 259
 Atlantic Ocean 256
 continuous models 361–362, 362
 diffusive models 247

- Thermocline (*cont.*)
 equatorial 18
 horizontal advection 247
 Indian Ocean 255–256
 main 18, 164, 340
 seasonal variability 530
 subduction process *see* Subduction theory 18
 transient response to decadal variability 365–370, 365, 366, 367, 368
 tropical–subpolar exchange of Intermediate Water 252–254
 tropical–subtropical water exchanges 248, 248–252, 249
 Equatorial Undercurrent source water 249
 upper 251
 ventilation 362, 364–365, 564
 Pacific Ocean tracer studies 433–435, 434, 435
- Thermohaline circulation 21–23, 24, 227, 302, 337, 563
 AAIW (Antarctic Intermediate Water) 438
 Agulhas Retroflection transport 310
 anthropogenic climate change 7
 Atlantic Ocean tracer studies 435–438, 437
 Bering Strait transport 306–307
 coupled ocean–atmosphere models 88–90, 89, 92
 future stability 93–94, 94
 deep-ocean monitoring 9
 deep/intermediate water mass formation 21
 diapycnal mixing 338–339
 flows over sills 22, 23
 high-resolution modelling 73–76, 77
 Indonesian Throughflow 309–310
 interocean exchange 304–307, 310
 large scale cells 305
 marginal seas 419
 Mediterranean outflow contribution 429
 models 86
 NADW (North Atlantic Deep Water) export 305
 Nordic Sea overflows 89, 90, 94
 numerical modelling 553, 554
 Southern Ocean 296–300, 299
 sudden climate change models 27
 tropical Pacific Ocean 220
 water mass transformation 317
see also GCMs (General Circulation Models)
- Thermohaline intrusions 346
- Thermostad 249, 252, 253
- Tidal current estimation 118
- Tide gauge data
 altimetry comparisons 142, 142, 161
 sea-level change measurements 28, 65, 66, 535
 WOCE Data System 188
- Time scales
 climate change 12, 50, 53, 54
 random walk phenomena 54
- climate prediction 595
 DBE (Deep Basin Experiment) 268, 270
 models 63
 coupled ocean–atmosphere 79
 high-resolution 63–64, 73, 77
 ocean change 49, 51
 rapid 6–7, 51
 WHP data 105
 Time series measurements 102, 532
 model performance evaluation 64
 stochastic variability 54–55, 55, 56
- Time-evolving ocean circulation
 modelling 539, 539
- TIROS 196, 204
- TIROS-N 32
- TOGA (Tropical Ocean–Global Atmosphere) study 3–4, 9, 35, 79, 91, 150, 215, 221, 222, 531, 534, 588, 591, 595
- COARE (Coupled Ocean–Atmosphere Response Experiment) 219
- global ocean surface circulation data 194
 meteorological data collection 120
 Pacific Ocean surface circulation computation 199
 surface drifter observations 14
- Tomographic integrals 58
- Tonga–Kermadec trench 444
- Tongue-like distributions 99
 Mediterranean outflow 419
 tracers 48, 52
- TOPEX/POSEIDON 5, 8, 28, 51, 65, 105, 142, 143, 198, 470, 471, 526, 538, 539, 542, 574, 590
- altimetry
 heat flux determinations 150
 sea-level variability resolution 148, 149
- development 35, 37
- launch 41
- ocean topography estimates 144, 145, 146, 147
- WOCE Data system 188
- Topographic steering, ACC (Antarctic Circumpolar Current) 290–291, 292
- Topographic waves *see* Rossby waves
- Total alkalinity measurements 497, 498, 499
- CRMs (certified reference materials) 499, 501, 502
 data quality 501, 502
- Total dissolved inorganic carbon
see TCO₂
- Total ocean circulation 589
- Tracer studies 4, 431–452, 470, 471, 473, 495, 526, 589, 591–592
- AABW (Antarctic Bottom Water) formation rate 296
- AAIW (Antarctic Intermediate Water) renewal in Atlantic Ocean 438–440, 439, 440, 441
- Atlantic Ocean deep thermohaline circulation 427, 435–438
- Brazil Basin 352
 CO₂ uptake estimates 492
 coupled ocean–atmosphere models 90
 DBE (Deep Basin Experiment) 267
 glacial meltwater addition around Antarctica 448, 448–449, 449
 interior circulation 209
 diapycnal mixing 347, 347, 348
 mesoscale/microscale lateral dispersion 345
- Pacific Ocean 433–435, 434, 435
 deep/bottom water circulation 444–446, 446
 Indian Ocean exchange 449–450, 451
 mid-depth circulation 440–444, 442
 thermocline ventilation 433–435, 434, 435
- tropical–subtropical thermocline water exchanges 249–250, 250
- principles 432–433
- Southern Ocean deep water formation 446–448
- subduction 364–365
- techniques 432–433
- WHP (WOCE Hydrographic Programme) 101
 one-time survey 104, 105
- Transient Tracers in the Ocean *see* TTO
- Transit navigation system 32
- Tritium (³H) tracer studies 432
 Indonesian Archipelago interocean exchange 449
- Pacific Ocean
 thermocline ventilation 433–435, 434, 435
 tropical–subtropical thermocline water exchange 249–250, 250
- TRM (Temporal–Residual–Mean) circulation 338, 340–345, 343
- TRMM 179, 180
- Tropical Atlantic Gradient Index *see* TAGI
- Tropical Atlantic Study *see* TAS
- Tropical Atmosphere Ocean mooring array *see* TAO mooring array
- Tropical cell 219, 251
- Tropical Instability Waves 201, 215, 221–222
- Tropical ocean circulation 215–246
 equatorial Atlantic 226–233
 flow patterns 215–216
 Indian Ocean 233–245
 Pacific Ocean 216–226
- water mass transformation patterns 215–216
- Tropical Ocean–Global Atmosphere study *see* TOGA study
- T-S (temperature/salinity) relation 336, 357, 358, 394
- Tsuchiya Jets 222, 225–226, 245
- TTO (Transient Tracers in the Ocean) 101, 431, 435, 437, 444, 497
- TAS 438
- Turbulent framework of ocean circulation 48, 51, 51, 56

- Turbulent mixing 337, 338
 abyssal currents 353
 bottom boundary layer 350
 mesoscale eddies 340, 341
 ocean currents 349–351
 thermohaline intrusions 346
 zonal jets 349
- UCDW (Upper Circumpolar Deep Water) 293, 294, 298
 Upper Circumpolar Deep Water *see* UCDW
- Upper ocean structure/currents 4, 5
 ADCPs 111
 WHP (WOCE Hydrographic Programme) 100
see also Surface circulation
- Upper ocean thermal fields 533–534
 WOCE Data System 187–188
- Upwelling 155
 equatorial 225, 247, 256
- Variability 529–532, 557–558, 596
 WOCE goals 37
- Velocity data sets 534
- Vema Channel 267, 269, 269, 353
- Ventilated thermocline model 359, 359
- Ventilation 206, 526, 563, 564
 deep convection 390, 391
 main thermocline 359
 mode waters formation 373–374
 shadow zone 225, 359, 366
 subduction 367–368
 tracer studies 432
 Pacific Ocean 433–435, 434, 435
- Vertical advection 340
- Vertical Current Meter floats 137
- Volcanic eruptions 6
- Voluntary Observing Ships *see* VOS
- Vortical mode motions 338
 tracers dispersion 345
- Vorticity 22
 equation 281–282
 potential vorticity definition 375
 potential vorticity flux 286–287
- VOS (Voluntary Observing Ships) 590, 592
 IMET automated meteorological data collection 121
 TOGA observing system 4
- Wacongne–Pacanowski cell 238, 239
- Warm water pathway/warm route *see* Meridional overturning circulation
- Water isotope tracer studies 432
 glacial meltwater addition around Antarctica 448, 448–449, 449
- Water mass formation
 coupled ocean–atmosphere models 90–91
- diapycnal volume fluxes 318–319, 319
 marginal seas 419
- Water mass transformation
 ocean surface 317–336
 tracer studies 431–452
 tropical ocean circulation 215–216
- Water samples, WHP one-time survey standards 103, 104
- Water vapour 14, 80, 82, 162
 coupled ocean–atmosphere models 80, 82, 93
 WOCE Data system 188
- Waves
 baroclinic 80, 148, 153
 barotropic 148, 151, 152–153
 equatorial 91, 148
 internal 348, 349, 350
 Rossby 148, 149, 151, 153, 154–155, 281
 tidal 205
 wave guide 29, 91
- WCRP (World Climate Research Programme) 3–4, 189
 global tracking system planning 193
 goals 3, 9
 planning 34, 36
- Weddell Sea 401, 446, 447, 448
 deep convection 21, 529
 Mediterranean Water 427
- Weddell Sea Bottom Water *see* WSBW
- Weddell Sea Deep Water *see* WSDW
- West Antarctic Ice Sheet 8
- West Spitsbergen Current 572
- Western boundary currents 18–19, 24, 206–207
 deep convection 390–391
 deep ocean circulation 211
- Deep Western Boundary Currents *see* DWBCs
- Global Drifter Programme data 197–198
 heat transport estimates 471, 472
 mode waters 373, 376
 moored arrays 471
 seasonal deep mixed layers 17
 SST (sea surface temperature) 322
 tropical Indian Ocean 239–242
 tropical–subtropical water exchanges 250
 wind-driven modelling studies 67, 68
see also named currents
- Western Mediterranean Deep Water *see* WMDM
- WGASF (Working Group on Air–Sea Fluxes) 535
- WHP (WOCE Hydrographic Programme) 8, 100–122
 aims 100
 climatologies 533
 coordinating centre (WHP Office) 106, 107
 cruise documentation summaries
 production 108
 data
 formats 109
- Products Committee 42
 quality assurance 107–108, 109
 reporting 108–109
 WOCE Data System 186–187
 deep helium field mapping 442–443, 442, 443
 float deployment 130
 JGOFS/WOCE global CO₂ survey 495, 496
- measurements
 methods 100
 standards 103, 106–111
- meteorological data collection 120
- one-time survey *see* One-time WHP survey
- participation base 101, 101
- planning 102–105
 heat flux lines 104–105
- Planning Office 38
- repeat hydrography 102, 103, 105–106, 108, 121, 557
- scale of survey 101–102, 103
- station spacing 104
- time-series stations 102
- tracer studies 431
- Wind
 air–sea momentum transfer 13–14
 COADS data 368, 456
 curl of wind stress 17–18, 206
 fields 152
 Global Drifter Programme 195
 lower troposphere 5
 satellite data 174–177
 scatterometers 174, 175–177, 176
 shipboard data collection 120
 surface flux data sets 534–535
- Wind stress 13–14, 13, 17
 atmosphere–ocean interactions 173
 satellite data 174–177
 curl 17–18, 153, 206
 numerical models 553
 sea ice momentum transfer 16
 sea-level variability 148, 151–153
 shelf circulation 29
 surface circulation 17
 thermocline response to decadal variability 366
 tropical Indian Ocean 233, 234
 tropical Pacific Ocean 222
 wind-driven circulation models 64, 65, 67
- Wind-driven circulation 17–21
 high-resolution modelling 64–69, 77
 interior circulation 209
- Wind-driven currents *see* Ekman transport
- Winter mixed layers 17, 21
- Wintertime convection 27
- WMDM (Western Mediterranean Deep Water) 422, 425
- WMO (World Meteorological Organization) 32, 33, 194
- WOCE (World Ocean Circulation Experiment) 3–4, 8, 12, 31–43, 48–51, 173
- achievements 43

- WOCE (*cont.*)
- AIMS (Analysis Interpretation Modelling Synthesis) phase 8, 9, 42, 42, 108, 109, 186, 525, 526, 556
 - boundary currents measurements 19, 20, 21
 - CO₂ global survey 489–520
 - Core Project 1 (Global Description) 38, 100
 - Core Project 2 (The Southern Ocean) 38
 - Core Project 3 (Gyre Dynamics) 38, 43, 49
 - data collection/assembly 526
 - data format issues 109
 - data quality 37, 39, 40–41, 106, 108
 - data-based analyses 542–544
 - atlases/climatologies 532–535
 - data management *see* WOCE data system
 - data sets *see* WOCE data sets
 - large-scale circulation/water mass descriptions 526–529
 - metadata 186
 - online data sources 526
 - process studies 529
 - quality assurance *see* Data quality assurance
 - variability studies 529–532
 - data-sharing policy 39–41, 185
 - deep circulation quantification 259–260
 - float programme 123–139
 - flow variability scale studies 49, 51
 - global data system 181–190
 - global-scale activities 49, 50
 - goals 7, 37, 79, 105, 106, 190, 525, 586, 589
 - heat flux/transport observations 15, 456
 - hydrographic sections 99–102
 - see also* WHP (WOCE Hydrographic Programme)
 - implementation 41–42
 - Implementation Plan 3, 4, 36, 37, 39, 99
 - IWP (Intergovernmental Panel) 39
 - modelling activities 59, 77, 95, 189, 535
 - NEG (Numerical Experimentation Group) 37–38, 42
 - observations 4–5, 58, 589–592
 - direct measurements 590–592
 - general strategy 589–590
- meteorology 120–121
- remote sensing 590
 - shipboard 99–122
- ocean circulation as non-equilibrium system 48, 51
- planning
- CCCO initiatives 33–36
 - Design Options Study Group 35–36
 - SCOR initiative 33, 34
 - SSG (Scientific Steering Group) initiatives 36–41
 - regional programmes 49
 - Scientific Plan 3, 36, 99
 - SMWG (Synthesis and Modelling Working Group) 42
 - standards/protocols 99
 - Surface Velocity Programme 128
 - synthesis phase 525–545
 - ocean state estimation 535–542, 544–545
 - temporal variability studies 105
 - tracer studies 433, 450, 451
- WOCE Data Products Committee 183–185
- WOCE Data Resource 185–186, 186, 189
- WOCE data sets 95, 533–535
- atmospheric circulation 558, 558–563
 - Global Data Set 189–190
 - hydrographic data 533
 - mean state of ocean 596
 - observational system design 542–544
 - online access 534, 535
 - representativeness 530, 557–558, 586–587
 - scale of variability 580–582
 - surface fluxes 534–535
 - tracer studies 90–91, 432, 444–446
 - upper ocean thermal fields 533–534
 - velocities 534
- WOCE Data System 181–190, 184
- adaptations 185
 - ADCPs (Acoustic Doppler Current Profilers) 188
 - bathymetry 188
 - data archive 189
 - data streams 186
 - DIU (Data Information Unit) 186
 - DPC (Data Products Committee) 183–185
 - floats 188
 - hydrographic programme 186–187
 - in-situ* sea-level data 188
 - international distribution of functional units 186, 187
- Internet uses 185
- metadata 186
 - moored current meter arrays 188
 - primary functions 183
 - satellite measurements 188
 - surface drifter data 187
 - surface meteorology/air-sea flux 188
 - surface salinity 188
 - upper ocean thermal data 187–188
- WOCE Global Data Set 189–190
- WOCE Hydrographic Programme
- see* WHP
- Working Group on Air–Sea Fluxes
- see* WGASF
- World Climate Research Programme
- see* WCRP
- World Data Centre 39
- World Meteorological Organization
- see* WMO
- World Ocean Circulation Experiment
- see* WOCE
- WSBW (Weddell Sea Bottom Water) 295, 334, 447
- WSDW (Weddell Sea Deep Water) 265, 266, 295, 296
- Wyrtki Jets 233, 236, 237, 242
- Wyville–Thomson ridge 401
- XBTs (Expendable Bathythermographs) 4, 50, 150, 215, 526, 588, 590, 591
- ACC (Antarctic Circumpolar Current) observations 277
- altimeter sea level data relation 157
 - data assimilation 539
 - data management 40, 181
 - high-density lines 102, 102
 - interannual variability measurements 532
 - models evaluation 64
 - ocean variability studies 530, 531
 - tropical Pacific Ocean 222
 - upper ocean thermal field data sets 533, 534
- WOCE Data System 187–188
- z*-coordinate models 81, 90, 344
- Zonal equatorial currents 18
- Zonal jets 349

International Geophysics Series

EDITED BY

RENATA DMOWSKA

*Division of Engineering and Applied Science
Harvard University
Cambridge, MA 02138*

JAMES R. HOLTON

*Department of Atmospheric Sciences
University of Washington
Seattle, Washington*

H. THOMAS ROSSBY

*University of Rhode Island
Kingston, Rhode Island*

- Volume 1* BENO GUTENBERG. Physics of the Earth's Interior. 1959*
- Volume 2* JOSEPH W. CHAMBERLAIN. Physics of the Aurora and Airglow. 1961*
- Volume 3* S. K. RUNCORN (ed.) Continental Drift. 1962*
- Volume 4* C. E. JUNGE. Air Chemistry and Radioactivity. 1963*
- Volume 5* ROBERT G. FLEAGLE AND JOOST A. BUSINGER. An Introduction to Atmospheric Physics. 1963*
- Volume 6* L. DUFOUR AND R. DEFAY. Thermodynamics of Clouds. 1963*
- Volume 7* H. U. ROLL. Physics of the Marine Atmosphere. 1965*
- Volume 8* RICHARD A. CRAIG. The Upper Atmosphere: Meteorology and Physics. 1965*
- Volume 9* WILLIS L. WEBB. Structure of the Stratosphere and Mesosphere. 1966*
- Volume 10* MICHELE CAPUTO. The Gravity Field of the Earth from Classical and Modern Methods. 1967*
- Volume 11* S. MATSUSHITA AND WALLACE H. CAMPBELL (eds.) Physics of Geomagnetic Phenomena. (In two volumes.) 1967*
- Volume 12* K. YA KONDRATYEV. Radiation in the Atmosphere. 1969*
- Volume 13* E. PALMÁN AND C. W. NEWTON. Atmospheric Circulation Systems: Their Structure and Physical Interpretation. 1969*
- Volume 14* HENRY RISHBETH AND OWEN K. GARRIOTT. Introduction to Ionospheric Physics. 1969*
- Volume 15* C. S. RAMAGE. Monsoon Meteorology. 1971*
- Volume 16* JAMES R. HOLTON. An Introduction to Dynamic Meteorology. 1972*
- Volume 17* K. C. YEH AND C. H. LIU. Theory of Ionospheric Waves. 1972*
- Volume 18* M. I. BUDYKO. Climate and Life. 1974*
- Volume 19* MELVIN E. STERN. Ocean Circulation Physics. 1975
- Volume 20* J. A. JACOBS. The Earth's Core. 1975*
- Volume 21* DAVID H. MILLER. Water at the Surface of the Earth: An Introduction to Ecosystem Hydrodynamics. 1977
- Volume 22* JOSEPH W. CHAMBERLAIN. Theory of Planetary Atmospheres: An Introduction to Their Physics and Chemistry. 1978*

* Out of Print

- Volume 23* JAMES R. HOLTON. An Introduction to Dynamic Meteorology, Second Edition. 1979*
- Volume 24* ARNETT S. DENNIS. Weather Modification by Cloud Seeding. 1980
- Volume 25* ROBERT G. FLEAGLE AND JOOST A. BUSINGER. An Introduction to Atmospheric Physics, Second Edition. 1980
- Volume 26* KUG-NAN LIOU. An Introduction to Atmospheric Radiation. 1980
- Volume 27* DAVID H. MILLER. Energy at the Surface of the Earth: An Introduction to the Energetics of Ecosystems. 1981.
- Volume 28* HELMUT G. LANDSBERG. The Urban Climate. 1981
- Volume 29* M. I. BUDYKO. The Earth's Climate: Past and Future. 1982*
- Volume 30* ADRIAN E. GILL. Atmosphere-Ocean Dynamics. 1982
- Volume 31* PAOLO LANZANO. Deformations of an Elastic Earth. 1982*
- Volume 32* RONALD T. MERRILL AND MICHAEL W. MCELHINNY. The Earth's Magnetic Field. Its History, Origin, and Planetary Perspective. 1983
- Volume 33* JOHN S. LEWIS AND RONALD G. PRINN. Planets and Their Atmospheres: Origin and Evolution. 1983
- Volume 34* ROLF MEISSNER. The Continental Crust: A Geophysical Approach. 1986
- Volume 35* M. U. SAGITOV, B. BODKI, V. S. NAZARENKO, AND KH. G. TADZHIDINOV. Lunar Gravimetry. 1986
- Volume 36* JOSEPH W. CHAMBERLAIN AND DONALD M. HUNTER. Theory of Planetary Atmospheres: An Introduction to Their Physics and Chemistry, Second Edition. 1987
- Volume 37* J. A. JACOBS. The Earth's Core, Second Edition. 1987
- Volume 38* J. R. APEL. Principles of Ocean Physics. 1987
- Volume 39* MARTIN A. UMAN. The Lightning Discharge. 1987
- Volume 40* DAVID G. ANDREWS, JAMES R. HOLTON AND CONWAY B. LEOVY. Middle Atmosphere Dynamics. 1987
- Volume 41* PETER WARNECK. Chemistry of the Natural Atmosphere. 1988
- Volume 42* S. PAL ARYA. Introduction to Micrometeorology. 1988
- Volume 43* MICHAEL C. KELLEY. The Earth's Ionosphere. 1989
- Volume 44* WILLIAM R. COTTON AND RICHARD A. ANTHES. Storm and Cloud Dynamics. 1989
- Volume 45* WILLIAM MENKE. Geophysical Data Analysis: Discrete Inverse Theory, Revised Edition. 1989
- Volume 46* S. GEORGE PHILANDER. El Niño, La Niña, and the Southern Oscillation. 1990
- Volume 47* ROBERT A. BROWN. Fluid Mechanics of the Atmosphere. 1991
- Volume 48* JAMES R. HOLTON. An Introduction to Dynamic Meteorology, Third Edition. 1992
- Volume 49* ALEXANDER A. KAUFMAN. Geophysical Field Theory and Method.
Part A: Gravitational, Electric, and Magnetic Fields. 1992
Part B: Electromagnetic Fields I. 1994
Part C: Electromagnetic Fields II. 1994
- Volume 50* SAMUEL S. BUTCHER, GORDON H. ORIANS, ROBERT J. CHARLSON, AND GORDON V. WOLFE. Global Biogeochemical Cycles. 1992
- Volume 51* BRIAN EVANS AND TENG-FONG WONG. Fault Mechanics and Transport Properties of Rocks. 1992
- Volume 52* ROBERT E. HUFFMAN. Atmospheric Ultraviolet Remote Sensing. 1992
- Volume 53* ROBERT A. HOUZE JR. Cloud Dynamics. 1993
- Volume 54* PETER V. HOBBS. Aerosol-Cloud-Climate Interactions. 1993
- Volume 55* S. J. GIBOWICZ AND A. KIKO. An Introduction to Mining Seismology. 1993
- Volume 56* DENNIS L. HARTMANN. Global Physical Climatology. 1994
- Volume 57* MICHAEL P. RYAN. Magmatic Systems. 1994
- Volume 58* THORNE LAY AND TERRY C. WALLACE. Modern Global Seismology. 1995
- Volume 59* DANIEL S. WILKS. Statistical Methods in the Atmospheric Sciences. 1995
- Volume 60* FREDERIK NEBEKER. Calculating the Weather. 1995
- Volume 61* MURRAY L. SALBY. Fundamentals of Atmospheric Physics. 1996

* Out of Print

- Volume 62* JAMES P. MCCALPIN. Paleoseismology. 1996
- Volume 63* RONALD T. MERRILL, MICHAEL W. McELHINNY, AND PHILLIP L. MCFADDEN. The Magnetic Field of the Earth: Paleomagnetism, the Core, and the Deep Mantle. 1996
- Volume 64* NEIL D. OPDYKE AND JAMES E. T. CHANNELL. Magnetic Stratigraphy. 1996
- Volume 65* JUDITH A. CURRY AND PETER J. WEBSTER. Thermodynamics of Atmospheres and Oceans. 1998
- Volume 66* LAKSHMI H. KANCHA AND CAROL ANNE CLAYSON. Numerical Models of Oceans and Oceanic Processes. 2000
- Volume 67* LAKSHMI H. KANCHA AND CAROL ANNE CLAYSON. Small Scale Processes in Geophysical Fluid Flows. 2000
- Volume 68* RAYMOND S. BRADLEY. Paleoclimatology, Second Edition. 1999
- Volume 69* LEE-LUENG FU AND ANNY CAZANAVE. Satellite Altimetry. 2000
- Volume 70* DAVID A. RANDALL. General Circulation Model Development. 2000
- Volume 71* PETER WARNECK. Chemistry of the Natural Atmosphere, Second Edition. 2000
- Volume 72* MICHAEL C. JACOBSON, ROBERT J. CHARLSON, HENNING RODHE AND GORDON H. ORIANS. Earth System Science: From Biogeochemical Cycles to Global Change. 2000
- Volume 73* MICHAEL W. McELHINNY AND PHILLIP L. MCFADDEN. Paleomagnetism: Continents and Oceans. 2000
- Volume 74* ANDREW E. DESSLER. The Chemistry and Physics of Stratospheric Ozone. 2000
- Volume 75* BRUCE DOUGLAS, MICHAEL KEARNEY AND STEPHEN LEATHERMAN. Sea Level Rise: History and Consequences. 2000
- Volume 76* ROMAN TEISSEYRE AND EUGENIUSZ MAJEWSKI. Earthquake Thermodynamics and Phase Transformations in the Earth's Interior. 2001

This Page Intentionally Left Blank